Alkali-Hybrid Spin-Exchange Optically-Pumped Polarized ^{3}He Targets Used for Studying Neutron Structure

Jaideep Singh
San Diego, CA

B.S. Physics, California Institute of Technology, 2000

A Dissertation presented to the Graduate Faculty
of the University of Virginia in Candidacy for the Degree of
Doctor of Philosophy

Department of Physics

University of Virginia
December, 2010

Advisor	Gordon D. Cates, Jr.
Member 1	Donald G. Crabb
Member 2	Kent D. Paschke
Outside Member	G. Wilson Miller IV

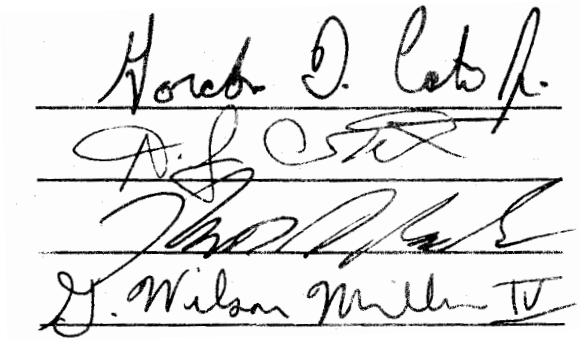

Alkali-Hybrid Spin-Exchange Optically-Pumped Polarized ^{3}He Targets Used For Studying Neutron Structure

Jaideep Singh
San Diego, CA

B.S. Physics, California Institute of Technology, 2000

A Dissertation presented to the Graduate Faculty
of the University of Virginia in Candidacy for the Degree of
Doctor of Philosophy

Department of Physics

University of Virginia
December, 2010

Abstract

This thesis describes the first application of alkali-hybrid spin-exchange optical pumping (SEOP) to polarized ^{3}He targets used in electron scattering experiments. Over the last decade, polarized ^{3}He targets have been used at the Thomas Jefferson National Accelerator Facility (JLab) to measure the structure of the neutron via its spin degrees of freedom. In this thesis, two experiments, E97110 & E02013, receive special attention. The first, E97110, measured the absolute inclusive cross section differences for a longitudinally polarized electron beam scattering from a traditional SEOP ^{3}He target polarized both parallel & perpendicular to the beam. These cross section differences were used to extract the ^{3}He spin structure functions $g_1(x, Q^2)$ & $g_2(x, Q^2)$ over a Bjorken-x range of $0.01 < x < 0.50$ for $Q^2 = 0.04, 0.06, 0.08, 0.10, 0.12, \& \ 0.24$ GeV^2. Integrals of g_1 & g_2 over x were used to extract I_A^n (the generalized Gerasimov-Drell-Hearn integral) and Γ_1^n (the first moment of g_1) for the neutron. Preliminary results for these quantities are used to test the predictions of Baryon Chiral Perturbation Theory.

The second, E02013, measured the asymmetry for a longitudinally polarized electron beam scattering from an alkali-hybrid SEOP ^{3}He target polarized perpendicular to the q-vector. The electric form factor of the neutron, G_E^n, was extracted from this asymmetry for $Q^2 = 1.7, 2.5, \& \ 3.4$ GeV^2. Near final results for G_E^n are

compared to predictions from a variety of nucleon models.

Alkali-hybrid SEOP using rubidium & potassium ([K]/[Rb] $\approx 5 \pm 2$), coupled with narrowband (laser linewidth is roughly equal to Rb absorption linewidth) laser diode arrays, have resulted in a consistent & reliable in-beam ^{3}He polarization increase from 37% to 65%. We describe how to implement these improvements and why they are effective. Furthermore, we summarize what we've learned over the past decade about the ^{3}He polarization limits of SEOP. Finally, we present a detailed analysis of ^{3}He polarimetry based on nuclear magnetic resonance (NMR) and electron paramagnetic resonance frequency shifts (EPR), with a special emphasis on corrections due to magnetic field gradients and polarization gradients within the target cell.

Contents

List of Figures

List of Tables

Acknowledgments

First and foremost, I owe my deepest gratitude to my advisor Gordon Cates. Ten years ago, he took a chance on me and, ever since, he has offered me a seemingly endless supply of support and encouragement. Gordon's infectious enthusiasm would make any goal seem attainable and his patience & guidance would get me there. There is simply no way I could have completed graduate school without his help. Thank you!

It has been a great pleasure to work with Al Tobias and Vladimir Nelyubin. We have spent a *long* time in the lab trying to make *many* things work - and a few things did work out in the end! I am deeply appreciative of the brutal determination, attention to detail, and humor that Al and Vladimir bring to any task. Thank you for your friendship and always willing to lend a helping hand - I've needed it!

I am very lucky to have been part of the UVa Physics Family. I am glad that Scott Rohrbaugh stuck around long enough for us to become the best of friends. I appreciate everything you do for me. Ryan Snyder has taught me a great deal about politics and forced me to think about the world outside the lab, which I've come to understand is a good thing. Karen Mooney has provided me with opportunities to get crushed in fantasy football, baked goods, a chance to teach one day of a lab course, an occasional hug, good humor, lots of good advice I prob-

ably should have taken, and so much more. I want to thank James Wang and Peter Dolph for allowing me to talk to/at them for hours on end in the office. My understanding (and I hope theirs as well!) of all aspects of the work we've done has become much deeper because of our conversations. Through our shared experiences, several aspects of the graduate school journey were made considerably more tolerable by Nadia Fomin, Josh Pierce, Paul Tanner, James Maxwell. I am very appreciative of the help (in all its different forms) I received during the Princeton-to-Charlottesville move from Brian Humensky, Ioannis Kominis, Dan Walter, Warren Griffith, and Brian Patton.

This thesis would not have been possible, let alone been relevant, without the considerable contributions our of JLab collaborators-of which there are too many to name. First and foremost, I want to express my gratitude to Todd Averett and his target group at William & Mary. I have benefited a great deal from our close collaboration and their generosity on all aspects of the target work. I want to thank Kees de Jager for supporting my graduate work while I was stationed at JLab. I want to thank J.P. Chen, Bogdan Wojtsekhowski, Franco Garibaldi, Nilanga Liyanage, Wolfgang Korsch, and Zein-Eddine Meziani (among many others) for both challenging us to provide better targets and the opportunity to use them. It has been a privilege to work with Mike Souza and Willie Shoup. None of the experiments described in this thesis could have been done without their technical glassblowing skills and their willingness to find a way make it work. I want to thank J.P. Chen, Alexandre Deur, Xiaochao Zheng, and Kevin Kramer for teaching me about the Hall A target when I first got to JLab. It has been an honor for me to have toiled away in the dungeons of Hall A with Patricia Solvignon, Vince Sulkosky, Aidan Kelleher, and Tim Holmstrom. Getting an experiment on the floor is a very

stressful exercise - and - I appreciate their willingness to put up with me and my smell. Anything I know about electron scattering, I've learned from Karl Slifer and Alexandre Deur. They have always been very generous with their time and patiently explained to me every aspect of the experiments.

After I finished college, I was unclear about what to do next. Steven Frautschi saw potential in me that I didn't see myself and strongly encouraged me to stick with science. Emlyn Hughes provided me with the guidance to do so. If they had not intervened, I would not have made it to this point. For this, I owe them a debt of gratitude. I want to thank Tammie and Dawn for helping me get to UVa and finding magical ways to keep me enrolled there. I want to thank Aidan Kelleher, Peter Dolph, Chiranjib Dutta, Seamus Riordan, and Vince Sulkosky for providing me with various plots, diagrams, and tables. I want to thank Don Crabb, Kent Paschke, Wilson Miller for agreeing to be on my defense committee and managing to find the time to slog through this thing. I want to thank Al, Dawn, & Karen for all of their help in submitting the final thesis packet. As I struggled mightily to finish my graduate school career, the Argonne MEP Group, in particular Zheng-Tian Lu and Roy Holt, displayed a remarkable amount of patience and offered only words of encouragement. I will always be grateful for that.

It is a great pleasure to thank all my friends who first don't seem to mind the unreturned phone calls and then readily accept my urgent pleas for food and shelter. Along those lines, I want to sincerely thank Karl & Patricia, Sean & Colleen, Ryan, Emma, Rachel & Dan, Will & Teresa, and Nadia & Josh. I will always cherish the welcome distractions provided by the House of Riffraff, The Walker Brothers, Erin & Matt, Anna & the ever-changing Miller's crew, and the rest of you - you know who you are. Outside of Charlottesville, I want to thank Alan, Matt & Heidi,

Ishy, Kevin, Nick, Shep, Jon, Walter & Emma, Matt & Sam, and Peter & Jannah for the many late night phone conversations and occasional visits. I want to thank the extended Rohrbaugh/Roy/Rooney Family, in particular Cindy and Nikki, for pulling for me, especially towards the end of my graduate career. I want to express my sincere gratitude to the Rosenwinkel Family, in particular Lester and Paula, for essentially adopting me for Thanksgiving, all federal holidays, and pretty much every other day of the year. If I have forgotten to mention you, then (1) not that it is an excuse - but - you know me and (2) I'm sorry.

I have learned a great deal of what life can be like outside of the lab thanks to Jess, Miku, and the Wisler & Domjan Families. These are lessons that I will never forget. Finally, I want to thank my parents and brother: Surjit, Harmesh, and Rajdeep. This has taken an unreasonably long time and you've unflinchingly stuck with me and supported me (in every way) the whole way. Words simply cannot express the love and appreciation I have for you - so I'll show you.

Chapter 1

Historical Introduction

1.1 Overview

Over the last 25 years, laser polarized noble gases have found applications in, just to name a few, polarized targets for electron scattering experiments [1], magnetic resonance imaging [2], tests of fundamental symmetries [3], and neutron scattering experiments [4]. During the past decade, significant progress has been made towards understanding & improving the dynamics of spin exchange optical pumping (SEOP) of noble gases. For polarizing ^{3}He, the two most important advances have been alkali-hybrid SEOP [5, 6] and the use of high power, spectrally-narrow diode lasers [7]. The application of these two technologies together to polarized ^{3}He targets has resulted in a dramatic increase in the typical ^{3}He polarizations (in-beam) from 37% to 65%.

The upper plot in Fig. (1.1) shows the number of days of beamtime required to perform a typical electron scattering experiment (see caption for details). Each band represents the range of ^{3}He polarizations that was acheived during electron

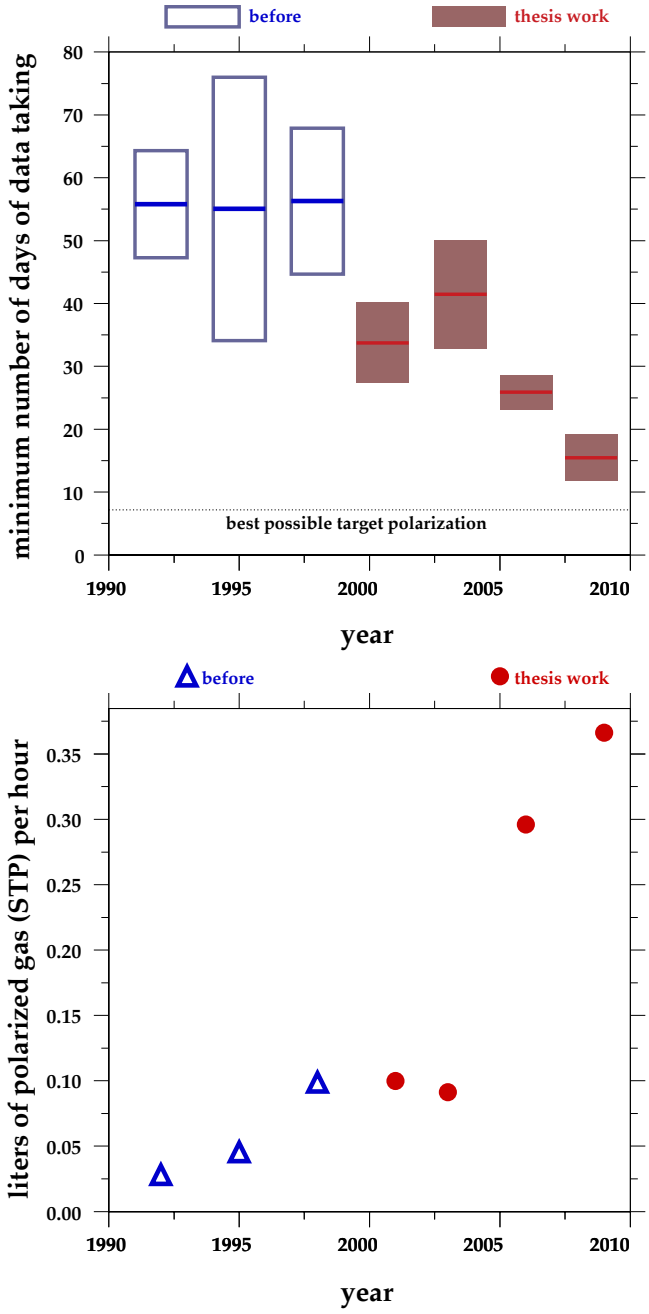

Figure 1.1: Improvement in SEOP Polarized ^{3}He Targets. The upper plot shows the number of days of data taking necessary to achieve a statistical precision of 10% on an asymmetry of 0.02 with a count rate of 0.5 Hz. These are typical numbers for a measurement of the neutron electric form factor G_E^n at high resolution ($\sqrt{Q^2}$). The lower plot shows the the number of polarized nuclei divided by the polarization time scale. This quantity is given by the product of the ^{3}He density, target cell volume, ^{3}He polarization, and polarization (i.e. spinup) rate.

scattering experiments at the time. The most obvious improvement is the factor of 3 increase in the average performance of the target cells. We are now within a factor of 2 of what is currently understood to be the highest possible performance for SEOP ^{3}He , based only on the limits of the ^{3}He polarization. The improvements described in this dissertation are critical for the polarized ^{3}He program at Thomas Jefferson National Accelerator Facility (JLab) after the 12 GeV upgrade. Because the scattering rates drop significantly at higher resolution ($\sqrt{Q^2}$, four-momentum transfer), one must compensate with increased luminosity. Higher polarizations and shorter polarization time constants are two key components to achieving this goal.

The second improvement is the substantial reduction in the variation in the performance of the target cells. These new technologies essentially guarantee consistent and reproducible high performance. Given the time & expense required to prepare a target cell for use in an electron scattering experiment and the recent scarcity of ^{3}He gas [8], one could argue that this advance is nearly as important as the improvement in performance. These advances also have a substantial impact on hyperpolarized magnetic resonance imaging (MRI). A crude metric to gauge the performance in this context is the amount of polarized gas produced per unit time, see lower plot in Fig. (1.1). Alkali-hybrid SEOP coupled with spectrally-narrow (narrowband) diode lasers can now produce twice as much polarized ^{3}He gas in half the time with half the laser power. This is roughly an order of magnitude improvement over traditional SEOP with spectrally-broad (broadband) diode lasers.

This dissertation is divided into two parts. In the first part, I'll present a description of polarized electron scattering, Chp. (2), and briefly summarize my contributions to the JLab Hall A Polarized ^{3}He Program, Chp. (3), with a particular

emphasis on ^{3}He polarimetry, Chp. (4). Two experiments in particular will receive special attention. The first is E97110: "the GDH Sum Rule, the Spin Structure of ^{3}He and the Neutron using Nearly Real Photons." Measurements of the neutron spin structure functions were made over a Q^2 range of 0.04 to 0.25 GeV^2 in the Summer of 2003. Moments of these spin structure functions can be related to the generalized Gerasimov-Drell-Hearn integral and spin polarizabilities. Baryon Chiral Perturbation Theory allows one to calculate the values and slopes of these quantities at and near $Q^2 = 0$. The interplay between theory & experiment will provide a better understanding of the effective hadronic degrees of freedom that are necessary to understand the long-distance scale structure of the neutron. Preliminary results for the spin structure function moment Γ_1^n and the generalized GDH integral I_A^n will be presented.

The second experiment is E02013: "Measurement of the Neutron Electric Form Factor G_n^E at High Q^2." Measurements of double polarization asymmetries for quasielastic kinematics were made over a Q^2 range of 1.7 to 3.4 GeV^2 in the Spring of 2006. The scattered neutron was detected in coincidence with the scattered electron to minimize backgrounds. This was the first experiment to feature alkali-hybrid SEOP polarized ^{3}He targets in electron scattering, which yielded ^{3}He polarizations consistently near or above 50% in-beam for the first time. Elastic form factors are related to electric charge and magnetic current density distributions. These are among the most fundamental properties of nucleons and their measurements, G_E^n in particular [9], were part of the original scientific motivation behind JLab. Final results for the G_E^n will be presented.

In the second part of this dissertation, I will discuss the spin exchange optical pumping of polarized ^{3}He targets with a special emphasis on the factors that ulti-

mately limit the ^{3}He polarization. In Chp. (5), I will describe optical pumping and how it is modified by alkali-hybrid mixtures. I have attempted to relax as many assumptions as possible in rederiving the relevant equations in order to identify potential sources of imperfections and estimate their size. Even small imperfections in optical pumping can dramatically reduce the photon economy (i.e. increase the laser intensity required to achieve unity alkali polarization). In Chp. (6), I will describe the polarization dynamics in target cells with two chambers. These calculations provide a framework for determining (1) the equilibrium ^{3}He polarizations in both chambers and (2) the proper interpretation of experimentally determined time constants associated with the polarization & diffusion processes.

In Chp. (7), I will present a brief summary of the parasitic experimental tests that we have performed over the last decade on the target cells constructed for use in JLab experiments. These tests have confirmed several features that are expected based on (1) numerical simulations of the optical pumping process and (2) experimental observations made by other groups in cells with different geometries & ^{3}He densities. This agreement gives us confidence that we are starting to truly understand (1) the limits of the ^{3}He polarization in these targets and (2) how to reliably extrapolate to more demanding experimental conditions. Finally, the appendices include, among other things, a catalog of reference data relevant to the optical pumping of alkali atoms & SEOP of ^{3}He and detailed derivations of several results used for extracting the alkali & ^{3}He polarizations & densities.

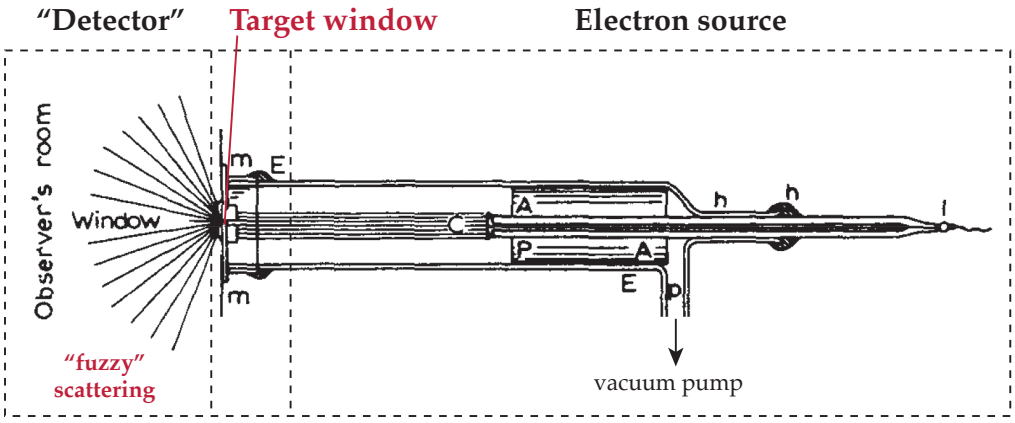

Figure 1.2: Lénárd's Cathode Ray Experiment. Electrons are accelerated from the cathode (C) towards a thin target window (which is sealed at points m & m). The electrons are scattered at small angles which is indicative of a "fuzzy" atomic charge distribution. [10]

1.2 Pictures of the Nucleon from Electron Scattering

The structure of an object can be functionally defined by its response to a probe. This response is used to infer the object's parts and the rules that determine how they behave and interact with each other. These parts and rules together form the degrees of freedom that describe the object in a manner that can be very different at various size scales. By varying the probe resolution, different size scales within the object can be studied. From this perspective, the goals of science are to enumerate the degrees of freedom at each size scale and then find the relationship, *if any*, that exists between these different scales.

1.2.1 Point Particle

The size scale relevant to nucleons covers the approximate range from 0.1 fm to 1 fm (1 fm $= 10^{-15}$ m). An extremely well-suited probe is electron scattering, which,

in its modern form, has been used to explore nucleon structure since the pioneering measurements of Hofstadter in the 1950's. However, the basic conceptual arguments regarding the need and utility of electron scattering can be traced at least as far back as Philipp E. A. von Lénárd's Nobel Lecture [10] titled "On cathode rays" delivered on May 28, 1906 (my emphasis in **bold**, his in *italics*):

> What are these fine constituents of atoms? That in all atoms they are the same, only present in varying numbers, we have already concluded from the law of proportionality between mass and absorption. We can now learn further details. **We can use the quanta of the cathode rays as small test particles which we allow to traverse the interior of the atoms and thus provide us with information thereon.** . . . As far as we know, cathode rays experience such a deflection owing only to electrical and magnetic forces. To assume magnetic forces within the atoms would imply the assumption of mobile electricity in the atoms, thus again electrical forces. We must therefore regard the diffusion of cathode rays in matter as proof for *the existence of electrical forces in the interior of the atoms.* **The magnitude of these forces can be estimated by considering the extent of the deflection** . . .

Lénárd studied the small angle deflections ($\theta_{\max} \approx 20^\circ$) of electrons through very thin sheets of various materials. He mostly used discharge tubes which provided an electron energy of about 30 keV, which can be converted into a size scale using:

$$\big(\text{energy scale}\big) \times (\text{size scale}) = \hbar c \approx 200\,\text{MeV} \cdot \text{fm} \tag{1.1}$$

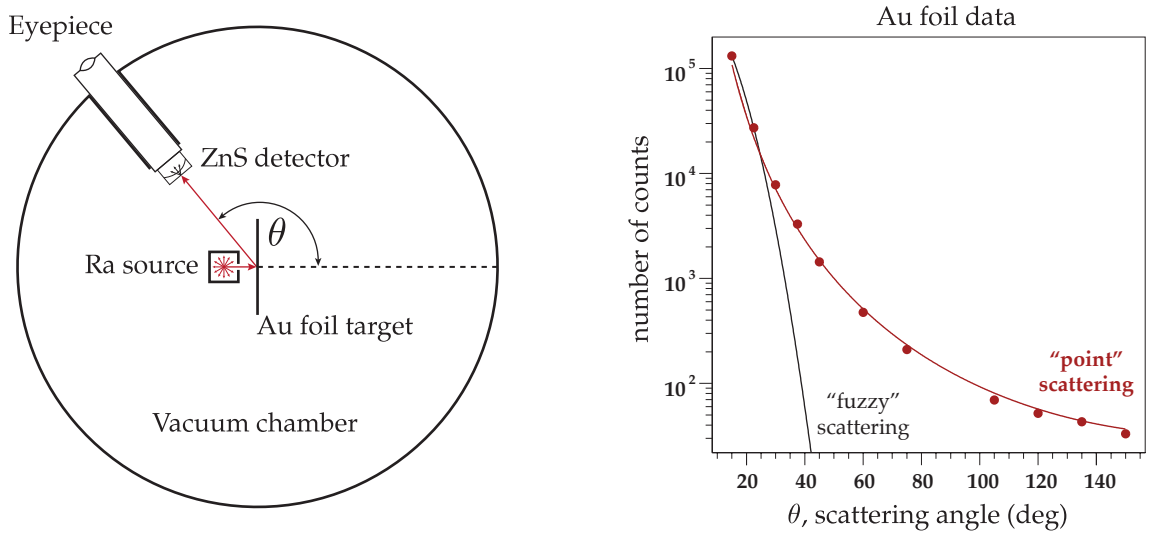

Figure 1.3: Geiger-Marsden Gold Foil Experiment. (Left) Schematic of experimental apparatus. (Right) Data on gold foil [11].

where $\hbar$ is the Planck constant divided by 2π, c is the speed of light, and the energy scale for small angular deflections is estimated by:

$$\left(\text{energy scale}\right) \approx E\theta \tag{1.2}$$

where E is the energy of the particle and θ is the deflection angle in radians. These formulas explicitly stipulate that higher energy and/or larger angles are required for higher resolution. Since Lénárd's apparatus, Fig. (1.2), could only probe size scales as small as 20000 fm, he understandably concluded that "The probable proper volume of the positive electricity, provided it too were not extremely small, should be regarded as completely penetrable for negative quanta." He did, however, anticipate Rutherford by noting that "the fastest rays are also capable of supplying the answer to the question whether perhaps these centres have a special, impenetrable proper volume." [10]

The true classical archetype for the scattering technique is Geiger and Marsden's famous gold foil experiment, Fig. (1.3). They originally observed (1909) that about 1 in 8000 α particles (^{4}He nuclei) fired at a 60 μm thick gold foil were reflected back at angles greater than 90° [12]. This inspired Rutherford (1911) to derive the Coulombic scattering formula that still bears his name [13]. Geiger and Marsden set out to confirm (1912) Rutherford's celebrated formula. Their *source* was a collimated beam of 6.0 & 7.7 MeV α particles from the decay of radium-226 and its daughter nuclei. Their *targets* were silver and gold with air equivalent thicknesses of 0.1 cm to 0.45 cm. Their *detector* was a zinc sulfide screen which produced visible scintillations when struck by a scattered α particle. They themselves were the *data acquisition system*: they simply counted the number of scintillations (100,000 total!) at 14 different scattering angles between 5° and 150°. Geiger and Marsden confirmed every aspect of the formula and provided strong evidence for a small dense positive core at the center of atoms [11]. Because the size scale that they probed was between 10 and 400 fm, they could not resolve any further nuclear structure beyond a simple point particle, see Fig. (1.4).

In scattering experiments, elastic scattering refers to the case when the probe and target particles remain in their ground state. For inelastic electron scattering, the target particle is excited out of its ground state or smashed apart creating new particles. The first inelastic electron scattering experiments were performed by J. Franck and G. Hertz [14]. A beam of electrons accelerated up to 100 eV were sent through a vapor of mercury atoms, see Fig. (1.5). The number of undeflected electrons (current) was measured as a function of accelerating voltage. Franck and Hertz found that at certain sharp & discrete steps, characteristic to mercury atoms, all of the electrons were deflected. Their results clearly showed the excitation of

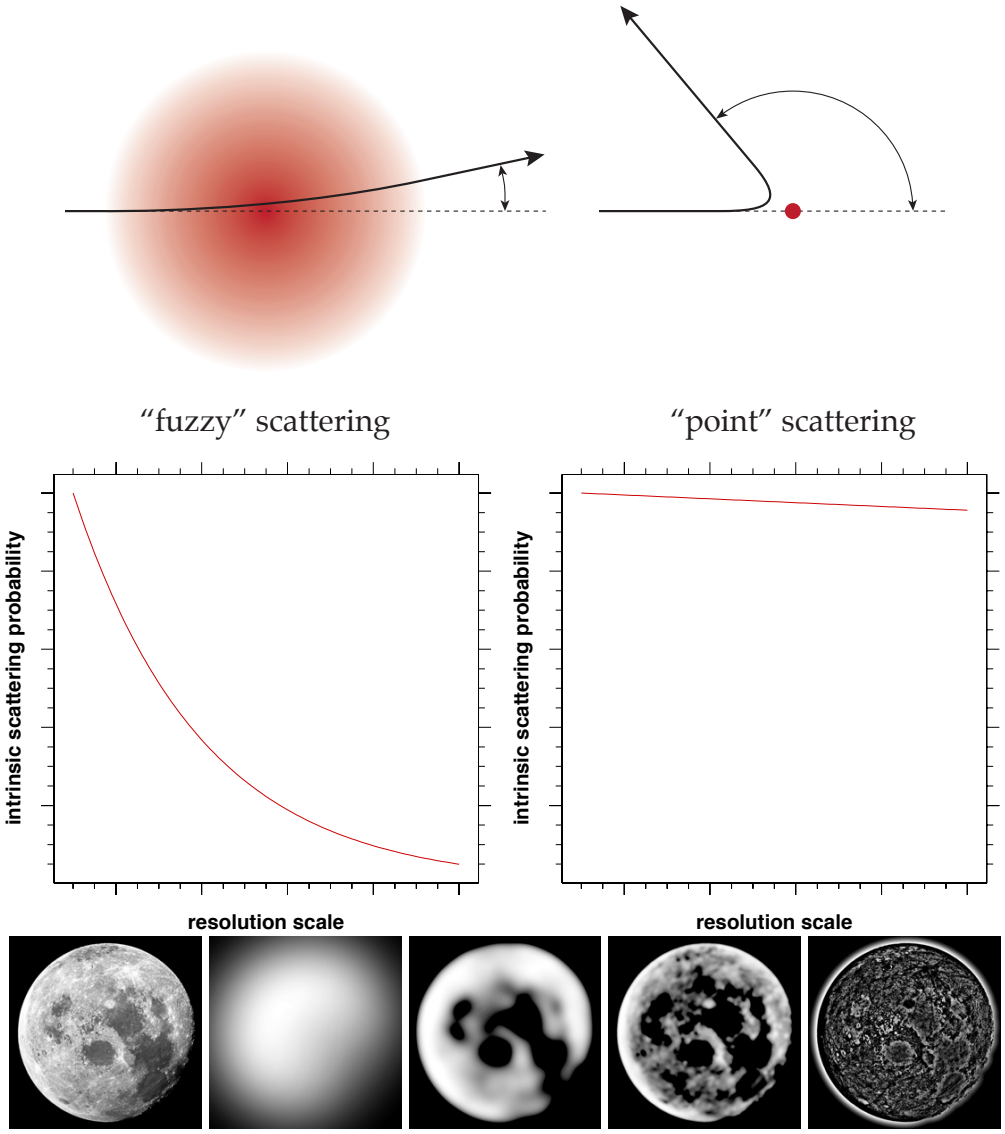

Figure 1.4: "Fuzzy" scattering vs. "Point" scattering. In the top left figure, the size of the nucleus is not resolved. This results in a small angle scattering from an apparent "fuzzy" atomic charge distribution as observed by Lénárd. In the top right figure, the nucleus is sufficiently resolved to result in large angle back scattering as observed by Geiger & Marsden. The two central plots depict the intrinsic scattering probability as a function of resolution scale for both "fuzzy" and "point" targets. The bottom pictures of the Moon are an attempt to demonstrate what we mean by "resolution scale." The far left picture is the Moon in its entirety. Each succeeding picture depicts the Moon at a different resolution scale starting at the lowest and ending at the highest.

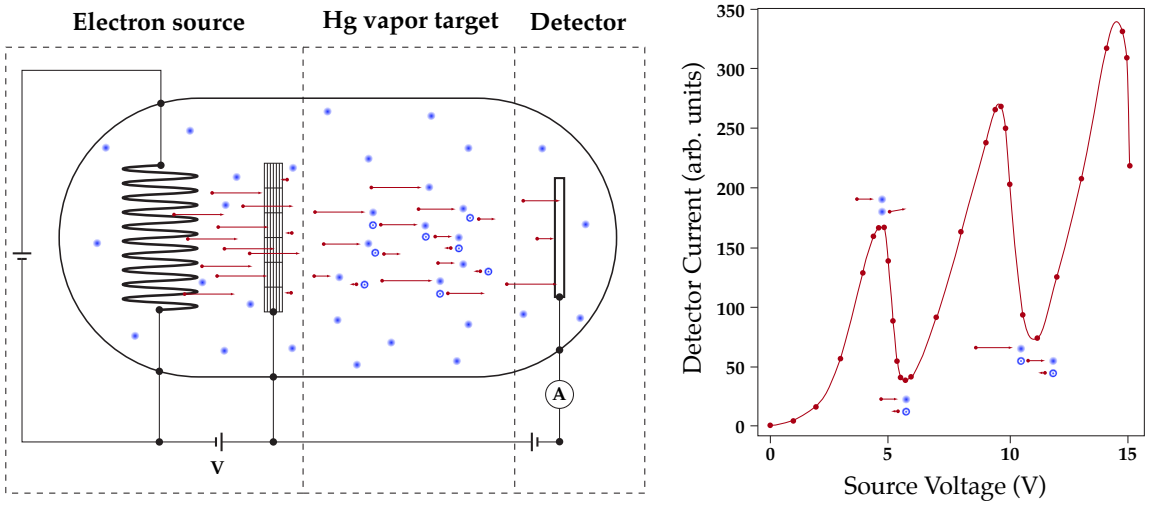

Figure 1.5: Franck-Hertz Experiment. The left figure is a schematic of the experiment. The right figure depicts the drops in the anode current when the accelerating voltage equals an integer multiple of the strong Hg intercombination line at 254 nm (4.9 eV). [14]

an atom's constituents, namely orbital electrons. They did not realize it at the time but they had provided a "most direct confirmation for the general interpretation of spectra" based on Bohr's quantum theory [15, 16]. Although they only probed mercury atoms at a size scale of 1 million fm (atomic scales), their experiment demonstrated the general principle that one could measure the collective excitation spectrum of a particle's constituents via inelastic scattering.

1.2.2 Protons, Neutrons, and a Cloud of Virtual Pions

Elastic scattering experiments of alpha rays from nuclei continued over the next two decades. Convinced by his experiments of alpha scattering from nitrogen in 1919, Rutherford declared that nuclei contained protons [17]. By his Bakerian lecture to the Royal Society in 1920, he was prepared to posit "the possible existence of an atom of mass 1 which has zero nucleus charge." [18] In 1932 his former student

James Chadwick conclusively identified neutrons ejected from beryllium by alpha scattering [19]. At sufficiently low resolution, the structure of the alpha particles themselves can be ignored and they can be thought of as heavy spinless electrons. However, at even moderate resolutions, the scattering process becomes sensitive to both the structure of the alpha particle and the strong interactions between the alpha and the target nucleus. These effects had already started to manifest themselves with Rutherford's experiments with light nuclei [20].

Electrons (and leptons in general) are a much cleaner probe in this regard. Their degrees of freedom are very well understood in the form of Quantum Electrodynamics (QED). In addition, their effect on the target can be treated perturbatively in powers of $\alpha \approx 1/137$. Neville Mott generalized Rutherford's formula to account for spin in scattering between two ideal point-like spin-1/2 particles [21]. These particles are also sometimes called Dirac particles because their relativistic behavior can be described by the Dirac equation. Deviations from the Mott formula were immediately observed [22] in the first proton-proton scattering experiments in the early 1930's. However, this was not conclusive evidence that protons were not Dirac particles, since these deviations were legitimately attributable to the strong interactions between nucleons.

The earliest and more compelling evidence that nucleons are not purely Dirac particles were measurements of proton and deuteron magnetic moments by Otto Stern. The ratio of a Dirac particle's magnetic moment to its spin is simply its charge to mass ratio. Stern found a value 2.5 times larger than what was expected for the proton [23]. Using his now famous molecular beam techniques, I. I. Rabi confirmed the result for the proton [24]. Both Stern and Rabi (separately) measured the deuteron magnetic moment and inferred a significantly non-zero and negative

value for the neutron [25, 26]. At Rabi's urging, this was directly confirmed by J.R. Dunning's group at Columbia in the mid-1930's [27]. The first precision measurement of the neutron magnetic moment was published in 1940 by Alvarez and Bloch [28].

For electrons, the anomalous magnetic moment is quite small and is directly attributable to the effects of a cloud of virtual photons & other particles that surrounds the bare electron. One had to wait for Yukawa's Meson Theory to use this picture to explain the anomalous magnetic moment of nucleons. Yukawa imagined an exchange of a new type of particle to mediate strong interactions between nucleons. He furthermore argued that these particles, unlike photons, must be massive in order to explain the apparent short range of the strong interaction. To complete the analogy, the anomalous magnetic moment of nucleons is the effect of a surrounding cloud of virtual pions & nucleons, Fig. (1.6). The substantial size of this anomalous magnetic moment is a direct consequence of the strength of interactions among nucleons and pions. W. Pauli showed that an anomalous magnetic moment can be accommodated by the Dirac equation without violating special relativity (Lorentz invariance) or conservation of charge (gauge invariance) [29]. Thus one could have reasonably argued that an anomalous magnetic moment by itself did not constitute proof that nucleons are not point particles. An anomalous magnetic moment, therefore, does not address the question of whether nucleons have any spatial extent.

At sufficiently high resolution, the non-point like structure of the nucleus should make itself apparent. M.E. Rose was among the first to address this point for nuclei [30]:

> It is pointed out that the finite size of the nucleus will give rise to large

> deviations from Mott scattering when the change in wave-length of the electrons is of order of the nuclear dimensions. This deviation from Mott scattering at large scattering angles therefore provides a possibility for determination of the shape of the charge distribution and size of nuclei.

M.N. Rosenbluth extended this argument to nucleons and explicitly stated that high energy elastic electron scattering "should yield data on the nature of the meson cloud of the proton." [31] These deviations are encoded in quantities called form factors. For a purely electromagnetic process involving a spin-1/2 particle, there are, in general, two form factors. It is convenient to associate one with the electrical properties of the target and the other with the magnetic properties of the target. The form factors for a point target are simply the target's charge & magnetic moment. For a non-point like particle, the form factors are no longer constants and vary with the resolution of the probe. In the kinematic regime where the target recoil is negligible (i.e. nonrelativistic), these form factors have a simple physical interpretation: they are the Fourier transforms of the static spatial charge and magnetization distributions of the particle in the lab frame.

The first attempt to measure nuclear charge distributions in the modern era of high energy electron scattering was by Lyman, Hanson, & Scott in 1951. They measured elastic scattering of 16 MeV electrons from carbon, aluminum, copper, silver and gold [34]. They probed a size scale of 5 to 25 fm and their results indicated a uniform charge distribution for heavy nuclei. After making the definitive measurements of several heavy nuclei in the mid-1950's, Robert Hofstadter and his students turned their attention to nucleon structure. They probed a size scale of 0.3 to 2 fm and found that the number of scattered electrons for a given angle

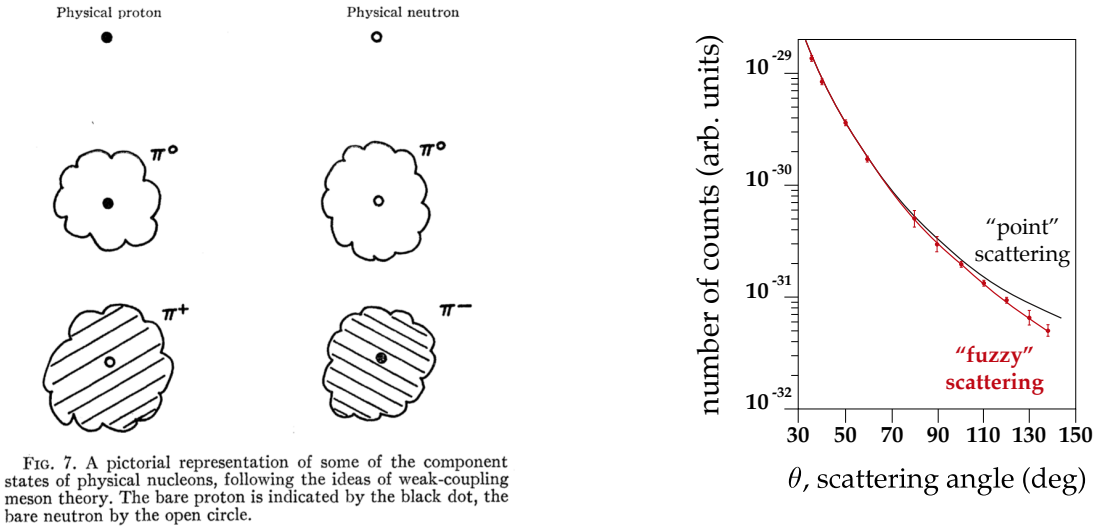

FIG. 7. A pictorial representation of some of the component states of physical nucleons, following the ideas of weak-coupling meson theory. The bare proton is indicated by the black dot, the bare neutron by the open circle.

Figure 1.6: Pictures of the Proton. The left figure is from a review article on nucleon structure from 1957 [32]. The right plot is from Hofstadter's measurement of elastic scattering of electrons from protons. [33].

were less than what one would expect for a Dirac like point particle with the same magnetic moment as the proton [33], Fig. (1.6). This indicated that the proton form factor was not constant and dropped quite rapidly as one increased the resolution. Hofstadter could describe their data with a exponentially decaying charge and magnetization distribution with a radius of about 0.8 fm [35]. However, for their highest resolution data, the target recoil was sizable, as it often is for light nuclei and nucleons, and the lab frame spatial distribution interpretation breaks down due to relativistic effects. Regardless, Hofstadter's measurements showed that nucleons have a spatial extent and found the size scale where their non-point like behavior finally becomes apparent.

1.2.3 Constituent Quarks

Throughout the 50's and 60's, many new mesons, baryons, and resonances were discovered. However, all approaches to describe these new strongly interacting particles using the ideas from QED failed. As a result, the predominant theoretical idea was to focus only on the most general properties of the scattering process [36–38]. Specifically it was argued that one should only be concerned with the initial and final state of the scattered particles and ignore the microscopic details of their interaction. For this reason, one could not give nucleons any special priority as being fundamental. All hadrons were considered equal, establishing a kind of "nuclear democracy" [39].

One powerful mathematical formulation of these arguments comes in the form of dispersion relations. The general properties that they encode are the conservation of probability and the idea that cause precedes effect. Combined with conservation of charge and enforcing consistency with special relativity, dispersion relations were used to derive an important sum rule by Gerasimov and Drell & Hearn [40, 41]. Nowadays referred to as the GDH sum rule, it describes the consequences of polarized photon scattering from a polarized target. The GDH sum rule relates a particle's deviations from point-like behavior (anomalous magnetic moment) to the collective excitations of its constituents (its differential polarized inelastic spectrum). A photon can only interact with global properties of a particle (charge, magnetic moment). Therefore this sum rule is only true for "zero" resolution. It has been generalized to electron scattering [42] and therefore can be related to the a particle's structure at all resolution scales.

An alternative and minority view at the time took advantage of the patterns found across hadrons. Gell-Man, Ne'eman, and Zweig showed that hadrons could

be ordered by their spin, isospin, and strangeness [43, 44]. Furthermore, the regularity of these patterns suggested that hadrons are composed of a discrete set of subnuclear particles referred to as "quarks" or "aces" [45, 46]. This idea is in complete analogy to atoms where different combinations of protons, neutrons, and electrons can fully explain their atomic number, weights, and chemistry. Just as Mendeleev had done with atoms and the periodic table a century earlier, a particle's properties could be predicted based its position in a table, see for example [47]. The model could explain nearly all the masses, charges, magnetic moments, spin, isospin, and strangeness on the basis of three fractionally charged flavors of constituents called up, down, and strange.

Using the structure of atoms as a guide, Dalitz was able to incorporate orbital angular momentum into the quark model [48, 49]. His symmetric quark model could explain several of the resonance states as orbital excitations of nucleons. It could not, however, explain the existence of certain hadrons that had three quarks all with the same quantum numbers. Much like Uhlenbeck and Goudsmit's conjecture of electron spin to explain Pauli's principle, Owen Greenberg [50] (also Han & Nambu [51]) proposed a new quantum number which is now referred to as "color." Although the mathematical utility of constituent quarks was not doubted, the physical reality of quarks was (except notably by Zweig and Dalitz) [45,46,49,52–55]. All searches for "free" quarks at the time (1960's) returned with negative results, see for example [56].

During this same time at the Stanford Linear Accelerator Center (SLAC), Panofsky & Allton (0.3 to 0.9 fm) [58] and Ohlsen (0.3 to 0.6 fm) [59] and Hand (0.2 to 0.7 fm) [60] performed the first series of inelastic studies on the proton. They demonstrated electropion production and observed the Δ resonance (near $W = 1.2$ GeV)

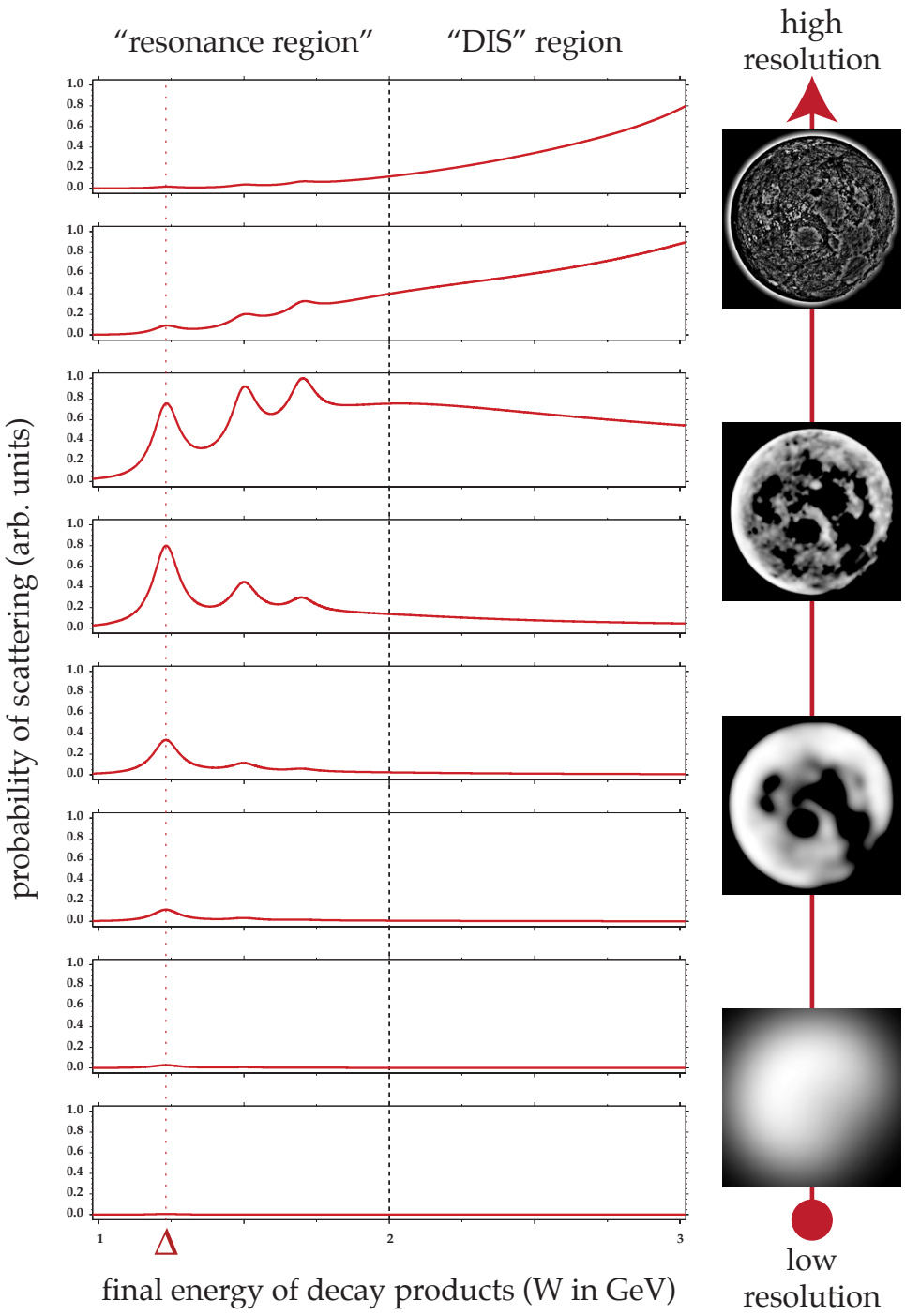

Figure 1.7: Response of the Nucleon at Different Resolutions. Compare the "resonance region" in the middle spectra to the spectrum in Fig. (1.5). Spectra were generated using QFS [57]. The resolution scale ($\sqrt{Q^2}$) increases going from bottom to top.

which is the lowest energy collective excitation of the nucleon, see the "resonance region" in Fig. (1.7). In 1965, Cone et al. (0.1 to 0.4 fm) expanded these studies at Harvard and observed all known resonances up to 1920 MeV [61]. These results were expected based on earlier results from pion-nucleon and nucleon-nucleon scattering.

As these resonances get heavier, more decay modes become available (i.e. the decay phase space increases due to more ways to conserve energy and momentum). More decay modes imply a shorter lifetime which leads to broader energy width. Therefore, it was expected that these resonances would become very wide. For resonance masses above twice the mass of nucleons, it was observed that the resonances essentially smear out into a gradually decreasing continuum, see the "DIS" region of the middle two spectra in Fig. (1.7). Just like the ground state nucleon, these resonances were expected to have analogous form factors that drop off appreciably at sufficiently high resolution ($\ll 1$ fm). For example, the Delta (Δ) resonance in Fig. (1.7) is only apparent at a range of resolutions scales that is on the order of its characteristic size. At resolutions much lower or higher than this range, the probability of scattering is flat and nearly zero. This is essentially the same argument made in the SLAC Proposal E4B "The Electron-Proton Inelastic Scattering Experiment:"

> Because the inelastic cross section contains q^2 dependencies which are similar to that of the form factors describing elastic scattering, the counting rates drop rapidly as a function of four-momentum transfer . . .

where "q^2" (the four-momentum transfer squared, Q^2 in modern notation) is the parameter that defines the resolution scale in electron scattering [62]. The expectation was that, at sufficiently high resolution ($\sqrt{Q^2}$), the probability of scattering in

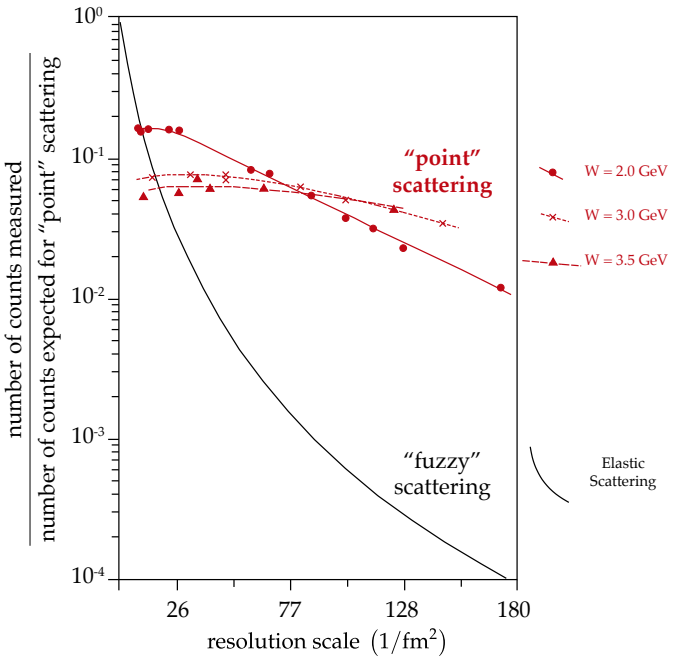

Figure 1.8: SLAC Deep Inelastic Scattering Data. Adapted from [63].

the "DIS" region (high W) would be nearly zero.

1.2.4 Partons

With this expectation, Friedman, Kendall, and Taylor performed their legendary deep inelastic scattering (DIS) experiments at the newly upgraded SLAC linear accelerator. Their original goals were to "search for new nucleon resonances" above 1.8 GeV (i.e. the right half of the spectra in Fig. (1.7)) and to "separate the inelastic longitudinal and transverse form factors." They fired 7 to 17 GeV electrons at a liquid hydrogen target and measured the scattering rates at 6 and 10 degrees [64]. Unexpectedly, they found [63] that the inelastic form factors for resonance masses above 2 GeV were essentially constant or, in other words, had no resolution dependence, see the "DIS" region in the top two spectra of Fig. (1.7). The immediate

interpretation of this observation was that the electrons were scattering elastically from point-like particles within the proton, see Fig. (1.8).

Bjorken had earlier considered [65] the possibility of such an observation and nowadays it is referred to Bjorken scaling. Feynman provided the first clear physical picture of what was being measured during this process [66]. He imagined the scattering process in a reference frame where the electron and nucleon are traveling at each other fast enough so that one could ignore the transverse motion of these objects he called partons. In this frame, the interaction would occur so quickly that the struck parton would be scattered out of the nucleon before it could interact with another parton. The struck parton would carry a fraction of the total momentum of the nucleon. In this picture, the electron scattering probes the longitudinal momentum distribution of partons within the nucleon. Unpolarized electron scattering indicated that partons behaved like point-like spin-1/2 fractionally charged particles. For this reason, it was difficult to avoid associating partons with quarks. Including the impressive data from neutrino-nucleon scattering, the evidence for the quark-parton model became overwhelming.

1.2.5 How are these pictures related?

At nuclear distance scale, above 1 fm, protons and neutrons interact as point particles would through pion exchange. One can very successfully model this interaction based on effective short range potentials inspired by atomic physics. On the 35th anniversary of the Lyman-Scott-Hansen electron scattering experiment, J.D. Walecka recalled Herb Anderson asking the question, "We have been doing nuclear physics for 50 years without quarks. Why do we need them now?" [67].

Quark and gluon degrees of freedom are absolutely necessary at very short

distance scales, below ≈ 0.2 fm. By the mid-1970's, all of the theoretical tools and experimental observations necessary to describe these degrees of freedom had become available. An early synthesis of the relevant ideas was fully outlined in 1973 by Gross & Wilczek [68, 69] and dubbed Quantum Chromodynamics. The charges that cause attraction and repulsion in QCD are labeled by three colors (in analogy to the two "colors" in QED: positive and negative electrical charge). The attraction and repulsion between quarks is mediated by gluons just like photons between electrical charges. Unlike photons, the gluons themselves carry charge. This difference is what explains the dramatic difference in the small distance scale behavior between QED and QCD. In QED, the strength of the interaction becomes much larger as two electrons are brought together. In QCD, the strength of the interaction becomes much smaller as two quarks are brought together. This property is called "asymptotic freedom" and allows theorists to make accurate calculations about quark behavior at distance scale below about 0.1 fm. At larger distance scales, the strength of the interactions between quarks becomes so large that enough energy is available for the creation of more quarks and gluons. For this reason, QCD calculations become intractable and one is left to wonder if "more is different."

What happens between 0.1 to 1 fm? It is believed that, through a mechanism called "confinement," quarks accumulate a cloud of virtual quarks and gluons. The resulting blobs are the constituent quarks of the original quark model of hadrons. To differentiate between the two, short distance scale quarks are sometimes referred to current quarks. A constituent quark obtains its quantum numbers from the current quark at its core. This current quark is referred to as the valence quark. Almost all of the mass of a constituent quark is generated by the cloud of virtual particles that surround the nearly massless valence quark. This

surrounding cloud of virtual quarks is referred to as the sea quarks. Finally, these constituent quarks then bind together to form hadrons in direct analogy to the binding of nucleons in nuclei.

One of the central goals of Nuclear Physics is to better understand how the transition from quarks to nuclei occurs between 0.1 and 1 fm. The nucleon is a natural place to investigate this transition since it has the size scale characteristic of the relevant physics. This intermediate size scale regime is a fertile ground for theorists to build effective models of nucleon structure in an effort to bridge the very long and very short distance scale physics of the strong interaction. There are several complimentary experimental approaches to this problem. The one emphasized here takes advantage of the spin degrees of freedom to access polarization observables.

1.3 Polarized He-3 Targets

1.3.1 The Importance of Polarization Observables

The spin of the nucleon is interesting in itself and also provides "an extra knob to turn" to access nucleon structure. The importance of these degrees of freedom was well known for a long time, but several technological barriers had to be overcome before double polarized (i.e. beam and target) scattering experiments could become practical. By the early 70's, polarized electron scattering from polarized nuclear targets had become realizable and the first such experiment was E80 at SLAC led by V.W. Hughes. The polarized electron beam was produced by photo-ionization of a Li-6 atomic beam. They could deliver a 120 Hz pulsed beam with an average beam current of 0.04 μA at 50% polarization. The target was

butanol doped by porphyrexide radicals which achieved a proton polarization of 50%. They measured asymmetries for elastic scattering [70] and deep inelastic scattering [71,72]. In the DIS region, their first results showed positive asymmetries as expected from the quark-parton model. A subsequent experiment, E130, took data in the resonance region for the first time and found a negative asymmetry for the delta resonance as expected from the constituent quark model [73].

Experiments of this type are now routine and a great deal has been learned about the spin structure of the nucleon, see for example [74]. For the sake of brevity, we'll highlight the famously surprising result [75] from the European Muon Collaboration. They found that the contribution to the spin of the nucleon due to the spin of the quarks was consistent with zero. After a considerable amount of experimental effort over the past two decades, we now know that the value for this quantity is closer to 0.3 [76]. At present, firm statements about the gluon contribution to the spin of the nucleon are impossible to make because of the limited kinematic coverage of data presently available. With that caveat in mind, a recent global analysis [76] of the world data has hinted, in the limited kinematic region explored, that the gluons contribute little to the spin of the nucleon. These two experimental observations have provided some credence to idea that quark orbital angular momentum plays a significant role in the dynamics of nucleons.

More recently, additional hints of nonzero quark orbital angular momentum have come from measurements of the proton form factors. High resolution measurements of the proton form factors at SLAC in 1989 seemed to indicate that there was no significant difference in the spatial distribution of charge and magnetization within the proton [77]. This view was upended by experiments at JLab in the early part of this decade. These later experiments took advantage of polarization

degrees of freedom to directly measure the ratio of the electric to magnetic form factor of the proton. This type of measurement is regarded as being relatively free of systematic effects that plague the determination of this ratio using data from unpolarized electron scattering [78]. These experiments famously observed & confirmed a linear decrease in the ratio of the electric to magnetic form factors with increasing resolution [79]. One natural explanation for this observation involves nonzero quark orbital angular momentum [74].

These two discoveries simply would not have been possible without the ability to control and measure the spin of the beam and target. One could argue that improvements in polarized beams & targets lays the foundation for future unexpected discoveries.

1.3.2 Effective Neutron Target

Most precision electron scattering experiments require many hours of beamtime to accumulate enough scattering events to achieve a prescribed statistical precision. A dense, free neutron target for these types of experiments simply does not exist. Two possible effective neutron targets are deuterons and ^{3}He nuclei. As an unpolarized target, deuterons are ideal because they are a simpler two body nuclear system and a single proton produces less background. As a polarized target, deuterons are less attractive because of the large uncanceled spin of the spectator proton and the tensor polarization effects due to the spin-1 nature of deuterons. On the other hand, the spins of the two spectator protons in the ^{3}He nucleus largely cancel due to the Pauli exclusion principle. In the most simple picture, a fully polarized ^{3}He nucleus can be thought of as a bag of loosely bound nucleons with an effective neutron polarization of 86% and an effective proton polarization of -2%.

1.3.3 Polarizing He-3

There are at least three ways to polarize ^{3}He nuclei. The first and most inefficient is the brute force method where one applies large magnetic fields and low temperatures to produce large Boltzmann polarizations. It would require a 50 T field to produce 1% polarization in ^{3}He at liquid helium temperatures.

The second is called metastability exchange optical pumping (MEOP) and was first demonstrated by Schearer, Colegrove, & Walters in 1963 [80]. In this method, an RF (radiofrequency) discharge excites ^{3}He atoms in the 1^1S_0 ground state into the 2^3S_1 metastable state. These metastable atoms are polarized via optically pumping (described in the following section) to the 2^3P states. Finally, metastable atoms exchange their electronic configuration with atoms in the ground state via collisions. The "metastability exchange" collisions are sudden with respect to the ^{3}He nuclear spin. Therefore, the nuclear polarization is preserved as the ^{3}He atom returns to the ground state. This method requires low pressures to insure sufficiently long lifetimes in the metastable state for optical pumping. This technique is the preferred polarization method for internal polarized ^{3}He targets.

The third method and, historically, the first one to be realized experimentally is a two step process referred to as spin exchange optical pumping (SEOP). Alkali atoms are first polarized via optical pumping. This electronic polarization is then transferred to ^{3}He nuclei via spin exchange collisions. This process is one of the main topics of this dissertation.

1.3.4 Spin Exchange Optical Pumping

There were three key ideas that had to established before the demonstration of spin exchange optical pumping of ^{3}He . The first was optical pumping, which involves the redistribution of the populations of the Zeeman levels of a particular state using polarized light. Kastler's key idea in 1950 was to suggest the use of *circularly* polarized light to selectively depopulate or populate a given atomic state [81]. This was soon demonstrated in sodium in 1952 by Brossel, Kastler, and Winter [82] and in 1953 by Hawkins and Dicke [83].

At the time, most optical pumping experiments on alkali atoms used light produced from a discharge lamp of the same alkali atom. These lamps produced a spectrum that was a mixture of wavelengths associated with both the D1 and D2 transitions. Due to electric dipole selection rules, optical pumping with light originating from the D1 & D2 transitions results in ground state polarizations of +100% & -50% respectively. In 1957, Franzen and Emslie were among the first to suggest that nearly "one hundred percent orientation of alkali atoms" could be obtained by "illuminating them with circularly polarized resonance radiation" comprised *only of D1 light* [84].

The last piece of the puzzle was the concept of spin exchange, which was first used to describe collisions between atomic hydrogen in 1956 by Purcell & Field [85] and Wittke & Dicke [86]. However, the prediction and observation of the Overhauser effect more directly led to the first demonstration of SEOP of ^{3}He . As it was originally imagined by Overhauser [87], conduction electrons in metals could, under the proper conditions, polarize nuclei via a hyperfine coupling between their spins. Carver and Slichter were soon able to verify this prediction [88]. As this result was a part of Carver's dissertation work [89], it's not surprising he, along

with Bouchiat and Varnum, sought to reproduce this effect in ^{3}He using optically pumped Rb. In 1960, they succeeded in polarizing a 3 amagat sample of ^{3}He to 0.01% [90]. They observed very short ($\approx$ 1 hr) ^{3}He relaxation time constants, which they noted limited the applicability of this method to polarized nuclear targets.

Because SEOP relies on a very weak coupling between alkali atoms and ^{3}He nuclei, a very high density of alkali atoms is required to provide a spin exchange rate high enough to overcome the ^{3}He relaxation rate. To provide some context, optical pumping experiments at the time were performed at alkali densities of one hundred to one million times smaller than the alkali densities used in the target cells described in this dissertation. Rb lamps used for optical pumping cannot provide the light intensity required to polarize such a high density of atoms. For this reason, the possibility of using SEOP was not seriously explored again until 25 years later when high power lasers of the appropriate wavelength became available.

1.3.5 SEOP Polarized He-3 Targets

Even as late as 1984, as reported in the *Proceedings of the Workshop on Polarized He-3 Beams and Targets*, not one mention is made of utilizing spin exchange optical pumping for polarizing ^{3}He . There is, however, a discussion about polarizing ^{3}He *ions*, produced by collisions with a charged particle beam, using optically pumped Rb atoms [91]. The ^{3}He nuclei would then be polarized by the hyperfine coupling between the spin of the valence electron of the ^{3}He ion and its nuclear spin. Within three years of this workshop, it was shown that small volumes (a few cm^3) of ^{3}He at a density of roughly 3 amg could be polarized to 40% using SEOP [92].

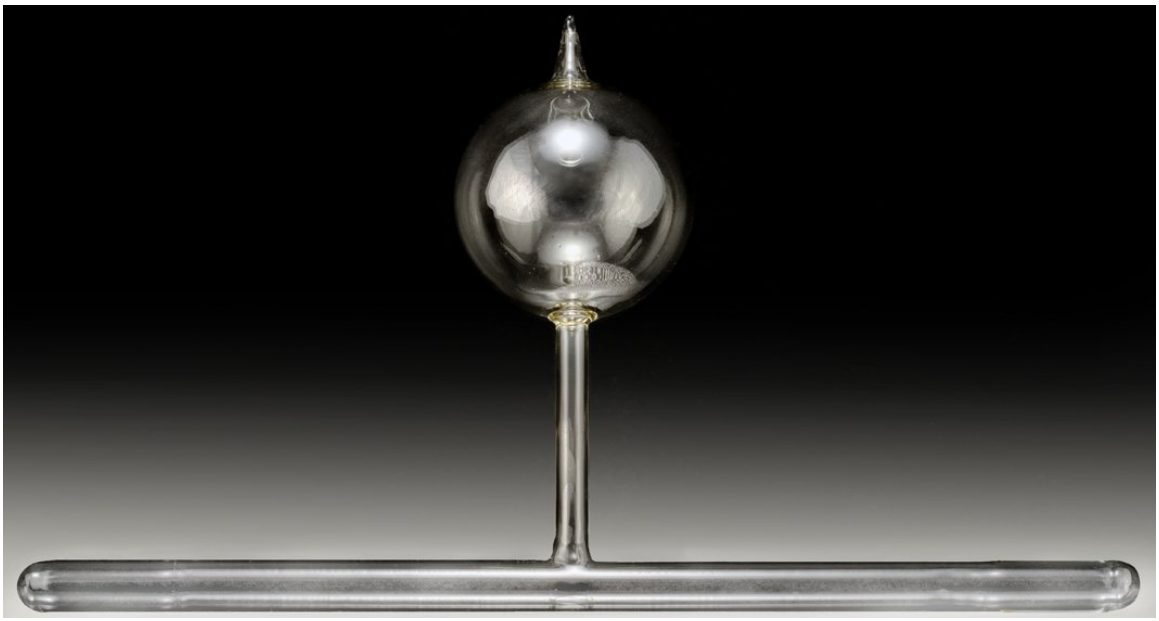

Figure 1.9: SEOP Polarized Target Cell Used for G_E^n (E02013). Image provided by Al Gavalya.

The basic design and operational parameters of the type of polarized ^{3}He targets that are the focus of this dissertation were established with the SLAC experiments E142 [93] & E154 [94]. The developments of these targets benefitted from several other polarized ^{3}He efforts that were already in progress [92, 95–97]. JLab style target cells have a pumping chamber (2.5 in to 3.5 in diameter sphere) and a target chamber (15 cm to 40 cm in length) connected via a transfer tube, see Fig. (1.9). These cells have a total volume that ranges from 200 cm^3 to 400 cm^3. The ^{3}He operating density in the target chamber is typically 10 amg, while the density in the pumping chamber is about 7 amg.

The prescription to insure sufficiently long wall relaxation time constants in target cells was developed during the run up to E142 [98]. The precision ^{3}He polarimetry techniques developed for E154, with a few modifications, are what we still use today [99]. Each of these advances were carried over to and built

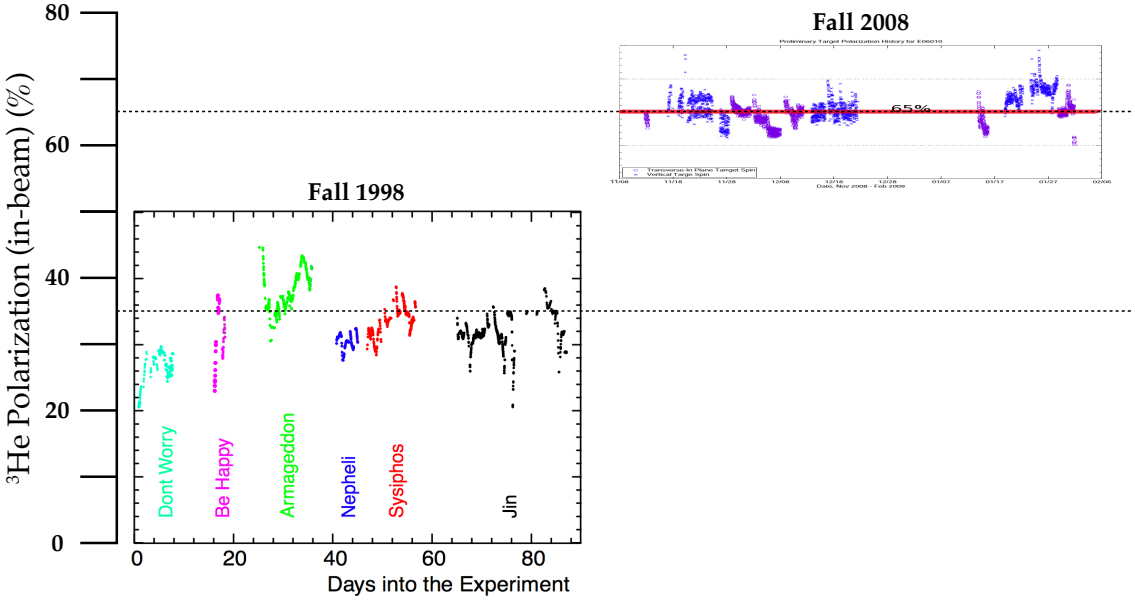

Figure 1.10: Target Polarization for the First (E94010) and Most Recent (E06010) JLab ^{3}He Experiments. Data from E94010, taken in the Fall of 1998, are on the left [101]. Preliminary data from E06010, taken in the Fall of 2008, are on the right (figure provided by C. Dutta).

upon by the JLab polarized ^{3}He program [100–105]. Starting from the first JLab ^{3}He experiment, E94010 [106], the capabilities of polarized ^{3}He targets at JLab have steadily advanced, with more than an order of magnitude increase in the appropriate figure of merit. The success of this program can be attested to by the fact that, averaged over the past decade, at least one new polarized ^{3}He experiment per year has completed data taking.

Bibliography

[1] P. L. Anthony, R. G. Arnold, H. R. Band, H. Borel, P. E. Bosted, V. Breton, G. D. Cates, T. E. Chupp, F. S. Dietrich, J. Dunne, R. Erbacher, J. Fellbaum, H. Fonvieille, R. Gearhart, R. Holmes, E. W. Hughes, J. R. Johnson, D. Kawall, C. Keppel, S. E. Kuhn, R. M. Lombard-Nelsen, J. Marroncle, T. Maruyama, W. Meyer, Z.-E. Meziani, H. Middleton, and J. Morgenstern. Determination of the neutron spin structure function. *Phys. Rev. Lett.*, 71(7):959–962, Aug 1993.

[2] M. S. Albert, G. D. Cates, B. Driehuys, W. Happer, B. Saam, C. S. Springer, and A. Wishnia. Biological magnetic resonance imaging using laser-polarized ^{129}Xe. *Nature*, 370(6486).

[3] D. Bear, R. E. Stoner, R. L. Walsworth, V. Alan Kostelecký, and Charles D. Lane. Limit on Lorentz and *CPT* Violation of the Neutron Using a Two-Species Noble-Gas Maser. *Phys. Rev. Lett.*, 85(24):5038–5041, Dec 2000.

[4] M. G. Huber, M. Arif, T. C. Black, W. C. Chen, T. R. Gentile, D. S. Hussey, D. A. Pushin, F. E. Wietfeldt, and L. Yang. Precision Measurement of the *n*-^{3}He Incoherent Scattering Length Using Neutron Interferometry. *Phys. Rev. Lett.*, 102(20):200401, May 2009.

[5] William Happer, Gordon D. Cates, Jr., Mikhail V. Romalis, and Christopher J Erickson. *U.S. Patent No. 6,318,092*, 2001.

[6] E. Babcock, et al. Hybrid Spin-Exchange Optical Pumping of ^{3}He. *Phys. Rev. Lett.*, 91(12):123003, Sep 2003.

[7] B. Chann, et al. Production of highly polarized ^{3}He using spectrally narrowed diode laser array bars. *J. Appl. Phys.*, 94(10):6908–6914, 2003.

[8] David Kramer. Doe begins rationing helium-3. *Physics Today*, 63(6):22–25, 2010.

[9] Franz Gross. Early history of jefferson laboratory. *Jefferson Lab 2009 Users Group Meeting*.

[10] Philipp E. A. von Lénárd. On cathode rays. In *Nobel Lectures, Physics 1901-1921*. Elsevier, Amsterdam, 1967.

[11] H. Geiger and E. Marsden. LXI. The Laws of Deflexion of a Particles through Large Angles. *Philosophical Magazine Series 6*, 25(148):604–623, 1913.

[12] H. Geiger and E. Marsden. On a Diffuse Reflection of the α-Particles. *Proc. Roy. Soc. 1909 A*, 82:495–500, 1909.

[13] E. Rutherford. LXXIX. The scattering of α and β particles by matter and the structure of the atom. *Philosophical Magazine Series 6*, 12(125):669–688, 1911.

[14] James Franck. Transformation of Kinetic Energy of Free Electrons into Excitation Energy of Atoms by Impacts. In *Nobel Lectures, Physics 1922-1941*. Elsevier, Amsterdam, 1965.

[15] Gustav Hertz. The Results of the Electron-Impact Tests in the Light of Bohr's Theory of Atoms. In *Nobel Lectures, Physics 1922-1941*. Elsevier, Amsterdam, 1965.

[16] Niels Bohr. The Structure of the Atom. In *Nobel Lectures, Physics 1922-1941*. Elsevier, Amsterdam, 1965.

[17] E. Rutherford. LIV. Collision of α Particles with Light Atoms IV. An Anomalous Effect in Nitrogen. *Philosophical Magazine Series 6*, 37(222):581–587, 1919.

[18] E. Rutherford. Bakerian Lecture. Nuclear Constitution of Atoms. *Proceedings of the Royal Society of London. Series A*, 97(686):374–400, 1920.

[19] J. Chadwick. The Existence of a Neutron. *Proceedings of the Royal Society of London. Series A*, 136(830):692–708, 1932.

[20] E. Rutherford. Collision of α particles with light atoms I. Hydrogen. *Philosophical Magazine Series 6*, 37(222):537–561, 1919.

[21] N. F. Mott. The Scattering of Fast Electrons by Atomic Nuclei. *Proceedings of the Royal Society of London. Series A*, 124(794):425–442, 1929.

[22] Milton G. White. Collisions of high energy protons in hydrogen. *Phys. Rev.*, 47(7):573–574, Apr 1935.

[23] I. Estermann and O. Stern. Über die magnetische Ablenkung von Wasserstoffmoleklen und das magnetische Moment des Protons. II. *Zeitschrift für Physik*, 85(1–2):17–24, 1933.

[24] I. I. Rabi, J. M. B. Kellogg, and J. R. Zacharias. The Magnetic Moment of the Proton. *Phys. Rev.*, 46(3):157–163, Aug 1934.

[25] I. Estermann and O. Stern. Über die magnetische Ablenkung von isotopen Wasserstoffmoleklen und das magnetische Moment des "Deutons". *Zeitschrift für Physik*, 86(1–2):132–134, 1933.

[26] I. I. Rabi, J. M. B. Kellogg, and J. R. Zacharias. The Magnetic Moment of the Deuton. *Phys. Rev.*, 46(3):163–165, Aug 1934.

[27] P. N. Powers, H. Carroll, H. Beyer, and J. R. Dunning. The Sign of the Magnetic Moment of the Neutron. *Phys. Rev.*, 52(1):38–39, Jul 1937.

[28] Luis W. Alvarez and F. Bloch. A Quantitative Determination of the Neutron Moment in Absolute Nuclear Magnetons. *Phys. Rev.*, 57(2):111–122, Jan 1940.

[29] W. Pauli. Relativistic Field Theories of Elementary Particles. *Rev. Mod. Phys.*, 13(3):203–232, Jul 1941.

[30] M. E. Rose. The Charge Distribution in Nuclei and the Scattering of High Energy Electrons. *Phys. Rev.*, 73(4):279–284, Feb 1948.

[31] M. N. Rosenbluth. High Energy Elastic Scattering of Electrons on Protons. *Phys. Rev.*, 79(4):615–619, Aug 1950.

[32] D. R. Yennie, M. M. Lévy, and D. G. Ravenhall. Electromagnetic Structure of Nucleons. *Rev. Mod. Phys.*, 29(1):144–157, Jan 1957.

[33] R. W. McAllister and R. Hofstadter. Elastic Scattering of 188 MeV Electrons from the Proton and the Alpha Particle. *Phys. Rev.*, 102(3):851–856, May 1956.

[34] E. M. Lyman, A. O. Hanson, and M. B. Scott. Scattering of 15.7 MeV Electrons by Nuclei. *Phys. Rev.*, 84(4):626–634, Nov 1951.

[35] E. E. Chambers and R. Hofstadter. Structure of the Proton. *Phys. Rev.*, 103(5):1454–1463, Sep 1956.

[36] Geoffrey F. Chew and S. C. Frautschi. Principle of equivalence for all strongly interacting particles within the *s*-matrix framework. *Phys. Rev. Lett.*, 7(10):394–397, Nov 1961.

[37] Andrew Pickering. *Constructing Quarks: A Sociological History of Particle Physics*. University of Chicago Press, Chicago, 1999.

[38] David J. Gross. Nobel Lecture: The discovery of asymptotic freedom and the emergence of QCD. *Rev. Mod. Phys.*, 77(3):837–849, Sep 2005.

[39] Geoffrey F. Chew. Nuclear democracy and bootstrap dynamics. In David Pines, editor, *Strong Interaction Physics: A Lecture Note Volume*. W. A. Benjamin, New York, 1964.

[40] S. B. Gerasimov. A sum rule for magnetic moments and the damping of the nucleon magnetic moment in nuclei. *Soviet Journal of Nuclear Physics*, 2(4):430–433, April 1966.

[41] S. D. Drell and A. C. Hearn. Exact Sum Rule for Nucleon Magnetic Moments. *Phys. Rev. Lett.*, 16(20):908–911, May 1966.

[42] Xiangdong Ji and Jonathan Osborne. Generalized sum rules for spin-dependent structure functions of the nucleon. *Journal of Physics G: Nuclear and Particle Physics*, 27(1):127–146, 2001.

[43] M. Gell-Mann and Y. Ne'eman. *The Eightfold Way*. W. A. Benjamin, New York, 1964.

[44] G. Zweig. An SU_3 model for strong interaction symmetry and its breaking.

[45] Michael Riordan. *The Hunting of the Quark: A True Story of Modern Physics*. Simon & Schuster, New York, 1987.

[46] Andrew Watson. *The Quantum Quark*. Cambridge University Press, Cambridge, 2008.

[47] V. E. Barnes, P. L. Connolly, D. J. Crennell, B. B. Culwick, W. C. Delaney, W. B. Fowler, P. E. Hagerty, E. L. Hart, N. Horwitz, P. V. C. Hough, J. E. Jensen, J. K. Kopp, K. W. Lai, J. Leitner, J. L. Lloyd, G. W. London, T. W. Morris, Y. Oren, R. B. Palmer, A. G. Prodell, D. Radojičić, D. C. Rahm, C. R. Richardson, N. P. Samios, J. R. Sanford, R. P. Shutt, and J. R. Smith. Observation of a hyperon with strangeness minus three. *Phys. Rev. Lett.*, 12(8):204–206, Feb 1964.

[48] R. H. Dalitz. Quark Models for the "Elementary Particles". In C. DeWitt and M. Jacob, editors, *High Energy Physics, Lectures delivered at Les Houches during the 1965 session of the Summer School of Theoretical Physics*, pages 251–323. Gordon and Breach Science Publishers, New York, 1965.

[49] R. H. Dalitz. Symmetries and the Strong Interactions. In Margaret Alston-Garnjost, editor, *Proceedings of the XIIIth International Conference on High Energy Physics, University of California, Berkeley, 1966*. University of California Press, Berkeley, 1967.

[50] O. W. Greenberg. Spin and unitary-spin independence in a paraquark model of baryons and mesons. *Phys. Rev. Lett.*, 13(20):598–602, Nov 1964.

[51] M. Y. Han and Y. Nambu. Three-triplet model with double $su(3)$ symmetry. *Phys. Rev.*, 139(4B):B1006–B1010, Aug 1965.

[52] Murray Gell-Mann. Current Topics in Particle Physics. In Margaret Alston-Garnjost, editor, *Proceedings of the XIIIth International Conference on High Energy Physics, University of California, Berkeley, 1966*. University of California Press, Berkeley, 1967.

[53] George Zweig. Origins of the Quark Model. In Nathan Isgur, editor, *Proceedings of Baryon 1980 : the IVth International Conference on Baryon Resonances, University of Toronto, 1980*. University of Toronto Press, Toronto, 1980.

[54] Frank E. Close and Avraham Gal. Obituary: Richard henry dalitz, frs (1925-2006). *Nuclear Physics A*, 771:2 – 7, 2006.

[55] Telegdi, Valentine L. Interview by Sara Lippincott. Pasadena, California, March 4 and 9, 2002. Oral History Project, California Institute of Technology Archives. Retrieved [supply date of retrieval] from the World Wide Web: `http://resolver.caltech.edu/CaltechOH:OH_Telegdi_V`.

[56] Lawrence W. Jones. A review of quark search experiments. *Rev. Mod. Phys.*, 49(4):717–752, Oct 1977.

[57] J. W. Jr. Lightbody and J. S. O. Connell. Modeling single arm electron scattering and nucleon production from nuclei by gev electrons. *Computers in Physics*, 2:57–64, May/June 1988.

[58] W. K. H. Panofsky and E. A. Allton. Form Factor of the Photopion Matrix Element at Resonance. *Phys. Rev.*, 110(5):1155–1165, Jun 1958.

[59] Gerald G. Ohlsen. Electroproduction of Pions from Hydrogen and Deuterium. *Phys. Rev.*, 120(2):584–592, Oct 1960.

[60] L. N. Hand. Experimental Investigation of Pion Electroproduction. *Phys. Rev.*, 129(4):1834–1846, Feb 1963.

[61] A. A. Cone, K. W. Chen, J. R. Dunning, C. Hartwig, N. F. Ramsey, J. K. Walker, and Richard Wilson. Baryon Spectroscopy by Inelastic Electron-Proton Scattering. *Phys. Rev. Lett.*, 14(9):326–328, Mar 1965.

[62] Panofsky, W.K.H. and Coward, D.H. and DeStaebler, H. and Litt, J. and Mo, L.W. and Taylor, R.E. and Friedman, J.I. and Kendall, H.W. and Van Speybroeckm L. and Peck, C. and Pine, J. *SLAC E4 Proposal: Proposals for Initial Electron Scattering Experiments Using the SLAC Spectrometer Facilities*. January 1966.

[63] M. Breidenbach, J. I. Friedman, H. W. Kendall, E. D. Bloom, D. H. Coward, H. DeStaebler, J. Drees, L. W. Mo, and R. E. Taylor. Observed behavior of highly inelastic electron-proton scattering. *Phys. Rev. Lett.*, 23(16):935–939, Oct 1969.

[64] E. D. Bloom, D. H. Coward, H. DeStaebler, J. Drees, G. Miller, L. W. Mo, R. E. Taylor, M. Breidenbach, J. I. Friedman, G. C. Hartmann, and H. W. Kendall. High-energy inelastic $e - p$ scattering at 6^o and 10^o. *Phys. Rev. Lett.*, 23(16):930–934, Oct 1969.

[65] J. D. Bjorken. Asymptotic sum rules at infinite momentum. *Phys. Rev.*, 179(5):1547–1553, Mar 1969.

[66] Richard P. Feynman. *Photon-Hadron Interactions*. Addison-Wesley, Reading Massachusetts, 1998.

[67] J. D. Walecka. Symposium—35 years of electron scattering. *AIP Conference Proceedings*, 161(1):213–223, 1987.

[68] David J. Gross and Frank Wilczek. Asymptotically free gauge theories. i. *Phys. Rev. D*, 8(10):3633–3652, Nov 1973.

[69] David J. Gross and Frank Wilczek. Asymptotically free gauge theories. ii. *Phys. Rev. D*, 9(4):980–993, Feb 1974.

[70] M. J. Alguard, W. W. Ash, G. Baum, J. E. Clendenin, P. S. Cooper, D. H. Coward, R. D. Ehrlich, A. Etkin, V. W. Hughes, H. Kobayakawa, K. Kondo, M. S. Lubell, R. H. Miller, D. A. Palmer, W. Raith, N. Sasao, K. P. Schüler, D. J. Sherden, C. K. Sinclair, and P. A. Souder. Elastic scattering of polarized electrons by polarized protons. *Phys. Rev. Lett.*, 37(19):1258–1261, Nov 1976.

[71] M. J. Alguard, W. W. Ash, G. Baum, J. E. Clendenin, P. S. Cooper, D. H. Coward, R. D. Ehrlich, A. Etkin, V. W. Hughes, H. Kobayakawa, K. Kondo, M. S. Lubell, R. H. Miller, D. A. Palmer, W. Raith, N. Sasao, K. P. Schüler, D. J. Sherden, C. K. Sinclair, and P. A. Souder. Deep inelastic scattering of polarized electrons by polarized protons. *Phys. Rev. Lett.*, 37(19):1261–1265, Nov 1976.

[72] M. J. Alguard, W. W. Ash, G. Baum, M. R. Bergstrom, J. E. Clendenin, P. S. Cooper, D. H. Coward, R. D. Ehrlich, V. W. Hughes, K. Kondo, M. S. Lubell, R. H. Miller, S. Miyashita, D. A. Palmer, W. Raith, N. Sasao, K. P. Schüler, D. J. Sherden, P. A. Souder, and M. E. Zeller. Deep-inelastic $e - p$ asymmetry measurements and comparison with the bjorken sum rule and models of proton spin structure. *Phys. Rev. Lett.*, 41(2):70–73, Jul 1978.

[73] G. Baum, M. R. Bergström, J. E. Clendenin, R. D. Ehrlich, V. W. Hughes, K. Kondo, M. S. Lubell, S. Miyashita, R. H. Miller, D. A. Palmer, W. Raith, N. Sasao, K. P. Schüller, and P. A. Souder. Measurement of asymmetry in spin-dependent $e - p$ resonance-region scattering. *Phys. Rev. Lett.*, 45(25):2000–2003, Dec 1980.

[74] Steven D. Bass. The spin structure of the proton. *Rev. Mod. Phys.*, 77(4):1257–1302, Nov 2005.

[75] J. Ashman et al. A measurement of the spin asymmetry and determination of the structure function g1 in deep inelastic muon-proton scattering. *Physics Letters B*, 206(2):364 – 370, 1988.

[76] Daniel de Florian, Rodolfo Sassot, Marco Stratmann, and Werner Vogelsang. Global analysis of helicity parton densities and their uncertainties. *Phys. Rev. Lett.*, 101(7):072001, Aug 2008.

[77] L. Andivahis, P. E. Bosted, A. Lung, L. M. Stuart, J. Alster, R. G. Arnold, C. C. Chang, F. S. Dietrich, W. Dodge, R. Gearhart, J. Gomez, K. A. Griffioen, R. S. Hicks, C. E. Hyde-Wright, C. Keppel, S. E. Kuhn, J. Lichtenstadt, R. A. Miskimen, G. A. Peterson, G. G. Petratos, S. E. Rock, S. Rokni, W. K. Sakumoto, M. Spengos, K. Swartz, Z. Szalata, and L. H. Tao. Measurements of the electric and magnetic form factors of the proton from $q2$=1.75 to 8.83 (gev/c)2. *Phys. Rev. D*, 50(9):5491–5517, Nov 1994.

[78] J Arrington, C D Roberts, and J M Zanotti. Nucleon electromagnetic form factors. *Journal of Physics G: Nuclear and Particle Physics*, 34(7):S23–S51, 2007.

[79] O. Gayou et al. Measurement of G_E^p/G_M^p in $\vec{e}p \rightarrow e\vec{p}$ to $Q^2 = 5.6$ GeV^2. *Phys. Rev. Lett.*, 88(9):092301, Feb 2002.

[80] L. D. Schearer, F. D. Colegrove, and G. K. Walters. Large he-3 nuclear polarization. *Phys. Rev. Lett.*, 10(3):108–110, Feb 1963.

[81] Kastler, Alfred. Quelques suggestions concernant la production optique et la détection optique d'une inégalité de population des niveaux de quantification spatiale des atomes. application à l'expérience de stern et gerlach et à la résonance magnétique. *J. Phys. Radium*, 11(6):255–265, 1950.

[82] Jean Brossel and Alfred Kastler and Jacques Winter. Gréation optique d'une inégalité de population entre les sous-niveaux zeeman de l'état fondamental des atomes. *J. Phys. Radium*, 13(12):668–9, 1952.

[83] W. B. Hawkins and R. H. Dicke. The polarization of sodium atoms. *Phys. Rev.*, 91(4):1008–1009, Aug 1953.

[84] W. Franzen and A. G. Emslie. Atomic orientation by optical pumping. *Phys. Rev.*, 108(6):1453–1458, Dec 1957.

[85] E. M. Purcell and G. B. Field. Influence of Collisions upon Population of Hyperfine States in Hydrogen. *Astrophysical Journal*, 124:542–+, November 1956.

[86] J. P. Wittke and R. H. Dicke. Redetermination of the hyperfine splitting in the ground state of atomic hydrogen. *Phys. Rev.*, 103(3):620–631, Aug 1956.

[87] Albert W. Overhauser. Polarization of nuclei in metals. *Phys. Rev.*, 92(2):411–415, Oct 1953.

[88] Thomas R. Carver and Charles P. Slichter. Experimental verification of the overhauser nuclear polarization effect. *Phys. Rev.*, 102(4):975–980, May 1956.

[89] Charles P. Slichter. The discovery and demonstration of dynamic nuclear polarization-a personal and historical account.

[90] M. A. Bouchiat, T. R. Carver, and C. M. Varnum. Nuclear polarization in *he*3 gas induced by optical pumping and dipolar exchange. *Phys. Rev. Lett.*, 5(8):373–375, Oct 1960.

[91] R. W. Dunford and T. E. Chupp. Discussion of polarized targets. *AIP Conference Proceedings*, 131(1):194–195, 1985.

[92] T. E. Chupp, M. E. Wagshul, K. P. Coulter, A. B. McDonald, and W. Happer. Polarized, high-density, gaseous ^3he targets. *Phys. Rev. C*, 36(6):2244–2251, Dec 1987.

[93] P.L. Anthony et al. Deep inelastic scattering of polarized electrons by polarized ^{3}He and the study of the neutron spin structure. *Phys. Rev. D*, 54(11):6620–6650, Dec 1996.

[94] K. Abe, T. Akagi, B. D. Anderson, P. L. Anthony, R. G. Arnold, T. Averett, H. R. Band, C. M. Berisso, P. Bogorad, H. Borel, P. E. Bosted, V. Breton, M. J. Buenerd, G. D. Cates, T. E. Chupp, S. Churchwell, K. P. Coulter, M. Daoudi, P. Decowski, R. Erickson, J. N. Fellbaum, H. Fonvieille, R. Gearhart, V. Ghazikhanian, K. A. Griffioen, R. S. Hicks, and R. Holmes. Precision determination of the neutron spin structure function $g1n$. *Phys. Rev. Lett.*, 79(1):26–30, Jul 1997.

[95] B. Larson, O. Häusser, P. P. J. Delheij, D. M. Whittal, and D. Thiessen. Optical pumping of rb in the presence of high-pressure *he*3 buffer gas. *Phys. Rev. A*, 44(5):3108–3118, Sep 1991.

[96] N. R. Newbury, A. S. Barton, P. Bogorad, G. D. Cates, M. Gatzke, B. Saam, L. Han, R. Holmes, P. A. Souder, J. Xu, and D. Benton. Laser polarized muonic helium. *Phys. Rev. Lett.*, 67(23):3219–3222, Dec 1991.

[97] N. R. Newbury, A. S. Barton, P. Bogorad, G. D. Cates, M. Gatzke, B. Saam, L. Han, R. Holmes, P. A. Souder, J. Xu, and D. Benton. Errata: Laser polarized muonic helium. *Phys. Rev. Lett.*, 69(2):391, Jul 1992.

[98] Hunter Leigh Middleton. *The Spin Structure of the Neutron Determined Using a Polarized ^{3}He Target*. PhD thesis, Princeton University, 1994.

[99] Mikhail V. Romalis. *Laser Polarizaed* ^{3}He *Target Used for a Precision Measurement of the Neutron Spin Structure*. PhD thesis, Princeton University, 1997.

[100] John Steffen Jensen. *Measurement of the Neutron (^{3}He) Spin Structure Function at Low Q^2: A Connection Between the Bjorken and Drell-Hearn-Gerasimov Sum Rules*. PhD thesis, California Institute of Technology, 2000.

[101] Ioannis Kominis. *Measurement of the Neutron (*^{3}He *) Spin Structure at Low Q^2 and the Extended Gerasimov-Drell-Hearn Sum Rule*. PhD thesis, Princeton University, 2001.

[102] Alexandre Deur. *Experimental Study of the spin structure of the Neutron (*^{3}He *) at Low Q^2: A Connection between the Bjorken and Gerasimov-Drell-Hearn Sum Rules*. PhD thesis, Universite Blaise Pascal, 2000.

[103] Karl J. Slifer. *Spin Structure of* ^{3}He *and the Neutron at Low* Q^2*; A Measurement of the Extended GDH Integral and the Burkhardt-Cottingham Sum Rule*. PhD thesis, Temple University, 2004.

[104] Xiaochao Zheng. *Precision Measurement of Neutron Spin Asymmetry* A_1^n *at Large* x_{bj} *Using CEBAF at 5.7 GeV*. PhD thesis, Massachusetts Institute of Technology, 2002.

[105] Kevin M. Kramer. *A Search for Higher Twist Effects the Neutron Spin Structure Function* $g_2^n(x, Q^2)$. PhD thesis, College of William & Mary, 2003.

[106] M. Amarian, L. Auerbach, T. Averett, J. Berthot, P. Bertin, W. Bertozzi, T. Black, E. Brash, D. Brown, E. Burtin, J. R. Calarco, G. D. Cates, Z. Chai, J.-P. Chen, Seonho Choi, E. Chudakov, E. Cisbani, C. W. de Jager, A. Deur, R. DiSalvo, S. Dieterich, P. Djawotho, M. Finn, K. Fissum, H. Fonvieille, S. Frullani, and H. Gao. Q^2evolution of the generalized gerasimov-drell-hearn integral for the neutron using a ^{3}He target. *Phys. Rev. Lett.*, 89(24):242301, Nov 2002.

Chapter 2

Nucleon Structure via Electron Scattering

2.1 Basic Elements of A Scattering Experiment

2.1.1 Units and Conventions

The speed of light ($c = 1$) and Planck constant divided by 2π ($\hbar = h/2\pi = 1$) are set equal to 1. Momentum and mass can be converted from energy units by dividing by c and c^2 respectively. One can convert between energy units and distance units by [1]:

$$\hbar c = (0.1973269631 \pm 0.0000000049)\ \text{GeV} \cdot \text{fm} \tag{2.1}$$

A useful approximation based on this relationship between energy and distance is:

$$\big(\text{energy scale}\big) \times (\text{size scale}) \approx \frac{1\ \text{GeV} \cdot \text{fm}}{5} \tag{2.2}$$

All vectors are relativistic four-vectors ($x = x^{\mu} = (x_0, \vec{x})$), unless noted otherwise. Three dimensional spatial vectors will be denoted with arrows. The metric tensor is given by:

$$g_{\mu\nu} = \begin{bmatrix} 1 & 0 & 0 & 0 \\ 0 & -1 & 0 & 0 \\ 0 & 0 & -1 & 0 \\ 0 & 0 & 0 & -1 \end{bmatrix} \tag{2.3}$$

The Levi-Civita symbol is defined in the following way using the Bjorken & Drell convention [2]:

$$\varepsilon_{\mu\nu\alpha\beta} = \left\{ \begin{array}{ll} +1 & (\mu\nu\alpha\beta) = \text{even permutation of (0123)} \\ -1 & (\mu\nu\alpha\beta) = \text{odd permutation of (0123)} \\ 0 & \text{otherwise} \end{array} \right\} \tag{2.4}$$

Note also that $\varepsilon^{\mu\nu\alpha\beta} = -\varepsilon_{\mu\nu\alpha\beta}$. All quantities are evaluated in the lab frame, unless otherwise noted.

2.1.2 Kinematic Variables

We'll only consider the case for a fixed target experiment. The kinematic variables are depicted in the Feynman diagram on the left half of Fig. (2.1). The incoming and outgoing electron momenta are p and p' respectively:

$$p = (E, \vec{p}) \qquad p' = (E', \vec{p}') \tag{2.5}$$

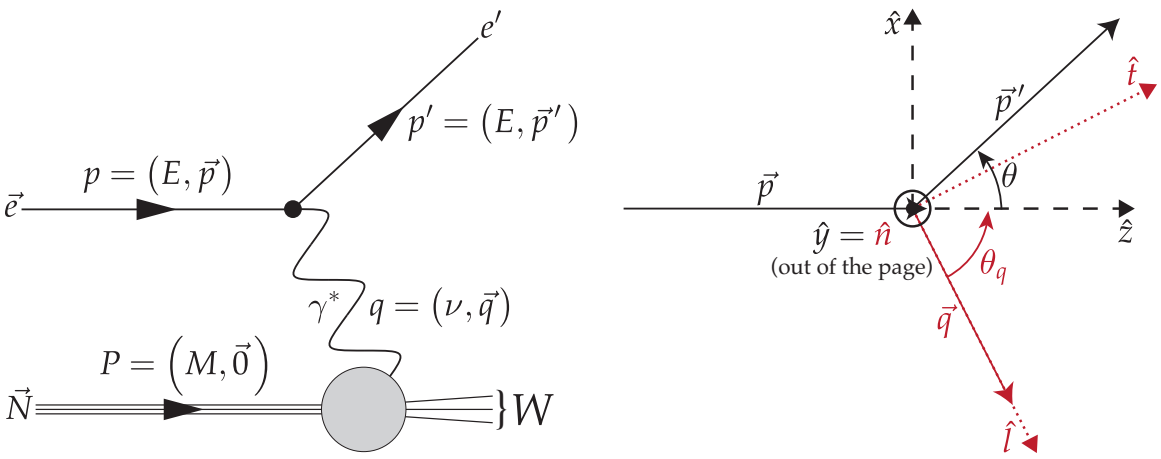

Figure 2.1: Kinematic Variables & Coordinate Systems for Electron Scattering

At JLab energies $E \gg m$, we can safely ignore the small electron rest mass (m):

$$p^2 = 0 \leftrightarrow E = |\vec{p}| \qquad p'^2 = 0 \leftrightarrow E' = |\vec{p}'| \tag{2.6}$$

The scattering angle between the incoming and outgoing electron is θ:

$$\vec{p} \cdot \vec{p}' = EE' \cos(\theta) \tag{2.7}$$

The momentum transfer carried by the exchanged virtual photon is q:

$$p - p' = q = (\nu, \vec{q}) \tag{2.8}$$

where the energy lost by the scattering electron is ν:

$$\nu = E - E' \geq 0 \tag{2.9}$$

By convention, the square of the invariant four-momentum transfer is $Q^2 = -q^2$:

$$Q^2 = \vec{q}^2 - \nu^2 = 2EE'(1 - \cos(\theta)) = 4EE' \sin^2\left(\frac{\theta}{2}\right) \tag{2.10}$$

The initial momentum of a target particle with rest mass M is:

$$P = \left(M, \vec{0}\right) \tag{2.11}$$

The total momentum of carried away by the decay products is P':

$$p + P = p' + P' \rightarrow P' = q + P \tag{2.12}$$

The invariant mass of the decay products is W:

$$P'^2 = W^2 = P^2 + 2q \cdot P + q^2 \tag{2.13}$$

which can be rewritten as:

$$W^2 = M^2 + 2M\nu - Q^2 \tag{2.14}$$

Three useful unitless quantities are the fraction of energy loss in the lab frame y, the Bjorken scaling variable x, and the parameter that completely specifies the virtual

photon polarization vector ε (see Sec. (2.5.7)):

$$y = \frac{q \cdot P}{p \cdot P} = \frac{\nu}{E} \tag{2.15}$$

$$x = \frac{Q^2}{2M\nu} \tag{2.16}$$

$$\varepsilon = \left[1 + \frac{2\vec{q}^2}{Q^2} \tan^2\left(\frac{\theta}{2}\right)\right]^{-1} \tag{2.17}$$

The smallest energy loss occurs for elastic scattering $W_{\min} = M$:

$$\nu_{\min} = \frac{Q^2}{2M} \tag{2.18}$$

$$x_{\max} = 1 \tag{2.19}$$

which can be solved to give:

$$y_{\min} = \frac{\nu_{\min}}{E} = \frac{\left(2E/M\right)\sin^2\left(\frac{\theta}{2}\right)}{1 + \left(2E/M\right)\sin^2\left(\frac{\theta}{2}\right)} \tag{2.20}$$

$$\frac{E'_{\max}}{E} = \frac{1}{1 + \left(2E/M\right)\sin^2\left(\frac{\theta}{2}\right)} \tag{2.21}$$

This also corresponds to the largest Q^2:

$$Q^2_{\max} = \frac{4E^2\sin^2\left(\frac{\theta}{2}\right)}{1 + \left(2E/M\right)\sin^2\left(\frac{\theta}{2}\right)} \tag{2.22}$$

Finally, plugging $\nu = \nu_{\min}$ into Eqn. (2.10) gives τ which is a common kinematic factor used *for elastic scattering only*:

$$\tau = \frac{Q^2}{4M^2} = \frac{\vec{q}^2}{Q^2} - 1 = \frac{\nu^2}{Q^2} \tag{2.23}$$

For the case of the largest energy loss, we cannot ignore the electron rest mass m and in this case $p' = (m, \vec{0})$, which gives:

$$E'_{\text{min}} = m \tag{2.24}$$

$$\nu_{\text{max}} = E - m \tag{2.25}$$

$$y_{\text{max}} = 1 - \frac{m}{E} \tag{2.26}$$

$$Q^2_{\text{min}} = 2Em \tag{2.27}$$

$$x_{\text{min}} = \frac{m}{M\left(1 - \frac{m}{E}\right)} \tag{2.28}$$

$$\frac{W_{\text{max}}}{M} = \sqrt{1 + \frac{2E}{M}\left(1 - \frac{m}{E} - \frac{m}{M}\right)} \tag{2.29}$$

2.1.3 Coordinate Systems

For inclusive scattering experiments, there are two coordinate systems useful for describing the kinematics, see right half of Fig. (2.1). The zxy-system is defined with respect to the incident electron momentum $\vec{p}$ where $\hat{z} = \hat{p}$. The ltn-system ($l$ongitudinal, $t$ransverse, $n$ormal) is defined with respect to the momentum transfer vector $\vec{q}$ where $\hat{q} = \hat{l}$. The incident & scattered electron momenta and consequently the q-vector all lie in the scattering plane which is defined by zx or equivalently lt. The $\hat{2}$ ($= \hat{y} = \hat{n}$) direction is normal to this plane and, by choice, points up. Applying the conservation of momentum gives:

$$\vec{p} = E\hat{z} = E\left(\hat{l}\cos(\theta_q) + \hat{t}\sin(\theta_q)\right) \tag{2.30}$$

$$\vec{p}' = E'\left(\hat{z}\cos(\theta) + \hat{x}\sin(\theta)\right) = E'\left(\hat{l}\cos(\theta + \theta_q) + \hat{t}\sin(\theta + \theta_q)\right) \tag{2.31}$$

$$\vec{q} = \vec{p} - \vec{p}' = \left(E - E'\cos(\theta)\right)\hat{z} - E'\sin(\theta)\hat{x} \tag{2.32}$$

where the zxy unit vectors are ($\theta \neq 0$):

$$\hat{z} = \hat{p} = \hat{l}\cos(\theta_q) + \hat{t}\sin(\theta_q) \tag{2.33}$$

$$\hat{x} = \frac{\hat{p}' - \hat{p}\cos(\theta)}{\sin(\theta)} = \hat{t}\cos(\theta_q) - \hat{l}\sin(\theta_q) \tag{2.34}$$

$$\hat{y} = \frac{\hat{p} \times \hat{p}'}{\sin(\theta)} = \hat{n} \tag{2.35}$$

the ltn units vectors are:

$$\hat{l} = \hat{q} = \hat{z}\cos(\theta_q) - \hat{x}\sin(\theta_q) \tag{2.36}$$

$$\hat{t} = \hat{n} \times \hat{l} = \hat{x}\cos(\theta_q) + \hat{z}\sin(\theta_q) \tag{2.37}$$

$$\hat{n} = \hat{y} \tag{2.38}$$

and finally θ_q is the angle between $\vec{p}$ & $\vec{q}$:

$$\cos(\theta_q) = \frac{E - E'\cos(\theta)}{|\vec{q}|} \tag{2.39}$$

$$\sin(\theta_q) = \frac{E'\sin(\theta)}{|\vec{q}|} \tag{2.40}$$

where $|\vec{q}| = \sqrt{Q^2 + \nu^2}$.

2.1.4 Measuring Cross Sections

In a typical scattering experiment, one fires a beam of particles at an interaction region filled with target centers. If the target center density is very dilute, then the rate at which the detector counts the scattered beam particles $N_{\text{count}}/\Delta t$ is given by:

$$\frac{N_{\text{count}}}{\Delta t} = \frac{N_{\text{beam}}}{\Delta t} \times p_{\text{int}} \times p_{\text{det}} \tag{2.41}$$

where $N_{\text{beam}}/\Delta t$ is the average number of incident beam particles per unit time, p_{int} is the interaction probability, and p_{det} is the detection probability. The interaction probability is given by:

$$p_{\text{int}} = \frac{\text{total effective area of target centers}}{\text{total area of the interaction region}} = \frac{\rho V_{\text{int}} \sigma}{A_{\text{int}}} = \rho L_{\text{int}} \sigma \tag{2.42}$$

where ρ is the number of target centers per unit volume, σ is the effective cross sectional area of each target center, and V_{int}, A_{int}, & L_{int} are the volume, cross sectional area, & length of the interaction region. The detection probability is given by:

$$p_{\text{det}} = \big(\text{detector efficiency}\big) \times (\text{effective size of the detector}) = f_{\text{det}} \Delta\Omega \tag{2.43}$$

where f_{det} is the detector efficiency and $\Delta\Omega$ is the solid angle subtended by the detector which can be estimated by:

$$\Delta\Omega = \frac{A_{\text{det}}}{4\pi r_{\text{det}}^2} \tag{2.44}$$

where A_{det} is the physical area of the detector and r_{det} is the distance of the detector from the target. All of the intrinsic properties of the scattering process are isolated in the differential scattering cross section given by:

$$\frac{d\sigma}{d\Omega} = \frac{(N_{\text{count}}/\Delta t)/f_{\text{det}}}{(N_{\text{beam}}/\Delta t)\rho\,(L_{\text{int}}\Delta\Omega)} \tag{2.45}$$

If the energy of the scattered particle is measured and not constrained kinematically, then the formula is generalized to include the size of the energy bin $\Delta E'$:

$$\frac{d^2\sigma}{d\Omega dE'} = \frac{(N_{\text{count}}/\Delta t)/f_{\text{det}}}{(N_{\text{beam}}/\Delta t)\rho\,(L_{\text{int}}\Delta\Omega)\,\Delta E'} \tag{2.46}$$

Finally, the relative uncertainty in the cross section due only to counting statistics ($\sigma_N = \sqrt{N}$) is given by $1/\sqrt{N_{\text{count}}}$ [3].

2.1.5 Asymmetries & Cross Section Differences

We'll consider cross sections in the Born approximation [4]. Quantum mechanically, this amounts to the assumption that the incoming and outgoing particles can be described by a plane wave. In the language of quantum field theory, this is equivalent to the one photon exchange diagram. For electromagnetic processes, this approximation is valid for $Z\alpha \ll 1$, where $\alpha \approx 1/137$ is the fine structure constant. In experiments where both the beam and target are polarized, the differential cross section can be written with both spin-independent & spin-dependent parts. We'll only consider the case of a longitudinally polarized beam, Sec. (2.4.2), with a helicity defined by $h_b = \hat{s}\cdot\hat{p}$, where the incident electron spin unit vector is given by $\hat{s} = \pm\hat{p}$. In this case, the differential cross section can be written as:

$$\sigma(h_b\hat{P}_t) = \left(\frac{d\sigma}{d\Omega}\right)_{h_b\hat{P}_t} \text{ or } \left(\frac{d^2\sigma}{d\Omega dE'}\right)_{h_b\hat{P}_t} = \bar{\sigma}\left(1 + h_b\hat{P}_t\cdot\left[\overleftrightarrow{A}\,\hat{q}\right]\right) \tag{2.47}$$

where $\bar{\sigma}$ is the unpolarized cross section (spin-independent part), $\hat{P}_t$ is the target polarization unit vector, $\hat{q}$ is the momentum transfer unit vector, and $\overleftrightarrow{A}$ is the asym-

metry matrix (spin-dependent part) defined with respect to the q-vector (lt axes):

$$\overleftrightarrow{A} = (A_{\text{long}}) \cdot \overleftrightarrow{1} + (A_{\text{trans}}) \cdot \hat{n} \times \qquad A_{\text{long}} = A_{\text{TT}} \qquad A_{\text{trans}} = A_{\text{LT}} \tag{2.48}$$

where $\overleftrightarrow{1}$ is the identity matrix, A_{long} is the longitudinal asymmetry (due to the transverse polarization of the virtual photon, Sec. (2.5.7)), A_{trans} is the transverse asymmetry (due to the interference between the longitudinal and transverse polarizations of the virtual photon, Sec. (2.5.7))), $\hat{n}$ is the unit vector normal to the scattering plane, and $\times$ refers to a cross product. As we'll see later in both polarized elastic & inelastic scattering, these two asymmetries naturally encode a more convenient separation of the physics. Experimentally, however, it is usually easier to measure the two asymmetries $A_{\parallel}$ & $A_{\perp}$ that are formed with respect to the target orientation relative to the zx axes:

$$A_{\parallel} = \frac{\sigma^{\overrightarrow{\Rightarrow}} - \sigma^{\overrightarrow{\Leftarrow}}}{\sigma^{\overrightarrow{\Rightarrow}} + \sigma^{\overrightarrow{\Leftarrow}}} \tag{2.49}$$

$$A_{\perp} = \frac{\sigma^{\overrightarrow{\Uparrow}} - \sigma^{\overrightarrow{\Uparrow}}}{\sigma^{\overrightarrow{\Uparrow}} + \sigma^{\overrightarrow{\Uparrow}}} \tag{2.50}$$

where $\rightarrow$ ($\leftarrow$) refers to positive (negative) beam helicity $h_b = +(-)$ and $\Rightarrow$ ($\Uparrow$) refers to a longitudinally (transversely) polarized target with a polarization unit vector of $\hat{P}_t = +\hat{z}(\hat{x})$. These two sets of asymmetries can be related to each other by a rotation in the scattering plane about the normal unit vector by the angle θ_q:

$$\begin{pmatrix} A_{\parallel} \\ A_{\perp} \end{pmatrix} = \begin{pmatrix} \cos(\theta_q) & \sin(\theta_q) \\ -\sin(\theta_q) & \cos(\theta_q) \end{pmatrix} \begin{pmatrix} A_{\text{long}} \\ A_{\text{trans}} \end{pmatrix} \tag{2.51}$$

Averaging over the beam helicity yields the unpolarized cross section (as expected):

$$\frac{1}{2}\sum_{h_b}\sigma(h_b\hat{P}_t) = \frac{\sigma(+\hat{P}_t)+\sigma(-\hat{P}_t)}{2} = \frac{\sigma^{\rightrightarrows}+\sigma^{\rightleftarrows}}{2} = \frac{\sigma^{\uparrow\uparrow}+\sigma^{\uparrow\downarrow}}{2} = \bar{\sigma} \tag{2.52}$$

The cross section difference between the two beam helicities $(\Delta\sigma)_{\hat{P}_t}$ is given by:

$$(\Delta\sigma)_{\hat{P}_t} = \sigma(+\hat{P}_t)-\sigma(-\hat{P}_t) = 2\bar{\sigma}\hat{P}_t\cdot[\overleftrightarrow{A}\,\hat{q}] = 2\bar{\Delta}_{\hat{P}_t} \tag{2.53}$$

$$(\Delta\sigma)_{\parallel} = \sigma^{\rightrightarrows}-\sigma^{\rightleftarrows} = 2\bar{\sigma}\hat{z}\cdot[\overleftrightarrow{A}\,\hat{q}] = 2\bar{\sigma}A_{\parallel} = 2\bar{\Delta}_{\parallel} \tag{2.54}$$

$$(\Delta\sigma)_{\perp} = \sigma^{\uparrow\uparrow}-\sigma^{\uparrow\downarrow} = 2\bar{\sigma}\hat{x}\cdot[\overleftrightarrow{A}\,\hat{q}] = 2\bar{\sigma}A_{\perp} = 2\bar{\Delta}_{\perp} \tag{2.55}$$

where $\bar{\Delta}_{\hat{P}_t}$ is the *mean* cross section difference. For an arbitrary target orientation, the asymmetry is given by:

$$A = \frac{\sigma^{\rightarrow}-\sigma^{\leftarrow}}{\sigma^{\rightarrow}+\sigma^{\leftarrow}} = \hat{P}_t\cdot\left[\overleftrightarrow{A}\,\hat{q}\right] = \left[\hat{P}_t\cdot\hat{z}\right]A_{\parallel}+\left[\hat{P}_t\cdot\hat{x}\right]A_{\perp} \tag{2.56}$$

$$= \left[\hat{P}_t\cdot\hat{q}\right]A_{\text{long}}+\left[\hat{P}_t\cdot(\hat{n}\times\hat{q})\right]A_{\text{trans}} \tag{2.57}$$

Finally, we'll consider the practical case when the beam & target polarizations are non-unity (< 1) and when there is some unpolarized background. In this case the total cross section is an average over the four possible combinations of beam helicity & target orientation $\{$ $(h_b = +1, +\hat{P}_t)$, $(h_b = -1, +\hat{P}_t)$, $(h_b = +1, -\hat{P}_t)$, $(h_b = -1, -\hat{P}_t)\}$ and the cross section for the unpolarized background $\bar{\sigma}_B$. The fraction of target particles is given by f and the fraction of background particles by $(1-f)$. Each configuration is weighted by the fraction of the beam particles with $\pm$ helicity $(1\pm P_b)/2$ and by the fraction of target particles with $\pm$ orientation $(1\pm P_t)/2$ where P_b & P_t are the beam & target polarizations. This weighted average cross section is

given by:

$$\begin{aligned}\sigma &= f\left[\frac{1+P_b}{2}\right]\left[\frac{1+P_t}{2}\right]\sigma(h_b=1,\hat{P}_t) + f\left[\frac{1-P_b}{2}\right]\left[\frac{1+P_t}{2}\right]\sigma(h_b=-1,\hat{P}_t) \\ &\quad + f\left[\frac{1+P_b}{2}\right]\left[\frac{1-P_t}{2}\right]\sigma(h_b=1,-\hat{P}_t) + f\left[\frac{1-P_b}{2}\right]\left[\frac{1-P_t}{2}\right]\sigma(h_b=-1,-\hat{P}_t) \\ &\quad + (1-f)\bar{\sigma}_B \end{aligned} \tag{2.58}$$

After some algebra, we find that the it can be written as:

$$\sigma(P_b,\vec{P}_t) = f\bar{\sigma}\left(1 + P_b\vec{P}_t\cdot\left[\overleftrightarrow{A}\,\hat{q}\right]\right) + (1-f)\bar{\sigma}_B \tag{2.59}$$

where the P_b is the beam polarization and $\vec{P}_t = P_t\hat{P}_t$ is the target polarization vector. The measured or raw asymmetry A_{raw} that is formed when the beam polarization is flipped is related to the physics asymmetry A by:

$$A_{\text{raw}} = \frac{\sigma(+P_b,\vec{P}_t) - \sigma(-P_b,\vec{P}_t)}{\sigma(+P_b,\vec{P}_t) + \sigma(-P_b,\vec{P}_t)} = DP_bP_tA \tag{2.60}$$

where the dilution factor D is given by:

$$D = \left[1 + \left(\frac{1-f}{f}\right)\frac{\bar{\sigma}_B}{\bar{\sigma}}\right]^{-1} \tag{2.61}$$

where f is the fraction of target particles and $\bar{\sigma}_B$ is the unpolarized cross section of the background. The absolute uncertainty in the raw asymmetry due only to counting statistics ($\sigma_N = \sqrt{N}$) is given by:

$$\sigma_{\text{raw}} = \sqrt{\frac{4N^{\rightarrow}N^{\leftarrow 2} + 4N^{\rightarrow 2}N^{\leftarrow}}{N^4}} = \sqrt{\frac{1-A_{\text{raw}}^2}{N}} \tag{2.62}$$

where $N = N^{\rightarrow} + N^{\leftarrow}$ is the total number of counts, $N^{\overrightarrow{\leftarrow}} = N(1 \pm A_{\text{raw}})/2$ is the total number of counts for $\pm$ beam helicity, and $A_{\text{raw}} = (N^{\rightarrow} - N^{\leftarrow})/(N^{\rightarrow} + N^{\leftarrow})$ is the raw asymmetry. This can be propagated through to the absolute uncertainty in the physics asymmetry A due only to the counting statistics from A_{raw}:

$$\sigma_A = \frac{1}{P_b P_t D\sqrt{N}} \tag{2.63}$$

where we've ignored the higher order effect of A_{raw}^2 which is negligible when $A_{\text{raw}} \ll 1$. To achieve an absolute precision of σ_A when the uncertainty is dominated by counting statistics, the minimum total number of counts must be:

$$N_{\text{min}} = \frac{1}{(P_b P_t D\sigma_A)^2} \tag{2.64}$$

2.1.6 The Scale for Cross Sections: Rutherford Formula

For the nonrelativistic case of elastic scattering of a beam of spinless point particles with charge Z_{beam} from a target of heavy (i.e. no recoil) spinless point particles of charge Z_{target} at rest, one can calculate the following differential cross section using classical mechanics [5]:

$$\frac{d\sigma}{d\Omega} = \frac{Z_{\text{beam}}^2 Z_{\text{target}}^2 \alpha^2}{16 T_{\text{KE}}^2 \sin^4\left(\frac{\theta}{2}\right)} \tag{2.65}$$

where α is the fine structure constant, T_{KE} is the kinetic energy of the beam particles, and θ is the scattering angle. This is the famous Rutherford scattering formula (in modern notation) and, generalized to relativistic beam velocities, it contains the

basic ingredients for all of the forthcoming scattering formulas:

$$\frac{d\sigma}{d\Omega} = \underbrace{\left[\frac{\alpha^2}{4E^2\beta^4\sin^4\left(\frac{\theta}{2}\right)}\right]}_{\text{scale}} \times \overbrace{\left[Z_{\text{beam}}\right]^2}^{\text{structure of beam}} \times \underbrace{\left[Z_{\text{target}}\right]^2}_{\text{structure of target}} \tag{2.66}$$

where E & β are the relativistic energy & speed of the beam particles. The electromagnetic structure of a point particle is given by its global properties. In the case of a spinless point particle, the only structure is it's charge Z. Next we'll consider the case for a beam with non-zero spin.

2.1.7 Beam with Spin: Mott Formula

The differential cross section for a relativistic beam of Dirac (spin-1/2 point) particles with charge $Z_{\text{beam}} = \pm 1$ elastically scattering from a heavy (i.e. no recoil) spinless point particle with charge Z was first derived by Mott in 1929 [6]. To lowest order in α for a beam of particles moving at a speed β, it is given by:

$$\frac{d\sigma}{d\Omega} = \left[\frac{\sigma_R}{\beta^4}\right] \times \left[1 - \beta^2 \sin^2\left(\frac{\theta}{2}\right)\right] \times [Z]^2 \tag{2.67}$$

where we've defined the scale to be the Rutherford cross section:

$$\left(\frac{d\sigma}{d\Omega}\right)_{\text{Rutherford}} = \sigma_R = \frac{\alpha^2}{4E^2\sin^4\left(\frac{\theta}{2}\right)} \tag{2.68}$$

In high energy electron scattering, $\beta = 1$ and, by convention, the first two terms are collectively known as the Mott cross section. This quantity sets the scale for

electron scattering experiments:

$$\left(\frac{d\sigma}{d\Omega}\right)_{\text{Mott}} = \sigma_M \equiv \sigma_R \cos^2\left(\frac{\theta}{2}\right) = \frac{\alpha^2}{4E^2 \sin^4\left(\frac{\theta}{2}\right)} \cos^2\left(\frac{\theta}{2}\right) \tag{2.69}$$

2.1.8 Target with Structure: Form Factors & Charge Distributions

If the heavy spinless target particles have some finite extent, then the Mott formula is multiplied by a quantity encodes these deviations from point scattering:

$$\frac{d\sigma}{d\Omega} = \left[\left(\frac{d\sigma}{d\Omega}\right)_{\text{Mott}}\right] \times \left|F\left(Q^2\right)\right|^2 \tag{2.70}$$

where $F\left(Q^2\right)$ is known as the form factor. An early derivation of this formula in the context of electron scattering from nuclei was given by Rose in 1948 [7]. All we've really done is replaced a constant (Z) with a function ($F\left(Q^2\right)$) which depends on Q^2. The form factor is normalized such that $F(0) = Z$. Therefore, the form factor for a point particle is just $F\left(Q^2\right) = Z$.

The physical interpretation of a form factor is straightforward at sufficiently low energies when $Q^2 \approx \vec{q}^2$. It is the Fourier transform of the charge distribution of the target:

$$F(Q^2) = \int \rho(\vec{r})\, e^{i\vec{q}\cdot\vec{r}}\, d^3r \tag{2.71}$$

The gross features of nuclear charge distributions are well described by the spherically symmetric Fermi distribution [8]:

$$\rho(r) = \rho_1(Z, A)\left[1 + \exp\left(\frac{r - c(A)}{z_1}\right)\right]^{-1} \tag{2.72}$$

where the parameters are given by:

$$\rho_1(Z,A) = \left(\frac{0.19/\text{fm}^3}{1+2.6/\sqrt[3]{A^2}}\right)\cdot\frac{Ze}{A} \qquad c(A) = (1.07\text{ fm})\cdot\sqrt[3]{A} \qquad z_1 = 0.55\text{ fm} \quad (2.73)$$

where ρ_1 is the central charge density, $c(A)$ encodes the size of the nucleus, and z_1 is a universal parameter that describes that size of the edge roll-off (skin thickness). This distribution is essentially flat at the center with an exponentially decaying edge. It underestimates (overestimates) the charge density at the center of light (heavy) nuclei. One method to parametrize the detailed shape of nuclear charge distributions was developed by Sick [9] using a sum of Gaussians (SOG):

$$\rho(r) = \frac{F(0)}{2(\gamma\sqrt{\pi})^3}\sum_{i=1}^{n}\frac{Q_i}{1+2R_i^2/\gamma^2}\left[\exp\left(-\frac{(r-R_i)^2}{\gamma^2}\right)+\exp\left(-\frac{(r+R_i)^2}{\gamma^2}\right)\right] \quad (2.74)$$

where γ is the width of the Gaussians, R_i is the relative position of the i-th Gaussian, Q_i the fraction of charged enclosed by the i-th Gaussian such that $\sum_{i=1}^{n} Q_i = 1$. $\{R_i, Q_i\}$ are obtained by fits to the data. A benefit to this parameterization is that the form factor can be represented using the same parameters by a simple form in a model independent way:

$$F(Q) = F(0)\exp\left(-\frac{Q^2\gamma^2}{4}\right)\sum_{i=1}^{n}\frac{Q_i}{1+2R_i^2/\gamma^2}\left[\cos(QR_i)+\left(\frac{2R_i^2}{\gamma^2}\right)\frac{\sin(QR_i)}{QR_i}\right] \quad (2.75)$$

where the normalization is given by $4\pi\int_0^\infty r^2\rho(r)\,dr = F(0)$. A comparison among the form factors (left) and their corresponding charge distributions (right) for six different spinless nuclei is depicted in Fig. (2.2). The solid blue line is the SOG charge distribution and the dashed red line gives the equivalent Fermi charge distribution.

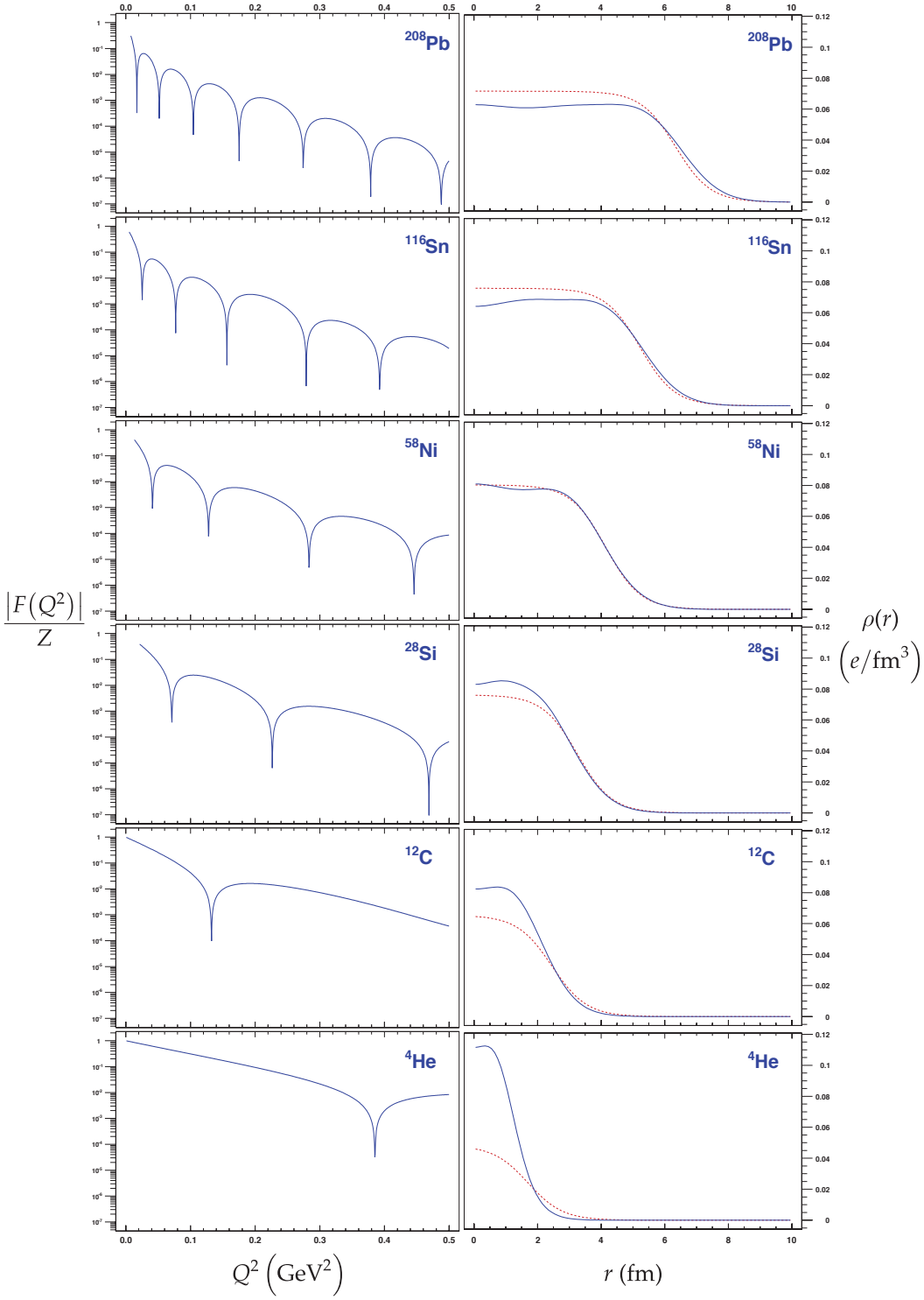

Figure 2.2: Form Factors & Nuclear Charge Distributions. Solid blue lines are from a SOG parameterization [10] and dashed red lines are Fermi distributions [8].

2.2 Magnetic Moments

2.2.1 Point Particles

Quantum mechanics requires that the magnetic moment vector $\vec{\mu}$ of a spin-S particle be proportional to its spin vector $\vec{S}$:

$$\vec{\mu} = \mu \left(\frac{\vec{S}}{S} \right) \tag{2.76}$$

where μ is its magnetic moment. The magnetic moment of a spin-1/2 point particle is prescribed by the Dirac equation to be [11]:

$$\mu_{\text{Dirac}} = \frac{Ze}{2M} \tag{2.77}$$

where Z & M are the particle's charge & mass respectively and e is the elementary unit of charge. The magnetic moments of a Dirac electron and Dirac proton are:

$$\mu_e = -\mu_{\text{B}} \qquad\qquad \mu_p = +\mu_{\text{N}} \tag{2.78}$$

where μ_B is the Bohr magneton:

$$\mu_B = \frac{e}{2m} = \frac{e\hbar}{2m}\,(\text{SI}) = \frac{e\hbar}{2mc}\,(\text{cgs}) \tag{2.79}$$

where m is the mass of the electron and μ_N is the nuclear magneton:

$$\mu_N = \frac{e}{2M_p} = \frac{e\hbar}{2M_p}\,(\text{SI}) = \frac{e\hbar}{2M_pc}\,(\text{cgs}) \tag{2.80}$$

where M_p is the mass of the proton. In general, nuclear (atomic) magnetic moments are written as:

$$\mu = g\mu_{N(B)}S \tag{2.81}$$

where g is called the g-factor.

The *classical* magnetic moment for a charged particle with orbital angular momentum $\vec{L}$ is [12]:

$$\vec{\mu} = \left(\frac{Ze}{2M}\right)\vec{L} \tag{2.82}$$

It is for this reason (by analogy) that the *intrinsic quantum mechanical* magnetic moment for a particle is also written as:

$$\vec{\mu} = g^\star\left(\frac{Ze}{2M}\right)\vec{S} \tag{2.83}$$

where $g^\star$ is also called the g-factor. The $\star$ is included to avoid confusion between the forms of the g-factor, which are related by:

$$\mu = g^\star\left(\frac{Ze}{2M}\right)S = g\mu_N S \tag{2.84}$$

$$g^\star = \frac{g}{Z}\left(\frac{M}{M_p}\right) \tag{2.85}$$

Similar equations can be written for atomic magnetic moments by replacing M_p with m and μ_N with μ_B. Note that for the electron & proton, $g = g^\star$, and for the neutron, $g^\star$ is undefined because an uncharged point particle would not be expected to have a magnetic moment. The natural choice appears to be the $g^\star$ convention since it measures a particle's magnetic moment in units of its own mass, whereas g measures a particle's magnetic moment in units of the proton's mass. On the

other hand, a benefit to the g convention is that, unlike $g^\star$, g is well-defined for a neutral particle. As we'll explore later, these two conventions lead to two different definitions for the anomalous magnetic moment.

The ratio of the magnetic moment to the spin of a point particle is given strictly by its charge to mass ratio:

$$\left(\frac{\mu}{S}\right)_{\text{point}} = \left(\frac{Z}{M}\right) e = \left(\frac{Z}{M}\right) 2\mu_{\text{N}} M_p \;\Rightarrow\; \mu_{\text{point}} = \left(\frac{Ze}{M}\right) S \tag{2.86}$$

which implies that $g^\star = 2$ for all point particles regardless of spin. To be explicit, by "point" particle, we mean, following Kim & Tsai [13], that it does not: (1) couple via the strong interaction, (2) have a permanent electric dipole moment, and (3) have any radiative corrections (it's a "bare" particle). There is some disagreement in the literature about what the magnetic moment for such a particle should be.

Using the formalism of Fierz & Pauli [14], Belinfante conjectured [15] that the magnetic moment for all point particles is given by:

$$\mu_{\text{point}}^{\text{Belinfante}} = \left(\frac{Ze}{2M}\right) \tag{2.87}$$

which implies that $g^\star = 1/S$. A key ingredient to the argument $g^\star = 1/S$ is the "minimal electromagnetic interaction" prescription [16]. In this prescription, one writes down the free Lagrangian for a field, performs a local gauge transformation, adds terms that couple the field to the electromagnetic field, and keeps only the terms necessary to insure gauge invariance. Pauli showed [17] how these additional terms (now known as Pauli terms) could be added to the Lagrangian that were gauge invariant, but were not required to insure gauge invariance. T.D. Lee showed [18] that fields with spins greater than $1/2$ that follow the "minimal

electromagnetic interaction" prescription do not have unique couplings. Because gauge invariance is not restrictive enough, these "proofs" that $g^\star = 1/S$ really just amounted to the choice that $g^\star = 1/S$.

An alternative approach to deduce $g^\star$ for spin $> 1/2$ point particles is to require that they have "good" high energy behavior. For example, Weinberg [19] and Kim & Tsai [13] have both made the argument that a point particle with "good" high energy behavior will obey the Gerasimov-Drell-Hearn sum rule, Sec. (2.5.6), implying that $g^\star = 2$. Pagels goes a step further [20] arguing that the coefficients of the lowest order terms of the forward Compton amplitude, Sec. (2.5.5), *define* the charge & the anomalous magnetic moment of a particle. This directly implies that $g^\star = 2$ regardless of spin. More recently, this conclusion has been reached using string theory considerations [21], within a general study of the low energy behavior of massive spin-3/2 particles [22], from a calculation of the graviton elastic scattering amplitude [23], and by assuming that helicity (defined in terms of light-cone variables) is conserved to lowest order in the infinite momentum frame [24].

In the Standard Model, additional ingredients (spontaneously broken gauge symmetries, renormalizability) add terms to the Lagrangian that do not strictly follow the "minimal electromagnetic interaction" prescription but do fix $g^\star = 2$ for charged leptons & $W^\pm$ bosons:

$$\mu_{e^\mp} = \mp\frac{e}{2m} \qquad \mu_{\mu^\mp} = \mp\frac{e}{2m_\mu} \qquad \mu_{\tau^\mp} = \mp\frac{e}{2m_\tau} \qquad \mu_{W^\pm} = \pm\frac{e}{M_W} \tag{2.88}$$

It is the $W^\pm$ magnetic moment that discriminates between the two possible forms of $g^\star$ for point particles and identifies $g^\star = 2$. This has been verified experimentally

for the $W^{\pm}$ at tree level [1]:

$$|g^{\star}_{W^{\pm}}| = 2.22^{+0.20}_{-0.19} \tag{2.89}$$

2.2.2 Anomalous Magnetic Moments

The anomalous magnetic moment (amm) is the part of the magnetic moment that differs from the expected point magnetic moment. In other words, the anomalous magnetic moment should be called the anomalous *part* of the magnetic moment. The amm is usually defined in such a way to indicate an excess of charge:

$$\mu = 2\left(Z\frac{M_p}{M} + \kappa\right)\mu_{\mathrm{N}} S = \frac{(Z+\kappa^{\star})\,e}{M} S \tag{2.90}$$

where the two definitions are a direct result of the two conventions for the g-factor. By convention it is a unitless quantity and is related to the g-factors by:

$$\kappa = \frac{g}{2} - Z\frac{M_p}{M} = Z\frac{M_p}{M}\left(\frac{g^{\star}}{2} - 1\right) \tag{2.91}$$

$$\kappa^{\star} = Z\left(\frac{g^{\star}}{2} - 1\right) = \frac{g}{2}\left(\frac{M}{M_p}\right) - Z \tag{2.92}$$

where the two definitions are related to each other by the ratio M/M_p:

$$\frac{\kappa}{M_p} = \frac{\kappa^{\star}}{M} = \frac{\mu - \mu_{\mathrm{point}}}{eS} = \frac{g}{2M_p} - \frac{Z}{M} = \frac{Z}{M}\left(\frac{g^{\star}}{2} - 1\right) \tag{2.93}$$

Recently Ji & Li have suggested [25] yet another definition for the amm:

$$\mu = \frac{\left(2ZS + \kappa_{\mathrm{Ji}}\right)e}{2M} = 2\left(Z + \frac{\kappa_{\mathrm{Ji}}}{2S}\right)\frac{M_p}{M}\mu_{\mathrm{N}} S \tag{2.94}$$

$$\kappa_{\mathrm{Ji}} = 2S\kappa^{\star} = 2S\left(\frac{M}{M_p}\right)\kappa = \left(\frac{gM}{M_p} - 2Z\right)S \tag{2.95}$$

This definition is a generalization of the one made by Pagels [20] for a spin-1 particle with charge of $+1$. Note that for the proton, all of these definitions become degenerate:

$$\kappa_{\text{Ji}}^{p} = \kappa_{p}^{\star} = \kappa_{p} = \frac{g_p}{2} - 1 = +1.793 \tag{2.96}$$

and for the neutron, they are all nearly degenerate because $M_n \approx M_p$:

$$\kappa_{\text{Ji}}^{n} = \kappa_{n}^{\star} = \frac{g_n}{2}\left(\frac{M_n}{M_p}\right) = -1.916 \approx \kappa_n = \frac{g_n}{2} = -1.913 \tag{2.97}$$

Differences among these definitions truly manifest themselves when applied to nuclei with $Z > 1$, $M > M_p$, and $S > 1/2$, see Tab. (2.2). For example, consider the ^{3}He nucleus:

$$\kappa_{\text{Ji}}^{3} = \kappa_{3}^{\star} = \frac{g_3}{2}\left(\frac{M_3}{M_p}\right) - 2 = -8.368 \tag{2.98}$$

$$\kappa_3 = \frac{g_3}{2} - \frac{2M_p}{M_3} = -2.796 \tag{2.99}$$

where M_3 is the ^{3}He nuclear mass. For complete nondegeneracy among the definitions, consider the deuteron:

$$\kappa_{\text{Ji}}^{d} = g_d\left(\frac{M_d}{M_p}\right) - 2 = -0.286 \tag{2.100}$$

$$\kappa_{d}^{\star} = \frac{g_d}{2}\left(\frac{M_d}{M_p}\right) - 1 = -0.143 \tag{2.101}$$

$$\kappa_d = \frac{g_d}{2} - \frac{M_p}{M_d} = -0.072 \tag{2.102}$$

where M_d is the deuteron mass. From an informal survey of the literature, unless otherwise noted, most authors are referring to $\kappa^\star$ when they refer to the anomalous

magnetic moment. Finally we'll note that, for a spin-1 particle with charge of $+1$, Brodsky & Hiller [26] explicitly define the anomalous magnetic moment to be $\kappa^\star$.

2.3 Elastic Scattering

2.3.1 Target with Structure & Spin: Rosenbluth Formula

The differential cross section for a relativistic beam of Dirac particles elastically scattering from a target composed of Dirac particle with charge Z and mass M including the effect of target recoil is

$$\left(\frac{d\sigma}{d\Omega}\right)_{\text{Dirac}} = [\sigma_M] \times \left(\frac{E'}{E}\right) \times Z^2 \left[1 + 2\tau \tan^2\left(\frac{\theta}{2}\right)\right] \tag{2.103}$$

where the factor (E'/E) appears when the recoil of the target is so large that the lab frame is no longer coincident with the center of mass frame and $\tau = Q^2/(4M^2)$ is a kinematic factor often used in elastic scattering given by Eqn. (2.23). A Dirac particle acquires an anomalous magnetic moment $\kappa^\star (\neq 0)$ through radiative corrections [27]. As mentioned before, it can be accounted for by including a Pauli term in the Quantum Electrodynamics (QED) Lagrangian [17]. Propagating this term through gives the following differential cross section for a relativistic beam of Dirac particles elastically scattering from a Dirac particle with an anomalous magnetic moment $\kappa^\star$:

$$\left(\frac{d\sigma}{d\Omega}\right)_{\text{amm}} = [\sigma_M] \times \left(\frac{E'}{E}\right) \times \left[Z^2 + \tau \left\{\kappa^{\star 2} + 2\left[Z + \kappa^\star\right]^2 \tan^2\left(\frac{\theta}{2}\right)\right\}\right] \tag{2.104}$$

Anomalous magnetic moments are often attributed to the effects of a cloud of

virtual particles that surround the bare particle. As the beam particle penetrates the cloud, it "sees" less of the cloud and more of the bare particle. This picture implies that there should be a resolution dependence of the anomalous magnetic moment $\kappa^\star = \kappa^\star\left(Q^2\right)$. This argument can be generalized to the charge as well. Making this argument and consequently these replacements $Z \to F_1\left(Q^2\right)$ and $\kappa^\star \to F_2\left(Q^2\right)$, Rosenbluth obtained the following differential cross section for elastically scattering of a beam of Dirac particles from an extended particle [28]:

$$\begin{aligned}\left(\frac{d\sigma}{d\Omega}\right)_{\text{Rosenbluth}} &= [\sigma_M] \times \left(\frac{E'}{E}\right) \\ &\quad \times \left[F_1^2\left(Q^2\right) + \tau\left\{F_2^2\left(Q^2\right) + 2\left[F_1\left(Q^2\right) + F_2\left(Q^2\right)\right]^2 \tan^2\left(\frac{\theta}{2}\right)\right\}\right]\end{aligned} \tag{2.105}$$

where $F_1\left(Q^2\right)$ and $F_2\left(Q^2\right)$ are the Dirac and Pauli form factors which are normalized at $Q^2 = 0$ in the following way:

$$F_1(0) = Z \tag{2.106}$$

$$F_2(0) = \kappa^\star \tag{2.107}$$

In principle, one could also introduce a pair of form factors for the electron as well. Measurements from electron-positron scattering imply that $|F_1^e\left(Q^2\right)| = 1$ for Q^2 well into the TeV range [1]. In addition, the electron Pauli from factor scales as m^2/Q^2 for $Q^2 \gg m^2$ where m is the electron mass [29]. Therefore, in this context, electrons can reliably be thought of as Dirac particles and the effect of its anomalous magnetic moment is completely negligible.

An alternative set of form factors is commonly used in the literature [30, 31]:

$$G_E(Q^2) = F_1(Q^2) - \tau F_2(Q^2) \tag{2.108}$$

$$G_M(Q^2) = F_1(Q^2) + F_2(Q^2) \tag{2.109}$$

These are known as the Sachs form factors with the following normalizations:

$$G_E(0) = F_1(0) - (0) \cdot F_2(0) = Z \tag{2.110}$$

$$G_M(0) = F_1(0) + F_2(0) = Z + \kappa^\star \tag{2.111}$$

The differential cross section in terms of Sachs form factors can be obtained using:

$$F_1(Q^2) = \frac{G_E(Q^2) + \tau G_M(Q^2)}{1+\tau} \tag{2.112}$$

$$F_2(Q^2) = \frac{G_M(Q^2) - G_E(Q^2)}{1+\tau} \tag{2.113}$$

which gives:

$$\left(\frac{d\sigma}{d\Omega}\right)_{\text{Sachs}} = [\sigma_M] \times \left(\frac{E'}{E}\right) \times \left[\frac{G_E^2(Q^2) + \tau G_M^2(Q^2)}{1+\tau} + 2\tau G_M^2(Q^2) \tan^2\left(\frac{\theta}{2}\right)\right] \tag{2.114}$$

This cross section can be written in terms of the virtual photon polarization [32]:

$$\left(\frac{d\sigma}{d\Omega}\right)_{\text{Sachs}} = [\sigma_M] \times \left(\frac{E'}{E}\right) \times \left(\frac{1}{1+\tau}\right) \underbrace{\left[G_E^2(Q^2) + \frac{\tau}{\varepsilon} G_M^2(Q^2)\right]}_{\text{reduced cross section}} \tag{2.115}$$

By varying the beam energy & scattering angle in such a way that Q^2 (and consequently τ) is fixed, one can attempt to disentangle G_E^2 from G_M^2 by plotting the

reduced cross section as a function of $\tan^2\left(\frac{\theta}{2}\right)$, ε, or some other variable that depends on the scattering angle θ at a fixed Q^2. This procedure is called Rosenbluth separation and is the standard method to obtain G_E & G_M using unpolarized targets. At high (low) Q^2, the unpolarized cross section is, generally speaking, more sensitive to G_M^2 (G_E^2). In either case, the sign of either form factor cannot be determined from Rosenbluth separation alone.

Finally, in general, a spin-S particle will have $2S+1$ form factors [33]. For example, the elastic cross section for an unpolarized spin-1 particle is given by [34]:

$$\frac{d\sigma}{d\Omega} = [\sigma_M] \times \left(\frac{E'}{E}\right) \times \left[A\left(Q^2\right) + B\left(Q^2\right)\tan^2\left(\frac{\theta}{2}\right)\right] \tag{2.116}$$

where the elastic response (or structure) functions A & B are combinations of the charge G_C, quadrupole G_Q, and magnetic G_M form factors as:

$$A\left(Q^2\right) = G_C^2\left(Q^2\right) + \frac{8}{9}\tau^2 G_Q^2\left(Q^2\right) + \frac{2}{3}\tau G_M^2\left(Q^2\right) \tag{2.117}$$

$$B\left(Q^2\right) = \frac{4}{3}\tau(1+\tau)G_M^2\left(Q^2\right) \tag{2.118}$$

The form factors have the normalizations $G_C(0) = Z$, $G_Q(0) = Q^\star$, and $G_M = Z + \kappa^\star$ where $Q^\star$ is the quadrupole moment in units of e/M^2.

2.3.2 Nucleons Inside Nuclear Targets: Quasi-elastic Scattering

In quasi-elastic scattering, the incident lepton scatters off of one of the nucleons inside the nucleus. The struck nucleon remains intact and is ejected out of the nucleus leaving behind a "spectator" nucleus. In the impulse approximation, the cross section for this process can be written as an incoherent sum of the nucleon

elastic cross sections:

$$\left(\frac{d^2\sigma}{d\Omega dE'}\right)_{\text{IA}} = Z\sigma_p^{\text{QE}} + (A-Z)\sigma_n^{\text{QE}} \tag{2.119}$$

where Z is the number of protons (charge of the nucleus) and $(A-Z)$ is the number of neutrons (atomic weight). Due to the motion of the nucleons inside the nucleus and binding effects, the elastic cross sections are smeared out and broadened. This is encoded by an integral over the momentum of the struck nucleon inside the nucleus before the scattering $\vec{k}$ and over the total change in energy of the spectator nucleus ν_s [35]:

$$\begin{aligned}\sigma^{\text{QE}} &= \sigma_M \int\int \left[\frac{G_E^2\left(Q'^2\right) + \tau' G_M^2\left(Q'^2\right)}{1+\tau'} K_2 + 2\tau' G_M^2\left(Q'^2\right)\tan^2\left(\frac{\theta}{2}\right) K_1\right] \\ &\quad \times S\left(\nu_s, \vec{k}\right) \times \delta\left(\nu' - \frac{Q'^2}{2M}\right)\, d\nu_s\, d^3k\end{aligned} \tag{2.120}$$

where K_1 & K_2 are kinematic factors, $\nu' = \nu - \nu_s$ is the energy change of the struck nucleon, $q' = (\nu', \vec{q})$ is the momentum transferred to the struck nucleon, $Q'^2 = -q'^2$, $\tau' = Q'^2/(4M^2)$, M is the mass of the struck nucleon, and the motion & binding effects are given by the nucleon spectral function $S(\nu_s, \vec{k})$. If the struck nucleon is detected in coincidence with the scattered electron, then the cross section also includes effects due to final state interactions:

$$\sigma^{\text{QE+FSI}} = \int \sigma^{QE}(k, k'')F(k'', k')\, d^4k'' \tag{2.121}$$

where $k''(k)$ is the momentum of the struck nucleon immediately after (before) being struck by the electron, k' is the final momentum of the struck nucleon after

leaving the nucleus, and $F(k'', k')$ encodes of the information due to final state interactions.

2.3.3 Polarization Observables

Following Donnelly & Raskin [36] (N.B. the sign convention for Q^2), the polarized part of the elastic scattering cross section for a spin-1/2 can be written as:

$$\bar{\Delta} = -h_b \bar{\sigma} \left[2\tau(1+\tau) G_M^2 v_{\mathrm{T}'} \cos(\theta^\star) - 2(1+\tau)\sqrt{2\tau(1+\tau)} G_E G_M v_{\mathrm{TL}'} \sin(\theta^\star)\cos(\phi^\star) \right] \tag{2.122}$$

where the unpolarized cross section $\bar{\sigma}$ is given by $\left(\frac{d\sigma}{d\Omega}\right)_{\mathrm{Sachs}}$ and the kinematic & geometric factors are given by:

$$v_{\mathrm{T}'} = \tan\left(\frac{\theta}{2}\right)\sqrt{\frac{Q^2}{|\vec{q}|^2} + \tan^2\left(\frac{\theta}{2}\right)} \tag{2.123}$$

$$v_{\mathrm{TL}'} = \frac{-Q^2}{|\vec{q}|^2\sqrt{2}} \tan\left(\frac{\theta}{2}\right) \tag{2.124}$$

$$\cos(\theta^\star) = \hat{P}_t \cdot \hat{q} \tag{2.125}$$

$$\sin(\theta^\star)\cos(\phi^\star) = \hat{P}_t \cdot (\hat{n} \times \hat{q}) \tag{2.126}$$

After some considerable algebra, for elastic scattering only, we can derive the following useful equalities:

$$-\frac{v_{\mathrm{T}'}}{v_{\mathrm{TL}'}}\sqrt{\frac{2\tau}{1+\tau}} = \sqrt{\tau\left(1+(1+\tau)\tan^2\left(\frac{\theta}{2}\right)\right)} = \sqrt{\frac{\tau(1+\varepsilon)}{2\varepsilon}} = \frac{(E+E')\tan\left(\frac{\theta}{2}\right)}{2M} \tag{2.127}$$

Putting this altogether allows us to identify the polarized part in terms of the components of the asymmetry matrix defined relative to the q-vector:

$$A_{\text{long}} = A_0 \left(\frac{(E+E')\tan\left(\frac{\theta}{2}\right)}{2M} \right) \tag{2.128}$$

$$A_{\text{trans}} = A_0 \left(\frac{G_E}{G_M} \right) \tag{2.129}$$

where the "scale asymmetry" A_0 is given by:

$$A_0 = -\left[\frac{2\tan\left(\frac{\theta}{2}\right)\sqrt{\tau(1+\tau)}}{\left(G_E/G_M\right)^2 + \tau/\varepsilon} \right] \tag{2.130}$$

We'll note that the transverse asymmetry is sensitive to the ratio and relative sign of the elastic form factors [37].

Assuming $(G_E/G_M)^2$ is small enough to ignore in the denominator, then A_{trans} is essentially proportional to G_E/G_M. To take advantage of this, we should orient, in the scattering plane, the target polarization vector perpendicular to the q-vector ($\hat{P}_t \cdot (\hat{n} \times \hat{q}) \approx 1$ & $\hat{P}_t \cdot \hat{q} \approx 0$) such that the physics asymmetry A would be more sensitive to A_{trans} than A_{long}:

$$\frac{G_E}{G_M} \approx -A \left[\frac{\sqrt{\tau}}{2\varepsilon\tan\left(\frac{\theta}{2}\right)\sqrt{1+\tau}[\hat{P}_t \cdot (\hat{n} \times \hat{q})]} \right] - \left[\frac{(\hat{P}_t \cdot \hat{q})(E+E')\tan\left(\frac{\theta}{2}\right)}{[\hat{P}_t \cdot (\hat{n} \times \hat{q})]2M} \right] \tag{2.131}$$

where we've ignored the higher order effects of $(G_E/G_M)^2$ in the denominator of A_0. If it cannot be neglected, then we must solve [38] the following quadratic equation:

$$\left(\frac{G_E}{G_M}\right)^2 - \mathcal{B}\left(\frac{G_E}{G_M}\right) + \mathcal{C} = 0 \tag{2.132}$$

where the factors $\mathcal{B}$ & $\mathcal{C}$ are given by:

$$\mathcal{B} = \frac{-2\tan\left(\frac{\theta}{2}\right)\sqrt{\tau(1+\tau)}[\hat{P}_t \cdot (\hat{n} \times \hat{q})]}{A} \qquad \mathcal{C} = \frac{\tau}{\varepsilon} - \mathcal{B}\left[\frac{(\hat{P}_t \cdot \hat{q})(E+E')\tan\left(\frac{\theta}{2}\right)}{[\hat{P}_t \cdot (\hat{n} \times \hat{q})]2M}\right] \tag{2.133}$$

and the two solutions are given by:

$$\frac{G_E}{G_M} = \frac{2\mathcal{C}/\mathcal{B}}{1+\sqrt{1-\frac{4\mathcal{C}}{\mathcal{B}^2}}} \quad \text{or} \quad \frac{\mathcal{B}}{2}\left[1+\sqrt{1-\frac{4\mathcal{C}}{\mathcal{B}^2}}\right] \tag{2.134}$$

Care must be taken to choose the correct solution given the kinematics and we'll note that when the ratio is small $G_E/G_M \ll 1$, the first solution is the correct one.

Furthermore, if A_{long} and A_{trans} can be measured independently & simultaneously, then their ratio directly gives G_E/G_M:

$$\frac{G_E}{G_M} = \frac{A_{\text{trans}}}{A_{\text{long}}}\left(\frac{(E+E')\tan\left(\frac{\theta}{2}\right)}{2M}\right) \tag{2.135}$$

In practice this could be done by defining two scattering planes (with their own corresponding q-vectors) by an appropriate placement of detectors. In one, the target polarization vector would be parallel to the q-vector ($\hat{P}_t \cdot (\hat{n} \times \hat{q}) \approx 0$ & $\hat{P}_t \cdot \hat{q} \approx 1$) making the physics asymmetry most sensitive to $A \approx A_{\text{long}}$. In the other, the target polarization vector would be perpendicular to the q'-vector ($\hat{P}_t \cdot (\hat{n}' \times \hat{q}') \approx 1$ & $\hat{P}_t \cdot \hat{q}' \approx 0$) making the physics asymmetry most sensitive to $A' \approx A_{\text{trans}}$. Although technically difficult, it has the advantage that the target polarization, beam polarization, and dilution factor all essentially cancel in the ratio $(A_{\text{trans}}/A_{\text{long}}) \approx (A'/A) = (A'_{\text{raw}}/A_{\text{raw}})$. Assuming the average beam & target polarizations are stable, this type of measurement can also be performed by switching the target spin

angle between parallel & perpendicular to the q-vector to measure A_{long} & A_{trans} separately.

One can alternatively measure the polarization transferred to an unpolarized target from a polarized beam [37, 39]. The polarization of the recoiling particle is related to the asymmetries by "turn-around" relations given by [36]:

$$P_{\text{long}} = +A_{\text{long}} \qquad\qquad P_{\text{trans}} = -A_{\text{trans}} \tag{2.136}$$

where $P_{\text{long(trans)}}$ is the longitudinal (transverse) polarization with respect to momentum transfer axis. If the target particle is initially at rest, then this axis corresponds with the recoiling particle's direction of propagation. The ratio G_E/G_M can expressed as the transferred polarization ratio, which does not require any knowledge of the beam polarization:

$$\frac{G_E}{G_M} = -\frac{P_{\text{trans}}}{P_{\text{long}}}\left(\frac{(E+E')\tan\left(\frac{\theta}{2}\right)}{2M}\right) \tag{2.137}$$

2.3.4 Nucleon Form Factors

There are two complications that make the interpretation of nucleon form factors difficult. First, unlike the spinless case, there are two form factors for spin-1/2 particles. One way to approach the solution to this problem is to expand the form factors for low Q^2 (assuming a spherically symmetric distribution):

$$F\left(Q^2\right) = F(0) - \frac{2\pi Q^2}{3}\int r^4 \rho(r)\, dr + \cdots \tag{2.138}$$

where the term linear in Q^2 is proportional to the root mean square (rms) radius of the distribution described by $\rho(r)$. Yennie, Lévy, & Ravenhall showed [40] that the rms charge radius was related to G_E in the following way:

$$\langle r^2 \rangle = \int r^2 \rho(r)\, d^3r = 4\pi \int r^4 \rho(r)\, dr = -6 \left[\left. \frac{dF_1}{dQ^2} \right|_{Q^2=0} - \frac{F_2(0)}{2M} \right] = -6 \left. \frac{dG_E}{dQ^2} \right|_{Q^2=0} \tag{2.139}$$

This reason, among others, lead to the interpretation of the G_E & G_M as the Fourier transform of the charge and magnetization distributions [31, 41–43]. Note that at sufficiently low Q^2, specifically $\tau \ll 1 \rightarrow Q^2 \ll 4M^2$, the choice between F_1 and G_E as the charge distribution is less critical.

Second, relativistic effects due to the recoil of the target are significant. For each Q^2, there is a frame of reference, called the Breit frame, where the target recoil is zero, $\nu = 0$. The Breit frame (also called the "brick wall" frame) travels along the direction of the momentum transfer (q-vector) in the scattering plane at a velocity given by $\nu/|\vec{q}|$, which is $\sqrt{\tau/(1+\tau)}$ for elastic scattering. It is in this frame that the form factor is interpreted as the Fourier transform of a distribution. To calculate the static charge and magnetization distributions of nucleons in the lab frame, one must first boost both G_E & G_M from the Breit frame into the lab frame. At sufficiently low Q^2 ($\tau \ll 1$), this is straightforward since the Breit frame travels at nonrelativistic velocities with respect to the lab frame. At higher Q^2, the Breit frame travels at relativistic velocities. It is difficult, in a model independent way, to disentangle relativistic "boost" effects from structure information. Regardless of their connection to static lab-frame distributions, nucleon form factors provide an important link between meson cloud effects at low Q^2 [44] and coherent hard scattering from three Dirac constituents at high Q^2 [45].

The first measurements of proton form factors [46,47] by Hofstadter & McAllister in the mid-1950's indicated that they were not constant and decreased with Q^2. Based on subsequent measurements [48] up to $Q^2 < 0.55\,\mathrm{GeV}^2$, the proton Dirac & Pauli proton factors were well parametrized by the "dipole" form factor:

$$F_1^p = F_2^p = G_D(Q^2) = \left[1 + \frac{Q^2}{Q_D^2}\right]^{-2} \tag{2.140}$$

where $Q_D^2 = 0.73\,\mathrm{GeV}^2$. This form factor can represent the Fourier transform of an exponentially decaying distribution with an R.M.S. radius given of 0.80 fm. Another early parameterization [49], motivated by the possibility of the breakdown of electrodynamics at short distances or alternatively arguments based on dispersion relations, has the form:

$$F(Q^2) = \sum_{i=0}^{N} \frac{a_i}{1 + b_i Q^2} \tag{2.141}$$

where a_i, b_i, and N are fit to the data. In the language of vector meson dominance, Sec. (2.3.5), these parameters can related to the number of vector mesons included in the sum (N), their masses ($1/\sqrt{b_i}$), and the product of the vector meson-photon coupling constant & the vector meson-nucleon-nucleon coupling constant (a_i). In the early 60's, both F_1^p & F_2^p [50] and G_E^p & G_M^p [31] were parametrized by this form. F_1 & F_2 were separated by essentially solving two simultaneous quadratic equations using the method of "intersecting ellipses" [51]. Data taken up to $Q^2 = 1\,\mathrm{GeV}^2$ and analyzed using this method indicated that, above $Q^2 \approx 0.5\,\mathrm{GeV}^2$, $(F_2^p/\kappa_p^\star)/F_1^p < 1$ as Q^2 increased. G_E^p & G_M^p were obtained by Rosenbluth separation and data taken up to $Q^2 = 1.8\,\mathrm{GeV}^2$ indicated that $G_M^p(Q^2) \approx G_M^p(0)G_E^p(Q^2)$. Measurements between the mid 60's and early 80's for the proton form factors (using Rosenbluth separation) extended to $Q^2 < 4\,\mathrm{GeV}^2$. Their coarse structure was described (within

10%) by the dipole form factor [52]:

$$\frac{G_E^p(Q^2)}{G_E^p(0)} = \frac{G_M^p(Q^2)}{G_M^p(0)} = G_D(Q^2) \tag{2.142}$$

where $Q_D^2 = 0.71\ \mathrm{GeV}^2$, $G_E^p(0) = 1$, and $G_M^p(0) = 1 + \kappa_p^\star$. By the mid-90's, measurements of G_E^p & G_M^p were extended up to $Q^2 = 7\ \mathrm{GeV}^2$ & $Q^2 = 30\ \mathrm{GeV}^2$ respectively. The world data at the time was parametrized by an empirical inverse polynomial form [56]:

$$F(Q^2)/F(0) = \frac{1}{1 + \sum_{i=1}^{N} a_i Q^i} \tag{2.143}$$

where a_i and N are determined by fits to the data. The upper (lower) half of Fig. (2.3) depicts a representative sample of parameterizations for G_M^p before (after) 1995. The experimental picture at that time can be summarized as $G_E^p/G_M^p \approx$ constant. Therefore it was quite striking when the first high Q^2 measurements [62] obtained from the polarization transfer technique indicated that G_E^p/G_M^p decreased linearly with increasing Q^2. The difference in these two techniques are thought [66, 67] to be due to, at least partly, previously unaccounted for radiative corrections due to two photon exchange at the nucleon vertex [68, 69]. Fig. (2.4) shows a comparison of the polarization transfer data with more recent Rosenbluth separation experiments.

Neutron form factor data are much more limited in both quantity & quality due to a lack of a free neutron target. For this reason, the traditional approach (until the mid-90's) was to extract neutron form factors from both elastic and quasi-elastic scattering from an unpolarized deuterium target. The first quasi-elastic experiments were carried out by Yearian & Hofstadter [70] in the late-50's and resulted in the conclusion that $F_2^n \approx F^p$ within large uncertainties assuming that $F_1^n = 0$.

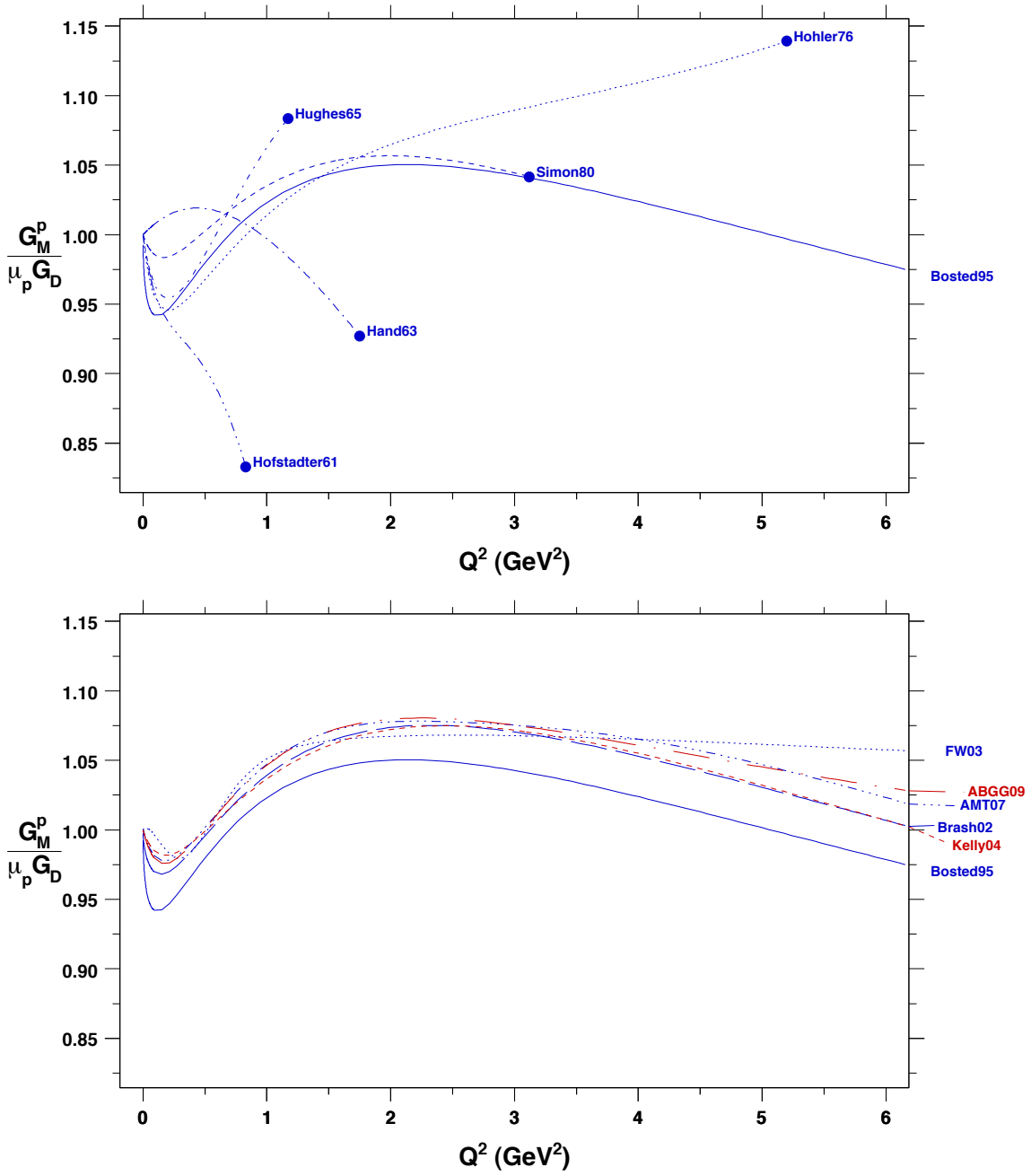

Figure 2.3: Parameterizations of G_M^p before & after 1995. The parameterizations are from Hofstadter61 [50], Hand63 [31], Hughes65 [53], Simon80 [54], Hohler76 [55], Bosted95 [56], Brash02 [57], FW03 [58], Kelly04 [59], AMT07 [60], & ABGG09 [61].

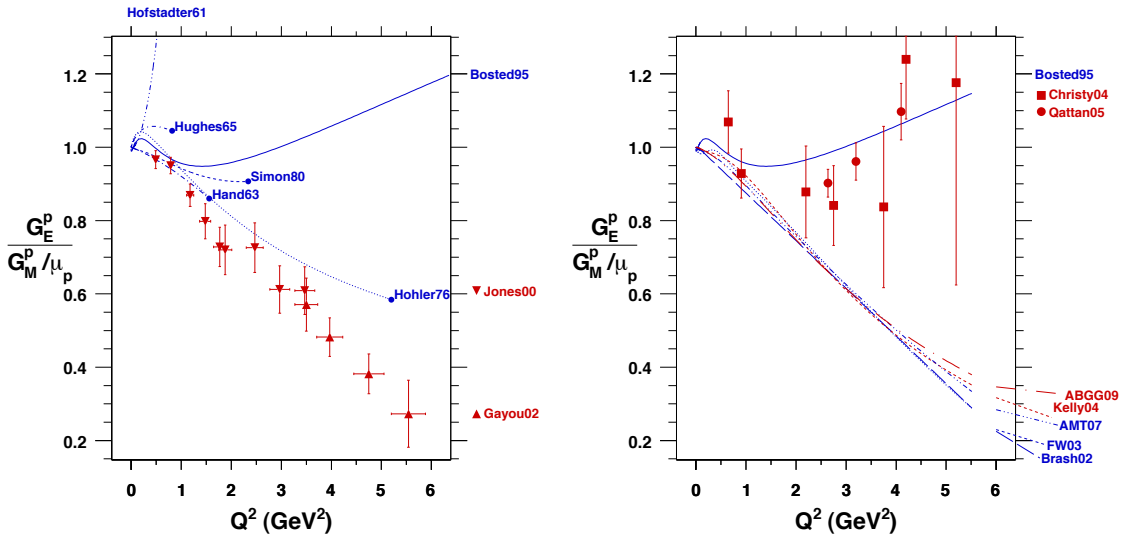

Figure 2.4: Comparison of $\mu_p G_E^p / G_M^p$ from the Polarization Transfer Method with Rosenbluth Separation. Polarization transfer data (left) are from Jones00 [62] and Gayou02 [63]. Rosenbluth separation data (right) from Christy04 [64] and Qattan05 [65].

This technique measures $(\sigma_p^{\mathrm{QE}} + \sigma_n^{\mathrm{QE}})$ which requires corrections due to the contribution from the proton (G_E^p & G_M^p) and nucleon motion & binding effects (nucleon spectral functions $S(\nu_s, \vec{k})$). Sensitivity to nucleon motion & binding effects can be reduced by also measuring a struck proton in coincidence with the scattered electron. In this method, the neutron form factors are extracted from the ratio $(\sigma_p^{\mathrm{QE}} + \sigma_n^{\mathrm{QE}})/\sigma_p^{\mathrm{QE+FSI}}$, which is mainly sensitive to final state interactions of the struck proton exiting the nucleus. Sensitivity to FSI can be reduced by also measuring a struck neutron in coincidence to the scattered electron. In this method, the neutron form factors are extracted from the ratio $\sigma_n^{\mathrm{QE+FSI}}/\sigma_p^{\mathrm{QE+FSI}}$, which is mainly sensitive to the neutron detection efficiency and differences between the proton & neutron FSI. All of these methods have been used to extract G_M^n and it is isolated from G_E^n by assuming that $G_E^n \approx 0$, by choosing a large scattering angle to enhance sensitivity to "magnetic" scattering, and/or by Rosenbluth separation. Within

$\pm 10\%$ up to $Q^2 = 6$ GeV^2, the coarse structure of G_M^n is also given by the dipole form factor as $G_M^n\left(Q^2\right) = G_M^n(0) G_D\left(Q^2\right)$ where $G_M^n(0) = \kappa_n^\star$. The upper (lower) half of Fig. (2.5) depicts a representative sample of parameterizations for G_M^p before (after) 1995.

Of the four electromagnetic nucleon form factors, G_E^n is the most difficult to extract cleanly. The most precise constraint to G_E^n comes from the neutron-electron scattering length b_{ne}. The first non-zero observation of this quantity (or equivalently a spin-& velocity-independent neutron-electron interaction) [71] came from neutron scattering from Pb by Havens, Rabi &, Rainwater [72] and from Xe by Fermi & Marshall [73] in 1947. Foldy argued [74] that this interaction could, at least partly, be attributed to the neutron's anomalous magnetic moment. Subsequent, higher precision experiments demonstrated [75] that almost all of the interaction was accounted for by the anomalous magnetic moment. In the language of elastic electron scattering, this process is measuring the slope of G_E^n at $Q^2 = 0$:

$$V_0 = \left(\frac{3m}{2\alpha r_e^2 M_n}\right) b_{ne} = \left(\frac{\alpha}{2r_e^3}\right) \left\langle r_n^2 \right\rangle = -\left(\frac{3\alpha}{r_e^3}\right) \left.\frac{dG_E^n}{dQ^2}\right|_{Q^2=0} \tag{2.144}$$

where the early experiments expressed their results as the equivalent potential V_0 on the surface of sphere with the classical electron radius $r_e = \alpha/m$. A world average of the results from modern versions of this type of neutron scattering give [76]:

$$\left\langle r_n^2 \right\rangle = -\left(0.1161 \pm 0.0022\right) \text{ fm}^2 \quad \Rightarrow \quad \left.\frac{dG_E^n}{dQ^2}\right|_{Q^2=0} = \left(0.4969 \pm 0.0094\right) / \text{GeV}^2 \tag{2.145}$$

The left side of Fig. (2.6) shows a comparison between this slope and low Q^2 electron scattering data & parameterizations.

For non-zero Q^2, until the mid-90's, G_E^n was extracted from both elastic and

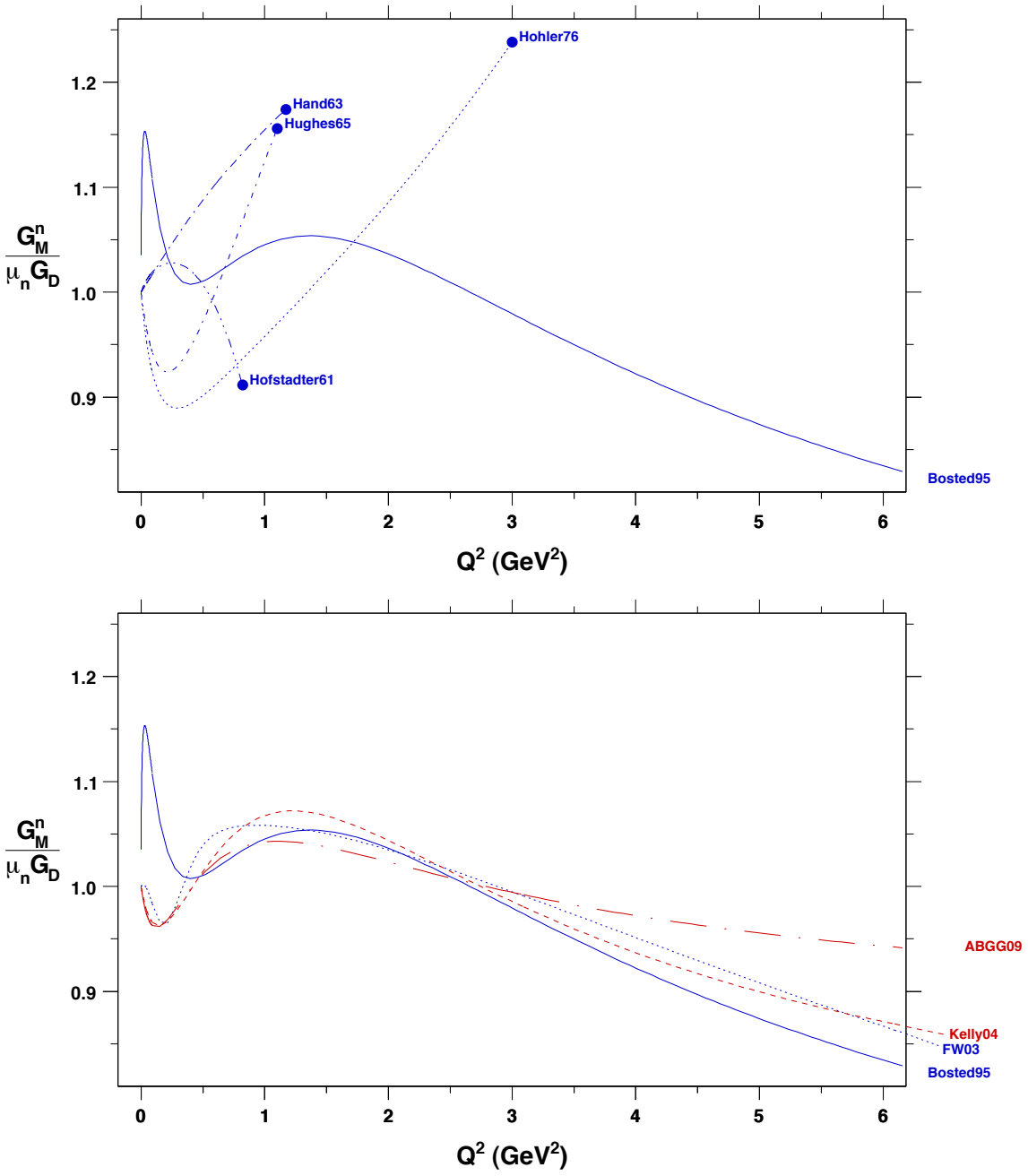

Figure 2.5: Parameterizations of G_M^n before & after 1995. The parameterizations are the same as in Fig. (2.5).

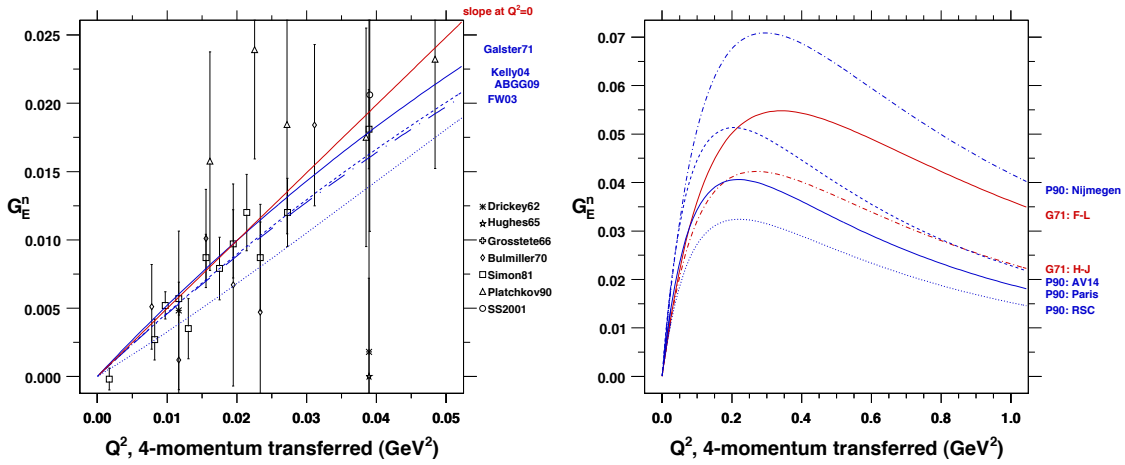

Figure 2.6: Left: G_E^n for $Q^2 \leq 0.05$ GeV^2. Data from Drickey62 [77], Hughes65 [53], Grosstete66 [78], Bulmiller70 [79], Simon81 [80], Platchkov90 [81], & SS2001 [82]. Right: Parameterizations of G_E^n with Different NN-potentials. Fits to data from Galster71 (G71) [83] using the Feshbach-Lomon (F-L) [84] and Hamada-Johnston (H-J) [85] potentials. Fits to data from Platchkov90 (P90) [81] using the Nijmegen [86], Argonne-14 (AV14) [87] (with $b = 21.2$), Paris [88], and Reid Soft Core (RSC) [89] potentials.

quasi-elastic scattering from unpolarized deuterium targets. Extracting G_E^n from quasi-elastic scattering [53, 90–95] is analogous to extracting G_M^n. The most precise determinations of G_E^n, however, came from elastic scattering [54,77–79,81,83,96]. At sufficiently low $Q^2 \ll 4M_d^2$, the $A^d(Q^2)$ deuteron elastic structure function is most sensitive to the charge & quadrupole form factors $G_C^d(Q^2)$ & $G_Q^d(Q^2)$. These two form factors can be written in terms of G_E^p & G_E^n using knowledge of the ground state wave function of the deuteron. This must be calculated from a theoretical model for the nucleon-nucleon (NN) potential. The extraction of G_E^n is especially sensitive to the choice of the NN-potential, see right side of Fig. (2.6). In 1971, Galster et al. [83] made an early use of this technique and parametrized G_E^n up to $Q^2 \approx 1$ GeV^2 as:

$$G_E^n(Q^2) = -G_M^n(0) G_D(Q^2) \frac{A_G \tau}{1 + B_G \tau} \tag{2.146}$$

where $\tau = Q^2/(4M_n^2)$ and a best fit to the world data at the time gave $A_G = 1.0$ & $B_G = 5.6$. In 1990, Platchkov et al. [81] repeated this analysis with their higher precision data ($0.04\,\mathrm{GeV}^2 \leq Q^2 \leq 0.70\,\mathrm{GeV}^2$) and their best fit (RSC) constrained by dG_E^n/dQ^2 is $A_G = 0.944$ & $B_G = 16.6$. In 2001, Schiavilla & Sick extracted G_E^n from a global analysis of the world data for G_Q^d, which they argue is less sensitive to the choice of NN-potential. Fig (2.7) shows a representative selection of the world data for G_E^n extracted from scattering from unpolarized deuterium targets before (upper) & after (lower) 1990.

Since the early-90's, the neutron form factors have been extracted from quasi-elastic polarized electron scattering. These experiments can be broken down into four categories based on the type of target: Metastability Exchange Optical Pumping (MEOP) ^{3}He targets [97–101], Spin Exchange Optical Pumping (SEOP) ^{3}He targets [102] & E02013, polarization transfer to unpolarized deuterium targets [103–108], & polarized deuterium targets [109–112]. The first experiments [97, 102] of this type had large systematic uncertainties due to corrections for the proton contribution [113]. All subsequent experiments measured the struck neutron in coincidence with the scattered electron. Corrections due to final state interactions (FSI) and meson exchange currents (MEC) for deuterium targets are made using the prescription of Arenhövel et al. (see [114] and references therein). The analysis of Golak et al. [115] has been used [99–101] to treat FSI & MEC for ^{3}He targets. Fig. (2.9) shows a comparison between extractions of G_E^n using spin-independent & spin-dependent observables.

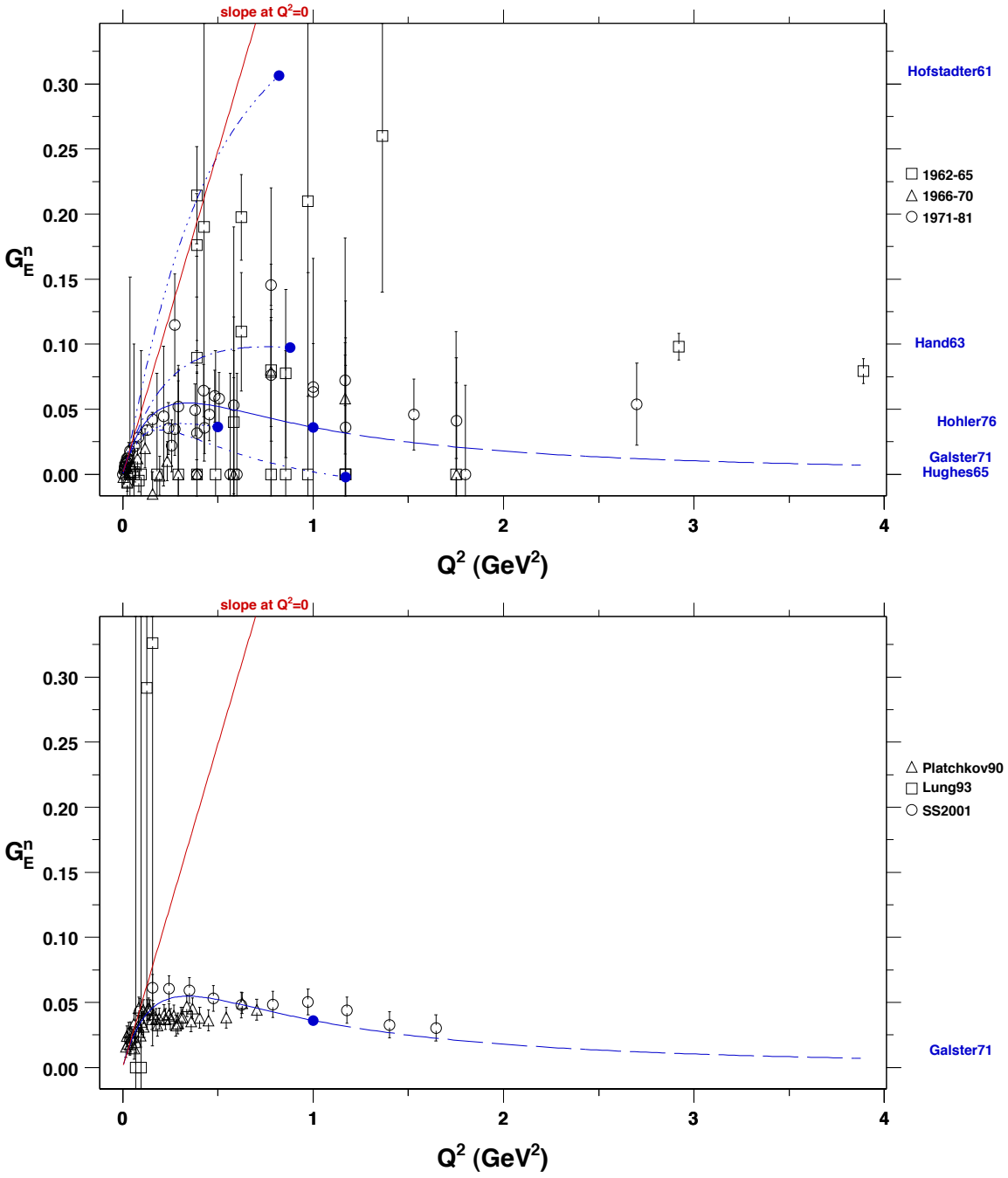

Figure 2.7: G_E^n from Elastic & Quasi-elastic Scattering from Unpolarized Deuterium Targets Before (upper) & After (lower) 1990. Data are from 1962-65 [53, 77, 90, 91], 1966-70 [78, 79, 92, 96], 1971-81 [80, 83, 93, 94], & after 1990 [81, 82, 95].

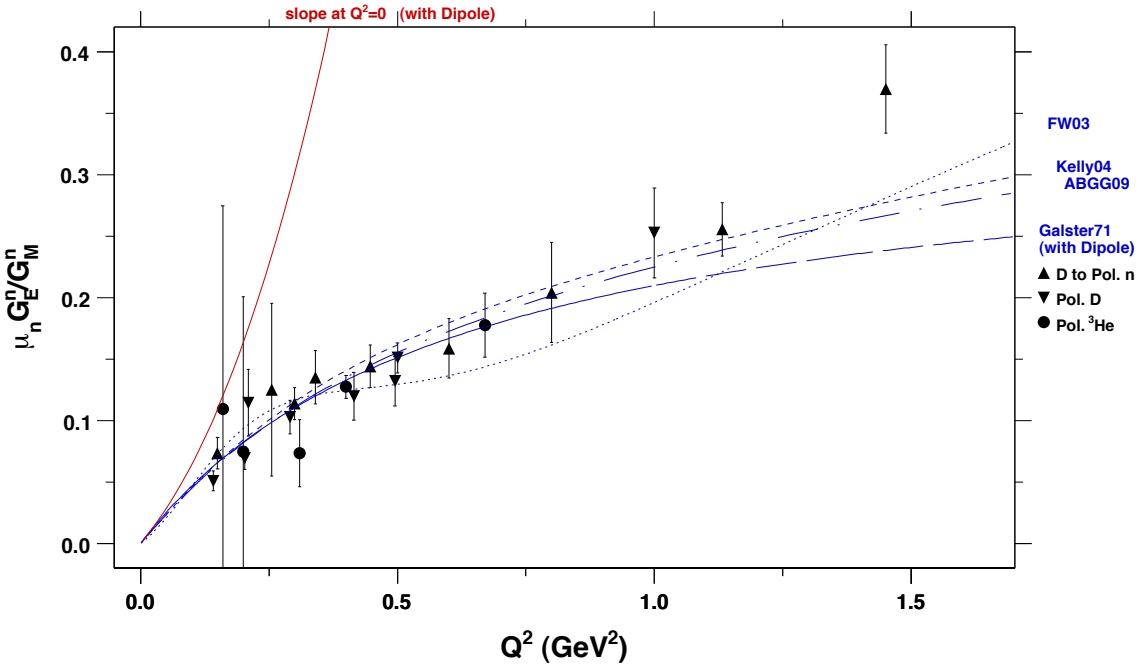

Figure 2.8: $\mu_n G_E^n / G_M^n$ from the Polarization Observables.

2.3.5 Perspectives From Theory

From the perspective of theory, the "physics" of a scattering cross section (σ) is provided by the modulus square of the scattering amplitude ($|\mathcal{M}|^2$). Form factors (F) always appear quadratically in cross section formulas, which implies that they are linear in the scattering amplitudes ($\mathcal{M}$). This scattering amplitude is described by a product of the matrix elements for the electron and the nucleon. The electron matrix element is determined from QED, whereas the nucleon matrix element is unknown. Most (but not all) theoretical approaches are essentially an exercise in constructing & evaluating the nucleon matrix element:

$$\left.\begin{array}{l} \sigma \sim |\mathcal{M}^2| \\ \sigma \sim F^2 \end{array}\right\} \Rightarrow F \sim \mathcal{M} \sim \langle N' | O | N \rangle \tag{2.147}$$

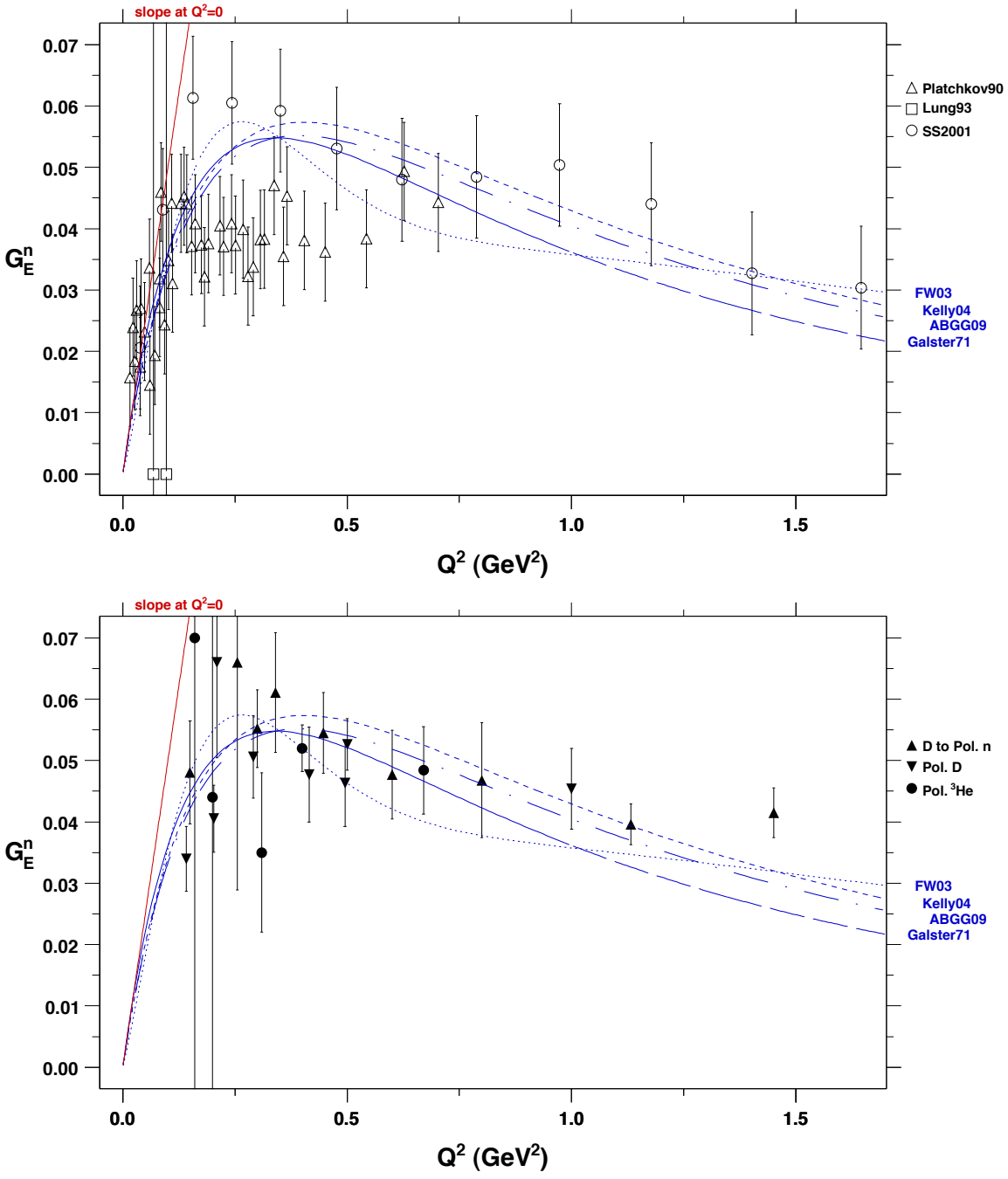

Figure 2.9: Comparison of G_E^n from Unpolarized (upper) & Polarized (Lower) Scattering Experiments Since 1990.

Finally, from the point of view of theory, it is usually more convenient to describe proton and neutron form factors by their isospin components:

$$F^p = F^S + F^V \tag{2.148}$$

$$F^n = F^S - F^V \tag{2.149}$$

$$F^S = \frac{F^p + F^n}{2} \tag{2.150}$$

$$F^V = \frac{F^p - F^n}{2} \tag{2.151}$$

where F^S & F^V are the isoscalar & isovector nucleon form factors. This isospin decomposition is valid for both conventions and ignores the small mass difference between protons & neutrons.

Dispersion Relations

Dispersion relations are mathematical relationships that are derived from the physical requirement of causality, see Sec.(2.5.4). They provide a general constraint to the form of the response of an object, represented by f, by relating the real part of f to its imaginary part:

$$\Re f(Q^2) = \frac{1}{\pi} \int_{Q_0^2}^{\infty} \frac{\Im f\left(Q'^2\right)}{Q'^2 + Q^2} \, dQ'^2 \tag{2.152}$$

In the context of elastic electron-nucleon scattering, f can be thought of as a complex-valued "generalized" form factor with a real part that is given by the usual nucleon form factors. The imaginary part of f represents the closely related process of nucleon-antinucleon ($N\overline{N}$) pair production from $e^{\pm}$ collisions [116]. From the perspective of quantum field theory, the Feynman diagrams for these two processes

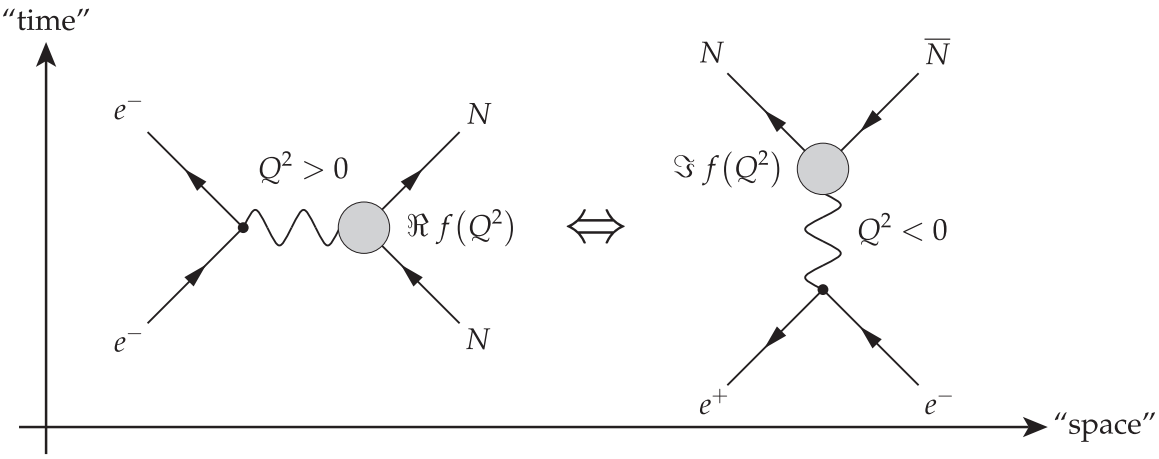

Figure 2.10: Elastic Scattering & $e^{\pm}$ Collisions. The elastic scattering ($e^{\pm}$ collision) diagram involves the exchange of a "space-like" ("time-like") virtual photon with $Q > 0$ ($Q^2 < 0$).

are nearly identical and differ by a 90° "rotation in spacetime," see Fig (2.10).

Vector Meson Dominance

The traditional modeling of form factors amounts to determining the imaginary part of f usually with hadronic degrees of freedom. After the $e^{\pm}$ annihilation, the virtual photon can fluctuate into an intermediate particle with mass m, which is suggested by the propagator-like form of the denominator with $Q' = m$. The dispersion relation can then be interpreted as a spectral decomposition [117, 118] and rewritten as:

$$F_{1,2}^{S,V} = \frac{1}{\pi} \int_{(m_0^{S,V})^2}^{\infty} \frac{w_{1,2}^{S,V}(m^2)}{m^2 + Q^2} \, dm^2 \tag{2.153}$$

where $w_{1,2}^{S,V} = \Im \, f_{1.2}^{S,V}$ is known as the spectral weight function. The integration threshold $m_0^{S(V)} = 2(3)m_\pi$ is given by isospin symmetry considerations. The spec-

tral weights give the naive nucleon distributions by [119]:

$$\rho(r) = \frac{1}{4\pi^2} \int_{m_0^2}^{\infty} \frac{e^{-mr}}{r} w(m^2)\, dm^2 \tag{2.154}$$

An early model called Vector Meson Dominance (VMD) [120, 121] argued that these intermediate particles are vector mesons, which have same same quantum numbers as a photon (zero charge, spin-1, odd parity). In this picture, a cloud of virtual vector mesons with mass m surround the "intrinsic" nucleon with a range $1/m$. The spectral function w is then a product of the photon-vector meson ($g_{\gamma V}$) coupling constant and the vector meson-NN (F_{VNN}) "form factor." The lightest vector mesons, ρ & ω, are expected to have the dominant weights. One can account for the possibility of strangeness in the nucleon by including a term for the ϕ-meson. Early motivations for VMD included the prediction of the existence of the ω-meson by Y. Nambu [122] and the strong resonances due to vector mesons in the $e^{\pm}$ collisional cross section [123]. The simplest versions of this model had limited success in describing the nucleon form factors [124, 125].

Modifications to the basic VMD model which improve the fit to experimental data include an additional term (related to the pion form factor F_π) for two pion exchange for the isovector form factors [126–130], an additional term for two kaon exchange for the isoscalar form factors [131, 132], an "intrinsic" form factor that acts as the core of the nucleon (that is surrounded by a cloud of vector mesons), and/or the requirement that the high Q^2 scaling behavior is constrained by pQCD, see Sec. (2.3.5). Fig (2.11) depicts Feynman diagrams that represent these processes.

The model of Iachello et al. [133] includes an intrinsic form factor (g) and has been updated to include pQCD scaling [134]. The model of Hohler et al. [55] was

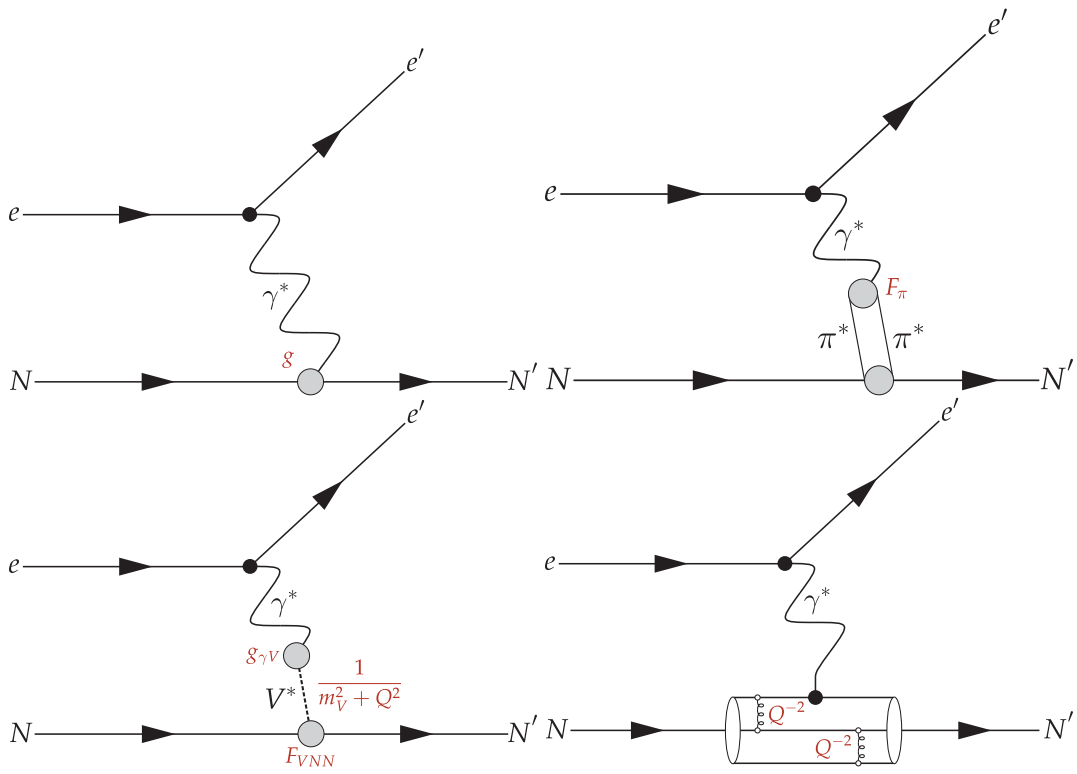

Figure 2.11: Feynman Diagrams Describing Different Approaches to Elastic Scattering. (UL) Intrinsic Form Factor, (UR) Two Pion Exchange, (LL) Vector Meson Exchange, (LR) pQCD.

among the first to include two pion exchange. It has been updated to include pQCD scaling [135] and new calculations for the contributions due to two pion & two kaon exchange [136]. Although it has its roots in VMD, this updated model is more properly described as a "dispersion relation analysis." The model of Gari & Krümpelmann [137–140] was among the first to include pQCD scaling. It has been extended by E.L. Lomon to include additional heavier vector mesons and two pion exchange [141–143].

Perturbative QCD

Partonic (quark & gluon) degrees of freedom can provide constraints to the asymptotic short distance scale behavior of the form factors using perturbative QCD (pQCD). Based on dimensional scaling rules, Brodsky & Farrar argued [144] that at very high Q^2 the form factors F_1 & F_2 should scale as $1/Q^4$ & $1/Q^6$ respectively. Lepage & Brodsky came to the same conclusion [145, 146] by factorizing the scattering process into two parts [147]: "soft" and "hard." The soft parts represent the probabilities of finding the nucleon (hadron) in a three (n) quark state before and after scattering. The hard part represents the virtual photon and gluon exchanges among the three (n) quarks. The simplest (lowest order) way for this to happen is for an exchange of two $(n-1)$ gluons. Each gluon exchange implies one $1/Q^2$ factor from the gluon propagator, which gives $1/Q^4$ for F_1. If one assumes that the nucleon (hadron) helicity is conserved during the scattering process to lowest order, then one additional gluon exchange is required to mediate a helicity flip. This implies a $1/Q^6$ scaling for F_2. Generalizing the dimensional scaling rules [148] and pQCD factorization analysis [149] to include quark orbital angular momentum (OAM) have reconfirmed these arguments and give:

$$\lim_{Q^2\to\infty} \frac{F_2}{F_1} \propto \frac{\left[\log(Q^2/\Lambda^2)\right]^2}{Q^2} \tag{2.155}$$

where Λ is a "soft scale related to the size of the nucleon." Ralston & Jain argue [150], that to properly include the effect of quark OAM, the transverse momenta of the quarks must be included in the calculation. Consequently they find that F_2 scales as $1/Q^5$ and F_2/F_1 scales as $1/Q$.

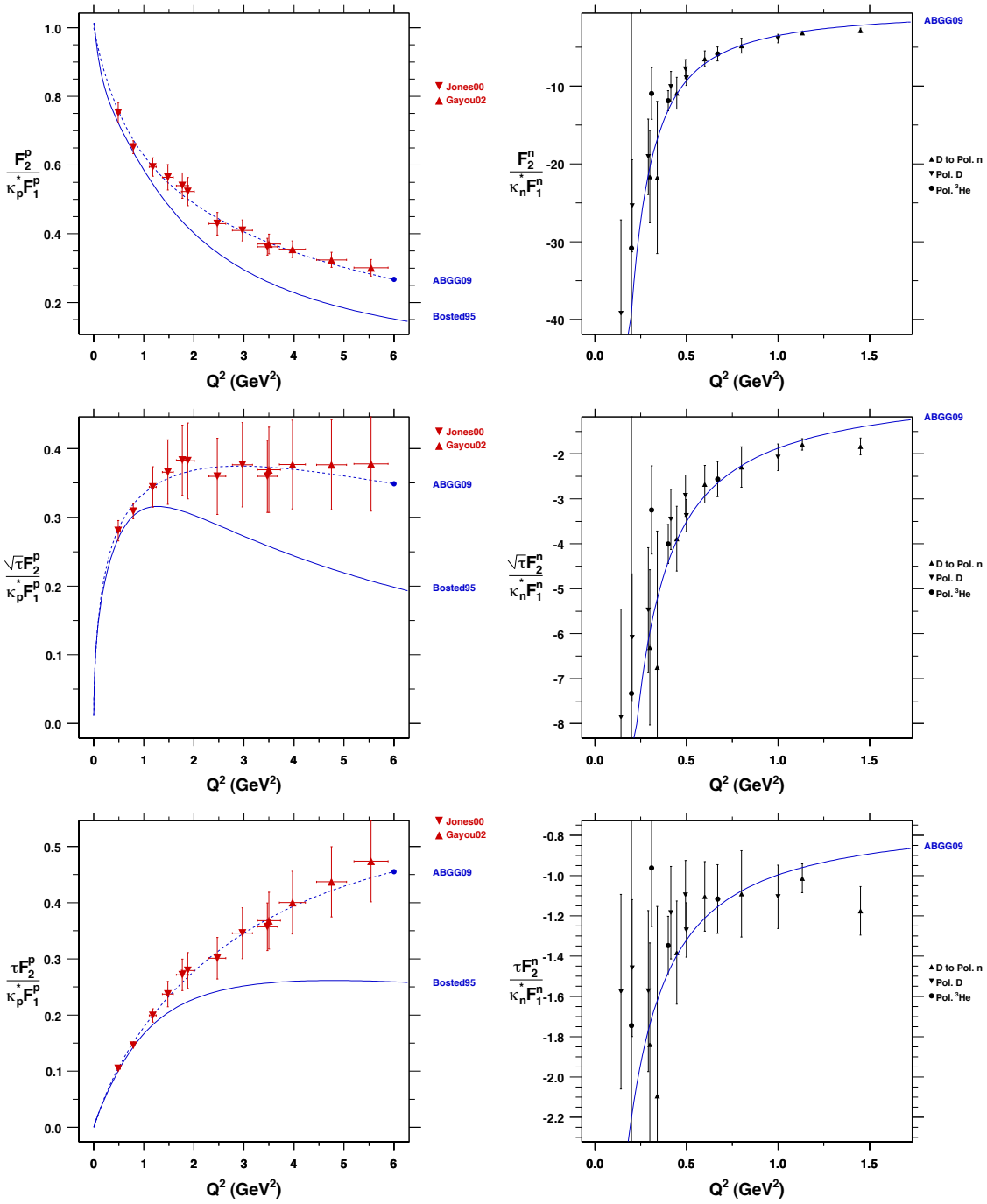

Figure 2.12: F_2/F_1 Ratios from the Polarization Observables.

Effective Chiral Field Theories

An alternative approach using hadronic degrees of freedom is to write down an "effective" field theory that approximates the low energy behavior of the "full" theory. In the context of QCD (the "full" theory), the concept of chiral symmetry is used to deduce the degrees of freedom for the effective theory [151]. The family of particles that include pions (light pseudoscalar mesons) are the required degrees of freedom. One way to implement this idea is called Chiral Perturbation Theory, which will be described more fully in Sec. (2.5.10). See [32] for a recent review of nucleon form factors calculated within this framework.

A soliton is a mathematical object that has a spatial distribution that is localized and stable in time [152–154]. The form factor of such an object can be calculated from knowledge of its spatial distribution. To obtain nucleon form factors using a soliton model, the soliton must represent a nucleon. This is usually done by designing a field theory with a Lagrangian that satisfies two criteria. First, it has terms that mimic the chiral symmetry properties of QCD. (Specifically, some form of the nonlinear sigma model [27] is included to spontaneously break the chiral symmetry that is also built into the Lagrangian). Second, it includes a type of non-linear interaction that necessarily results in a soliton solution. Soliton models differ on how these two criteria are satisfied. In the limit where the number of colors is infinite ($N_c \gg 1$, for example [155]), the effective field theories that represent these models have a deep relationship with QCD [156].

Chiral Soliton Models start with a Lagrangian (originally proposed by Skyrme [157]) with only pion degrees of freedom. The solutions are "topological" chiral solitons that are named Skyrmions [158]. One of the invariant parameters that describes the topology of a Skyrmion (the winding number) can be related to the

baryon number B. When $B = 1$, the Skyrmion can be thought of as a baryon and more specifically a nucleon. Its spatial (chiral) profile (specified as a part of the solution to the Lagrangian) is related to its baryon density and moment of inertia density. These densities represent the charge and magnetization densities of the nucleon which can be immediately inverted to give the nucleon form factors [159]. This form of the model is only useful at very low Q^2. Holzwarth has extended this model [160,161] to higher Q^2 by including the effects of the lightest vectors mesons (ρ & ω) and boosting the densities [162] from the Skyrmion rest frame to the Breit frame.

Chiral Quark Soliton Models use a Lagrangian (the Nambu & Jona-Lasinio Model [163, 164]) which involve both pion and quark degrees of freedom [165]. In this case, the solutions are "non-topological" solitons which represent a localized three valence quark bound state [166]. Consequently, the baryon number of this object is due to the valence quarks. The pion degrees of freedom result in sea quarks that surround the valence quarks which are bound by their individual interaction with the sea. Remarkably this model manages to approximate the chiral symmetry properties of QCD and produce a nucleon-like object that has a spatial extent, three quarks, and a pion cloud. In these models, form factors are obtained by calculating the matrix element for the nucleon electromagnetic current (which will be described shortly). See [32,167] for a recent review of Chiral Soliton Models & Chiral Quark Soliton Models as they relate to form factors.

Relativistic Constituent Quark Models

Quark degrees of freedom can also be used to represent the nucleon in the form of the nucleon wavefunction $|N, h, P\rangle$. This wavefunction can then be used to calcu-

late the matrix element of nucleon electromagnetic current which is related to the form factors by [2]:

$$\langle P', S' | J^{\mu} | P, S \rangle = \bar{u}(P', S') \left[\gamma^{\mu} F_1(Q^2) + i\sigma^{\mu\nu} q_v \left(\frac{F_2(Q^2)}{2M} \right) \right] u(P, S) \tag{2.156}$$

where $S(S')$ & $P(P')$ are the initial (final) nucleon spin vector and momentum, $\bar{u}$ & u are Dirac spinors, M is the mass of the nucleon, and γ^{μ} & $\sigma^{\mu\nu}$ are the given by the Dirac matrices. The wavefunction can usually be decomposed into helicity non-flip ($h' = \hat{S}' \cdot \hat{P}' = h = \hat{S} \cdot \hat{P}$) and flip ($h' = -h$) parts that directly correspond to the Dirac F_1 and Pauli F_2 form factors respectively.

In the constituent quark model, the nucleon wavefunction is represented by an effective three-quark wavefunction that is written as [168]:

$$|P, S\rangle = \xi_{\text{spatial}} \zeta_{\text{flavor}} \chi_{\text{spin}} \phi_{\text{color}} \tag{2.157}$$

where the total wavefunction must be antisymmetric under an interchange of any two quarks. This is accomplished by an antisymmetric color wavefunction ϕ_{color} and a totally symmetric spatial-flavor-spin product wavefunction $\xi_{\text{spatial}} \zeta_{\text{flavor}} \chi_{\text{spin}}$. For nucleons (and more generally spin-1/2 baryons), the spin-flavor product and spatial wavefunctions are each separately symmetric. The spatial wavefunction is usually represented in the momentum basis and its exact form is either chosen to have some simple functional form or deduced from a chosen intra-nucleon potential that confines the quarks. If the energy scale of the confining potential is much larger than the constituent quark masses, then the wavefunction must be constructed within a relativistic framework. Finally, depending on the Lorentz frame in which the incoming (outgoing) wavefunction is constructed, it must be

boosted into the appropriate frame that corresponds to the motion of the nucleon before (after) scattering. Relativistic constituent quark models differ in:

1. the choice of relativistic framework (i.e. instant, point, light-front) [169–171]
2. the functional form of the spatial wavefunction (e.g. "power law" [172–174], Gaussian [175]) or (equivalently) the intra-nucleon potential [176, 177]
3. the effective form factor of the constituent quarks themselves (e.g. [178, 179])
4. the inclusion of quark-quark interactions (e.g. [176, 178])
5. the inclusion of pion effects (e.g. [179, 180])

See [32, 167] for a recent review of different models and comparisons to data.

Lattice QCD & Dyson-Schwinger Equations

An alternative approach using quark degrees of freedom is to solve QCD non-perturbatively by calculating the appropriate correlation function. Once again the matrix element of the nucleon electromagnetic current provides that link that connects the nucleon form factors with calculable quantities which, in this case, are the correlation functions. In quantum field theory, a two-point correlation function gives the probability amplitude [27] for the process where a particle is first created at a spacetime point x_1, then propagates from x_1 to x_2, and finally is annihilated at x_2. It is denoted by $\langle \Omega | \, T(\phi(x_1)\phi(x_2)) \, | \Omega \rangle$ where Ω is the ground state of the theory, T is the time ordering operator, and ϕ is a (scalar) field that corresponds to the particle. This quantity can be calculated by finding the Green's function $G(x_1, x_2)$ that solves the field equations that governs the particle's behavior. Nonperturbative ap-

proaches for finding the Green's function (and thereby calculating the correlation function) are Lattice QCD (LQCD) and the Dyson-Schwinger equations (DSE).

A two-point Green's function can be represented by path integrals [27] in the following way:

$$\langle\Omega|\, T\left(\phi(x_1)\phi(x_2)\right)|\Omega\rangle = G(x_1,x_2) = \lim_{T\to\infty(1-i\epsilon)} \frac{\int \mathcal{D}\phi\ \phi(x_1)\phi(x_2)\exp\left[i\int_{-T}^{+T}\ \mathcal{L}\ d^4x\right]}{\int \mathcal{D}\phi\ \exp\left[i\int_{-T}^{+T}\ \mathcal{L}\ d^4x\right]} \tag{2.158}$$

where $\int\ \mathcal{D}\phi$ denotes a path (functional) integral and $\mathcal{L}$ is the Lagrangian (density) of the field theory. These integrals are numerically computed by discretizing the paths by representing QCD on a spacetime lattice [181–183]. The lattice spacing is inversely proportional to both the energy scale probed and the computational cost. Elastic scattering from a nucleon can be represented by a three-point Green's function [184]. The nucleon is created at x_1, it then propagates to x_2 where it interacts with the incoming electron via a virtual photon, and finally it propagates to x_3 where it is annihilated. Only certain types of diagrams, representing a subset of all the paths from x_1 to x_2 to x_3, are calculated with the currently available computational resources [185]. These diagrams are chosen so that the isovector form factors can be calculated (i.e. the uncomputed diagrams are needed for the isoscalar form factors). LQCD calculations vary in the size of the lattice (number of lattice points), the energy scale studied (the lattice spacing), how the valence quarks are represented on the lattice (i.e. naive, Wilson, or staggered), and whether the sea quarks are included (i.e. no sea quarks refers to a "quenched" calculation). See [32, 67] for a recent discussion of Lattice QCD calculations of nucleon form factors.

The Dyson-Schwinger equations [186, 187] are a set of nonlinear integral equations that recursively relate a group of m n-point Green's function, where n repre-

sents the number of fields and m depends on the exact form of the interaction. Because there are an unlimited number of field configurations, there are, correspondingly, an infinite number (or "ladder") of coupled equations. The benefit, however, is that each of these n-point Green's functions is exact and non-perturbative. For this approach to be useful, the number of coupled equations needed to be solved must be finite and still be representative of the underlying field theory. This procedure is called "truncation" and results in approximate, but non-perturbative solutions for the Green's functions. A truncation procedure has been developed to treat hadrons using QCD [188,189]. Because the Green's functions are non-perturbative (all higher order diagrams are included), the three quarks include a surrounding cloud of sea quarks. In a recent approach [190], these three "dressed" quarks are represented by a quark and diquark pair. The nucleon is "bound" by an interchange of quarks between the single quark and diquark pair. The Green's function is obtained from the three-body (Faddeev) field equations which represent a sum over all possible quark-virtual photon interactions & quark interchanges. See [67] for a recent discussion of this approach.

Generalized Parton Distributions

Finally, a new framework has been developed to describe nucleons called Generalized Parton Distributions (GPDs). GPDs are related to both the parton distribution functions (Sec. (2.4.3)) obtained from deep inelastic scattering and the nucleon electromagnetic form factors. Because GPDs are partially determined by nucleon form factors [191,192], we'll end the discussion here. See [193,194] for a review of GPDs and [32,195] for a special emphasis on the connection between GPDs and nucleon form factors.

2.4 Inelastic Scattering at High Q^2

We'll introduce inelastic scattering in the context of high Q^2 first. At this scale, the "containers of information" (F_1, F_2, g_1, & g_2) are more easily understood with respect to quark & gluon degrees of freedom. In Sec. (2.5), we'll develop the relationship between the theoretical frameworks used to describe the high & low Q^2 regimes. Sec. (2.4.1) & (2.4.2) are general for all Q^2.

2.4.1 General Formulation

Following Anselmino, Efremov, & Leader [196,197], the differential scattering cross section for polarized lepton-nucleon inelastic scattering can be written as:

$$\frac{d^2\sigma}{d\Omega dE'}(p,s,P,S;p',s',q) = \frac{\alpha^2}{2MQ^4}\left(\frac{E'}{E}\right) L^{\mu\nu}(p,s;p',s')W_{\mu\nu}(P,S;q) \tag{2.159}$$

where M is the nucleon mass, (p,s) are the momentum & spin for the incident lepton, (p',s') are the momentum & spin for the scattered lepton, (P,S) are the momentum and spin for the target nucleon, and $L_{\mu\nu}$ & $W_{\mu\nu}$ are the leptonic & hadronic tensors. Each tensor is given by the $\mu\nu$ component of the modulus squared matrix element of the corresponding electromagnetic current and explicitly, for the hadronic tensor, it is:

$$\begin{aligned} W_{\mu\nu}(P,S;q) &= \frac{1}{2\pi}\int \sum_X \langle P,S|\, J_\mu(x)\,|X\rangle\,\langle X|\, J_\nu(0)\,|P,S\rangle \exp(iq\cdot x)\, d^4x & (2.160)\\ &= \frac{1}{2\pi}\int \langle P,S|\left[J_\mu(x), J_\nu(0)\right]|P,S\rangle \exp(iq\cdot x)\, d^4x & (2.161)\end{aligned}$$

where $J_\mu(x)$ is the nucleon electromagnetic current evaluated at a spacetime point x, $|X\rangle$ is some final state, and the sum over all final states $\sum_X |X\rangle \langle X| = 1$ is a completeness relation. Both tensors can be split into symmetric (s) and antisymmetric (a) components relative to a swap between the indices $\mu \leftrightarrow \nu$:

$$L_{\mu\nu}(p,s;p',s') = L^s_{\mu\nu}(p;p') + iL^a_{\mu\nu}(p,s;p') + L^{s'}_{\mu\nu}(p,s;p',s') + iL^{a'}_{\mu\nu}(p;p',s') \tag{2.162}$$

$$W_{\mu\nu}(P,S;q) = W^s_{\mu\nu}(P;q) + iW^a_{\mu\nu}(P,S;q) \tag{2.163}$$

The only terms that depend on the scattered electron spin are the two primed leptonic terms $L^{s'}_{\mu\nu}$ & $L^{a'}_{\mu\nu}$. These terms sum to zero when the scattered electron polarization is not measured. The mean differential cross section is obtained by averaging over the incident lepton & target nucleon spins and summing over the scattered lepton spin:

$$\bar{\sigma} = \frac{\sum_{s,S,s'}}{4}\left[\frac{d^2\sigma}{d\Omega dE'}(p,s,P,S;p',s',q)\right] = \frac{\alpha^2}{2MQ^4}\left(\frac{E'}{E}\right)2L^{\mu\nu}_s(p;p')W^s_{\mu\nu}(P;q) \tag{2.164}$$

The mean difference in the differential cross section for opposite target spin orientations (after summing over the scattered lepton spin) is given by:

$$\begin{aligned}\bar{\Delta} &= \frac{\sum_{s'}}{2}\left[\frac{d^2\sigma}{d\Omega dE'}(p,s,P,+S;p',s',q) - \frac{d^2\sigma}{d\Omega dE'}(p,s,P,-S;p',s',q)\right] \\ &= \frac{\alpha^2}{2MQ^4}\left(\frac{E'}{E}\right)2L^{\mu\nu}_a(p,s;p')W^a_{\mu\nu}(P,S;q)\end{aligned} \tag{2.165}$$

The symmetric and antisymmetric components of the leptonic tensor are given by:

$$L^s_{\mu\nu} = p_\mu p'_\nu + p'_\mu p_\nu - g_{\mu\nu}(p \cdot p' - m^2) = p_\mu p'_\nu + p'_\mu p_\nu - g_{\mu\nu}\left(\frac{Q^2}{2}\right) \quad (2.166)$$

$$L^a_{\mu\nu} = m\varepsilon_{\mu\nu\alpha\beta}s^\alpha q^\beta \quad (2.167)$$

where m is the lepton mass and we've used $-q^2 = Q^2 = 2(p \cdot p' - m^2)$. The symmetric and antisymmetric components of the hadronic tensor are given by:

$$\begin{aligned}\frac{W^s_{\mu\nu}}{2M} &= \left[-g_{\mu\nu} - \frac{q_\mu q_\nu}{Q^2}\right] W_1(P \cdot q, Q^2) \\ &\quad + \left[\left(P_\mu + \frac{P \cdot q}{Q^2}q_\mu\right)\left(P_\nu + \frac{P \cdot q}{Q^2}q_\nu\right)\right] \frac{W_2(P \cdot q, Q^2)}{M^2}\end{aligned} \quad (2.168)$$

$$\begin{aligned}\frac{W^a_{\mu\nu}}{2M} &= \varepsilon_{\mu\nu\alpha\beta}q^\alpha \\ &\quad \times \left\{\left[MS^\beta\right] G_1(P \cdot q, Q^2) + \left[(P \cdot q)S^\beta - (S \cdot q)P^\beta\right] \frac{G_2(P \cdot q, Q^2)}{M}\right\}\end{aligned} \quad (2.169)$$

where W_1 & W_2 describe the spin-independent response of the nucleon with units of (energy)$^{-1}$ and G_1 & G_2 describe the spin-dependent response of the nucleon with units of (energy)$^{-3}$. Noting that $g_{\mu\nu}g^{\mu\nu} = 4$ and taking advantage of the conservation of current [198] in the form of $q^\mu L_{\mu\nu} = q^\nu L_{\mu\nu} = 0$, we can contract the indices for Eqn. (2.164) and get the unpolarized part:

$$\bar{\sigma} = \frac{\alpha^2}{Q^4}\left(\frac{E'}{E}\right)\left[2\left(Q^2 - 2m^2\right)W_1 + \left(\frac{4(p \cdot P)(p' \cdot P)}{M^2} - Q^2\right)W_2\right] \quad (2.170)$$

Noting that $\varepsilon_{\mu\nu\alpha\beta}\varepsilon^{\mu\nu\alpha'\beta'} = -2\left[\delta^{\alpha'}_{\alpha}\delta^{\beta'}_{\beta} - \delta_{\alpha}\delta^{\beta'}\delta_{\beta}\delta^{\alpha'}\right]$ [199], we can contract the indices for Eqn. (2.165) and get the polarized part:

$$\begin{aligned}\bar{\Delta} &= \frac{4m\alpha^2}{Q^4}\left(\frac{E'}{E}\right)\left[\left\{(q\cdot s)(q\cdot S) + Q^2(s\cdot S)\right\}MG_1\right. \\ &\qquad \left. + Q^2\left\{(q\cdot P)(s\cdot S) - (q\cdot S)(s\cdot P)\right\}G_2/M\right] \quad (2.171)\end{aligned}$$

2.4.2 Longitudinally Polarized Beam on a Fixed Target

The equations in the previous section are frame independent and do not make the assumption that the lepton mass is negligible. In this section, we'll choose to work in the lab frame, ignore the lepton mass, and consider the situation where the nucleon target is at rest. It is straightforward to show that the mean unpolarized cross section $\bar{\sigma}$ is given by:

$$\bar{\sigma} = \sigma_M \times \left[W_2(\nu, Q^2) + 2W_1(\nu, Q^2)\tan^2\left(\frac{\theta}{2}\right)\right] \quad (2.172)$$

To calculate $\overleftrightarrow{A}$ under these conditions, we'll note that the lepton (s) and target (S) spin vectors are given by:

$$s^{\mu} = \frac{h_b E}{m}\left(1, \hat{p}\right) \quad (2.173)$$

$$S^{\mu} = \left(0, \hat{P}_t\right) \quad (2.174)$$

where h_b is the helicity of the electron beam and $\hat{P}_t$ is the target polarization unit vector. After some algebra, we find:

$$\overleftrightarrow{A} = -\left(\frac{2(\sigma_R - \sigma_M)}{\bar{\sigma}}\right)\left[M\left(E\hat{p} + E'\hat{p}'\right)G_1(\nu, Q^2) - 2EE'\left(\hat{p} - \hat{p}'\right)G_2(\nu, Q^2)\right] \quad (2.175)$$

For a target polarization in the scattering plane that is either parallel or perpendicular to the electron beam, we find the following two asymmetries:

$$\begin{aligned} A_{\parallel} &= -\left(\frac{2(\sigma_R - \sigma_M)}{\bar{\sigma}}\right)\left[M\left(E + E'\cos(\theta)\right)G_1(\nu, Q^2) - Q^2 G_2(\nu, Q^2)\right] \\ A_{\perp} &= -\left(\frac{2(\sigma_R - \sigma_M)}{\bar{\sigma}}\right)\left[E'\sin(\theta)\right]\left[MG_1(\nu, Q^2) + 2EG_2(\nu, Q^2)\right] \end{aligned} \tag{2.176}$$

2.4.3 Partons and Structure Functions

If the nucleon is made up of some number of Dirac constituents (spin-1/2 point particles) with a mass that is some fraction of the nucleon mass xM, then at sufficiently high Q^2, the electron should elastically scatter off these constituents, which we'll call partons. These partons recoil causing the incident electron to lose some energy given by:

$$\nu = \frac{Q^2}{2(xM)} \rightarrow x = \frac{Q^2}{2M\nu} \tag{2.177}$$

The elastic cross section for electron-parton collisions (ignoring the possible anomalous magnetic moment of the parton) is given by:

$$\frac{d\sigma}{d\Omega} = \sigma_M \times \left(\frac{E'}{E}\right) \times \left[1 + 2\tau\tan^2\left(\frac{\theta}{2}\right)\right] Z^2 \tag{2.178}$$

where $\tau = Q^2/(4(xM)^2)$ and Z is the parton charge. If the parton mass is not fixed but is probabilistic, then we have to multiply the cross section by the probability of having a mass fraction between x and $x + dx$:

$$\frac{d\sigma}{d\Omega} = \sigma_M \times \left(\frac{E'}{E}\right) \times \left[1 + 2\tau\tan^2\left(\frac{\theta}{2}\right)\right] Z^2 P(x)dx \tag{2.179}$$

If there are different types (flavors) of partons and the scattering occurs hard & fast enough, then the total cross section is simply an incoherent sum over all parton types (in direct analogy to quasi-elastic scattering):

$$\left[\frac{d\sigma}{d\Omega}\right]_{\text{tot}} = \sum_i \sigma_M \times \left(\frac{E'}{E}\right) \times \left[1 + 2\tau \tan^2\left(\frac{\theta}{2}\right)\right] Z_i^2 P_i(x) dx \tag{2.180}$$

It is straightforward to show that (at constant Q^2) $dx = (Ex)/(E'\nu)dE'$ and plugging this into the total electron-parton elastic cross section gives the inelastic electron-nucleon cross section:

$$\frac{d^2\sigma}{d\Omega dE'} = \frac{1}{dE'}\left[\frac{d\sigma}{d\Omega}\right]_{\text{tot}} = \sum_i \sigma_M \times \left(\frac{E'}{E}\right) \times \left[1 + 2\tau \tan^2\left(\frac{\theta}{2}\right)\right] Z_i^2 P_i(x) \frac{Ex}{E'\nu} \tag{2.181}$$

Rearranging a few things, we find:

$$\frac{d^2\sigma}{d\Omega dE'} = \sigma_M \left[\frac{1}{\nu}\left(x\sum_i Z_i^2 P_i(x)\right) + \frac{2}{M}\left(\frac{1}{2}\sum_i Z_i^2 P_i(x)\right)\tan^2\left(\frac{\theta}{2}\right)\right] \tag{2.182}$$

By comparing this to the inelastic cross section from the previous section, we can immediately make the following identifications:

$$\nu W_2(\nu, Q^2) \;\rightarrow\; x\sum_i Z_i^2 P_i(x) = F_2(x) \tag{2.183}$$

$$M W_1(\nu, Q^2) \;\rightarrow\; \frac{1}{2}\sum_i Z_i^2 P_i(x) = F_1(x) \tag{2.184}$$

We find that, in the deep ($Q^2 \to \infty$) inelastic ($\nu \to \infty$) scattering regime, the inelastic response functions W_1 and W_2 no longer depend on ν and Q^2 separately. They only depend on a single scaling variable called Bjorken x (famously predicted by Bjorken [200]). The traditional interpretation [121, 201] of x is that it is the fraction

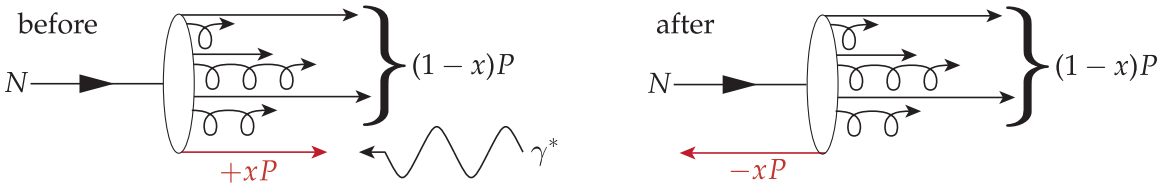

Figure 2.13: Deep Inelastic Scattering in the Breit Frame. At high Q^2, the partons are traveling essentially collinear to each other with very small transverse momenta.

of the nucleon's longitudinal momentum P carried by the struck parton in the Breit frame, see Fig. (2.13).

In this high Q^2 regime, it is more convenient to refer to the unitless (unpolarized) structure function F_1 and F_2. We see for Dirac particles that:

$$F_2(x) = 2xF_1(x) \tag{2.185}$$

which is known as the Callan-Gross relation [202] and its experimental verification was among the earliest & strongest evidence that charged partons are Dirac particles. In the quark-parton model, $F_2(x)$ given by [203]:

$$F_2(x) \;=\; x\sum_i Z_i^2 \left[p_i(x) + \bar{p}_i(x)\right] \tag{2.186}$$

where i refers to the parton flavors (up, down, strange, charm, bottom, top, gluons), Z_i is the parton charge in units of the elementary charge, and $p_i(x)$ & $\bar{p}_i(x)$ are the parton and antiparton fractional momentum distributions. Gluons are their own antiparticles so they only have one fractional momentum distribution $p_i(x) + \bar{p}_i(x) \to g(x)$. However, since gluons are chargeless $Z_g = 0$, they do not contribute to the sum. For protons and neutrons, considering only the three lightest

quark flavors (u = up, d = down, s = strange), we get:

$$F_2^p(x) = x\left[\frac{4}{9}\left(u^p(x)+\bar{u}^p(x)\right)+\frac{1}{9}\left(d^p(x)+\bar{d}^p(x)\right)+\frac{1}{9}\left(s^p(x)+\bar{s}^p(x)\right)\right] \quad (2.187)$$

$$F_2^n(x) = x\left[\frac{4}{9}\left(u^n(x)+\bar{u}^n(x)\right)+\frac{1}{9}\left(d^n(x)+\bar{d}^n(x)\right)+\frac{1}{9}\left(s^n(x)+\bar{s}^n(x)\right)\right] \quad (2.188)$$

Assuming charge symmetry for the u and d quarks and that the s distributions are the same for protons and neutrons:

$$u(x) = u^p(x) = d^n(x) \quad d(x) = d^p(x) = u^n(x) \quad s(x) = s^p(x) = s^n(x) \quad (2.189)$$

we find:

$$F_2^p(x) = x\left[\frac{4}{9}\left(u(x)+\bar{u}(x)\right)+\frac{1}{9}\left(d(x)+\bar{d}(x)\right)+\frac{1}{9}\left(s(x)+\bar{s}(x)\right)\right] \quad (2.190)$$

$$F_2^n(x) = x\left[\frac{4}{9}\left(d(x)+\bar{d}(x)\right)+\frac{1}{9}\left(u(x)+\bar{u}(x)\right)+\frac{1}{9}\left(s(x)+\bar{s}(x)\right)\right] \quad (2.191)$$

where the nucleon is described by a total of 6 quark and antiquark distributions. The physical significance of these distributions can be seen by the following sum rules:

$$U_v = \int_0^1 (u-\bar{u})\,dx = 2 \text{ valence up quarks} \quad (2.192)$$

$$D_v = \int_0^1 (d-\bar{d})\,dx = 1 \text{ valence down quark} \quad (2.193)$$

$$S_v = \int_0^1 (s-\bar{s})\,dx = 0 \text{ valence strange quarks} \quad (2.194)$$

The Gross-Llewellyn-Smith [204] & Adler [205, 206] sum rules relate the unpolarized proton structure functions from neutrino & antineutrino scattering experi-

ments to $U_v + D_v = 3$ & $U_v - D_v = 1$ respectively. They have both been verified to better than 10% [203]. At finite Q^2, these distributions and structure functions become a function of both x and Q^2: $F(x) \to F(x, Q^2)$. This soft dependence on Q^2 is refered to as a "scaling violation."

2.4.4 Scaling Violations & High Q^2 Evolution

A striking success of QCD is its ability to describe how Bjorken scaling is violated in DIS once we know the quark distributions at some reference Q^2 [198,203]. These violation occur due to gluon emission. Before the quark emits a gluon, it carries a momentum fraction y of the nucleon. After emitting a gluon, it carries a momentum fraction $x(< y)$ of the nucleon or alternatively a relative fraction x/y of its original momentum fraction. The probability of emitting a gluon which carries away the remaining momentum $(y - x)$ is given by the "splitting function" $P_{qq}(x/y)$. Analogous arguments can be made for when the parent parton and/or the struck parton is a gluon and this results in four splitting functions: P_{qq},P_{qg},P_{gq}, & P_{gg}. The parton distribution probed by the virtual photon $p(x, Q^2)$ depends on both the parent parton distribution $p(y, Q^2)$ and the splitting functions. This relationship is defined by the Dokshitzer-Gribov-Lipatov-Altarelli-Parisi (DGLAP) evolution equation given by [207]:

$$\frac{dp(x, Q^2)}{d(\log Q^2)} = \frac{\alpha_S(Q^2)}{2\pi} \int_x^1 \left[\sum_f q_f(y, Q^2) P_{pq}(z) + g(y, Q^2) P_{pg}(z) \right] \frac{dy}{y} \tag{2.195}$$

where the sum over flavors f is dropped when the parton being considered is a quark and the strong coupling constant α_s has a Q^2 dependence famously given

by [203,208,209]:

$$\alpha_s(Q^2) = \frac{4\pi}{\left[11 - 2N_f/3\right]\log(Q^2/\Lambda^2_{\rm QCD})} \tag{2.196}$$

where N_f is the number of quark flavors resolvable at Q^2 and $\Lambda_{\rm QCD} \approx 0.2$ GeV is the QCD scale.

2.4.5 Spin Structure Functions & Moments

In the deep ($Q^2 \to \infty$) inelastic ($\nu \to \infty$) scattering regime, the spin-dependent response functions G_1 & G_2 also exhibit Bjorken scaling [210,211]:

$$\lim_{(\nu,Q^2)\to\infty} M^2\nu G_1(\nu, Q^2) = g_1(x) \tag{2.197}$$

$$\lim_{(\nu,Q^2)\to\infty} M\nu^2 G_2(\nu, Q^2) = g_2(x) \tag{2.198}$$

where $g_1(x)$ and $g_2(x)$ are the unitless spin structure functions. In the quark-parton model, $g_1(x)$ is given by [212]:

$$g_1(x) = \sum_{i,m} mZ_i^2 \left[p_i^m(x) + \bar{p}_i^m(x)\right] \tag{2.199}$$

where $m = \pm 1/2$ labels the spin state of the quark. Assuming charge symmetry for the u and d quarks and that the s distributions are the same for protons and neutrons, then g_1 can be written as:

$$g_1^p(x) = \frac{1}{2}\left[\frac{4}{9}\Delta u(x) + \frac{1}{9}\Delta d(x) + \frac{1}{9}\Delta s(x)\right] \tag{2.200}$$

$$g_1^n(x) = \frac{1}{2}\left[\frac{4}{9}\Delta d(x) + \frac{1}{9}\Delta u(x) + \frac{1}{9}\Delta s(x)\right] \tag{2.201}$$

where the quark polarized distribution Δq is given by:

$$\Delta q(x) = \left[q^{\uparrow}(x) - q^{\downarrow}(x)\right] + \left[\bar{q}^{\uparrow}(x) - \bar{q}^{\downarrow}(x)\right] \tag{2.202}$$

Summing over quark flavors and integrating over x gives:

$$\Delta\Sigma = \int_0^1 (\Delta u + \Delta d + \Delta s)\ dx \tag{2.203}$$

which represents the fraction of the spin of the proton that is carried by the spin of the quarks. For the proton, $\Delta\Sigma$ has been found to be only about $1/3$ at $Q^2 = 5\ \mathrm{GeV}^2$ [213].

Because $g_2(x)$ is expected to be zero in the quark parton model, it does not have a simple physical interpretation. Using a technique called operator product expansion, see Sec. (2.4.7), it can be written as:

$$g_2(x, Q^2) = \underbrace{-g_1(x, Q^2) + \int_x^1 \frac{g_1(y, Q^2)}{y}\, dy}_{g_2^{\mathrm{WW}}} + g_2^{(3)}(x, Q^2) \tag{2.204}$$

where g_2^{WW} was first derived by Wandzura & Wilzcek [214] and is completely determined by g_1. The second term, $g_2^{(3)}$, is related to higher order spin-dependent correlations (higher twists) between quarks and gluons. At finite Q^2, the distributions and spin structure functions become a function of both x and Q^2: $g(x) \rightarrow g(x, Q^2)$. Analogous DGLAP evolution equations can be written for the polarized parton distributions with the substitutions $q_f \rightarrow \Delta q_f$ and $g \rightarrow \Delta G$ [215], where ΔG is the gluon polarization. Integrating the spin structure functions over x gives their

moments:

$$\Gamma_1(Q^2) = \int_0^1 g_1(x, Q^2)\, dx \tag{2.205}$$

$$\Gamma_2(Q^2) = \int_0^1 g_2(x, Q^2)\, dx \tag{2.206}$$

2.4.6 Bjorken Sum Rule

Following Close [216], the number of valence quarks for the proton and neutron are given by:

$$U_v^p - D_v^p = +1 \qquad U_v^n - D_v^n = -1 \tag{2.207}$$

which indicate that the quark distributions are related to nucleon isospin matrix element by:

$$U_v^{p,n} - D_v^{p,n} = \int_0^1 \left(u_{p,n}(x) - \bar{u}_{p,n}(x)\right) - \left(d_{p,n}(x) - \bar{d}_{p,n}(x)\right)\, dx = \langle p, n | \, 2\tau_3 \, | p, n \rangle \tag{2.208}$$

where $|p, n\rangle$ is the nucleon wavefunction in terms of its quark content and τ_3 is the isospin operator that acts in the quark flavor space. By analogy the quark polarization distributions are related to isospin-spin matrix element:

$$\int_0^1 \left(\Delta u_{p,n}(x) - \Delta d_{p,n}(x)\right)\, dx = \langle p, n | \, 2\tau_3 S_z \, | p, n \rangle \tag{2.209}$$

where S_z is the spin operator that acts in the quark spin space. The isospin & isospin-spin matrix elements are directly related to the vector & axial matrix ele-

ments responsible for neutron beta decay [168]. Their ratios given by:

$$\frac{\langle \tau_3 S_z \rangle_p}{\langle \tau_3 \rangle_p} = \frac{\text{spin flip (Gamow} - \text{Teller)}}{\text{non flip (Fermi)}} = \frac{\langle p^\uparrow | \tau_+ S_+ | n^\downarrow \rangle}{\langle p^\uparrow | \tau_+ | n^\uparrow \rangle} = \frac{\langle p^\uparrow | A_+^z | n^\downarrow \rangle}{\langle p^\uparrow | V_+^z | n^\uparrow \rangle} = \frac{g_A}{g_V} \tag{2.210}$$

where τ_+ & S_+ are the isospin & spin ladder operators, V_+^z & A_+^z are the vector & axial currents, and g_V & g_A are the weak vector & axial coupling constants. Since $\langle 2\tau_3 \rangle_p = +1$ for the proton, we immediately find that $\langle 2\tau_3 S_z \rangle_p = g_A/g_V$. This can be related to the proton and neutron spin structure moments giving the celebrated Bjorken Sum Rule (once referred to as the "worthless equation") [210, 211, 217]:

$$\Gamma_1^p - \Gamma_1^n = \frac{1}{2}\int_0^1 \left(\frac{4-1}{9}\right)(\Delta u(x) - \Delta d(x))\, dx = \frac{1}{6}\langle 2\tau_3 S_z \rangle = \frac{1}{6}\left(\frac{g_A}{g_V}\right) \tag{2.211}$$

Calculations from pQCD for 3 quarks flavors give the Q^2 evolution as [218]:

$$\Gamma_1^p(Q^2) - \Gamma_1^n(Q^2) = \frac{1}{6}\left(\frac{g_A}{g_V}\right)\left[1 - \frac{\alpha_s(Q^2)}{\pi} - 3.5833\frac{\alpha_s^2(Q^2)}{\pi^2} - 20.2153\frac{\alpha_s^3(Q^2)}{\pi^3}\right] \tag{2.212}$$

and has been verified to better than 10% [212].

2.4.7 Operator Product Expansion

Operator product expansion (OPE) is a general prescription for separating the perturbative, short-distance scale physics from the nonperturbative, long-distance scale physics in asymptotically free quantum field theories. OPE allows us to understand the behavior of the matrix element $\langle N' | A(x)B(0) | N \rangle$ as $x \to 0$ for *all* states $|N'\rangle$ & $|N\rangle$ [219], where $A(x)$ & $B(x)$ are called "local" operators because they depend on the position & time ($x = x^\mu = (t, \vec{x})$, not to be confused with Bjorken-x).

Wilson [220] has argued that the "operator product" $A(x)B(0)$ can be written as the following expansion:

$$A(x)B(0) = \sum_n C_n(x)O_n(0) \tag{2.213}$$

where $C_n(x)$ is a complex valued "coefficient function" that contains the short-distance physics and $O_n(0)$ is a local operator that describes the long-distance scale physics. The units of A, B, C_n, and O_n are given by [energy]^a, [energy]^b , [energy]^{c_n}, and [energy]^{o_n} respectively. By simple dimensional analysis, the "dimensions" a, b, c_n & o_n satisfy the relationship $c_n = a + b - o_n$. This expansion is analogous to a Taylor series expansion in the sense that the terms are ordered in powers of o_n [221]. The operators $\{O_n\}$ are formed by combinations of x and the fields & derivative operators of the quantum field theory in question. These combinations are constrained by the quantum numbers of the operator product and the symmetry properties of underlying theory [222]. Because the operators $\{O_n\}$ can be thought of as forming a "basis" in a linear "operator space," the expansion can be considered a linear decomposition with weights given by the coefficient functions [27].

In the context of deep inelastic scattering, OPE is a systematic technique for calculating higher order QCD corrections to the parton distributions [221, 223]. It can be applied by recalling that the hadronic tensor is the Fourier transform of the matrix element of the electromagnetic current product $J_\mu(x)J_\nu(0)$, see Eqn. (2.161). The Fourier transform implies that q and x are conjugate variables such that $Q^2 \to \infty$ corresponds to $x \to 0$. As a consequence, the dominant terms of the expansion in this limit are ones for which $C_n(x)$ have the form $1/x^{c_n}$ where $c_n > 0$. The exact form of $C_n(x)$ is given by dimensional analysis in combination with a calculation

of the Green's function that corresponds to the matrix element of O_n:

$$\langle N|\, O_n(0)\, |N\rangle = x_{\mu_1} \cdots x_{\mu_{J_n}} \underbrace{\langle N|\, O_n^{\mu_1 \cdots \mu_{J_n}}(0)\, |N\rangle}_{\text{Green's function}} \tag{2.214}$$

where $O^n_{\mu_1 \cdots \mu_n}$ is a Lorentz tensor of rank J_n and has units of [energy]$^{J_n+\tau_n}$. The quantity τ_n is called "twist" and it determines the dimensions of C_n by $c_n = a + b - \tau_n$ [224]. The most dominant terms in the expansion have the largest c_n which corresponds to the smallest twists. By applying dispersion relations, the coefficient functions $\{C_n\}$ can be related to the moments of the F_1, F_2, g_1, & g_2 [196, 197]. Lattice QCD can then be used to calculate these moments via a direct numerical calculation of the Green's function $\left\langle O_n^{\mu_1 \cdots \mu_{J_n}} \right\rangle$ [225].

2.5 Inelastic Scattering at Low Q^2

At low Q^2, it's usually more useful to talk about "virtual" photons interacting with the nucleon as a whole rather than electrons "elastically" scattering off of partons. In the Breit frame, the electron beam acts as a source of virtual photons being fired at a nucleon target, see Fig. (2.14). The virtual photon flux $\Gamma^\star$ is the number of virtual photons being fired at the nucleon per unit solid angle per unit time. The number of photons that are absorbed or scattered by the nucleon is given by the total virtual photoabsorption cross section $\sigma^\star_{\text{tot}}$. The *electron* inelastic scattering cross section is therefore written as a product of these two quantities $\Gamma^\star \sigma^\star_{\text{tot}}$. Photon scattering in this context is more generally referred to as Compton scattering. This framework uses the same language as real Compton scattering, which we'll introduce first.

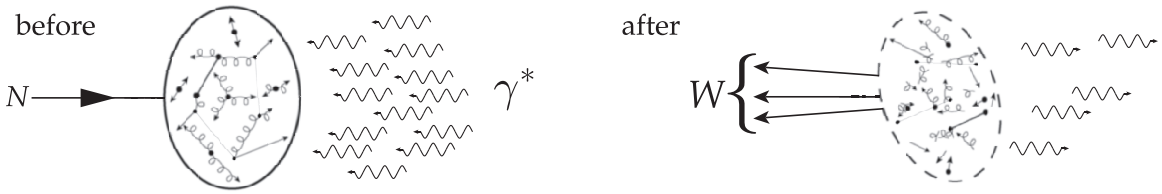

Figure 2.14: Inelastic Scattering at Low Q^2 in the Breit Frame. A virtual photon beam is fired at a nucleon. The absorbed photons excite the nucleon into a "blob" which then disintegrates into some hadronic debris.

2.5.1 Polarization Vector for Real Photons

The polarization vector for arbitrarily polarized real photons can be written in the circular polarization basis as, see Sec. (E.4.4):

$$\vec{\varepsilon} = \sqrt{\frac{1+P_\gamma}{2}} e^{-i\phi_\gamma} \hat{\varepsilon}_+ + \sqrt{\frac{1-P_\gamma}{2}} e^{+i\phi_\gamma} \hat{\varepsilon}_- \tag{2.215}$$

where P_γ is the degree of circular polarization and ϕ_γ is the angle of the residual linear polarization in the xy-plane as measured from the x-axis. Right (left) circularly polarized photons have a positive (negative) helicity $h_\gamma = P_\gamma = +1(-1)$. It will be more useful to represent this vector in the linear polarization basis:

$$\vec{\varepsilon} = \left[\sqrt{1-P_\gamma} \frac{e^{+i\phi_\gamma}}{2} + \sqrt{1+P_\gamma} \frac{e^{-i\phi_\gamma}}{2} \right] \hat{x} + \left[\sqrt{1-P_\gamma} \frac{e^{+i\phi_\gamma}}{2i} - \sqrt{1+P_\gamma} \frac{e^{-i\phi_\gamma}}{2i} \right] \hat{y} \tag{2.216}$$

The polarization state of a photon can also be described by its density matrix:

$$\overleftrightarrow{\rho} = \vec{\varepsilon}^* \vec{\varepsilon} = \begin{pmatrix} \varepsilon_x^* \varepsilon_x & \varepsilon_x^* \varepsilon_y & 0 \\ \varepsilon_y^* \varepsilon_x & \varepsilon_y^* \varepsilon_y & 0 \\ 0 & 0 & 0 \end{pmatrix} \tag{2.217}$$

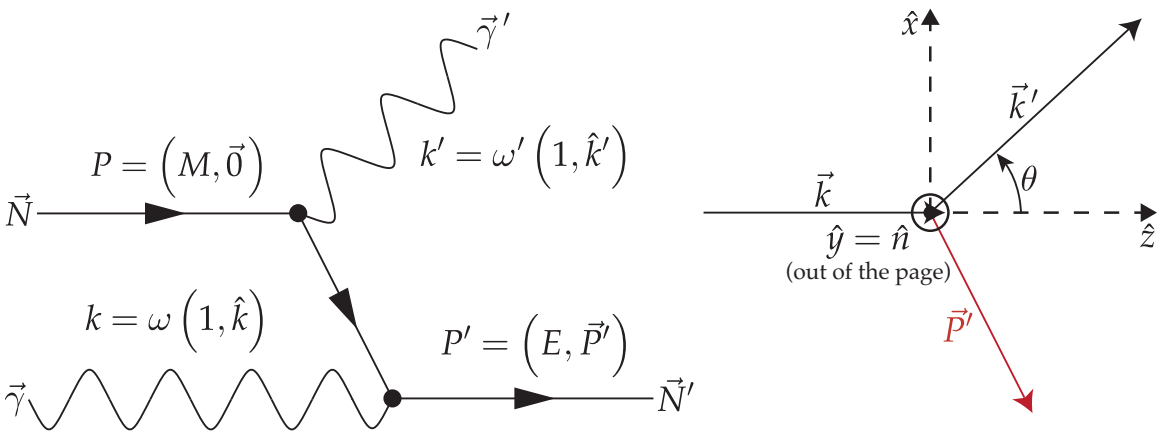

Figure 2.15: Kinematic Variables for Real Compton Scattering

The polarization vector can be written covariantly as $\varepsilon^\mu = (0, \vec{\varepsilon})$ which gives the corresponding covariant photon density matrix:

$$\rho^{\mu\nu} = \varepsilon^{\mu *}\varepsilon^\nu = \begin{pmatrix} 0 & 0 & 0 & 0 \\ 0 & \varepsilon_x^*\varepsilon_x & \varepsilon_x^*\varepsilon_y & 0 \\ 0 & \varepsilon_y^*\varepsilon_x & \varepsilon_y^*\varepsilon_y & 0 \\ 0 & 0 & 0 & 0 \end{pmatrix} \tag{2.218}$$

2.5.2 Real Compton Scattering from a Spin-1/2 Particle

A real photon with initial energy ω scatters from a particle at rest with mass M & charge Z through an angle θ with final energy ω', Fig. (2.15). In the lab frame, the directions of incoming and outgoing momenta of the photon are given by $\hat{k} = \hat{z}$ and $\hat{k}' = \hat{x}\sin(\theta) + \hat{z}\cos(\theta)$ respectively. For the case of elastic scattering ($P^2 = P'^2 = M^2$ where P & P' are the initial & final momenta of the particle), applying the conservation of momentum in the lab frame yields [226]:

$$\frac{\omega'}{\omega} = \frac{1}{1 + \left(2\omega/M\right)\sin^2\left(\frac{\theta}{2}\right)} \tag{2.219}$$

which is the identical to the formula for the elastic scattering of relativistic electrons with $\omega \leftrightarrow E$ & $\omega' \leftrightarrow E'$. In the Born approximation, the differential scattering cross section has the general form [27]:

$$\frac{d\sigma}{d\Omega} = \left(\frac{\omega'}{\omega}\right)^2 \left(\frac{1}{4M}\right)^2 \left(\frac{1}{4\pi}\right)^2 \left|4\pi\alpha\varepsilon_f^{\mu *}\varepsilon_i^{\nu} T_{\mu\nu}\right|^2 \tag{2.220}$$

where $\varepsilon_f^{\mu *}$ (ε_i^{ν}) is the final (initial) photon polarization vector and the Compton tensor is represented by:

$$T_{\mu\nu} = i \int \langle P', S' | \, T(J_\mu(x) J_\nu(0)) \, | P, S \rangle \, e^{ik'\cdot x} \, d^4x \tag{2.221}$$

where $S(S')$ is the initial (final) target polarization vector and J_μ is the electromagnetic current of the target particle. Its useful to rewrite the cross section in terms of the initial ($\rho_i^{\beta\nu}$) and final ($\rho_f^{\mu\alpha}$) photon densities:

$$\frac{d\sigma}{d\Omega} = r_c^2 \left(\frac{\omega'}{\omega}\right)^2 \left[\frac{1}{4}\rho_f^{\mu\alpha}\rho_i^{\beta\nu} T^*_{\alpha\beta} T_{\mu\nu}\right] \tag{2.222}$$

where $r_c = \alpha/M$ is the "classical" radius for a charged point particle [227]. Using the form of the Compton tensor for Dirac particles prescribed by QED, Lipps & Tolhoek have found [228, 229]:

$$\frac{1}{4}\rho_f^{\mu\alpha}\rho_i^{\beta\nu} T^*_{\alpha\beta} T_{\mu\nu} = Z^4 \sum_{n=0}^{4} \{\Phi_n\} \tag{2.223}$$

and $\{\Phi_n\}$ are a group of functions that involves every combination of n of the 4 polarization vectors that describe the photon and the target particle before and after scattering. Since we're only interested in specifying the initial polarizations,

we'll sum over the final polarizations to get:

$$\sum_{\varepsilon_f}\sum_{S'}\left[\frac{1}{4}\rho_f^{\mu\alpha}\rho_i^{\beta\nu}T^*_{\alpha\beta}T_{\mu\nu}\right] = Z^4(2\cdot 2)\left[\Phi_0+\Phi_1(\varepsilon_i)+\Phi_1(S)+\Phi(\varepsilon_i,S)\right] \tag{2.224}$$

where the Φ_n functions (N.B. the sign convention of [228] and the typo in [229], for example compare to [230]) for photons of elliptically polarized light are given by:

$$\begin{aligned}
\Phi_0 &= \frac{1}{8}\left[1+\cos^2(\theta)+\frac{(\omega-\omega')}{M}(1-\cos(\theta))\right] && (2.225)\\
\Phi_1(\varepsilon) &= +\frac{1}{8}\left[-\sqrt{1-P_\gamma^2}\cos(2\phi_\gamma)\right]\sin^2(\theta) && (2.226)\\
\Phi_1(S) &= 0 && (2.227)\\
\Phi_2(\varepsilon,S) &= -\frac{1}{8}\left[P_\gamma\right](1-\cos(\theta))\,\vec{P}_t\cdot\left[\frac{\vec{k}}{M}\cos(\theta)+\frac{\vec{k}'}{M}\right] && (2.228)
\end{aligned}$$

We can write the cross section as the sum of each type of photon polarization (none, circular, linear):

$$\sum_{\vec{\varepsilon}'}\sum_{\vec{P}'_t}\frac{d\sigma}{d\Omega} = Z^4\sigma_{\rm KN}\left(F_0 - P_\gamma\vec{P}_t\cdot\left[\overleftrightarrow{G}_0\,\hat{k}\right]-\sqrt{1-P_\gamma^2}\cos(2\phi_\gamma)H_0\right) \tag{2.229}$$

where the scale is given by $\sigma_{\rm KN}$ which is labeled after Klein & Nishina who first calculated [231] the polarization independent part F_0 for photon-electron scattering, the circular polarization dependent part is given by the matrix $\overleftrightarrow{G}_0$, and the part that depends only on the residual linear polarization of the light is H_0. By noting

that $1-\cos(\theta) = M(1/\omega' - 1/\omega)$, these terms are given by:

$$\begin{aligned}
\sigma_{\rm KN} &= \frac{\alpha^2}{2M^2}\left(\frac{\omega'}{\omega}\right)^2 && (2.230)\\
F_0 &= \frac{\omega'}{\omega} + \frac{\omega}{\omega'} - \sin^2(\theta) && (2.231)\\
\overleftrightarrow{G}_0 &= G_0^z \overleftrightarrow{1} + G_0^x \hat{n}\times && (2.232)\\
G_0^z &= \left(\frac{\omega}{\omega'} - \frac{\omega'}{\omega}\right)\cos(\theta) && (2.233)\\
G_0^x &= \left(1 - \frac{\omega'}{\omega}\right)\sin(\theta) && (2.234)\\
H_0 &= \sin^2(\theta) && (2.235)
\end{aligned}$$

Averaging over all initial photon polarizations ($P_\gamma = \pm 1$ and $\phi_\gamma = 0, \pi/2$) gives the usual Klein-Nishina formula. This result was generalized by Powell (among others) to include the effect of an anomalous magnetic moment ($\kappa^\star \neq 0$) [17,232]:

$$\left(\frac{d\sigma}{d\Omega}\right)_{\rm Powell} = \sigma_{\rm KN}\left(Z^4 F_0 + \left[\frac{8\omega\omega'}{M^2}\right]\left[\sum_{n=1}^{4} f_n \kappa^{\star n}\sin^2\left(\frac{\theta}{2}\right) + \left(\frac{\kappa^\star}{2}\right)^4\right]\right) \qquad (2.236)$$

where $\{f_n\}$ are given in Tab. (2.1). Integrating over $d\Omega$ gives the total cross section:

$$\frac{\sigma_{\rm tot}}{2\pi\alpha^2/M^2} = Z^4\left[u + \frac{1+\eta}{(1+2\eta)^2} + \frac{2\{1-(1+\eta)u\}}{\eta^2}\right] + \sum_{n=1}^{4} a_n\left[u - \frac{b_n}{(1+2\eta)^2}\right]\kappa^{\star n} \qquad (2.237)$$

where $\{a_n, b_n\}$ are given in Tab. (2.1) and η & u are given by:

$$\eta = \frac{\omega}{M} \qquad u = \frac{\log(1+2\eta)}{2\eta} \qquad (2.238)$$

n	f_n	a_n	b_n
1	$\sin^2\left(\frac{\theta}{2}\right)$	$+2$	$1+3\eta$
2	$1+\frac{1}{4}\sin^2\left(\frac{\theta}{2}\right)$	$+1/2$	$1+3\eta-8\eta^2$
3	$1-\frac{1}{2}\sin^2\left(\frac{\theta}{2}\right)$	-1	$1+3\eta+4\eta^2$
4	$\frac{1}{8}\cos^2\left(\frac{\theta}{2}\right)$	$-1/4$	$1+3\eta+4\eta^2+2\eta^3$

Table 2.1: Parameters for AMM Compton Scattering calculated by Powell [232].

In the low energy limit $\omega \ll M$, $u \approx 1-\eta+4\eta^2/3+\cdots$, $\eta \to 0$, and we recover the classical result first derived by Thomson for electrons [227]:

$$\lim_{\omega\to 0}\sigma_{\text{tot}} = \frac{8\pi}{3}\left(\frac{Z^4\alpha^2}{M^2}\right) \tag{2.239}$$

This is the limit regardless of the spin of the particle [233].

2.5.3 Forward Compton Scattering & The Optical Theorem

The probability for a particle to be scattered in the same direction as its original momentum is described by the "forward" scattering amplitude ($\mathcal{M}(0)$). The conservation of probability (unitarity) implies that the imaginary part of this amplitude ($\Im M(0)$) encodes the amount of attenuation of a beam of particles due to scattering. The total scattering cross section (σ_{tot}) quantifies precisely the same thing which implies that $\Im\mathcal{M}(0)$ is proportional to σ_{tot}. This exact form of this relationship is the content of the optical theorem which states [234, 235]:

$$\frac{d\sigma}{d\Omega} = |\mathcal{M}(\theta)|^2 \quad \Rightarrow \int \frac{d\sigma}{d\Omega}\, d\Omega = \sigma_{\text{tot}} = \frac{4\pi}{\omega}\Im\mathcal{M}(0) \tag{2.240}$$

where $\mathcal{M}(\theta)$ is the scattering amplitude. By inspecting Eqn. (2.220), we can write down the Compton scattering amplitude:

$$\mathcal{M}(\theta) = \left(\frac{\alpha\omega'}{4M\omega}\right)\varepsilon_f^{\mu *}\varepsilon_i^{\nu} T_{\mu\nu}(\theta) \tag{2.241}$$

where the angular dependence is buried deep in $T_{\mu\nu}$. For forward scattering $\theta = 0$, the initial and final photon polarizations are the same ($\varepsilon_f = \varepsilon_i$) which allows us to identify $\varepsilon_f^{\mu *}\varepsilon_i^{\nu}$ with the initial photon density matrix $\rho_i^{\mu\nu}$. In addition $P' = P$ and $S' = S$ which implies that the forward Compton tensor is now given by:

$$T_{\mu\nu}(\theta = 0) = i\int d^4x\, e^{ik'\cdot x}\left\langle P,S\right| T(J_\mu(x)J_\nu(0))\left|P,S\right\rangle \tag{2.242}$$

If the particle in question is a nucleon, then we can immediately relate the forward Compton tensor to the nucleon hadronic tensor given in Eqn. (2.161) by:

$$\int(\cdots)\left\langle\left[J_\mu(x),J_\nu(0)\right]\right\rangle = 2\int(\cdots)\left\langle T(J_\mu(x)J_\nu(0))\right\rangle \quad \Rightarrow \quad T_{\mu\nu}(\theta=0) = i\pi W_{\mu\nu} \tag{2.243}$$

where the integral over the commutator product "double counts" the time-ordered product. This relationship can be used to relate the nucleonic structure functions contained in $W_{\mu\nu}$ to the total real photon absorption cross sections via the optical theorem. For the case of real Compton scattering from a polarized nucleon with an unobserved final photon state, we find:

$$\sigma_{\text{tot}} = \sum_{\varepsilon_f}\sum_{S'}\frac{4\pi}{\omega}\Im\mathcal{M}(0) = \frac{8\pi}{\omega}\left(\frac{\alpha}{4M}\right)\Im\left\{\varepsilon_i^{\mu *}\varepsilon_i^{\nu}T_{\mu\nu}(\theta=0)\right\} = \frac{4\pi^2\alpha}{\omega}\Im\left\{\rho_i^{\mu\nu}\frac{iW_{\mu\nu}}{2M}\right\} \tag{2.244}$$

The sum over ε_f results in an additional factor of 2, whereas the sum over S' is implicit in the structure of $W_{\mu\nu}$. To explicitly evaluate the tensor contraction, we'll note that $q = k = k' = \omega(1, \hat{z})$ & $Q^2 = 0$ and use the following useful identity:

$$\varepsilon_{\mu\nu\alpha\beta} M^\mu N^\nu A^\alpha B^\beta = \begin{array}{l} +M^0[(\vec{N} \times \vec{A}) \cdot \vec{B}] - B^0[(\vec{M} \times \vec{N}) \cdot \vec{A}] \\ +A^0[(\vec{B} \times \vec{M}) \cdot \vec{N}] - N^0[(\vec{A} \times \vec{B}) \cdot \vec{M}] \end{array} \tag{2.245}$$

which gives:

$$\rho_i^{\mu\nu} \frac{i W_{\mu\nu}}{2M} = \frac{i}{M} \left(F_1 - P_\gamma \left[\hat{P}_t \cdot \hat{q} \right] g_1 \right) \tag{2.246}$$

For pure circularly polarized photons, $P_\gamma = h_\gamma = \pm 1$ and the total real photoabsorption cross sections are [236]:

$$\sigma_{3/2} \equiv \sigma_{\text{tot}} \left(h_\gamma \hat{P}_t \cdot \hat{q} = +1 \right) = \left(\frac{4\pi^2 \alpha}{M\omega} \right) \left[F_1 - g_1 \right] \tag{2.247}$$

$$\sigma_{1/2} \equiv \sigma_{\text{tot}} \left(h_\gamma \hat{P}_t \cdot \hat{q} = -1 \right) = \left(\frac{4\pi^2 \alpha}{M\omega} \right) \left[F_1 + g_1 \right] \tag{2.248}$$

$$\sigma_{\text{T}} \equiv \frac{\sigma_{3/2} + \sigma_{1/2}}{2} = \left(\frac{4\pi^2 \alpha}{M\omega} \right) F_1 \tag{2.249}$$

$$\sigma'_{\text{TT}} = -\sigma_{\text{TT}} \equiv \frac{\sigma_{3/2} - \sigma_{1/2}}{2} = -\left(\frac{4\pi^2 \alpha}{M\omega} \right) g_1 \tag{2.250}$$

We can now compare the spin-independent cross section σ_{T} to the total Powell cross section to find the functional form for the structure function $F_1(\nu, Q^2)$ at $Q^2 = 0$ for a Dirac particle with an anomalous magnetic moment:

$$F_1(\nu, 0) = \frac{\alpha\eta}{2\pi} \left[Z^4 \left[u + \frac{1+\eta}{(1+2\eta)^2} + \frac{2\left\{1 - (1+\eta)\, u\right\}}{\eta^2} \right] + \sum_{n=1}^{4} a_n \left[u - \frac{b_n}{(1+2\eta)^2} \right] \kappa^{\star n} \right] \tag{2.251}$$

where $\omega = \nu$ and $\eta = \omega / M$, see Tab. (2.1).

2.5.4 Dispersion Relations

"Dispersion relations" are a consequence of the requirement that cause precedes effect (causality), see for example [237]. For example, a target particle will not be scattered until it is struck by the beam. The mathematical consequence of causality is that the Fourier transform of the scattering amplitude vanishes for all times $t < 0$, where $t = 0$ is when the interaction takes place [238]. This immediately implies, by the Titsmarch theorem [239], that the real and imaginary parts of the scattering amplitude are related by:

$$\Re\{\mathcal{M}(\nu)\} = +\frac{1}{\pi}\,\mathrm{PV}\int_{-\infty}^{+\infty}\frac{\Im\{\mathcal{M}(\omega)\}}{\omega-\nu}\,d\omega \tag{2.252}$$

$$\Im\{\mathcal{M}(\nu)\} = -\frac{1}{\pi}\,\mathrm{PV}\int_{-\infty}^{+\infty}\frac{\Re\{\mathcal{M}(\omega)\}}{\omega-\nu}\,d\omega \tag{2.253}$$

where PV refers to the Cauchy principal value and we've assumed that $|\mathcal{M}(\omega)| \to 0$ as $\omega \to 0$. If $\mathcal{M}$ exhibits crossing symmetry such that $\mathcal{M}(-\omega) = +(-)\mathcal{M}^*(\omega)$, then $\Re\mathcal{M}$ is an even (odd) function and $\Im\mathcal{M}$ is an odd (even) function. This can be used to reduce the integration limits to $\omega > 0$:

$$\Re\{\mathcal{M}(\nu)\}_{\mathrm{even}} = \frac{2}{\pi}\,\mathrm{PV}\int_{0}^{+\infty}\frac{\omega\Im\{\mathcal{M}(\omega)\}_{\mathrm{odd}}}{\omega^2-\nu^2}\,d\omega \tag{2.254}$$

$$\Re\{\mathcal{M}(\nu)\}_{\mathrm{odd}} = \frac{2}{\pi}\,\mathrm{PV}\int_{0}^{+\infty}\frac{\nu\Im\{\mathcal{M}(\omega)\}_{\mathrm{even}}}{\omega^2-\nu^2}\,d\omega \tag{2.255}$$

which can be done for $\Im\mathcal{M}$ as well. We'll assume that $\mathcal{M}$ can be decomposed into an even symmetric part $f(\omega)$ and an odd symmetric part $g(\omega)$. Dispersion relations can be formed independently for $f(\omega)$ and $g(\omega)$. In this case, we can improve the convergence of the integral as $|\omega| \to \infty$ by forming a dispersion relation for

$f(\omega)/\omega^{2n}$ and $g(\omega)/\omega^{2n+1}$ where n is an integer ≥ 0:

$$\Re\left\{\frac{f(\nu)}{\nu^{2n}}\right\} = \frac{2}{\pi}\,\mathrm{PV}\int_0^\infty \Im\left\{\frac{f(\omega)}{\omega^{2n}}\right\}\frac{\omega}{\omega^2-\nu^2}\,d\omega \tag{2.256}$$

$$\Re\left\{\frac{g(\nu)}{\nu^{2n+1}}\right\} = \frac{2}{\pi}\,\mathrm{PV}\int_0^\infty \Im\left\{\frac{g(\omega)}{\omega^{2n+1}}\right\}\frac{\omega}{\omega^2-\nu^2}\,d\omega \tag{2.257}$$

where $\Re\{\cdots\}$ is even in both cases implying that $\Im\{\cdots\}$ is odd. The assumption that the ω^k factor in the denominator does not introduce a pole at $\omega = 0$ is called the "no subtraction hypothesis." [238] This form of the dispersion relation is suggestive of a Taylor expansion of $f(\omega)$ & $g(\omega)$ about $\omega = 0$.

2.5.5 Low Energy Theorems and Expansions

The Compton scattering amplitude can be written as a series of terms that are composed of scalar quantities formed from combinations of the initial & final photon & particle polarizations & momenta. Each of these scalars are multiplied by coefficients that are functions of the initial & final photon energies and the electromagnetic properties of the particle. Gauge invariance (conservation of charge [240]), Lorentz invariance ("intrinsic" or dynamical probability of interaction is independent of reference frame [27]), and crossing symmetry constrains the exact form of these terms and their corresponding coefficients. Based on these arguments, the Low Energy Theorem states that the lowest order terms (in photon energies) are given solely by the particle's mass M, charge Z, and anomalous magnetic moment $\kappa^\star$ [241,242]. In other words, it states that the longest wavelength photons are only sensitive to the global properties of the system (target particle).

If the wavelength is shortened slightly (resolution is increased), then these photons are additionally sensitive to the characteristic size of the particle and to the

ability of its internal degrees of freedom to reconfigure itself in response to the electric and magnetic fields associated with the photons [243–246]. The "electromagnetic" size of the particle characterized by the root mean square radius ($\langle r^2_{E,M} \rangle$) of its charge and magnetization distributions. The measure of its ability to reconfigure itself is known as its polarizability (α_E, β_M). In atomic systems, polarizabilities are directly related to the medium's index of refraction and, in the context of quantum mechanics, provide a link between microscopic structure and the macroscopic optical phenomenon caused by it (i.e. refraction, absorption, Faraday rotation). Because $\langle r^2_{E,M} \rangle$, α_E, β_M have to be calculated from a theory that describes the detailed electromagnetic structure of the particle, the terms that involve them are said to be a consequence of a Low Energy "Expansion."

In general, each coefficient includes terms that have even and odd powers of the photon energies [246]. For the special case of forward scattering, the even & odd terms decouple and the forward real Compton scattering amplitude can be written as:

$$\mathcal{M}(\theta = 0) = f(\omega)\,[\vec{\varepsilon}^{\,*} \cdot \vec{\varepsilon}] + g(\omega)\left[i\hat{P}_t \cdot (\vec{\varepsilon}^{\,*} \times \vec{\varepsilon})\right] \tag{2.258}$$

where f (g) is a real function even (odd) in ω and spin independent (dependent) given by [236]:

$$f(\omega) = -\frac{\alpha Z^2}{M} + (\alpha_E + \beta_M)\,\omega^2 + O(\omega^4) \tag{2.259}$$

$$g(\omega) = \left(-\frac{\alpha \kappa^{\star 2}}{2M^2}\right)\omega + (\gamma_0)\,\omega^3 + O(\omega^5) \tag{2.260}$$

where Z, $\kappa^\star$, & M are the charge, anomalous magnetic moment, and mass of the spin-1/2 particle and α_E, β_M, & γ_0 are the electric, magnetic, and forward-spin polarizabilities. In atomic systems, the electric polarizability is related to the index

of refraction n by $n-1=[\mathrm{N}]\alpha_E$ where [N] is the number density of the medium. Furthermore, the forward-spin polarizability is responsible for the Faraday effect (i.e. Faraday rotation) and is calculated explicitly for alkali atoms in Sec. (E).

2.5.6 Gerasimov-Drell-Hearn Sum Rule

The real part of the forward Compton scattering amplitude is given to lowest orders in ω by the Low Energy Theorem & Expansion. The imaginary part of the forward Compton scattering amplitude is given by the total photoabsorption cross sections via the optical theorem. Making this connection explicitly order by order gives:

$$-\left(\frac{4\pi^2\alpha Z^2}{M}\right) \quad ? \quad \int_{\nu_0}^{\infty}\left(\sigma_{3/2}+\sigma_{1/2}\right)\,d\nu\to\infty \tag{2.261}$$

$$\frac{2\pi^2\alpha\kappa^{\star 2}}{M^2} = +\int_{\nu_0}^{\infty}\left(\frac{\sigma_{3/2}-\sigma_{1/2}}{\nu}\right)\,d\nu = I_{\mathrm{GDH}} \tag{2.262}$$

$$\alpha_E+\beta_M = +\frac{1}{4\pi^2}\int_{\nu_0}^{\infty}\left(\frac{\sigma_{3/2}+\sigma_{1/2}}{\nu^2}\right)\,d\nu = I_{\mathrm{Baldin}} \tag{2.263}$$

$$\gamma_0 = -\frac{1}{4\pi^2}\int_{\nu_0}^{\infty}\left(\frac{\sigma_{3/2}-\sigma_{1/2}}{\nu^3}\right)\,d\nu \tag{2.264}$$

where ν_0 is the inelastic threshold and, in this case, the amplitudes are defined to ignore elastic scattering. The first line is nonsensical both because the bracketed term on the l.h.s. & the cross sections are positive definite and because the integral does not converge. The second line gives the Gerasimov-Drell-Hearn sum rule for *any* spin-1/2 object [247, 248]. The third line is known as the Baldin sum rule [244] and is an unpolarized analog to the GDH sum rule. Finally, the last simply provides a definition for the forward spin polarizability.

In a paper received on October 26, 1964 and published on April 26, 1965, C.K.

Iddings [249] anticipated the GDH sum rule in the course of studying the hyperfine structure of Hydrogen (at the urging of V.W. Hughes). The main ingredients were present (dispersion relations and low energy theorem) but the sum rule was not explicitly formed [250]. Therefore, the earliest known publication of the GDH sum rule is S.B. Gerasimov's submission to *Yadernaya Fizika* on March 9, 1965 (published October 1965 [247], translated by J.G. Adashko for *Soviet Journal of Nuclear Physics* in April 1966 [251]). Quoting S.D. Drell and A.C. Hearn, their paper's contribution "is very simply that of joining the dispersion relation [Eq. (3)] and the low energy theorem [Eq. (4)] with the no-subtraction assumption" (received April 20, 1966, published May 16, 1966) [248]. Using current algebra techniques, Masataka Hosoda and Kunio Yamamoto derived the sum rule for Dirac particles [252] (received May 20, 1966) and extended the argument for all spin-1/2 and spin-3/2 nuclei [253] (received June 6, 1966). At the time, there was some discussion in the literature as to whether the sum rule holds for composite objects as well [254–256], for example the ^{3}He nucleus. In his original paper, Gerasimov claims without proof that the sum rule is true for nuclei and uses the sum rule to study nuclear binding effects. The issue was essentially settled by the early 70's in favor of the generality of the sum rule [257–262], see in particular Brodsky & Primack [258]. The generalization to spin greater than $1/2$ was written down in the original Gerasimov paper and has been rederived many times [19, 20, 25, 26, 257, 263].

Making the identification that $\sigma_{3/2(1/2)}$ refers to the cross section when the photon helicity is parallel (antiparallel) with the particle's spin, the $S \geq 1/2$ general-

ization for all three conventions of the anomalous magnetic moment is written as:

$$\frac{I_{\rm GDH}(m_S)}{4\pi^2\alpha|m_S|} = \frac{1}{4\pi^2\alpha|m_S|}\int_0^\infty \left(\frac{\sigma_P - \sigma_A}{\nu}\right)\, d\nu = \left(\frac{\kappa}{M_P}\right)^2 = \left(\frac{\kappa^\star}{M}\right)^2 = \left(\frac{\kappa_{\rm Ji}}{(2S)M}\right)^2 \tag{2.265}$$

where m_S is the S_z component of the particle's spin state (e.g. $m_S = \pm 1/2$ for $S = 1/2$), M_p is the mass of the proton, and the three conventions for the anomalous magnetic moment are:

$$\kappa \equiv \frac{g}{2} - Z\frac{M_P}{M} \qquad \kappa^\star \equiv \frac{g}{2}\left(\frac{M}{M_P}\right) - Z \qquad \kappa_{\rm Ji} \equiv gS\frac{M}{M_P} - 2ZS \tag{2.266}$$

where the total magnetic moment of the particle is given by $\mu = g\mu_N S$. It is useful to express the sum rule in terms of the Gerasimov cross section defined by:

$$\sigma_G \equiv \frac{2\pi^2\alpha\hbar^2}{M_P^2c^2} = 63.7104\ \mu{\rm b}\ \ ({\rm SI}) \tag{2.267}$$

which gives:

$$I_{\rm GDH}(m_S) = 2\sigma_G|m_{\rm S}|\kappa^2 = 2\sigma_G|m_{\rm S}|\left(\frac{\kappa^\star}{M/M_P}\right)^2 = 2\sigma_G|m_{\rm S}|\left(\frac{\kappa_{\rm Ji}}{(2S)M/M_P}\right)^2 \tag{2.268}$$

Recently, X.Ji and Y.Li [25] have derived a closely related form of sum rule:

$$I_{\rm JL} = \sum_{m_S=-S}^{+S}\frac{|m_S|}{2}I_{\rm GDH}(m_S) = \pi^2\alpha\left[\frac{2S(S+1)(2S+1)}{3}\right]\left(\frac{\kappa_{\rm Ji}}{(2S)M}\right)^2 \tag{2.269}$$

See Helbing for a recent review of the GDH sum rule and the status of its verification for protons [264].

Species	^{1}H	^{1}n	^{2}H	^{3}He	^{3}H
Z	$+1$	0	$+1$	$+2$	$+1$
S	$1/2$	$1/2$	1	$1/2$	$1/2$
m_S	$\pm 1/2$	$\pm 1/2$	$0, \pm 1$	$\pm 1/2$	$\pm 1/2$
$M(M_P)$	1.0000	1.0014	1.9990	2.9932	2.9937
$\mu(\mu_N)$	$+2.7928$	-1.9130	$+0.8574$	-2.1275	$+2.9790$
g	$+5.5857$	-3.8261	$+0.8574$	-4.2550	$+5.9579$
κ	$+1.7928$	-1.9130	-0.0715	-2.7957	$+2.6449$
$\kappa^\star$	$+1.7928$	-1.9157	-0.1430	-8.3679	$+7.9182$
$\kappa_{\rm Ji}$	$+1.7928$	-1.9157	-0.2860	-8.3679	$+7.9182$
$I_{\rm GDH}(m_S)(\mu{\rm b})$	204.78	233.16	$0, 0.65194$	497.95	445.70

Table 2.2: GDH Sum Rule evaluated for the proton, neutron, deuteron, and helion. Data from [265, 266].

2.5.7 Polarization Vector for Virtual Photons

There are two differences between real photons and virtual photons. First, virtual photons are "off mass shell" or, in other words, they are not constrained to have the same rest mass as real photons ($q^2 = -Q^2 \neq 0$). Second, a direct consequence of the first, virtual photons may have a component of their polarization parallel to its momentum ($\vec{\varepsilon} \cdot \vec{q} \neq 0$). The polarization state of the virtual photon involved in electron scattering is prescribed by the leptonic tensor. It is straightforward to show (after some tedious algebra) that the leptonic tensor (summed over the final electron spin state s') for a longitudinally polarized electron beam with polarization $P_b = h_b = \pm 1$ can be written as [37, 267]:

$$\sum_{s'} L^{\mu\nu} = \left(\frac{2Q^2}{1-\varepsilon} \right) \rho^{\mu\nu} \tag{2.270}$$

where ε is the virtual photon polarization parameter and $\rho^{\mu\nu}$ in the lab frame is given by:

$$\begin{bmatrix} \gamma_\beta^2\varepsilon & \gamma_\beta\sqrt{\varepsilon(1+\varepsilon)/2} & ih_b\gamma_\beta\sqrt{\varepsilon(1-\varepsilon)/2} & \beta\gamma_\beta^2\varepsilon \\ \gamma_\beta\sqrt{\varepsilon(1+\varepsilon)/2} & (1+\varepsilon)/2 & ih_b\sqrt{1-\varepsilon^2}/2 & \beta\gamma_\beta\sqrt{\varepsilon(1+\varepsilon)/2} \\ -ih_b\gamma_\beta\sqrt{\varepsilon(1-\varepsilon)/2} & -ih_b\sqrt{1-\varepsilon^2}/2 & (1-\varepsilon)/2 & -ih_b\beta\gamma_\beta\sqrt{\varepsilon(1-\varepsilon)/2} \\ \beta\gamma_\beta^2\varepsilon & \beta\gamma_\beta\sqrt{\varepsilon(1+\varepsilon)/2} & ih_b\beta\gamma_\beta\sqrt{\varepsilon(1-\varepsilon)/2} & \beta^2\gamma_\beta^2\varepsilon \end{bmatrix} \tag{2.271}$$

where β is the velocity of the Breit frame relative to the lab frame and, along with γ_β, it is given by:

$$\beta = \frac{\nu}{|\vec{q}|} \qquad \gamma_\beta = \frac{|\vec{q}|}{Q} \qquad \beta\gamma_\beta = \frac{\nu}{Q} \qquad \gamma_\beta^2 = \frac{1}{1-\beta^2} \tag{2.272}$$

Careful inspection of $\rho^{\mu\nu}$ allows us to interpret it as the virtual photon density matrix for a polarization vector given by:

$$\varepsilon^\mu = \left(\gamma_\beta\sqrt{\varepsilon} \ , \ \sqrt{\frac{1+\varepsilon}{2}} \ , \ ih_b\sqrt{\frac{1-\varepsilon}{2}} \ , \ \beta\gamma_\beta\sqrt{\varepsilon} \right)^{\mathrm{T}} \tag{2.273}$$

The polarization vector has the normalization $\varepsilon^{\mu *}\varepsilon_\mu = \varepsilon - 1$. By noting that $q = (v, \vec{q}) = Q(\beta\gamma_\beta, 0, 0, \gamma_\beta)$, we find $\varepsilon^\mu q_\mu = 0$. It is useful to rewrite ε^μ as a sum of mutually orthogonal transverse (T) & longitudinal (L) parts $\vec{\varepsilon}_{\mathrm{T}} \cdot \vec{\varepsilon}_{\mathrm{L}} = 0$:

$$\varepsilon^\mu = \varepsilon_{\mathrm{T}}^\mu + \varepsilon_{\mathrm{L}}^\mu \tag{2.274}$$

$$\varepsilon_{\mathrm{T}}^\mu = \left(0 \ , \ \sqrt{\frac{1+\varepsilon}{2}} \ , \ ih_b\sqrt{\frac{1-\varepsilon}{2}} \ , \ 0 \right)^{\mathrm{T}} \tag{2.275}$$

$$\varepsilon_{\mathrm{L}}^\mu = \sqrt{\varepsilon}\left(\gamma_\beta \ , \ 0 \ , \ 0 \ , \ \beta\gamma_\beta \right)^{\mathrm{T}} \tag{2.276}$$

which gives the following spatial dot & cross products:

$$\vec{\varepsilon}^* \cdot \vec{\varepsilon} = |\vec{\varepsilon}_{\rm T}|^2 + |\vec{\varepsilon}_{\rm L}|^2 = 1 + \beta^2\gamma_\beta^2\varepsilon \tag{2.277}$$

$$\vec{\varepsilon}^* \times \vec{\varepsilon} = \vec{\varepsilon}_{\rm T}^* \times \vec{\varepsilon}_{\rm T} + (\vec{\varepsilon}_{\rm T}^* - \vec{\varepsilon}_{\rm T}) \times \vec{\varepsilon}_{\rm L} = ih_b P_\gamma \left[\overleftrightarrow{1} - (\lambda_{\rm LT})\,\hat{n}\times\right]\hat{q} \tag{2.278}$$

where $\hat{q}$ is the direction of the momentum of the virtual photon and $\hat{n}$ is a unit vector that is perpendicular to the scattering plane, see Sec. (2.1.3). Comparing these relationships to those for real photons leads to the interpretation of ε as a measure of the degree of virtually or non-realness of the photon ($\varepsilon = 0$ for real photons), P_γ as the degree of circular polarization as before, and $\lambda_{\rm LT}$ as the ratio of the longitudinal linear polarization to the transverse linear polarization:

$$P_\gamma = \sqrt{1-\varepsilon^2} \qquad \lambda_{\rm LT} = \frac{\beta\gamma_\beta\sqrt{\varepsilon}}{\sqrt{(1+\varepsilon)/2}} = \frac{\beta\gamma_\beta\sqrt{2\varepsilon(1-\varepsilon)}}{P_\gamma} \tag{2.279}$$

In the limit of $Q^2 \to 0$, $\varepsilon \to 0$ and the virtual photons become circularly polarized real photons. In the limit of $Q^2 \to \infty$, $\varepsilon \to 1$ and the virtual photons becomes completely linearly polarized.

2.5.8 Virtual Compton Scattering

There are a few different processes that could be referred to as "virtual Compton scattering" [203]. Bethe-Heitler (BH) is the process where the incoming or outgoing electron emits a "soft" (low energy) photon. Virtual Compton scattering (VCS) is the process (generally speaking) where the incoming nucleon absorbs a virtual photon from the electron and then emits a real photon. Doubly virtual Compton scattering (V^2CS) is the term used to describe electron scattering and the one that

we're interested in the following sections.

It is straightforward to the generalize the various integrals in Sec. (2.5.6) by simply allowing the integrands to have a Q^2 dependence. What's desired, however, is a sum "rule"' which equates the generalized integral (to be measured) to some fundamental property of the system (to be calculated) over the entire Q^2 range. This can be done by generalizing the forward Compton scattering amplitude for the case of virtual photons and calculating the virtual photoabsorption cross sections using the optical theorem:

$$\sigma_V = \frac{4\pi^2\alpha}{K}\Im\left\{\rho^{\mu\nu}\frac{iW_{\mu\nu}}{2M}\right\} \tag{2.280}$$

where we've introduced the parameter K in place of ω to make units "work out." Unlike the case for real photons, there is some ambiguity as to what the parameter K should represent. There are three standard conventions for this virtual photon flux "factor" K (that reduce to ν for real photons):

1. $K_0 = \nu$
2. $K_G = |\vec{q}| = \sqrt{\nu^2 + Q^2} = \nu\sqrt{1 + \frac{4M^2x^2}{Q^2}}$, Gilman convention, "the magnitude of the laboratory photon three-momentum" [268].
3. $K_H = (W^2 - M^2)/(2M) = \nu - Q^2/(2M) = \nu(1 - x)$, Hand convention, "the laboratory photon energy producing a final state of total center-of-mass energy" W after absorption by a nucleon at rest [269].

It's important to note that the extraction of structure functions (F_1, F_2, g_1, g_2) and their moments do not depend on the choice of K.

Using the Eqn. (2.245), we find:

$$\begin{aligned}\rho_i^{\mu\nu}\frac{iW_{\mu\nu}}{2M} &= \frac{i}{M}\left[(1-\varepsilon)F_1+\varepsilon\gamma_\beta^2\left(\frac{M}{\nu}\right)F_2\right.\\ &\left.-h_b P_\gamma \hat{P}_t\cdot\left\{\hat{q}\left(g_1-\frac{g_2}{\beta^2\gamma_\beta^2}\right)+(\hat{n}\times\hat{q})\left(\frac{\lambda_{\rm LT}}{\beta\gamma_\beta}\right)\left(\frac{g_1+g_2}{\beta\gamma_\beta}\right)\right\}\right] \quad (2.281)\end{aligned}$$

It is conventional [236] to split the total photoabsorption cross section σ_V into parts that depend on 1, ε, $\hat{P}_t\cdot\hat{q}$, and $\hat{P}_t\cdot(\hat{n}\times\hat{q})$:

$$\sigma_V=\sigma_{\rm T}+\varepsilon\sigma_{\rm L}-h_b(\hat{P}_t\cdot\hat{q})\sqrt{1-\varepsilon^2}\sigma_{\rm TT}-h_b\hat{P}_t\cdot(\hat{n}\times\hat{q})\sqrt{2\varepsilon(1-\varepsilon)}\sigma_{\rm LT} \quad (2.282)$$

where the individual cross sections are given by:

$$\begin{aligned}\sigma_{\rm T} &= \frac{\sigma_{1/2}+\sigma_{3/2}}{2}=\sigma_K[F_1] && (2.283)\\ \sigma_{\rm L} &= \sigma_K\left[\gamma_\beta^2\left(\frac{M}{\nu}\right)F_2-F_1\right] && (2.284)\\ \sigma_{\rm TT} &= -\sigma'_{\rm TT}=\sigma_{\rm long}=\frac{\sigma_{1/2}-\sigma_{3/2}}{2}=\sigma_K\left[g_1-\frac{g_2}{\beta^2\gamma_\beta^2}\right] && (2.285)\\ \sigma_{\rm LT} &= -\sigma'_{\rm LT}=\sigma_{\rm trans}=\sigma_K\left[\frac{g_1+g_2}{\beta\gamma_\beta}\right] && (2.286)\\ \sigma_K &= \frac{4\pi^2\alpha}{MK} && (2.287)\end{aligned}$$

where $\beta\gamma_\beta=\nu/Q$ and $\gamma_\beta^2=1+\nu^2/Q^2$. These virtual photoabsorption cross sections are directly related to the inclusive inelastic electron scattering cross section by:

$$\frac{d^2\sigma}{d\Omega dE'}=\frac{\alpha^2}{2MQ^4}\left(\frac{E'}{E}\right)\left\{\sum_{s'}L^{\mu\nu}\right\}W_{\mu\nu}=\frac{\alpha^2}{Q^4}\left(\frac{E'}{E}\right)\left(\frac{2Q^2}{1-\varepsilon}\right)\rho^{\mu\nu}\frac{W_{\mu\nu}}{2M}=\Gamma_V\sigma_V \quad (2.288)$$

where Γ_V is the virtual photon flux (number of virtual photons per unit time per unit solid angle):

$$\Gamma_V = \frac{\alpha}{2\pi^2}\left(\frac{E'}{E}\right)\frac{K}{Q^2}\left[\frac{1}{1-\varepsilon}\right] = \frac{2(\sigma_R - \sigma_M)}{\sigma_K M(1-\varepsilon)} \tag{2.289}$$

In this case, there are two extra cross sections: $\sigma_{\rm L}$, which is solely due to the longitudinal polarization component of the virtual photon, and $\sigma_{\rm LT}$, which is an interference term between the longitudinal and transverse polarization components of the virtual photon. In the real photon limit $Q^2 \to 0$, we find:

$$K \to \nu \qquad \varepsilon \to 0 \qquad \sigma_{\rm TT} \to \sigma_K g_1 \qquad \sigma_{\rm LT} \to 0 \qquad \varepsilon\sigma_{\rm L} \propto F_2 \tag{2.290}$$

2.5.9 Generalized Spin-Dependent Integrals and Sum Rules

All that's left now is to associate each virtual photoabsorption cross section with it's corresponding virtual Compton amplitude. We'll still use the mechanism of dispersion relations, but one must account for elastic scattering which has large contributions at low Q^2. In terms of calculating the amplitude, this is a subtle technical issue pertaining to the pole structure of the amplitude for ν below the inelastic threshold [236, 270]. In terms of writing down a sum rule, we'll simply place a bar over the amplitude to symbolically indicate the elastic contribution has been removed. The forward virtual Compton scattering amplitude has the same form as Eqn. (2.258). However, it is conventional to use Eqns. (2.277) & (2.278) to separate the components that are due to the longitudinal polarization of the virtual

photon:

$$\begin{aligned}\mathcal{M}_V(\theta_\gamma = 0) &= f_{\rm T}(\nu, Q^2)\,[\vec{\varepsilon}^{\,*}_{\rm T}\cdot\vec{\varepsilon}_{\rm T}] + f_{\rm L}(\nu, Q^2)\left[\frac{\vec{\varepsilon}^{\,*}_{\rm L}\cdot\vec{\varepsilon}_{\rm L}}{\beta^2\gamma_\beta^2}\right] \\ &\quad + g_{\rm TT}(\nu, Q^2)\left[i\hat{P}_t\cdot\left(\frac{\vec{\varepsilon}^{\,*}_{\rm T}\times\vec{\varepsilon}_{\rm T}}{h_b P_\gamma}\right)\right] \\ &\quad + g_{\rm LT}(\nu, Q^2)\left[i\hat{P}_t\cdot\left\{\frac{(\vec{\varepsilon}^{\,*}_{\rm T}-\vec{\varepsilon}_{\rm T})\times\vec{\varepsilon}_{\rm L}}{h_b P_\gamma \lambda_{\rm LT}/(\beta\gamma_\beta)}\right\}\right] \qquad (2.291)\end{aligned}$$

Anticipating their use in a dispersion relation, we'll perform a low energy expansion of the real part of the elastic-subtracted spin-dependent amplitudes [236]:

$$\Re\bar{g}_{\rm TT}(\nu, Q^2) = \left(\frac{2\alpha I_A(Q^2)}{M^2}\right)\nu + \left(\gamma_0(Q^2)\right)\nu^3 + O(\nu^5) \qquad (2.292)$$

$$\Re\bar{g}_{\rm LT}(\nu, Q^2) = \left(\frac{2\alpha Q I_3(Q^2)}{M^2}\right) + \left(Q\delta_{\rm LT}(Q^2)\right)\nu^2 + O(\nu^4) \qquad (2.293)$$

where we've defined the expansion parameters as functions of Q^2 such that in the real photon limit:

$$I_A(Q^2)\to -\frac{\kappa^{\star 2}}{4} \quad \gamma_0(Q^2)\to\gamma_0 \quad Q I_3(Q^2)\to 0 \quad Q\delta_{\rm LT}(Q^2)\to 0 \qquad (2.294)$$

By inspection, the imaginary parts of these amplitudes are given by:

$$\Im g_{\rm TT} = \frac{K}{4\pi}\sigma_{\rm TT} = \frac{\pi\alpha}{M}\left[g_1 - \frac{g_2}{\beta^2\gamma_\beta^2}\right] \qquad \Im g_{\rm LT} = \frac{K}{4\pi}\sigma_{\rm LT} = \frac{\pi\alpha}{M}\left[\frac{g_1+g_2}{\beta^2\gamma_\beta^2}\right] \qquad (2.295)$$

where $\beta\gamma_\beta = \nu/Q = Q/(2Mx)$. Equating the real part of the amplitudes order by order to the corresponding photoabsorption cross sections via the optical theorem

gives [236,271,272]:

$$I_A(Q^2) = \frac{M^2}{4\pi^2\alpha}\int_{\nu_0}^{\infty}\left[\frac{K(\nu,Q^2)}{\nu}\right]\left[\left[\frac{\sigma_{\rm TT}}{\nu}\right]d\nu = \frac{2M^2}{Q^2}\int_0^{x_0}\left[g_1 - \frac{4M^2}{Q^2}x^2 g_2\right]dx \tag{2.296}$$

$$\gamma_0(Q^2) = \frac{1}{2\pi^2}\int_{\nu_0}^{\infty}\left[\frac{K(\nu,Q^2)}{\nu}\right]\left[\frac{\sigma_{\rm TT}}{\nu^3}\right]d\nu = \frac{16\alpha M^2}{Q^6}\int_0^{x_0}x^2\left[g_1 - \frac{4M^2}{Q^2}x^2 g_2\right]dx \tag{2.297}$$

$$I_3(Q^2) = \frac{M^2}{4\pi^2\alpha}\int_{\nu_0}^{\infty}\left[\frac{K(\nu,Q^2)}{\nu}\right]\left[\frac{\sigma_{\rm LT}}{Q}\right]d\nu = \frac{2M^2}{Q^2}\int_0^{x_0}\left[g_1+g_2\right]dx \tag{2.298}$$

$$\delta_{\rm LT}(Q^2) = \frac{1}{2\pi^2}\int_{\nu_0}^{\infty}\left[\frac{K(\nu,Q^2)}{\nu}\right]\left[\frac{\sigma_{\rm LT}}{Q\nu^2}\right]d\nu = \frac{16\alpha M^2}{Q^6}\int_0^{x_0}x^2\left[g_1+g_2\right]dx \tag{2.299}$$

where $dx/x = -d\nu/\nu$ at constant Q^2. We can now identify the first line as essentially the generalized GDH integral, the second line as the generalized forward (transverse) spin polarizability, and the last line defines the forward longitudinal spin polarizability which has no real photon analog. While K & $\sigma_{\rm (TT,LT)}$ are flux-factor-convention dependent, their product $K\sigma_{\rm (TT,LT)}$ and, consequently, the integrands are not.

An alternative approach is to define the elastic-subtracted amplitudes in such a way that g_1 & g_2 are decoupled and that the resulting integrals relate to partial spin structure moments in the following way:

$$I_{1,2}(Q^2) = \frac{2M^2}{Q^2}\bar{\Gamma}_{1,2}(Q^2) \qquad I_3(Q^2) = I_1(Q^2) + I_2(Q^2) \tag{2.300}$$

where the partial moments are given by:

$$\bar{\Gamma}_{1,2}(Q^2) = \int_0^{x_0} g_{1,2}(x,Q^2)\,dx. \tag{2.301}$$

and x_0 corresponds to inelastic threshold. In terms of the photoabsorption cross sections, I_1 and I_2 can be written as:

$$I_1(Q^2) = \frac{M^2}{4\pi^2\alpha}\int_{\nu_0}^{\infty}\left[\frac{1}{1+Q^2/\nu^2}\right]\left[\frac{K(\nu,Q^2)}{\nu}\right]\left[\frac{+\sigma_{TT}+Q\sigma_{LT}/\nu}{\nu}\right]d\nu \quad (2.302)$$

$$I_2(Q^2) = \frac{M^2}{4\pi^2\alpha}\int_{\nu_0}^{\infty}\left[\frac{1}{1+Q^2/\nu^2}\right]\left[\frac{K(\nu,Q^2)}{\nu}\right]\left[\frac{-\sigma_{TT}+\nu\sigma_{LT}/Q}{\nu}\right]d\nu \quad (2.303)$$

Along these lines, Ji & Osbourne [270] define (with slightly different normalizations) the spin-dependent forward Compton amplitude in analogy to the antisymmetric part of the hadronic tensor:

$$\begin{aligned}\mathcal{M}_V(\theta_\gamma=0) &= \left\{i\varepsilon_{\mu\nu\alpha\beta}\rho^{\mu\nu}\left(\frac{q^\alpha}{M}\right)S^\beta\right\}S_1(\nu,Q^2)\\ &\quad+\left\{i\varepsilon_{\mu\nu\alpha\beta}\rho^{\mu\nu}\left(\frac{q^\alpha}{M}\right)\left[\left(\frac{P\cdot q}{M^2}\right)S^\beta - S\cdot\left(\frac{q}{M}\right)\frac{P^\beta}{M}\right]\right\}S_2(\nu,Q^2)\end{aligned} \quad (2.304)$$

Comparing this to the cross sections in Eqn. (2.280) gives:

$$\Im\left\{S_1(\nu,Q^2)\right\} = \frac{\pi\alpha}{\nu}g_1(\nu,Q^2) = \left(\frac{M}{\nu}\right)\Im\left\{\frac{g_{TT}+\beta^2\gamma_\beta^2 g_{LT}}{1+\beta^2\gamma_\beta^2}\right\} \quad (2.305)$$

$$\Im\left\{S_2(\nu,Q^2)\right\} = \frac{\pi\alpha M}{\nu^2}g_2(\nu,Q^2) = \left(\frac{M}{\nu}\right)^2\Im\left\{\left(-g_{TT}+\beta^2\gamma_\beta^2 g_{LT}\right)\left(1+\beta^2\gamma_\beta^2\right)\right\} \quad (2.306)$$

By convention, the corresponding low energy expansions are given by [236]:

$$\begin{aligned}
\Re\bar{S}_1(\nu,Q^2) &= \left(\frac{2\alpha I_1(Q^2)}{M}\right)+\left(\frac{2\alpha}{M}\left[\frac{I_A(Q^2)-I_1(Q^2)}{Q^2}\right]+M\delta_{\rm LT}(Q^2)\right)\nu^2+O(\nu^4)\\
\Re\nu\bar{S}_2(\nu,Q^2) &= \left(2\alpha I_2(Q^2)\right)-\left(2\alpha\left[\frac{I_A(Q^2)-I_1(Q^2)}{Q^2}\right]\right)\nu^2\\
&\quad+\frac{1}{Q^2}\left(2\alpha\left[\frac{I_A(Q^2)-I_1(Q^2)}{Q^2}\right]+M^2\left[\delta_{\rm LT}(Q^2)-\gamma_0(Q^2)\right]\right)\nu^4+O(\nu^6)
\end{aligned} \tag{2.307}$$

Finally, we'll note two other conventions found in the literature for the generalized GDH integral [271]:

$$I_B(Q^2) = \frac{M^2}{4\pi^2\alpha}\int_{\nu_0}^{\infty}\left[\frac{1}{\sqrt{1+Q^2/\nu^2}}\right]\left[\frac{K(\nu,Q^2)}{\nu}\right]\left[\left[\frac{\sigma_{\rm TT}}{\nu}\right]d\nu \tag{2.308}$$

$$= \frac{2M^2}{Q^2}\int_0^{x_0}\left[\frac{1}{\sqrt{1+4M^2x^2/Q^2}}\right]\left[g_1-\frac{4M^2}{Q^2}x^2g_2\right]dx \tag{2.309}$$

$$I_C(Q^2) = \frac{M^2}{4\pi^2\alpha}\int_{\nu_0}^{\infty}\left[\frac{1}{1-Q^2/(2M\nu)}\right]\left[\frac{K(\nu,Q^2)}{\nu}\right]\left[\left[\frac{\sigma_{\rm TT}}{\nu}\right]d\nu \tag{2.310}$$

$$= \frac{2M^2}{Q^2}\int_0^{x_0}\left[\frac{1}{1-x}\right]\left[g_1-\frac{4M^2}{Q^2}x^2g_2\right]dx \tag{2.311}$$

At the real photon point, each of these unitless generalized integrals reduces to the same value and are related to the GDH integral by:

$$I_1(0)=I_A(0)=I_B(0)=I_C(0)=\frac{M^2}{4\pi^2\alpha}\int_{\nu_0}^{\infty}\left[\frac{\sigma_{\rm TT}}{\nu}\right]d\nu=-\frac{M^2}{8\pi^2\alpha}I_{\rm GDH}=-\frac{\kappa^{\star 2}}{4} \tag{2.312}$$

which implies that (to lowest order):

$$\bar{\Gamma}_1(Q^2)=\frac{Q^2}{2M^2}\left[-\frac{\kappa^{\star 2}}{4}+Q^2\left.\frac{dI_1(Q^2)}{dQ^2}\right|_{Q^2=0}+\cdots\right] \tag{2.313}$$

2.5.10 Chiral Perturbation Theory

Chiral Perturbation Theory (ChPT) [273–278] is an effective field theory that represents QCD at low energies. In this energy regime, QCD becomes nonperturbative and the interactions between quark and gluons become very strong. We can hide the nonperturbative physics by dealing only with "effective" interactions among "bound states" of quarks and gluons, namely hadrons. Compared to some reference energy scale, these effective interactions are weak and can therefore be treated perturbatively. It has been shown [279] that if one includes every effective interaction that is consistent with the symmetries of the underlying theory, then the effective theory is equivalent to the underlying theory. ChPT is a systematic implementation of these ideas which relies on the spontaneous breaking of the approximate chiral symmetry of QCD.

Chiral Symmetry

The QCD Lagrangian [203] with N_f quark flavors and N_c colors can be written as:

$$\mathcal{L}_{\text{QCD}} = \left[\begin{array}{ll} \bar{q}\left(i\gamma^\mu\partial_\mu - \mathtt{M}\right)q & \text{(quark kinetic energy)} \\ -\frac{1}{2}\left[\partial^\mu A^\nu_a - \partial^\nu A^\mu_a\right]\left[\partial_\mu A^a_\nu - \partial_\nu A^a_\mu\right] & \text{(gluon kinetic energy)} \\ +\frac{g_s\lambda_a}{2}\bar{q}\gamma^\mu A^a_\mu q & \text{(quark}-\text{gluon interaction)} \\ +\frac{ig_s}{2}f_{abc}A^\mu_b A^\nu_c\left[\partial_\mu A^a_\nu - \partial_\nu A^a_\mu\right] & \text{(three gluon interaction)} \\ +\frac{g_s^2}{8}f_{abc}f^{ade}A^\mu_b A^\nu_c A^d_\mu A^e_\nu & \text{(four gluon interaction)} \end{array}\right] \tag{2.314}$$

where γ^μ are the usual Dirac matrices, q is the quark field, $\mathtt{M}$ is the quark mass matrix, A^μ_a is one of the eight ($a = 1..8$) gluon vector fields, g_s is the strong coupling constant, λ_a is one the eight Gell-Mann matrices, and f_{abc} are the antisymmetric

structure constants. This can be rewritten in a much more compact notation:

$$\mathcal{L}_{\rm QCD} = \bar{\psi}\left(i\gamma^\mu D_\mu - \mathtt{M}\right)\psi - \frac{1}{2}G^a_{\mu\nu}G^{\mu\nu}_a \tag{2.315}$$

where $D_\mu = \partial - ig\lambda_a A^a_\mu/2$ is the "covariant derivative" and $G^{\mu\nu}_a = \partial^\mu A^\nu_a - \partial^n u A^\mu_a + g f_{abc} A^\mu_b A^\nu_c$ is the "dual gluon field tensor." If we decompose the quark fields into their "chiral" components:

$$q = q_L + q_R \qquad q_L = \left(\frac{1+\gamma_5}{2}\right)q \qquad q_R = \left(\frac{1-\gamma_5}{2}\right)q \tag{2.316}$$

where q_L (q_R) is the "left-handed" ("right-handed") chiral quark field, then the QCD Lagrangian can be written as:

$$\begin{aligned}\mathcal{L}_{\rm QCD} &= i\bar{\psi}_L\gamma^\mu D_\mu\psi_L + i\bar{\psi}_R\gamma^\mu D_\mu\psi_R - \bar{\psi}_L\mathtt{M}\psi_R - \bar{\psi}_R\mathtt{M}\psi_L - \frac{1}{2}G^a_{\mu\nu}G^{\mu\nu}_a & (2.317)\\ &= \mathcal{L}^0_{\rm QCD} - \bar{\psi}_L\mathtt{M}\psi_R - \bar{\psi}_R\mathtt{M}\psi_L & (2.318)\end{aligned}$$

where we've used the anticommutation property $\{\gamma^5, \gamma^\mu\}$ of the Dirac matrices and $\mathcal{L}^0_{\rm QCD}$ does not contain terms that mix chiral quark fields.

A chiral transformation can be defined as $q_{L,R} \rightarrow \exp(i\theta_{L,R})$ and, for example, performing this transformation yields:

$$\bar{\psi}_L\gamma^\mu D_\mu\psi_L \rightarrow e^{+i(\theta_L-\theta_L)}\bar{\psi}_L\gamma^\mu D_\mu\psi_L = \bar{\psi}_L\gamma^\mu D_\mu\psi_L \qquad \bar{\psi}_L\mathtt{M}\psi_R \rightarrow -e^{+i(\theta_R-\theta_L)}\bar{\psi}_L\mathtt{M}\psi_R \tag{2.319}$$

where, in general, $\theta_L \neq \theta_R$. This implies that $\mathcal{L}^0_{\rm QCD}$ is invariant under chiral transformation and is therefore said to exhibit chiral symmetry. The quark mass term in not invariant and is therefore said to break this symmetry "explicitly." If the quark

masses are set to zero ($\mathtt{M} = 0$), then the QCD Lagrangian exhibits chiral symmetry. In this limit (called the chiral limit), the chirality of a quark is given by its helicity.

Spontaneous Symmetry Breaking

In the chiral limit, the QCD Lagrangian can be decomposed into two parts labeled by handedness. Therefore, solutions to the Lagrangian are expected to have a definite parity. As a consequence, the hadronic spectrum (quark bound states) should consist of pairs of hadrons with identical properties but opposite parity. For approximate chiral symmetry, these "parity doublets" would still exist but with slightly different masses directly attributable to the non-zero quark masses. In the real world, parity doublets with small mass separations are not a feature of the hadronic spectrum. For this reason (among others), it is strongly believed that the approximate chiral symmetry of QCD is spontaneously broken.

Spontaneous symmetry breaking (SSB) occurs when the a continuous global symmetry exhibited by the equations of motion is not exhibited by the ground state of the system. SSB implies:

1. the existence of massless pseudoscalar (Goldstone) bosons
2. that the interactions among these bosons decrease in strength with increasing separation (decreasing energy scale).

With the exception of their mass, the lightest mesons (i.e. spin-0 pseudoscalar meson nonet: π,η,K) have exactly the properties of the Goldstone bosons that would be present due to the breaking of chiral symmetry. In the language of condensed matter physics, SSB is a phase transition that occurs as the energy scale is varied. If the quark masses are much smaller than the energy scale at which this phase tran-

sition occurs in QCD (Λ_χ), then the Goldstone bosons acquire small masses that are proportional to the quark masses. For this reason, the group of lightest mesons are known as "pseudo"-Goldstone bosons. The SSB mechanism not only allows us to identify the correct degrees of freedom, but also implies that their interactions can be treated perturbatively.

Effective Lagrangian & Power Counting: Mesonic ChPT

A low energy effective theory of QCD should be described by a set of $(N_f^2 - 1)$ light pseudoscalar bosons with a Lagrangian that exhibits approximate chiral symmetry. For simplicity, we'll consider only the case of up and down quarks ($N_f = 2$). One can construct a chiral symmetric field using pionic degrees of freedom in the following way [278]:

$$U(x) = \exp\left(i\sqrt{2}\phi(x)/F\right) \qquad \phi(x) = \begin{pmatrix} +\pi^0/\sqrt{2} & \pi^+ \\ \pi^- & -\pi^0/\sqrt{2} \end{pmatrix} \tag{2.320}$$

where F is a low energy constant (LEC). In this case, F refers to the pion decay constant and is related to the SSB energy scale by:

$$\Lambda_\chi = 4\pi F \tag{2.321}$$

The effective Lagrangian contains any and all interaction terms involving U that are allowed by the symmetries of QCD. Since SSB implies that the interactions "turn off" as the energy scale goes to zero, only derivatives of U ($\partial_\mu U$) appear in chiral limit. In momentum space, the derivative of U transforms into the product of the pion momentum and U, $\partial_\mu U \to p_\mu U$. This insures that the interaction vanishes

in the limit that the pion momentum goes to zero ($p_\mu \to 0$).

Since chiral symmetry is only approximate, the effective Lagrangian can also contain interaction terms with the field U itself. These additional terms are due to explicit chiral symmetry breaking and therefore necessarily include a factor proportional to the up and down quark masses. Therefore the effective Lagrangian is composed of all allowed combinations of $\mathtt{M}U$ and $\partial_\mu U$, where $\mathtt{M}$ is the quark mass matrix. If the pion momentum is small compared to the SSB energy scale ($p_\mu \ll 1$ GeV), then U can be expanded by a Taylor series:

$$U = \overleftrightarrow{1} + \frac{i\sqrt{2}\phi(x)}{F} - \frac{2\phi^2}{F^2} + \cdots \tag{2.322}$$

As such, each term involving the field U or its derivative actually represents a infinite set of terms involving $\phi(x)$ and its derivatives.

Using dimensional analysis, Weinberg [279] was the first to outline a systematic prescription for determining the relative importance of each of these terms. The units of U and $\partial_\mu U$ are 1 and p respectively. The units of the quark mass matrix $\mathtt{M}$ in terms of the pion momentum p can be inferred by expanding the product $\mathtt{M}U$. It can be shown that the lowest order term results in the following relationship:

$$m_\pi^2 = B\,(m_u + m_d) \tag{2.323}$$

where $m_{\pi,u,d}$ are the masses of the pion, up quark, & down quark and B is another LEC which, in this case, is related to chiral quark condensate $\langle 0|\,\bar{q}q\,|0\rangle$ (i.e. the vacuum expectation value of the quark-antiquark field operators). This implies that the units of $\mathtt{M}$ is p^2. The units of each term in the expansion can now be given by p^D where D is the chiral dimension and this process is called "power counting." This

allows one to know ahead of time which diagrams make the largest contributions. The effective Lagrangian can be systematically grouped by D and calculated order by order.

The coupling constants that describe each of these terms are known as Low Energy Constants (LEC). LECs have to be renormalized which implies that they depend on the energy scale being probed. The number of LECs that describe all the terms with a specific chiral order D increases with D. Thus to calculate higher order terms, one needs to know the values of an increasing number of LECs. Fortunately, each LEC can be related to some experimental observable. Theoretical values of LEC usually come from some low energy model for QCD and may one day be calculated directly by Lattice QCD.

Including the Nucleon and Δ: Baryon ChPT

When considering low energy interactions among pions, the pion mass and momenta are considered small perturbations relative to the scale set by SSB (m_π/Λ_χ , $p < \Lambda_\chi \ll 1$). This leads naturally to a power counting scheme that systematically organizes the infinite number of terms that constitute the effective Lagrangian. The situation is not as well defined when a nucleon is included among the hadronic initial and final states due to the large nucleon mass ($m_N/\Lambda_\chi \approx 1$). The general strategy is to isolate a part of the nucleon momentum that is small relative to the nucleon mass or equivalently the SSB energy scale:

$$P^\mu = m_N v^\mu + k^\mu \qquad \frac{k}{m_N} \ll 1 \tag{2.324}$$

where P^μ is the total nucleon momentum and k^μ is some small momentum relative to the nucleon rest mass. By construction, this small nucleon momentum k contributes at the same order as the pion mass ($k/\Lambda_\chi \approx m_\pi/\Lambda_\chi$). There are two basic frameworks for accomplishing this goal [277, 278, 280, 281]: Heavy Baryon ChPT (HBChPT) and Relativistic (aka Lorentz Invariant) Baryon ChPT (RBChPT).

In HBChPT, the nucleon field ($\Phi(x)$) itself is split into two nucleon velocity-dependent fields ($H_v(x)$ and $N_v(x)$) labeled as "light" and "heavy:"

$$\Phi = \begin{pmatrix} p^+ \\ n^0 \end{pmatrix} \qquad H_v(x) = e^{im_N v\cdot x} P_v^- \Phi(x) \quad N_v(x) = e^{im_N v\cdot x} P_v^+ \Phi(x) \qquad P_v^\pm = \frac{1 \pm \gamma^\mu v_\mu}{2} \tag{2.325}$$

where $P_v^\pm$ is the velocity projection operator. The Dirac equation for the nucleon field is used to derive the equations of motion for the "heavy" field component. This equation of motion is essentially a modified form of the Dirac equation and is used to eliminate the "heavy" field from the effective Lagrangian. Alternatively within the path integral representation, the "heavy" field can be "integrated out." In either case, what results is an expansion in powers of k/m_N & k/Λ_χ and consequently a power counting scheme. The fact that this approach is nonrelativisitic can lead to problems evaluating certain types of "loop" diagrams (i.e. the types of diagrams that lead to mass renormalization in QED). RBChPT was developed in part to address this situation.

A loop diagram involves an integral from 0 to ∞ over the undetermined momentum of the virtual particle that makes the loop and has the general form:

$$H = C \int \frac{d^4k}{(2\pi)^4} \frac{1}{(k^2 + a_1 k + a_0)(k^2 + b_1 k + b_0)} \tag{2.326}$$

where C, $a_{0,1}$, & $b_{0,1}$ are constants that depend on the coupling constant, nucleon mass, pion mass, and external momenta. The basic idea in RBChPT is to split this integral into two pieces, $H = R + I$. The first piece (R) is essentially an integral over k from m_π to ∞. It is well behaved ("regular") and dropped because it can be absorbed by the coupling constant (after redefining the coupling constant). The second piece (I) is essentially an integral over k from 0 to m_π. This integral blows up at $k = 0$ (i.e. infrared divergent) and is compensated by a counter term. The final steps are to expand the integrand via a Taylor series in powers of k/m_N and then integrate term by term. The benefit of this approach, asides from being manifestly Lorentz invariant, is that it is expected to have, in certain situations, a higher energy domain of applicability than HBChPT. Finally, we note in passing that the Δ-resonance can be handled in a similar manner with three modifications:

1. The mass difference between the Δ and the nucleon is treated as another order parameter ($(m_\Delta - m_N)/\Lambda_\chi < 1$) in the power counting scheme.

2. A more complicated set of equations of motion (Rarita Schwinger equations [282]) are required to describe the Δ since it is a spin-$3/2$ object.

3. The probability of creating a Δ resonance depends strongly on Q^2. This can be described phenomenologically with a Δ "form factor."

2.5.11 Predictions from BChPT for Spin-Dependent Quantities

The Heavy BChPT result, calculated by Ji et al. [283], for the slopes of the generalized GDH integrals can be given in closed form:

$$\left.\frac{dI_1}{dQ^2}\right|_0 = \frac{\pi M_N}{48 m_\pi}\left[\frac{g_A}{4\pi F_\pi}\right]^2 [1 + 3\kappa_V + 2(1+3\kappa_S)\tau_3] \tag{2.327}$$

$$\left.\frac{dI_A}{dQ^2}\right|_0 = \frac{M_N^2}{6 m_\pi^2}\left[\frac{g_A}{4\pi F_\pi}\right]^2 \left[1 - \frac{\pi m_\pi}{4 M_N}(13 + 2\tau_3 + 2\kappa_V)\right] \tag{2.328}$$

where $M_N = 0.9389$ GeV is the average nucleon mass, $m_\pi = 0.1380$ GeV is the average pion mass, $g_A = 1.267$ is the axial coupling constant, $F_\pi = 0.09242$ GeV is the pion decay constant, $\tau_3 = +(-)1$ for protons (neutrons), $\kappa_S = \kappa_p^\star + \kappa_n^\star = -0.123$ is the isoscalar anomalous magnetic moment, $\kappa_V = \kappa_p^\star - \kappa_n^\star = +3.709$ is the isovector anomalous magnetic moment, and we've ignored the small mass difference between protons and neutrons. For the same quantities, the numerical values for the Relativistic BChPT calculation by Bernard et al. [284] are:

$$\left.\frac{dI_1^p}{dQ^2}\right|_0 = \frac{M_p^2}{16\pi\alpha}\left[\frac{-0.4 + 1.2}{\text{GeV}^4}\right] = +\frac{1.92}{\text{GeV}^2} \tag{2.329}$$

$$\left.\frac{dI_1^n}{dQ^2}\right|_0 = \frac{M_n^2}{16\pi\alpha}\left[\frac{-1.7 + 1.9}{\text{GeV}^4}\right] = +\frac{0.48}{\text{GeV}^2} \tag{2.330}$$

$$\left.\frac{dI_A^p}{dQ^2}\right|_0 = \frac{M_p^2}{16\pi\alpha}\left[\frac{+3.2 + 1.8}{\text{GeV}^4}\right] = +\frac{12.0}{\text{GeV}^2} \tag{2.331}$$

$$\left.\frac{dI_A^n}{dQ^2}\right|_0 = \frac{M_n^2}{16\pi\alpha}\left[\frac{-0.3 - 1.8}{\text{GeV}^4}\right] = -\frac{5.05}{\text{GeV}^2} \tag{2.332}$$

where $M_p = 0.9383$ GeV is the proton mass, $M_n = 0.9396$ GeV is the neutron mass, and $\alpha = 1/137.036$ is the fine structure constant. The slope for I_A at the real photon point differs in sign for the proton and only a factor of 2 for the neutron. In a later publication [272], Bernard et al. found indications that the Δ-resonance does not

change the sign of the slope.

Kao et al. have applied Heavy BChPT to calculate the Q^2 dependence of the generalized polarizabilities [285]. The slopes and values at the real photon point from the pion loop are given by:

$$\gamma_0(Q^2=0) = \frac{2\alpha}{3m_\pi^2}\left[\frac{g_A}{4\pi F_\pi}\right]^2\left[1-\frac{\pi m_\pi}{8M_N}(15+3\kappa_V+(6+\kappa_S)\tau_3)\right] \quad (2.333)$$

$$\delta_{\rm LT}(Q^2=0) = \frac{\alpha}{3m_\pi^2}\left[\frac{g_A}{4\pi F_\pi}\right]^2\left[1+\frac{\pi m_\pi}{8M_N}(-3+\kappa_V+(-6+4\kappa_S)\tau_3)\right] \quad (2.334)$$

$$\left.\frac{d\gamma_0}{dQ^2}\right|_0 = +\frac{4\alpha}{45m_\pi^4}\left[\frac{g_A}{4\pi F_\pi}\right]^2\left[1-\frac{\pi m_\pi}{1024M_N}(5451+267\kappa_V+(-75+21\kappa_S)\tau_3)\right] \quad (2.335)$$

$$\left.\frac{d\delta_{\rm LT}}{dQ^2}\right|_0 = -\frac{\alpha}{18m_\pi^4}\left[\frac{g_A}{4\pi F_\pi}\right]^2\left[1+\frac{\pi m_\pi}{80M_N}(54-9\kappa_V-(27+24\kappa_S)\tau_3)\right] \quad (2.336)$$

They also estimated the contribution from the Δ-resonance and found that the Δ makes almost no contribution to $\delta_{\rm LT}$.

Within the Relativistic BChPT framework, Bernard et al. [272] provide a closed form formula for the first four terms in the pion loop expansion for the transverse spin polarizability:

$$\begin{aligned}\gamma_0(Q^2=0) = \frac{2\alpha}{3m_\pi^2}\left[\frac{g_A}{4\pi F_\pi}\right]^2\Bigg\{&1-\frac{\pi m_\pi}{8M_N}\left[15+3\kappa_V+(6+\kappa_S)\tau_3\right]\\&-\frac{5m_\pi^2}{4M_N^2}\left[10+3\kappa_V+\frac{3}{5}\kappa_S+3\left(2+\frac{\kappa_V}{5}+\kappa_S\right)\tau_3\right]\\&-\frac{m_\pi^2}{M_N^2}\log\left(\frac{m_\pi}{M_N}\right)\left[15+4\kappa_V+3\kappa_S+(11+3\kappa_V+4\kappa_S)\tau_3\right]\\&+\frac{15\pi m_\pi^3}{64M_N^3}\left[65+32\kappa_V+21\kappa_S+(60+17\kappa_V-42\kappa_S)\tau_3\right]\Bigg\} \quad (2.337)\end{aligned}$$

and for the longitudinal spin polarizability:

$$\begin{aligned}\delta_{\rm LT}(Q^2=0) &= \frac{\alpha}{3m_\pi^2}\left[\frac{g_A}{4\pi F_\pi}\right]^2\left\{1+\frac{\pi m_\pi}{8M_N}\left[-3+\kappa_V+(-6+4\kappa_S)\,\tau_3\right]\right.\\ &+\frac{m_\pi^2}{32M_N^2}\left[64+93\kappa_V+9\kappa_S-(160+3\kappa_V-57\kappa_S)\,\tau_3\right]\\ &+\frac{3m_\pi^2}{16M_N^2}\log\left(\frac{m_\pi}{M_N}\right)\left[32-\kappa_V+3\kappa_S-(32+\kappa_V-19\kappa_S)\,\tau_3\right]\\ &\left.-\frac{3\pi m_\pi^3}{128M_N^3}\left[394-75\kappa_V+15\kappa_S-(156+45\kappa_V-135\kappa_S)\tau_3\right]\right\}\end{aligned} \tag{2.338}$$

The two lowest order terms in the Relativistic BChPT calculation exactly matches the Heavy BChPT calculation. The large difference in $\gamma_0(0)$ for the proton is due to the large contributions from the higher order terms within Relativisitic BChPT. The estimate for the Δ contribution is consistent between these two calculations. Tab. (2.3) lists the numerical values for these calculations at each order, the estimates for the Δ-resonance contributions, and the values from the phenomenological MAID model [286, 287].

2.5.12 Polarization Observables in Inelastic Scattering

The subscripts $_{\rm L}$ & $_{\rm T}$ refer to components of the virtual photon polarization vector. The subscripts $_{\rm long}$ & $_{\rm trans}$ refer to the orientation relative to the q-vector. The cross product between two transverse polarization components ($_{\rm TT}$) results in a longitudinal vector ($_{\rm long}$). On the other hand, the cross product between a longitudinal and a transverse polarization component ($_{\rm LT}$) results in a transverse vector ($_{\rm trans}$). Finally, the subscripts $\parallel$ & $\perp$ refer to the orientation relative to the momentum of the incoming electron beam.

quantity	Baryon ChPT		MAID		units
	Heavy	Relativistic	2003	2007	
$I_A^p(0) = I_1^p(0)$	$-\kappa_p^{\star 2}/4 = -0.804$		-0.644	-0.650	unitless
$I_A^n(0) = I_1^n(0)$	$-\kappa_n^{\star 2}/4 = -0.917$		-0.487	-0.521	unitless
$dI_A^p/dQ^2\|_0$	-14.6	$+12.0$	-4.53	-2.87	GeV^{-2}
$dI_A^n/dQ^2\|_0$	-10.3	-5.05	-7.75	-6.04	GeV^{-2}
$dI_1^p/dQ^2\|_0$	$+7.09$	$+1.92$	$+3.47$	$+5.35$	GeV^{-2}
$dI_1^n/dQ^2\|_0$	$+5.76$	$+0.48$	$+1.12$	$+2.07$	GeV^{-2}
ref.	[283]	[284]	[286]	[287]	
γ_0^p, loop	-3.91	$+4.64$			10^{-4} fm^4
γ_0^n, loop	-0.78	$+1.82$			10^{-4} fm^4
$\gamma_0^{p,n}$, Δ	-2.85	-2.83 ± 0.80			10^{-4} fm^4
γ_0^p, tot	-6.75	$+1.80 \pm 0.80$	-0.63	-0.73	10^{-4} fm^4
γ_0^n, tot	-3.63	-1.00 ± 0.80	$+0.10$	-0.01	10^{-4} fm^4
δ_{LT}^p, loop	$+1.53$	$+2.04$			10^{-4} fm^4
δ_{LT}^n, loop	$+3.26$	$+2.66$			10^{-4} fm^4
$\delta_{\mathrm{LT}}^{p,n}$, Δ	$+0.04$	-0.10 ± 0.25			10^{-4} fm^4
δ_{LT}^p, tot	$+1.57$	$+1.95 \pm 0.25$	$+1.38$	$+1.34$	10^{-4} fm^4
δ_{LT}^n, tot	$+3.30$	$+2.55 \pm 0.25$	$+2.32$	$+2.03$	10^{-4} fm^4
$d\gamma_0^p/dQ^2\|_0$, loop	-60.3	(≈ 0)			10^{-4} fm^4/GeV^2
$d\gamma_0^n/dQ^2\|_0$, loop	-62.6	$(-)$			10^{-4} fm^4/GeV^2
$d\gamma_0^{p,n}/dQ^2\|_0$, Δ	-29.8	$(+)$			10^{-4} fm^4/GeV^2
$d\gamma_0^p/dQ^2\|_0$, tot	-90.1	$(+)$	-26.6	-21.2	10^{-4} fm^4/GeV^2
$d\gamma_0^n/dQ^2\|_0$, tot	-92.4	$(-)$	-44.3	-38.8	10^{-4} fm^4/GeV^2
$d\delta_{\mathrm{LT}}^p/dQ^2\|_0$, loop	-19.8	$(-)$			10^{-4} fm^4/GeV^2
$d\delta_{\mathrm{LT}}^n/dQ^2\|_0$, loop	-25.4	$(-)$			10^{-4} fm^4/GeV^2
$d\delta_{\mathrm{LT}}^{p,n}/dQ^2\|_0$, Δ	-0.32	(≈ 0)			10^{-4} fm^4/GeV^2
$d\delta_{\mathrm{LT}}^p/dQ^2\|_0$, tot	-20.7	$(-)$	-25.3	-22.9	10^{-4} fm^4/GeV^2
$d\delta_{\mathrm{LT}}^n/dQ^2\|_0$, tot	-25.7	$(-)$	-41.3	-35.7	10^{-4} fm^4/GeV^2
ref.	[285]	[272]	[286]	[287]	

Table 2.3: Values from BChPT & MAID for Spin-Dependent Quantities.

Normalizing the total virtual photoabsorption cross section by $\sigma_{\rm T}$ allows us to define three new quantities:

$$\frac{\sigma_V}{\sigma_{\rm T}} = 1 + \varepsilon R - h_b(\hat{P}_t \cdot \hat{q})\sqrt{1-\varepsilon^2}A_1 - h_b\hat{P}_t \cdot (\hat{n} \times \hat{q})\sqrt{2\varepsilon(1-\varepsilon)}A_2 \tag{2.339}$$

where R, A_1, & A_2 are given by:

$$R \equiv \frac{\sigma_{\rm L}}{\sigma_{\rm T}} = \left[1+\gamma^2\right]\left[\frac{F_2}{2xF_1}\right] - 1 \tag{2.340}$$

$$A_1 \equiv \frac{\sigma_{\rm TT}}{\sigma_T} = \frac{\sigma_{1/2}-\sigma_{3/2}}{\sigma_{1/2}+\sigma_{3/2}} = \frac{g_1 - \gamma^2 g_2}{F_1} \tag{2.341}$$

$$A_2 \equiv \frac{\sigma_{\rm LT}}{\sigma_T} = \frac{2\sigma_{\rm LT}}{\sigma_{1/2}+\sigma_{3/2}} = \gamma\left[\frac{g_1+g_2}{F_1}\right] \tag{2.342}$$

where γ is a common kinematic factor:

$$\gamma \equiv \frac{1}{\beta\gamma_\beta} = \frac{Q}{\nu} = \frac{2Mx}{Q} \tag{2.343}$$

Eqn. (2.176) can be used to equate measured cross section differences to g_1 and g_2:

$$\Delta\sigma_\parallel = 2\bar{\sigma}A_\parallel = -\frac{8\alpha^2}{MQ^2}\left(\frac{1-y}{y}\right)\left[\left(1-\frac{y}{2}-\frac{y^2\gamma^2}{4}\right)g_1 - \left(\frac{y\gamma^2}{2}\right)g_2\right] \tag{2.344}$$

$$\Delta\sigma_\perp = 2\bar{\sigma}A_\perp = -\frac{8\alpha^2}{MQ^2}\left(\frac{1-y}{y}\right)\gamma\sqrt{1-y-\frac{y^2\gamma^2}{4}}\left[\left(\frac{y}{2}\right)g_1 + g_2\right] \tag{2.345}$$

where $y = \nu/E$ and we're using the "$d\Omega dE'$" convention (as opposed to the "$dxdy$" convention):

$$\Delta\sigma_{\parallel,\perp} \equiv \left[\frac{d^2\sigma}{d\Omega dE'}\right]_{\parallel,\perp} \qquad \frac{d^2\sigma}{dxdy} = \frac{d^2\sigma}{d\Omega dE'}\left[\frac{2\pi My}{1-y}\right] \tag{2.346}$$

These can be inverted to extract g_1 and g_2:

$$g_1 = -\frac{MQ^2}{8\alpha^2}\left[\frac{y}{(1-y)(2-y)}\right]\left[2\Delta\sigma_{\parallel} + \left(\frac{y\gamma}{\sqrt{1-y-y^2\gamma^2/4}}\right)\Delta\sigma_{\perp}\right] \quad (2.347)$$

$$g_2 = -\frac{MQ^2}{8\alpha^2}\left[\frac{y}{(1-y)(2-y)}\right]\left[-y\Delta\sigma_{\parallel} + \frac{2}{\gamma}\left(\frac{1-y/2-y^2\gamma^2/4}{\sqrt{1-y-y^2\gamma^2/4}}\right)\Delta\sigma_{\perp}\right] \quad (2.348)$$

Using the following:

$$g_1 = \frac{F_1(A_1+\gamma A_2)}{1+\gamma^2} \qquad g_2 = \frac{F_1(A_2-\gamma A_1)}{\gamma(1+\gamma^2)} \quad (2.349)$$

we find:

$$A_{\parallel} = D(A_1+\eta A_2) \qquad A_{\perp} = d(A_2-\xi A_1) \quad (2.350)$$

where, after some considerable algebra, the kinematic factors are given by [288]:

$$D = \frac{y(1+y\gamma^2/2)(2-y)}{y^2(1+\gamma^2)+2(1+R)(1-y-y^2\gamma^2/4)} \quad (2.351)$$

$$\eta = \frac{\gamma(1-y-y^2\gamma^2/4)}{(1-y/2)(1+y\gamma^2/2)} \quad (2.352)$$

$$d = \frac{2y(1+y\gamma^2/2)\sqrt{1-y-y^2\gamma^2/4}}{y^2(1+\gamma^2)+2(1+R)(1-y-y^2\gamma^2/4)} \quad (2.353)$$

$$\xi = \frac{\gamma(1-y/2)}{1+y\gamma^2/2} \quad (2.354)$$

Bibliography

[1] C. Amsler et al. (Particle Data Group). Review of Particle Physics. *Physics Letters B*, 667(1-5):1 – 6, 2008. Review of Particle Physics.

[2] James D. Bjorken and Sidney D. Drell. *Relativistic Quantum Mechanics*. McGraw-Hill, Inc., New York, 1964.

[3] William R. Leo. *Techniques for Nuclear and Particle Physics Experiments: A How-to Approach*. Springer-Verlag, Berlin, second revised edition, 1994.

[4] Ernest M. Henley and Alejandro Garcia. *Subatomic Physics*. World Scientific Pub. Co., Hackensack, NJ, third edition, 2007.

[5] E. Rutherford. LXXIX. The scattering of α and β particles by matter and the structure of the atom. *Philosophical Magazine Series 6*, 12(125):669–688, 1911.

[6] N. F. Mott. The Scattering of Fast Electrons by Atomic Nuclei. *Proceedings of the Royal Society of London. Series A*, 124(794):425–442, 1929.

[7] M. E. Rose. The Charge Distribution in Nuclei and the Scattering of High Energy Electrons. *Phys. Rev.*, 73(4):279–284, Feb 1948.

[8] Beat Hahn, D. G. Ravenhall, and Robert Hofstadter. High-Energy Electron Scattering and the Charge Distributions of Selected Nuclei. *Phys. Rev.*, 101(3):1131–1142, Feb 1956.

[9] I. Sick. Model-independent nuclear charge densities from elastic electron scattering. *Nuclear Physics A*, 218(3):509 – 541, 1974.

[10] H. De Vries, C. W. De Jager, and C. De Vries. Nuclear charge-density-distribution parameters from elastic electron scattering. *Atomic Data and Nuclear Data Tables*, 36(3):495 – 536, 1987.

[11] P. A. M. Dirac. The Quantum Theory of the Electron. *Proceedings of the Royal Society of London. Series A*, 117(778):610–624, 1928.

[12] Arthur Beiser. *Concepts of Modern Physics*. McGraw-Hill, Inc., New York, fifth edition, 1995.

[13] Kwang Je Kim and Yung-Su Tsai. Magnetic Dipole and Electric Quadrupole Moments of the $W^{\pm}$ Meson. *Phys. Rev. D*, 7(12):3710–3721, Jun 1973.

[14] M. Fierz and W. Pauli. On Relativistic Wave Equations for Particles of Arbitrary Spin in an Electromagnetic Field. *Proceedings of the Royal Society of London. Series A. Mathematical and Physical Sciences*, 173(953):211–232, 1939.

[15] F. J. Belinfante. Intrinsic Magnetic Moment of Elementary Particles of Spin 3/2. *Phys. Rev.*, 92(4):997, Nov 1953.

[16] C. R. Hagen and W. J. Hurley. Magnetic Moment of a Particle with Arbitrary Spin. *Phys. Rev. Lett.*, 24(24):1381–1384, Jun 1970.

[17] W. Pauli. Relativistic Field Theories of Elementary Particles. *Rev. Mod. Phys.*, 13(3):203–232, Jul 1941.

[18] T. D. Lee. Minimal Electromagnetic Interaction and C, T Noninvariance. *Phys. Rev.*, 140(4B):B967–B976, Nov 1965.

[19] Steven Weinberg. Dynamic and Algebraic Symmetries. In Stanley Deser, Marc Grisaru, and Hugh Pendleton, editors, *Lectures on Elementary Particles and Quantum Field Theory: 1970 Brandeis University Summer Institute in Theoretical Physics, Volume 1*. M.I.T. Press, 1971.

[20] Heinz Pagels. Decays $\pi \to 2\gamma$, $\eta \to 2\gamma$ and Sum Rules for Nucleon Compton Scattering. *Phys. Rev.*, 158(5):1566–1576, Jun 1967.

[21] Sergio Ferrara, Massimo Porrati, and Valentine L. Telegdi. $g = 2$ as the natural value of the tree-level gyromagnetic ratio of elementary particles. *Phys. Rev. D*, 46(8):3529–3537, Oct 1992.

[22] S. Deser, A. Waldron, and V. Pascalutsa. Massive spin 3/2 electrodynamics. *Phys. Rev. D*, 62(10):105031, Oct 2000.

[23] Barry R. Holstein. Factorization in graviton scattering and the "natural" value of the g factor. *Physical Review D (Particles, Fields, Gravitation, and Cosmology)*, 74(8):085002, 2006.

[24] Cédric Lorcé. Electromagnetic properties for arbitrary spin particles: Natural electromagnetic moments from light-cone arguments. *Physical Review D (Particles and Fields)*, 79(11):113011, 2009.

[25] Xiangdong Ji and Yingchuan Li. Sum rules and spin-dependent polarizabilities of the deuteron in effective field theory. *Physics Letters B*, 591(1-2):76 – 82, 2004.

[26] Stanley J. Brodsky and John R. Hiller. Universal properties of the electromagnetic interactions of spin-one systems. *Phys. Rev. D*, 46(5):2141–2149, Sep 1992.

[27] Michael E. Peskin and Daniel E. Schroeder. *An Introduction to Quantum Field Theory*. Perseus Books, Reading, MA, 1995.

[28] M. N. Rosenbluth. High Energy Elastic Scattering of Electrons on Protons. *Phys. Rev.*, 79(4):615–619, Aug 1950.

[29] D. Drechsel and K. Bermuth. Comment on Rosenbluth scattering with Pauli moment for the electron. *J. Phys. G: Nucl. Part. Phys.*, 17:1779–1782, 1991.

[30] L. N. Hand, D. G. Miller, and R. Wilson. Alternative Nucleon form Factors. *Phys. Rev. Lett.*, 8(3):110–112, Feb 1962.

[31] L. N. Hand, D. G. Miller, and Richard Wilson. Electric and Magnetic Form Factors of the Nucleon. *Rev. Mod. Phys.*, 35(2):335–349, Apr 1963.

[32] C.F. Perdrisat, V. Punjabi, and M. Vanderhaeghen. Nucleon electromagnetic form factors. *Progress in Particle and Nuclear Physics*, 59(2):694 – 764, 2007.

[33] M. Gourdin. Weak and electromagnetic form factors of hadrons. *Physics Reports*, 11(2):29 – 98, 1974.

[34] R Gilman and F Gross. Electromagnetic structure of the deuteron. *Journal of Physics G: Nuclear and Particle Physics*, 28(4):R37–R116, 2002.

[35] Omar Benhar, Donal Day, and Ingo Sick. Inclusive quasielastic electron-nucleus scattering. *Reviews of Modern Physics*, 80(1):189, 2008.

[36] T. W. Donnelly and A. S. Raskin. Considerations of polarization in inclusive electron scattering from nuclei. *Annals of Physics*, 169(2):247 – 351, 1986.

[37] NORMAN DOMBEY. Scattering of Polarized Leptons at High Energy. *Rev. Mod. Phys.*, 41(1):236–246, Jan 1969.

[38] M. K. Jones et al. Proton G_E/G_M from beam-target asymmetry. *Physical Review C (Nuclear Physics)*, 74(3):035201, 2006.

[39] Raymond G. Arnold, Carl E. Carlson, and Franz Gross. Polarization transfer in elastic electron scattering from nucleons and deuterons. *Phys. Rev. C*, 23(1):363–374, Jan 1981.

[40] D. R. Yennie, M. M. Lévy, and D. G. Ravenhall. Electromagnetic Structure of Nucleons. *Rev. Mod. Phys.*, 29(1):144–157, Jan 1957.

[41] J. D. Walecka. Spectral functions in the static theory. *Nuovo Cimento*, 11(6):821–836, Mar 1959.

[42] F. J. Ernst, R. G. Sachs, and K. C. Wali. Electromagnetic Form Factors of the Nucleon. *Phys. Rev.*, 119(3):1105–1114, Aug 1960.

[43] R. G. Sachs. High-Energy Behavior of Nucleon Electromagnetic Form Factors. *Phys. Rev.*, 126(6):2256–2260, Jun 1962.

[44] Dieter Drechsel and Thomas Walcher. Hadron structure at low Q^2. *Reviews of Modern Physics*, 80(3):731, 2008.

[45] George Sterman and Paul Stoler. Hadronic Form Factors and Perturbative QCD. *Annual Review of Nuclear and Particle Science*, 47(1):193–233, 1997.

[46] Robert Hofstadter and Robert W. McAllister. Electron Scattering from the Proton. *Phys. Rev.*, 98(1):217–218, Apr 1955.

[47] R. W. McAllister and R. Hofstadter. Elastic Scattering of 188-Mev Electrons from the Proton and the Alpha Particle. *Phys. Rev.*, 102(3):851–856, May 1956.

[48] E. E. Chambers and R. Hofstadter. Structure of the Proton. *Phys. Rev.*, 103(5):1454–1463, Sep 1956.

[49] E. Clementel and C. Villi. On the scattering of high energy electrons by protons. *Nuovo Cimento*, 4(5):1207–1211, Nov 1956.

[50] Robert Hofstadter and Robert Herman. Electric and Magnetic Structure of the Proton and Neutron. *Phys. Rev. Lett.*, 6(6):293–296, Mar 1961.

[51] R. Hofstadter, C. de Vries, and Robert Herman. Dirac and Pauli Form Factors of the Neutron. *Phys. Rev. Lett.*, 6(6):290–293, Mar 1961.

[52] M. Goitein, J. R. Dunning, and Richard Wilson. Comparison of Elastic Electron-Proton Scattering Cross Sections with Some Theoretical Predictions. *Phys. Rev. Lett.*, 18(23):1018–1022, Jun 1967.

[53] E. B. Hughes, T. A. Griffy, M. R. Yearian, and R. Hofstadter. Neutron Form Factors from Inelastic Electron-Deuteron Scattering. *Phys. Rev.*, 139(2B):B458–B471, Jul 1965.

[54] G.G. Simon, Ch. Schmitt, F. Borkowski, and V.H. Walther. Absolute electron-proton cross sections at low momentum transfer measured with a high pressure gas target system. *Nuclear Physics A*, 333(3):381 – 391, 1980.

[55] G. Höhler, E. Pietarinen, I. Sabba-Stefanescu, F. Borkowski, G. G. Simon, V. H. Walther, and R. D. Wendling. Analysis of electromagnetic nucleon form factors. *Nuclear Physics B*, 114(3):505 – 534, 1976.

[56] P. E. Bosted. Empirical fit to the nucleon electromagnetic form factors. *Phys. Rev. C*, 51(1):409–411, Jan 1995.

[57] E. J. Brash, A. Kozlov, Sh. Li, and G. M. Huber. New empirical fits to the proton electromagnetic form factors. *Phys. Rev. C*, 65(5):051001, Apr 2002.

[58] J. Friedrich and Th. Walcher. A coherent interpretation of the form factors of the nucleon in terms of a pion cloud and constituent quarks. *European Physical Journal A*, 17(4):607–623, Aug 2003.

[59] J. J. Kelly. Simple parametrization of nucleon form factors. *Phys. Rev. C*, 70(6):068202, Dec 2004.

[60] J. Arrington, W. Melnitchouk, and J. A. Tjon. Global analysis of proton elastic form factor data with two-photon exchange corrections. *Physical Review C (Nuclear Physics)*, 76(3):035205, 2007.

[61] W. M. Alberico, S. M. Bilenky, C. Giunti, and K. M. Graczyk. Electromagnetic form factors of the nucleon: New fit and analysis of uncertainties. *Physical Review C (Nuclear Physics)*, 79(6):065204, 2009.

[62] M. K. Jones et al. G_E^p/G_M^p Ratio by Polarization Transfer in $\vec{e}p \rightarrow e\vec{p}$. *Phys. Rev. Lett.*, 84(7):1398–1402, Feb 2000.

[63] O. Gayou et al. Measurement of G_E^p/G_M^p in $\vec{e}p \rightarrow e\vec{p}$ to $Q^2 = 5.6$ GeV^2. *Phys. Rev. Lett.*, 88(9):092301, Feb 2002.

[64] M.E. Christy et al. Measurements of electron-proton elastic cross sections for $0.4 < Q^2 < 5.5$ (GeV/c)^2. *Phys. Rev. C*, 70(1):015206, Jul 2004.

[65] I.A. Qattan et al. Precision Rosenbluth Measurement of the Proton Elastic Form Factors. *Phys. Rev. Lett.*, 94(14):142301, Apr 2005.

[66] J. Arrington. Evidence for two-photon exchange contributions in electron-proton and positron-proton elastic scattering. *Phys. Rev. C*, 69(3):032201, Mar 2004.

[67] J Arrington, C D Roberts, and J M Zanotti. Nucleon electromagnetic form factors. *Journal of Physics G: Nuclear and Particle Physics*, 34(7):S23–S51, 2007.

[68] Richard Wilson. Some features of electromagnetic interactions. In T. W. Preist and L. L. J. Vick, editors, *Particle Interactions at High Energies: Scottish Universities' Summer School 1966*. Plenum Press, New York, 1967.

[69] Carl E. Carlson and Marc Vanderhaeghen. Two-Photon Physics in Hadronic Processes. *Annual Review of Nuclear and Particle Science*, 57(1):171–204, 2007.

[70] M. R. Yearian and Robert Hofstadter. Magnetic Form Factor of the Neutron. *Phys. Rev.*, 110(2):552–564, Apr 1958.

[71] N. F. Ramsey. The Rabi School. *European Journal of Physics*, 11(3):137–141, 1990.

[72] W. W. Havens, I. I. Rabi, and L. J. Rainwater. Interaction of Neutrons with Electrons in Lead. *Phys. Rev.*, 72(7):634–636, Oct 1947.

[73] E. Fermi and L. Marshall. On the Interaction Between Neutrons and Electrons. *Phys. Rev.*, 72(12):1139–1146, Dec 1947.

[74] L. L. Foldy. The Electron-Neutron Interaction. *Phys. Rev.*, 83(3):688, Aug 1951.

[75] Leslie L. Foldy. Neutron-Electron Interaction. *Rev. Mod. Phys.*, 30(2):471–481, Apr 1958.

[76] Hartmut Abele. The neutron. Its properties and basic interactions. *Progress in Particle and Nuclear Physics*, 60(1):1 – 81, 2008.

[77] D. J. Drickey and L. N. Hand. Precise Neutron and Proton Form Factors at Low Momentum Transfers. *Phys. Rev. Lett.*, 9(12):521–524, Dec 1962.

[78] B. Grossetête, D. Drickey, and P. Lehmann. Elastic Electron-Deuteron Scattering. *Phys. Rev.*, 141(4):1425–1434, Jan 1966.

[79] F. A. Bumiller, F. R. Buskirk, J. W. Stewart, and E. B. Dally. Form-Factor Ratio G_E^n/G_E^p at Low Momentum Transfers. *Phys. Rev. Lett.*, 25(26):1774–1778, Dec 1970.

[80] G. G. Simon, Ch. Schmitt, and V. H. Walther. Elastic electric and magnetic e-d scattering at low momentum transfer. *Nuclear Physics A*, 364(2-3):285 – 296, 1981.

[81] S. Platchkov et al. The deuteron $A(Q^2)$ structure function and the neutron electric form factor. *Nuclear Physics A*, 510(4):740 – 758, 1990.

[82] R. Schiavilla and I. Sick. Neutron charge form factor at large q^2. *Phys. Rev. C*, 64(4):041002, Sep 2001.

[83] S. Galster et al. Elastic electron-deuteron scattering and the electric neutron form factor at four-momentum transfers $5\,\mathrm{fm}^{-2} < q^2 < 14\,\mathrm{fm}^{-2}$. *Nuclear Physics B*, 32(1):221 – 237, 1971.

[84] E. Lomon and H. Feshbach. A Nucleon-Nucleon Interaction Consistent with Theory and Experiment. *Rev. Mod. Phys.*, 39(3):611–621, Jul 1967.

[85] T. Hamada and I. D. Johnston. A potential model representation of two-nucleon data below 315 MeV. *Nuclear Physics*, 34(2):382 – 403, 1962.

[86] M. M. Nagels, T. A. Rijken, and J. J. de Swart. Low-energy nucleon-nucleon potential from Regge-pole theory. *Phys. Rev. D*, 17(3):768–776, Feb 1978.

[87] R. B. Wiringa, R. A. Smith, and T. L. Ainsworth. Nucleon-nucleon potentials with and without $\Delta(1232)$ degrees of freedom. *Phys. Rev. C*, 29(4):1207–1221, Apr 1984.

[88] M. Lacombe, B. Loiseau, R. Vinh Mau, J. Côtè, P. Pirès, and R. de Tourreil. Parametrization of the deuteron wave function of the Paris N—N potential. *Physics Letters B*, 101(3):139 – 140, 1981.

[89] Roderick V. Reid. Local phenomenological nucleon-nucleon potentials. *Annals of Physics*, 50(3):411 – 448, 1968.

[90] C. W. Akerlof, K. Berkelman, G. Rouse, and M. Tigner. Neutron Form Factors from Inelastic Electron-Deuteron Scattering. *Phys. Rev.*, 135(3B):B810–B815, Aug 1964.

[91] J. R. Dunning Jr. et al. Electromagnetic Structure of the Neutron and Proton. *Phys. Rev. Lett.*, 13(21):631–635, Nov 1964.

[92] R. J. Budnitz et al. Neutron Form Factors from Quasi-Elastic Electron-Deuteron Scattering. *Phys. Rev.*, 173(5):1357–1390, Sep 1968.

[93] K.M. Hanson et al. Large-Angle Quasielastic Electron-Deuteron Scattering. *Phys. Rev. D*, 8(3):753–778, Aug 1973.

[94] W. Bartel et al. Measurement of proton and neutron electromagnetic form factors at squared four-momentum transfers up to 3 $(\mathrm{GeV}/c)^2$. *Nuclear Physics B*, 58(2):429 – 475, 1973.

[95] A. Lung et al. Measurements of the electric and magnetic form factors of the neutron from $Q^2 = 1.75$ to 4.00 $(\mathrm{GeV}/c)^2$. *Phys. Rev. Lett.*, 70(6):718–721, Feb 1993.

[96] D. Benaksas, D. Drickey, and D. Frèrejacque. Deuteron Electromagnetic Form Factors for 3 $\mathrm{F}^{-2} < q^2 < 6\ \mathrm{F}^{-2}$. *Phys. Rev.*, 148(4):1327–1331, Aug 1966.

[97] C.E. Jones-Woodward et al. Determination of the neutron electric form factor in quasielastic scattering of polarized electrons from polarized ^{3}He . *Phys. Rev. C*, 44(2):R571–R574, Aug 1991.

[98] M. Meyerhoff et al. First measurement of the electric form factor of the neutron in the exclusive quasielastic scattering of polarized electrons from polarized ^{3}He . *Physics Letters B*, 327(3-4):201 – 207, 1994.

[99] J. Becker et al. Determination of the neutron electric form factor from the reaction $^3\vec{\mathrm{H}}\mathrm{e}(\vec{e},e'n)$ at medium momentum transfer. *Eur. Phys. J. A*, 6(3):329–344, nov 1999.

[100] D. Rohe et al. Measurement of the Neutron Electric Form Factor G_E^n at 0.67 $(\mathrm{GeV}/c)^2$ via $^3\vec{\mathrm{H}}\mathrm{e}(\vec{e},e'n)$. *Phys. Rev. Lett.*, 83(21):4257–4260, Nov 1999.

[101] J. Bermuth et al. The neutron charge form factor and target analyzing powers from scattering. *Physics Letters B*, 564(3-4):199 – 204, 2003.

[102] A. K. Thompson et al. Quasielastic Scattering of Polarized Electrons from Polarized ^{3}He and Measurement of the Neutron's Form Factors. *Phys. Rev. Lett.*, 68(19):2901–2904, May 1992.

[103] T. Eden et al. Electric form factor of the neutron from the $^2\mathrm{H}(\vec{e},e'\vec{n})p$ reaction at $Q^2 = 0.255$ $(\mathrm{GeV}/c)^2$. *Phys. Rev. C*, 50(4):R1749–R1753, Oct 1994.

[104] C. Herberg et al. Determination of the neutron electric form factor in the $D(\vec{e},e'\vec{n})p$ reaction and the influence of nuclear binding. *Eur. Phys. J. A*, 5(2):131–135, jun 1999.

[105] M. Ostrick et al. Measurement of the Neutron Electric Form Factor G_E^n in the Quasifree $^2\mathrm{H}(\vec{e},e'\vec{n})p$ Reaction. *Phys. Rev. Lett.*, 83(2):276–279, Jul 1999.

[106] R. Madey et al. Measurements of G_E^n/G_M^n from the $^2\mathrm{H}(\vec{e},e'\vec{n})^1\mathrm{H}$ Reaction to $Q^2 = 1.45$ $(\mathrm{GeV}/c)^2$. *Phys. Rev. Lett.*, 91(12):122002, Sep 2003.

[107] B. Plaster et al. Measurements of the neutron electric to magnetic form factor ratio G_E^n/G_M^n via the $^2\mathrm{H}(\vec{e},e'\vec{n})^1\mathrm{H}$ reaction to $Q^2 = 1.45$ $(\mathrm{GeV}/c)^2$. *Physical Review C (Nuclear Physics)*, 73(2):025205, 2006.

[108] D. I. Glazier et al. Measurement of the electric form factor of the neutron at $Q^2 = 0.3$–0.8 $(\mathrm{GeV}/c)^2$. *Eur. Phys. J. A*, 24(1):101–109, apr 2005.

[109] I. Passchier et al. Charge Form Factor of the Neutron from the Reaction $^2\vec{\mathrm{H}}(\vec{e}, e'n)p$. *Phys. Rev. Lett.*, 82(25):4988–4991, Jun 1999.

[110] H. Zhu et al. Measurement of the Electric Form Factor of the Neutron through $\vec{d}(\vec{e}, e'n)p$ at $Q^2 = 0.5$ $(\mathrm{GeV}/c)^2$. *Phys. Rev. Lett.*, 87(8):081801, Aug 2001.

[111] G. Warren et al. Measurement of the Electric Form Factor of the Neutron at $Q^2 = 0.5$ and 1.0 GeV^2/c^2. *Phys. Rev. Lett.*, 92(4):042301, Jan 2004.

[112] E. Geis et al. Charge Form Factor of the Neutron at Low Momentum Transfer from the $^2\vec{\mathrm{H}}(\vec{e}, e'n)^1\mathrm{H}$ Reaction. *Physical Review Letters*, 101(4):042501, 2008.

[113] B. Blankleider and R. M. Woloshyn. Quasi-elastic scattering of polarized electrons on polarized ^{3}He . *Phys. Rev. C*, 29(2):538–552, Feb 1984.

[114] H. Arenhövel, W. Leidemann, and E. L. Tomusiak. General survey of polarization observables in deuteron electrodisintegration. *Eur. Phys. J. A*, 23(1):147–190, jan 2005.

[115] J. Golak, G. Ziemer, H. Kamada, H. Witała, and W. Glöckle. Extraction of electromagnetic neutron form factors through inclusive and exclusive polarized electron scattering on a polarized ^{3}He target. *Phys. Rev. C*, 63(3):034006, Feb 2001.

[116] R. Ent. Elastic Form Factors. In Frank Close, Sandy Donnachie, and Graham Shaw, editors, *Electromagnetic Interactions and Hadronic Structure*. Cambridge University Press, 2007.

[117] Geoffrey F. Chew, Robert Karplus, Stephen Gasiorowicz, and Fredrik Zachariasen. Electromagnetic Structure of the Nucleon in Local-Field Theory. *Phys. Rev.*, 110(1):265–276, Apr 1958.

[118] P. Federbush, M. L. Goldberger, and S. B. Treiman. Electromagnetic Structure of the Nucleon. *Phys. Rev.*, 112(2):642–665, Oct 1958.

[119] John Dirk Walecka. *Electron Scattering for Nuclear and Nucleon Structure*. Cambridge University Press, Cambridge, 2001.

[120] J. J. Sakurai. *Currents and Mesons*. University of Chicago Press, Chicago, IL, 1969.

[121] Richard P. Feynman. *Photon-Hadron Interactions*. Addison-Wesley, Reading Massachusetts, 1998.

[122] Yoichiro Nambu. Possible Existence of a Heavy Neutral Meson. *Phys. Rev.*, 106(6):1366–1367, Jun 1957.

[123] T B W Kirk and Richard Wilson. Ten years of accelerator physics. *Reports on Progress in Physics*, 35(2):529–585, 1972.

[124] L. H. Chann et al. Nucleon Form Factors and Their Interpretation. *Phys. Rev.*, 141(4):1298–1307, Jan 1966.

[125] L. H. Chann et al. Errata: Nucleon Form Factors and Their Interpretation. *Phys. Rev.*, 147(4):1174, Jul 1966.

[126] William R. Frazer and Jose R. Fulco. Effect of a Pion-Pion Scattering Resonance on Nucleon Structure. *Phys. Rev. Lett.*, 2(8):365–368, Apr 1959.

[127] William R. Frazer and Jose R. Fulco. Partial-Wave Dispersion Relations for the Process $\pi + \pi \to N + \bar{N}$. *Phys. Rev.*, 117(6):1603–1608, Mar 1960.

[128] William R. Frazer and Jose R. Fulco. Effect of a Pion-Pion Scattering Resonance on Nucleon Structure. II. *Phys. Rev.*, 117(6):1609–1614, Mar 1960.

[129] G. Höhler and E. Pietarinen. The ρNN vertex in vector-dominance models. *Nuclear Physics B*, 95(2):210 – 230, 1975.

[130] M.A. Belushkin, H.-W. Hammer, and Ulf-G. Meißner. Novel evaluation of the two-pion contribution to the nucleon isovector form factors. *Physics Letters B*, 633(4-5):507 – 511, 2006.

[131] H.-W. Hammer and M. J. Ramsey-Musolf. $K\bar{K}$ continuum and isoscalar nucleon form factors. *Phys. Rev. C*, 60(4):045204, Sep 1999.

[132] H.-W. Hammer and M. J. Ramsey-Musolf. Errata: $K\bar{K}$ continuum and isoscalar nucleon form factors. *Phys. Rev. C*, 62(4):049902, Sep 2000.

[133] F. Iachello, A. D. Jackson, and A. Lande. Semi-phenomenological fits to nucleon electromagnetic form factors. *Physics Letters B*, 43(3):191 – 196, 1973.

[134] R. Bijker and F. Iachello. Reanalysis of the nucleon spacelike and timelike electromagnetic form factors in a two-component model. *Phys. Rev. C*, 69(6):068201, Jun 2004.

[135] P. Mergell, Ulf-G. Meißner, and D. Drechsel. Dispersion-theoretical analysis of the nucleon electromagnetic form factors. *Nuclear Physics A*, 596(3-4):367 – 396, 1996.

[136] M. A. Belushkin, H.-W. Hammer, and Ulf-G. Meißner. Dispersion analysis of the nucleon form factors including meson continua. *Physical Review C (Nuclear Physics)*, 75(3):035202, 2007.

[137] M. Gari and W. Krümpelmann. Semiphenomenological synthesis of meson and quark dynamics and the E.M. structure of the nucleon. *Zeitschrift für Physik A Hadrons and Nuclei*, 322(4):689–693, Dec 1985.

[138] Manfred Gari and W. Krümpelmann. The electromagnetic form factor of the neutron. *Physics Letters B*, 173(1):10 – 14, 1986.

[139] M. F. Gari and W. Krümpelmann. The electric neutron form factor and the strange quark content of the nucleon. *Physics Letters B*, 274(2):159 – 162, 1992.

[140] M. F. Gari and W. Krümpelmann. Errata: The electric neutron form factor and the strange quark content of the nucleon. *Physics Letters B*, 282(3-4):483 – 484, 1992.

[141] Earle L. Lomon. Extended Gari-Krümpelmann model fits to nucleon electromagnetic form factors. *Phys. Rev. C*, 64(3):035204, Aug 2001.

[142] Earle L. Lomon. Effect of recent Rp and Rn measurements on extended Gari-Krümpelmann model fits to nucleon electromagnetic form factors. *Phys. Rev. C*, 66(4):045501, Oct 2002.

[143] Earle L. Lomon. Effect of revised *Rn* measurements on extended Gari-Krümpelmann model fits to nucleon electromagnetic form factors. arXiv:nucl-th/0609020v2(MIT-CTP-3765), Sep 2006.

[144] Stanley J. Brodsky and Glennys R. Farrar. Scaling Laws at Large Transverse Momentum. *Phys. Rev. Lett.*, 31(18):1153–1156, Oct 1973.

[145] G. Peter Lepage and Stanley J. Brodsky. Exclusive Processes in Quantum Chromodynamics: The Form Factors of Baryons at Large Momentum Transfer. *Phys. Rev. Lett.*, 43(8):545–549, Aug 1979.

[146] G. Peter Lepage and Stanley J. Brodsky. Errata: Exclusive Processes in Quantum Chromodynamics: The Form Factors of Baryons at Large Momentum Transfer. *Phys. Rev. Lett.*, 43(21):1625, Nov 1979.

[147] G. Peter Lepage and Stanley J. Brodsky. Exclusive processes in perturbative quantum chromodynamics. *Phys. Rev. D*, 22(9):2157–2198, Nov 1980.

[148] Xiangdong Ji, Jian-Ping Ma, and Feng Yuan. Generalized Counting Rule for Hard Exclusive Processes. *Phys. Rev. Lett.*, 90(24):241601, Jun 2003.

[149] A. V. Belitsky, Xiangdong Ji, and Feng Yuan. Perturbative QCD Analysis of the Nucleon's Pauli Form Factor $F_2(Q^2)$. *Phys. Rev. Lett.*, 91(9):092003, Aug 2003.

[150] John P. Ralston and Pankaj Jain. QCD form factors and hadron helicity nonconservation. *Phys. Rev. D*, 69(5):053008, Mar 2004.

[151] H Georgi. Effective Field Theory. *Annual Review of Nuclear and Particle Science*, 43(1):209–252, 1993.

[152] A.C. Scott, F.Y.F. Chu, and D.W. McLaughlin. The soliton: A new concept in applied science. *Proceedings of the IEEE*, 61(10):1443–1483, Oct. 1973.

[153] Claudio Rebbi and Giulio Soliani. *Solitons and Particles*. World Scientific, Singapore, 1984.

[154] Sidney Coleman. Classical lumps and their quantum decendants. In *Aspects of Symmetry: selected Erice Lectures*. Cambridge University Press, Cambridge, 1985.

[155] Edward Witten. Baryons in the $1/N$ expansion. *Nuclear Physics B*, 160(1):57 – 115, 1979.

[156] Edward Witten. Current algebra, baryons, and quark confinement. *Nuclear Physics B*, 223(2):433 – 444, 1983.

[157] T. H. R. Skyrme. A Non-Linear Field Theory. *Proceedings of the Royal Society of London. Series A. Mathematical and Physical Sciences*, 260(1300):127–138, 1961.

[158] M Oka and A Hosaka. Nucleons as Skyrmions. *Annual Review of Nuclear and Particle Science*, 42(1):333–365, 1992.

[159] Eric Braaten, Sze-Man Tse, and Charles Willcox. Electroweak form factors of the Skyrmion. *Phys. Rev. D*, 34(5):1482–1492, Sep 1986.

[160] G. Holzwarth. Electro-magnetic nucleon form factors and their spectral functions in soliton models. *Zeitschrift für Physik A Hadrons and Nuclei*, 356(1):339–350, Dec 1996.

[161] G. Holzwarth. Electromagnetic Form Factors of the Nucleon in the Chiral Soliton Model. arXiv:hep-ph/0201138v1(SI-TH-02-01), Jan 2002.

[162] Xiangdong Ji. A relativistic skyrmion and its form factors. *Physics Letters B*, 254(3-4):456 – 461, 1991.

[163] Y. Nambu and G. Jona-Lasinio. Dynamical Model of Elementary Particles Based on an Analogy with Superconductivity. I. *Phys. Rev.*, 122(1):345–358, Apr 1961.

[164] Y. Nambu and G. Jona-Lasinio. Dynamical Model of Elementary Particles Based on an Analogy with Superconductivity. II. *Phys. Rev.*, 124(1):246–254, Oct 1961.

[165] Chr. V. Christov, A. Z. Grski, K. Goeke, and P. V. Pobylitsa. Electromagnetic form factors of the nucleon in the chiral quark soliton model. *Nuclear Physics A*, 592(4):513 – 538, 1995.

[166] Chr. V. Christov, A. Blotz, H. C. Kim, P. Pobylitsa, T. Watabe, Th. Meissner, E. Ruiz Arriola, and K. Goeke. Baryons as non-topological chiral solitons. *Progress in Particle and Nuclear Physics*, 37:91 – 191, 1996.

[167] Charles Earl Hyde-Wright and Kees de Jager. ELECTROMAGNETIC FORM FACTORS OF THE NUCLEON AND COMPTON SCATTERING. *Annual Review of Nuclear and Particle Science*, 54(1):217–267, 2004.

[168] Bogdan Povh, Klaus Rith, Christoph Scholz, and Frank Zetsche. *Particles and Nuclei: An Introduction to the Physical Concepts*. Springer-Verlag, Berlin, sixth edition, 2008.

[169] P. A. M. Dirac. Forms of Relativistic Dynamics. *Rev. Mod. Phys.*, 21(3):392–399, Jul 1949.

[170] B. Juliá-Díaz, D. O. Riska, and F. Coester. Baryon form factors of relativistic constituent-quark models. *Phys. Rev. C*, 69(3):035212, Mar 2004.

[171] B. Juliá-Díaz, D. O. Riska, and F. Coester. Errata: Baryon form factors of relativistic constituent-quark models. *Physical Review C (Nuclear Physics)*, 75(6):069902, 2007.

[172] Felix Schlumpf. Relativistic constituent quark model of electroweak properties of baryons. *Phys. Rev. D*, 47(9):4114–4121, May 1993.

[173] Felix Schlumpf. Errata: Relativistic constituent quark model of electroweak properties of baryons. *Phys. Rev. D*, 49(11):6246, Jun 1994.

[174] Gerald A. Miller and Michael R. Frank. Q^2 independence of QF_2/F_1 Poincaré invariance, and the nonconservation of helicity. *Phys. Rev. C*, 65(6):065205, Jun 2002.

[175] P. L. Chung and F. Coester. Relativistic constituent-quark model of nucleon form factors. *Phys. Rev. D*, 44(1):229–241, Jul 1991.

[176] R. F. Wagenbrunn, S. Boffi, W. Klink, W. Plessas, and M. Radici. Covariant nucleon electromagnetic form factors from the Goldstone-boson-exchange quark model. *Physics Letters B*, 511(1):33 – 39, 2001.

[177] M. De Sanctis, M. M. Giannini, E. Santopinto, and A. Vassallo. Electromagnetic form factors and the hypercentral constituent quark model. *Physical Review C (Nuclear Physics)*, 76(6):062201, 2007.

[178] E. Pace, G. Salm, F. Cardarelli, and S. Simula. A light-front description of electromagnetic form factors for $J \leq 3/2$ hadrons. *Nuclear Physics A*, 666-667:33 – 37, 2000. The Structure of the Nucleon.

[179] Franz Gross and Peter Agbakpe. Shape of the nucleon. *Physical Review C (Nuclear Physics)*, 73(1):015203, 2006.

[180] Gerald A. Miller. Light front cloudy bag model: Nucleon electromagnetic form factors. *Phys. Rev. C*, 66(3):032201, Sep 2002.

[181] Kenneth G. Wilson. Confinement of quarks. *Phys. Rev. D*, 10(8):2445–2459, Oct 1974.

[182] A Hasenfratz and P Hasenfratz. Lattice Gauge Theories. *Annual Review of Nuclear and Particle Science*, 35(1):559–604, 1985.

[183] G. Peter Lepage. Lattice QCD for Novices. In Jos L. Goity, editor, *Strong Interactions at Low and Intermediate Energies*. World Scientific, Co., 2000.

[184] C. Alexandrou and G. Koutsou and J. W. Negele and A. Tsapalis. Nucleon electromagnetic form factors from lattice qcd. *Physical Review D (Particles and Fields)*, 74(3):034508, 2006.

[185] S. Boinepalli, D. B. Leinweber, A. G. Williams, J. M. Zanotti, and J. B. Zhang. Precision electromagnetic structure of octet baryons in the chiral regime. *Physical Review D (Particles and Fields)*, 74(9):093005, 2006.

[186] William Marciano and Heinz Pagels. Quantum chromodynamics. *Physics Reports*, 36(3):137 – 276, 1978.

[187] Carl M. Bender, Kimball A. Milton, and Van M. Savage. Solution of Schwinger-Dyson equations for *PT*-symmetric quantum field theory. *Phys. Rev. D*, 62(8):085001, Sep 2000.

[188] C.D. Roberts. Hadron properties and Dyson-Schwinger equations. *Progress in Particle and Nuclear Physics*, 61(1):50 – 65, 2008. Quarks in Hadrons and Nuclei - 29th Course, International Workshop on Nuclear Physics.

[189] G. Eichmann, I. C. Cloët, R. Alkofer, A. Krassnigg, and C. D. Roberts. Toward unifying the description of meson and baryon properties. *Physical Review C (Nuclear Physics)*, 79(1):012202, 2009.

[190] I. C. Cloët, G. Eichmann, B. El-Bennich, T. Klähn, and C. D. Roberts. Survey of Nucleon Electromagnetic Form Factors. *Few-Body Systems*, 46(1):1–36, Jun 2009.

[191] M. Diehl, Th Feldmann, R. Jakob, and P. Kroll. Generalized parton distributions from nucleon form factor data. *The European Physical Journal C - Particles and Fields*, 39:1–39, 2005. 10.1140/epjc/s2004-02063-4.

[192] M. Guidal, M. V. Polyakov, A. V. Radyushkin, and M. Vanderhaeghen. Nucleon form factors from generalized parton distributions. *Phys. Rev. D*, 72(5):054013, Sep 2005.

[193] M. Diehl. Generalized parton distributions. *Physics Reports*, 388(2-4):41 – 277, 2003.

[194] Sigfrido Boffi and Barbara Pasquini. Generalized parton distributions and the structure of the nucleon. *La Rivista del Nuovo Cimento*, 30:387–449, 2007.

[195] Xiangdong Ji. GENERALIZED PARTON DISTRIBUTIONS. *Annual Review of Nuclear and Particle Science*, 54(1):413–450, 2004.

[196] M. Anselmino, A. Efremov, and E. Leader. The theory and phenomenology of polarized deep inelastic scattering. *Physics Reports*, 261(1-2):1 – 124, 1995.

[197] M. Anselmino, A. Efremov, and E. Leader. Errata: The theory and phenomenology of polarized deep inelastic scattering. *Physics Reports*, 281(5-6):399 – 400, 1997.

[198] Francis Halzen and Alan D. Martin. *Quarks & Leptons*. John Wiley & Sons, New York, 1984.

[199] Charles W. Misner, Kip S. Thorne, and John Archibald Wheeler. *Gravitation*. W. H. Freeman and Company, New York, 1973.

[200] J. D. Bjorken. Asymptotic Sum Rules at Infinite Momentum. *Phys. Rev.*, 179(5):1547–1553, Mar 1969.

[201] J. D. Bjorken and E. A. Paschos. Inelastic Electron-Proton and γ-Proton Scattering and the Structure of the Nucleon. *Phys. Rev.*, 185(5):1975–1982, Sep 1969.

[202] C. G. Callan and David J. Gross. High-Energy Electroproduction and the Constitution of the Electric Current. *Phys. Rev. Lett.*, 22(4):156–159, Jan 1969.

[203] Anthony W. Thomas and Wolfram Weise. *The Structure of the Nucleon*. Wilet-VCH, Berlin, 2001.

[204] David J. Gross and C. H. Llewellyn Smith. High-energy neutrino-nucleon scattering, current algebra and partons. *Nuclear Physics B*, 14(2):337 – 347, 1969.

[205] Stephen L. Adler. Sum Rules Giving Tests of Local Current Commutation Relations in High-Energy Neutrino Reactions. *Phys. Rev.*, 143(4):1144–1155, Mar 1966.

[206] Stephen L. Adler. Errata: Sum Rules Giving Tests of Local Current Commutation Relations in High-Energy Neutrino Reactions. *Phys. Rev.*, 151(4):1342, Nov 1966.

[207] G. Altarelli and G. Parisi. Asymptotic freedom in parton language. *Nuclear Physics B*, 126(2):298 – 318, 1977.

[208] David J. Gross and Frank Wilczek. Ultraviolet Behavior of Non-Abelian Gauge Theories. *Phys. Rev. Lett.*, 30(26):1343–1346, Jun 1973.

[209] H. David Politzer. Reliable Perturbative Results for Strong Interactions? *Phys. Rev. Lett.*, 30(26):1346–1349, Jun 1973.

[210] J. D. Bjorken. Applications of the Chiral $U(6) \bigotimes U(6)$ Algebra of Current Densities. *Phys. Rev.*, 148(4):1467–1478, Aug 1966.

[211] J. D. Bjorken. Errata: Applications of the Chiral $U(6) \bigotimes U(6)$ Algebra of Current Densities. *Phys. Rev.*, 160(5):1582, Aug 1967.

[212] E. W. HUGHES and R. VOSS. SPIN STRUCTURE FUNCTIONS. *Annual Review of Nuclear and Particle Science*, 49(1):303–339, 1999.

[213] A. Airapetian et al. Precise determination of the spin structure function g_1 of the proton, deuteron, and neutron. *Physical Review D (Particles and Fields)*, 75(1):012007, 2007.

[214] S. Wandzura and F. Wilczek. Sum rules for spin-dependent electroproduction- test of relativistic constituent quarks. *Physics Letters B*, 72(2):195 – 198, 1977.

[215] Johannes Blümlein and Helmut Böttcher. QCD analysis of polarized deep-inelastic scattering data and parton distributions. *Nuclear Physics B*, 636(1-2):225 – 263, 2002.

[216] F. E. Close. *An Introduction to Quarks and Partons*. Academic Press, London, 1979.

[217] J. D. Bjorken. Inelastic Scattering of Polarized Leptons from Polarized Nucleons. *Phys. Rev. D*, 1(5):1376–1379, Mar 1970.

[218] S. A. Larin and J. A. M. Vermaseren. The α_S^3 corrections to the Bjorken sum rule for polarized electroproduction and to the Gross-Llewellyn Smith sum rule. *Physics Letters B*, 259(3):345 – 352, 1991.

[219] Steven Weinberg. *The Quantum Theory of Fields, Volume II: Madern Applications*. Cambridge University Press, Cambridge, 2000.

[220] Kenneth G. Wilson. Non-Lagrangian Models of Current Algebra. *Phys. Rev.*, 179(5):1499–1512, Mar 1969.

[221] George Sterman. *An Introduction to Quantum Field Theory*. Cambridge University Press, Cambridge, 1993.

[222] H. David Politzer. Asymptotic freedom: An approach to strong interactions. *Physics Reports*, 14(4):129 – 180, 1974.

[223] Jiro Kodaira, Satoshi Matsuda, Ken Sasaki, and Tsuneo Uematsu. QCD higher order effects in spin-dependent deep inelastic electroproduction. *Nuclear Physics B*, 159(1-2):99 – 124, 1979.

[224] David J. Gross and S. B. Treiman. Light-Cone Structure of Current Commutators in the Gluon-Quark Model. *Phys. Rev. D*, 4(4):1059–1072, Aug 1971.

[225] M. Göckeler, R. Horsley, E. M. Ilgenfritz, H. Perlt, P. Rakow, G. Schierholz, and A. Schiller. Polarized and unpolarized nucleon structure functions from lattice QCD. *Phys. Rev. D*, 53(5):2317–2325, Mar 1996.

[226] Arthur H. Compton. A Quantum Theory of the Scattering of X-rays by Light Elements. *Phys. Rev.*, 21(5):483–502, May 1923.

[227] J. D. Jackson. *Classical Electrodynamics*. John Wiley & Sons, New York, second edition, 1975.

[228] F.W. Lipps and H.A. Tolhoek. Polarization phenomena of electrons and photons. I: General method and application to Compton scattering. *Physica*, 20(1-6):85 – 98, 1954.

[229] F.W. Lipps and H.A. Tolhoek. Polarization phenomena of electrons and photons. II: Results for Compton scattering. *Physica*, 20(1-6):385 – 405, 1954.

[230] U. FANO. Remarks on the Classical and Quantum-Mechanical Treatment of Partial Polarization. *J. Opt. Soc. Am.*, 39(10):859–863, 1949.

[231] O. Klein and T. Nishina. Über die Streuung von Strahlung durch freie Elektronen nach der neuen relativistischen Quantendynamik von Dirac. *Zeitschrift für Physik*, 52(11-12):853–868, Nov 1929.

[232] John L. Powell. Note on the Bremsstrahlung Produced by Protons. *Phys. Rev.*, 75(1):32–34, Jan 1949.

[233] C. G. Bollini. Total Compton Cross Section for Arbitrary Spin. *Phys. Rev.*, 121(1):314–318, Jan 1961.

[234] Roger G. Newton. Optical theorem and beyond. *American Journal of Physics*, 44(7):639–642, 1976.

[235] Steven Weinberg. *The Quantum Theory of Fields, Volume I: Foundations*. Cambridge University Press, Cambridge, 1999.

[236] D. Drechsel, B. Pasquini, and M. Vanderhaeghen. Dispersion relations in real and virtual Compton scattering. *Physics Reports*, 378(2-3):99 – 205, 2003.

[237] J. D. Jackson. Introduction to dispersion relation techniques. In G. R. Screaton, editor, *Dispersion Relations: Scottish Universities' Summer School 1960*. Oliver and Boyd, Edinburgh, 1961.

[238] Jon Mattews and Robert L. Walker. *Mathematical Methods of Physics*. W. A. Benjanmin, New York, second edition, 1970.

[239] George B. Arfken and Hans J. Weber. *Mathematical Methods for Physicists*. Academic Press, San Diego, fourth edition, 1995.

[240] David Griffiths. *Introduction to Elementary Particles*. John Wiley & Sons, New York, 1987.

[241] F. E. Low. Scattering of Light of Very Low Frequency by Systems of Spin-1/2. *Phys. Rev.*, 96(5):1428–1432, Dec 1954.

[242] M. Gell-Mann and M. L. Goldberger. Scattering of Low-Energy Photons by Particles of Spin-1/2. *Phys. Rev.*, 96(5):1433–1438, Dec 1954.

[243] Abraham Klein. Low-Energy Theorems for Renormalizable Field Theories. *Phys. Rev.*, 99(3):998, Aug 1955.

[244] A. M. Baldin. Polarizability of nucleons. *Nuclear Physics*, 18:310 – 317, 1960.

[245] V.S. Barashenkov, H.J. Kaiser, and A.A. Ogreba. Elastic scattering of γ-Quanta by a particle with spin. *Physics Letters*, 2(1):33 – 34, 1962.

[246] S. Scherer, A. Yu. Korchin, and J. H. Koch. Virtual Compton scattering off the nucleon at low energies. *Phys. Rev. C*, 54(2):904–919, Aug 1996.

[247] S. B. Gerasimov. A sum rule for magnetic moments and the damping of the nucleon magnetic moment in nuclei. *Yadernaya Fizika (Journal of Nuclear Physics)*, 2(4):598–602, October 1965.

[248] S. D. Drell and A. C. Hearn. Exact Sum Rule for Nucleon Magnetic Moments. *Phys. Rev. Lett.*, 16(20):908–911, May 1966.

[249] C. K. Iddings. Structure of the Proton and the Hyperfine Shift in Hydrogen. *Phys. Rev.*, 138(2B):B446–B458, Apr 1965.

[250] Ralf Pantforder. *Investigations on the foundation and possible modifications of the Gerasimov-Drell-Hearn sum rule*. PhD thesis, Bonn U., 1998.

[251] S. B. Gerasimov. A sum rule for magnetic moments and the damping of the nucleon magnetic moment in nuclei. *Soviet Journal of Nuclear Physics*, 2(4):430–433, April 1966.

[252] Masataka Hosoda and Kunio Yamamoto. Sum Rule for the Magnetic Moment of the Dirac Particle. *Progress of Theoretical Physics*, 36(2):425–426, 1966.

[253] Masataka Hosoda and Kunio Yamamoto. Sum Rules for Magnetic Moments of Spin 1 and 3/2 Nuclei. *Progress of Theoretical Physics*, 36(2):426–427, 1966.

[254] Norman Dombey. Forward Compton Scattering at High Energy and the Drell-Hearn-Gerasimov Sum Rule. *Phys. Rev. Lett.*, 19(17):985–987, Oct 1967.

[255] Norman Dombey. Errata: Forward Compton Scattering at High Energy and the Drell-Hearn-Gerasi-Mov Sum Rule. *Phys. Rev. Lett.*, 19(22):1305, Nov 1967.

[256] G. Barton and Norman Dombey. Drell-Hearn-Gerasimov Sum Rule: Examples and Counterexamples. *Phys. Rev.*, 162(5):1520–1525, Oct 1967.

[257] Gaku Konisi and Kunio Yamamoto. Sum Rule for the Magnetic Moment of Arbitrary Spin Particle and Simple Application to Nucleus. *Progress of Theoretical Physics*, 37(3):538–543, 1967.

[258] Stanley J. Brodsky and Joel R. Primack. Electromagnetic Interactions of Loosely-Bound Composite Systems. *Phys. Rev.*, 174(5):2071–2073, Oct 1968.

[259] Hugh Osborn. Relativistic Corrections to Nonrelativistic Two-Particle Dynamical Calculations: Demonstration of the Validity of the Drell-Hearn-

Gerasimov Sum Rule for Weakly Bound Composite Particles. *Phys. Rev.*, 176(5):1523–1533, Dec 1968.

[260] Richard A. Krajcik and Leslie L. Foldy. Electromagnetic Interactions with an Arbitrary Loosely Bound System. *Phys. Rev. Lett.*, 24(10):545–548, Mar 1970.

[261] Richard A. Krajcik and Leslie L. Foldy. Errata: Electromagnetic Interactions with an Arbitrary Loosely Bound System. *Phys. Rev. Lett.*, 24(13):762, Mar 1970.

[262] F. E. Close and L. A. Copley. Electromagnetic interactions of weakly-bound composite systems. *Nuclear Physics B*, 19(2):477 – 500, 1970.

[263] J. L. Friar. Low-energy theorem for Compton scattering and the Drell-Hearn-Gerasimov sum rule: Exchange currents. *Phys. Rev. C*, 16(4):1504–1512, Oct 1977.

[264] Klaus Helbing. The Gerasimov-Drell-Hearn sum rule. *Progress in Particle and Nuclear Physics*, 57(2):405 – 469, 2006.

[265] David R. Lide (Editor-in Chief). *CRC Handbook of Chemistry and Physics*. CRC Press, Boca Raton, FL, 75$^{\text{th}}$ student edition, 1994.

[266] Peter J. Mohr and Barry N. Taylor. CODATA recommended values of the fundamental physical constants: 2002. *Rev. Mod. Phys.*, 77(1):1–107, Mar 2005.

[267] N. Dombey. Introduction to Photoproduction and Electroproduction. In J. Cumming and H. Osborn, editors, *Hadronic Interactions of Electrons and*

Photons: Proceedings of the Eleventh Session of the Scottish Universities Summer School in Physics, 1970. Academic Press, 1971.

[268] Frederick J. Gilman. Kinematics and Saturation of the Sum Rules and Inequalities for Inelastic Electron-Nucleon Scattering. *Phys. Rev.*, 167(5):1365–1371, Mar 1968.

[269] L. N. Hand. Experimental Investigation of Pion Electroproduction. *Phys. Rev.*, 129(4):1834–1846, Feb 1963.

[270] Xiangdong Ji and Jonathan Osborne. Generalized sum rules for spin-dependent structure functions of the nucleon. *Journal of Physics G: Nuclear and Particle Physics*, 27(1):127–146, 2001.

[271] D. Drechsel, S. S. Kamalov, and L. Tiator. Gerasimov-Drell-Hearn sum rule and related integrals. *Phys. Rev. D*, 63(11):114010, Apr 2001.

[272] Véronique Bernard, Thomas R. Hemmert, and Ulf-G. Meißner. Spin structure of the nucleon at low energies. *Phys. Rev. D*, 67(7):076008, Apr 2003.

[273] J. Gasser and H. Leutwyler. Chiral perturbation theory to one loop. *Annals of Physics*, 158(1):142 – 210, 1984.

[274] H. Leutwyler. On the foundations of chiral perturbation theory. *Annals of Physics*, 235(1):165 – 203, 1994.

[275] G. Ecker. Chiral perturbation theory. *Progress in Particle and Nuclear Physics*, 35:1 – 80, 1995.

[276] Véronique Bernard and Ulf-G. Meißner. Chiral perturbation theory. *Annual Review of Nuclear and Particle Science*, 57(1):33–60, 2007.

[277] Véronique Bernard. Chiral perturbation theory and baryon properties. *Progress in Particle and Nuclear Physics*, 60(1):82 – 160, 2008.

[278] S. Scherer. Chiral perturbation theory: Introduction and recent results in the one-nucleon sector. *Progress in Particle and Nuclear Physics*, 64(1):1 – 60, 2010.

[279] Steven Weinberg. Phenomenological lagrangians. *Physica A: Statistical and Theoretical Physics*, 96(1-2):327 – 340, 1979.

[280] Elizabeth Jenkins and Aneesh V. Manohar. Baryon chiral perturbation theory using a heavy fermion lagrangian. *Physics Letters B*, 255(4):558 – 562, 1991.

[281] T. Becher and H. Leutwyler. Baryon chiral perturbation theory in manifestly lorentz invariant form. *Eur. Phys. J. C*, 9(4):643–671, jul 1999.

[282] William Rarita and Julian Schwinger. On a Theory of Particles with Half-Integral Spin. *Phys. Rev.*, 60(1):61, Jul 1941.

[283] Xiangdong Ji, Chung-Wen Kao, and Jonathan Osborne. Generalized drell-hearn-gerasimov sum rule at order $O(p^4)$ in chiral perturbation theory. *Physics Letters B*, 472(1-2):1 – 4, 2000.

[284] Véronique Bernard, Thomas R. Hemmert, and Ulf-G. Meißner. Novel analysis of chiral loop effects in the generalized gerasimov-drell-hearn sum rule. *Physics Letters B*, 545(1-2):105 – 111, 2002.

[285] Chung Wen Kao, Thomas Spitzenberg, and Marc Vanderhaeghen. Burkhardt-cottingham sum rule and forward spin polarizabilities in heavy baryon chiral perturbation theory. *Phys. Rev. D*, 67(1):016001, Jan 2003.

[286] D. Drechsel, O. Hanstein, S. S. Kamalov, and L. Tiator. A unitary isobar model for pion photo- and electroproduction on the proton up to 1 gev. *Nuclear Physics A*, 645(1):145 – 174, 1999.

[287] D. Drechsel, S. S. Kamalov, and L. Tiator. Unitary isobar model –maid2007. *Eur. Phys. J. A*, 34(1):69–97, oct 2007.

[288] S.E. Kuhn, J.-P. Chen, and E. Leader. Spin structure of the nucleon–status and recent results. *Progress in Particle and Nuclear Physics*, 63(1):1 – 50, 2009.

Chapter 3

The Hall A Polarized ^{3}He Program

E97110 (Small Angle GDH) & E02013 (G_E^n) will be described and preliminary & final results will be presented. These two experiments are a part of the Hall A polarized ^{3}He program summarized in Tab. (3.1). Generally speaking, the program seeks to elucidate the electromagnetic structure of the neutron at different resolutions and in different kinematic regimes. The experimental motif is electron scattering from a polarized ^{3}He target. One could summarize the three basic components of these and, in general, all electron scattering experiments as:

1. the "Beam," which includes a source, an accelerator, and a "beamline" used to measure & control properties of the electron beam before scattering.

2. the "Target," which includes the target material and all other equipment used to measure & control properties of the target material.

3. the "Detector," which includes the data acquisition system (DAQ) and any equipment used to redirect & measure the properties of the scattered electrons and/or particles associated with the reaction.

In our case, the "Beam" is the Continuous Electron Beam Accelerator Facility (CEBAF) at the Thomas Jefferson National Accelerator Facility (Jefferson Lab or JLab) in Newport News, VA. The "Target" is a spin-exchange optical pumping (SEOP) polarized ^{3}He target which is used as an effective polarized neutron target. The implementation of the "Target" and the "Detector" are specific to each experiment and will be described in the appropriate sections. My main contributions to these experiments have been:

1. to provide a better understanding of the physics of SEOP, including alkali-hybrid SEOP, see Chps. (5) & (6)
2. the design & optimization of the optical pumping apparatus, see Chp. 5)
3. the design, construction, & characterization of the glass target cells, see Secs. (3.2) & (3.3)

3.1 Effective Polarized Neutron

In the simplest picture, the "neutron-in-^{3}He" spin structure functions $g^3_{1,2}$ are equal to the neutron spin structure functions $g^n_{1,2}$. This naive picture neglects several important nuclear corrections which depend crucially on the kinematics being considered. Under most conditions, the largest of these corrections are due to the effective polarizations of the neutron ($P_n < 1$) and proton ($P_p \neq 0$) within a ^{3}He nucleus. These effective polarizations depend on the exact form of the ^{3}He ground state wavefunction. This wavefunction describes the motion of three nucleons and can be represented by a linear combination of angular momentum basis states.

	yr	quantity	Q^2 GeV^2	W GeV	$\langle P_b \rangle$	$\langle P_t \rangle$	ref.
E94010	98	$I_A, \gamma_0, \delta_{\rm LT}$	0.1–0.9	M_n–2.5	0.70	0.35	[1–7]
E95001	99	G_M	0.1–0.6	$\approx M_n$	0.70	0.30	[8–11]
E99117	01	A_1	2.7–4.8	2.0–2.5	0.80	0.40	[12, 13]
E97103	01	g_2	0.6–1.3	1.8–2.5	0.76	0.40	[14]
E01012	03	Γ_1	1.2–3.0	1.1–1.8	0.78	0.38	[15]
E97110	03	$I_A, \gamma_0, \delta_{\rm LT}$	0.04–0.24	M_n–2.0	0.71	0.37	[16]
E02013	06	G_E	1.4–3.4	$\approx M_n$	0.85	0.47	[17]
E06010	08–09	$A_{\rm N}$	1.0–3.0	1.8–2.2	0.80	0.65	[18]
E07013	08–09	$A_{\rm N}$	1.3–3.1	2.3–3.1			[19]
E06014	09	d_2	2.0–6.0	1.7–3.0			[20]
E05015	09	$A_{\rm N}$	1.0–2.3	$\approx M_n$			[21]
E08005	09	$A_{\rm N}$	0.7–1.0	$\approx M_n$			[22]
E05102	09	$A_{\rm T,L}(G_E)$	(0.36)	$\approx M_n$			[23]

Table 3.1: Hall A Polarized ^{3}He Experiments up to 2009. $M_n = 0.94$ GeV is neutron mass. $\langle P_{b,t} \rangle$ are the average beam and target polarizations. Note the dramatic improvement in the $\langle P_t \rangle$ starting with E02013. $A_{\rm N}$ is the target single spin asymmetries measured with the target spin normal to the scattering plane. d_2^n is related to higher moments of g_1 & g_2. $A_{\rm T,L}$ are the beam-target asymmetries measured with the target spin transverse & longitudinal to the q-vector in the the scattering plane. E05102 also made a parasitic measurement G_E^n.

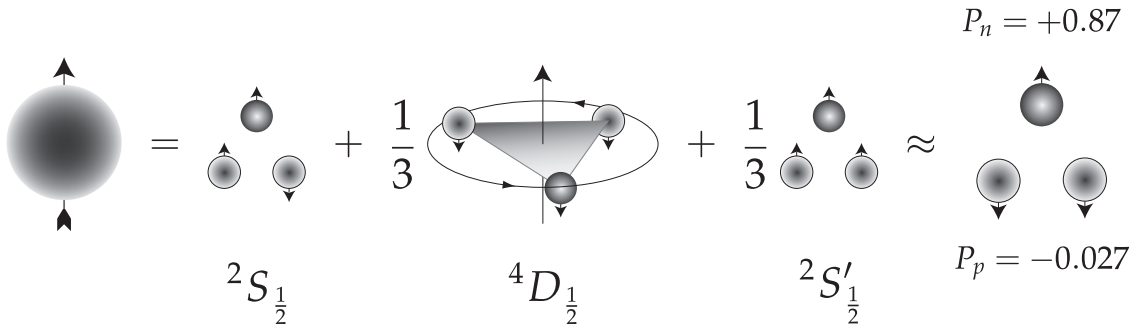

Figure 3.1: Effective Neutron and Proton Polarizations in ^{3}He from [26].

A total of 9 degrees of freedom are required to fully specify the motion of each nucleon in a three-nucleon (or alternatively "trinucleon") system; however, we can eliminate the 3 "external" degrees of freedom that specify the absolute motion of the center of mass. It is conventional [24] to specify the remaining 6 "internal" degrees of freedom using the LS-coupling scheme of Derrick & Blatt [25]:

1. the three intranucleon distances r_{12}, r_{23}, and r_{13}

2. the three Euler angles that represent the rotation of the triangle formed by r_{12}, r_{23}, and r_{13}

In this scheme, the total orbital angular momentum L (specified by the Euler angles) couples to the total nucleonic spin S. The sum $(L + S)$ results in the total angular momentum J of the trinucleon system. In the ground state, J must equal the spin I of the trinucleon nucleus (i.e. $J = I = 1/2$).

The three largest contributions to the ground state ^{3}He wavefunction are depicted in Fig. (3.1). The spin-isospin component of the S basis state is antisymmetric, whereas the spin-isospin component of the S' basis state has mixed symmetry. The contribution of the P basis states is suppressed because they have the opposite parity of the S basis states. There is a relatively large contribution from the D basis

	Reid Soft Core	AV14	"Best Fit"
$P(S)$	0.8864	0.89680	0.8920
$P(D)$	0.0837	0.08931	0.0945
$P(S')$	0.0154	0.01314	0.0135
Δ	0.0609	0.0639	0.0675
Δ'	0.0114	0.0127	0.0135
P_n	$+0.878$	$+0.872$	$+0.865$
P_p	-0.023	-0.025	-0.027
ref.	[28, 29]	[30]	[26]

Table 3.2: Contributions to the Ground State ^{3}He Wavefunction and the Effective Nucleon Polarizations for Different NN-potentials. "Best Fit" refers to the best fit for Δ & Δ' from several different NN-potentials (see [26] for more details).

states due to the tensor LS-coupling within nuclei [27]. The relative contributions of each of these basis states is given in Tab. (3.2).

Using the following result for the trinucleon magnetic moment from [31]:

$$\mu = \mu_S \left[P(S) + P(S') - P(D)\right] - 2\tau_3\mu_V \left[P(S) - \frac{P(S')}{3} + \frac{P(D)}{3}\right] + \left[\frac{3+2\tau_3}{6}\right] P(D) \tag{3.1}$$

where $\mu_{S,V} = (\mu_p \pm \mu_n)/2$ are the isoscalar & isovector nucleon magnetic moments and $2\tau_3 = \pm 1$ is the isospin of the trinucleon nucleus ($2\tau_3 = +1$ for ^{3}He), it has been shown [26] that the effective nucleon polarizations can be written as:

$$P_n = 1 - 2\Delta \qquad\qquad P_p = -2\Delta' \tag{3.2}$$

where Δ and Δ' are related to the ground state wavefunction contributions by:

$$\Delta = \frac{P(S') + 2P(D)}{3} \qquad \Delta' = \frac{P(D) - P(S')}{6} \qquad \Delta - \Delta' = \frac{1 - P(S)}{2} \tag{3.3}$$

where the contribution of the P basis states is taken to be zero ($P(P) = 0$) and the effective nucleon polarizations (P_n & P_p) are listed in Tab. (3.2).

Another group of corrections involve nuclear binding effects and the Fermi motion of the nucleons within the nucleus. These types of corrections involve "convolution integrals" over the neutron & proton spin structure functions and have been considered for the quasielastic [29,30,32], resonance [33,34], & DIS kinematic regimes [35,36]. It has been argued that the convolution integrals essentially reduce to the result obtained from the "effective polarization method" for g_1 in the DIS regime [35] and for integrals of g_1 down to the resonance region [33]:

$$g_1^3 = P_n g_1^n + 2P_p \left[\frac{M_n}{M_p}\right] g_1^p \qquad \text{in the DIS region} \tag{3.4}$$

$$I_A^3 = P_n I_A^n + 2P_p \left[\frac{M_n}{M_p}\right]^2 I_A^p \qquad \text{including the resonance and DIS regions} \tag{3.5}$$

where the superscripts $(3, n, p)$ refer to "neutron-in-^{3}He," neutron, & proton and the neutron to proton mass ratio (M_n/M_p) is usually approximated as 1. Analogous expressions exist for g_2 & I_1. Recently, corrections due to "off-shell" effects, meson exchange currents, the Δ isobar, and nuclear shadowing & antishadowing have also been considered in the DIS regime [36].

Finally we'll note that we've defined the "neutron-in-^{3}He" spin structure functions ($g_{1,2}^3$) such that $g_{1,2}^3 = g_{1,2}^n$ absent nuclear corrections. We'll denote this convention as the "effective neutron" convention. This is different than the "per nu-

cleon" convention also used in the literature where the "neutron-in-^{3}He" spin structure functions are defined as "per nucleon," see for example [37, 38]. In the "per nucleon" convention, $g_{1,2}^3 = g_{1,2}^n/3$ absent nuclear corrections. Unless otherwise noted, we'll use the "effective neutron" convention. Lastly, the ^{3}He spin structure functions $g_{1,2}^{^3\mathrm{He}}$ ($M = 2808.4$ MeV) are distinguished from the "neutron-in-^{3}He" spin structure functions $g_{1,2}^3$ ($M = 939.57$ MeV) based on the mass used in Eqns. (2.347) & (2.348).

3.2 Target Cell Fabrication & Characterization

Several aspects of target cell preparation are now standard. For the sake of brevity, we refer to previous dissertations. Details regarding target cell fabrication can be found in [39]. Details regarding the UVa/Princeton gas filling station can be found in [40]. Details regarding the the determination of the target cell volumes and wall & window thicknesses can be found in [41]. Details regarding the determination of the target cell ^{3}He density can be found in [41] and Sec. (E.8.3). Finally, a catalog of cells and their measured properties can be found at the group web site:

`http://galileo.phys.virginia.edu/research/groups/spinphysics/`

The application of alkali-hybrid SEOP is a new contribution to the ^{3}He program. Therefore, in the following section, I will describe in some detail how to create alkali-hybrid mixtures for use in target cells.

3.3 Creating Alkali Hybrid Mixes

3.3.1 Predicting the Hybrid Vapor Ratio

To estimate the vapor number density above an impure sample of an alkali metal, we use Raoult's law:

$$[\mathrm{A}] = f_{\mathtt{A}}[\mathrm{A}]_{\mathrm{pvp}} \tag{3.6}$$

where $[\mathrm{A}]_{\mathrm{pvp}}$ is the vapor number density above a pure sample of the alkali metal and $f_{\mathtt{A}}$ is the mole fraction of pure alkali metal within the impure mix (liquid or solid). Raoult's law is a very good approximation because the interaction between two alkali atoms of the same species is very similar to the interaction between two alkali atoms of different species. If two alkali metals are mixed together, then the hybrid vapor ratio above the mix is simply:

$$\frac{[\mathrm{A1}]}{[\mathrm{A2}]} = \frac{f_1}{f_2} \cdot \frac{[\mathrm{A1}]_{\mathrm{pvp}}}{[\mathrm{A2}]_{\mathrm{pvp}}} \tag{3.7}$$

3.3.2 Finding the Desired Mole Fraction

Our goal is to produce some prescribed hybrid vapor ratio of alkali to Rb, $\left([\mathrm{A}]/[\mathrm{Rb}]\right)_{\mathrm{goal}}$, with some prescribed operating alkali number density, [A]. Therefore, we have to work backwards from the hybrid vapor ratio and operating alkali density to find the mole fraction ratio in the solid mix that would produce it. In principle, this is done by assuming that there are no other impurities in the alkali mix and solving the following system of equations numerically for the operating

temperature T_{op} and the mole fraction ratio $f_{\text{A}}/f_{\text{Rb}}$:

$$[\text{A}]_{\text{goal}} = f_{\text{A}}[\text{A}]_{\text{pvp}}(T_{\text{op}}) \quad \& \quad \left(\frac{[\text{A}]}{[\text{Rb}]}\right)_{\text{goal}} = \frac{f_{\text{A}}}{f_{\text{Rb}}} \cdot \frac{[\text{A}]_{\text{pvp}}(T_{\text{op}})}{[\text{Rb}]_{\text{pvp}}(T_{\text{op}})} \quad \& \quad f_{\text{A}} + f_{\text{Rb}} = 1 \tag{3.8}$$

where we've explicitly written out the temperature dependence of the pure vapor pressure curves.

In practice, however, we're able to derive a simple formula for the required mole fraction ratio. This is done by first finding a parameterization of the pure vapor pressure ratio as a function of the pure alkali density. Note that normally, we obtain the pure vapor pressure ratio for two alkali metals by specifying an operating temperature. Instead what we want now is to obtain the pure vapor pressure ratio by specifying the number density of a pure alkali metal corresponding to that operating temperature. This is done by fitting ratios from the CRC formula, see App. (A.3), to the following functional form:

$$\left(\frac{[\text{A}]}{[\text{Rb}]}\right)_{\text{pvp}} = \frac{\left([\text{A}]_{\text{pvp}}/[\text{A}]_0\right)^n}{\left([\text{Rb}]/[\text{A}]\right)_0} \tag{3.9}$$

where $\left([\text{Rb}]/[\text{A}]\right)_0$ is the pure vapor pressure ratio for a density of $[\text{A}]_0$ of a pure alkali metal and the fit parameters n, $\left([\text{Rb}]/[\text{A}]\right)_0$, & $[\text{A}]_0$ are listed in Tab. (3.3).

Plugging this parameterization of the pure vapor pressure ratio into the hybrid vapor ratio equation, we find:

$$\left(\frac{[\text{A}]}{[\text{Rb}]}\right)_{\text{goal}} = \frac{f_{\text{A}}}{f_{\text{Rb}}} \cdot \left(\frac{[\text{A}]}{[\text{Rb}]}\right)_{\text{pvp}} = \frac{f_{\text{A}}}{f_{\text{Rb}}} \cdot \frac{\left([\text{A}]_{\text{pvp}}/[\text{A}]_0\right)^n}{\left([\text{Rb}]/[\text{A}]\right)_0} = \frac{f_{\text{A}}}{f_{\text{Rb}}} \cdot \frac{\left([\text{A}]_{\text{goal}}/[\text{A}]_0/\text{f}_{\text{A}}\right)^n}{\left([\text{Rb}]/[\text{A}]\right)_0} \tag{3.10}$$

Under our conditions, the alkali metal is lighter than Rb, which implies that pure vapor pressure ratio $\left([\text{A}]/[\text{Rb}]\right)_{\text{pvp}}$ is less than one, and the desired operating alkali

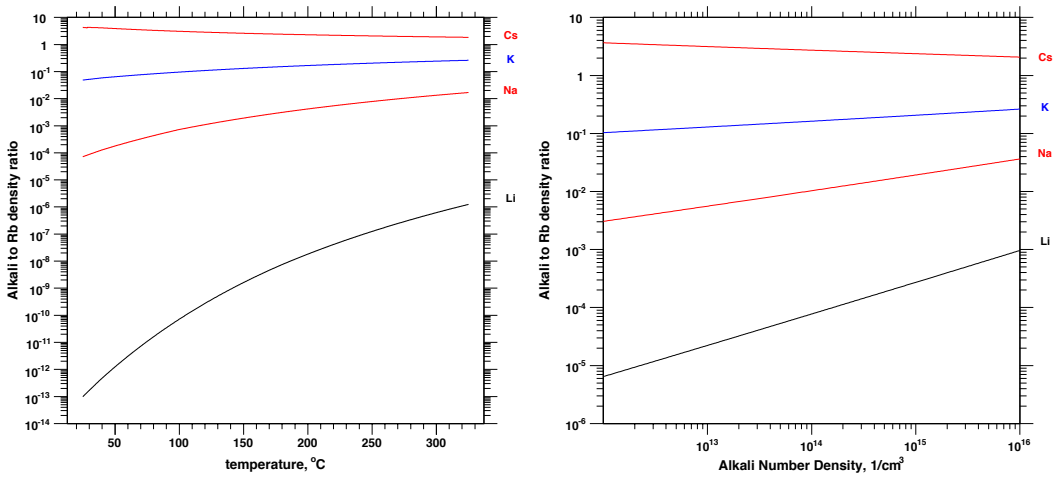

Figure 3.2: Alkali to Rb pure vapor pressure curve ratio vs. Temperature and Pure Alkali Density. These use the CRC formulas [42].

to Rb ratio is never less than 1. Therefore, the mole fraction of the alkali metal will be high, $f_A \geq 0.8$. When this is true or when the coefficient n is much less than 1, we can make approximation $\left(f_A\right)^n \approx 1$, which allows us to analytically solve for the required mole fraction:

$$\frac{f_{Rb}}{f_A} \approx \frac{\left([A]_{goal}/[A]_0\right)^n}{\left([Rb]/[A]\right)_0} \cdot \left(\frac{[Rb]}{[A]}\right)_{goal} \tag{3.11}$$

Finally, we can use Eqn. (A.38) to calculate the required operating temperature for the prescribed alkali operating density.

Traditionally for pure Rb cells, the operating temperature is about 190 °C. This corresponds to a Rb density of about $6\times10^{14}/\text{cm}^3$. Since the alkali-^{3}He spin exchange rate constants are roughly the same, we'll specify that we want roughly the same total (alkali+Rb) density for the hybrid cells. Tab. (3.4) lists the molecular weights needed for this method and Tab. (3.5) lists the required mole fraction ratios for typical hybrid vapor ratios.

CRC Pure Alkali to Pure Rb Ratio				
	Li	**Na**	**K**	**Cs**
$T_{\mathtt{min}}$ (K)	453.65	370.87	336.53	312.46
$T_{\mathtt{min}}$ (°C)	180.5	97.72	63.38	39.31
$[\mathrm{A}]_{\mathtt{min}}$ $(1/\mathrm{cm}^3)$	3.79×10^{6}	3.18×10^{9}	3.23×10^{10}	1.90×10^{11}
$\left([\mathrm{A}]/[\mathrm{Rb}]\right)_{\mathtt{min}}$	8.87×10^{-9}	6.06×10^{-4}	0.0727	3.36
$T_{\mathtt{max}}$ (K)	1050	700	600	550
$T_{\mathtt{max}}$ (°C)	777	427	327	277
$[\mathrm{A}]_{\mathtt{max}}$ $(1/\mathrm{cm}^3)$	1.81×10^{16}	1.10×10^{16}	1.17×10^{16}	2.12×10^{16}
$\left([\mathrm{A}]/[\mathrm{Rb}]\right)_{\mathtt{max}}$	8.68×10^{-4}	0.0301	0.252	1.72
$[\mathrm{A}]_0$ $(1/\mathrm{cm}^3)$		10^{14}		
$\left([\mathrm{Rb}]/[\mathrm{A}]\right)_0$	16800	112	6.31	0.427
n	0.516	0.259	0.0970	-0.0575

Table 3.3: Alkali to Rb Pure Vapor Pressure Curve Ratio. These parameters are used in Eqns. (3.9), (3.10), & (3.11). The function is fit to values from the CRC formula [42] over a temperature range that covers the higher melting point to a temperature that corresponds to at least $10^{16}/\mathrm{cm}^3$. The formula reproduces the CRC values to $\pm3.5\%$ for Li and $\pm1.0\%$ for all others.

Element	Symbol	Mol. Wgt. g/mol	Melting °C	Melting K	Boiling °C	Boiling K
Lithium	Li	6.941	180.5	453.65	1342	1615
Sodium	Na	22.989770	97.72	370.87	883	1156
Potassium	K	39.0983	63.38	336.53	759	1032
Rubidium	Rb	85.4678	39.31	312.46	688	961
Cesium	Cs	132.90545	28.44	301.59	671	944
Calcium	Ca	40.078	842	1115	1484	1757
Chlorine	Cl	35.453	-101.5	171.65	-34.04	239.11

Table 3.4: Physical Properties of Selected Elements. Molecular weights from [43] and temperatures from [42].

3.3.3 Glovebox Method

In this method, an appropriate amount of Rb is added to approximately one gram of the alkali metal:

$$\frac{\text{mass of Rb}}{\text{mass of A}} = \left(\frac{\text{Mol. Wgt. of Rb}}{\text{Mol. Wgt. of A}}\right)\left[\frac{f_{Rb}}{f_A}\right]_{\text{need}} \tag{3.12}$$

Because alkali metals are highly reactive to both water vapor and oxygen, the alkali handling is done in a dry N_2 environment within a glovebox. Care is taken to ensure that the glovebox has low levels of contaminants that react with the alkali metals. Both alkali metals are weighed to within 0.3 mg and inserted into an empty ampuole. The mix is then heated to a temperature above the highest individual melting point of the two metals. The ampuole is then capped with rubber stopper and removed from the glovebox. The ampuole is sealed under the flow of argon gas. Once the ampuole is sealed, it is once again heated above the melting point and vigorously agitated. In all went well, the two metals have been melted and mixed together to produce a homogeneous hybrid mix.

3.3.4 Reaction Method

An alternative technique [44,45] is to reduce appropriate amounts of RbCl and ACl with calcium chips. The reaction is given by:

$$2\text{ACl} + \text{excess Ca} + \text{metal impurities} \xrightarrow{\text{HEAT}} 2\text{A} + \text{CaCl}_2 + \big(\text{Ca} + \text{metal impurities}\big) \tag{3.13}$$

where A is Li, Na, or K. The reaction is catalyzed by heat provided by a flame that is kept under the melting point of calcium. High vapor pressure impurities are

pumped away. The mass ratio of RbCl to ACl needed to produce a necessary ratio of Rb to A in the solid mix is given by:

$$\frac{\text{mass of RbCl}}{\text{mass of ACl}} = \left(\frac{\text{Mol. Wgt. of RbCl}}{\text{Mol. Wgt. of ACl}}\right)\left[\frac{f_{Rb}}{f_A}\right]_{\text{need}} \tag{3.14}$$

The minimum amount of calcium to add is obtained from this inequality:

$$\frac{\text{mass of Ca}}{\text{mass of ACl}} \geq \frac{1}{2}\left(1+\left[\frac{f_{Rb}}{f_A}\right]_{\text{need}}\right)\left(\frac{\text{Mol. Wgt. of Ca}}{\text{Mol. Wgt. of ACl}}\right) \tag{3.15}$$

Tab. (3.4) lists molecular weight and melting point data needed for this method and Tab. (3.5) lists the required mass ratios for typical hybrid vapor ratios. We have not attempted this method because we've found the glovebox method adequate for our purposes. In addition, it is not clear how one determines that all of the alkali salt has been reacted.

Hybrid Mole Fractions			
	Li	**Na**	**K**
1:1 & $3\times10^{14}/\mathrm{cm}^3$			
$f_{\mathtt{Rb}}/f_{\mathtt{A}}$	1.05×10^{-4}	0.0119	0.176
$m_{\mathtt{Rb}}$ (mg)	1.29	44.1	385
$m_{\mathtt{RbCl}}/m_{\mathtt{ACl}}$	3.00×10^{-4}	0.0246	0.285
$m_{\mathtt{Ca}}/m_{\mathtt{ACl}}$	0.473	0.347	0.316
$T_{\mathtt{op}}$ (K)	843	577	493
$T_{\mathtt{op}}$ ($^{\mathrm{o}}$C)	570	303	220
5:1 & $6\times10^{14}/\mathrm{cm}^3$			
$f_{\mathtt{Rb}}/f_{\mathtt{A}}$	3.00×10^{-5}	2.84×10^{-3}	0.0377
$m_{\mathtt{Rb}}$ (mg)	0.370	10.6	82.4
$m_{\mathtt{RbCl}}/m_{\mathtt{ACl}}$	8.56×10^{-5}	5.88×10^{-3}	0.0611
$m_{\mathtt{Ca}}/m_{\mathtt{ACl}}$	0.473	0.344	0.279
$T_{\mathtt{op}}$ (K)	872	596	508
$T_{\mathtt{op}}$ ($^{\mathrm{o}}$C)	599	323	235
20:1 & $6\times10^{14}/\mathrm{cm}^3$			
$f_{\mathtt{Rb}}/f_{\mathtt{A}}$	7.50×10^{-6}	7.10×10^{-4}	9.43×10^{-3}
$m_{\mathtt{Rb}}$ (mg)	0.0924	2.64	20.6
$m_{\mathtt{RbCl}}/m_{\mathtt{ACl}}$	2.14×10^{-5}	1.47×10^{-3}	0.0153
$m_{\mathtt{Ca}}/m_{\mathtt{ACl}}$	0.473	0.343	0.271
$T_{\mathtt{op}}$ (K)	872	596	507
$T_{\mathtt{op}}$ ($^{\mathrm{o}}$C)	599	323	234

Table 3.5: Required Mole Fraction Ratios, Mass Ratios, and Operating Temperatures. The mass of Rb is specified assuming an alkali mass of 1 gram. The desired operating hybrid vapor ratios of alkali to Rb are 1:1, 5:1, and 20:1. The difference between these values and ones obtained from a "full" numerical solution is about a few percent.

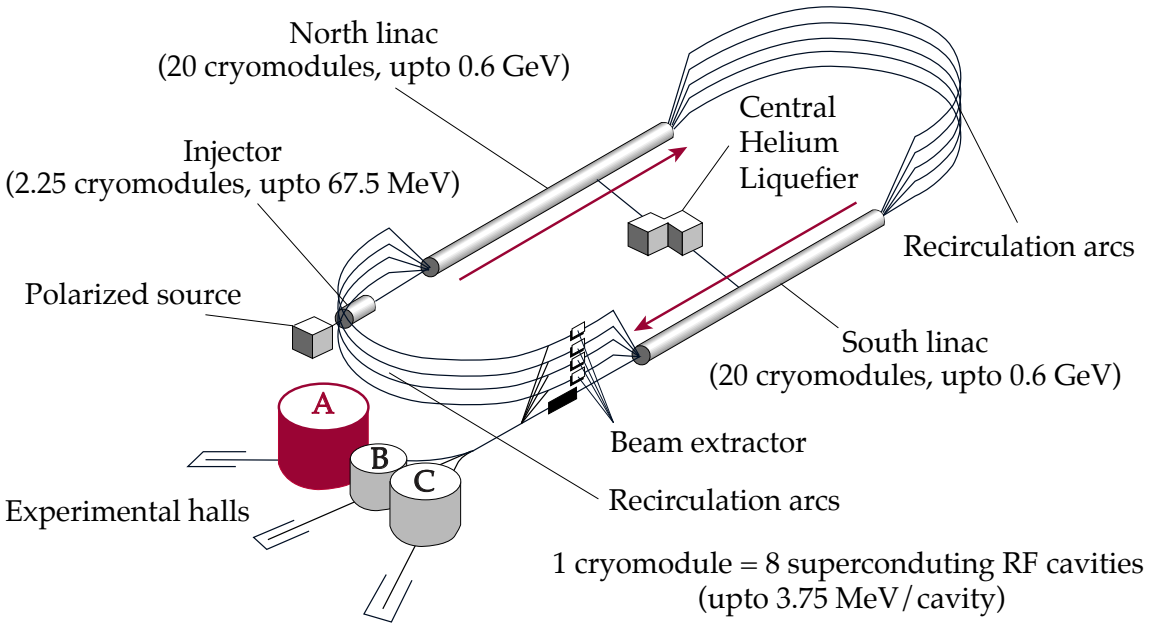

Figure 3.3: Schematic of CEBAF as of 2009. Adapted from [46].

3.4 The Electron Beam

CEBAF can simultaneously deliver up to three CW (continuous wave) interleaved polarized electron beams at three different energies to three experimental halls (A, B, & C). Each hall consists of a beamline, a set of targets, and a set of specialized detectors. The experiments listed in Tab. (3.1) took place in Hall A.

3.4.1 CEBAF

The electrons start at the polarized source where they are photoemitted. In a solid-state analogy to optical pumping, a circularly polarized laser beam selectively photoemits electrons from one of two energy levels of a strained GaAs crystal. The helicity of the laser (and consequently the helicity of the electron beam) is rapidly toggled at 30 Hz in a pseudorandom pattern. For an accurate measurement of elec-

tron scattering asymmetries, the properties of the electron beam must not change very much when the helicity is toggled. This is mainly achieved by careful control of the purity of the circular polarization of the laser beam through which one can suppress helicity-correlated differences in the intensity, size, location, and energy of the electron beam (see for example [47]). Each hall has a designated laser that is pulsed at 499 MHz with a unique phase offset. The timing of the pulses from the three lasers is such that the GaAs crystal is struck at a rate of 1497 MHz. The electrons leave the polarized source and enter the Injector at 100 keV. The Injector then accelerates the electrons up to about 70 MeV before injecting them into the North linear accelerator (linac).

The North linac is composed of 20 cryomodules each of which is a group of 8 superconducting RF cavities. Presently, one pass through the North linac can accelerate electrons up to 0.6 GeV. These electrons are then recirculated back into an identical South linac. The beam can then either be delivered into one of the three halls or recirculated back into the North linac. An energy up to 6 GeV can be obtained by a maximum of 5 passes through the linacs via the recirculating arcs. Finally, a beam extractor separates the beams and redirects them into the three experimental halls. More details about CEBAF can be found in [48] and references therein.

3.4.2 Hall A Beamline

The beamline in Hall A controls the position & angle of the beam on the target, measures its properties (e.g. current, position, energy, polarization), and provides a "dump" for the unscattered portion of the beam. All "invasive" measurements require dedicated beamtime, whereas "noninvasive" measurements can be per-

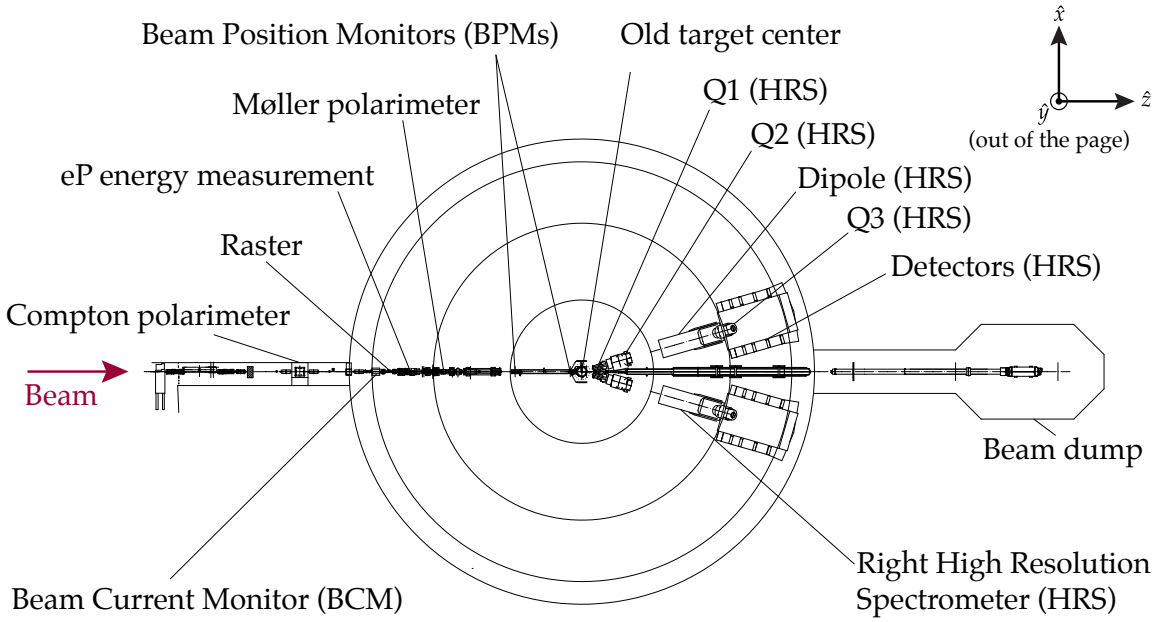

Figure 3.4: Schematic of the Hall A Beamline and High Resolution Spectrometers (HRS) as of 2009. Adapted from [46].

formed during physics data taking. Since the intrinsic size of the beam is a few hundred microns, an electromagnet called the Raster is used to scan the beam over an area of a few mm^2. Measurements from a pair of beam position monitors (BPMs) (noninvasive) are used to extrapolate the position on the target and the incident angle. Beam current monitors (BCMs) (noninvasive) measure both the instantaneous current and the total charge accumulated over a run. The beam energy can be measured in one of three ways: the "Tiefenbach" method (noninvasive), an "ARC" measurement (invasive), or an "eP" measurement (invasive). The Tiefenbach method and the ARC measurement both infer the momentum of the beam by its angular deflection in a magnetic field. An eP measurement extracts the beam energy by measuring the recoil angles of protons and electrons via elastic scattering from a thin polyethylene (CH_2) tape. The beam polarization is obtained from scattering asymmetries measured for Compton scattering (see Sec. (2.5.2)) from a

date		run number		angle	cell	$\langle E \rangle$	$\langle P_b^0 \rangle$
start	end	first	last	(deg)		MeV	(Møller)
07/15	07/23	2294	2709	6	penelope	2134.3	0.742
07/25	07/28	2782	2948	6	priapus	4208.8	0.652
07/28	07/30	2949	3059	6	priapus	2134.9	0.747
07/31	08/05	3061	3260	6	priapus	2844.8	0.767
08/08	08/13	3266	3487	9	priapus	3775.5	0.765
08/14	08/16	3488	3641	9	priapus	1147.3	0.762
08/16	08/21	3642	3850	9	priapus	2233.9	0.761
08/21	08/25	3851	4066	9	priapus	4404.2	0.756
08/26	08/30	4067	4218	9	priapus	3318.8	0.778

Table 3.6: Run Information for Production Data for E97110.

laser beam (noninvasive) and Møller scattering (see for example [49–52]) from a magnetized iron foil (invasive). More details about the Hall A instrumentation can be found in [46] and references therein.

3.5 E97110: Small Angle GDH

3.5.1 Introduction

E97110 ("The GDH Sum Rule and the Spin Structure of ^{3}He and the Neutron Using Nearly Real Photons") ran between March and August 2003. We measured the "neutron-in-^{3}He" spin structure functions g_1^3 & g_2^3, see Sec. (2.4.5), or equivalently the ^{3}He virtual photoabsorption cross sections σ_{TT}^3 & σ_{LT}^3, see Sec. (2.5.8). Integrals of these quantities are related to the generalized Gerasimov-Drell-Hearn (GDH) integrals (I_A, I_1) and generalized spin polarizabilities (γ_0, δ_{LT}) for the neutron, see Sec. (2.5.9). In the Bjorken limit ($Q^2 \to \infty$), the generalized GDH integral I_1 is related to the Bjorken sum rule, see Sec. (2.4.6). In the real photon limit ($Q^2 = 0$), both

generalized GDH integrals I_1 & I_A reduce to the GDH sum rule, see Sec. (2.5.6). Baryon Chiral Perturbation Theory (BChPT), see Sec. (2.5.10), is the relevant theoretical approach for the low Q^2 kinematic regime covered by this experiment. Our data extends the measurement of the Bjorken integral to low Q^2 and is a test of BChPT, which predicts the values & slopes of I_1, I_A, γ_0, & δ_{LT} at $Q^2 = 0$, see Tab. (2.3).

We measured the inclusive scattering of polarized electrons from a polarized ^{3}He target using the standard Hall A equipment and a "septum" magnet. During the March to May running, the septum magnet was miswired which severely reduced its acceptance; therefore, only the production data from the July to August data taking period will be described here. Data were taken over a Q^2 range of 0.04 to 0.24 GeV^2 at scattering angles of 6 and 9 degrees with the beam energies listed in Tab. (3.6). Both g_1^3 & g_2^3 (or equivalently σ_{TT}^3 & σ_{LT}^3) were extracted because data was taken for both parallel & perpendicular target polarizations, see Sec. (2.5.12).

A previous experiment, E94010, measured the same quantities at a higher Q^2 range of 0.1–0.9 GeV^2, see Fig. (3.5). They found that the generalized GDH integral (I_A) starts at about 0 at high Q^2 and drops below the GDH sum rule for their lowest Q^2 point. The MAID model [53] and both Heavy & Relativistic BChPT calculations, which predict a negative slope at $Q^2 = 0$ (i.e. a "turnover" a low Q^2), are consistent with the data. Our data covers the Q^2 range where this "turnover" is expected and allows for an extraction of the slope at $Q^2 = 0$.

The generalized spin polarizabilities for the the lowest Q^2 points of E94010 were also extracted. The results for both γ_0 and δ_{LT} are consistent with the MAID model. The Heavy BChPT calculations appear inconsistent with the data, which may be an indication that the Q^2 range represented by the data is still too high to

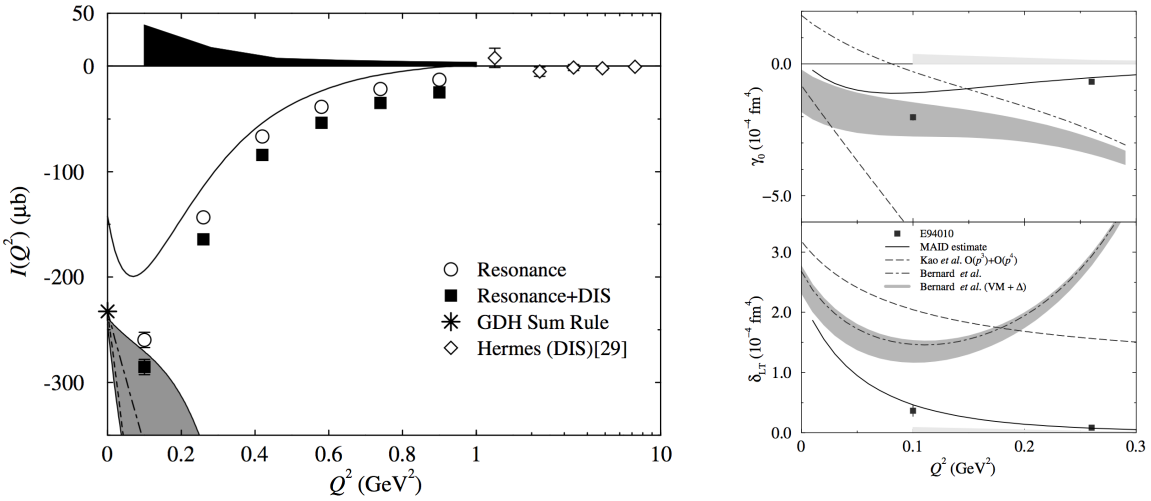

Figure 3.5: E94010 Results for I_A, γ_0, & $\delta_{\rm LT}$ from [1,3].

be applicable. The Relativistic BChPT calculation (with the Δ contribution) shows good agreement γ_0 but not $\delta_{\rm LT}$. This is intriguing because the calculations indicate that the Δ contribution to $\delta_{\rm LT}$ is essentially zero. The Q^2 range accessible to E97110 is more appropriate to the BChPT calculations. Our data more fully explores the low Q^2 regime, allows for an extraction of the slope at $Q^2 = 0$, and may allow for an extrapolation to $Q^2 = 0$.

At the low Q^2 covered in this experiment, the dominant contribution to I_A, I_1, γ_0, & $\delta_{\rm LT}$ is expected to be from the resonance region and, in particular, the Δ-resonance. The kinematics were chosen to provide complete coverage of the resonance region and also the quasielastic region, see Fig. (3.6). The low Q^2 regime is accessed by detecting electrons at small angles. Due to the size of the High Resolution Spectrometers (HRS), see Fig. (3.4), the smallest central scattering angle that can be detected, for the HRS alone, is 12.5 degrees. For this experiment (and a few others), scattering angles below this limit was accessed with the use of a septum magnet. Placed between the target and the right HRS, the septum magnet bent the

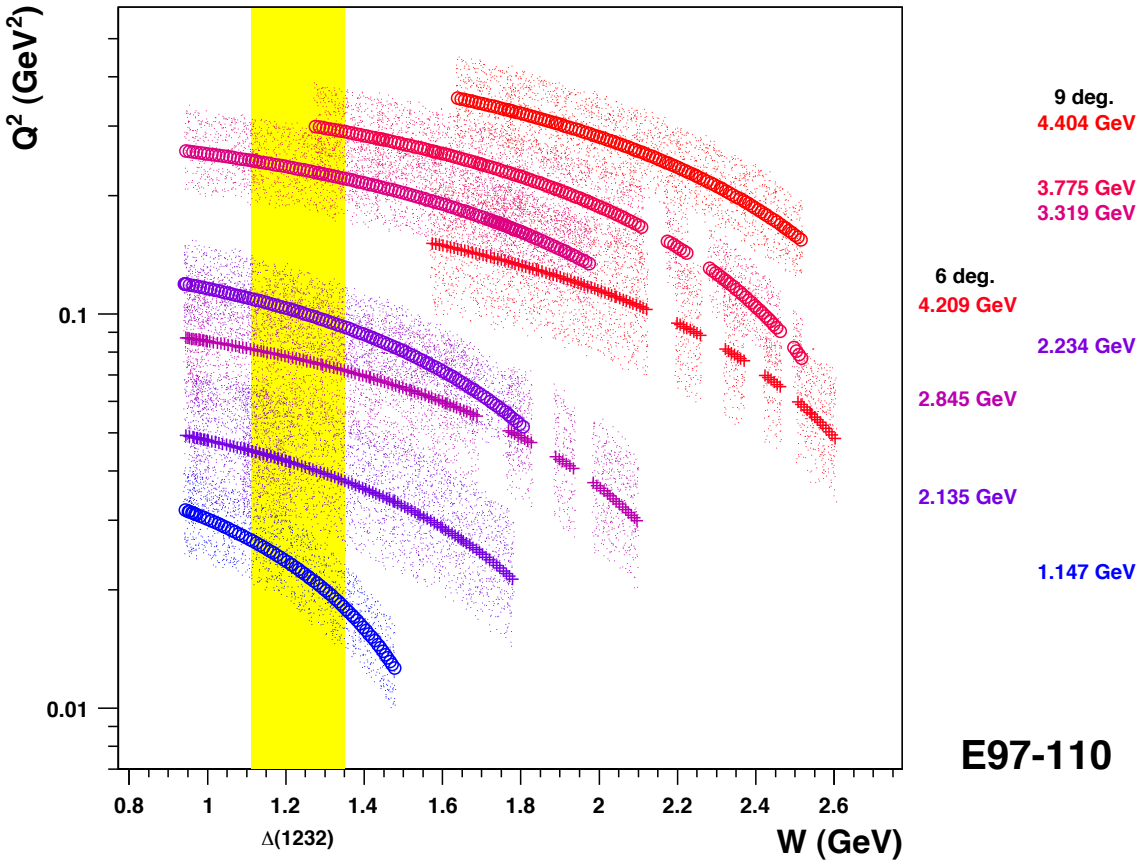

Figure 3.6: Kinematic Coverage for E97110. The yellow band denotes the Δ-resonance region.

trajectory of scattered electrons towards the HRS. The left HRS detected scattering from an downstream carbon target and used to check for false asymmetries & monitor the beam luminosity. The experimental layout is depicted in Fig (3.7).

3.5.2 The Polarized He-3 Target

The standard polarized ^{3}He target (i.e. the same as E94010) was used for this experiment. The target was polarized using traditional spin-exchange optical pumping (i.e. pure Rb) with three or four 30 Watt broadband laser diode arrays. Two sets of laser beams and Helmholtz coils were required to pump parallel ("longitudinal") and perpendicular ("transverse") to the beamline. The target polarization was monitored using NMR and EPR. Absolute calibration of the NMR signal was obtained from EPR and water NMR. The target ladder included carbon foils used for optics calibration, a "no target" position, and a "reference cell" used to account for scattering due to the glass and N_2 .

Two target cells were used for this experiment: "Penelope" and "Priapus." These cell were fabricated at Princeton by Mike Souza and filled at the University of Virginia (UVa). Because we detected electrons that scattered at very small angles, we made two modifications to reduce the size of radiative corrections:

1. Corning 1720 (C1720) glass was used instead of General Electric 180 (GE180) because C1720 has a radiation thickness that is longer by a factor of 1.5, see App. (B.6).

2. The sides walls of the target chamber were made thinner by a factor of two.

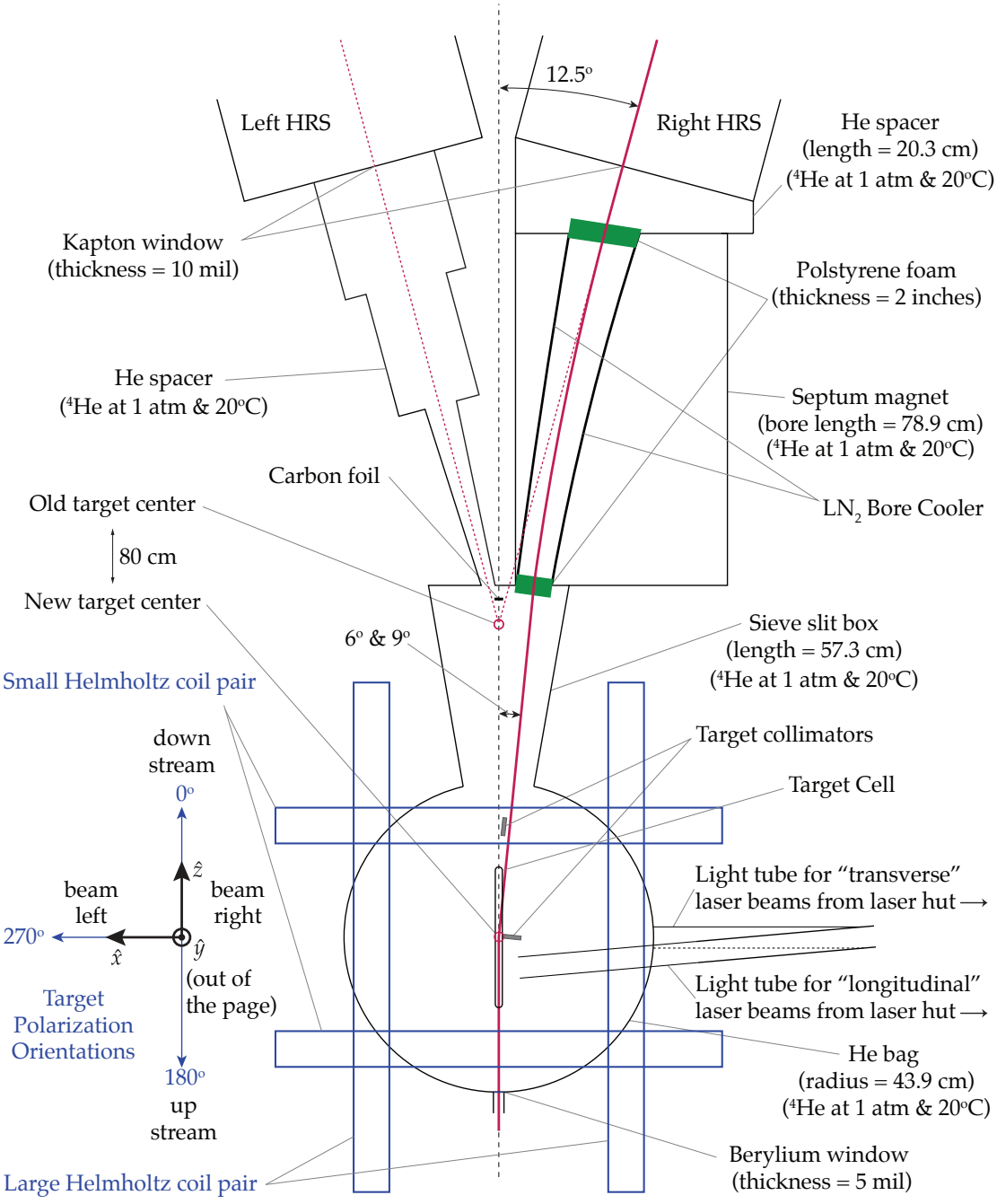

Figure 3.7: Experimental Layout Near that Target Region for E97110.

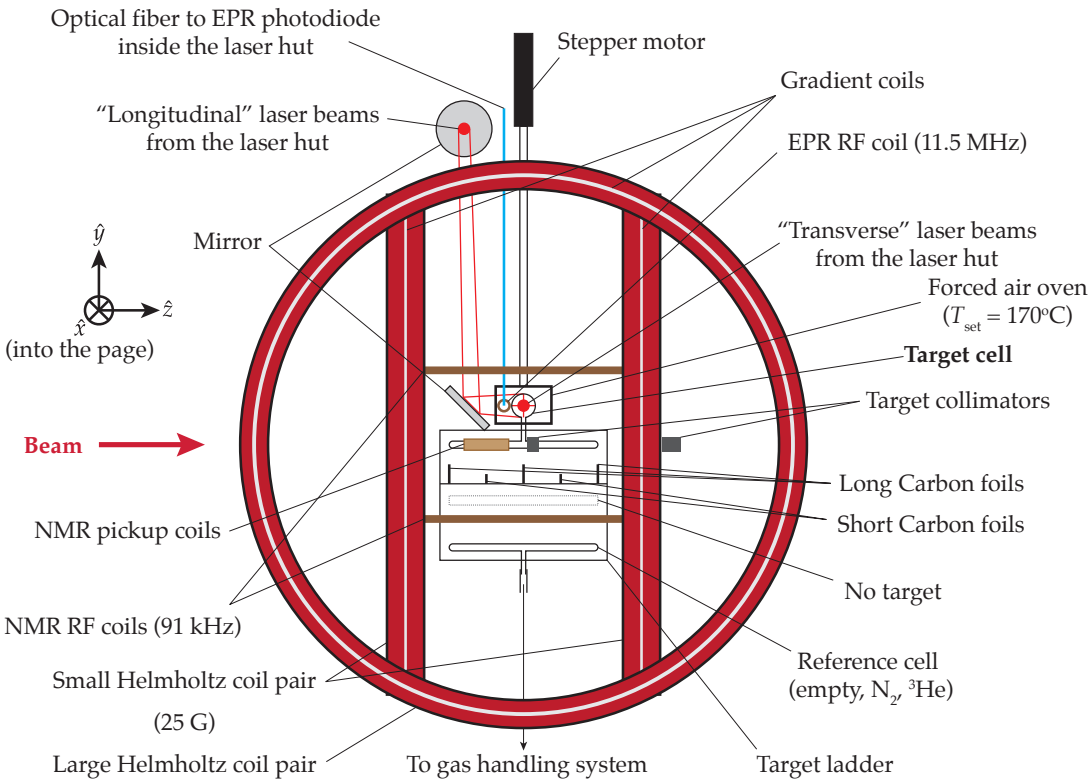

Figure 3.8: Standard Polarized ^{3}He Target for E97110.

cell	Penelope	Ref. Cell 1	Priapus	Ref. Cell 2
window, upstream (μm)	132 ± 2	127 ± 2	128 ± 2	131 ± 2
window, downstream (μm)	138 ± 2	120 ± 2	142 ± 2	150 ± 2
wall, beam right (μm)	622 ± 10	638 ± 10	600 ± 10	610 ± 10
wall, beam left (μm)	694 ± 10	693 ± 10	760 ± 10	711 ± 10
outer diameter (cm)	1.9249	1.920	1.9160	1.920
external length (cm)	39.6875	39.5288	39.3700	39.5288
$\langle [^3\mathrm{He}] \rangle_{\mathrm{op}}$ (amg)	10.65	-	10.46/10.49	-
$\langle [\mathrm{N}_2] \rangle_{\mathrm{op}}$ (amg)	0.107	9.48	0.111/0.112	9.50/9.38

Table 3.7: Cell Parameters. Densities for Priapus refer to 6/9 degrees.

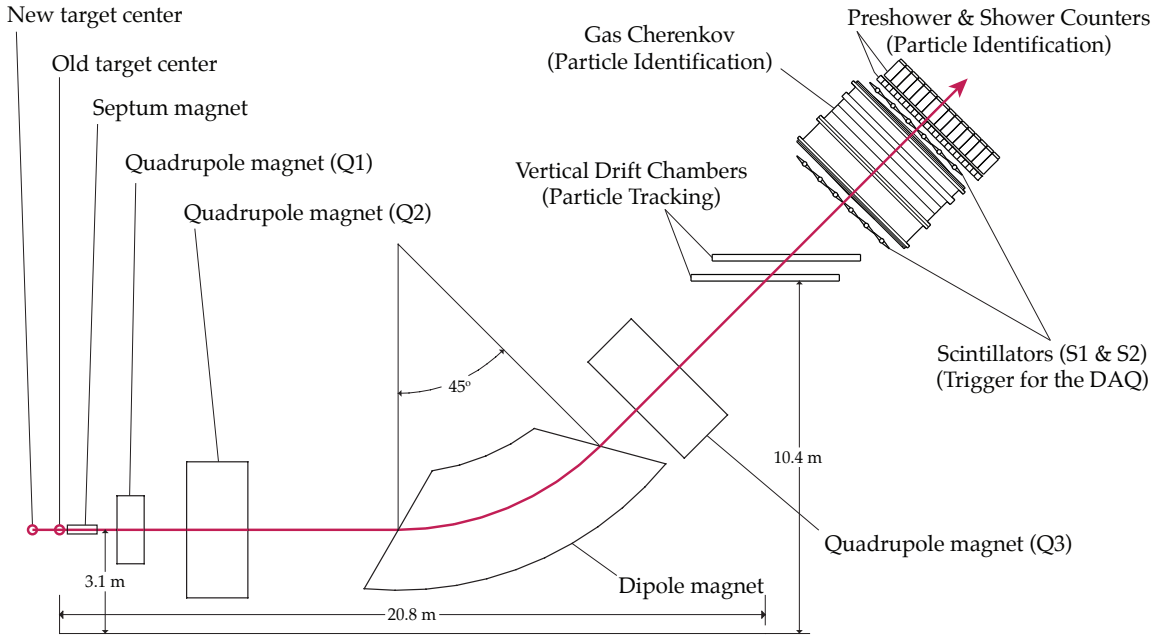

Figure 3.9: Schematic of the HRS Detector Package. Adapted from [46].

3.5.3 The "Detector"

In general, after scattering from the target, the scattered electrons enter the "Detector." The goal of the "Detector" is to count the number of "good" scattered electrons for a given momentum & scattering angle. A "good" electron has the following properties:

1. Its initial properties, such as helicity, are unambiguous.
2. Its momentum and scattering angle are unambiguous.
3. It successfully triggers the data acquisition system (DAQ).
4. It scatters from the target material and not from any surrounding material.
5. It is an electron as opposed to some other negatively charged particle.

For this experiment, the "Detector" was the septum/right HRS pair. The right HRS was placed at 12.5 degrees relative to the "old target center." The orientation and magnetic field of the septum magnet was chosen to bend electrons scattered at 6 and 9 degrees out to the right HRS. The HRS consists of a quadrupole-quadrupole-dipole-quadrupole (QQDQ) "magnetic transport system" and a "detector package." For this experiment, the detector package consisted of a pair of vertical drift chambers (VDCs), a pair of scintillators, a Cerenkov detector, and an electromagnetic calorimeter. These detectors measured the final trajectory & momentum of the scattered particle, triggered the DAQ, and identified the particle as an electron.

A significant fraction of beamtime was allotted to taking data required to calibrate the magnetic transport system of the septum magnet/HRS pair. The magnetic transport system bends the scattered electrons vertically by an angle inversely proportional to its momentum. This approximately maps the particle's momentum to a vertical displacement. In addition, the magnetic transport system is designed such that the particle's relative scattering angle is approximately mapped to a horizontal displacement. Finally, the scattered particle exits the magnetic transport system and enters the detector package.

The final trajectory & momentum of the scattered particle was measured by a pair of VDCs. In reality, the scattered particle's final trajectory is a complicated quasi-linear combination of its initial trajectory & momentum before entering the HRS. With detailed knowledge of the magnetic transport system, the particle's initial trajectory & momentum was deconvoluted from its final trajectory & momentum. The initial trajectory allowed us to determine whether the particle scattered from the target material or some surrounding material.

Next, the data taking by the DAQ was triggered by a pair of scintillators. Only negatively charged particles were bent up into the detector package. Therefore, given the kinematics, the most likely particles were electrons, muons, and negatively charged pions. Electrons can be very effectively distinguished by other particles due to their small mass which implies:

1. For the same momentum, electrons are faster ($\beta = 1/\sqrt{1+(m/p)^2}$).

2. At JLab energies, electrons suffer greater energy loss due to bremsstrahlung.

The first method indirectly determines the particle's speed via the Cerenkov effect. A flash of light (Cerenkov radiation) is emitted when a charged particle travels through a medium with a velocity greater than the speed of light in that medium. Therefore, the index of refraction of the material in the Cerenkov detector is chosen such that an electron will emit a flash of light whereas a pion would not. The second method is a direct measurement of the energy loss by the particle in a shower counter. In a carefully designed shower counter:

1. Electrons lose all of their energy near the front of the counter.

2. Heavier particles lose a relatively small fraction of their energy more uniformly throughout the counter.

Therefore, both the total energy deposited in the counter and spatial distribution of the energy loss can be used to distinguish electrons from heavier particles.

With the exception of the VDCs, all of the detectors have the same basic operating principle. Some or all of the energy of the charged particle is converted into light by some physical mechanism. This light is then collected using mirrors or waveguides and detected by sensitive photomultiplier tubes (PMTs).

3.5.4 Analysis & Results

Overview

Full details of the analysis can be found in [54]. The goal was to compute the generalized GDH integrals, I_A & I_1, and the generalized spin polarizabilities, γ_0 & $\delta_{\rm LT}$, for the neutron at $Q^2 = 0.04$, 0.06, 0.08, 0.10, 0.12, & 0.24 GeV^2. First, the "experimental" parallel & perpendicular cross section differences, $\Delta\sigma_{\parallel}^{\rm exp}$ & $\Delta\sigma_{\perp}^{\rm exp}$, were formed from the unpolarized cross section $\sigma^{\rm phys}$ and the parallel & perpendicular asymmetries, $A_{\parallel}^{\rm phys}$ & $A_{\perp}^{\rm phys}$:

$$\Delta\sigma_{\parallel,\perp}^{\rm exp} = 2A_{\parallel,\perp}^{\rm phys}\sigma^{\rm phys} \tag{3.16}$$

These experimental cross section differences $\Delta\sigma_{\parallel,\perp}^{\rm exp}$ underwent "radiative corrections" which result in the ("Born") cross section differences $\Delta\sigma_{\parallel,\perp}^{\rm born}$ in the Born approximation. We then interpolated these cross section differences, binned by the invariant mass W, from constant beam energy to constant Q^2. After subtracting out the contribution from quasielastic scattering that "leaks" into the resonance region, $\Delta\sigma_{\parallel,\perp} = \Delta\sigma_{\parallel,\perp}^{\rm born} - \Delta\sigma_{\parallel,\perp}^{\rm QE}$, we extracted the "neutron-in-^{3}He" spin structure functions using the results of Sec. (2.5.12) in the form of:

$$g_1^3 = -\frac{M_n Q^2}{8\alpha^2}\left[\frac{y}{(1-y)(2-y)}\right]\left[2\Delta\sigma_{\parallel} + \left(\frac{y\gamma}{\sqrt{1-y-y^2\gamma^2/4}}\right)\Delta\sigma_{\perp}\right] \tag{3.17}$$

$$g_2^3 = -\frac{M_n Q^2}{8\alpha^2}\left[\frac{y}{(1-y)(2-y)}\right]\left[-y\Delta\sigma_{\parallel} + \frac{2}{\gamma}\left(\frac{1-y/2-y^2\gamma^2/4}{\sqrt{1-y-y^2\gamma^2/4}}\right)\Delta\sigma_{\perp}\right] \tag{3.18}$$

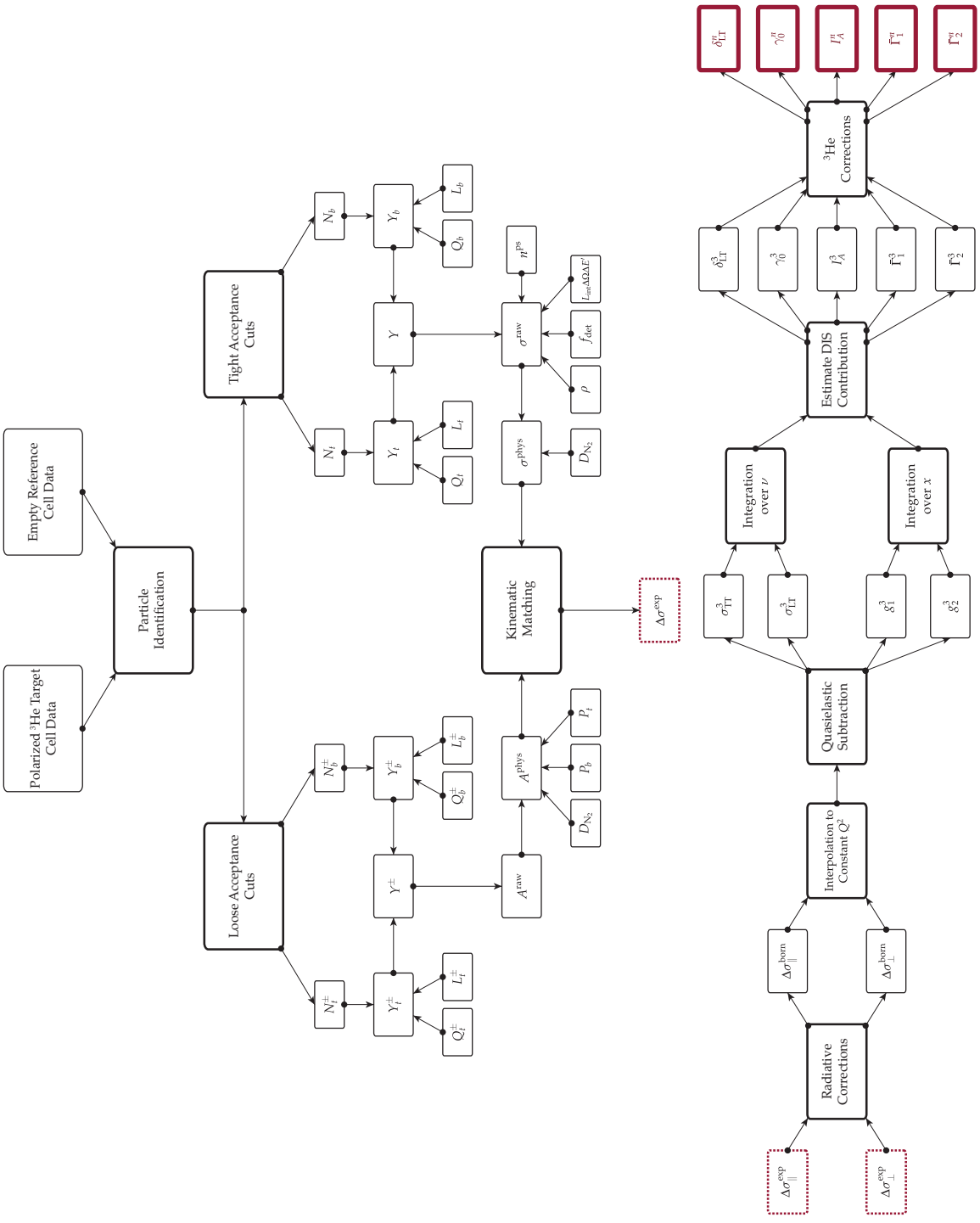

Figure 3.10: Analysis Flowchart.

where $M_n = 939.57$ MeV is the neutron mass, $y = \nu/E$, and $\gamma = Q/\nu$. These spin structure functions are integrated to give the following "neutron-in-^{3}He" quantities:

$$I_A^3(Q^2) = \frac{2M_n^2}{Q^2}\int_0^{x_0}\left[g_1^3(x,Q^2) - \frac{4M_n^2}{Q^2}x^2 g_2^3(x,Q^2)\right]dx \tag{3.19}$$

$$\bar{\Gamma}_1^3 = \frac{Q^2}{2M_n^2}I_1^3(Q^2) = \int_0^{x_0} g_1^3(x,Q^2)dx \tag{3.20}$$

where $x_0 = 1/[1 + m_\pi(m_\pi + 2M_n)/Q^2]$ is the pion threshold (m_π is the pion mass). We'll also note that the generalized GDH integrand (for I_A^3 in the "Hand" convention $K = (1-x)\nu$) is given by:

$$\frac{(1-x)\sigma_{\mathrm{TT}}^3}{\nu} = -\left[\frac{16\pi^2 M_n \alpha x^2}{Q^4}\right]\left[g_1^3 - \frac{4M_n^2}{Q^2}x^2 g_2^3\right] \tag{3.21}$$

Finally, using the "effective polarization method," we extracted the neutron spin structure moment $\bar{\Gamma}_1^n$ (only covering the inelastic regime):

$$\bar{\Gamma}_1^n = \frac{\bar{\Gamma}_1^3 - 2P_p\bar{\Gamma}_1^p}{P_n} \tag{3.22}$$

where we've ignored the small mass difference between protons and neutrons $M_n = M_p$. These steps are summarized in the analysis flowchart in Fig. (3.10). We'll now discuss these steps in more detail.

Unpolarized Cross Sections & Asymmetries

For each kinematic setting, data were taken for (1) parallel & perpendicular polarized ^{3}He target orientations, (2) an "empty" reference cell, and (3) a reference cell filled with about 9.4 amagats of N_2 . Identical "detector & acceptance cuts"

were placed on each data set to select electrons scattering from the inner part of the target cell with well-reconstructed momenta & scattering angles. Relatively "tight" ("loose") acceptance cuts were made to select a clean (large) subset of the data for the calculation of the unpolarized cross section (perpendicular & parallel asymmetries). The total and helicity gated yields (Y & $Y^{\pm}$) for each data set were calculated by:

$$Y = \frac{N}{(Q/e)L} \qquad Y^{\pm} = \frac{N^{\pm}}{(Q^{\pm}/e)L^{\pm}} \tag{3.23}$$

where $N, N^{\pm}$ are the total number of counts surviving the cuts, $Q, Q^{\pm}$ are the total charge of the electron beam delivered to the target, e is the charge of the electron, and $L, L^{\pm}$ are the "lifetimes."

For the kinematics of this experiment, the scattering rates were high enough to potentially damage the detectors in the HRS. Consequently, the beam current was kept between 1 to 10 μA to limit the rate in the detectors. A current calibration was performed to verify the linear response of the BCM belows 5 μA. Over 90% of the runs had a charge asymmetry $(Q^{+} - Q^{-})/(Q^{+} - Q^{-})$ of less than 200 ppm.

After an event is triggered, the DAQ and detectors require a finite amount of time to "reset" and be available for the next event. The fraction of time that the DAQ & detectors is unavailable is referred to as the "deadtime." The livetime L is simply 1 minus the deadtime. At sufficiently low rates ($<$ 4kHz) or equivalently low deadtime $<$ 15%, the number of "good" electrons missed during the deadtime can be accounted for by simply dividing N by L. Over 80% of the runs had a deadtime less than 10% and all of the runs had a deadtime less than 15%.

Any background (i.e. scattering not due to the contents of the target cell) that is still present after the acceptance cuts is subtracted away using data from the empty reference cell run. This gives the "corrected" yields for the target cell, Y & $Y^{\pm}$, and

the reference cell with N_2 , Y_2^N :

$$Y = Y_t - Y_b \qquad Y^{\pm} = Y_t^{\pm} - Y_b^{\pm} \qquad Y^{N_2} = Y_t^{N_2} - Y_b \tag{3.24}$$

where the subscript t refers to raw (uncorrected) yield and the subscript b refers to the empty reference cell. The N_2 dilution factor D_{N_2} is calculated from the corrected yields by Eqn. (2.61):

$$D_{N_2} \equiv \frac{\sigma^{\text{phys}}}{\sigma^{\text{raw}}} = 1 - \left(\frac{\rho_{N_2}^{\text{tc}}}{\rho_{N_2}^{\text{ref}}}\right)\left(\frac{Y^{N_2}}{Y}\right) \tag{3.25}$$

where σ^{phys} is the "true" unpolarized ^{3}He cross section, σ^{exp} is unpolarized ^{3}He cross section measured from a target cell "diluted" by a small of N_2 , $\rho_{N_2}^{\text{tc}}$ is the density of N_2 in the target cell, and $\rho_{N_2}^{\text{ref}}$ is the density of N_2 in the reference cell. The nitrogen dilution factor was typically around 0.92.

The unpolarized cross section is calculated using Eqn. (2.46):

$$\left[\frac{d^2\sigma}{d\Omega dE'}\right]^{\text{phys}} = \sigma^{\text{phys}} = \frac{\sigma^{\text{raw}}}{D_{N_2}} = \frac{Y/f_{\text{det}}}{\rho\,(L_{\text{int}}\Delta\Omega\Delta E')} \tag{3.26}$$

where f_{det} is the combined efficiencies of the detectors, ρ is the number density of ^{3}He in the target chamber of the target cell, and $(L_{\text{int}}\Delta\Omega\Delta E')$ is the "acceptance factor." The scintillator trigger efficiency and particle identification efficiencies were over 0.99 throughout the experiment. Because the raw rates were very high in this experiment, a multitrack correction was applied to account for the fact that it was quite likely that more than one track in the VDC counted as a "good" electron. These factors are all folded into f_{det}. The ^{3}He density was determined from "temperature tests," see Sec. (4.6.3), and are listed in Tab. (3.7). The acceptance factor

was calculated from a Monte Carlo simulation of the magnetic transport system of the septum/right HRS pair.

The parallel & perpendicular asymmetries were calculated using Eqn. (2.60):

$$A_{\parallel,\perp}^{\text{phys}} = \frac{A_{\parallel,\perp}^{\text{raw}}}{D_{\text{N}_2}\, P_b P_t} = \frac{1}{D_{\text{N}_2}\, P_b P_t}\left[\frac{Y^+ - Y^-}{Y^+ + Y^-}\right] \tag{3.27}$$

The target polarization P_t will be discussed is Sec. (4.6). The beam polarization was measured at each energy using the Møller polarimeter. During these measurements, it was found that the polarization changed when the Hall C beam was turned on. The beam polarization was being diluted by "bleedthrough" of the Hall C beam into Hall A. Combined with the polarization of the bleedthrough (P_C), the beam polarization was corrected on a run by run basis using:

$$P_{\text{beam}} = P_{\text{beam}}^0\left[1 - \frac{I'_{\text{C}}}{I_A}\left(1 - \frac{P_{\text{C}}}{P_{\text{beam}}^0}\right)\right] \tag{3.28}$$

where P_{beam} is the beam polarization with the Hall C beam on, P_{beam}^0 is the beam polarization with the Hall C beam off, I_A is the Hall A beam current, and the amount of bleedthrough I'_C into Hall A depends on the Hall A slit position S and the Hall C beam current I_C:

$$\frac{I'_C}{I_A} = \frac{m}{1000}\left(\frac{I_C}{I_A} - R_0\right) \qquad \text{valid for } S = -1 \text{ and } I_C > R_0 I_A \tag{3.29}$$

$$\frac{I'_C}{I_A} = \frac{m}{1000}\left(\frac{I_C}{I_A}\left[\frac{S}{60}\right]^2 - R_0\right) \qquad \text{valid for } 0 \le S \le 60 \text{ and } I_C > R_0 I_A (60/S)^2 \tag{3.30}$$

where m & R_0 were empirically determined and listed in Tab. (3.8). This correction

time period	**slit position**	m	R_0
before run 3263	$S = -1$	4.310	$+0.43735$
	$0 \leq S \leq 60$	3.791	$+0.04685$
after run 3263	$S = -1$	1.902	-0.06572
	$0 \leq S \leq 60$	3.226	$+0.05505$

Table 3.8: Bleedthrough correction parameters. $S = -1$ corresponds to the case when the Hall A slit is "out."

can be as large as 15% relative, see Fig. (3.11). These results are consistent with the beam polarizations extracted from the Compton polarimeter.

For the asymmetries, a loose acceptance cut was chosen to reduce the statistical uncertainty. For the unpolarized cross section, a tight acceptance cut was chosen to select a particularly "clean" subset of the data. Since two different subsets of data were used, the kinematics of the asymmetry and unpolarized cross were slightly different. Therefore, before the "experimental" cross section differences $\Delta\sigma^{\rm exp}_{\parallel,\perp}$ were calculated, the asymmetries and unpolarized cross section were interpolated to the same kinematics (i.e. "kinematically matched").

Radiative Corrections

The experimental cross section differences are not the same as the "Born" cross section differences (i.e. one photon exchange). This is because $\Delta\sigma^{\rm exp}$ (1) includes higher order diagrams beyond the Born approximation and (2) is actually a convolution of cross sections from different kinematics due to the energy lost by the

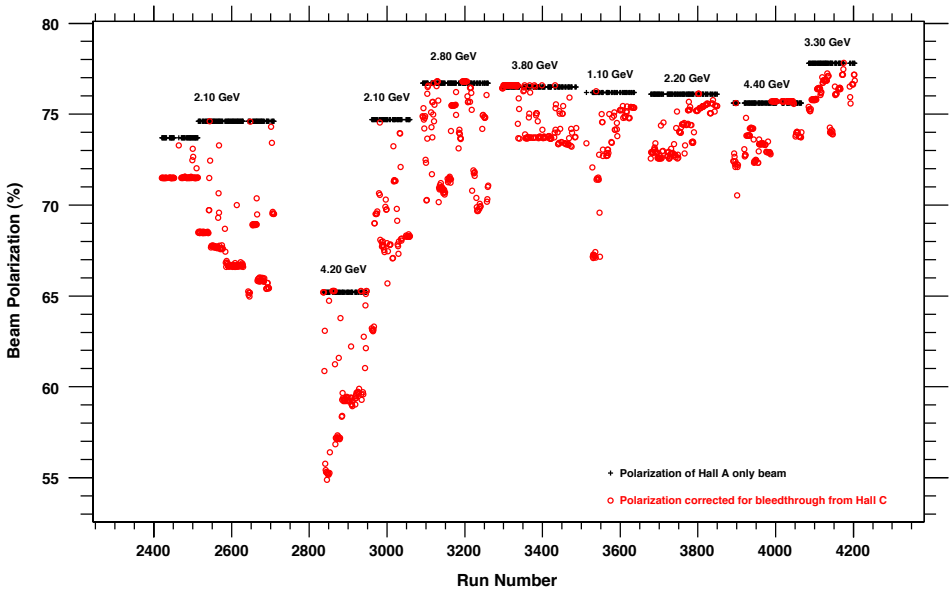

Figure 3.11: Beam Polarization Before and After Bleedthrough Correction.

electron before and after scattering:

$$\Delta\sigma^{\text{exp}}(E,\nu) = \int_0^T \frac{dt}{T} \int_0^\nu d\nu_b \int_0^\nu d\nu_a P(\nu_b,t)\,(1+\delta_{\text{HO}})\,\Delta\sigma^{\text{born}}(E_0,\nu_0) P(\nu_a, T-t) \quad (3.31)$$

where the incident beam energy is E, the total energy lost is ν, T is the total radiation thickness, ν_b is the energy lost before scattering, ν_a is the energy lost after scattering, δ_{HO} is the contribution due to higher order diagrams, $P(\nu', t')$ is the probability (per unit energy bin) of losing energy ν' after a radiation thickness of t', $E_0 = E - \nu_b$ is energy before scattering, and $\nu_0 = \nu - \nu_b - \nu_a$ is energy lost during scattering. "Radiative corrections" refers to the process of "unfolding" the Born cross section difference from the experimental cross section difference. The radiation thicknesses for this experiment are based on Fig. (3.7) & Tab. (3.7) and are listed in Sec. (B.6).

The polarized elastic tail contribution $\Delta\sigma^{\text{elastic}}_{^3\text{He}}$ was calculated using the FOR-

TRAN program ROSETAIL.F, which uses the formalism of Mo & Tsai [55,56] and the notation of Stein et al [57]. The ^{3}He elastic form factors used to generate the tail are given by Eqn. (2.75) where $\{Q_i, R_i\}$ are from Table 1 of [58] and $\gamma = (0.8\text{ fm})/\sqrt{3/2}$ (N.B. the typo in Eqn. (1) of [58], for discussion see [59]). After the elastic tail have been subtracted out from $\Delta\sigma^{\text{exp}}$, the spectra were "smoothened out" using a cubic spline and interpolated in order to "fill in any gaps" in the data. Energy losses that occur before & after scattering due to materials in the path of the incident & scattered electrons lead to "external" radiative corrections. External corrections are spin-independent (i.e. "unpolarized") and are performed using the FORTRAN program RADCOR.F, which uses the formalism of Mo & Tsai [55,56]. Energy losses that occur in the field of the nucleus that causes scattering lead to "internal" radiative corrections. Internal corrections are spin-dependent (i.e. "polarized") and are performed using the FORTRAN program POLRAD.F, which is based on the original program & formalism of [60]. The radiative corrections, $\Delta_{RC}^{\text{external}}$ & $\Delta_{RC}^{\text{internal}}$, are calculated from the difference between the spectra output from the programs and the input "smoothed" spectra. Finally, the Born cross section differences are given by:

$$\Delta\sigma^{\text{born}} = \Delta\sigma^{\text{exp}} - \Delta\sigma_{^3\text{He}}^{\text{elastic}} - \Delta_{\text{RC}}^{\text{external}} - \Delta_{\text{RC}}^{\text{internal}} \tag{3.32}$$

Preliminary Results for Neutron Quantities & Discussion

The Born cross section differences were rebinned by W and then interpolated to constant Q^2. For the results presented here, the contribution from the quasielastic tail has not been subtracted away yet.. The "neutron-in-^{3}He" spin structure functions, g_1^3 & g_2^3, at constant Q^2 were then extracted from these parallel & perpendicular cross section differences, see Eqns. (3.17) & (3.18). The generalized

GDH integrand for I_A^3 using the "Hand" convention was calculated using g_1^3 & g_2^3, see Eqn. (3.21). The first moment $\bar{\Gamma}_1^3$ was calculated by integrating over g_1^3, see Eqn. (3.20). Since our data only covered the resonance region, the small contribution from the DIS region was calculated using the Thomas & Bianchi parameterization [61]. Finally, $\bar{\Gamma}_1$ for the neutron was extracted using the effective polarization method, see Eqn. (3.22).

Preliminary results for $g_{1,2}^3$ are depicted in Figs. (3.12). Just as for E94010, g_2^3 is, to a very good approximation, the negative of g_1^3, as naively expected by the Wandzura & Wilzcek relation, see Eqn. (2.204). The generalized GDH integrand is shown in (3.13). The large negative peak near $W = 1.2$GeV due to the Δ-resonance is readily apparent. Whereas the statistical uncertainties are very small, the systematic uncertainties are quite large. This intergrand still includes the tail of the quasielastic peak.

Fig. 3.14) depicts the preliminary results for $\bar{\Gamma}_1^n$ and I_A^n. These plots include radiative corrections but not the final polarimetry results described in Sec. (4.6). There is excellent agreement between the second lowest Q^2 point for E94010 and the highest Q^2point for E97110 at $Q^2 \approx 0.25$ GeV^2. Within the quoted systematic uncertainies, the lowest Q^2 point for E94010 and the second highest Q^2point for E97110 at $Q^2 \approx 0.1$ GeV^2 are in agreement. Although the systematic uncertainies are quite large, the E97110 data indicate that generalized GDH integral "turns over" at ≈ 0.1 GeV^2 which is in good agreement with the MAID model. Finally, we'll note that the lowest three Q^2points appear to indicate a much shallower slope for the GDH integral at low Q^2than both the BChPT predictions and the MAID model at $Q^2 = 0$.

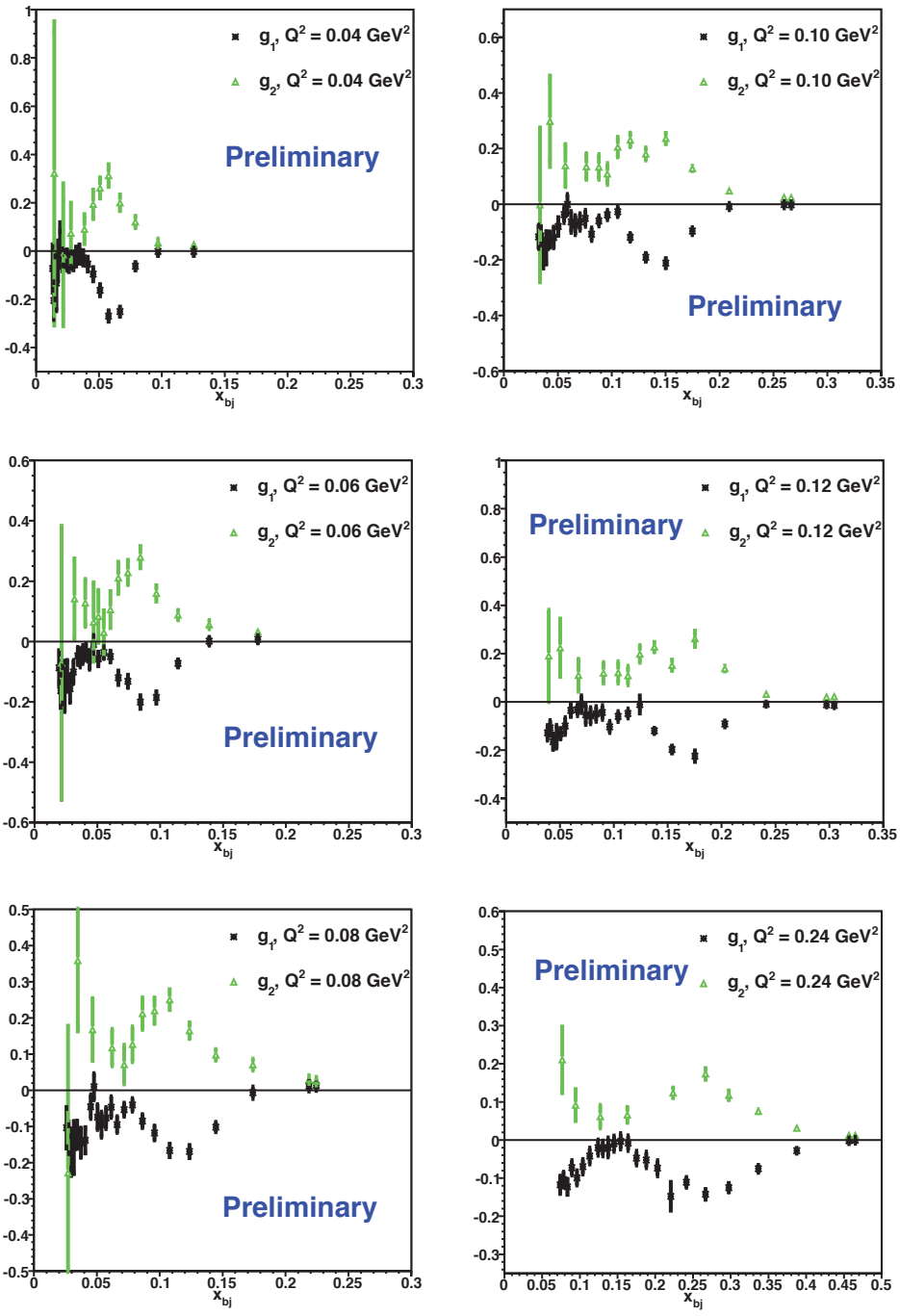

Figure 3.12: Preliminary Results for g_1^3 and g_2^3. (Provided by V. Sulkosky)

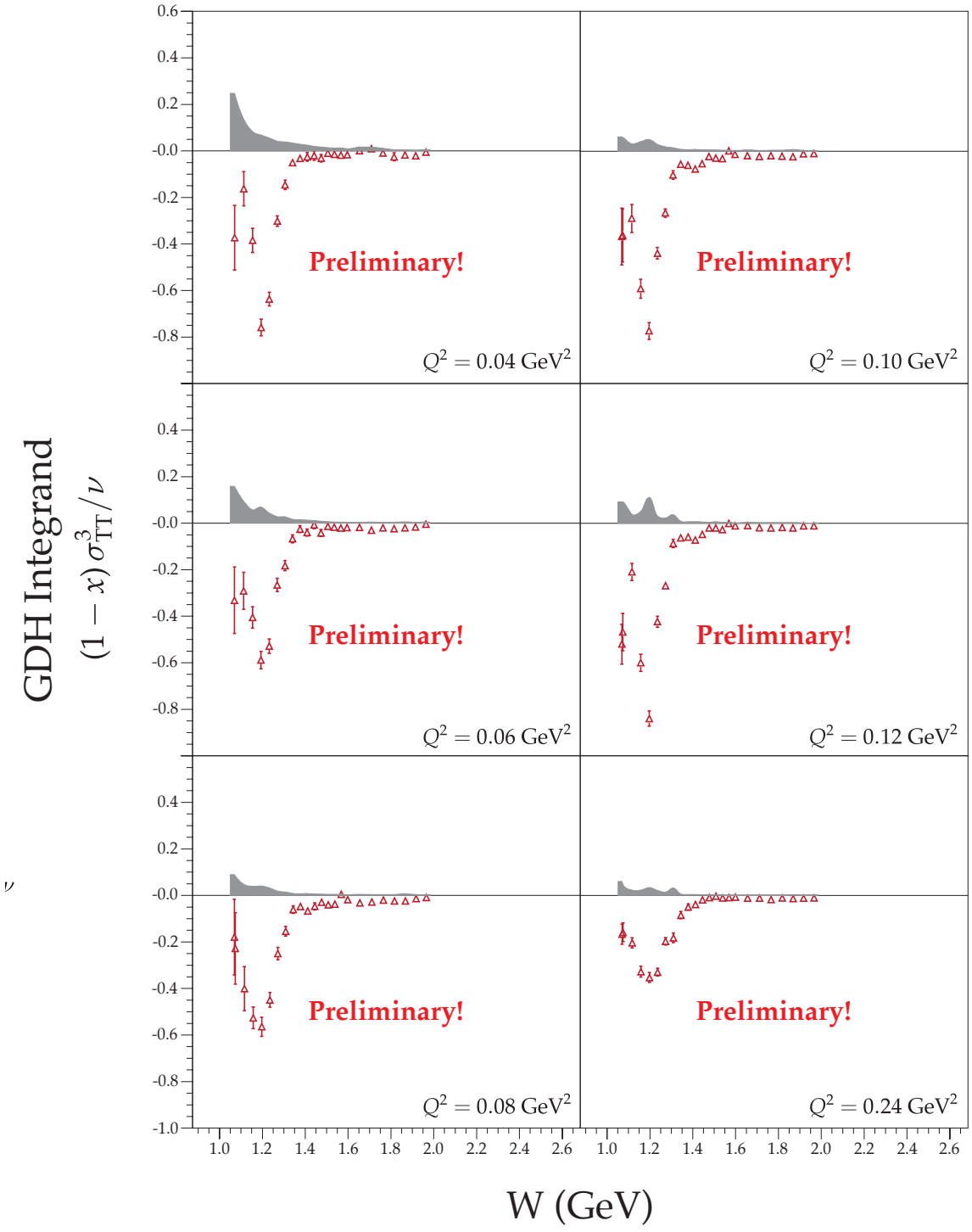

Figure 3.13: Preliminary Results for $(1-x)\sigma^3_{TT}/\nu$. (Provided by V. Sulkosky)

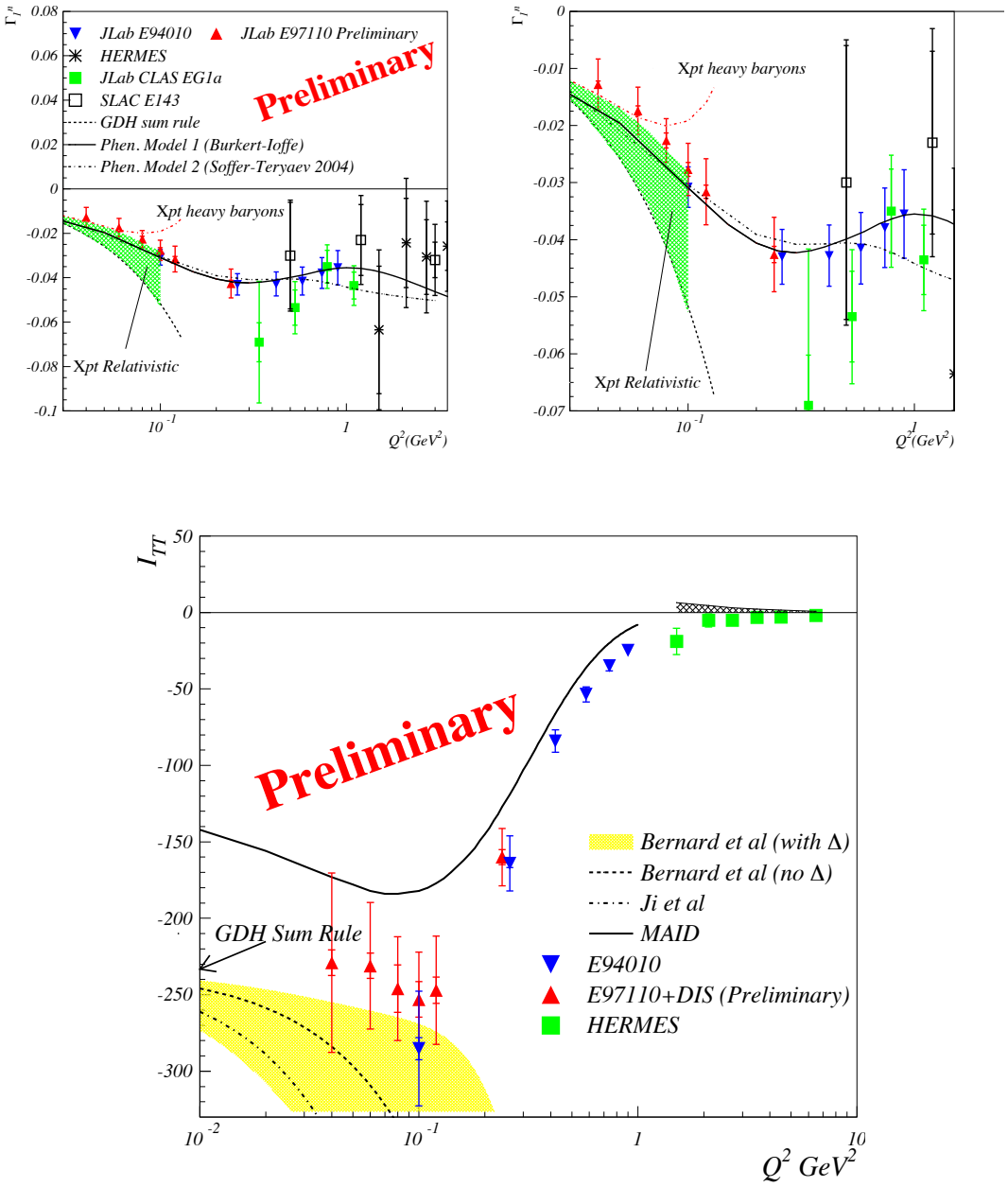

Figure 3.14: Preliminary Results for $\bar{\Gamma}_1^n$ & I_A^n. (Provided by V. Sulkosky) The contribution due to the quasielastic tail has not been removed in the data presented in these plots.

3.6 E02013: GEN

3.6.1 Introduction

E02013 ("Measurement of the Neutron Electric Form Factor G_E^n at High Q^2") ran from February to May 2006. The double polarization method was used to measure the transverse asymmetry A_{trans}, which is directly related to ratio of the electric to magnetic form factor G_E^n/G_M^n. Combined with recent precision measurements [62] of G_M^n over the same Q^2 range, the neutron electric form factor G_E^n was extracted. Although complicated by relativistic effects, electromagnetic form factors of nucleons encode information about the spatial distribution of their charge and magnetization, see Sec. (2.3.4). At low Q^2, these distributions are indicative of a virtual pion cloud. At high Q^2, these distributions are attributable to quarks degrees of freedom. In this regime ($Q^2 > 1$ GeV), the ratio of the proton's electric to magnetic form factor drops linearly with increasing Q^2, see Fig. (2.4). This surprising observation may have intriguing implications about the spatial distributions of quarks withing in the nucleon.

Precise data free of significant nuclear effects & model dependence for the neutron electric form factor are limited and, before this experiment, essentially no data existed above $Q^2 = 1.65$ GeV^2, see Fig. (2.9). Towards that end, since the mid-90's, G_E^n has been exclusively accessed via polarization observables from quasielastic scattering from deuterium and ^{3}He targets. Although limited in Q^2 range and statistics, these data seem to indicate that, unlike for the proton, G_E^n/G_M^n increases linearly, see Fig. (2.8), and $\tau F_2^n/\kappa_n^\star F_1^2$ is constant for increasing Q^2, see Fig. (2.12). Our data doubled the Q^2 range of G_E^n extracted from polarization observables and helped determine whether these trends continue, see Sec. (3.6.4).

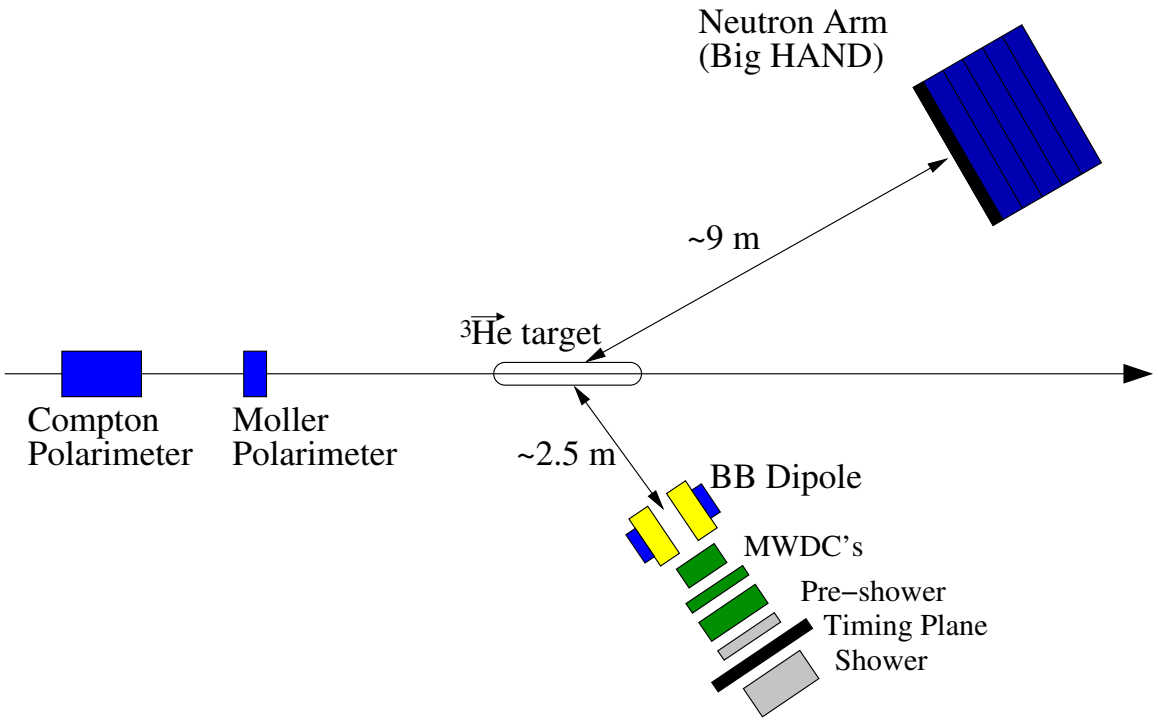

Figure 3.15: Schematic of E02013. (Provided by S. Riordan)

We measured the semi-inclusive quasielastic scattering of polarized electrons from a polarized ^{3}He target. The scattered electron was detected in coincidence with the recoiling neutron, see Fig. (3.15). Data were taken for Q^2 values of 1.4, 1.7, 2.5, & 3.4 GeV^2, see Tab. (3.9). Our data are a critical test of theoretical models can successfully reproduce the proton form factor ratio. In addition, our data provide important constraints to generalized parton distribution (GPD) models at high Q^2.

3.6.2 The Polarized He-3 Target

The target for this experiment was significantly different than the standard Hall A polarized ^{3}He target described in the previous section:

Q^2 (GeV^2)	**1.4**	**1.7**	**2.5**	**3.4**
kinematic	1	4	2a,2b	3a,3b
dates	03/05–03/08	05/03–05/12	03/09–03/21 04/17–04/24	03/24–04/17 04/24–05/03
cell	barbara	edna	dolly edna	edna
$\langle P_b \rangle$	(0.85)	0.85	0.85	0.83
$\langle P_t \rangle$	(0.40)	0.49	0.45	0.48
E (GeV)	1.52	2.08	2.64	3.29
$-\theta$ (deg)	56	52	52	52
E' (GeV)	0.88	1.13	1.28	1.41
β_n	0.80	0.87	0.91	0.94
$-\theta_n$ (deg)	36	33	28	25
d_{ND} (m)	8.2	8.2	11	11

Table 3.9: Nominal Experimental Parameters for E02013

1. To shield the target cell from fringe fields from Big Bite, the target cell was enclosed in a large iron box, see Fig. (3.16). The field inside the box was sufficiently uniform to maintain high target polarization and minimize any losses during an adiabatic fast passage (AFP) spin flip.

2. A second set of NMR coils was used to monitor the relative polarization in the pumping chamber. This helped minimize the uncertainty in the polarization gradient corrections between the two chambers, see Sec. (6.4.3).

3. The UNRAT optics system, see Sec. (**??**), in combination with 75 m armored optical fibers were used to deliver the optical pumping laser light to the target. This mitigated the need to install a shielded laser hut (saving much needed space in the Hall). In addition, this significantly reduced any possible optical pumping inefficiencies due to "skew" pumping, see Sec. (5.4.1).

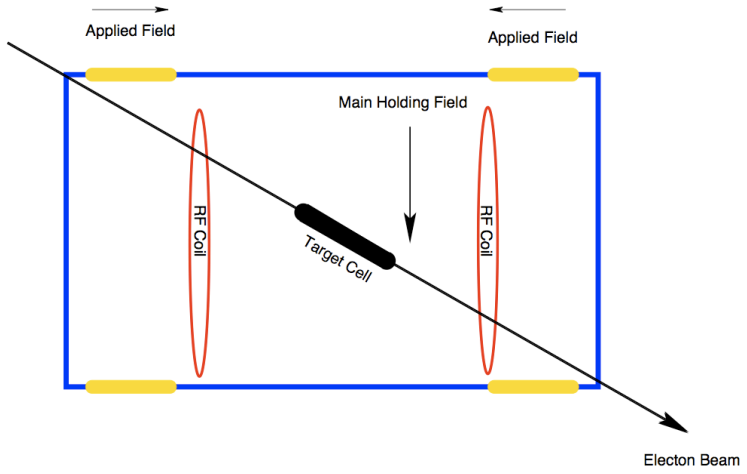

Figure 3.16: Schematic of the Target for E02013. (Provided by A. Kelleher)

4. Alkali-hybrid SEOP, see Chp. (5), was used for the first time in a polarized ^{3}He target for electron scattering. This resulted in record high (at the time) in-beam target polarizations, see Fig. (3.17), that, in addition, were significantly higher than the proposal goal.

5. The target cell had a significantly larger pumping chamber which reduced the sensitivity to beam depolarization, see. (6.3).

The changes in the target were so successful that pumping chamber NMR coils, the UNRAT optics system, alkali-hybrid SEOP cells, and larger pumping chambers are all now part of the standard polarized ^{3}He target. Further details about the target and polarimetry can be found in [63, 64].

3.6.3 The "Detector"

Because G_E^n is a naturally small quantity and nucleon elastic scattering cross sections drop off as Q^{-12}(!), a very acceptance large electron spectrometer was re-

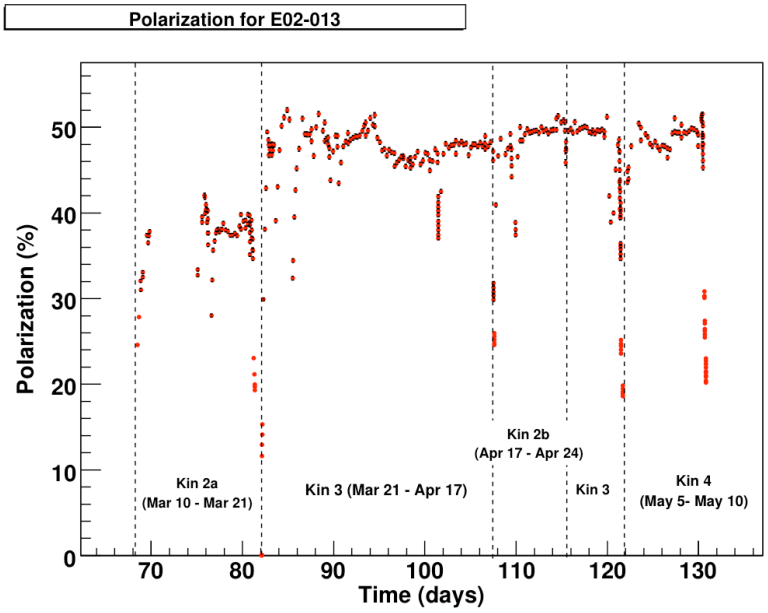

Figure 3.17: Target Polarization During E02013. (Provided by A. Kelleher)

quired to accumulate statistics at sufficiently high rate. To that end, a non-superconducting non-focusing dipole magnet called "Big Bite" was installed in Hall A. Big Bite has a combined momentum & solid angle acceptance that is about 70 times larger than that for the HRS. It was outfitted with, see Fig. (3.18):

1. a set of three custom built multiwire drift chambers used for tracking.

2. a set of preshower & shower counters for triggering the DAQ, particle identification, and coarse tracking.

3. a single scintillator plane used to obtain precise timing information necessary for forming a coincidence with the neutron detector.

Except for the first kinematic setting, Big Bite was kept at fixed position with respect to the target.

One additional criteria for being a "good" electron was required for this experiment: scattering quasielastically from a neutron. This was accomplished by tagging each electron scattering event measured in Big Bite with a coincident neutron event in a neutron detector. The main task of the neutron detector was to identify neutrons and determine their momentum via their time of flight. For each beam energy, the neutron detector had to be moved to a different location as prescribed by the kinematics. The distance between the target and the neutron detector was chosen to achieve a given timing resolution for the time of flight determination. The physical size (cross sectional area) of the detector was chosen to match the kinematic acceptance of Big Bite.

The neutron detector consisted of a pair scintillating layers in front of a set of seven alternating layers of converter material and scintillating material, see Fig. (3.18). A converter layer, composed of iron or lead, increased the probability that the neutron will create an electromagnetic shower. First, charged particles (protons) were distinguished from uncharged particles (neutrons and gammas) by their greater likelihood of producing a signal in surface layers of scintillators (the "veto" layer). Second, the time of flight (calculated by a timing signal from the Big Bite spectrometer and the signal from the inner scintillators of the neutron detector) was used to help distinguish neutrons from gammas.

3.6.4 Analysis & Results

Overview

Full details of the analysis can be found in [63–65]. The goal is to extract G_E^n from the quasielastic transverse asymmetry A_{trans} for polarized electron scattering from

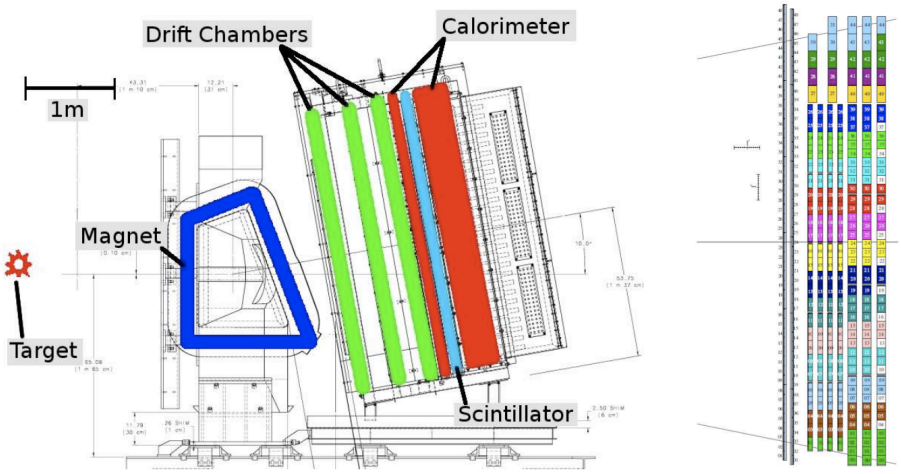

Figure 3.18: Schematic of the Big Bite & Neutron Detector. (Provided by A. Kelleher)

a polarized ^{3}He target. Using Eqns. (2.57), (2.128), & (2.129), the physics asymmetry can be written as [66]:

$$A_{\text{phys}} = A_0(\Lambda)\left\{\left[\hat{P}_t\cdot\hat{q}\right]\left(\frac{(E+E')\tan\left(\frac{\theta}{2}\right)}{2M_n}\right)+\left[\hat{P}_t\cdot(\hat{n}\times\hat{q})\right]\Lambda\right\}=\sum_{n=0}^{\infty}T_n\Lambda^n \tag{3.33}$$

where $\Lambda = G_E^n/G_M^n$, $A_0(\Lambda)$ is the "scale" asymmetry that depends on Λ & is defined by Eqn. (2.130), and the vectors are defined in Secs. (2.1.3) & (2.3.3). The experiment was designed such that $\hat{P}_t\cdot(\hat{n}\times\hat{q}) \gg \hat{P}_t\cdot\hat{q}\approx 0$, which makes $A_{\text{phys}} \approx A_{\text{trans}}$. Since Λ is small, $A_0(\Lambda)$ is Taylor expanded about $\Lambda = 0$, and, multiplying everything out, yields the "polynomial sum" in Eqn. (3.33), where the expansion coefficients T_n are given by:

$$T_{2n} = -\left[\hat{P}_t\cdot\hat{q}\right]\sqrt{1-\varepsilon^2}\left(-\frac{\varepsilon}{\tau}\right)^n \tag{3.34}$$

$$T_{2n+1} = -\left[\hat{P}_t\cdot(\hat{n}\times\hat{q})\right]\sqrt{\frac{2\varepsilon(1-\varepsilon)}{\tau}}\left(-\frac{\varepsilon}{\tau}\right)^n \tag{3.35}$$

The ratio $\Lambda = G_E^n/G_M^n$ was solved for numerically using the polynomial sum truncated at fifth order in Λ. Finally, G_E^n was extracted by multiplying Λ by G_M^n from a recent precision measurement from Hall B at JLab [62]. We'll now describe these steps in more detail.

"Good" Electron Selection

Tracking information from Big Bite identifies negatively charged particles scattered from the target and determines the 4-momentum transfer q. Cuts on the energy deposited in preshower & shower separates electrons from pions. The timing information from the scintillator in Big Bite combined with the signal from the Neutron Detector creates a coincidence signal and determines the momentum of the scattered nucleon p_n via time of flight. Quasielastic neutron events are distinguished from inelastic events by a cut on the invariant mass $W = \sqrt{M_n^2 + 2M_n\nu - Q^2} \approx M_n$ and a coincidence signal from the neutron detector. Cuts on the missing mass $W' = \sqrt{(P_3 + q - p_n)^2}$, where $P_3 = (M_3, \vec{0})$ is the initial momentum of the ^{3}He nucleus with mass M_3, help eliminate the pion electroproduction events.

The missing momentum $(\vec{q} - \vec{p}_n)$ is a measure of the the neutron momentum within the ^{3}He nucleus before scattering. Scattering from neutrons with low initial momenta are considered quasi-free. Therefore cuts are placed on the missing momentum to selects these events. This cut minimizes the effect of final state interactions (FSI) due to scattering of the struck nucleon from the spectator nucleons. In addition, this cut preferentially selects neutrons in the S basis state of the ^{3}He ground state wavefunction, which modifies the calculation of the effective neutron polarization P_n inside the ^{3}He nucleus presented in Sec. (3.1).

Extracting A_{phys}

The raw asymmetry is formed from events $N^{\pm}$ that survive these cuts and is related to the physics asymmetry by:

$$A_{\text{raw}} = \frac{N^+ - N^-}{N^+ + N^-} = D_{\text{N}_2}\ D_B D_p D_{\text{FSI}} P_b P_t P_n A_{\text{phys}} + A'_{\text{N}_2}\ + A'_B + A'_p + A'_{\text{other}} \quad (3.36)$$

where $D_{\text{N}_2\ ,B,p,\text{FSI}}$ & $A'_{\text{N}_2\ ,B,p,\text{FSI}}$ are the dilution factors & "apparent asymmetries" due to N_2 in the target cell, background, protons, & final state interactions/other sources and $P_{b,t,n}$ are the beam, ^{3}He , and effective neutron polarizations. The apparent asymmetries are defined by $A'_X = (N^+_X - N^-_X)/(N^+ + N^-)$, where $N^{\pm}_X$ are events due to X that survived past the cuts. The dilution and apparent asymmetry due to the background is measured using a subset of the data selected by an "inverse" cut on the time of flight. The dilution due to nitrogen is measured using a reference cell with N_2 , while the apparent asymmetry is taken to be 0. Corrections, D_p & A'_p, due to the possible misidentification of protons as neutrons are calculated using a Monte Carlo simulation and cross-checked by comparing yields from different nuclear targets. The correction, D_{FSI}, due to final state interactions (already suppressed by a cut on the missing momentum) are calculated from theory.

Extracting G_E^n

The scattering angle of the electron varies over the acceptance of the Big Bite spectrometer. Therefore, A_{phys} is really a "kinematic weighted average" over the acceptance of Big Bite [66]:

$$A_{\text{phys}} = \sum_{n=0}^{\infty} \langle T_n \Lambda \rangle_{\text{BB}} \approx \sum_{n=0}^{5} \langle T_n \rangle_{\text{BB}} \langle \Lambda \rangle^n_{Q^2} \quad (3.37)$$

where $\langle \cdots \rangle_{\mathrm{BB}}$ refers to the average over the acceptance of Big Bite. By assuming that Λ varies linearly with Q^2 across the acceptance, we can calculate acceptance averaged expansion coefficients $\langle T_n \rangle_{\mathrm{BB}}$ using a Monte Carlo simulation. Furthermore, $\langle \Lambda \rangle_{Q^2}$ can be interpreted as the neutron form factor ratio at an average $\langle Q^2 \rangle$ given by $\langle T_1 Q^2 \rangle_{\mathrm{BB}} / \langle T_1 \rangle_{\mathrm{BB}}$. The ratio $\langle \Lambda \rangle_{Q^2}$ can be solved for numerically by truncating the polynomial sum at fifth order $n = 5$. Finally, $G_E^n(Q^2)$ is obtained by $\langle \Lambda \rangle_{Q^2} G_M^n(Q^2)$.

Near Final Results & Discussion

Near final results are depicted for the $Q^2 = 1.7$, 2.5, & 3.4 GeV points in Fig. (3.19). The E02013 data has nearly the doubled Q^2 range over which G_E^n has been measured. The pQCD scaling with two different values for the "soft scale" parameter Λ do not describe the high Q^2 data of this experiment very well. The relativistic constitutent quark model and the vector meson domiinace model depicted in the plot are all within one sigma of the data, but consistently overestimate the measured values. The calculation using a solution to the Dyson-Schwinger Equations (i.e. the diquark model) appears to describe the data the best. Finally, although the highest Q^2 measurement before this experiment ($Q^2 \approx 1.4$ GeV^2) appears to be quite higher than the lowest Q^2 point for this experiment ($Q^2 \approx 1.7$ GeV^2), the difference between these two measurements is not statistically significant.

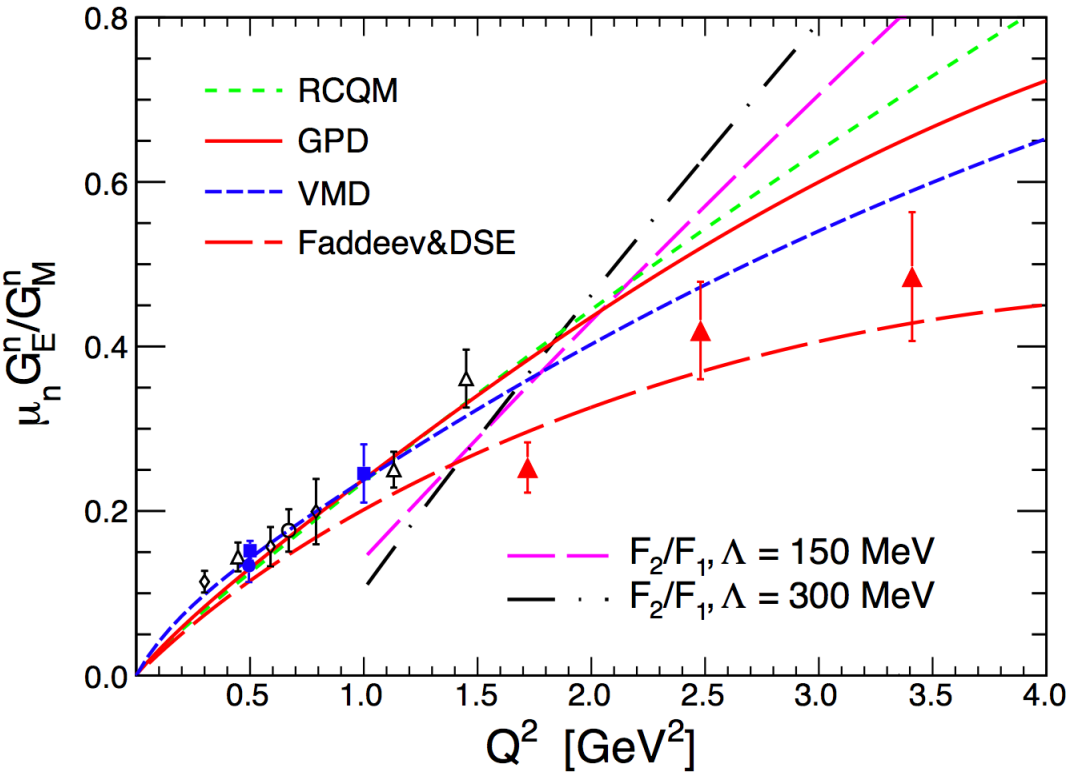

Figure 3.19: Ratio of G_E^n to G_M^n with near final Results for E02013. (Provided by S. Riordan) Red triangles are the data from E02013. The other data are the same as discussed in Sec. (2.3.4) and shown in Fig. (2.8). The F_2/F_1 ratios are calculations from pQCD [67], see Sec. (2.3.5). RCQM is the prediction from Miller's relativisitic constituent quark model [68], see Sec. (2.3.5). GPD is a parameterization of generalized parton distributions from prior nucleon form factor data [69, 70], see Sec. (2.3.5). VMD is the generalized vector meson dominance model of Lomon [71, 72], see Sec. (2.3.5). Fadeev & DSE is the prediction from a solution to the Dyson-Schwinger Equations [73], see Sec. (2.3.5).

Bibliography

[1] M. Amarian et al. Q^2 Evolution of the Generalized Gerasimov-Drell-Hearn Integral for the Neutron using a ^{3}He Target. *Phys. Rev. Lett.*, 89(24):242301, Nov 2002.

[2] M. Amarian et al. Q^2 Evolution of the Neutron Spin Structure Moments using a ^{3}He Target. *Phys. Rev. Lett.*, 92(2):022301, Jan 2004.

[3] M. Amarian et al. Measurement of the Generalized Forward Spin Polarizabilities of the Neutron. *Phys. Rev. Lett.*, 93(15):152301, Oct 2004.

[4] A. Deur et al. Experimental Determination of the Evolution of the Bjorken Integral at Low Q^2. *Phys. Rev. Lett.*, 93(21):212001, Nov 2004.

[5] Z.-E. Meziani et al. Higher twists and color polarizabilities in the neutron. *Physics Letters B*, 613(3-4):148 – 153, 2005.

[6] A. Deur, V. Burkert, J.P. Chen, and W. Korsch. Experimental determination of the effective strong coupling constant. *Physics Letters B*, 650(4):244 – 248, 2007.

[7] K. Slifer et al. ^{3}He Spin-Dependent Cross Sections and Sum Rules. *Phys. Rev. Lett.*, 101(2):022303, Jul 2008.

[8] W. Xu et al. Transverse Asymmetry $A_{T'}$ from the Quasielastic $^3\vec{\mathrm{He}}(\vec{e},e')$ Process and the Neutron Magnetic Form Factor. *Phys. Rev. Lett.*, 85(14):2900–2904, Oct 2000.

[9] F. Xiong et al. Precision Measurement of the Spin-Dependent Asymmetry in the Threshold Region of $^3\vec{\mathrm{He}}(\vec{e},e')$. *Phys. Rev. Lett.*, 87(24):242501, Nov 2001.

[10] W. Xu et al. Plane-wave impulse approximation extraction of the neutron magnetic form factor from quasielastic $^3\vec{\mathrm{He}}(\vec{e},e')$ at $Q^2 = 0.3$ to 0.6 $(\mathrm{GeV}/c)^2$. *Phys. Rev. C*, 67(1):012201, Jan 2003.

[11] B. Anderson et al. Extraction of the neutron magnetic form factor from quasielastic $^3\vec{\mathrm{He}}(\vec{e},e')$ at $Q^2 = 0.1$ to 0.6 $(\mathrm{GeV}/c)^2$. *Phys. Rev. C*, 75(3):034003, Mar 2007.

[12] X. Zheng et al. Precision Measurement of the Neutron Spin Asymmetry A_1^n and Spin-Flavor Decomposition in the Valence Quark Region. *Phys. Rev. Lett.*, 92(1):012004, Jan 2004.

[13] X. Zheng et al. Precision measurement of the neutron spin asymmetries and spin-dependent structure functions in the valence quark region. *Phys. Rev. C*, 70(6):065207, Dec 2004.

[14] K. Kramer. Q^2 Dependence of the Neutron Spin Structure Function g_2^n at Low Q^2. *Phys. Rev. Lett.*, 95(14):142002, Sep 2005.

[15] P. Solvignon et al. Quark-Hadron Duality in Neutron (^{3}He) Spin Structure. *Phys. Rev. Lett.*, 101(18):182502, Oct 2008.

[16] Chen, J.-P. and and Cates, G. and Garibaldi, F. et al. *JLab Proposal 97-110: The GDH Sum Rule, the Spin Structure of ^{3}He and the Neutron using Nearly Real Photons*. December 1997.

[17] Wojtsekhowski, B. and Cates, G. and McCormick K. and Reitz, B. et al. *JLab Proposal 02-013: Measurement of the Neutron Electric Form Factor G_E^n at High Q^2*. December 2001.

[18] Jiang, X. and Chen, J.-P., and Peng, J.-C. Peng, and Gao, H. and Cisbani, E. et al. *JLab Proposals 06-010/011: Measurement of Single Target-Spin Asymmetry in Semi-Inclusive Pion Electroproduction on a Transversely Polarized ^{3}He Target*. January 2006.

[19] Jiang, X. and Averett, T. and Holmstrom, T. and Gilman, R. et al. *JLab Proposal 07-013: Target Normal Single-Spin Asymmetry in Inclusive DIS $n^\uparrow(e,e')$ with a polarized ^{3}He Target*. December 2006.

[20] Sawatzky, Brad and Choi, S. and Jiang, X. and Meziani, Z.-E. et al. *JLab Proposal 06-014: Measurement of the Neutron d_2: Towards the Electric χ_E and the Magnetic χ_B Color Polarizabilities*. December 2005.

[21] Averett, T. and Jiang, X. and Chen, J.-P. et al. *JLab Proposal 05-015: Measurement of the Target Single-Spin Asymmetry in Quasi-Elastic ^{3}He$\uparrow$ (e,e')*. December 2004.

[22] Sulkosky, V. and Averett, T. and Higinbotham, D.W. et al. *JLab Proposal 08-005: Measurement of the Target Single-Spin Asymmetry A_y in Quasi-Elastic ^{3}He$\uparrow$ $(e,e'n)$*. December 2007.

[23] Širca, S. and Gilad, S. and Higinbotham, D.W. and Korsch, W. and Norum, B.E. et al. *JLab Proposal 05-102: Measurement of A_x and A_z asymmetries in the quasi-elastic $^3\vec{\mathrm{H}}\mathrm{e}(\vec{e},e'd)$ reaction*. June 2005.

[24] L. M. DELVES and A. C. PHILLIPS. Present Status of the Nuclear Three-Body Problem. *Rev. Mod. Phys.*, 41(3):497–530, Jul 1969.

[25] G. Derrick and J. M. Blatt. Classification of triton wave functions. *Nuclear Physics*, 8:310 – 324, 1958.

[26] J. L. Friar, B. F. Gibson, G. L. Payne, A. M. Bernstein, and T. E. Chupp. Neutron polarization in polarized ^3He targets. *Phys. Rev. C*, 42(6):2310–2314, Dec 1990.

[27] Edward Gerjuoy and Julian Schwinger. On Tensor Forces and the Theory of Light Nuclei. *Phys. Rev.*, 61(3-4):138–146, Feb 1942.

[28] I. R. Afnan and N. D. Birrell. Comparison of the unitary pole and Adhikari-Sloan expansions in the three-nucleon system. *Phys. Rev. C*, 16(2):823–838, Aug 1977.

[29] B. Blankleider and R. M. Woloshyn. Quasi-elastic scattering of polarized electrons on polarized ^{3}He. *Phys. Rev. C*, 29(2):538–552, Feb 1984.

[30] A. Kievsky, E. Pace, G. Salmè, and M. Viviani. Neutron electromagnetic form factors and inclusive scattering of polarized electrons by polarized ^{3}He and ^{3}H targets. *Phys. Rev. C*, 56(1):64–75, Jul 1997.

[31] E. L. Tomusiak, M. Kimura, J. L. Friar, B. F. Gibson, G. L. Payne, and J. Dubach. Trinucleon magnetic moments. *Phys. Rev. C*, 32(6):2075–2086, Dec 1985.

[32] C. Ciofi degli Atti, E. Pace, and G. Salmè. Investigation of the neutron form factors by inclusive quasielastic scattering of polarized electrons off polarized ^{3}He: A theoretical overview. *Phys. Rev. C*, 51(3):1108–1119, Mar 1995.

[33] C. Ciofi degli Atti and S. Scopetta. On the Extraction of the Neutron Spin Structure Functions and the Gerasimov – Drell – Hearn Integral from $^3\vec{\mathrm{H}}\mathrm{e}(\vec{e},e')X$ data. *Physics Letters B*, 404(3-4):223 – 229, 1997.

[34] S. A. Kulagin and W. Melnitchouk. Spin structure functions of ^{3}He at finite Q^2. *Phys. Rev. C*, 78(6):065203, Dec 2008.

[35] C. Ciofi degli Atti, S. Scopetta, E. Pace, and G. Salmè. Nuclear effects in deep inelastic scattering of polarized electrons off polarized ^{3}He and the neutron spin structure functions. *Phys. Rev. C*, 48(3):R968–R972, Sep 1993.

[36] F. Bissey, V. Guzey, M. Strikman, and A. Thomas. Complete analysis of spin structure function g_1 of ^{3}He. *Phys. Rev. C*, 65(6):064317, Jun 2002.

[37] M. Anselmino, A. Efremov, and E. Leader. The theory and phenomenology of polarized deep inelastic scattering. *Physics Reports*, 261(1-2):1 – 124, 1995.

[38] M. Anselmino, A. Efremov, and E. Leader. Errata: The theory and phenomenology of polarized deep inelastic scattering. *Physics Reports*, 281(5-6):399 – 400, 1997.

[39] Hunter Leigh Middleton. *The Spin Structure of the Neutron Determined Using a Polarized ^{3}He Target*. PhD thesis, Princeton University, 1994.

[40] Ioannis Kominis. *Measurement of the Neutron (^{3}He) Spin Structure at Low Q^2 and the Extended Gerasimov-Drell-Hearn Sum Rule*. PhD thesis, Princeton University, 2001.

[41] Mikhail V. Romalis. *Laser Polarizaed ^{3}He Target Used for a Precision Measurement of the Neutron Spin Structure*. PhD thesis, Princeton University, 1997.

[42] David R. Lide (Editor-in Chief). *CRC Handbook of Chemistry and Physics*. CRC Press, Boca Raton, FL, 75th student edition, 1994.

[43] M.A. Zucker, A.R. Kishore, R. Sukumar, and R.A. Dragoset. Elemental Data Index (version 2.1). [Online] Available: http://physics.nist.gov/EDI [2008, April 20].

[44] Christopher James Erickson. *Measurements Of The Magnetic Field Dependence Of The Spin Relaxation Rate In Alka¿¿¿li Metal Vapors*. PhD thesis, Princeton University, 2000.

[45] P.H. Schmidt. The Purification of Cesium and Rubidium Metals by Chloride Reduction under High Vacuum Conditions. *Journal of the Electrochemical Society*, 116:1279–1282, September 1969.

[46] J. Alcorn et al. Basic instrumentation for Hall A at Jefferson Lab. *Nuclear Instruments and Methods in Physics Research Section A: Accelerators, Spectrometers, Detectors and Associated Equipment*, 522(3):294 – 346, 2004.

[47] T. B. Humensky et al. SLAC's polarized electron source laser system and minimization of electron beam helicity correlations for the E-158 parity violation experiment. *Nuclear Instruments and Methods in Physics Research Section A: Ac-*

celerators, Spectrometers, Detectors and Associated Equipment, 521(2-3):261 – 298, 2004.

[48] Christoph W. Leemann, David R. Douglas, and Geoffrey A. Krafft. The Continuous Electron Beam Accelerator Facility: CEBAF at the Jefferson Laboratory. *Annual Review of Nuclear and Particle Science*, 51(1):413–450, 2001.

[49] Adam M. Bincer. Scattering of Longitudinally Polarized Fermions. *Phys. Rev.*, 107(5):1434–1438, Sep 1957.

[50] G. W. Ford and C. J. Mullin. Scattering of Polarized Dirac Particles on Electrons. *Phys. Rev.*, 108(2):477–481, Oct 1957.

[51] G. W. Ford and C. J. Mullin. Errata: Scattering of Polarized Dirac Particles on Electrons. *Phys. Rev.*, 110(6):1485, Jun 1958.

[52] A. Rączka and R. Rączka. Møller Scattering of Arbitrarily Polarized Electrons. *Phys. Rev.*, 110(6):1469–1471, Jun 1958.

[53] D. Drechsel, O. Hanstein, S. S. Kamalov, and L. Tiator. A unitary isobar model for pion photo- and electroproduction on the proton up to 1 GeV. *Nuclear Physics A*, 645(1):145 – 174, 1999.

[54] Vincent Anthony Sulkosky. *THE SPIN STRUCTURE OF* ^{3}He *AND THE NEUTRON AT LOW* Q^2*:A MEASUREMENT OF THE GENERALIZED GDH INTEGRAND*. PhD thesis, College of William and Mary, 2007.

[55] L. W. Mo and Y. S. Tsai. Radiative Corrections to Elastic and Inelastic ep and up Scattering. *Rev. Mod. Phys.*, 41(1):205–235, Jan 1969.

[56] Y. S. Tsai. *SLAC-PUB-0848: Radiative Corrections to Electron Scattering*. January 1971.

[57] S. Stein et al. Electron scattering at 4^o with energies of 4.5–20 GeV. *Phys. Rev. D*, 12(7):1884–1919, Oct 1975.

[58] A. Amroun et al. ^{3}H and ^{3}He electromagnetic form factors. *Nuclear Physics A*, 579(3-4):596 – 626, 1994.

[59] I. Sick. Elastic electron scattering from light nuclei. *Progress in Particle and Nuclear Physics*, 47(1):245 – 318, 2001.

[60] I. Akushevich, A. Ilyichev, N. Shumeiko, A. Soroko, and A. Tolkachev. POLRAD 2.0. FORTRAN code for the radiative corrections calculation to deep inelastic scattering of polarized particles. *Computer Physics Communications*, 104(1-3):201 – 244, 1997.

[61] E. Thomas and N. Bianchi. First Regge parameterisation of polarized DIS cross section. *Nuclear Physics B - Proceedings Supplements*, 82:256 – 261, 2000. Proceedings of the International Conference on the Structure and Interactions of the Photon, including the 12th International Workshop on Photon-Photon Collisions.

[62] J. Lachniet et al. Precise Measurement of the Neutron Magnetic Form Factor G_M^n in the Few-GeV^2 Region. *Phys. Rev. Lett.*, 102(19):192001, May 2009.

[63] Aidan M. Kelleher. *A MEASUREMENT OF THE NEUTRON ELECTRIC FORM FACTOR AT VERY LARGE MOMENTUM TRANSFER USING POLARIZED ELECTRONS SCATTERING FROM A POLARIZED HELIUM-3 TARGET*. PhD thesis, College of William and Mary, 2010.

[64] Ameya Suresh Kolarkar. *PRECISION MEASUREMENTS OF THE NEUTRON ELECTRIC FORM FACTOR AT HIGH MOMENTUM TRANSFERS*. PhD thesis, University of Kentucky, 2008.

[65] Seamus Patrick Riordan. *Measurements of the Electric Form Factor of the Neutron at Q^2= 1.7 and 3.5* GeV^2. PhD thesis, Carnegie Mellon, 2008.

[66] G. B. Franklin. G_E^n asymmetry corrections for finite angular acceptance. *Carnegie Mellon Technical Note*.

[67] A. V. Belitsky, Xiangdong Ji, and Feng Yuan. Perturbative QCD Analysis of the Nucleon's Pauli Form Factor $F_2(Q^2)$. *Phys. Rev. Lett.*, 91(9):092003, Aug 2003.

[68] Gerald A. Miller. Light front cloudy bag model: Nucleon electromagnetic form factors. *Phys. Rev. C*, 66(3):032201, Sep 2002.

[69] M. Diehl, Th Feldmann, R. Jakob, and P. Kroll. Generalized parton distributions from nucleon form factor data. *The European Physical Journal C - Particles and Fields*, 39:1–39, 2005. 10.1140/epjc/s2004-02063-4.

[70] M. Guidal, M. V. Polyakov, A. V. Radyushkin, and M. Vanderhaeghen. Nucleon form factors from generalized parton distributions. *Phys. Rev. D*, 72(5):054013, Sep 2005.

[71] Earle L. Lomon. Extended Gari-Krümpelmann model fits to nucleon electromagnetic form factors. *Phys. Rev. C*, 64(3):035204, Aug 2001.

[72] Earle L. Lomon. Effect of revised *Rn* measurements on extended Gari-Krümpelmann model fits to nucleon electromagnetic form factors. arXiv:nucl-th/0609020v2(MIT-CTP-3765), Sep 2006.

[73] I. C. Cloët, G. Eichmann, B. El-Bennich, T. Klähn, and C. D. Roberts. Survey of Nucleon Electromagnetic Form Factors. *Few-Body Systems*, 46(1):1–36, Jun 2009.

Chapter 4

^{3}He Polarimetry

The ^{3}He polarization can be measured using two independent techniques. The first is Nuclear Magnetic Resonance (NMR) technique of Adiabatic Fast Passage (AFP). The second, referred to as "EPR", is the Electron Paramagnetic Resonance (EPR) frequency shift polarimetry. NMR is a relative polarization monitor that can be calibrated using a signal from a sample of water or by comparison to EPR. We'll describe how to perform these measurements and how to extract ^{3}He polarization from them. In addition, we'll describe a potentially large systematic error for EPR due to the AC Zeeman Effect. The water NMR signal and the EPR frequency shift can both be used to determine the sign of the ^{3}He polarization relative to the holding field. Finally, we'll describe the polarimetry analysis for E97110 (Small Angle GDH).

4.1 Introduction

The ^{3}He polarization is obtained by measuring the effect of the magnetic field $\vec{B}_{\mathrm{He}}$ produced by the polarized ^{3}He gas in the cell. This magnetic field depends on the geometry of the cell and the location $\vec{r}$ of the measurement by [1]:

$$\vec{B}_{\mathrm{He}}(\vec{r},t) = \vec{\nabla} \times \vec{A}(\vec{r},t) \qquad \vec{A}(\vec{r},t) = \frac{\mu_0}{4\pi} \int \frac{\vec{M}(\vec{u},t) \times (\vec{r}-\vec{u})}{|\vec{r}-\vec{u}|^3} d^3u \tag{4.1}$$

where $\vec{A}(\vec{r},t)$ is the magnetic vector potential of the polarized ^{3}He gas, t is time, μ_0 is magnetic permeability of free space (i.e. the relative magnetic permeability of air and glass is essentially unity), $\vec{M}(\vec{u},t)$ is the magnetization of the polarized ^{3}He gas at a location $\vec{u}$, and the integral is performed over the inner volume of the cell. The magnetization is defined as the average magnetic moment per unit volume:

$$\vec{M}(\vec{u},t) = \langle \vec{\mu}(\vec{u},t) \rangle \, n(\vec{u},t) \tag{4.2}$$

where n is local ^{3}He number density and $\langle \vec{\mu} \rangle$ is the combined statistical & quantum mechanical expectation value of the ^{3}He magnetic dipole moment:

$$\langle \vec{\mu}(\vec{u},t) \rangle = g\mu_N \left\langle \vec{S}(\vec{u},t) \right\rangle = \frac{g\mu_N}{2} P_{\mathrm{He}} \vec{p}(\vec{u},t) \tag{4.3}$$

where g is the ^{3}He g-factor in units of the nuclear magneton μ_N, $\vec{S}$ is the spin-1/2 vector operator, P_{He} is the ^{3}He polarization, and $\vec{p}$ is the polarization vector. Because B_{He} is so small (on order of mG under our typical conditions), a technique called "Adiabatic Fast Passage" (AFP) is used to isolate $\vec{B}_{\mathrm{He}}$ from larger surrounding fields by reversing the sign of $\hat{B}_{\mathrm{He}}$ (i.e. "flipping the spins"). The time depen-

dence of this spin-flip process is encoded in the polarization vector which will be calculated in the next section.

4.2 Adiabatic Fast Passage of the Polarization Vector

Both NMR & EPR make use of AFP to rotate the polarization vector (i.e. flip the spins) of the ^{3}He nuclei with a relatively small loss of polarization. In this section, the motion of the polarization vector will be calculated quantum mechanically. The Hamiltonian for a spin-1/2 particle in a longitudinal ($\hat{z}$) "holding" field with magnitude B and a transverse ($\hat{y}$) RF (radiofrequency) field with magnitude $2B_1$ & frequency $\omega_{\mathtt{rf}}$ is:

$$\mathcal{H} = -g\mu_N \vec{S} \cdot \left[B\hat{z} + 2B_1 \cos\left(\omega_{\mathtt{rf}} t\right) \hat{y}\right] = -s\hbar \left[\left(\omega_{\mathtt{rf}} + \Delta\right) S_z + 2\omega_1 \cos\left(\omega_{\mathtt{rf}} t\right) S_y\right] \quad (4.4)$$

where s is the sign of the particle's magnetic moment ($s = g/|g|$) and:

$$\Delta = |\gamma|B - \omega_{\mathtt{rf}} \qquad \omega_1 = |\gamma|B_1 \qquad \omega_0 = |\gamma|B_0 \qquad \gamma = \frac{g\mu_N}{\hbar} \quad (4.5)$$

where Δ is the "detuning", B_0 & ω_0 are the field & frequency at which $\Delta = 0$, and γ is the particle's gyromagnetic ratio. We can represent the general spin state Ψ of the particle in the $\{|\pm\rangle\}$ basis as:

$$|\Psi\rangle = a(t) \exp\left[+\frac{is(\omega_{\mathtt{rf}} + \Delta)t}{2}\right] |+\rangle + b(t) \exp\left[-\frac{is(\omega_{\mathtt{rf}} + \Delta)t}{2}\right] |-\rangle \quad (4.6)$$

Plugging this into Schrodinger's equation, $i\hbar\partial|\Psi\rangle/\partial t = \mathcal{H}|\Psi\rangle$, results in two coupled differential equations for the coefficients a & b:

$$\frac{da}{dt} = \dot{a} = +\frac{sb\omega_1}{2}\left(1+\exp\left[-si2\omega_{\mathtt{rf}}t\right]\right)\exp\left[-is\Delta t\right] \tag{4.7}$$

$$\frac{db}{dt} = \dot{b} = -\frac{sa\omega_1}{2}\left(1+\exp\left[+si2\omega_{\mathtt{rf}}t\right]\right)\exp\left[+is\Delta t\right] \tag{4.8}$$

We'll now make the time honored "rotating wave approximation" (RWA) [2] and simply drop the term occurring at a frequency $2\omega_{\mathtt{rf}}$:

$$\dot{a} = +\frac{sb\omega_1}{2}\exp\left[-is\Delta t\right] \qquad \dot{b} = -\frac{sa\omega_1}{2}\exp\left[+is\Delta t\right] \tag{4.9}$$

Note that this term *does* have a small effect: (1) The main resonance is shifted to $\omega_0\left(1+\frac{\omega_1^2}{4\omega_0^2}+\cdots\right)$ (i.e. the "Bloch-Siegert" shift [3]) and (2) There are, in general, resonances at frequencies $\omega_n = \frac{\omega_0}{2n+1}$ where $n \geq 0$ [4]. However, all resonances for $n \neq 0$ are very weak under our conditions. Solving the equation for da/dt in Eqn. (4.9) for b, differentiating with respect to t, and plugging in the equation for db/dt gives:

$$\ddot{a} + is\Delta\dot{a} + \frac{\omega_1^2}{4}a = 0 \tag{4.10}$$

This is solved straightforwardly using the substitution $a = e^{i\lambda t}$:

$$\lambda = \frac{-s\Delta \pm \Omega}{2} \qquad \Omega = \sqrt{\Delta^2+\omega_1^2} \tag{4.11}$$

where Ω is the venerable Rabi frequency [5]. Note that the RWA is valid only for $\Omega \ll 2\omega_{\mathtt{rf}}$. After enforcing unit normalization ($\langle\Psi\,|\,\Psi\rangle = 1$), the general solution

for Ψ in the $\{|\pm\rangle\}$ basis can be written as:

$$
\begin{aligned}
|\Psi\rangle &= A(t)\exp\left[+is\frac{\omega_{\mathtt{rf}}}{2}t\right]|+\rangle + B(t)\exp\left[-is\frac{\omega_{\mathtt{rf}}}{2}t\right]|-\rangle && (4.12)\\
A(t) &= a_1\exp\left[+i\frac{\Omega}{2}t\right] + |a_2|\exp\left[-i\frac{\Omega}{2}t - i\phi\right] && (4.13)\\
B(t) &= ia_1\sqrt{\frac{1-s\frac{\Delta}{\Omega}}{1+s\frac{\Delta}{\Omega}}}\exp\left[+i\frac{\Omega}{2}t\right] - i|a_2|\sqrt{\frac{1+s\frac{\Delta}{\Omega}}{1-s\frac{\Delta}{\Omega}}}\exp\left[-i\frac{\Omega}{2}t - i\phi\right] && (4.14)\\
|a_2|^2 &= \frac{1}{2}\left[1-s\frac{\Delta}{\Omega}\right] - a_1^2\left[\frac{1-s\frac{\Delta}{\Omega}}{1+s\frac{\Delta}{\Omega}}\right] && (4.15)
\end{aligned}
$$

where the real constants a_1 & ϕ are specified by initial conditions. The components of the expectation value of $\langle\Psi|\,\vec{S}\,|\Psi\rangle$ are:

$$
\begin{aligned}
\langle S_x\rangle &= -sa_1|a_2|\left\{\left[\frac{\Omega+s\Delta}{\omega_1}\right]\sin(s\omega_{\mathtt{rf}}t+\Omega t+\phi) - \left[\frac{\Omega-s\Delta}{\omega_1}\right]\sin(s\omega_{\mathtt{rf}}t-\Omega t-\phi)\right\}\\
&\quad +s\left[2|a_1|^2\left(\frac{\Omega-s\Delta}{\omega_1}\right) - \frac{\omega_1}{2\Omega}\right]\sin(s\omega_{\mathtt{rf}}t) && (4.16)\\
\langle S_y\rangle &= -sa_1|a_2|\left\{\left[\frac{\Omega+s\Delta}{\omega_1}\right]\cos(s\omega_{\mathtt{rf}}t+\Omega t+\phi) - \left[\frac{\Omega-s\Delta}{\omega_1}\right]\cos(s\omega_{\mathtt{rf}}t-\Omega t-\phi)\right\}\\
&\quad +s\left[2|a_1|^2\left(\frac{\Omega-s\Delta}{\omega_1}\right) - \frac{\omega_1}{2\Omega}\right]\cos(s\omega_{\mathtt{rf}}t) && (4.17)\\
\langle S_z\rangle &= \frac{s\Delta}{2\Omega}\left[\frac{4|a_1|^2}{1+s\frac{\Delta}{\Omega}} - 1\right] + 2a_1|a_2|\cos(\Omega t+\phi) && (4.18)
\end{aligned}
$$

We'll specify the initial condition that, when the detuning is large ($|\Delta| \gg \omega_1$), $|\Psi_0\rangle = |\pm\rangle$, which implies that the constants are:

$$
\left\{\begin{array}{l} a_1 = \frac{1}{2}\left[1+s\frac{\Delta}{\Omega}\right] \\ a_2 = 0 \end{array}\right\} \text{ for } s\Delta > 0 \qquad \left\{\begin{array}{l} a_1 = 0 \\ a_2 = \frac{1}{2}\left[1-s\frac{\Delta}{\Omega}\right] \end{array}\right\} \text{ for } s\Delta < 0 \quad (4.19)
$$

If the fraction of particles with the initial condition $|\Psi_0\rangle = |\pm\rangle$ is given by $f_{\Psi_0} = (1 \pm P_{\mathrm{He}})/2$, then the statistical average of the expectation value of $\vec{S}$ is given by:

$$\left\langle \vec{S} \right\rangle = \sum_{\Psi_0} f_{\Psi_0} \left\langle \vec{S} \right\rangle_{\Psi_0} = \left(\frac{1+P_{\mathrm{He}}}{2} \right) \left\langle \vec{S} \right\rangle_{+} + \left(\frac{1-P_{\mathrm{He}}}{2} \right) \left\langle \vec{S} \right\rangle_{-} = \frac{P_{\mathrm{He}}}{2} \vec{p} \tag{4.20}$$

where the polarization vector is given by:

$$\vec{p} = s \left[\left(\frac{\omega_1}{\Omega} \right) \left\{ \underbrace{\hat{x} \sin(s\omega_{\mathtt{rf}} t) + \hat{y} \cos(s\omega_{\mathtt{rf}} t)}_{\hat{y}_{\mathrm{rot}}} \right\} + \frac{\Delta}{\Omega} \hat{z} \right] = s \left[\left(\frac{\omega_1}{\Omega} \right) \hat{y}_{\mathrm{rot}} + \frac{\Delta}{\Omega} \hat{z} \right] \tag{4.21}$$

In the reference frame rotating at a frequency $-s\omega_{\mathtt{rf}}$ about the axis $\hat{z}$ defined by holding field, the bracketed term $\hat{y}_{\mathrm{rot}}$ is the unit vector in the transverse direction to $\hat{z}$. In this "rotating" frame, the polarization vector $\vec{p}$ is parallel to an effective field given by:

$$\vec{B}_{\mathrm{eff}} = \frac{\omega_1 \hat{y}_{\mathrm{rot}} + \Delta \hat{z}}{|\gamma|} = \frac{\vec{\Omega}}{|\gamma|} \quad \rightarrow \quad \vec{p} = s \frac{\vec{\Omega}}{\Omega} = s \hat{B}_{\mathrm{eff}} \tag{4.22}$$

If the detuning Δ is varied slow enough, then $\vec{p}$ will follow adiabatically (i.e. stay aligned) with $\vec{B}_{\mathrm{eff}}$, see Fig. (4.1). At the "resonance" condition $\Delta = 0$, the polarization vector is aligned with the RF field transverse to the holding field.

The detuning Δ is swept by ramping either the holding field B or the RF frequency $\omega_{\mathtt{rf}}$. The rate of change of Δ is considered "slow" if the fractional change in Ω over one period of Ω is very small:

$$\delta_A \equiv \left(\text{fractional change in } \Omega\right) \times \left(\text{one period of } \Omega\right) = \left| \frac{1}{\Omega} \frac{\partial \Omega}{\partial t} \right| \left(\frac{2\pi}{\Omega} \right) \ll 1 \tag{4.23}$$

This condition is most severely tested for the maximum value of δ_A and, assuming

a linear sweep of Δ, it is given by:

$$\delta_A \leq \frac{4\pi}{\omega_1\sqrt{27}}\left|\frac{\dot{\Delta}}{\omega_1}\right| \qquad \dot{\Delta} = |\gamma|\frac{dB}{dt} - \frac{d\omega_{\mathtt{rf}}}{dt} \tag{4.24}$$

Therefore, $\delta_A \ll 1$ is "adiabatic" condition. In this section, we've ignored the effect of relaxation, which will be described more fully in Sec. (4.3.4), which provides a lower limit on the rate of change:

$$\delta_F \equiv \text{polarization loss} = (\text{relaxation rate}) \times (\text{time scale of relaxation}) \ll 1 \tag{4.25}$$

This condition is most severely tested for ^{3}He near resonance:

$$\delta_F \leq \frac{1}{T_2}\left|\frac{\omega_1}{\dot{\Delta}}\right| = \frac{D}{B_1^2}\left(\frac{\partial B}{\partial z}\right)^2\left|\frac{\omega_1}{\dot{\Delta}}\right| \tag{4.26}$$

where T_2 is the transverse relaxation rate, D is the ^{3}He diffusion coefficient, and we've assumed that the dominant ^{3}He relaxation mechanism at resonance is due to longitudinal magnetic field gradients [6–9], see Fig. (4.5). In summary, the rate of change of the effective field must be *slow* enough for the spins to follow *adiabatically* and *fast* enough to avoid polarization loss near resonance:

$$\delta_F \ll 1 \ll \frac{1}{\delta_A} \quad \rightarrow \quad \frac{D}{B_1^2}\left(\frac{\partial B}{\partial z}\right)^2 \ll \left|\frac{\dot{B}}{B_1} - \frac{\dot{\omega}_{\mathtt{rf}}}{\omega_1}\right| \ll \frac{\omega_1\sqrt{27}}{4\pi} \tag{4.27}$$

where $\dot{\omega}_{\mathtt{rf}} = 0$ ($\dot{B} = 0$) for field (frequency) sweep AFP. Under our typical conditions for ^{3}He , $\dot{B} \approx 1$ G/s, $2B_1 \approx 100$ mG, $D \approx 0.2$ cm^2/s, & $\partial B/\partial z = 10$ mG/cm, the AFP conditions are well satisfied ($0.0004 \ll 1 \ll 20$).

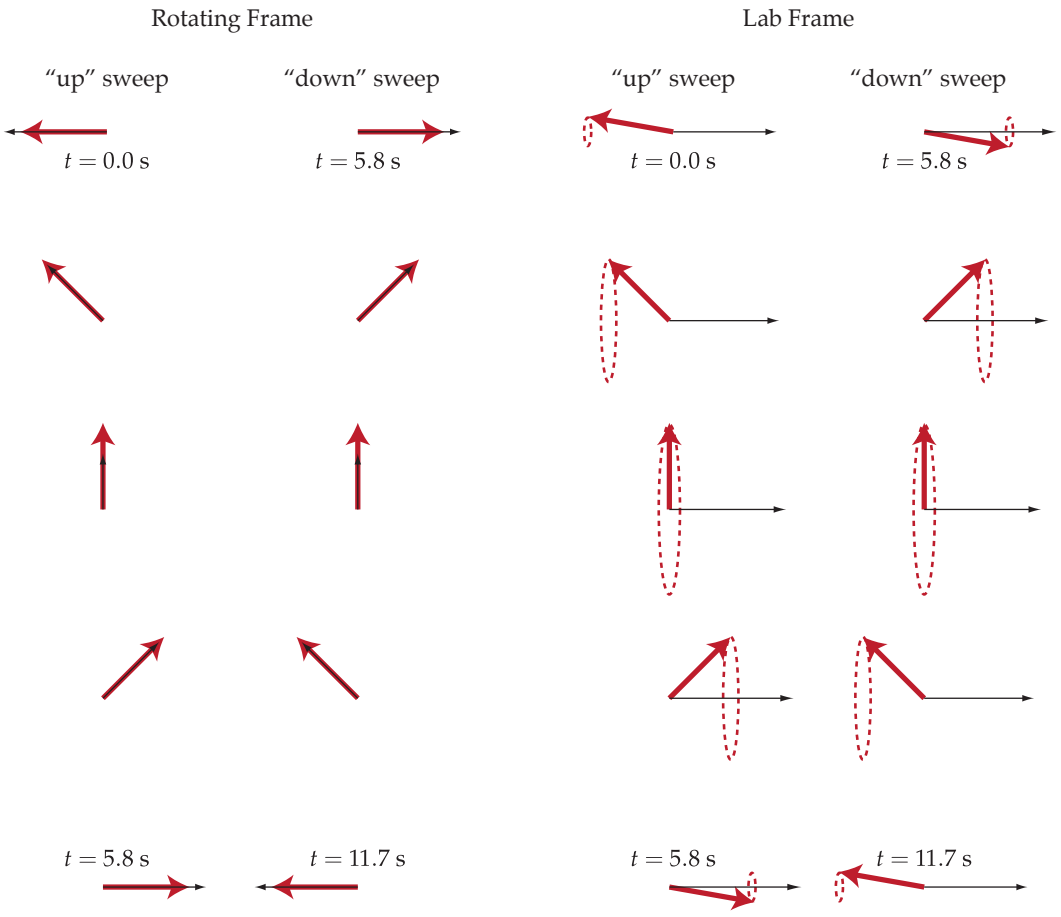

Figure 4.1: Adiabatic Fast Passage of SEOP Polarized ^{3}He Spins in the Rotating & Lab Frames. The thick red (thin black) arrow is the polarization vector (effective field) in the rotating and lab frames. In the lab frame, the polarization vector is precessing about the holding field at a RF frequency $\omega_{\mathtt{rf}}$.

4.3 NMR

According to Eqn. (4.21), the components of the polarization vector that are perpendicular to the holding field oscillate in time with a frequency of $\omega_{\mathtt{rf}}$. This motion of the spins results in an oscillating magnetic field due to the polarized ^{3}He gas, see Fig. (4.1). In the NMR technique [4,10], a set of appropriately oriented "pickup" coils are placed near the cell. The oscillating $\vec{B}_{\mathrm{He}}$ induces a small oscillating voltage in these pickup coils, which is then amplified by a lock-in amplifier referenced to $\omega_{\mathtt{rf}}$. Away from resonance $|\Delta| \gg \omega_1$, the induced voltage is small, while, near resonance $|\Delta| \approx 0$, the induced voltage is large. In the following sections, we will derive the lineshape (voltage measured by the lock-in as a function of time) of the NMR signal as the detuning Δ is swept linearly. The equations that follow are equally valid for both field and frequency sweep AFP.

4.3.1 Pickup Coil Voltage

The voltage $\mathcal{V}$ induced in the pickup coils by the flipping spins is given by Faraday's Law [11]:

$$\mathcal{V}(t) = -\frac{d}{dt}\int \vec{B}_{\mathrm{He}}(\vec{r},t)\cdot d\vec{a} \tag{4.28}$$

where $d\vec{a}$ infinitesimal area vector on the surface of the pickup coil. By representing the field as the magnetic vector potential and applying Stokes's Theorem, the flux integral over the area of the coils can be reduced to an integral around the path of the coils [12–14]:

$$\int \vec{B}_{\mathrm{He}}(\vec{r},t)\cdot d\vec{a} = \int \left(\nabla\times\vec{A}(\vec{r},t)\right)\cdot d\vec{a} = \oint \vec{A}(\vec{r},t)\cdot d\vec{l} \tag{4.29}$$

which gives:

$$\mathcal{V} = -\frac{\mu_0}{4\pi} \int \oint \frac{d\vec{M}(\vec{u}, t)}{dt} \times \left[\frac{\vec{r} - \vec{u}}{|\vec{r} - \vec{u}|^3} \right] \cdot d\vec{l}\, d^3u \tag{4.30}$$

where $\vec{u}$ is the displacement vector from the origin to the infinitesimal volume element d^3u inside the cell and $\vec{r}$ is the displacement vector from the origin to the infinitesimal line element $d\vec{l}$ of the pickup coil.

The total time derivative of some vector $\vec{V}$ in the lab frame is related to its time derivative in the rotating frame by:

$$\left[\frac{d\vec{V}}{dt} \right]_{\text{lab}} = \left[\frac{\partial \vec{V}}{\partial t} \right]_{\text{rot}} + \left[\left(\vec{\omega} + t \frac{d\vec{\omega}}{dt} \right) \times \vec{V} \right]_{\text{rot}} \tag{4.31}$$

where $\vec{\omega}$ is the possibly time varying angular velocity of the rotating frame relative to the lab frame. The $d\omega/dt$ term is sometimes referred to as the "Euler force" term [15] and it can neglected if the relative change in ω is small over the time scale during which the vector $\vec{V}$ is changing the most. In our case, this occurs for the magnetization vector during the time $t_0 \approx \omega_1/|\dot{\Delta}|$ near resonance, and with $\omega = -s\omega_{\texttt{rf}}$, we find:

$$\delta_R \equiv \left| \frac{1}{\omega} \frac{\partial \omega}{\partial t} \left(\frac{|\Delta \vec{V}|}{|d\vec{V}/dt|} \right) \right| = \left(\frac{\dot{\omega}_{\texttt{rf}}}{\omega_{\texttt{rf}}} \right) \left(\frac{\omega_1}{|\dot{\Delta}|} \right) \ll 1 \tag{4.32}$$

This is easily satisfied under our conditions because $\omega_1 \ll \omega_{\texttt{rf}}$ and we'll simply ignore the Euler force ($\dot{\omega}_{\texttt{rf}}$) terms going forward. Using the components (p_x, p_y, p_z) of the polarization vector in the rotating frame, we find that the time derivative of the polarization vector in the lab frame is:

$$\left[\frac{d\vec{p}}{dt} \right]_{\text{lab}} = \left(\frac{dp_x}{dt} \right) \hat{x}_{\text{rot}} + \left(\frac{dp_y}{dt} \right) \hat{y}_{\text{rot}} + \left(\frac{dp_z}{dt} \right) \hat{z} - s\omega_{\texttt{rf}} \hat{z} \times \vec{p} \tag{4.33}$$

which gives the total time derivative of the magnetization vector in the lab frame:

$$\left[\frac{d\vec{M}}{dt}\right]_{\text{lab}} = \left[\frac{g\mu_N P_{\text{He}} n}{2}\right]\left[\frac{\omega_1}{\Omega}\right]\left[\omega_{\texttt{rf}}\hat{x}_{\text{rot}} - s\frac{\dot{\Omega}}{\Omega}\hat{y}_{\text{rot}} + s\frac{\dot{\Delta}\omega_1}{\Omega^2}\hat{z}\right] \tag{4.34}$$

where $\hat{x}_{\text{rot}}$ is given by:

$$\hat{x}_{\text{rot}} = \left(\frac{s}{\omega_{\texttt{rf}}}\right)\frac{d\hat{y}_{\text{rot}}}{dt} = \hat{y}_{\text{rot}} \times \hat{z} = \hat{x}\cos(s\omega_{\texttt{rf}}t) - \hat{y}\sin(s\omega_{\texttt{rf}}t) \tag{4.35}$$

The terms related to $\hat{y}_{\text{rot}}$ and $\hat{z}$ are negligible when the RWA and adiabatic condition are valid (i.e. under our conditions):

$$\left|-s\frac{\dot{\Omega}}{\Omega}\right| \ll \frac{\Omega}{2\pi} \ll \frac{\omega_{\texttt{rf}}}{\pi} < \omega_{\texttt{rf}} \qquad \left|s\frac{\dot{\Delta}\omega_1}{\Omega^2}\right| \leq \frac{|\dot{\Delta}|}{\omega_1} \ll \frac{\omega_1\sqrt{27}}{4\pi} \ll \omega_{\texttt{rf}} \tag{4.36}$$

Dropping these small terms, we can the write the induced voltage as:

$$\mathcal{V} = -\mathcal{V}_x\cos(\omega_{\texttt{rf}}t) + s\mathcal{V}_y\sin(\omega_{\texttt{rf}}t) \tag{4.37}$$

where $\mathcal{V}_N$ is defined as:

$$\mathcal{V}_N = \left[\frac{\mu_0 g\mu_N\omega_{\texttt{rf}}}{8\pi}\right]\int\oint P_{\text{He}}(\vec{u})n(\vec{u})\left(\frac{\omega_1(\vec{u})}{\Omega(\vec{u})}\right)\hat{N}(\vec{u}) \times \left[\frac{\vec{r}-\vec{u}}{|\vec{r}-\vec{u}|^3}\right]\cdot d\vec{l}\,d^3u \tag{4.38}$$

where we've explicitly written out the position dependence of P_{He}, n, ω_1, & Ω and assumed that P_{He} & n do not change much during the measurement.

4.3.2 The Flux Factor

Any spatial gradients in the ^{3}He polarization P_{He}, ^{3}He density n, the RF field $\vec{B}_1$, and the holding field $\vec{B}$ are folded into the integral. Gradients in the magnitude of B_1 and B affect the shape, height, and resonance location of ω_1/Ω. Gradients in the pointing of the RF & holding fields affect the pointing of $\hat{x}_{\mathrm{rot}}$. Because these gradients are expected to be small, we'll parametrize their effect by two unitless quantities $f(\vec{u})$ and G_∇^n, which are equal to unity in the absence of all gradients.

First, a possible polarization and/or density gradient will be contained in the function $f(\vec{u})$:

$$P_{\mathrm{He}}(\vec{u})n(\vec{u}) = \langle P_{\mathrm{He}} \rangle_V \langle n \rangle_V f(\vec{u}) \qquad \int f(\vec{u}) \frac{d^3u}{V} = 1 \tag{4.39}$$

where the brackets $\langle \cdots \rangle_V$ refer to the average over a region with volume V. Second, the effect due to magnetic field gradients can considered by expanding both the lineshape ω_1/Ω and unit vector $\hat{N}$ about the center $\vec{u}_0$ of the region that contains the spins:

$$\begin{aligned}
\left[\frac{\omega_1}{\Omega}\right]_{\vec{u},t} &= \left[\frac{\omega_1}{\Omega}\right]_{\vec{u}_0,t} + (\vec{u}-\vec{u}_0)\cdot\left[\vec{\nabla}\frac{\omega_1}{\Omega}\right]_{\vec{u}_0,t}\cdots \\
&= \left[\frac{\omega_1}{\Omega}\right]_{\vec{u}_0,t} + (\vec{u}-\vec{u}_0)\cdot\left[\vec{\nabla}B_0\right]\frac{\partial}{\partial B_0}\left[\frac{\omega_1}{\Omega}\right]_{\vec{u}_0,t}\cdots \qquad (4.40) \\
\vec{N}(\vec{u}) &= \vec{N}(\vec{u}_0) + (\vec{u}-\vec{u}_0)\cdot\left[\vec{\nabla}\vec{N}\right]_{\vec{u}_0} + \cdots \qquad (4.41)
\end{aligned}$$

Putting this altogether gives:

$$\int\oint P_{\mathrm{He}}(\vec{u})n(\vec{u})\left(\frac{\omega_1(\vec{u})}{\Omega(\vec{u})}\right)\hat{N}(\vec{u})\times\left[\frac{\vec{r}-\vec{u}}{|\vec{r}-\vec{u}|^3}\right]\cdot d\vec{l}\,d^3u = P_{\mathrm{He}}n\left[\frac{\omega_1}{\Omega}\right]_{\vec{u}_0,t}G_\nabla^N(t)\Phi_N \tag{4.42}$$

where P_{He} & n are volume average quantities and we've defined the "flux factor" Φ_N which contains all the geometrical information about the system:

$$\Phi_N = \int \oint f(\vec{u})\, \hat{N}(\vec{u}_0) \times \left[\frac{\vec{r}-\vec{u}}{|\vec{r}-\vec{u}|^3}\right] \cdot d\vec{l}\, d^3u = c\frac{VN_tL}{d^2} \tag{4.43}$$

where V is the volume of the region containing the spins, L is the length of the coils, N_t is the number of turns, d is the distance between the center of the spin region & the center of the pickup coils, and c is a unitless (and possibly negative) number that contains all of the information about the integral & is of order 0.1 under our conditions. The "gain" due to magnetic field gradients is defined as:

$$\begin{aligned} G_\nabla^N(t) &= \frac{1}{\Phi_N}\int \oint f(\vec{u}) \left\{1 + (\vec{u}-\vec{u}_0)\cdot\left[\vec{\nabla}\frac{\omega_1}{\Omega}\right]_{\vec{u}_0,t}\left[\frac{\Omega}{\omega_1}\right]_{\vec{u}_0,t} + \cdots\right\} \\ &\quad \cdot\left[\vec{N}(\vec{u}_0) + (\vec{u}-\vec{u}_0)\cdot\left[\vec{\nabla}\vec{N}\right]_{\vec{u}_0} + \cdots\right] \times \left[\frac{\vec{r}-\vec{u}}{|\vec{r}-\vec{u}|^3}\right]\cdot d\vec{l}\, d^3u \end{aligned} \tag{4.44}$$

In practice, the pickup coils are usually placed near the target chamber. Therefore, it is usually easier to discuss the flux factors from the target chamber Φ_N^{tc} of the cell separately from the flux factors from the pumping chamber Φ_N^{pc} and transfer tube Φ_N^{tt}. Putting this altogether, we find:

$$P_{\mathrm{He}} n \left[\frac{\omega_1}{\Omega}\right]_{\vec{u}_0,t} G_\nabla^N(t)\Phi_N = P_{\mathrm{tc}} n_{\mathrm{tc}} \left[\frac{\omega_1}{\Omega}\right]_{\vec{u}_0,t} G_\nabla^{N,\mathrm{tc}}(t) G_\Phi^N \Phi_N^{\mathrm{tc}} \tag{4.45}$$

where $\vec{u}_0$ is now chosen to be the center of the target chamber and we've defined the "gain" due to the flux G_Φ^N:

$$G_\Phi^N = 1 + \frac{P_{\mathrm{tt}} n_{\mathrm{tt}} G_\nabla^{N,\mathrm{tt}} \Phi_N^{\mathrm{tt}} + P_{\mathrm{pc}} n_{\mathrm{pc}} G_\nabla^{N,\mathrm{pc}} \Phi_N^{\mathrm{pc}}}{P_{\mathrm{tc}} n_{\mathrm{tc}} G_\nabla^{N,\mathrm{tc}} \Phi_N^{\mathrm{tc}}} \to 1 + \frac{P_{\mathrm{tt}} n_{\mathrm{tt}} \Phi_N^{\mathrm{tt}} + P_{\mathrm{pc}} n_{\mathrm{pc}} \Phi_N^{\mathrm{pc}}}{P_{\mathrm{tc}} n_{\mathrm{tc}} \Phi_N^{\mathrm{tc}}} \tag{4.46}$$

where the arrow denotes the value in the absence of magnetic field gradients. Finally, each component of the induced voltage can be written as:

$$\mathcal{V}_N = \left[\frac{\mu_0 g \mu_N \omega_{\mathtt{rf}}}{8\pi}\right] P_{\mathrm{tc}} n_{\mathrm{tc}} \left[\frac{\omega_1}{\Omega}\right]_{\vec{u}_0,t} G_{\nabla}^{N,\mathrm{tc}}(t) G_{\Phi}^{N}(t) \Phi_N^{\mathrm{tc}} \tag{4.47}$$

4.3.3 Signal Shaping Effects

A lock-in amplifier is used to amplify the NMR signal from the pickup coils through a preamplifier. This device essentially performs Fourier cosine and sine transforms of the input signal at some reference frequency and outputs the RMS amplitudes of the two components [16]:

$$\mathcal{V} = -\mathcal{V}_x \cos(\omega_{\mathtt{rf}} t) + s\mathcal{V}_y \sin(\omega_{\mathtt{rf}} t) \quad \Rightarrow \quad \left\{ \begin{array}{c} \mathcal{V}_x/\sqrt{2} \\ \mathcal{V}_y/\sqrt{2} \end{array} \right\} \quad \Rightarrow \quad \mathcal{V}_{\mathrm{in}} = \frac{\mathcal{V}_x}{\sqrt{2}} \sqrt{1 + \frac{\mathcal{V}_y^2}{\mathcal{V}_x^2}} \tag{4.48}$$

where the signals from the two channels are added in quadrature by choosing the phase of the lock-in such that most of the signal is "in" the x-channel. In practice, the pickup coils are oriented such that their area vectors are approximately aligned with $\hat{x}$ and, as a consequence, Φ_y is much smaller than Φ_x. This is done to maximize the voltage induced by the polarized ^{3}He and minimize the voltage induced by the RF field in the $\hat{y}$ direction. Under these conditions, $(\mathcal{V}_y/\mathcal{V}_x)^2 \ll 1$ and $\mathcal{V}_{\mathrm{in}} = \mathcal{V}_x/\sqrt{2}$.

The lock-in "performs" the Fourier transform using a mixer followed by a low pass filter, which distorts the lineshape of the signal in the following way:

$$\frac{d\mathcal{V}_{\mathrm{out}}}{dt} = \frac{\mathcal{V}_{\mathrm{in}} - \mathcal{V}_{\mathrm{out}}}{\tau} \quad \Leftrightarrow \quad \mathcal{V}_{\mathrm{out}}(t) = \frac{1}{\tau} \int_{-\infty}^{t} \exp\left(\frac{u-t}{\tau}\right) \mathcal{V}_{\mathrm{in}}(u)\, du \tag{4.49}$$

where τ is the lockin time constant. Note that since $-\infty < u \leq t$, the quantity $(u - t)$

will always be less than or equal to zero. The output signal is a time averaging of the input signal with exponential weighting. Putting this altogether, we find:

$$\mathcal{V}_{\text{out}}(t) = G_{\text{L}} G_{\text{P}} Q(\omega_0) \left[\frac{\mu_0 g \mu_N \omega_0}{8\pi\sqrt{2}} \right] P_{\text{tc}} n_{\text{tc}} \Phi_x^{\text{tc}} \ell(t) \tag{4.50}$$

where $G_{\text{L}} = 10$ V/(lockin sensitivity) is the gain of the lockin, G_{P} is the gain of the preamp, and $Q(\omega)$ is the frequency dependent response of the pickup coil circuit & BNC cables used for signal transmission, and the lineshape $\ell(t)$ of the signal is given by:

$$\ell(t) = \frac{1}{\tau} \int_{-\infty}^{t} \exp\left(\frac{u-t}{\tau} \right) \left[\frac{Q(\omega_{\texttt{rf}}(u))}{Q(\omega_0)} \right] \left[\frac{\omega_{\texttt{rf}}(u)}{\omega_0} \right] \left[\frac{G_{\nabla}^{x,\text{tc}}(u) G_{\Phi}^{x}(u)}{\sqrt{1 + \Delta^2(u)/\omega_1^2}} \right] du \tag{4.51}$$

4.3.4 Accounting for Relaxation: Modified Bloch Equations

Thus far, we've ignored the possibility of the relaxation of polarization to its equilibrium value. For the case of proton NMR from a sample of liquid water, this is an important omission because the relaxation time constants ($T_{1,2} \approx 3$ s) are on order of the total sweep time ($2t_0 \approx 6$ s). In other words, the "fast" condition ($\delta_F = 2t_0/T_{1,2} \ll 1$) is violated and the magnitude of the polarization changes significantly during the sweep, see Figs. (4.2) & (4.3). The equations that govern the time evolution of the magnetization vector as it approaches equilibrium in the presence of static and RF fields are the modified Bloch equations (MBE) [4]. In the lab frame, as the magnetization approaches the equilibrium value of $\vec{M}^{\infty}$ at a relaxation rate $1/T$, the equations are, in SI units:

$$\left[\frac{d\vec{M}}{dt} \right]_{\text{lab}} = \mu_0 \gamma \left(\vec{M} \times \vec{H}_{\text{tot}} \right) - \left(\frac{\vec{M} - \vec{M}^{\infty}}{T} \right) \tag{4.52}$$

where we've assumed that the relative magnetic permeability of the air, glass, & water are all unity and $\mu_0\vec{H}_{\text{tot}} = B\hat{z} + 2B_1\cos(\omega_{\text{rf}}t)\hat{y}$ in the lab frame. Using Eqn. (4.31) to rewrite these equations in the rotating frame and allowing for different longitudinal & transverse relaxation rates $1/T_1$ & $1/T_2$ and equilibrium polarization $\vec{M}^{\infty}_{\text{long}}$ & $\vec{M}^{\infty}_{\text{trans}}$, we find:

$$\left[\frac{d\vec{M}}{dt}\right]_{\text{rot}} = \mu_0\gamma\left(\vec{M}\times\vec{H}_{\text{tot}}\right) - \left(\frac{\vec{M}_{\text{long}} - \vec{M}^{\infty}_{\text{long}}}{T_1}\right) - \left(\frac{\vec{M}_{\text{trans}} - \vec{M}^{\infty}_{\text{trans}}}{T_2}\right) - \left(\vec{\omega} + t\frac{d\vec{\omega}}{dt}\right)\times\vec{M} \quad (4.53)$$

where H_{tot} in the rotating frame is given by:

$$\vec{H}_{\text{tot}} = \left[\vec{H}_{\text{long}}\right] + \left[\vec{H}_{\text{trans}}\right] = \left[\frac{B}{\mu_0}\hat{z}\right] + \left[\frac{B_1}{\mu_0}\left\{\hat{y}_{\text{rot}} + \hat{y}_{\text{rot}}\cos(2\omega t) + \hat{x}_{\text{rot}}\sin(2\omega t)\right\}\right] \quad (4.54)$$

In the RWA (i.e. dropping the 2ω terms) and ignoring the Euler force ($\dot{\omega}$) terms, $H_{\text{tot}} = \vec{B}_{\text{eff}}/\mu_0$ in the rotating frame where $\vec{B}_{\text{eff}}$ is given by Eqn. (4.22). It is more convenient to represent the magnetization vector with the polarization vector in the rotating frame:

$$\vec{M} = \frac{g\mu_N}{2}nP_{\text{scale}}\left[p_x\hat{x}_{\text{rot}} + p_y\hat{y}_{\text{rot}} + p_z\hat{z}\right] \quad (4.55)$$

where P_{scale} is some reference polarization used to set the scale for the polarization vector. We can now rewrite the MBE Eqn. (4.53), again ignoring the Euler force ($\dot{\omega}$)

terms following Eqn. (4.32), in the following way:

$$\frac{dp_x}{dt} = +s\Delta p_y - \left(\frac{p_x - p_x^\infty}{T_2}\right) - s\omega_1 p_z \tag{4.56}$$

$$\frac{dp_y}{dt} = -\left(\frac{p_y - p_y^\infty}{T_2}\right) - s\Delta p_x \tag{4.57}$$

$$\frac{dp_z}{dt} = +s\omega_1 p_x - \left(\frac{p_z - p_z^\infty}{T_1}\right) \tag{4.58}$$

where $B_1 = \omega_1/|\gamma|$ is the magnitude of the RF field in the rotating frame, $\Delta = (|\gamma|B - \omega_{\mathtt{rf}})$ is the detuning, B is the magnitude of the holding field, s is the sign of the particle's magnetic moment, $1/T_1$ & $1/T_2$ are the longitudinal & transverse relaxation rates, and the equilibrium values are defined by:

$$\vec{M}_{\text{long}}^\infty = \frac{g\mu_N}{2} n P_{\text{scale}} \left[p_x^\infty \hat{x}_{\text{rot}} + p_y^\infty \hat{y}_{\text{rot}}\right] \tag{4.59}$$

$$\vec{M}_{\text{trans}}^\infty = \frac{g\mu_N}{2} n P_{\text{scale}} p_z^\infty \hat{z} \tag{4.60}$$

These differential equations must be solved numerically using the appropriate initial conditions (p_x^0, p_y^0, p_z^0). The values $(p_x^{\text{eq}}, p_y^{\text{eq}}, p_z^{\text{eq}})$ for the polarization components that give $d\vec{p}/dt = 0$ are:

$$\begin{aligned} p_x^{\text{eq}} &= \frac{p_x^\infty + sT_2\left(\Delta p_y^\infty - \omega_1 p_z^\infty\right)}{1 + \omega_1^2 T_1 T_2 + \Delta^2 T_2^2} \\ p_y^{\text{eq}} &= p_y^\infty - s\Delta T_2 p_x^{\text{eq}} \\ p_z^{\text{eq}} &= p_z^\infty + s\omega_1 T_1 p_x^{\text{eq}} \end{aligned} \tag{4.61}$$

Because $\omega_{\mathtt{rf}} \gg \omega_1 \gg 1/T_1, 1/T_2$ under our conditions, $\omega_{\mathtt{rf}} p_y$ is much greater than the rotating frame derivatives $\dot{p}_y$ & $\dot{p}_z$ (which are essentially the approximations made in Sec. (4.3.1)) and, in this case, $\omega_{\mathtt{rf}} p_y \gg \dot{p}_x$. Using these approximations and

following the arguments of Sec. (4.3.3), we find:

$$\mathcal{V}_{\text{out}}(t) = G_{\text{L}} G_{\text{P}} Q(\omega_0) \left[\frac{\mu_0 g \mu_N \omega_0}{8\pi\sqrt{2}} \right] P_{\text{scale}} n_{\text{tc}} \Phi_x^{\text{tc}} \ell_B(t) \tag{4.62}$$

and the lineshape $\ell_B(t)$ of the signal is given by:

$$\ell_B(t) = \frac{1}{\tau} \int_{-\infty}^{t} \exp\left(\frac{u-t}{\tau} \right) \left[\frac{Q(\omega_{\mathtt{rf}}(u))}{Q(\omega_0)} \right] \left[\frac{\omega_{\mathtt{rf}}(u)}{\omega_0} \right] \left[G_{\nabla}^{x,\text{tc}}(u) G_{\Phi}^{x}(u) p_y(u) \right] \, du \tag{4.63}$$

and it is straightforward to show that when the fast condition, Eqn. (4.25), is met, p_y reduces to ω_1/Ω.

For the case of protons in liquid water (i.e. thermal polarization), see Fig. (4.3), we'll make the choice to set the scale polarization to the thermal equilibrium polarization $P_{\text{scale}} = \chi H_0$ at the resonance field $B_0 = \omega_0/|\gamma|$:

$$P_{\text{th}}(B,T) = \tanh\left(\frac{g\mu_N B}{2kT} \right) \approx \frac{g\mu_N B}{2kT} = \frac{g\mu_N \mu_0 H}{2kT} = \chi H \tag{4.64}$$

where $P_{\text{th}}(B,T)$ is the thermal equilibrium polarization for a spin-1/2 particle due to a field B at a temperature T, k is the Boltzmann constant, and the magnetic χ_0 & "reduced" magnetic χ susceptibilities are given by:

$$\chi_0 = \frac{g\mu_N n}{2} \chi = \frac{\gamma^2 \hbar^2 n \mu_0}{4kT} \qquad \chi = \frac{g\mu_N \mu_0}{2kT} = \frac{\gamma \hbar \mu_0}{2kT} \tag{4.65}$$

We'll make the same classic argument originally put forth by Bloch [20] that the equilibrium polarizations approached are the thermal equilibrium polarizations

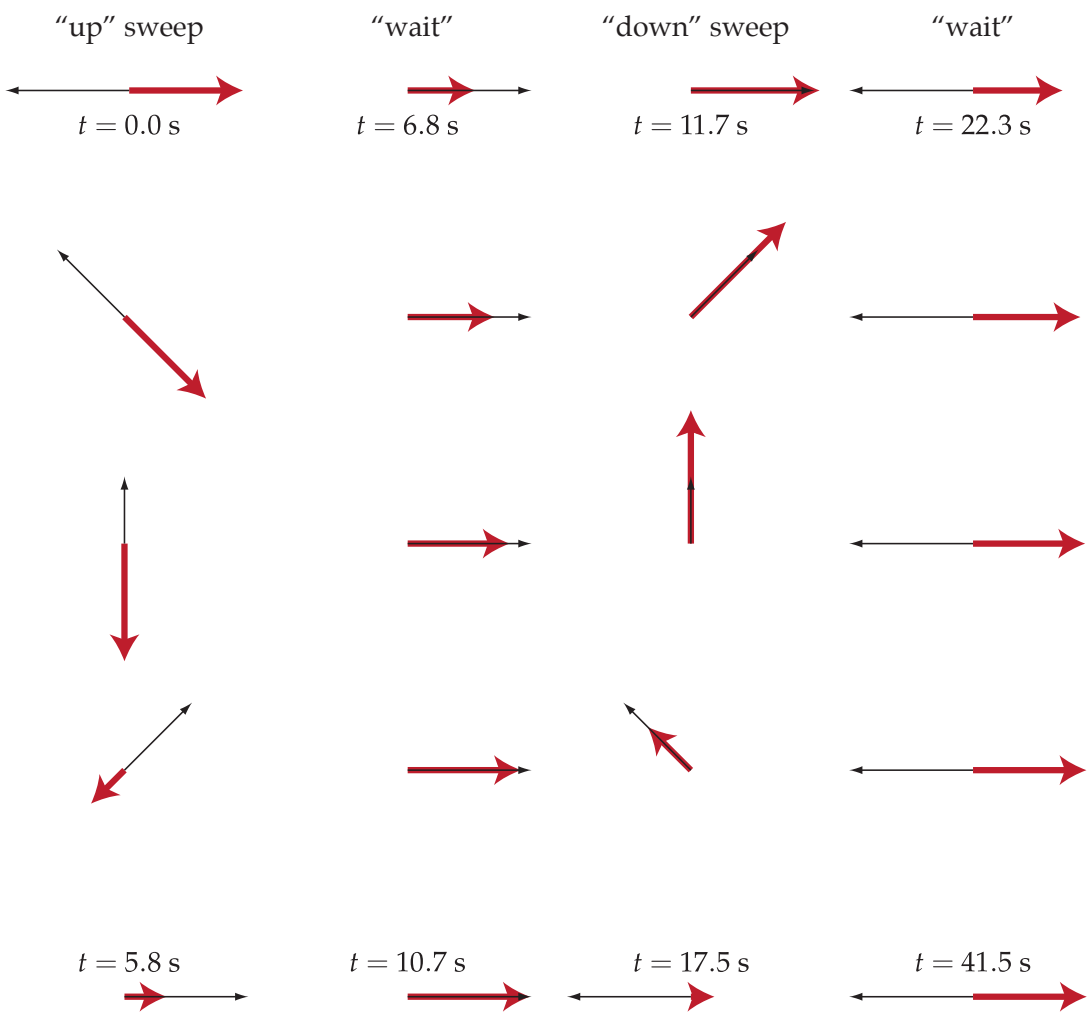

Figure 4.2: Adiabatic Passage of Thermally Polarized Proton Spins in the Rotating Frame. The thick red (thin black) arrow is the polarization vector (effective field).

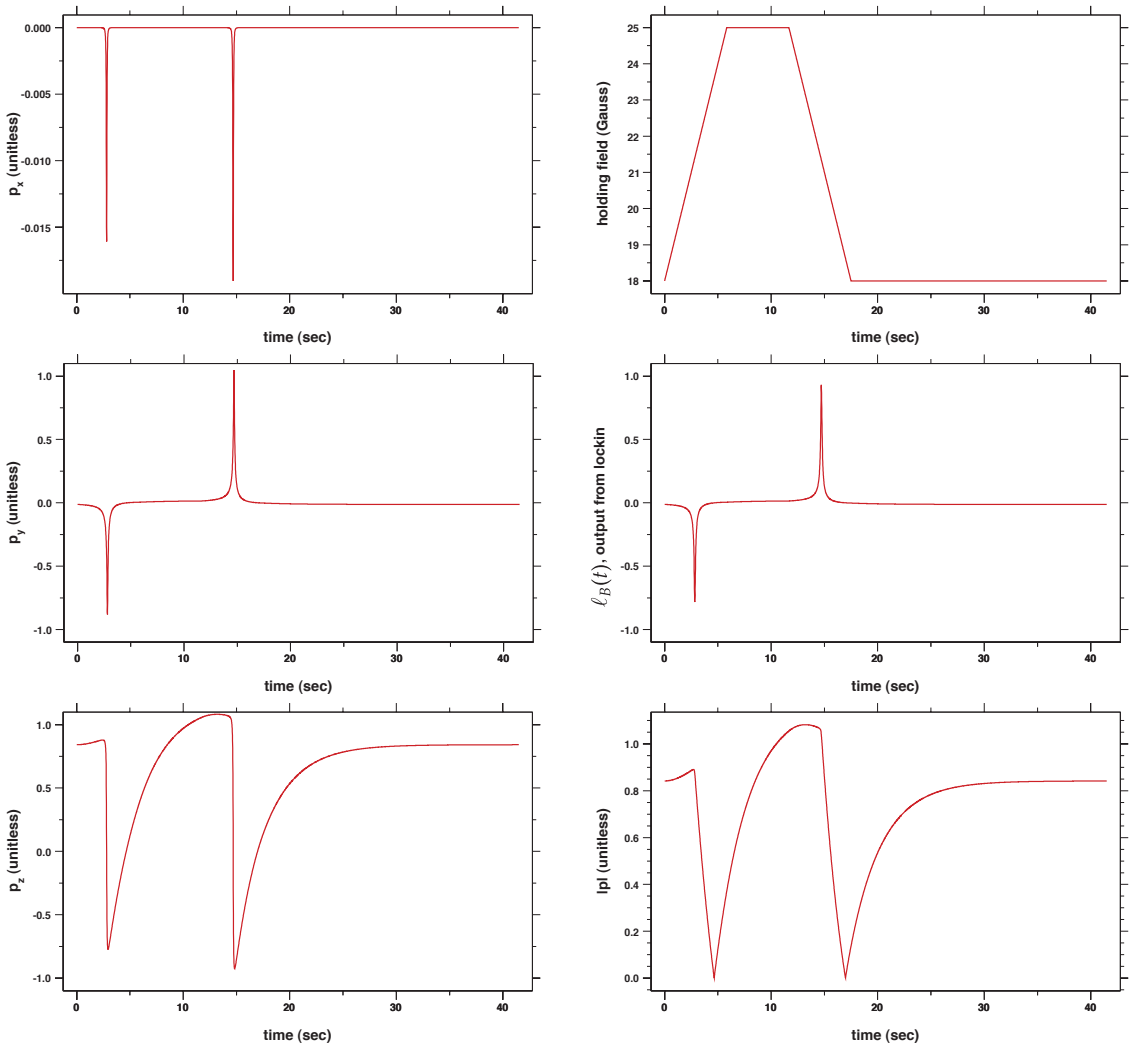

Figure 4.3: Numerical Solution to MBE for Thermal Protons in Liquid Water. Solution was found using the "standard" 4^{th} order Runge-Kutta algorithm [17–19] with a time step size of 4.15 μs, $T_1 = 3.65$ s, $T_2 = 3.25$ s, $\dot{B} = 1.2$ G/s, "wait" time between sweeps of 5.83 s, "wait" time between sweep cycles of 24 s, $B_1 = 53$ mG, $\nu_{\mathtt{rf}} = 91$ kHz, a lockin time constant of $\tau = 30$ ms, and no field gradients $G_{\nabla}^{x,\text{tc}} = 1$.

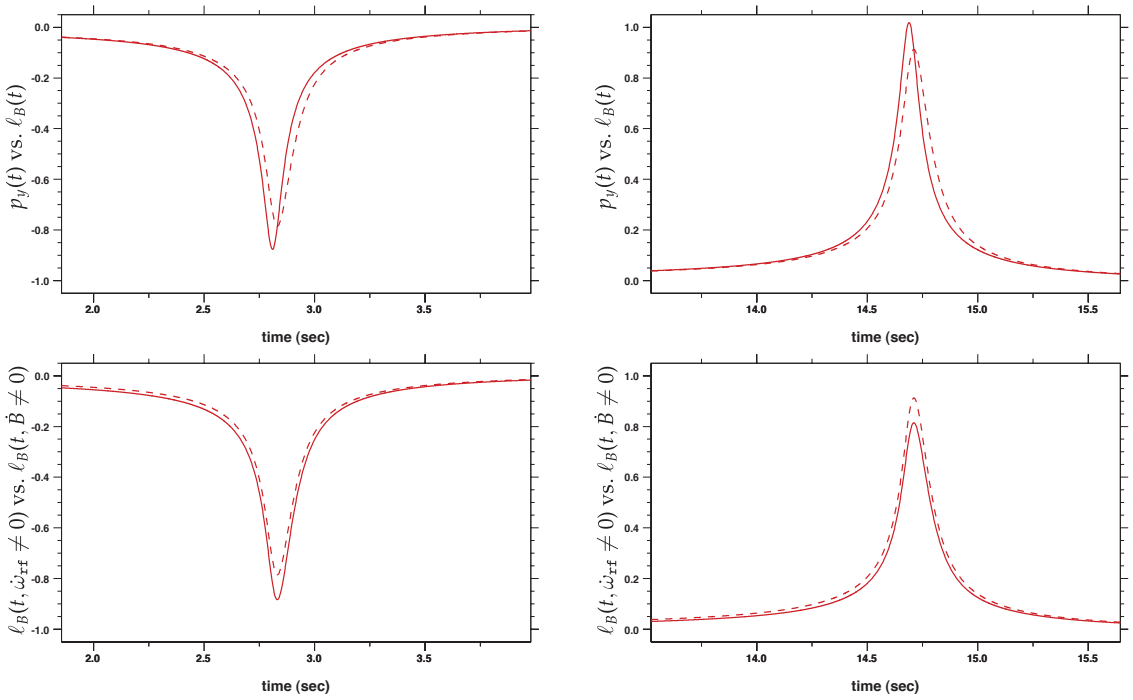

Figure 4.4: Top: Lockin Input (solid) vs. Lockin Output (dashed) for Field Sweep AFP. Bottom: Frequency Sweep AFP (solid) vs. Field Sweep AFP (dashed) for Lockin Output. The lockin time constant was $\tau = 30$ ms and we've assumed that $Q(\omega_{\mathtt{rf}}) = Q(\omega_0)$ for all $\omega_{\mathtt{rf}}$. The field sweep was from 18 G to 25 G with $\nu_{\mathtt{rf}} = 91.54$ kHz, whereas the frequency sweep was from 105.4 kHz to 75.56 kHz with $B_0 = 21.37$ G. All other input parameters were the same as Fig. (4.3).

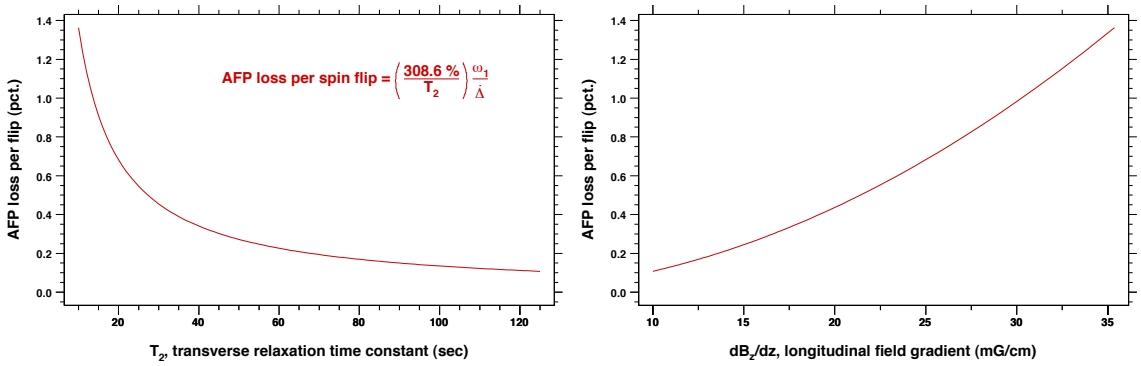

Figure 4.5: ^{3}He AFP polarization loss per spin flip vs. T_2 and dB_z/dz. We've used Eqn. (4.26) using $D = 0.2$ cm^2/s, $B_1 = 50$ mG, and $\dot{B} = 1.2$ G/s. See caption of Fig. (4.6) for other ^{3}He input parameters.

due to the static and RF fields in the rotating frame:

$$p_x^\infty = 0 \qquad p_y^\infty = \frac{B_1}{B_0} \qquad p_z^\infty = \frac{B}{B_0} \tag{4.66}$$

The initial conditions used in the numerical solution to these equations are the values $(p_x^{\mathrm{eq}}, p_y^{\mathrm{eq}}, p_z^{\mathrm{eq}})$ given by:

$$\begin{aligned} p_x^0 &= p_x^{\mathrm{eq}} = -s\omega_1 T_2 \left(\frac{\omega_{\mathtt{rf}}}{\omega_0}\right)\eta & (4.67)\\ p_y^0 &= p_y^{\mathrm{eq}} = \frac{\omega_1}{\omega_0}\left[1 + \Delta\omega_{\mathtt{rf}} T_2^2 \eta\right] & (4.68)\\ p_z^0 &= p_z^{\mathrm{eq}} = \frac{B}{B_0} - \omega_1^2 T_1 T_2 \left(\frac{\omega_{\mathtt{rf}}}{\omega_0}\right)\eta & (4.69)\\ \eta &= \left[1 + \omega_1^2 T_1 T_2 + \Delta^2 T_2^2\right]^{-1} & (4.70) \end{aligned}$$

For the case of SEOP polarized ^{3}He (i.e. nonthermal polarization), see Fig. (4.6), the scale polarization is the ^{3}He polarization immediately before the measurement $P_{\mathrm{scale}} = P_{\mathrm{He}}$. The equilibrium polarization are:

$$p_x^\infty = 0 \qquad p_y^\infty = \chi H_1 / P_{\mathrm{He}} \tag{4.71}$$

$$p_z^\infty = \chi H / P_{\mathrm{He}} \quad \text{(spindown)} \qquad p_z^\infty = P_{\mathrm{He}}^\infty / P_{\mathrm{He}} \quad \text{(spinup)} \tag{4.72}$$

where p_z^∞ depends on whether the ^{3}He polarization is decaying to its thermal equilibrium value (i.e. a "spindown") or building up to its equilibrium value due to spin-exchange (i.e. a "spinup"). The initial conditions used as input for the numerical solution are given by:

$$p_x^0 = 0 \qquad p_y^0 = \frac{\omega_1}{\Omega(t=0)} \qquad p_z^0 = \frac{\Delta(t=0)}{\Omega(t=0)} \tag{4.73}$$

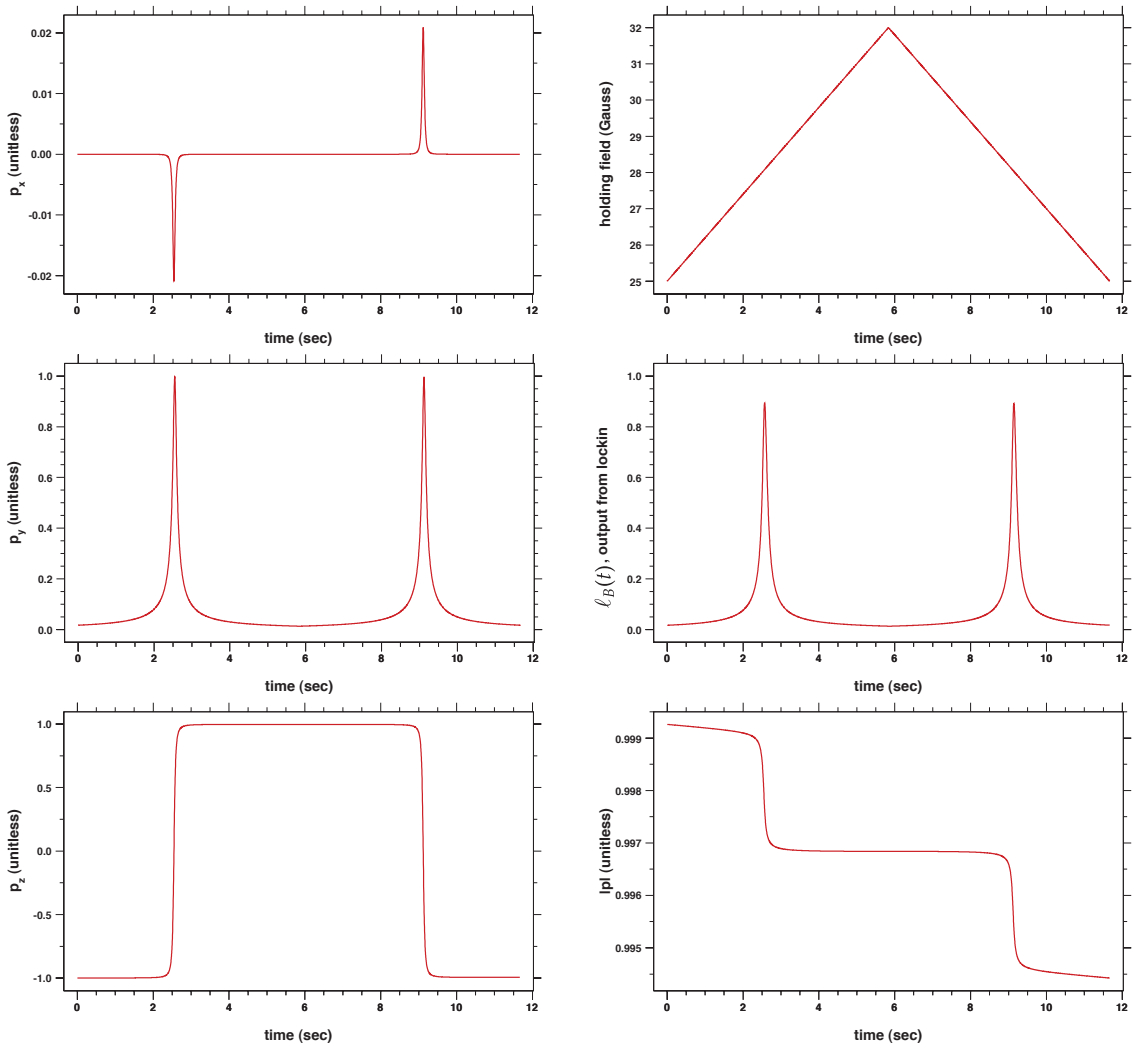

Figure 4.6: Numerical Solution to MBE for SEOP Polarized ^{3}He . Solution was found using the "standard" 4$^{\text{th}}$ order Runge-Kutta algorithm [17–19] with a time step size of 1.17 μs, $T_1 = 10$ hr, $T_2 = 60$ s, $\dot{B} = 1.2$ G/s, $B_1 = 53$ mG, $\nu_{\mathtt{rf}} = 91$ kHz, $P_{\text{He}} = 0.38$, $P_{\text{He}}^{\infty} = 0.42$, a lockin time constant of $\tau = 30$ ms, and no field gradients $G_{\nabla}^{x,\text{tc}} = 1$.

4.4 EPR Frequency Shift Polarimetry

4.4.1 Introduction

The *optical* detection of *radiofrequency* magnetic resonance in alkali atoms has a long history that is intimately linked to the development of optical pumping, see for example [21–26] and the optical pumping references in Sec. (5.2.2). Early on, it was predicted and observed that the radiofrequency spectra of optically pumped alkali atoms are shifted due to spin exchange collisions, see for example [27,28]. The "EPR" method described here [29–35] is a direct descendant of those techniques, which takes advantage of the vaporized alkali metal present in the pumping chamber of the target cell. These alkali metal atoms experience a small "effective" field due to the presence of polarized ^{3}He gas. According to Eqn. (4.21), when the NMR RF frequency is far from resonance $\Delta \gg \omega_1$, the effective field due to the ^{3}He nuclei points in the z-direction. This field (10's of mG) produces small but precisely detectable Zeeman shifts (10's of kHz) in the alkali EPR spectrum that is proportional to the ^{3}He polarization and density. The average EPR transition frequency is located by exciting the EPR transitions with a set of EPR RF coils and observing the resulting change in some probe that is sensitive to the alkali polarization. This probe has traditionally been the intensity of the D2 fluorescence that results from optical pumping. The EPR RF coil frequency is modulated to transform the signal from the photodiode into an error signal (i.e. a voltage linearly proportional to the detuning from resonance). A proportional/integral (PI) feedback loop uses this error signal to lock the RF coil frequency to the intensity averaged EPR frequency while the direction of the ^{3}He spins is reversed via AFP. This reversal isolates the ^{3}He contribution to the EPR frequency and consequently the ^{3}He polarization can

be extracted from this frequency shift, Sec. (4.4.4). Additional sources of frequency shifts correlated with the spin reversal include a drift in the baseline magnetic field, the NMR RF AC Zeeman shift, Sec. (4.4.5), and a coupling between the fluorescence intensity to magnetic field gradients, Sec. (4.4.6).

4.4.2 The Error Signal: "FM Sweep" Lineshape

The EPR transitions are driven using a small RF coil, located near the pumping chamber, producing an RF field perpendicular to the main holding field. The modulation of the EPR RF frequency is described by:

$$\omega_{\mathrm{RF}} = \omega_m + (\Delta\omega)_m + \Omega_{\mathrm{mod}} \cos(\omega_{\mathrm{mod}} t) \tag{4.74}$$

where ω_{RF} is the EPR coil frequency, $(\Delta\omega)_m$ 1s the detuning between the coil frequency and the EPR transition frequency ω_m between the m and $m-1$ states, m is the z-component of the total alkali angular momentum, Ω_{mod} is the FM amplitude, and ω_{mod} is the FM frequency. This excitation induces EPR transitions in the alkali metal atoms and slightly lowers the alkali polarization. Because of the rapid and efficient spin-exchange between alkali metal atoms, the equilibrium alkali polarization tracks the modulation of the excitation. When the excitation is off resonance, the alkali polarization is high. When the excitation is on resonance, the alkali polarization is lowered. This results in a modulation of the alkali polarization which in turn results in a modulation of the intensity of the fluorescence.

Although the presence of N_2 molecules greatly suppresses the number of radiative decays, a few percent of the transitions back to the ground state still occur radiatively. The amount of D1 and D2 fluorescence is roughly the same due to

the collisional mixing of the excited states by the N_2 molecules. However, a filter is placed in front of a photodiode to allow transmission of only the D2 fluorescence. This is because the large D1 background from the pump laser light could potentially saturate the photodiode.

Combining Eqns. (5.70) & (5.20), assuming a pump light polarization of unity, and neglecting the small contribution of off-resonant D2 absorption to the population of the $P_{3/2}$ excited state, we can write the power of the D2 fluorescence measured by the photodiode (on the order of mW under our typical operating conditions) as:

$$\begin{aligned} P_{\mathrm{D2}} &= A_{\mathrm{pd}} \sum_q \int h\nu \, d\Phi_f^{q,2} \, d\nu \\ &= \int\int \left[\frac{A_{\mathrm{pd}}}{4\pi |\vec{u}|^2} \right] f'_{\mathrm{rad}} f_d \, [1 - P_{\mathrm{A}}] \, [\mathrm{Rb}] V_{\mathrm{pc}} h\nu R W(\nu, \vec{r}, \vec{u}) \left(\frac{d^3u}{V_{\mathrm{pc}}} \right) \left(\frac{d\nu}{\nu_2} \right) \end{aligned} \quad (4.75)$$

where A_{pd} is the area the photodiode, f'_{rad} is probability that atom decays radiatively ($\approx \left(0.43\% \cdot \mathrm{amg}\right) / [\mathrm{N_2}]$), $f_d \approx 1/7$ is the probability of that the atom decays from the $P_{3/2}$ excited state, P_{A} is the alkali polarization, [Rb] is the Rb number density, V_{pc} is the pumping chamber volume, h is Planck's constant, R is the unpolarized absorption rate, ν_2 is the frequency of the D2 transition, and W is a geometric factor that describes the transmission probability of a fluorescence photon with frequency ν from a volume element d^3u located at $\vec{u}$ to the surface of the photodiode located at $\vec{r}$:

$$W(\nu, \vec{r}, \vec{u}) = \sum_{k,q} \left[\frac{\sigma_2(\nu)}{\int \sigma_2(\nu) \, (d\nu/\nu_2)} \right] \Lambda_k^q \left(\frac{d_k}{d} \right) f_q(\theta) T_q(\nu, \vec{u}, \vec{r}) H(R_{\mathrm{pc}} - |\vec{r} + \vec{u}|) \quad (4.76)$$

where the parameters are defined in Sec. (5.4.3). At equilibrium, the alkali polar-

ization term can be rewritten using:

$$R(1-P_{\mathrm{A}}) = P_{\mathrm{A}}\left(\Gamma_{\mathrm{A}}+\gamma_{\mathtt{rf}}\right) = R\left[\frac{\Gamma_{\mathrm{A}}+\gamma_{\mathtt{rf}}}{R+\Gamma_A+\gamma_{\mathtt{rf}}}\right] \approx P_0\Gamma_{\mathrm{A}} + P_0^2\gamma_{\mathtt{rf}} \quad \leftrightarrow \quad \gamma_{\mathtt{rf}} \ll R+\Gamma_{\mathrm{A}} \tag{4.77}$$

where $\gamma_{\mathtt{rf}}$ is the relaxation rate due the EPR RF excitation, Γ_{A} is the alkali relaxation rate without the EPR RF excitation, and P_0 is the alkali polarization without the EPR RF excitation.

The photodiode current is converted into a voltage by a transimpedance amplifier circuit which is then fed into a lockin amplifier:

$$\mathcal{V}_{\mathrm{in}} = -R_{\mathrm{pd}}\alpha_{\mathrm{pd}}\int I_{\mathrm{scale}}(1-P_{\mathrm{A}})\,d\mathcal{Z} = \int V_{\mathrm{scale}}P_0\left[1+P_0\left(\frac{\gamma_{\mathtt{rf}}}{\Gamma_{\mathrm{A}}}\right)\right]d\mathcal{Z} \tag{4.78}$$

where α_{pd} is the photodiode sensitivity, R_{pd} is transimpedance resistor, I_{scale} & V_{scale} are the "scale" intensity and voltage that hides all of the other factors, $d\mathcal{Z} = (d^3u/V_{\mathrm{pc}})(d\nu/\nu_2)$. The frequency modulation is hidden in the frequency dependence of the EPR RF excitation relaxation rate $\gamma_{\mathtt{rf}}$ given by Eqn. (E.872), which is a sum of Lorentzian lineshapes for each transition:

$$\gamma_{\mathtt{rf}}(\omega_{\mathrm{RF}}) = \sum_m D_a\Gamma_{\mathrm{RF}}^m\left[\frac{\gamma_m^2}{(\omega_{\mathrm{RF}}-\omega_m)^2+\gamma_m^2}\right] \tag{4.79}$$

where $D_a = 1$ ($D_a = D = [\mathrm{K}]/[\mathrm{Rb}]$) when probing Rb (K) transitions, m labels the $m \leftrightarrow (m-1)$ transition, Γ_{RF}^m is the relaxation rate at resonance (which is proportional to the square of the EPR RF field, see Eqns. (E.872) & (E.407)) and γ_m is the effective alkali hyperfine relaxation rate (on order of 10's of kHz) which is dominated by alkali-alkali spin-exchange collisions [36–38]. The Fourier integral (per-

formed by the lockin mixer) is evaluated by integrating by parts to give [39]:

$$\mathcal{F}_c(\mathcal{V}_{\text{in}}) = \int \cos(\omega_{\text{mod}} t)\mathcal{V}_{\text{in}}\, dt = \frac{\sin(\omega_{\text{mod}} t)}{\omega_{\text{mod}}}\mathcal{V}_{\text{in}} - \frac{1}{\omega_{\text{mod}}}\int \frac{d\mathcal{V}_{\text{in}}}{dt}\sin(\omega_{\text{mod}} t)\, dt \quad (4.80)$$

The high frequency parts are integrated away by the low pass filter to give the lockin output:

$$\mathcal{V}_{\text{out}}(t) = -\frac{G_{\text{L}}}{\omega_{\text{mod}}\tau}\int\int \exp\left[\frac{t'-t}{\tau}\right]\sin(\omega_{\text{mod}} t')V_{\text{scale}}\left(\frac{P_0^2}{\Gamma_{\text{A}}}\right)\frac{d\gamma_{\texttt{rf}}}{dt'}\, d\mathcal{Z}\, dt' \quad (4.81)$$

where τ is the lockin time constant and G_{L} is the lockin gain. Expanding the derivative of $\gamma_{\texttt{rf}}$ using the chain rule $d\gamma_{\texttt{rf}}/dt = (d\gamma_{\texttt{rf}}/d\omega_{\text{RF}})(d\omega_{\text{RF}}/dt)$, noting that $\sin^2(\omega_{\text{mod}} t) = 1 - \cos^2(\omega_{\text{mod}} t)$, dropping the high frequency terms, and averaging the derivative near resonance, we find:

$$\mathcal{V}_{\text{out}}(t) = G_{\text{L}}\Omega_{\text{mod}}\int V_{\text{scale}}\left(\frac{P_0^2}{\Gamma_{\text{A}}}\right)\left\langle\frac{d\gamma_{\texttt{rf}}}{d\omega_{\text{RF}}}\right\rangle d\mathcal{Z} \quad (4.82)$$

where the time averaged derivative near resonance is given by:

$$\left\langle\frac{d\gamma_{\texttt{rf}}(\omega_{\text{RF}})}{d\omega_{\text{RF}}}\right\rangle = \sum_m \frac{2D_a\Gamma_{\text{RF}}^m\gamma_m^2(\omega_m - \omega_{\text{RF}})}{\left(\gamma_m^2 + (\Delta\omega)_m^2\right)^2 + \left(\gamma_m^2 + 3(\Delta\omega)_m^2\right)\Omega_{\text{mod}}^2 + \frac{3}{8}\Omega_{\text{mod}}^4} \quad (4.83)$$

where $(\Delta\omega)_m = \langle\omega_{\texttt{EPR}}\rangle - \omega_m$ and $\langle\omega_{\texttt{EPR}}\rangle$ is the intensity averaged EPR frequency.

Because of the frequency modulation of the EPR excitation, the lineshape that is produced when the lockin response is plotted against the detuning of the EPR excitation is the derivative of a Lorentzian-like lineshape, see Fig. (4.7). This "FM sweep" lineshape directly determines the behavior of the feedback loop [30] used to lock to the EPR transition. Modulation and lock-in parameters (i.e. modula-

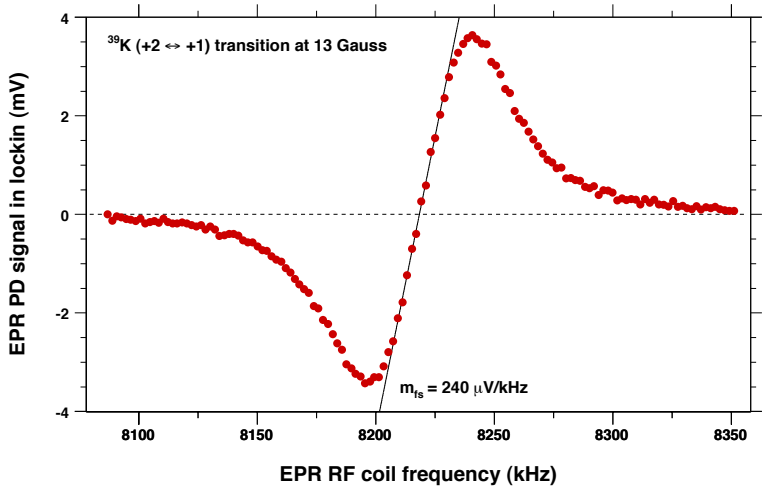

Figure 4.7: FM Sweep lineshape. This is an example of a "good" FM sweep because (1) the slope has the correct sign, (2) the lineshape is visibly symmetric, (3) there does not appear to be an offset, and (4) the zero-crossing is in the middle of the lineshape.

tion amplitude, modulation frequency, lockin sensitivity, lockin phase, lockin time constant, absolute & relative gains on the PI feedback box) must be adjusted to produce an optimal FM sweep lineshape. The "feedback slope" is typically quoted in units of μV per kHz and provides a conversion between the detuning of EPR RF coil frequency and the voltage response of the excitation/sensing electronics:

$$m_{\mathtt{fs}} \equiv \frac{1}{G_{\mathrm{L}}}\left|\frac{d\mathcal{V}_{\mathrm{out}}}{d\omega_{\mathrm{RF}}}\right| = \sum_m \int \frac{\left[2V_{\mathrm{scale}}P_0^2/\Gamma_{\mathrm{A}}\right]\left[\Omega_{\mathrm{mod}}D_a\Gamma_{\mathrm{RF}}^m\gamma_m^2\right]}{\left(\gamma_m^2+(\Delta\omega)_m^2\right)^2+\left(\gamma_m^2+3(\Delta\omega)_m^2\right)\Omega_{\mathrm{mod}}^2+\frac{3}{8}\Omega_{\mathrm{mod}}^4}\,d\mathcal{Z} \quad (4.84)$$

Increasing the modulation amplitude increases the slope when $\Omega_{\mathrm{mod}} \ll \gamma_m$. An increase in the temperature increases the alkali vapor number density. This increases the alkali-alkali spin-exchange rate, which broadens the RF lineshape, reduces the slope, and, consequently, reduces the signal to noise ratio of the EPR measurement

at higher temperatures:

$$m_{\mathtt{fs}} \propto \frac{D_a[\mathrm{Rb}]\gamma_m^2}{\gamma_m^4} \propto \frac{D_a[\mathrm{Rb}][\mathrm{A}]^2}{[\mathrm{A}]^4} = \frac{D_a[\mathrm{Rb}]}{[\mathrm{A}]^2} \tag{4.85}$$

where [A] is the total alkali density and the $1/\Gamma_\mathrm{A}$ factor cancels the Γ_A factor hidden in V_scale. This scaling also indicates that when $D > 1$ for a hybrid cell, the signal to noise ratio is roughly a factor D better for EPR with K transitions than EPR with Rb transitions.

The analog voltage signal from the lockin is then processed by a PI feedback box and converted into a frequency correction that is applied to the central frequency of the Voltage Controlled Oscillator (VCO) that controls the frequency of the EPR RF coils. The gains of the PI feedback box are chosen based on the feedback slope extracted from the FM sweep lineshape:

$$\frac{\text{frequency correction}}{\text{frequency detuning}} = m_{\mathtt{fs}} G_\mathrm{L} G_\mathrm{atten} G_\mathrm{abs}^\mathrm{PI} G_\mathrm{VCO} = \text{-0.1 to -100} \tag{4.86}$$

where G_atten is the unitless gain of attenuator (if present), $G_\mathrm{abs}^\mathrm{PI}$ is the absolute gain of the PI feedback, G_VCO is the gain of the VCO in kHz/μV, and the absolute size of the correction to detuning ratio is determined empirically by whatever works best. Once the zero crossing of the FM sweep lineshape is determined by the excitation/sensing electronics, the EPR RF coil frequency is recorded by a counter as a function of time. The ^{3}He spins are then flipped twice relative to the holding field using NMR RF frequency sweep AFP. Enough counter data is taken with the ^{3}He in either state to result in a high precision determination of the intensity averaged EPR frequencies of the alkali atoms. The difference in these frequencies is largely insensitive to the holding field and is, to first order, proportional to the

^{3}He effective field.

4.4.3 Intensity Averaged EPR Frequency Difference

When the lockin output voltage is zero, the PI feedback loop has locked the EPR RF coil frequency to a fluorescence intensity weighted average EPR frequency:

$$\mathcal{V}_{\text{out}} = 0 \quad \rightarrow \quad \omega_{\text{RF}} = \langle \omega_{\text{EPR}} \rangle \equiv \frac{\sum_m \int A_m(P_0) \omega_m d\mathcal{Z}}{\sum_m \int A_m(P_0) d\mathcal{Z}} \tag{4.87}$$

where $A_m(P_0)$ is a position, temperature, photon frequency, and alkali polarization dependent weight function for the m-th EPR transition which has a frequency ω_m. The quantity of interest is the intensity averaged frequency difference after the ^{3}He spins are flipped via NMR RF frequency sweep AFP. This quantity isolates any factors that either change sign after the ^{3}He spin reversal or are in any way correlated with the spin reversal process. The most important term that changes sign is the ^{3}He effective field. Because it is small relative to the holding field, we can Taylor expand the the EPR transition frequency to give:

$$\omega_m^{\uparrow\downarrow} = \bar{\omega}_m^{\uparrow\downarrow} \pm \frac{d\omega_m^{\uparrow\downarrow}}{dB} B_{\text{He}} + \cdots \tag{4.88}$$

where $\bar{\omega}_m^{\uparrow\downarrow}$ is the EPR transition frequency in the absence of the polarized ^{3}He gas and the derivative is evaluated at the field that corresponds to $\bar{\omega}_m^{\uparrow\downarrow}$. The superscript $\uparrow\downarrow$ is used to indicate that the possibility that the quantity may have a correlation to the spin reversal process independent of the ^{3}He polarization.

The weight function $A_m(P_0)$ is also sensitive to the ^{3}He polarization through its dependence on the alkali polarization [12]. A-^{3}He spin exchange causes a small

change in the equilibrium alkali polarization which can be determined from:

$$\frac{dP_0^{\uparrow\downarrow}}{dt} = +R(1-P_0^{\uparrow\downarrow}) + \gamma_{se}(\pm P_{He} - P_0^{\uparrow\downarrow}) - \Gamma_A^0 P_0^{\uparrow\downarrow} = 0 \quad \text{(at equilibrium)} \tag{4.89}$$

where R is the optical pumping rate, $\gamma_{se} = k_{se}[^3\text{He}]$, k_{se} is the A-^{3}He spin-exchange rate constant, $[^3\text{He}]$ is the ^{3}He number density in the pumping chamber, and $\Gamma_A = \Gamma_A^0 + \gamma_{se}$. Using this equation, the equilibrium alkali polarization can be written in terms of ^{3}He spin independent $\bar{P}$ and dependent (ΔP) terms:

$$P_0^{\uparrow\downarrow} = \bar{P} \pm (\Delta P) \qquad \bar{P} = \frac{R}{R+\Gamma_A} \qquad (\Delta P) = \frac{\gamma_{se} P_{He}}{R+\Gamma_A} \tag{4.90}$$

By Taylor expanding about $\bar{P}$, the weight function can also be written as a sum of ^{3}He spin independent and dependent terms:

$$A_m^{\uparrow\downarrow}(P_0) = A_m^{\uparrow\downarrow}(\bar{P}) \pm \frac{dA_m}{dP}(\Delta P) + \cdots \tag{4.91}$$

Plugging the Taylor expansions for ω_m and $A_m(P_0)$ into the frequency difference and dropping all higher order terms involving the ^{3}He polarization, we find:

$$\begin{aligned}
\omega_{RF}^{\uparrow} - \omega_{RF}^{\downarrow} = \Delta\omega_{RF} \;=\; & \left\langle \frac{d\omega_m^{\uparrow}}{dB} B_{He} \right\rangle_{\uparrow} + \left\langle \frac{d\omega_m^{\downarrow}}{dB} B_{He} \right\rangle_{\downarrow} + \left\langle \bar{\omega}_m^{\uparrow} \right\rangle_{\uparrow} - \left\langle \bar{\omega}_m^{\downarrow} \right\rangle_{\downarrow} \\
& + \left\langle \bar{\omega}_m^{\uparrow} \left[\frac{1}{A_m^{\uparrow}(\bar{P})} \frac{dA_m^{\uparrow}}{dP}(\Delta P) - \left\langle \frac{1}{A_m^{\uparrow}(\bar{P})} \frac{dA_m^{\uparrow}}{dP}(\Delta P) \right\rangle \right] \right\rangle_{\uparrow} \\
& + \left\langle \bar{\omega}_m^{\downarrow} \left[\frac{1}{A_m^{\downarrow}(\bar{P})} \frac{dA_m^{\downarrow}}{dP}(\Delta P) - \left\langle \frac{1}{A_m^{\downarrow}(\bar{P})} \frac{dA_m^{\downarrow}}{dP}(\Delta P) \right\rangle \right] \right\rangle_{\downarrow}
\end{aligned} \tag{4.92}$$

where the brackets $\langle \cdots \rangle_{\uparrow\downarrow}$ indicate an fluorescence intensity average defined by:

$$\langle X \rangle_{\uparrow\downarrow} = \frac{\sum_m \int A_m^{\uparrow\downarrow}(\bar{P}) X \, d\mathcal{Z}}{\sum_m \int A_m^{\uparrow\downarrow}(\bar{P}) \, d\mathcal{Z}} \tag{4.93}$$

$$A_m(\bar{P}) = \bar{P}^2 \left[\frac{f'_{\rm rad} f_d [{\rm A}] V_{\rm pc} W \left\{ A_{\rm pd} / |\vec{u}|^2 \right\} \nu \Gamma_{\rm rf}^m \gamma_m^2}{(\gamma_m^2 + (\Delta\omega)_m^2)^2 + (\gamma_m^2 + 3(\Delta\omega)_m^2)\Omega_{\rm mod}^2 + \frac{3}{8}\Omega_{\rm mod}^4} \right] \tag{4.94}$$

4.4.4 Extracting the Helium Polarization

The first two terms of Eqn. (4.92 are the dominant terms and they indicate that $B_{\rm He}$ can be calculated by:

$$B_{\rm He} = \frac{(\Delta B)}{2} = (\Delta\nu_{\rm RF}) \times \left(\frac{d\nu}{dB} \right)^{-1} \tag{4.95}$$

where $\omega_{\rm RF} = 2\pi\nu_{\rm RF}$ and the derivative of the frequency with respect to the field is given by Eqns. (E.264) or (E.265). For ^{85}Rb (^{39}K) it is necessary to evaluate the derivative up to first (second) order in field to insure an accuracy below 0.1%. Traditionally, it is assumed that the alkali polarization is near unity and only the end transition $(m = F) \leftrightarrow (m - 1 = F - 1)$ is being excited by the EPR RF coils. When this is a good approximation, $B_{\rm He}$ can be calculated using the analytic form of $B(\nu)$, Eqn. (E.245), which is only valid for the end transition:

$$B_{\rm He} = \frac{(\Delta B)}{2} = \frac{B\left(\nu_{\rm RF}^{\uparrow}\right) - B\left(\nu_{\rm RF}^{\downarrow}\right)}{2} \tag{4.96}$$

The ^{3}He polarization is extracted from the ^{3}He effective field using:

$$B_{\rm He} = \frac{2\mu_0}{3} \left(\kappa_0 - 1 + \kappa_{\rm geo} \right) [^3{\rm He}\,] g \mu_N \frac{P_{\rm He}}{2} \qquad \mu_0 \mu_N = (1.70530)\ {\rm mG/amg} \tag{4.97}$$

where μ_0 is the magnetic permeability of free space, κ_0 is an empirical shift con-

stant, κ_{geo} is a geometric factor, [^{3}He] is the He-3 number density in the pumping chamber, g is the ^{3}He g-factor, μ_N is the nuclear magneton, $P_{\text{He}} = 2\langle S_z \rangle$ is the ^{3}He polarization. Under typical operating conditions, about $1/6$ of the ^{3}He effective field felt by the alkali atoms is due to the classical magnetic field produced by the bulk magnetization of the polarized ^{3}He gas. The rest is due to the very short but frequent A-^{3}He spin-exchange collisions. During these spin-exchange collisions, the alkali valence electron is essentially located within the ^{3}He nucleus thus facilitating a hyperfine-like Fermi contact interaction between their spins. The classical field and effective field due to spin exchange are distinguished in at least three important ways:

1. The size of the classical magnetic field is dependent on the geometry of the target cell; whereas the spin-exchange effective field is not.

2. The size of the classical magnetic field is independent of the alkali metal being perturbed; whereas the size of the spin-exchange effective field *does* depend on the alkali metal.

3. The classical magnetic field can be, in principle, detected by a sufficiently sensitive external magnetic field probe; whereas the spin-exchange effective field can not be detected in the way.

Because the spin-exchange effective field is difficult to calculate precisely from theory, it is usually clumped together with the classical magnetic field and parametrized by a unitless temperature dependent quantity called κ_0, which has been measured empirically. The temperature dependence of κ_0 is given by:

$$\kappa_0 = \kappa_0(T_{\text{ref}}) + m_\kappa (T - T_{\text{ref}}) \tag{4.98}$$

alkali	temp. range °C	$\kappa_0(T_{\text{ref}})$	σ_{κ_0}	m_κ	σ_{m_κ}	T_{ref} (°C)	source
Rb	110–350	6.108	0.095	0.00916	0.00026	170	[34,35]
K	150–225	5.99	0.11	0.0086	0.0020	200	[35,40]
Na	210–350	4.72	0.09	0.00914	0.00056	200	[35]

Table 4.1: Values for κ_0. The absolute value of κ_0 is based only on the precision Rb measurement of Romalis & Cates [34]. The measurements of Newbury et al [32] and Barton et al [33] are excluded because they were performed over a substantially lower temperature range. The Rb temperature dependence is a weighted average of Romalis & Cates and Babcock et al. [35]. The K to Rb κ_0 ratio was measured by Baranga et al [40]. The K & Na κ_0 ratio with Rb along with the temperature dependencies were measured by Babcock et al. There are some inconsistencies between the Na κ_0 between Eqn. (8) and Tabs. I & II (quoted here) of [35].

where T & T_{ref} are in degrees Celsius and the parameters for Rb, K, and Na are listed in Tab. (4.1).

The geometric factor κ_{geo} is the ratio of the classical magnetic field produced by the ^{3}He for the cell geometry to the classical magnetic field produced by a uniformly polarized spherical ^{3}He sample:

$$\kappa_{\text{geo}} = \frac{\left\langle \hat{z} \cdot \vec{B}(\vec{u}) \right\rangle}{\left\langle \hat{z} \cdot \vec{B}_{\text{sphere}} \right\rangle} = \left\langle \frac{3}{8\pi} \int \left[\frac{P(\vec{u}')n(\vec{u}')}{P_{\text{pc}} n_{\text{pc}}} \right] \frac{3(\hat{z} \cdot \hat{n})^2 - 1}{|\vec{u} - \vec{u}'|^3} \, d^3u' \right\rangle \tag{4.99}$$

where $\hat{z}$ is the direction of the holding field and consequently the magnetization vector, $\vec{B}_{\text{sphere}}$ is constant inside a uniformly magnetized sphere, $\hat{n}$ is the unit vector from a volume element d^3u' at $\vec{u}'$ to the observation point $\vec{u}$, $P(\vec{u}')n(\vec{u}')$ is the polarization-density product at $\vec{u}'$, and the brackets $\langle \cdots \rangle$ indicate a weighted average defined by Eqn. (4.93). This factor κ_{geo} is also closely related to the "demagnetization factor" (or "coefficient of induced magnetization" or "demagnetizing factor") D used in calculations of the field inside of permanent magnets [41], see

shape	**orientation**	$D/(4\pi)$
sphere	-	$1/3$
prolate spheroid	major axis	$\left[\rho^2 \text{atanh}\,(e) - \rho^2 e\right]/e^3$
prolate spheroid	minor axis	$\left[e - \rho^2 \text{atanh}\,(e)\right]/(2e^3)$
oblate spheroid	major axis	$\left[\rho \text{asin}\,(e) - \rho^2 e\right]/(2e^3)$
oblate spheroid	minor axis	$\left[e - \rho \text{asin}\,(e)\right]/(e^3)$
infinite elliptical cylinder	major axis	$\rho/(1+\rho)$
infinite elliptical cylinder	minor axis	$1/(1+\rho)$
infinite cylinder	cylinder axis	0

Table 4.2: Demagnetization Factors for Different Uniformly Magnetized Shapes. The classical magnetic field inside a uniformly magnetized ellipsoid is constant and given by $\vec{B} = (2/3)\mu_0\kappa_{\text{geo}}\vec{M} = \mu_0\left(1 - D/(4\pi)\right)\vec{M}$. The factors listed here are from Osborn [42] who also lists the results for a general ellipsoid. Orientation denotes the direction of the magnetization. A prolate (oblate) spheroid is an ellipsoid formed from the revolution of an ellipse about its minor (major) axis. The ratio of the minor to major axis of the ellipse is ρ where $\rho = 1$ for a circle. The eccentricity of the ellipse is $e = \sqrt{1-\rho^2}$ where $e = 0$ for a circle. The result for the infinite cylinder is the same for a cylinder of any (but uniform) cross section.

Tab. (4.2):

$$\kappa_{\text{geo}} = \frac{1 - D/(4\pi)}{2/3} \tag{4.100}$$

This indicates that the value of κ_{geo} is 1 for a spherical pumping chamber, $3/2$ for an infinitely long cylindrical pumping chamber magnetized along its axis, and $3/4$ for an infinitely long circular cylindrical pumping chamber magnetized perpendicular to its axis.

For the case of a target cell (in direct analogy to the "flux gain" G_Φ^x see Eqn. (4.46)), κ_{geo} can be written as:

$$\kappa_{\text{geo}} = 1 + \kappa_{\text{pc}} + \kappa_{\text{tt}}\left(\frac{P_{\text{tt}} n_{\text{tt}}}{P_{\text{pc}} n_{\text{pc}}}\right) + \kappa_{\text{tc}}\left(\frac{P_{\text{tc}} n_{\text{tc}}}{P_{\text{pc}} n_{\text{pc}}}\right) \tag{4.101}$$

where the factor of 1 indicates that the pumping chamber is nearly a uniformly po-

larized sphere, $\kappa_{\rm pc}$ is the factor that accounts for the non-sphericity of the pumping chamber (i.e. the pull-off tip), $\kappa_{\rm tt}$ is the contribution from the transfer tube, and $\kappa_{\rm tc}$ is the contribution from the target chamber. We can estimate the size of these three factors by modeling them as spheres which gives $\kappa_x = -(3V_x)/(8\pi d_x^3)$, where V_x is the volume of the region and d is the distance from the center of the region to the center of the pumping chamber. For typical target cell geometries, we find $\kappa_{\rm geo} \approx 0.97$. Therefore ignoring these terms introduces only about a 0.5% error on $(\kappa_0 - 1 + \kappa_{\rm geo})$ and $B_{\rm He}$.

Since the effective field due to ^{3}He is largely independent of the cell geometry (when the pumping chamber is spherical), we can pull it out of the fluorescence intensity averaging:

$$\frac{(\Delta B)}{2} = \frac{\Delta\nu_{\rm RF}}{d\nu/dB} = B_{\rm He}\left[\frac{1}{2}\frac{dB}{d\omega}\left(\left\langle\frac{d\omega_m^{\uparrow}}{dB}\right\rangle_{\uparrow} + \left\langle\frac{d\omega_m^{\downarrow}}{dB}\right\rangle_{\downarrow}\right)\right] \tag{4.102}$$

In calculating $B_{\rm He}$, we have, thus far, assumed that only the end transition is being excited. In other words, the slope $d\nu/dB$ used to convert from frequency to magnetic field is evaluated for the end transition. If the alkali polarization is very high, the different transitions are well resolved ($\omega_m - \omega_{m-1} \gg \gamma_m + \gamma_{m-1}$), or the holding field is sufficiently low, then the bracketed term in Eqn. (4.102) is to a very good approximation 1.

The slope $d\nu/dB$ is nearly constant and independent of the transition at low field. Only higher terms order in the magnetic field have a dependence on the transition, see Eqn. (E.265). "Low" field is judged by the strength of the Zeeman interaction relative to the hyperfine interaction. For ^{39}K and ^{85}Rb, low field therefore is defined to be much less than $B_{\rm hfs} = 165$ gauss and $B_{\rm hfs} = 1080$ gauss respectively.

The largest possible correction to the slope comes from the transition adjacent to the end transition. We can estimate the lowest order contribution to the correction by calculating the weighted average slope with weights given by the strength of the transition, the relative populations of the states involved in the transitions, and the frequency difference between the transitions:

$$\frac{dB}{d\omega}\left\langle\frac{d\omega_m}{dB}\right\rangle - 1 \approx \frac{4x}{2I+1}\left[1+\left(\frac{1+\bar{P}}{a(1-\bar{P})}\right)\frac{(1+v^2)^2+(1+3v^2)u^2+3u^4/8}{1+u^2+3u^4/8}\right]^{-1} \tag{4.103}$$

where $x = B_0/B_{\text{hfs}}$ is the relative field, $u = 2\Omega_{\text{mod}}/(\gamma_m + \gamma_{m-1})$ is the relative modulation amplitude, $v = 8\pi\nu_{\text{hfs}}x^2/(2I+1)^2/(\gamma_m + \gamma_{m-1})$ is the relative frequency difference between the transitions (see Eqn. (E.263)), and $\bar{P}$ is the average alkali polarization. The transition matrix element ratio (see Eqn. (E.877)) is $a = 7/3$ (2), the nuclear spin is $I = 5/2$ (3/2), and the hyperfine splitting is $\nu_{\text{hfs}} = 3036$ (0.462) MHz for ^{85}Rb (^{39}K). Under our typical conditions, $B_0 = 25$ G, the ^{39}K transitions are very well resolved implying that $v \gg 1$ and the correction is completely negligible. The worst case scenario occurs when $u \gg 1, v$, for ^{85}Rb, we find that the correction is 0.5% when $\bar{P} = 0.7$. However, under our typical conditions, $u < 1$ & $v \approx 1$ implying that the correction is 0.2% when $\bar{P} = 0.7$.

4.4.5 AC Zeeman Shift Due to the NMR RF Field

Introduction

The oscillating NMR RF field used for AFP also causes a small frequency shift $(\Delta\nu)_{\texttt{rf}}$, in this case, due to the AC Zeeman effect. If the magnitude of the NMR RF field changes during AFP, then its corresponding frequency shift is different for the two directions of the ^{3}He spins causing a correlation described by the second pair

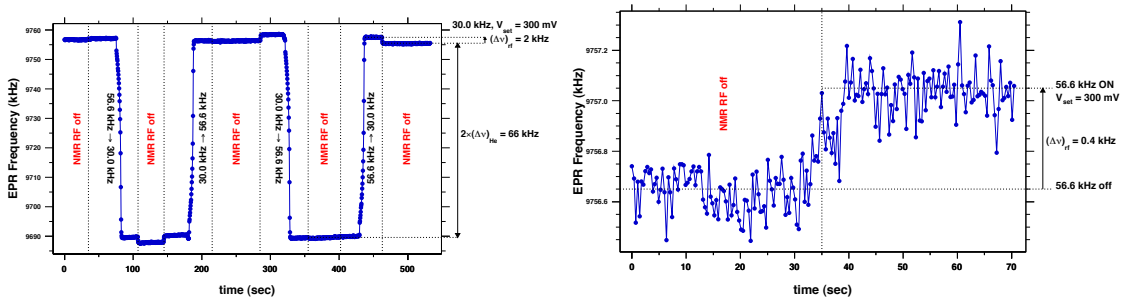

Figure 4.8: Typical EPR Measurement Sequence. The He spins are flipped using frequency sweep NMR-AFP. The top plot shows the entire data set which includes four ^{3}He spin flips. The shift due to the NMR RF field at 30.0 kHz can be seen at 75 sec $< t <$ 175 sec, 250 sec $< t <$ 325 sec, and finally 425 sec $< t <$ 500 sec. Note that the sign of the RF shift is independent of the direction of the ^{3}He spins. The shift due to the NMR RF field at 56.6 kHz is much smaller, but is visible at 0 sec $< t <$ 70 sec, see the bottom plot. Because the NMR RF coil resonates at about 20 kHz, the amplitude of the RF field at 30.0 kHz is much larger than the amplitude of the RF field at 56.6 kHz for the same function generator set amplitude $V_{\text{set}} = 300$ mV.

of terms in Eqn. (4.92). Under this condition, the partially canceled frequency shift due to the NMR RF field also contributes to & contaminates the EPR frequency difference: $\Delta\nu_{\text{EPR}} = 2 \times (\Delta\nu)_{\text{He}} + [(\Delta\nu)^{\uparrow}_{\text{rf}} - (\Delta\nu)^{\downarrow}_{\text{rf}})]$. This could potentially be a large systematic error in the determination of the ^{3}He polarization.

The result of a typical EPR measurement at UVa is shown in Fig. (4.8). At the start of an EPR polarization measurement, the total static magnetic field seen by the alkali atoms is $B = B_0 + B_{\text{He}}$, which corresponds to an EPR frequency of:

$$(\nu^{\uparrow}_{\text{EPR}})_{\text{off}} = \nu_0 + (\Delta\nu)_{\text{He}} \tag{4.104}$$

Under our typical conditions, $B_0 = 13$ G and, for the "well state" transition of ^{39}K, the EPR frequency is around 9.7 MHz. After measuring this EPR frequency for several seconds, the NMR RF field is turned on with a frequency of 56.6 kHz. This

NMR RF field causes an additional shift in the EPR frequency:

$$(\nu_{\mathtt{EPR}}^{\uparrow})_{\text{on}} = \nu_0 + (\Delta\nu)_{\text{He}} + (\Delta\nu)_{\mathtt{rf}}^{\uparrow} \tag{4.105}$$

After again measuring the EPR frequency for several seconds, the NMR RF frequency is swept over a period of 6 seconds from 56.6 kHz, through resonance at 42.2 kHz, to 30.0 kHz. The rate is chosen to be fast enough to minimize the ^{3}He relaxation at resonance, but slow enough for the ^{3}He spins to follow the effective field in the rotating frame adiabatically. After the spins have been flipped, the total static magnetic field felt by the alkali atoms is $B = B_0 - B_{\text{He}}$ which corresponds to an EPR frequency of:

$$(\nu_{\mathtt{EPR}}^{\downarrow})_{\text{on}} = \nu_0 - (\Delta\nu)_{\text{He}} + (\Delta\nu)_{\mathtt{rf}}^{\downarrow} \tag{4.106}$$

and then we turn the NMR RF off to measure:

$$(\nu_{\mathtt{EPR}}^{\downarrow})_{\text{off}} = \nu_0 - (\Delta\nu)_{\text{He}} \tag{4.107}$$

To conclude the EPR measurement, we follow the same steps already mentioned, but in reverse order: (1) the NMR RF on at 30.0 kHz, (2) measure the EPR frequency, (3) sweep the NMR RF frequency from 30.0 kHz to 56.6 kHz, (4) measure the EPR frequency, (5) turn the NMR RF off, and (6) measure the EPR frequency. In addition to this measurement sequence, Fig. (4.8) also shows the results of an analogous measurement sequence for which the NMR frequency sweep from 30.0 kHz to 56.6 kHz and then back to 30.0 kHz. Using these measurements, there are

two frequency differences that can be used to extract the ^{3}He polarization:

$$\Delta(\nu_{\mathtt{EPR}})_{\mathrm{on}} = (\nu^{\uparrow}_{\mathtt{EPR}})_{\mathrm{on}} - (\nu^{\downarrow}_{\mathtt{EPR}})_{\mathrm{on}} = 2 \times (\Delta\nu)_{\mathrm{He}} + \left[(\Delta\nu)^{\uparrow}_{\mathtt{rf}} - (\Delta\nu)^{\downarrow}_{\mathtt{rf}})\right] \quad (4.108)$$

$$\Delta(\nu_{\mathtt{EPR}})_{\mathrm{off}} = (\nu^{\uparrow}_{\mathtt{EPR}})_{\mathrm{off}} - (\nu^{\downarrow}_{\mathtt{EPR}})_{\mathrm{off}} = 2 \times (\Delta\nu)_{\mathrm{He}} \quad (4.109)$$

If there is no shift associated with the NMR RF field ($(\Delta\nu)^{\uparrow}_{\mathtt{rf}} = (\Delta\nu)^{\downarrow}_{\mathtt{rf}} = 0$) or if the size of frequency shift associated with the NMR RF field stays the same after the ^{3}He spins are flipped ($[(\Delta\nu)^{\uparrow}_{\mathtt{rf}} - (\Delta\nu)^{\downarrow}_{\mathtt{rf}})] = 0$), then the two frequency differences are identical. However, at least at UVa, this is not the case.

Based on Figs. (4.8) & (4.9), we'll make the following observations of the what we call "NMR RF Shift" Effect:

1. the size of $(\Delta\nu)_{\mathtt{rf}}$ has no measurable dependence on the sign and magnitude of the ^{3}He polarization

2. the size of $(\Delta\nu)_{\mathtt{rf}}$ at 13 G appears to in the kHz range for both ^{85}Rb and ^{39}K

3. the sign of $(\Delta\nu)_{\mathtt{rf}}$ is positive for both the "well" state transition $-(I+1/2) \leftrightarrow -(I-1/2)$ and the "hat" state transition $+(I+1/2) \leftrightarrow +(I-1/2)$

4. the size of $(\Delta\nu)_{\mathtt{rf}}$ increases with the NMR RF amplitude and decreases with the NMR RF frequency

Originally, we thought that $(\Delta\nu)_{\mathtt{rf}} \neq 0$ was due to a direct coupling between the NMR RF coils and the photodiode used for EPR. We tested this hypothesis by increasing the distance between the EPR photodiode and the NMR RF coils. The fluorescence from the cell needed as an input to the EPR feedback circuit was captured by an optical fiber instead of the photodiode directly. Because we used a very long optical fiber, the distance between the EPR photodiode and NMR RF

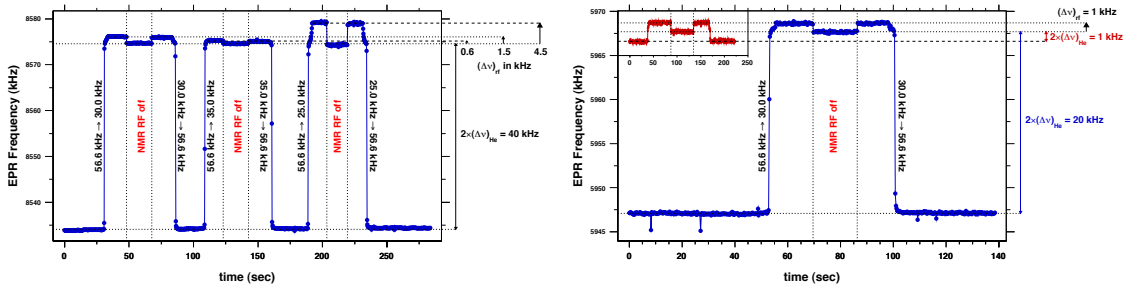

Figure 4.9: EPR in the High Energy or "Hat" State for ^{39}K (top) and ^{85}Rb (bottom) at 13 Gauss. In the top plot, we see that the shift depends on NMR frequency. This is because circuit used to drive the NMR RF coils resonates at about 20 kHz. In the bottom plot, we see that the NMR RF shift in independent of the size of the shift due to the polarized ^{3}He gas.

coils was several meters. When we performed the EPR measurement under these conditions, we still observed a frequency shift when the NMR RF was turned on and off.

Our new hypothesis (which we believe is correct) is that the NMR RF field directly interacts with the alkali atoms to produce a frequency shift via the AC Zeeman effect. Under our experimental conditions, $B_0 > 10$ Gauss, $\nu_0 > 5$ MHz, $\nu_{\mathtt{rf}} = (40 \pm 20)$ kHz, $B_{\mathtt{rf}} < 0.5$ Gauss, and, using the results of Sec. (4.4.5), the size of the shift is given by:

$$(\Delta\nu)_{\mathtt{rf}} = \frac{F(F+1) - m(m-1)}{4\nu_{\mathtt{EPR}}} \left[\frac{\partial\nu}{\partial B} B_{\mathtt{rf}}\right]^2 \tag{4.110}$$

where $F = I \pm 1/2$, I is the nuclear spin of the alkali atom, $\nu_{\mathtt{EPR}}$ is the frequency of the $|F, m\rangle \leftrightarrow |F, m-1\rangle$ transition, $\partial\nu/\partial B$ is given by Eqn. (E.265), and $B_{\mathtt{rf}}$ is the amplitude of the NMR RF Field in the lab frame. Tab. (4.3) lists the quantitative size of the shift for ^{85}Rb and ^{39}K under our conditions. Because, for incidental historical reasons, the NMR RF coils resonate at 20 kHz (see Fig. (4.11)), the NMR RF field

amplitude is higher at 30.0 kHz than at 56.6 kHz for the same set control voltage, which implies $(\Delta\nu)^{\uparrow}_{\mathtt{rf}} \neq (\Delta\nu)^{\downarrow}_{\mathtt{rf}}$. Therefore, in order to avoid all these difficulties, it is much better to use $\Delta(\nu_{\mathtt{EPR}})_{\mathrm{off}}$ than $\Delta(\nu_{\mathtt{EPR}})_{\mathrm{on}}$ to calculate the ^{3}He polarization. To do this, all you have to do is take data with the NMR RF field off before and after the AFP frequency sweep.

Calculating the Shift Due to the NMR RF Field: The AC Zeeman Effect

To calculate the shift due to the AC Zeeman effect, we'll follow and in some cases generalize the basic arguments found in problem 2.7 of [43]. Since we are only interested in a given Zeeman transition within the EPR spectrum, we'll focus only on the states involved in the transition. This results in a two state system ($|m\rangle$ & $|m-1\rangle$) with a Hamiltonian written as:

$$\mathcal{H}_0 = \hbar\omega_0 F_z \tag{4.111}$$

where F_z is the z-component of the total atomic angular momentum, $\hbar$ is the Planck constant divided by 2π, and ω_0 is the EPR frequency for the transition for a magnetic field B_0. If another much smaller magnetic field $B_1 \ll B_0$ is turned on, then we can write the additional Zeeman interaction as:

$$\mathcal{H}_1 = -\mu \cdot \vec{B}_1 = -g\mu_B \vec{F} \cdot \vec{B}_1 \tag{4.112}$$

where g is the effective or Landé g-factor, μ_B is the Bohr magneton, and $\vec{F}$ is the total atomic angular momentum. In general, g depends on the total magnetic field in the z-direction, the hyperfine manifold F, and the magnetic substate m. Its form can be obtained by considering the case when $\vec{B}_1$ is in the z-direction (the same

direction as $\vec{B}_0$). In this case, the total Hamiltonian can be written in two ways:

$$\mathcal{H} = \mathcal{H}_0 + \mathcal{H}_1 = \hbar\omega F_z = \hbar\omega_0 F_z - g\mu_B F_z B_1 \tag{4.113}$$

Taylor expanding $\omega = \omega(B_0 + B_1)$ about B_0 gives:

$$\omega(B_0 + B_1) = \omega(B_0) + (B_0 + B_1 - B_0)\frac{\partial\omega}{\partial B} = \omega_0 + B_1\frac{\partial\omega}{\partial B} \tag{4.114}$$

Putting this together gives the form of the effective g-factor:

$$\hbar\omega F_z - \hbar\omega_0 F_z = -g\mu_B F_z B_1 \quad \rightarrow \quad g = -\left(\frac{\hbar}{\mu_B}\right)\frac{\partial\omega}{\partial B} \tag{4.115}$$

where the derivative is evaluated at B_0.

We'll now consider the case of an oscillating RF field in the x-direction:

$$\mathcal{H} = \hbar\omega_0 F_z - g\mu_B F_x B_{\mathtt{rf}} \cos(\omega_{\mathtt{rf}} t) \tag{4.116}$$

where $B_{\mathtt{rf}}$ is the amplitude of the RF field in the lab frame and $\omega_{\mathtt{rf}}$ is the angular frequency of the RF field. In general, the non-zero matrix elements of F_z and $F_x = (F_+ + F_-)/2$ are:

$$\langle m|\, F_z\, |m\rangle = m \qquad\qquad \langle m-1|\, F_z\, |m-1\rangle = m-1 \tag{4.117}$$

$$\langle m-1|\, F_x\, |m\rangle = \langle m|\, F_x\, |m-1\rangle = (1/2)\sqrt{F(F+1) - m(m-1)} \tag{4.118}$$

Using these formulas, we can rewrite the Hamiltonian using the Pauli spin matrices:

$$\mathcal{H} = \hbar\omega_0 \bar{m} + \hbar\omega_0 \sigma_z/2 + \hbar\Omega_{\mathtt{rf}}\sigma_x \cos(\omega_{\mathtt{rf}} t)/2 \tag{4.119}$$

where $\bar{m} = m - 1/2$ is the mean m associated with the transition and $\Omega_{\mathtt{rf}}$ is given by:

$$\Omega_{\mathtt{rf}} = \frac{\partial \omega}{\partial B} B_{\mathtt{rf}} \sqrt{F(F+1) - m(m-1)} \tag{4.120}$$

Since $\hbar\omega_0\bar{m}$ is an overall constant energy offset, we can safely drop it from the Hamiltonian. For convenience, we'll relabel two eigenstates of $\mathcal{H}_0$ as $|a\rangle = |m\rangle$ and $|b\rangle = |m-1\rangle$. The eigenstates of the full Hamiltonian $\mathcal{H}$ are denoted as $|1\rangle$ & $|2\rangle$ and can be expanded as:

$$|1\rangle = a_1 \exp(-i\omega_0 t/2)\,|a\rangle + b_1 \exp(+i\omega_0 t/2)\,|b\rangle \tag{4.121}$$

$$|2\rangle = a_2 \exp(-i\omega_0 t/2)\,|a\rangle + b_2 \exp(+i\omega_0 t/2)\,|b\rangle \tag{4.122}$$

where orthonormality enforces:

$$|a_1|^2 + |b_1|^2 = |a_2|^2 + |b_2|^2 = 1 \qquad a_1^* a_2 + b_1^* b_2 = 0 \tag{4.123}$$

Because we've chose to expand $|1\rangle$ & $|2\rangle$ in this way, they automatically satisfy the Schrodinger equations with $a_1 = b_2 = 1$ & $a_2 = b_1 = 0$ when there is no RF field $\Omega_{\mathtt{rf}} = 0$. Our goal now is to obtain a solution correct to the lowest order for the case when $0 < \Omega_{\mathtt{rf}} \ll \omega_0$.

Applying Schrodinger equation to $|1\rangle$, we get a pair of coupled equations:

$$\begin{aligned} i\hbar(\dot{a}_1 - i\omega_0 a_1/2)\exp(-i\omega_0 t/2) &= +(\hbar\omega_0 a_1/2)\exp(-i\omega_0 t/2) \\ &\quad +(\hbar\Omega_{\mathtt{rf}} b_1/2)\exp(+i\omega_0 t/2)\cos(\omega_{\mathtt{rf}} t) \quad (4.124) \\ i\hbar(\dot{b}_1 + i\omega_0 b_1/2)\exp(+i\omega_0 t/2) &= -(\hbar\omega_0 b_1/2)\exp(+i\omega_0 t/2) \\ &\quad +(\hbar\Omega_{\mathtt{rf}} a_1/2)\exp(-i\omega_0 t/2)\cos(\omega_{\mathtt{rf}} t) \quad (4.125) \end{aligned}$$

After rearranging a few things we get:

$$\dot{a}_1 = -(i\Omega_{\mathtt{rf}} b_1/2)\exp(+i\omega_0 t)\cos(\omega_{\mathtt{rf}} t) \tag{4.126}$$

$$\dot{b}_1 = -(i\Omega_{\mathtt{rf}} a_1/2)\exp(-i\omega_0 t)\cos(\omega_{\mathtt{rf}} t) \tag{4.127}$$

Since $\Omega_{\mathtt{rf}}$ is small, it's not unreasonable to assume that $|a_1| \approx 1$. In other words, we'll make the ansatz that $a_1 = \exp(-i\omega_! t)$. Using this form of a_1 allows us to directly integrate $\dot{b}_1$ to give:

$$\begin{aligned} b_1 = \int \dot{b}_1\, dt &= -(i\Omega_{\mathtt{rf}}/2)\int \exp(-i(\omega_1+\omega_0)t)\cos(\omega_{\mathtt{rf}} t)\, dt \qquad (4.128)\\ &= -(i\Omega_{\mathtt{rf}}/4)\int \left[\exp(-i(\omega_1+\omega_0-\omega_{\mathtt{rf}})t) + \exp(-i(\omega_1+\omega_0+\omega_{\mathtt{rf}})t)\right] dt \\ &= -(i\Omega_{\mathtt{rf}}/4)\left[\frac{\exp(-i(\omega_1+\omega_0-\omega_{\mathtt{rf}})t)}{-i(\omega_1+\omega_0-\omega_{\mathtt{rf}})} + \frac{\exp(-i(\omega_1+\omega_0+\omega_{\mathtt{rf}})t)}{-i(\omega_1+\omega_0+\omega_{\mathtt{rf}})}\right] \\ &= \frac{\Omega_{\mathtt{rf}}}{4}\left[\frac{\exp(-i(\omega_1+\omega_0-\omega_{\mathtt{rf}})t)}{\omega_1+\omega_0-\omega_{\mathtt{rf}}} + \frac{\exp(-i(\omega_1+\omega_0+\omega_{\mathtt{rf}})t)}{\omega_1+\omega_0+\omega_{\mathtt{rf}}}\right] \qquad (4.129)\end{aligned}$$

Using this solution for b_1 and the ansatz for a_1, we now apply the equation for $\dot{a}_1$:

$$\begin{aligned} \dot{a}_1 &= -(i\Omega_{\mathtt{rf}} b_1/2)\exp(+i\omega_0 t)\cos(\omega_{\mathtt{rf}} t) \\ -i\omega_1\exp(-i\omega_1 t) &= -i\frac{\Omega_{\mathtt{rf}}^2}{8}\exp(+i\omega_0 t)\cos(\omega_{\mathtt{rf}} t) \\ &\quad \times\left[\frac{\exp(-i(\omega_1+\omega_0-\omega_{\mathtt{rf}})t)}{\omega_1+\omega_0-\omega_{\mathtt{rf}}} + \frac{\exp(-i(\omega_1+\omega_0+\omega_{\mathtt{rf}})t)}{\omega_1+\omega_0+\omega_{\mathtt{rf}}}\right] \\ \omega_1 &= \frac{\Omega_{\mathtt{rf}}^2}{8}\cos(\omega_{\mathtt{rf}} t)\left[\frac{\exp(+i\omega_{\mathtt{rf}} t)}{\omega_1+\omega_0-\omega_{\mathtt{rf}}} + \frac{\exp(-i\omega_{\mathtt{rf}} t)}{\omega_1+\omega_0+\omega_{\mathtt{rf}}}\right] \\ &= \frac{\Omega_{\mathtt{rf}}^2}{16}\left[\exp(+i\omega_{\mathtt{rf}} t)+\exp(-i\omega_{\mathtt{rf}} t)\right]\left[\frac{\exp(+i\omega_{\mathtt{rf}} t)}{\omega_1+\omega_0-\omega_{\mathtt{rf}}} + \frac{\exp(-i\omega_{\mathtt{rf}} t)}{\omega_1+\omega_0+\omega_{\mathtt{rf}}}\right] \\ &= \frac{\Omega_{\mathtt{rf}}^2}{16}\left[\frac{1+\exp(+2i\omega_{\mathtt{rf}} t)}{\omega_1+\omega_0-\omega_{\mathtt{rf}}} + \frac{1+\exp(-2i\omega_{\mathtt{rf}} t)}{\omega_1+\omega_0+\omega_{\mathtt{rf}}}\right] \qquad (4.130)\end{aligned}$$

Our first approximation will be to drop the rapidly oscillating terms to get:

$$\omega_1 = \frac{\Omega_{\mathtt{rf}}^2}{8}\left[\frac{\omega_1+\omega_0}{(\omega_1+\omega_0)^2-\omega_{\mathtt{rf}}^2}\right] \tag{4.131}$$

Our second approximation is that $\omega_1 \ll \omega_0$, which allows us to solve for ω_1:

$$\begin{aligned}
\omega_1 &= \frac{\Omega_{\mathtt{rf}}^2}{8}\left[\frac{\omega_0}{\omega_0^2-\omega_{\mathtt{rf}}^2}\right]\left[1+\frac{\omega_1}{\omega_0}\right]\left[1+\frac{2\omega_1\omega_0+\omega_1^2}{\omega_0^2-\omega_{\mathtt{rf}}^2}\right]^{-1} && (4.132)\\
&\approx \frac{\Omega_{\mathtt{rf}}^2}{8}\left[\frac{\omega_0}{\omega_0^2-\omega_{\mathtt{rf}}^2}\right]\left[1-\frac{\omega_1}{\omega_0}\left(\frac{\omega_0^2+\omega_{\mathtt{rf}}^2}{\omega_0^2-\omega_{\mathtt{rf}}^2}\right)\right] && (4.133)\\
&= \frac{\Omega_{\mathtt{rf}}^2}{8}\left[\frac{\omega_0}{\omega_0^2-\omega_{\mathtt{rf}}^2}\right]\left[1+\frac{\Omega_{\mathtt{rf}}^2(\omega_0^2+\omega_{\mathtt{rf}}^2)}{8(\omega_0^2-\omega_{\mathtt{rf}}^2)^2}\right]^{-1} && (4.134)
\end{aligned}$$

For self-consistency, this approximation necessarily implies that $\Omega_{\mathtt{rf}} \ll \omega_0$ which is roughly equivalent to our earlier assertion that $B_{\mathtt{rf}} \ll B_0$. Our third and final approximation is that the frequency of the RF field is far from resonance, $\omega_{\mathtt{rf}} \ll \omega_0$, which finally gives:

$$\omega_1 = \frac{\Omega_{\mathtt{rf}}^2}{8}\left[\frac{\omega_0}{\omega_0^2-\omega_{\mathtt{rf}}^2}\right]\left[1+\frac{\Omega_{\mathtt{rf}}^2(\omega_0^2+\omega_{\mathtt{rf}}^2)}{8(\omega_0^2-\omega_{\mathtt{rf}}^2)^2}\right]^{-1} \approx \frac{\Omega_{\mathtt{rf}}^2}{8\omega_0} \tag{4.135}$$

We can follow this same calculation for $|2\rangle$ where a_2 plays the same role as b_1, b_2 plays the same role as a_1, and we must flip the sign of ω_0:

$$\begin{aligned}
a_2 &= \frac{\Omega_{\mathtt{rf}}}{4}\left[\frac{\exp(-i(\omega_2-\omega_0-\omega_{\mathtt{rf}})t)}{\omega_2-\omega_0-\omega_{\mathtt{rf}}}+\frac{\exp(-i(\omega_2-\omega_0+\omega_{\mathtt{rf}})t)}{\omega_2-\omega_0+\omega_{\mathtt{rf}}}\right] && (4.136)\\
b_2 &= \exp(-i\omega_2 t) && (4.137)\\
\omega_2 &\approx -\frac{\Omega_{\mathtt{rf}}^2}{8\omega_0} && (4.138)
\end{aligned}$$

Putting this altogether gives:

$$
\begin{aligned}
|1\rangle &= \exp(-i(\omega_0/2+\omega_1)t)\,|a\rangle + b_1 \exp(+i\omega_0 t/2)\,|b\rangle && (4.139)\\
|2\rangle &= a_2 \exp(-i\omega_0 t/2)\,|a\rangle + \exp(+i(\omega_0/2-\omega_2)t)\,|b\rangle && (4.140)\\
b_1 &= +\frac{\Omega_{\mathtt{rf}}}{4\omega_0}\exp(-i(\omega_1+\omega_0)t)\cos(\omega_{\mathtt{rf}}t) && (4.141)\\
a_2 &= -\frac{\Omega_{\mathtt{rf}}}{4\omega_0}\exp(-i(\omega_2-\omega_0)t)\cos(\omega_{\mathtt{rf}}t) && (4.142)\\
\omega_1 = -\omega_2 &= \frac{\Omega_{\mathtt{rf}}^2}{8\omega_0} && (4.143)
\end{aligned}
$$

To lowest order, the energy levels are:

$$
\begin{aligned}
\langle 1|\,\mathcal{H}\,|1\rangle &= \langle 1|\, i\hbar\frac{\partial\,|1\rangle}{\partial t} \approx +\hbar(\omega_0/2+\omega_1) && (4.144)\\
\langle 2|\,\mathcal{H}\,|2\rangle &= \langle 2|\, i\hbar\frac{\partial\,|2\rangle}{\partial t} \approx -\hbar(\omega_0/2-\omega_2) && (4.145)
\end{aligned}
$$

and finally the frequency is:

$$
\begin{aligned}
\omega &= \frac{\langle 1|\,\mathcal{H}\,|1\rangle - \langle 2|\,\mathcal{H}\,|2\rangle}{\hbar} = \omega_0+\omega_1-\omega_2 = \omega_0+\frac{\Omega_{\mathtt{rf}}^2}{4\omega_0}\\
&= \omega_0\left[1+\left(\frac{\partial\omega}{\partial B}\frac{B_{\mathtt{rf}}}{2\omega_0}\right)^2 (F(F+1)-m(m-1))\right] && (4.146)
\end{aligned}
$$

The AC Zeeman frequency shift due to an RF field for the transition $|F,m\rangle \leftrightarrow |F,m-1\rangle$ when $B_{\mathtt{rf}} \ll B_0$ and $\nu_{\mathtt{rf}} \ll \nu_0$ is, to lowest order, given by:

$$
(\Delta\nu)_{\mathtt{rf}} = \frac{F(F+1)-m(m-1)}{4\nu_0}\left[\frac{\partial\nu}{\partial B}B_{\mathtt{rf}}\right]^2 \qquad (4.147)
$$

where $B_{\mathtt{rf}}$ is the magnitude of the RF field in the lab frame, ν_0 is the frequency of the transition when $B_{\mathtt{rf}} = 0$, and the derivative for $F = I \pm 1/2$ is given by (up to

B_0 Gauss	isotope	I	m $\pm[I]/2$	ν_0 MHz	$\partial\nu/\partial B$ kHz/G	$(\Delta\nu)_{\mathtt{rf}}$ kHz/G^2	$(\Delta\nu)_{\mathrm{He}}$ kHz/amg
13	^{85}Rb	5/2	+3	6.01	458	52.4	−7.08
			−3	6.13	476	55.4	+7.36
	^{39}K	3/2	+2	8.59	622	45.0	−9.01
			−2	9.67	788	64.2	+11.4
23	^{85}Rb	5/2	+3	10.55	451	28.9	−6.97
			−3	10.93	484	32.1	+7.48
	^{39}K	3/2	+2	14.54	569	22.3	−8.24
			−2	17.91	863	41.6	+12.5

Table 4.3: EPR Frequency Shifts for the End Transitions Due to the NMR RF Field & Polarized ^{3}He. We've assumed that $B_{\mathtt{rf}} \ll B_0$ and $\nu_{\mathtt{rf}} \ll \nu_0$. The $-(+)$ sign for m refers to the "well" ("hat") state. For the shift due to the polarized ^{3}He, we've assumed a spherical sample at a temperature of 200 °C and 100% polarization. The sign of the polarization is taken to be the same as the sign of the alkali m state.

fifth order in field) Eqn. (E.265). For the special case of end transitions, $F = I + 1/2$ and $m = I + 1/2$ for $I + 1/2 \leftrightarrow I - 1/2$ & $m = -I + 1/2$ for $-I + 1/2 \leftrightarrow -I - 1/2$ and the frequency shift is:

$$(\Delta\nu)_{\mathtt{rf}} = \frac{[I]}{4\nu_0}\left[\frac{\partial\nu}{\partial B}B_{\mathtt{rf}}\right]^2 \tag{4.148}$$

An Experimental Study of the NMR RF Shift Effect

To study the NMR RF Shift effect, we took data for:

1. fields of 13 Gauss and 23 Gauss
2. NMR RF frequencies of 25.0 kHz, 30.0 kHz, 35.0 kHz, and 56.6 kHz
3. NMR RF set amplitude from 25 mV up to 600 mV or whatever value the NMR RF amplifier would overload
4. ^{39}K in the "well" state

At typical sequence is depicted in Fig. (4.10). For each data set, we would measure the EPR frequency, the current in the Helmholtz coils, and the current in the NMR RF coils. For all of the measurements, the current in the Helmholtz coils was very stable and the ^{3}He polarization had reached equilibrium. Therefore any change in the EPR frequency was mostly due to the NMR RF field.

After collecting this data, we plot the shift vs. NMR RF set amplitude, see Fig. (4.12). The expected quadratic behavior is readily seen. We don't expect the NMR RF frequency to play a direct role in the shift. Therefore we measured the current in the NMR RF coils vs. NMR RF frequency for a fixed set amplitude V_{set}, see Fig. (4.11). To make all the data comparable, we convert the shift into the amplitude of the RF field causing it using Eqn. (4.148). Since the same set amplitude doesn't correspond to the same current in the NMR RF coils for different NMR RF frequencies, we plot the data vs. the current in the RF coils instead. When we do this, if our calculation is correct, then all the data should lie on a line. To better than 5%, this is true and we get a slope of 182 mG/A.

4.4.6 Sensitivity to Magnetic Field Gradients

The last two terms in Eqn. (4.92) relate to differences in the fluorescence intensity due to changes in the alkali polarization induced by spin-exchange with ^{3}He . If

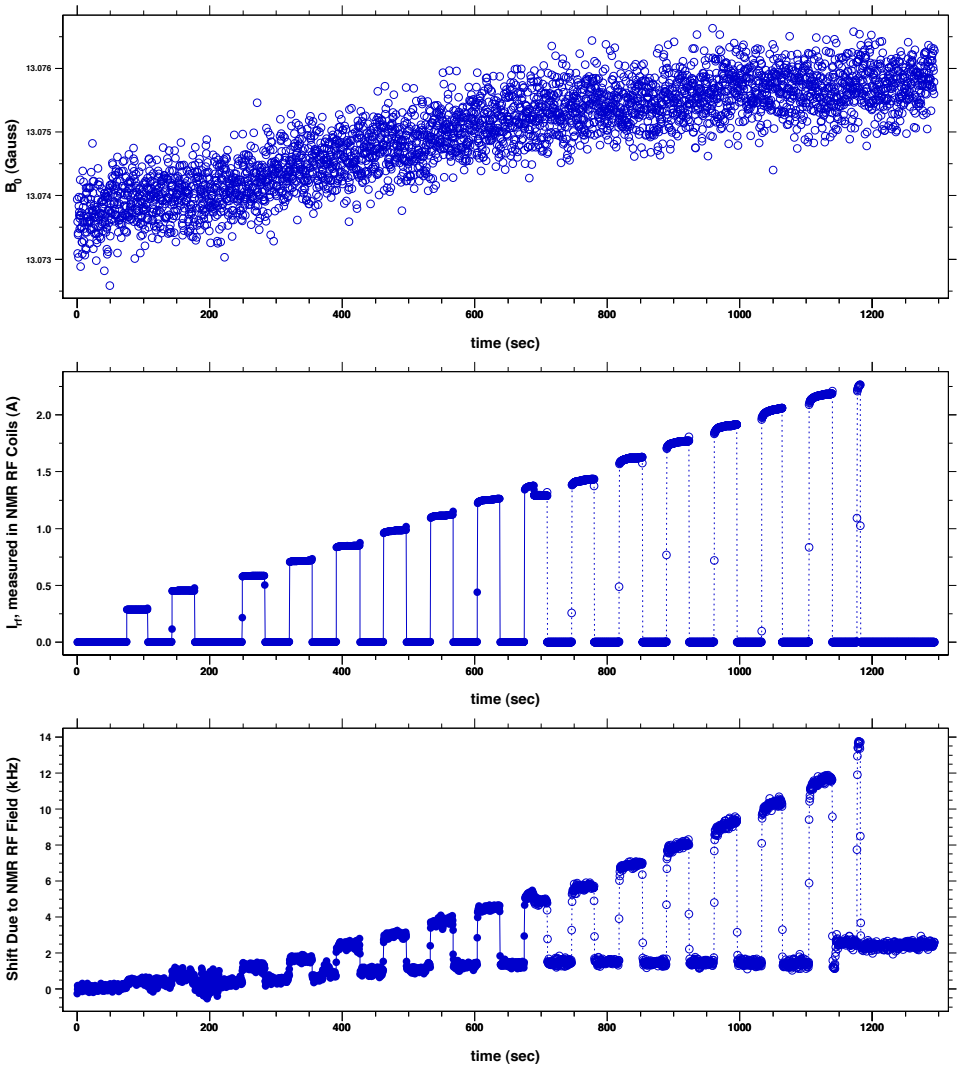

Figure 4.10: Shift in the EPR Frequency for an NMR RF Field at 25 kHz. The top plot shows the magnitude of the holding field as measured from the current in the Helmholtz coils. Over the course of the measurement, it was stable to a few mG. The middle plot shows the current in NMR RF coils. During the measurement, the RF field was turned off and on at linearly increasing amplitudes. The bottom plot shows the locked EPR frequency as the NMR RF field is varied. The measurement was done at the end of a spin-up, so we assume that the ^{3}He polarization was at equilibrium. The field due to the polarized ^{3}He is about 40 mG, which corresponds to a frequency shift of about 30 kHz. The magnitude of the NMR RF field is increased linearly, whereas the shift is increasing in a quadratic manner. At around $t = 700$ sec, there was a glitch in the RF amplitude. In addition, the NMR RF amplifier overloaded at around $t = 1175$ sec. Both of these features can be seen in both the bottom two plots.

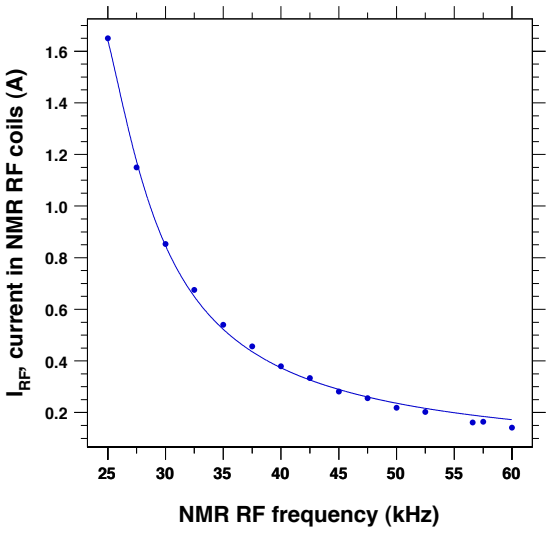

Figure 4.11: Current in NMR RF coils for a set amplitude of $V_{\text{set}} = 300$ mV. The NMR RF coils resonate at about 20 kHz.

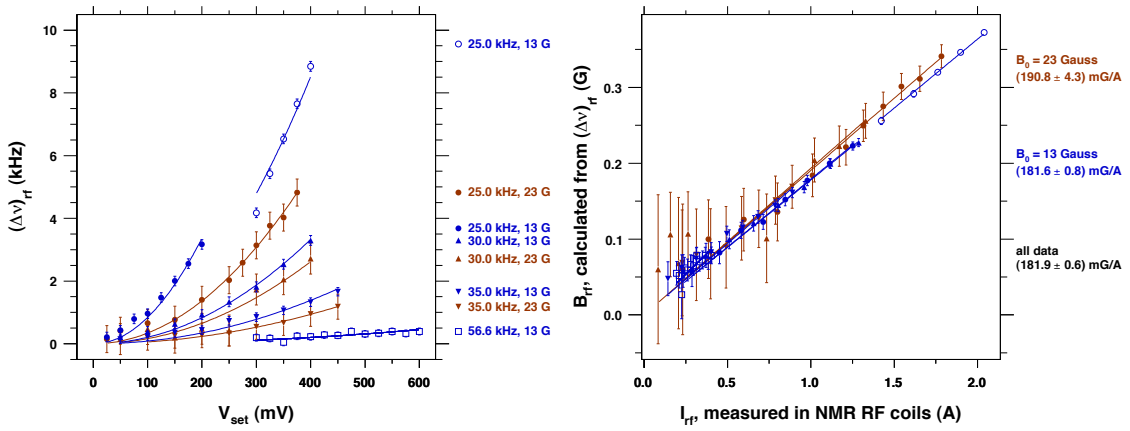

Figure 4.12: Measurement of $(\Delta\nu)_{\mathtt{rf}}$ under different conditions. We measured the NMR RF shift at two different fields, four different NMR RF frequencies, and several NMR RF field amplitudes. The top plot shows the shift plotted against set amplitude. Except for the 25.0 kHz, 13 Gauss data set, there was a linear relationship between the current in the NMR RF coils and the set amplitude. For the 25.0 kHz, 13 gauss data set, a glitch occurred during the measurement, see Fig. (4.10). For the bottom plot, we've inserted the measured shift into Eqn. (4.148) and solved for the amplitude of the NMR RF field in the lab frame. Once this value for $B_{\mathtt{rf}}$ is plotted against the measured current $I_{\mathtt{rf}}$ in the NMR RF coils, the data cluster along a line.

the holding field were perfectly uniform throughout the pumping chamber, then it's contribution to the EPR frequency would be independent of position and the two terms would be identically zero. To make this more manifest, we'll expand EPR frequency about its value at the center of the cell (located at $\vec{u}_0$) which gives:

$$\begin{aligned}\left\langle \bar{\omega}_m \left[\frac{1}{A_m(\bar{P})} \frac{dA_m}{dP}(\Delta P) - \left\langle \frac{1}{A_m(\bar{P})} \frac{dA_m}{dP}(\Delta P) \right\rangle \right] \right\rangle \\ = \left\langle \left((\vec{u} - \vec{u}_0) \cdot \vec{\nabla} B_0 \frac{d\bar{\omega}_m}{dB} \cdots \right) \left[\frac{1}{A_m(\bar{P})} \frac{dA_m}{dP}(\Delta P) - \left\langle \frac{1}{A_m(\bar{P})} \frac{dA_m}{dP}(\Delta P) \right\rangle \right] \right\rangle\end{aligned} \tag{4.149}$$

An estimate of the scale of this effect can be made by replacing $(\vec{u} - \vec{u}_0)$ with the characteristic size of the pumping chamber and using Eqn. (4.90) for ΔP, we find:

$$R_{\mathrm{pc}} \left(\frac{\partial B_0}{\partial z} \right) \left(\frac{d\bar{\omega}_m}{dB} \right) \left(\frac{P_{\mathrm{He}} \gamma_{\mathrm{se}}}{R + \Gamma_{\mathrm{A}}} \right) \approx 2 \text{ Hz} \tag{4.150}$$

where, under typical operating conditions, $R_{\mathrm{pc}} = 3$ cm, $\partial B_0/\partial z = 10$ mG/cm, $d\bar{\omega}_m/dB = 470$ kHz/G, $P_{\mathrm{He}} = 0.5$, $\gamma_{\mathrm{se}} = 20$ Hz, and $R = 100$ kHz. In other words, the fractional change in the fluorescence weight function $A_m(\bar{P})$ would have to be a few orders of magnitude to make a significant contribution to the frequency difference. This is mostly because the spin-exchange rate is very small compared to the optical pumping rate. Even if the magnetic field gradient were increased by an order of magnitude and the optical pumping rate were decreased by an order of magnitude, this gradient coupling effect would only introduce a 1% systematic error on the measurement of the ^{3}He polarization.

4.4.7 Summary & Discussion

The EPR technique provides a precise measurement of the ^{3}He polarization that is very insensitive to systematic effects. Because most of the frequency shift is due to spin-exchange collisions, the measurement is relatively insensitive to the geometry of cell. Fluorescence photons detected by the photodiode from the parts of the pumping chamber where the alkali polarization & optical pumping rates are both very high are very insensitive to the effects of the adjacent transition and magnetic field gradients. If the NMR RF is turned off after each NMR RF frequency sweep AFP, then the measurement is completely insensitive to the AC Zeeman effects due to the NMR RF field. Furthermore, if the NMR signal is calibrated by EPRs taken when pumping to both the low and high energy states, then the average calibration constant suppresses sensitivity to both the NMR RF shift effect and shifts due to magnetic field gradients. This is because the shift due to the effective field of the polarized ^{3}He gas changes sign when the laser helicity is flipped while the sign of the shifts due to these two classes of systematics remains unchanged.

The largest source of uncertainty comes from knowledge of κ_0 & its temperature dependence, the pumping chamber temperature, and the pumping chamber ^{3}He density. For a 1% measurement, the main holding field must stable to within 200 ppm over the course of the measurement. Correcting for the effects of a systematic drift in the holding field are discussed in Sec. (4.6.8). If one is interested in the target chamber polarization, then a polarization gradient correction must be applied, see Sec. (4.6.8).

4.5 Sign Determination

4.5.1 The Sign of the ^{3}He Polarization

Before going on further, it is imperative to reemphasize two important points:

1. The frequency shift due to polarized ^{3}He is measured relative to the EPR frequency when the ^{3}He polarization is zero. In other words, the "baseline" EPR frequency is due to the all the fields *not* associated with the ^{3}He.

2. The sign of the ^{3}He polarization is measured relative to the sign of the holding field (which is positive by definition).

The sign of the frequency shift $\Delta\nu$ is determined by the product $g_K\left(\vec{P}\cdot\hat{B}_0\right)$. Since the magnetic moment of ^{3}He is negative ($g_K < 0$), the sign of the polarization is negative to the sign of the frequency shift:

$$\text{sign}\left[\vec{P}\cdot\hat{B}_0\right] = -\text{sign}\left[\Delta\nu\right] \tag{4.151}$$

The physical interpretation of this result is straightforward to understand. When the holding field and the field due to ^{3}He are parallel (antiparallel), then the two fields add (subtract). The resulting EPR frequency is consequently greater (smaller) than the zero ^{3}He polarization EPR frequency. Thus the frequency shift is positive (negative). Because the magnetic moment of ^{3}He is negative, the polarization of ^{3}He and the magnetic field due to the ^{3}He are always of opposite sign:

$$\text{sign}\left[\vec{P}\right] = -\text{sign}\left[\vec{B}_{\text{He}}\right] \tag{4.152}$$

whereas the sign of the expectation value of the spin state is always the same as the sign of the polarization:

$$\text{sign}\left[\vec{P}\right] = \text{sign}\left[\left\langle \vec{K} \right\rangle\right] \tag{4.153}$$

A graphical depiction of this argument is given at the bottom of Figs. (4.13) & (4.14). To summarize:

- well shape $\Rightarrow \Delta\nu > 0 \Rightarrow B_{\text{He}}$ is parallel to B_0

  $\left({}^3\text{He is in low energy state}\right) \Rightarrow B_{\text{He}} > 0 \Rightarrow P < 0$

- hat shape $\Rightarrow \Delta\nu < 0 \Rightarrow B_{\text{He}}$ is antiparallel to B_0

  $\left({}^3\text{He is in high energy state}\right) \Rightarrow B_{\text{He}} < 0 \Rightarrow P > 0$

The sign of the ^{3}He polarization can also be inferred from the water signal. Assuming that the electronics are identical for both ^{3}He and water, then the field produced by the ^{3}He is parallel to the field produced by the water when the ^{3}He peak points in the same direction as the up sweep for the water signal during field sweep NMR, where the "up" sweep is defined as a sweep from low field to HIGH field. Since the magnetic moment of ^{3}He is negative, this implies that the sign of the ^{3}He polarization is negative. On the other hand, if the ^{3}He peak points in the opposite direction of the "up" sweep from the field sweep water NMR signal, then the sign of the ^{3}He polarization is positive.

4.5.2 The Sign of the Alkali Polarization

If the spin system in the cell is at equilibrium, then one can be certain that the sign of the alkali polarization is the same as the sign of the ^{3}He polarization. The

phrase "at equilibrium" means that both the alkali and ^{3}He polarizations have reached their saturation values. The alkali and ^{3}He spins are not at equilibrium after the first spin flip and before the second spin flip during an EPR measurement. During this middle period of an EPR measurement, the signs of the alkali and ^{3}He polarizations are opposite.

This observation can used to define a looser and more useful definition for "at equilibrium:" the spin system is "at equilibrium" when the difference between the number of alkali spin flips and the number of ^{3}He spin flips is even. The alkali spins are usually flipped by rotating the quarter waveplate used to circularly polarize the laser beam by 90 degrees. Suppose that both the alkali and ^{3}He polarizations are zero and the laser has just been turned on. In this case, the polarizations of both the alkali atoms and ^{3}He nuclei are changing with time. However, since neither set of spins have been flipped, the signs of the polarizations should be the same. In summary, as long as nothing "weird" has happened, the sign of the alkali polarization should be the same as the sign of the ^{3}He polarization.

An alternative way to determine the sign of the alkali polarization is from the EPR frequency and the magnitude of the holding field. To lowest order, the frequencies are linear in field and independent of the m_F state. However, the higher order terms (hidden in δg) give an m_F dependence to the EPR frequency. For example, at $B_0 = 25$ gauss, the difference in EPR frequencies between the $m_F = +(I + 1/2) \leftrightarrow +(I - 1/2)$ transition and the $m_F = -(I + 1/2) \leftrightarrow -(I - 1/2)$ transition are -450 kHz and -4000 kHz for ^{85}Rb and ^{39}K respectively. To use this method, one needs to know the magnitude of the holding field to only about 20% for ^{39}K EPR frequencies and to about 4% for ^{85}Rb EPR frequencies. At 25 gauss, this corresponds to only about 5 gauss for ^{39}K EPR frequencies and to about 1 gauss for

^{85}Rb EPR frequencies.

Finally, the signs of the alkali polarizations in a hybrid cell are always essentially the same. This is because the alkali spin exchange is very fast (>MHz). The alkali atoms can always be thought of as being "at equilibrium" with each other.

4.5.3 The Sign of the Light Polarization

Once the sign of the alkali polarization is known, the sign of the light polarization can be determined from knowledge of the laser beam propagation direction relative to the holding field. This is a very tricky argument because (1) there are two different coordinate systems involved in this discussion and (2) there are two different conventions for labeling the circular polarization of light. First let's start with the two different coordinate systems. From the point of view of the alkali atom, the most natural coordinate system is the one in which the positive z direction points along the direction of the holding field. Let's call this the atomic coordinate system. On the other hand, from the point of view of the photon in the laser beam, the most natural coordinate system is the one in which the positive z direction points along the direction of propagation of the laser beam. Let's call this the light coordinate system.

When the laser beam is traveling parallel to the the holding field, the atomic system and the light system are one and the same. However, when the laser beam is traveling antiparallel to the holding field, the atomic system and the light system point in opposite directions!

Suppose we've found that the polarization of ^{85}Rb is negative. This means that the $m_F = -3$ state is being filled and the $m_F = +3$ is being depopulated by the polarized light. If we ignore the nuclear spin, then this corresponds to the $m_J = +1/2$

state being filled while the $m_J = -1/2$ is being depopulated. For this to happen, the Rb atom must be selectively undergoing transitions from the $\left|S_{1/2}, +1/2\right\rangle$ state to the $\left|P_{1/2}, -1/2\right\rangle$ state. This implies that the angular momentum carried by the photon in the atomic system must be -1. Consequently, the electric field vector of the laser light is rotating clockwise around the z-axis of the atomic system. To be clear, "rotating" is really just shorthand for "rotating at a fixed point as a function of time."

If the laser beam is traveling parallel to the holding field, then our work is done. We can conclude that the electric field vector is rotating clockwise around the laser beam propagation direction. Whether we call that "right" or "left" circularly polarized light is a matter of convention that is discussed later. What happens in the scenario where the laser beam is propagating antiparallel to the holding field? Recall that the z direction in the light system points antiparallel to the z direction in the atomic system. This means that the electric field vector is rotating counter-clockwise around the laser beam propagation direction, even though it is rotating clockwise around the holding field. This argument is depicted graphically in the upper and middle portions of Figs. (4.13) & (4.14).

"Helicity" vs. "Optics" Sign Convention

Now we can finally address the question of what "handedness" to label circularly polarized light: "right" or "left." One approach is to define a quantity called helicity, which is the sign of the projection of the angular momentum of the photon about the photon propagation direction $\vec{J_\gamma}$ onto the photon momentum $\vec{k}$:

$$h = \text{sign}\left[\vec{J_\gamma} \cdot \vec{k}\right] \tag{4.154}$$

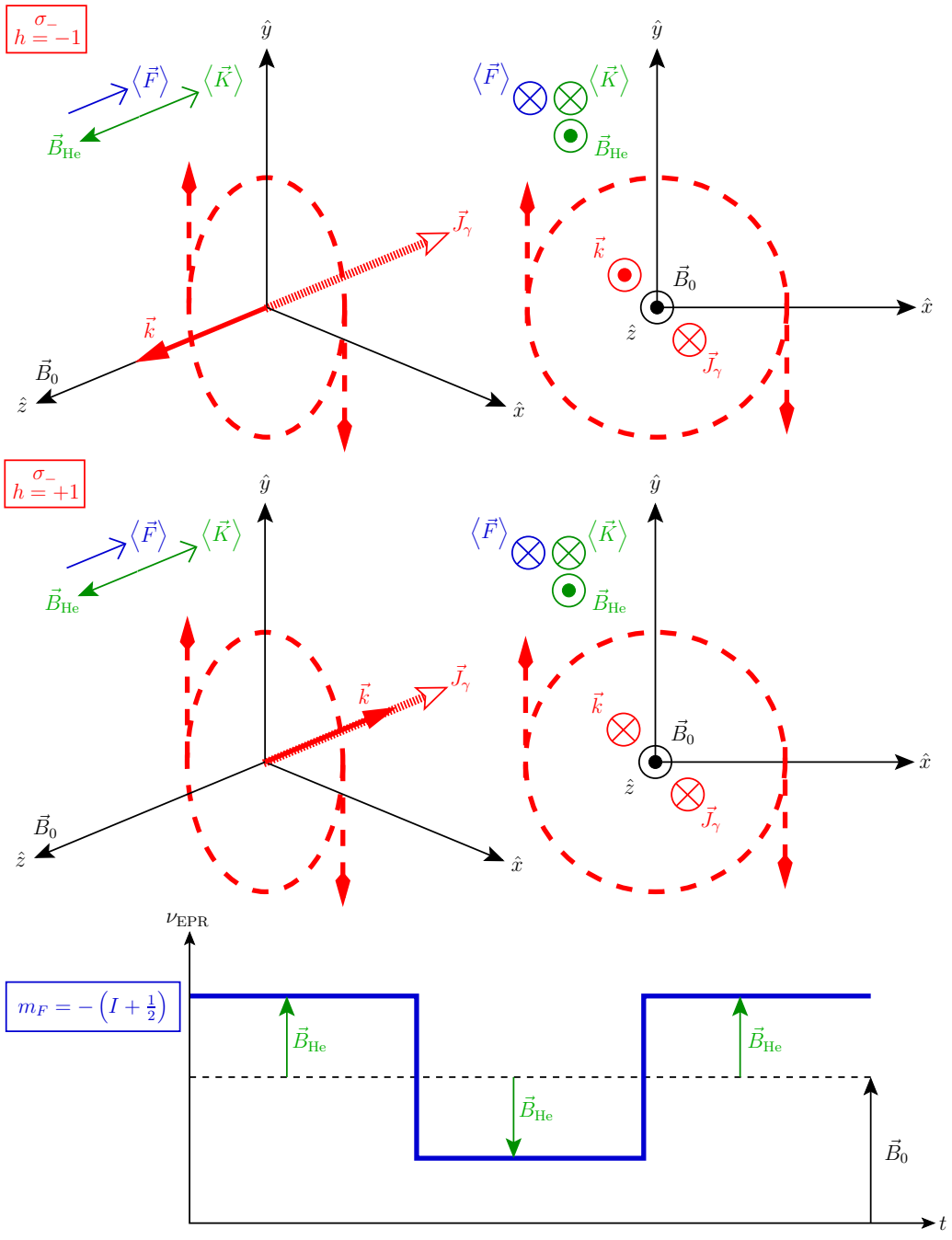

Figure 4.13: "Well" Spectrum. The field due to ^{3}He points parallel to the holding field. The sign of the ^{3}He and alkali polarizations are negative. The angular momentum of the light is antiparallel to the holding field. The EPR frequency shift measurement probes the $m_F = -(I + 1/2) \leftrightarrow -(I - 1/2)$ transition. Using the helicity convention, the upper (middle) figure represents "left" ("right") circularly polarized light traveling parallel (antiparallel) to the holding field.

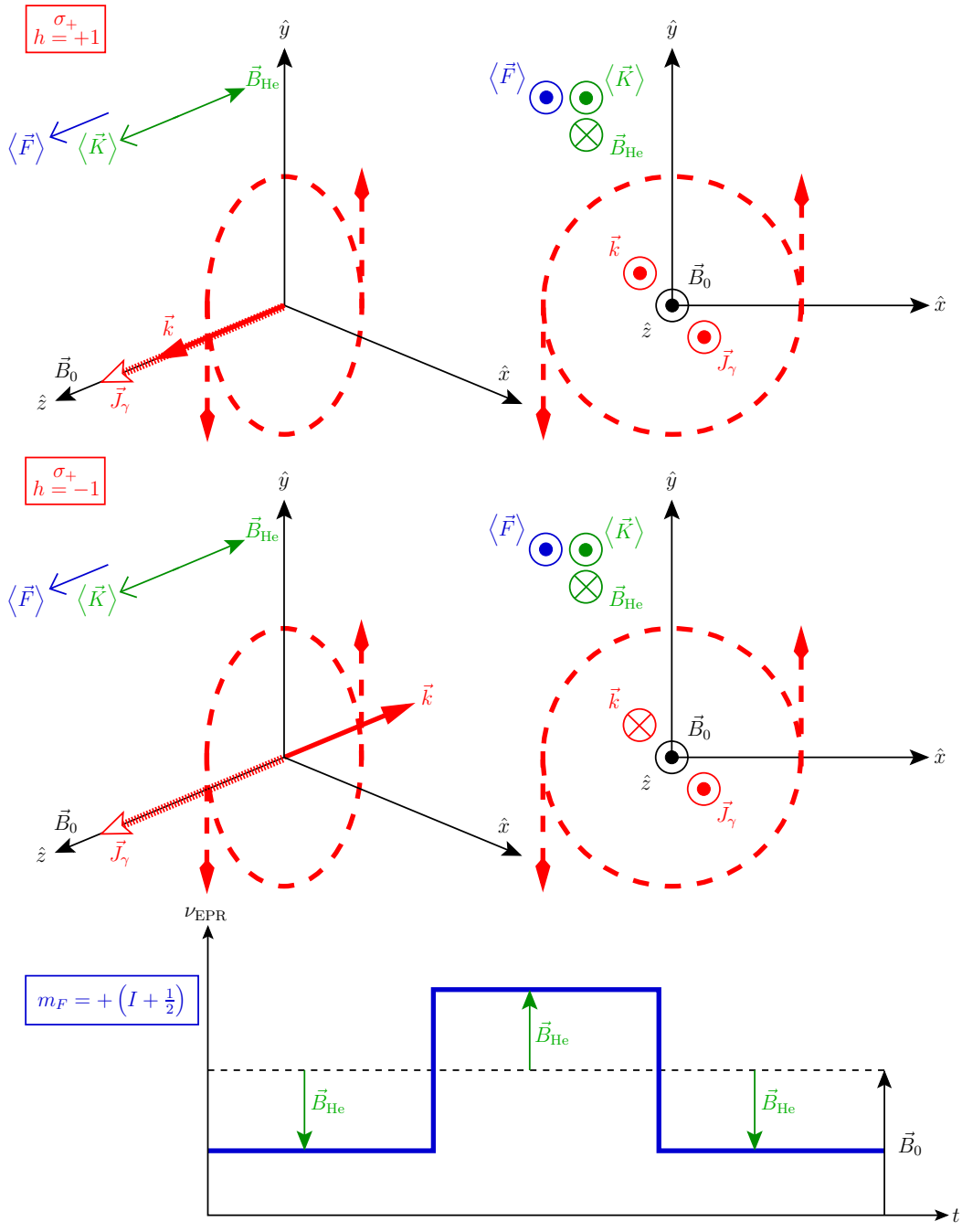

Figure 4.14: "Hat" Spectrum. The field due to ^{3}He points antiparallel to the holding field. The sign of the ^{3}He and alkali polarizations are positive. The angular momentum of the light is parallel to the holding field. The EPR frequency shift measurement probes the $m_F = +(I + 1/2) \leftrightarrow +(I - 1/2)$ transition. Using the helicity convention, the upper (middle) figure represents "right" ("left") circularly polarized light traveling parallel (antiparallel) to the holding field.

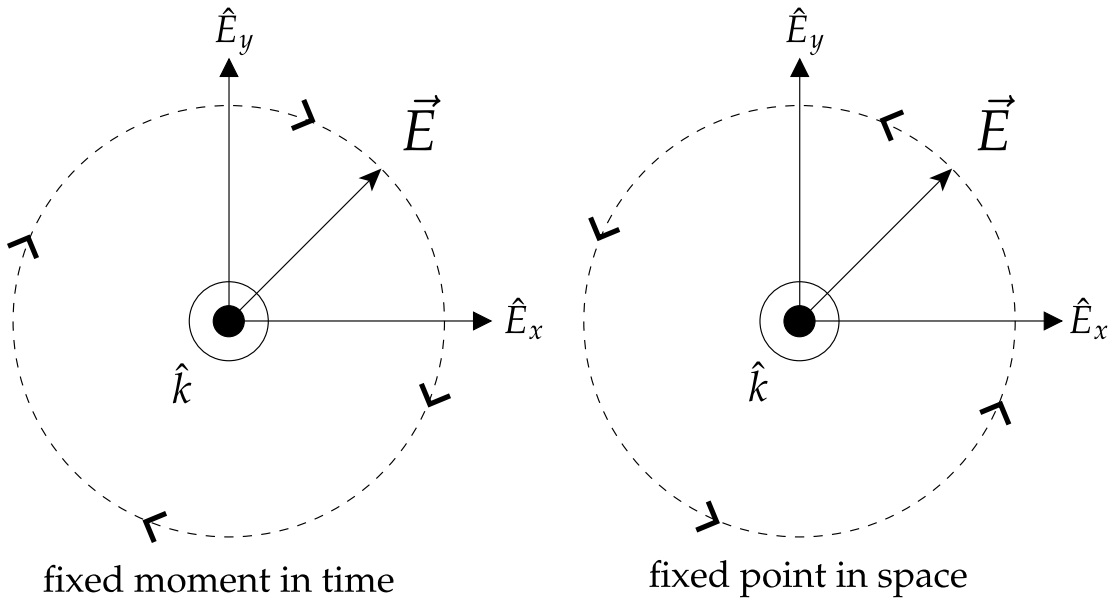

Figure 4.15: Right (helicity) circularly polarized light. Left: fixed time, forward in space. Right: fixed space, forward in time.

The helicity obeys the right hand rule: it is positive when the electric field vector rotates counter-clockwise about the light propagation direction. Once again, to be clear, by "rotate," we mean "rotating as *a function of time* at a fixed point." Let's call this the "helicity" convention. In this convention, it is natural to call light with positive (negative) helicity , "right" ("left") circularly polarized.

The other convention is the "standard optics" convention. In this case, we imagine how the electric field vector rotates as *a function of position* at a fixed time. Suppose we can "freeze" time and "look" at the electric field vector at different positions. If we were to connect that electric field vectors from location to location, we would end up with a "corkscrew" shape. A "right" handed laser beam in the helicity convention looks like a "left" handed corkscrew. The difference between these two conventions is depicted in Fig. (4.15). Useful discussions on this point can be found in [44, 45].

4.6 Polarimetry for E97110

4.6.1 NMR Calibration Constant

For this experiment, the NMR signal was calibrated using NMR signals from two sources with known absolute polarizations. The first source was protons in liquid water with a known thermal polarization given the magnetic field and temperature. The second source was the polarized ^{3}He itself with a pumping chamber polarization determined by an EPR measurement. The NMR signal data was fit to an appropriate analytic model function $\ell_{\text{model}}(t)$ which yielded the NMR signal amplitude S. By comparing to Eqn. (4.62), we find that this amplitude is given by:

$$S = c_S \left[\frac{G_{\text{L}}}{G_{\text{L}}^n}\right] G_{\text{P}} Q(\omega_0) g \nu_0 P_{\text{scale}} n_{\text{tc}} \Phi_x^{\text{tc}} \ell_B^{\text{fit}} = \frac{P_{\text{scale}} n_{\text{tc}} \ell_B^{\text{fit}}}{c_X} \tag{4.155}$$

where G_{L}^n is the nominal gain of the lockin, G_{L} is the actual gain of the lockin, G_{P} is the gain of the preamp, $Q(\omega_0)$ is the frequency response of the pickup coil detection circuitry at the resonance frequency $\omega_0 = 2\pi\nu_0$, g is the g-factor of the particle in units of the nuclear magneton, P_{scale} & n_{tc} are the average scale polarization & density in the target chamber, Φ_x^{tc} is the flux factor, ℓ_B^{fit} is the lineshape factor from a fit to $\ell_B(t)$ using the model function $\ell_{\text{model}}(t)$, $\ell_B(t)$ is NMR lineshape obtained from the numerical solution to the MBE which includes the effects of the lockin time constant & magnetic field gradients, and c_S is a constant independent of the signal source and signal detection circuitry:

$$c_S \;=\; \text{constant} \;=\; \frac{\mu_0 \mu_N}{4\sqrt{2}} = \frac{1}{4\sqrt{2}} \left(\frac{17.0530\ \text{nV}}{\text{amg} \cdot \text{cm}^2 \cdot \text{kHz}}\right) \tag{4.156}$$

In theory, we could attempt to calculate the calibration constant c_X by plugging in each factor in Eqn. (4.155). In practice, however, it is more useful to express c_X in terms of ratios, which are expected to have smaller uncertainties:

$$c_X = \left[\frac{\hat{G}_\mathrm{L}/\hat{G}_\mathrm{L}^n}{G_\mathrm{L}/G_\mathrm{L}^n}\right]\left[\frac{\hat{G}_\mathrm{P}}{G_\mathrm{P}}\right]\left[\frac{\hat{Q}(\omega_0)}{Q(\omega_0)}\right]\left[\frac{\hat{g}}{g}\right]\left[\frac{\hat{\nu}_0}{\nu_0}\right]\left[\frac{\hat{\Phi}_x^\mathrm{tc}}{\Phi_x^\mathrm{tc}}\right]\left[\frac{\hat{P}_\mathrm{tc}\hat{n}_\mathrm{tc}\hat{\ell}_B^\mathrm{fit}}{\hat{S}}\right] \tag{4.157}$$

where the "hat" (ˆ) labels quantities for a calibration measurement. The "non-hat" quantities refer to values during a "production" ^{3}He polarization measurement and yields a ^{3}He polarization given by:

$$P_\mathrm{tc} = \frac{c_X S}{n_\mathrm{tc}\ell_B^\mathrm{fit}} \tag{4.158}$$

4.6.2 Response of the Detection Circuitry

The lockin amplifier used for this experiment (SRS 844) amplified the input signal to produce an output signal given by $V_\mathrm{out} = V_\mathrm{in}(10\ \mathrm{V/sens.}) = G_\mathrm{L}V_\mathrm{in}$. The voltage recorded by the DAQ was rescaled by the nominal gain to give $V_\mathrm{DAQ} = V_\mathrm{out}/G_\mathrm{L}^n = (G_\mathrm{L}/G_\mathrm{L}^n)V_\mathrm{in}$. The ratio of the true gain to the nominal gain is 1.000 ± 0.029 ($\pm$0.25 dB for frequencies below 50 MHz [16]). Although a precise determination of this ratio could have been determined easily by a direct measurement, this was not done. Therefore, comparing two signals from the lockin at two different sensitivity settings results in a 4.1% relative uncertainty. All NMR measurements of the polarized ^{3}He cell were taken with the lockin sensitivity at 30 mV. Since all water calibration were performed with the lockin sensitivity at 100 mV, 300 mV, or 1 V, the ratio of lockin gains is 1.000 ± 0.041 for the water calibration constant. On the other hand, the EPR calibrations were performed at the same sensitivity and,

consequently, the ratio of the lockin gains cancels.

The same argument applies for the preamp (SRS 560) which has a gain accuracy of 3.5% relative (± 0.30 dB for nominal gains up to 1000 and frequencies below 300 kHz [46]). The preamp gain was 1 for ^{3}He measurements and 100 or 200 for water calibrations. Again, since the true gain was not measueed, we've assumed that the preamp gain ratio for water calibration was 1.000 ± 0.050, whereas this factor cancels for EPR calibrations.

The relative frequency response of the detection circuitry was monitored by measurements of its "Q-Curve." The pickup coils, preamp (with a nominal gain of 1 and frequency filters off), and BNC cabling can be modeled [12, 14, 47, 48] as an equivalent series RLC-circuit with the induced signal $\mathscr{E}$ as a voltage source. In this model, the voltage measured by the lockin is across the equivalent capacitor, which we'll assume also has a large intrinsic resistance in parallel. It is straightforward to show that the amplitude of the frequency response is given by [47]:

$$\begin{aligned} Q(\omega) &= \left|\frac{V_{\text{out}}}{\mathscr{E}}\right| = \left[\left(1+\rho-u^2\right)^2 + \frac{u^2}{q^2}\right]^{-1/2} \times \exp(-\alpha) \qquad (4.159) \\ 2\alpha^2 &= \rho + u^2\left[-1+\sqrt{1+\frac{1/q^2-2\rho}{u^2}+\frac{\rho^2}{u^4}}\right] \approx \frac{1}{2q^2} \quad \left(\text{when } u \gg 1/q, \sqrt{\rho}\right) \end{aligned}$$

where $u = \omega/\omega_0$, $\omega_0 = 1/\sqrt{LC}$, $\rho = R_s/R_p$ is the ratio of the series resistance R_s to the parallel resistance R_p, $q = Q_0/(1+\rho Q_0^2)$, $Q_0 = (1/R_s)\sqrt{L/C}$, and α is due to the attenuation of the signal due to the BNC cable. The Q-curve is measured by recording the signal induced in the pickup coils due to a small "Q"-coil which creates an RF field at a fixed amplitude. The lockin voltage (in the "R" channel) vs.

Q-coil frequency is fit to:

$$f(\omega) = \left| AQ(\omega) + b + m\left(\frac{\omega - \omega_{\text{ref}}}{\omega_0}\right)\right| \tag{4.160}$$

where $\omega_{\text{ref}} = 2\pi(91\text{ kHz})$, we've included a linear background to account for the "drift" in signal due to the "warming-up" of the Q-coil, and the absolute value insures that the voltage measured is positive, see Fig. (4.16). The results for E97110 are listed in Tab. (4.4), where the fits values for $|\rho|$ were always below 0.003. The response at 91 kHz $Q(91\text{ kHz})$ changed by $(-4.6 \pm 0.5)\%$ relative after the cell Penelope ruptured on 07/23. Finally, the response while the oven is hot (i.e. operating conditions for ^{3}He) is lower by $(1.8 \pm 0.3)\%$ relative than the response while the oven is cold (i.e. operating conditions for water calibrations). Since relatively few Q-curve measurements were taken, we've used the variation in the July measurements to assign a 1% relative uncertainity to the stability of the frequency response.

4.6.3 Target Density

The number density in the two chambers of the target cell can be calculated from the temperature t and volume v ratios defined by:

$$v = V_{\text{pc}}/V_{\text{tc}} \qquad\qquad t = T_{\text{pc}}/T_{\text{tc}} \tag{4.161}$$

where the temperatures of the pumping & target chambers are given **in Kelvin** by T_{pc} & T_{tc} respectively, and the volumes of the pumping & target chambers are V_{pc} & V_{tc} respectively. Assuming that the pressure is uniform throughout the cell and

date	**conditions**	**res. freq. (kHz)**	q	Q(91 kHz)
07/09 19:33	cold	146.873 ± 0.009	28.3 ± 0.1	1.5930 ± 0.0004
07/10 00:24	cold	147.237 ± 0.014	32.8 ± 0.3	1.5907 ± 0.0006
07/10 00:37	cold	147.238 ± 0.014	32.8 ± 0.3	1.5907 ± 0.0006
07/12 17:29	cold	147.632 ± 0.004	28.9 ± 0.1	1.5900 ± 0.0002
07/12 18:14	cold	147.686 ± 0.008	28.0 ± 0.1	1.5873 ± 0.0003
08/05 19:01	cold	153.080 ± 0.004	40.1 ± 0.1	1.5261 ± 0.0002
08/30 19:24	cold	153.425 ± 0.004	41.3 ± 0.1	1.5272 ± 0.0002
08/30 19:34	cold	153.424 ± 0.004	41.3 ± 0.1	1.5273 ± 0.0002
08/30 22:29	cold	153.440 ± 0.004	41.3 ± 0.1	1.5266 ± 0.0002
09/01 21:56	cold	153.072 ± 0.005	40.1 ± 0.1	1.5264 ± 0.0002
09/01 22:06	cold	153.072 ± 0.005	40.1 ± 0.1	1.5264 ± 0.0002
09/02 10:52	hot	155.932 ± 0.010	43.5 ± 0.3	1.5017 ± 0.0003
09/02 11:02	hot	155.962 ± 0.010	43.4 ± 0.3	1.5005 ± 0.0003
07/09	penelope cold			1.590 ± 0.002
07/23	penelope hot			1.563 ± 0.004
07/23	priapus cold			1.5267 ± 0.0005
09/01	priapus hot			1.501 ± 0.003

Table 4.4: Results of "Q-Curve" Measurements for E97110. The rupture of the cell Penelope on 07/23 is thought to have changed the response of the pickup coils. Only two measurements were made while the cell & oven were hot. These measurements were scaled to estimate the "hot" response before 07/23.

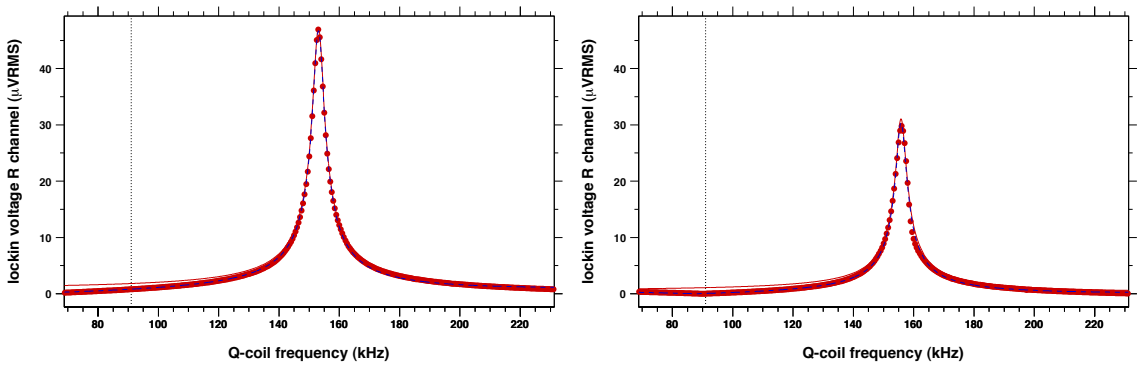

Figure 4.16: Q-curve Measurements. The left (right) plot is depicts the fit to the 09/01 22:06 (09/02 10:52) measurement when the oven was cold (hot). The solid points are data, the dashed line is the fit to Eqn. (4.160), and the solid line the response, Eqn. (4.159), scaled by the normalization parameter A. The vertical dotted line is at 91 kHz, which was the NMR RF frequency for all NMR measurements. The "kink" in the hot measurement (right plot) is an artifact due to the fact that the R channel of the lockin does not record sign information.

that the ^{3}He behaves as an ideal gas, we find:

$$P_{\text{cell}} = n_{\text{fill}} \left[\frac{1+v}{t+v}\right] RT_{\text{pc}} = n_{\text{pc}} RT_{\text{pc}} = n_{\text{tc}} RT_{\text{tc}} \tag{4.162}$$

where n_{fill} is the fill density, R is the ideal gas constant, and we've ignored the effect of the small transfer tube volume. This immediately yields the densities:

$$n_{\text{pc}} = n_{\text{fill}} \left[\frac{1+v}{t+v}\right] \qquad n_{\text{tc}} = n_{\text{pc}} t = n_{\text{fill}} \left[\frac{1+v}{t+v}\right] t \tag{4.163}$$

Target Chamber Temperatures

The target chamber temperatures were monitored at 5 different locations along the length of the chamber using RTDs (Resistance Temperature Detector), see Fig. (4.18) and Tab. (4.7). There are several ways [12,49] to model the temperature distribution in the target chamber and, provided the model results in a reasonable/smoothly-

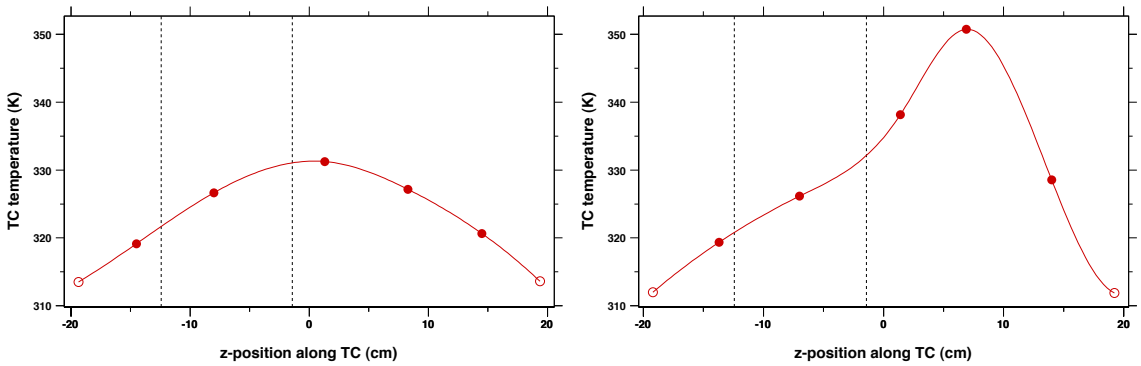

Figure 4.17: Target Chamber Temperature Gradient. The solid points are the measured temperatures. The open points are the extrapolated values used to construct the cubic spline (denoted by the solid curve). The left (right) plot is for the cell Penelope (Priapus) during the 6 (9) degree running. The vertical dashed lines represent the edges of the pickup coils.

varying function, the average target chamber density is very insensitive to the details of the model. Therefore, we used a cubic spline where the temperature at the ends of the target chamber were determined by a linear extrapolation of two nearest temperature readings, see Fig. (4.17). Since n_{tc} is defined to be the average density in the target chamber, the value T_{tc} is understood to be $1/\langle 1/T_{\mathrm{tc}}\rangle$, the inverse of the average value of the inverse temperature in the target chamber.

"Temperature Tests"

The laser light heats the ^{3}He gas in the pumping chamber by a significant amount [50, 51]. In addition, the light may also heat the RTDs monitoring the pumping chamber temperature by some unknown amount. Therefore, the temperature of the ^{3}He gas in the pumping chamber can not be assumed to be the same as the surface temperature of the pumping chamber. A "temperature test" is used to infer the ^{3}He gas temperature in the pumping chamber when the lasers are on by comparing the size of the NMR signal with the lasers on & off. This test assumes

that the ^{3}He gas temperature is the same as the surface temperature of the glass for those parts of the cell that are not being hit by the laser light.

The ratio of NMR signals with the laser on & off are given by:

$$\frac{S^{\rm on}}{S^{\rm off}} = \frac{c_X^{\rm off} P^{\rm on} n^{\rm on} \ell^{\rm on}}{c_X^{\rm on} P^{\rm off} n^{\rm off} \ell^{\rm off}} \tag{4.164}$$

Because any change in the polarization or calibration constant can mimic a change in the density when the laser is turned on/off, it is more useful to work with the normalized NMR signal ratio ρ defined by:

$$\rho \equiv \frac{n^{\rm on}}{n^{\rm off}} = \frac{S^{\rm on} c_X^{\rm on} P^{\rm off} \ell^{\rm off}}{S^{\rm off} c_X^{\rm off} P^{\rm on} \ell^{\rm on}} \tag{4.165}$$

For the case where we can measure the NMR signal in both chambers simultaneously, we can take the ratio of the pumping & target chamber normalized NMR signal ratios to get:

$$\frac{\rho_{\rm pc}}{\rho_{\rm tc}} = \frac{n_{\rm pc}^{\rm on}}{n_{\rm pc}^{\rm off}} \times \frac{n_{\rm tc}^{\rm off}}{n_{\rm tc}^{\rm on}} = \frac{n_{\rm pc}^{\rm on}}{n_{\rm tc}^{\rm on}} \times \frac{n_{\rm tc}^{\rm off}}{n_{\rm pc}^{\rm off}} = \frac{t^{\rm off}}{t^{\rm on}} \tag{4.166}$$

which we can easily solve for $t^{\rm on}$:

$$t^{\rm on} = t^{\rm off} \rho_{\rm tc}/\rho_{\rm pc} \quad \rightarrow \quad T_{\rm pc}^{\rm on} = T_{\rm pc}^{\rm off} \left[\frac{S_{\rm tc}^{\rm on} S_{\rm pc}^{\rm off}}{S_{\rm tc}^{\rm off} S_{\rm pc}^{\rm on}}\right] \left[\frac{c_{\rm tc}^{\rm on} c_{\rm pc}^{\rm off}}{c_{\rm tc}^{\rm off} c_{\rm pc}^{\rm on}}\right] \left[\frac{P_{\rm tc}^{\rm off} P_{\rm pc}^{\rm on}}{P_{\rm tc}^{\rm on} P_{\rm pc}^{\rm off}}\right] \left[\frac{\ell_{\rm tc}^{\rm off} \ell_{\rm pc}^{\rm on}}{\ell_{\rm tc}^{\rm on} \ell_{\rm pc}^{\rm off}}\right] \left[\frac{T_{\rm tc}^{\rm on}}{T_{\rm tc}^{\rm off}}\right] \tag{4.167}$$

If we only have NMR measurement in the pumping chamber, then we must start with this equation:

$$\rho_{\rm pc} = \frac{n_{\rm pc}^{\rm on}}{n_{\rm pc}^{\rm off}} = \frac{1+v}{t^{\rm on}+v} \times \frac{t^{\rm off}+v}{1+v} = \frac{t^{\rm off}+v}{t^{\rm on}+v} \tag{4.168}$$

Solving for t^{on} gives:

$$t^{\text{on}} = \frac{t^{\text{off}} + v}{\rho_{\text{pc}}} - v \;\; \rightarrow \;\; T_{\text{pc}}^{\text{on}} = T_{\text{tc}}^{\text{on}} \left(\frac{V_{\text{pc}}}{V_{\text{tc}}}\right) \left(-1 + \left[1 + \frac{T_{\text{pc}}^{\text{off}} V_{\text{tc}}}{T_{\text{tc}}^{\text{off}} V_{\text{pc}}}\right] \left[\frac{S_{\text{pc}}^{\text{off}}}{S_{\text{pc}}^{\text{on}}}\right] \left[\frac{c_{\text{pc}}^{\text{off}}}{c_{\text{pc}}^{\text{on}}}\right] \left[\frac{P_{\text{pc}}^{\text{on}}}{P_{\text{pc}}^{\text{off}}}\right] \left[\frac{\ell_{\text{pc}}^{\text{on}}}{\ell_{\text{pc}}^{\text{off}}}\right]\right) \tag{4.169}$$

If we can only measure the NMR signal in the target chamber, then we must start with this equation:

$$\rho_{\text{tc}} = \frac{n_{\text{tc}}^{\text{on}}}{n_{\text{tc}}^{\text{off}}} = t^{\text{on}} \left[\frac{1+v}{t^{\text{on}}+v}\right] \times \frac{1}{t^{\text{off}}} \left[\frac{t^{\text{off}}+v}{1+v}\right] = \frac{t^{\text{on}}}{t^{\text{off}}} \left[\frac{t^{\text{off}}+v}{t^{\text{on}}+v}\right] \tag{4.170}$$

Solving for t^{on} gives:

$$\frac{1}{t^{\text{on}}} = \frac{1}{\rho_{\text{tc}}} \left[\frac{1}{t^{\text{off}}} + \frac{1}{v}\right] - \frac{1}{v} \tag{4.171}$$

Rearranging some things and writing it out explicitly gives for NMR in the target chamber only:

$$T_{\text{pc}}^{\text{on}} = T_{\text{tc}}^{\text{on}} \left(-\frac{V_{\text{tc}}}{V_{\text{pc}}} + \left[\frac{T_{\text{tc}}^{\text{off}}}{T_{\text{pc}}^{\text{off}}} + \frac{V_{\text{tc}}}{V_{\text{pc}}}\right] \left[\frac{S_{\text{tc}}^{\text{off}}}{S_{\text{tc}}^{\text{on}}}\right] \left[\frac{c_{\text{tc}}^{\text{off}}}{c_{\text{tc}}^{\text{on}}}\right] \left[\frac{P_{\text{tc}}^{\text{on}}}{P_{\text{tc}}^{\text{off}}}\right] \left[\frac{\ell_{\text{tc}}^{\text{on}}}{\ell_{\text{tc}}^{\text{off}}}\right]\right)^{-1} \tag{4.172}$$

Results for E97110

For E97110, only target chamber pickup coils were used, therefore, we'll apply Eqn. (4.172). This test is very sensitive to systematic differences between the NMR signals when the laser is turned off. For example, in our case, a 1% relative difference between the "laser on" and "laser off" normalized NMR signals translates into about a 5 degree difference between the calculated and measured pumping chamber temperatures. Changes in the NMR signal are due to changes in both the density (what we're interested in) and the calibration constant & polarization. During these tests, there was usually a 0.3 K difference in target chamber temperature when the lasers turned on/off. We have assumed that variations in the calibration

date	**notes**	**# meas.**	$\langle \Delta t \rangle$	S_{tc}^{on}/S_{tc}^{off}	P_{tc}^{on}/P_{tc}^{off}	$(\Delta T)_{\neq 1}$	$(\Delta T)_{=1}$
07/16	penelope	5	26	1.049	1.001	23	24
07/24	-	4	20	1.072	1.018	33	55
07/28	-	3	22	1.051	1.000	31	31
07/30	-	5	25	1.052	1.017	13	31
08/03	-	7	24	1.048	1.010	16	27
08/12	4 lasers	5	26	1.047	1.001	20	21
08/13	-	6	15	1.056	1.004	24	29
08/29	cooling jets on	5	19	1.065	0.997	43	39
08/29	cooling jets off	5	20	1.053	0.999	26	25
08/29	1 laser	7	15	1.025	0.998	17	15
			min			K	K

Table 4.5: Temperature Test Results for E97110. All tests were done with the cell Priapus and 3 lasers unless otherwise noted. The average time interval between measurements is $\langle \Delta t \rangle$. The difference between the calculated pumping chamber temperature and the measured value with the lasers on is (ΔT). A temperature test using only one laser was performed to estimate the size of the temperature difference when there was less heating. The calculated temperature was obtained by assuming that alkali vapor density (1) remains fixed ($(\Delta T)_{\neq 1}$, P_{tc}^{on}/P_{tc}^{off} listed in table) and (2) changes instantaneously ($(\Delta T)_{=1}$,$P_{tc}^{on}/P_{tc}^{off} = 1.0000 \pm 0.0002$).

constant due to target chamber temperature fluctuations is linear; therefore, we find $c_{tc}^{on}/c_{tc}^{off} = 1.000 \pm 0.001$.

The signals are typically measured five times with the laser sequence ON-off-ON-off-ON with about a 20 minute interval between measurements, see Tab. (4.5). Since most measurements are performed when the polarization is near its equilibrium value, it does not change much when the laser is on. However, the polarization may change significantly when the lasers are off because of the rapid (relative to the cell lifetime) spin exchange with the unpolarized alkali vapor. This may cause a systematic difference in the polarization when the lasers are turned off.

Studies of the polarization dynamics in the cell, see Sec. (6.1), indicate that the polarization ratio P_{tc}^{on}/P_{tc}^{off} is most sensitive to alkali vapor density when the lasers are turned off. Although the glass and ^{3}He gas is expected to reach thermal equilibrium very quickly (several seconds), it is not clear how fast the alkali vapor density changes. Therefore, we've calculated the polarization ratio assuming that the alkali vapor density (1) remains fixed throughout the temperature test and (2) changes instantaneously to its new equilibrium value when the laser is turned on/off. For the first case, because the alkali vapor density remains high, the spin exchange rate is relatively fast and the polarization ratios calculated from a numerical simulation are listed in Tab. (4.5). For the second case, because the laser off pumping chamber temperature is relatively low (compared to hybrid cells), the spin exchange rate is relatively slow and a numerical simulation indicates that the polarization ratio is essentially unity, $P_{tc}^{on}/P_{tc}^{off} = (1.0000 \pm 0.0002)$. On average, in our case, the assumption that the polarization ratio is unity results in calculated pumping chamber temperatures that are about 5 degrees hotter. Combing all of the second period temperature tests and averaging the results from the two assumptions for

the behavior of the alkali vapor density, we find:

$$\Delta T = T_{pc}^{calc} - T_{pc}^{meas} = (28 \pm 8)\ \mathrm{K} + [0.4 \pm 0.6]\left(T_{pc}^{meas} - 465\ \mathrm{K}\right) \tag{4.173}$$

where the uncertainties in the calibration constant & polarization ratios have been folded into uncertainties quoted in the equation. The pumping chamber temperature was systematically 13 K lower when the laser light was incident from the transverse direction (i.e. "transverse pumping"). Since a temperature test was not possible under this condition, we've used the correction given by Eqn. (4.173) for both longitudinal & transverse pumping. This was reasonable since the large uncertainty in the linear term (0.4 ± 0.6) resulted in a larger uncertainty in the calculated temperatures for transverse pumping.

Finally, we'll note that the pumping chamber polarization ratio is much more sensitive to the details of the dynamics and, in our case, we find $P_{pc}^{on}/P_{pc}^{off} = 1.10 \pm 0.05$ for case (1) and $P_{pc}^{on}/P_{pc}^{off} = 1.03 \pm 0.02$ for case (2). This causes a difference in the ratio of the polarizations between the pumping & target chambers when the lasers are turned on/off. Combined with the change in the ratio of pumping chamber to target chamber density, this causes a systematic difference in the lineshape factor when the lasers are turned on/off. Under our conditions, we found that $\ell_{tc}^{on}/\ell_{tc}^{off} = 1.0025 \pm 0.0025$. Since we ignored this factor in the analysis, we've assumed that $\ell_{tc}^{on}/\ell_{tc}^{off} = 1.000 \pm 0.005$, which results in only a small change in the final value & uncertainty in the pumping chamber temperature.

4.6.4 NMR Pickup Coil Flux Factor

The flux factor was calculated by a numeric integration of Eqn. (4.43). We assumed two identical pickup coils on either side of the target chamber, each with 120 turns using 32 gauge (AWG) wire. Measurements of the coil-to-coil (`cc1`, `cc2`, `cc3`, `cc4`) and coil-to-cell (`atp`, `atm`, `btp`, `btm`) distances were usually made for each water calibration and for each time the polarized ^{3}He cell was installed or removed, see Tab. (4.6) and Fig. (4.18). The coil-to-coil distances were more reliable, so the cell-to-coil distances were rescaled using the target chamber outer diameter (`tcod`), for example:

$$\texttt{atp}' = \texttt{atp}\left[\frac{\texttt{cc1}/2 + \texttt{cc2}/2 - \texttt{tcod}}{\texttt{atp} + \texttt{btp}}\right] \tag{4.174}$$

The vertical (y) position of the coil with respect to the target chamber was determined by the encoder reading from the stepper motor used to raise/lower the target ladder assembly, see Fig. (3.8).

The density gradient in the target chamber was determined by the temperature distribution, see Sec. (4.6.3). The polarization gradient was estimated using the results of Sec. (6.4.6). Combining the polarization and density gradients, we find for the target chamber:

$$f(\vec{u}) = \left[1 + \frac{1}{2}\left(1 - \frac{4|\vec{u}\cdot\hat{z}|}{L_{\rm tc}}\right)\frac{\Delta P_{\rm tc}}{\langle P_{\rm tc}\rangle}\right]\frac{1/\langle 1/T_{\rm tc}\rangle}{T_{\rm tc}(\vec{u}\cdot\hat{z})} \tag{4.175}$$

where $\Delta P_{\rm tc}/\langle P_{\rm tc}\rangle$ is difference in the polarization between the center & ends of the target chamber relative to the average target chamber polarization and the values used for this experiment are listed in Tab. (4.7).

The water cell used for this experiment had a different target chamber wall thickness than for the two polarized ^{3}He cells, see Tab. (4.8). Because the flux fac-

date	**cell**	atp	atm	btm	btp	cc1	cc2	cc4	cc3
07/10	water	0.267	0.373	0.254	0.297	2.469	2.522	2.591	2.601
07/12	water	1.003	1.430	0.254	0.417	3.368	3.307	3.683	3.622
08/05	water	0.772	1.445	0.267	0.470	3.317	3.251	3.622	3.614
09/01	water	0.792	1.494	0.274	0.472	3.352	3.302	3.582	3.588
07/12	penelope	0.970	1.372	0.406	0.371	3.368	3.307	3.683	3.622
07/23	priapus	0.780	1.157	0.401	0.514	3.347	3.288	3.677	3.625
08/07	priapus	0.790	1.273	0.437	0.587	3.317	3.251	3.622	3.614
08/29	priapus	0.770	1.041	0.366	0.442	3.330	3.330	3.617	3.569
09/01	-1 mm	-0.56	-0.27	+1.57	+1.07	+0.94	+0.94	+0.73	+0.73
	$+1$ mm	+0.52	+0.24	-1.24	-0.79	-0.92	-0.92	-0.72	-0.72
08/29	-1 mm	-0.50	-0.44	+1.41	+1.01	+0.94	+0.94	+0.84	+0.84
	$+1$ mm	+0.47	+0.40	-1.02	-0.72	-0.92	-0.92	-0.83	-0.83

Table 4.6: Measured Coil-to-cell & Coil-to-coil Distances for E97110. The first 8 rows are the distances in cm. The pickup coils were moved on July 12 due to space constraints and on July 23 because the cell Penelope ruptured. The last 4 rows are the percent change in the flux factor Φ_x^{tc} when the distance corresponding to that column is changed by ± 1 mm for the water cell (09/01) and the cell Priapus (08/29). The flux gain $G_\Phi^x(0)$ changes by less than 0.1% relative for a ± 1 mm variation in the coil positions.

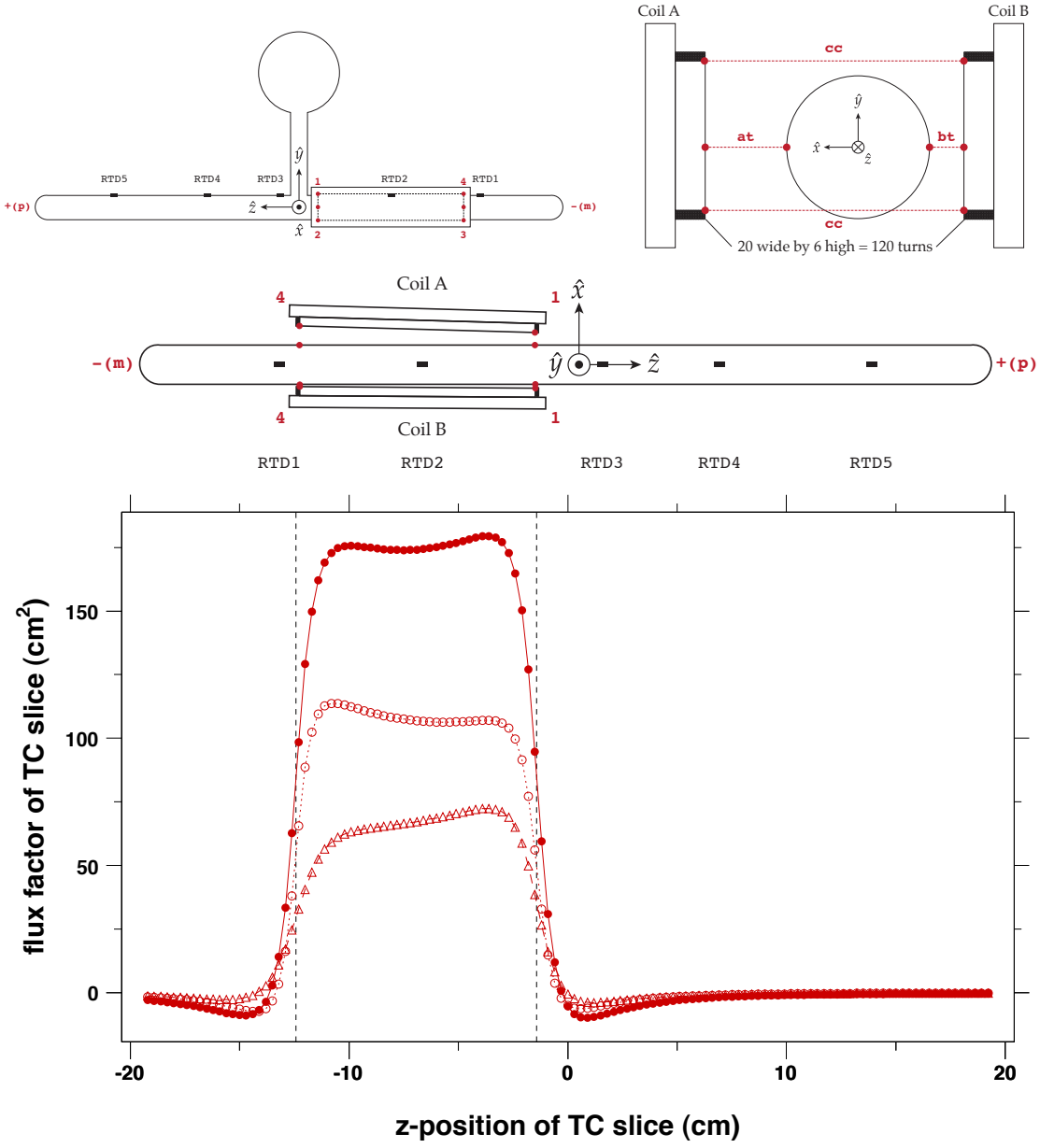

Figure 4.18: Pickup Coil and Target Chamber Geometry. The positive z-axis points towards the beam dump. The positive y-axis points towards the pumping chamber and $\hat{x} = \hat{y} \times \hat{z}$. The origin is the center of the target chamber. Each pickup coil is 20 turns wide by 6 turns high with a wire diameter of 202 μm. The lower plot is the flux factor per z-slice in the target chamber of Priapus during the 9 degree running, where the solid circles is the sum of the coil A (open triangles) and coil B (open circles) contributions.

parameter	water	penelope	priapus	
			6 deg	9 deg
T_{pc}^{calc} (°C)	24	227	216	221
`rtd1` (cm) , T_{tc} (°C)	24	-14.5 , 46.0	-13.7 , 43.8	46.2
`rtd2` (cm) , T_{tc} (°C)	24	-8.0 , 53.5	-7.0 , 55.6	53.0
`rtd3` (cm) , T_{tc} (°C)	24	$+1.3$, 58.1	$+1.4$, 77.9	65.0
`rtd4` (cm) , T_{tc} (°C)	24	$+8.3$, 54.0	$+6.9$, 86.4	77.6
`rtd5` (cm) , T_{tc} (°C)	24	$+14.5$, 47.5	$+14.0$, 55.4	55.4
$1/\langle 1/T_{tc}\rangle$ (°C)		51.3	58.5	56.1
$v = V_{pc}/V_{tc}$		1.023	1.141	
$n_{pc}/n_{tc} = 1/t$	1	0.649	0.679	0.666
n_{tc} (amg)	2482	10.82	10.53	10.62
$\langle I_{beam}\rangle$ (μA)		2.23	4.29	8.00
lifetime (hrs)		54	56	56
$\left(1 - P_{tc}^{\infty}/P_{pc}^{\infty}\right)_{beam}$ (%)		2.9	3.0	3.7
$\left(1 - P_{tc}^{\infty}/P_{pc}^{\infty}\right)_{0}$ (%)	0	2.5	2.2	2.2
$\left(\Delta P_{tc}/\langle P_{tc}\rangle\right)_{beam}$ (%)		1.42	1.50	1.88
$\left(\Delta P_{tc}/\langle P_{tc}\rangle\right)_{0}$ (%)	0	1.20	1.08	1.10

Table 4.7: Temperature/Density and Polarization Gradient Parameters for E97110. NMR measurements were made with lasers on in the longitudinal configuration. The polarization gradient parameters are given for both no beam (subscript 0) and with a beam current of $\langle I_{beam}\rangle$ (subscript beam).

tor drops off a $1/d^2$, where d is the distance between the coils and the spins, the numerical integration took into account the size of the coil wire to determine the relative position of each turn. The integration was performed using $2 \times$ (3 by 14) line elements per turn, $(2 \times 64 + 1) \times (16 \times 4)^2$ volume elements for the target chamber, $(2 \times 8 + 1) \times (8 \times 4)^2$ volume elements for the transfer tube, and 13025 volume elements for the pumping chamber. The flux gain $G_\Phi^x(0)$ is calculated using the parameters from Tab. (4.7) assuming that there are no magnetic field gradients. Final results for the flux factor and flux gain for each measurement of the coil positions are listed in Tab. (4.9). The uncertainty in the flux factor due to the uncertainty in the coil position measurements is about 2.6% relative per 1 mm of uncertainty of the measurements, see Tab. (4.6). From measurements of the coil positions from the start and end of the 9 degree running with Priapus, we've assigned a 0.6% relative uncertainty due to the stablity of the coil positions. Finally, we've assigned a 0.7% relative uncertaintity due to our understanding of the polarization & temperature/density gradients along the target chamber.

4.6.5 NMR Lineshape Model Functions

Since a full numerical calculation of the NMR lineshape via the MBE is very time consuming, the data were fit to analytic model functions. These functions are approximate but reproduce all the salient features of the lineshape. For the case of polarized ^{3}He (i.e. no relaxation), the model function is given by:

$$\ell_{\text{model}}(t) = S\left[1 + \left(\frac{H(t) - H_0}{H_1}\right)^2\right]^{-1/2} + m_b H(t) + c_b \tag{4.176}$$

where we've allowed for the possibility of a linear background.

	water	penelope	priapus
pcodV	6.72	6.16	6.33
pcodH	6.50	6.11	6.28
pcwall	0.193	0.193	0.193
ttod	1.25	1.26	1.27
ttlen	6.53	6.20	6.02
ttwall	0.173	0.181	0.181
tcod	1.92	1.91	1.91
tclen	39.9	39.7	39.4
tcwallA	0.115	0.0694	0.0760
tcwallB	0.115	0.0622	0.0600

Table 4.8: Cell Dimensions Used for Flux Factor Calculation. All units are cm. The vertical & horizontal diameters of the pumping chamber are pcodV & pcodH respectively. The wall thickness of the target chamber near coils A & B are tcwallA & tcwallB respectively. Water cell dimensions were from [52].

For the case of thermally polarized protons in water (i.e. with relaxation), a model function can be found by noting that (1) since $\eta \ll 1$, p_x starts small, $p_x^0 = p_x^{\text{eq}} \ll p_y^{\text{eq}} \ll p_z^{\text{eq}}$, and (2) a numerical solution to the MBE confirms that p_x stays small as the detuning is swept, $p_x \ll p_y, p_z$ for all t, see Fig. (4.3). Therefore, by setting p_x & $\dot{p}_x$ to zero in Eqn. (4.56), we find that the ratio of p_z to p_y is approximately Δ/ω_1 and, consequently, the polarization vector can be written as:

$$\vec{p} \approx \frac{p}{\Omega}\left[\omega_1 \hat{y}_{\text{rot}} + \Delta\hat{z}\right] = p\hat{B}_{\text{eff}} \tag{4.177}$$

where p is the magnitude of the polarization relative to the thermal polarization due to a field with magnitude B_0. Once again the polarization vector is parallel to the effective field in the rotating frame. However, in this case, the magnitude of

date	cell	coil A		coil B		A+B	
		Φ_x^{tc}	$G_\Phi^x(0)$	Φ_x^{tc}	$G_\Phi^x(0)$	Φ_x^{tc}	$G_\Phi^x(0)$
07/10	water	3781	0.949	3944	0.951	7725	0.950
07/12	water	1850	0.910	3689	0.948	5539	0.935
08/05	water	2001	0.915	3577	0.948	5578	0.936
09/01	water	2014	0.918	3626	0.950	5640	0.938
	NG	0.76	-2.14	0.73	-1.26	0.74	-1.56
07/12	TG	-0.22	0.12	-0.21	0.08	-0.22	0.09
	penelope	2174	0.954	4032	0.970	6206	0.965
	NG	-0.91	-2.23	-1.06	-1.49	-1.00	-1.77
07/23	TG	-0.23	0.14	-0.21	0.10	-0.22	0.11
	priapus	2344	0.948	3680	0.964	6024	0.958
	NG	-1.25	-2.22	-1.29	-1.52	-1.27	-1.79
08/07	TG	-0.30	0.17	-0.26	0.12	-0.28	0.14
	priapus	2425	0.950	3667	0.965	6092	0.959
	NG	-1.26	-2.26	-1.28	-1.49	-1.27	-1.78
08/29	TG	-0.29	0.17	-0.27	0.12	-0.28	0.14
	priapus	2343	0.950	3769	0.965	6111	0.959

Table 4.9: Results for Flux Factors and Flux Gains for E97110. The flux factors Φ_x^{tc} are given in cm^2 and the flux gains $G_\Phi^x(0)$ are unitless. For the polarized ^{3}He cells, the first row is the result ignoring polarization & temperature gradients, the second row includes the effect of a temperature/density gradient (TG) along the target chamber, and the third row includes both the temperature/density gradient and the polarization gradient (TG/PG) along the target chamber length. The first & second rows are given as the percent difference from the third row. The flux gain quoted here is calculated assuming that there are no magnetic field gradients, see Sec. (4.6.6) for further discussion.

the polarization vector p is not unity and its time evolution is governed by:

$$\frac{dp}{dt} \approx \frac{d}{dt}\left[s\sqrt{p_y^2 + p_z^2}\right] = \frac{1}{p}\left[p_y\frac{dp_y}{dt} + p_z\frac{dp_z}{dt}\right] = \frac{p_{\text{eq}}(t) - p}{T} \tag{4.178}$$

where we've made the additional approximation that $T_2 = T_1$ giving $T = T_1$ and $p_{\text{eq}}(t)$ is the "equilibrium" polarization:

$$p_{\text{eq}}(t) = \frac{\omega_1^2 + \Delta(t)\left(\omega_0 + q\Delta(t)\right)}{\omega_0\Omega(t)} \qquad q = \left\{\begin{array}{ll} 0 & \text{frequency sweep} \\ 1 & \text{field sweep} \end{array}\right\} \tag{4.179}$$

where $q = 0$ is the frequency sweep AFP and $q = 1$ for field sweep AFP. In direct analogy to the lockin time constant equation (4.49), we can immediately write down the integral form of this equation:

$$p(t) = \frac{1}{T}\int_{-\infty}^{t} \exp\left(\frac{u-t}{T}\right) p_{\text{eq}}(u)\, du \tag{4.180}$$

In our case, the detuning is ramped "up," held fixed for a some amount of time t_w, and then ramped "down:"

$$\Delta(t) = \left\{\begin{array}{ll} \Delta_{\text{start}} & t \le 0 \\ \Delta_{\text{start}} + \dot{\Delta}t & t \le 2t_0 \\ \Delta_{\text{end}} & t \le 2t_0 + t_w \\ \Delta_{\text{end}} - \dot{\Delta}(t - 2t_0 - t_w) & t \le 4t_0 + t_w \\ \Delta_{\text{start}} & t > 4t_0 + t_w \end{array}\right\} \tag{4.181}$$

where Δ_{start} is the initial detuning, and the final detuning Δ_{end} & sweep rate $\dot{\Delta}$ are:

$$\Delta_{\text{end}} = \Delta_{\text{start}} + \dot{\Delta} 2t_0 \qquad \dot{\Delta} = \frac{\Delta_{\text{end}} - \Delta_{\text{start}}}{2t_0} \tag{4.182}$$

To derive an analytic solution for this equation, we'll make the usual approximations [12, 53, 54] that (1) far from resonance $|\Delta| \gg \omega_1$, the equilibrium polarization is:

$$p_{\text{eq}}(t) \approx s_z \left(1 + q\frac{\Delta(t)}{\omega_0}\right) \qquad s_z \equiv \frac{\Delta}{|\Delta|} \tag{4.183}$$

where s_z is the sign of the detuning and (2) sufficiently close to resonance ($|u - t_0| \leq t_a$ & $|u - 3t_0 - t_w| \leq t_a$), the exponential is expanded as:

$$\exp\left(\frac{u-t}{T}\right) = \exp\left(-s_r \beta z(t)\right) \sum_{n=0}^{\infty} \frac{\left[s_r \beta z(u)\right]^n}{n!} \tag{4.184}$$

where we've defined the unitless quantities z and β given by:

$$\frac{u-t}{T} = s_r \beta (z(u) - z(t)) \qquad z(t) = \frac{\Delta(t)}{\omega_1} \qquad \beta = \frac{\omega_1}{|\dot{\Delta}|T} \qquad s_r = \frac{\dot{\Delta}}{|\dot{\Delta}|} \tag{4.185}$$

where s_r is the sign of the detuning sweep rate that that the opposite (same) sign as the detuning before (after) resonance. The integrals near resonance are evaluated using the following:

$$\frac{s_r \beta \omega_1}{\omega_0} \int \left[\sum_{n=0}^{\infty} \frac{(s_r \beta z)^n}{n!}\right] \left[\frac{1 + \frac{\omega_0}{\omega_1} z + q z^2}{\sqrt{1+z^2}}\right] dz = \sum_{n=0}^{\infty} c_n(s_r) I_n(z) \tag{4.186}$$

where the coefficients c_n and integrals $I_n(z)$ are defined by:

$$c_n(s_r) = \frac{(s_r\beta)^n}{n!}\left[n + s_r\beta\frac{\omega_1}{\omega_0}\left(1+\frac{qn(n-1)}{\beta^2}\right)\right] \quad (4.187)$$

$$I_n(z) = \int \frac{z^n}{\sqrt{1+z^2}}dz = \frac{z^{n+1}}{n+1}\left[{}_2F_1\left(\frac{1}{2},\frac{n+1}{2};\frac{n+3}{2};-z^2\right)\right] \quad (4.188)$$

where ${}_2F_1$ is the generalized hypergeometric function. For our purposes, truncating the sum to sixth order in z gives us considerable flexibility in choosing t_a and the closed form of the first seven integrals are given by:

$$I_0 = \text{asinh}(z) \qquad I_1 = \sqrt{1+z^2} \qquad I_2 = \tfrac{z}{2}I_1 - \tfrac{1}{2}I_0 \qquad I_3 = \left[\tfrac{z^2}{3} - \tfrac{2}{3}\right]I_1 \quad (4.189)$$

$$I_4 = \left[\tfrac{z^3}{4} - \tfrac{3z}{8}\right]I_1 + \tfrac{3}{8}I_0 \qquad I_5 = \left[\tfrac{z^4}{5} - \tfrac{4z^2}{15} + \tfrac{8}{15}\right]I_1 \qquad I_6 = \left[\tfrac{z^5}{6} - \tfrac{5z^3}{24} + \tfrac{5z}{16}\right]I_1 - \tfrac{5}{16}I_0$$

Putting all this together, we find:

$$\begin{aligned}
p\left[t \le u_0\right] &= -s_r\left(1+\frac{q\Delta_{\text{start}}}{\omega_0}\right) \\
p\left[t \le u_1\right] &= p'(u_0,t) - s_r I_\ell\left[\left(1+\frac{q\Delta_{\text{start}}}{\omega_0}\right),\left(+\frac{q\dot{\Delta}}{\omega_0}\right),u_0,t\right] \\
p\left[t \le u_2\right] &= p'(u_1,t) + \exp(-s_r\beta z(t))\sum_{n=0}^{6} c_n(+s_r)\left[I_n(z(t)) - I_n(z(u_1))\right] \\
p\left[t \le u_3\right] &= p'(u_2,t) + s_r I_\ell\left[\left(1+\frac{q\Delta_{\text{start}}}{\omega_0}\right),\left(+\frac{q\dot{\Delta}}{\omega_0}\right),u_2,t\right] \\
p\left[t \le u_4\right] &= p'(u_3,t) + s_r\left(1+\frac{q\Delta_{\text{end}}}{\omega_0}\right)\left(1-\exp\left[\frac{u_3-t}{T}\right]\right) \\
p\left[t \le u_5\right] &= p'(u_4,t) + s_r I_\ell\left[\left(1+\frac{q\Delta_{\text{end}}+q\dot{\Delta}u_4}{\omega_0}\right),\left(-\frac{q\dot{\Delta}}{\omega_0}\right),u_4,t\right] \\
p\left[t \le u_6\right] &= p'(u_5,t) + \exp(+s_r\beta z(t))\sum_{n=0}^{6} c_n(-s_r)\left[I_n(z(t)) - I_n(z(u_5))\right] \\
p\left[t \le u_7\right] &= p'(u_6,t) - s_r I_\ell\left[\left(1+\frac{q\Delta_{\text{end}}+q\dot{\Delta}u_4}{\omega_0}\right),\left(-\frac{q\dot{\Delta}}{\omega_0}\right),u_6,t\right] \quad (4.190)
\end{aligned}$$

where the times $u_0 \cdots u_7$ are given by:

$$u_0 = 0 \qquad u_1 = t_0 - t_a \qquad u_2 = t_0 + t_a \qquad u_3 = 2t_0 \qquad u_4 = 2t_0 + t_w$$
$$u_5 = 3t_0 + t_w - t_a \qquad u_6 = 3t_0 + t_w + t_a \qquad u_7 = 4t_0 + t_w \tag{4.191}$$

and p' & I_ℓ are both functions of t given by:

$$p'(u,t) = \exp\left(\frac{u-t}{T}\right) p(u) \tag{4.192}$$
$$I_\ell(b,m,u,t) = b + m(t-T) - [b + m(u-T)] \exp\left[\frac{u-t}{T}\right] \tag{4.193}$$

When the resonance region integral sum is truncated at 6th order, then the higher order terms contribute less than 0.1% over one T. Therefore a reasonable value for the transition time t_a between the two approximations is:

$$t_a = \left\{ \begin{array}{ll} t_1 & T > t_1 \\ T & T \leq t_1 \end{array} \right\} \qquad t_1 = \frac{10\omega_1}{\dot{\Delta}} \tag{4.194}$$

Finally, the model function used to fit water data is given by:

$$\ell_{\text{model}}(t) = S\left(\frac{\omega_{\mathtt{rf}}(t)}{\omega_0}\right) p(t) + q_b t^2 + m_b t + c_b \tag{4.195}$$

where we've allowed for a quadratic background. This function is valid for both frequency & field sweep AFP. In addition, although the heights of the up and down sweeps are different due to relaxation, individual fits to the up and down sweeps should result in the same value of the normalization S.

4.6.6 Lineshape Factor

Introduction

The lineshape factor is calculated in the following way:

$$\ell_B^{\text{fit}} = [A_{\texttt{F0T0}}] \left[\frac{A_{\texttt{aGT0}}}{A_{\texttt{a0T0}}}\right] \left[\frac{A_{\texttt{a00d}}}{A_{\texttt{a000}}}\right] \tag{4.196}$$

where the first term accounts for the differences between the full numerical solution to the Modified Bloch Equations, Sec. (4.3.4), & the model function, see previous section, and the signal averaging by the lockin amplifier. $A_{\texttt{F0T0}}$ is the normalization parameter determined by a fit to a numerical solution of Eqn. (4.49) where the lockin time constant τ is 30 msec and the lockin input $\mathcal{V}_{\text{in}}'$ is given by $p_y(t)$ which is determined by the numerical solution of MBE.

The second term accounts for distortions due to (1) magnetic field gradients along the target chamber and (2) the small signals from the pumping chamber & transfer tube. $A_{\texttt{a0T0}}$ is the normalization parameter determined by a fit to a numerical solution of Eqn. (4.49) where $\tau = 30$ msec and $\mathcal{V}_{\text{in}}'(t) = \ell_{\text{model}}(t)$. $A_{\texttt{aGT0}}$ is the normalization parameter determined by a fit to a numerical solution of Eqn. (4.49) where $\tau = 30$ msec and the lockin input is:

$$\begin{aligned}
\mathcal{V}_{\text{in}}'(t) &= G_{\nabla}^{x,\text{tc}}(t) G_{\Phi}^{x}(t) p_y(t) \approx \sum_{n=-64}^{+64} \frac{\phi_x^{\text{tc}}(z_n)}{\mathbf{\Phi}_x^{\text{tc}}} \ell_{\text{model}}(t, z_n) \\
&\quad + \frac{P_{\text{tt}} n_{\text{tt}}}{P_{\text{tc}} n_{\text{tc}}} \sum_{m=-8}^{+8} \frac{\phi_x^{\text{tt}}(y_m)}{\mathbf{\Phi}_x^{\text{tc}}} \ell_{\text{model}}(t, y_m) + \frac{P_{\text{pc}} n_{\text{pc}}}{P_{\text{tc}} n_{\text{tc}}} \sum_{k=0}^{13024} \frac{\phi_x^{\text{pc}}(\vec{u}_k)}{\mathbf{\Phi}_x^{\text{tc}}} \ell_{\text{model}}(t, \vec{u}_k) \\
&\rightarrow G_{\Phi}^{x}(0) \ell_{\text{model}}(t) \qquad \text{(no magnetic field gradients)}
\end{aligned} \tag{4.197}$$

where $\phi_x^{\text{tc}}(z_n)$ is the partial flux factor, Sec (4.3.2), for the nth-slice at location z_n

along the target chamber, $\Phi_x^{\rm tc} = \sum_{n=-64}^{+64} \phi_x^{\rm tc}(z_n)$ is the total target chamber flux factor, and $\ell_{\rm model}(t, z_n)$ is the model function, which has a position dependence through the holding field sweep range.

Analogous terms are included for the pumping chamber & transfer tube to account for distortions to the lineshape due to a vertical magnetic field gradient. The flux gain $G_\Phi^x(0)$, as defined by the terms to the right of the arrow in Eqn. (4.46), assumes that the resonance occurs at the same time for the target and pumping chambers. Since the flux factor from the pumping chamber and transfer tube are negative, the total signal at resonance is reduced by about 5% compared to the signal from the target chamber alone. The presence of a vertical ($\partial B_z/\partial y$) magnetic field gradient shifts the resonance peak of the pumping chamber (and transfer tube) relative to the target chamber. If the shift is large enough ($\Delta y \partial B_z/\partial y \gg B_1$), then the total signal at resonance is nearly the same as the signal from the target chamber alone. For this experiment, there was an additional shift between the pumping & target chamber due to the fact that the pickup coils were offset in the z-direction relative to the centers of the target & pumping chambers.

The lowest order correction to $G_\nabla^{x,\rm tc}$ from Eqn. (4.40) depends on:

$$\begin{aligned}
[\vec{u} - \vec{u}_0] \cdot \vec{\nabla} B_0 \;\; = \;\; & \Delta z \left(\frac{B_z}{B_0}\right) \left[\frac{\partial B_z}{\partial z} + \frac{\Delta x}{\Delta z}\frac{\partial B_z}{\partial x} + \frac{\Delta y}{\Delta z}\frac{\partial B_z}{\partial y} \right. \\
& + \frac{B_x}{B_z}\left(\frac{\partial B_x}{\partial z} + \frac{\Delta x}{\Delta z}\frac{\partial B_x}{\partial x} + \frac{\Delta y}{\Delta z}\frac{\partial B_x}{\partial y}\right) \\
& \left. + \frac{B_y}{B_z}\left(\frac{\partial B_y}{\partial z} + \frac{\Delta x}{\Delta z}\frac{\partial B_y}{\partial x} + \frac{\Delta y}{\Delta z}\frac{\partial B_y}{\partial y}\right)\right] \qquad (4.198)
\end{aligned}$$

In our case, most of field is in the z-direction which means that $B_z \approx B_0$ and $B_x, B_y \ll B_z$. In addition, since the target chamber is long and narrow, $\Delta z \approx 11$ cm is roughly the length of the pickup coils, while $\Delta x = \Delta y \approx 1.7$ cm is roughly the target cham-

ber inner diameter. For these two reasons, the lineshape is most sensitive to gradients in B_z and, in particular, $\partial B_z/dz$. For the same reason, the contribution from the transfer tube is most sensitive to $\partial B_z/\partial y$. Due to the spherical shape of the pumping chamber, the contribution from the pumping chamber includes gradients in B_z in all three directions.

The fields and gradients were determined by a magnetic field mapping [14] in the target region with the septum magnet set to $I_{\text{sep}} = 175, 250, 325$ Amps. We made the questionable assumptions that the fringe field from the septum magnet was (1) linear in septum current and (2) did not change when the magnet was switched from the "6 degree" configuration to the "9 degree" configuration. By combing the data sets, we determined the fields with the septum magnet on and off, see Fig. (4.19). By comparing to a numerical calculation of the field due to a Helmholtz pair, we determined that the dominant gradient with the septum off was not due to the Helmholtz coils. As shown in Fig. (4.20), the gradient along the target chamber of B_z at the center of the pickup coils decreases with increasing septum current. Finally, by combining the gradients in the longitudinal (along the target chamber) and vertical (along the transfer tube) directions, we calculated the field shift between the pumping and target chamber for each septum current Fig. (4.20).

The third term accounts for a slow drift in the holding field during a water calibration. $A_{\texttt{a00d}}$ is the normalization parameter determined by a fit to the average of N model functions, where N is the total number of measurements each with a different starting field. $A_{\texttt{a000}}$ is the normalization parameter determined by a fit to the model function using the average starting field. The starting field for each measurement was determined by the value of the current in the Helmholtz coils

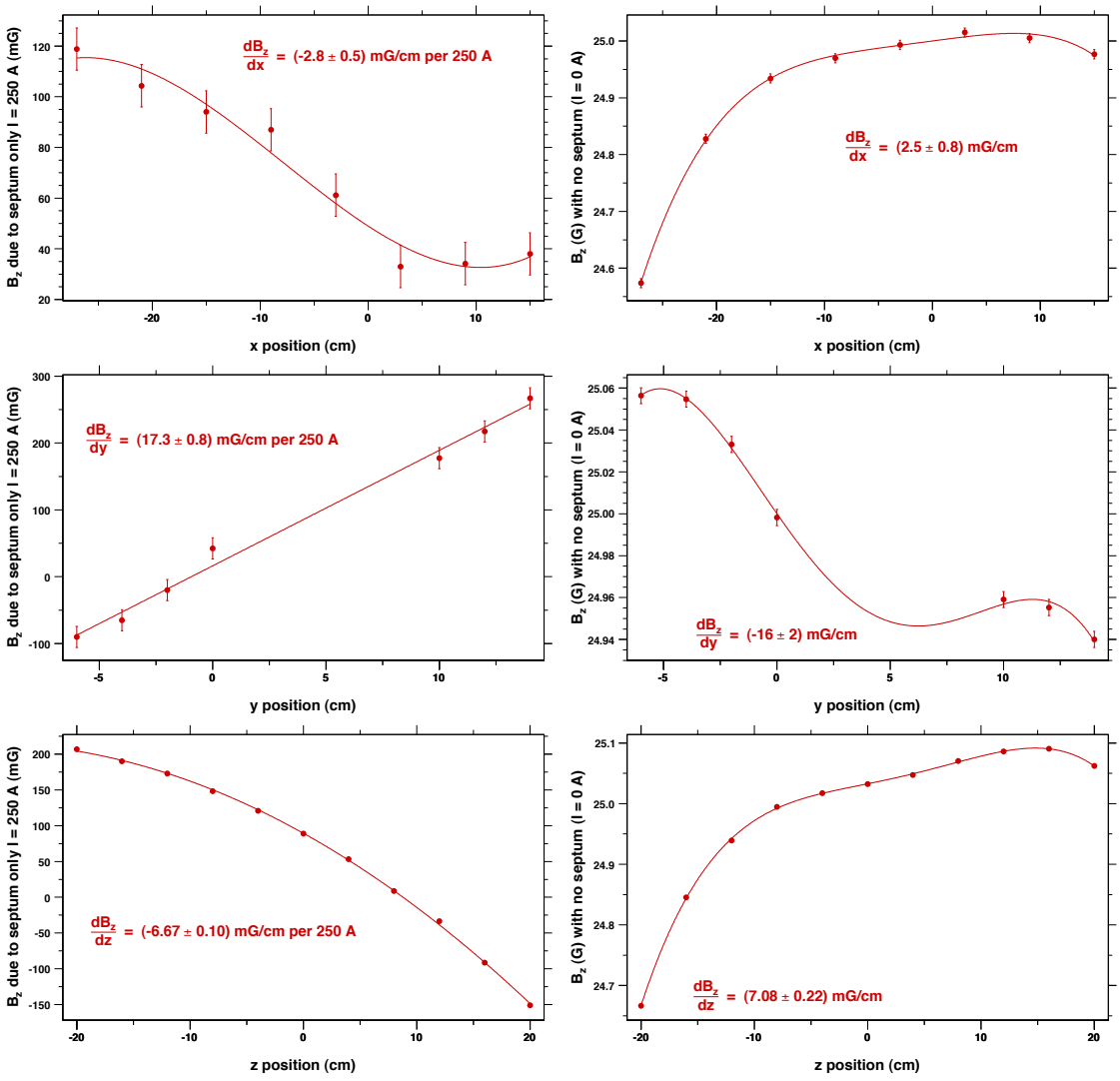

Figure 4.19: Spatial Variation of B_z with and without the Septum Magnet (2nd period). The gradients listed in the plots are evaluated at the center of the pickup coil region in the target chamber.

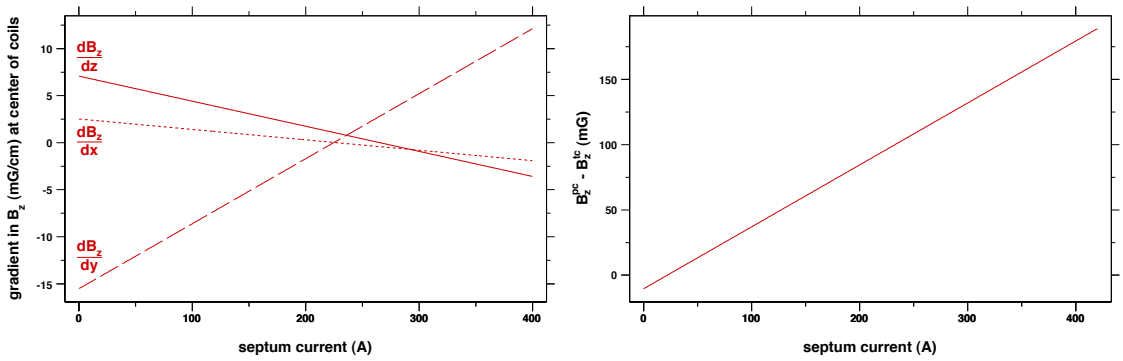

Figure 4.20: Magnetic Field Gradients vs. Septum Current. (Left) Gradients in the target chamber at the center of the pickup coils. (Right) The holding field at the center of the pumping chamber relative to the target chamber.

date	r.m.s. drift (mG)	total drift (mG)	$A_{\mathrm{a00d}}/A_{\mathrm{a000}}$
07/08	8.7	39.1	0.9938
07/10	8.4	35.5	0.9943
07/12	12.8	49.7	0.9877
08/05	5.1	28.4	0.9994
08/31-1	5.0	24.9	0.9979
08/31-2	6.9	32.0	0.9958
09/01-1	5.2	24.9	0.9973
09/01-2	5.4	24.9	0.9975

Table 4.10: Drift Corrections for Water Calibrations.

which was recorded about every 3 seconds, see Fig. (4.21). The typical size of of the drifts and corresponding correction factor is listed in Tab. (4.10).

Determination of Parameters for Numerical Solution to MBE

The various parameters used in the numerical calculation of the water and ^{3}He lineshape factors are listed in Tab. (4.11). The RF frequency of the B_1 field was 91 kHz throughout the experiment. The total field sweep range was 7 Gauss at a rate of 1.2 G/s [14]. The starting fields (B_{start}) were determined from the location of the

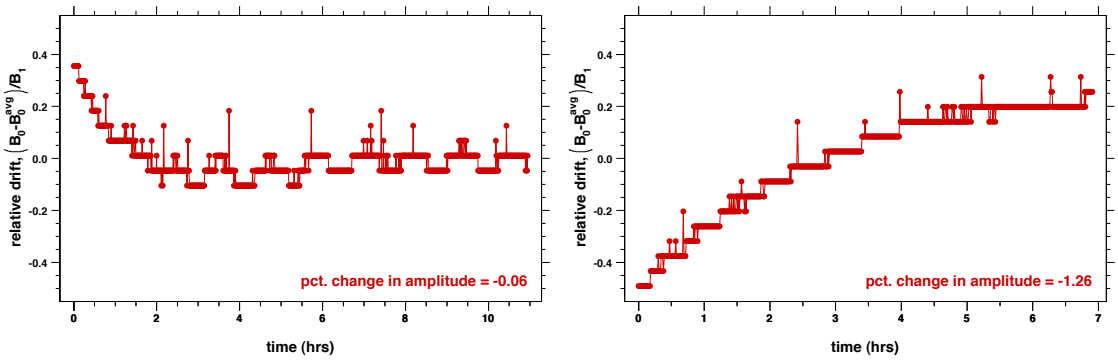

Figure 4.21: Slow Drift in the Holding Field During Water Calibrations. The relative drift is defined by the difference from the average field scaled by $B_1 = 61.8$ mG, which is the characteristic size of the broadened resonance peak. The size of the signal drops by 30% at a distance of one B_1 away from resonance. The smallest (largest) correction was due to the drift depicted in the plot on the left (right).

parameter	**water**	**he3**	**units**
ν_0	91	91	kHz
B_{start}	17.8	24.5	G
B_{end}	24.8	31.5	G
B_1	48.4	49.9	mG
μ	2.79285	-2.12750	μ_N
$2t_0$	5.83	5.83	sec
t_w	5.83	0	sec
T_1	3.76	360000	sec
T_2	3.35	27.6–60.6	sec
t_w^{cycle}	24	0	sec
num. of sweeps	350–1000	1	unitless
sweep type (+1 = field, -1 = freq.)	1	1	unitless
τ, lockin time constant	30	30	msec
P_{scale} (0 for thermal pol.)	0	0.38	unitless
P_z^{∞} (0 for thermal pol.)	0	0.42	unitless

Table 4.11: Parameters Used for the Numerical Solution to the Modified Bloch Equations.

resonance peaks from the fits to the NMR data. The signal averaging of the lockin causes the resonance peak to shift to a later time. Since the "up" and "dn" sweeps were in different directions, the shift due to the lockin signal averaging largely cancels in the average of the up and dn peak locations.

The amplitude of B_1 was determined by the width parameter from fits to ^{3}He NMR data taken at 5 different NMR RF amplitude settings. This width was broadened to due the signal averaging of the lockin and due to magnetic field gradients. Therefore, the value of B_1 put into the numerical lineshape calculation was varied until the broadened fit width matched the fit width in the data. The average value of B_1 (or equivalently H_1) from this method was about 10% lower than the value determined using the "H_1 coil" method [14, 55]. The magnitude of B_1 was different for water because those measurements were taken with the aluminum covers removed. The ^{3}He NMR data during production running was taken with the aluminum covers in place.

The sweep time ($2t_0$) and wait time (t_w) were programmed into the function generator controlling the holding field. The wait time between sweeps was determined by the data transfer time of the DAQ. The T_1 for water in the water cell was determined by comparing the ratio of the up and dn peak fits amplitudes in two different ways. In the first method, the water data and numerical calculations of the lineshape were both fit to the model function which included relaxation. The T used in this model function was varied until the ratio of the up and dn peaks was 1.00094, which was the ratio of the up and dn fit amplitudes determined by the numerical calculation of the lineshape. In the second method, the water data and numerical calculations of the lineshape were both fit to the model function used for the ^{3}He NMR data (square root of a Lorentzian). The T_1

used in the numerical calculation of the lineshape was varied until the ratio of the up and dn peaks was -0.86259, which was the ratio of the up and dn fit amplitudes determined from the data after the effect of magnetic field gradients had been removed. The first method gave $T = 3.85$s, while the second method gave $T_1 = 3.67$s. The uncertainty in the ratio of the up and dn peaks from fits to the data (about 1 percent) corresponds to an uncertainty in T_1 of 0.25 sec. The average value of $T_1 = (3.76 \pm 0.25)$ s used in this analysis varies considerably from the value $T_1 = 3.0$ s used in past [14,56]. Finally, T_2 was calculated from the difference in the transverse and longitudinal relaxation rates ($T_2^{-1} - T_1^{-1} = 33$ mHz) used in the past [14,57].

From Eqn. (6.14), we find that the ^{3}He T_1 is given by:

$$\frac{1}{T_1} = \Gamma_{\rm tc} + d_{\rm tc}\left(1 - \frac{P_{\rm pc}}{P_{\rm tc}}\right) \tag{4.199}$$

where $\Gamma_{\rm tc}$ is the relaxation rate in the target chamber, $d_{\rm tc}$ is the diffusion rate per nucleus of ^{3}He nuclei exiting the target camber, and $P_{\rm pc}/P_{\rm tc}$ is the ratio of pumping chamber to target chamber polarizations. As the polarization reaches equilibrium, the longitudinal relaxation rate T_1^{-1} approaches 0. Because T_1 is very long (hours) relative to the sweep time, the final lineshape is relatively insensitive to the value of T_1 for ^{3}He ; therefore, we used $T_1 = 100$ hrs. T_2 was determined by the AFP loss per spin flip using:

$$\texttt{afp loss per spin flip} = \frac{308.6\%}{T_2}\left[\frac{\omega_1}{\dot{\Delta}}\right] = (308.6\%)\, D\left[\frac{\partial B_z/\partial z}{B_1}\right]^2\left[\frac{\omega_1}{\dot{\Delta}}\right] \tag{4.200}$$

where $D = 0.189$ cm^2/s is the ^{3}He diffusion coefficient in the target chamber under operating conditions, $\dot{\Delta}$ is the detuning sweep rate, and 308.6% was determined

by varying T_2 in the numerical calculation of the lineshape, see Fig. (4.5). First, T_2 was calculated from dedicated measurements of the AFP loss at 5 different septum currents, see left plot of Fig. (4.22). These measurements were performed by taking 5 consecutive NMR measurements with a short time interval, typically $\Delta t = 3$ minutes. Most of these AFP loss measurements were taken when the target chamber polarization was near its equilibrium value. This insured that the change in polarization between measurements was almost entirely due to the AFP loss. Second, T_2 was calculated by averaging the square of the longitudinal gradient throughout the target chamber, see left plot of Fig. (4.22). Although the gradient in the region defined by the pickup coils decreases with increasing septum current, the r.m.s. gradient throughout the target chamber increases with septum current. Since we were interested in the change in the average polarization throughout the target chamber, we averaged the gradients throughout the target chamber. These two methods were average to calculate the T_2 as a function of septum current, see right plot of Fig. (4.22).

Discussion & Uncertainty Analysis

The lineshape factors for the up and dn sweep for each water calibration are listed in Tab. (4.12). The lineshape factors for ^{3}He are a function of septum current, see upper left Fig, (4.23). The functional form of the ^{3}He lineshape was determined by considering the effect of broadening mechanisms in general. The signal averaging due to the lockin, magnetic field gradients, and slow magnetic drifts all broaden the apparent width and reduce the apparent height of the resonance peak. The basic effect of each broadening mechanism can be essentially described by the fol-

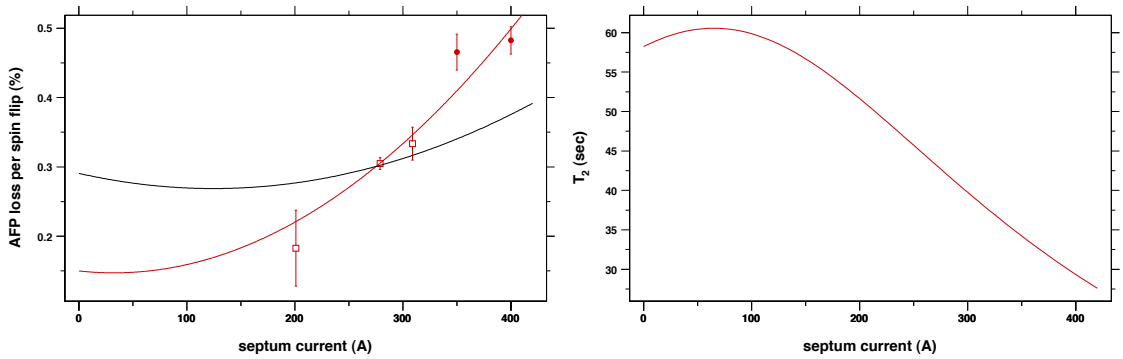

Figure 4.22: AFP Loss and T_2 for ^{3}He NMR Measurements. (Left) AFP loss as a function of septum current. The open squares (closed circles) are from dedicated measurements of AFP loss during the 6 degree (9 degree) configuration. The red line through the data points is a fit constrained by 0.15% for zero septum current. The black line is based on a calculation of the magnetic field gradient in the target chamber. (Right) Average T_2 using the two methods described in the text as a function of septum current.

date	$A^{\mathrm{up}}_{\mathtt{FOTO}}$	$A^{\mathrm{dn}}_{\mathtt{FOTO}}$	$A^{\mathrm{up}}_{\mathtt{aGTO}}/A^{\mathrm{up}}_{\mathtt{aOTO}}$	$A^{\mathrm{dn}}_{\mathtt{aGTO}}/A^{\mathrm{dn}}_{\mathtt{aOTO}}$	$\ell_B^{\mathrm{fit,up}}$	$\ell_B^{\mathrm{fit,dn}}$
07/08	0.9018	0.8996	0.9177	0.9189	0.8224	0.8215
07/10	0.9018	0.8995	0.9177	0.9189	0.8229	0.8219
07/12	0.9018	0.8995	0.9027	0.9041	0.8041	0.8033
08/05	0.9018	0.8998	0.9034	0.9048	0.8141	0.8136
08/31-1	0.9018	0.8997	0.9053	0.9067	0.8147	0.8140
08/31-2	0.9018	0.8997	0.9053	0.9067	0.8130	0.8123
09/01-1	0.9018	0.8997	0.9053	0.9067	0.8142	0.8135
09/01-2	0.9018	0.8997	0.9053	0.9067	0.8144	0.8137

Table 4.12: Lineshape Factors for Water Calibrations. The drift corrections are listed in Tab. (4.10).

lowing integral:

$$f(t) = \int w(t,t_0)\ell(t,t_0)\,dt_0 \rightarrow f(z) = \int \frac{w(z_0)}{\sqrt{1+(z-z_0)^2}}\,dz_0 \tag{4.201}$$

where $w(t,t_0)$ is a weight function that describes the probability of the resonance peak occurring at t_0, z is a unitless parameter that defines the distance from resonance, and z_0 is an resonance offset caused by the broadening mechanism. If the resonance offset z_0 is uniformly distributed over the range $-b$ to $+b$, the height of the signal at $z = 0$ is reduced in the following way [13,58]:

$$f(0) = \int_{-b}^{+b} \frac{1/2b}{\sqrt{1+z_0^2}}\,dz_0 = \frac{\text{asinh}(b)}{b} \tag{4.202}$$

Furthermore, a fit to the numerical calculation of the entire lineshape yields:

$$A(b) = \left[\frac{\text{asinh}(0.8b)}{(0.8b)}\right] \qquad w(b) = \sqrt{1+\frac{(0.8b)^2}{2}} \tag{4.203}$$

where $A(b)$ the is fit value for the amplitude and $w(b)$ is the fit value for the width. Therefore, a single "broadening parameter" b can be used to describe how both the amplitude and width change due to a broadening mechanism. This is very useful since the amplitude is very sensitive to various normalization factors whereas the width is not. *If we can determine the relationship between the width and broadening parameter, then we can use the broadening parameter to determine the amplitude (or equivalently the lineshape factor).* This result can be used to model both the effect of (1) a linear magnetic field gradient with a uniform flux profile and (2) a slow linear drift

in the following way:

$$b = \frac{\text{characteristic size of the broadening}}{\text{characteristic size of the peak}} = \frac{(\partial B_z/\partial z)L_{\text{coil}}/2}{B_1} = \frac{(dB_z/dt)\Delta T/2}{B_1} \tag{4.204}$$

where L_{coil} is the length of the pickup coil, dB_z/dt is the field drift rate, and ΔT is the total length of the measurement.

In our case, the weight function is much more complicated and the signal is broadened by both the lockin and magnetic field gradients. Only one additional higher order term was required to provide a fit to the calculation (which accounted for these effects) to better than 0.1%:

$$b(I) = m\left(\frac{I - I_0}{B_1}\right) \tag{4.205}$$

$$\ell_B^{\text{fit}}(I) = \ell_0\left[\frac{\text{asinh}(b)}{b} - (cb)^3\right] \tag{4.206}$$

$$B_1^{\text{fit}}(I) = B_1^0\left[\sqrt{1 + \frac{b^2}{2}} - (cb)^4\right] \tag{4.207}$$

$$\alpha(I) = \alpha_0 + b^2 \tag{4.208}$$

where $B_1 = 49.9$ mG and m, I_0, & c are determined by fitting to the results of the numerical calculation of the lineshape and are listed in Tab. (4.13). The parameters that relate the septum current to the broadening parameter used to determine the lineshape factor are very similar to the parameters used to relate the septum current to the broadening parameter for the width parameter. In other words, even with the complicated weight function due to the variation in the flux factor throughout the target chamber, the calculated lineshape factor & width parameter both still depend on a single broadening parameter, which has the simple linear

	penelope	**priapus6**	**priapus9a**	**priapus9b**
ℓ_0^{up}	0.9013	0.8991	0.8992	0.8993
I_0	350.78	358.97	358.13	357.70
m	0.1133	0.1141	0.1138	0.1136
c	0.3434	0.3305	0.3321	0.3321
ℓ_0^{dn}	0.8983	0.8968	0.8965	0.8966
I_0	346.55	347.03	348.50	348.09
m	0.1106	0.1204	0.1152	0.1150
c	0.3408	0.3456	0.3338	0.3340
B_1^0	56.54	56.16	56.22	56.23
I_0	330.99	333.90	333.44	333.19
m	0.1240	0.1281	0.1276	0.1274
c	0.5392	0.5296	0.5315	0.5316
α_0		0.4253		
I_0		62.62		
m		0.0994		

Table 4.13: ^{3}He Lineshape Factor, Width Parameter, and AFP Loss Parameters. For the 9 degree configuration with the cell Priapus, a coil position measurement was performed when the cell was installed (a) and before the cell was removed (b) at the end of the experiment. The final value for 9 degree configuration with the cell Priapus is the average of these two measurements.

relationship to the septum current.

Modeling the ^{3}He lineshape factor in terms of the broadening parameters allows us (1) to estimate the uncertainties due to the magnetic field measurements. and (2) test the reliability of the calculation. First, the longitudinal gradient at the center of the coil region is given as:

$$\frac{\partial B_z}{\partial z} = \left(m_z = -6.67 \pm 0.10 \text{ mG/cm}\right) \frac{I}{250 \text{ A}} + \left(b_z = 7.08 \pm 0.22 \text{ mG/cm}\right) \quad (4.209)$$

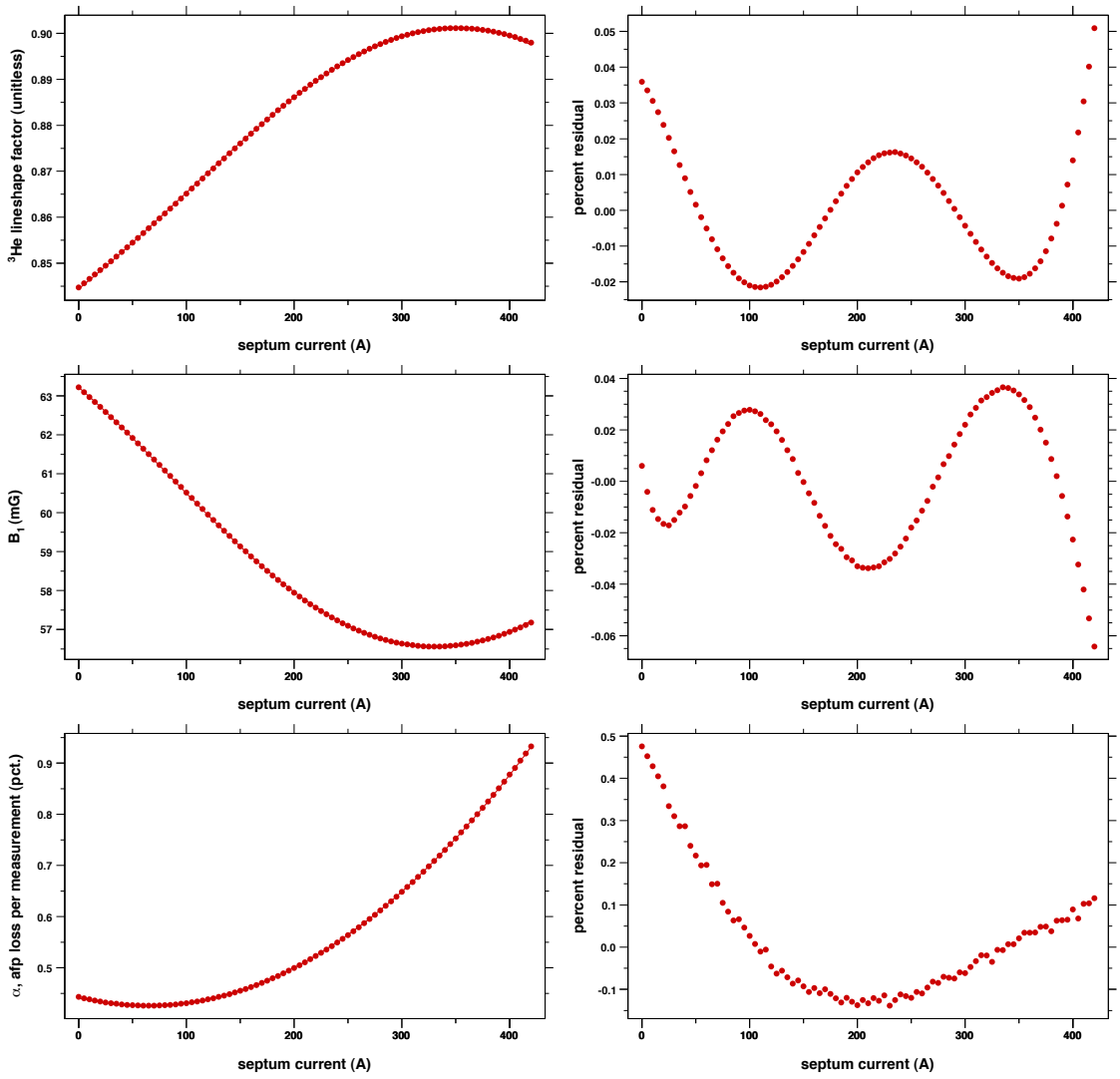

Figure 4.23: Calculated ^{3}He Lineshape Factor, Width Parameter, and AFP loss vs. Septum Current.

which can be propagated using Eqn. (4.204) into an uncertainty in b:

$$\sigma_b^2 = \sigma_{m_z}^2 \left(\frac{(I/250\text{ A})L_{\text{coil}}}{2B_1} \right)^2 + \sigma_{b_z}^2 \left(\frac{L_{\text{coil}}}{2B_1} \right)^2 = \left(\frac{I/(420\text{ A})}{54.0} \right) + \left(\frac{1}{41.2} \right)^2 \quad (4.210)$$

where $L_{\text{coil}} = 11$ cm. This can then be propagated into an uncertainty into the lineshape factor and fit width as:

$$\sigma_\ell = \frac{\partial \ell}{\partial b}\sigma_b \qquad \sigma_{B_1^{\text{fit}}} = \frac{\partial B_1^{\text{fit}}}{\partial b}\sigma_b \quad (4.211)$$

Second, our numerical calculation should be able to reproduce septum current functional dependence of both the width parameter & the lineshape factor equally well. In other words, if we see that the width parameter from the calculation matches (doesn't match) the width parameter from the data, then we can safely conclude that the corresponding lineshape factor is (isn't) reliable. Fig, (4.24) show the results of fits to the data (points) and numerical calculation (line). The numerical calculation appears to describe the the width parameter from the data very well when the septum current is over 250 A. Over the range 50–250 A, the numerical calculation appears to systematically overestimate the width parameter for the data. For a zero septum current, the calculation does reproduce the increase in the width parameter. The implication is that, for zero septum current and septum currents above 250 A, we can trust the value of the lineshape factor from the calculation. On the other hand, below 250 A, the implication is that the calculation underestimates the lineshape factor.

Two things happen that affect the lineshape of the NMR signal when the septum magnet is turned on and the current is increased. First, within the pickup region, the background magnetic field gradient is canceled to some degree by the

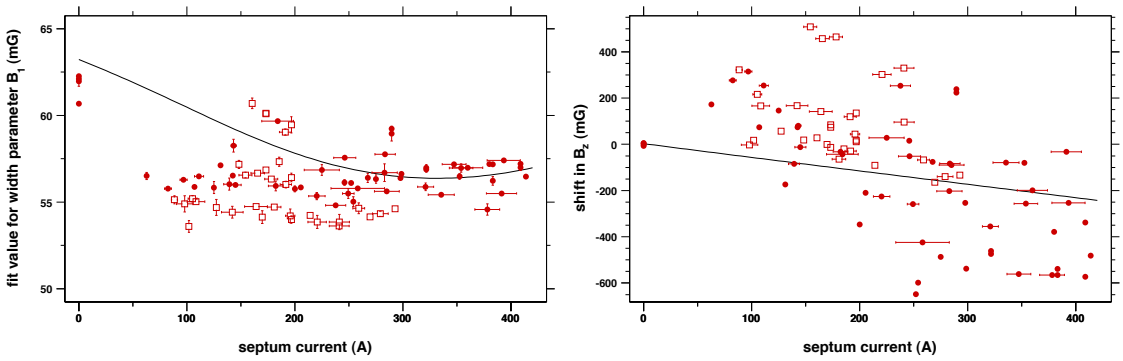

Figure 4.24: Comparison between Fits to Data and Calculations. The open squares (closed circles) are data from the 6 degree (9 degree) configuration. The solid curve is from the numerical calculation of the lineshape. (Left) Width parameter as a function of septum current. (Right) Holding field shift parameter as a function of septum current (relative to $I_{\text{sep}} = 0$).

fringe field from the septum magnet. Second, the resonance peak from the pumping chamber and transfer tube becomes shifted relative to the resonance peak of the target chamber. Both of these effects imply that we should see a "broad" peak with a smaller amplitude (i.e. lineshape factor) at low septum currents relative to a "narrow" peak with a larger amplitude at higher septum currents. The data (based on the width parameter) supports this conclusion qualitatively. However, our calculation, based on measurements of the background and septum fringe fields, indicates a smooth transition from no cancellation at $I_{\text{sep}} = 0$ to complete cancellation at $I_{\text{sep}} \approx 354$A. However, the data appears to indicate that the cancellation is nearly complete & essentially constant for all septum currents above $I_{\text{sep}} = 50$ A. In other words, the calculation indicates a smooth transition, whereas the data implies a "step-function" transition. This implies that there is a nonlinear relationship between the broadening parameter b and the septum current I. This is not an unreasonable conclusion since we observed that the septum magnet appeared to "saturate" at higher septum currents.

The calculation of the lineshape for the water calibration gave an average width parameter of 63.4 mG. This was in excellent agreement with the weighted average of the width parameter from the water calibration data 62.54 ± 0.76. For this reason, we've assumed that our calculation of the water lineshape factors is quite reliable and we've used the values listed in Tab. (4.12). To estimate the uncertainty, we first calculate the broadening parameter that corresponds to the a septum current of 0 A from the ^{3}He lineshape data, Tab. (4.13):

$$b_{\text{water}}(I = 0) \approx \left\langle \frac{m(0 - I_0)}{48.4} \right\rangle = -0.831 \tag{4.212}$$

Using Eqn. (4.210), we find that the uncertainty in our water broadening parameter due to our measurements of magnetic field gradients is $\sigma_b^{\text{water}} \approx 0.024$. This propagates into an uncertainty in the lineshape factor of 0.23% relative. The dominant uncertainty in b_{water} comes from our knowledge of B_1 which is only good to about 10% relative. This translates into $\sigma_b^{\text{water}} = 0.08$ which propagates into an uncertainty of the lineshape factor of 0.85% relative. Finally, the T_1 used to calculate the lineshape was varied by ± 0.25sec which translated into a variation of the lineshape factors of $\pm 0.95\%$ relative. The total uncertainty for the water lineshape is therefore 1.29% relative.

For the ^{3}He lineshape, we'll note that the data seems to imply the broadening parameter b is a constant for septum current above 50 A. This implies that the lineshape factor is also a constant, which we'll take to be equal to the $I = I_0$ or equivalently $b = 0$ value. For the final value of the ^{3}He lineshape factor, we'll split the difference between the constant value and value calculated taking into account

the septum current:

$$b(I) = m\left(\frac{I - I_0}{B_1}\right) \tag{4.213}$$

$$\ell_B^{\text{fit}}(I) = \frac{\ell_0}{2}\left[1 + \frac{\text{arcsinh}(b)}{b} - (cb)^3\right] \tag{4.214}$$

$$\sigma_\ell^{^3\text{He}}(I) = \frac{\ell_0}{2}\left[1 - \frac{\text{arcsinh}(b)}{b} + (cb)^3\right] \tag{4.215}$$

where uncertainty in the ^{3}He lineshape factor includes half the difference between these two values, see Fig. (4.25). The net effect is that the lineshape factor for ^{3}He measurements with septum currents between 50 and 250 A have a larger lineshape factor with greater uncertainty compared to the fit of calculation alone. The dominant uncertainty in the ^{3}He lineshape factor is due to the uncertainty in relationship between the septum current and broadening parameter, see Tab. (4.14). Given the lack of complete agreement between the data & calculation for the ^{3}He width parameter and given our lack of understanding of the differences in the septum fringe field between the 6 & 9 degree configurations, we've assigned a 3% relative uncertainity in our calculation of the ^{3}He lineshape factors.

4.6.7 Water Calibration Constant

The water calibration constant is given as:

$$c_W = \left[\frac{\hat{G}_{\text{L}}/\hat{G}_{\text{L}}^n}{G_{\text{L}}/G_{\text{L}}^n}\right]\left[\frac{R_W}{G_{\text{P}}Q(\omega_0)\Phi_x^{\text{tc}}}\right]\left[\frac{\hat{g}}{g}\right]\left[\frac{\hat{\nu}_0}{\nu_0}\right] \tag{4.216}$$

where $\hat{g}/g = g_{\text{proton}}^{\text{shielded}}/g_{\text{helion}}^{\text{shielded}} = -1/(0.7617861313)$ [59], the NMR RF frequency was 91 kHz for all NMR measurements, and R_W is a factor that accounts for all the

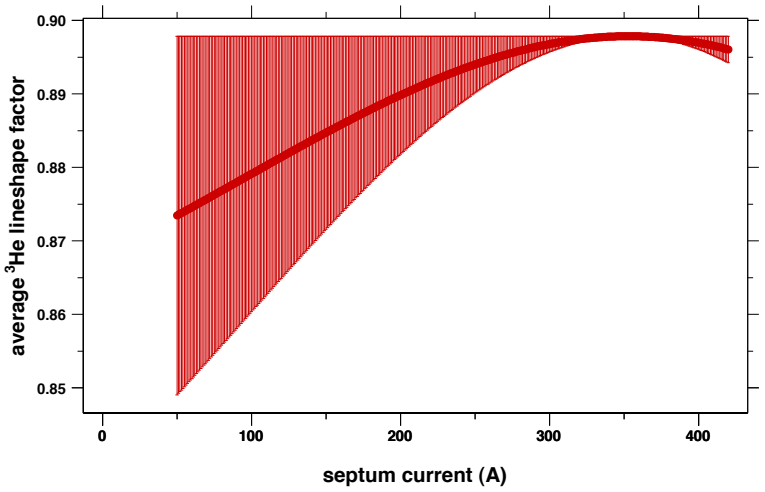

Figure 4.25: Average ^{3}He Lineshape Factor with Uncertainties. The lineshape factor and uncertainties are given by Eqns. (4.214) & (4.215).

source	water	penelope	priapus6	priapus9
total (% rel.)	1.29	0.98 to 1.50	0.39 to 2.47	0.39 to 2.80
$b(I)$	n/a	0.85 to 1.39	0.16 to 2.37	0.00 to 2.69
B_1	0.84	0.39 to 0.50	0.16 to 0.64	0.18 to 0.71
T_1	0.95	neg.	neg.	neg.
T_2	neg.	0.15	0.15	0.15
$\partial B_z/\partial z$	0.25	0.26	0.27	0.28
τ, lockin time constant	neg.	neg.	neg.	neg.
drift	neg.	n/a	n/a	n/a
$I_{\rm sep}^{\rm min}$–$I_{\rm sep}^{\rm max}$ (A)	0	148–197	87–293	58–420
$\langle I_{\rm sep} \rangle$ (A)	0	170	192	255

Table 4.14: Percent Relative Uncertainties in the Water & ^{3}He Lineshape Factors. The ^{3}He lineshape factor uncertainties depend on the septum current. The largest uncertainties occur for the lowest septum currents. The uncertainty in T_2 for ^{3}He comes from the difference in the determination of the afp loss described in Fig. (4.22). The uncertainty due to the lockin signal averaging is very small since time constant was always 30 msec and only ratios of lineshape factors were used to calculate the calibration constant.

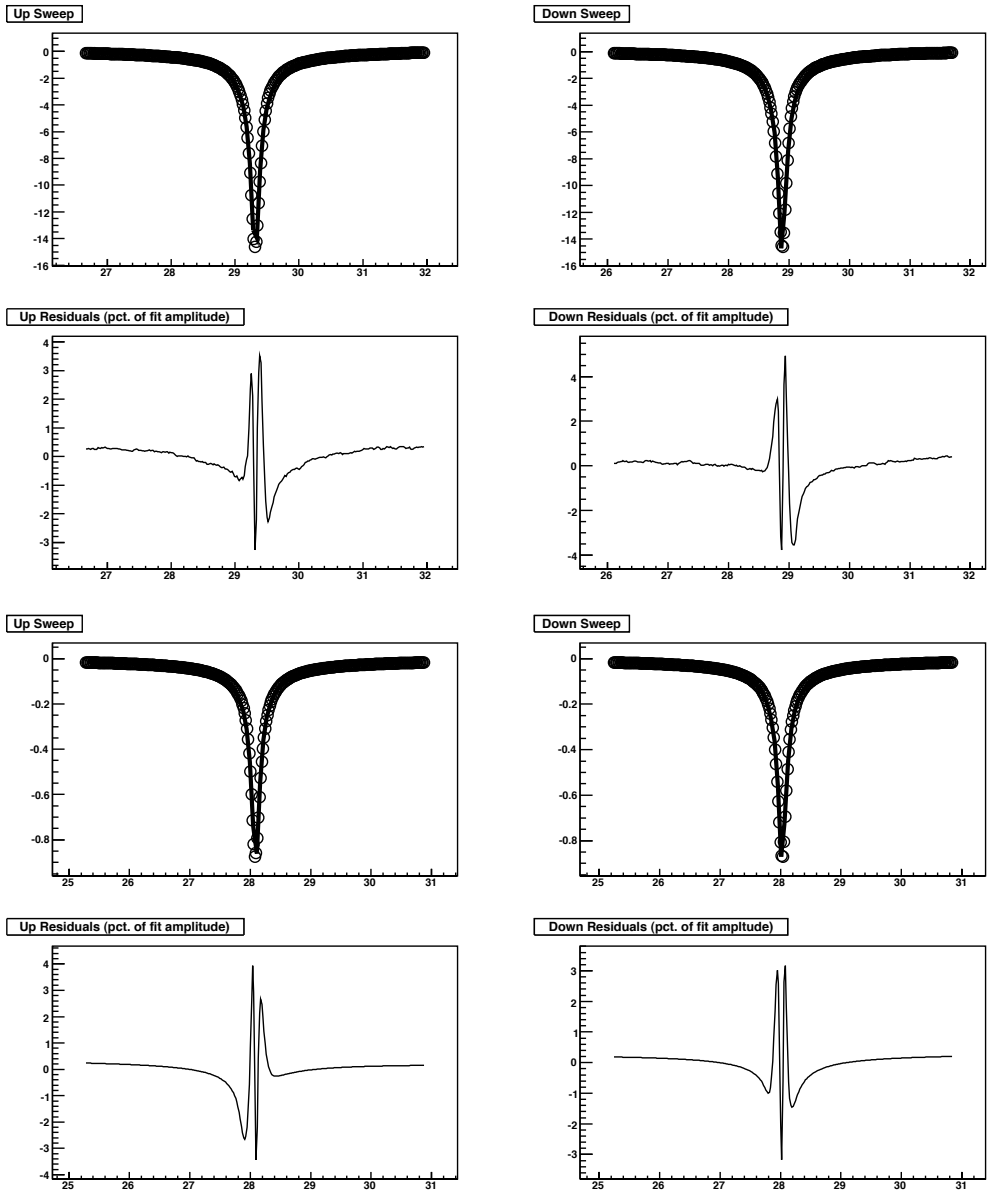

Figure 4.26: Measured and Calculated ^{3}He NMR Lineshape. The top (bottom) two plots show the measured (calculated) lineshape and residuals. The x-axis is the holding field in Gauss. The y-axis is in mV (arb. units) for the top (bottom) plot. For both residuals plots, the y-axis is given as the percentage of the fit amplitude. The shape and size of the residuals from the calculation match the data very well which gives us some confidence in the lineshape calculation.

variations among water calibrations measurements and should be a constant:

$$R_W = \frac{\hat{G}_P \hat{Q}(\omega_0) \hat{\Phi}_x^{tc} \hat{P}_{tc} \hat{n}_{tc} \hat{\ell}_B^{fit}}{\hat{S}} \tag{4.217}$$

Before the water cell was installed, the phase of the lockin was adjusted such that all of the ^{3}He signal was in the x-channel. It was assumed that the phase of the water signal is nearly identical to the phase of the ^{3}He NMR signal. Because the water NMR signal is so small, several (≤ 1000) sweeps are taken per water calibration measurement. Each sweep was split in the middle and analyzed separately as up and dn sweeps. A linear background was fit to each sweep and then subtracted from each sweep. Sweeps that are considered excessively noisy were not included in the average. The criteria used to determine whether a sweep was too noisy was based on the following parameters calculated for each sweep:

1. range ≤ 160 μV - the difference between the highest and lowest signals measured during the sweep

2. standard deviation ≤ 150 μV - the r.m.s. variation of signal during the sweep

3. maximum derivative ≤ 1800 μV/G - the forward difference is used to estimate the numerical derivative of each sweep and the largest absolute value is the maximum derivative

Each of these quantities was calculated after the linear background subtraction. If any of these cut parameters were identically zero, then it was concluded that the lockin was saturated and the sweep is thrown out. Large values for the standard deviation usually implied that the sweep contained a visibly apparent oscillation probably due to vibrations. Large values for the maximum derivative usually im-

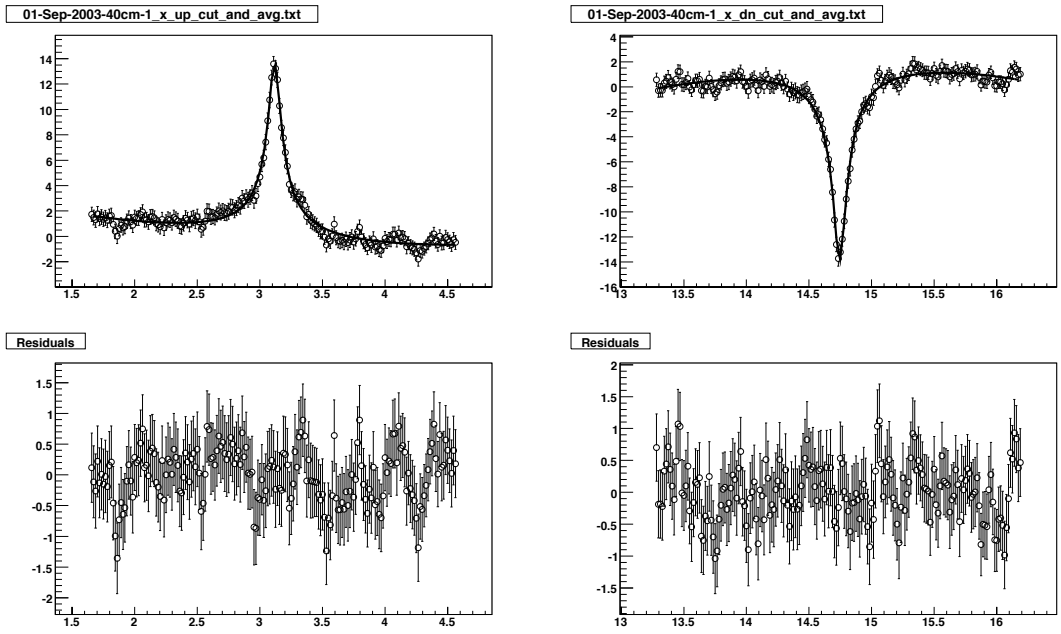

Figure 4.27: Water Calibration NMR Signal. The x-axis are seconds from the start of the sweep and the y-axis is in μV.

plied that there was an abrupt shift in the signal during these sweeps. If the up (dn) sweep failed to meet the cut criteria, then the dn (up) sweep was also thrown out. Anywhere from 13% to 54% of the sweeps would not meet the noise criteria and be thrown out. (The drift correction from the previous section used an average of the sweeps that were kept.) The mean and standard deviation were calculated on a point by point basis for each measurement. The water calibration amplitude $\hat{S}$ was then determined from a fit of the averaged water NMR signal using the model function that takes into account relaxation with $T = 3.76$ sec. The standard deviation on each point of the sweep, typically $0.6\mu V$, was used to the determine the weight used for the fit and is reflected in uncertainty of the amplitude. Only the region near the resonance peak (about half the sweep) was used in the fit, see Fig. (4.27).

date	G_P/sens.	**kept/sweeps**	R_W^{up}	stat	R_W^{dn}	stat	$\langle R_W \rangle$	stat
07/08	100/1V	595/686	-1658	21	-1685	18	(-1671)	(14)
07/10	200/300mV	291/350	-1732	36	-1635	29	-1684	23
07/12	200/300mV	314/600	-1763	111	-1505	60	-1634	63
08/05	100/1V	518/950	-1881	157	-1687	109	-1784	95
08/31-1	200/100mV	573/965	-1707	51	-1677	40	(-1692)	(32)
08/31-2	200/100mV	461/1000	-1542	37	-1672	40	-1607	27
09/01-1	200/100mV	526/1000	-1563	36	-1622	31	-1593	24
09/01-2	200/100mV	433/710	-1598	36	-1642	30	-1620	23
		before rupture of penelope					**-1678**	**21**
		after rupture of penelope					**-1614**	**13**

Table 4.15: Water Calibration Fits. The units of R_W are amg $\cdot$ cm^2/mV. The values in parenthesis were not included for the final weighted average.

The results of the fits are listed in Tab. (4.15). Two of the water calibrations were thrown out. First, the 07/08 calibration was taken without any measurements of the coil positions. Between the 07/08 and 07/10 measurements, the coils were repositioned to minimize background pickup from the NMR RF field itself. For comparison, the value listed in the table for this measurement used the same flux factor as the 07/10 measurement. Second, the 08/31-1 calibration was found to have many sweeps taken while the lockin was saturated. Because the rupture of the cell Penelope could have modified the NMR signal detection apparatus in a way that we may have not accounted for, the R_W value was calculated for the time period before and after the rupture separately. Final results and a list of uncertainties are listed in Tab. (4.16).

cell/angle	**calibration constant**	**stat , syst (% rel.)**
penelope	0.2266 amg/mV	$\pm 1.3 \pm 8.2$
priapus6	0.2339 amg/mV	$\pm 0.9 \pm 8.2$
priapus9	0.2310 amg/mV	$\pm 0.9 \pm 8.2$
source	**quantity**	**% rel. uncertainty**
preamp gain [46]	$\hat{G}_p/G_p$	5.0
lockin gain [16]	$(\hat{G}_L/\hat{G}_L^n)/(G_L/G_L^n)$	4.1
coil positions	$\hat{\Phi}_x/\Phi_x$	3.7
$b(I_{\rm sep})$	^{3}He $\hat{\ell}_B^{\rm fit}$	3.0
B_1,T_1	water $\hat{\ell}_B^{\rm fit}$	1.3
pickup coils/BNC cables	$\hat{Q}(\omega_0)/Q(\omega_0)$	1.0
polaization/density gradient	$\hat{\Phi}_x/\Phi_x$	0.7
coil stablity	$\hat{\Phi}_x/\Phi_x$	0.6
temperature	$\hat{P}_{\rm scale}$	0.3
temperature	$\hat{n}_{\rm tc}$	neg.
NMR RF func. gen.	$\hat{\nu}_0/\nu_0$	neg.
[59]	$\hat{g}/g$	neg.

Table 4.16: Water Calibration Constants.

4.6.8 Analysis of the EPR Measurements

Accounting for Baseline Field Drifts

A typical EPR measurement taken during E97110 is depicted in Fig. (4.28). The ^{3}He spins are flipped twice providing two measurements of the frequency shift due to ^{3}He . Each measurement consisted of three "time slices:" (1) before the first AFP, (2) between the two AFPs, (3) after the second AFP. The data were cut such that the "transition regions" associated with spin flip were excluded from the analysis. To account for a drift in the background field (e.g. due to a change in septum set point during the EPR measurement), the EPR frequencies within each time slice were fit to a line:

$$\nu_1(t) = m_1 t + b_1 \qquad \nu_2(t) = m_2 t + b_2 \qquad \nu_3(t) = m_3 t + b_3 \tag{4.218}$$

wherer m_n & b_n are the slopes & offsets in the n time slice. The numerical derivative of the EPR frequency vs. time data was taken to determine the time that corresponded to the "middle" of the AFP spin flip. The centers $t_{a,b}$ of the peaks in the derivative were taken to the middle of the spin flip. The frequencies were extrapolated to the middle of each spin flip using the linear fits to give $\nu_1(t_a)$ & $\nu_2(t_a)$ for the first flip and $\nu_3(t_b)$ & $\nu_3(t_b)$ for the second flip. The uncertainty on each of these frequencies was given by [60]:

$$\sigma_\nu = \sqrt{m^2\sigma^2_{t_{a,b}} + \sigma^2_m t^2_{a,b} + \sigma^2_b + 2\sigma^2_{bm} t_{a,b}} \tag{4.219}$$

where the uncertainty in the slope σ_m, uncertainty in the offset σ_b, and covariance between the slope & offset σ^2_{bm} were determined from the linear fit. If the covari-

ance term is neglected, then the uncertainty in the frequency at the midpoint is greatly overestimated. Eqn. (E.245) was used to convert the frequencies into their corresponding fields using the assumption that only the end transitions were being excited. The effective field due to the ^{3}He was calculated by:

$$B_{\mathrm{He}} = \frac{\Delta B}{2} = \frac{1}{4}\left[B(\nu_1(t_a)) - B(\nu_2(t_a)) + B(\nu_3(t_b)) - B(\nu_2(t_b))\right] \tag{4.220}$$

which was used to extract the ^{3}He polarization in the target chamber using Eqn. (4.97):

$$P_{\mathrm{tc}} = \left[\frac{3B_{\mathrm{He}}}{\mu_0\left(\kappa_0 - 1 + \kappa_{\mathrm{geo}}\right) n_{\mathrm{pc}} g \mu_N}\right]\left(\frac{1}{1-\alpha/2}\right)\left(\frac{P_{\mathrm{tc}}}{P_{\mathrm{pc}}}\right) \tag{4.221}$$

where α is the AFP loss per EPR measurement (two spin flips) and $(P_{\mathrm{tc}}/P_{\mathrm{pc}})$ is the polarization gradient correction factor used to obtain the polarization in the target chamber.

The analysis was also performed by simply taking the average of the frequencies within a time slice. Under most conditions, the resulting ^{3}He polarization was within 1% relative of the value determined by the extrapolated frequencies. In addition, there was no systematic difference between the two methods. Occasionally, an EPR measurement was taken while the septum magnet was being ramped to a new set point. This caused a corresponding change in the fringe field due to the septum magnet that was visibly apparent during the EPR measurement. In these cases, the extrapolated frequencies resulted in polarizations that were up to 5% relative different than the value determined from the average frequencies. In all cases, the extrapolated frequencies were used to determine the ^{3}He polarization.

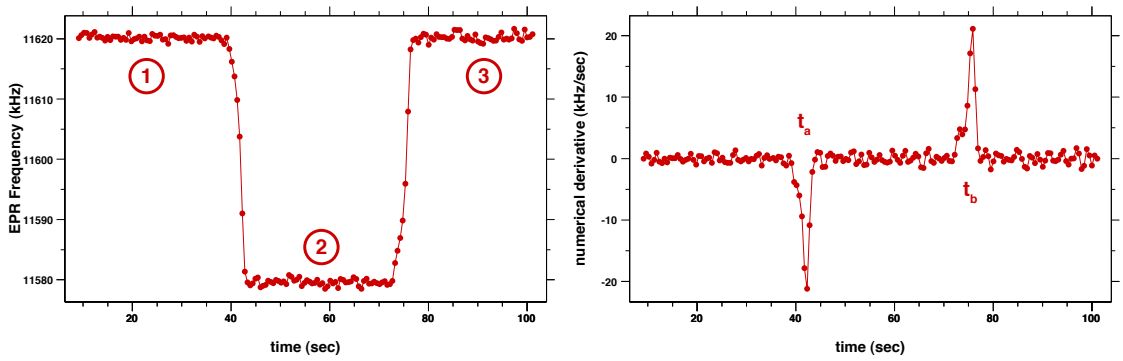

Figure 4.28: Typical EPR Measurement with ^{85}Rb at 24.4 Gauss. The right plot is the numerical derivative of the left plot.

Correcting for AFP Losses

The AFP loss for the EPR measurements were typically larger than for NMR measurements for four reasons. First, the magnetic field gradients were larger in the pumping chamber. Second, the ^{3}He spins were in the opposite state for a longer period of time which increased the contribution to spin-exchange to the AFP loss. Third, the effect of spin-exchange while in the opposite state is more immediately felt in the pumping chamber than the target chamber. Fourth, the NMR RF field used for AFP had a smaller amplitude than for the EPR measurements. AFP loss data was taken at various septum currents, see left side of Fig. (4.29), and was very well described by:

$$\alpha = \alpha_0 + \left(\frac{I_{\text{sep}}}{I_2}\right)^2 + \left(\frac{I_{\text{sep}}}{I_4}\right)^4 \tag{4.222}$$

where $\alpha_0 = 0.527$, $I_0 = 2077$ A, and $I_4 = 251.3$ A. For septum currents above 300 A, the AFP losses became large enough that gradient correction coils were required to partially cancel gradients due to the fringe field of the septum. These coils were only used during EPR measurements and significantly reduced the AFP losses, see right side of Fig. (4.29). For EPR measurements taken while the gradient correc-

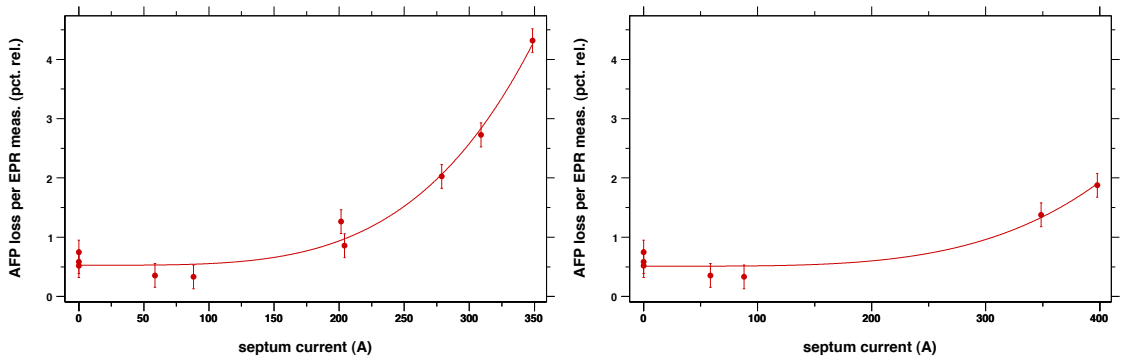

Figure 4.29: AFP Losses During EPR Measurements. The left plot is data taken without the gradient correction coils. The right plot is data taken with the gradient correction coils at septum current greater than 300 A and without the gradient correction coils for septum currents below 100 A.

tions coils were on, the fit was constrained to give the same AFP loss at zero current and the other fit parameters were $I_2 = 1.322\text{E}7$ A and $I_4 = 367.4$ A. If we assume that the losses due to AFP occur mainly during the spin flips, then the pumping chamber polarization extracted from Eqn. (4.97) corresponds to $P_0(1 - \alpha/2)$, where P_0 is the ^{3}He pumping chamber polarization before the measurement. We've assigned a 0.2% relative uncertainty due to the AFP loss correction, which is mainly due to our level of understanding on the dependence of the AFP loss in the pumping chamber as a funcion of septum current.

Polarization Gradient Correction

The EPR measurements resulted in the polarization in the pumping chamber. A polarization gradient correction was applied to determine the polarization in the target chamber. The size of the correction was sensitive to the relaxation attributed to the electron beam and the detailed polarization and diffusion dynamics within the cell. In order to estimate the size of this correction, we assumed that the polarizations were at equilibrium when the electron beam was turned off. Immediately

after the beam is turned off, the time evolution of the polarizations are given by Eqns. (6.40) & (6.41), where $m_{\rm pc} = 0$ and $m_{\rm tc} = +\Gamma_b P_{\rm tc}(t=0)$, which gives the ratio of target to pumping chamber polarization to lowest order in t:

$$y_t \equiv \frac{P_{\rm tc}(t)}{P_{\rm pc}(t)} \approx \frac{P_{\rm tc}(t=0)}{P_{\rm pc}(t=0)} \left[\frac{1 + \Gamma_b t + O(t^2)}{1 + O(t^2)} \right] \qquad t\Gamma_{\rm f} \ll 1 \tag{4.223}$$

where Γ_b is the relaxation rate due to the electron beam in the target chamber. This is only valid for $t\Gamma_{\rm f} \ll 1$, where $\Gamma_{\rm f} \approx d_{\rm tc}/f_{\rm pc}$ is the fast time constant, $d_{\rm tc}$ is the diffusion rate out of the target chamber, and $f_{\rm pc} = 1 - f_{\rm tc}$ is the fraction of ^{3}He nuclei in the pumping chamber. When $t\Gamma_{\rm f} \gg 1$, we can combine Eqns. (6.31) by dropping the fast exponential term and after some considerable algebra we find:

$$y_t \approx y_0 \left[\frac{(x_b - x_t) + x_b(x_t - 1)\left(1 - f_{\rm tc}\Gamma_b/d_{\rm tc}\right)}{x_t(x_b - 1)} \right] \qquad t\Gamma_{\rm f} \gg 1 \tag{4.224}$$

where $y_t = P_{\rm tc}(t)/P_{\rm pc}(t)$ is the ratio of polarization at time t, $y_0 = P^{\infty}_{\rm tc,0}/P^{\infty}_{\rm pc,0} \approx 1 - \Gamma_{\rm tc}/d_{\rm tc}$ is the ratio of equilibrium polarizations without the beam, $x_t = P_{\rm pc}(t)/P^{\infty}_{\rm pc,0}$ is the polarization in the pumping chamber relative to its equilibrium value without the beam, $x_b = P^{\infty}_{{\rm pc},b}/P^{\infty}_{\rm pc,0} = 1/(1 + \tau_{\rm su} f_{\rm tc}\Gamma_b)$ is the ratio of the equilibrium polarization in the pumping chamber with and without the beam (i.e. the pumping chamber polarization immediately after the beam is turned off defining $t = 0$), and $\tau_{\rm su}$ is the spin-up time constant without the beam. We've expressed the ratio of the target chamber to pumping chamber polarizations in this form because $P_{\rm pc}$, $P^{\infty}_{\rm pc,0}$, $P^{\infty}_{\rm tc,0}$, & $\tau_{\rm su}$ were measured directly and Γ_b & $d_{\rm tc}$ were calculated using the results of

Secs. (6.3.1) & (6.4.1):

$$\Gamma_b = \left[\frac{1}{42\text{ hrs}}\right]\left[\frac{I_{\text{beam}}}{10\ \mu\text{A}}\right]\left[\frac{2.0\text{ cm}^2}{A_{\text{tc}}}\right]\left[\frac{n_a}{0.5}\right] \quad (4.225)$$

$$d_{\text{tc}} = \left[0.80\text{ hrs}^{-1}\right]\left[\frac{A_{\text{tt}}}{0.5\text{ cm}^2}\right]\left[\frac{6\text{ cm}}{L_{\text{tt}}}\right]\left[\frac{90\text{ cm}^3}{V_{\text{tc}}}\right]\left[\frac{10\text{ amg}}{n_{\text{tc}}}\right]\left[\frac{\Upsilon\left(T_{\text{pc}}, T_{\text{tc}}\right)}{4/3}\right] \quad (4.226)$$

where I_{beam} is the beam current, $A_{\text{tc(tt)}}$ is the cross sectional area of the target chamber (transfer tube), n_a is the mean number of nuclear spin flips per atomic ion, see Eqn. (6.107), L_{tt} is the length of the transfer tube, V_{tc} is the volume fo the target chamber, and Υ is defined by Eqn. (6.129). The uncertainties in this correction were mainly due to the approximations made in deriving these results, the 15% uncertainty in d_{tc} due to the uncertainty of crossetional area of the transfer tube, and the 15% uncertainty in Γ_b due to the uncertainty in n_a, see Sec. (6.3.4). The largest error in the approximation occurs when $t\Gamma_{\text{f}} \approx 1$, see Fig. (4.30). For $t < t_a$ ($t \geq t_a$), we used Eqn. (4.223) (Eqn. (4.224)) where $t_a = 1.2/\Gamma_{\text{f}}$ was chosen to minize the approximation error. The total uncertainty in this correction is given by $(0.4 + 0.05 I_{\text{beam}}/(10\ \mu\text{A}))$ percent relative, where I_{beam} is the beam current.

Discussion of Uncertainties

The dominant uncertainties are due to the knowledge of κ_0 itself and due to our understanding the polarization dynamics between the two chambers. Since the polarization conditions varied from one EPR measurement to another, we've assigned a fairly large 1% relative uncertainty due to the polarization gradient correction. The statistical uncertainty on B_{He} due to the the linear fits were usually 0.9% relative. The contribution to the EPR frequency shift due the AC Zeeman effect by the NMR RF field (which was *not* turned off during the measurement)

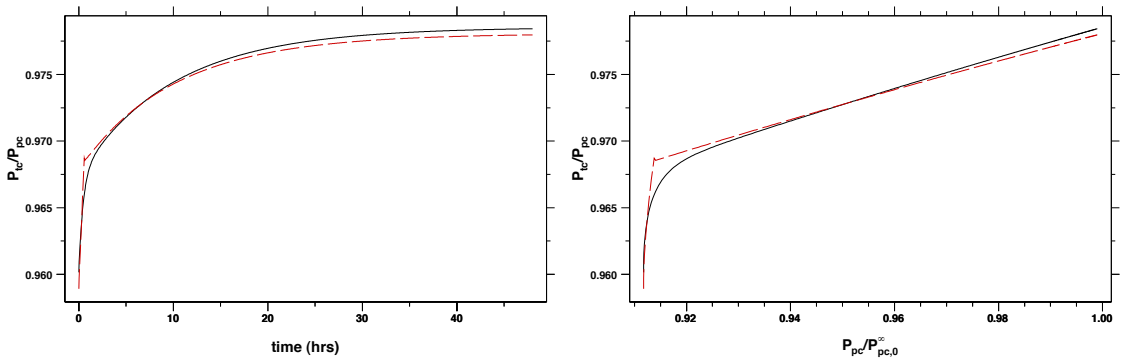

Figure 4.30: Time Evolution of the Polarization Gradient. A 10 μA electron beam is turned off at $t = 0$. The polarization in the target chamber immediately starts to increase linearly whereas the pumping chamber polarization is constant to first order in t. After some time, the target chamber to pumping chamber polarization ratio increases linearly with the pumping chamber polarization. The broken red (solid black) line is the approximate (full) calculation.

is about 1.2%. We've assumed that, during the frequency sweep AFP, the NMR RF field does not change in magnitude by more than 50% relative, which introduces a 0.6% relative uncertainty on B_{He}. Since the temperature dependnace of κ_0 is anticorrelated to n_{pc}, the total uncertainty on their product due to the uncertainty on the pumping chamber tempertaure is greatly supprsessed, which in our case contribites 0.2% relative. The effect of magnetic field gradients, altrhouhg large and vargiable in the pumping chmabre due to the septum fringe fields, is expected to tbe greatly suppressed due to the very small A–He spin-exchange rate to optical pumping rate. Finally, we've used $\kappa_{\mathrm{geo}} = 0.97$ which introduces a 0.2% relative uncertainty.

source	quantity	% rel. uncertainty
total sytematic		2.0
statistical		0.9
[12]	κ_0	1.5
polarization gradient	$P_{\rm tc}/P_{\rm pc}$	1.0
NMR RF shift	$\Delta\nu$	0.6
afploss correction	$B_{\rm He}$	0.2
slope $d\nu/dB$	$B_{\rm He}$	0.2
$T_{\rm pc}$,$T_{\rm tc}$	$(\kappa_0 n_{\rm pc})$	0.2
$\kappa_{\rm geo}$	κ_0	0.2
magnetic field gradients	$\Delta\nu$	0.1

Table 4.17: EPR Measurement Uncertainties.

4.6.9 EPR-NMR Calibration Constant

The EPR-NMR calibration constant is given as:

$$c_{\rm epr} = \left[\frac{\hat{\Phi}_x^{\rm tc}}{\Phi_x^{\rm tc}}\right]\left[\frac{\hat{\ell}_B^{\rm fit}}{\hat{S}}\right]\left[\frac{t}{\kappa_0 - 1 + \kappa_{\rm geo}}\right]\left[\frac{3\hat{B}_{\rm He}}{g\mu_0\mu_N}\right]\left(\frac{1}{1-\hat{\alpha}/2}\right)\left(\frac{\hat{P}_{\rm tc}}{\hat{P}_{\rm pc}}\right) = \frac{R_{\rm epr}}{\Phi_x^{\rm tc}} \quad (4.227)$$

where t is the rato of pumping chamber to target chamber temperatures and $R_{\rm epr}$ isolates all the factors that vary from one measurement to the next. Six dedicated EPR-NMR calibration measurements were taken and are listed in Tab. (4.18). Each measurement typically consisted of four NMR measurements interleaved with three EPR measurements. AFP losses were determined directly from the data. For most of the measurements, the polarization gradient was well understood since they were performed well after the electron beam had been turned off. Once again, we've separated the calibration into two groups before and after Penelope ruptured. The uncertainty in the coil positions measurement for the Penelope calibration is zero since the cell was not moved. On the other hand, the uncertainty

date	**notes**	I_{sep} (A)	I_{beam} (μA)	B_{He} (mG)	$\sigma^{\text{stat}}_{B_{\text{He}}}$ (mG)	$\langle S \rangle$ (mV)	R_{epr}
07/17	penelope	204.2	0	46.96	0.54	-18.08	2120
07/25	-	88.1	0	42.72	0.54	-15.67	1979
08/03	-	0	0	46.57	0.73	-17.35	1956
08/16	-	58.6	4.8	43.91	0.72	-16.44	1996
08/30	-	0	0	40.56	0.27	-14.49	1927
08/30	1 laser	0	0	40.13	0.37	-13.65	2054

Table 4.18: EPR-NMR Calibration Measurements. All measurements are with Priapus and full (3 or 4) laser power unless otherwise noted. $R_{\texttt{epr}}$ has units of amg $\cdot$ cm^2/mV and can be directly compared to $R_{\texttt{w}}(g^{\text{sheilded}}_{\text{proton}}/g^{\text{sheilded}}_{\text{He}})$.

in the coil position measurements for Priapus larger since the cell was removed and reinstalled during the switch from 6 to 9 degree configuration. Once again the sensistivty to the uncertainty in the pumping chamber temperature is suppresd in the ratio κ_0/t. The final value and uncertainties are listed in Tab. (4.19).

4.6.10 Final Results for the Target Polarization

The polarization was monitored about every four hours during the experiement with both NMR and stand-alone EPR measurements. The time dependence of the polarization was modeled using a simple cubic spline. AFP losses in the target chamber were accounted for after each measurement. Polarizations were determined on a run-by-run basis by averaging the cubic spline over the duration of the run. Since the water calibration constant had a significantly larger uncertainty than the EPR-NMR calibration constant, the EPR-NMR calibration was given twice the weight. The stand-alone EPR measurements had a smaller systematic uncertainty than the NMR measurements, but were taken less frequently. Therfore, we gave

cell/angle	**calibration constant**	**stat , syst (% rel.)**
penelope	0.2185 amg/mV	$\pm 1.2 \pm 3.7$
priapus6	0.2180 amg/mV	$\pm 0.5 \pm 4.3$
priapus9	0.2152 amg/mV	$\pm 0.5 \pm 4.0$
source	**quantity**	**% rel. uncertainty**
$b(I_{\rm sep})$	^{3}He $\hat{\ell}_B^{\rm fit}$	3.0
coil positions	$\hat{\Phi}_x/\Phi_x$	0.0/2.2/1.5
[12]	κ_0	1.5
pickup coils/BNC cables	$\hat{Q}(\omega_0)/Q(\omega_0)$	1.0
polaization/density gradient	$\hat{\Phi}_x/\Phi_x$	0.7
NMR RF shift	$\Delta\nu$	0.6
coil stablity	$\hat{\Phi}_x/\Phi_x$	0.6
$T_{\rm pc}$,$T_{\rm tc}$	(κ_0/t)	0.5
polarization gradient	$P_{\rm tc}/P_{\rm pc}$	0.4
slope $d\nu/dB$	$B_{\rm He}$	0.2
$\kappa_{\rm geo}$	κ_0	0.2
magnetic field gradients	$\Delta\nu$	0.1
NMR RF func. gen.	$\hat{\nu}_0/\nu_0$	neg.
preamp gain [46]	$\hat{G}_p/G_p$	neg.
lockin gain [16]	$(\hat{G}_L/\hat{G}_L^n)/(G_L/G_L^n)$	neg.

Table 4.19: EPR-NMR Calibration Constants.

equal weights to the NMR and EPR polarizations to yield the final polarization:

$$P_{\text{final}} = \frac{P^{\mathtt{W}}_{\text{NMR}} + 2P^{\mathtt{epr}}_{\text{NMR}} + 3P_{\text{EPR}}}{6} \tag{4.228}$$

where $P^{\mathtt{W(epr)}}_{\text{NMR}}$ is the NMR polarization using the water (EPR-NMR) calibration constant and P_{EPR} is the EPR polarization. Since the EPR measurements were taken less frequently for Priapus during the 6 degree running, the polarization for this data set was given by:

$$P_{\text{final}} = \frac{P^{\mathtt{W}}_{\text{NMR}} + 4P^{\mathtt{epr}}_{\text{NMR}} + P_{\text{EPR}}}{6} \tag{4.229}$$

Between runs 3891 and 3903, the polarization mysteriously dropped from 0.4 to 0.2 over the course of six hours. Since we did not know when the drop occurred, we've simply performed a linear interpolation from 0.4 to 0.2 over these runs and assigned very large uncertainties (50% relative) for these runs.

Since there are several correlations between the three measurements, we estimated the uncertainty on the polarization using:

$$\left[\frac{\sigma}{P}\right]_{\text{final}} = \frac{1}{6}\left[\frac{\sigma}{P}\right]^{\mathtt{W}}_{\text{NMR}} + \frac{1}{3}\left[\frac{\sigma}{P}\right]^{\mathtt{epr}}_{\text{NMR}} + \frac{1}{2}\left[\frac{\sigma}{P}\right]_{\text{EPR}} \tag{4.230}$$

where we've used an analogous equation for the Priapus 6 degree data set. The total statistical unertainty is about 0.6% relative. The total systematic uncertainty on the polarization density product is about 3.9% relative, where we've added a 1% relative uncertainty due to the run-by-run interpolation. The total systematic uncertainty on the polarization is about 4.2% relative, which also includes an additional 1.5% uncertainty due to the density.

cell	penelope	priapus6	priapus9
$\langle P^{\mathtt{W}}_{\mathrm{NMR}} \rangle$	0.390	0.424	0.392
stat.	1.27	0.88	0.88
syst.	8.23	8.23	8.23
$\langle P^{\mathtt{epr}}_{\mathrm{NMR}} \rangle$	0.376	0.395	0.365
stat.	1.20	0.47	0.47
syst.	3.73	4.34	4.01
$\langle P_{\mathrm{EPR}} \rangle$	0.379	0.391	0.365
stat.	0.87	0.87	0.87
syst.	2.02	2.02	2.02
$\langle P_{\mathrm{final}} \rangle$	0.390	0.399	0.372
stat.	0.67	0.54	0.54
syst.	3.76	3.96	3.85

Table 4.20: Average ^{3}He Polarizations. The statistical (stat.) and systematic (syst.) uncertainties are quoted at % relative. Only the final systematic uncertainty (last row) include the 1% relative interpolatation uncertainty. These uncertainties are for the polarization density product. An additional 1.6% relative uncertainty must be added in quadrature to obtain the uncertainties on the polarizations themselves.

The final polarizations are depicted in Fig. (4.31). The polarizations from NMR measurements using the EPR-NMR calibration constant agreed within 1% relative with the polarizations from stand alone EPR measurements. For Penelope, the polarizations from NMR measurements using the water calibration constant were typically 3.7% relative higher than from calibrations using EPR. For Priapus, the polarizations from NMR measurements using the water calibration constant were typically 7.3% relative higher than from calibrations using EPR. This is not unreasonable since the total systematic uncertainty of the water calibration constant is 8.3% relative. The final average polarizations, statistcal uncertainties, and systematic uncertaintites are listed in Tab. (4.20).

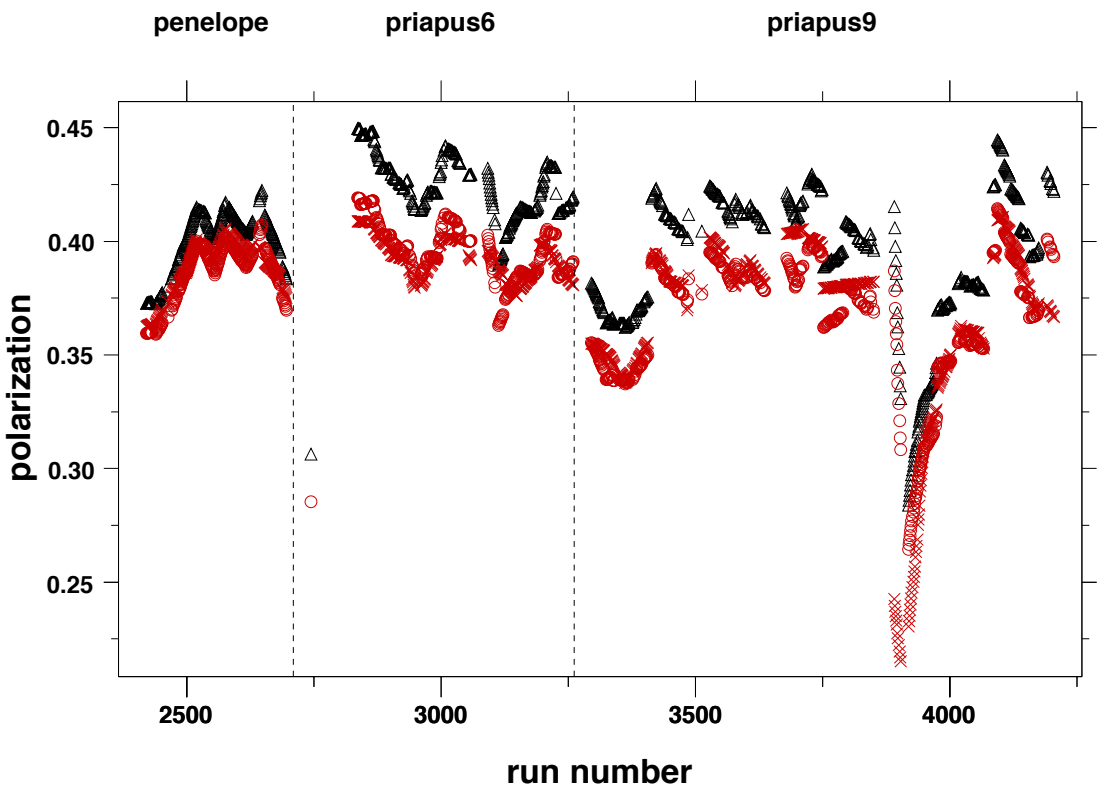

Figure 4.31: Final ^{3}He Target Chamber Polarizations. The open black triangles (red circles) are from NMR measurements using the water (EPR-NMR) calibration constant. The red crosses are from stand-alone EPR measurements.

Bibliography

[1] J.D. Jackson. *Classical Electrodynamics*. John Wiley & Sons, New York, 2nd edition, 1975.

[2] I. I. Rabi, N. F. Ramsey, and J. Schwinger. Use of Rotating Coordinates in Magnetic Resonance Problems. *Reviews of Modern Physics*, 26(2):167–171, Apr 1954.

[3] F. Bloch and A. Siegert. Magnetic Resonance for Nonrotating Fields. *Phys. Rev.*, 57(6):522–527, Mar 1940.

[4] A. Abragam. *Principles of Nuclear Magnetism*. Oxford University Press, Oxford, 1961.

[5] I. I. Rabi. Space quantization in a gyrating magnetic field. *Phys. Rev.*, 51(8):652–654, Apr 1937.

[6] Rodger L. Gamblin and Thomas R. Carver. Polarization and relaxation processes in ^{3}He gas. *Phys. Rev.*, 138(4A):A946–A960, May 1965.

[7] L. D. Schearer and G. K. Walters. Nuclear spin-lattice relaxation in the presence of magnetic-field gradients. *Phys. Rev.*, 139(5A):A1398–A1402, Aug 1965.

[8] G. D. Cates, S. R. Schaefer, and W. Happer. Relaxation of spins due to field inhomogeneities in gaseous samples at low magnetic fields and low pressures. *Phys. Rev. A*, 37(8):2877–2885, Apr 1988.

[9] G. D. Cates, D. J. White, Ting-Ray Chien, S. R. Schaefer, and W. Happer. Spin relaxation in gases due to inhomogeneous static and oscillating magnetic fields. *Phys. Rev. A*, 38(10):5092–5106, Nov 1988.

[10] C. P. Slichter. *Principles of Magnetic Resonance*. Springer, Berlin, 3rd, enlarged, updated, corrected edition, 1996.

[11] Edward M. Purcell. *Electricity & Magnetism*. McGraw-Hill, New York, 2nd edition, 1984.

[12] Mikhail V. Romalis. *Laser Polarizaed* ^{3}He *Target Used for a Precision Measurement of the Neutron Spin Structure*. PhD thesis, Princeton University, 1997.

[13] Ioannis Kominis. *Measurement of the Neutron (*^{3}He *) Spin Structure at Low* Q^2 *and the Extended Gerasimov-Drell-Hearn Sum Rule*. PhD thesis, Princeton University, 2001.

[14] Kevin M. Kramer. *A Search for Higher Twist Effects the Neutron Spin Structure Function* $g_2^n(x, Q^2)$. PhD thesis, College of William & Mary, 2003.

[15] Cornelius Lanczos. *The Variational Principles of Mechanics*. Dover Publications, Inc., New York, 4th edition, 1986.

[16] *Manual for Model SR844 RF Lock-In Amplifier, Revision 2.7 (7/2007)*. Stanford Research Systems, Sunnyvale, CA, 2007.

[17] Forman S. Acton. *Numerical Methods That Usually Work*. Mathematical Association of America, Washington, DC, 1990.

[18] Forman S. Acton. *Real Computing Made Real: Preventing Errors in Scientific and Engineering Calculations*. Dover Publications, Mineola, New York, 1996.

[19] William H. Press, Brian P. Flannery, Saul A. Teukolsky, and William T. Vetterling. *Numerical Recipes in C: The Art of Scientific Computing*. Cambridge University Press, Cambridge, 1st edition, 1988.

[20] F. Bloch. Nuclear induction. *Phys. Rev.*, 70(7-8):460–474, Oct 1946.

[21] F. Bitter. The Optical Detection of Radiofrequency Resonance. *Phys. Rev.*, 76(6):833–835, Sep 1949.

[22] William E. Bell and Arnold L. Bloom. Optical Detection of Magnetic Resonance in Alkali Metal Vapor. *Phys. Rev.*, 107(6):1559–1565, Sep 1957.

[23] G W Series. Radio-frequency spectroscopy of excited atoms. *Reports on Progress in Physics*, 22(1):280, 1959.

[24] A. Gozzini, editor. *Topics in Radiofrequency Spectroscopy (Proceedings of the International School of Physics, Enrico Fermi, XVII Course, 1960)"*. Academic Press, New York, 1962.

[25] F. Bitter. Magnetic Resonance in Radiating or Absorbing Atoms. *Appl. Opt.*, 1(1):1–10, 1962.

[26] Alfred Kastler. Optical Methods for Studying Hertzian Resonances. In *Nobel Lectures, Physics 1963-1970*. Elsevier, Amsterdam, 1972.

[27] L. C. Balling, R. J. Hanson, and F. M. Pipkin. Frequency Shifts in Spin-Exchange Optical Pumping Experiments. *Phys. Rev.*, 133(3A):A607–A626, Feb 1964.

[28] L. C. Balling, R. J. Hanson, and F. M. Pipkin. Errata: Frequency Shifts in Spin-Exchange Optical Pumping Experiments. *Phys. Rev.*, 135(7AB):AB1, Sep 1964.

[29] B. C. Grover. Noble-gas nmr detection through noble-gas-rubidium hyperfine contact interaction. *Phys. Rev. Lett.*, 40(6):391–392, Feb 1978.

[30] Stephen Robert Schaefer. *Determination of Spin-exchange Parameters in an Optically Pumped Rb + Kr System*. PhD thesis, Princeton University, 1988.

[31] S. R. Schaefer, G. D. Cates, Ting-Ray Chien, D. Gonatas, W. Happer, and T. G. Walker. Frequency shifts of the magnetic-resonance spectrum of mixtures of nuclear spin-polarized noble gases and vapors of spin-polarized alkali-metal atoms. *Physical Review A*, 39(11):5613–5623, Jun 1989.

[32] N. R. Newbury, A. S. Barton, P. Bogorad, G. D. Cates, M. Gatzke, H. Mabuchi, and B. Saam. Polarization-dependent frequency shifts from Rb-^{3}He collisions. *Physical Review A*, 48(1):558–568, Jul 1993.

[33] A. S. Barton, N. R. Newbury, G. D. Cates, B. Driehuys, H. Middleton, and B. Saam. Self-calibrating measurement of polarization-dependent frequency shifts from Rb-^{3}He collisions. *Physical Review A*, 49(4):2766–2770, Apr 1994.

[34] M. V. Romalis and G. D. Cates. Accurate ^{3}He polarimetry using the Rb Zeeman frequency shift due to the Rb-^{3}He spin-exchange collisions. *Physical Review A*, 58(4):3004–3011, Oct 1998.

[35] Earl Babcock, Ian A. Nelson, Steve Kadlecek, and Thad G. Walker. ^{3}He polarization-dependent EPR frequency shifts of alkali-metal-^{3}He pairs. *Physical Review A*, 71(1):013414, Jan 2005.

[36] A. Ben-Amar Baranga, S. Appelt, C. J. Erickson, A. R. Young, and W. Happer. Alkali-metal-atom polarization imaging in high-pressure optical-pumping cells. *Phys. Rev. A*, 58(3):2282–2294, Sep 1998.

[37] W. Happer and H. Tang. Spin-exchange shift and narrowing of magnetic resonance lines in optically pumped alkali vapors. *Phys. Rev. Lett.*, 31(5):273–276, Jul 1973.

[38] I. M. Savukov and M. V. Romalis. Effects of spin-exchange collisions in a high-density alkali-metal vapor in low magnetic fields. *Phys. Rev. A*, 71(2):023405, Feb 2005.

[39] M. Liang. A Guide for the EPR Measurement at Jefferson Lab. *JLAB E94010 Technical Note*, 2001.

[40] A. Ben-Amar Baranga, S. Appelt, M. V. Romalis, C. J. Erickson, A. R. Young, G. D. Cates, and W. Happer. Polarization of 3*he* by spin exchange with optically pumped rb and k vapors. *Phys. Rev. Lett.*, 80(13):2801–2804, Mar 1998.

[41] James Clerk Maxwell. *A Treatise on Electricity and Magnetism: Volume Two*. Dover Publications, Inc., New York, 3rd, unabridged edition, 1954.

[42] J. A. Osborn. Demagnetizing factors of the general ellipsoid. *Phys. Rev.*, 67(11-12):351–357, Jun 1945.

[43] Dmitry Budker, Derek K. Kimball, and David P. DeMille. *Atomic Physics: An Exploration Through Problems and Solutions*. Oxford University Press, Oxford, Great Britain, 1st edition, 2004.

[44] Frank S. Crawford Jr. *Waves*. McGraw-Hill, New York, 1968.

[45] David S. Kliger, James W. Lewis, and Cora Einterz Randall. *Polarized Light in Optics and Spectroscopy*. Academic Press, Boston, 1990.

[46] *Manual for Model SR560 Low Noise Preamplifier, Revision 2.8 (12/2006)*. Stanford Research Systems, Sunnyvale, CA, 2006.

[47] William R. Leo. *Techniques for Nuclear and Particle Physics Experiments: A How-to Approach*. Springer-Verlag, Berlin, second revised edition, 1994.

[48] Sebastien Incerti. Monitoring of the pick-up coils. *JLAB E94010 Technical Note*, 22, 1999.

[49] Patricia H. Solvignon. *Measurement of the neutron (^{3}He) spin structure functions in the resonance region*. PhD thesis, Temple University, 2006.

[50] D. K. Walter, W. M. Griffith, and W. Happer. Energy Transport in High-Density Spin-Exchange Optical Pumping Cells. *Phys. Rev. Lett.*, 86(15):3264–3267, Apr 2001.

[51] Steven R. Parnell, Martin H. Deppe, Salma Ajraoui, Juan Parra-Robles, Stephen Boag, and Jim M. Wild. Measurement of laser heating in spin exchange optical pumping by nmr diffusion sensitization gradients. *Journal of Applied Physics*, 107(9):094904, 2010.

[52] Vince Sulkosky (Private Communication).

[53] Hunter Leigh Middleton. *The Spin Structure of the Neutron Determined Using a Polarized ^{3}He Target*. PhD thesis, Princeton University, 1994.

[54] Sebastien Incerti and Enkeleida Lakuriqi. Model of the water signal shape from the Bloch equations. *JLAB E94010 Technical Note*, 10, 1998.

[55] Sebastien Incerti. Estimation of the NMR RF field amplitude. *JLAB E94010 Technical Note*, 18, 1999.

[56] John Steffen Jensen. *Measurement of the Neutron (^{3}He) Spin Structure Function at Low Q^2: A Connection Between the Bjorken and Drell-Hearn-Gerasimov Sum Rules*. PhD thesis, California Institute of Technology, 2000.

[57] Alexander Deur. About the NMR Relaxation times T_1 and T_2 and Procedure to Fill the Reference Cell. *JLAB E94010 Technical Note*, 12, 1998.

[58] Sebastien Incerti. Estimation of the magnetic longitudinal gradient between the pick-up coils. *JLAB E94010 Technical Note*, 23, 1999.

[59] J. L. Flowers, B. W. Petley, and M. G. Richards. A measurement of the nuclear magnetic moment of the helium-3 atom in terms of that of the proton. *Metrologia*, 30(2):75, 1993.

[60] Philip R. Bevington and D. Keith Robinson. *Data Reduction and Error Analysis for the Physical Sciences*. McGraw-Hill, Boston, MA, 2nd edition, 1992.

Chapter 5

Optical Pumping of Alkali-Hybrid Mixtures

5.1 Introduction

5.1.1 Traditional SEOP

In traditional SEOP [1], a single alkali species, usually Rb, is optically pumped with broadband laser diode arrays. Optical pumping occurs by exciting the D1 transition of the vaporized Rb atoms by circularly polarized laser light tuned to the appropriate wavelength (795 nm). Constrained by the conservation of energy and angular momentum, only one of the two Zeeman levels ($m_J = \pm 1/2$) of the $5S_{1/2}$ ground state is excited to the $5P_{1/2}$ state, where we've ignored the Rb nuclear spin. Collisions with ^{3}He & N_2 almost completely disorients the Zeeman levels of the excited states. This insures that the Rb atom decays back to either Zeeman level of the ground state with equal probability. Radiation trapping effects are greatly suppressed by the addition of small amount of N_2 which nonradiatively quenches

the $5P \rightarrow 5S_{1/2}$ transitions. Within milliseconds the Rb polarization reaches an equilibrium value of P_{Rb} given by the balance between the optical pumping rate R and the relaxation rate Γ_{Rb}:

$$P_{\mathrm{Rb}} = \frac{R}{R + \Gamma_{\mathrm{Rb}}} \tag{5.1}$$

The optical pumping rate is given by the following integral over laser frequency ν:

$$R = \int_0^\infty \Phi(\nu)\, \sigma_1^{\mathrm{Rb}}(\nu)\, d\nu \tag{5.2}$$

where $\Phi(\nu)$ is the total photon flux and $\sigma_1^{\mathrm{Rb}}(\nu)$ is the unpolarized Rb D1 photon-absorption cross section. The dominant mechanism of Rb spin relaxation are polarization destroying collisions with other Rb atoms, ^{3}He atoms, and N_2 molecules.

Spin exchange between Rb and ^{3}He is largely mediated by a hyperfine-like Fermi contact interaction. This couples the spin of the valence electron spin of the Rb atom to the nucleus of the ^{3}He atom. In the fast diffusion limit, see Sec. (6.1.6), the spin-exchange rate is given by:

$$\langle \gamma_{\mathrm{se}} \rangle = f_{\mathrm{pc}} k_{\mathrm{se}} [\mathrm{Rb}] \tag{5.3}$$

where f_{pc} is the fraction of ^{3}He nuclei in the pumping chamber and k_{se} is the Rb-^{3}He spin-exchange rate constant. After several hours, the ^{3}He polarization reaches an equilibrium value of P_{He} given by:

$$P_{\mathrm{He}} = \frac{P_{\mathrm{Rb}} \langle \gamma_{\mathrm{se}} \rangle}{\langle \gamma_{\mathrm{se}} \rangle + \langle \Gamma_{\mathrm{He}} \rangle} \tag{5.4}$$

where, in the fast diffusion limit, $\langle \Gamma_{\mathrm{He}} \rangle$ is the volume averaged ^{3}He spin relaxation rate.

According to these equations, if one could provide enough laser power to keep a very high density of Rb polarized, then the ^{3}He polarization could be, in principle, made to equilibrate at unity:

$$P_{\mathrm{He}} = \left[\lim_{\langle\gamma_{\mathrm{se}}\rangle\to\infty} \frac{\langle\gamma_{\mathrm{se}}\rangle}{\langle\gamma_{\mathrm{se}}\rangle + \langle\Gamma_{\mathrm{He}}\rangle}\right]\left[\lim_{R\to\infty} \frac{R}{R+\Gamma_{\mathrm{Rb}}}\right] = 1 \tag{5.5}$$

However, in practice with SEOP, the ^{3}He polarization has never been recorded higher than 0.85 and has rarely been made to exceed 0.80. The performance is even lower in SLAC/JLab style target cells. There are two main reasons for non-unity ^{3}He polarization. First, it has been reported that there is a previously unaccounted for ^{3}He spin-relaxation mechanism [2]. This so-called 'X'-factor is dependent on the alkali density and/or has an alkali vapor pressure-like temperature dependence, see Sec. (6.2.1). Second, it is difficult to provide enough photon flux throughout the entire pumping chamber because of light absorption by the Rb vapor. This absorption results in a spatial variation of the photon flux governed by:

$$\frac{d\Phi(\vec{r},\nu)}{dz} = -\Phi(\vec{r},\nu)\sigma_1^{\mathrm{Rb}}(\nu)[\mathrm{Rb}]\,(1 - P_{\mathrm{Rb}}(\vec{r})) \tag{5.6}$$

where z is the depth into the cell and [Rb] is the number density of Rb atoms. Because the Rb polarization rate (kHz) is much faster than its diffusion rate (mHz), the *local* Rb polarization is given by the *local* optical-pumping rate, which in turn depends on the *local* photon flux [3–5]. On the other hand, because the ^{3}He diffusion rate (mHz) is much faster than its polarization rate (μHz), the ^{3}He polarization depends on the average Rb polarization in the pumping chamber $\langle P_{\mathrm{Rb}}\rangle_{\mathrm{pc}}$. Thus the

^{3}He equilibrium polarization is more realistically given by:

$$P_{\mathrm{He}} = \frac{\langle P_{\mathrm{Rb}} \rangle_{\mathrm{pc}} \langle \gamma_{\mathrm{se}} \rangle}{\langle \gamma_{\mathrm{se}} \rangle (1 + X) + \langle \Gamma_{\mathrm{He}} \rangle} \tag{5.7}$$

To approach the $1/(1 + X)$ limit, the alkali density must be increased such that $\langle \Gamma_{\mathrm{He}} \rangle / \langle \gamma_{\mathrm{se}} \rangle \ll 1$ while enough photon flux must be supplied to insure $\langle P_{\mathrm{Rb}} \rangle_{\mathrm{pc}} \approx 1$.

5.1.2 An Outline of Alkali-Hybrid SEOP

In alkali-hybrid SEOP [6,7], a mix of two alkali species, in our case potassium (K) & rubidium (Rb), are used. As in traditional SEOP, Rb is polarized via optical pumping. When the K to Rb vapor density ratio $D = [\mathrm{K}]/[\mathrm{Rb}]$ is small ($D \ll 1000$), polarization conserving alkali-alkali spin exchange collisions dominate and insure that $P_{\mathrm{K}} = P_{\mathrm{Rb}} = P_{\mathrm{A}}$. Now ^{3}He is polarized by both Rb-^{3}He & K-^{3}He spin-exchange collisions. The equations for the equilibrium polarizations have the same form provided we relabel the subscript Rb $\rightarrow$ A and account for the spin exchange & relaxation due to K:

$$\Gamma_{\mathrm{A}} = \Gamma_{\mathrm{Rb}} + D(\Gamma_{\mathrm{K}} + 2k_A[\mathrm{Rb}]) \tag{5.8}$$

$$\langle \gamma_{\mathrm{se}} \rangle = f_{\mathrm{pc}} k_{\mathrm{se}}[\mathrm{Rb}] \left[1 + D \left(\frac{k'_{\mathrm{se}}}{k_{\mathrm{se}}} \right) \right] \tag{5.9}$$

where Γ_{K} is the K spin-relaxation rate, k_A is the mean Rb-K spin relaxation rate, and k'_{se} is the K-^{3}He spin-exchange rate constant. For the same $\langle \gamma_{\mathrm{se}} \rangle$, the Rb density is smaller & the alkali relaxation rate is larger for alkali-hybrid SEOP than traditional SEOP. K has a much smaller spin-relaxation rate than Rb and consequently the increase in the alkali relaxation rate is not too substantial. At the optimal D, where

the reduction in the Rb density maximally compensates for the increased alkali relaxation rate, alkali-hybrid SEOP requires less laser power traditional SEOP to keep the entire alkali vapor polarized throughout the pumping chamber.

5.2 Generalized Alkali Rate Equations

5.2.1 The Effect of the Alkali Nuclear Spin

The valence electron and nucleus of an alkali atom couple via the hyperfine interaction. Any collisional process that is "slow" relative to the hyperfine frequency (1 GHz $= 10^{-3}$/ps) interacts with the total (electronic+nuclear) angular momentum of the alkali atom. These types of processes include Rb-noble gas van der Waals molecular interactions [8, 9], which have a typical lifetime of 10^4 ps, and diffusion to the cell wall [10]. In the high pressure (10 atm) regime, the lifetime of Rb-^{3}He van der Waals molecules is heavily suppressed and diffusion effects are only important very close (10 μm) to the wall of the pumping chamber. Binary collisions involving alkali atoms in vapor form have a characteristic duration $|T_d|$ of 1 ps, see Sec. (5.4.5). In this case, there are no slow processes and we can make the standard argument [11] that optical pumping, spin exchange, and spin relaxation are sudden with respect to the alkali nuclear spin. Consequently, the presence of a non-zero alkali nuclear spin is relevant only in-between collisions and optical pumping cycles, during which the alkali valence electron & nucleus recouple via the hyperfine interaction. This recoupling conserves but redistributes the total atomic angular momentum between the valence electron and nuclear spins. Under these conditions, the distribution of angular momentum within the alkali vapor is characterized by a quantity called spin temperature β. Because the angular mo-

mentum is slowly leaked into and stored by the alkali nuclear spin, the observed alkali rates are slower by the ratio of the average atomic azimuthal angular momentum to the average electronic azimuthal spin, $\langle F_z \rangle / \langle S_z \rangle = 1 + \epsilon(I, P)$, where I is the nuclear spin, P is the electronic polarization, and $\epsilon(I, P)$ is known as the "paramagnetic coefficient" [1, 11]. This so-called "nuclear slowing down factor" $(1 + \epsilon(I, P))$ depends on the spin temperature and must be averaged over each alkali isotope. For the case of SEOP of ^{3}He , the nuclear slowing down factor does not effect the equilibrium alkali polarization, see howeever Sec. (5.4.4).

5.2.2 Depopulation and Repopulation Optical Pumping

In general, optical pumping [12–28] is the process of generating nonthermal equilibrium populations in the ground and excited states in a sample of atoms or molecules using polarized light. In our case, the optical pumping cycle of alkali metal atom consists of depopulation pumping into the excited state and then repopulation pumping into the ground state. We'll consider the possibility of pumping both the D1 and D2 transitions. We'll also assume that the pump beam is a statistical mixture of purely circularly polarized photons. In this case, the rate equations for $s_\pm$, the fractional population of the $m = \pm 1/2$ level of the $S_{1/2}$ ground state, are:

$$\begin{aligned}
\dot{s}_\pm &= -s_\pm \left[2R_\mp + \frac{R'_\mp}{2} + \frac{3R'_\pm}{2} \right] && \text{(depopulation)} \\
&\quad + \left(\frac{s}{2} - s_\pm \right) \Gamma_s && \text{(spin relaxation)} \\
&\quad + \frac{p_\pm \Lambda_p}{\tau_p^0} + \frac{p_\mp (1 - \Lambda_p)}{\tau_p^0} + \frac{d_\pm \Lambda_d}{\tau_d^0} + \frac{d_\mp (1 - \Lambda_d)}{\tau_d^0} + \frac{d'_\pm}{\tau_d^0} && \text{(repopulation)} \\
&\quad + p_\mp (2R_\mp) + d_\mp (R'_\mp / 2) + d'_\pm (3R'_\pm / 2) && \text{(stimulated emission)}
\end{aligned} \tag{5.10}$$

where $R_\pm$ ($R'_\pm$) is the D1 (D2) absorption/stimulated emission rate of photons carrying ± 1 unit of angular momentum, $s = s_+ + s_-$ is the total fractional population of the ground state, Γ_s is the ground state spin relaxation rate, $p_\pm$ ($d_\pm$) is the fractional population of the $m = \pm 1/2$ level of the $P_{1/2}$ ($P_{3/2}$) excited state, $d'_\pm$ ($d_\pm$) is the fractional population of the $m = \pm 3/2$ level of the $P_{3/2}$ excited state, and $\Lambda_{p,d}$ is the probability of decaying from the $m = \pm 1/2$ excited level to the $m = \pm 1/2$ ground level. The partial lifetimes of the $P_{1/2}$ & $P_{3/2}$ excited state, τ_p^0 & τ_d^0 respectively, are the given by:

$$\frac{1}{\tau_p^0} = \Gamma_q + \frac{1}{\tau_{\text{spon}}} \qquad\qquad \frac{1}{\tau_d^0} = \Gamma'_q + \frac{1}{\tau'_{\text{spon}}} \tag{5.11}$$

where Γ_q & $1/\tau_{\text{spon}}$ (Γ'_q & $1/\tau'_{\text{spon}}$) are the nonradiative quenching & spontaneous decay rates for the $P_{1/2}$ ($P_{3/2}$) excited state. Analogously, the rate equations for the fractional excited state level populations are:

$$\dot{p}_\pm = +(s_\mp - p_\pm)(2R_\pm) + \left(\frac{p}{2} - p_\pm\right)\Gamma_p - \frac{p_\pm}{\tau_p^0} + \sum_m \left[d_m \Gamma_{d,m\to p,\pm} - p_\pm \Gamma_{p,\pm\to d,m}\right] \tag{5.12}$$

$$\begin{aligned}\dot{d}_\pm = {} & +(s_\mp - d_\pm)(R'_\pm/2) - \frac{d_\pm}{\tau_d^0} + \sum_m \left[d_m \Gamma_{d,m\to d,\pm 1/2} - d_\pm \Gamma_{d\pm 1/2\to d,m}\right] \\ & + \sum_m \left[p_m \Gamma_{p,m\to d,\pm 1/2} - d_\pm \Gamma_{d,\pm 1/2\to p,m}\right]\end{aligned} \tag{5.13}$$

$$\begin{aligned}\dot{d}'_\pm = {} & +(s_\pm - d'_\pm)(3R'_\pm/2) - \frac{d'_\pm}{\tau_d^0} + \sum_m \left[d_m \Gamma_{d,m\to d,\pm 3/2} - d'_\pm \Gamma_{d\pm 3/2\to d,m}\right] \\ & + \sum_m \left[p_m \Gamma_{p,m\to d,\pm 3/2} - d'_\pm \Gamma'_{d,\pm 3/2\to p,m}\right]\end{aligned} \tag{5.14}$$

where $p = p_+ + p_-$ ($d = d_+ + d_- + d'_+ + d'_-$) is the total fractional population of the $P_{1/2}$ ($P_{3/2}$) excited state, Γ_p is the orientation desctruction rate for the $P_{1/2}$ excited state, and $\Gamma_{J,m\to J',m'}$ is the transfer rate from the (J,m) level to the (J',m') level. These equations obey the constraint $s + p + d = 1$.

It is more convenient to express these equations in the multipole representation

which allows us to greatly reduce the number of linearly independant transfer rates, see Sec. (D.1.1). At equilibrium, the total population of the ground & excited states satisfy the following three equation:

$$\begin{aligned}
\dot{s}=0 &= -sR(1-\overline{P}_\gamma P_s) - sR'\left(1+\frac{\overline{P}'_\gamma P_s}{2}\right) + \frac{p}{\tau_p^0} + \frac{d}{\tau_d^0} \\
&\quad + pR(1+\overline{P}_\gamma P_p) + \frac{dR'}{2}\left(1+\frac{Q_d}{2}+\frac{3\overline{P}'_\gamma P_d}{2}\right) \qquad (5.15)\\
\dot{p}=0 &= +sR(1-\overline{P}_\gamma P_s) - pR(1+\overline{P}_\gamma P_p) - \frac{p}{\tau_p^0} - p\Gamma_m + d\Gamma'_m \qquad (5.16)\\
\dot{d}=0 &= +sR'\left(1+\frac{\overline{P}'_\gamma P_s}{2}\right) - \frac{d}{\tau_d^0} - d\Gamma'_m + p\Gamma_m - \frac{dR'}{2}\left(1+\frac{Q_d}{2}+\frac{3\overline{P}'_\gamma P_d}{2}\right) \qquad (5.17)
\end{aligned}$$

where $R = R_+ + R_-$ ($R' = R'_+ R'_-$) is the total unpolarized D1 (D2) absorption & stimulated emission rate, $\overline{P}_\gamma = (R_+ - R_-)/R$ ($\overline{P}'_\gamma = (R'_+ - R'_-)/R'$) is the D1 (D2) cross section-weighted mean photon polarization, $P_s = (s_+ - s_-)/s$ is the ground state polarization, $P_p = (p_+ - p_-)/p$ is the $P_{1/2}$ excited state orientation, $P_d = (d'_+ + d_+/3 - d_-/3 - d'_-)/d$ is the $P_{3/2}$ excited state orientation, $Q_d = (d'_+ - d_+ - d_- + d'_-)/d$ is the $P_{3/2}$ excited state alignment, and $R_d = (d'_+ - 3d_+ + 3d_- - d'_-)/d$ is the $P_{3/2}$ excited state octopole moment. When only the $m = J$ state is populated (each state is equally populated), each of these quantities is unity (zero). The mixing rates Γ_m & Γ'_m are related to the multipole mixing rates by:

$$\Gamma_m = \sqrt{2}\Gamma^{(0\to 0)}_{1/2\to 3/2} \qquad \Gamma'_m = \frac{\Gamma^{(0)}_{3/2\to 1/2} + Q_d\Gamma^{(2\to 0)}_{3/2\to 1/2}}{\sqrt{2}} \qquad (5.18)$$

Solving these equations gives the relative fractional populations of the two excited

states:

$$\frac{p}{s} = f_p \tau_p R \left[1 - \overline{P}_\gamma P_s + g'_m \left(\frac{R'}{R} \right) \left(1 + \frac{\overline{P}'_\gamma P_s}{2} \right) \right] \tag{5.19}$$

$$\frac{d}{s} = f_d \tau_d R \left[1 - \overline{P}_\gamma P_s + \frac{1}{g_m} \left(\frac{R'}{R} \right) \left(1 + \frac{\overline{P}'_\gamma P_s}{2} \right) \right] \tag{5.20}$$

where f_p (f_d) is the probability that the atom decays from the $P_{1/2}$ ($P_{3/2}$) excited state and g_m (g'_m) is the relative mixing rate from the $P_{1/2}$ ($P_{3/2}$) excited state:

$$f_p = \left[\frac{1 - g_m}{1 - g_m g'_m} \right] \qquad f_d = g_m \left[\frac{1 - g'_m}{1 - g_m g'_m} \right] \qquad g_m = \frac{\tau_p \Gamma_m}{1 + \tau_p \Gamma_m} \qquad g'_m = \frac{\tau_d \Gamma'_m}{1 + \tau_d \Gamma'_m} \tag{5.21}$$

where $f_p + f_d = 1$ and the full lifetimes of the $P_{1/2}$ & $P_{3/2}$ excited states at equilibrium, τ_p & τ_d respectively, are the given by:

$$\frac{1}{\tau_p} = \frac{1}{\tau_p^0} + R(1 + \overline{P}_\gamma P_p) \qquad \frac{1}{\tau_d} = \frac{1}{\tau_d^0} + \frac{R'}{2} \left(1 + \frac{Q_d}{2} + \frac{3\overline{P}'_\gamma P_d}{2} \right) \tag{5.22}$$

These lifetimes differ from the partial lifetimes τ_p^0 & τ_d^0 only by terms due to stimulated emmission.

At equilibrium, the ground state polarization satifies:

$$\begin{aligned} \frac{d(sP_s)}{dt} = 0 \quad = \quad & +sR(\overline{P}_\gamma - P_s) - sR' \left(\frac{\overline{P}'_\gamma}{2} + P_s \right) - sP_s\Gamma_s \\ & + \frac{pP_p}{\tau_p^0}(2\Lambda_p - 1) + \frac{dP_d}{\tau_d^0} + \frac{3d(P_d - R_d)}{5\tau_d^0} \left[\Lambda_d - \frac{2}{3} \right] \\ & - pR(\overline{P}_\gamma + P_p) + dR' \left[\overline{P}'_\gamma \left(\frac{1 + 2Q_d}{4} \right) + \frac{3}{5} \left(P_d + \frac{R_d}{4} \right) \right] \end{aligned} \tag{5.23}$$

where we're anticipating that $\Lambda_d - 2/3 \approx 0$ and the excited state polarization mo-

ments satisfy the following coupled equations:

$$\begin{aligned}
\frac{d(pP_p)}{dt} = 0 &= +sR(\overline{P}_\gamma - P_s) - pR(\overline{P}_\gamma + P_p) - pP_p\left[\Gamma_p + \frac{1}{\tau_p^0} + \Gamma_m\right] \\
&\quad + \frac{d}{10}\left[3P_d\Gamma'_{11} + R_d\Gamma'_{31}\right] \qquad (5.24)\\
\frac{d(dP_d)}{dt} = 0 &= +sR'\left[\frac{5}{6}\overline{P}'_\gamma + \frac{2}{3}P_s\right] - dR'\left[\frac{\overline{P}'_\gamma}{3}\left(\frac{5}{4} + Q_d\right) + \frac{1}{10}\left(7P_d + \frac{R_d}{2}\right)\right] \\
&\quad - dP_d\left[\Gamma_d^{(1)} + \frac{1}{\tau_d^0} + \frac{\Gamma'_{00}}{2}\right] + pP_p\frac{\Gamma_{11}}{3} - \frac{d\Gamma'_{20}}{10}(4P_d + R_d) \qquad (5.25)\\
\frac{d(dQ_d)}{dt} = 0 &= +sR'\left[\frac{1}{2} + \overline{P}'_\gamma P_s\right] - dR'\left[\frac{3\overline{P}'_\gamma}{5}\left(P_d + \frac{R_d}{4}\right) + \left(\frac{1+2Q_d}{4}\right)\right] \\
&\quad - dQ_d\left[\Gamma_d^{(2)} + \frac{1}{\tau_d^0} + \frac{\Gamma'_{00}}{2}\right] + p\Gamma_{02} - \frac{d\Gamma'_{20}}{2} \qquad (5.26)\\
\frac{d(dR_d)}{dt} = 0 &= +sR'\left(\frac{3P_s}{2}\right) - dR'\left[\frac{3}{4}\overline{P}'_\gamma Q_d + \frac{3}{10}\left(\frac{3P_d}{2} + R_d\right)\right] \\
&\quad - dR_d\left[\Gamma_d^{(3)} + \frac{1}{\tau_d^0} + \frac{\Gamma'_{00}}{2}\right] + pP_p\Gamma_{13} - \frac{d\Gamma'_{20}}{10}(9P_d - 4R_d) \qquad (5.27)
\end{aligned}$$

where $\Gamma_d^{(k)}$ is the k-th multipole *destruction* rate and the mixing rates between the $P_{1/2}$ & $P_{3/2}$ levels differ from the multipole mixing rates only in normalization:

$$\begin{aligned}
\Gamma^{(0)}_{1/2\to3/2} &= \frac{\Gamma_m}{\sqrt{2}} \quad \Gamma^{(1)}_{1/2\to3/2} = \frac{\Gamma_{11}}{\sqrt{10}} \quad \Gamma^{(2)}_{1/2\to3/2} = \frac{\Gamma_{20}}{\sqrt{2}} \quad \Gamma^{(3)}_{1/2\to3/2} = \frac{\Gamma_{31}}{\sqrt{10}} \\
\Gamma^{(0)}_{3/2\to1/2} &= \frac{\Gamma'_{00}}{\sqrt{2}} \quad \Gamma^{(1)}_{3/2\to1/2} = \frac{\Gamma'_{11}}{\sqrt{10}} \quad \Gamma^{(2)}_{3/2\to1/2} = \frac{\Gamma'_{20}}{\sqrt{2}} \quad \Gamma^{(3)}_{3/2\to1/2} = \frac{\Gamma'_{31}}{\sqrt{10}} \qquad (5.28)
\end{aligned}$$

These can be solved to give the excited state polarization moments:

$$pP_p = \frac{sR}{\gamma_p}\left[\overline{P}_\gamma\left(1-\frac{p}{s}\right)-P_s+\frac{d}{2sR}\left(\frac{3P_d\Gamma'_{11}+R_d\Gamma'_{31}}{5}\right)\right] \tag{5.29}$$

$$dP_d = \frac{sR'}{\gamma_d^{(1)}}\left[\frac{5\overline{P}'_\gamma}{6}\left(1-\frac{d}{2s}\left[1+\frac{4Q_d}{5}\right]\right)+\frac{2P_s}{3}-\frac{d}{2s}\left[1+\frac{2\Gamma'_{20}}{R'}\right]\frac{R_d}{10}+\frac{p}{sR'}\frac{\Gamma_{11}P_p}{3}\right] \tag{5.30}$$

$$dQ_d = \frac{sR'}{\gamma_d^{(2)}}\left[\frac{1}{2}-\frac{d}{4s}+\overline{P}'_\gamma P_s-\frac{d}{2s}\frac{3\overline{P}'_\gamma}{10}(4P_d+R_d)+\frac{p}{sR'}\Gamma_{02}-\frac{d}{2sR'}\Gamma'_{20}\right] \tag{5.31}$$

$$dR_d = \frac{sR'}{\gamma_d^{(3)}}\left[\frac{3P_s}{2}-\frac{d}{2s}\frac{3}{2}\left(\overline{P}'_\gamma Q_d+\frac{3}{5}P_d\right)+\frac{p}{sR'}P_p\Gamma_{13}-\frac{d}{2sR'}\frac{9P_d\Gamma'_{20}}{5}\right] \tag{5.32}$$

where $\gamma_d^{(k)}$ is the k-th multipole *relaxation* rate given by:

$$\gamma_p = \Gamma_p+\frac{1}{\tau_p^0}+\Gamma_m+R \tag{5.33}$$

$$\gamma_d^{(1)} = \Gamma_d^{(1)}+\frac{1}{\tau_d^0}+\frac{\Gamma'_{00}}{2}+\frac{7R'}{10}+\frac{2\Gamma'_{20}}{5} \tag{5.34}$$

$$\gamma_d^{(2)} = \Gamma_d^{(2)}+\frac{1}{\tau_d^0}+\frac{\Gamma'_{00}}{2}+\frac{R'}{2} \tag{5.35}$$

$$\gamma_d^{(3)} = \Gamma_d^{(3)}+\frac{1}{\tau_d^0}+\frac{\Gamma'_{00}}{2}+\frac{3R'}{10}-\frac{2\Gamma'_{20}}{5} \tag{5.36}$$

Using these equations, we can finally solve for the ground state polarization:

$$P_s = \frac{R_1-R_2/2}{R_0+\Gamma_s} \tag{5.37}$$

where the polarized D1 & D2 optical pumping rates R_1 & R_2 are given by:

$$R_1 = 2\Lambda_1\left(1-\frac{p}{s}\right)\overline{P}_\gamma R \qquad\qquad R_1 = 2\Lambda_2\left(1-\frac{d}{2s}\right)\overline{P}'_\gamma R' \tag{5.38}$$

and the total unpolarized (D1+D2) optical pumping rate R_0 is given by:

$$R_0 = 2\Lambda_0 R+2\Lambda'_0 R' \tag{5.39}$$

and the effective branching ratios Λ_1, Λ_2, Λ_0, and Λ_0' are given by:

$$2\Lambda_1 = 2\Lambda_0 + \frac{d}{2s\tau_p^0 R}\left[\frac{2\Lambda_p - 1 - \tau_p^0 R}{\overline{P}_\gamma(1-p/s)}\right]\left[\frac{3P_d\Gamma'_{11} + R_d\Gamma'_{31}}{5\gamma_p}\right] \quad (5.40)$$

$$2\Lambda_0 = \frac{\tau_p^0(\Gamma_p + \Gamma_m) + 2\Lambda_p}{\tau_p^0(\Gamma_p + \Gamma_m + R) + 1} \quad (5.41)$$

$$2\Lambda_2 = 2\Lambda_0' - \frac{1}{\tau_d^0\gamma_d^{(1)}} + \left[\frac{d/(2s)}{\overline{P}'_\gamma\left[1 - d/(2s)\right]}\right]\Delta\Lambda \quad (5.42)$$

$$2\Lambda_0' = \frac{\tau_d^0\gamma_d^{(1)} - 2/3}{\tau_d^0\gamma_d^{(1)}} \quad (5.43)$$

and $\Delta\Lambda$ is given by:

$$\Delta\Lambda = \frac{6(P_d - R_d)}{5\tau_d^0 R'}\left[\frac{2}{3} - \Lambda_d\right] + \left[\frac{2}{3\tau_d^0\gamma_d^{(1)}} - 1\right]\overline{P}'_\gamma Q_d - \frac{6P_d}{5} + \left[1 - 3\tau_d^0\gamma_d^{(1)} + \frac{2\Gamma'_{20}}{R'}\right]\frac{R_d}{10\tau_d^0\gamma_d^{(1)}} - \frac{2p}{3d}\left[\frac{\Gamma_{11}}{\tau_d^0 R'\gamma_d^{(1)}}\right]P_p \quad (5.44)$$

Both nonradiative quenching [29] and spontaneous emission are "sudden" with respect to the electron spin (at least for alkali species lighter than Cs [30]). As a consequence, the electron spin is conserved during the decay, which implies the following values for the branching ratios: $\Lambda_p = 1/3$ and $\Lambda_d = 1 - \Lambda_p = 2/3$. If the $P_{1/2}$ orientation destruction rate is very small, the D2 to D1 optical pumping rate ratio is very small, and there is very little mixing between the $P_{1/2}$ & $P_{3/2}$ levels, then $\Lambda_1 = \Lambda_0 = \Lambda_p \approx 1/3$. This implies that a large orientation destruction rate of the $P_{1/2}$ level is beneficial, since $\Lambda_1 = \Lambda_0 \approx 1/2$ when $\tau_p\Gamma_p \gg 1$. If the D2 optical pumping rate is very small, but much larger than the D1 optical pumping rate, and there is very little mixing between the $P_{1/2}$ & $P_{3/2}$ levels, then (after some straightforward but very tedious algebra) we find $\Lambda_2 = \Lambda_0'$. This implies that there

quantity	$S_{1/2}$	$P_{1/2}$	$P_{3/2}$	**units**
$n = s, p, d$	1-7E-07	2.84E-06	4.07E-06	-
P_n	0.978	4.02E-03	8.37E-05	-
Q_d	-	-	6.93E-05	-
R_d	-	-	8.41E-05	-
Γ_q^n	-	0.529	0.393	GHz
τ_{spon}^n	-	27.7	26.2	ns
τ_n	-	1.77	2.32	ns
$\Gamma_n^{(1)}$	1.08E-06	104	472	GHz
$\Gamma_n^{(2)}$	-	-	570	GHz
$\Gamma_n^{(3)}$	-	-	469	GHz
Γ_m^n	-	2.01	1.01	GHz
Γ_{11}^n	-	-0.207	-0.104	GHz
g_m^n	-	0.781	0.702	-
f_n	-	0.485	0.515	-
abs. width	-	126	150	GHz
abs. shift	-	51.8	7.31	GHz

Table 5.1: Typical Excited State Polarization Moments and Multipole Rates. We've assumed broadband pumping of the Rb D1 transition with $R = 100$ kHz and $R'/R = 0.0011$. The rates were calculated using data from Sec. (D.4) assuming $T_{\text{pc}} = 210^{\text{o}}\text{C}$, $[^3\text{He}]_{\text{pc}} = 6.5$ amg, and $[\text{N}_2]/[^3\text{He}] = 0.01$. For a pure Rb cell, this corresponds to $[\text{Rb}] = 1.38 \times 10^{15}/\text{cm}^3$ and $1/\gamma_{\text{se}} = 3$ hrs. Under these conditions, all of the effective branching ratios are 0.500 ± 0.001.

is a buffer gas pressure (corresponding to $\tau_d^0 \gamma_d^{(1)} = 2/3$) at which the ground state polarization changes sign. Historically, finding this zero crossing was one early method used to determine the $P_{3/2}$ excited state multipole destruction rate [31].

Tab. (5.1) lists typical rates for nonradiative quenching, spontaneous emission, excited state mixing, and multipole destruction. Nonradiative quenching is almost entirely due to collisions with N_2 molecules. Excited state mixing is due to collisions with ^{3}He atoms and N_2 molecules. The ground state spin relaxation and excited state multipole destruction are dominated by collisions with ^{3}He atoms

and other alkali atoms. Starting from Eqn. (5.19), we've made the tacit assumption that the absorption/stimulated emission rate is much smaller than the spontaneous decay and nonradiative quenching rates, $R \ll 1/\tau_{\text{spon}} \ll \Gamma_q$. This is reasonable since it would require about 5 & 65 kW of laser power to equal the spontaneous decay & quenching rates, under our conditions. Furthermore, the excited state multipole destruction rates are much larger than the excited state decay rates, $\tau^0_{p,d}\Gamma_{p,d} \gg 1$. This implies that the excited state polarization moments are all nearly zero, $P_p, P_d, Q_d, R_d < 0.01$, and that all four effective branching ratios are nearly $1/2$, $2\Lambda_1 = 2\Lambda_0 = 2\Lambda_2 = 2\Lambda'_0 = 1$.

5.2.3 Two Species Rate Equations

Using the results of the previous, the polarization rate equation for traditional SEOP with Rb is written as:

$$\frac{d[1+\bar{\epsilon}(\beta)]P_{\text{Rb}}}{dt} = +(R_1 - R_2/2) - R_0 P_{\text{Rb}} - \Gamma_{\text{Rb}} P_{\text{Rb}} \tag{5.45}$$

where we've hidden the explicit position dependence for the sake of clarity, $1+\bar{\epsilon}$ is the isotope averaged nuclear slowing down factor discussed in Sec. (5.2.1), $R_{1,2}$ & R_0 are the polarized & unpolarized Rb optical pumping rates, and the Rb spin relaxation rate is written as:

$$\Gamma_{\text{Rb}} = k_{\text{Rb}}[\text{Rb}] + k_{\text{He}}[^3\text{He}] + k_{\text{N}_2}[\text{N}_2] + k_{\text{se}}[^3\text{He}]\left(1 - \frac{P_{\text{He}}}{P_{\text{Rb}}}\right) \tag{5.46}$$

where k_{Rb} is the Rb-Rb spin relaxation rate constant, k_{He} is the Rb-He spin relaxation rate constant, k_{N_2} is the Rb-N_2 spin relaxation rate constant, and the last term

reminds us that spin exchange to ^{3}He is a relaxation process only when the polarizations are unequal.

In the case of alkali-hybrid SEOP, we have a pair of coupled differential equations that include terms for Rb-K spin relaxation and spin exchange collisions:

$$\begin{aligned}\frac{d[1+\bar{\epsilon}_{\mathrm{Rb}}(\beta_{\mathrm{Rb}})]P_{\mathrm{Rb}}}{dt} &= +(R_1 - R_2/2) - R_0 P_{\mathrm{Rb}} - \Gamma_{\mathrm{Rb}} P_{\mathrm{Rb}} - k_{\mathrm{K}}[\mathrm{K}]P_{\mathrm{Rb}} + A_{\mathrm{se}}[\mathrm{K}](P_{\mathrm{K}} - P_{\mathrm{Rb}}) \\ \frac{d[1+\bar{\epsilon}_{\mathrm{K}}(\beta_{\mathrm{K}})]P_{\mathrm{K}}}{dt} &= +(K_1 - K_2/2) - K_0 P_{\mathrm{K}} - \Gamma_{\mathrm{K}} P_{\mathrm{K}} - k'_{\mathrm{Rb}}[\mathrm{Rb}]P_{\mathrm{K}} + A_{\mathrm{se}}[\mathrm{Rb}](P_{\mathrm{Rb}} - P_{\mathrm{K}})\end{aligned} \tag{5.47}$$

where k_{K} is the Rb spin relaxation rate constant due to K, A_{se} is the Rb-K spin exchange rate constant, k'_{Rb} is the K spin relaxation rate constant due to Rb, $K_{1,2}$ & K_0 are the polarized & unpolarized K optical pumping rates, and the K spin relaxation rate is given by:

$$\Gamma_{\mathrm{K}} = k'_{\mathrm{K}}[\mathrm{K}] + k'_{\mathrm{He}}[^3\mathrm{He}] + k'_{\mathrm{N_2}}[\mathrm{N_2}] + k'_{\mathrm{se}}[^3\mathrm{He}]\left(1 - \frac{P_{\mathrm{He}}}{P_{\mathrm{K}}}\right) \tag{5.48}$$

where k'_{K} is the K-K spin relaxation rate constant, k'_{He} is the K-He spin relaxation rate constant, $k'_{\mathrm{N_2}}$ is the K-N_2 spin relaxation rate constant, and k'_{se} is the K-He spin exchange rate constant. Solving these coupled equations for the equilibrium alkali polarizations gives:

$$P_{\mathrm{Rb}} = \frac{R_1 - R_2/2 + \eta_{\mathrm{K}} D\left[K_1 - K_2/2\right]}{R_0 + \Gamma_{\mathrm{Rb}} + k_{\mathrm{K}}[\mathrm{K}] + \eta_{\mathrm{K}} D\left\{K_0 + \Gamma_{\mathrm{K}} + k'_{\mathrm{Rb}}[\mathrm{Rb}]\right\}} \tag{5.49}$$

$$P_{\mathrm{K}} = \frac{K_1 - K_2/2 + (\eta_{\mathrm{Rb}}/D)\left[R_1 - R_2/2\right]}{K_0 + \Gamma_{\mathrm{K}} + k'_{\mathrm{Rb}}[\mathrm{Rb}] + (\eta_{\mathrm{Rb}}/D)\left\{R_0 + \Gamma_{\mathrm{Rb}} + k_{\mathrm{K}}[\mathrm{K}]\right\}} \tag{5.50}$$

where $D = [\mathrm{K}]/[\mathrm{Rb}]$ is the hybrid ratio and η_{Rb} (η_{K}) is the relative alkali spin ex-

change rate from K to Rb (Rb to K) given by:

$$\eta_{\mathrm{K}} = \frac{A_{\mathrm{se}}[\mathrm{Rb}]}{A_{\mathrm{se}}[\mathrm{Rb}] + K_0 + \Gamma_{\mathrm{K}} + k'_{\mathrm{Rb}}[\mathrm{Rb}]} \qquad \eta_{\mathrm{Rb}} = \frac{A_{\mathrm{se}}[\mathrm{K}]}{A_{\mathrm{se}}[\mathrm{K}] + R_0 + \Gamma_{\mathrm{Rb}} + k_{\mathrm{K}}[\mathrm{K}]} \tag{5.51}$$

In general there are three different regimes for the alkali polarizations depending on the relative size of the alkali spin exchange rates compared to the optical pumping rates. When the relative alkali spin exchange rates are very low, $\eta_{\mathrm{Rb}}, \eta_{\mathrm{K}} \ll 1$, the polarizations are:

$$P_{\mathrm{Rb}} = \frac{R_1 - R_2/2}{R_0 + \Gamma_{\mathrm{Rb}} + k_{\mathrm{K}}[\mathrm{K}]} \qquad P_{\mathrm{K}} = \frac{K_1 - K_2/2}{K_0 + \Gamma_{\mathrm{K}} + k'_{\mathrm{Rb}}[\mathrm{Rb}]} \tag{5.52}$$

Note that for this case, in general, $P_{\mathrm{Rb}} \neq P_{\mathrm{K}}$. When the relative alkali spin exchange rates are very high, $\eta_{\mathrm{Rb}}, \eta_{\mathrm{K}} \approx 1$, the polarizations are the same:

$$P_{\mathrm{Rb}} = P_{\mathrm{K}} = \frac{R_1 - R_2/2 + D\left[K_1 - K_2/2\right]}{R_0 + \Gamma_{\mathrm{Rb}} + D\left\{K_0 + \Gamma_{\mathrm{K}} + 2k_{\mathrm{A}}[\mathrm{Rb}]\right\}} \tag{5.53}$$

where $k_{\mathrm{A}} = (k_{\mathrm{K}} + k'_{\mathrm{Rb}})/2$ is the mean Rb-K spin relaxation rate constant. Finally, the last regimes are a mixture of the previous two: $\eta_{\mathrm{Rb}} \ll 1$ & $\eta_{\mathrm{K}} \approx 1$ or $\eta_{\mathrm{Rb}} \approx 1$ & $\eta_{\mathrm{K}} \ll 1$.

Under our typical conditions, we're directly pumping only the Rb D1 transition, which implies $A_{\mathrm{se}}[\mathrm{K}] \gtrsim R_0 \gtrsim R_1 \gg R_2 > K_0 \gtrsim K_1 \approx K_2$. and it is more useful to write the K polarizations as:

$$P_{\mathrm{K}} = \eta_{\mathrm{K}} \left[P_{\mathrm{Rb}} + \left(\frac{K_1 - K_2/2}{A_{\mathrm{se}}[\mathrm{Rb}]} \right) \right] \tag{5.54}$$

To insure that K is polarized mainly due to spin exchange collisions with Rb and

not off-resonant optical pumping, the Rb density must be sufficiently high [Rb] $\gg$ $K_0/A_{se} \approx 0.4 \times 10^{11}$ cm^{-3}/(75 W). Furthermore, to insure that the polarization ratio P_K/P_{Rb} is nearly unity, the Rb density must be sufficiently high [Rb] $\gg \Gamma_K/A_{se} \approx$ 10^{12} cm^{-3}/(1 kHz). To maximize the alkali polarization, the main source of polarization must be the on-resonant optical pumping of Rb and not the off-resonant optical pumping of K. This condition can be satisfied by a sufficiently small K to Rb vapor ratio $D \ll R_0/(\eta_K K_0)$. To summarize, for a fixed spin exchange rate to ^{3}He , γ_{se}, the hybrid ratio D must be sufficiently small to insure $\eta_K \approx 1$ and to satisfy $D \ll R_0/K_0 \approx 10^3$ (10^4) assuming broadband (narrowband) light and $T_d = 0$, see Sec. (5.4.5).

5.3 Laser Light for Optical Pumping

5.3.1 Spatial Characteristics

The beam from a fiber-coupled laser diode array typically used for optical pumping can be modeled as a Gaussian beam.Ignoring aberrations due the shape and orientation of the beam shaping & polarizing optics, the intensity profile is given by the fundamental mode by:

$$I(r,z) = \frac{2P_0}{\pi w^2(z)} \exp\left[-\frac{2r^2}{w^2(z)}\right] \tag{5.55}$$

where P_0 is the total power, r is the radial distance from the center of the beam, and the beam radius $w(z)$ at some location z is given by:

$$w(z) = w_0\sqrt{1 + \psi_0^2\left(\frac{z - z_0}{w_0}\right)^2} \tag{5.56}$$

where w_0 is the beam waist, z_0 is the location of the beam waist, and ψ_0 is the far field divergence of the beam. These three parameters, w_0, z_0, ψ_0, (i.e. Gaussian beam parameters) obey the constraint $w_0\psi_0 = M^2\lambda/\pi$, where λ is the wavelength of the light. The beam quality factor M^2 is unity for an ideal Gaussian beam and around 300 for the types of beam we use for optical pumping. Once the Gaussian beam parameters have been empirically determined, the size of the beam can be calculated at any location.

The Gaussian beam parameters also determine the divergence $\psi(z) = \partial w/\partial z$ of the beam. This quantity describes the beam's "angular spread." In other words, the angle θ_r formed by the propagation vector of a photon located at distance r from the center of beam is given by:

$$\tan(\theta_r) = \left[\frac{r}{w(z)}\right]\psi(z) = \frac{r}{w(z)}\frac{\partial w(z)}{\partial z} = \psi_0\left(\frac{r}{w}\right)\left[1 + \left(\frac{w_0}{\psi_0(z - z_0)}\right)^2\right]^{-1/2} \tag{5.57}$$

where θ_r is measured relative to the propagation vector at the center of the beam. Far from beam waist, $z \gg z_0$, and for small divergences, this angle is $\theta_r \approx \psi_0(r/w)$.

5.3.2 Forward Propagation

The photon flux $\Phi(\vec{r}, \nu)$ is defined as the number of photons per unit area per unit time per unit frequency interval. In general, it has a complicated shape and varies significantly as a function of the depth into the cell z and the laser frequency ν. At the front of the cell, however, $\Phi(z = 0, r, \nu)$ can be written simply as a product of a spatial profile, assuming a Gaussian beam, and a frequency spectrum. For the laser diode arrays typically used for optical pumping, the spectrum can be reasonably

represented by unit normalized Gaussian distribution:

$$\Phi(0,r,\nu) = \left[\frac{I(r,z_{\text{cell}})}{h\nu}\right] G(\nu) = \left[\frac{I(r,z_{\text{cell}})}{h\nu}\right] \left[\frac{2\sqrt{\log(2)/\pi}}{\texttt{FWHM}} \exp\left(-4\log(2)\frac{\left(\nu-\nu_\gamma\right)^2}{\texttt{FWHM}^2}\right)\right] \tag{5.58}$$

where z_{cell} is the location of the front of the cell relative to the beam waist location, h is Planck's constant, FWHM is the full width half maximum of the distribution, and ν_γ is the center of the distribution. This is a very good model when the diode is "fresh," but after it has aged the spectrum becomes broadened and distorted. A "broadband" laser has a FWHM that is much larger than the absorption linewidth, while a "narrowband" laser has a FWHM that is about equal to the absorption linewidth. Under typical operating conditions, the Rb D1 pressure broadened absorption linewidth is about 120 GHz (0.25 nm), while broadband & narrowband lasers typically have FWHM of 950 GHz (2 nm) & 95 GHz (0.2 nm) respectively.

As the light propagates through the alkali vapor, it polarizes layer after layer of alkali atoms until the light is fully absorbs or exits the cell [32]. A "hole is burnt" into the part of the laser spectrum that is near resonance, which modifies the shape of the spectrum significantly. Using the results of Sec. (E.6.4) and dropping the negligible field dependant terms, the frequency dependent attenuation of the beam is given by:

$$\begin{aligned}\left[\frac{1}{\Phi}\frac{d\Phi}{dz}\right]_{\mathcal{R},\mathcal{L}} &= \sum_a \left\{p_a\left(1 \pm P_p^a\cos(\theta)\right) - s_a\left(1 \mp P_s^a\cos(\theta)\right)\right\}\sigma_1^a[\mathrm{A}]_a \\ &\quad + \left\{\frac{d_a}{2}\left(1 + \frac{Q_d}{2} \pm \frac{3}{2}P_d\cos(\theta)\right) - s_a\left(1 \pm \frac{P_s^a\cos(\theta)}{2}\right)\right\}\sigma_2^a[\mathrm{A}]_a \end{aligned} \tag{5.59}$$

where a labels the alkali metal, $\sigma_{1(2)}^a$ is the D1 (D2) absorption cross section, the second (first) term on each line is due to absorption (stimulated emission), the first (second) line is due to the D1 (D2) transition, the upper (lower) sign is taken for $\mathcal{R}$

($\mathcal{L}$) right (left) handed photons (helicity convention, see Sec. (4.5.3)), and the flux of right & left handed photons is given by:

$$\Phi_{\mathcal{R}}(\vec{r},\nu) = \Phi(\vec{r},\nu)\left[\frac{1+P_\gamma(\vec{r},\nu)}{2}\right] \qquad \Phi_{\mathcal{L}}(\vec{r},\nu) = \Phi(\vec{r},\nu)\left[\frac{1-P_\gamma(\vec{r},\nu)}{2}\right] \quad (5.60)$$

where P_γ is the polarization of the light. The attenuation depends on the "skew" angle θ between the polarization vector of the alkali atoms (i.e. the magnetic holding field direction) and the propagation direction of the photons (i.e. the k-vector). For a Gaussian beam with divergence ψ and beam radius w, the skew angle at a radial distance r from the center of the beam and at an azimuthal angle ϕ measured relative to the propagation axis of the beam center is given by:

$$\cos(\theta) = \cos(\theta_0)\cos(\theta_r) + \sin(\theta_0)\sin(\theta_r)\cos(\phi) = \frac{\cos(\theta_0) + (\psi r/w)\sin(\theta_0)\cos(\phi)}{\sqrt{1+(\psi r/w)^2}} \quad (5.61)$$

where θ_0 is the angle between the holding field and the k-vector at the center of the beam. The propagation equations for $\Phi_{\mathcal{R}}$ & $\Phi_{\mathcal{L}}$ can be written in terms of the total flux Φ and polarization P_γ:

$$\begin{aligned}
\frac{1}{\Phi}\frac{d\Phi}{dz} &= \sum_a \left\{ p_a\left(1+P_\gamma P_p^a\cos(\theta)\right) - s_a\left(1-P_\gamma P_s^a\cos(\theta)\right)\right\}\sigma_1^a[\mathrm{A}]_a \\
&\quad + \left\{\frac{d_a}{2}\left(1+\frac{Q_d}{2}+\frac{3}{2}P_\gamma P_d\cos(\theta)\right) - s_a\left(1+P_\gamma\frac{P_s^a\cos(\theta)}{2}\right)\right\}\sigma_2^a[\mathrm{A}]_a \quad (5.62)\\
\frac{dP_\gamma}{dz} &= \frac{1}{\Phi}\left[\frac{d\Phi_{\mathcal{R}}}{dz} - \frac{d\Phi_{\mathcal{L}}}{dz}\right] - \frac{P_\gamma}{\Phi}\frac{d\Phi}{dz} \\
&= \left(1-P_\gamma^2\right)\cos(\theta)\sum_a\left\{\left[p_a P_p^a + s_a P_s^a\right]\sigma_1^a + \left[\frac{3d_a P_d^a}{4} - \frac{s_a P_s^a}{2}\right]\sigma_2^a\right\}[\mathrm{A}]_a \quad (5.63)
\end{aligned}$$

This implies that, as the alkali atoms become polarized, they (1) "purify" the degree of circular polarization of the laser beam as it propagtes through the polarized

alkali vapor and (2) the alkali atoms become nearly transparent to the beam.

5.4 Limits to the Alkali Polarization

5.4.1 Sources of Imperfection: Introduction

Stimulated Emission

An imperfection in optical pumping could be described as a mechanism that reduces the effective polarization of the pump light. The two types that we'll discuss in this section either directly reduce the pump light polarization or compete against the pump light. An example of the first type is the nonzero population of the excited states which reduces the effective light polarization from $\overline{P}_\gamma$ to $\overline{P}_\gamma(1 - p/s)$.

Skew Pumping

Another example of this type is referred to as "skew pumping" [33], which is due to a nonzero angle θ between the propagation vector of the light and the magnetic field that defines the quantization axis of the atoms. This effect can be accounted for by simply replacing $\overline{P}_\gamma$ with $\overline{P}_\gamma \cos(\theta)$, see Sec. (E.6.3).

Off-resonant Absorption

For the second type of mechanism, we can write the ground state polarization as (assuming $2\Lambda(1 - p/s) = 1$ for simplicity):

$$P_s = \frac{\overline{P}_\gamma R + P_x \Gamma_x}{R + \Gamma_x + \Gamma_s} \approx \overline{P}_\gamma \left[1 - \left(1 - \frac{P_x}{\overline{P}_\gamma}\right) \frac{\Gamma_x}{R} - \frac{\Gamma_s}{R} + \cdots\right] \tag{5.64}$$

where P_x and Γ_x are the polarization and rate of the competing mechanism. For sufficiently high optical pumping rates, $R \gg \Gamma_x + \Gamma_s$, the effect of the competing mechanism can be made arbitrarily small. However, if the competing mechanism depends on the laser intensity or the optical pumping rate and $P_x < P_\gamma$, then it provides a fundamental limit to the ground state alkali polarization [7]. Off resonant pumping of the D2 transition is an example of this type of mechanism.

5.4.2 Excitation Energy Transfer Collisions

The rates Γ_m & Γ'_m in Eqns. (5.16) & (5.17) represent collisions of the form:

$$\mathrm{Rb}(P_{1/2}) + X \leftrightarrow \mathrm{Rb}(P_{3/2}) + X + \Delta E \tag{5.65}$$

where ΔE is the energy change during the collision and X could be a Rb atom, a ^{3}He atom, or a N_2 molecule [34]. These collisions are generally referred to as excitation energy transfer collisioins. When the population of the P excited states of alkali atoms are being redistributed, these collisions are also refered to fine structure mixing collisions. If the collision partner is another Rb atom, then these collisions may represent another ground state relaxation mechanism.

There are two scenarios that could describe the collision. In the first, the excited atom simply changes energy and enters a different excited state. Since the collision is electrostatic in origin, the spin state of the ground state alkali atom is not expected to change. In the second scenario, the excited atom and ground state atom can "swap" states. Since the mean electronic spin polarization in the excited state is essentially zero, the net change in the ground state polarization is towards zero. To provide an upper limit for the ground state relaxation rate, we'll assume

that every collision proceeds as the second scenario, which gives:

$$\Gamma^a_{\text{EET}} = \sum_{b,J,J'} \sigma^{b\to a}_{J\to J'} v_b p_{b,J} [\text{A}]_b \tag{5.66}$$

where J (J') labels the initial (final) excited state, a (b) labels the initial (final) excited alkali species, $p_{b,J}$ is the relative population of alkali atoms in the excited state, v_b is the mean relative thermal velocity between the alkali atoms, and $\sigma^{b\to a}_{J\to J'}$ is the cross section of transfer for the process:

$$B(P_J) + A(S_{1/2}) \leftrightarrow B(S_{1/2}) + A(P_{J'}) \tag{5.67}$$

In hybrid cells, A & B could be Rb & Rb, K & K, Rb & K, and K & Rb, see Sec. (D.4.3).

It has been shown [35–37] that the cross section for this process roughly scales as $1/(\Delta E)^n$ where ΔE is the energy difference between the intial & final excited state energies. For this reason, the largest cross sections are expected for Na atoms for $P_{1/2} \leftrightarrow P_{3/2}$ collisions between similar atoms, $P_k \leftrightarrow P_k$ collisions between similar alkali atoms, and K & Rb for collisions between dissimilar atoms. We'll note that $P_k \leftrightarrow P_k$ collisions between similar atoms are usually indistinuishable from multipole destruction collisions with similar alkali atoms. We do not have to limit ourselves to collisions involving only the P states. As was observed by [38], cells lacking N_2 emit a "purple glow." This is attributable to the process $\text{Rb}(5P_J) + \text{Rb}(5P_{J'}) \to \text{Rb}(6P_{J'''}) + \text{Rb}(S_{1/2}) \to 2\text{Rb}(S_{1/2}) + \gamma(\lambda = 421\text{ nm})$. A more recent study [39] observed no less than 8 additional peaks in the fluoresecene spectra attributable to transitions between higher excited states to the $5P$ and $5S$ levels. The addition of 50 torr of N_2 reduced the intensity of fluoresence by a factor of

two, which implies very large cross sections ($> 10^6$ Å^2) for collisions between two excited atoms.

If we take the cross section for $P_J \leftrightarrow P_J$ collisions between Rb atoms to be equal to the Rb-Rb multipole destruction scross section (10^4 Å^2), then, using the results in Tab. (5.1), we estimate an upper limit of $\Gamma_{\mathrm{EET}} \leq 0.005R$. Although the cross section for this process is very large, the sensitivity of the ground state polarization to this mechanism is suppressed by the very low population of the excited state.

Polarization Transfer in Fine Structure Mixing Collisions

It has been shown that orientation and alignment can be transfered between $P_{1/2}$ the $P_{3/2}$ levels during mixing collisions, see for example [40]. Both the magnitude and sign of the polarization transferred is sensitive to the magnitude of the magnetic field and the presence of nonzero nuclear spin. Polarization transfer can cause an imperfection in optical pumping to the extent that it causes an imbalanace between the effective branching ratios. To lowest order, the effect on the alkali polarization can be given by:

$$\frac{2\Lambda_1 R - 2\Lambda_2 R'/2}{2\Lambda_0 R + 2\Lambda_0' R'} \approx 1 - \left(\frac{\Lambda_1}{\Lambda_0} - 1\right) - \frac{R'}{R}\left[\frac{3}{2} + \frac{\Lambda_2 + 2\Lambda_0' - 3\Lambda_0}{2\Lambda_0}\right] \tag{5.68}$$

When $\Lambda_1 < \Lambda_0$, the effective polarization of the light is reduced. When $\Lambda_2 + 2\Lambda_0' > 3\Lambda_0$, the effect of off-resonant absorption is enhanced. Under our conditions, the multipole destruction rates are far greater than the mixing rates which insures that the excited state polarization moments are nearly zero. This greatly suppresses the sensitivity of the ground state polarization to the polarization transfer in the excited state.

5.4.3 Radiation Trapping

"Radiation trapping" [41–45] occurs when the fluorescence photons undergo several cycles of reabsorption and emission by the atomic vapor before exiting the cell. The unpolarized optical thickness of an alkali atom for wavelengths near the Dn transitions can be estimated by:

$$\frac{1}{\sigma_n(\nu)[\mathrm{A}]} = (2.13\ \mathrm{mm}) \left[1 + \left(\frac{2\Delta_n}{\Gamma_n}\right)^2\right] \left(\frac{1}{3f_n}\right) \left(\frac{\Gamma_n}{120\ \mathrm{GHz}}\right) \left(\frac{10^{14}/\mathrm{cm}^3}{[\mathrm{A}]}\right) \tag{5.69}$$

where Δ_n is detuning from resonance, Γ_n is the pressure broadened width, f_n is the oscillator strength, and [A] is the alkali density. Because the pumping chamber radius is several orders of magnitude larger than the unpolarized optical thickness, radiation trapping could potentially limit the alkali polarization. Although this situation is greatly mitigated by nonradiative quenching collisions with N_2 molecules, a few percent of decays still occur via spontaneous emission.

The flux element of fluorescence photons carrying $q = 0, \pm 1$ units of angular momentum from the Dn transition at some point $\vec{r}$ (relative to the center of the cell) in the cell from a volume element located a displacement of $\vec{u}$ (relative to $\vec{r}$) is given by:

$$d\Phi_f^{q,n} = \sum_k \left[\frac{\sigma_n(\nu)}{\int \sigma_n(\nu)\, d\nu}\right] \frac{1}{\tau^n_{\mathrm{spon}}} \Lambda_k^q p_k^n(\vec{u}+\vec{r})[\mathrm{A}] \frac{f_q(\theta)}{4\pi u^2} T_q(\nu, \vec{u}, \vec{r}) H(R_{\mathrm{pc}} - |\vec{r}+\vec{u}|)\, d^3u \tag{5.70}$$

where we've summed over all the excited states k with population p_k^n, Λ_k^q is the branching ratio, [A] is the alkali density, $H(x)$ is the Heaviside step-function defined such that it is 1 (0) when $\vec{r}+\vec{u}$ points to a location inside (outside) the cell,

R_{pc} is the pumping chamber radius, f_q is an angular factor given by [46]:

$$f_{\pm 1} = \frac{1+\cos^2(\theta)}{4} \qquad f_0 = \frac{\sin^2(\theta)}{2} \tag{5.71}$$

and T_q is the probability of transmission given by:

$$T_q(\nu, \vec{u}, \vec{r}) = \exp\left[-\sum_n \int_0^1 \sigma_n(\nu)[\mathrm{A}]\left(1 - q|\cos(\theta)|c_n P_{\mathrm{A}}(x\vec{u}+\vec{r})\right)\, dx\right] \tag{5.72}$$

where P_{A} is the position dependent alkali polarization and $c_1 = 1$ ($c_2 = -1/2$) for D1 (D2) transitions.

Far from the wall of the pumping chamber, the transmission function can be approximated by a step function that is nonzero only within a small region near $\vec{r}$ of radius $(\sigma_n[\mathrm{A}](1 - qc_n|\cos(\theta))|P_{\mathrm{A}}(\vec{r}))$. Making this approximation, we find:

$$d\Phi_f^{q,n} = \sum_k \frac{\Lambda_k^q p_k^n(\vec{r}) f_q(\theta)\sin(\theta)}{\tau_{\mathrm{spon}}^n\left[1 - qc_n|\cos(\theta)|P_{\mathrm{A}}(\vec{r})\right]\left[\int \sigma_n(\nu)\, d\nu\right]} d\theta \tag{5.73}$$

Using this flux element, we can calculate the unpolarized & polarized D1 optical pumping rates due to the reabsorption of fluorescence photons using:

$$P_F F = \int |\cos(\theta)| d\left[\Phi_f^{+1,1} - \Phi_f^{-1,1}\right]\int \sigma_1\, d\nu \qquad F = \int d\left[\Phi_f^{+1,1} + \Phi_f^{0,1} + \Phi_f^{-1,1}\right]\int \sigma_1\, d\nu \tag{5.74}$$

where P_F is the polarization of the fluorescence photons. The D2 optical pumping rates can be calculated in a similar fashion. Assuming that $P_p = P_d = Q_d = R_d = 0$, setting $\cos(\theta) = 1$ in the denominator, and using Eqns. (5.19) & (5.20), we find that

the unpolarized D1 and D2 optical pumping rates are given by:

$$\begin{aligned}\frac{F}{R} &= f_{\rm rad} f_p \left(\frac{1}{3}\right)\left[\frac{1-P_s^2/3}{1-P_s^2}\right]\left[1-\overline{P}_\gamma P_s + g'_m \frac{R'}{R}\left(1+\frac{\overline{P}'_\gamma P_s}{2}\right)\right] \\ \frac{F'}{R} &= f'_{\rm rad} f_d \left(\frac{25}{96}\right)\left[\frac{1-8P_s^2/75}{1-P_s^2/4}\right]\left[1-\overline{P}_\gamma P_s + \frac{1}{g_m}\frac{R'}{R}\left(1+\frac{\overline{P}'_\gamma P_s}{2}\right)\right]\end{aligned} \tag{5.75}$$

where the fraction of decays, $f_{\rm rad}$ & $f'_{\rm rad}$, from the $P_{1/2}$ & $P_{3/2}$ excited states that are radiative are given by (ignoring stimulated emission):

$$f_{\rm rad} = \frac{\tau_p^0}{\tau_{\rm spon}} = \frac{1}{1+\tau_{\rm spon}\Gamma_q} \qquad f'_{\rm rad} = \frac{\tau_d^0}{\tau'_{\rm spon}} = \frac{1}{1+\tau'_{\rm spon}\Gamma'_q} \tag{5.76}$$

and the polarizations of the D1 & D2 fluorescence photons are given by:

$$P_F = \frac{4}{15}\left[\frac{P_s}{1-P_s^2/3}\right] \qquad P'_F = -\frac{64}{375}\left[\frac{P_s}{1-8P_s^2/75}\right] \tag{5.77}$$

The sign of these polarizations reflect the fact that the alkali vapor is relatively more transparent to D1 (D2) photons that have the same (opposite) polarization as the alkali atoms. The numerical factors are mainly due to the integral over θ and, given the crudeness of our approximation for T_q, they should not be taken too literally. Finally, it is important to note that polarization of the fluoresence that is reabsorbed by the alkali atoms is very geometry dependant [15]. Our calculation assumed a spherical pumping chamber. On the other hand, the polarization of the fluoresence inside a long, thin cylindrical pumping chamber with its axis oriented parallel (perpendicular) to the holding field is expected to be larger (smaller) due to the angular factors given by Eqn. (5.71).

5.4.4 Excited State Hyperfine Coupling

Introduction

Thus far, we've assumed that the alkali nuclear spin has no effect on the ground state electronic polarization. If the alkali nuclear spin did couple to something besides the alkali valence electron, then this coupling would provide a pathway for the alkali electron polarization to "leak out" of the atom. If this occurred while the atom was in the ground state, then this mechanism would only contribute to Γ_s. However, if a leak through the nuclear spin occurred while the atom was in an excited P state, then the effective relaxation rate due to this mechanism would have to be proportional to the optical pumping rate R.

As discussed previously, the excited state orientation is very quickly lost in collisions with the buffer gas. In this case, the angular momentum stored by the nuclear spin can leak out through hyperfine interactions with the disoriented electron itself [47]. It is usually assumed [1, 11, 48] that processes that occur during the optical pumping cycle are "sudden" with respect to the alkali nucleus. This implies that the angular momentum stored by the alkali nuclear spin is fully conserved throughout the optical pumping cycle. Bhaskar et al. [49] have considered the more general case when only a "fraction ϵ_n of the nuclear spin is conserved" during the optical pumping cycle. Following their reasoning, the time rate of change in the mean azimuthal angular momentum of the ground state, $\langle F_z \rangle = \langle I_z \rangle + \langle S_z \rangle$,

due only to depopulation & repopulation pumping can be written as:

$$\begin{aligned}\frac{d\langle F_z\rangle}{dt} &= -R\langle I_z\rangle + R\left(\frac{s_z}{2}\right) + R\mathrm{Tr}\left(\frac{\rho F_z \vec{s}\cdot\vec{\Theta}}{2}\right) - R\langle S_z\rangle \qquad \text{(depopulation)} \\ &\quad + R\langle I_z\rangle \epsilon_n - R\mathrm{Tr}\left(\frac{\rho F_z \vec{s}\cdot\vec{\Theta}}{2}\right) \qquad \text{(repopulation)} \\ &= R\left(\frac{s_z}{2} - \langle S_z\rangle\right) + R\langle I_z\rangle(\epsilon_n - 1) = R\left(\frac{s_z}{2} - \langle S_z\rangle\right) + R\langle \Delta I_z\rangle \qquad (5.78)\end{aligned}$$

where $\langle I_z\rangle$ & $\langle S_z\rangle$ are the mean azimuthal nuclear & electronic spins, s_z is z component of the mean photon polarization vector $\vec{s}$, $\rho = \varphi + \vec{S}\cdot\vec{\Theta}$ is the density matrix for the ground state, $\vec{S}$ is the electron spin vector, and φ & $\vec{\Theta}$ are the "purely nuclear operators" defined in [11]. Our goal is to estimate the change in the nuclear spin $\langle \Delta I_z\rangle$ due to the excited state hyperfine coupling.

Probability of a Spin Flip

Once excited to the $P_{1/2}$ state, the alkali atom undergoes an average of $n = \tau\Gamma_p$ disorienting collisions before decaying to the ground state $(1/\tau_p^0)$ or transfering collisionally to the $P_{3/2}$ excited state (Γ_m), where $\tau = \tau_p^0/(1 + \tau_p^0\Gamma_m)$ is the mean time the atom spends in the excited state. After a few collisions, the orientation comes to equilibrium and is nearly zero, see Tab. (5.1). Immediately after a disorienting collision, the state of the atomic angular momentum can be written as the uncoupled product $|\psi(0)\rangle = |\pm\rangle\,|m\rangle$, where m $(\pm)$ labels the nuclear spin (electron angular momentum) state. During the short time between collisions, the nucleus and electron start to recouple and, in the mixed hyperfine coupled basis labeled by

$|F_\pm, m_F\rangle$, see Sec. (E.3.4), the atomic state evolves as:

$$|\psi(t)\rangle = (a_1 b_1 - a_2 b_2)\,|F_+, m \pm 1/2\rangle\, e^{-i\omega_+ t} \mp (a_1 b_2 + a_2 b_1)\,|F_-, m \pm 1/2\rangle\, e^{-i\omega_- t} \quad (5.79)$$

where b_1 & b_2 are the Clebsch-Gordon coefficients given by Eqns. (E.215) & (E.216), a_1 & a_2 are magnetic field dependant hyperfine mixing coefficients given by Eqns. (E.212) & (E.213), and $\omega_\pm = E_\pm/\hbar$ are the hyperfine precession frequecies corresponding to the energies $E_\pm$ given by Eqn. (E.197). At low fields, the probability of a spin flip at some time t since the last collision is given by:

$$P^{\pm}_{\text{flip}}(t) = |\langle \mp, m \pm 1 \mid \psi(t)\rangle|^2 = \frac{2\left(I(I+1) - m^2\right) \mp 2m}{[I]^2}\,[1 \mp \upsilon x + \cdots]\,[1 - \cos(\omega_{\text{hfs}}(x)t)] \quad (5.80)$$

where I is the nuclear spin, $J = 1/2$ is the total angular momentum of the electron in the $P_{1/2}$ excited state, $x = B_0/B_{\text{hfs}}$ is the Breit-Rabi parameter, B_0 is the magnitude of the holding field, B_{hfs} is the field at which the strength of Zeeman interaction equals the strength of the hyperfine coupling, see Sec. (E.3.3) and Tab. (A.6), $\upsilon = 2(m \pm 1/2)/[I]$, $[I] = 2I + 1$, and $\omega_{\text{hfs}}(x)$ is the hyperfine splitting between the F_+ & $F_+ - 1$ hyperfine levels given by:

$$\omega_{\text{hfs}}(x) = 2\pi F \left[A + \frac{3B}{4IJ}\right](1 + \upsilon x + \cdots) \quad (5.81)$$

where A & B are the hyperfine structure constants for the excited state, see Tab. (A.6). For sufficiently small magnetic fields, the hyperfine mixing is small, $F_\pm$ nearly equals $I \pm J$, and a_1 (a_2) is nearly unity (zero) with a small quadratic (linear) field dependant term. Under our conditions, $B_0 \leq 30$ G and, for the $P_{1/2}$ excited state of ^{85}Rb (^{87}Rb), $B_{\text{hfs}} = 388$ (870) G which gives $x \leq 0.08$. For our purposes, this

is sufficiently small and we'll drop all the field (x) dependant terms.

This probability of a spin flip $P^{\pm}_{\text{flip}}(t)$ must be averaged (1) over all the possible time intervals between disorienting collisions and (2) over each nuclear state. Assuming P_p is at equilibrium and ignoring the time dependance of the relative populations of the nuclear states, the time averaging (with the stipuation that the quenching/transfer collision occurs after the disorienting collision) is given by:

$$\overline{\alpha}^2 \equiv \int_0^\infty \left\{ \int_0^{t'} \left[1 - \cos\left(\omega_{\text{hfs}}(0)t\right)\right] e^{-t\Gamma_p} \, \frac{dt}{1/\Gamma_p} \right\} e^{-\frac{t'}{\tau}} \, \frac{dt'}{\tau} = \frac{\alpha^2}{\left(1+n^{-1}\right)\left[\left(1+n^{-1}\right)^2 + \alpha^2\right]} \tag{5.82}$$

where $\alpha = \omega_{\text{hfs}}(0)/\Gamma_p$. Under our conditions, $n \gg 1$ & $\alpha \ll 1$, which implies that $\overline{\alpha} \approx \alpha$ and allows us to safely ignore the short amount of time ($\approx 1/\Gamma_p$) that it takes for the electron orientation to come to equilibrium. The probability that the atom exits the excited state before undergoing even a single disorienting collision is suppresed by a factor of $1/n^2$.

Since we've ignored the small Zeeman splitting of the hyperfine energy levels, ω_{hfs} is independant of m and the average over the electron & nuclear states is given by:

$$\sum_m \left(\frac{1 \pm P_p}{2}\right) \rho_{mm} \left(\frac{2\left(I(I+1) - m^2\right) \mp 2m}{[I]^2}\right) = \left(\frac{1 \pm P_p}{2}\right) \frac{\epsilon(I, P_s)\left(1 \mp P_s\right)}{[I]^2} \tag{5.83}$$

where $P_s = 2\left\langle S_z \right\rangle$ (P_p) is the ground state polarization (excited state orientation), ρ_{mm} is the diagonal element of the density matrix corresponding to the relative population of the nuclear state labelled by m, and the paramagnetic coefficient $\epsilon(I, P)$ is defined by [11]:

$$\epsilon(I, P) = 2\left\langle \vec{I}^2 - I_z^2 \right\rangle = 2\left\langle I(I+1) - m^2 \right\rangle = \frac{\langle I_z \rangle}{\langle S_z \rangle} = \frac{\langle m \rangle}{\langle S_z \rangle} \tag{5.84}$$

Putting this altogether, the approximate mean time-averaged probability $P_1^{\pm}$ for a single $\pm$ flip is given by:

$$P_1^{\pm} = \left\langle \left\langle P_{\text{flip}}^{\pm}(t) \right\rangle_t \right\rangle_m = \left[\frac{(1 - P_p P_s) \pm (P_p - P_s)}{2} \right] \left[\frac{\epsilon(I, P_s)}{[I]^2} \right] \overline{\alpha}^2 \tag{5.85}$$

Effective Relaxation Rate

We'll assume that the probability of k spin flips out of n collisions can be simply described by a binomial distribution. In that case, the average change in the nuclear spin is given by:

$$\langle \Delta I_z \rangle = n \left(P_1^+ - P_1^- \right) = \left(P_p - P_s \right) n \overline{\alpha}^2 \left[\frac{\epsilon(I, P_s)}{[I]^2} \right] = \left(P_p - P_s \right) P_n \tag{5.86}$$

where $P_n = nP_1$ and P_1 is the "unpolarized" probability of a single spin flip. From the perspective of the ground state, the excited state hyperfine coupling appears as a spin relaxation mechanism that pushes the ground state polarization towards P_p. The effective relaxation rate due to the hyperfine coupling in the excited state, after averaging over the different isotopes of Rb labelled by i, is given by:

$$\frac{\Gamma_{\text{hfs}}}{R} = \sum_i (\eta_i \eta_p') P_n^i = \sum_i (\eta_i \eta_p') \left[\frac{\left(\omega_{\text{hfs}}^i(0) \right)^2 \tau}{\Gamma_p} \right] \left(\frac{\overline{\alpha}_i^2}{\alpha_i^2} \right) \left[\frac{\epsilon(I_i, P_s)}{[I_i]^2} \right] \tag{5.87}$$

where η_i is the fractional abundance of the isotope, $\eta_p' = p/(p+d)$ is the relative population of the $P_{1/2}$ excited state, $1/\tau$ is the sum of total excited state decay rate & the collisional transfer rate, Γ_p is the orientation destruction rate, and, under our conditions ($n \gg 1$), $\overline{\alpha}/\alpha \approx 1$. This calculation is in agreement with the results of Bhaskar et al. [49] for ^{133}Cs when (1) alkali-alkali spin exchange is the fastest process (i.e. the mean time T between alkali-alkali spin exchange collisions ap-

proaches zero, $T \to 0$), (2) the ground state alkali polarization is very low $P_s \to 0$ (i.e. $\epsilon(I, P_s \to 0) \to 4I(I+1)/3$), and (3) the excited state electron is completely disoriented ($P_p = 0$). Tab. (5.2) lists the parameters used to calculate the effective relaxation rate.

A similar calculation for the hyperfine coupling in the $P_{3/2}$ excited state is more involved since there are more than two hyperfine manifolds. (There are $2J+1$ manifolds when $I \geq J$.) For our purposes (i.e. order of magnitude), we may safely ignore this complication and simply treat the $P_{3/2}$ level as if it had $J = 1/2$. In that case, the formulas are unchanged provided we substitute the $P_{3/2}$ rates, population, & hyperfine constants in the place of the $P_{1/2}$ ones in the appropriate places.

5.4.5 On- & Off-Resonant Absorption Rates

The unpolarized absorption/stimulated emission rates R & R' for the D1 & D2 transitions are given by:

$$R^{\{\prime\}} = R_+^{\{\prime\}} + R_-^{\{\prime\}} = \int_0^\infty \left[\Phi_{\mathcal{R}}(\nu) + \Phi_{\mathcal{L}}(\nu)\right] \sigma_{1\{2\}}(\nu)\, d\nu = \int_0^\infty \Phi\sigma_{1\{2\}}\, d\nu \tag{5.88}$$

where $\sigma_{1\{2\}}$ is the unpolarized absorption cross sections for the D1 (D2) transition. The polarized absorption/stimulated emission rates $\overline{P}_\gamma R$ & $\overline{P}'_\gamma R'$ for the D1 & D2 transitions are given by:

$$\overline{P}_\gamma^{\{\prime\}} R^{\{\prime\}} = R_+^{\{\prime\}} - R_-^{\{\prime\}} = \int_0^\infty \left[\Phi_{\mathcal{R}}(\nu) - \Phi_{\mathcal{L}}(\nu)\right] \sigma_{1\{2\}}(\nu)\, d\nu \tag{5.89}$$

The unpolarized absorption cross section for the Dn transition is given as

$$\sigma_n(\nu) = \pi r_e c f_n L_n(\nu) \tag{5.90}$$

excited state	$P_{1/2}$	$P_{1/2}$	$P_{3/2}$	$P_{3/2}$	
isotope	^{85}Rb	^{87}Rb	^{85}Rb	^{87}Rb	**units**
I	2.50	1.50	2.50	1.50	
J	0.50	0.50	1.50	1.50	
F	3	2	4	3	
A_{hfs}	121	406	25.0	84.7	MHz
B_{hfs}	0	0	26.0	12.5	MHz
ω_{hfs} $(F \leftrightarrow F-1)$	2.27	5.10	0.760	1.68	GHz
τ	0.394	0.394	0.413	0.413	ns
Γ_p	104	104	472	472	GHz
n	40.9	40.9	195	195	
α	2.19E-02	4.92E-02	1.61E-03	3.55E-03	
$\epsilon(I_i, 1)$	5	3	5	3	
$[I]$	6	4	6	4	
P_1	6.20E-05	4.21E-04	3.55E-07	2.33E-06	
P_n	2.53E-03	1.72E-02	6.91E-05	4.53E-04	
η_i	0.7217	0.2783	0.7217	0.2783	
η'_p	0.412	0.412	0.588	0.588	
Γ^i_{hfs}/R	7.53E-04	1.97E-03	2.93E-05	7.42E-05	

Table 5.2: Parameters for Estimating the Excited State Hyperfine Coupling. Hyperfine structure constants A & B are from Tab. (A.6). Parameters τ and Γ_p were calculated from Tab. (5.1). We'll note that these values are quite sensitive to the relative populations of the excited P states and the mixing rates between them. Because of the relatively large uncertainties in the off resonant absorption rate and the fine structure mixing cross sections & their temperature dependance, these values may easily be too large or too small by an order of magnitude. Details of how these rates were determined are described in Sec. (D.4.3).

.

where r_e is the classical electron radius, c is the speed of light in a vacuum, f_n is the oscillator strength, and $L_n(\nu)$ is the unit normalized absorption lineshape. Because of the relatively high ^{3}He pressure in the cells, the pressure broadened linewidth (120 GHz) is much larger than both the Doppler linewidth (1 GHz) the hyperfine splitting (3 GHz). In this pressure broadened regime, the alkali lineshape is given by a modified Lorentzian profile:

$$L_n(\nu) = \frac{\Gamma_n g(x)/(2\pi)}{\Delta_n^2 + \Gamma_n^2/4} \qquad x \equiv 2\pi\Delta_n T_d \tag{5.91}$$

where $\Delta_n = \nu - \nu_n$ is the detuning, ν_n the pressure shifted transition frequency, Γ_n is the unperturbed full width at half maximum pressure broadening linewidth, T_d is the effective duration of alkali-buffer gas collisions, and x is the relative detuning. The pressure shifts, pressure widths, and oscillator strengths for the D1 & D2 transitions of the alkali atoms are listed in Tab. (5.5).

The exact form of $g(x)$ depends on critically on the interatomic potential between the alkali atom and the perturber atom. For a van der Waals potential, Walkup et al. calculated $g(x)$ in three regimes [50]:

$$g(x) \approx \left\{ \begin{array}{cc} \left(\pi/6/0.3380\right)\sqrt{|x|} & x < -2.4 \\ 1 - \left(0.2245/0.3380\right)x & -1.5 < x < 0.5 \\ \left(0.8464/0.3380\right)\sqrt{x}\exp\left[-2.1341x^{\frac{5}{9}}\right] & x > 2.4 \end{array} \right\} \tag{5.92}$$

where $x \approx 0$ is near resonance, $x \ll 0$ is referred to the as the classically allowed or "quasistatic" wing, $x \gg 0$ is referred to as the classically forbidden wing. Near resonance, the lineshape is modified to include a small asymmetry term. When T_d is nonzero, the off resonant lineshape is, relative to the a pure Lorentzian lineshape,

much larger on the quasistatic wing and much smaller on the classically forbidden wing.

Combining the incident photon flux with the Rb D1 absorption cross section, assuming $T_d = 0$, gives the unpolarized absorption rate at the front of the cell:

$$R(0,r) = P_0 \sigma_1^{\mathrm{Rb}}(\nu_\gamma) \left[\frac{2}{h\nu_\gamma \pi w^2}\right] \exp\left(-\frac{2r^2}{w^2}\right) \left[\frac{V\left(\Delta_1^{\mathrm{Rb}}, \frac{\mathtt{FWHM}}{2\sqrt{2\log(2)}}, \frac{\Gamma_1^{\mathrm{Rb}}}{2}\right)}{L_1^{\mathrm{Rb}}(\nu_\gamma)}\right] \tag{5.93}$$

where ν_γ is the peak frequency of the laser spectrum, $\Delta_1^{\mathrm{Rb}} = \nu_\gamma - \nu_1^{\mathrm{Rb}}$ is the detuning from the pressure shifted Rb D1 transition frequency ν_1^{Rb}, and $V(\Delta, \sigma, \gamma)$ is the Voigt profile [46, 51] defined by:

$$V(\Delta, \sigma, \gamma) = \int_{-\infty}^{\infty} G(\Delta', \sigma) L(\Delta - \Delta', \gamma)\, d\Delta' \tag{5.94}$$

where G is a Gaussian with a full width half maximum of $2\sigma\sqrt{2\log(2)}$ and L is Lorentzian with a full width half maximum of 2γ. The quantity $f_\gamma = V/L_1^{\mathrm{A}}$ can be thought of as the fraction of the total power that is participates in the absorption and it is sensitive to the ratio of the laser linewidth to the absorption linewidth $\mathtt{FWHM}/\Gamma_n^{\mathrm{A}}$, see Fig. (5.1).

In the broadband limit, $\mathtt{FWHM}/\Gamma_n^{\mathrm{A}} \to \infty$, the absorption cross section looks like a δ-function $L_1^{\mathrm{Rb}} \to \delta(\nu - \nu_1^{\mathrm{Rb}})$, $V \to G(\nu_1^{\mathrm{Rb}})$, and the absorption rate at the center of the beam ($r = 0$) is given by:

$$R(0,0) = 115\ \mathrm{kHz} \left[\frac{P}{75\ \mathrm{W}}\right] \left[\frac{23\ \mathrm{cm}^2}{\pi w^2/2}\right] \left[\frac{2\ \mathrm{nm}}{\mathtt{FWHM}}\right] \left[3 f_1^{\mathrm{Rb}}\right] \exp\left[-\frac{4\log(2)\left(\Delta_1^{\mathrm{Rb}}\right)^2}{\mathtt{FWHM}^2}\right] \tag{5.95}$$

In the narrowband limit, $\mathtt{FWHM}/\Gamma_n^{\mathrm{A}} \to 0$, the laser spectrum looks like a δ-function

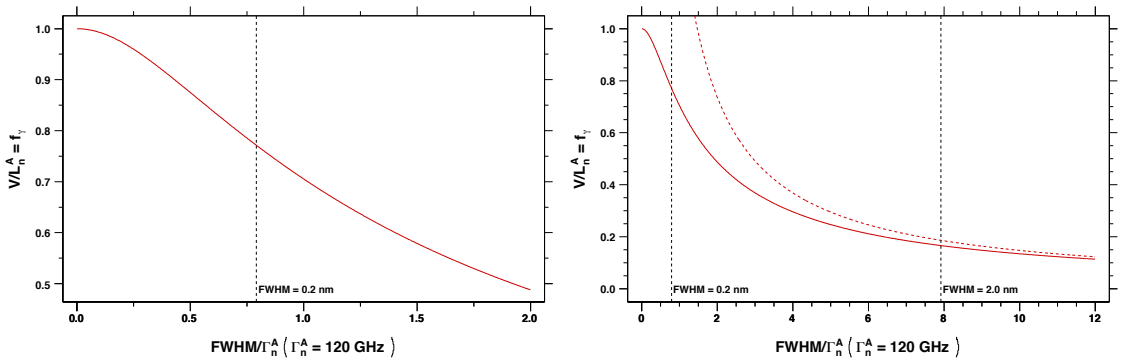

Figure 5.1: Effective Fraction of "Useful" Photons. The black vertical dashed line shows the fraction $f_\gamma = 0.17$ (0.77) for a typical broadband (narrowband) laser with $\texttt{FWHM} = 2$ (0.2) nm. The dashed red curve in the right plot is the fraction in the broadband limit.

$G(\nu) \to \delta(\nu - \nu_\gamma)$, $V/L_1^{\mathrm{Rb}}(\nu_\gamma) \to 1$, the absorption rate at the center of the beam is given by (assuming $T_d = 0$):

$$R(0,0) = 612 \text{ kHz} \left[\frac{P}{75 \text{ W}}\right] \left[\frac{23 \text{ cm}^2}{\pi w^2/2}\right] \left[\frac{120 \text{ GHz}}{\Gamma_1^{\mathrm{Rb}}}\right] \left[\frac{3 f_1^{\mathrm{Rb}}}{1 + 4(\Delta_1^{\mathrm{Rb}})^2/(\Gamma_1^{\mathrm{Rb}})^2}\right] \tag{5.96}$$

The Rb D2 ($\Delta_2^{\mathrm{Rb}} = -7$ THz), K D1 ($\Delta_1^{\mathrm{K}} = -12$ THz), and K D2 ($\Delta_2^{\mathrm{K}} = -14$ THz) transitions are far enough away from the Rb D1 transition that the laser spectrum looks like a δ-function relative to the tail of the absorption line, where we have ignored the tail of the emission spectrum. In this limit, $V/L_n^{\mathrm{A}} \to 1$ (since each photon is roughly the same detuning from the other transition frequencies) and, assuming a pure Lorentzian lineshape (i.e. $T_d = 0 \to g(x) = 1$), the central incident off resonant absorption rate is given by:

$$\mathrm{A}_n^0(0,0) = 51.3 \text{ Hz} \left[\frac{P}{75 \text{ W}}\right] \left[\frac{23 \text{ cm}^2}{\pi w^2/2}\right] \left[\frac{\Gamma_n^{\mathrm{A}}}{140 \text{ GHz}}\right] \left[\frac{10 \text{ THz}}{\Delta_n^{\mathrm{A}}}\right]^2 \left[\frac{3 f_n^{\mathrm{A}}}{2}\right] \tag{5.97}$$

For an attractive potential, $T_d > 0$, the Rb D1 transition is on the quasistatic wing

of the other three transitions and the off resonant absorption rate can be written as:

$$\mathrm{A}_n^{\mathrm{qs}}(0,0) \approx 3.88 \times \mathrm{A}_n^0(0,0)\sqrt{\left|\left(\frac{\Delta_n^{\mathrm{A}}}{10\ \mathrm{THz}}\right)\frac{T_d^n}{0.1\ \mathrm{ps}}\right|} \tag{5.98}$$

For a repulsive potential, $T_d < 0$, the Rb D1 transition is on the classically forbidden wing of the other three transitions and the off resonant absorption rate can be written as:

$$\mathrm{A}_n^{\mathrm{cf}}(0,0) \approx 0.0168 \times \mathrm{A}_n^0(0,0)\sqrt{\left(\frac{\Delta}{10\ \mathrm{THz}}\right)\frac{T_d^n}{0.1\ \mathrm{ps}}}\exp\left[-5.92\left\{(\Delta T_d^n)^{5/9}-1\right\}\right] \tag{5.99}$$

The off resonant absorption rate is extremely sensitive to the sign and magnitude of T_d. For example, Romalis et al. [52] have measured T_d (near resonance) of order -0.1 ps for Rb-He collisions, $+1.0$ ps for Rb-N_2 collisions, and $+3.5$ ps for Rb-^{129}Xe collisions. This gives 2 Hz, 1 kHz, and 2 kHz, respectively, for the off resonant absorption rate for the Rb D2 transition. The ratio of off-resonant to on-resonant absorption rates for different values of T_d are depicted in Fig. (5.2).

Using the framework of Walkup allows us to quantitatively describe the effect on the absorption spectrum due to van der Waals interactions between excited Rb atoms and He atoms using a single parameter T_d. The measured value for T_d near resonance in Rb-He systems is too small and has the "wrong" sign to fully account for the alkali X-factor. On the other hand, Walkup's framework predicts a temperature scaling for pressure broadening & shift and certain relationships between the pressure broadening & shift that is not consistent with the measurements of Romalis et al. In other words, the value for T_d measured near resonance may not be the appropriate value for calculating off resonance effects.

Alternatively, Hirano et al [53] have calculated *ab initio* the potential curves and

excitation spectrum for Rb-He "exciplex" molecules. These molecules are formed from a single excited Rb atom and n He atoms. For $n = 1$, they found that the peak wavelengths that corresponded to the energy difference between the lowest three vibrational states of the $\Pi_{3/2}$ level and the $\Sigma_{1/2}$ level are 830 nm, 805 nm, and 790 nm. Each peak has a FWHM of about 15 nm each. Their results compare favorably to their spectral measurements made at temperatures below 100 K and a He density of 3.4 amg. Based on both their calculation and experimental results, this seems to indicate that the formation of RbHe molecules would increase the off resonant absorption cross section for the D2 transition at frequencies lower (wavelengths higher) than the unperturbed D2 frequency. Recently, Sell et al [54] have found that the cross section for Rb fine structure mixing due to collisions with He gas is quadratic in He density. This was not observed before [34] because the He density at which the three body rate equals the binary rate is very high (roughly 3.4 amg). The existence of a three body rate could be indicative of the formation of a short lived RbHe molecule facilitated by a collision with another He atom. This interpretation provides additional evidence for the formation of RbHe molecules. If so, they would negatively affect the optical pumping process by generating "satellite" absorption lines with locations & widths that contaminate the D1 atomic line.

5.4.6 Maximum Alkali Polarization

Including imperfections to optical pumping, the Rb polarization can written as:

$$P_{\mathrm{Rb}} = \frac{2\Lambda \overline{P}_{\gamma} R \cos(\theta)(1 - X'_{\mathrm{A}})}{2\Lambda R(1 + X_{\mathrm{A}}) + \Gamma_{\mathrm{A}}} \tag{5.100}$$

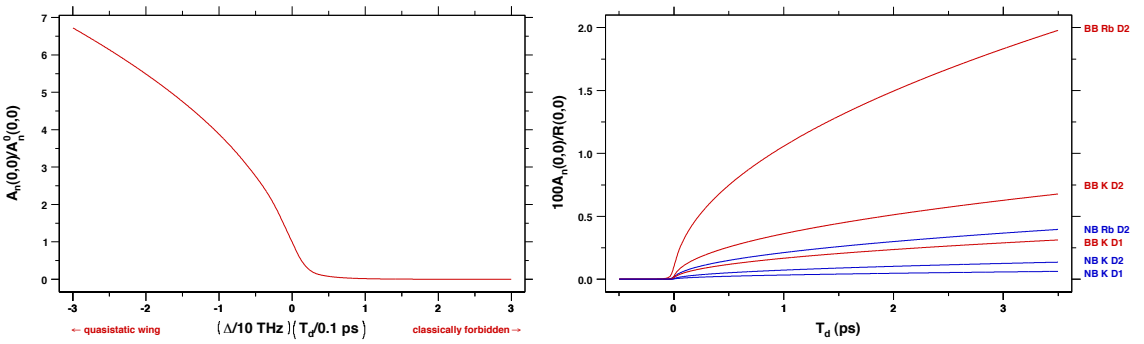

Figure 5.2: Sensitivity of the Off Resonant Absorption Rate to the T_d Parameter. The red (blue) lines are evaluated in the broadband (narrowband) limit. These curves were calculated assuming $T_{pc} = 235^oC$, $[^3He]_{pc} = 6.5$ amg, and $[N_2]/[^3He] = 0.01$. The shifts, widths, and oscillator strengths of each transition are listed in Tab. (5.5).

where Γ_A is the total Rb relaxation rate that independent of the light and X_A & X'_A due to imperfections in the optical pumping or alternatively light-dependent alkali relaxation mechanisms. Mechanisms of such type have been observed by the Wisconsin & NIST groups [7,55,56]. Assuming the imperfections are small and $\eta_K = 1$, we can write the alkali X-factors to lowest order as:

$$\begin{aligned} X'_A &\approx \frac{p}{s} + \frac{R'}{2R} - \frac{DK}{R} + \frac{DK'}{2R} - \frac{P_F F}{\overline{P}_\gamma R} + \frac{P'_F F'}{2\overline{P}_\gamma R} + \left[1 - \frac{P_p}{\overline{P}_\gamma}\right]\frac{\Gamma_{hfs}}{R} + \left[1 - \frac{P_d}{\overline{P}_\gamma}\right]\frac{\Gamma'_{hfs}}{R} \\ X_A &\approx \frac{R'}{R} + \frac{DK}{R} + \frac{DK'}{R} + \frac{F}{R} + \frac{F'}{R} \end{aligned} \tag{5.101}$$

Assuming the optical pumping rate is very high $R_1 \gg \Gamma_A$ and $\overline{P}_\gamma \approx \overline{P}'_\gamma$, the alkali polarization, to lowest order, can be written as:

$$\begin{aligned} P_{Rb} \approx \overline{P}_\gamma \cos(\theta) \Bigg[1 - \frac{p}{s} - \frac{3R'}{2R} - \frac{3DK'}{2R} - \left(1 - \frac{P_F}{\overline{P}_\gamma}\right)\frac{F}{R} - \left(1 + \frac{P'_F}{2\overline{P}_\gamma}\right)\frac{F'}{R} \\ - \left(1 - \frac{P_p}{\overline{P}_\gamma}\right)\frac{\Gamma_{hfs}}{R} - \left(1 - \frac{P_d}{\overline{P}_\gamma}\right)\frac{\Gamma'_{hfs}}{R} - \frac{\Gamma_A}{2\Lambda R}\Bigg] \end{aligned} \tag{5.102}$$

In the very high laser power limit, where $\Gamma_A/R \to 0$ but $[Rb] \gg K_0/A_{se}$, this can

rewritten using Eqn. 5.64) as:

$$\frac{P_{\mathrm{Rb}}}{\overline{P}_{\gamma}} \rightarrow \cos(\theta)P_{\infty} \approx 1 - \{1 - \cos(\theta)\} - \left[X_{\mathrm{A}} + X'_{\mathrm{A}}\right] = 1 - \left[\sum_{k}\left(1 - \frac{P_x^k}{\overline{P}_{\gamma}}\right)\frac{\Gamma_x^k}{R}\right] \quad (5.103)$$

where P_{∞} is the limiting alkali polarization. If one removes the contribution of skew pumping and off-resonant K absorption, then P_{∞} reduces to the same quantity defined in [7].

The effect of stimulated emission can be estimated using Eqn. (5.19). Skew pumping effects can be estimated using $\theta \approx \theta_0 + \psi$, where θ_0 is the central pointing of the beam and ψ is the divergence of the beam. The off resonant absorption rates can be estimated using the results of the previous section assuming $T_d = 0$. The effect of different values for D & T_d is depicted in Fig. (5.3). The parameters used for estimating the effects of radiation trapping & excited state hyperfine coupling are listed in Tabs. (5.1) & (5.2). A list of estimates for each alkali X-factor is listed in Tab. (5.3). The two largest factors are the hyperfine coupling in the $P_{1/2}$ excited state and radiation trapping of D1 fluorescence photons. Both of these factors do not depend on the spectral linewidth of the laser. Although these estimates relatively crude in some cases, it does provide a guide to the most important limiting factors and their scaling behavior under typical conditions in polarized ^{3}He target cells. Because of the relatively large hyperfine interaction in the $P_{1/2}$ excited state, the effective relaxation rate due to excited state hyperfine coupling is about 2% of the unpolarized optical pumping rate. This suprisingly large rate lowers the highest achievable alkali polarization to 0.97, which is consistent, within ± 0.05 absolute uncertainties, with published results for various measurements of the absolute alkali polarization (e.g. > 0.95 in [55], > 0.97 in [2], > 0.98 in [7], > 0.97 in [57]).

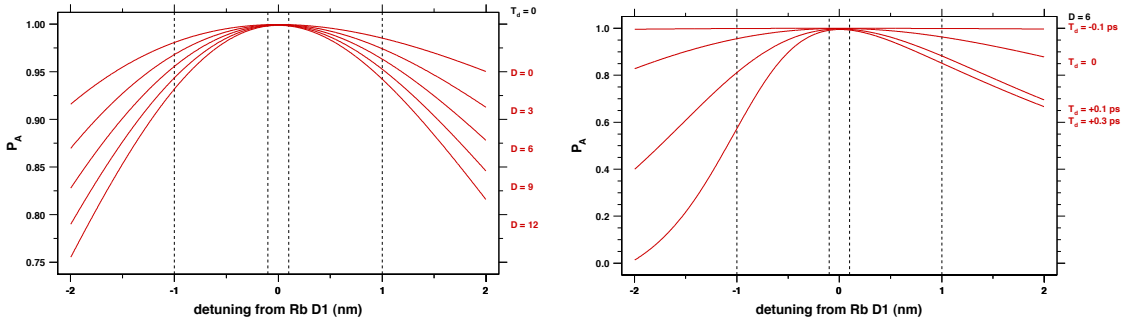

Figure 5.3: Sensitivity of the Maximum Alkali Polarization to the D and T_d. Only the contributions due to off-resonant absorption were included in the calculation of P_A. These curves were calculated assuming $T_{pc} = 235^oC$, $[^3He]_{pc} = 6.5$ amg, and $[N_2]/[^3He] = 0.01$. The outer (inner) vertical dashed lines depict the FWHM of a typical broadband (narrowband) laser. The true alkali polarization is found by averaging P_A over the laser spectral profile. A narrowband laser has a much smaller sensitivity to imperfections due to off-resonant absorption.

5.4.7 Photon Cost

If we are only directly pumping the Rb D1 transition, then it is convenient to rewrite Eqn. (**??**) as:

$$\frac{d\Phi(\nu)}{dz} = -\Phi(\nu)\sigma_1^{Rb}(\nu)[Rb]\left[1 + X_\gamma(\nu) - P_\gamma(\nu)P_{Rb}\cos(\theta)\left\{1 - X'_\gamma(\nu)\right\}\right] \qquad (5.104)$$

where $X_\gamma(\nu)$ & $X'_\gamma(\nu)$ are, in general, additional light absorption mechanisms that spoil the transparency of the alkali vapor when $P_\gamma P_{Rb}\cos(\theta) = 1$. Nonzero values of these "photon X-factors" could potentially limit the volume averaged alkali polarization by preventing the light from penetrating to the back end of the cell.

Integrating over ν, assuming that $R \gg \Gamma_A$ throughout the pumping chamber &

source	P_x	$100\left(\Gamma_x/R\right)$	$100\left(X_{\mathrm{A}}+X'_{\mathrm{A}}\right)$	**scaling**
$P_{1/2}$ HFS	$+0.01$	2.008	1.987	$[\mathrm{N_2}]^{-1}[^3\mathrm{He}]^{-1}$
D1 rad. trap.	$+0.40$	0.907	0.544	$[\mathrm{N_2}]^{-1}$
K D2 abs.	-0.50	0.144	0.217 $\{0.043\}$	$D[^3\mathrm{He}]^{1\{2\}}\Delta^{-2}$
skew pump.	$+0.00$	0.137	0.137	θ^2
Rb D2 abs.	-0.50	0.080	0.120 $\{0.024\}$	$[^3\mathrm{He}]^{1\{2\}}\Delta^{-2}$
$P_{3/2}$ HFS	$+0.00$	0.012	0.012	$[\mathrm{N_2}]^{-1}[^3\mathrm{He}]^{-1}$
stim. emis.	$+0.00$	0.011	0.011 $\{0.057\}$	$I_0\left(\mathtt{FWHM}\{[^3\mathrm{He}]\}\right)^{-1}[\mathrm{N_2}]^{-1}$
D2 rad. trap.	-0.19	0.003	0.003	$[\mathrm{N_2}]^{-1}$
total			**3.03 {2.81}**	
P_∞			**0.973 {0.974}**	
P_{Rb}			**0.970 {0.972}**	

Table 5.3: Estimates for Alkali X-Factors. These values were calculated assuming $D = [\mathrm{K}]/[\mathrm{Rb}] = 6$, $T_{\mathrm{pc}} = 235^{\mathrm{o}}\mathrm{C}$, $[^3\mathrm{He}]_{\mathrm{pc}} = 6.5$ amg, $[\mathrm{N_2}]/[^3\mathrm{He}] = 0.01$, $T_d = 0$, $I_0 = 75$ W/23 cm^2, and $\theta = 3^{\mathrm{o}}$. The values without (with) the curly brackets $\{\cdots\}$ were calculated in the broadband (narrowband) laser spectrum limit with $\mathtt{FWHM} = 2$ (0.2) nm. The detuning from the Rb D1 transition frequency is denoted by Δ. The maximum alkali polarization estimated from this table is signifcantly larger than the value of 0.91 from [7] for traditional SEOP with broadband lasers. It should be noted, however, that off resonant pumping makes a larger contribution as the light penetrates deeper into the cell (where the on resonant optical pumping rate is smaller). This implies that the average X_{A} due to off resonant pumping can be very sensitive to the cell geometry, alkali number density, and laser intensity. Even for such a high estimate for P_∞ listed in this table, the photon cost can be significant, see Sec. (5.4.7). Finally, [7] found no apparent ^{3}He pressure dependence on P_{A}. This may be because those measurements were taken in a regime where the decrease in off resonant pumping of the Rb D2 transition was partially/wholly compensated by the increase in the $P_{1/2}$ excited state hyperfine coupling with decreasing ^{3}He pressure.

$\eta_K = 1$ such that $P_K = P_{Rb}$, and keeping only the lowest order X terms, we find:

$$\frac{d\int \Phi\, d\nu}{dz} = -R[\mathrm{Rb}]\left[\frac{\Gamma_A}{2\Lambda R} + X_{abs}\right] \tag{5.105}$$

where X_{abs} and the cross section weighted photon X-factors are given by:

$$\begin{aligned} X_{abs} &= \left\{1 - \overline{P}_\gamma^2\right\} + \sin^2(\theta) + \overline{X}_\gamma + \overline{X}'_\gamma + X_A + X'_A & (5.106)\\ \overline{X}_\gamma &= -2\left(\frac{p}{s}\right)_{Rb} + \frac{R'}{R} + \frac{DK}{R} + \frac{DK'}{R} & (5.107)\\ \overline{X}'_\gamma &= +2\left(\frac{p}{s}\right)_{Rb} + \frac{R'}{2R} + D\left(\frac{P_K}{P_{Rb}}\right)\left[-\frac{K}{R} + \frac{K'}{2R}\right] & (5.108) \end{aligned}$$

Assuming $\overline{P}_\gamma = 1$, $P_K = P_{Rb}$, and using the results from the last section, we find $100\left(\overline{X}_\gamma + \overline{X}_\gamma\right) = 0.34$ (0.07) and $100X_{abs} = 3.6$ (2.8) for broadband (narrowband) lasers. At the front of the cell, $\Gamma_A/(2\Lambda R) \approx 10^{-2}$, imperfect optical pumping increases the local photon cost by about a factor of 4.

To estimate the laser power required to maintain a high alkali polarization throughout the pumping chamber, it is useful to write R as $\beta P_0 \sigma_1^{Rb}(\nu_\gamma) f_\gamma$, where β describes the transverse spatial profile of the beam and f_γ is the fraction of photons useful for optical pumping. If we make the assumption that only photons within this fraction are lost as the the light propagates through the vapor then we find:

$$\frac{d\int \Phi\, d\nu}{dz} = \frac{d\beta P_0 d\nu}{dz} = \beta\left[\frac{d(1-f_\gamma)P_0}{dz} + \frac{d(f_\gamma P_0)}{dz}\right] = \beta\frac{d(f_\gamma P_0)}{dz} \tag{5.109}$$

where we've assumed that the divergence of the beam is small enough that $d\beta/dz \approx$

0 and now we have:

$$\frac{d(f_\gamma P_0)}{dz} = -(f_\gamma P_0)\sigma_1^{\mathrm{Rb}}(\nu_\gamma)[\mathrm{Rb}]X_{\mathrm{abs}} - \frac{[\mathrm{Rb}]\Gamma_{\mathrm{A}}}{2\Lambda\beta} \tag{5.110}$$

This can be solved go give:

$$(f_\gamma P_0)(z) = (f_\gamma P_0)(0)\exp\left(-\frac{z}{z_x}\right) - \frac{\Gamma_{\mathrm{A}}}{2\Lambda\beta\sigma^1_{\mathrm{Rb}}(\nu_\gamma)X_{\mathrm{abs}}}\left[1-\exp\left(-\frac{z}{z_x}\right)\right] \tag{5.111}$$

where $1/z_x = \sigma_1^{\mathrm{Rb}}(\nu_\gamma)[\mathrm{Rb}]X_{\mathrm{abs}}$ is the optical depth in the presence of imperfections. In our case, using $[\mathrm{A}] = 10^{15}/\mathrm{cm}^3$, we find $z_x \approx 6.2$ (8.0) mm for broadband (narrowband) lasers, which, in either case is much less than the diameter of the pumping chamber (60–85 mm) that we typically use.

To determine the power needed at the front of the cell (i.e. the total power from the laser), we'll impose the boundary condition that $(f_\gamma P_0)$ at the back of the cell, $z = \ell$, is still large enough to keep alkali polarization high:

$$P_{\mathrm{A}}^{\mathrm{min}} = \frac{2\Lambda\overline{P}_\gamma\beta(f_\gamma P_0)(\ell)\sigma_1^{\mathrm{Rb}}(\nu_\gamma)\cos(\theta)(1-X'_{\mathrm{A}})}{2\Lambda\beta(f_\gamma P_0)(\ell)\sigma_1^{\mathrm{Rb}}(\nu_\gamma)(1+X_{\mathrm{A}})+\Gamma_{\mathrm{A}}} \tag{5.112}$$

Solving this equation for $(f_\gamma P_0)(\ell)$, then plugging it into Eqn. (5.111), and solving for the power at the front of cell, we get:

$$P_0(z=0) = P_{\mathrm{scale}}\left[\frac{n_{\mathrm{back}}+n_{\mathrm{path}}}{100}\right]\frac{\exp\left(+\ell/z_x\right)}{10} \tag{5.113}$$

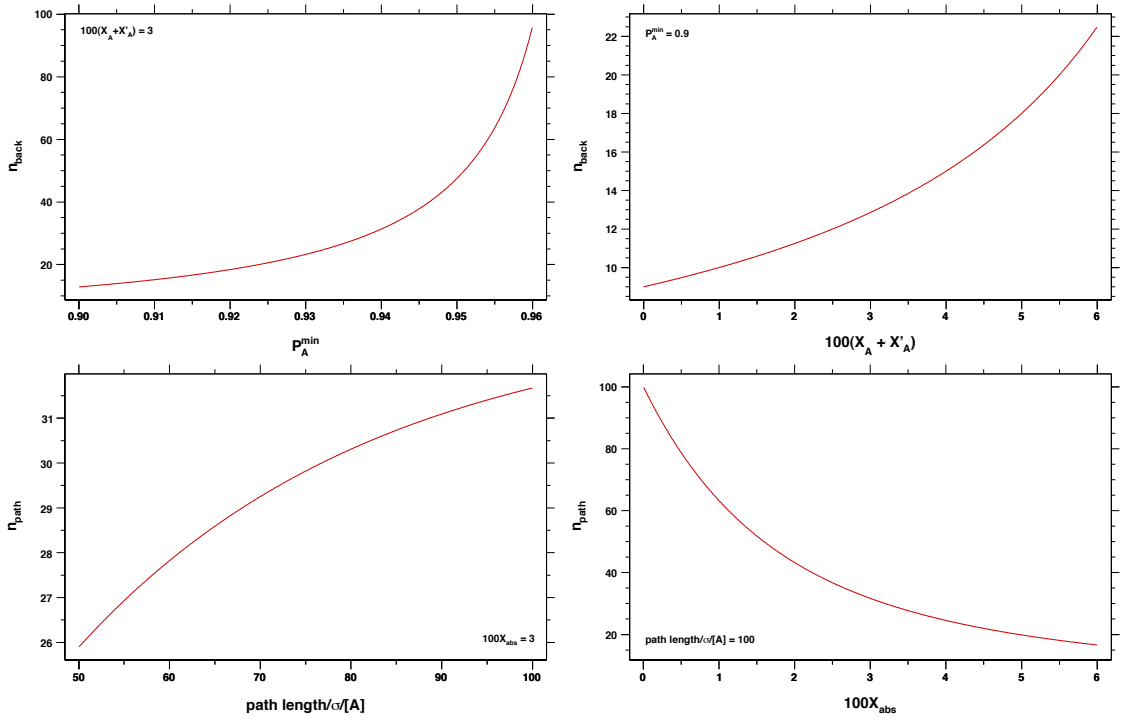

Figure 5.4: Photon Cost Factors. The unitless factor n_{back} is the due to the requirement that the laser power is large enough to penetrate to the back of the cell. The factor n_{path} is a relative measure of the amount of photons absorbed over the path length due to Γ_{A}.

where P_{scale}, n_{back}, and n_{path} are given by:

$$P_{\text{scale}} = \frac{1000\Gamma_{\text{A}}}{2\Lambda f_\gamma \beta \sigma^1_{\text{Rb}}(\nu_\gamma)} \tag{5.114}$$

$$n_{\text{back}} = \frac{P^{\text{min}}_{\text{A}}}{1-\left\{1-\overline{P}_\gamma\right\}-\left\{1-\cos(\theta)\right\}-(X_{\text{A}}+X'_{\text{A}})-P^{\text{min}}_{\text{A}}} \tag{5.115}$$

$$n_{\text{path}} = \frac{1-\exp\left(-\ell/z_x\right)}{X_{\text{abs}}} \tag{5.116}$$

Fig. (5.4) depicts the sensitivity of n_{back} & n_{path} to $P^{\text{min}}_{\text{A}}$ & $\ell/\sigma^{\text{Rb}}_1(\nu_\gamma)/[\text{Rb}]$ and the alkali & photon X-factors.

Assuming a Gaussian beam profile at the front of the cell (i.e. $\beta = I(r, z_{\text{cell}}/(h\nu_\gamma P_0))$

and and using $V/L_1^{\mathrm{Rb}}(\nu_\gamma)$ for f_γ, we can write the scale power as:

$$P_{\mathrm{scale}} = \frac{159\,\mathrm{W}}{(2\Lambda)(3f_n^{\mathrm{A}})}\left[\frac{0.771}{f_\gamma}\right]\left[\frac{\Gamma_{\mathrm{A}}}{1\,\mathrm{kHz}}\right]\left[\frac{\Gamma_n^{\mathrm{A}}}{120\,\mathrm{GHz}}\right]\left[\frac{795\,\mathrm{nm}}{\lambda_n^{\mathrm{A}}}\right]\left[\frac{\pi w^2/2}{23\,\mathrm{cm}^2}\right] \times\left[1+\left(\frac{2\Delta_n^{\mathrm{A}}}{\Gamma_n^{\mathrm{A}}}\right)^2\right]\exp\left(\frac{2r^2}{w^2}\right) \tag{5.117}$$

For a spherical cell, the laser power requirement is most severe at the center of the cell, $r = 0$, where the path length is equal to the cell diameter $\ell = 2R_{\mathrm{pc}}$.

It is useful to express the Rb density in terms of the spin exchange rate γ_{se} to ^{3}He and D:

$$[\mathrm{Rb}] = 13.7\times10^{14}/\mathrm{cm}^3\left[\frac{\gamma_{\mathrm{se}}}{1/(3\,\mathrm{hrs})}\right]\left[\frac{1}{1+0.764D}\right] \tag{5.118}$$

which we can use to express the argument of exponential factor of Eqn. (5.113) as:

$$\frac{\ell}{z_x} = 4.50\,[100X_{\mathrm{abs}}]\left[\frac{\ell}{7\,\mathrm{cm}}\right]\left[\frac{\gamma_{\mathrm{se}}}{1/(3\,\mathrm{hrs})}\right]\left[\frac{1}{1+0.764D}\right] \times\left[1+\left(\frac{2\Delta_n}{\Gamma_n}\right)^2\right]^{-1}(3f_n)\left[\frac{120\,\mathrm{GHz}}{\Gamma_n}\right] \tag{5.119}$$

When $\ell/z_x \ll 1$, n_{path} becomes independent of X_{abs}, and the laser power requirement becomes:

$$P_0(z=0) \approx \frac{P_{\mathrm{scale}}}{1000}\left[n_{\mathrm{back}}+n_{\mathrm{path}}\right]\left[1+n_{\mathrm{path}}X_{\mathrm{abs}}\right] \tag{5.120}$$

$$n_{\mathrm{path}} \approx \ell\sigma_1^{\mathrm{Rb}}(\nu_\gamma)[\mathrm{Rb}] = 450\left[\frac{\ell}{7\,\mathrm{cm}}\right]\left[\frac{\gamma_{\mathrm{se}}}{1/(3\,\mathrm{hrs})}\right]\left[\frac{1}{1+0.764D}\right] \times\left[1+\left(\frac{2\Delta_n}{\Gamma_n}\right)^2\right]^{-1}(3f_n)\left[\frac{120\,\mathrm{GHz}}{\Gamma_n}\right] \tag{5.121}$$

where $\ell/z_x \approx n_{\mathrm{path}}X_{\mathrm{abs}} \ll 1$ in this limit. Therefore, we see that, when $X_{\mathrm{abs}} \to 0$,

	$100(X_A + X'_A)$	$100X_{abs}$	P_{scale} (W)	n_{path}	ℓ/z_x	P_0 (W)
sph. cow 1/12 hrs	0.00	0.00	652	116	0.0	8.1E+01
sph. cow 1/3 hrs	0.00	0.00	652	463	0.0	3.1E+02
skew only	0.14	0.27	652	262	1.3	6.3E+02
skew + off-res.	0.26	0.51	652	177	2.4	1.3E+03
all sources	2.81	3.07	652	33	14.2	4.4E+07
narrowband only	2.76	2.91	144	34	13.5	4.7E+06
hybrid only	3.03	3.50	1652	27	2.9	1.2E+03
both	2.79	2.97	365	31	2.5	1.8E+02

Table 5.4: Illustrative Example of the Photon Cost for "Transversity-Style" Target Cells. Unless otherwise noted, the following parameters were used in the calculation: $1/\gamma_{se} = 3$ hrs, $R_{pc} = 3.6$ cm, and $P_A^{min} = 0.9$. The first six (last two) rows were calculated using $D = 0$ ($D = 6$). Rows 1–5 & 7 (6 & 8) were calculated using $\texttt{FWHM} = 2.0$ & $f_\gamma = 0.17$ ($\texttt{FWHM} = 0.2$ & $f_\gamma = 0.77$). All other parameters were from Tab. (5.3) and $n_{back} \approx 10$. According to this crude model, it would require $P_0 \approx 200$ W of narrowband light to polarize the alkali vapor > 0.9 throughout the pumping chamber. With a ^{3}He X-factor of 0.2, beam current of 10 μA, and cell lifetime of 30 hrs, the expected ^{3}He polarization is about 0.65. The target cells used for the "Transversity" experiments, see Tab. (3.1), achieved this level of performance with roughly $P_0 \approx 100$ W.

we've recovered the "naive" $R_{pc}^3\gamma_{se}$ photon cost scaling that is usually expected for spherical cells, where $P_{scale} \propto w^2$ and we've assumed $w = R_{pc}$. On the other hand, when $100X_{abs} \geq 1$, the laser power requirement can very easily obtain an exponential $\exp[\cdots R_{pc}\gamma_{se}/(1 + 0.8D)\cdots]$ dependence. This effect can be greatly suppressed with a hybrid cell ($D > 1.3$). In addition, pumping with a narrowband laser significantly reduces the sensitivity to off-resonant absorption effects and increases f_γ. Illustrative examples of the photon cost using Eqn. (5.113) for the most recent ^{3}He experiments and for upcoming ^{3}He experiments are listed in Tab. (5.4) and depicted in Fig. (5.5) respectively. Generally speaking, the biggest gains comes first from alkali-hybrid SEOP and then in combination with narrowband lasers.

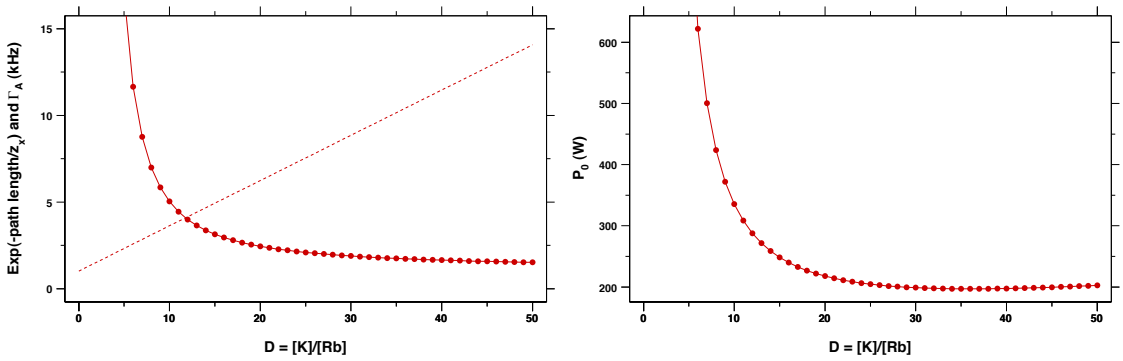

Figure 5.5: Illustrative Example of the Photon Cost for "GEN II-Style" Target Cells. In the left plot, the solid circles (dashed line) is the exponential factor $\exp(-\ell/z_x)$ (alkali relaxation rate Γ_A). In the right plot, the minimum power requirement occurs near $D = 35$, where it should be noted that this crude model assumes $P_K = P_{Rb}$ (i.e. $\eta_K = 1$) for all values of D. The following parameters were used in the calculation: $1/\gamma_{se} = 3.5$ hrs, $R_{pc} = 5.9$ cm, and $P_A^{min} = 0.9$. All other parameters are from Tab. (5.3). According to this crude model, it would require 250 W of narrowband light for a $D \approx 35$ hybrid ratio to polarize the alkali vapor > 0.9 throughout the pumping chamber. With a ^{3}He X-factor of 0.15, beam current of 60 μA, and cell lifetime of 25 hrs, the expected ^{3}He polarization is about 0.65.

5.5 Numerical Simulations

The effects discussed in this chapter become quite complicated as we consider a realistic situation as one might encounter in an actual target cell. In particular, one simplifying assumption made in the previous section is the invariance of the pump beam spectral profile. Eqn. (5.59) indicates that this profile is modified dramatically as the laser propagates through the alkali vapor. Absorption is largest near the center of the profile, which, deeper into the cell, results in a spectrum with a "hole" at center. The optical pumping rate associated with such a profile is lower than that for a Gaussian profile with the same total power as given by Eqn. (5.95) (Eqn. (5.96)) for broadband (narrowband) lasers. As a consquence, the alkali X-factor associated with off resonant absorption depends on both the geometry of

the cell and the shape of the pump beam spectral profile.

With the dynamics involved in a real target being complicated, the easiest way to see the impact of the effects discussed previously is to perform a numerical simulation of a realistic target cell. In this way, it is straightforward to appreciate the considerable impact of the both alkali hybrid mixtures and narrowband light. The conditions for optimizing a target design also become quickly apparent.

5.5.1 Simulation Ingredients

The simulation is a numerical integration of Eqn. (5.59) over a discretized path through the pumping chamber. Assuming cylindrical symmetry, a spherical pumping chamber is divided into 100 radial bins, each with a different path length. The path for each radial bin is divided into slices with a thickness of 100 μm, which is chosen as a balance between computational time and accuracy. The spectral profile of the laser is binned by helicity and divided into 3000 frequency bins that represent a $\pm$1500 GHz ($\pm$3.2 nm) window centered at the D1 absorption line of one of the two alkali species. The pressure broadened alkali absorption cross section is determined from Eqn. (E.800) and the parameters listed in Tab. (5.5), where T_d is input by the user. At the beginning of each slice, the D1 & D2 optical pumping rates for both alkali species are calculated by a numerical integration of Eqns. (5.88) & (5.89).

Armed with the optical pumping rates and the alkali relaxation rates determined from Tab. (5.6), Sec. (D.2) & Sec. (D.3), the alkali polarizations are calculated using Eqn. (5.49) & (5.50). The alkali X-factors are calculated using this initial alkali polarization and, subsequently, these factors are then used to recalculate the final alkali polarization. Since the alkali X-factors are relatively small, only a sin-

parameter	Na	K	Rb	Cs	units
λ_1 (air)	589.5924	769.896	794.7603	894.347	nm
λ_1 (vac.)	589.7558	770.108	794.9789	894.593	nm
ν_1	508333.2	389286.3	377107.4	335116.0	GHz
$\nu_{so} = \nu_2 - \nu_1$	515.6	1729.9	7123.0	16609.8	GHz
f_1	0.322	0.340	0.342	0.344	
f_2	0.647	0.682	0.695	0.7131	
D1 width	17	15.6	18.7	25	GHz/amg
n	(0.35)	0.41	0.11	(0.35)	
D2 width	20	21.4	20.8	22	GHz/amg
n	(0.35)	0.23	0.34	(0.35)	
D1 shift ($n = 1.1$)	1.0	2.5	5.64	6.4	GHz/amg
D2 shift ($n = 1.6$)	0.6	1.5	0.68	2.3	GHz/amg
T_{ref}	450	410	353	393	K
ref.	[58]	shift only: [59]	[52]	[60]	

Table 5.5: Optical Pumping Parameters. The wavelengths and oscillator strengths ($f_{1,2}$) are from the NIST Atomic Spectra Database Version 3 [61]. The parameters have be rescaled from ^{4}He to ^{3}He by the square root of the ratio of the reduced mass where we're assuming that the only difference is the relative thermal velocity. The width and shift parameters have a temperture dependence given by $(T/T_{ref})^n$, where n is the temperature coefficient. The K pressure broadening numbers as well as the Rb pressure broadening temperature coefficients are from our preliminary measurements and will be published separately. The other pressure broadenign temperature coefficients are set to an average between the value assuming a van der Waals potential ($n = 0.3$) and typical theoretical calulations ($n \approx 0.4$) [62]. The pressure shift temperature coefficients are set equal to Rb, the only one that's been measured.

parameter	alkali	value	rel. err.	experiment	theory
σ_{se}^{A}	Na	101	0.5%	[24]	[24]
	K	158	4%	[24]	[24]
$\left(\text{Å}^2\right)$	Rb	174	4%	[24,63]	
	Cs	186	4%	[24]	[24]
σ_{sd}^{A}	Na	0.00557	10%	[64]	
	K	0.0128	10%	[65,66]	
$\left(\text{Å}^2\right)$	Rb	0.0994	10%	[65–69]	
	Cs	2.08	10%	[66,70]	
k_{se}	Na	1.27	10%	[64]	[71–73]
	K	1.38	3%	[56,74]	[71–73]
(Hz/amg)	Rb	1.81	3%	[67,69,74–76]	
	Cs	2.97	10%	[74]	[71,72]
k_{He}	Na	0.15	30%	[64]	[77]
	K	4.7	10%	[78,79]	[77]
(Hz/amg)	Rb	55.9	2%	[66,69,80,81]	
	Cs	530	10%	[82,83]	[77]
k_{N_2}	Na	150	100%	no measurement	
	K	150	30%	[84]	
(Hz/amg)	Rb	290	10%	[66,68,80,81,85]	
	Cs	2100	20%	[82,83]	

Table 5.6: Spin Exchange & Spin Destruction Parameters at $T = 200^{o}$C. See Chp. (D) for more details about data selection and temperature dependences.

gle iteration is required to converge to a final equilibrium alkali polarization. This final alkali polarization is used to attenuate the spectral profile, which is then fed into the next path slice. Finally, the volume averaged alkali polarization is calculated by weighing the polarization in each radial bin & path slice by the fractional volume of that bin-slice.

5.5.2 Hybrid vs. Traditional SEOP

In order to illustrate the impact of using the hybrid alkali mixtures and narrowband lasers, it is useful to focus our attention on examples that are reasonably close to those used in the experiments described in Chp. (3). We will thus consider the baseline parameters listed in Tab. (5.7) for a 3 in diameter spherical pumping chamber. We will further restrict our attention to a spin-exchange rate such that $\gamma_{se} = 1/(3 \text{ hrs})$. Noting from Sec. (6.1.6) that the equilibrium ^{3}He polarization in the fast diffusion limit is given by:

$$P_{He} = \frac{f_{pc}\gamma_{se}\left\langle P_A\right\rangle_{pc}}{f_{pc}\gamma_{se}(1+X)+\left\langle\Gamma\right\rangle} \tag{5.122}$$

and that typically $f_{pc} \approx 0.55$, $X \approx 0.25$, $\Gamma_s \approx 1/(20 \text{ hrs (with beam)}$, this implies:

$$P_{He} = \left\langle P_A\right\rangle_{pc}(66\%) \tag{5.123}$$

where $\left\langle P_A\right\rangle_{pc}$ is the volume averaged alkali polarization inside the pumping chamber. While targets were certainly run with a range of values for γ_{se}, the value of $1/(3 \text{ hrs})$ was reasonably typical, and as will come evident, close to the fastest value we could practically achieve. In Fig. (5.6), we show the volume averaged alkali polarization as a function of $D = [K]/[Rb]$. We show this dependence for two assumed values for the spectral with of the illuminating light, $\Delta\nu = 0.2$ nm and 2.0 nm, which as discussed earlier, are typical values for narrowband and broadband lasers respectively. In both cases, we assume a total power of 75 W. Furthermore, we assume here that T_d, the effective collision time, is zero. This represents a fairly optimistic or best case scenario, in which off resonant absorption

parameter	value	units
$[^3\mathrm{He}\,]_{\mathrm{pc}}$	6.5	amg
$[\mathrm{N_2}\,]/[^3\mathrm{He}\,]$	0.01	
$1/\gamma_{\mathrm{se}}$	3	hrs
D	0 (pure) 6 (hybrid)	
ΔT	0	K
$2R_{\mathrm{pc}}$	3	in
w/R_{pc}	1	
P_0	75	W
detuning	0	nm
`FWHM`	0.2 (narrowband) 2.0 (broadband)	nm nm
P_γ	0.99	
θ	3	deg
ψ	0	deg
op alkali	2 (Rb)	
se alkail	1 (K)	
T_d (op D1)	0	ps
T_d (op D2)	0	ps
T_d (se D1)	0	ps
T_d (se D2)	0	ps
off resonance absorption scale factor	1	
radiation trapping	0	
stimulated emission	0	
excitation energy transfer	0	
EET polarization transfer	0	
excited state hyperfine coupling	0	
diffusion layer correction	0	

Table 5.7: Baseline Input Parameters to the Numerical Simulation. The optically pumped alkali atom is labelled as "op alkali," whereas the hybrid alkali species is labelled as "se alkali." The alkali species are enumerated as Na = 0, K = 1, Rb = 2, and Cs = 3. The density ratio of "se alkali" to "op alkali" is given by D. The alkali vapor pressure temperature and alkali number densities are determined from γ_{se} and D. The cell temperature is given by the sum of ΔT and the alkali vapor pressure temperature. The cell diameter is given by $2R_{\mathrm{pc}}$. The laser beam radius, power, linewidth, polarization, skew angle, and divergence are given by w, P_0, `FWHM`, P_γ, θ, and ψ respectively.

is still present but not enhanced by the interatomic interactions between Rband ^{3}He which are known to exist at some level.

It is immediately clear from this that regardless of the laser linewidth, the maximum alkali polarization occurs for $D = 6$. Furthermore, the variation is sufficiently slow that any value for D between say 4 and 10, results an alkali polarization fairly clos to the maximum. This important results tells us that we do not need to be overly precise in our alkali mixtures to achieve nice performance. It is also clear from this Fig. (5.6) that for any value of $D \geq 1$, the use of narrowband light results in greatly improved polarization.

Next, in Fig. (5.7), we consider how to optimize a target depending on the amount of laser power available. This process begins by constructing curves of the sort shown in Fig. (5.6) and the resulting alkali polarization. Fig. (5.7) shows the best value of P_{A} that can obtained as a function of laser power, and next to each plotted point is an annotation indicatin the value of D for which that alkali polarization was achieved. For example, when $P_0 = 75$ W, this value is $D = 6$ for both the narrowband and broadband cases.

Finally, we show in Fig. (5.8) for $P_0 = 75$ W the alkali polarization as a function of depth into the cell. This plot provides insight into both the way in which the laser's spectral profile and the ratio D affects the spatial variation of the alkali polarization. One qualitative feature is immediatly apparent. The narrowband light is associated with a sharp drop-off of polarization, whereas, the broadband light is associated with a more gradual rolloff. In the latter case, this is associated with the reduced optical pumping rate R that results from a depletion of light near the absorption maximum and the relative increase in the off resonant absorption. It it also clear that for any type of laser light the point at which alkali polarization

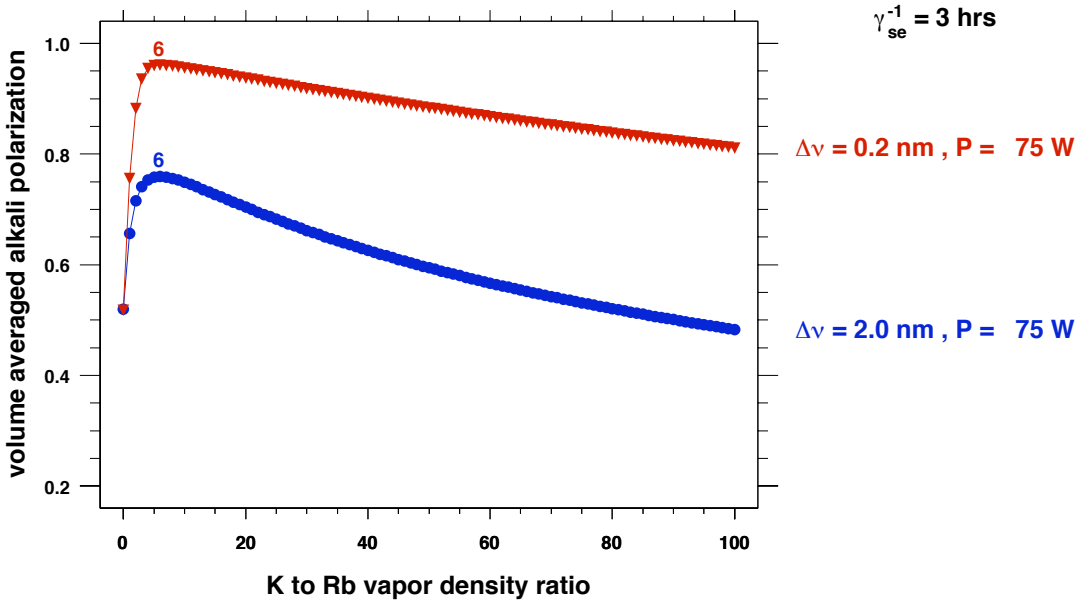

Figure 5.6: Alkali Polarization vs. Alkali-Hybrid Ratio.

is reduced is pushed further into the cell by employing a hybrid alkali mixture. That is, as discussed earlier, hybrid mixtures greatly improve the photon economy.

5.5.3 The Effect of Imperfect Optical Pumping

Fig. (5.9) depicts the alkali polarization as a function of depth into the cell for three different values of the alkali X-factor. In all three cases, we consider a hybrid cell using narrowband lasers. To provide a baseline for comparison, we also include the results for a pure Rb cell using broadband lasers with a zero alkali X-factor. The results is fairly dramatic. Even for a relatively small alkali X-factor, for example $X_A = 0.01$ which implies a maximum alkali polarization per slice of 0.99, the depth into the cell that the light can penetrate is reduced by 30% relative. The implication, as described earlier, is that even small imperfections can greatly increase the photon cost of polarizing a high density ($\geq 10^{15}/\text{cm}^3$) of alkali vapor.

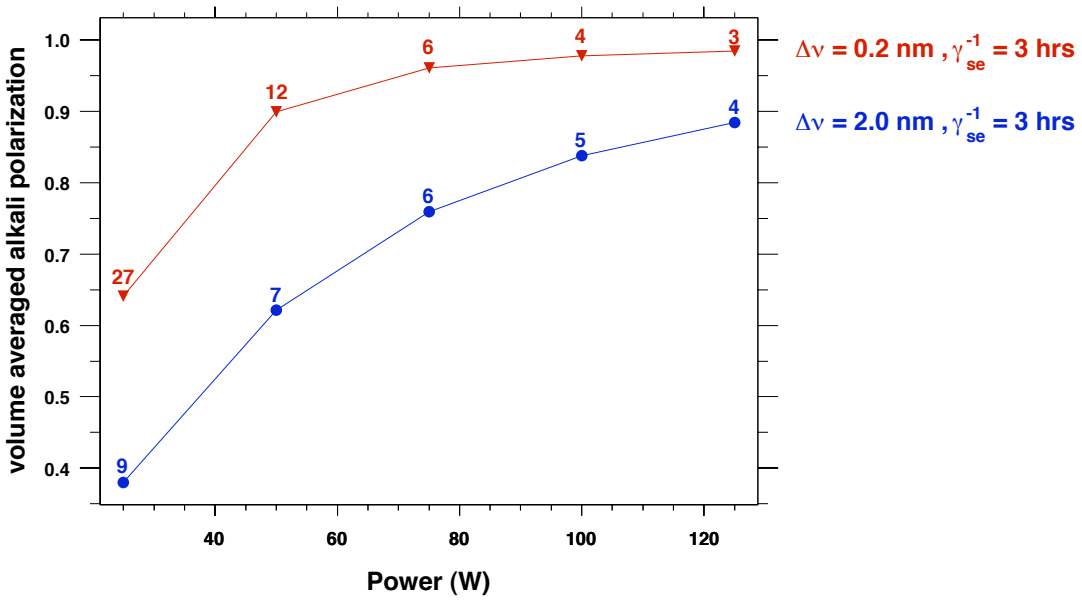

Figure 5.7: Optimal Alkali-Hybrid Ratio vs. Laser Power.

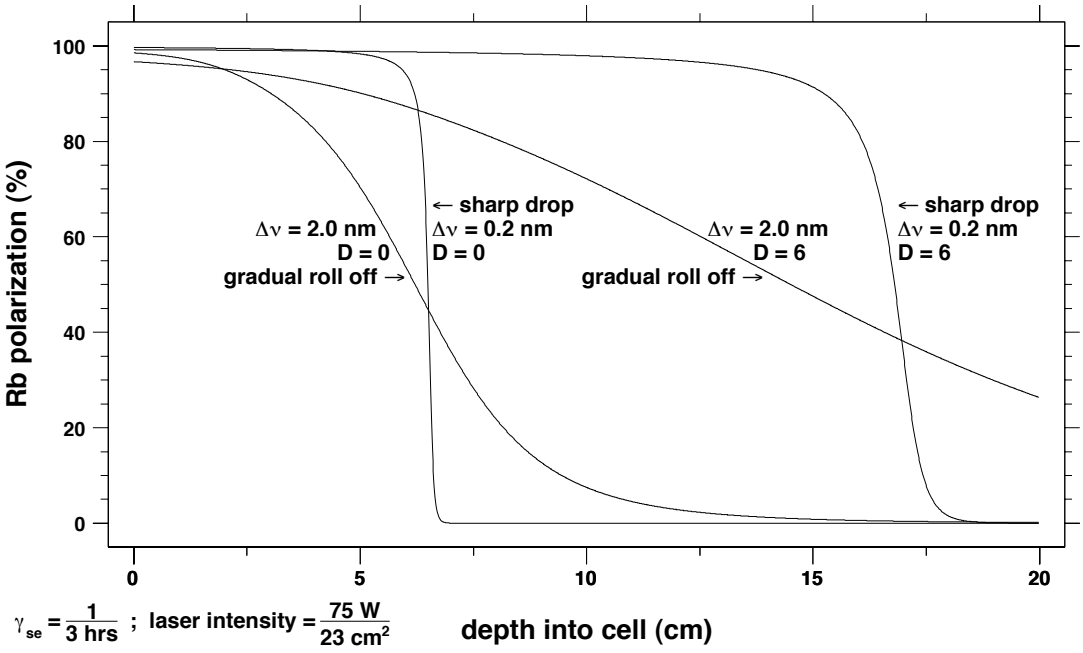

Figure 5.8: Alkali Polarization vs. Depth into Pumping Chamber.

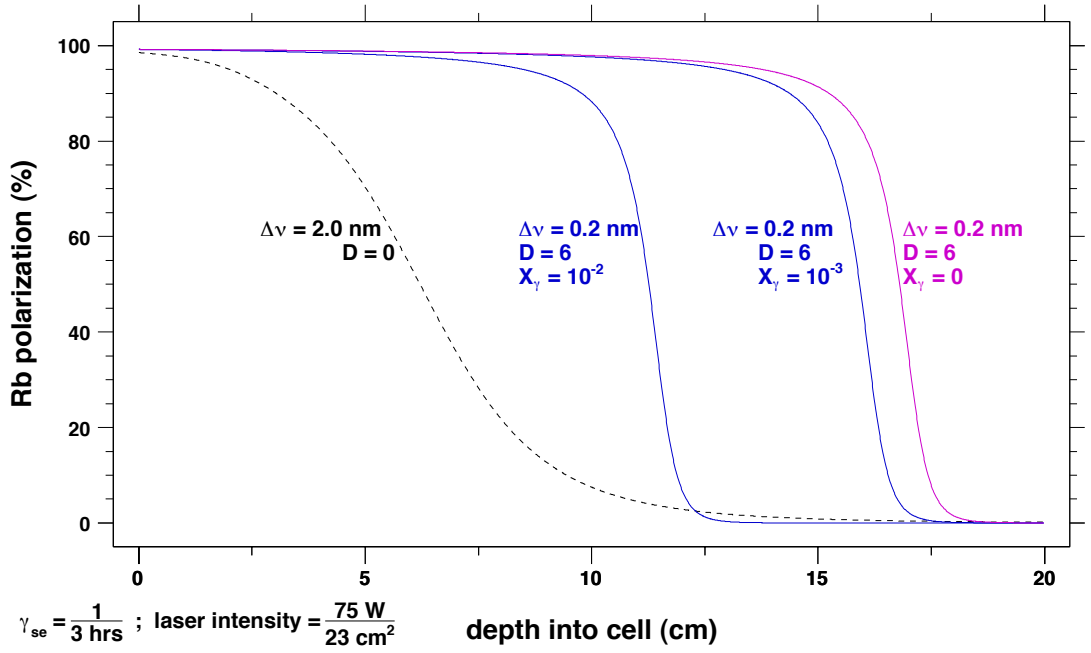

Figure 5.9: Alkali Polarization Profile with Imperfect Optical Pumping.

Alkali X-factors of this size are known to exist, which explains the relatively poor performance of pure Rb cell using broadband light. The combination of hybrid cells and narrowband pumping significanty reduce our sensitivity to these small imperfections, regardless of their origin.

5.5.4 Conclusion

There are several conclusions from the above discussion that are worth noting. First, the use of alkali-hybrid mixtures greatly improves the photon economy that can be achieved. Regarding the question of narrowband versus broadband lasers, it is tempting to believe that , if money were no object, broadband lasers could do as well as narrowband lasers if sufficient laser power were used. Unfortunately, even in the absence of the various effects summarized in Tab. (5.3), there will still

be unwanted off resonant pumping that limits the maximum alkali polarization that can be achieved and that influences the optimal value for D. In fact, off resonant pumping associated with a given lasder sourece, limits somewhat the maximum alkali polarization that can be achieved. This is even true for a laser with an arbitrarily narrow spectral profile. It is worth noting, however, that these effects can be reduced by polarizing the ^{3}He at lower pressures where broadening is reduced.

There are, however, important effects in addition to off resonant pumping that result in what are effectively alkali X-factors. They include hyperfine interactions in the excited states, radiation trapping, skew pumping, and the other phenomenona listed in Sec. (5.4.6). These effects like off resonant pumping limit the maximum alkali polarization that can be achieved regardless of the laser power employed. The addition of more N_2 (quenching gas) can reduce some of these effects, but in eletron scattering, this is generally not an acceptable solution.

It is natural to ask whether there are further large gains to be had based on the lessons learned here. Sodium, for instance, is even more efficient at transferring polarization to the ^{3}He nuclei than either K or Rb, see Fig. (5.10). It is the case, however, that Na would need to be run at higher temperatures, see Tab. (5.8), where some of the other alkali spin relaxation mechanisms are greatly aggravated. The benefits of Na-Rb SEOP probably require more study as do other potential hybrid alkali mixtures.

Given the benefits of additioanl quenchnig gas, it might be interesteing to explore the use of H_2 instead of N_2 . The cross section for quenching is about 10 times smaller [34], but, because it is 14 times lighter than N_2 , the quenching rate is only 3 times smaller than N_2 for the same density. Using H_2 instead of N_2 could allow

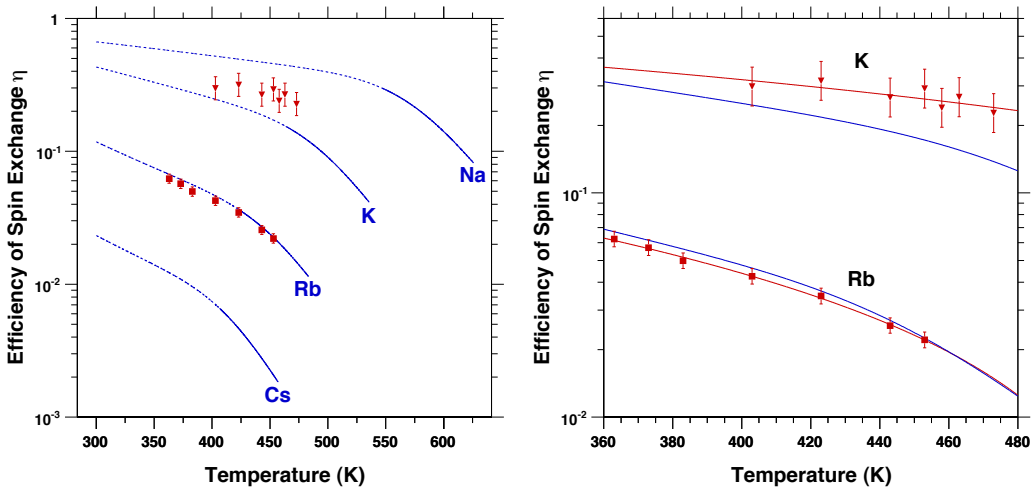

Figure 5.10: Spin Exchange Efficiency for Na, K, Rb, & Cs. The spin exchange efficiency is defined as the fraction of angular momentum that successfully transferred from the alkali atom to the ^{3}He nucleus: $1/\eta_A = 1 + (k_{sd}/k_{se}) + (k'_{sd}/k_{se})([A]/[^3He]) + (k''_{sd}/k_{se})([N_2]/[^3He])$. At low temperatures and alkali densities, it is approximately $k_{se}/(k_{se} + k_{sd})$. At high temperatures, it approaches $k_{se}[^3He]/(k'_{sd}[A])$. The blue lines are calculated from the values in Tab. (**??**). The red data points are from [69]. In the left figure, the solid blue lines represent an alkali density range of $(10^{14}$ to $10^{15})/cm^3$. In the right figure, the red line is a parameterization of the data given by $\eta_K(T) = 0.756 - 0.00109T$ and $\eta_{Rb}(T) = 0.337 - 0.00102T(1 - 0.0007T)$.

parameter	**Na**	**K**	**Rb**	**Cs**	**units**
λ_{D1} (air)	589.6	769.9	794.8	894.3	nm
spin orbit splitting	5.2E+02	1.7E+03	7.1E+03	1.7E+04	GHz
naive X_α^{D2} (2.0 nm)	1.1E+01	3.7E–02	1.6E–03	2.6E–04	
naive X_α^{D2} (0.2 nm)	9.0E–02	5.7E–03	3.6E–04	7.8E–05	
$k_{se}^{-1}/(10^{15}/cm^3)$	5.86	5.39	4.12	2.51	hrs
$[A]_3$ for $\gamma_{se}^{-1} = 3$ hrs	1.95	1.80	1.37	0.84	$10^{15}/cm^3$
T_3 for $[A]_3$	634.3	537.6	483.5	453.2	K
$\sigma_{sd}^A/\sigma_{se}^A$	5.5E–05	8.1E–05	5.7E–04	1.1E–02	
k_{He}/k_{se} at T_3	0.31	5.2	33	155	
X_{ani}	0.16	0.057	0.046	0.026	

Table 5.8: Basic Alkali Parameters for SEOP.

us to, for example, increase the quenching rate by a factor of 10 thereby suppressing the alkali X-factors associated with excited state by a factor of 10, while only doubling the dilution factor. H_2 has the disadvantage that it reacts (albeit slowly) with the alkali metal to form hydrides. It is certainly intriging to look at the huge gains that have been made in SEOP and ask the quection of what can be done to further advance th technique.

Bibliography

[1] Thad G. Walker and William Happer. Spin-exchange optical pumping of noble-gas nuclei. *Rev. Mod. Phys.*, 69(2):629–642, Apr 1997.

[2] E. Babcock, et al. Limits to the polarization for spin-exchange optical pumping of ^{3}he. *Phys. Rev. Lett.*, 96(8):083003, 2006.

[3] Young, A.R. and Appelt, S. and Baranga, A. Ben-Amar and Erickson, C. and Happer, W. Three-dimensional imaging of spin polarization of alkali-metal vapor in optical pumping cells. *Applied Physics Letters*, 70:3081–3083, 1997.

[4] A. Ben-Amar Baranga, S. Appelt, C. J. Erickson, A. R. Young, and W. Happer. Alkali-metal-atom polarization imaging in high-pressure optical-pumping cells. *Phys. Rev. A*, 58(3):2282–2294, Sep 1998.

[5] S. Appelt, T. Unlu, K. Zilles, N. J. Shah, S. Baer-Lang, and H. Halling. Experimental studies of rubidium absolute polarization at high temperatures. *Applied Physics Letters*, 75(3):427–429, 1999.

[6] William Happer, Gordon D. Cates, Jr., Mikhail V. Romalis, and Christopher J Erickson. *U.S. Patent No. 6,318,092*, 2001.

[7] Earl Babcock, Ian Nelson, Steve Kadlecek, Bastiaan Driehuys, L.W. Anderson, F.W. Hersman, and Thad G. Walker. Hybrid Spin-Exchange Optical Pumping of He. *Physical Review Letters*, 91(12):123003, 2003.

[8] C. C. Bouchiat, M. A. Bouchiat, and L. C. L. Pottier. Evidence for Rb-Rare-Gas Molecules from the Relaxation of Polarized Rb Atoms in a Rare Gas. Theory. *Phys. Rev.*, 181(1):144–165, May 1969.

[9] M. A. Bouchiat, J. Brossel, and L. C. Pottier. Evidence for Rb-Rare-Gas Molecules from the Relaxation of Polarized Rb Atoms in a Rare Gas. Experimental Results. *The Journal of Chemical Physics*, 56(7):3703–3714, 1972.

[10] Françoise Masnou-Seeuws and Marie-Anne Bouchiat. Étude théorique de la relaxation d'atomes alcalins par collisions sur une paroi et sur un gaz". *J. Phys. France*, 28(5), 1967.

[11] S. Appelt, A. Ben-Amar Baranga, C. J. Erickson, M. V. Romalis, A. R. Young, and W. Happer. Theory of spin-exchange optical pumping of ^{3}He and ^{129}Xe. *Phys. Rev. A*, 58(2):1412–1439, Aug 1998.

[12] ALFRED KASTLER. Optical Methods of Atomic Orientation and of Magnetic Resonance. *J. Opt. Soc. Am.*, 47(6):460–465, 1957.

[13] Robert L. de Zafra. Optical Pumping. *American Journal of Physics*, 28(7):646–654, 1960.

[14] Arnold L. Bloom. Optical pumping. *Scientific American*, 203:72–80, Oct. 1960.

[15] G. V. Skrotskii and T. G. Izyumova. OPTICAL ORIENTATION OF ATOMS AND ITS APPLICATIONS. *SOV PHYS USPEKHI*, 4(2):177–204, 1961.

[16] Jay R. Singer, editor. *Advances in Quantum Electronics, Proceedings of the Second International Conference on Quantum Electronics (Berkeley 1961)*. Columbia University Press, 1961.

[17] Thomas R. Carver. Optical Pumping. *Science*, 141(3581):599–608, 1963.

[18] Reuben Benumof. Optical Pumping Theory and Experiments. *American Journal of Physics*, 33(2):151–160, 1965.

[19] Robert Bernheim. *Optical Pumping: An Introduction*. W. A. Benjamin, New York, 1965.

[20] Claude Cohen-Tannaoudji and Alfred Kastler. Optical pumping. In E. Wolf, editor, *Progress in Optics*, volume 5, pages 1–81. North-Holland Publishing Company, Amsterdam, 1966.

[21] F. G. Major. Optical pumping. In B. Bederson and Wade L. Fite, editors, *Methods of Experimental Physics: Atom and Electron Physics, Atomic Interactions, Part B*, volume 7, pages 1–28. Academic Press, New York, 1968.

[22] W. Happer. Optical pumping theory. In Sydney Geltman, Kalayana T. Mahanthappa, and Wesley E. Brittin, editors, *Atomic Collision Processes (Lectures in Theoretical Physics, Boulder Summer Institute 1968)*, volume XI-C, pages 273–315. Gordon and Breach Science Publishers, New York, 1969.

[23] G. W. Series. Optical pumping and related topics. In S. M. Kay and A. Maitland, editors, *Quantum Optics (Scottish Universitites Summer School in Physics 1969)*, volume 10, pages 395–482. Academic Press, London, 1970.

[24] William Happer. Optical Pumping. *Rev. Mod. Phys.*, 44(2):169–249, Apr 1972.

[25] L. C. Balling. Optical pumping. In D. W. Goodwin, editor, *Advances in Quantum Electronics*, volume 3, pages 1–167. Academic Press, 1975.

[26] G. W. Series. Thirty years of optical pumping. *Contemporary Physics*, 22(5):487–509, 1981.

[27] Happer, W. and Van Wijngaarden, W. A. An optical pumping primer. *Hyperfine Interactions*, 38(1–4):435–470, Dec 1987.

[28] R. J. Knize, Z. Wu, and W. Happer. Optical Pumping and Spin Exchange in Gas Cells. In Sir David Bates and Benjamin Bederson, editors, *Advances in Atomic and Molecular Physics*, volume 24, pages 223–267. Academic Press, 1988.

[29] A. Sieradzan and F. A. Franz. Quenching, depolarization, and transfer of spin polarization in rb-N_2 collisions. *Phys. Rev. A*, 25(6):2985–2995, Jun 1982.

[30] F. A. Franz, R. Boggy, and C. E. Sooriamoorthi. Relative transition probabilities in deexcitation of atomic states by collisional quenching: Cs $6p122 \rightarrow 6s122$. *Phys. Rev. A*, 11(1):1–9, Jan 1975.

[31] J. Fricke, J. Haas, E. Lüscher, and F. A. Franz. Cross sections for excited-state mixing in cesium-noble-gas collisions from $d2$ optical pumping. *Phys. Rev.*, 163(1):45–53, Nov 1967.

[32] N. D. Bhaskar, M. Hou, B. Suleman, and W. Happer. Propagating, optical-pumping wave fronts. *Phys. Rev. Lett.*, 43(7):519–521, Aug 1979.

[33] B. Chann, E. Babcock, L. W. Anderson, and T. G. Walker. Skew light propagation in optically thick optical pumping cells. *Phys. Rev. A*, 66(3):033406, Sep 2002.

[34] L. Krause. Sensitized fluorescence and quenching. In J. Wm. McGowan, editor, *Advances in Chemical Physics, Vol. XXVIII: The Excited State in Ch¿¿¿emical Physics*. Interscience, New York, 1975.

[35] L. Krause. Collisional excitation transfer between the2p$\frac{1}{2}$and2p3/2levels in alkali atoms. *Appl. Opt.*, 5(9):1375–1382, 1966.

[36] M. Movre S. Knezovic, C. Vadla. Fine structure excitation transfer between the potassium 4^2P states induced by collisions with caesium atoms. *Zeitschrift fr Physik D*, 22:449–450, 1992.

[37] M. Movre K. Neimax V. Horvatic, C. Vadla. The collision cross sections for the fine-structure mixing of caesium 6P levels induced by collisions with potassium atoms. *Zeitschrift fr Physik D*, 36:101–104, 1996.

[38] Brian Timothy Saam. *Pulse-NMR studies of spin relaxation relevant to laser-polarized noble gases*. PhD thesis, Princeton University, 1996.

[39] Indrajit Saha, Panayiotis Nikolaou, Nicholas Whiting, and Boyd M. Goodson. Characterization of violet emission from Rb optical pumping cells used in laser-polarized xenon NMR experiments. *Chemical Physics Letters*, 428(4-6):268 – 276, 2006.

[40] M. Elbel. Energy and polarization transfer. In W. Hanle and H. Kleinpoppen, editors, *Progress in Atomic Spectroscopy: Part B*. Plenum Press, New York, 1979.

[41] Andreas F. Molisch and Bernhard P. Oehry. *Radiation trapping in atomic vapours*. Oxford University Press, Oxford, 1998.

[42] T. Holstein. Imprisonment of Resonance Radiation in Gases. *Phys. Rev.*, 72(12):1212–1233, Dec 1947.

[43] D. Tupa, L. W. Anderson, D. L. Huber, and J. E. Lawler. Effect of radiation trapping on the polarization of an optically pumped alkali-metal vapor. *Phys. Rev. A*, 33(2):1045–1051, Feb 1986.

[44] D. Tupa and L. W. Anderson. Effect of radiation trapping on the polarization of an optically pumped alkali-metal vapor in a weak magnetic field. *Phys. Rev. A*, 36(5):2142–2147, Sep 1987.

[45] M. A. Rosenberry, J. P. Reyes, D. Tupa, and T. J. Gay. Radiation trapping in rubidium optical pumping at low buffer-gas pressures. *Phys. Rev. A*, 75(2):023401, Feb 2007.

[46] Alan Corney. *Atomic and laser spectroscopy*. Oxford University Press, Oxford, 1978.

[47] Thad Walker (Private Communication).

[48] W. Happer, E. Miron, S. Schaefer, D. Schreiber, W. A. van Wijngaarden, and X. Zeng. Polarization of the nuclear spins of noble-gas atoms by spin exchange with optically pumped alkali-metal atoms. *Phys. Rev. A*, 29(6):3092–3110, Jun 1984.

[49] N. D. Bhaskar, J. Camparo, W. Happer, and A. Sharma. Light narrowing of magnetic resonance lines in dense, optically pumped alkali-metal vapor. *Phys. Rev. A*, 23(6):3048–3064, Jun 1981.

[50] R. Walkup, B. Stewart, and D. E. Pritchard. Collisional line broadening due to van der waals potentials. *Phys. Rev. A*, 29(1):169–173, Jan 1984.

[51] R. J. Wells. Rapid approximation to the voigt/faddeeva function and its derivatives. *Journal of Quantitative Spectroscopy and Radiative Transfer*, 62(1):29 – 48, 1999.

[52] M. V. Romalis, E. Miron, and G. D. Cates. Pressure broadening of Rb D_1 and D_2 lines by ^{3}He, 4He, N_2, and Xe: Line cores and near wings. *Phys. Rev. A*, 56(6):4569–4578, Dec 1997.

[53] K. Hirano, K. Enomoto, M. Kumakura, Y. Takahashi, and T. Yabuzaki. Emission spectra of $rb * hen$ exciplexes in a cold 4*he* gas. *Phys. Rev. A*, 68(1):012722, Jul 2003.

[54] J. F. Sell, M. A. Gearba, B. M. Patterson, T. Genda, B. Naumann, and R. J. Knize. Enhancement of rb fine-structure transfer in 4he due to three-body collisions. *Opt. Lett.*, 35(13):2146–2148, 2010.

[55] B. Chann, et al. Production of highly polarized ^{3}He using spectrally narrowed diode laser array bars. *J. Appl. Phys.*, 94(10):6908–6914, 2003.

[56] Earl V. Babcock. *Spin-Exchange Optical Pumping with Alkali-Metal Vapors*. PhD thesis, University of Wisconsin-Madison, 2005.

[57] E. Babcock, S. Boag, M. Becker, W. C. Chen, T. E. Chupp, T. R. Gentile, G. L. Jones, A. K. Petukhov, T. Soldner, and T. G. Walker. Effects of high-flux neutron beams on ^{3}He cells polarized in situ with spin-exchange optical pumping. *Phys. Rev. A*, 80(3):033414, Sep 2009.

[58] J F Kielkopf. Measurement of the width, shift and asymmetry of the sodium D lines broadened by noble gases. *Journal of Physics B: Atomic and Molecular Physics*, 13(19):3813–3821, 1980.

[59] N. Lwin, D. G. McCartan, and E. L. Lewis. The Determination of Collision Damping Constants. *Astrophysical Journal*, 213:599–606, April 1977.

[60] A. H. Couture, T. B. Clegg, and B. Driehuys. Pressure shifts and broadening of the Cs D_1 and D_2 lines by He, N_2, and Xe at densities used for optical pumping and spin exchange polarization. *Journal of Applied Physics*, 104(9):094912, 2008.

[61] Kramida A.E. Reader J. Ralchenko, Yu. and NIST ASD Team (2008). Nist atomic spectra database (version 3.1.5), [online]. available: http://physics.nist.gov/asd3 [2010, may 17]. *National Institute of Standards and Technology, Gaithersburg, MD.*

[62] D F T Mullamphy, G Peach, V Venturi, I B Whittingham, and S J Gibson. Collisional broadening of alkali doublets by helium perturbers. *Journal of Physics B: Atomic, Molecular and Optical Physics*, 40(6):1141–1152, 2007.

[63] D. K. Walter, W. M. Griffith, and W. Happer. Magnetic Slowing Down of Spin Relaxation due to Binary Collisions of Alkali-Metal Atoms with Buffer-Gas Atoms. *Phys. Rev. Lett.*, 88(9):093004, Feb 2002.

[64] P. I. Borel, L. V. Søgaard, W. E. Svendsen, and N. Andersen. Spin-exchange and spin-destruction rates for the ^{3}He-Na system. *Phys. Rev. A*, 67(6):062705, Jun 2003.

[65] R. J. Knize. Spin destruction in rubidium-rubidium and potassium-potassium collisions. *Phys. Rev. A*, 40(11):6219–6222, Dec 1989.

[66] Stephen John Kadlecek. *Spin Relaxation in Alkali Vapors*. PhD thesis, University of Wisconsin-Madison, 1999.

[67] B. Larson, O. Häusser, P. P. J. Delheij, D. M. Whittal, and D. Thiessen. Optical pumping of Rb in the presence of high-pressure ^{3}He buffer gas. *Phys. Rev. A*, 44(5):3108–3118, Sep 1991.

[68] M. E. Wagshul and T. E. Chupp. Laser optical pumping of high-density Rb in polarized ^{3}He targets. *Phys. Rev. A*, 49(5):3854–3869, May 1994.

[69] A. Ben-Amar Baranga, S. Appelt, M. V. Romalis, C. J. Erickson, A. R. Young, G. D. Cates, and W. Happer. Polarization of ^{3}He by Spin Exchange with Optically Pumped Rb and K Vapors. *Phys. Rev. Lett.*, 80(13):2801–2804, Mar 1998.

[70] N. D. Bhaskar, J. Pietras, J. Camparo, W. Happer, and J. Liran. Spin Destruction in Collisions between Cesium Atoms. *Phys. Rev. Lett.*, 44(14):930–933, Apr 1980.

[71] Thad G. Walker. Estimates of spin-exchange parameters for alkali-metal–noble-gas pairs. *Phys. Rev. A*, 40(9):4959–4964, Nov 1989.

[72] D. K. Walter, W. Happer, and T. G. Walker. Estimates of the relative magnitudes of the isotropic and anisotropic magnetic-dipole hyperfine interactions in alkali-metal–noble-gas systems. *Phys. Rev. A*, 58(5):3642–3653, Nov 1998.

[73] T. V. Tscherbul, P. Zhang, H. R. Sadeghpour, and A. Dalgarno. Collision-induced spin exchange of alkali-metal atoms with ^{3}He: An ab initio study. *Physical Review A (Atomic, Molecular, and Optical Physics)*, 79(6):062707, 2009.

[74] Guodong Wang. *Polarizing He-3 by spin exchange with potassium*. PhD thesis, California Institute of Technology, 2004.

[75] K.P. Coulter, A.B. McDonald, W. Happer, T.E. Chupp, and M.E. Wagshul. Neutron polarization with polarized ^{3}He. *Nuclear Instruments and Methods in Physics Research Section A: Accelerators, Spectrometers, Detectors and Associated Equipment*, 270(1):90 – 94, 1988.

[76] B. Chann, E. Babcock, L. W. Anderson, and T. G. Walker. Measurements of ^{3}He spin-exchange rates. *Phys. Rev. A*, 66(3):032703, Sep 2002.

[77] Thad G. Walker, Joseph H. Thywissen, and William Happer. Spin-rotation interaction of alkali-metal–He-atom pairs. *Phys. Rev. A*, 56(3):2090–2094, Sep 1997.

[78] F. A. Franz and C. Volk. Electronic spin relaxation of the $4S_{1/2}$ state of K induced by K-He and K-Ne collisions. *Phys. Rev. A*, 26(1):85–92, Jul 1982.

[79] T. G. Walker, I. A. Nelson, and S. Kadlecek. Method for deducing anisotropic spin-exchange rates. *Phys. Rev. A*, 81(3):032709, Mar 2010.

[80] F. A. Franz and C. Volk. Spin relaxation of rubidium atoms in sudden and quasimolecular collisions with light-noble-gas atoms. *Phys. Rev. A*, 14(5):1711–1728, Nov 1976.

[81] Daniel Karl Walter. *Optical Probes of Angular Momentum and Energy Transport in Spin-Exchange Optical ¿¿¿Pumping Systems*. PhD thesis, Princeton Univeristy, 2002.

[82] F. A. Franz and C. E. Sooriamoorthi. Spin relaxation within the $6P_{1/2}$ and $6S_{1/2}$ states of cesium measured by white-light optical pumping. *Phys. Rev. A*, 10(1):126–140, Jul 1974.

[83] N. Beverini, P. Minguzzi, and F. Strumia. Foreign-Gas-Induced Cesium Hyperfine Relaxation. *Phys. Rev. A*, 4(2):550–555, Aug 1971.

[84] Stephen Kadlecek, L. W. Anderson, and Thad Walker. Measurement of potassium-potassium spin relaxation cross sections. *Nuclear Instruments and Methods in Physics Research Section A: Accelerators, Spectrometers, Detectors and Associated Equipment*, 402(2-3):208 – 211, 1998. Proceedings of the 7th RCNP International Workshop on Polarized He Beams and Gas Targets and Their Application.

[85] Jacques Vanier, Jean-F. Simard, and Jean-S. Boulanger. Relaxation and frequency shifts in the ground state of Rb-85. *Phys. Rev. A*, 9(3):1031–1040, Mar 1974.

Chapter 6

^{3}He Polarization Dynamics in Target Cells

6.1 Polarization Dynamics

6.1.1 Nuclei Number Rate Equations

A cell is composed of a pumping and target chamber that are connected by a transfer tube, see Fig. (6.1). In Sec. (6.4.2), we will consider in more detail the polarization dynamics within the transfer tube; however, for now, we will simply ignore the small transfer tube volume. The ^{3}He nuclei in the pumping chamber are polarized via spin-exchange collisions with polarized alkali atoms with a rate constant k_{se}, see Sec. (D.3.1). The ^{3}He nuclei in the target chamber are polarized via transfer through the transfer tube. Because of the low alkali vapor pressure in the target chamber, we will ignore the spin exchange with alkali atoms in the target chamber. The number of ^{3}He nuclei is $N^{\pm}_{pc,tc}$ where the superscript $\pm$ labels the spin state and the subscript labels the chamber. Similarly the total number of ^{3}He nuclei

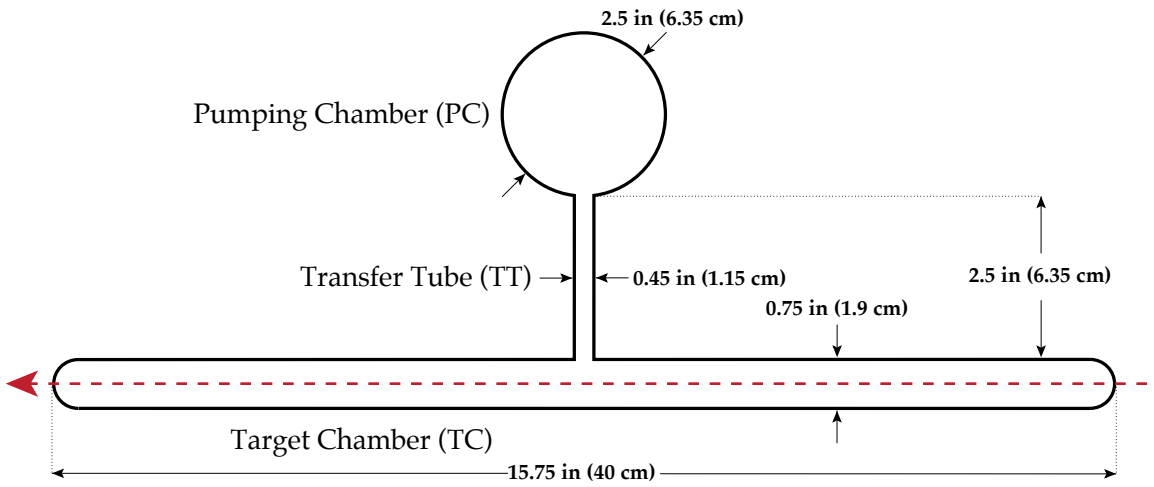

Figure 6.1: Basic Geometry of a "Standard" Small Pumping Chamber Cell. Drawn to 5:2 scale with nominal outer dimensions. Dashed red line represents path of electron beam.

in a given chamber is $N_{\mathrm{pc,tc}}\left(=N^{+}_{\mathrm{pc,tc}}+N^{-}_{\mathrm{pc,tc}}\right)$. Consequently the total number of ^{3}He nuclei is $N\left(=N_{\mathrm{pc}}+N_{\mathrm{tc}}\right)$ and the fraction of ^{3}He nuclei in either chamber is $f_{\mathrm{pc,tc}}\left(=N_{\mathrm{pc,tc}}/N\right)$.

Assuming that the alkali polarization reaches equilibrium very quickly and remains constant while the ^{3}He polarization approaches equilibrium, the rate of change of the number of $\pm$ nuclei in either chamber is governed by the following equations:

$$\begin{aligned}
\frac{dN^{+}_{\mathrm{pc}}}{dt} &= k_{\mathrm{se}}[A^{+}]N^{-}_{\mathrm{pc}}-k_{\mathrm{se}}[A^{-}]N^{+}_{\mathrm{pc}}+\left(\frac{N_{\mathrm{pc}}}{2}-N^{+}_{\mathrm{pc}}\right)\Gamma_{\mathrm{pc}}+N^{+}_{\mathrm{tc}}d_{\mathrm{tc}}-N^{+}_{\mathrm{pc}}d_{\mathrm{pc}}\\
\frac{dN^{-}_{\mathrm{pc}}}{dt} &= k_{\mathrm{se}}[A^{-}]N^{+}_{\mathrm{pc}}-k_{\mathrm{se}}[A^{+}]N^{-}_{\mathrm{pc}}+\left(\frac{N_{\mathrm{pc}}}{2}-N^{-}_{\mathrm{pc}}\right)\Gamma_{\mathrm{pc}}+N^{-}_{\mathrm{tc}}d_{\mathrm{tc}}-N^{-}_{\mathrm{pc}}d_{\mathrm{pc}}\\
\frac{dN^{+}_{\mathrm{tc}}}{dt} &= N^{+}_{\mathrm{pc}}d_{\mathrm{pc}}-N^{+}_{\mathrm{tc}}d_{\mathrm{tc}}+\left(\frac{N_{\mathrm{tc}}}{2}-N^{+}_{\mathrm{tc}}\right)\Gamma_{\mathrm{tc}}\\
\frac{dN^{-}_{\mathrm{tc}}}{dt} &= N^{-}_{\mathrm{pc}}d_{\mathrm{pc}}-N^{-}_{\mathrm{tc}}d_{\mathrm{tc}}+\left(\frac{N_{\mathrm{tc}}}{2}-N^{-}_{\mathrm{tc}}\right)\Gamma_{\mathrm{tc}}
\end{aligned} \tag{6.1}$$

where $[A^{\pm}]$ is the alkali number density in the pumping chamber for the $\pm$ spin state. The spin-relaxation rates per nucleus $\Gamma_{\mathrm{pc,tc}}$ represent interactions which show no preference for either state and therefore push equilibrium towards equal numbers of $\pm$ nuclei. The transfer rate $d_{\mathrm{tc(pc)}}$ is the probability per unit time per nucleus that a nucleus will exit the target (pumping) chamber and enter the pumping (target) chamber, where we have neglected the transfer tube volume. Alternatively, one could define $d_{\mathrm{tc(pc)}}$ as the fraction of particles in the target (pumping) chamber that transfer out per unit time.

6.1.2 Total Nuclei Number Equilibrium

The rates of change of the total number of nuclei in the two chambers are given by:

$$\begin{aligned} \frac{dN_{\rm pc}}{dt} &= \frac{dN^{+}_{\rm pc}}{dt} + \frac{dN^{-}_{\rm pc}}{dt} = N_{\rm tc}d_{\rm tc} - N_{\rm pc}d_{\rm pc} \\ \frac{dN_{\rm tc}}{dt} &= \frac{dN^{+}_{\rm tc}}{dt} + \frac{dN^{-}_{\rm tc}}{dt} = N_{\rm pc}d_{\rm pc} - N_{\rm tc}d_{\rm tc} \\ \frac{dN}{dt} &= \frac{dN_{\rm pc}}{dt} + \frac{dN_{\rm tc}}{dt} = 0 \end{aligned} \tag{6.2}$$

When the total number of nuclei in either chamber reaches equilibrium, the total transfer rates into and out of each chamber must balance:

$$N_{\rm tc}d_{\rm tc} = N_{\rm pc}d_{\rm pc} \quad \rightarrow \quad f_{\rm tc}d_{\rm tc} = f_{\rm pc}d_{\rm pc} \tag{6.3}$$

Equilibrium in this regard is achieved when the temperature of the two chambers has stabilized and when the pressure throughout the cell is constant. To estimate how long if takes for the pressure to equalize throughout the cell, we'll look at two limits. The slow limit is found by calculating the finite one dimensional diffusion time scale:

$$\tau \approx \frac{L^2_{\rm tt}}{\pi^2 D} \approx 20 \text{ sec} \tag{6.4}$$

where $L_{\rm tt}$ is the transfer tube length and $D \approx 0.2$ cm^2/s is the ^{3}He diffusion constant under operating conditions.

The fast limit is found by applying Poiseuille's equation for viscous incompressible flow through a tube due to a pressure differential [1]:

$$\frac{d}{dt}\left(\rho_{\rm pc}V_{\rm pc}\right) = -\frac{A^2_{\rm tt}}{8\pi\eta L_{\rm tt}}\left(p_{\rm pc} - p_{\rm tc}\right) \tag{6.5}$$

where ρ_{pc} is the mass density of the ^{3}He in the pumping chamber, V_{pc} is the pumping chamber volume, A_{tt} is the cross sectional area of the transfer tube, η is the viscosity, p_{pc} is the pumping chamber pressure, and p_{tc} is the target chamber pressure. We'll assume that the temperature in the pumping chamber is instantaneously changed to its operating value. Consequently the pressure in the pumping chamber is initially higher than the pressure in the target chamber. The change in the mass flow rate from the pumping chamber can be rewritten as:

$$\frac{d}{dt}\left(\rho_{pc}V_{pc}\right) = \frac{d}{dt}\left(\text{M.W.} \times \frac{p_{pc}V_{pc}}{RT_{pc}}\right) \tag{6.6}$$

where M.W. is the molecular weight of ^{3}He and R is the ideal gas constant. Using the fact the total number of particles in the cell is constant, we can rewrite the pressure in the target chamber in terms of the pressure in the pumping chamber:

$$p_{tc} = n_{tc}RT_{tc} = \left(N - N_{pc}\right)\frac{RT_{tc}}{V_{tc}} = \frac{V_{pc}}{V_{tc}}\frac{T_{tc}}{T_{pc}}\left(N - N_{pc}\right)\frac{RT_{pc}}{V_{pc}} = \frac{v}{t}\left(\frac{NRT_{pc}}{V_{pc}} - p_{pc}\right) \tag{6.7}$$

where v and t are the pumping chamber to target chamber ratios of the volumes and temperatures, respectively. Putting this altogether we get:

$$\frac{d}{dt}\left(\text{M.W.} \times \frac{p_{pc}V_{pc}}{RT_{pc}}\right) = -\frac{A_{tt}^2}{8\pi\eta L_{tt}}\left[p_{pc} - \frac{v}{t}\left(\frac{NRT_{pc}}{V_{pc}} - p_{pc}\right)\right] \tag{6.8}$$

which can be rewritten as:

$$\frac{dp_{pc}}{dt} = \frac{p_{pc}^{\infty} - p_{pc}}{\tau} \tag{6.9}$$

where the time constant τ and equilibrium pressure $p_{\rm pc}^{\infty}$ are given as:

$$\tau = \frac{8\pi\eta L_{\rm tt} \times \text{M.W.} \times V_{\rm pc} f_{\rm tc}}{A_{\rm tt}^2 R T_{\rm pc}} \quad \& \quad p_{\rm pc}^{\infty} = \frac{f_{\rm pc} N R T_{\rm pc}}{V_{\rm pc}} \tag{6.10}$$

To calculate τ, we have estimated the viscosity $\eta \approx D$ by using the diffusion constant D which is reasonable for a mono-atomic gas [2]. Therefore the fast limit for the pressure equilibration time scale is about 0.3 μsec.

Finally, we estimate how long it takes for the temperature of the glass wall of the pumping chamber to equilibrate. Once again using the finite one dimensional diffusion timescale [3]:

$$\tau \approx \frac{t_{\rm pc}^2}{\pi^2 D_g} = \frac{t_{\rm pc}^2 C_p^g \rho_g}{\pi^2 k_g} \approx 2 \text{ sec} \tag{6.11}$$

where we have the following values for the thermal conductivity of glass $k_g = 1$ W/m/K [4], the heat capacity of glass $C_p^g = 1$ J/g/K, the density of glass $\rho_g = 2.5$ g/cm^3, and the thickness of the pumping chamber $t_{\rm pc} = 3$ mm. All of these time estimates indicate that the cell temperature & pressure equilibrate very quickly compared to the polarization timescale. In reality, the main factor that determines how quickly the cell reaches thermal equilibrium are the time scales related to the forced air oven heater feedback system, which can be several minutes.

6.1.3 Polarization Rate Equations

Polarization for any spin-1/2 particle is defined as:

$$P_{\rm pc,tc} = \frac{N_{\rm pc,tc}^{+} - N_{\rm pc,tc}^{-}}{N_{\rm pc,tc}^{+} + N_{\rm pc,tc}^{-}} = \frac{N_{\rm pc,tc}^{+} - N_{\rm pc,tc}^{-}}{N_{\rm pc,tc}} = f_{\rm pc,tc}^{+} - f_{\rm pc,tc}^{-} \tag{6.12}$$

Combining the nuclei number rate Eqns. (6.1) in the manner defined above, noting the following relationships:

$$f^{\pm}_{\mathrm{pc,tc}} = \frac{1}{2}\left(1 \pm P_{\mathrm{pc,tc}}\right) \qquad f_{\mathrm{pc,tc}} = f^{+}_{\mathrm{pc,tc}} + f^{-}_{\mathrm{pc,tc}} \qquad 1 = f_{\mathrm{pc}} + f_{\mathrm{tc}} \tag{6.13}$$

and, to reiterate, assuming that the alkali polarization reaches equilibrium very quickly and remains constant during the ^{3}He polarization build-up, the polarizations in the two chambers of the cell are given by:

$$\begin{aligned} \frac{dP_{\mathrm{pc}}}{dt} &= \gamma_{\mathrm{se}}\left(P_A - P_{\mathrm{pc}}\right) - \Gamma_{\mathrm{pc}}P_{\mathrm{pc}} - d_{\mathrm{pc}}P_{\mathrm{pc}} + \left(\frac{d_{\mathrm{tc}}N_{\mathrm{tc}}}{N_{\mathrm{pc}}}\right)P_{\mathrm{tc}} \\ \frac{dP_{\mathrm{tc}}}{dt} &= \left(\frac{d_{\mathrm{pc}}N_{\mathrm{pc}}}{N_{\mathrm{tc}}}\right)P_{\mathrm{pc}} - d_{\mathrm{tc}}P_{\mathrm{tc}} - \Gamma_{\mathrm{tc}}P_{\mathrm{tc}} \end{aligned} \tag{6.14}$$

where $\gamma_{\mathrm{se}}\,(= k_{\mathrm{se}}[A])$ is the spin-exchange rate per nucleus and P_A is the pumping chamber volume averaged equilibrium alkali polarization. If we assume that the total nuclei number in each chamber has reached equilibrium before the polarization process is initiated (i.e. the cell is brought to operating temperature before the lasers are turned on), then we can take advantage of the relationship defined by Eqn. (6.3) to give the following:

$$\frac{dP_{\mathrm{pc}}}{dt} = \gamma_{\mathrm{se}}\left(P_A - P_{\mathrm{pc}}\right) - \Gamma_{\mathrm{pc}}P_{\mathrm{pc}} - d_{\mathrm{pc}}\left(P_{\mathrm{pc}} - P_{\mathrm{tc}}\right) = aP_{\mathrm{pc}} + bP_{\mathrm{tc}} + B \tag{6.15}$$

$$\frac{dP_{\mathrm{tc}}}{dt} = d_{\mathrm{tc}}\left(P_{\mathrm{pc}} - P_{\mathrm{tc}}\right) - \Gamma_{\mathrm{tc}}P_{\mathrm{tc}} = cP_{\mathrm{pc}} + dP_{\mathrm{tc}} \tag{6.16}$$

where the following substitutions are made:

$$a = -\left(\gamma_{\mathrm{se}} + \Gamma_{\mathrm{pc}} + d_{\mathrm{pc}}\right) \qquad b = d_{\mathrm{pc}} \qquad c = d_{\mathrm{tc}} \qquad d = -\left(\Gamma_{\mathrm{tc}} + d_{\mathrm{tc}}\right) \qquad B = \gamma_{\mathrm{se}}P_A \tag{6.17}$$

The coupled rate equations can be rewritten as a matrix equation:

$$\frac{d}{dt}\begin{bmatrix} P_{pc} \\ P_{tc} \end{bmatrix} = \begin{bmatrix} a & b \\ c & d \end{bmatrix}\begin{bmatrix} P_{pc} \\ P_{tc} \end{bmatrix} + \begin{bmatrix} B \\ 0 \end{bmatrix} \quad \rightarrow \quad \frac{d\vec{P}}{dt} = \mathbf{M}\vec{P} + \vec{B} \tag{6.18}$$

6.1.4 Analytic Solution to Polarization Rate Equations

Eqn. (6.18) is solved by finding the eigenvalues of the rate matrix **M**. These eigenvalues:

$$\Gamma_{\pm} = -\frac{1}{2}\left[a + d \pm \sqrt{(a-d)^2 + 4bc}\right] \tag{6.19}$$

are the characteristic rates of the system and, as will be explained shortly, are labeled slow and fast:

$$\Gamma_s = \frac{1}{2}\left[d_{pc}+d_{tc}+\gamma_{se}+\Gamma_{pc}+\Gamma_{tc}-\left(d_{pc}+d_{tc}\right)\sqrt{1-2\left(f_{pc}-f_{tc}\right)u+u^2}\right] \tag{6.20}$$

$$\Gamma_f = d_{pc} + d_{tc} + \gamma_{se} + \Gamma_{pc} + \Gamma_{tc} - \Gamma_s \tag{6.21}$$

and u is given by:

$$u = \frac{\gamma_{se} + \Gamma_{pc} - \Gamma_{tc}}{d_{pc} + d_{tc}} = \frac{\text{difference in the total rates between the two chambers}}{\text{sum of the transfer rates}} \tag{6.22}$$

These rates can be written as:

$$\Gamma_s = \langle\gamma_{se}\rangle + \langle\Gamma\rangle - \delta\Gamma \tag{6.23}$$

$$\Gamma_f = \left(d_{pc} + d_{tc}\right) + \left(\gamma_{se} - \langle\gamma_{se}\rangle\right) + \left(\Gamma_{pc} + \Gamma_{tc} - \langle\Gamma\rangle\right) + \delta\Gamma \tag{6.24}$$

where again we have made use of Eqn. (6.3) in the form of:

$$\frac{d_{\rm pc}-d_{\rm tc}}{d_{\rm pc}+d_{\rm tc}}=\frac{d_{\rm tc}\left(\frac{f_{\rm tc}}{f_{\rm pc}}\right)-d_{\rm tc}}{d_{\rm tc}\left(\frac{f_{\rm tc}}{f_{\rm pc}}\right)+d_{\rm tc}}=\frac{f_{\rm tc}-f_{\rm pc}}{f_{\rm tc}+f_{\rm pc}}=f_{\rm tc}-f_{\rm pc} \tag{6.25}$$

and we have defined the following quantities:

$$\begin{aligned}
\langle\gamma_{\rm se}\rangle &\equiv \gamma_{\rm se}f_{\rm pc} && (6.26)\\
\langle\Gamma\rangle &\equiv \Gamma_{\rm pc}f_{\rm pc}+\Gamma_{\rm tc}f_{\rm tc} && (6.27)\\
\delta\Gamma &\equiv \frac{d_{\rm pc}+d_{\rm tc}}{2}\left[\sqrt{1-2\left(f_{\rm pc}-f_{\rm tc}\right)u+u^2}-1+\left(f_{\rm pc}-f_{\rm tc}\right)u\right] && (6.28)\\
&\approx f_{\rm pc}f_{\rm tc}\frac{\left(\gamma_{\rm se}+\Gamma_{\rm pc}-\Gamma_{\rm tc}\right)^2}{d_{\rm pc}+d_{\rm tc}}+O\left(\frac{\left(\gamma_{\rm se}+\Gamma_{\rm pc}-\Gamma_{\rm tc}\right)^3}{\left(d_{\rm pc}+d_{\rm tc}\right)^2}\right) && (6.29)
\end{aligned}$$

where the brackets $\langle\cdots\rangle$ refer to an average over all nuclei. Note that the correction term $\delta\Gamma$ is small and consequently $\Gamma_{\rm s}=\langle\gamma_{\rm se}\rangle+\langle\Gamma\rangle$ is a very good approximation when:

1. The transfer rates are the fastest rates in the cell, $d_{\rm pc},d_{\rm tc}\gg\gamma_{\rm se},\Gamma_{\rm pc},\Gamma_{\rm tc}$.

2. The difference in the total rates of the pumping chamber and target chamber is small, $\gamma_{\rm se}+\Gamma_{\rm pc}\approx\Gamma_{\rm tc}$.

Both of these scenarios are true during the spindown of a long lifetime cell ($>$ 40 hrs). Fig. (6.2) depicts the slow and fast time constants (note that a time constant is defined to be the inverse rate, $\tau\equiv 1/\gamma$) to different orders for two cell types.

The solutions to the coupled rate equations are given by:

$$\begin{aligned}
P_{\rm pc}(t) &= P_{\rm pc}^{\infty}+\left[P_{\rm pc}^{0}-P_{\rm pc}^{\infty}-c_{\rm pc}\right]\exp\left(-\Gamma_{\rm s}t\right)+c_{\rm pc}\exp\left(-\Gamma_{\rm f}t\right) && (6.30)\\
P_{\rm tc}(t) &= P_{\rm tc}^{\infty}+\left[P_{\rm tc}^{0}-P_{\rm tc}^{\infty}-c_{\rm tc}\right]\exp\left(-\Gamma_{\rm s}t\right)+c_{\rm tc}\exp\left(-\Gamma_{\rm f}t\right) && (6.31)
\end{aligned}$$

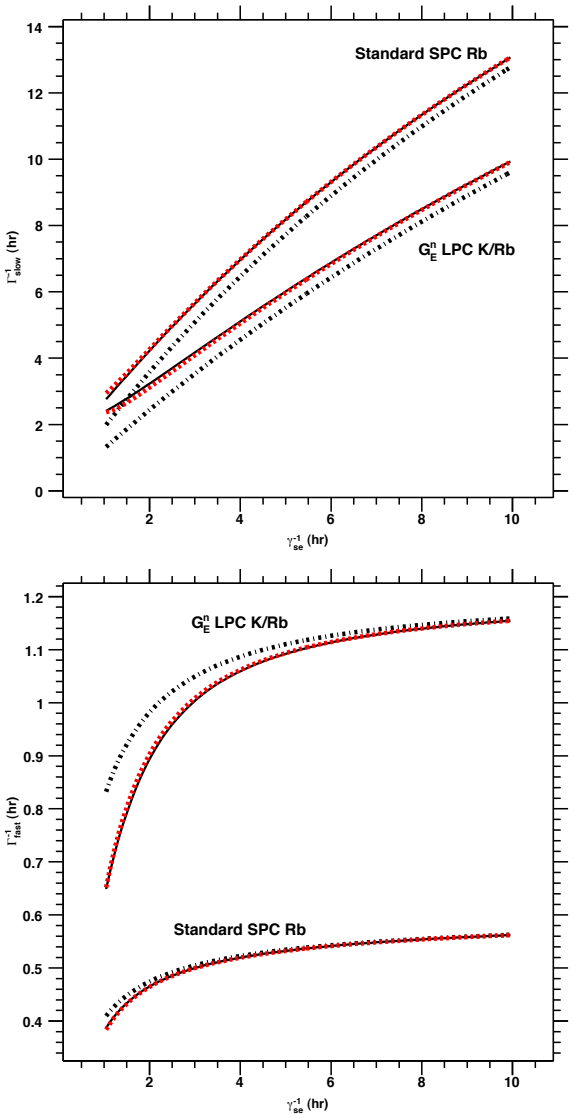

Figure 6.2: Slow (upper) and Fast (lower) Time Constants for Two Chambered Cells. Time constants (inverse rates) are plotted as a function of the spin-exchange time constant (γ_{se}^{-1}). Leading order (dotted black), next to leading order (dashed red), and full (solid black) calculations are depicted. The next to leading order (dashed red) is nearly identical to the full calculation (solid black). A typical "Standard SPC Rb" cell has dimensions $L_{tt} = 6$ cm & $V_{pc} = 90$ cc and contains pure Rb; whereas a typical "G_E^n LPC K/Rb" cell has dimensions $L_{tt} = 9$ cm & $V_{pc} = 310$ cc and contains a hybrid mix of mostly K and some Rb. The observed spin-up time constant, which is essentially Γ_s^{-1}, is always longer than the spin-exchange time constant. In addition, the spin-up time constants for the two different cells converge for sufficiently fast spin exchange.

where $P^0_{\rm pc,tc}$ are set by the initial conditions and the equilibrium ($t \to \infty$) polarizations are found by setting the rate equations to zero:

$$P^\infty_{\rm pc} = \frac{Bd}{bc - ad} \qquad \& \qquad P^\infty_{\rm tc} = -\left(\frac{c}{d}\right) P^\infty_{\rm pc} \tag{6.32}$$

The above can be written in a more illuminating form by using Eqn. (6.3) and after some algebra:

$$P^\infty_{\rm pc} = P_A \left[\frac{\gamma_{\rm se} f_{\rm pc}}{\gamma_{\rm se} f_{\rm pc} + \Gamma_{\rm pc} f_{\rm pc} + \Gamma_{\rm tc} f_{\rm tc} \left(1 + \frac{\Gamma_{\rm tc}}{d_{\rm tc}}\right)^{-1}} \right] \tag{6.33}$$

$$P^\infty_{\rm tc} = P^\infty_{\rm pc} \left[1 + \frac{\Gamma_{\rm tc}}{d_{\rm tc}}\right]^{-1} \tag{6.34}$$

Finally, the coefficients $c_{\rm pc,tc}$ can be obtained by satisfying the coupled rate equations and after some algebra:

$$c_{\rm pc} = \frac{\Gamma_{\rm s}\left(P^\infty_{\rm pc} - P^0_{\rm pc}\right) - bP^0_{\rm tc} - aP^0_{\rm pc} - B}{\Gamma_{\rm f} - \Gamma_{\rm s}} \tag{6.35}$$

$$c_{\rm tc} = \frac{\Gamma_{\rm s}\left(P^\infty_{\rm tc} - P^0_{\rm tc}\right) - dP^0_{\rm tc} - cP^0_{\rm pc}}{\Gamma_{\rm f} - \Gamma_{\rm s}} \tag{6.36}$$

These can be written in terms of the rates themselves:

$$\frac{c_{\rm pc}}{c_{\rm scale}} = f_{\rm tc}\left(P^0_{\rm pc} - P^0_{\rm tc}\right) + \frac{\Gamma_{\rm s}\left(P^\infty_{\rm pc} - P^0_{\rm pc}\right) + \gamma_{\rm se}\left(P^0_{\rm pc} - P_A\right) + \Gamma_{\rm pc}P^0_{\rm pc}}{d_{\rm pc} + d_{\rm tc}} \tag{6.37}$$

$$\frac{c_{\rm tc}}{c_{\rm scale}} = f_{\rm pc}\left(P^0_{\rm tc} - P^0_{\rm pc}\right) + \frac{\Gamma_{\rm s}\left(P^\infty_{\rm tc} - P^0_{\rm tc}\right) + \Gamma_{\rm tc}P^0_{\rm tc}}{d_{\rm pc} + d_{\rm tc}} \tag{6.38}$$

$$c_{\rm scale} = 1 + \frac{\gamma_{\rm se} + \Gamma_{\rm pc} + \Gamma_{\rm tc} - 2\Gamma_{\rm s}}{d_{\rm pc} + d_{\rm tc}} \tag{6.39}$$

6.1.5 Time Evolution Near $t = 0$

Near $t = 0$ when $t\Gamma_f \ll 1$, we can Taylor expand the exponentials to second order:

$$\begin{aligned} P_{pc}(t) &= P_{pc}^{\infty} + \left[P_{pc}^{0} - P_{pc}^{\infty} - c_{pc}\right]\left[1 - \Gamma_s t + \frac{\Gamma_s^2}{2}t^2\right] + c_{pc}\left[1 - \Gamma_f t + \frac{\Gamma_f^2}{2}t^2\right] \\ &= P_{pc}^{0} + m_{pc}t + \frac{q_{pc}}{2}t^2 \qquad (6.40) \\ P_{tc}(t) &= P_{tc}^{\infty} + \left[P_{tc}^{0} - P_{tc}^{\infty} - c_{tc}\right]\left[1 - \Gamma_s t + \frac{\Gamma_s^2}{2}t^2\right] + c_{tc}\left[1 - \Gamma_f t + \frac{\Gamma_f^2}{2}t^2\right] \\ &= P_{tc}^{0} + m_{tc}t + \frac{q_{tc}}{2}t^2 \qquad (6.41) \end{aligned}$$

where the linear slopes are given by:

$$\begin{aligned} m_{pc} &= P_A\gamma_{se} - P_{pc}^{0}\left(\gamma_{se} + \Gamma_{pc}\right) + \left(P_{tc}^{0} - P_{pc}^{0}\right)d_{pc} \qquad (6.42) \\ m_{tc} &= -P_{tc}^{0}\Gamma_{tc} + \left(P_{pc}^{0} - P_{tc}^{0}\right)d_{tc} \qquad (6.43) \end{aligned}$$

and the quadratic slopes are given by:

$$\begin{aligned} q_{pc} &= \left(P_{pc}^{\infty} - P_{pc}^{0}\right)\Gamma_f\Gamma_s - \left(\Gamma_f + \Gamma_s\right)m_{pc} \qquad (6.44) \\ q_{tc} &= \left(P_{tc}^{\infty} - P_{tc}^{0}\right)\Gamma_f\Gamma_s - \left(\Gamma_f + \Gamma_s\right)m_{tc} \qquad (6.45) \end{aligned}$$

For the special case of zero initial polarization, $P_{pc}^{0} = P_{tc}^{0} = 0$:

$$\begin{aligned} P_{pc}(t) &= \gamma_{se}P_A\left[1 - \frac{t}{2}\left(\gamma_{se} + \Gamma_{pc} + d_{pc}\right)\right]t \qquad (6.46) \\ P_{tc}(t) &= \gamma_{se}P_A\left(\frac{d_{tc}}{2}\right)t^2 \qquad (6.47) \end{aligned}$$

6.1.6 Fast Transfer Limit

In the limit the transfer rates approach infinity, $d_{\mathrm{pc,tc}} \to \infty$, the rates, equilibrium polarizations, and coefficients become:

$$\Gamma_{\mathrm{f}} \to \infty \tag{6.48}$$

$$\Gamma_{\mathrm{s}} \to \langle\gamma_{\mathrm{se}}\rangle + \langle\Gamma\rangle \tag{6.49}$$

$$P_{\mathrm{pc}}^{\infty} \to P_A\left[\frac{\gamma_{\mathrm{se}} f_{\mathrm{pc}}}{\gamma_{\mathrm{se}} f_{\mathrm{pc}} + \Gamma_{\mathrm{pc}} f_{\mathrm{pc}} + \Gamma_{\mathrm{tc}} f_{\mathrm{tc}}}\right] = P_A\left[\frac{\langle\gamma_{\mathrm{se}}\rangle}{\langle\gamma_{\mathrm{se}}\rangle + \langle\Gamma\rangle}\right] = \frac{f_{\mathrm{pc}}\gamma_{\mathrm{se}} P_A}{\Gamma_{\mathrm{s}}} \tag{6.50}$$

$$P_{\mathrm{tc}}^{\infty} \to P_{\mathrm{pc}}^{\infty} \tag{6.51}$$

$$c_{\mathrm{pc}} \to f_{\mathrm{tc}}\left(P_{\mathrm{pc}}^{0} - P_{\mathrm{tc}}^{0}\right) \tag{6.52}$$

$$c_{\mathrm{tc}} \to f_{\mathrm{pc}}\left(P_{\mathrm{tc}}^{0} - P_{\mathrm{pc}}^{0}\right) \tag{6.53}$$

which gives for the polarizations in the two chambers:

$$\begin{aligned} P_{\mathrm{pc}}(t) = P_{\mathrm{tc}}(t) \to\ & P_{\mathrm{pc}}^{\infty} + \left[P_{\mathrm{pc}}^{0} f_{\mathrm{pc}} + P_{\mathrm{tc}}^{0} f_{\mathrm{tc}} - P_{\mathrm{pc}}^{\infty}\right]\exp\left(-\Gamma_{\mathrm{s}} t\right) \\ & = P^{\infty}\left[1 - \exp\left(-\Gamma_{\mathrm{s}} t\right)\right] + \left\langle P^{0}\right\rangle \exp\left(-\Gamma_{\mathrm{s}} t\right) \end{aligned} \tag{6.54}$$

After the fast exponential has decayed away, the polarization in the two chambers evolves identically as if the initial polarization in the two chambers had been a volume of average of the true initial polarizations in the two chambers.

Near $t = 0$ when $t\Gamma_{\mathrm{s}} \ll 1$, we can Taylor expand the exponential to second order:

$$P(t) = P^{\infty} + \left[\left\langle P^{0}\right\rangle - P^{\infty}\right]\left[1 - \Gamma_{\mathrm{s}} t + \frac{\Gamma_{\mathrm{s}}^{2}}{2} t^{2}\right] \tag{6.55}$$

$$= \left\langle P^{0}\right\rangle + \left[f_{\mathrm{pc}}\gamma_{\mathrm{se}} P_A - \Gamma_{\mathrm{s}}\left\langle P^{0}\right\rangle\right] t\left(1 - \frac{\Gamma_{\mathrm{s}}}{2} t\right) \tag{6.56}$$

6.2 Relaxation Mechanisms

In this section, we discuss the various relaxation mechanisms that contribute to Γ_{pc} and Γ_{tc}. Although the wall relaxation can make the dominant contribution these relaxation rates, not much is known the their origin. As a practical matter, an empiracally determined procedure has been developed to reduce wall relaxation rates to a level that are tolerable. The most imporant and ultimately limiting relaxation mechanism is the X-factor, which is discussed in the next section.

6.2.1 The X-Factor

The Wisconsin & NIST groups have determined [5] that there is a relaxation mechanism that appears to be proportional to the spin exchange rate γ_{se}. Becasue this mechanism scale with γ_{se}, it can not be "turned off" by increasing γ_{se} and therefore limits the ^{3}He polarization. The relaxation rate associated with the X-factor can be written in the following way:

$$\Gamma_x = X\gamma_{se} = \left[X_0 + X_1\left(\frac{S}{V}\right)\right]\gamma_{se} \tag{6.57}$$

where X is the X-factor and X_0 (X_1) is the part of X that is independant (dependant) on the surface to volume ratio S/V. This could mean that this mechanism is due to collisions with alkali atoms, has a temperature dependance that roughly follows that alkali metal vapor pressure curve, or some combination of the two.

Based on the data presented in [5], we can make the following statements. For smaller values of S/V (e.g. larger spheres), X is on average smaller and the variations in X are smaller. For larger values of S/V (e.g. smaller spheres), X is on

average larger and the variations in X are larger. The preceding two statements can be quantified and collapsed into the following inequality:

$$\approx 0.1 \leq X \leq (0.4 \text{ cm}) \left(\frac{S}{V} \right) \tag{6.58}$$

This inequality implies that $X_0 \approx 0.1$ and $X_1 \approx 0.4$ cm. For $S/V \approx 2.5/\text{cm}$ or, equivalently, for a sphere with a ≈ 9.5 in diameter, the contribution from X_0 equals the contribututon from X_1.

The lower limit of the inequality, namely X_0, is intriguing since it suggests a more fundamental limit to the ^{3}He polarization. One obvious mechanism for $X_0 \neq 0$ is anisotropic spin exchange between the alkali atom and ^{3}He nucleus. To understand the origin of anisotropic spin exchange, its useful to recall the Hamiltonian that describes the interaction between two dipoles $\vec{\mu}_1$ & $\vec{\mu}_2$ separated by a displacement $\vec{r}$ [6]:

$$\mathcal{H}_{\text{dip}} = -\frac{\mu_0}{4\pi} \left[\left(\frac{8\pi}{3} \delta(\vec{r}) - \frac{1}{|\vec{r}|^3} \right) \vec{\mu}_1 \cdot \vec{\mu}_2 + \frac{3(\vec{r} \cdot \vec{\mu}_1)(\vec{r} \cdot \vec{\mu}_2)}{|\vec{r}|^5} \right] \tag{6.59}$$

where μ_0 is the magnetic constant and $\delta(\vec{r})$ is a Dirac δ-function. The first term generates isotropic spin exchange that we're familiar with, whereas the second term generates anisotropic spin exchange.

Walter et al. have shown [7] that the anisotropic spin exchange from a fully polarized alkali atom to a ^{3}He nucleus tends to polarize the ^{3}He nucleus to $-1/2$. Furthermore, they calculated the effective X-factor due to this mechanism X_{ani} to be as high as 0.16 for Na and as low as 0.03 for Cs. The same calculation finds 0.06 for K and 0.05 for Rb. These theoretical values can only account for half of the observed X_0 for pure Rb and K-Rb hybrid mixtures.

Recently a method for experimentally determining X_{ani} has been suggested by Walker et al. [8]. The technique involves comparing the relaxation of the alkali metal in the presence of ^{3}He and ^{4}He. They've applied this method to K and found $X_0 = 0.11 \pm 0.13$. Although the uncertainty of this result is quite large, the central value is exactly what one would expect based on Eqn. (6.58). Both $X_0 \approx 0$ and $X_0 \approx 0.24$ are within 1σ of the central value, which implies that the limiting ^{3}He polarization is as low as 0.81. We note in passing that a ^{3}He polarzation greater than this value, to our knowledge, has never been reported.

6.2.2 Magnetic Field Gradients

The relaxation rate due to magnetic field inhomogeneities is given as [9,10]:

$$\Gamma_{\nabla B} = D\frac{\left|\vec{\nabla} B_t\right|^2}{B_z}\left(1+\omega^2\tau_c^2\right)^{-1} \tag{6.60}$$

where $D = 0.2$ cm^2/s is the diffusion constant, B_t is the transverse component of the magnetic field, B_z is the longitudinal component of the field, ω is the Larmor frequency associated with B_z, and $\tau_c \approx D/\bar{v}^2$ is the mean time between collisions. This equation indicates the transverse gradients (relative to the holding field) contributes to T_1. On the other hand, as discussed in Sec. (4.2), longitudinal gradients contribute to T_2, see Eqn. (4.26).

6.2.3 Spin Relaxation Due to Nuclear Dipolar Interactions

The theoretical minimum spin-relaxation rate is due to a direct coupling between two nearby ^{3}He nuclei. Newbury et al. [11] have calculated this ^{3}He -^{3}He nuclear

dipolar spin-relaxation rate per nucleus at 23 ^{o}C:

$$\Gamma_{\text{dip}} = \frac{\left[{}^{3}\text{He}\right]}{(744\ \text{amg} \cdot \text{hrs})} \tag{6.61}$$

This rate decreases with increasing temperature, see Sec. (D.5.1) for a parameterization of the temperature dependence.

6.3 Relaxation Associated with the Beam

6.3.1 Basic Mechanism of Beam Depolarization

Ionizing radiation increases the nuclear spin relaxation in the target chamber. Also known as "beam depolarization," it is essentially a two step process. First, the beam ionizes an ^{3}He atom which results in an free electron and an atomic ion $^{3}\text{He}^{+}$. There is also the possibility that the atomic ion bonds with an neutral ^{3}He atom to form an molecular ion $^{3}\text{He}_{2}^{+}$. Second, interactions with ^{3}He ions induce ^{3}He nuclear spin flips. Therefore, the total relaxation rate due to ionization by the

beam is given by:

$$
\begin{aligned}
\Gamma_{\text{beam}} &= \left[\begin{array}{c}\text{ionization rate}\\ \text{per target chamber atom}\end{array}\right] \cdot \left[\begin{array}{c}\text{mean number of nuclear spin flips}\\ \text{per atomic ion}\end{array}\right] \\
&= \left[\left(\begin{array}{c}\text{electrons}\\ \text{per unit time}\end{array}\right) \cdot \left(\begin{array}{c}\text{atomic ions created}\\ \text{per electron}\end{array}\right) \cdot (\text{atoms in tc})^{-1}\right] \cdot (n_a + n_m) \\
&= \left[\left(\frac{I}{e}\right) \cdot \left(\frac{\text{total energy lost}}{\text{mean energy per ion}}\right) \cdot \left(\frac{1}{V_{\text{tc}}[\text{He}]_{\text{tc}}}\right)\right] \cdot (n_a + n_m) \\
&= \left[\left(\frac{I}{e}\right) \cdot \left(\frac{\left[\frac{1}{\rho}\frac{dE}{dx}\right] L_{\text{tc}}[\text{He}]_{\text{tc}}}{E_i}\right) \cdot \left(\frac{1}{V_{\text{tc}}[\text{He}]_{\text{tc}}}\right)\right] \cdot (n_a + n_m) \\
&= \left(\frac{I}{e}\frac{1}{E_i}\left[\frac{1}{\rho}\frac{dE}{dx}\right]\frac{1}{A_{\text{tc}}}\right) \cdot (n_a + n_m) \\
&= \Gamma_{\text{ion}} \cdot (n_a + n_m) \qquad (6.62)
\end{aligned}
$$

where I is the electron beam current, E_i is the mean energy for ion-electron pair creation, A_{tc} is the mean cross sectional area of the target chamber, Γ_{ion} is the ionization rate per ^{3}He atom in the target chamber, and n_a & n_m are the average number of spins lost per atomic ion created due to interactions with atomic & molecular ions respectively.

6.3.2 Beam Energy Lost to Ionizing Interactions

The electron beam loses energy to ionizing collisions and to radiation in the form of bremsstrahlung. For the electron energies relevant to JLab, the dominant mode of energy loss is bremsstrahlung, see Fig. 6.3). We will show, however, that the dominant mode of *ionization* is collisional energy loss. The energy lost to collisions per unit density per unit length is given by the celebrated Bethe-Bloch formula

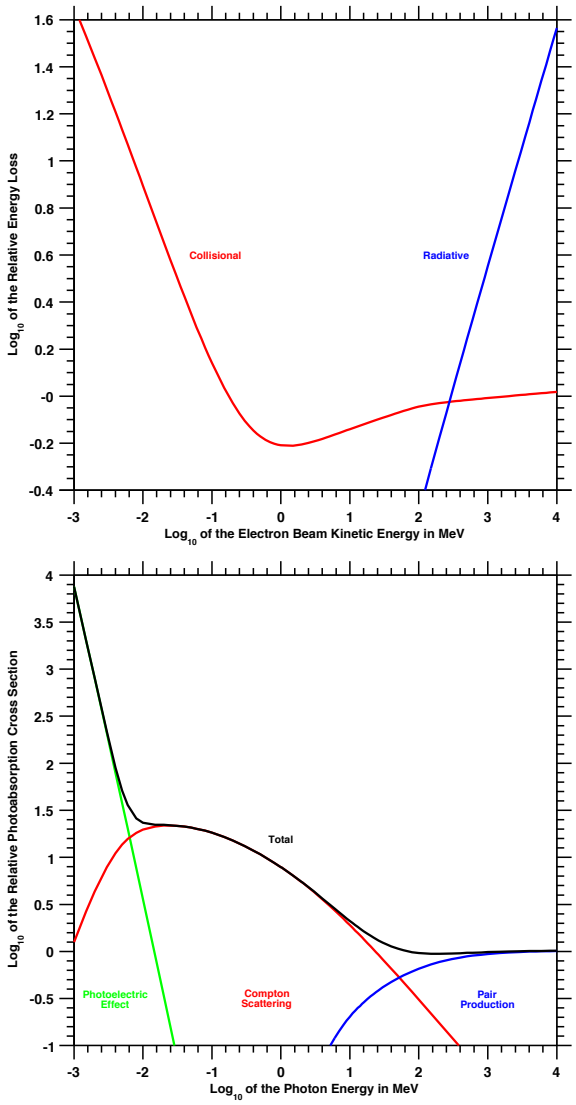

Figure 6.3: Upper: Relative Energy Loss to Collisions and to Radiation for Electrons in Helium gas at 1 atm and 20 °C. Energy loss is relative to the collisional energy loss for an electron beam energy of 2 GeV. Data is from NIST-ESTAR [12]. Lower: Relative Photoabsorption Cross Sections in Helium. Cross section is relative to the total photoabsorption cross section of a 2 GeV photon. Data is from NIST-XCOM [13].

and, for an electron beam, it is [14]:

$$\left[\frac{1}{\rho}\frac{dE}{dx}\right]_{\rm c} = 2\pi r_{\rm e}^2 m_{\rm e}c^2 \frac{Z}{\beta^2}\left[\log\left([\gamma-1]^2[\gamma+1]\right) - \delta + 2\log\left(\frac{m_{\rm e}c^2}{I_{\rm BB}}\right) - F(\gamma) - 2\frac{C_s}{Z}\right] \tag{6.63}$$

$$2\pi r_{\rm e}^2 m_{\rm e}c^2 = 6.85\,{\rm eV/amagat/cm} \tag{6.64}$$

$$F(\gamma) = \left[1+\frac{2}{\gamma}-\frac{1}{\gamma^2}\right]\log(2) - \frac{1}{8}\left[1-\frac{1}{\gamma}\right]^2 - \frac{1}{\gamma^2} \tag{6.65}$$

$$\gamma = \frac{1}{\sqrt{1-\beta^2}} = \frac{E_{\rm beam}}{m_{\rm e}c^2} \tag{6.66}$$

where Z is the target atomic number, $\beta(=v/c)$ is the electron velocity relative to the speed of light, $I_{\rm BB}$ is the mean excitation potential of the target material, δ is the density correction, and C_s is the shell correction. The shell correction is significant only when the incident electron velocity is roughly equal to or slower than the bound electron orbital velocity. For JLab beam energies, this is not the case; therefore the shell correction will be neglected ($C_s = 0$). The density correction δ is given by [14, 15]:

$$\delta(Y) = \left\{\begin{array}{ll} \delta_0 \exp\left[2\left(Y - Y_0'\right)\right] & Y \le Y_0' \\ 2\left(Y - Y_a'\right) + \left[\delta_0 - 2\left(Y_0' - Y_a'\right)\right]\left[\frac{Y_1'-Y}{Y_1'-Y_0'}\right]^m & Y_0' < Y \le Y_1' \\ 2\left(Y - Y_a'\right) & Y_1' < Y \end{array}\right\} \tag{6.67}$$

$$Y = \log\left(\beta\gamma\right) \tag{6.68}$$

$$Y_{a,0,1}' = Y_{a,0,1} - \log\sqrt{[{\rm N}]/[{\rm N}]_0} \tag{6.69}$$

where Y_a, Y_0, Y_1, m, and $[{\rm N}]_0$ depend on the target material at 1 atm & 20 °C and for ^{3}He are listed in Tab. (6.1).

For a ^{3}He density of 8.3 amg or higher, the equivalent beam energy for $Y = Y_1'$ is 700 MeV or less. Therefore for typical ^{3}He experiments at JLab, the density

parameter	value	comments
Z	2	atomic number
$I_{\rm BB}$	41.8 eV	mean excitation potential
C_s	0	for shell correction
δ_0	0	for density correction (1 atm & 20 $^{\rm o}$C)
Y_a	5.5697	
Y_0	5.0696	
Y_1	8.3174	
m	5.8347	
$[{\rm N}]_0$	0.93141 amg	

Table 6.1: Bethe-Bloch Formula Parameters for Electron-Helium Interactions. All values taken from [15].

correction is:

$$\delta(Y) = 2\log(\beta\gamma) - 2Y_a + \log\left([{\rm N}]/[{\rm N}]_0\right) \tag{6.70}$$

Plugging this into Eqn. (6.63) for ^{3}He :

$$\left[\frac{1}{\rho}\frac{dE}{dx}\right]_{\rm c} = \frac{4\pi r_{\rm e}^2 m_{\rm e}c^2}{\beta^2}\left[\log\left(\frac{[\gamma-1]^2[\gamma+1]}{[\beta\gamma]^2}\right) + 2Y_a - \log\left(\frac{[{\rm N}]}{[{\rm N}]_0}\right) + 2\log\left(\frac{m_{\rm e}c^2}{I_{\rm BB}}\right) - F(\gamma)\right] \tag{6.71}$$

and noting that for JLab beam energies $\geq$ 700 MeV:

$$\beta \approx 1 \quad \& \quad \gamma \gg 1 \tag{6.72}$$

$$\log\left(\frac{[\gamma-1]^2[\gamma+1]}{[\beta\gamma]^2}\right) \approx \log(\gamma) = \log\left(\frac{E_{\rm beam}}{m_{\rm e}c^2}\right) \tag{6.73}$$

$$F(\gamma) \approx \log(2) - \frac{1}{8} \tag{6.74}$$

we get:

$$\left[\frac{1}{\rho}\frac{dE}{dx}\right]_{\mathrm{c}} = 4\pi r_{\mathrm{e}}^2 m_{\mathrm{e}} c^2 \left[\log\left(\frac{E_{\mathrm{beam}}}{m_{\mathrm{e}}c^2}\right) + 2Y_a - \log\left(\frac{[\mathrm{N}]}{[\mathrm{N}]_0}\right) + 2\log\left(\frac{m_{\mathrm{e}}c^2}{I_{\mathrm{BB}}}\right) - \log(2) + \frac{1}{8}\right] \tag{6.75}$$

$$= 4\pi r_{\mathrm{e}}^2 m_{\mathrm{e}} c^2 \left[\log\left(\frac{E_{\mathrm{beam}}}{1\ \mathrm{GeV}}\right) - \log\left(\frac{[\mathrm{N}]}{10\ \mathrm{amg}}\right) + 34.6\right] \tag{6.76}$$

$$4\pi r_{\mathrm{e}}^2 m_{\mathrm{e}} c^2 = 510\ \mathrm{keV}\cdot\mathrm{barn} = 13.70\ \mathrm{eV/amagat/cm} \tag{6.77}$$

Above electron beam energies of 700 MeV, the previous equation gives the energy loss due to collisions in helium to much better than one percent compared to the full formula Eqn. (6.63).

Collisional energy loss leads directly to ionization of atoms in the target material. On the other hand, energy loss to radiation ionizes atoms only if the emitted bremsstrahlung photons subsequently interact with the target atoms. To provide an upper limit for the ionization contribution from radiation, we assume the following:

1. The photoelectric effect, Compton scattering, and pair production can all result in ionization.

2. One rescattered/reabsorbed bremsstrahlung photon ionizes at most one atom.

3. Every photon must travel half the length of the target chamber before exiting.

The energy loss to radiation that contributes to ionization per unit density per unit length is given by:

$$\left[\frac{1}{\rho}\frac{dE}{dx}\right]_{\mathrm{ri}} = \left(\frac{\text{total energy lost to radiation}}{\text{per unit density per unit length}}\right)\cdot\left(\text{fraction of energy that ionizes}\right) \tag{6.78}$$

Bremsstrahlung can produce any number of photons with any energy such that the total energy does not exceed the energy of the incident electron. The probability that any of these photons subsequently ionizes depends on its energy; therefore, we must convolute the bremsstrahlung spectrum with the total photoabsorption cross section over all photon energies:

$$\left[\frac{1}{\rho}\frac{dE}{dx}\right]_{\text{ri}} = E\int_0^1 u\left[\frac{1}{\rho}\frac{d^2\Phi(u)}{du\cdot dx}\right]\langle f(u)\rangle\, du \tag{6.79}$$

where $u(=h\nu/E)$ (unitless) is the photon energy as a fraction of the electron energy, $d^2\Phi(u)/du/dx$ is the number of bremsstrahlung photons created per frequency bin per unit length, and $\langle f(u)\rangle$ is the average fraction of photons reabsorbed or rescattered:

$$\langle f(u)\rangle = 1-\exp\left(-\sigma_\gamma(u)[\text{He}]_{\text{tc}}L_{\text{tc}}/2\right) \tag{6.80}$$

In this case, we'll assume $[\text{He}]_{\text{tc}} = 10$ amg and $L_{\text{tc}} = 40$ cm.

Bethe and Heitler [16] have shown that the energy per frequency bin of the bremsstrahlung spectrum is roughly constant, see Fig. (6.4), and when the electron energy is so high that complete screening can be assumed, this constant is [17]:

$$\frac{1}{E}\left[\frac{1}{\rho}\frac{dE}{dx}\right]_{\text{rad}} = \Phi_{\text{rad}} \equiv \int_0^1 u\left[\frac{1}{\rho}\frac{d^2\Phi(u)}{du\cdot dx}\right]du = 4\alpha r_{\text{e}}^2\left(Z^2\left[L(Z)-f(Z\alpha)\right]+ZL'(Z)\right) \tag{6.81}$$

$$4\alpha r_{\text{e}}^2 = 2.318 \text{ millibarns} \tag{6.82}$$

where for Helium $L(2) = 4.79$, $f(2\alpha) = 2.56\times10^{-4}$, $L'(2) = 5.621$ and therefore $\Phi_{\text{rad}} = 70.47$ millibarns. This reduces the convolution integral to an integral over

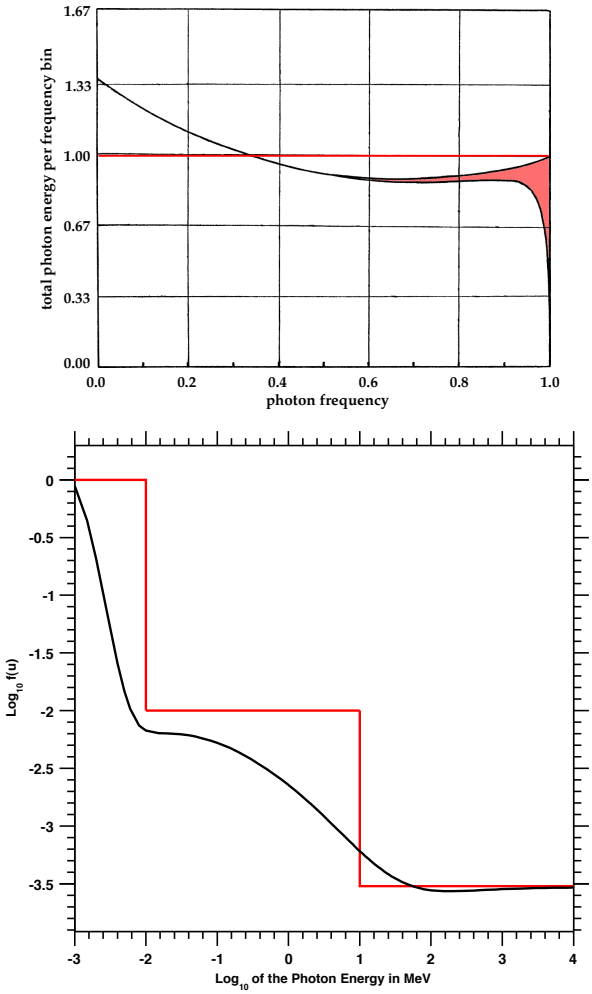

Figure 6.4: Upper: Bremsstrahlung Spectrum (adapted without permission from [16]). The horizontal axis is the photon frequency relative to the beam energy ($u = h\nu/E$). The vertical axis is the total photon energy per frequency bin normalized to the average value over all frequencies $\left(\frac{u}{\Phi_{\rm rad}}\left[\frac{1}{\rho}\frac{d^2\Phi(u)}{du\cdot dx}\right]\right)$. The lower bound of the pink shaded region corresponds to a beam energy of 500 MeV; while, the upper bound to the limit of infinite beam energy. In the convolution integral, Eqn. (6.79), this curve is taken to be independent of both u & $E_{\rm beam}$ and set equal to 1, which corresponds to the horizontal red line. Lower: Average Fraction of Bremsstrahlung Photons Absorbed as a Function of Photon Energy. The horizontal axis is the log base 10 of the photon energy in MeV. The vertical axis is the log base 10 of $\langle f(u)\rangle$ evaluated for a 10 amg/40 cm cell. The black curve is the true form of $\langle f(u)\rangle$ and the red curve is the rectangular approximation used for the integral Eqn. (6.84). In summary, the integral of Eqn. (6.79) is a convolution of the black curves in these two plots; whereas we approximate this integral by taking a convolution of the red curves in these plots.

$\langle f(u)\rangle$:

$$\left[\frac{1}{\rho}\frac{dE}{dx}\right]_{\text{ri}} \approx E\Phi_{\text{rad}}\int_0^1 \langle f(u)\rangle\, du = \left[\frac{1}{\rho}\frac{dE}{dx}\right]_{\text{rad}}\int_0^1 \langle f(u)\rangle\, du \tag{6.83}$$

To approximate this integral, we first note that small photon energies have large photoabsorption cross sections (see Fig. (6.3)) but represent a small frequency range in the bremsstrahlung spectrum. Therefore we separate $\langle f(u)\rangle$ into three rectangular frequency bins and find:

$$\begin{aligned}
\int_0^1 \langle f(u)\rangle\, du &\approx \sum_n u_n \langle f(u)\rangle_n = \frac{\left(10^{-2}\text{ MeV}\right)\cdot(1.00)}{E_{\text{beam}}} \\
&\quad + \frac{\left(10\text{ MeV } - 10^{-2}\text{ MeV}\right)\cdot(0.01)}{E_{\text{beam}}} \\
&\quad + \frac{\left(E_{\text{beam}} - 10\text{ MeV } - 10^{-2}\text{ MeV}\right)\cdot\left(3\times10^{-4}\right)}{E_{\text{beam}}} \\
&\approx \frac{0.01\text{ MeV}}{E_{\text{beam}}} + \frac{0.1\text{ MeV}}{E_{\text{beam}}} + 3\times10^{-4} \\
&\approx \frac{0.11\text{ MeV}}{E_{\text{beam}}} + 3\times10^{-4}
\end{aligned} \tag{6.84}$$

Using the above approximation for the integral in Eqn. (6.79) and dividing by the energy loss due to collisions gives the following estimate for the ratio:

$$\eta \equiv \frac{\left[\frac{1}{\rho}\frac{dE}{dx}\right]_{\text{ri}}}{\left[\frac{1}{\rho}\frac{dE}{dx}\right]_{\text{c}}} \approx \frac{0.015 + 0.042\cdot\left(\frac{E_{\text{beam}}}{1\text{ GeV}}\right)}{\log\left(\frac{E_{\text{beam}}}{1\text{ GeV}}\right) + 34.6} < 0.02 \text{ (for } E_{\text{beam}} \leq 16\text{ GeV)} \tag{6.85}$$

Even though the energy loss to radiation is about 3 to 30 times larger than the energy loss due to collisions at JLab energies, it contributes very little to the ionization.

6.3.3 Mean Energy for Helium Ion-Electron Pair Creation

The mean energy per ion-electron creation has been measured in helium a number of times, see Tab. (6.2). The early measurements found about 32 eV per pair. As later authors noted on more than one occasion [18–21], these early measurements were performed on insufficiently pure helium samples. Later measurements, which took great care to purify the helium sample, obtained results about 10 eV per pair higher. We need to know the value for pure He because we are interested in knowing how many He ions are created. Consequently, we use a weighted average of five "modern" measurements that went to great lengths to purify their He sample. As a side note, the mean energy per ion-electron creation E_i is entirely different than the mean excitation potential I_{BB}. It is merely a coincidence that they have nearly the same value for He. We are finally in a position to calculate the mean ionization rate per atom:

$$\Gamma_{\text{ion}} = \left(\frac{1}{eE_i} \left[\frac{1}{\rho} \frac{dE}{dx} \right]_{\text{c}} \right) \frac{I}{A_{\text{tc}}} = \beta \frac{I}{A_{\text{tc}}} \tag{6.86}$$

where e is the elementary charge, I is the beam current, A_{tc} is the mean cross sectional area of the target chamber, and β^{-1} is tabulated in Tab. (6.3) for various beam energies. The dependence of β on the beam energy is soft; consequently the mean ionization rate per atom within 5 percent over all JLab energies is:

$$\Gamma_{\text{ion}} = \left(0.0095 \, \frac{\text{cm}^2}{\mu\text{A} \cdot \text{hr}} \right) \frac{I}{A_{\text{tc}}} = \left(\frac{1}{21 \text{ hrs}} \right) \cdot \left(\frac{I}{10 \, \mu\text{A}} \right) \cdot \left(\frac{2.0 \text{ cm}^2}{A_{\text{tc}}} \right) \tag{6.87}$$

E_i(eV)	year	comments	ref.
26.2	1925	purified in charcoal at liquid air temps, possible double ionization of He?	[22]
31	1927	purified in charcoal at liquid air temperatures	[23]
31.0	1944	value listed in [24] and [25]	[26]
29.9	1951	tank He at 99.95% purity with traces amounts of N_2 and O_2	[27]
30.9	1952	cited in [19, 28]	[29]
(32.5 ± 0.5)	1952	$He/Ar/CH_4$ mixture	[30]
29.7	1952	He with 0.13% Ar	[18]
41.3		purified with charcoal at liquid air temperatures	
(26.0 ± 1.6)	1953	was purified, but not pure enough?	[31]
$(42.7 \pm 0.2)^*$	1953	purified with charcoal at liquid air temperatures	[19]
33.8	1954	tank He with less than 0.02% N_2	[32]
$(44.2 \pm 0.9)^*$	1954	purified with Ca-Mg chips at 470°C	[28]
$(46.0 \pm 0.5)^*$	1954	two sets of He samples with different purification methods	[20]
$(42.3 \pm 0.3)^*$	1955	purified with charcoal at liquid air temperatures	[33]
$(40.3 \pm 0.8)^*$	1956	purified with charcoal at liquid air temperatures	[34]
55,60 (±5%)	1957	used He-ethylene mix, but applied an "impurity" correction	[35]
29.9/35.2	1954	theoretical calculation for impure He sample	[21]
41.1		theoretical calculation for pure He	
42.7,42.3	1964	sensitivity to impurities discussed, but no original sources listed	[36]
41	1994		[14]
		$E_i(\text{weighted mean}) = (43.2 \pm 0.1)\,\text{eV}$	

Table 6.2: Mean Energy per Ion-e^- Pair Creation in He Gas. Only measurements performed on carefully purified samples (*) are used in the calculation of the weighted mean. The different measurement techniques and their respective sensitivities to impurities are discussed in the 1958 review article by Valentine and Curran [37].

E_{beam} (GeV)	$\left[\frac{1}{\rho}\frac{dE}{dx}\right]_c$	η (%)	β^{-1} $\left(\text{hr}\cdot\mu\text{A/cm}^2\right)$
0.7	0.97	0.1	110.1
1.0	0.98	0.2	109.0
2.0	1.00	0.3	106.8
4.0	1.02	0.5	104.8
8.0	1.04	1.0	102.8
16.0	1.06	1.8	100.9
32.0	1.08	3.6	99.04
64.0	1.10	7.0	97.26

Table 6.3: Variation of Ionizing Energy Loss Parameters with Electron Beam Energy. The second column is the energy lost to collisions relative to the value at 2 GeV. The maximum relative ionization contribution from radiation, η, is estimated assuming a ^{3}He density of 10 amg and a target chamber length of 40 cm.

6.3.4 Spin Relaxation Due to Atomic and Molecular Helium Ions

Atomic ions contribute to polarization loss due to a "spin-exchange"-like interaction between the ^{3}He nucleus and the unpaired electron in the atomic ion. Because charge exchange occurs readily, electrons from highly polarized neutral atoms jump to lowly polarized atomic ions. The newly formed atomic ion partially depolarizes until it undergoes charge exchange and so on. The cumulative effect is at most one nuclear spin flip [38]. In addition to this process, molecular ions also lose polarization to the rotational degrees of freedom via a spin-rotation interaction [39]. Little mention is made in the literature about relaxation due to interactions with free electrons, consequently, we'll show in the next section that their effect is negligible. Before estimating the number of spin flips induced by both processes, it is useful to first estimate the fraction of ions of both types and their typical lifetimes. First we write down the rate equations for the density of atomic ions and molecular ions (in the target chamber) assuming that most of the atoms are neutral:

$$\frac{d[\mathrm{He}^+]_{\mathrm{tc}}}{dt} = +\Gamma_{\mathrm{ion}}[\mathrm{He}]_{\mathrm{tc}} - \sum_i k_i[X_i]_{\mathrm{tc}}[\mathrm{He}^+]_{\mathrm{tc}} - k_m[\mathrm{He}^+]_{\mathrm{tc}}[\mathrm{He}]^2_{\mathrm{tc}} + D\nabla^2[\mathrm{He}^+]_{\mathrm{tc}} \quad (6.88)$$

$$\frac{d[\mathrm{He}_2^+]_{\mathrm{tc}}}{dt} = +k_m[\mathrm{He}^+]_{\mathrm{tc}}[\mathrm{He}]^2_{\mathrm{tc}} - \sum_j [X_j]_{\mathrm{tc}}\left(k'_j + k''_j[\mathrm{He}]_{\mathrm{tc}}\right)[\mathrm{He}_2^+]_{\mathrm{tc}} + D\nabla^2[\mathrm{He}_2^+]_{\mathrm{tc}} \quad (6.89)$$

where k_m, k_i, k'_j, & k''_j are the rate constants for molecular formation, atomic ion charge transfer to X_i, binary molecular charge transfer to X_j, and three body molecular charge transfer to X_j, see Tab. (D.17). Losses due to diffusion can be estimated

parameter	value	units	description
$[He]_{tc}$	10	amg	operating target chamber density
$[N_2]_{tc}$	0.1	amg	operating target chamber density
ρ	1.0	-	ratio of N_2 to ^3He densities relative to 0.01
h	1.0	-	density of ^3He relative to 10 amg
I	10	μA	beam current
A_{tc}	2	cm^2	target chamber cross sectional area
Γ_{ion}	$1/20$	hrs^{-1}	ionization rate per atom
D	1.8	cm^2/s	^3He self-diffusion constant at STP
$k_m[He]_{tc}^2$	6.0	GHz	molecular ion formation rate
$k_n[N_2]_{tc}$	2.7	GHz	atomic ion rate of charge transfer to N_2
$k'_n[N_2]_{tc}$	3.0	GHz	molecular ion binary rate of charge transfer to N_2
$k''_n[N_2]_{tc}[He]_{tc}$	9.8	GHz	molecular ion 3-body rate of charge transfer to N_2
τ_a	115	ps	mean lifetime of atomic ions
τ_m	78	ps	mean lifetime of molecular ions
τ_{ex}	6.7	ps	mean time between atomic charge transfers
h_a^∞	1.5×10^{-15}	-	fraction of nuclei that are in atomic ions
h_m^∞	7.2×10^{-16}	-	fraction of nuclei that are in molecular ions
A_a/h	8.66	GHz	atomic ion hyperfine coupling constant [38]
$\gamma_m N/h$	29	MHz	molecular ion spin-rotation coupling constant [39]
Q_m	≤ 1	-	relative molecular ion relaxation rate
n_m	≤ 0.002	-	spin flips due to molecular ions per atomic ion created
Ω	0.36	radians	amount of nuclear spin precession in between charge transfers
r	17	-	mean number of atomic charge transfers before neutralization
n_a	0.50 ± 0.07	-	spin flips due to atomic ions per atomic ion created

Table 6.4: Parameters Relevant to Relaxation Due to Ion Formation. These values are calculated for typical operating conditions.

by:

$$D\nabla^2 \rightarrow \gamma_d \approx D\pi^2 \left[\frac{1}{R^2} + \frac{1}{L^2}\right] \tag{6.90}$$

where D is the ^{3}He self-diffusion constant, R is the characteristic diffusion size in the radial direction, and L is the characteristic diffusion size along the target chamber. Using the intrinsic radius of the beam ≈ 100 μm and the target chamber length ≈ 40 cm, we get $\gamma_d \approx 200$ kHz. Since all of the other rates are on the order of GHz, we can safely ignore the effect of diffusion. In other words, the exact details of the transverse spatial distribution of beam current is irrelevant. All that matters is the total current that passes through the target chamber. Charge recombination is assumed to be negligible. Dividing out the total ^{3}He density and assuming that N_2 is the only other gas in the target chamber, we get rate equations for the fraction of atoms ions h_a and molecular ions h_m, where we have assumed $h_a, h_m \ll 1$:

$$\begin{aligned}
\frac{dh_a}{dt} &= +\Gamma_{\text{ion}} - \frac{h_a}{\tau_a} && (6.91)\\
\tau_a^{-1} &= k_n[\text{N}_2]_{\text{tc}} + k_m[\text{He}]_{\text{tc}}^2 && (6.92)\\
\frac{dh_m}{dt} &= +k_m h_a[\text{He}]_{\text{tc}}^2 - \frac{h_m}{\tau_m} && (6.93)\\
\tau_m^{-1} &= [\text{N}_2]_{\text{tc}}\left(k_n' + k_n''[\text{He}]_{\text{tc}}\right) && (6.94)
\end{aligned}$$

where τ_a and τ_m are the mean atomic and molecular ion lifetimes. The equilibrium fractions are obtained from setting the rates to zero and give:

$$\begin{aligned}
h_a^\infty &= \Gamma_{\text{ion}}\tau_a = \frac{\Gamma_{\text{ion}}}{k_n[\text{N}_2]_{\text{tc}} + k_m[\text{He}]_{\text{tc}}^2} && (6.95)\\
h_m^\infty &= k_m[\text{He}]_{\text{tc}}^2\tau_m h_a^\infty = \frac{\Gamma_{\text{ion}}}{[\text{N}_2]_{\text{tc}}\left(k_n' + k_n''[\text{He}]_{\text{tc}}\right)}\left(1 + \frac{k_n[\text{N}_2]_{\text{tc}}}{k_m[\text{He}]_{\text{tc}}^2}\right)^{-1} && (6.96)
\end{aligned}$$

Under our conditions, we find $\tau_a, \tau_m \approx 100$ ps and $h_a^\infty, h_m^\infty \approx 10^{-15}$, which justifies our previous assumption that there are very few ions.

The presence of a foreign gas such as N_2 greatly limits the lifetime of molecular ions. Whereas molecular ions have the potential to depolarize many nuclei, their effect is greatly reduced because they are so short lived. Relaxation due to molecular ions is discussed in [39] and they derive an expression for n_m of the following form:

$$\Gamma_{\text{ion}} n_m = \left\langle \frac{\gamma_m N}{h} \right\rangle h_m^\infty Q_m \rightarrow n_m = \left\langle \frac{\gamma_m N}{h} \right\rangle \left(\frac{h_m^\infty}{\Gamma_{\text{ion}}} \right) Q_m \tag{6.97}$$

where $\gamma_m N/h$ is the molecular spin-rotation coupling constant and Q_m is the unitless relative relaxation rate that depends on the magnitude of the magnetic field and the density of ^{3}He . Since Q_m can be at most 1, the maximum value for n_m is given as:

$$n_m \leq \frac{\left\langle \frac{\gamma_m N}{h} \right\rangle}{[N_2]_{\text{tc}} \left(k_n' + k_n''[\text{He}]_{\text{tc}}\right)} \left(1 + \frac{k_n [N_2]_{\text{tc}}}{k_m [\text{He}]_{\text{tc}}^2} \right)^{-1} \approx 0.002 \tag{6.98}$$

Relaxation due to atomic ions is discussed in [38] and their calculation gives:

$$\begin{aligned}
n_a(r,\Omega) &= 1 + \frac{a_1}{1-r\gamma_1} + \Re\left(\frac{a_2}{1-r\gamma_2}\right) \\
a_1 &= \frac{-|\gamma_2|^2 + \Omega^2/2}{|\gamma_2|^2 + 2\gamma_1(1+\gamma_1)} \\
a_2 &= \frac{2\left(\Omega^2/2 - \gamma_1\gamma_2^*\right)(\gamma_1 - \gamma_2^*)}{\left(\gamma_2^* - \gamma_2\right)\left[|\gamma_2|^2 + 2\gamma_1(1+\gamma_1)\right]} \\
\gamma_1 &= S + T - \frac{2}{3} \\
\gamma_2 &= \left(\frac{i\sqrt{3}-1}{2}\right)S - \left(\frac{i\sqrt{3}+1}{2}\right)T - \frac{2}{3} \\
S &= (Q+R)^{1/3} \\
T &= (Q-R)^{1/3} \\
Q &= \frac{1}{108}\left(4 + 9\Omega^2\right) \\
R &= \frac{\Omega}{12\sqrt{3}}\left(8 - 13\Omega^2 + 16\Omega^4\right)^{1/2} \\
\Omega &= 2\pi\left(\frac{A_a}{h}\right)\tau_{\text{ex}} \\
r &= \frac{\tau_a}{\tau_{\text{ex}}}
\end{aligned} \tag{6.99}$$

where τ_{ex} is the mean time between atomic charge exchange collisions, A_a/h is the atomic ion hyperfine coupling constant, r is the mean number of charge exchange collisions before the atomic ion is neutralized, and Ω is a measure of "how much" the nuclear spin and unpaired electron interact before a charge exchange collision occurs. Note that since Q and R are positive definite, γ_1 and a_1 are necessarily real and we can and *must* choose T to be real as well. In our specific case, τ_a and τ_{ex} can

be calculated by:

$$\tau_{ex}^{-1} = k_{ex}[He]_{tc} \tag{6.100}$$

$$\tau_{a}^{-1} = k_{n}[N_2]_{tc} + k_{m}[He]_{tc}^{2} \tag{6.101}$$

where k_{ex} is the binary He-He charge transfer rate constant, k_n is the binary He-N_2 charge transfer rate constant, and k_m is the three body He molecular ion formation rate constant.

Fig. (6.5) depicts n_a for various values of r, Ω, ^{3}He density, and N_2 to ^{3}He density ratio. The red point in the left plot corresponds to our typical conditions with $n_a = 0.50 \pm 0.07$, where all of the uncertainty comes from our (lack of) knowledge of the atomic charge transfer and molecular formation rate constants. It is quite tedious to calculate n_a directly from the above set of equations. Therefore we have prepared a "homemade" parameterization in matrix form which reproduces the full calculation of n_a to better than 2.0% for ^{3}He densities from 5 to 15 amg with N_2 to ^{3}He density ratios from 0% to 5%:

$$n_a(h,\rho) = \begin{bmatrix} 1 & h-1 & (h-1)^2 & (h-1)^3 \end{bmatrix} M_a \begin{bmatrix} 1 \\ \rho - 1 \\ (\rho-1)^2 \\ (\rho-1)^3 \end{bmatrix} \tag{6.102}$$

where M_a is a 4 by 4 matrix given by:

$$M_a = \begin{bmatrix} +5.0539\text{E}-1 & -8.1948\text{E}-2 & +1.1033\text{E}-2 & -8.6382\text{E}-4 \\ -6.5344\text{E}-1 & +4.7939\text{E}-2 & +9.9539\text{E}-4 & -4.4021\text{E}-4 \\ +1.8737\text{E}-1 & +1.0659\text{E}-1 & -2.2923\text{E}-2 & +2.0191\text{E}-3 \\ +2.5606\text{E}-1 & -1.2834\text{E}-1 & -9.7831\text{E}-3 & -3.7214\text{E}-5 \end{bmatrix} \tag{6.103}$$

and h and ρ are given by:

$$h = \frac{[^3\text{He}\,]_{\text{tc}}}{10\ \text{amg}} \qquad \& \qquad \rho = 100 \cdot \frac{[\text{N}_2\,]_{\text{tc}}}{[^3\text{He}\,]_{\text{tc}}} \tag{6.104}$$

The right half of Fig. (6.5) shows a comparison between the full calculation for n_a and the matrix parameterization as a function of ^{3}He density for different N_2 to ^{3}He density ratios. The desired amount of N_2 in the cell is usually about one percent or $\rho = 1$. In this case, the matrix form of n_a collapses to give:

$$n_a(h, \rho = 1) = 0.50539 - 0.65344 \cdot (h-1) + 0.18737 \cdot (h-1)^2 + 0.25606 \cdot (h-1)^3 \tag{6.105}$$

If the ^{3}He density is 10 amg or $h = 1$, the matrix collapses to give:

$$n_a(h = 1, \rho) = 0.50539 - 0.081948 \cdot (\rho-1) + 0.011033 \cdot (\rho-1)^2 - 0.00086382 \cdot (\rho-1)^3 \tag{6.106}$$

Over a ^{3}He density range of 9 amg to 12 amg and a N_2 to ^{3}He density ratio range of 0.5% to 2%, the following reproduces the full calculation to better than 3%:

$$n_a = 0.50618 - [0.62409 - 0.05691 \cdot (\rho-1)] \cdot (h-1) - 0.075812 \cdot (\rho-1) \tag{6.107}$$

6.4 Polarization Diffusion

Up to now, we have not specified by mechanism by which the particles transfer between chambers. For the cells described in this dissertation, the transfer mechanism is diffusion.

6.4.1 Diffusion Rate Per Atom

To calculate the diffusion rates, we'll follow the arguments presented in [40, 41]. The flux of particles $\vec{J}$ of the ith type due to diffusion is [1]:

$$\vec{J_i} = -nD\left[\vec{\nabla} f_i - k_T \log(T) - k_p \log(p)\right] \tag{6.108}$$

where f_i is the fraction of particles of the ith particle type such that $\sum_i f_i = 1$, D is the diffusion constant, $k_{T(p)}$ is the thermal diffusion (barodiffusion) ratio, n is the total density of particles, and $T(p)$ is the temperature (pressure) of the gas. Reducing the problem to one dimension $\left(\vec{\nabla} \to \hat{z}\frac{d}{dz}\right)$, labeling i as the up and down spins, and subtracting one from the other gives us the net polarization flux through the transfer tube:

$$J_{\text{tt}} = \hat{z} \cdot \left(\vec{J_+} - \vec{J_-}\right) = -n(z)D(z)\hat{z} \cdot \vec{\nabla}\left(f_+ - f_-\right) = -n(z)D(z)\frac{dP(z)}{dz} \tag{6.109}$$

Note that we have assumed that the diffusion ratios k_T and k_p depend only on the type of chemical species and not on the specific spin state. To solve this equation for J_{tt}, we'll make the assumption that J_{tt} is constant, $\frac{dJ_{\text{tt}}}{dz} \approx 0$, and that there

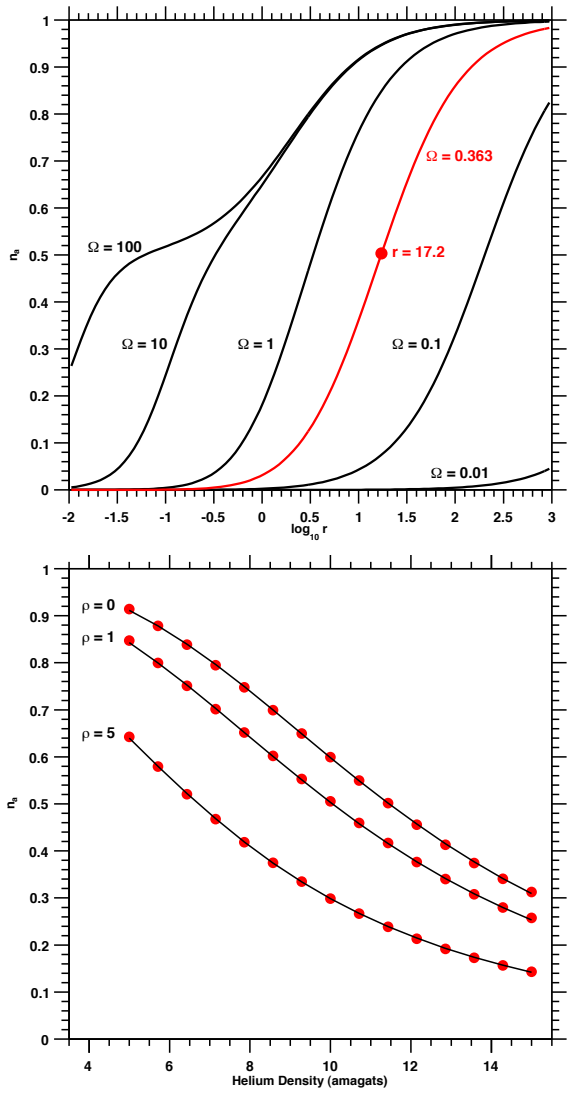

Figure 6.5: Mean Number of Spin Flips Due to Atomic Ions. Upper: n_a as function of r and Ω. This is a recreation of Fig. (1) from [38] with the addition of the red curve which corresponds to a ^{3}He density of 10 amg. The red point corresponds to values for n_a and r when the N_2 to ^{3}He density (ρ) is 1%. Lower: n_a as a function of ^{3}He density for three different values of ρ. The black curves are obtained from the full calculation, Eqns. (6.99); whereas the red points are obtained from the matrix parameterization, Eqn. (6.102). This parameterization reproduces the full calculation to better 2% over ($0.5 \leq h \leq 1.5$) and ($0 \leq \rho \leq 5$). Note that increasing the relative density of N_2 helps suppress n_a.

is a linear temperature gradient between the two chambers [41]. The temperature dependence of the diffusion constant can be seen by considering the diffusion relation for a gas using kinetic theory [2]:

$$\begin{aligned} D &\approx \bar{v} l_{\text{mfp}} = \sqrt{\frac{8RT}{\pi M}} \frac{1}{n\sigma} = D_0 \sqrt{\frac{T}{T_0}} \left(\frac{n_0}{n}\right) \left(\frac{\sigma_0}{\sigma}\right) = D_0 \left(\frac{T}{T_0}\right)^{m-1} \left(\frac{n_0}{n}\right) \quad (6.110) \\ &= D_0 \left(\frac{T}{T_0}\right)^{m} = \left(0.235\ \text{cm}^2/\text{s}\right) \left(\frac{T}{400\ \text{K}}\right)^{0.7} \left(\frac{10\ \text{amg}}{n}\right) \quad (6.111) \end{aligned}$$

where $\bar{v}$ is the mean thermal velocity, l_{mfp} is the mean free path, n is the gas density, and σ is the collisional cross section. At constant pressure, the density has an inverse temperature dependence and the cross section has some temperature dependence that has to be determined empirically:

$$m = \frac{1}{2}\left(\text{from the velocity}\right) + 1\left(\text{from the density}\right) + m_\sigma\left(\text{from the cross section}\right) \quad (6.112)$$

Using this form of the diffusion constant, moving some things around, and integrating along the transfer tube length gives:

$$\begin{aligned} J_{\text{tt}} &= -n(z) D_0 \left(\frac{T}{T_0}\right)^{m-1} \frac{n_0}{n(z)} \frac{dP(z)}{dz} \\ -\frac{J_{\text{tt}} T_0^{m-1}}{D_0 n_0} \int_0^{L_{\text{tt}}} T(z)^{1-m}\, dz &= \int_0^{L_{\text{tt}}} \frac{dP(z)}{dz} dz \\ -\frac{J_{\text{tt}} T_0^{m-1}}{D_0 n_0} \frac{L_{\text{tt}}}{T_{\text{pc}} - T_{\text{tc}}} \int_{T_{\text{tc}}}^{T_{\text{pc}}} u^{1-m}\, du &= P(L_{\text{tt}}) - P(0) \\ -\frac{J_{\text{tt}} T_0^{m-1}}{D_0 n_0} \frac{L_{\text{tt}}}{T_{\text{pc}} - T_{\text{tc}}} \left(\frac{T_{\text{pc}}^{2-m} - T_{\text{tc}}^{2-m}}{2-m}\right) &= P_{\text{pc}} - P_{\text{tc}} \quad (6.113) \end{aligned}$$

parameter	value	units
D_0	2.79	cm^2/s
T_0	353	K
n_0	0.773	amg
m	1.70	-

Table 6.5: ^{3}He Self-Diffusion Constant Parameters from [42].

Finally solving for J_{tt} gives:

$$J_{tt} = -\left(P_{pc} - P_{tc}\right)\left[D_0\left(\frac{T_{tc}}{T_0}\right)^{m-1}\frac{n_0}{n_{tc}}\right]\frac{n_{tc}}{L_{tt}}\frac{(2-m)(t-1)}{(t^{2-m}-1)} \quad \& \quad t = \frac{T_{pc}}{T_{tc}} \tag{6.114}$$

where D_0 is the diffusion constant at a reference temperature T_0 and density n_0 listed in Tab. (6.5), T_{tc} & n_{tc} are the temperature and density of the target chamber, and t is the ratio of the pumping chamber to target chamber temperature. Note that J_{tt} is the total rate per unit area, whereas we want the rate per atom. Multiplying by the transfer tube cross sectional area A_{tt}, dividing by the number of particles in each chamber, and comparing to Eqns. (6.15) & (6.16) give the following relations for the diffusion rates per atom:

$$\begin{aligned} d_{pc} &= -\frac{J_{tt}A_{tt}}{V_{pc}n_{pc}\left(P_{pc}-P_{tc}\right)} = \frac{A_{tt}}{V_{pc}L_{tt}}\left[D_0\left(\frac{T_{pc}}{T_0}\right)^{m-1}\frac{n_0}{n_{pc}}\right]\frac{(2-m)\left(1-t^{-1}\right)}{(1-t^{m-2})} \\ d_{tc} &= -\frac{J_{tt}A_{tt}}{V_{tc}n_{tc}\left(P_{pc}-P_{tc}\right)} = \frac{A_{tt}}{V_{tc}L_{tt}}\left[D_0\left(\frac{T_{tc}}{T_0}\right)^{m-1}\frac{n_0}{n_{tc}}\right]\frac{(2-m)(t-1)}{(t^{2-m}-1)} \end{aligned} \tag{6.115}$$

where we have made use of the following identity:

$$\left[\left(\frac{T_{pc}}{T_0}\right)^{m-1}\right]\frac{\left(1-t^{-1}\right)}{(1-t^{m-2})} = \left[\left(\frac{T_{tc}}{T_0}\right)^{m-1}\right]\frac{(t-1)}{(t^{2-m}-1)} \tag{6.116}$$

Therefore the following quantities are averages over a linear temperature gradient:

$$\langle nD\rangle = \left[n_0 D_0 \left(\frac{T_{\rm pc}}{T_0}\right)^{m-1}\right] \frac{(2-m)\left(1-t^{-1}\right)}{\left(1-t^{m-2}\right)} = \left[n_0 D_0 \left(\frac{T_{\rm tc}}{T_0}\right)^{m-1}\right] \frac{(2-m)(t-1)}{\left(t^{2-m}-1\right)} \tag{6.117}$$

$$= \left(0.706\ \text{amg}\cdot\text{cm}^2/\text{s}\right)\left(\frac{T_{\rm pc}}{400\ \text{K}}\right)^{0.7}\left[\frac{1-t^{-1}}{1-t^{-0.3}}\right] = \left(0.706\ \text{amg}\cdot\text{cm}^2/\text{s}\right)\left(\frac{T_{\rm tc}}{400\ \text{K}}\right)^{0.7}\left[\frac{t-1}{t^{0.3}-1}\right] \tag{6.118}$$

$$\langle D\rangle = \left[D_0 \left(\frac{T_{\rm pc}}{T_0}\right)^{m} \frac{n_0}{n_{\rm pc}}\right] \frac{(m-1)\left(1-t^{-1}\right)}{\left(t^{m-1}-1\right)} = \left[D_0 \left(\frac{T_{\rm tc}}{T_0}\right)^{m} \frac{n_0}{n_{\rm tc}}\right] \frac{(m-1)(t-1)}{\left(1-t^{1-m}\right)} \tag{6.119}$$

$$= \left(0.187\ \text{cm}^2/\text{s}\right)\left[\frac{T_{\rm pc}}{400\ \text{K}}\right]^{1.7}\left[\frac{10\ \text{amg}}{n_{\rm pc}}\right]\left[\frac{1-t^{-1}}{t^{0.7}-1}\right] = \left(0.187\ \text{cm}^2/\text{s}\right)\left[\frac{T_{\rm tc}}{400\ \text{K}}\right]^{1.7}\left[\frac{10\ \text{amg}}{n_{\rm tc}}\right]\left[\frac{t-1}{1-t^{-0.7}}\right] \tag{6.120}$$

Note that the pumping chamber and target chamber operating densities are related by:

$$n_{\rm pc} = \frac{n_{\rm tc}}{t} = n_{\rm fill}\left(\frac{1+v}{t+v}\right) \quad \& \quad v = \frac{V_{\rm pc}}{V_{\rm tc}} \quad \& \quad t = \frac{T_{\rm pc}}{T_{\rm tc}} \tag{6.121}$$

where v is the ratio of the pumping chamber volume to the target chamber volume and we have tacitly assumed that the fraction of nuclei in the transfer tube is negligible. Combining this relation with Eqns. (6.115) & (6.3) gives:

$$f_{\rm pc} = \frac{v}{t+v} \tag{6.122}$$

$$f_{\rm tc} = \frac{t}{t+v} \tag{6.123}$$

$$d_{\rm pc} = \left(\frac{t}{v}\right) d_{\rm tc} \tag{6.124}$$

$$d_{\rm tc} = \frac{A_{\rm tt}}{V_{\rm tc} L_{\rm tt} n_{\rm fill}}\left[D_0 n_0 \left(\frac{273.15\ \text{K}}{T_0}\right)^{m-1}\right] \frac{(t+v)(2-m)(t-1)}{t(1+v)\left(t^{2-m}-1\right)} \left(\frac{T_{\rm tc}}{273.15\ \text{K}}\right)^{m-1} \tag{6.125}$$

where:

$$\left[D_0 n_0 \left(\frac{273.15\ \text{K}}{T_0}\right)^{m-1}\right] = 6488.21\ \frac{\text{cm}^2\cdot\text{amg}}{\text{hr}} \tag{6.126}$$

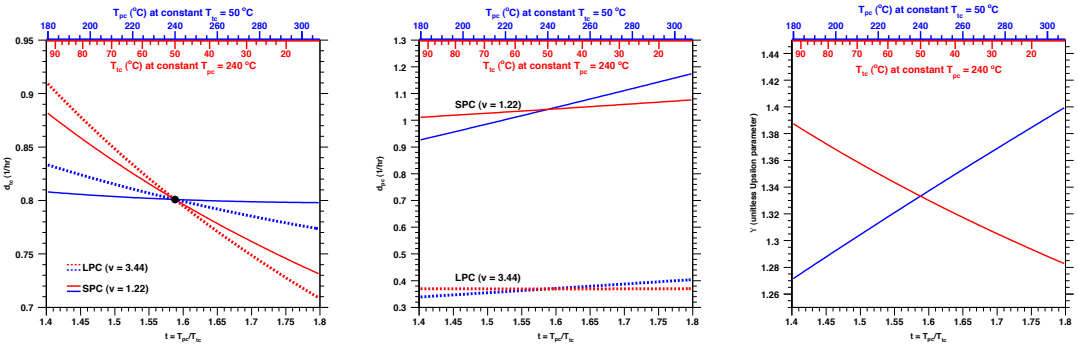

Figure 6.6: Diffusion Rates per Nuclei As a Function of Temperature. Upper Left: d_{tc} as function of temperatures. Upper Right: d_{pc} as a function of temperatures. Lower: Unitless temperature parameter $\Upsilon(t, T_{\text{tc}})$ as a function of temperature. Solid curves are for SPC (small pumping chamber cells), whereas dotted curves are for LPC (large pumping chamber cells). Only the volume ratio v is varied between the SPC and LPC curves with all else being equal. The blue curves and axis represent varying pumping chamber temperatures for a constant target chamber temperature. The red curves and axis represent varying target chamber temperatures for a constant pumping chamber temperature.

The diffusion rate out of the target chamber per atom can be alternatively written as:

$$d_{\text{tc}} = \left(0.60\ \text{hr}^{-1}\right)\left(\frac{A_{\text{tt}}}{0.5\ \text{cm}^2}\right)\left(\frac{6\ \text{cm}}{L_{\text{tt}}}\right)\left(\frac{90\ \text{cm}^3}{V_{\text{tc}}}\right)\left(\frac{10\ \text{amg}}{n_{\text{tc}}}\right)\left(\frac{0.3t-0.3}{t^{0.3}-1}\right)\left(\frac{T_{\text{tc}}}{273.15\ \text{K}}\right)^{0.7} \tag{6.127}$$

$$= \left(0.80\ \text{hrs}^{-1}\right)\left(\frac{A_{\text{tt}}}{0.5\ \text{cm}^2}\right)\left(\frac{6\ \text{cm}}{L_{\text{tt}}}\right)\left(\frac{90\ \text{cm}^3}{V_{\text{tc}}}\right)\left(\frac{10\ \text{amg}}{n_{\text{tc}}}\right)\left(\frac{\Upsilon\left(T_{\text{pc}}, T_{\text{tc}}\right)}{4/3}\right) \tag{6.128}$$

$$\Upsilon\left(T_{\text{pc}}, T_{\text{tc}}\right) = 0.3\left(\frac{t-1}{t^{0.3}-1}\right)\left(\frac{T_{\text{tc}}}{273.15\ \text{K}}\right)^{0.7} \tag{6.129}$$

where Υ is a dimensionless factor, usually between 1.2 and 1.5, that depends only on the cell temperatures. Note that when the cell is at a uniform temperature, $T_{\text{pc}} = T_{\text{tc}}$:

$$\lim_{t\to 1}\Upsilon = \lim_{t\to 1} 0.3\left(\frac{t-1}{t^{0.3}-1}\right)\left(\frac{T_{\text{tc}}}{273.15\ \text{K}}\right)^{0.7} = \lim_{t\to 1} 0.3\left(\frac{1}{0.3}\right)\left(\frac{T_{\text{tc}}}{273.15\ \text{K}}\right)^{0.7} = \left(\frac{T_{\text{tc}}}{273.15\ \text{K}}\right)^{0.7} \tag{6.130}$$

6.4.2 Depolarization Within the Transfer Tube

Thus far we have neglected the polarization dynamics in the transfer tube since only a small fraction of ^{3}He nuclei are in the transfer tube volume. In this section, we will estimate the size of the correction needed to account for spin relaxation in the transfer tube. First we need to estimate the fraction of nuclei in the transfer tube volume. This is obtained from an integral over the transfer tube length:

$$f_{\mathrm{tt}} = \frac{N_{\mathrm{tt}}}{N_{\mathrm{tot}}} = \frac{A_{\mathrm{tt}}}{n_{\mathrm{fill}} V_{\mathrm{tot}}} \int_0^{L_{\mathrm{tt}}} n_{\mathrm{tt}}(z)\, dz \tag{6.131}$$

Assuming a linear temperature gradient with one end being at the pumping chamber temperature and the other end being at the target chamber temperature:

$$T(z) = T_{\mathrm{pc}} + \left(T_{\mathrm{tc}} - T_{\mathrm{pc}}\right) \frac{z}{L_{\mathrm{tt}}} \tag{6.132}$$

gives the following equivalent integral over temperature:

$$f_{\mathrm{tt}} = \frac{V_{\mathrm{tt}}}{n_{\mathrm{fill}} V_{\mathrm{tot}}} \frac{P}{R\left(T_{\mathrm{tc}} - T_{\mathrm{pc}}\right)} \int_{T_{\mathrm{pc}}}^{T_{\mathrm{tc}}} \frac{dT}{T} \tag{6.133}$$

Rewriting in terms of densities gives:

$$f_{\mathrm{tt}} = \frac{V_{\mathrm{tt}}}{V_{\mathrm{tot}}} \left[\frac{n_{\mathrm{fill}}}{n_{\mathrm{pc}}} - \frac{n_{\mathrm{fill}}}{n_{\mathrm{tc}}}\right]^{-1} \log\left(\frac{n_{\mathrm{tc}}}{n_{\mathrm{pc}}}\right) \tag{6.134}$$

If we make the assumption that $f_{\mathrm{tt}} \ll 1$, then we can use Eqn. (6.121) and $f_{\mathrm{pc}}/f_{\mathrm{tc}} = v/t$ to get:

$$f_{\mathrm{tt}} = \frac{V_{\mathrm{tt}}}{V_{\mathrm{tc}}} \frac{\log(t)}{\left(1 + f_{\mathrm{pc}}/f_{\mathrm{tc}}\right)(t-1)} \tag{6.135}$$

Under typical conditions, $t = 1.7$, f_{pc}/f_{tc} varies very roughly from 1 to 2, $V_{tt} = 4$ cc, and $V_{tc} = 90$ cc, which gives $f_{tt} \leq 0.02$. This justifies our approximation that the fraction of nuclei in the transfer tube is very small.

Next, we'll model the transfer tube as a virtual "chamber" somewhere between the pumping and target chambers. The spin relaxation that occurs throughout the physical transfer tube will be averaged to find the equivalent spin relaxation in this virtual chamber. Under these assumptions, it is straightforward to generalize the two chamber polarization rate equations, Eqn. (6.14), into three chamber polarization rate equations:

$$\frac{dP_{pc}}{dt} = \gamma_{se}\left(P_A - P_{pc}\right) - \Gamma_{pc}P_{pc} - d_{pc}^{tt}\left(P_{pc} - P_{tt}\right) \tag{6.136}$$

$$\frac{dP_{tt}}{dt} = -\Gamma_{tt}P_{tt} - d_{tt}^{pc}\left(P_{tt} - P_{pc}\right) - d_{tt}^{tc}\left(P_{tt} - P_{tc}\right) \tag{6.137}$$

$$\frac{dP_{tc}}{dt} = d_{tc}^{tt}\left(P_{tt} - P_{tc}\right) - \Gamma_{tc}P_{tc} \tag{6.138}$$

where P_{tt} is the effective transfer tube polarization and Γ_{tt} is the average transfer tube relaxation rate. Note that we now have four diffusion rates which correspond to diffusion from the pumping and target chambers into the virtual chamber and vice versa. At nuclei number equilibrium, they must satisfy:

$$f_{pc}d_{pc}^{tt} = f_{tt}d_{tt}^{pc} \quad \& \quad f_{tc}d_{tc}^{tt} = f_{tt}d_{tt}^{tc} \tag{6.139}$$

where the subscripts and superscripts on d refer to the source and destination chambers respectively. At equilibrium, the polarizations in the three chambers

are:

$$\frac{P_{\rm tc}^{\infty}}{P_{\rm tt}^{\infty}} = \left[1+\frac{\Gamma_{\rm tc}}{d_{\rm tc}^{\rm tt}}\right]^{-1} \tag{6.140}$$

$$\frac{P_{\rm tt}^{\infty}}{P_{\rm pc}^{\infty}} = \left[1+\frac{\Gamma_{\rm tt}}{d_{\rm tt}^{\rm pc}}+\left(\frac{\Gamma_{\rm tc}}{d_{\rm tc}^{\rm tt}}\right)\left(\frac{d_{\rm tt}^{\rm tc}}{d_{\rm tt}^{\rm pc}}\right)\left(1+\frac{\Gamma_{\rm tc}}{d_{\rm tc}^{\rm tt}}\right)^{-1}\right]^{-1} \tag{6.141}$$

$$\begin{aligned}\frac{P_{\rm pc}^{\infty}}{P_A} = &\left[1+\frac{\Gamma_{\rm pc}}{\gamma_{\rm se}}+\frac{d_{\rm pc}^{\rm tt}}{\gamma_{\rm se}}\left(\frac{\Gamma_{\rm tt}}{d_{\rm tt}^{\rm pc}}\left[1+\frac{\Gamma_{\rm tc}}{d_{\rm tc}^{\rm tt}}\right]+\frac{\Gamma_{\rm tc}}{d_{\rm tc}^{\rm tt}}\frac{d_{\rm tt}^{\rm tc}}{d_{\rm tt}^{\rm pc}}\right)\right.\\ &\left.\times\left(\left[1+\frac{\Gamma_{\rm tt}}{d_{\rm tt}^{\rm pc}}\right]\left[1+\frac{\Gamma_{\rm tc}}{d_{\rm tc}^{\rm tt}}\right]+\frac{\Gamma_{\rm tc}}{d_{\rm tc}^{\rm tt}}\frac{d_{\rm tt}^{\rm tc}}{d_{\rm tt}^{\rm pc}}\right)^{-1}\right]^{-1}\end{aligned} \tag{6.142}$$

If we assume that the system is at nuclei number equilibrium, then we can use Eqn. (6.139) to write these equilibrium polarizations in a more illuminating form:

$$P_{\rm pc}^{\infty} = \frac{P_A\gamma_{\rm se}f_{\rm pc}}{\gamma_{\rm se}f_{\rm pc}+\Gamma_{\rm pc}f_{\rm pc}+\left[\left(1+\frac{\Gamma_{\rm tc}}{d_{\rm tc}^{\rm tt}}\right)\Gamma_{\rm tt}f_{\rm tt}+\Gamma_{\rm tc}f_{\rm tc}\right]\left[1+\Gamma_{\rm tc}f_{\rm tc}\left(\frac{1}{f_{\rm tc}d_{\rm tc}^{\rm tt}}+\frac{1}{f_{\rm pc}d_{\rm pc}^{\rm tt}}\right)+\left(1+\frac{\Gamma_{\rm tc}}{d_{\rm tc}^{\rm tt}}\right)\frac{f_{\rm tt}}{f_{\rm pc}}\frac{\Gamma_{\rm tt}}{d_{\rm pc}^{\rm tt}}\right]^{-1}} \tag{6.143}$$

$$\frac{P_{\rm tc}^{\infty}}{P_{\rm pc}^{\infty}} = \left[1+\Gamma_{\rm tc}f_{\rm tc}\left(\frac{1}{f_{\rm tc}d_{\rm tc}^{\rm tt}}+\frac{1}{f_{\rm pc}d_{\rm pc}^{\rm tt}}\right)+\left(1+\frac{\Gamma_{\rm tc}}{d_{\rm tc}^{\rm tt}}\right)\left(\frac{f_{\rm tt}}{f_{\rm pc}}\right)\left(\frac{\Gamma_{\rm tt}}{d_{\rm pc}^{\rm tt}}\right)\right]^{-1} \tag{6.144}$$

In the limit that the diffusion rates approach infinity, $d_{\rm pc}^{\rm tt}, d_{\rm tc}^{\rm tt} \to \infty$, the above equations reduce to a very satisfying result:

$$\frac{P_{\rm tc}^{\infty}}{P_{\rm pc}^{\infty}} \to 1 \qquad \& \qquad P_{\rm pc}^{\infty} \to P_A\frac{\gamma_{\rm se}f_{\rm pc}}{\gamma_{\rm se}f_{\rm pc}+\Gamma_{\rm pc}f_{\rm pc}+\Gamma_{\rm tt}f_{\rm tt}+\Gamma_{\rm tc}f_{\rm tc}} = P_A\frac{\langle\gamma_{\rm se}\rangle}{\langle\gamma_{\rm se}\rangle+\langle\Gamma\rangle} \tag{6.145}$$

In the limit that the fraction of nuclei in the transfer tube approaches zero, $f_{\rm tt} \to 0$, the three chamber equilibrium polarization equations reduce to the familiar two

chamber results, Eqns. (6.33) & (6.34):

$$P_{\rm pc}^{\infty} = \frac{P_A \gamma_{\rm se} f_{\rm pc}}{\gamma_{\rm se} f_{\rm pc} + \Gamma_{\rm pc} f_{\rm pc} + \Gamma_{\rm tc} f_{\rm tc} \left[1 + \Gamma_{\rm tc} f_{\rm tc} \left(\frac{1}{f_{\rm tc} d_{\rm tc}^{\rm tt}} + \frac{1}{f_{\rm pc} d_{\rm pc}^{\rm tt}}\right)\right]^{-1}} \tag{6.146}$$

$$\frac{P_{\rm tc}^{\infty}}{P_{\rm pc}^{\infty}} = \left[1 + \Gamma_{\rm tc} f_{\rm tc} \left(\frac{1}{f_{\rm tc} d_{\rm tc}^{\rm tt}} + \frac{1}{f_{\rm pc} d_{\rm pc}^{\rm tt}}\right)\right]^{-1} \tag{6.147}$$

To make this reduction manifest, note our prior assumption that the nuclei flux is constant throughout the transfer tube:

$$J_{\rm tt} = \text{constant} = \frac{d_{\rm tc} N_{\rm tc}}{A_{\rm tt}} \left(P_{\rm pc} - P_{\rm tc}\right) = \frac{d_{\rm tc}^{\rm tt} N_{\rm tc}}{A_{\rm tt}} \left(P_{\rm tt} - P_{\rm tc}\right) = \frac{d_{\rm pc}^{\rm tt} N_{\rm pc}}{A_{\rm tt}} \left(P_{\rm pc} - P_{\rm tt}\right) \tag{6.148}$$

If, in addition to the above identities, we make the assumption that the polarization varies linearly along the transfer tube and then dropping common factors gives:

$$d_{\rm tc} f_{\rm tc} L_{\rm tt} = d_{\rm tc}^{\rm tt} f_{\rm tc} x L_{\rm tt} = d_{\rm pc}^{\rm tt} f_{\rm pc} \left(1 - x\right) L_{\rm tt} \tag{6.149}$$

where x is the "fractional distance" along the physical transfer tube length where the virtual chamber "is located." To recap, assuming a constant nuclei flux, a linear temperature gradient along the transfer tube, and a linear polarization gradient along the transfer tube, we get the following relationship among the diffusion rates for the two chamber and three chamber systems:

$$f_{\rm tc} \left(\frac{1}{f_{\rm tc} d_{\rm tc}^{\rm tt}} + \frac{1}{f_{\rm pc} d_{\rm pc}^{\rm tt}}\right) = f_{\rm tc} \left(\frac{x}{d_{\rm tc} f_{\rm tc}} + \frac{1 - x}{d_{\rm tc} f_{\rm tc}}\right) = \frac{1}{d_{\rm tc}} \tag{6.150}$$

which insures that the three chamber solutions Eqns. (6.146) & (6.147) reduce to the two chamber solutions Eqns. (6.33) & (6.34) in the limit that the fraction of nuclei

in the transfer tube approaches zero.

The most significant source of spin relaxation in the transfer tube is spin exchange with alkali vapor. This vapor has a negligible polarization since it is not directly exposed to laser light. Because there is a temperature gradient along the transfer tube, there is also an alkali vapor density gradient as well as ^{3}He density gradient. Therefore we collapse the alkali density gradient into a ^{3}He density weighted average alkali density:

$$\langle [A] \rangle_{\text{tt}} = \frac{\int_0^{L_{\text{tt}}} [A](z) n(z)\, dz}{\int_0^{L_{\text{tt}}} n(z)\, dz} = \frac{\int_{T_{\text{pc}}}^{T_{\text{tc}}} [A](T) \left(\frac{P}{RT}\right) \left(\frac{L\, dT}{T_{\text{tc}} - T_{\text{pc}}}\right)}{\int_{T_{\text{pc}}}^{T_{\text{tc}}} \left(\frac{P}{RT}\right) \left(\frac{L\, dT}{T_{\text{tc}} - T_{\text{pc}}}\right)} = \frac{\int_{T_{\text{pc}}}^{T_{\text{tc}}} [A](T) \frac{dT}{T}}{\int_{T_{\text{pc}}}^{T_{\text{tc}}} \frac{dT}{T}} \tag{6.151}$$

The temperature dependence of the alkali density is obtained from the vapor pressure curve combined with the ideal gas law:

$$[A](T) = \frac{\exp\left(A_{\text{vp}} - \frac{B_{\text{vp}}}{T}\right)}{RT} = \exp\left[-B_{\text{vp}}\left(T^{-1} - T_{\text{pc}}^{-1}\right)\right]\left(\frac{T_{\text{pc}}}{T}\right)[A]_{\text{pc}} \tag{6.152}$$

where A_{pc} & B_{pc} are the vapor pressure constants listed in Tab. (A.7) and $[A]_{\text{pc}}$ is the alkali density in the pumping chamber. Plugging in this form of the alkali density and performing the integral in the numerator:

$$\begin{aligned}
\int_{T_{\text{pc}}}^{T_{\text{tc}}} [A](T) \frac{dT}{T} &= T_{\text{pc}}[A]_{\text{pc}} \exp\left(\frac{B_{\text{vp}}}{T_{\text{pc}}}\right) \int_{T_{\text{pc}}}^{T_{\text{tc}}} \frac{\exp\left(-\frac{B_{\text{vp}}}{T}\right)}{T^2}\, dT \\
&= \frac{T_{\text{pc}}}{B_{\text{vp}}}[A]_{\text{pc}} \exp\left(\frac{B_{\text{vp}}}{T_{\text{pc}}}\right)\left[\exp\left(-\frac{B_{\text{vp}}}{T_{\text{tc}}}\right) - \exp\left(-\frac{B_{\text{vp}}}{T_{\text{pc}}}\right)\right] \\
&= \frac{T_{\text{pc}}}{B_{\text{vp}}}[A]_{\text{pc}}\left[-1 + \exp\left(\frac{B_{\text{vp}}}{T_{\text{pc}}} - \frac{B_{\text{vp}}}{T_{\text{tc}}}\right)\right] \\
&= \frac{T_{\text{tc}}[A]_{\text{tc}} - T_{\text{pc}}[A]_{\text{pc}}}{B_{\text{vp}}}
\end{aligned} \tag{6.153}$$

Dividing this by the integral in the denominator gives:

$$\langle [A] \rangle_{tt} = \frac{T_{pc}[A]_{pc} - T_{tc}[A]_{tc}}{B_{vp} \log\left(\frac{T_{pc}}{T_{tc}}\right)} \tag{6.154}$$

The average alkali spin-exchange rate in the transfer tube is:

$$\langle \gamma_{se} \rangle_{tt} = \gamma_{se} \left(\frac{T_{pc}}{B_{vp} \log\left(\frac{T_{pc}}{T_{tc}}\right)} \right) \tag{6.155}$$

where we've taken advantage of the fact that, under typical operating conditions, the alkali density in the target chamber is negligible, see Tab. (6.6).

In principle, the same type of calculation should be done for all other sources of spin relaxation in the transfer tube, such as the nuclear dipolar relaxation. However, since:

1. the spin exchange with essentially unpolarized alkali vapor dominates the spin relaxation
2. the nuclear dipolar relaxation has a soft temperature dependence
3. we ignore, if any, the temperature dependence of the wall relaxation

it is much easier to simply use the geometric mean of the pumping chamber relaxation rate and the total non-beam related relaxation for the target chamber, which gives:

$$\Gamma_{tt} = \langle \gamma_{se} \rangle_{tt} + \langle \Gamma_{dip} \rangle_{tt} + \langle \Gamma_{wall} \rangle_{tt} + \langle \Gamma_{other} \rangle_{tt} \approx \langle \gamma_{se} \rangle_{tt} + \sqrt{\Gamma_{pc} \Gamma^0_{tc}} \tag{6.156}$$

T (°C)	[Rb] (10^{14} cm^{-3})	$1/\gamma_{se}$ (hrs)	[K] (10^{14} cm^{-3})	$1/\gamma_{se}$ (hrs)	[Na] (10^{14} cm^{-3})	$1/\gamma_{se}$ (hrs)
25.0	1.29×10^{-4}	3.16×10^{5}	5.88×10^{-6}	8.59×10^{6}	7.88×10^{-9}	5.78×10^{9}
50.0	1.47×10^{-3}	2.79×10^{4}	8.71×10^{-5}	5.80×10^{5}	2.07×10^{-7}	2.20×10^{8}
75.0	1.08×10^{-2}	3.80×10^{3}	8.62×10^{-4}	5.86×10^{4}	3.37×10^{-6}	1.35×10^{7}
100.0	6.01×10^{-2}	679	5.78×10^{-3}	8.73×10^{3}	3.87×10^{-5}	1.18×10^{6}
125.0	0.270	152	3.04×10^{-2}	1.66×10^{3}	2.91×10^{-4}	1.56×10^{5}
150.0	1.01	40.5	0.131	385	1.72×10^{-3}	2.64×10^{4}
175.0	3.25	12.6	0.478	106	8.32×10^{-3}	5.47×10^{3}
180.3	4.08	10.0	0.617	81.9	1.13×10^{-2}	4.02×10^{3}
200.0	9.21	4.44	1.52	33.3	3.39×10^{-2}	1.34×10^{3}
225.0	23.5	1.74	4.28	11.8	0.120	380
229.3	27.2	1.50	5.05	10.0	0.147	311
241.2	40.8	1.00	7.91	6.39	0.253	180
250.0	54.5	0.749	10.9	4.64	0.374	122
275.0	117	0.349	25.4	1.99	1.05	43.4
297.1	217	0.188	50.5	1.00	2.43	18.8
300.0	235	0.174	55.0	0.919	2.69	16.9
315.0	346	0.118	84.6	0.597	4.55	10.0
325.0	443	9.22×10^{-2}	111	0.454	6.36	7.16
350.0	794	5.14×10^{-2}	212	0.238	14.0	3.25
375.0	1.36×10^{3}	3.01×10^{-2}	385	0.131	29.0	1.57
391.6	1.89×10^{3}	2.16×10^{-2}	557	9.06×10^{-2}	45.5	1.00
400.0	2.23×10^{3}	1.83×10^{-2}	667	7.57×10^{-2}	56.7	0.803

Table 6.6: Pure Alkali Number Density and ^{3}He Spin-Exchange Rate vs. Temperature.

6.4.3 Polarization Gradient Between Pumping & Target Chambers

The polarization gradient between the two chambers is given by:

$$\Delta \equiv 1 - \frac{P_{\text{tc}}^{\infty}}{P_{\text{pc}}^{\infty}} = 1 - \left[1 + \Gamma_{\text{tc}} f_{\text{tc}} \left(\frac{1}{f_{\text{tc}} d_{\text{tc}}^{\text{tt}}} + \frac{1}{f_{\text{pc}} d_{\text{pc}}^{\text{tt}}} \right) + \left(1 + \frac{\Gamma_{\text{tc}}}{d_{\text{tc}}^{\text{tt}}} \right) \left(\frac{f_{\text{tt}}}{f_{\text{pc}}} \right) \left(\frac{\Gamma_{\text{tt}}}{d_{\text{pc}}^{\text{tt}}} \right) \right]^{-1} \tag{6.157}$$

Assuming a linear polarization gradient along the physical transfer tube and placing the third virtual chamber half way between the two chambers gives the following:

$$2 d_{\text{tc}} f_{\text{tc}} = d_{\text{tc}}^{\text{tt}} f_{\text{tc}} = d_{\text{pc}}^{\text{tt}} f_{\text{pc}} \tag{6.158}$$

Note that this amounts to choosing $x = 1/2$ in Eqn. (6.149). Using the above relationship and Eqn. (6.150) allows us to write the polarization gradient as:

$$\Delta_{3 \text{ chamber}} = 1 - \left[1 + \frac{\Gamma_{\text{tc}}}{d_{\text{tc}}} + \left(1 + \frac{\Gamma_{\text{tc}}}{2 d_{\text{tc}}} \right) \left(\frac{f_{\text{tt}}}{f_{\text{tc}}} \right) \left(\frac{\Gamma_{\text{tt}}}{2 d_{\text{tc}}} \right) \right]^{-1} \tag{6.159}$$

which should be compared to the equation for a two chamber cell neglecting the transfer tube volume:

$$\Delta_{2 \text{ chamber}} = 1 - \left[1 + \frac{\Gamma_{\text{tc}}}{d_{\text{tc}}} \right]^{-1} \tag{6.160}$$

We will now perform a binomial expansion to estimate the size of (1) the polarization loss in the transfer tube and (2) the lowest order term of the polarization gradient. Under typical conditions, the diffusion rate d_{tc} is faster than the relaxation rates in the transfer and target chamber. Applying this approximation to

second order in d_{tc} gives:

$$\Delta = 1 - \left(1 - \left[\Gamma_{tc} + \frac{\Gamma_{tt}}{2}\frac{f_{tt}}{f_{tc}}\right] d_{tc}^{-1} + \left[\Gamma_{tc}^2 + \frac{\Gamma_{tt}^2}{4}\frac{f_{tt}^2}{f_{tc}^2} + \frac{3\Gamma_{tc}\Gamma_{tt}}{4}\frac{f_{tt}}{f_{tc}}\right] d_{tc}^{-2}\right) + O\left(\frac{\Gamma_{tc}^3}{d_{tc}^3}\right) \tag{6.161}$$

$$= \left[1 + \frac{1}{2}\frac{f_{tt}}{f_{tc}}\frac{\Gamma_{tt}}{\Gamma_{tc}}\left(1 \underbrace{- \frac{1}{2}\frac{f_{tt}}{f_{tc}}\frac{\Gamma_{tt}}{d_{tc}} - \frac{3}{2}\frac{\Gamma_{tc}}{d_{tc}}}\right) - \frac{\Gamma_{tc}}{d_{tc}}\right]\frac{\Gamma_{tc}}{d_{tc}} \tag{6.162}$$

Note that under typical conditions, f_{tt}/f_{tc} is roughly the same order of magnitude as Γ_{tc}/d_{tc}. Therefore we can drop the under-braced terms, which are essentially third order, to give the lowest order terms of the polarization gradient:

$$\Delta = \left[1 + \frac{1}{2}\frac{f_{tt}}{f_{tc}}\frac{\Gamma_{tt}}{\Gamma_{tc}} - \frac{\Gamma_{tc}}{d_{tc}}\right]\frac{\Gamma_{tc}}{d_{tc}} + O\left(\frac{\Gamma_{tc}^3}{d_{tc}^3}\right) \tag{6.163}$$

Therefore the polarization lost traversing through the transfer tube is a second order correction. When there is no beam depolarization in the target chamber, the polarization gradient is written as:

$$\Delta_0 = \left[1 + \frac{1}{2}\frac{f_{tt}}{f_{tc}}\frac{\Gamma_{tt}}{\Gamma_{tc}} - \frac{\Gamma_{tc}^0}{d_{tc}}\right]\frac{\Gamma_{tc}^0}{d_{tc}} = \left[1 + \frac{1}{2}\left(\frac{\langle\gamma_{se}\rangle_{tt}}{\Gamma_{tc}^0} + \sqrt{\frac{\Gamma_{pc}}{\Gamma_{tc}^0}}\right)\frac{f_{tt}}{f_{tc}} - \frac{\Gamma_{tc}^0}{d_{tc}}\right]\frac{\Gamma_{tc}^0}{d_{tc}} \tag{6.164}$$

where we have used Eqn. (6.156). The relaxation in the target chamber that is independent of the beam current, Γ_{tc}^0, can be estimated from the lifetime of the cell

assuming that the wall relaxation is independent of temperature:

$$\Gamma_{\text{lifetime}} = \tau_{\text{lifetime}}^{-1} = \Gamma_{\text{wall}} + \Gamma_{\text{dip}}\left(T_{\text{lifetime}}\right) \tag{6.165}$$

$$\Gamma_{\text{tc}}^{0} = \Gamma_{\text{wall}} + \Gamma_{\text{dip}}\left(T_{\text{tc}}\right) \tag{6.166}$$

$$= \Gamma_{\text{lifetime}} - \Gamma_{\text{dip}}\left(T_{\text{lifetime}}\right) + \Gamma_{\text{dip}}\left(T_{\text{tc}}\right) \tag{6.167}$$

$$= \Gamma_{\text{lifetime}}\left[1 + \frac{\Gamma_{\text{dip}}\left(T_{\text{tc}}\right) - \Gamma_{\text{dip}}\left(T_{\text{lifetime}}\right)}{\Gamma_{\text{lifetime}}}\right] \tag{6.168}$$

where T_{tc} is the target chamber temperature under operating conditions and T_{lifetime} is the target chamber temperature during the lifetime measurement. Note that the target chamber temperature affects both the density of the target chamber and the nuclear dipolar rate constant. Finally, we can write the contributions to the polarization gradient from both sources up to next to leading order:

$$\Delta = \Delta_0 + \Delta_{\text{beam}} \tag{6.169}$$

$$\Delta_0 = \frac{\Gamma_{\text{tc}}^{0}}{d_{\text{tc}}}\left[1 + \frac{1}{2}\left(\frac{\langle\gamma_{\text{se}}\rangle_{\text{tt}}}{\Gamma_{\text{tc}}^{0}} + \sqrt{\frac{\Gamma_{\text{pc}}}{\Gamma_{\text{tc}}^{0}}}\right)\frac{f_{\text{tt}}}{f_{\text{tc}}} - \frac{\Gamma_{\text{tc}}^{0}}{d_{\text{tc}}}\right] \tag{6.170}$$

$$\Delta_{\text{beam}} = \frac{\Gamma_{\text{beam}}}{d_{\text{tc}}}\left[1 - \frac{\left(2\Gamma_{\text{tc}}^{0} + \Gamma_{\text{beam}}\right)}{d_{\text{tc}}}\right] \tag{6.171}$$

It is now useful to enumerate every assumption and approximation used to derive these relationships:

1. The transfer tube volume is very small compared to the volume of the cell.

2. The target chamber has a negligible vapor pressure of alkali metal.

3. The alkali vapor reaches equilibrium polarization very fast relative to the ^{3}He polarization.

4. The alkali polarization is independent of the ^{3}He polarization.

5. The cell is at thermal equilibrium throughout the ^{3}He polarization process.

6. The diffusion rates per nucleus are the fastest rates in the system.

7. The beam energy is in the range of 1–16 GeV.

8. Only a tiny fraction of the ^{3}He atoms in the target chamber are ionized at any instant of time.

9. Very little of the ionization is due to bremsstrahlung.

10. The electrons created during ionization contribute little to the beam depolarization.

11. Diffusion in the radial direction of the target chamber is essentially instantaneous.

12. Molecular ^{3}He ions contribute little to the beam depolarization.

13. There is a linear temperature gradient along the transfer tube.

14. There is a constant polarization flux through the transfer tube.

15. The wall relaxation is uniform throughout the cell and independent of temperature.

6.4.4 Discussion and Representative Examples

To get a qualitative and lowest order quantitative handle on the polarization gradient, we'll drop all the higher order terms (including the polarization lost in the

transfer tube). Using the reasonable approximation that $\Gamma^0_{\rm tc} = \Gamma_{\rm lifetime}$, the beam independent polarization gradient becomes:

$$\Delta_0 = \frac{\Gamma^0_{\rm tc}}{d_{\rm tc}} + \text{higher order terms} \tag{6.172}$$

$$= \left(\frac{1\text{ hr}}{6488.21\text{ cm}^2\cdot\text{amg}}\right)\left(\frac{L_{\rm tt}\cdot V_{\rm tc}\cdot n_{\rm tc}}{\tau_{\rm lifetime}\cdot A_{\rm tt}\cdot\Upsilon\left(T_{\rm pc},T_{\rm tc}\right)}\right) \tag{6.173}$$

$$= \left(\frac{1}{36}\right)\left(\frac{40\text{ hrs}}{\tau_{\rm lifetime}}\right)\left(\frac{0.5\text{ cm}^2}{A_{\rm tt}}\right)\left(\frac{L_{\rm tt}}{6\text{ cm}}\right)\left(\frac{V_{\rm tc}}{80\text{ cm}^3}\right)\left(\frac{n_{\rm tc}}{10\text{ amg}}\right)\left(\frac{4/3}{\Upsilon\left(T_{\rm pc},T_{\rm tc}\right)}\right) \tag{6.174}$$

and the beam dependent polarization gradient is:

$$\Delta_{\rm beam} = \frac{\Gamma_{\rm ion} n_a}{d_{\rm tc}} + \text{higher order terms} \tag{6.175}$$

$$= \left(\frac{1}{681262\ \mu\text{A}\cdot\text{amg}}\right)\left(\frac{I\cdot n_a\cdot L_{\rm tc}\cdot L_{\rm tt}\cdot n_{\rm tc}}{A_{\rm tt}\cdot\Upsilon\left(T_{\rm pc},T_{\rm tc}\right)}\right) \tag{6.176}$$

$$= \left(\frac{1}{38}\right)\left(\frac{I}{10\ \mu\text{A}}\right)\left(\frac{n_a}{0.5}\right)\left(\frac{L_{\rm tc}}{40\text{ cm}}\right)\left(\frac{0.5\text{ cm}^2}{A_{\rm tt}}\right)\left(\frac{L_{\rm tt}}{6\text{ cm}}\right)\left(\frac{n_{\rm tc}}{10\text{ amg}}\right)\left(\frac{4/3}{\Upsilon\left(T_{\rm pc},T_{\rm tc}\right)}\right) \tag{6.177}$$

Both sources contribute equals amounts to the polarization gradient ($\Delta_0 = \Delta_{\rm beam}$) to lowest order when the following relationship between cell lifetime and beam current is true:

$$I\cdot\tau_{\rm lifetime} = \left(420\ \mu\text{A}\cdot\text{hrs}\cdot\text{cm}^2\right)\left(\frac{A_{\rm tc}}{2.0\text{ cm}^2}\right)\left(\frac{0.5}{n_a}\right) \tag{6.178}$$

In other words, the contribution to the total polarization gradient due to a beam current of 10 μA in a cell with a lifetime of 42 hrs is the same. Some representative values for past experiments are given in Tab. (6.7) assuming a beam current of 10 μA and a cell lifetime of 42 hr. The lowest order, next to leading order, and full calculation for both a 2 chamber and 3 chamber cell model all produce that same

polarization gradient within 10 percent relative. The parameter that varies largest on a cell to cell basis is the transfer tube cross sectional area. Unfortunately the polarization gradient also happens to be very sensitive to this parameter. Increasing the relative amount of N_2 in the cell helps suppress beam depolarization. Alternatively, a long lifetime cell helps suppress the polarization gradient that is independent of the beam. The largest uncertainty comes from our imprecise knowledge of the various ionic rate constants used to calculate the beam depolarization. In practical terms, n_a is known to only about 15 percent.

The next largest source of uncertainty is in our knowledge of the wall relaxation. The target chamber has a larger surface area to volume ratio than the pumping chamber, so, naively, one would imagine that the wall relaxation would be greater in the target chamber. We also don't know its temperature dependence; however, the relative change in the target chamber temperature is at the level of 10 percent. Finally, we use a fairly simple diffusion model to estimate the diffusion rates per nucleus. If we apply a 10 percent uncertainty to the diffusion rates as well, then our overall uncertainty is about 20 percent relative on a usually 5 percent relative correction.

6.4.5 Estimating Diffusion and Beam Parameters Empirically

In principle, it is possible to estimate these parameters empirically from data rather than having to rely upon theoretical calculations. To obtain information on the diffusion rates, spin-up data can be taken on the target chamber, or even better both chambers, and then fit to Eqn. (6.31). This method would probably benefit from taking spin-up data under different initial conditions, for example:

1. Start with both chambers at zero polarization, $P^0_{\mathrm{tc}} = 0$ and $P^0_{\mathrm{pc}} = 0$.

parameter	E142	E154	GDH	A1n	g2n	saGDH	GEn-spc	GEn-LPC	units
$[^3\mathrm{He}\,]_{\mathrm{fill}}$	7.88	8.83	9.62	8.69	8.19	8.78	8.25	7.40	amg
$[\mathrm{N}_2\,]_{\mathrm{fill}}$	0.0663	0.0776	0.0964	0.0824	0.0940	0.0913	0.125	0.112	amg
R_{pc}	2.64	2.62	2.94	3.02	3.02	2.93	2.90	4.12	cm
A_{tt}	0.704	0.709	1.01	0.537	0.537	0.645	0.385	0.385	cm^2
L_{tt}	5.9	6.2	6.02	6.52	6.52	6.11	10.1	8.89	cm
A_{tc}	3.09	3.56	2.27	2.05	2.05	2.47	2.03	2.03	cm^2
L_{tc}	29.8	29.8	39.6	25.6	39.5	39.5	40.3	40.3	cm
T_{pc}	435	465	492	505	505	485	558	558	K
T_{tc}	338	343	330	333	333	331	309	309	K
V_{pc}	77.0	75.0	106	115	115	105	102	292	cm^3
V_{tt}	4.15	4.39	6.08	3.50	3.50	3.94	3.88	3.42	cm^3
V_{tc}	92	106	89.8	52.4	80.9	97.5	81.8	81.8	cm^3
t	1.28	1.35	1.49	1.51	1.51	1.46	1.80	1.80	-
v	0.83	0.71	1.18	2.19	1.42	1.07	1.24	3.58	-
f_{pc}	0.394	0.343	0.442	0.591	0.484	0.424	0.408	0.664	-
f_{tt}	0.024	0.023	0.030	0.021	0.017	0.019	0.020	0.010	-
f_{tc}	0.605	0.656	0.557	0.408	0.515	0.575	0.591	0.335	-
n_{pc}	6.81	7.31	7.85	7.48	6.75	7.17	6.07	6.29	amg
n_{tc}	8.77	9.90	11.7	11.34	10.23	10.51	10.96	11.36	amg
p_{op}	10.8	12.4	14.1	13.8	12.4	12.7	12.4	12.8	atm
ρ	0.84	0.87	1.00	0.94	1.14	1.03	1.51	1.51	-
Ω	0.413	0.366	0.309	0.319	0.354	0.345	0.33	0.319	rad
r	19.9	18.0	15.4	16.0	16.2	16.4	14.0	13.7	-
n_a	0.6007	0.5191	0.3998	0.4243	0.4761	0.4672	0.4066	0.3849	-
n_m^{max}	0.0024	0.0019	0.0012	0.0014	0.0013	0.0014	0.0008	0.0007	-
τ_{beam}	54.6	73.1	60.9	51.7	46.0	56.5	53.4	56.5	hr
τ_{tc}^0	40.8	40.6	38.4	37.3	38.4	39.0	36.7	34.6	hr
τ_{tc}	23.3	26.1	23.5	21.7	20.9	23.1	21.8	21.5	hr
τ_{tt}	32.4	20.4	12.0	8.4	8.5	14.1	9.6	9.4	hr
Υ	1.27	1.30	1.32	1.33	1.33	1.31	1.35	1.35	-
d_{pc}^{-1}	0.533	0.566	0.581	1.207	1.089	0.839	1.846	4.828	hr
d_{tc}^{-1}	0.820	1.081	0.731	0.832	1.159	1.138	2.669	2.434	hr
Δ_0^0, Eqn. (6.172)	2.00	2.66	1.91	2.23	3.02	2.92	7.27	7.04	% rel.
Δ_0^1, Eqn. (6.170)	2.01	2.69	2.04	2.45	3.17	2.97	7.23	6.94	% rel.
Δ_{beam}^0, Eqn. (6.177)	1.50	1.48	1.20	1.61	2.52	2.02	5.00	4.31	% rel.
Δ_{beam}^1, Eqn. (6.171)	1.41	1.38	1.14	1.51	2.31	1.86	4.02	3.52	% rel.
Δ^0, Eqn. (6.172;6.177)	3.51	4.14	3.11	3.84	5.54	4.93	12.3	11.4	% rel.
Δ^1, Eqn. (6.170;6.171)	3.43	4.07	3.18	3.96	5.47	4.82	11.3	10.5	% rel.
$\Delta_{2\mathrm{ch}}$, Eqn. (6.160)	3.39	3.98	3.02	3.70	5.25	4.70	10.9	10.2	% rel.
$\Delta_{3\mathrm{ch}}$, Eqn. (6.159)	3.43	4.07	3.18	3.95	5.47	4.83	11.3	10.5	% rel.

Table 6.7: Polarization Gradient for Representative Cells with $I = 10$ μA and $\tau_{\mathrm{lifetime}} = 42$ hr.

2. Start with both chambers at the opposite polarization, $P^0_{\rm tc} = -P^\infty_{\rm tc}$ and $P^0_{\rm pc} = -P^\infty_{\rm pc}$. This could easily be accomplished by reversing the spins by AFP after the polarization has reached equilibrium.

3. Start with one chamber at the equilibrium polarization, while the other chamber is at zero, $P^0_{\rm tc} = 0$ and $P^0_{\rm pc} = +P^\infty_{\rm pc}$. This could be accomplished by a transient burst of on-resonance RF localized near the target chamber.

Another way to get the diffusion rate $d_{\rm tc}$ is to do the following:

1. Start with zero polarization in both chambers, $P^0_{\rm pc} = P^0_{\rm tc} = 0$.

2. Monitor the polarization of both chambers during a spinup over a time scale much shorter than the diffusion time scale, $t \ll 1/\Gamma_{\rm f}$.

3. Fit the pumping chamber polarization data to a second order polynomial.

4. Fit the target chamber polarization data to a third order polynomial.

5. From Eqns. (6.46) & (6.47), the ratio of the quadratic coefficient from the target chamber ($q_{\rm tc}$) to the linear coefficient from the pumping chamber ($m_{\rm pc}$) gives the target chamber diffusion rate, $d_{\rm tc}$:

$$\frac{q_{\rm tc}}{m_{\rm pc}} = \frac{\gamma_{\rm se} P_A d_{\rm tc}/2}{\gamma_{\rm se} P_A} = \frac{d_{\rm tc}}{2} \tag{6.179}$$

To obtain information about the beam depolarization, one can compare the equilibrium polarizations with beam on and off. This works best when the diffusion

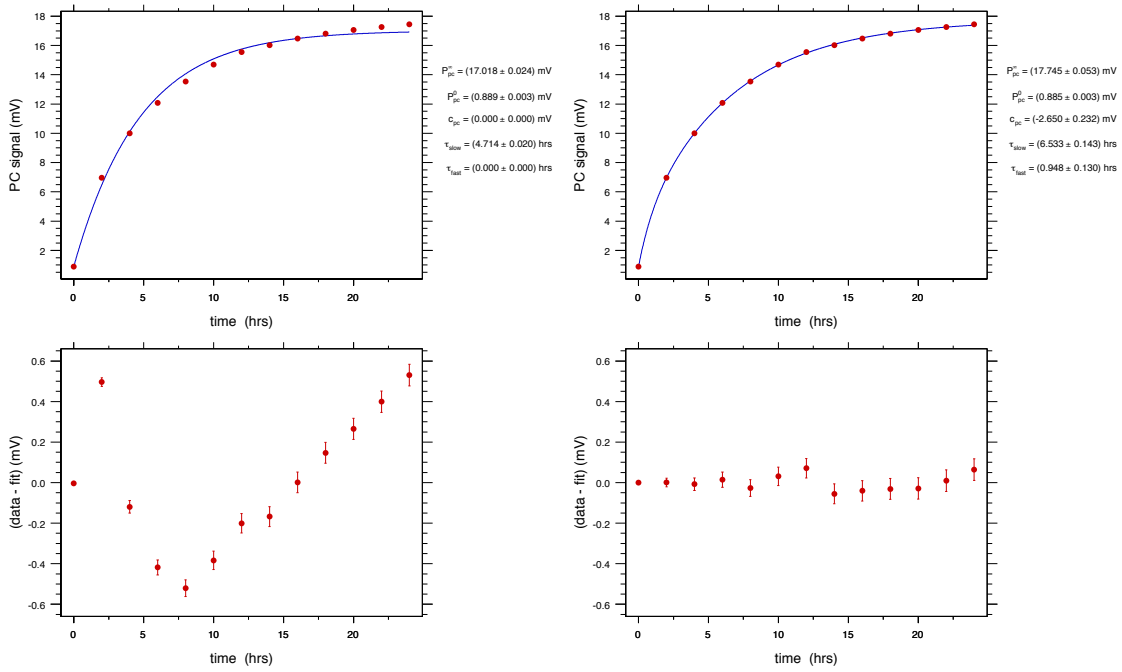

Figure 6.7: Spinup Curves for Hyrbid Cells

rates are much faster than all other rates. Under those conditions:

$$P^{\infty} = P^{\infty}_{\rm pc} = P^{\infty}_{\rm tc} = \frac{P_A \gamma_{\rm se} f_{\rm pc}}{\gamma_{\rm se} f_{\rm pc} + \Gamma_{\rm pc} f_{\rm pc} + \Gamma_{\rm tc} f_{\rm tc}} \tag{6.180}$$

$$P^{\infty}_{\rm off} = \frac{P_A \gamma_{\rm se} f_{\rm pc}}{\gamma_{\rm se} f_{\rm pc} + \Gamma_{\rm pc} f_{\rm pc} + \Gamma^0_{\rm tc} f_{\rm tc}} \tag{6.181}$$

$$P^{\infty}_{\rm on} = \frac{P_A \gamma_{\rm se} f_{\rm pc}}{\gamma_{\rm se} f_{\rm pc} + \Gamma_{\rm pc} f_{\rm pc} + \Gamma^0_{\rm tc} f_{\rm tc} + \Gamma_{\rm beam} f_{\rm tc}} \tag{6.182}$$

$$\frac{P^{\infty}_{\rm off}}{P^{\infty}_{\rm on}} = 1 + \frac{\Gamma_{\rm beam} f_{\rm tc}}{\gamma_{\rm se} f_{\rm pc} + \Gamma_{\rm pc} f_{\rm pc} + \Gamma^0_{\rm tc} f_{\rm tc}} = 1 + \tau^{\rm off}_{\rm slow} \Gamma_{\rm beam} f_{\rm tc} \tag{6.183}$$

$$\Gamma_{\rm beam} = \frac{\Gamma^{\rm off}_{\rm s}}{f_{\rm tc}} \left[\frac{P^{\infty}_{\rm off}}{P^{\infty}_{\rm on}} - 1 \right] \tag{6.184}$$

This method requires knowledge of the "slow" spin-up time constant with the beam off, $\Gamma_{\rm s}$.

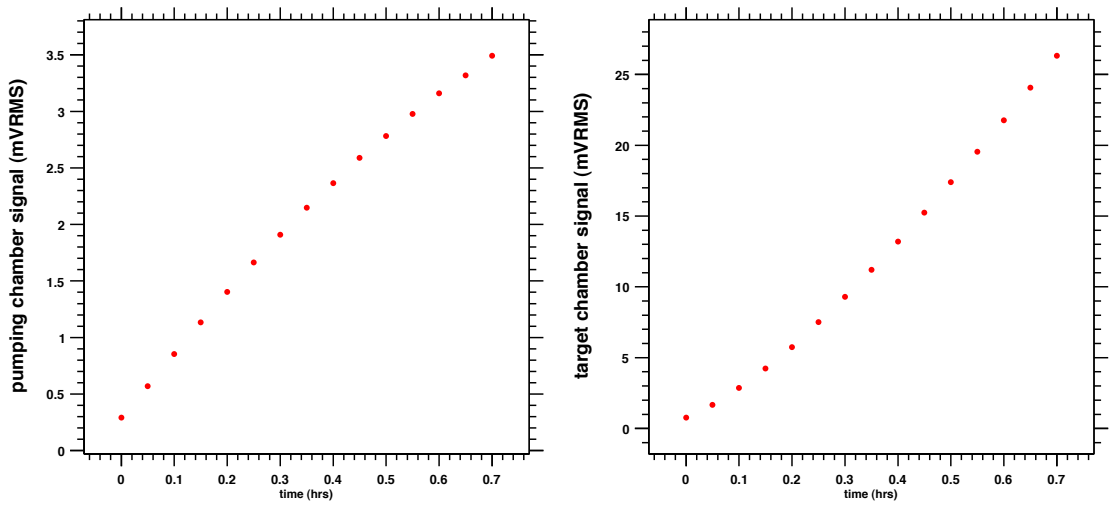

Figure 6.8: Polarization Buildup at $t = 0$ With $P_{pc}^0 = P_{tc}^0 = 0$.

6.4.6 Polarization Gradient Within the Target Chamber

Thus far we've assumed that the polarization is uniform throughout the target chamber. However, the polarization at the ends of the target chamber must be lower than the polarization at the junction between the transfer tube and the target chamber. In addition, the beam depolarizes only within an area defined by the beam raster. To account for a spatial variation in polarization due to these effects, we'll model the transfer tube-target chamber junction as a delta function source for polarization and the beam raster area as a sink for polarization. Therefore, Eqn. (6.16) is generalized to:

$$\frac{dP_{tc}(r,z,t)}{dt} = d_{tc}\mathcal{A}\left(P_{pc} - P_{tc}\right)\delta(z)\delta(r - r_{tc}) - \left(\Gamma_{tc}^0 + \Gamma_{beam}\Theta(r - r_0)\right)P_{tc} + D\nabla^2 P_{tc} \tag{6.185}$$

where $\mathcal{A}$ is the characteristic area of the polarization source, $\Theta(r - r_0)$ is the Heaviside function, r_0 is the radius of the beam raster, and D is the diffusion constant evaluated at the target chamber temperature and density.

To solve this equation, we'll have to make some simplifying arguments. First, we will consider the system only at equilibrium, $t \to \infty$; therefore the polarization has reached a steady state value throughout the cell, $dP_{\text{tc}}/dt = 0$. Second, we will assume that the polarization dynamics within the pumping chamber are sensitive to only the volume averaged target chamber polarization $\langle P_{\text{tc}} \rangle$ (as opposed to some small region localized near the transfer tube-target chamber junction). This is true when the diffusion rates are fast relative to all other polarization/relaxation rates in the cell. This implies that P_{tc}^{∞} in all previous equations is to be interpreted as the volume averaged target chamber polarization.

Third, we will assume that the gradient in the radial direction is negligible relative to the gradient in the longitudinal direction [40]. To justify this assumption, consider the characteristic distance that a ^{3}He atom travels during the characteristic relaxation time under typical conditions:

$$\lambda = \sqrt{\frac{D}{\Gamma_{\text{tc}}}} \approx \sqrt{\frac{0.2 \text{ cm}^2/\text{sec}}{1/20 \text{ hrs}^{-1}}} \approx 120 \text{ cm} \tag{6.186}$$

The polarization gradient within the target chamber scales as the ratio between the characteristic size and this characteristic diffusion length:

$$\frac{r_{\text{tc}} = 0.85 \text{ cm}}{\lambda} \approx 0.007 \ll \frac{L_{\text{tc}}/2 = 20 \text{ cm}}{\lambda} \approx 0.17 < 1 \tag{6.187}$$

This justifies our third assumption and finally we get:

$$0 = d_{\text{tc}} \ell \left(P_{\text{pc}}^{\infty} - \langle P_{\text{tc}} \rangle \right) \delta(z) - \Gamma_{\text{tc}} P_{\text{tc}} + D \frac{d^2 P_{\text{tc}}}{dz^2} \tag{6.188}$$

where ℓ is the characteristic size of the polarization source. Note the we have tacitly

defined the coordinate system such that the transfer tube-target chamber junction occurs at $z = 0$ and the target chamber ends are at $z = \pm L_{\text{tc}}/2$.

Finally we can solve this equation by performing a Laplace transform and solving for $\mathcal{L}P_{\text{tc}}$:

$$\begin{aligned} -\Gamma_{\text{tc}}\mathcal{L}P_{\text{tc}} + D\left[k_z^2\mathcal{L}P_{\text{tc}} - k_z P_{\text{tc}}(0) - P'_{\text{tc}}(0)\right] &= -d_{\text{tc}}\ell\left(P_{\text{pc}}^{\infty} - \langle P_{\text{tc}}\rangle\right) \\ \left[-\Gamma_{\text{tc}} + Dk_z^2\right]\mathcal{L}P_{\text{tc}} &= Dk_z P_{\text{tc}}(0) + DP'_{\text{tc}}(0) - d_{\text{tc}}\ell\left(P_{\text{pc}}^{\infty} - \langle P_{\text{tc}}\rangle\right) \\ \mathcal{L}P_{\text{tc}} &= \frac{k_z P_{\text{tc}}(0) + P'_{\text{tc}}(0) - \frac{d_{\text{tc}}\ell}{D}\left(P_{\text{pc}}^{\infty} - \langle P_{\text{tc}}\rangle\right)}{k_z^2 - \frac{\Gamma_{\text{tc}}}{D}} \end{aligned} \tag{6.189}$$

where k_z is the conjugate variable to z and $P_{\text{tc}}(0)$ & $P'_{\text{tc}}(0)$ are the polarization and first derivative of the polarization evaluated at $z = 0$. Substituting the characteristic diffusion length and taking the inverse Laplace transform gives:

$$\begin{aligned} \mathcal{L}P_{\text{tc}} &= \frac{k_z P_{\text{tc}}(0) + P'_{\text{tc}}(0) - \frac{d_{\text{tc}}\ell}{D}\left(P_{\text{pc}}^{\infty} - \langle P_{\text{tc}}\rangle\right)}{k_z^2 - \lambda^{-2}} \\ \mathcal{L}^{-1}\mathcal{L}P_{\text{tc}} &= P_{\text{tc}}(0)\mathcal{L}^{-1}\left(\frac{k_z}{k_z^2 - \lambda^{-2}}\right) + \lambda\left[P'_{\text{tc}}(0) - \frac{d_{\text{tc}}\ell}{D}\left(P_{\text{pc}}^{\infty} - \langle P_{\text{tc}}\rangle\right)\right]\mathcal{L}^{-1}\left(\frac{\lambda^{-1}}{k_z^2 - \lambda^{-2}}\right) \\ P_{\text{tc}}(z) &= P_{\text{tc}}(0)\cosh\left(\frac{z}{\lambda}\right) + \lambda\left[P'_{\text{tc}}(0) - \frac{d_{\text{tc}}\ell}{D}\left(P_{\text{pc}}^{\infty} - \langle P_{\text{tc}}\rangle\right)\right]\sinh\left|\frac{z}{\lambda}\right| \end{aligned} \tag{6.190}$$

The inverse Laplace transforms performed above are only valid for $|k_z|\lambda > 1$ or analogously $|z| < \lambda$. Since $\lambda \approx 120$ cm and the maximum value is $|z| = L_{\text{tc}}/2 = 20$ cm, the above solution is valid and we can expand the hyperbolic trig functions to lowest order to give:

$$P_{\text{tc}}(z) = P_{\text{tc}}(0) + |z|\left[P'_{\text{tc}}(0) - \frac{d_{\text{tc}}\ell}{D}\left(P_{\text{pc}}^{\infty} - \langle P_{\text{tc}}\rangle\right)\right] + O\left(\frac{|z|}{\lambda}\right)^2 \tag{6.191}$$

The value of the first derivative of the polarization at $z = 0$ can be estimated by analogy to Eqn. (6.109):

$$J_{\rm tc}(z) = n_{\rm tc} D P'_{\rm tc}(z) \tag{6.192}$$

We'll assume that the net total number of particles entering the target chamber at the transfer tube-target chamber junction is conserved, which implies:

$$J_{\rm tt} A_{\rm tt} = \left[J_{\rm tc}(\text{at 0 towards } +z) + J_{\rm tc}(0\text{at 0 towards } -z) \right] A_{\rm tc} \tag{6.193}$$

Note that the number of particles entering the target chamber are equally split and directed towards either end of the target chamber. Combining this with Eqn. (6.115) gives:

$$P'_{\rm tc}(0) = \frac{J_{\rm tc}(0)}{n_{\rm tc} D} = \frac{1}{2} \frac{A_{\rm tt}}{A_{\rm tc}} \frac{J_{\rm tt}}{n_{\rm tc} D} = \frac{d_{\rm tc} L_{\rm tc}}{2D} \left(\langle P_{\rm tc} \rangle - P^{\infty}_{\rm pc} \right) \tag{6.194}$$

The difference in polarization at equilibrium between the two chambers is obtained from Eqn. (6.34):

$$P^{\infty}_{\rm pc} - \langle P_{\rm tc} \rangle = \langle P_{\rm tc} \rangle \left(1 + \frac{\Gamma_{\rm tc}}{d_{\rm tc}} \right) - \langle P_{\rm tc} \rangle = \langle P_{\rm tc} \rangle \frac{\Gamma_{\rm tc}}{d_{\rm tc}} \tag{6.195}$$

Putting this altogether, calculating the average value of $P_{\rm tc}$ along the target chamber, and solving for $P_{\rm tc}(0)$:

$$\begin{aligned} \langle P_{\rm tc} \rangle = \frac{1}{L_{\rm tc}} \int_{-L_{\rm tc}/2}^{+L_{\rm tc}/2} P_{\rm tc}(z)\, dz &= \frac{1}{L_{\rm tc}} \int_{-L_{\rm tc}/2}^{+L_{\rm tc}/2} P_{\rm tc}(0) - |z| \langle P_{\rm tc} \rangle \frac{\Gamma_{\rm tc}}{D} \left(\ell + \frac{L_{\rm tc}}{2} \right) dz \\ &= P_{\rm tc}(0) - \frac{L_{\rm tc}}{4} \langle P_{\rm tc} \rangle \frac{\Gamma_{\rm tc}}{D} \left(\ell + \frac{L_{\rm tc}}{2} \right) dz \qquad (6.196) \\ P_{\rm tc}(0) &= \langle P_{\rm tc} \rangle \left[1 + \frac{L_{\rm tc}}{4} \frac{\Gamma_{\rm tc}}{D} \left(\ell + \frac{L_{\rm tc}}{2} \right) \right] \qquad (6.197) \end{aligned}$$

Finally, using this form of $P_{tc}(0)$ and rearranging a few things gives:

$$P_{tc}(z) = \langle P_{tc} \rangle \left[1 + \left(1 - \frac{4|z|}{L_{tc}} \right) \left(1 + \frac{2\ell}{L_{tc}} \right) \left(\frac{L_{tc}^2}{8} \right) \frac{\Gamma_{tc}}{D} \right] \tag{6.198}$$

The total center to end relative polarization gradient is given by:

$$\frac{\Delta P_{tc}}{\langle P_{tc} \rangle} = \left(1 + \frac{2\ell}{L_{tc}} \right) \left(\frac{L_{tc}^2}{4} \right) \frac{\Gamma_{tc}}{D} \tag{6.199}$$

Finally, to quantify things, we need to estimate ℓ, the characteristic size of the polarization source. In this case, the "polarization source" is the transfer tube; therefore it's reasonable to use the transfer tube diameter or the square root of the transfer tube cross sectional area. For $\ell = \sqrt{A_{tt}} \ll L_{tc}$, we find:

$$\frac{\Delta P_{tc}}{\langle P_{tc} \rangle} = (3\% \text{ relative}) \left(\frac{L_{tc}}{40 \text{ cm}} \right)^2 (\Gamma_{tc} \cdot 20 \text{ hrs}) \left(\frac{n_{tc}}{11 \text{ amg}} \right) \left(\frac{333.15 \text{ K}}{T_{tc}} \right)^{0.7} \tag{6.200}$$

Therefore, under typical conditions, the polarization decreases linearly from the center of the target chamber to the ends. The polarization across the target chamber varies by about $\pm 1.5\%$ relative to the target chamber average.

Bibliography

[1] L.D. Landau and E.M. Lifshitz. *Fluid Mechanics (Course of Theoretical Physics, Vol. 6)*. Butterworth-Heinemann, Oxford, second revised english edition, 1998.

[2] L.D. Landau and E.M. Lifshitz. *Physical Kinetics (Course of Theoretical Physics, Vol. 10)*. Butterworth-Heinemann, Oxford, english edition, 1998.

[3] Richard Haberman. *Elementary Applied Partial Differential Equations*. Prentice-Hall, INC., Upper Saddle River, NJ, 3rd edition, 1998.

[4] David R. Lide (Editor-in Chief). *CRC Handbook of Chemistry and Physics*. CRC Press, Boca Raton, FL, 75th student edition, 1994.

[5] E. Babcock, et al. Limits to the polarization for spin-exchange optical pumping of ^{3}he. *Phys. Rev. Lett.*, 96(8):083003, 2006.

[6] J.D. Jackson. *Classical Electrodynamics*. John Wiley & Sons, New York, 2nd edition, 1975.

[7] D. K. Walter, W. Happer, and T. G. Walker. Estimates of the relative magnitudes of the isotropic and anisotropic magnetic-dipole hyperfine interactions in alkali-metal–noble-gas systems. *Phys. Rev. A*, 58(5):3642–3653, Nov 1998.

[8] T. G. Walker, I. A. Nelson, and S. Kadlecek. Method for deducing anisotropic spin-exchange rates. *Phys. Rev. A*, 81(3):032709, Mar 2010.

[9] Rodger L. Gamblin and Thomas R. Carver. Polarization and relaxation processes in ^{3}He gas. *Phys. Rev.*, 138(4A):A946–A960, May 1965.

[10] L. D. Schearer and G. K. Walters. Nuclear spin-lattice relaxation in the presence of magnetic-field gradients. *Phys. Rev.*, 139(5A):A1398–A1402, Aug 1965.

[11] N.R. Newbury, A.S. Barton, G.D. Cates, W. Happer, and H. Middleton. Gaseous ^{3}He-^{3}He magnetic dipolar spin relaxation. *Phys. Rev. A*, 48(6):4411–4420, Dec 1993.

[12] M.J. Berger, J.S. Coursey, M.A. Zucker, and J. Chang. *ESTAR, PSTAR, and ASTAR: Computer Programs for Calculating Stopping-Power and Range Tables for Electrons, Protons, and Helium Ions*. (version 1.2.3). [Online] Available: http://physics.nist.gov/Star [2006, November 2]. National Institute of Standards and Technology, Gaithersburg, MD, 2005.

[13] M.J. Berger, J.H. Hubbell, S.M. Seltzer, J. Chang, J.S. Coursey, R. Sukumar, and D.S. Zucker. *XCOM: Photon Cross Section Database*. (version 1.3). [Online] Available: http://physics.nist.gov/xcom [2006, November 2]. National Institute of Standards and Technology, Gaithersburg, MD, 2005.

[14] William R. Leo. *Techniques for Nuclear and Particle Physics Experiments: A How-to Approach*. Springer-Verlag, Berlin, second revised edition, 1994.

[15] R.M. Sternheimer, M.J. Berger, and S.M. Seltzer. Density Effect for the Ionization Loss of Charged Particles In Various Substances. *Atomic Data and Nuclear Data Tables*, 30(2):261–271, March 1984.

[16] H. Bethe and W. Heitler. On the Stopping of Fast Particles and on the Creation of Positive Electrons. *Proceedings of the Royal Society of London. Series A, Containing Papers of a Mathematical and Physical Character*, 146(856):83–112, August 1934.

[17] Particle Data Group. Review of Particle Physics. *Physics Letters B*, 592:1–1109, 2004.

[18] William P. Jesse and John Sadauskis. Alpha-Particle Ionization in Mixtures of the Noble Gases. *Phys. Rev.*, 88(2):417–418, Oct 1952.

[19] William P. Jesse and John Sadauskis. Alpha-Particle Ionization in Pure Gases and the Average Energy to Make an Ion Pair. *Phys. Rev.*, 90(6):1120–1121, Jun 1953.

[20] T.E. Bortner and G.S. Hurst. Ionization of Pure Gases and Mixtures of Gases by 5-Mev Alpha Particles. *Phys. Rev.*, 93(6):1236–1241, Mar 1954.

[21] G.A. Erskine. The Effect of Contaminating Gases on the Energy per Ion Pair in Helium. *Proceedings of the Physical Society. Section A*, 67(7):640–642, 1954.

[22] R.W. Gurney. Ionisation by Alpha-Particles in Monoatomic and Diatomic Gases. *Proceedings of the Royal Society of London. Series A, Containing Papers of a Mathematical and Physical Character*, 107(742):332–340, February 1925.

[23] J.F. Lehmann. The Absorption of Slow Cathode Rays in Various Gases. *Proceedings of the Royal Society of London. Series A, Containing Papers of a Mathematical and Physical Character*, 115(772):624–639, August 1927.

[24] Hans H. Staub. Detection Methods. In E. Segrè, editor, *Experimental Nuclear Physics, Volume I*, pages 1–165, New York, 1953. John Wiley and Sons.

[25] Bruno Rossi. *High-Energy Physics*. Prentice-Hall, Incorporated, New York, 1952.

[26] L.H. Gray. *Proceedings of the Cambridge Philosophical Society*, 40:72, 1944.

[27] C.J. Bakker and E. Segrè. Stopping Power and Energy Loss for Ion Pair Production for 340-Mev Protons. *Phys. Rev.*, 81(4):489–492, Feb 1951.

[28] Lloyd O. Herwig and Glenn H. Miller. Alpha-Particle Ionization Yields in a Gridded Chamber. *Phys. Rev.*, 94(5):1183, Jun 1954.

[29] W. Haberli, P. Huber, and E. Baldinger. *Helv. Phys. Acta*, 25:467, 1952.

[30] J.M. Valentine. Energy per Ion Pair for Electrons in Gases and Gas Mixtures. *Proceedings of the Royal Society of London. Series A, Mathematical and Physical Sciences*, 211(1104):75–85, February 1952.

[31] Robert H. Frost and Carl E. Nielsen. The Specific Probable Ionization of Electrons Observed with a Wilson Cloud Chamber. *Phys. Rev.*, 91(4):864–870, Aug 1953.

[32] Leon M. Dorfman. Absorption of Tritium Beta Particles in Hydrogen and Other Gases. *Phys. Rev.*, 95(2):393–396, Jul 1954.

[33] William P. Jesse and John Sadauskis. Ionization in Pure Gases and the Average Energy to Make an Ion Pair for Alpha and Beta Particles. *Phys. Rev.*, 97(6):1668–1670, Mar 1955.

[34] Jerome Weiss and William Bernstein. Energy Required to Produce One Ion Pair in Several Noble Gases. *Phys. Rev.*, 103(5):1253, Sep 1956.

[35] W.G. Stone and L.W. Cochran. Ionization of Gases by Recoil Atoms. *Phys. Rev.*, 107(3):702–704, Aug 1957.

[36] Emilio Segrè. *Nuclei and Particles: An Introduction to Nuclear and Subnuclear Physics*. W.A. Benjamin, INC., New York, 1964.

[37] J.M. Valentine and S.C. Curran. Average energy expenditure per ion pair in gases and gas mixtures. *Reports on Progress in Physics*, 21(1):1–29, 1958.

[38] K.D. Bonin, D.P. Saltzberg, and W. Happer. Relaxation of gaseous spin-polarized ^{3}He targets due to creation of $^3He^+$. *Phys. Rev. A*, 38(9):4481–4487, Nov 1988.

[39] K.D. Bonin, T.G. Walker, and W. Happer. Relaxation of gaseous spin-polarized ^{3}He targets due to ionizing radiation. *Phys. Rev. A*, 37(9):3270–3282, May 1988.

[40] T. E. Chupp, R. A. Loveman, A. K. Thompson, A. M. Bernstein, and D. R. Tieger. Tests of a high density polarized *he*3 target for electron scattering. *Phys. Rev. C*, 45(3):915–930, Mar 1992.

[41] Mikhail V. Romalis. *Laser Polarizaed* ^{3}He *Target Used for a Precision Measurement of the Neutron Spin Structure*. PhD thesis, Princeton University, 1997.

[42] Xiaochao Zheng. *Precision Measurement of Neutron Spin Asymmetry* A_1^n *at Large* x_{bj} *Using CEBAF at 5.7 GeV*. PhD thesis, Massachusetts Institute of Technology, 2002.

Chapter 7

Progress Towards Reaching the Limiting ^{3}He Polarization

In this final chapter, we illustrate the dramatic gains that have occurred in target performance and summarize the main lessons learned regarding optimization. The data presented here were taken from the various measurements that were performed as target cells were being tested for upcoming experiments. Quoted values for ^{3}He polarization P_{He} are generally fairly accurate ($\pm 5\%$), but the numbers for some other quantities may be somewhat less accurate, as will be discussed later. More importantly, the conditions of these various tests varied considerably over the past decade during which they occurred. Few of these measurements were part of an organized, systematic exploration of target cell performance, since our immediate goal had been to determine the best cells to use for upcoming experiments. With these caveats in mind, the broad trends discussed in the previous two chapters are clearly evident.

7.1 The Impact of Alkali-Hybrid Mixtures

Tab. (7.1) is a list of target cells & their performance using broadband lasers. This table is not meant to be complete, but merely representative of the cells of that time period. The value for D listed in this table was determined by measuring the total absorption of the pressure broadened Rb & K absorptions lines, see Sec. (E.8.4), and then extrapolating this value to operating temperatures using their vapor pressure curves, see Sec. (A.3).

The first 6 cells listed in Tab. (7.1) are 2.5 in diameter pumping-chamber target-style cells containing only Rb that were pumped with 60 W of broadband (2 nm) laser power. These cells were considered "state of art" circa 2002 and, in fact, two of them (Priapus and Penelope) were used in E97110 described in Sec. (3.5). At the time, the expectation was that the highest ^{3}He polarization that could be achieved in target cells (in the fast diffusion limit & not including beam relaxation) was given by:

$$P_{\mathrm{He}}^{\mathrm{naive}} = P_{\mathrm{A}}\left[1 - \frac{\Gamma_{\mathrm{He}}}{\Gamma_s}\right] \tag{7.1}$$

where Γ_s^{-1} is the spin up time constant, $\Gamma_{\mathrm{He}}^{-1}$ is the cell lifetime measured at room temperature, and we've assumed their difference is equal to the volume averaged spin exchange rate given by:

$$\Gamma_s - \Gamma_{\mathrm{He}} = f_{\mathrm{pc}} k_{\mathrm{se}}[\mathrm{A}] \tag{7.2}$$

where f_{pc} is the fraction of ^{3}He nuclei that are in the pumping chamber, k_{se} is the A-^{3}He spin exchange rate constant, and [A] is the alkali number density. Using the measured values for these quantities and assuming $P_{\mathrm{A}} = 1$, we find $P_{\mathrm{He}}^{\mathrm{naive}} > 0.60$. If

one directly attributed the low ^{3}He polarization solely to a low alkali polarization, then the following equation can be used to estimate the average alkali polarization in the pumping chamber:

$$P_{\mathrm{A}}^{\mathrm{calc}} = P_{\mathrm{He}} \left[1 - \frac{\Gamma_{\mathrm{He}}}{\Gamma_s} \right]^{-1} \tag{7.3}$$

Indeed, it was a common belief that the ^{3}He polarizations measured in these cells were an indication of alkali polarizations at the level of $P_{\mathrm{A}}^{\mathrm{calc}} \approx 0.70$, see for example [1].

As described in Sec. (5.5.2), alkali-hybrid SEOP was expected to utilize the laser power more efficiently in transferring the light polarization to ^{3}He nuclear polarization. As a pratical matter, this statement implies that one would achieve:

1. higher alkali polarization for the same laser power and

2. the same alkali polarization for a higher alkali density.

This was, in fact, borne out as evidenced by the last 9 cells listed in Tab. (7.1). These cells had both 2.5 in & 3.5 in pumping chamber diameters and were specifically designed (and used) for E02013 described in Sec. (3.6). Several comments could be made about their performance, but we'll highlight the most relevant.

While the worst cells performed no worse than pure Rb cells, the best cells, when pumped with sufficient laser power, achieved ^{3}He polarizations in excess of 0.50. Since the lifetime of these cells did not vary significantly, it was safe to assume that the difference in performance was attributable to the alkali-hybrid ratio D. We found that the best performing cells had D in the range $3 \leq D \leq 7$ or equivalently 5 ± 2, which is in surprisingly good agreement with the results of the simulation shown in Fig. (5.6). However, these hybrid cells also failed to achieve $P_{\mathrm{He}}^{\mathrm{naive}} \approx 0.8$.

cell	P_{He}	**lasers**	I_0 W/cm^2	Γ_{s}^{-1} hrs	$\Gamma_{\mathrm{He}}^{-1}$ hrs	D (PB)	$P_{\mathrm{He}}^{\mathrm{naive}}$	$P_{\mathrm{A}}^{\mathrm{calc}}$
Proteus	0.46	3/6 60 W	3.8	27	74	0	0.63	0.73
Priapus	0.44	3/6 60 W	3.8	21	56	0	0.62	0.71
Penelope	0.44	3/6 60 W	3.8	17	54	0	0.69	0.64
Phubar	0.39	3/6 60 W	3.8	18	46	0	0.61	0.64
Powell	0.38	3/6 60 W	3.8	13	25	0	0.49	0.77
Prasch	0.33	3/6 60 W	3.8	13	33	0	0.62	0.53
Boris	0.39	3/1 40 W	1.8			2.4		
Edna	0.54	3/2 55 W	1.8	4.9	28	3.5	0.83	0.65
Samantha	0.53	3/1 40 W	1.8	4.6	22	4.1	0.79	0.67
AL TTC	0.54	5/2 97 W	6.1	8.0			0.69	0.78
	0.53	5/1 49 W	3.1		26	4.4		
	0.45	3/1 30 W	1.9					
Barbara	0.53	5/2 97 W	3.1	6.0		4.8		
	0.43	3/1 30 W	1.0					
Gloria	0.58	3/2 53 W	1.7	5.0	35	6.9	0.86	0.68
Anna	0.39	3/1 30 W	1.0	7.0				
	0.31	2/1 20 W	0.6			9.3		
	0.24	1/1 10 W	0.3					
Simone	0.45	2/2 60 W	3.8		32	9.6		
Dolly	0.42	5/2 90 W	2.9			21		
	0.42	3/1 30 W	1.0	5.6		21		

Table 7.1: Cell Performance with Broadband Lasers. For the pure Rb (hybrid) cells, the oven set temperature was 180 °C (235 °C). The entry n/m P_0 in the "lasers" column indicates that n lasers with a total power of P_0 was incident on the pumping chamber. The second number m refers to the number of beamlines. Finally, I_0 refers to the laser intensity at the front of cell estimated by $2P_0/(\pi w^2)$, where w is the radius of the pumping chamber.

It was tempting to believe that a low alkali polarization ($P_A \approx 0.7$) was once again the culprit. Before we had the diagnostic tools to verify this directly, all we could do was significantly increase the laser power to indirectly test this hypothesis.

7.2 Limits to the Alkali and He-3 Polarizations, Part I

To illustrate the point made at the end of the previous section, we'll discuss the performance of two cells listed in Tab. (7.1), AL TTC and Dolly, as a function of laser power. AL TTC had a 2.5 in diameter pumping chamber with a D within the optimal range. Doubling the laser power resulted in very little improvement in the ^{3}He polarization $0.53 \rightarrow 0.54$. Given that this cell had a 2.5 in diameter pumping chamber and that the size of the laser beam was adjusted to match the size of the pumping chamber, this cell was pumped with the highest laser intensity I_0 (power per unit area) available in our lab at time. Dolly was a 3.5 in diameter pumping-chamber cell with a D that was well outside the optimal range. In this case, tripling the laser power resulted in essentially no improvement in the ^{3}He polarization $0.42 \rightarrow 0.42$, see [2] for more details regarding the conditions of the high laser power measurement.

While one could argue that this laser power was not sufficient to saturate the alkali polarization in a pure Rb cell, it was difficult to make this argument for the case of a hybrid cell, since they did exihibit an increase in ^{3}He polarization. The most straightforward explanation for these observations was that the laser power that was being supplied was sufficient to achieve the highest alkali polarization possible under those experimental conditions. If the ^{3}He relaxation rate did not increase significantly with temperature, then this would necessarily imply that

$P_A \approx 0.7$ was the highest attainable alkali polarization. This conclusion was difficult to defend, because, even at that time, several authors had reported alkali polarizations from direct measurements with broadband laser light in excess of 0.90 [3, 4]. On the other hand, anecdotal evidence had existed for years that the "hot" cell lifetime (i.e. the lifetime measured with the lasers off and the cell near operating temperature), after the A-^{3}He spin exchange rate had been subtracted out, appeared to be shorter than the "cold" cell lifetime (i.e. the lifetime measured with the lasers off and the cell at room temperature). This observation was difficult to verify accurately because of the factor of two variation in the spin exchange rate constants k_{se} that were reported in the literature at that time.

The first reliable measurements (see Sec. (D.3.1) for a more detailed discussion) of the A-^{3}He spin exchange rate constant was made by the Princeton Group [5]. These results were later confirmed by the Wisconsin Group [6], who further demonstrated unambiguously that the hot lifetime was indeed shorter than the cold lifetime. Subsequently, they demonstrated that the excess ^{3}He relaxation present while the cell is hot appeared to be linearly proportional to the alkali density [7]. This implies the following relationship among the hot & cold cell lifetimes and the spin up time constant:

$$\Gamma_{He}^{hot} = \Gamma_{He} + f_{pc} k_{se}[A] X \qquad \rightarrow \qquad \Gamma_s - \Gamma_{He} = f_{pc} k_{se}[A](1 + X) \tag{7.4}$$

which implies that the equilibrium ^{3}He polarization is given by:

$$P_{He} = \frac{P_A}{1 + X}\left[1 - \frac{\Gamma_{He}}{\Gamma_s}\right] \tag{7.5}$$

where X is due to some ^{3}He relaxation mechanism that scales with the alkali den-

sity or has the same temperature dependance of the alkali vapor pressure curve (i.e. $\approx T^{20}$).

Accepting the X-factor hypothesis, the limiting ^{3}He polarization is given by $P_A/(1+X)$, which, by comparing Eqns. (7.3) & (7.5), we find is equal to P_A^{calc}. By ignoring the fact that these cells were tested under different conditions, we simply took an average of P_A^{calc} and estimated $P_A/(1+X) = 0.67 \pm 0.09$ for pure Rb cells & 0.70 ± 0.06 for hybrid cells within the optimal range. By assuming that X was independant of D, we concluded that the alkali polarization was nearly the same for pure Rb cells and hybrid cell within the optimal range. Since both the typical spin up time constant was much shorter and the laser intensity was usually lower for our tests of hybrid cells, we essentially verified our previous claim that hybrid cells would polarize a higher alkali density to the same alkali polarization for the same laser power. Measurements of Γ_s, Γ_{He}, and P_{He} alone did not allow us to establish to what extent the ^{3}He polarization was limited by nonunity P_A and nonzero X when pumping with broadband lasers.

7.3 The Impact of Narrowband Lasers

Tab. (7.2) is a list of target cells & their performance using narrowband lasers. With the exception of Sosa, Simone, & Dolly, each of these cells had a 3.0 in diameter pumping chamber and was designed & constructed for use in the "Transversity" group of experiments listed in Tab. (3.1). Using the experience gained from the E02013 target cell production run, we adjusted our alkali-hybrid mixture preparation prescription, see Sec. (3.3), to insure that we obtained cells with a D within the optimal range, 5 ± 2. Of the cells listed in Tab. (7.2), only two fell significantly

cell	P_{He}	Lasers	I_0	Γ_s^{-1}	Γ_{He}^{-1}	D (PB/EPR)	P_{He}^*	P_A	X
Sosa	0.58	2NB/1BB	1.9	17	78	0/0		0.95	0.29
Alex	0.59	2NB/1BB	2.6	4.8	33	1.2/1.5	0.59	0.96	0.39
Stephanie	0.64	3NB	2.7	4.5	48	1.5/1.7		0.99	0.40
Brady	0.72	3NB	2.6	5.2	36	2.2/2.9	0.43	0.99	0.18
Moss	0.63	1NB/1BB	1.8	5.4	33	-/2.9	0.56	0.97	0.29
Tigger	0.51	1NB/1BB	1.8	4.9	13	-/4.2		0.95	0.13
Samantha	0.70	3NB	2.6	4.6	22	4.1/5.4	0.56	0.99	0.12
Maureen	0.69	3NB	2.7		29	-/6.3		0.98	
Astralweeks	0.70	2NB/1BB	2.6	6.6	49	6.2/8.5	0.31	0.97	0.20
Simone	0.62	2NB/1BB	3.8		32	9.6/16		0.90	
Dolly	0.62	1NB/1BB	1.3	5.8		21/-			

Table 7.2: Cell Performance with Narrowband Lasers. The labels "nNB" & "mBB" refer to the number of narrowband (n) and (m) broadband lasers used for the measurement. Each laser had a power incident on the pumping chamber of about 20 W.

outside that range, which indicated that we indeed achieved a sufficient level of control over the ratio D. Of the cells that were pumped with three narrowband lasers (and no broadband lasers), three out of four achvieved ^{3}He polarizations near or above 0.70. Regardless of D, so long as even one narrowband laser was used, all but one cell listed in Tab. (7.2) achieved or significantly exceeded the best performance, using only broadband lasers, listed in Tab. (7.1). The cell, Tigger, with the poorest performance had an unusually short lifetime. Even so, this cell still outperformed every pure Rb cell that we had ever pumped in our apparatus using only broadband lasers.

For the best performance, as it related to D, we found that the optimal range using narrowband lasers was $3 \leq D \leq 9$ or equivalently $D = 6 \pm 3$. This result was consistent with what we found for broadband lasers and was in complete agreement with the finding from the previous simulations that the optimal value of D

was relatively insensitive to the laser linewidth. We'll note that Sosa, a 3.5 in diameter pumping-chamber pure Rb cell, achieved the highest ^{3}He polarization that we've ever obtained for a pure Rb target cell. This was due to both the fact that it had an unusually long lifetime and that it was pumped using mostly narrowband laser power.

7.4 "Masing" Effects

During these set of tests, we observed that the ^{3}He polarization was much lower when pumping to the high energy state, see Fig. (4.14), than when pumping to the low energy state, see Fig. (4.13). These lower polarizations are listed as P^*_{He} in Tab. (7.2) and, for example, the cell Astralweeks was only able to obtain a ^{3}He polarization of 0.31 when pumped to the high energy state. We were able to suppress this effect by applying a sufficiently large longitudinal magnetic field gradient (≈ 10 mG/cm) along the holding field direction. This gradient was small enough not to significantly reduce the ^{3}He polarization due to the relaxation, see Sec. (6.2.2).

Because of the dependence on the sign of the ^{3}He polarization and the response to a magnetic field gradient, we called this effect the "masing" effect due to its similarities to the masing effect described in [8,9]. However, unlike the effect decribed in [8], we could find no obvious coupling between the ^{3}He magnetization and our NMR pickup coils. Furthermore, such an effect had been observed in several JLab experiments and there was anecdotal evidence that this effect only occured in the pumping chamber. We believe that we have verified this by our simultaneous NMR measurements of the pumping & target chambers using two sets of NMR

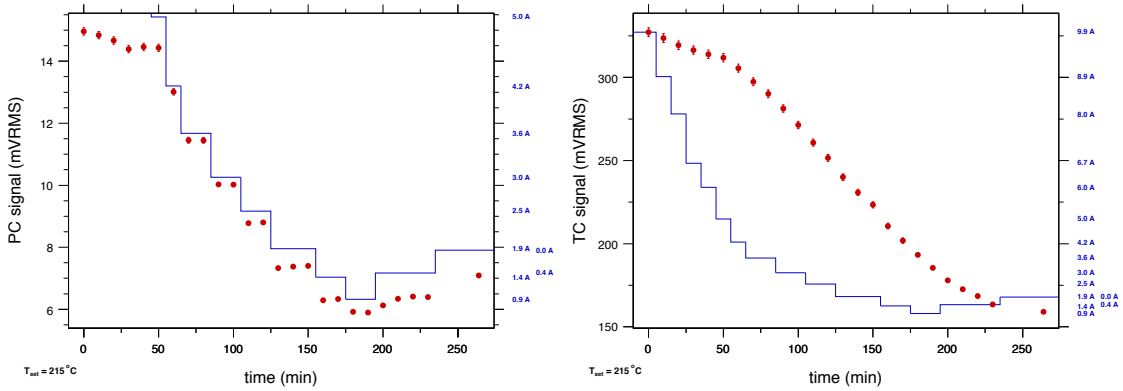

Figure 7.1: Masing Effect in the Target Cell Astralweeks. The red data points are the NMR signal in either chamber. The solid blue lines are the current in the gradient coil. The left (right) plot is for the pumping (target) chamber. .

pickup coils. Fig. (7.1) shows the NMR signal in the pumping & target chambers as a function of time a the current in the gradient coils is varied. As the current was lowered in a stepwise fashion, the NMR signal in the pumping chamber also dropped in a stepwise fashion. Whereas the NMR signal dropped almost instantaneously in the pumping chamber, the NMR signal in the target chamber appeared to exhibit a time lag of several minutes and then only slowly & smoothtly lowered in size. We took this as evidence that the masing effect occurred only in the pumping chamber. Regardless of the physical origin of this effect, a magnetic field gradient can suppress it and is absolutely required to achieve high polarization when pumping to the high energy state.

7.5 Limits to the Alkali and He-3 Polarizations, Part II

We were able to measure the alkali polarization directly using EPR RF spectrocopy, which is a standard diagnostic tool in spin exchange optical pumping, see for example [3, 4, 6]. Fig. (7.2) shows a typical EPR RF spectra in a hybrid cell which a

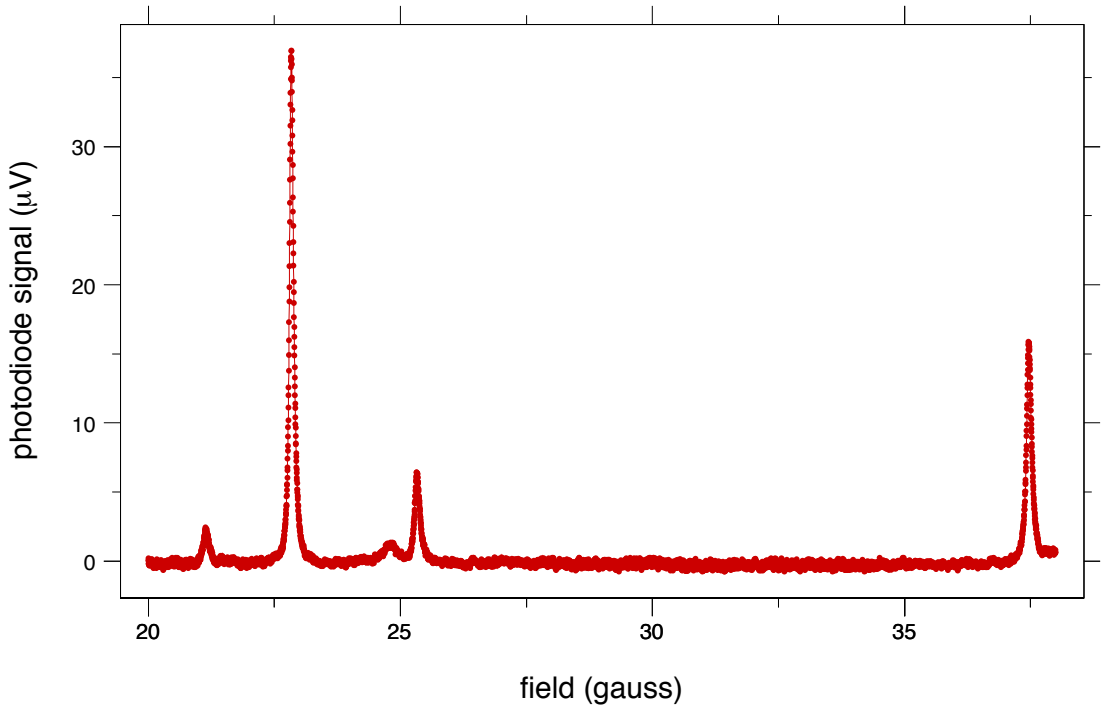

Figure 7.2: Alkali EPR RF Spectra at 18.3 MHz. .

D =? and represents an alkali polarization of P_A =?. It is straightfoward to show that the ratio of areas under consecutive peaks for the same alkali isotope can be related to the alkali polarization, see Sec. (E.10.3). In addition, the alkali-bybrid ratio D under operating conditions can also be determined using these spectra, see Sec.(E.10.4).

Armed with this additional diagnostic tool, we retested three cells, Samantha, Simone, & Dolly, from Tab. (7.1) using narrowband lasers. The improvement in performance, $0.42 \rightarrow 0.62$, for Dolly was particularly striking. As noted before, increasing the broadband (only) laser power for Dolly by a factor of three resulted in no gains in ^{3}He polarization. On the other hand, simply replacing one broadband laser with one narrowband laser resulted in a ^{3}He polarization nearly 50% relative higher with half the total laser power. Of the three, Samantha had a D

that was closest to the optimal value and showed an increase from 0.53, using only broadband lasers, to 0.70, using only narrowband lasers. While Samantha had a near unity alkali polarization, Simone, with a D outside the optimal range, had the lowest measured alkali polarization of the all the cells tested. Unfortunately, this cell ruptured before we could perform any alkali polarization measurements.

Regardless, given the improvements in performance of these three cells with narrowband lasers and by direct measurements of the alkali polarization in other cells, it was safe to infer that pumping with broadband lasers resulted in alkali polarizations that were nonunity. Furthermore, we have never measured an alkali polarization in excess of 0.90 using only broadband lasers. On the other hand, for the cells with a D within the optimal range, the alkali polarizations were never below 0.95. Under ideal conditions (i.e. three narrowband lasers with no broadband lasers), these cells obtained alkali polarization in excess of 0.97 in every case.

Because of the variations in laser conditions, it was difficult to draw firm conclusions about the relationship between D and the alkali polarization. With that said, a decrease in alkali polarization for increasing values of D beyond the optimal value was the bevahiour that one would expect based on the results of the simulation and the results of the Wisconsin Group [10]. A natural explanation for this was due to the increased sensistiity to off resonant pumping of the K D2 transition, which scales with D. This would also explain the dramatic improvement one obtains using narrowband lasers compared to broadband lasers.

As mentioned previously, the limiting ^{3}He polarization is given by $P_{\mathrm{A}}/(1+X)$. Since pumping with narrowband lasers, under ideal conditions, can result in nearly unity alkali polarization, the value of X determines the limiting ^{3}He polarization obtainable for a given cell. A direct measurement of the alkali polarization,

in combination with the other measurements that we already performed on the target cells, allowed us to extract X for any cell of interest using the following equation:

$$X = \frac{P_A}{P_{He}} \left[1 - \frac{\Gamma_{He}}{\Gamma_s} \right] - 1 \tag{7.6}$$

Before discussing the values of X listed in Tab. (7.2), it is important to note that three points. First, we measured the alkali polarization using two different probes that were sensitive to differnt regions of the pumping chamber. Faraday rotation, see Sec. (E.9.2), utilizes a probe beam that was sensitive to the alkali polarization along its path through the cell. On the other hand, the intensity of the D2 fluorescence measured by the photodiode, see Sec.(4.4.2), was sensitive to some region in the pumping chamber that was closest to the photodiode. It was entirely possible that neither of these methods was truly representative of the volume averaged alkali polarization. With that said, we have found satisfactory agreement between these two methods.

Second, the cold lifetime Γ_{He}^{-1} is partly due to the dipolar interactions among the ^{3}He nuclei themselves. The relaxation rate associated with this interaction has known dependences on the ^{3}He temperature and density, see Sec.(D.5.1), that were not accounted for in our preliminary determinations of X. The third and final point concerns the proper interpretation of Γ_s. As discussed in Sec. (6.1.4), the spin up curves measured in two chambered cells was always the sum of two exponentials, one with a fast time constant and one with a slow time contant. However, the spin up time constants used to detemine X were the results of single exponential fits to the data, which was appropriate only in the fast diffusion limit. This necessitates corrections of order Γ_s/d_{tc}, which have not been made yet, where d_{tc} ($\approx 1/\text{hr}$) was the diffusion rate between the two chambers.

The range of X that we've extracted for 3 in diameter pumping chamber cells was $0.12 \leq X \leq 0.40$. The lowest values for X that we've measured (≈ 0.12) were among the lowest values observed by the Wisconsin & NIST Groups [7]. Both of these observations were in completement aggreement with their measurements that indicated $\approx 0.1 \leq X \leq (0.4 \text{ cm})\, S/V$, where S/V is the surface to volume ratio of the cell. Using $P_A/(1+X)$ and assuming $P_A = 1$, we inverted our measured X range to find $0.7 \leq P_{He} \leq 0.9$. This has indicated that we may be, for the first time, truly approaching the limits of ^{3}He polarization attainable in target cells.

7.6 Summary & Outlook

Fig. (7.3) depicts the ^{3}He polarization as a function of the alkali-hybrid ratio D and the laser intensity I_0. The most salient features of these two plots can be summarized by the following statement: *To insure the best performance, a target cell, with a D within the range* 5 ± 2, *should be pumped by narrowband lasers ($\Delta\nu \approx 0.2$ nm) with an intensity of at least* 2.5 W/cm^2.

Given the values of X that we've measured in our target cells, it was tempting to think that, at suffiently high laser intensity and alkali density (i.e. temperature), we should obtain polarizations in excess of 0.80. If one were not concerned with damaging the cells, this could be tested, with the cells and laser intensity presently available, by simply increasing the cell temperature by an additional 25 ^{o}C. On the other hand, if we have truly identified all of the factors limiting the ^{3}He polarization, then a 4.5 in diameter pumping chamber cell with a 45 hr lifetime and $X = 0.15$ should achieve a ^{3}He polarization of 0.80 at present operating temperatures.

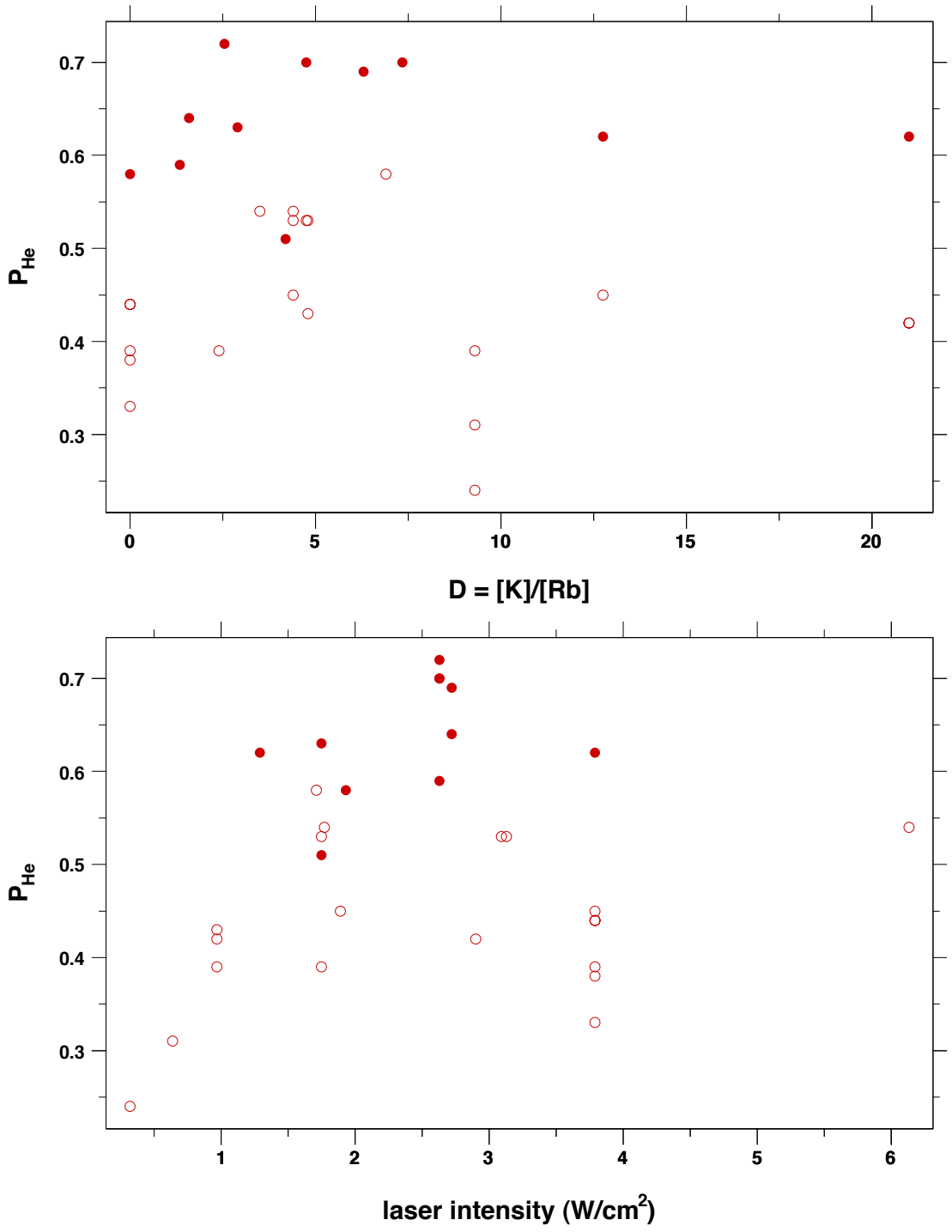

Figure 7.3: Target Cell Performance as a Function of Alkali-Hybrid Ratio and Laser Intensity .

Although, as a practical matter, it has been shown that the alkali polarization can be made unity under the appropriate conditions, it is still interesting to determine the mechanism that limits the alkli polarization at high D and/or when pumping with broadband lasers. Whatever the mechanism, the relaxation rate associated with it must scale with the D1 optical pumping rate (i.e. laser power). One potentially useful probe of some of these dynamics may be the relative population of the excited state of the alkali atoms. They may be monitored by measuring the spectrum of fluroecnes emitted by the deexciting atoms.

Finally, we'll end with some speculative comments about the nature of X. Based only the measurements listed in Tab. (7.2), one could argue that X appears to decrease with decreasing lifetimes or with increasing values for D. More measurements along these lines may be profitable. In calculating X, we have assumed that the relaxation mechanism that was associated with X was only present in the pumping chamber and not in the target chamber. Our only justification for this assumption was the observation [7] that this mechanism appeared to increase with alkali density and/or temperature, both of which are higher in the pumping chamber. It would be interesting to find a way to measure X separately for the two chambers.

Bibliography

[1] J. Alcorn et al. Basic instrumentation for Hall A at Jefferson Lab. *Nuclear Instruments and Methods in Physics Research Section A: Accelerators, Spectrometers, Detectors and Associated Equipment*, 522(3):294 – 346, 2004.

[2] Aidan M. Kelleher. *A MEASUREMENT OF THE NEUTRON ELECTRIC FORM FACTOR AT VERY LARGE MOMENTUM TRANSFER USING POLARIZED ELECTRONS SCATTERING FROM A POLARIZED HELIUM-3 TARGET*. PhD thesis, College of William and Mary, 2010.

[3] A. Ben-Amar Baranga, S. Appelt, C. J. Erickson, A. R. Young, and W. Happer. Alkali-metal-atom polarization imaging in high-pressure optical-pumping cells. *Phys. Rev. A*, 58(3):2282–2294, Sep 1998.

[4] S. Appelt, T. Unlu, K. Zilles, N. J. Shah, S. Baer-Lang, and H. Halling. Experimental studies of rubidium absolute polarization at high temperatures. *Applied Physics Letters*, 75(3):427–429, 1999.

[5] A. Ben-Amar Baranga, S. Appelt, M. V. Romalis, C. J. Erickson, A. R. Young, G. D. Cates, and W. Happer. Polarization of ^{3}He by Spin Exchange with Optically Pumped Rb and K Vapors. *Phys. Rev. Lett.*, 80(13):2801–2804, Mar 1998.

[6] B. Chann, E. Babcock, L. W. Anderson, and T. G. Walker. Measurements of ^{3}He spin-exchange rates. *Phys. Rev. A*, 66(3):032703, Sep 2002.

[7] E. Babcock, et al. Limits to the polarization for spin-exchange optical pumping of ^{3}he. *Phys. Rev. Lett.*, 96(8):083003, 2006.

[8] Mikhail V. Romalis. *Laser Polarizaed* ^{3}He *Target Used for a Precision Measurement of the Neutron Spin Structure*. PhD thesis, Princeton University, 1997.

[9] M. V. Romalis and W. Happer. Inhomogeneously broadened spin masers. *Phys. Rev. A*, (2):1385–1402, Aug 1999.

[10] E. Babcock, et al. Hybrid Spin-Exchange Optical Pumping of ^{3}He. *Phys. Rev. Lett.*, 91(12):123003, Sep 2003.

Appendix A

Units, Physical Constants, and Alkali Reference Data

A.1 Units & Physical Constants

All units are in SI unless otherwise noted. The following relationship sets a useful scale for nuclear reactions:

$$\hbar c = 197.32696 \text{ MeV} \cdot \text{fm} = 0.19732696 \text{ GeV} \cdot \text{fm} \tag{A.1}$$

If we set $\hbar = c = 1$, then nuclear energy & distance scales are related by:

$$\begin{aligned} \text{GeV}^2 &= 25.681900/\text{fm}^2 && \text{(A.2)} \\ 1/\text{GeV}^2 &= 0.389379304 \text{ mb} && \text{(A.3)} \\ 1 \text{ b} &= 10^{-24} \text{ cm}^2 && \text{(A.4)} \\ 1 \text{ amu} &= 931.494028 \text{ MeV} && \text{(A.5)} \end{aligned}$$

symbol	value	units	description
c	299 792 458	m/s	speed of light in vacuum
μ_0	$4\pi \times 10^{-7}$	N/A^2	magnetic constant
ϵ_0	$8.854\,187\,817 \times 10^{-12}$	$C^2/(N \cdot m^2)$	electric constant
e	$1.602\,176\,5 \times 10^{-19}$	C	elementary charge
m	$9.109\,382 \times 10^{-31}$	kg	electron mass
g_S	$-2.002\,319\,304\,36$	unitless	electron g-factor
r_e	$2.817\,940\,29 \times 10^{-15}$	m	classical electron radius
μ_B	$9.274\,009 \times 10^{-24}$	J/T	Bohr magneton
μ_N	$5.050\,783 \times 10^{-27}$	J/T	Nuclear magneton
h	$6.626\,069 \times 10^{-34}$	$J \cdot s$	Planck constant
α^{-1}	137.035 999 7	unitless	inverse fine structure constant
N_A	$6.022\,142 \times 10^{23}$	#/mol	Avogadro constant
k	$1.380\,65 \times 10^{-23}$	J/K	Boltzmann constant
R	8.314 5	$J/(mol \cdot K)$	molar gas constant
amu	$1.660\,538\,8 \times 10^{-27}$	kg	$\left(\text{mass } {}^{12}C\right)/12$

Table A.1: Physical Constants. These values are from CODATA 2006 [1].

The following relationships are useful for ^{3}He polarimetry:

$$\mu_0\mu_N = \frac{1.70530\ \text{mG}}{\text{amg}} = \frac{17.0530\ \text{nV}}{\text{amg} \cdot \text{cm}^2 \cdot \text{kHz}} \tag{A.6}$$

$$\mu_B/k = 6.7171 \times 10^{-5}\ \text{K/G} \tag{A.7}$$

$$\mu_B/h = 1.3996246\ \text{MHz/G} \tag{A.8}$$

$$\mu_N/k = 3.65826 \times 10^{-8}\ \text{K/G} \tag{A.9}$$

$$\mu_N/h = 0.7622594\ \text{kHz/G} \tag{A.10}$$

The following relationships are useful for determining atomic cross sections & rate constants:

$$R = kN_A \tag{A.11}$$

$$k/h = 20.8366\ \text{GHz/K} \tag{A.12}$$

$$1\ \text{amg} = \frac{101325\ \text{Pa}}{k \cdot (273.15\ \text{K})} = 2.68678 \times 10^{19}/\text{cm}^3 \tag{A.13}$$

$$10^{15}/\text{cm}^3 = 37.2193\ \mu\text{amg} \tag{A.14}$$

$$1\ \text{Å}^2 = 10^{-16}\ \text{cm}^2 \tag{A.15}$$

$$1\ \text{Hz/amg} = 3.72193 \times 10^{-20}\ \frac{\text{cm}^3}{\text{s}} = 3.72193 \times 10^{-4}\ \text{Å}^2 \cdot \frac{\text{cm}}{\text{s}} \tag{A.16}$$

$$10^{-18}\ \text{cm}^3/\text{s} = 0.01\ \text{Å}^2 \cdot \frac{\text{cm}}{\text{s}} = 10^6\ \text{b} \cdot \frac{\text{cm}}{\text{s}} = 26.8678\ \frac{\text{Hz}}{\text{amg}} \tag{A.17}$$

$$1\ \text{MHz}/\left(10^{15}/\text{cm}^3\right) = 10^{-9}\ \text{cm}^3/\text{s} = 10^7\ \text{Å}^2 \cdot (\text{cm/s}) \tag{A.18}$$

$$\Delta\nu = -474.3\ \text{GHz} \left(\frac{\Delta\lambda}{+1\ \text{nm}}\right) \left(\frac{795\ \text{nm}}{\lambda}\right)^2 \tag{A.19}$$

$$\bar{v}_{\text{rel.}} = 1.00089 \times 10^5\ \frac{\text{cm}}{\text{s}} \sqrt{\left(\frac{T}{473.15\ \text{K}}\right) \left(\frac{10\ \text{g/mol}}{\mu_{\text{reduced}}}\right)} \tag{A.20}$$

where one amagat (amg) is the density of a universal gas at a temperature & pressure of 273.15 K & 1 atm. The following relationships are useful when calculating the polarizability of alkali atoms:

$$\epsilon_0 = 1/(c^2\mu_0) \tag{A.21}$$

$$\alpha = \frac{e^2}{4\pi\epsilon_0\hbar c} = \left(\frac{mc}{\hbar}\right) r_e \tag{A.22}$$

$$r_e = \frac{e^2}{4\pi\epsilon_0 mc^2} = \left(\frac{\hbar}{mc}\right) \alpha \tag{A.23}$$

$$r_e c = \frac{\hbar\alpha}{m} = 0.84479725 \times 10^{-15}\ \text{THz} \cdot \text{cm}^3/\text{mm} \tag{A.24}$$

Element	Ground State	$S_{1/2}$ g_J/g_S	$P_{1/2}$ g_J	$P_{3/2}$ g_J	$\nu_{\mathtt{so}}$ (GHz)	$y=1$ (T)
Lithium	2	1.000 003 4	−0.667	−1.335	9.994 18	0.712
Sodium	3	1.000 000 9	−0.665 8	−1.334 2	515.730	36.7
Potassium	4	1.000 018 44			1 730.32	123
Rubidium	5	1.000 005 9			7 124.94	508
Cesium	6	1.000 104 474	−0.665 90	−1.334 0	16 614.2	1180
Theory (if $g_S=-2$)		1.000 000 000	−0.665 894 −2/3	−1.334 106 −4/3		
Reference	[3]		[2]		(E.57)	(E.59)

Table A.2: Alkali atom ground state and first excited states fine structure.

A.2 Alkali Atom Fine & Hyperfine Structure

An excellent source of alkali D line data has been complied by Daniel Steck at `http://steck.us/alkalidata/`. The spin-orbit splitting is simply the difference between the D2 and D1 transition frequencies: $\nu_2 - \nu_1 = \nu_{\mathtt{so}}$. The strength of the Zeeman interaction relative to the spin-orbit (hyperfine [only for $J=1/2$]) coupling is quantified by the unitless parameter y (x) which is given by:

$$y = \left[\frac{g_S}{-2}\right]\frac{2\mu_B B_0}{h\nu_{\mathrm{so}}} \qquad\qquad x = \left(g_I\mu_N - g_J\mu_B\right)\frac{B_0}{h\nu_{\mathrm{hfs}}} \tag{A.25}$$

where B_0 is the magnetic field. The relative energy of a particular manifold F is given by [2]:

$$E_F = \frac{AK}{2} + \frac{B}{2}\left[\frac{3K(K+1) - 2I(I+1)2J(J+1)}{2I(2I-1)2J(2J-1)}\right] \tag{A.26}$$

where $K = F(F+1) - I(I+1) - J(J+1)$, I is the nuclear spin, and J is the total electronic angular momentum. This formula can be used to calculate the fine structure energy levels with the substitutions $B=0$, $F \to J$, $I \to S$, and $J \to L$.

Element	D1					D2				
	λ_1 (nm, air)	τ_1 (ns)	f_1	τ_1 (ns)	f_1	λ_2 (nm, air)	τ_2 (ns)	f_2	τ_2 (ns)	f_2
Lithium	670.791	26.9	0.251	27.3	0.247	670.776	26.9	0.502	27.9	0.494
Sodium	589.592 4	16.2	0.322	16.4	0.318	588.995 0	16.1	0.647	16.3	0.637
Potassium	769.896	26.2	0.340	27	0.35	766.490	25.8	0.682	27	0.70
Rubidium	794.760 3	27.7	0.342	28.5	0.32	780.026 8	26.2	0.695	26.5	0.67
Cesium	894.347	34.8	0.344	31	0.39	852.113	30.53	0.7131	31	0.81
Reference	[3]			[4]		[3]			[4]	

Table A.3: Alkali atom D1 and D2 transition wavelengths (λ), lifetimes (τ), and oscillator strengths (f). Data from NIST Atomic Spectra Database [3] and Radzig & Smirnov [4]. These oscialltor strengths are for low buffer gas density. At higher buffer gas density, the oscialltor strengths decreases, for example, see [5, 6]. Although the sum ($f_1 + f_2$) varies from 0.75 to 1.06, the ratio f_2/f_1 equals 2 to better 4% relative for the alkali atoms listed in the table.

Element	D1			D2			
	λ_1 (air, nm)	λ_1 (vac, nm)	ν_1 (GHz)	λ_2 (air, nm)	λ_2 (vac, nm)	ν_2 (GHz)	ν_{so} (GHz)
Lithium	670.791	670.976	446 800.6	670.776	670.961	446 810.6	10.0
Sodium	589.592 4	589.755 8	508 333.2	588.995 0	589.158 2	508 848.8	515.6
Potassium	769.896	770.108	389 286.3	766.490	766.701	391 016.1	1 729.9
Rubidium	794.760 3	794.978 9	377 107.4	780.026 8	780.241 4	384 230.4	7 123.0
Cesium	894.347	894.593	335 116.0	852.113	852.347	351 725.8	16 609.8

Table A.4: Alkali atom D1 & D2 air & vacuum transition wavelengths (λ), transition frequencies (ν), and spin-orbit splitting (ν_{so}). Data are from the NIST Atomic Spectra Database [3]. The air wavelengths are calculated from the vacuum wavelengths assuming "standard air" using the 1972 formula of Peck & Reeder [7].

	Mass (amu)	**Abd.**	I	μ (μ_N)	g_I	$\epsilon(I, P_A)$ $P_A = 0$	$\epsilon(I, P_A)$ $P_A = 1$	$s = 1 + \epsilon$ $P_A = 0$	$s = 1 + \epsilon$ $P_A = 1$
Li	6.941					4.823	2.924	5.823	3.924
^{6}Li	6.0151223	0.0759	1	+0.822056	+0.822056	8/3	2	11/3	3
^{7}Li	7.0160040	0.9241	3/2	+3.25644	+2.17096	5	3	6	4
Na	22.989770					5	3	6	4
^{23}Na	22.9897697	1.0	3/2	+2.21752	+1.47835	5	3	6	4
K	39.0983					5.003	3.001	6.003	4.001
^{39}K	38.9637069	0.93258	3/2	+0.39146	+0.26097	5	3	6	4
^{40}K	39.9639987	0.000117	4	−1.298	−0.3245	80/3	8	83/3	9
^{41}K	40.9618260	0.06730	3/2	+0.21487	+0.14325	5	3	6	4
Rb	85.4678					9.811	4.443	10.81	5.443
^{85}Rb	84.911789	0.7217	5/2	+1.35302	+0.541208	35/3	5	38/3	6
^{87}Rb	86.909184	0.2783	3/2	+2.7512	+1.8341	5	3	6	4
Cs	132.90545					21	7	22	8
^{133}Cs	132.905447	1.0	7/2	+2.579	+0.7369	21	7	22	8

Table A.5: Alkali Isotopic & Nuclear Data. $\epsilon(I, P_A)$ is the paramagnetic coefficient and s is the nuclear slowing down factor. For $P_A = 0$, $\epsilon = 4I(I+1)/3$ and for $P_A = 1$, $\epsilon = 2I$. Data is from the NIST Handbook of Basic Atomic Spectroscopic Data [8].

	$S_{1/2}$			$P_{1/2}$			$P_{3/2}$	
	A/h (MHz)	ν_{hfs} (MHz)	$x=1$ (G)	A/h (MHz)	ν_{hfs} (MHz)	$x=1$ (G)	A/h (MHz)	B/h (MHz)
^{6}Li	152.136 841	228.205 261	81.4	17.38	26.06	27.9	−1.155	−0.1
^{7}Li	401.752 043 3	803.504 086 6	287	45.92	91.83	98.4	−3.055	−0.22
^{23}Na	885.813 064 4	1 771.626 128	632	94.3	188.6	202	18.69	2.9
^{39}K	230.859 860 1	461.719 720 2	165	28.85	57.70	61.8	6.06	2.8
^{40}K	−285.731	−1 285.79	459	−34.52	−155.3	167	−7.59	−3.5
^{41}K	127.006 935 2	254.013 870 4	90.6	15.25	30.50	32.7	3.40	3.3
^{85}Rb	1 011.910 813	3 035.732 439	1 080	120.72	362.16	388	25.01	25.88
^{87}Rb	3 417.341 306 4	6 834.682 612 8	2 440	406.2	812.4	870	84.845	12.52
^{133}Cs	2 298.157 942 5	9 192.631 770	3 280	291.9	1 167	1 250	50.34	−0.4
Ref.	[2]	(E.186)	(E.188)	[2,9]	(E.186)	(E.188)	[2]	

Table A.6: Alkali atom ground state and first excited states hyperfine structure. All of the data is from the 1977 RMP [2] except for the ^{40}K $P_{1/2}$ data which is from [9]. There is still an unresolved discrepancy for the excited state hyperfine structure constants for K between [9] and [10].

A.3 Alkali Metal Vapor Pressure Curves

A.3.1 The Clausius-Clapeyron Equation

The saturated vapor pressure above a liquid (solid) is described by the Clausius-Clapeyron equation. It is a consequence of the equality between the chemical potentials of the vapor and liquid (solid). The derivation can be found in any undergraduate text on thermodynamics (e.g. Kittel & Kroemer [11]):

$$\Delta v \cdot \partial P = L \cdot \partial T / T \tag{A.27}$$

where P is the pressure, T is the temperature, L is the latent heat of vaporization (sublimation) per particle, and Δv is given by:

$$\Delta v = v_{\mathtt{v}} - v_{\mathtt{l(s)}} = \frac{V_{\mathtt{v}}}{N_{\mathtt{v}}} - \frac{V_{\mathtt{l(s)}}}{N_{\mathtt{l(s)}}} \tag{A.28}$$

where V is the volume occupied by the particles, N is the number of particles, and the subscripts $\mathtt{v}$ & $\mathtt{l(s)}$ refer to the vapor & liquid (solid) respectively.

Following the derivation in Nesmeyanov [12], we'll make the approximation that the average volume per vapor atom is much greater than the average volume per liquid (solid) atom:

$$v_{\mathtt{v}} \gg v_{\mathtt{l(s)}} \quad \Rightarrow \quad \Delta v \approx v_{\mathtt{v}} = \frac{V_{\mathtt{v}}}{N_{\mathtt{v}}} \tag{A.29}$$

Since the vapor has a very low density, we can apply the ideal gas law:

$$PV_{\mathtt{v}} = N_{\mathtt{v}} kT \tag{A.30}$$

to get:

$$\left(kT/P\right) \cdot \partial P = L \cdot \partial T/T \tag{A.31}$$

Expanding the latent heat as a function of temperature,

$$L(T) = L_0 + L_1 T + L_2 T^2 + \cdots \tag{A.32}$$

and a little rearrangement gives:

$$\frac{\partial P}{P} = \left(\frac{L_0}{kT^2} + \frac{L_1}{kT} + \frac{L_2}{k} + \cdots\right) \partial T \tag{A.33}$$

Integrating the above equation term by term and making substitutions for the coefficients gives the vapor pressure curve:

$$\log P_{\text{vp}} = A - \frac{B}{T} + CT + D \log T \tag{A.34}$$

Note that the coefficients A, B, C, & D depend on whether a liquid or solid is being considered, the choice of units for the vapor pressure P_{vp}, and the base for the logarithm. The temperature T, however, is always in Kelvin.

A.3.2 Number Density Formulas

The number density is obtained from the vapor pressure curve by once again applying the ideal gas law:

$$[\text{A}] = \frac{N_{\text{v}}}{V_{\text{v}}} = \frac{P_{\text{vp}}}{kT} \tag{A.35}$$

For all alkali metals, the number density (in units of $1/\mathrm{cm}^3$) from the 1995 CRC [13] can be written in the following equivalent forms:

$$[\mathrm{A}] = \left[\left(\frac{101325\ \mathrm{Pa}}{1\ \mathrm{atm}}\right)\left(10^{A-B/T}\ \mathrm{atm}\right)\right]\cdot\left[\frac{1}{kT}\left(\frac{1\ \mathrm{m}}{100\ \mathrm{cm}}\right)^3\right] \tag{A.36}$$

$$= [\mathrm{A}]_0\left(\frac{T_0}{T}\right)\exp\left(b\left[1-\frac{T_0}{T}\right]\right) \tag{A.37}$$

where A & B are parameters from the CRC and $[\mathrm{A}]_0$, T_0, & b are parameters derived from them. These parameters are different for the vapor pressure above liquid and solid. At the melting point, the liquid and solid CRC formulas give values that are consistent within the quoted accuracy, see Tab. (A.8). Note that T_0 is the temperature corresponding to a density of $[\mathrm{A}]_0$.

The inversion formula used to obtain the temperature given the number density is of the form:

$$T = \frac{T_0}{1-\sum_{n=1}^{N} a_n\cdot\left(\log[\mathrm{A}]/[\mathrm{A}]_0\right)^n} \tag{A.38}$$

The coefficients $\{a_n\}$ are found from a fit to the Eqn. (A.38). The value of highest order N is found by keeping the temperature residuals under 0.02 K (0.005K) for liquids (solids) over the temperature range noted in the CRC. If only the lowest order term is kept ($N = 1$), then we get the following formula that is good to ± 2.5 K for Li and ± 1.2 K for all others:

$$T = \frac{T_0}{1-a_1\cdot\log[\mathrm{A}]/[\mathrm{A}]_0} \tag{A.39}$$

The values for parameters A, B, T_0, $[\mathrm{A}]_0$, b, & $\{a_n\}$ are listed in Tab. (A.7).

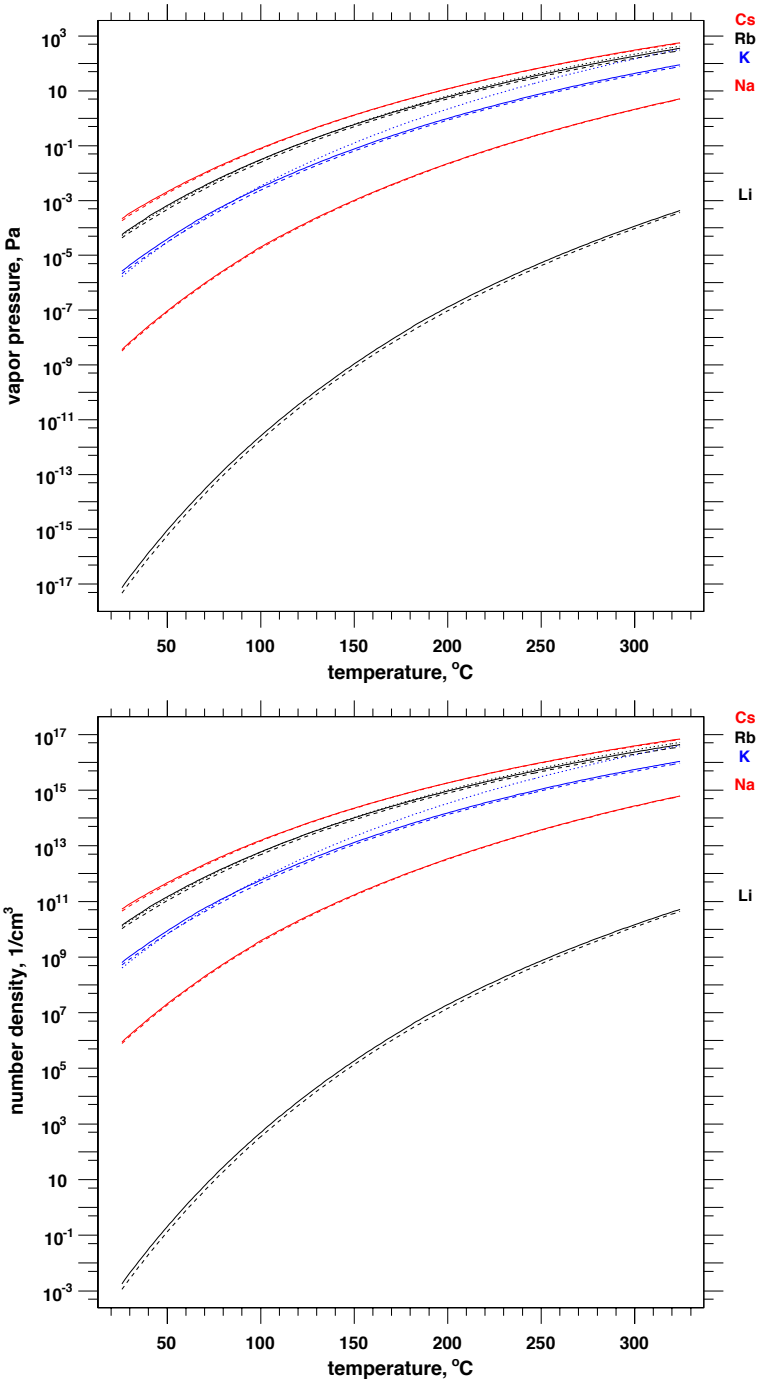

Figure A.1: Number Density and Vapor Pressure Curves. The solid lines represent the CRC formula [13]. The dashed lines represent the Nesmeyanov formula [12]. The dotted lines represent Killian [14].

CRC					
over solid	**Li**	**Na**	**K**	**Rb**	**Cs**
$T_{\mathtt{min}}$ (K)			298		
$T_{\mathtt{min}}$ (°C)			25		
$[\mathrm{A}]_{\mathtt{min}}$ (1/cm^3)	1.49×10^{-3}	7.72×10^{5}	5.78×10^{8}	1.27×10^{10}	4.82×10^{10}
$T_{\mathtt{mp}}$ (K)	453.7	370.87	336.53	312.46	301.59
$T_{\mathtt{mp}}$ (°C)	180.5	97.72	63.38	39.31	28.44
$[\mathrm{A}]_{\mathtt{mp}}$ (1/cm^3)	3.61×10^{6}	3.07×10^{9}	3.12×10^{10}	5.47×10^{10}	6.88×10^{10}
A	5.667	5.298	4.961	4.857	4.711
B (K)	8310	5603	4646	4215	3999
T_0 (K)	378.51	336.79	302.76	295.75	283.12
$[\mathrm{A}]_0$ (1/cm^3)	10^3	10^8	10^9	10^{10}	10^{10}
b	50.552	38.306	35.334	32.816	32.523
$a_1 \times 10^2$	2.0181	2.6806	2.9125	3.1447	3.1752
$a_2 \times 10^5$	0.41582	0.94564	1.3149	0	
$a_3 \times 10^8$	5.2686		0		
a_4			0		
over liquid	**Li**	**Na**	**K**	**Rb**	**Cs**
$T_{\mathtt{mp}}$ (K)	453.7	370.87	336.53	312.46	301.59
$T_{\mathtt{mp}}$ (°C)	180.5	97.72	63.38	39.31	28.44
$[\mathrm{A}]_{\mathtt{mp}}$ (1/cm^3)	3.79×10^{6}	3.18×10^{9}	3.22×10^{10}	5.66×10^{10}	7.11×10^{10}
$T_{\mathtt{max}}$ (K)	1000	700	600	550	
$T_{\mathtt{max}}$ (°C)	727	427	327	277	
$[\mathrm{A}]_{\mathtt{max}}$ (1/cm^3)	7.90×10^{15}	1.10×10^{16}	1.17×10^{16}	1.24×10^{16}	2.12×10^{16}
A	5.055	4.704	4.402	4.312	4.165
B (K)	8023	5377	4453	4040	3830
T_0 (K)	800.94	546.90	463.79	422.98	406.51
$[\mathrm{A}]_0$ (1/cm^3)			10^{14}		
b	23.065	22.638	22.108	21.993	21.694
$a_1 \times 10^2$	4.5321	4.6214	4.7377	4.7636	4.8324
$a_2 \times 10^5$	4.6950	4.9639	5.4499	5.5431	5.8187
$a_3 \times 10^6$	1.4241	1.6648	1.6322	1.7177	1.9172
$a_4 \times 10^8$	2.8057	4.5433		0	

Table A.7: CRC Number Density Parameters. The parameters listed are used in Eqns. (A.36), (A.37), (A.38), & (A.39). The CRC [13] vapor pressure formulas have a quoted accuracy of 5%. The inversion formula for the temperature reproduces the CRC values to within ±0.02 K (±0.005 K) given the vapor pressure above a liquid (solid). If only the lowest order term is used (a_1), then the inversion formula reproduces the CRC values to ±2.5 K for Li and ±1.2 K for all others. The fit to Li is worse because the data covers a much larger number density range.

	Melting		CRC		% diff.	avg.
	°C	K	over solid	over liquid		
Li	180.5	453.65	3.61×10^{6}	3.79×10^{6}	4.8	3.70×10^{6}
Na	97.72	370.87	3.07×10^{9}	3.18×10^{9}	3.6	3.12×10^{9}
K	63.38	336.53	3.12×10^{10}	3.22×10^{10}	3.4	3.17×10^{10}
Rb	39.31	312.46	5.47×10^{10}	5.66×10^{10}	3.5	5.57×10^{10}
Cs	28.44	301.59	6.88×10^{10}	7.11×10^{10}	3.3	6.99×10^{10}

Table A.8: CRC Number Density at the Melting Point. The CRC solid and liquid vapor pressure curves give two different values at the melting point. However, the difference is always less than 5%, which is the quoted accuracy for the CRC formula.

A.3.3 Comparison with other standard formulas

The Nesmeyanov [12] formula for the alkali number density (in $1/\text{cm}^3$) is written as:

$$[\text{A}] = \left[\left(\frac{101325\ \text{Pa}}{760\ \text{mmHg}}\right)\left(10^{A-B/T+CT+D\log_{10}T}\ \text{mmHg}\right)\right]\cdot\left[\frac{1}{kT}\left(\frac{1\ \text{m}}{100\ \text{cm}}\right)^3\right] \quad \text{(A.40)}$$

There are no uncertainties quoted. Nesmeyanov does not list values for the K vapor pressure above a solid; therefore, we'll extrapolate to lower temperatures using the liquid values.

Killian [14] made measurements of K and Rb and fit them to:

$$[\text{A}] = \left[\left(\frac{1\ \text{Pa}}{10\ \text{barye}}\right)\left(10^{A-B/T}\ \text{barye}\right)\right]\cdot\left[\frac{1}{kT}\left(\frac{1\ \text{m}}{100\ \text{cm}}\right)^3\right] \quad \text{(A.41)}$$

There were no uncertainties quoted. In addition, Killian quotes the pressure in "bars." His formula is incorrect by 6 orders of magnitude if one interprets his "bar" as 10^5 Pascals. However, it has been noted [15] that there exists another pressure unit "barye," which is equivalent to 0.1 Pascals. We'll assume that "barye" is the

unit meant by Killian.

The parameters A, B, C, & D for Nesmeyanov & Killian are listed in Tab. (A.9). Fig. (A.1) shows both the vapor pressures and number densities from all three sources; whereas Fig. (A.2) depicts the percent difference between Nesmeyanov & Killian relative to the CRC. Nesmeyanov appears to be systematically 10% to 30% lower. The Killian values for Rb compare favorably to the CRC and are about 10% lower over the temperature range covered by Killian's measurements. Outside that range, the Killian values are within -10% and $+20\%$ of the CRC values. Within the measurement range, the Killian K values compare favorably to the CRC, but outside that range, the Killian values diverge from the CRC significantly.

A.3.4 Alkali Dimers

Dimers are weakly bound molecules formed by two alkali atoms. Only Nesmeyanov includes a formula for alkali dimers in vapor form [12]:

$$[\mathrm{A}_2] = \left[\left(\frac{101325\ \mathrm{Pa}}{760\ \mathrm{mmHg}}\right)\left(10^{A-B/T+CT+D\log_{10}T}\ \mathrm{mmHg}\right)\right] \cdot \left[\frac{1}{kT}\left(\frac{1\ \mathrm{m}}{100\ \mathrm{cm}}\right)^3\right] \quad \text{(A.42)}$$

No uncertainties are quoted. The Cs liquid and solid dimer number densities have a large discrepancy at the melting point. Therefore, we'll use the liquid vapor pressure to extrapolate down to lower temperatures for Cs.

The ratio of the Nesmeyanov dimer to monomer density (or vapor pressure) is

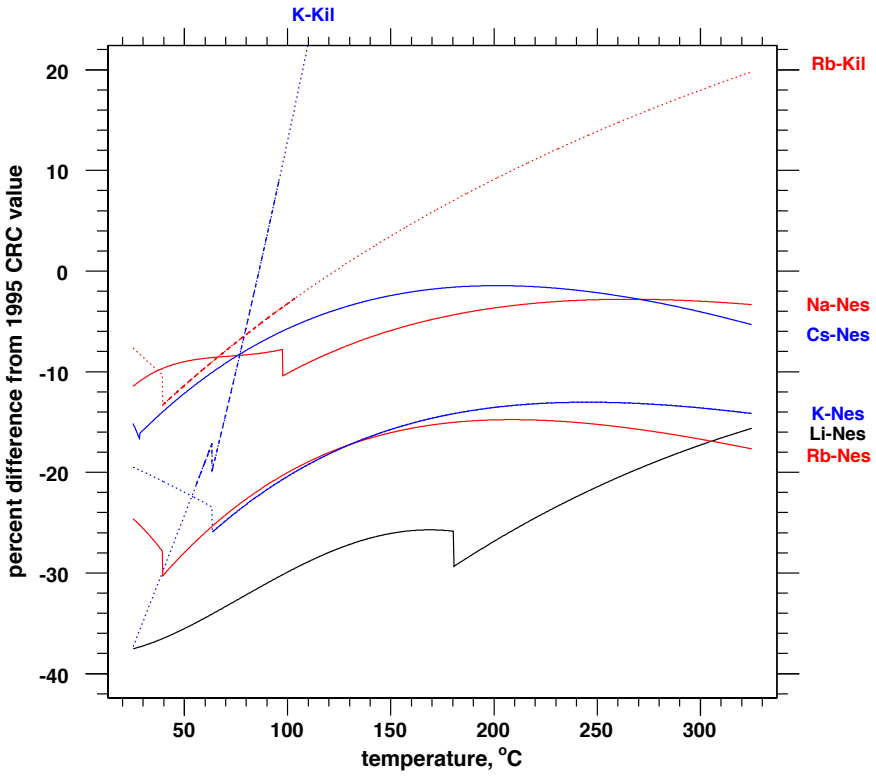

Figure A.2: Relative Difference Between Formulas. The solid lines represent the % difference between Nesmeyanov and the CRC. The dashed lines represent the % difference between Killian and the CRC over the temperature range measured in Killian. The dotted lines represent extrapolations outside the temperature ranges quoted for the formulas. The discontinuities are mainly attributable to the CRC formulas and occur only at the melting point.

Nesmeyanov					
over solid	**Li**	**Na**		**Rb**	**Cs**
$T_{\mathtt{min}}$ (K)			298		
$T_{\mathtt{min}}$ (°C)			25		
$[\mathrm{A}]_{\mathtt{min}}$ ($1/\mathrm{cm}^3$)	9.29×10^{-4}	6.83×10^{5}		9.59×10^{9}	4.10×10^{10}
$T_{\mathtt{mp}}$ (K)	453.7	370.87		312.46	301.59
$T_{\mathtt{mp}}$ (°C)	180.5	97.72		39.31	28.44
$[\mathrm{A}]_{\mathtt{mp}}$ ($1/\mathrm{cm}^3$)	2.68×10^{6}	2.83×10^{9}		3.95×10^{10}	5.72×10^{10}
$-A$	54.87864	-133.42927		94.04826	219.48200
B (K)	6450.944	9302.868		1961.258	-1088.676
$-C$ (1/K) $\times 10^2$	1.487480	-3.114431		3.771687	8.336185
D	24.82251	-49.37679		42.57526	94.88752
over liquid	**Li**	**Na**	**K**	**Rb**	**Cs**
$T_{\mathtt{mp}}$ (K)	453.7	370.87	336.53	312.46	301.59
$T_{\mathtt{mp}}$ (°C)	180.5	97.72	63.38	39.31	28.44
$[\mathrm{A}]_{\mathtt{mp}}$ ($1/\mathrm{cm}^3$)	2.68×10^{6}	2.85×10^{9}	2.39×10^{10}	3.95×10^{10}	5.96×10^{10}
$T_{\mathtt{bp}}$ (K)	1615	1156	1032	961	944
$T_{\mathtt{bp}}$ (°C)	1342	883	759	688	671
$[\mathrm{A}]_{\mathtt{bp}}$ ($1/\mathrm{cm}^3$)	4.23×10^{18}	5.50×10^{18}	6.08×10^{18}	6.49×10^{18}	6.85×10^{18}
A	10.34540	10.86423	13.83624	15.88253	8.22127
B (K)	8345.574	5619.406	4857.902	4529.635	4006.048
C (1/K) $\times 10^4$	-0.8840	0.0345	3.4940	5.8663	-6.0194
$-D$	0.68106	1.0411	2.21542	2.99138	0.19623

Killian		
	K	**Rb**
$T_{\mathtt{min}}$ (K)	328.8	312.5
$T_{\mathtt{min}}$ (°C)	55.6	39.4
$[\mathrm{A}]_{\mathtt{mp}}$ ($1/\mathrm{cm}^3$)	1.19×10^{10}	4.93×10^{10}
$T_{\mathtt{max}}$ (K)	369.2	376.8
$T_{\mathtt{max}}$ (°C)	96.1	103.6
$[\mathrm{A}]_{\mathtt{max}}$ ($1/\mathrm{cm}^3$)	4.76×10^{11}	7.38×10^{12}
A	11.83	10.55
B (K)	4964	4132

Table A.9: Alternative Number Density Parameters. The Nesmeyanov [12] parameters are used in Eqn. (A.40) and the Killian [14] parameters are using in Eqn. (A.41).

fit to the following two forms:

$$\frac{[A_2]}{[A]} = \frac{\exp\left(-b\left(\frac{T_0}{T}-1\right)+c\left(\frac{T}{T_0}-1\right)+d\cdot\log\left(\frac{T}{T_0}\right)\right)}{\left([A]/[A_2]\right)_0} \tag{A.43}$$

$$= \frac{\left([A]/[A]_0\right)^n}{\left([A]/[A_2]\right)_0} \tag{A.44}$$

The first form is fit to values over a temperature range that covers 298 K to 600 K. Even though this range covers the discontinuity at the melting point, the fit still reproduces the Nesmeyanov values to within $\pm 5\%$. The second form is fit to values over a temperture range that runs from the melting point to a temperature that corresponds to at least 10^{16}. Because of the larger range covered, it only reproduces the Nesmeyanov values to $\pm 10\%$. Note that the ratio $\left([A]/[A_2]\right)_0$ corresponds to a temperature T_0 for the first form and to the density $[A]_0$ for the second form.

The values for the Nesmeyanov Dimer parameters A, B, C, & D for liquids and solids, as well as the parameters derived from them for the first fit formula b, c, d, T_0, & $\left([A]/[A_2]\right)_0$ are listed in Tab. (A.11). The parameters for the second fit formula n, $[A]_0$, & $\left([A]/[A_2]\right)_0$ are listed in Tab. (A.10).

Nesmeyanov Dimer to Monomer Ratio					
	Li	**Na**	**K**	**Rb**	**Cs**
$T_{\mathtt{min}}$ (K)	453.65	370.87	336.53	312.46	301.59
$T_{\mathtt{min}}$ (°C)	180.5	97.72	63.38	39.31	28.44
$[\mathrm{A}]_{\mathtt{min}}$ $(1/\mathrm{cm}^3)$	2.68×10^{6}	2.85×10^{9}	2.39×10^{10}	3.95×10^{10}	5.96×10^{10}
$\left([\mathrm{A_2}]/[\mathrm{A}]\right)_{\mathtt{min}}$	5.93×10^{-5}	3.48×10^{-4}	2.49×10^{-5}	3.48×10^{-5}	2.09×10^{-5}
$T_{\mathtt{max}}$ (K)	1050	700	600	550	
$T_{\mathtt{max}}$ (°C)	777	427	327	277	
$[\mathrm{A}]_{\mathtt{max}}$ $(1/\mathrm{cm}^3)$	1.62×10^{16}	1.04×10^{16}	1.00×10^{16}	1.04×10^{16}	2.06×10^{16}
$\left([\mathrm{A_2}]/[\mathrm{A}]\right)_{\mathtt{max}}$	0.0357	0.0253	4.85×10^{-3}	5.39×10^{-3}	5.24×10^{-3}
$[\mathrm{A}]_0$ $(1/\mathrm{cm}^3)$			10^{14}		
$\left([\mathrm{A}]/[\mathrm{A_2}]\right)_0$	119	148	1350	1210	1920
n	0.284	0.284	0.407	0.404	0.433

Table A.10: Dimer to Monomer Ratio vs. Monomer Density. This parameters are used in Eqn. (A.44). The temperature range of the fit covers the higher melting point to a temperature that corresponds to monomer density of at least 10^{16} $1/\mathrm{cm}^3$. These parameters reproduce the Nesmeyanov [12] values to within $\pm10\%$.

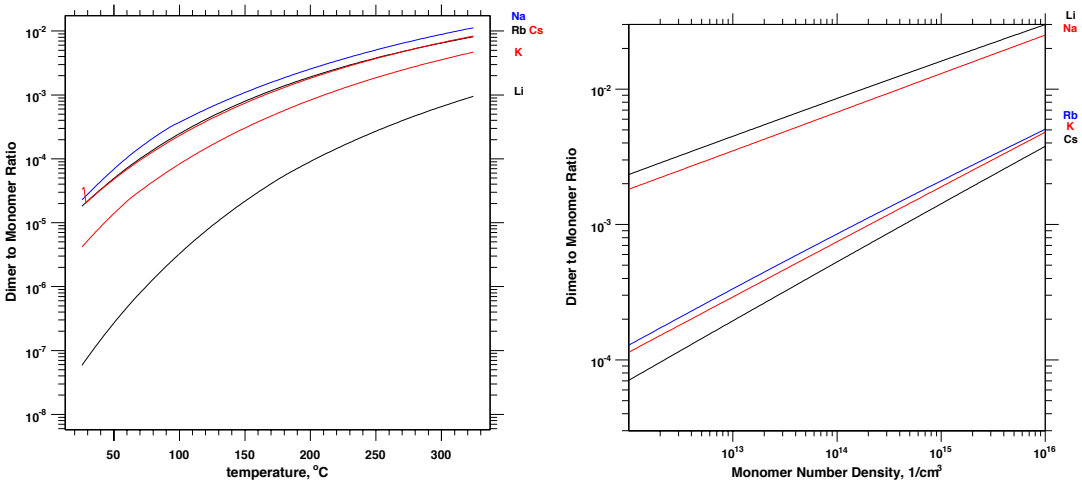

Figure A.3: Dimer to Monomer Ratio vs. Temperature and Monomer Density. (Nesmeyanov [12] formulas)

Nesmeyanov Dimers					
over solid	**Li**	**Na**	**K**	**Rb**	**Cs**
$T_{\mathtt{min}}$ (K)			298		
$T_{\mathtt{min}}$ (°C)			25		
$[A_2]_{\mathtt{min}}$ ($1/cm^3$)	5.14×10^{-11}	14.9	1.85×10^{3}	1.67×10^{5}	1.31×10^{6}
$T_{\mathtt{mp}}$ (K)	453.7	370.87	336.53	312.46	301.59
$T_{\mathtt{mp}}$ (°C)	180.5	97.72	63.38	39.31	28.44
$[A_2]_{\mathtt{mp}}$ ($1/cm^3$)	148	1.01×10^{6}	5.93×10^{5}	1.27×10^{6}	2.15×10^{6}
$-A$	74.04758	338.13794	75.58292	211.33010	211.02760
B (K)	8491.378	−1842.920	4578.883	966.918	727.545
$-C$ $(1/K)\times10^2$	2.035840	9.791968	2.667904	7.829240	7.947950
D	33.06458	139.75985	34.61890	91.59149	91.64953
over liquid	**Li**	**Na**	**K**	**Rb**	**Cs**
$T_{\mathtt{mp}}$ (K)	453.7	370.87	336.53	312.46	301.59
$T_{\mathtt{mp}}$ (°C)	180.5	97.72	63.38	39.31	28.44
$[A_2]_{\mathtt{mp}}$ ($1/cm^3$)	148	1.01×10^{6}	5.92×10^{5}	1.27×10^{6}	1.21×10^{6}
$T_{\mathtt{bp}}$ (K)	1615	1156	1032	961	944
$T_{\mathtt{bp}}$ (°C)	1342	883	759	688	671
$[A_2]_{\mathtt{bp}}$ ($1/cm^3$)	6.22×10^{17}	7.14×10^{17}	3.52×10^{17}	3.98×10^{17}	4.13×10^{17}
A	18.37849	5.33624	17.05231	41.27530	18.22054
B (K)	11139.618	6866.162	6806.144	7226.316	6064.472
C $(1/K)\times10^3$	0.16342	−1.06668	0.12351	3.33213	0.09016
$-D$	3.03209	−1.23023	2.98966	11.85510	3.45395
$T_{\mathtt{min}}$ (K)			298		
$\left([A_2]/[A]\right)_{\mathtt{min}}$	5.44×10^{-8}	2.17×10^{-5}	4.12×10^{-6}	1.72×10^{-5}	1.74×10^{-5}
$T_{\mathtt{max}}$ (K)			600		
$\left([A_2]/[A]\right)_{\mathtt{max}}$	9.67×10^{-4}	1.20×10^{-2}	4.91×10^{-3}	8.32×10^{-3}	8.57×10^{-3}
T_0 (K)			500		
$\left([A_2]/[A]\right)_0$	1.70×10^{-4}	3.70×10^{-3}	1.30×10^{-3}	2.82×10^{-3}	2.73×10^{-3}
b	10.939	26.735	17.484	11.862	9.019
c	−5.303	22.388	9.816	2.482	0.228
$-d$	−5.361	42.561	19.449	7.623	2.224

Table A.11: Dimer Number Density Parameters. These values are from Nesmeyanov [12] and are used in Eqn. (A.42). The ratio Dimer to Monomer density ratio is fit to Eqn. (A.43) over a temperature range of 298 K to 600 K. The Cs dimer density is discontinuous at the melting point, so we use the liquid parameters even below the melting point. The K monomer number density below the melting point is estimated using the liquid parameters. The fit reproduces the Nesmeyanov values to within 5%.

Bibliography

[1] Peter J. Mohr, Barry N. Taylor, and David B. Newell. CODATA recommended values of the fundamental physical constants: 2006. *Rev. Mod. Phys.*, 80(2):633–730, Jun 2008.

[2] E. Arimondo, M. Inguscio, and P. Violino. Experimental determinations of the hyperfine structure in the alkali atoms. *Rev. Mod. Phys.*, 49(1):31–75, Jan 1977.

[3] Kramida A.E. Reader J. Ralchenko, Yu. and NIST ASD Team (2008). NIST Atomic Spectra Database (version 3.1.5), [Online]. Available: http://physics.nist.gov/asd3 [2010, May 17]. *National Institute of Standards and Technology, Gaithersburg, MD.*

[4] A.A. Radzig and B.M. Smirnov. *Reference Data on Atoms, Molecules, and Ions*. Springer-Verlag, Berlin, 1985.

[5] David E. Gilbert and Shang Yi Ch'en. Pressure Effects of Foreign Gases on the Absorption Lines of Cesium. VI. Intensity Measurements of the Cesium Resonance Lines and Their Associated Satellites in the Presence of Various Foreign Gases. *Phys. Rev.*, 188(1):40–45, Dec 1969.

[6] M. V. Romalis, E. Miron, and G. D. Cates. Pressure broadening of Rb D_1 and D_2 lines by ^{3}He, 4He, N_2, and Xe: Line cores and near wings. *Phys. Rev. A*, 56(6):4569–4578, Dec 1997.

[7] EDSON R. PECK and KAYE REEDER. Dispersion of Air. *J. Opt. Soc. Am.*, 62(8):958–962, 1972.

[8] W.C. Martin J.E. Sansonetti and S.L. Young (2005). Handbook of Basic Atomic Spectroscopic Data (version 1.1.2). [Online] Available: http://physics.nist.gov/Handbook [2010, May 17]. *National Institute of Standards and Technology, Gaithersburg, MD.*

[9] Stephan Falke, Eberhard Tiemann, Christian Lisdat, Harald Schnatz, and Gesine Grosche. Transition frequencies of the D lines of ^{39}K, ^{40}K, and ^{41}K measured with a femtosecond laser frequency comb. *Phys. Rev. A*, 74(3):032503, Sep 2006.

[10] Dipankar Das and Vasant Natarajan. High-precision measurement of hyperfine structure in the D lines of alkali atoms. *Journal of Physics B: Atomic, Molecular and Optical Physics*, 41(3):035001, 2008.

[11] Charles Kittel and Herbert Kroemer. *Thermal Physics*. W.H. Freeman, New York, 2nd edition, 1980.

[12] Andrei Nikolaevich Nesmeyanov. *Vapor Pressure of the Elements*. Academic Press, New York, translated (by J.S. Carasso) edition, 1963.

[13] David R. Lide (Editor-in Chief). *CRC Handbook of Chemistry and Physics*. CRC Press, Boca Raton, FL, 75$^{\text{th}}$ student edition, 1994.

[14] Thomas J. Killian. Thermionic Phenomena Caused By Vapors of Rubidium and Potassium. *Physical Review*, 27:578–587, May 1926.

[15] Brian R. Patton. *NMR Studies of Angular Momentum Transfer and Nuclear Spin Relaxation*. PhD thesis, Princeton University, 2007.

Appendix B

Radiation Thicknesses for E97110

B.1 Introduction

Catalog of radiation lengths and materials for E97110. Also a catalog of collisional thickness and most probable energy loss. Still needs a list of uncertainties and a more complete list of references. Better equation references. More discussion about the "1/18" term. Maybe explicitly write out bremmstrahlung spectrum? better table placement. reference/verify for GE180 composition. make comment about $\beta \approx 1$ and about the energy independence of B for our beam energies and momenta. references for densities of oxides. δ subscripts on stuff.

B.2 Formulas for Calculating Radiation Lengths

Bremsstrahlung is radiation emitted when an electron is accelerated in the Coulombic fields of both the nucleus [1] and electrons [2, 3] of an atom. The amount of

energy an electron loses to bremsstrahlung at a given frequency is given by:

$$d^2E = -h\nu\,[\mathrm{N}]\,\frac{d\sigma(\nu,E)}{d\nu}\,dx\,d\nu \tag{B.1}$$

where $h\nu$ is the energy of the radiated photons, [N] is the number density of the atoms, $d\sigma(\nu,E)/d\nu$ is differential cross section for the production of a photon, dx is the thickness of the material, and $d\nu$ is width of frequency range. To calculate the amount of energy lost per unit depth over all frequencies, one must integrate over the entire bremsstahlung frequency spectrum:

$$\int \frac{d^2E}{dx} = \frac{dE}{dx} = -[\mathrm{N}]\int_0^E h\nu\,\frac{d\sigma(\nu,E)}{d\nu}\,d\nu \tag{B.2}$$

It is convenient to change the integration variable to $u \equiv h\nu/E$, which is the fraction of the electron energy carried away by the radiated photons:

$$\frac{dE}{dx} = -[\mathrm{N}]E\int_0^1 u\,\frac{d\sigma(u,E)}{du}\,du \tag{B.3}$$

For electron energies over 50 MeV, the integrand is nearly independent of the electron energy E [4]:

$$\int_0^1 u\,\frac{d\sigma(u,E)}{du}\,du \approx \int_0^1 u\,\frac{d\sigma(u)}{du}\,du \equiv \sigma_{\mathrm{rad}} \tag{B.4}$$

Consequently $\sigma_{\rm rad}$, to a very good approximation, depends only on the charge of the nucleus Z and is given by [5–7]:

$$\sigma_{\rm rad}(Z) = 4\alpha r_e^2 \left[Z^2\left(L_{\rm rad}(Z) - f(Z\alpha)\right) + ZL'_{\rm rad}(Z)\right] \tag{B.5}$$

$$4\alpha r_e^2 = 2.31787 \text{ millibarns} \tag{B.6}$$

where α is the fine structure constant and r_e is the classical electron radius. The term proportional to Z^2 is due to the field of the nucleus and the term proportional to Z is due to the field of the atomic electrons. When evaluated in the complete screening limit, the radiation integrals $L_{\rm rad}$ & $L'_{\rm rad}$ are given by:

$$L_{\rm rad}(Z) = \left\{\begin{array}{cc} 5.31 & Z=1 \\ 4.79 & Z=2 \\ 4.74 & Z=3 \\ 4.71 & Z=4 \\ \log\left(184.15Z^{-1/3}\right) & Z\geq 5 \end{array}\right\} \tag{B.7}$$

$$L'_{\rm rad}(Z) = \left\{\begin{array}{cc} 6.144 & Z=1 \\ 5.621 & Z=2 \\ 5.805 & Z=3 \\ 5.924 & Z=4 \\ \log\left(1194Z^{-2/3}\right) & Z\geq 5 \end{array}\right\} \tag{B.8}$$

where $f(z)$ is known as the "Coulomb correction" [8]:

$$f(z) = z^2\sum_{\nu=1}^{\infty}\frac{1}{\nu\left(\nu^2+z^2\right)} \approx z^2\left[\frac{1}{1+z^2} + 0.20206 - 0.0369z^2 + 0.0083z^4 - 0.002z^6\right] \tag{B.9}$$

and we have dropped the Z^2 "1/18" term altogether [4]. When the Coulomb correction is neglected, L_{rad} is approximated by $\log\left(183/\sqrt[3]{Z}\right)$. If only the lowest terms in the Coulomb correction are kept, then L_{rad} is approximated by $\log\left(191/\sqrt[3]{Z}\right)$. Note that the original calculation of L'_{rad} [2] contains an error [3] that results in this commonly used but incorrect form of $L'_{\text{rad}} = \log\left(1440/\sqrt[3]{Z^2}\right)$.

Returning to the approximation that σ_{rad} is independent of the electron energy, the energy of the electron decays exponentially as it penetrates the material:

$$\frac{dE}{E} = -[\text{N}]\sigma_{\text{rad}}dx \rightarrow E(x) = E(0)\exp\left(-[\text{N}]\sigma_{\text{rad}}(Z)x\right) \tag{B.10}$$

If the material is a uniform mixture of different atoms and one makes the reasonable assumption that the electron interacts with only one atom at a time, then the cumulative energy loss is given by:

$$E(x) = E(0)\Pi_k \exp\left(-[\text{N}]_k\sigma_{\text{rad}}(Z_k)x\right) = E(0)\exp\left(-\sum_k [\text{N}]_k\sigma_{\text{rad}}(Z_k)x\right) \tag{B.11}$$

where k labels the atomic isotope. It is convenient to characterize a material by the thickness required for an electron to lose $1 - 1/e$ of its energy. This parameter is called the *radiation length* and is given by:

$$\bar{X}_0 \equiv \left[\sum_k [\text{N}]_k\sigma_{\text{rad}}(Z_k)\right]^{-1} \tag{B.12}$$

In practice, it's more convenient to work with mass densities ρ then with number densities [N]:

$$\bar{X}_0 = \frac{1}{[\text{N}]\sigma_{\text{rad}}(Z)} = \frac{A}{\rho N_A \sigma_{\text{rad}}(Z)} = \frac{X_0}{\rho} \tag{B.13}$$

where A is the molecular weight of the isotope and N_A is the Avogadro constant. Note that even though $\bar{X}_0$ and X_0 have different units, they are interchangeably called the radiation length in the literature [7, 9]. We will distinguish the two by a bar and their units. For a single isotope, the radiation length in mass per unit "area" is given by:

$$X_0 = \frac{A}{N_A \sigma_{\text{rad}}(Z)} \tag{B.14}$$

For a composite material, the radiation length in mass per unit "area" is given by the sum:

$$X_0^{-1} = \sum_k \frac{w_k N_A \sigma_{\text{rad}}(Z_k)}{A_k} = \sum_k \frac{w_k}{X_0^k} \tag{B.15}$$

where w_k is the fraction by mass for the k-th isotope. Finally the unitless *radiation thickness* is given by:

$$t = \sum_j \frac{\rho_j \ell_j}{X_0^j} \tag{B.16}$$

where the sum over j runs over each composite material with physical thickness ℓ_j and mass density ρ_j.

B.3 Formulas for Calculating Collisional Energy Loss

Electrons can undergo elastic collisions with atomic electrons within the materials along the beam path. Very often these collisions result in the ionization of the struck atom. Consequently the process is interchangeably called "ionization loss," "collisional loss," and "loss to ionizing collisions." We will also use these term interchangealby. The mean energy loss is given by the celebrated Bethe-Bloch equation, while the most probable energy loss was first calculated by Landau [10]. Both equations have the form of energy lost to collisions per unit mass density per unit

length [9]:

$$\left[\frac{\Delta}{\rho x}\right] = \left[\frac{\xi}{\rho x}\right]\left[2\log\left(\frac{pc}{I}\right) - \delta(X) + g\right] \tag{B.17}$$

$$\left[\frac{\xi}{\rho x}\right] = \frac{Za}{A\beta^2} \tag{B.18}$$

$$a = 2\pi N_A r_e^2 m_e c^2 = 0.15353747\ \text{MeV} \cdot \frac{\text{cm}^2}{\text{mol}} \tag{B.19}$$

where Z & A are the effective atomic number and weight (in g/mol) of the material, p & E are the electron's momentum and energy, ρ & x are the material's mass density and thickness, I is the mean excitation potential of the material, $\delta(X)$ is the density correction [11], and we'll call ξ the "collisional" thickness as used in Tsai's 848 [12]. The specific form of g depends on which energy loss is desired:

$$\bar{g} = \log(\gamma - 1) - F(\gamma) \qquad \text{mean energy loss (Bethe} - \text{Bloch)} \tag{B.20}$$

$$g_{\text{mp}} = \log\left[\frac{2\xi}{m_e c^2}\right] - \beta^2 + 0.198 \qquad \text{most probable (Landau)} \tag{B.21}$$

$$F(\gamma) = \left[1 + \frac{2}{\gamma} - \frac{1}{\gamma^2}\right]\log(2) - \frac{1}{8}\left[1 - \frac{1}{\gamma}\right]^2 - \frac{1}{\gamma^2} \tag{B.22}$$

$$\approx \log(2) - \frac{1}{8} = 0.568 \text{ for } \gamma \gg 1 \tag{B.23}$$

$$\beta = \frac{v}{c} = \frac{pc}{E} \tag{B.24}$$

$$\gamma = \frac{1}{\sqrt{1-\beta^2}} = \frac{E}{m_{\text{e}} c^2} \tag{B.25}$$

Note that constant term in g_{mp} was originally calculated by Landau to be 0.373 and subsequently recalculated more accurately [13] to be 0.198. The energy lost

per unit length can be written alternatively as:

$$\frac{dE}{dx} = -(m_e c^2)[\mathrm{N}]\sigma_{\mathrm{coll}} \tag{B.26}$$

$$\sigma_{\mathrm{coll}} = 2\pi r_e^2 \left(\frac{Z}{\beta^2}\right) B = \frac{A}{N_A m_e c^2}\left[\frac{\xi}{\rho x}\right] B \tag{B.27}$$

$$B = \left[2\log\left(\frac{pc}{I}\right) - \delta(X) + g\right] \tag{B.28}$$

where σ_{coll} is the collisional cross section and B is called the stopping number when $g = \bar{g}$.

The density correction δ is given by [14]:

$$\delta(X) = \left\{ \begin{array}{ll} \delta\left(X_0^\delta\right) \times 10^{2\left(X - X_0^\delta\right)} & X \leq X_0^\delta \\ 2\log(10)\left(X - X_a^\delta\right) + a_\delta\left(X_1^\delta - X\right)^{m_\delta} & X_0^\delta < X < X_1^\delta \\ 2\log(10)\left(X - X_a^\delta\right) & X \geq X_1^\delta \end{array} \right\} \tag{B.29}$$

$$X = \log_{10}\left(\frac{p}{m_e c}\right) \tag{B.30}$$

$$X_a^\delta = \frac{-C_\delta}{2\log(10)} \tag{B.31}$$

$$C_\delta = 2\log\left(\frac{\hbar\omega_p}{I}\right) - 1 \tag{B.32}$$

$$a_\delta = \frac{\delta\left(X_0^\delta\right) + 2\log(10)\left(X_a^\delta - X_0^\delta\right)}{\left(X_1^\delta - X_0^\delta\right)^{m_\delta}} \tag{B.33}$$

$$\delta(X_0^\delta) = \left\{ \begin{array}{ll} 0.0 & \text{insulators} \\ 0.06, 0.08, 0.10, 0.12, \text{ or } 0.14 & \text{conductors} \end{array} \right\} \tag{B.34}$$

where ω_p,X_0^δ, X_1^δ, m_δ , and $\delta(X_0^\delta)$ depend on the material. The density correction below X_0^δ depends on whether the material is an insulator or conductor [15]. The plasma frequency [16] is a function of the electron number density in the material,

$[N_e]$:

$$\omega_p = \sqrt{4\pi[N_e]r_e c^2} \tag{B.35}$$

$$[N_e] = \langle Z\rangle [N] = \frac{\langle Z\rangle N_A \rho}{\langle A\rangle} = N_A \rho \left\langle \frac{Z}{A} \right\rangle \tag{B.36}$$

Note that above $X \geq X_1^\delta$, the mean energy loss becomes depends only logrithamically on energy and the most probable loss becomes independant of energy:

$$\frac{p}{m_e c} \geq \frac{p_1}{m_e c} = 10^{X_1^\delta} \tag{B.37}$$

$$\delta(p > p_1) = 2\log(10)\left(X - X_a^\delta\right) = 2\log\left(\frac{p}{p_a}\right) \tag{B.38}$$

$$\frac{p_a}{m_e c} = 10^{X_a^\delta} = \exp\left(-\frac{C_\delta}{2}\right) = \left(\frac{I}{\hbar\omega_p}\right)^2 \sqrt{e} \tag{B.39}$$

$$\left[\frac{\Delta}{\rho x}\right] = \left[\frac{\xi}{\rho x}\right]\left[2\log\left(\frac{p_a c}{I}\right) + g\right] \tag{B.40}$$

We use the density correction parameters from [14]. If the density of a material is different than that listed in [14], then the following substitutions are made [16]:

$$X_a^{\delta\prime} = X_a^\delta - \frac{1}{2}\log_{10}\left(\frac{[N]}{[N]_0}\right) \tag{B.41}$$

$$X_0^{\delta\prime} = X_0^\delta - \frac{1}{2}\log_{10}\left(\frac{[N]}{[N]_0}\right) \tag{B.42}$$

$$X_1^{\delta\prime} = X_1^\delta - \frac{1}{2}\log_{10}\left(\frac{[N]}{[N]_0}\right) \tag{B.43}$$

where $[N]_0$ is the number density listed in table and $[N]$ is the desired number density. This is particularly useful for gases because table blah uses the density for 20°C and 1 atm.

If the material is not listed, then one must calculate effective values for I & Z/A

using Bragg's additivity law. If the constituents are elements, the mean ionization potential is underestimated because electrons are more tightly bound in molecules than in the free atoms of the constituent elements. Therefore we'll use the "13 percent rule" to compenstate [17]. If the constituents are molecules such as various types of glass, we do not incease the ionziation potentials. This is because the binding effect was accounted for when the molecular ionization potential were calculated from their constitutent elements. Consequently the effective Z/A and I values are given by [17]:

$$\left\langle \frac{Z}{A} \right\rangle = \frac{\sum_i n_i Z_i}{\sum_i n_i A_i} = \sum_i w_i \left\langle \frac{Z}{A} \right\rangle_i \tag{B.44}$$

$$\log \langle I \rangle = \sum_i \frac{n_i Z_i}{Z} \log \left(I' \right)_i = \left\langle \frac{A}{Z} \right\rangle \sum_i w_i \left\langle \frac{Z}{A} \right\rangle_i \log \left(I \right)_i \tag{B.45}$$

where n_i are the number of atoms of the i-th type in the molecule, I' is the modified elemental ionization potential, w_i is the fraction of the i-th molecule by weight in the mixture, and I is the molecular ionization potential. Once the effective plasma frequency, ionization potential, and Z/A for the material have been calculated, then one uses Tab. (B.1) to select appropriate value of $X^{\delta}_{a,0,1}$. Finally the density correction δ, collisional thickness ξ, and energy loss are calculated only after first deriving effective density correction parameters for a given material.

B.4 Materials in the Path of the Beam

The electron beam exits the beam pipe and enters the target region through a 5 mil beryllium window. The target region is enclosed in a helium "bag." For now, we will assume that the helium gas displaces all of the air and that its temperature &

Phase of Material and Conditions			X_0^δ	X_1^δ
Solids & Liquids	$I < 100$ eV	$C_\delta > -3.681$	0.2	2.0
		$C_\delta \leq -3.681$	$-0.326C_\delta - 1.0$	2.0
	$I \geq 100$ eV	$C_\delta > -5.215$	0.2	3.0
		$C_\delta \leq -5.215$	$-0.326C_\delta - 1.5$	3.0
Gases, 20°C at 1 atm		$-10.000 < C_\delta$	1.6	4.0
		$-10.500 < C_\delta \leq -10.000$	1.7	4.0
		$-11.000 < C_\delta \leq -10.500$	1.8	4.0
		$-11.500 < C_\delta \leq -11.000$	1.9	4.0
		$-12.250 < C_\delta \leq -11.500$	2.0	4.0
		$-13.804 < C_\delta \leq -12.250$	2.0	5.0
		$-13.804 \leq C_\delta$	$-0.326C_\delta - 2.5$	5.0

Table B.1: General Parameterization of the Density Correction [16, 17]. C_δ is calculated from the plasma frequency. For all cases $m_\delta = 3.0$ and X_a^δ & a_δ are calculated using equations blah.

pressure are 20°C & and 1 atm. The electron beam then enters the target chamber portion of the cell which is made of C1720 glass. The end "windows" are much thinner than the side "walls." About 10 amagats of polarized ^{3}He and 0.1 amg of unpolarized N_2 fill the target chamber. For now, we'll also make the traditional approximation that the scattering occurs at the center of the target. This effects the thickness of polarized ^{3}He, unpolarized N_2, and glass wall traversed by the scattered electron.

After scattering, the electron passes through more polarized ^{3}He, unpolarized N_2, and the side wall of the cell. The distance travelled through these two materials after scattering is inversely proportional to the sine of the central scattering angle. After exiting the cell, the electrons travel out of the helium "bag" and through the sieve slit box. At this point the electrons enter the bore of the septum magnet.

Both the entrance and exit apertures of the septum bore were covered by 2 inch thick pieces of polystyrene "foam." The density of this foam is discussed in detail in the next section. The sieve slit box is filled with helium gas. Howver there is some ambiguity regarding whether the septum bore and the small amount of space between the septum and the HRS were filled with air or helium gas.

The spacing of the sieve slit box and septum magnet were almost certainly changed during the six to nine degree switch. In addition, the path of the central ray within the septum bore is different bewteen six and nine degrees. The only consequence of these two differences is that the amount of helium gas traversed by the scattered electron is different. Since this makes up only a tiny fraction of the radiation thickness. we will assume the geometry for nine degrees is identical to the geometry for six degrees. Finally, according to E. Folts, the electrons enter the HRS through a 10 mil Kapton window.

B.5 Density of the Polystyrene Foam

Solid polystyrene, used in scintillators, has a density of 1.032 g/cm^3 [7]. The density of the polystyrene foam that we used was measured independently by V. Sulkosky and A. Deur:

$$\rho = \left(\frac{0.03151 + 0.03220}{2} \right) g/cm^3 = 0.03186\ g/cm^3 \tag{B.46}$$

Clearly a large fraction of the polystyrene foam is occupied by some unknown gas. In principle, this gas affects the radiation length of the foam:

$$\frac{1}{X_0} = \frac{w_p}{X_p} + \frac{w_g}{X_g} \tag{B.47}$$

where w is the fraction by mass and the subscipts p & g refer to the polystyrene & the gas. Taking advantage of $w_p + w_g = 1$ and $w_g = \rho_g/\rho$, we find:

$$\frac{X_p}{X_0} - 1 = \frac{\rho_g}{\rho}\left[\frac{X_p}{X_g} - 1\right] \tag{B.48}$$

If the gas is at room temperature and 1 atm, then the gas density is on order of 10^{-3} g/cm^3 and consequently the true radiation length of the foam differs from the radiation legnth of polystyrene at the level of a fraction of a percent. Since the difference in the two measurements for the density of the foam is larger than the estimated correction due to the trapped gas, we neglect it's effect on the radiation length:

$$\left[\frac{\rho}{X_0}\right]_{\text{foam}} \approx \frac{\rho_{\text{foam}}}{X_{\text{polystyrene}}} \tag{B.49}$$

B.6 Reference Tables for E97110

Physical constants are listed in Tab. (A.1). Target cell parameters are listed in Tab. (3.7).

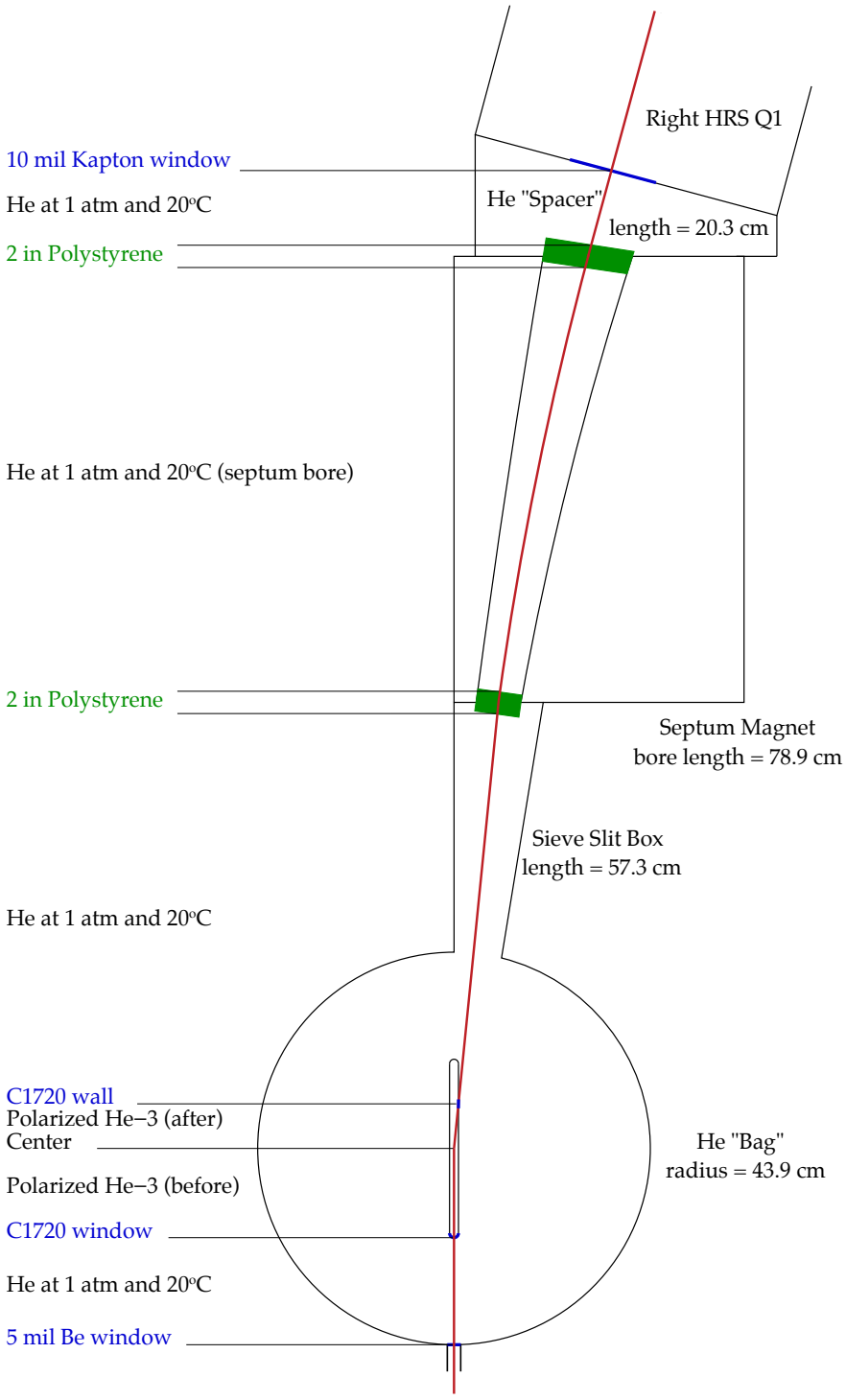

Figure B.1: Scaled Geometry of Target Region.

Z -	**atom**	A amu	σ_{rad} barns	X_0 g/cm^2
1	H	1.00794	0.02655	63.0435
2	^{3}He	3.01603	0.07047	71.0736
2	He	4.00260	0.07047	94.3224
4	Be	9.01218	0.22956	65.1900
5	B	10.81100	0.34073	52.6868
6	C	12.01070	0.46711	42.6969
7	N	14.00670	0.61226	37.9879
8	O	15.99940	0.77597	34.2382
11	Na	22.98977	1.37637	27.7362
12	Mg	24.30500	1.61235	25.0315
13	Al	26.98154	1.86596	24.0112
14	Si	28.08550	2.13706	21.8231
19	K	39.09830	3.74958	17.3151
20	Ca	40.07800	4.12249	16.1434
33	As	74.92160	10.41949	11.9401
38	Sr	87.62000	13.51897	10.7624
56	Ba	137.32700	27.45233	8.3066

Table B.2: Radiation Length by Atomic Species.

material	polystyrene	polyimide film (Kapton)
formula	$C_6H_5CH{=}CH_2$	$(C_{22}H_{10}N_2O_5)_n$
C by wt.	0.922582	0.691133
O by wt.	-	0.209235
N by wt.	-	0.073270
H by wt.	0.077418	0.026362
X_0 (g/cm^2)	43.7911	40.5761

Table B.3: Radiation Length of Polymers. [7, 18]

material	**by wt.**	$X_0\,(\mathrm{g/cm^2})$	**by** X_0
SiO_2	0.599	27.0460	0.594
Al_2O_3	0.182	27.9399	0.175
CaO	0.074	19.0098	0.104
MgO	0.088	28.0227	0.084
B_2O_3	0.047	38.4158	0.033
Na_2O	0.010	29.1660	0.009
K_2O	0.000	18.9019	negligible
As_2O_3	0.000	14.1807	negligible
$X_0 = 26.8379\ \mathrm{g/cm^2}$ $\rho = 2.53\ \mathrm{g/cm^3}$ $\bar{X}_0 = 10.608\ \mathrm{cm}$			

Table B.4: Radiation Length of Corning 1729 (C1720). [19]

material	**by wt.**	$X_0\,(\mathrm{g/cm^2})$	**by** X_0
SiO_2	0.605	27.0460	0.435
BaO	0.183	9.0195	0.394
Al_2O_3	0.144	27.9399	0.100
CaO	0.065	19.0098	0.066
SrO	0.003	12.0367	0.005
$X_0 = 19.4246\ \mathrm{g/cm^2}$ $\rho = 2.76\ \mathrm{g/cm^3}$ $\bar{X}_0 = 7.038\ \mathrm{cm}$			

Table B.5: Radiation Length of GE180. [20]

	Z/A	I eV	I' (g) eV	I' (l/s) eV	ρ g/cm^3	$-C$	X_0	X_1	a	m	$\delta(X_0)$
H	0.9922	19.2	19.2	19.2	8.3748E−05	9.5835	1.8639	3.2718	0.14095	5.7273	0.00
He	0.4997	41.8	41.8	47.2	1.6632E−04	11.1393	2.2017	3.6122	0.13443	5.8347	0.00
^{3}He	0.6631	41.8	41.8	47.2	1.2533E−04	11.1393	2.2017	3.6122	0.13443	5.8347	0.00
Be	0.4438	63.7	63.7	72.0	1.8480E+00	2.7847	0.0592	1.6922	0.76146	2.4339	0.14
B	0.4625	76.0	76.0	85.9	2.3700E+00	2.8477	0.0305	1.9688	0.56221	2.4512	0.14
C	0.4995	78.0	70.0	81.0	2.0000E+00	2.9925	-0.0351	2.4860	0.20489	3.0036	0.10
N	0.4998	82.0	82.0	82.0	1.1653E−03	10.5400	1.7378	4.1323	0.15955	3.2125	0.00
O	0.5000	95.0	97.0	106.0	1.3315E−03	10.7004	1.7541	4.3213	0.11778	3.2913	0.00
Na	0.4785	149.0	149.0	168.4	9.7100E−01	5.0526	0.2880	3.1962	0.07608	3.6452	0.08
Mg	0.4937	156.0	156.0	176.3	1.7400E+00	4.5297	0.1499	3.0668	0.08162	3.6166	0.08
Al	0.4818	166.0	166.0	187.6	2.6989E+00	4.2395	0.1708	3.0127	0.07934	3.6345	0.12
Si	0.4985	173.0	173.0	195.5	2.3300E+00	4.4351	0.2014	2.8715	0.14840	3.2546	0.14
K	0.4860	190.0	190.0	214.7	8.6200E−01	5.6423	0.3851	3.1724	0.20027	2.9233	0.10
Ca	0.4990	191.0	191.0	215.8	1.5500E+00	5.0396	0.3228	3.1191	0.15475	3.0745	0.14
As	0.4405	347.0	347.0	392.1	5.7300E+00	5.0510	0.1767	3.5702	0.06725	3.4176	0.08
Sr	0.4337	366.0	366.0	413.6	2.5400E+00	5.9867	0.4585	3.6778	0.07058	3.4435	0.14
Ba	0.4078	491.0	491.0	554.8	3.5000E+00	6.3153	0.4190	3.4547	0.18267	2.8906	0.14

Table B.6: Density Corrections Parameters for Elemental Materials. I' are the ionization potentials to be used when calculating effective molecular ionization potentials. The densities are given for the natural form of the element (gas, diatomic gas, liquid, solid) at 1 atm and 20^{o}C.

	Z/A	I eV	ρ g/cm^3	$-C$	X_0	X_1	a	m
Al_2O_3	0.4904	145.2	3.9700E+00	3.5682	0.0402	2.8665	0.08499	3.5458
As_2O_3	0.4549	276.6	3.8600E+00	4.9606	0.2000	3.0000	0.18402	3.0000
BaO	0.4174	451.1	5.7000E+00	5.6349	0.3370	3.0000	0.21620	3.0000
B_2O_3	0.4884	99.6	1.8120E+00	3.6027	0.1843	2.7379	0.11547	3.3832
CaO	0.4993	176.1	3.3000E+00	4.1209	-0.0172	3.0171	0.12127	3.1936
MgO	0.4962	143.8	3.5800E+00	3.6404	0.0575	2.8580	0.08313	3.5968
K_2O	0.4883	189.9	2.3200E+00	4.6463	0.0480	3.0110	0.16789	3.0121
SiO_2	0.4993	139.2	2.3200E+00	4.0029	0.1385	3.0025	0.08407	3.5064
Na_2O	0.4840	148.8	2.2700E+00	4.1892	0.1652	2.9793	0.07501	3.6943
SrO	0.4439	326.4	5.7000E+00	4.9259	0.2000	3.0000	0.18244	3.0000
C1720	0.4967	141.0	2.5300E+00	3.9477	0.2000	3.0000	0.13788	3.0000
GE180	0.4829	171.8	2.7600E+00	4.2834	0.2000	3.0000	0.15317	3.0000
kapton	0.5126	79.6	1.4200E+00	3.3497	0.1509	2.5631	0.15971	3.1921
polystyrene	0.5377	68.7	1.0600E+00	3.2999	0.1647	2.5031	0.16454	3.2224

Table B.7: Density Correction Parameters for Composite Materials. For all these materials $\delta(X_0) = 0$.

	Z/A	I eV	ρ g/cm^3	$-C$	X_0	X_1	a	m
			1.4330E−03		1.6726	3.0831		
^{3}He	0.6631	41.8	1.4080E−03	11.1393	1.6764	3.0869	0.13443	5.8347
			1.4120E−03		1.6758	3.0863		
			1.3370E−04		2.2080	4.6025		
			1.3870E−04		2.2000	4.5945		
			1.4000E−04		2.1980	4.5925		
N_2	0.4998	82.0	1.1850E−02	10.5400	1.2342	3.6287	0.15350	3.2125
			1.1870E−02		1.2338	3.6283		
			1.1720E−02		1.2366	3.6311		
polystyrene	0.5377	68.7	3.1860E−02	3.2999	0.9257	3.2641	0.16454	3.2224

Table B.8: Density Correction Parameters for Materials at Different Mass Densities.

material	X_0	ρ	$\bar{X}_0$	ℓ	t	**fraction of tot**
	g/cm^2	g/cm^3	cm	cm	-	-
C1720 Window	26.8379	2.530E+00	1.0608E+01	1.320E−02	1.244E−03	0.5879
Polarized ^{3}He	71.0736	1.433E−03	4.9596E+04	1.983E+01	3.998E−04	0.1889
Beryllium Window	65.1900	1.848E+00	3.5276E+01	1.270E−02	3.600E−04	0.1701
Unpolarized N_2	37.9879	1.337E−04	2.8406E+05	1.983E+01	6.981E−05	0.0330
Helium Gas	94.3224	1.664E−04	5.6687E+05	2.409E+01	4.250E−05	0.0201
Total Before	2.116E-03					
C1720 Wall	26.8379	2.530E+00	1.0608E+01	5.951E−01	5.610E−02	0.8641
Polystyrene Foam	43.7911	3.186E−02	1.3745E+03	1.016E+01	7.392E−03	0.1139
Kapton Window	40.5761	1.420E+00	2.8575E+01	2.540E−02	8.889E−04	0.0137
Helium Gas	94.3224	1.664E−04	5.6687E+05	1.912E+02	3.373E−04	0.0052
Polarized ^{3}He	71.0736	1.433E−03	4.9596E+04	8.612E+00	1.737E−04	0.0027
Unpolarized N_2	37.9879	1.337E−04	2.8406E+05	8.612E+00	3.032E−05	0.0005
Total After	6.492E-02					

Table B.9: Radiation Thicknesses Before & After Scattering from Penelope at 6 deg.

material	X_0	ρ	$\bar{X}_0$	ℓ	t	**fraction of tot**
	g/cm^2	g/cm^3	cm	cm	-	-
Unpolarized N_2	37.9879	1.185E−02	3.2062E+03	1.975E+01	6.160E−03	0.7938
C1720 Window	26.8379	2.530E+00	1.0608E+01	1.270E−02	1.197E−03	0.1543
Beryllium Window	65.1900	1.848E+00	3.5276E+01	1.270E−02	3.600E−04	0.0464
Helium Gas	94.3224	1.664E−04	5.6687E+05	2.417E+01	4.264E−05	0.0055
Total Before	7.760E-03					
C1720 Wall	26.8379	2.530E+00	1.0608E+01	6.104E−01	5.754E−02	0.8359
Polystyrene Foam	43.7911	3.186E−02	1.3745E+03	1.016E+01	7.392E−03	0.1074
Unpolarized N_2	37.9879	1.185E−02	3.2062E+03	8.574E+00	2.674E−03	0.0389
Kapton Window	40.5761	1.420E+00	2.8575E+01	2.540E−02	8.889E−04	0.0129
Helium Gas	94.3224	1.664E−04	5.6687E+05	1.912E+02	3.374E−04	0.0049
Total After	6.883E-02					

Table B.10: Radiation Thicknesses Before & After Scattering from Ref. Cell 1 at 6 deg.

material	X_0	ρ	$\bar{X}_0$	ℓ	t	**fraction of tot**
	g/cm^2	g/cm^3	cm	cm	-	-
C1720 Window	26.8379	2.530E+00	1.0608E+01	1.280E−02	1.207E−03	0.5827
Polarized ^{3}He	71.0736	1.408E−03	5.0496E+04	1.967E+01	3.896E−04	0.1881
Beryllium Window	65.1900	1.848E+00	3.5276E+01	1.270E−02	3.600E−04	0.1738
Unpolarized N_2	37.9879	1.387E−04	2.7383E+05	1.967E+01	7.184E−05	0.0347
Helium Gas	94.3224	1.664E−04	5.6687E+05	2.425E+01	4.278E−05	0.0207
Total Before	2.071E-03					
C1720 Wall	26.8379	2.530E+00	1.0608E+01	5.740E−01	5.411E−02	0.8599
Polystyrene Foam	43.7911	3.186E−02	1.3745E+03	1.016E+01	7.392E−03	0.1175
Kapton Window	40.5761	1.420E+00	2.8575E+01	2.540E−02	8.889E−04	0.0141
Helium Gas	94.3224	1.664E−04	5.6687E+05	1.913E+02	3.374E−04	0.0054
Polarized ^{3}He	71.0736	1.408E−03	5.0496E+04	8.591E+00	1.701E−04	0.0027
Unpolarized N_2	37.9879	1.387E−04	2.7383E+05	8.591E+00	3.137E−05	0.0005
Total After	6.293E-02					

Table B.11: Radiation Thicknesses Before & After Scattering from Priapus at 6 deg.

material	X_0	ρ	$\bar{X}_0$	ℓ	t	**fraction of tot**
	g/cm^2	g/cm^3	cm	cm	-	-
Unpolarized N_2	37.9879	1.187E−02	3.1994E+03	1.975E+01	6.173E−03	0.7903
C1720 Window	26.8379	2.530E+00	1.0608E+01	1.310E−02	1.235E−03	0.1581
Beryllium Window	65.1900	1.848E+00	3.5276E+01	1.270E−02	3.600E−04	0.0461
Helium Gas	94.3224	1.664E−04	5.6687E+05	2.417E+01	4.264E−05	0.0055
Total Before	7.811E-03					
C1720 Wall	26.8379	2.530E+00	1.0608E+01	5.836E−01	5.501E−02	0.8295
Polystyrene Foam	43.7911	3.186E−02	1.3745E+03	1.016E+01	7.392E−03	0.1115
Unpolarized N_2	37.9879	1.187E−02	3.1994E+03	8.601E+00	2.688E−03	0.0405
Kapton Window	40.5761	1.420E+00	2.8575E+01	2.540E−02	8.889E−04	0.0134
Helium Gas	94.3224	1.664E−04	5.6687E+05	1.912E+02	3.374E−04	0.0051
Total After	6.632E-02					

Table B.12: Radiation Thicknesses Before & After Scattering from Ref. Cell 2 at 6 deg.

material	X_0	ρ	$\bar{X}_0$	ℓ	t	**fraction of tot**
	g/cm^2	g/cm^3	cm	cm	-	-
C1720 Window	26.8379	2.530E+00	1.0608E+01	1.280E−02	1.207E−03	0.5822
Polarized ^{3}He	71.0736	1.412E−03	5.0352E+04	1.967E+01	3.907E−04	0.1885
Beryllium Window	65.1900	1.848E+00	3.5276E+01	1.270E−02	3.600E−04	0.1737
Unpolarized N_2	37.9879	1.400E−04	2.7138E+05	1.967E+01	7.249E−05	0.0350
Helium Gas	94.3224	1.664E−04	5.6687E+05	2.425E+01	4.278E−05	0.0206
Total Before	2.073E-03					
C1720 Wall	26.8379	2.530E+00	1.0608E+01	3.835E−01	3.616E−02	0.8050
Polystyrene Foam	43.7911	3.186E−02	1.3745E+03	1.016E+01	7.392E−03	0.1646
Kapton Window	40.5761	1.420E+00	2.8575E+01	2.540E−02	8.889E−04	0.0198
Helium Gas	94.3224	1.664E−04	5.6687E+05	1.943E+02	3.428E−04	0.0076
Polarized ^{3}He	71.0736	1.412E−03	5.0352E+04	5.740E+00	1.140E−04	0.0025
Unpolarized N_2	37.9879	1.400E−04	2.7138E+05	5.740E+00	2.115E−05	0.0005
Total After	4.492E-02					

Table B.13: Radiation Thicknesses Before & After Scattering from Priapus at 9 deg.

material	X_0	ρ	$\bar{X}_0$	ℓ	t	**fraction of tot**
	g/cm^2	g/cm^3	cm	cm	-	-
Unpolarized N_2	37.9879	1.172E−02	3.2404E+03	1.975E+01	6.095E−03	0.7882
C1720 Window	26.8379	2.530E+00	1.0608E+01	1.310E−02	1.235E−03	0.1597
Beryllium Window	65.1900	1.848E+00	3.5276E+01	1.270E−02	3.600E−04	0.0466
Helium Gas	94.3224	1.664E−04	5.6687E+05	2.417E+01	4.264E−05	0.0055
Total Before	7.733E-03					
C1720 Wall	26.8379	2.530E+00	1.0608E+01	3.899E−01	3.676E−02	0.7795
Polystyrene Foam	43.7911	3.186E−02	1.3745E+03	1.016E+01	7.392E−03	0.1568
Unpolarized N_2	37.9879	1.172E−02	3.2404E+03	5.747E+00	1.774E−03	0.0376
Kapton Window	40.5761	1.420E+00	2.8575E+01	2.540E−02	8.889E−04	0.0188
Helium Gas	94.3224	1.664E−04	5.6687E+05	1.943E+02	3.428E−04	0.0073
Total After	4.716E-02					

Table B.14: Radiation Thicknesses Before & After Scattering from Ref. Cell 2 at 9 deg.

material	ρ	ℓ	ξ	mp	dE
	g/cm^3	cm	MeV	MeV	MeV
Polarized ^{3}He	1.433E−03	1.983E+01	2.893E−03	0.064	0.102
C1720 Window	2.530E+00	1.320E−02	2.547E−03	0.038	0.072
Beryllium Window	1.848E+00	1.270E−02	1.599E−03	0.024	0.046
Helium Gas	1.664E−04	2.409E+01	3.076E−04	0.007	0.012
Unpolarized N_2	1.337E−04	1.983E+01	2.035E−04	0.004	0.008
Total Before			7.550E-03	0.137	0.240
C1720 Wall	2.530E+00	5.951E−01	1.148E−01	2.151	3.208
Polystyrene Foam	3.186E−02	1.016E+01	2.672E−02	0.577	0.861
Helium Gas	1.664E−04	1.912E+02	2.441E−03	0.060	0.092
Kapton Window	1.420E+00	2.540E−02	2.839E−03	0.044	0.081
Polarized ^{3}He	1.433E−03	8.612E+00	1.257E−03	0.027	0.044
Unpolarized N_2	1.337E−04	8.612E+00	8.838E−05	0.002	0.003
Total After			1.481E-01	2.861	4.289

Table B.15: Before (p = 2134.3 MeV) & After (p = 1806.4 MeV) Scattering from Penelope at 6 deg.

material	ρ	ℓ	ξ	mp	dE
	g/cm^3	cm	MeV	MeV	MeV
Unpolarized N_2	1.185E−02	1.975E+01	1.796E−02	0.399	0.601
C1720 Window	2.530E+00	1.270E−02	2.450E−03	0.036	0.069
Beryllium Window	1.848E+00	1.270E−02	1.599E−03	0.024	0.046
Helium Gas	1.664E−04	2.417E+01	3.086E−04	0.007	0.012
Total Before			2.232E-02	0.466	0.728
C1720 Wall	2.530E+00	6.104E−01	1.178E−01	2.209	3.290
Polystyrene Foam	3.186E−02	1.016E+01	2.672E−02	0.577	0.861
Unpolarized N_2	1.185E−02	8.574E+00	7.795E−03	0.167	0.260
Helium Gas	1.664E−04	1.912E+02	2.442E−03	0.060	0.092
Kapton Window	1.420E+00	2.540E−02	2.839E−03	0.044	0.081
Total After			1.576E-01	3.057	4.584

Table B.16: Before ($p = 2134.3$ MeV) & After ($p = 1806.4$ MeV) Scattering from Ref. Cell 1 at 6 deg.

material	ρ g/cm^3	ℓ cm	ξ MeV	mp MeV	dE MeV
Polarized ^{3}He	1.408E−03	1.967E+01	2.819E−03	0.063	0.101
C1720 Window	2.530E+00	1.280E−02	2.470E−03	0.037	0.070
Beryllium Window	1.848E+00	1.270E−02	1.599E−03	0.024	0.046
Helium Gas	1.664E−04	2.425E+01	3.096E−04	0.007	0.012
Unpolarized N_2	1.387E−04	1.967E+01	2.094E−04	0.005	0.008
Total Before			7.407E-03	0.136	0.237
C1720 Wall	2.530E+00	5.740E−01	1.108E−01	2.071	3.102
Polystyrene Foam	3.186E−02	1.016E+01	2.672E−02	0.577	0.863
Helium Gas	1.664E−04	1.913E+02	2.442E−03	0.060	0.092
Kapton Window	1.420E+00	2.540E−02	2.839E−03	0.044	0.081
Polarized ^{3}He	1.408E−03	8.591E+00	1.231E−03	0.026	0.043
Unpolarized N_2	1.387E−04	8.591E+00	9.146E−05	0.002	0.003
Total After			1.441E-01	2.780	4.184

Table B.17: Before (p = 3145.3 MeV) & After (p = 1941.5 MeV) Scattering from Priapus at 6 deg.

material	ρ	ℓ	ξ	mp	dE
	g/cm^3	cm	MeV	MeV	MeV
Unpolarized N_2	1.187E−02	1.975E+01	1.800E−02	0.400	0.609
C1720 Window	2.530E+00	1.310E−02	2.528E−03	0.038	0.072
Beryllium Window	1.848E+00	1.270E−02	1.599E−03	0.024	0.046
Helium Gas	1.664E−04	2.417E+01	3.086E−04	0.007	0.012
Total Before			2.244E-02	0.469	0.739
C1720 Wall	2.530E+00	5.836E−01	1.126E−01	2.107	3.154
Polystyrene Foam	3.186E−02	1.016E+01	2.672E−02	0.577	0.863
Unpolarized N_2	1.187E−02	8.601E+00	7.836E−03	0.168	0.261
Helium Gas	1.664E−04	1.912E+02	2.442E−03	0.060	0.092
Kapton Window	1.420E+00	2.540E−02	2.839E−03	0.044	0.081
Total After			1.524E-01	2.956	4.451

Table B.18: Before ($p = 3145.3$ MeV) & After ($p = 1941.5$ MeV) Scattering from Ref. Cell 2 at 6 deg.

material	ρ g/cm^3	ℓ cm	ξ MeV	mp MeV	dE MeV
Polarized ^{3}He	1.412E−03	1.967E+01	2.827E−03	0.063	0.101
C1720 Window	2.530E+00	1.280E−02	2.470E−03	0.037	0.070
Beryllium Window	1.848E+00	1.270E−02	1.599E−03	0.024	0.046
Helium Gas	1.664E−04	2.425E+01	3.096E−04	0.007	0.012
Unpolarized N_2	1.400E−04	1.967E+01	2.113E−04	0.005	0.008
Total Before			7.417E-03	0.136	0.237
C1720 Wall	2.530E+00	3.835E−01	7.400E−02	1.354	2.075
Polystyrene Foam	3.186E−02	1.016E+01	2.672E−02	0.577	0.864
Helium Gas	1.664E−04	1.943E+02	2.481E−03	0.061	0.093
Kapton Window	1.420E+00	2.540E−02	2.839E−03	0.044	0.081
Polarized ^{3}He	1.412E−03	5.740E+00	8.250E−04	0.017	0.029
Unpolarized N_2	1.400E−04	5.740E+00	6.166E−05	0.001	0.002
Total After			1.069E-01	2.054	3.144

Table B.19: Before (p = 3219.9 MeV) & After (p = 2007.0 MeV) Scattering from Priapus at 9 deg.

material	ρ	ℓ	ξ	mp	dE
	g/cm^3	cm	MeV	MeV	MeV
Unpolarized N_2	1.172E−02	1.975E+01	1.777E−02	0.395	0.602
C1720 Window	2.530E+00	1.310E−02	2.528E−03	0.038	0.072
Beryllium Window	1.848E+00	1.270E−02	1.599E−03	0.024	0.046
Helium Gas	1.664E−04	2.417E+01	3.086E−04	0.007	0.012
Total Before			2.221E-02	0.464	0.732
C1720 Wall	2.530E+00	3.899E−01	7.524E−02	1.378	2.110
Polystyrene Foam	3.186E−02	1.016E+01	2.672E−02	0.577	0.864
Unpolarized N_2	1.172E−02	5.747E+00	5.170E−03	0.109	0.173
Helium Gas	1.664E−04	1.943E+02	2.480E−03	0.061	0.093
Kapton Window	1.420E+00	2.540E−02	2.839E−03	0.044	0.081
Total After			1.124E-01	2.169	3.321

Table B.20: Before ($p = 3219.9$ MeV) & After ($p = 2007.0$ MeV) Scattering from Ref. Cell 2 at 9 deg.

cell	**angle**	p	**before**		**after**		**total**	
	deg.	MeV	mp	dE	mp	dE	mp (MeV)	dE (MeV)
penelope	6	400.0	0.137	0.226	2.860	4.065	2.998	4.291
penelope	6	2134.3	0.138	0.239	2.861	4.314	2.998	4.553
priapus	6	400.0	0.135	0.222	2.780	3.957	2.914	4.178
priapus	6	2134.9	0.135	0.234	2.780	4.199	2.915	4.433
priapus	6	2844.8	0.135	0.236	2.780	4.241	2.915	4.477
priapus	6	4208.9	0.135	0.239	2.780	4.297	2.915	4.536
priapus	9	400.0	0.135	0.222	2.054	2.972	2.189	3.194
priapus	9	1147.3	0.135	0.230	2.054	3.086	2.189	3.316
priapus	9	2233.9	0.135	0.235	2.054	3.157	2.189	3.392
priapus	9	3318.8	0.135	0.238	2.054	3.199	2.189	3.437
priapus	9	3775.5	0.135	0.239	2.054	3.213	2.189	3.452
priapus	9	4404.2	0.135	0.240	2.054	3.230	2.189	3.470
refcell 1	6	400.0	0.466	0.689	3.056	4.345	3.522	5.033
refcell 1	6	2134.3	0.467	0.727	3.057	4.610	3.524	5.337
refcell 2	6	400.0	0.468	0.692	2.955	4.209	3.423	4.901
refcell 2	6	2134.9	0.469	0.731	2.956	4.466	3.424	5.197
refcell 2	6	2844.8	0.469	0.737	2.956	4.510	3.424	5.247
refcell 2	6	4208.9	0.469	0.746	2.956	4.570	3.424	5.316
refcell 2	9	400.0	0.463	0.685	2.167	3.139	2.630	3.824
refcell 2	9	1147.3	0.464	0.709	2.168	3.259	2.632	3.968
refcell 2	9	2233.9	0.464	0.724	2.168	3.334	2.632	4.058
refcell 2	9	3318.8	0.464	0.733	2.168	3.378	2.632	4.111
refcell 2	9	3775.5	0.464	0.736	2.168	3.393	2.632	4.128
refcell 2	9	4404.2	0.464	0.739	2.168	3.410	2.632	4.149

Table B.21: Collisional Energy Loss for Penelope, Priapus, and the Ref. Cells for Different Electron Momenta. Note that the energy loss is insensistive to the electon momentum. Because of this insensitivity in our momentum range, we use average momenta for each cell and angle in the calculation of the collisional thickness ξ, the most probable energy loss mp, and the mean energy loss dE.

Bibliography

[1] H. Bethe and W. Heitler. On the Stopping of Fast Particles and on the Creation of Positive Electrons. *Proceedings of the Royal Society of London. Series A, Containing Papers of a Mathematical and Physical Character*, 146(856):83–112, August 1934.

[2] John A. Wheeler and Willis E. Lamb. Influence of atomic electrons on radiation and pair production. *Phys. Rev.*, 55(9):858–862, May 1939.

[3] John A. Wheeler and Willis E. Lamb. Erratum: Influence of atomic electrons on radiation and pair production. *Phys. Rev.*, 101(6):1836, Mar 1956.

[4] Hans A. Bethe and Julius Askin. Passage of Radiations through Matter. In E. Segrè, editor, *Experimental Nuclear Physics, Volume I*, pages 166–357, New York, 1953. John Wiley and Sons.

[5] Yung-Su Tsai. Pair production and bremsstrahlung of charged leptons. *Rev. Mod. Phys.*, 46(4):815–851, Oct 1974.

[6] Yung-Su Tsai. Erratum: Pair production and bremsstrahlung of charged leptons. *Rev. Mod. Phys.*, 49(2):421–423, Apr 1977.

[7] Particle Data Group. Review of Particle Physics. *Physics Letters B*, 592:1–1109, 2004.

[8] Handel Davies, H. A. Bethe, and L. C. Maximon. Theory of Bremsstrahlung and Pair Production. II. Integral Cross Section for Pair Production. *Phys. Rev.*, 93(4):788–795, Feb 1954.

[9] William R. Leo. *Techniques for Nuclear and Particle Physics Experiments: A How-to Approach*. Springer-Verlag, Berlin, second revised edition, 1994.

[10] L.D. Landau. On the energy loss of fast particles by ionization. *J. Phys. USSR*, 8:201, 1944.

[11] Enrico Fermi. The ionization loss of energy in gases and in condensed materials. *Phys. Rev.*, 57(6):485–493, Mar 1940.

[12] Yung-Su Tsai. Radiative Corrections to Electron Scattering. *SLAC-PUB-0848*, Jan 1971.

[13] H. D. Maccabee and D. G. Papworth. Correction to Landau's energy loss formula. *Physics Letters A*, 30:241–242, October 1969.

[14] R.M. Sternheimer, M.J. Berger, and S.M. Seltzer. Density Effect for the Ionization Loss of Charged Particles In Various Substances. *Atomic Data and Nuclear Data Tables*, 30(2):261–271, March 1984.

[15] R. M. Sternheimer. General expression for the density effect for the ionization loss of charged particles. *Phys. Rev. B*, 24(11):6288–6291, Dec 1981.

[16] R. M. Sternheimer and R. F. Peierls. General expression for the density effect for the ionization loss of charged particles. *Phys. Rev. B*, 3(11):3681–3692, Jun 1971.

[17] Stephen M. Seltzer and Martin J. Berger. Evaluation of the Collision Stopping Power of Elements and Compounds for Electrons and Positrons. *Int. J. Appl. Radiat. Isot.*, 33:1189–1218, 1982.

[18] M.J. Berger, J.S. Coursey, M.A. Zucker, and J. Chang. *ESTAR, PSTAR, and ASTAR: Computer Programs for Calculating Stopping-Power and Range Tables for Electrons, Protons, and Helium Ions*. (version 1.2.3). [Online] Available: http://physics.nist.gov/Star [2007, February 15]. National Institute of Standards and Technology, Gaithersburg, MD, 2005.

[19] Mikhail V. Romalis. *Laser Polarizaed* ^{3}He *Target Used for a Precision Measurement of the Neutron Spin Structure*. PhD thesis, Princeton University, 1997.

[20] Alexander Deur (Private Communication).

Appendix C

Clebsch-Gordon Coefficients

C.1 General Formula

Adapted from equation (17.27) in Wigner's *Group Theory* [1] into equation $14^3(5)$ in Condon & Shortley [2]:

$$\begin{aligned}\langle (J_1, J_2)\, m_1, m_2 | J, m\rangle &= \sqrt{\frac{(J+J_1-J_2)!\,(J-J_1+J_2)!\,(J_1+J_2-J)!\,(J+m)!\,(J-m)!\,(2J+1)}{(J+J_1+J_2+1)!\,(J_1-m_1)!\,(J_1+m_1)!\,(J_2-m_2)!\,(J_2+m_2)!}} \\ &\quad \times \delta_m^{(m_1+m_2)} \sum_{\kappa=\kappa_1}^{\kappa_2} \frac{(-1)^{\kappa+J_2+m_2}\,(J+J_2+m_1-\kappa)!\,(J_1-m_1+\kappa)!}{(J-J_1+J_2-\kappa)!\,(J+m-\kappa)!\kappa!\,(\kappa+J_1-J_2-m)!} \end{aligned} \tag{C.1}$$

$$\kappa_a = \max\left[0, J_2 - J_1 + m\right] \tag{C.2}$$

$$\kappa_b = \min\left[J+m, J_2 - J_1 + J\right] \tag{C.3}$$

$$\kappa_1 = \min\left[\kappa_a, \kappa_b\right] \tag{C.4}$$

$$\kappa_2 = \max\left[\kappa_a, \kappa_b\right] \tag{C.5}$$

where κ is summed over all non-negative integers between κ_1 and κ_2. Note the usual rules:

$$\langle (J_1, J_2)\, m_1, m_2 | J, m \rangle = (-1)^{J - J_1 - J_2} \langle (J_2, J_1)\, m_2, m_1 | J, m \rangle \tag{C.6}$$

$$J_1, J_2, J \geq 0 \qquad J = |J_1 - J_2| \ldots (J_1 + J_2) \tag{C.7}$$

$$m_1 = -J_1 \cdots + J_1 \qquad m_2 = -J_2 \cdots + J_2 \qquad m = m_1 + m_2 = -J \cdots + J \tag{C.8}$$

The formulas for $\vec{J_1} + (1/2, 1, 3/2, 2)$ are catalogued in Condon & Shortley [2] in tables 1^3, 2^3, 3^3, & 4^3. Tables of coefficients for $(1/2 + 1/2)$ upto $(2 + 2)$ are avaiable in *The Review of Particle Physics* [3].

C.2 For the case $\vec{J_1} + \frac{\vec{1}}{2}$

$$\begin{aligned}
\left\langle \left(J_1, \frac{1}{2}\right), m_1, \pm\frac{1}{2} | J_1 + \frac{1}{2}, m_1 \pm \frac{1}{2} \right\rangle &= \left\langle \left(J - \frac{1}{2}, \frac{1}{2}\right), m \mp \frac{1}{2}, \pm\frac{1}{2} | J, m \right\rangle \\
&= \sqrt{\frac{J_1 \pm m + \frac{1}{2}}{[J_1]}} = \sqrt{\frac{J_1 \pm m_1 + 1}{[J_1]}} \\
&= \sqrt{\frac{J \pm m}{2J}}
\end{aligned} \tag{C.9}$$

$$\begin{aligned}
\left\langle \left(J_1, \frac{1}{2}\right), m_1, \pm\frac{1}{2} | J_1 - \frac{1}{2}, m_1 \pm \frac{1}{2} \right\rangle &= \left\langle \left(J + \frac{1}{2}, \frac{1}{2}\right), m \mp \frac{1}{2}, \pm\frac{1}{2} | J, m \right\rangle \\
&= \mp\sqrt{\frac{J_1 \mp m + \frac{1}{2}}{[J_1]}} = \mp\sqrt{\frac{J_1 \mp m_1}{[J_1]}} \\
&= \mp\sqrt{\frac{J \mp m + 1}{2(J+1)}}
\end{aligned} \tag{C.10}$$

C.3 Expansion of Zero Field Eigenbasis for $I = 0$

$$\left|S_{\frac{1}{2}}, \frac{1}{2}, +\frac{1}{2}\right\rangle = \left|+\frac{1}{2}\right\rangle_S \tag{C.11}$$

$$\left|S_{\frac{1}{2}}, \frac{1}{2}, -\frac{1}{2}\right\rangle = \left|-\frac{1}{2}\right\rangle_S \tag{C.12}$$

$$\left|P_{\frac{1}{2}}, \frac{1}{2}, +\frac{1}{2}\right\rangle = \sqrt{\frac{2}{3}}\left|+1\right\rangle_L \left|-\frac{1}{2}\right\rangle_S - \sqrt{\frac{1}{3}}\left|0\right\rangle_L \left|+\frac{1}{2}\right\rangle_S \tag{C.13}$$

$$\left|P_{\frac{1}{2}}, \frac{1}{2}, -\frac{1}{2}\right\rangle = \sqrt{\frac{1}{3}}\left|0\right\rangle_L \left|-\frac{1}{2}\right\rangle_S - \sqrt{\frac{2}{3}}\left|-1\right\rangle_L \left|+\frac{1}{2}\right\rangle_S \tag{C.14}$$

$$\left|P_{\frac{3}{2}}, \frac{3}{2}, +\frac{3}{2}\right\rangle = \left|+1\right\rangle_L \left|+\frac{1}{2}\right\rangle_S \tag{C.15}$$

$$\left|P_{\frac{3}{2}}, \frac{3}{2}, +\frac{1}{2}\right\rangle = \sqrt{\frac{1}{3}}\left|+1\right\rangle_L \left|-\frac{1}{2}\right\rangle_S + \sqrt{\frac{2}{3}}\left|0\right\rangle_L \left|+\frac{1}{2}\right\rangle_S \tag{C.16}$$

$$\left|P_{\frac{3}{2}}, \frac{3}{2}, -\frac{1}{2}\right\rangle = \sqrt{\frac{2}{3}}\left|0\right\rangle_L \left|-\frac{1}{2}\right\rangle_S + \sqrt{\frac{1}{3}}\left|-1\right\rangle_L \left|+\frac{1}{2}\right\rangle_S \tag{C.17}$$

$$\left|P_{\frac{3}{2}}, \frac{3}{2}, -\frac{3}{2}\right\rangle = \left|-1\right\rangle_L \left|-\frac{1}{2}\right\rangle_S \tag{C.18}$$

Bibliography

[1] Eugene P. Wigner. *Group Theory and Its Application to the Quantum Mechanics of Atomic Spectra*. Academic Press, New York, 1959.

[2] E.U.Condon and G.H. Shortley. *The Theory of Atomic Spectra*. Cambridge University Press, London, 1967.

[3] C. Amsler et al. (Particle Data Group). Review of Particle Physics. *Physics Letters B*, 667(1-5):1 – 6, 2008. Review of Particle Physics.

Appendix D

Cross Sections & Rate Constants Relevant to SEOP of He-3

D.1 Notation & Conventions

D.1.1 The Language of Multipole Relaxation

If we assume that there are no coherences, see Sec. (E.5.1), then the state of a spin-1/2 system can be specified by the populations $n_\pm$ of the $m = \pm 1/2$ Zeeman levels. However, it is usually more useful to describe the state of the system using the total population $n = (n_+ + n_-)$ and the polarization $P_n = (n_+ - n_-)/n$:

$$\frac{n}{\sqrt{2}} \begin{bmatrix} 1 \\ P_n \end{bmatrix} = \frac{1}{\sqrt{2}} \begin{bmatrix} +1 & +1 \\ +1 & -1 \end{bmatrix} \begin{bmatrix} n_+ \\ n_- \end{bmatrix} \tag{D.1}$$

where the peculiar normalization is standard in the literacture [1]. The time evolution of this system is then prescribed by two characteristic rates which determine

the change in the total population and the polarization. The rate associated with the total population is simply the inverse of the mean lifetime of the state, whereas the rate associated with the polarization is the spin relaxation rate.

Repeating this analysis for a system with total angular momentum $J = 1$, we could choose the individual populations of each $m = -1, 0, +1$ Zeeman level to describe the state of the system. Once again, it is more useful to form three special linear combinations of these populations: the total population $n = (n_+ + n_0 + n_-)$, the "orientation" $P_n = (n_+ - n_-)/n$, and the "alignment" $Q_n = (n_+ - 2n_0 + n_-)/n$:

$$\begin{bmatrix} n/\sqrt{3} \\ nP_n/\sqrt{2} \\ nQ_n/\sqrt{6} \end{bmatrix} = \begin{bmatrix} +1/\sqrt{3} & +1/\sqrt{3} & +1/\sqrt{3} \\ +1/\sqrt{2} & 0 & -1/\sqrt{2} \\ +1/\sqrt{6} & -2/\sqrt{6} & +1/\sqrt{6} \end{bmatrix} \begin{bmatrix} n_+ \\ n_0 \\ n_- \end{bmatrix} \tag{D.2}$$

The orientation for a system with total angular momentum J plays the same role as polarization for a spin-S system. The alignment is essentially a relative measure of the net population of the "end" levels ($m = \pm J$) and is proportional to the magnetic quadrupole moment of the system. When optical pumping from a $J = 1$ ground state to a $J = 0$ excited state, linearly (circularly) polarized light propagating parallel to the holding field will produce nonzero alignment (orientation) in the ground state [2]. In this system, there are three characteristic rates: the inverse of the lifetime, the "disorientation" rate, and the "disalignment" rate.

To generalize these arguments, a system with total angular momentum J can be represented by $(2J + 1)$ mutually othogonal linear combinations of the $(2J + 1)$ individual $m = -J .. + J$ populations. The first four combinations specify the system's population (n), magnetic dipole moment (orientation, P_n), magnetic quadrupole moment (alignment, Q_n), and magnetic octopole moment (R_n), which are defined

in the following way:

$$nP_n = \frac{\langle J_z \rangle}{J} \qquad nQ_n = \frac{\langle 3J_z^2 - J^2 \rangle}{J(2J-1)} \qquad nR_n = \frac{\langle J_z \left(5J_z^2 + 1 - 3J^2\right) \rangle}{J(2J-1)(J-1)} \tag{D.3}$$

These quantities are normalized such that they equal 1 when all the atoms are in the $m = J$ state. The lowest J system that has all four of these moments is $J = 3/2$:

$$\begin{bmatrix} n/2 \\ 3nP_n/\sqrt{20} \\ nQ_n/2 \\ nR_n/\sqrt{20} \end{bmatrix} = \begin{bmatrix} +1/2 & +1/2 & +1/2 & +1/2 \\ +3/\sqrt{20} & +1/\sqrt{20} & -1/\sqrt{20} & -3/\sqrt{20} \\ +1/2 & -1/2 & -1/2 & +1/2 \\ +1/\sqrt{20} & -3/\sqrt{20} & +3/\sqrt{20} & -1/\sqrt{20} \end{bmatrix} \begin{bmatrix} n'_+ \\ n_+ \\ n_- \\ n'_- \end{bmatrix} \tag{D.4}$$

These linear combinations are the diagonal matrix elements of the density matrix in the spherical tensor representation, see for example [1, 3–5]. Each of these $(2J+1)$ spherical components of the density matrix evolves at one of the $(2J+1)$ characteristic rates which are referred to as the "multipole relaxation rates." The two rates that are most relevant to our calculations are the "monopole" relaxation rate (i.e. the rate at which the total population of a state is changing) and the "dipole" relaxation rate (i.e. the rate at which the orientation is changing).

D.1.2 The "Relaxation Rate"

It is straightforward, see for example [6], that the k-th multipole relaxation rate $\gamma_J^{(k)}$ for a system with total angular momentum angular J can be written as:

$$\gamma_J^{(k)} = \gamma_J^{(0)} + \Gamma_J^{(k)} \tag{D.5}$$

where $\gamma_J^{(0)}$ is the monopole relaxation rate and $\Gamma_J^{(k)}$ is the k-th multipole "destruction" rate. In other other words, the total rate of change of the k-th multipole is given by sum of the rate at which the Zeeman levels of the J state are being depopulated ($\gamma_J^{(0)}$)and the rate at which population of the Zeeman levels within a J state are being redistributed ($\Gamma_J^{(k)}$):

$$\frac{d(nP_n^k)}{dt} = \left(\frac{dn}{dt}\right) P_n^k + n\left(\frac{dP_n^k}{dt}\right) = -\gamma_J^{(0)} n P_n^k - \Gamma_J^{(k)} n P_n^k = -\gamma_J^{(k)} n P_n^k \tag{D.6}$$

where P_n^k is the k-th multipole.

In the ground state of alkali atoms, the total angular momentum is due to the electron spin and the lifetime is determined by the optical pumping rate. Historically, the mulitipole relaxation rate of the ground state of an alkali atom is determined by "relaxation in the dark" [7]. In this case, the lifetime of the ground state is infinite (i.e. $\gamma_J^{(0)} = 0$) and the ground state multipole relaxation rate Γ_s is called the spin relaxation rate, the spin depolarization rate, or the spin destruction rate interchangeably. By convention, see for example [8], the rate of change of the polarization P_s and the populations $s_\pm$ are given by $-\Gamma_s P_s$ and $+\left(s/2 - s_\pm\right)\Gamma_s = -\left(s_\pm - s_\mp\right)\Gamma_s/2$ respectively.

In the P_J excited states of alkali atoms, the total angular momentum is due to both the electron spin and orbital angular momentum. In this case, there are three processes of interest: decay from the P_J state to the $S_{1/2}$ ground state, mixing (i.e. transfer) between the P_J and $P_{J'}$ states, and mixing (i.e. redistribution) among the $(2J+1)$ Zeeman levels within a P_J state. Decays are due to spontaneous emission, stimulated emission, and quenching colliions with buffer gas molecules. Fine structure mixing is due to collisions with the buffer gases or other

alkali atoms. The sum of the decay and mixing rates give the monopole relaxation rate. Unfortunately, in the literature, the convention for the definition of the multipole destruction rate in the excited state is different than for the ground state, see for example [9]. Specifically, the rate of change of the orientation P_p and the populations $p_\pm$ are usually written as $-2\Gamma'_p P_p$ and $+\left(p-2p_\pm\right)\Gamma'_p = -\left(p_\pm - p_\mp\right)\Gamma'_p$ respectively. *In this document, we'll use the ground state convention for the excited state rates, rate constants, and cross sections (i.e.* $\Gamma_p = 2\Gamma'_p$*).* Futhermore, when we refer to the "disorientation" rate of the excited state, we actually mean the multipole destruction rate.

D.1.3 The "Cross Section"

What is usually measured in the lab, under "atomic" conditions, is $\Gamma = [\mathrm{N}_a]\langle\sigma v\rangle$, where the brackets indicate an average using the Maxwell distribution weighted by the relative thermal velocity. Generally speaking, see for example [10, 11], the cross section is isolated from the rate constant using the mean thermal velocity (as opposed to the most probable or root mean square velocity) by:

$$\sigma = \frac{\Gamma}{[\mathrm{N}_a]v} = \frac{\langle\sigma v\rangle}{\langle v\rangle} \qquad v = \langle v\rangle = \bar{v}_{\mathrm{rel.}} = \sqrt{\frac{8RT}{\pi}\left(\frac{1}{M_a}+\frac{1}{M_b}\right)} \tag{D.7}$$

where $[\mathrm{N}_a]$ is the number density of particle a, $\bar{v}_{\mathrm{rel.}}$ is the mean relative thermal velocity between particle a & b with molar masses M_a & M_b, R is the molar gas constant, and T is the absolute temperature. Therefore, when comparing to theory, it is important to recall that σ is really $\langle\sigma v\rangle / \langle v\rangle$. Unless otherwise noted, all cross sections and rate constants are calculated using the mean thermal velocity and are derived from the multipole destruction rate.

	$\langle\sigma_{se}\rangle$	err.	$\langle\sigma_{exp}\rangle$	exp. err.	$\langle\sigma_A/\sigma_{Rb}\rangle_{th}$	std. dev. (5)
Na	**100.7**	0.5	100.7	0.5 (2)	0.568	0.104
K	**158.3**	6.3	171.2	21.8 (2)	0.906	0.019
Rb	**173.5**	6.6	173.5	6.6 (5)	-	-
Cs	**186.2**	8.0	183.3	9.7 (3)	1.108	0.062
	Å^2	Å^2	Å^2	Å^2		

Table D.1: Alkali-Alkali Spin Exchange Cross Section in Å^2 at $T = 200\,°\text{C} = 473.15\,\text{K}$. All values are averaged and scaled from [10] with the addition of a new measurement for Rb from [14]. The number in parenthesis refers to the numbers of values used to calculate the each weighted average. The uncertainties on the experimental values are those originally quoted by the authors. The final column is the standard deviation of the ratios from theoretical calculations.

D.2 Ground State Alkali-Alkali Collisions

D.2.1 Spin Exchange

The alkali-alkali spin exchange rate constants are estimated by:

$$A_{se}^{ab} = \bar{v}\sqrt{\sigma_{se}^{a}\sigma_{se}^{b}} = \left[\frac{1\,\text{MHz}}{10^{15}/\text{cm}^3}\right]\sqrt{\left[\frac{\sigma_{se}^{a}}{100\text{Å}^2}\right]\left[\frac{\sigma_{se}^{b}}{100\text{Å}^2}\right]\left[\frac{10\,\text{g/mol}}{M_a}+\frac{10\,\text{g/mol}}{M_b}\right]} \tag{D.8}$$

where σ_{se} is the alkali-alkali spin exchange cross section. The A-A spin exchange rate constant is assumed to be independent of temperature just as e^--A spin exchange [12]. Therefore the cross section is assumed to have a $1/\sqrt{T}$ temperature dependence which cancels the $\sqrt{T}$ temperature depenance of the thermal velocity. Using the geometric mean of cross sections for dissimilar atoms appears justified by theoretical calculations [13].

D.2.2 Spin Destruction

The alkali-alkali spin destruction rate constants are estimated by:

$$A_{\mathrm{sd}}^{ab} = \bar{v}\sqrt{\sigma_{\mathrm{sd}}^{a}\sigma_{\mathrm{sd}}^{b}} = \left[\frac{1\ \mathrm{kHz}}{10^{15}/\mathrm{cm}^3}\right]\sqrt{\left[\frac{\sigma_{\mathrm{sd}}^{a}}{0.1\text{Å}^2}\right]\left[\frac{\sigma_{\mathrm{sd}}^{b}}{0.1\text{Å}^2}\right]\left[\frac{10\ \mathrm{g/mol}}{M_a}+\frac{10\ \mathrm{g/mol}}{M_b}\right]} \tag{D.9}$$

where σ_{sd} is the alkali-alkali spin destruction cross section. The A-A spin destruction rate constant is assumed to be independent of temperature, because most measurements have observed a (mostly) linear increase in relaxation rate with increasing the alkali density. This implies that the cross section has a $1/\sqrt{T}$ temperature dependence. The observed alkali-alkali spin destruction rate is written as [15]:

$$k_{\mathrm{obs}} = k_{\mathrm{sd}}/s = k_a + \left(\frac{k_b^0}{1+B/B_D}\right)\left(\frac{[\mathrm{A}]}{10^{15}\ \mathrm{cm}^{-3}}\right)^n \tag{D.10}$$

where k_a is the magnetic field independent part due to binary collisions, k_b is the field dependent part that is due to singlet and triplet alkali dimers, B_D is the magnetic decoupling width, n is a small next to leading order alkali power dependence, and [A] is the alkali number density.

For $B \ll 230$ Gauss, the spin destruction cross section is obtained by

$$\sigma_{\mathrm{sd}} = k_{\mathrm{sd}}/\bar{v} = s(k_a + k_b)/\bar{v} \tag{D.11}$$

where s is the nuclear slowing down factor. For k_b values from [15], we average over [A] and multiply by k_B^0 to get an effective k_b:

$$\langle k_b \rangle = k_b^0 \frac{\left([\mathrm{A}]_{\mathrm{max}}/10^{15}\ \mathrm{cm}^{-3}\right)^n}{1+n} \tag{D.12}$$

	k_a	k_b^0	B_D	n	$[\mathrm{A}]_{\max}$	$\langle k_b \rangle$	s	$s\left(k_a + \langle k_b \rangle\right)$	ref.
K	7.5E-15	8.2E-15	230	1/4	2.0	7.80E-15	6	9.18E-14	[15]
Rb	1.5E-14	2.6E-14	1150	1/4	2.5	2.62E-14	10.8	4.45E-13	[15]
Rb	1.50E-14	2.88E-14	1150	0	2.5	2.88E-14	10.8	4.74E-13	[16]
Cs	1.9E-13	1.8E-13	2900	0	0.78	1.80E-13	22	8.14E-12	[15]
	cm^3/s	cm^3/s	G		$10^{15}/\mathrm{cm}^3$	cm^3/s		cm^3/s	

Table D.2: Kadlecek Measurements of Alkali-Alkali Spin Destruction Magnetic Decoupling Parameters.

D.3 Ground State Alkali-Buffer Gas Collisions

D.3.1 Spin Exchange with He-3 Nuclei

The ^{3}He polarization evolution is given as:

$$P_{\mathrm{He}}(t) = P_{\mathrm{A}} k_{\mathrm{se}} [\mathrm{A}] \tau \left(1 - \exp(-t/\tau)\right) \tag{D.13}$$

where P_{A} is the volume average alkali polarization, k_{se} is the spin exchange rate constant, [A] is the alkali number density, and τ^{-1} is the total ^{3}He relaxation rate. These are related to the isotropic spin exchange k_{iso} and anisotropic spin exchange k_{ani} rate constants as:

$$k_{\mathrm{se}} = k_{\mathrm{iso}} - k_{\mathrm{ani}}/2 \tag{D.14}$$

$$1/\tau = 1/\tau_0 + k_{\mathrm{se}}[\mathrm{A}](1 + X) \tag{D.15}$$

where $1/\tau_0$ is the ^{3}He relaxation rate that is independent of the alkali density and X accounts for an extra alkali density/temperature dependent relaxation mecha-

	$\langle\sigma_{sd}\rangle$	σ_{sd}	measurement	value	rel. err.	reference
Na	**0.0056**	0.0056	k_{sd}	5.2E-14	0.08	[17]
K	**0.0128**	0.0128	k_a, k_b	(7.5,8.2)E-15	0.10	[15]
	0.0112	σ_{rms} (500 K)		1.00E-18	0.10	[18], *superseded by* [15]
	0.0255	$\bar{\sigma}$ (533 K)		2.4E-18	0.08	[19], *no density measurement*
Rb	**0.0994**	0.0919	k_a, k_b	(1.5,2.6)E-14	0.10	[15]
	0.0978	k_a, k_b		(1.50,2.88)E-14	0.10	[16], *superseded by* [15]
	0.0871	k_{sd}/s		3.9E-14	0.10	[20]
	0.1675	k_{sd}		8.11E-13	0.04	[21]
	0.1714	k_{sd}		8.3E-13	0.07	[22], *large* Rb-^{3}He *contribution*
	0.1583	$\bar{\sigma}$ (463 K)		1.6E-17	0.13	[19], *no density measurement*
Cs	**2.0825**	2.0965	k_a, k_b	(1.9,1.8)E-13	0.10	[15]
		2.0300	$\bar{\sigma}$ (473 K)	2.03E-16	0.20	[23]
	Å^2	Å^2	k in cm^3/s, σ in cm^2			

Table D.3: Alkali-Alkali Spin Destruction Cross Section in Å^2 at $T = 200\,^{\circ}\text{C} = 473.15\,\text{K}$. The relative uncertainties are those originally quoted by the authors. All values, except those in *italics,* are used in the weighted mean. The final uncertainty for each value is about 10%. Only measurements where the alkali density was measured independently was used, thereby ruling out [19]. Measurement [22] is not included because the large temperature dependent Rb-^{3}He spin relaxation rate was not accounted for and could lead to error as large as 50%.

nism. If X was completely due to anisotropic spin exchange, then it is given by:

$$X_{\text{ani}} = \frac{3k_{\text{ani}}/(2k_{\text{iso}})}{1 - k_{\text{ani}}/(2k_{\text{iso}})} \tag{D.16}$$

When the laser is turned off, the alkali polarization reaches approaches a new equilibrium due to spin exchange with ^{3}He given by:

$$P_{\text{A}}(t) = P_{\text{He}}(t)k_{\text{se}}[^3\text{He}]\tau_{\text{A}}/s\left(1 - \exp(-t/\tau_{\text{A}})\right) \tag{D.17}$$

where $[^3\text{He}]$ is the ^{3}He number density, τ_{A}^{-1} is the observed A relaxation rate, and s is the nuclear slowing down factor. Assuming only a single-chambered cell, the rate constants can be obtained by:

$$k_{\text{rate}} = \frac{P_{\text{He}}^{\infty}}{P_{\text{A}}[\text{A}]\tau} = \frac{\left(dP_{\text{He}}/dt|_{t=0}\right)}{P_{\text{A}}[\text{A}]} = k_{\text{se}} \tag{D.18}$$

$$k_{\text{repol}} = \frac{sP_{\text{A}}^{\infty}}{P_{\text{He}}[^3\text{He}]\tau_{\text{A}}} = \sqrt{\frac{s\left(dP_{\text{A}}/dt|_{t=0}\right)}{[^3\text{He}][\text{A}]P_{\text{A}}\tau_{\text{A}}}} = k_{\text{se}} \tag{D.19}$$

$$k_{\text{relax}} = \frac{1 - \tau/\tau_0}{[\text{A}]\tau} = k_{\text{se}}(1 + X) \tag{D.20}$$

The rate constant is been found to be temperature independent [17, 20, 24].

	Na	K	Rb	Cs	
k_{se}	**4.74**	**5.15**	**6.74**	**11.1**	$10^{-20}\,cm^3/s$
$1/\langle k_{se}\rangle$	5.86	5.39	4.12	2.51	$hrs\cdot 10^{15}/cm^3$
$\langle k_{se}\rangle$	1.27	1.38	1.81	2.97	Hz/amg
rel. err.	10	3.1	2.5	10	pct.
$\langle k_{exp}\rangle$	6.10	5.04	6.74	13.6	$10^{-20}\,cm^3/s$
rel. err.	10	3.3	2.5	10	pct.
$\langle k_{th}\rangle$	3.76	6.27		9.18	$10^{-20}\,cm^3/s$
std. dev.	0.13	0.08		0.12	

Table D.4: Alkali-^{3}He Spin Exchange Rate Constant. The experimental values are the weighted average from Tab. D.6. The theoretical values are obtained from the theoretical ratio to Rb from Tab. (D.5) and the experimental value for Rb.

	$\langle k^A_{iso}/k^{Rb}_{iso}\rangle$	$\bar{\sigma}_{iso}\times 10^8$	$k_{iso}\times 10^{20}$	$k_{iso}\times 10^{20}$	k_{ani}/k_{iso}	X_{ani}	$k_{iso}\times 10^{20}$
Na	0.56	1.2	21	2.3	0.100	0.158	6.7
K	0.93	2.1	35	4.9	0.037	0.057	9.0
Rb		2.1	35	5.6	0.030	0.046	10
Cs	1.36	2.7	44	8.1	0.017	0.026	
		$Å^2$	cm^3/s	cm^3/s			cm^3/s
		[25] (100 °C)		[26] (190 °C)			[27] (200 °C)

Table D.5: Alkali-^{3}He Spin Exchange Rate Constant Parameters from Theory. The rate constants from [27] were scaled to 473.15 K by $T^{1.275}$ using a parameterization of the temperature dependence based on their calculations.

	k_{se}	err.	ref.	method
Na	6.1	0.6	[17]	repolarization
K	5.5	0.2	[28]	rate/repolarization
K	*6.1*	0.4	[29]	*superseded by* [28]
K	4.0	0.3	[30]	relaxation
Rb	6.5	0.4	[30]	relaxation
Rb	6.8	0.2	[24]	rate/repolarization
Rb	6.7	0.6	[20]	repolarization
Rb	*6.1*	0.2	[22]	*relaxation*
Rb	*12.0*	2.0	[31]	*relaxation*
Cs	13.6	1.3	[30]	relaxation
	$10^{-20}\,\mathrm{cm}^3/\mathrm{s}$			

Table D.6: Measurements of Alkali-^{3}He Spin Exchange Rate Constant. All values, except those in *italics*, are used in the weighted mean. There are three general methods for extraction the spin exchange rate: "Repolarization" refers to measuring the alkali polarization due to spin exchange with ^{3}He with no optical pumping; "Rate" refers to measuring the equilibrium ^{3}He polarization, A polarization, and ^{3}He spin up time constant; "Relaxation" refers to measuring the ^{3}He relaxation when the cell is hot and with the lasers off. In all cases, the A density is needed to extract the rate constant. The first two methods measure k_{se} while the last method measures $k_{se}(1 + X)$. For this reason, older relaxation method measurements are not included in the final average.

	k_{473}	err.	quant.	value	temp.	notes
Na	**0.15**	**0.05**				
	0.23	0.13	$k_{se}+k_{sd}$	$(8\pm1)\times10^{-20}\,cm^3/s$	600	[17]
	0.11	0.01	k_{se}^{Na}/k_{se}^{Rb}	0.0020 ± 0.0002	473.15	Tab. D.8
K	**4.7**	**0.3**				
	12	1	$k_{sd}/\bar{v}$	$(8.0\pm0.8)\times10^{-25}\,cm^2$	325	for ^{4}He, [32]
	3.5	0.3	k_{sd}	$(8.9\pm0.9)\times10^{-20}\,cm^3/s$	423	rescaled from ^{4}He, [33]
	4.9	0.5	k_{se}^{K}/k_{se}^{Rb}	0.088 ± 0.009	473.15	Tab. D.8
Rb	**55.9**	**0.9**				fit to Tab. D.9
Cs	**530**	**30**				
	490	50	$k_{sd}/\bar{v}$	$(2.43\pm0.24)\times10^{-23}\,cm^2$	288	for ^{4}He, [34]
	550	50	$k_{sd}/\bar{v}$	$(2.8\pm0.3)\times10^{-23}\,cm^2$	290	for ^{4}He, [35]
	560	60	k_{se}^{Cs}/k_{se}^{Rb}	10 ± 1	473.15	Tab. D.8
	Hz/amg					

Table D.7: Alkali-^{3}He Spin Destruction Rate Constant. For measurements made on ^{4}He, the rate constants are rescaled by the square root of the ratio of reduced masses. All values are rescaled to 473.15 K using the Rb temperature scaling of $T^{3.31}$. Values from theoretical calculations are scaled relative to the experimental value for Rb.

D.3.2 Spin Destruction Due to He Atoms

The spin destruction rate constant for A-^{3}He collisions has a temperature dependence given by:

$$k_{sd}(T) = k_{473}\left(\frac{T}{473.15\,K}\right)^n \tag{D.21}$$

From a fit of world data (Tab. D.9) for Rb-^{3}He collisions, we find $k_{473} = (55.9 \pm 0.9)$ Hz/amg and $n = 3.31 \pm 0.12$. We'll assume that the rate constants for all other alkali have the same temperature dependence.

	T	$\bar{\sigma}_{sd}$	k_{sd} (at 473.15)	k_{sd}^{A}/k_{sd}^{Rb}
Na	428.15	1.2	0.083	0.0020
K	459.15	65	3.6	0.088
Rb	459.15	750	41	
Cs	423.15	6000	406	10
	K	10^{-10} Å^2	Hz/amg	

Table D.8: Theoretical Estimate for Spin Destruction in A-^{3}He Pairs Due to the Spin-Rotation Interaction. Calculations are from [36]. Based on the experimental data for K, Rb, and Cs, the uncertainty is estimated to be about 10%. The rate constant is rescaled to 473.15 K using the Rb temperature scaling of $T^{3.31}$.

T	k_{sd}	quantity	value	notes
305	12.40	$k_{sd}/\bar{v}$	3.1E-24 cm^2	for ^{4}He, [37]
363	22.80	$\Gamma_{sd}+\Gamma_{se}$	278 Hz	[^{3}He] = 11.3 amg, [38]
378	24.03	$k_{sd}+k_{se}$	0.96E-18 cm^3/s	[20]
383	28.02	$\Gamma_{sd}+\Gamma_{se}$	337 Hz	[^{3}He] = 11.3 amg, [38]
383	22.90	$k_{sd}+k_{se}$	0.92E-18 cm^3/s	[20]
393	28.81	$k_{sd}+k_{se}$	1.14E-18 cm^3/s	[20]
403	33.24	$\Gamma_{sd}+\Gamma_{se}$	396 Hz	[^{3}He] = 11.3 amg, [38]
403	33.06	$k_{sd}+k_{se}$	1.30E-18 cm^3/s	[20]
413	36.03	$k_{sd}+k_{se}$	1.41E-18 cm^3/s	[20]
418	36.53	$k_{sd}+k_{se}$	1.43E-18 cm^3/s	[20]
423	38.47	$\Gamma_{sd}+\Gamma_{se}$	455 Hz	[^{3}He] = 11.3 amg, [38]
423	41.58	$k_{sd}+k_{se}$	1.61E-18 cm^3/s	[20]
428	40.15	$k_{sd}+k_{se}$	1.56E-18 cm^3/s	[20]
433	43.61	$k_{sd}+k_{se}$	1.69E-18 cm^3/s	[20]
438	44.99	$k_{sd}+k_{se}$	1.74E-18 cm^3/s	[20]
443	48.81	$k_{sd}+k_{se}$	1.88E-18 cm^3/s	[20]
520	73.90	k_{sd}/v_{rms}	1.3E-13 cm^2	for ^{4}He, [15]
K	Hz/amg			

Table D.9: Rb-^{3}He Spin Destruction Rate Constant vs. Temperature. Each measurement has an uncertainty of about 10%.

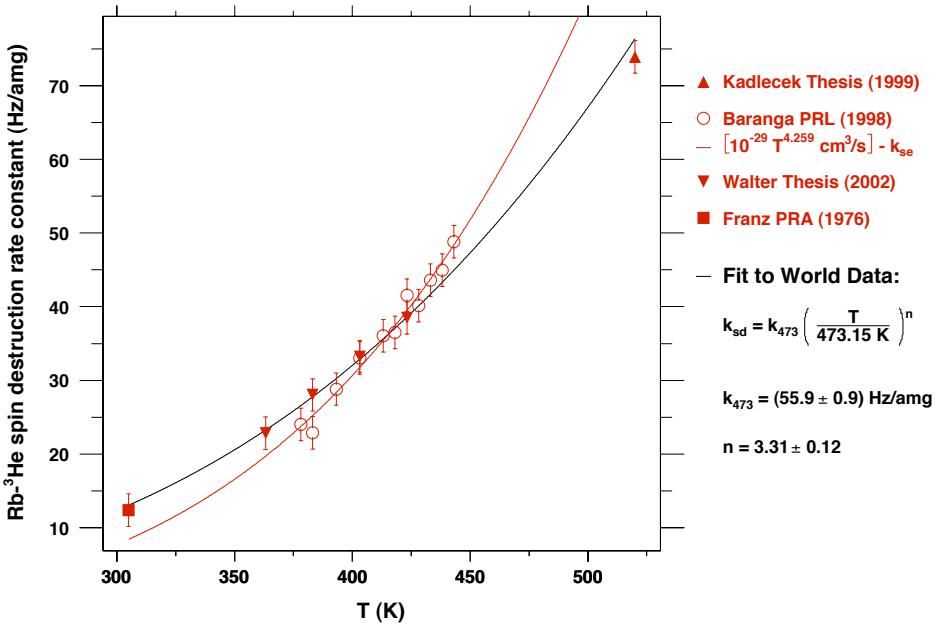

Figure D.1: Fit to Rb-^{3}He Spin Destruction Rate Constant World Data.

D.3.3 Spin Destruction Due to Nitrogen Molecules

The spin destruction rate constant for A-N_2 collisions has a temperature dependence given by:

$$k_{\mathrm{sd}}(T) = k_{473}\left(\frac{T}{473.15\,\mathrm{K}}\right)^{n} \tag{D.22}$$

From a weighted mean of the two fits of the world data (Tab. D.11) for Rb-N_2 collisions, we find $k_{473} = (290 \pm 30)$ Hz/amg and $n = 2.00 \pm 0.25$. We'll assume that the rate constants for all other alkali have the same temperature dependence.

	k_{473}	err.	quantity	value	temp.	notes
Na	**150?**					no data, set to K value
K	**150**	**50**				
	200	20	k_{sd}/v_{rms}	$(7.9 \pm 0.8) \times 10^{-23}\,cm^2$	437	[18]
Rb	**290**	**30**	$(n = 2.00 \pm 0.25)$			
	266	3	$(n = 1.74 \pm 0.06)$			fit to Tab. D.11 w/o [15]
	390	40	$(n = 3.29 \pm 2.00)$			fit to [15] data in Tab. D.11
Cs	**2100**	**200**				
	2050	110	$k_{sd}/\bar{v}$	$(5.52 \pm 0.55) \times 10^{-22}\,cm^2$	288	[34]
	2210	110	$k_{sd}/\bar{v}$	$(6.00 \pm 0.44) \times 10^{-22}\,cm^2$	290	[35]
	Hz/amg					

Table D.10: Alkali-N_2 Spin Destruction Rate Constant. The Rb mean values come from weighted average of the two fits weighted by the number of distinct temperature points for each set. All values are rescaled to 473.15 K using the Rb temperature scaling of T^2. The Rb values from [15] are significantly larger that the data. Since the K value is from [18] which is a similar measurement of the Rb values from [15], the K value is rescaled to the mean Rb value.

T	k_{sd}	quantity	value	notes
300	118.06	$k_{sd}/\bar{v}$	8.0E-23 cm^2	[39]
305	123.41	$k_{sd}/\bar{v}$	8.3E-23 cm^2	[37]
363	173.08	Γ_{sd}	703 Hz	$[N_2] = 4.07$ amg, [38]
363	162.31	Γ_{sd}	1244 Hz	$[N_2] = 7.68$ amg, [38]
383	185.01	Γ_{sd}	1418 Hz	$[N_2] = 7.68$ amg, [38]
393	196.47	Γ_{sd}	798 Hz	$[N_2] = 4.07$ amg, [38]
403	203.02	Γ_{sd}	1556 Hz	$[N_2] = 7.68$ amg, [38]
423	220.60	Γ_{sd}	896 Hz	$[N_2] = 4.07$ amg, [38]
423	221.94	Γ_{sd}	1701 Hz	$[N_2] = 7.68$ amg, [38]
463	252.04	k_{sd}	(9.38 ± 0.22)E-18 cm^3/s	[21]
480	404.90	k_{sd}/v_{vrms}	2.0E-22 cm^2	[15]
500	*419.50*	Γ_{sd}/s	(21.2 ± 0.1) Hz	*760 torr, [16], superseded by [15]*
520	526.80	k_{sd}/v_{vrms}	2.5E-22 cm^2	[15]
K	Hz/amg			

Table D.11: Alkali-N_2 Spin Destruction Rate Constant. All values have a 10% uncertainty unless otherwise noted.

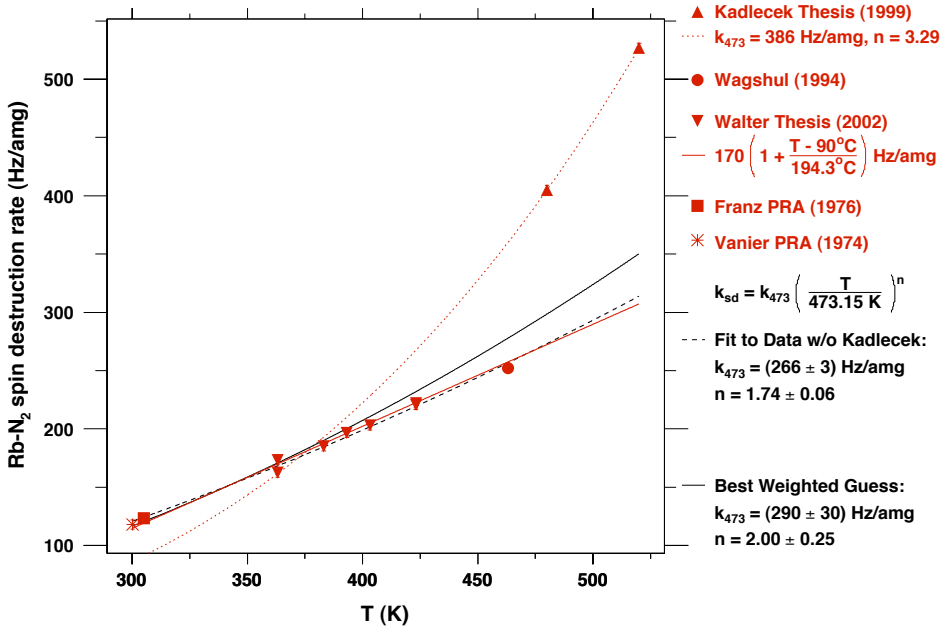

Figure D.2: Fit to Rb-N_2 Spin Destruction Rate Constant World Data.

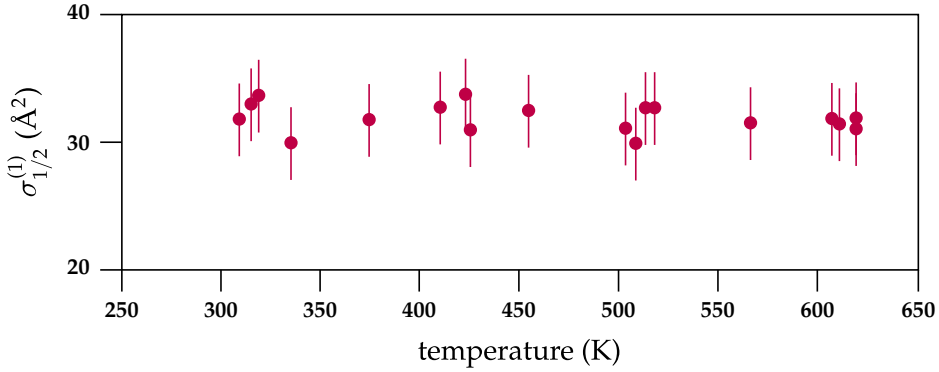

Figure D.3: Temperature Dependence of the Rb $5P_{1/2}$ Orientation Destruction Cross Section by He. Data are from Doebler & Kamke [40] with an average value of 33.1 Å^2.

D.4 Excited State Alkali Collisions

D.4.1 Multipole Destruction

The cross section has no temperature dependence by experiment [40]. The cross section has a soft temperature dependence by theory [41].

Because $\Delta E(m_J \leftrightarrow m'_J) \ll kT$

$$\sigma_{1/2}(\pm 1) = \sigma_{1/2}(\pm 1/2 \rightarrow \mp 1/2) \tag{D.23}$$

$$Z_0 = \sigma_{3/2}(\pm 1/2 \rightarrow \mp 1/2) \tag{D.24}$$

$$Z_1 = \sigma_{3/2}(\pm 3/2 \rightarrow \pm 1/2) = \sigma_{3/2}(\pm 1/2 \rightarrow \pm 3/2) \tag{D.25}$$

$$Z_2 = \sigma_{3/2}(\pm 3/2 \rightarrow \mp 1/2) = \sigma_{3/2}(\mp 1/2 \rightarrow \pm 3/2) \tag{D.26}$$

$$Z_3 = \sigma_{3/2}(\pm 3/2 \rightarrow \mp 3/2) \tag{D.27}$$

the collisions are assumed to be rotationally invariant (isotropic),

$$\sigma^{(1)}_{1/2} = 2\sigma_{1/2}(\pm 1) \tag{D.28}$$

$$\sigma^{(1)}_{3/2} = \frac{1}{5}Z_0 + \frac{2}{5}Z_1 + \frac{8}{5}Z_2 + \frac{9}{5}Z_3 \tag{D.29}$$

$$\sigma^{(2)}_{3/2} = 2Z_1 + 2Z_2 \tag{D.30}$$

$$\sigma^{(3)}_{3/2} = \frac{9}{5}Z_0 + \frac{8}{5}Z_1 + \frac{2}{5}Z_2 + \frac{1}{5}Z_3 \tag{D.31}$$

$$(0) = 3Z_0 - 4Z_1 + 4Z_2 - 3Z_3 \tag{D.32}$$

We've labeled things such that $\sigma^{(0)}_J$ is the depopulation cross section, $\sigma^{(1)}_J$ is the destruction cross section, and their sum $\sigma^{(0)}_J + \sigma^{(1)}_J$ is the relaxation cross section. Using the theory of [**?**] for s:

$$\sigma^{(1)}_{3/2} = 0.92s \qquad \sigma^{(2)}_{3/2} = 1.14s \qquad \sigma^{(3)}_{3/2} = 1.01s \tag{D.33}$$

Na	He	$\sigma^{(1)}_{1/2}$	33.4	3.4	$\sigma_{1/2}(\pm 1)$	16.7	1.7	[**?**]
Na	He	$\sigma^{(1)}_{3/2}$	99.0	23.1	$\sigma^{(0)}_{3/2} + \sigma^{(1)}_{3/2}$	146.0	22.0	[**?**]
Na	He	$\sigma^{(2)}_{3/2}$	81.0	14.7	$\sigma^{(0)}_{3/2} + \sigma^{(2)}_{3/2}$	128.0	13.0	[**?**]
Na	He	$\sigma^{(3)}_{3/2}$	120.0	18.4	$\sigma^{(0)}_{3/2} + \sigma^{(3)}_{3/2}$	167.0	17.0	[**?**]
Na	He	$\sigma^{(1)}_{1/2}$	28.1	4.0	$\sigma_{1/2}(\pm 1)$	14.1	2.0	[**?**]
Na	He	$\sigma^{(1)}_{1/2}$	26.3	3.6	$\sigma_{1/2}(\pm 1)$	13.2	1.8	[**?**]
Na	He	$\sigma^{(1)}_{3/2}$	61.2	7.1	Z_0	14.0	5.0	[?]
Na	He	$\sigma^{(2)}_{3/2}$	102.8	10.0	Z_1	28.3	2.5	[?]
Na	He	$\sigma^{(3)}_{3/2}$	80.8	14.1	Z_2	23.1	2.5	[?]
Na	He	(0)	-0.9	7.4	Z_3	5.6	0.6	[?]
Na	Na	$\sigma^{(1)}_{1/2}$	1.8E+04	1E+03	$\left\langle v\sigma^{(1)}_{1/2} \right\rangle$	1.8E-07	1.0E-08	[**?**], 550 K
Na	Na	$\sigma^{(1)}_{3/2}$	2.4E+04	1E+03	$\left\langle v\sigma^{(1)}_{3/2} \right\rangle$	2.4E-07	1.0E-08	[?], 550 K
Na	Na	$\sigma^{(2)}_{3/2}$	2.4E+04	4E+03	$\left\langle v\sigma^{(2)}_{3/2} \right\rangle$	2.4E-07	4.0E-08	[?], 530 K
Na	Na	$\sigma^{(3)}_{3/2}$	2.3E+04	2E+03	-	-	-	[?,**?**], 540 K

Table D.12: Table.

K	He	$\sigma^{(1)}_{1/2}$	92.0	4.6	$\sigma_{1/2}(\pm 1)$	46.0	2.3	[**?**]
K	He	$\sigma^{(1)}_{1/2}$	48.0	8.0	$\sigma_{1/2}(\pm 1)$	24.0	4.0	[**?**]
K	He	$\sigma^{(1)}_{3/2}$	86.0	14.0	$\sigma^{(1)}_{3/2}$	86.0	14.0	[**?**]
K	He	$\sigma^{(2)}_{3/2}$	127.0	37.0	$\sigma^{(2)}_{3/2}$	127.0	37.0	[?]
K	He	$\sigma^{(3)}_{3/2}$	103.5	24.1	$\sigma^{(3)}_{3/2}$	103.5	24.1	[?, ?]
K	He	$\sigma^{(1)}_{1/2}$	44.6	5.2	$\sigma_{1/2}(\pm 1)$	22.3	2.6	[**?**]
K	He	$\sigma^{(1)}_{3/2}$	96.8	13.4	Z_0	17.3	7.8	[?]
K	He	$\sigma^{(2)}_{3/2}$	129.6	17.3	Z_1	32.5	4.3	[?]
K	He	$\sigma^{(3)}_{3/2}$	99.2	23.0	Z_2	32.3	4.3	[?]
K	He	(0)	-0.6	12.6	Z_3	16.0	1.8	[?]
K	N2	$\sigma^{(1)}_{1/2}$	58.7	9.0	$\sigma^{(1)}_{1/2}$	58.7	9.0	[**?**]
K	N2	$\sigma^{(1)}_{3/2}$	155.0	23.0	$\sigma^{(1)}_{3/2}$	155.0	23.0	[?]
K	N2	$\sigma^{(2)}_{3/2}$	228.0	34.0	$\sigma^{(2)}_{3/2}$	228.0	34.0	[?]
K	N2	$\sigma^{(3)}_{3/2}$	174.0	26.0	$\sigma^{(3)}_{3/2}$	174.0	26.0	[?]
K	K	$\sigma^{(1)}_{1/2}$	5.7E+04	9E+03	$\sigma_{1/2}(\pm 1)$	2.9E+04	4.5E+03	[**?**]
K	K	$\sigma^{(1)}_{3/2}$	8.1E+04	1.9E+04	Z_0	2.0E+04	8.0E+03	[?]
K	K	$\sigma^{(2)}_{3/2}$	1.1E+05	2.2E+04	Z_1	3.1E+04	6.0E+03	[?]
K	K	$\sigma^{(3)}_{3/2}$	9.9E+04	2.7E+04	Z_2	2.6E+04	5.0E+03	[?]
K	K	(0)	-2.0E+02	1.6E+04	Z_3	1.3E+04	4.0E+03	[?]

Table D.13: Table.

Rb	He	$\sigma^{(1)}_{1/2}$	24.0	4.8	$\sigma^{(1)}_{1/2}$	24.0	4.8	[**?**, **?**]
Rb	He	$\sigma^{(1)}_{3/2}$	97.5	19.5	s	105.9	21.2	[**?**, ?]
Rb	He	$\sigma^{(2)}_{3/2}$	120.8	24.2	s	105.9	21.2	[?, ?]
Rb	He	$\sigma^{(3)}_{3/2}$	107.0	21.4	s	105.9	21.2	[?, ?]
Rb	He	$\sigma^{(1)}_{3/2}$	107.9	10.8	s	117.3	11.7	[**?**, ?]
Rb	He	$\sigma^{(2)}_{3/2}$	133.8	13.4	s	117.3	11.7	[?, ?]
Rb	He	$\sigma^{(3)}_{3/2}$	118.5	11.9	s	117.3	11.7	[?, ?]
Rb	He	$\sigma^{(1)}_{1/2}$	33.1	1.7	$\sigma^{(1)}_{1/2}$	33.1	1.7	[**?**]
Rb	He	$\sigma^{(1)}_{3/2}$	126.0	6.3	$\sigma^{(1)}_{3/2}$	126.0	6.3	[?]
Rb	He	$\sigma^{(2)}_{3/2}$	157.0	7.9	$\sigma^{(2)}_{3/2}$	157.0	7.9	[?]
Rb	He	$\sigma^{(3)}_{3/2}$	138.7	6.9	$\sigma^{(3)}_{3/2}$	138.7	6.9	[?, ?]
Rb	He	$\sigma^{(1)}_{1/2}$	23.0	4.6	$\sigma^{(1)}_{1/2}$	23.0	4.6	[?]
Rb	He	$\sigma^{(1)}_{1/2}$	11.6	2.0	$\sigma_{1/2}(\pm 1)$	5.8	1.0	[**?**], 1–7 T
Rb	He	$\sigma^{(1)}_{1/2}$	32.0	2.0	$\sigma_{1/2}(\pm 1)$	16.0	1.0	[**?**]
Rb	He	$\sigma^{(1)}_{3/2}$	240.0	30.0	Z_0	34.0	4.0	[?]
Rb	He	$\sigma^{(2)}_{3/2}$	278.0	32.0	Z_1	64.0	7.0	[?]
Rb	He	$\sigma^{(3)}_{3/2}$	203.3	23.3	Z_2	75.0	9.0	[?]
Rb	He	(0)	-0.0	19.2	Z_3	48.7	6.7	[?]
Rb	N2	$\sigma^{(1)}_{1/2}$	105.0	25.0	$\sigma^{(1)}_{1/2}$	105.0	25.0	[**?**]
Rb	N2	$\sigma^{(1)}_{1/2}$	65.0	4.0	$\sigma_{1/2}(\pm 1)$	32.5	2.0	[?]
Rb	N2	$\sigma^{(1)}_{3/2}$	219.4	24.2	Z_0	60.0	2.0	[?]
Rb	N2	$\sigma^{(2)}_{3/2}$	290.0	26.0	Z_1	78.3	6.5	[?]
Rb	N2	$\sigma^{(3)}_{3/2}$	267.6	17.8	Z_2	66.8	6.5	[?]
Rb	N2	(0)	-3.7	15.2	Z_3	38.5	6.0	[?]
Rb	Rb	$\sigma^{(1)}_{1/2}$	4.5E+04	4E+03	$\Gamma^{(1)}_{1/2}/\beta_n$	1.23	0.10	[**?**], 440 K
Rb	Rb	$\sigma^{(1)}_{3/2}$	6.4E+04	3E+03	$\Gamma^{(1)}_{3/2}/\beta_n$	1.71	0.08	[?], 440 K
Rb	Rb	$\sigma^{(2)}_{3/2}$	7.5E+04	4E+03	$\Gamma^{(2)}_{3/2}/\beta_n$	1.99	0.10	[?], 440 K
Rb	Rb	$\sigma^{(3)}_{3/2}$	6.6E+04	3E+03	-	-	-	[?, ?], 440 K

Table D.14: Table. $\beta_n = \beta 10^{-2}\,[\mathrm{N}]\,\lambda_n^3/\tau_n$

Cs	He	$\sigma^{(1)}_{1/2}$	6.1	1.2	$\sigma^{(1)}_{1/2}$	6.1	1.2	[?, ?]
Cs	He	$\sigma^{(1)}_{1/2}$	25.0	8.0	$\sigma_{1/2}(\pm 1)$	12.5	4.0	[**?**], 0 T
Cs	He	$\sigma^{(1)}_{1/2}$	9.8	1.4	$\sigma_{1/2}(\pm 1)$	4.9	0.7	[**?**], 0 T
Cs	He	$\sigma^{(1)}_{1/2}$	12.0	0.8	$\sigma_{1/2}(\pm 1)$	6.0	0.4	[**?**], 0 T
Cs	He	$\sigma^{(1)}_{1/2}$	22.2	2.0	$\sigma_{1/2}(\pm 1)$	11.1	1.0	[?], 0.8 T
Cs	He	$\sigma^{(1)}_{1/2}$	23.6	1.0	$\sigma_{1/2}(\pm 1)$	11.8	0.5	[**?**], 0.98 T
Cs	He	$\sigma^{(1)}_{1/2}$	12.8	4.2	$\sigma_{1/2}(\pm 1)$	6.4	2.1	[?] 1–7 T
Cs	He	$\sigma^{(1)}_{3/2}$	100.0	18.8	"σ^2_M"	32.0	6.0	[**?**, 11]
Cs	He	$\sigma^{(1)}_{3/2}$	80.0	12.0	$\sigma^{(1)}_{3/2}$	80.0	12.0	[**?**], 0.53 T
Cs	He	$\sigma^{(2)}_{3/2}$	86.0	21.0	$\sigma^{(2)}_{3/2}$	86.0	21.0	[?], 0.53 T
Cs	He	$\sigma^{(3)}_{3/2}$	82.0	15.9	$\sigma^{(3)}_{3/2}$	82.0	15.9	[?, ?], 0.53 T
Cs	He	$\sigma^{(1)}_{3/2}$	89.0	13.0	$\sigma^{(1)}_{3/2}$	89.0	13.0	[?], 0.57 T
Cs	He	$\sigma^{(2)}_{3/2}$	83.0	21.0	$\sigma^{(2)}_{3/2}$	83.0	21.0	[?], 0.57 T
Cs	He	$\sigma^{(3)}_{3/2}$	85.6	16.4	$\sigma^{(3)}_{3/2}$	85.6	16.4	[?, ?], 0.57 T

Table D.15: Table.

alkali	transition	σ_{473} (Å^2)	T (K)	σ_q (Å^2)	refs.
Na	D1 & D2	37.7	see Fig. (D.4)		[44,45]
K	D1 & D2	26.9	353	34	[48]
Rb	D1	44.4	340	58	[49]
	D2	33.0		43	
Cs	D1	55.5	315	77	[50]
	D2	49.7		69	

Table D.16: Alkali-N_2 Quenching Cross Sections. Data are rescaled from the 1975 Krause review article [44]. We estimate that the uncertainties are on the order of 10% relative.

D.4.2 Nonradiative Quenching

The quenching cross section due to collisions with atoms has been found to be negligibly small $\left(< 10^{-2}\ \text{Å}^2\right)$ [42,43]. This is because a collision that conserves energy through a change purely in translational kinetic energy is essentially impossible at our temperatures. On the other hand, the rotational and vibrational degrees of freedom of a molecule, such at N_2, provides several pathways for the excitation energy of the alkali atom to be absorbed in a quenching collision. We'll assume that the velocity averaged quenching cross section has the same power law temperature dependance ($\ll 1000$ K) for all the alkali atoms, see Fig. (D.4), which gives for the rate constant:

$$k_q(T) = \sigma_q \bar{v} = \frac{1.34\ \text{GHz}}{0.1\ \text{amg}} \left(\frac{\sigma_{473}}{50\ \text{Å}^2}\right) \left(\frac{T}{473.15\ \text{K}}\right)^{0.5+n} \sqrt{\frac{10\ \text{g/mol}}{M_\text{A}} + \frac{1}{2.8}} \tag{D.34}$$

where σ_{473} is the quenching cross section at $T = 473.15$ K listed in Tab. (D.16), $n = -0.81 \pm 0.19$, and M_A is the molar mass of the alkali atom.

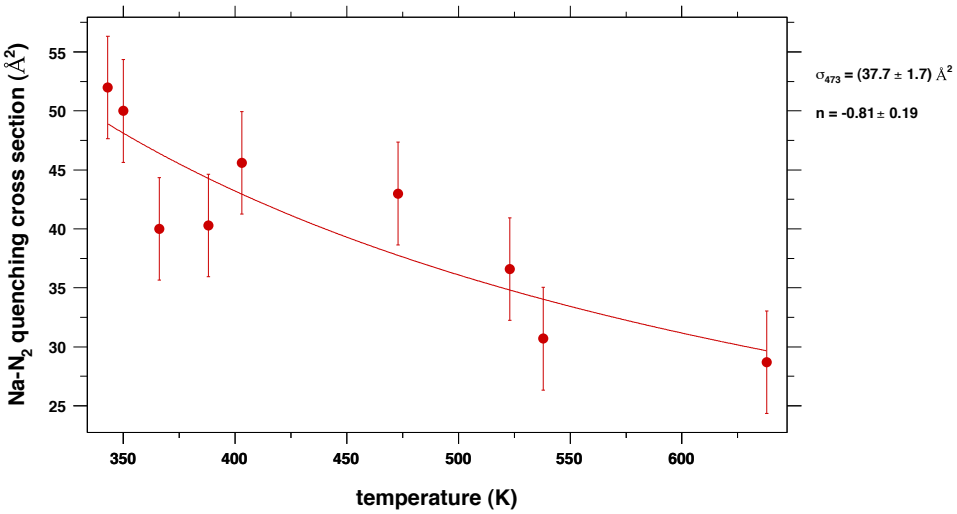

Figure D.4: Temperature Dependence of the Velocity Averaged Na-N_2 Quenching Cross Section at Low Temperatures. Data points are from the 1975 Krause review article [44] with the addition of [45]. At high temperatures ($\geq$ 1500 K), the velocity-averaged quenching cross section has been found to be independant of temperature [46]. Note, however, that the "energy dependant" (i.e. unaveraged) quenching cross section has been found to decrease linearly with the relative kinetic energy [45, 47].

D.4.3 Excitation Energy Transfer

Gallagher says that Rb-He has a $T^{2.59}$ and Cs-He is $T^{3.84}$, we'll assume this trend contiures. so that K-He has a $T^{1.15}$ and Cs-He is $T^{0.20}$. [51] Assuming rotational invariance during the collosional transfer process, the individual cross sections are given by:

$$F_3 = \sigma_m(1/2, \pm 1/2 \rightarrow 3/2, \pm 3/2) \tag{D.35}$$

$$F_0 = \sigma_m(1/2, \pm 1/2 \rightarrow 3/2, \pm 1/2) \tag{D.36}$$

$$F_1 = \sigma_m(1/2, \pm 1/2 \rightarrow 3/2, \mp 1/2) \tag{D.37}$$

$$F_2 = \sigma_m(1/2, \pm 1/2 \rightarrow 3/2, \mp 3/2) \tag{D.38}$$

which are combined to give:

$$\sigma^{(0\rightarrow 0)}_{1/2\rightarrow 3/2} = \frac{(F_3 + F_2) + (F_0 + F_1)}{\sqrt{2}} \tag{D.39}$$

$$\sigma^{(1\rightarrow 1)}_{1/2\rightarrow 3/2} = \frac{3(F_3 - F_2) + (F_0 - F_1)}{\sqrt{10}} \tag{D.40}$$

$$\sigma^{(0\rightarrow 2)}_{1/2\rightarrow 3/2} = \frac{(F_3 + F_2) - (F_0 + F_1)}{\sqrt{2}} \tag{D.41}$$

$$\sigma^{(1\rightarrow 3)}_{1/2\rightarrow 3/2} = \frac{(F_3 - F_2) - 3(F_0 - F_1)}{\sqrt{10}} \tag{D.42}$$

In the other direction, we have the analgous equations where $F \rightarrow G$ and these two are related by detailed balancing:

$$\frac{F}{G} = \frac{(2J_2 + 1)}{(2J_1 + 1)} \exp\left(-\frac{(E_2 - E_1)}{kT}\right) \tag{D.43}$$

D.5 Helium Collisions

D.5.1 Magnetic Dipolar Spin Relaxation

The theoretical minimum spin-relaxation rate is due to a direct coupling between two nearby ^{3}He nuclei. Newbury et al. [52] have calculated this ^{3}He -^{3}He nuclear dipolar spin-relaxation rate per nucleus at 23 ^{o}C:

$$\Gamma_{\text{dip}} = \frac{\left[{}^3\text{He}\right]}{(744\ \text{amg}\cdot\text{hrs})} \tag{D.44}$$

Fig. (D.5) [52, adapted from Figs. 2 and 3] depicts the temperature dependence of the relaxation rate from 0 K to 10 K and 1 K to 550 K calculated using one particular choice for the He-He inter-atomic potential. Newbury et al. state that two alternative models for the inter-atomic potential give consistent results within a few percent. An analytical form of the temperature dependence is not given; therefore we have prepared a "homemade" parameterization of this curve:

$$\Gamma_{\text{dip}}(T) = \frac{\left[{}^3\text{He}\right]}{(744\ \text{amg}\cdot\text{hrs})\cdot f_{\text{dip}}\left(T/T_{\text{ref}}\right)} \tag{D.45}$$

$$f_{\text{dip}}(t) = c_0 t^{c_1} + c_2 + c_3 t + \frac{c_4}{1+c_5 t} \tag{D.46}$$

where $T_{\text{ref}} = 296.15$ K is the reference temperature and the values of the unitless parameters are:

$$\begin{aligned} c_0 &= +1.2319\text{E}{+0} & c_1 &= +2.8591\text{E}{-1} & c_2 &= -2.1793\text{E}{-1} \\ c_3 &= -1.4426\text{E}{-2} & c_4 &= +5.3315\text{E}{-1} & c_5 &= +1.2376\text{E}{+3} \end{aligned} \tag{D.47}$$

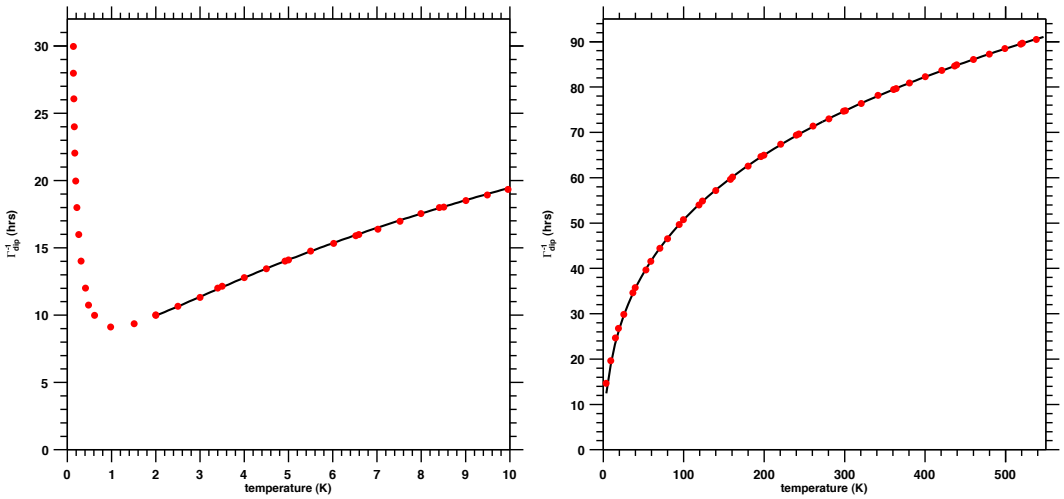

Figure D.5: Temperature Dependence of Nuclear Dipolar Relaxation for a Density of 10 amg. Note that both vertical axes are the spin-relaxation time constants Γ_{dip}^{-1}. Red points were located "by eye" from Figs. (2) & (3) in [52]. Black curve is the parametrization, Eqn. (D.46), that was fit to the red points. They agree to better than half a percent from 2 K to 550 K.

Note that at $T = T_{\text{ref}} = 23\ ^{\circ}\text{C} = 296.15$ K, the temperature function $f_{\text{dip}}(1)$ equals 1 as expected:

$$f_{\text{dip}}(T_{\text{ref}}) = c_0 + c_2 + c_3 + \frac{c_4}{1 + c_5} = 1 \tag{D.48}$$

This parametrization reproduces the curve in Fig. (D.5) to better than 0.5% from 2 K to 550 K. All things considered, a reasonable estimate for the uncertainty associated with this calculation/parametrization is about 5%.

D.5.2 Charge Exchange & Transfer

See rates.

reaction	type	binary	3-body	ref
$He^+ + He \rightarrow He + He^+$	charge exchange	15 ± 5	-	[53]
$He^+ + N_2 \rightarrow He + N_2^+$	charge transfer	27 ± 8	-	[54]
$He^+ + O_2 \rightarrow He + O_2^+$		23 ± 7	-	
$He^+ + 2He \rightarrow He + He_2^+$	molecular formation	-	0.060 ± 0.012	[55]
$He_2^+ + He \rightarrow He + He_2^+$	charge exchange	6 ± 3	-	[56]
$He_2^+ + CO_2 \rightarrow 2He + CO_2^+$	charge transfer	48 ± 13	-	[57]
$He_2^+ + (0,1)He + N_2 \rightarrow (2,3)He + N_2^+$	charge transfer	30 ± 3	9.8 ± 1.4	[58]
$He_2^+ + (0,1)He + H_2 \rightarrow (2,3)He + H_2^+$	charge transfer	11 ± 3	6.5 ± 3.6	[59]
$He_2^+ + (0,1)He + H_2O \rightarrow (2,3)He + H_2O^+$		22 ± 11	87 ± 18	
$He_2^+ + (0,1)He + O_2 \rightarrow (2,3)He + O_2^+$		27 ± 8	25 ± 7	

Table D.17: Atomic and Molecular Ion Reaction Rate Constants. Binary rate constants are in GHz/amg and 3-body rate constants are in GHz/amg^2. All values are assumed to be measured at 300 K and to have negligible temperature dependence within the quoted uncertainties.

Bibliography

[1] Alain Omont. Irreducible components of the density matrix. Application to optical pumping. *Progress in Quantum Electronics*, 5:69 – 138, 1979.

[2] G. V. Skrotskii and T. G. Izyumova. OPTICAL ORIENTATION OF ATOMS AND ITS APPLICATIONS. *SOV PHYS USPEKHI*, 4(2):177–204, 1961.

[3] K. Blum. Density matrix formalism and applications in spectroscopy. In W. Hanle and H. Kleinpoppen, editors, *Progress in Atomic Spectroscopy: Part A*. Plenum Press, New York, 1978.

[4] W. E. Baylis. Collisional depolarization in the excited state. In W. Hanle and H. Kleinpoppen, editors, *Progress in Atomic Spectroscopy: Part B*. Plenum Press, New York, 1979.

[5] Dmitry Budker, Derek F. Kimball, and David P. DeMille. *Atomic physics: an exploration through problems and solutions*. Oxford University Press, Oxford, 2nd edition, 2008.

[6] C. H. Wang and W. J. Tomlinson. Collision-Induced Anisotropic Relaxation in Gases. *Phys. Rev.*, 181(1):115–124, May 1969.

[7] W. Franzen. Spin Relaxation of Optically Aligned Rubidium Vapor. *Phys. Rev.*, 115(4):850–856, Aug 1959.

[8] T. E. Chupp, M. E. Wagshul, K. P. Coulter, A. B. McDonald, and W. Happer. Polarized, high-density, gaseous ^{3}He targets. *Phys. Rev. C*, 36(6):2244–2251, Dec 1987.

[9] W. Berdowski, T. Shiner, and L. Krause. m_J Mixing in Oriented $4^2P_{3/2}$ Potassium Atoms Induced by Collisions with Inert Gases. *Phys. Rev. A*, 4(3):984–992, Sep 1971.

[10] William Happer. Optical Pumping. *Rev. Mod. Phys.*, 44(2):169–249, Apr 1972.

[11] E. L. Lewis. Collisional relaxation of atomic excited states, line broadening and interatomic interactions. *Physics Reports*, 58(1):1 – 71, 1980.

[12] S. J. Davis and L. C. Balling. Temperature Dependence of the *e*-Na and *e*-Rb Spin-Exchange Cross Sections. *Phys. Rev. A*, 8(2):1136–1138, Aug 1973.

[13] A. Dalgarno and M. R. H. Rudge. Spin-Change Cross-Sections for Collisions Between Alkali Atoms. *Proceedings of the Royal Society of London. Series A, Mathematical and Physical Sciences*, 286(1407):519–524, 1965.

[14] D. K. Walter, W. M. Griffith, and W. Happer. Magnetic Slowing Down of Spin Relaxation due to Binary Collisions of Alkali-Metal Atoms with Buffer-Gas Atoms. *Phys. Rev. Lett.*, 88(9):093004, Feb 2002.

[15] Stephen John Kadlecek. *Spin Relaxation in Alkali Vapors*. PhD thesis, University of Wisconsin-Madison, 1999.

[16] S. Kadlecek, L. W. Anderson, and T. G. Walker. Field Dependence of Spin Relaxation in a Dense Rb Vapor. *Phys. Rev. Lett.*, 80(25):5512–5515, Jun 1998.

[17] P. I. Borel, L. V. Søgaard, W. E. Svendsen, and N. Andersen. Spin-exchange and spin-destruction rates for the ^{3}He-Na system. *Phys. Rev. A*, 67(6):062705, Jun 2003.

[18] Stephen Kadlecek, L. W. Anderson, and Thad Walker. Measurement of potassium-potassium spin relaxation cross sections. *Nuclear Instruments and Methods in Physics Research Section A: Accelerators, Spectrometers, Detectors and Associated Equipment*, 402(2-3):208 – 211, 1998. Proceedings of the 7th RCNP International Workshop on Polarized He Beams and Gas Targets and Their Application.

[19] R. J. Knize. Spin destruction in rubidium-rubidium and potassium-potassium collisions. *Phys. Rev. A*, 40(11):6219–6222, Dec 1989.

[20] A. Ben-Amar Baranga, S. Appelt, M. V. Romalis, C. J. Erickson, A. R. Young, G. D. Cates, and W. Happer. Polarization of ^{3}He by Spin Exchange with Optically Pumped Rb and K Vapors. *Phys. Rev. Lett.*, 80(13):2801–2804, Mar 1998.

[21] M. E. Wagshul and T. E. Chupp. Laser optical pumping of high-density Rb in polarized ^{3}He targets. *Phys. Rev. A*, 49(5):3854–3869, May 1994.

[22] B. Larson, O. Häusser, P. P. J. Delheij, D. M. Whittal, and D. Thiessen. Optical pumping of Rb in the presence of high-pressure ^{3}He buffer gas. *Phys. Rev. A*, 44(5):3108–3118, Sep 1991.

[23] N. D. Bhaskar, J. Pietras, J. Camparo, W. Happer, and J. Liran. Spin Destruction in Collisions between Cesium Atoms. *Phys. Rev. Lett.*, 44(14):930–933, Apr 1980.

[24] B. Chann, E. Babcock, L. W. Anderson, and T. G. Walker. Measurements of ^{3}He spin-exchange rates. *Phys. Rev. A*, 66(3):032703, Sep 2002.

[25] Thad G. Walker. Estimates of spin-exchange parameters for alkali-metal–noble-gas pairs. *Phys. Rev. A*, 40(9):4959–4964, Nov 1989.

[26] D. K. Walter, W. Happer, and T. G. Walker. Estimates of the relative magnitudes of the isotropic and anisotropic magnetic-dipole hyperfine interactions in alkali-metal–noble-gas systems. *Phys. Rev. A*, 58(5):3642–3653, Nov 1998.

[27] T. V. Tscherbul, P. Zhang, H. R. Sadeghpour, and A. Dalgarno. Collision-induced spin exchange of alkali-metal atoms with ^{3}He: An ab initio study. *Physical Review A (Atomic, Molecular, and Optical Physics)*, 79(6):062707, 2009.

[28] Earl V. Babcock. *Spin-Exchange Optical Pumping with Alkali-Metal Vapors*. PhD thesis, University of Wisconsin-Madison, 2005.

[29] Earl Babcock, Ian Nelson, Steve Kadlecek, Bastiaan Driehuys, L.W. Anderson, F.W. Hersman, and Thad G. Walker. Hybrid Spin-Exchange Optical Pumping of He. *Physical Review Letters*, 91(12):123003, 2003.

[30] Guodong Wang. *Polarizing He-3 by spin exchange with potassium*. PhD thesis, California Institute of Technology, 2004.

[31] K.P. Coulter, A.B. McDonald, W. Happer, T.E. Chupp, and M.E. Wagshul. Neutron polarization with polarized ^{3}He. *Nuclear Instruments and Methods in*

Physics Research Section A: Accelerators, Spectrometers, Detectors and Associated Equipment, 270(1):90 – 94, 1988.

[32] F. A. Franz and C. Volk. Electronic spin relaxation of the $4S_{1/2}$ state of K induced by K-He and K-Ne collisions. *Phys. Rev. A*, 26(1):85–92, Jul 1982.

[33] T. G. Walker, I. A. Nelson, and S. Kadlecek. Method for deducing anisotropic spin-exchange rates. *Phys. Rev. A*, 81(3):032709, Mar 2010.

[34] F. A. Franz and C. E. Sooriamoorthi. Spin relaxation within the $6P_{1/2}$ and $6S_{1/2}$ states of cesium measured by white-light optical pumping. *Phys. Rev. A*, 10(1):126–140, Jul 1974.

[35] N. Beverini, P. Minguzzi, and F. Strumia. Foreign-Gas-Induced Cesium Hyperfine Relaxation. *Phys. Rev. A*, 4(2):550–555, Aug 1971.

[36] Thad G. Walker, Joseph H. Thywissen, and William Happer. Spin-rotation interaction of alkali-metal–He-atom pairs. *Phys. Rev. A*, 56(3):2090–2094, Sep 1997.

[37] F. A. Franz and C. Volk. Spin relaxation of rubidium atoms in sudden and quasimolecular collisions with light-noble-gas atoms. *Phys. Rev. A*, 14(5):1711–1728, Nov 1976.

[38] Daniel Karl Walter. *Optical Probes of Angular Momentum and Energy Transport in Spin-Exchange Optical Pumping Systems*. PhD thesis, Princeton Univeristy, 2002.

[39] Jacques Vanier, Jean-F. Simard, and Jean-S. Boulanger. Relaxation and frequency shifts in the ground state of Rb-85. *Phys. Rev. A*, 9(3):1031–1040, Mar 1974.

[40] H. Doebler and B. Kamke. Temperature dependence of the disorientation cross section $\sigma^1_{1/2}$ in rubidium-rare gas collisions. *Zeitschrift fr Physik A*, 280(2):111–116, June 1977.

[41] B Brouillaud and R Gayet. Depolarisation of the 5p 2 P 1/2 state of rubidium induced by collisions with helium or xenon. *Journal of Physics B: Atomic and Molecular Physics*, 10(11):2143, 1977.

[42] G. Copley, B. P. Kibble, and L. Krause. Experimental Evidence for the Absence of Quenching of Sodium Resonance Radiation by Inert Gases. *Phys. Rev.*, 163(1):34–35, Nov 1967.

[43] B. Staudenmayer E. Speller and V. Kempter. Quenching cross sections for alkali-inert gas collisions. *Zeitschrift fr Physik A*, 291(4):311–318, Dec 1979.

[44] L. Krause. Sensitized fluorescence and quenching. In J. Wm. McGowan, editor, *Advances in Chemical Physics, Vol. XXVIII: The Excited State in Chemical Physics*. Interscience, New York, 1975.

[45] I. Tanarro, F. Arqueros, and J. Campos. Quenching of Na($3p^2$P) atoms by N_2 and CO molecules at low temperatures. *The Journal of Chemical Physics*, 77(4):1826–1829, 1982.

[46] P. J. Lijnse and R. J. Elsenaar. The temperature dependence of the quenching of Na-D-doublet by N_2 and H_2O in flames of 1500–2500 K. *Journal of Quantitative Spectroscopy and Radiative Transfer*, 12(7):1115 – 1128, 1972.

[47] John R. Barker and Jr. Ralph E. Weston. Energy-dependent cross sections for quenching of Na($3p^2$P) by several gases. *The Journal of Chemical Physics*, 65(4):1427–1442, 1976.

[48] G. Copley and L. Krause. Trapping and quenching of potassium resonance radiation. *Can. J. Phys.*, 47(5):533–539, 1969.

[49] E. S. Hrycyshyn and L. Krause. Inelastic collisions between excited alkali atoms and molecules. VII. Sensitized fluorescence and quenching in mixtures of rubidium with H_2, HD, D_2, N_2, CH_4, CD_4, C_2H_4, and C_2H_6. *Can. J. Phys.*, 48(22):2761–68, 1970.

[50] D. A. McGillis and L. Krause. Inelastic collisions between excited alkali atoms and molecules. IV. Sensitized fluorescence and quenching in mixtures of cesium with N_2, H_2, HD, and D_2. *Can. J. Phys.*, 46(9):1051–1057, 1968.

[51] Gallagher, Alan. Rubidium and Cesium Excitation Transfer in Nearly Adiabatic Collisions with Inert Gases. *Phys. Rev.*, 172(1):88–96, Aug 1968.

[52] N.R. Newbury, A.S. Barton, G.D. Cates, W. Happer, and H. Middleton. Gaseous ^{3}He-^{3}He magnetic dipolar spin relaxation. *Phys. Rev. A*, 48(6):4411–4420, Dec 1993.

[53] Donald Rapp and W.E. Francis. Charge Exchange between Gaseous Ions and Atoms. *The Journal of Chemical Physics*, 37(11):2361–2645, Dec 1962.

[54] J. Heimerl, R. Johnsen, and Manfred A. Biondi. Ion-Molecule Reactions, $He^+ + O_2$ and $He^+ + N_2$, at Thermal Energies and Above. *The Journal of Chemical Physics*, 51(11):5041–5048, Dec 1969.

[55] J.D.C. Jones, D.G. Lister, D.P. Wareing, and N.D. Twiddy. The temperature dependence of the three-body reaction rate coefficient for some rare-gas atomic ion-atom reactions in the range 100-300 K. *J. Phys. B: Atom. Molec. Phys.*, 13:3247–3255, 1980.

[56] K.D. Bonin, T.G. Walker, and W. Happer. Relaxation of gaseous spin-polarized ^{3}He targets due to ionizing radiation. *Phys. Rev. A*, 37(9):3270–3282, May 1988.

[57] D.K. Bohme, N.G. Adams, M. Mosesman, D.B. Dunkin, and E.E. Ferguson. Flowing Afterglow Studies of the Reactions of the Rare-Gas Molecular Ions He_2^+, Ne_2^+, and Ar_2^+ with Molecules and Rare-Gas Atoms. *The Journal of Chemical Physics*, 52(10):5094–5101, May 1970.

[58] J.M. Pouvesle, A. Bouchoule, and J. Stevefelt. Modeling of the charge transfer afterglow excited by intense electrical discharges in high pressure helium nitrogen mixtures. *The Journal of Chemical Physics*, 77(2):817–825, Jul 1982.

[59] C.B. Collins and F.W. Lee. Measurement of the rate coefficients for the bimolecular and termolecular ion-molecule reactions of He_2^+ with selected atomic and molecular species. *The Journal of Chemical Physics*, 68(4):1391–1401, Feb 1978.

Appendix E

Alkali Atoms and Polarized Light

The two basic quantities that must be known about a ^{3}He target cell are its helium density & polarization. To better understand & fully optimize the performance of these cells, it is essential to know the alkali vapor density & polarization as well. The atomic polarizability determines how light is modified after traversing a sample of alkali atoms. The imaginary part of the polarizability is responsible for absorption. The width of the absorption line is pressure broadened and consequently linearly proportional to the helium density. The real part of the atomic polarizability causes Faraday rotation of the the plane of polarization of a linearly polarized probe beam. The amount of rotation is proportional to the alkali density. We probe the Zeeman levels of the alkali atom via EPR RF spectroscopy. Slightly exciting one of the transitions lowers the alkali polarization by a small amount. By sweeping the holding field while keeping the RF frequency fixed, we map out the EPR RF spectrum of the alkali atoms. Ratios of areas under the peaks in this spectrum are related to the alkali polarization and alkali density ratio. Finally the locations of these peaks are shifted due interactions with the polarized helium gas.

The size of these frequency shifts are proportional to the He polarization. The goal of this note is to present all of the theoretical derivations needed to understand "where the formulas come from."

First, we'll derive the fine & hyperfine structure of the alkali atoms. Then we'll show how to describe polarized light using the Jones calculus. Using standard semi-classical arguments, we'll study how the matrix elements of the density operator changes under a harmonic perturbation. As a consequence, we'll calculate the transition matrix elements due to electric & magnetic dipole interactions. The coherences of the density matrix also depend on the populations of the density matrix, which are at a spin temperature equilibrium. To interpret pressure broadening & Faraday rotation, we'll calculate the atomic polarizability. Finally we'll provide an overview of the experimental techniques and summarize how to extract information from the experimental observables associated with the wavelength tunable probe beam. This note is meant to be detailed, explicit, and self-contained.

E.1 Atomic Notations & Conventions

All quantities will be denoted in SI. Angular momentum operators will be unitless:

$$\hat{\vec{J}}^2 |J, m_J\rangle = J(J+1) |J, m_J\rangle \tag{E.1}$$

$$\hat{J}_z |J, m_J\rangle = m_J |J, m_J\rangle, m_J = -J..J \tag{E.2}$$

$$\hat{J}_\pm = \hat{J}_x \pm i\hat{J}_y \tag{E.3}$$

$$\hat{J}_\pm |J, m_J\rangle = \sqrt{J(J+1) - m_J(m_J \pm 1)} |J, m_J \pm 1\rangle \tag{E.4}$$

The statistical weight is denoted by $[J]$ and is defined by $[J] = 2J + 1$. The magnetic moment arising from spin will be written:

$$\vec{\mu}_S = \frac{\mu_S}{S}\vec{S} \tag{E.5}$$

$$\frac{\mu_S}{S} = g_S \mu_x \tag{E.6}$$

The magnetic moment arising from the orbital angular momentum will be written:

$$\vec{\mu}_L = \mu_L \vec{L} \tag{E.7}$$

$$\mu_L = g_L \mu_x \tag{E.8}$$

Note that the sign of the magnetic moment is carried implicitly in g or alternatively μ_J. For example, $g \approx -2$ for the electron, $g \approx 2(2.79)$ for the proton, and $g \approx 2(-1.91)$ for the neutron. In all cases, the g-factor will be left unevaluated in the equations. However, equations will be written such that approximations can be made without loss of accuracy, for example:

$$-\frac{3}{2}g_S = 3\underbrace{\left[\frac{g_S}{-2}\right]}_{\approx 1.00116} \approx 3 \tag{E.9}$$

For the electron spin, g_S does not equal -2 exactly due to radiative corrections. There is no reason why g_L must equal exactly -1. This point is discussed at great length in section IX.5.1 of *Molecular Beams* [1]. Based on experimental results from alkali atoms, $|g_L|$ differs from unity on order of parts per million. Therefore, for $L \geq 1$, we'll take $g_L = -1.0$.

The units are carried in μ_x, which is the Bohr magneton (μ_B) for the electron

and the nuclear magneton (μ_N) for nuclei. The different angular momenta will be identified as:

- $\vec{S}$ is the sum of the spins of each electron in the atom,
- $\vec{L}$ is the sum of the orbital angular momenta of each electron in the atom,
- $\vec{J}\left(=\vec{L}+\vec{S}\right)$ is the total electronic angular momentum of the atom,
- $\vec{I}$ is the spin of the nucleus,
- $\vec{F}\left(=\vec{I}+\vec{J}\right)$ is the total internal angular momentum of the atom.

Operators and matrices will usually be denoted by hats $\hat{M}$. Hamiltonians will be $\mathcal{H}$, energies will be E, frequencies will be ν (with units of Hz), and angular frequencies ω (with units of rad·Hz).

E.2 The Fine Structure of Alkali Atoms

E.2.1 Zero Field Eigenbasis

The basic structure of the atomic Hamiltonian is summarized below, more details can be found in any good atomic physics book such as Woodgate [2] or Foot [3]:

1. The electrostatic interaction within an atom can be expressed as a central and a non-central force.
2. The central force is a Coulomb interaction between the electrons and an effective nuclear charge.
3. The non-central force is the residual electrostatic repulsion among the electrons.

4. For most atoms, the non-central force dominates over the spin-orbit coupling.

5. Because the non-central forces are larger, the orbital angular momenta of the electrons are correlated.

6. Because of Fermi-Dirac statistics, the total electronic spin and the total electronic orbital angular momentum is zero for closed shells.

7. Because of spherical symmetry, the non-central force is independent of orbital angular momentum for closed shells. Therefore, the non-central force is relevant only between the valence electrons.

8. In this limit, the spin-orbit coupling occurs between the total valence electronic spin and the total valence electronic orbital angular momentum.

9. Finally, all higher order interactions, such as quadrupole interactions, will usually be ignored.

Consider $\mathcal{H}_0$ with $\mathcal{H}_{\rm es}$, electrostatic interaction, and $\mathcal{H}_{\rm so}$, spin-orbit coupling:

$$\mathcal{H}_0 = \mathcal{H}_{\rm es} + \mathcal{H}_{\rm so} \tag{E.10}$$

Under the conditions described before, the form of $\mathcal{H}_{\rm so}$ is

$$\vec{J}^2 = (\vec{L}+\vec{S})^2 = \vec{L}^2 + 2\vec{L}\cdot\vec{S} + \vec{S}^2 \tag{E.11}$$

$$\mathcal{H}_{\rm so} = A_{\rm so}\vec{L}\cdot\vec{S} = \frac{A_{\rm so}}{2}(\vec{J}^2 - \vec{L}^2 - \vec{S}^2) \tag{E.12}$$

From the second form of $\mathcal{H}_{\rm so}$ above, it should be clear that J, L, and S are good quantum numbers, i.e., they commute with the Hamiltonian. A useful eigenbasis

with those quantum number is the LS-coupling scheme $\{|J, m_J\rangle\}$. Each group of degenerate eigenstates is labeled by a Russell-Saunders term [3,4] of the form

$$n^{2S+1}L_J \tag{E.13}$$

where n is the principal quantum number which labels the valence configuration. L labels the valence orbital in the following way:

- $L = 0 \rightarrow L = S$
- $L = 1 \rightarrow L = P$
- $L = 2 \rightarrow L = D$, and so on

All closed shells have

$$\vec{L}_{\text{shell}} = \vec{S}_{\text{shell}} = 0 \tag{E.14}$$

For a neutral alkali metal atom, $\vec{J}$, $\vec{L}$, and $\vec{S}$ all refer to the single valence electron. In the ground state, $J = \frac{1}{2}$ and the RS term is $n^2S_{\frac{1}{2}}$. The first two excited states have $J = \frac{1}{2}$ and $J = \frac{3}{2}$ and are labeled $n^2P_{\frac{1}{2}}$ and $n^2P_{\frac{3}{2}}$. Appendix C.3 contains an expansion of the LS-coupling basis $\{|J, m_J\rangle\}$ in the uncoupled L, S basis $\{|L, m_L\rangle\,|S, m_S\rangle\}$.

Spin-orbit coupling breaks the degeneracy of these n^2P states and results in *fine structure*. Fine structure also refers to other corrections, including relativistic ones, that are of the same order of magnitude. However, except for Hydrogen, these corrections are much smaller than the spin-orbit coupling. (where did i read that?) Regardless, these corrections only shift the energies collectively, independent of m_J and they do not mix the eigenstates. The transitions from the ground state to the first two excited states $n^2S_{\frac{1}{2}} \rightarrow n^2P_{\frac{1}{2}}$ and $n^2S_{\frac{1}{2}} \rightarrow n^2P_{\frac{3}{2}}$ are called the D1 and D2 transitions respectively.

E.2.2 Hamiltonian

The Hamiltonian describing the atom in a magnetic field $\vec{B}$ is

$$\mathcal{H} = \mathcal{H}_0 - \vec{\mu}_L \cdot \vec{B} - \vec{\mu}_S \cdot \vec{B} = \mathcal{H}_{\text{es}} + \mathcal{H}_{\text{so}} - \vec{\mu}_L \cdot \vec{B} - \vec{\mu}_S \cdot \vec{B} \tag{E.15}$$

To recap:

- The first term H_{es} contains all the terms that do not involve the electron spin.
- The second term is the spin-orbit interaction.
- The third and fourth terms are the Zeeman terms for the orbital and spin angular momentum respectively.

Using $\vec{B} = B\hat{z}$ & $J_z = L_z + S_z$:

$$\begin{aligned}
\mathcal{H} &= \mathcal{H}_{\text{es}} + \mathcal{H}_{\text{so}} - \vec{\mu}_L \cdot \vec{B} - \vec{\mu}_S \cdot \vec{B} && \text{(E.16)}\\
&= \mathcal{H}_{\text{es}} + \frac{A_{\text{so}}}{2}\left(\vec{J}^2 - \vec{L}^2 - \vec{S}^2\right) - g_L\mu_B L_z B - g_S\mu_B S_z B && \text{(E.17)}\\
&= \mathcal{H}_{\text{es}} + \frac{A_{\text{so}}}{2}\left(\vec{J}^2 - \vec{L}^2 - \vec{S}^2\right) - g_L\mu_B \left(J_z - S_z\right) B - g_S\mu_B S_z B && \text{(E.18)}\\
&= \mathcal{H}_{\text{es}} + \left(-\frac{A_{\text{so}}}{2}\left(\vec{L}^2 + \vec{S}^2\right) - g_L\mu_B B J_z\right) + \mathcal{H}' && \text{(E.19)}\\
\mathcal{H}' &= \frac{A_{\text{so}}}{2}\vec{J}^2 - \left(g_S - g_L\right)\mu_B B S_z && \text{(E.20)}\\
g_S &\simeq -2 && \text{(E.21)}\\
g_L &= \left\{ \begin{array}{cc} 0 & , L = 0 \\ -1 & , L > 0 \end{array} \right\} && \text{(E.22)}
\end{aligned}$$

The Hamiltonian is separated into three terms intentionally. States within a $n^{2S+1}L$ term with the same m_J but different J are mixed by the Zeeman interaction. This

means that the first two terms are diagonal simultaneously in the $\{|J, m_J\rangle\}$ basis and the eigenbasis of $\mathcal{H}$. Therefore, only $\mathcal{H}'$ has to be diagonalized.

E.2.3 Energies

Matrix Subblocks

Let's specialize to the case $S = \frac{1}{2}$, since an alkali metal atom is being considered. J can be $L \pm \frac{1}{2}$. Therefore in the $\{|J, m_J\rangle\}$ basis, the S_z term is block diagonal with subblocks no greater than 2 by 2 in size. The 2 by 2 subblocks are made of the states with different J and same m_J. For the special case of $m_J = \pm\left(L + \frac{1}{2}\right)$, there are no other states to mix with. Thus, they reside in subblocks of size 1 by 1. This is true for the $m_J = \pm\frac{1}{2}$ states of the ground state term $n^2S_{\frac{1}{2}}$ and the $m_J = \pm\frac{3}{2}$ states of the excited state term $n^2P_{\frac{3}{2}}$. On the other hand, the $m_J = \pm\frac{1}{2}$ states of the terms $n^2P_{\frac{1}{2},\frac{3}{2}}$ mix and therefore need to be diagonalized. To diagonalize $\mathcal{H}$, we only have to diagonalize each subblock of $\mathcal{H}'$,

$$\mathcal{H}' = \frac{A_{\text{so}}}{2}\vec{J}^2 - \left(g_S - g_L\right)\mu_B B S_z \tag{E.23}$$

$$\hat{\mathcal{H}}' = \frac{A_{\text{so}}}{2}\begin{bmatrix} \left(L+\frac{1}{2}\right)\left(L+\frac{3}{2}\right) & 0 \\ 0 & \left(L-\frac{1}{2}\right)\left(L+\frac{1}{2}\right) \end{bmatrix} - \left(g_S - g_L\right)\mu_B B \begin{bmatrix} \alpha_+ & \beta_- \\ \beta_+ & \alpha_- \end{bmatrix} \tag{E.24}$$

$$\alpha_\pm = \left\langle L \pm \frac{1}{2}, m_J \middle| \hat{S}_z \middle| L \pm \frac{1}{2}, m_J \right\rangle \tag{E.25}$$

$$\beta_\pm = \left\langle L \mp \frac{1}{2}, m_J \middle| \hat{S}_z \middle| L \pm \frac{1}{2}, m_J \right\rangle \tag{E.26}$$

The first term can be simplified to give:

$$\frac{A_{\rm so}}{2}\,\hat{\vec{J}}^2 = \frac{A_{\rm so}}{2}\left(L+\frac{1}{2}\right)\left(L+\frac{1}{2}+\begin{bmatrix}1 & 0\\ 0 & -1\end{bmatrix}\right) \tag{E.27}$$

$\alpha_\pm$ & $\beta_\pm$ in the second term are most easily calculated in the uncoupled $\{|L\rangle\,|S\rangle\}$ basis:

$$|L,m_L\rangle\,|S,m_S\rangle = |m_L,m_S\rangle = |m_L\rangle_L\,|m_S\rangle_S \tag{E.28}$$

$$|J,m_J\rangle = \sum |m_L,m_S\rangle \underbrace{\langle m_L,m_S|J,m_J\rangle}_{\rm Clebsch-Gordon} \tag{E.29}$$

Using formulas for Clebsch-Gordon coefficients from the appendix (C.2):

$$\begin{aligned}\left\langle m_J\mp\frac{1}{2},\pm\frac{1}{2}\mid L+\frac{1}{2},m_J\right\rangle &= \frac{1}{\sqrt{[L]}}\sqrt{L+\frac{1}{2}\pm m_J}\\ \left\langle m_J\mp\frac{1}{2},\pm\frac{1}{2}\mid L-\frac{1}{2},m_J\right\rangle &= \frac{\mp 1}{\sqrt{[L]}}\sqrt{L+\frac{1}{2}\mp m_J}\end{aligned} \tag{E.30}$$

For $\alpha_\pm$:

$$\begin{aligned}
\alpha_\pm &= \left\langle L \pm \frac{1}{2}, m_J \right| \hat{S}_z \left| L \pm \frac{1}{2}, m_J \right\rangle && \text{(E.31)}\\
&= \sum_{m_S, m'_S = -\frac{1}{2}}^{\frac{1}{2}} \langle m_J - m'_S, m'_S | \hat{S}_z | m_J - m_S, m_S \rangle \\
&\qquad \times \langle J, m_J | m_J - m'_S, m'_S \rangle \langle m_J - m_S, m_S | J, m_J \rangle && \text{(E.32)}\\
&= \sum_{m_S = -\frac{1}{2}}^{\frac{1}{2}} m_S \left| \langle m_J - m_S, m_S | J, m_J \rangle \right|^2, J = L \pm \frac{1}{2} && \text{(E.33)}\\
&= \frac{1}{2} \left(\frac{L + \frac{1}{2} \pm m_J - L - \frac{1}{2} \pm m_J}{[L]} \right) && \text{(E.34)}\\
&= \pm \left(\frac{m_J}{[L]} \right) = \pm(\alpha) && \text{(E.35)}
\end{aligned}$$

For $\beta_\pm$:

$$\begin{aligned}
\beta_\pm &= \left\langle L \mp \frac{1}{2}, m_J \right| \hat{S}_z \left| L \pm \frac{1}{2}, m_J \right\rangle && \text{(E.36)}\\
&= \sum_{m_S, m'_S = -\frac{1}{2}}^{\frac{1}{2}} \langle m_J - m'_S, m'_S | \hat{S}_z | m_J - m_S, m_S \rangle \\
&\qquad \times \left\langle L \mp \frac{1}{2}, m_J | m_J - m'_S, m'_S \right\rangle \left\langle m_J - m_S, m_S | L \pm \frac{1}{2}, m_J \right\rangle && \text{(E.37)}\\
&= \sum_{m_S = -\frac{1}{2}}^{\frac{1}{2}} m_S \left\langle L \mp \frac{1}{2}, m_J | m_J - m_S, m_S \right\rangle \left\langle m_J - m_S, m_S | L \pm \frac{1}{2}, m_J \right\rangle && \text{(E.38)}\\
&= +\frac{1}{2} \left(\frac{-\sqrt{\left(L + \frac{1}{2} \mp m_J\right)\left(L + \frac{1}{2} \pm m_J\right)}}{[L]} \right) - \frac{1}{2} \left(\frac{+\sqrt{\left(L + \frac{1}{2} \pm m_J\right)\left(L + \frac{1}{2} \mp m_J\right)}}{[L]} \right) && \text{(E.39)}\\
&= -\left(\frac{\sqrt{\left(L + \frac{1}{2}\right)^2 - m_J^2}}{[L]} \right) = -(\beta) && \text{(E.40)}
\end{aligned}$$

To solve for the energies, we only to diagonalize the last term in $\mathcal{H}'$:

$$\mathcal{H}' = \frac{A_{\text{so}}}{2}\left(L+\frac{1}{2}\right)\left(L+\frac{1}{2}+\begin{bmatrix}1 & 0\\ 0 & -1\end{bmatrix}\right)-\left(g_S-g_L\right)\mu_B B\begin{bmatrix}\alpha_+ & \beta_-\\ \beta_+ & \alpha_-\end{bmatrix} \tag{E.41}$$

$$= \frac{A_{\text{so}}}{2}\left(L+\frac{1}{2}\right)\left(L+\frac{1}{2}+\begin{bmatrix}1 & 0\\ 0 & -1\end{bmatrix}\right)+\left(g_L-g_S\right)\mu_B B\begin{bmatrix}\alpha & -\beta\\ -\beta & -\alpha\end{bmatrix} \tag{E.42}$$

$$= \frac{A_{\text{so}}}{2}\left(L+\frac{1}{2}\right)^2+\frac{A_{\text{so}}}{2}\left(L+\frac{1}{2}\right)\left(\begin{bmatrix}1 & 0\\ 0 & -1\end{bmatrix}+2\frac{\left(g_L-g_S\right)\mu_B B}{A_{\text{so}}\left(L+\frac{1}{2}\right)}\begin{bmatrix}\alpha & -\beta\\ -\beta & -\alpha\end{bmatrix}\right) \tag{E.43}$$

$$= \frac{A_{\text{so}}}{2}\left(L+\frac{1}{2}\right)^2+\frac{A_{\text{so}}}{2}\left(L+\frac{1}{2}\right)\underbrace{\begin{bmatrix}1+2\alpha y & -2\beta y\\ -2\beta y & -\left(1+2\alpha y\right)\end{bmatrix}}_{\hat{M}} \tag{E.44}$$

$$y = \left(g_L-g_S\right)\frac{\mu_B B}{A_{\text{so}}\left(L+\frac{1}{2}\right)} \tag{E.45}$$

Diagonalization

This is done by solving the secular equation:

$$0 = \det\left(\hat{M}-\hat{I}\lambda\right) \tag{E.46}$$

$$0 = \begin{vmatrix}1+2\alpha y-\lambda & -2\beta y\\ -2\beta y & -\left(1+2\alpha y+\lambda\right)\end{vmatrix} \tag{E.47}$$

$$0 = -\left(1+2\alpha y-\lambda\right)\left(1+2\alpha y+\lambda\right)-\left(2\beta y\right)^2 \tag{E.48}$$

$$0 = \lambda^2-\left(1+2\alpha y\right)^2-\left(2\beta y\right)^2 \tag{E.49}$$

$$\lambda = \pm\sqrt{\left(1+2\alpha y\right)^2+\left(2\beta y\right)^2} \tag{E.50}$$

$$= \pm\sqrt{1+4\alpha y+4\left(\alpha^2+\beta^2\right)y^2} \tag{E.51}$$

Using the eqns. (E.35) and (E.40), the following useful relations are derived:

$$\alpha^2 + \beta^2 = \frac{m_J^2 + \left(L + \frac{1}{2}\right)^2 - m_J^2}{[L]^2} = \frac{\left(L + \frac{1}{2}\right)^2}{2^2\left(L + \frac{1}{2}\right)^2} = \frac{1}{4} \tag{E.52}$$

$$4\alpha^2 + 4\beta^2 = 1 \tag{E.53}$$

We get the eigenvalues:

$$\pm\left(\lambda = \sqrt{1 + 4\alpha y + y^2}\right) \tag{E.54}$$

The total energy is therefore:

$$E = E_0 - \frac{A_{\text{so}}}{2}\left(L(L+1) + \frac{1}{2}\left(\frac{1}{2} + 1\right)\right) - g_L \mu_B m_J B + E' \tag{E.55}$$

$$E' = \frac{A_{\text{so}}}{2}\left(L + \frac{1}{2}\right)^2 \pm \frac{A_{\text{so}}}{2}\left(L + \frac{1}{2}\right)\lambda \tag{E.56}$$

The $\pm\lambda$ eigenvalue is used for states evolving from the $J = L \pm \frac{1}{2}$ term. In the zero field case, $B = 0$, we find the spin-orbit (fine structure) splitting between the two terms is:

$$\Delta E = \frac{A_{\text{so}}[L]}{2} = h\nu_{\text{so}} \tag{E.57}$$

Relabeling the energies without spin-orbit coupling and without field as E_0^L and relating A_{so} to the zero field spin-orbit splitting $h\nu_{\text{so}}$, for $L > 0$, we get:

$$E = E_0^L - \frac{h\nu_{\text{so}}}{2[L]} + \mu_B m_J B \pm \frac{h\nu_{\text{so}}}{2}\sqrt{1 + \frac{4m_J}{[L]}y + y^2} \tag{E.58}$$

$$y = \left(2\left[\frac{g_S}{-2}\right] - 1\right)\frac{\mu_B B}{h\nu_{\text{so}}} \tag{E.59}$$

where $\pm$ refers to the states with $J = L \pm \frac{1}{2}$. When $L = 0$, $g_L = 0$ and *the positive root* of the square root is taken, which gives the energies for the $n^2S_{\frac{1}{2}}$ term:

$$
\begin{aligned}
L &= 0 \rightarrow J = S \rightarrow m_J = m_S = \pm\frac{1}{2} && \text{(E.60)}\\
y &= \left[\frac{g_S}{-2}\right]\frac{2\mu_B B}{h\nu_{\text{so}}} && \text{(E.61)}\\
E_{\pm\frac{1}{2}} &= E_0^S - \frac{h\nu_{\text{so}}}{2} + \frac{h\nu_{\text{so}}}{2}\sqrt{1 \pm \frac{4}{2}y + y^2} && \text{(E.62)}\\
&= E_0^S - \frac{h\nu_{\text{so}}}{2} + \frac{h\nu_{\text{so}}}{2}\left(1 \pm y\right) && \text{(E.63)}\\
&= E_0^S \pm \frac{h\nu_{\text{so}}}{2}\left(\left[\frac{g_S}{-2}\right]\frac{2\mu_B B}{h\nu_{\text{so}}}\right) && \text{(E.64)}\\
&= E_0^S \pm \left[\frac{g_S}{-2}\right]\mu_B B && \text{(E.65)}\\
&= E_0^S - g_S\mu_B B m_S && \text{(E.66)}
\end{aligned}
$$

where $\pm$ refers to the sign of $m_S = \pm\frac{1}{2}$. Note that y is a unitless quantity that gives the relative measure of the size of the Zeeman interaction with respect to the spin-orbit interaction. For example the Zeeman interaction is comparable to the spin-orbit interaction ($y \approx 1$) for potassium and rubidium when $B \approx 124$ T & 510 T respectively, see table (A.2). Because of the strength of the spin-orbit interaction, J is almost always a very good quantum number for most alkali metals.

The energies of the $m_J = \pm(L + \frac{1}{2})$ states in the $J = L + \frac{1}{2}$ term are:

$$y = \left(2\left[\frac{g_S}{-2}\right] - 1\right)\frac{\mu_B B}{h\nu_{\rm so}} \tag{E.67}$$

$$E_{\pm\left(L+\frac{1}{2}\right)} = E_0^L - \frac{h\nu_{\rm so}}{2[L]} \pm \mu_B\left(L+\frac{1}{2}\right)B + \frac{h\nu_{\rm so}}{2}\sqrt{1 \pm \frac{4\left(L+\frac{1}{2}\right)}{[L]}y + y^2} \tag{E.68}$$

$$= E_0^L - \frac{h\nu_{\rm so}}{2[L]} \pm \mu_B\left(L+\frac{1}{2}\right)B + \frac{h\nu_{\rm so}}{2}\sqrt{1 \pm 2y + y^2} \tag{E.69}$$

$$= E_0^L - \frac{h\nu_{\rm so}}{2[L]} \pm \mu_B\left(L+\frac{1}{2}\right)B + \frac{h\nu_{\rm so}}{2}(1 \pm y) \tag{E.70}$$

$$= E_0^L + \frac{L}{[L]}h\nu_{\rm so} \pm \mu_B\left(L+\frac{1}{2}\right)B \mp \frac{h\nu_{\rm so}}{2}(1+g_S)\frac{\mu_B B}{h\nu_{\rm so}} \tag{E.71}$$

$$= E_0^L + \frac{L}{[L]}h\nu_{\rm so} \pm \mu_B B\left(L + \frac{1}{2} - \frac{1+g_S}{2}\right) \tag{E.72}$$

$$= E_0^L + \frac{L}{[L]}h\nu_{\rm so} \pm \left(L + \left[\frac{g_S}{-2}\right]\right)\mu_B B \tag{E.73}$$

Low Field Energies

At low field, see table (A.2), to second order in B, the energies for the $J = L \pm \frac{1}{2}$ terms with $L > 0$ are:

$$E = E_0^L - \frac{h\nu_{\rm so}}{2[L]} + \mu_B m_J B \pm \frac{h\nu_{\rm so}}{2}\left(1 + \frac{2m_J}{[L]}y + \frac{1}{2}\left(1 - \frac{4m_J^2}{[L]^2}\right)y^2 + O(y^3)\right) \tag{E.74}$$

$$\pm\left(\frac{E - E_0^L}{h\nu_{\rm so}}\right) = \mp\frac{1}{2[L]} + \pm m_J\frac{\mu_B B}{h\nu_{\rm so}} + \frac{1}{2} + \frac{m_J}{[L]}y + \frac{1}{4}\left(1 - \frac{4m_J^2}{[L]^2}\right)y^2 + O(y^3)$$

$$= \frac{1}{2}\left(1 \mp \frac{1}{[L]}\right) \pm m_J\frac{\mu_B B}{h\nu_{\rm so}} + \frac{m_J}{[L]}\left(2\left[\frac{g_S}{-2}\right] - 1\right)\frac{\mu_B B}{h\nu_{\rm so}} + \frac{1}{4}\left(1 - \frac{4m_J^2}{[L]^2}\right)y^2$$

$$= \frac{L + \frac{1}{2} \mp \frac{1}{2}}{[L]} + \frac{m_J}{[L]}\left(2\left[\frac{g_S}{-2}\right] - 1 \pm [L]\right)\frac{\mu_B B}{h\nu_{\rm so}} + \frac{1}{4}\left(1 - \frac{4m_J^2}{[L]^2}\right)y^2 \tag{E.75}$$

The energies for the three lowest RS terms of alkali metals to second order in B

are:

$$E^S_{\frac{1}{2},-\frac{1}{2}} = E^S_0 - \left[\frac{g_S}{-2}\right]\mu_B B \tag{E.76}$$

$$E^S_{\frac{1}{2},+\frac{1}{2}} = E^S_0 + \left[\frac{g_S}{-2}\right]\mu_B B \tag{E.77}$$

$$E^P_{\frac{1}{2},-\frac{1}{2}} = E^P_0 - \left(\frac{2}{3}\right)h\nu_{\rm so} - \left[2+\frac{g_S}{2}\right]\left(\frac{1}{3}\right)\mu_B B - \left(\frac{2}{9}y^2\right)h\nu_{\rm so} \tag{E.78}$$

$$E^P_{\frac{1}{2},+\frac{1}{2}} = E^P_0 - \left(\frac{2}{3}\right)h\nu_{\rm so} + \left[2+\frac{g_S}{2}\right]\left(\frac{1}{3}\right)\mu_B B - \left(\frac{2}{9}y^2\right)h\nu_{\rm so} \tag{E.79}$$

$$E^P_{\frac{3}{2},-\frac{3}{2}} = E^P_0 + \left(\frac{1}{3}\right)h\nu_{\rm so} - \left[\frac{1}{2}-\frac{g_S}{4}\right]2\mu_B B \tag{E.80}$$

$$E^P_{\frac{3}{2},-\frac{1}{2}} = E^P_0 + \left(\frac{1}{3}\right)h\nu_{\rm so} - \left[\frac{1}{2}-\frac{g_S}{4}\right]\left(\frac{2}{3}\right)\mu_B B + \left(\frac{2}{9}y^2\right)h\nu_{\rm so} \tag{E.81}$$

$$E^P_{\frac{3}{2},+\frac{1}{2}} = E^P_0 + \left(\frac{1}{3}\right)h\nu_{\rm so} + \left[\frac{1}{2}-\frac{g_S}{4}\right]\left(\frac{2}{3}\right)\mu_B B + \left(\frac{2}{9}y^2\right)h\nu_{\rm so} \tag{E.82}$$

$$E^P_{\frac{3}{2},+\frac{3}{2}} = E^P_0 + \left(\frac{1}{3}\right)h\nu_{\rm so} + \left[\frac{1}{2}-\frac{g_S}{4}\right]2\mu_B B \tag{E.83}$$

where the bracketed terms evaluate to 1 when the approximation $g_S \approx -2$ is made.

E.2.4 Eigenstates: Fine Structure Mixing

Orthonormality of the Mixing Coefficients

At zero field, with $S = \frac{1}{2}$, and for a given $L > 0$, there are in general two states with the same m_J, but with different J. Note however that when $|m_J| = L + \frac{1}{2}$, there is only one state with the quantum numbers m_J, J, and L. As noted before, the B-field mixes states with the same L, the same m_J, but different J. The result of the mixing are two states with the same m_J but with different J. At low field, the mixed states are, to a very good approximation, the zero field eigenstates with a small admixture of the other eigenstate. The mixed states, labeled by $\pm$, approach

the the zero field states with $J = L \pm \frac{1}{2}$ as the field approaches zero. Because J is still a very good quantum number, we will represent $\{|L_\pm, m_J\rangle\}$ in the $\{|J, m_J\rangle\}$ basis:

$$|L_\pm, m_J\rangle = a_1^\pm \left| L + \frac{1}{2}, m_J \right\rangle + a_2^\pm \left| L - \frac{1}{2}, m_J \right\rangle \tag{E.84}$$

where $a_1^\pm, a_2^\pm$ are the fine structure mixing coefficients, which we choose to be real. To repeat, a zero field, $L_\pm = P_{L\pm\frac{1}{2}}$. The mixed eigenstates must be orthonormal:

$$\left\langle m_J^\pm | m_J^\pm \right\rangle = \left(a_1^\pm\right)^2 + \left(a_2^\pm\right)^2 = 1 \tag{E.85}$$

$$\left\langle m_J^- | m_J^+ \right\rangle = a_1^- a_1^+ + a_2^- a_2^+ = 0 \tag{E.86}$$

Some algebra gives:

$$\left(a_2^\pm\right)^2 = 1 - \left(a_1^\pm\right)^2 \tag{E.87}$$

$$\left(a_1^- a_1^+\right)^2 = \left(a_2^- a_2^+\right)^2$$

$$\left(a_1^- a_1^+\right)^2 = 1 + \left(a_1^- a_1^+\right)^2 - \left(a_1^-\right)^2 - \left(a_1^+\right)^2$$

$$1 = \left(a_1^-\right)^2 + \left(a_1^+\right)^2 \tag{E.88}$$

$$\left(a_1^-\right)^2 = \left(a_2^+\right)^2 \tag{E.89}$$

$$\left(a_2^-\right)^2 = \left(a_1^+\right)^2 \tag{E.90}$$

$$\frac{a_1^-}{a_2^+} = -\frac{a_2^-}{a_1^-} \tag{E.91}$$

$$a_1^\pm = \pm a_2^\mp \tag{E.92}$$

To recap, orthonormality implies equation (E.92).

Solving for the Mixing Coefficients

The values for $a_{1,2}^{\pm}$ come from the diagonalization of eqn. (E.44) where $\lambda_{\pm}$ are the eigenvalues given by eqn. (E.54) and α and β are defined by eqns. (E.35) and (E.40):

$$\hat{M}\left|a\right\rangle = \pm\lambda\left|a\right\rangle \tag{E.93}$$

$$\begin{bmatrix} 1+2\alpha y & -2\beta y \\ -2\beta y & -\left(1+2\alpha y\right) \end{bmatrix} \begin{bmatrix} a_1^{\pm} \\ a_2^{\pm} \end{bmatrix} = \pm\lambda \begin{bmatrix} a_1^{\pm} \\ a_2^{\pm} \end{bmatrix} \tag{E.94}$$

$$\left(1+2\alpha y\right)a_1^{\pm} - 2\beta y a_2^{\pm} = \pm\lambda a_1^{\pm} \tag{E.95}$$

$$-2\beta y a_2^{\pm} - \left(1+2\alpha y\right)a_1^{\pm} = \pm\lambda a_2^{\pm} \tag{E.96}$$

These last two equations are redundant. Taking the former, using the normalization condition, and some algebra gives:

$$\left(1+2\alpha y \mp \lambda\right)a_1^{\pm} = 2\beta y a_2^{\pm} \tag{E.97}$$

$$\left(1+2\alpha y \mp \lambda\right)^2\left(a_1^{\pm}\right)^2 = 4\beta^2 y^2\left(1-\left(a_1^{\pm}\right)^2\right) \tag{E.98}$$

$$a_1^{\pm} = \frac{2\beta y}{\sqrt{\left(1+2\alpha y \mp \lambda\right)^2 + 4\beta^2 y^2}} \tag{E.99}$$

$$a_2^{\pm} = \frac{1+2\alpha y \mp \lambda}{\sqrt{\left(1+2\alpha y \mp \lambda\right)^2 + 4\beta^2 y^2}} \tag{E.100}$$

The $\pm$ sign is taken for states evolving from the $J = L \pm \frac{1}{2}$ term. Again even though J is not a rigorously good quantum number like m_J, at low fields it is still very good. This can be more easily seen by expanding $a_{1,2}^{\pm}$ at low field to second order in $y(B)$.

Low Field Expansion

The low field expansions are performed using the following useful relations (from equations 20.10 and 20.11 of the *Mathematical Handbook* [5]):

$$\sqrt{1+x} \simeq 1+\frac{1}{2}x-\frac{1}{8}x^2+\frac{1}{16}x^3-\frac{5}{128}x^4+O(x^5) \tag{E.101}$$

$$\frac{1}{\sqrt{1+x}} \simeq 1-\frac{1}{2}x+\frac{3}{8}x^2-\frac{5}{16}x^3+\frac{35}{128}x^4+O(x^5) \tag{E.102}$$

$$\begin{aligned}\sqrt{1+ax+bx^2} &\simeq 1+\frac{a}{2}x+\left(\frac{b}{2}-\frac{a^2}{8}\right)x^2+\left(\frac{a^3}{16}-\frac{ab}{4}\right)x^3 \\ &\quad+\left(\frac{3a^2b}{16}-\frac{b^2}{8}-\frac{5a^4}{128}\right)x^4+O(x^5)\end{aligned} \tag{E.103}$$

$$\begin{aligned}\frac{1}{\sqrt{1+ax+bx^2}} &\simeq 1-\frac{a}{2}x+\left(\frac{3a^2}{8}-\frac{b}{2}\right)x^2+\left(\frac{3ab}{4}-\frac{5a^3}{16}\right)x^3 \\ &\quad+\left(\frac{35a^4}{128}+\frac{3b^2}{8}-\frac{15a^2b}{16}\right)x^4+O(x^5)\end{aligned} \tag{E.104}$$

First we'll expand the eigenvalue to fourth order in y (field):

$$\lambda = \sqrt{1+4\alpha y+y^2} \tag{E.105}$$

$$\begin{aligned}&\simeq 1+2\alpha y+\left(\frac{1}{2}-2\alpha^2\right)y^2+\left(4\alpha^3-\alpha\right)y^3+\left(3\alpha^2-\frac{1}{8}-10\alpha^4\right)y^4+O(y^5) \\ &\simeq 1+2\alpha y+2\beta^2y^2-4\beta^2\alpha y^3+\left(3\alpha^2-\frac{1}{8}-10\alpha^4\right)y^4+O(y^5)\end{aligned} \tag{E.106}$$

Now let's consider the denominator of $a_{1,2} = \frac{n_{1,2}}{\sqrt{d}}$:

$$
\begin{aligned}
d &= \left(1 + 2\alpha y \mp \lambda\right)^2 + 4\beta^2 y^2 \\
&= 1 + 4\alpha^2 y^2 + \lambda^2 + 4\alpha y \mp 2\lambda \mp 4\alpha y\lambda + 4\beta^2 y^2 \\
&= 1 + 4\alpha^2 y^2 + 1 + 4\alpha y + y^2 + 4\alpha y \mp 2\lambda \mp 4\alpha y\lambda + 4\beta^2 y^2 \\
&= 2 + 8\alpha y + 2y^2 \mp 2\lambda \mp 4\alpha y\lambda \\
&= 2 + 8\alpha y + 2y^2 \mp 2\left(1 + 2\alpha y\right)\lambda \\
&\simeq 2 + 8\alpha y + 2y^2 \mp 2\left(1 + 2\alpha y\right)\left(1 + 2\alpha y + 2\beta^2 y^2 - 4\beta^2 \alpha y^3 + \left(3\alpha^2 - \frac{1}{8} - 10\alpha^4\right) y^4\right) \\
&\simeq 2 + 8\alpha y + 2y^2 \mp 2\left(2\alpha y + 4\alpha^2 y^2 + 4\alpha\beta^2 y^3 - 8\beta^2\alpha^2 y^4\right) \\
&\quad \mp 2\left(1 + 2\alpha y + 2\beta^2 y^2 - 4\beta^2 \alpha y^3 + \left(3\alpha^2 - \frac{1}{8} - 10\alpha^4\right) y^4\right) \\
&\simeq 2 + 8\alpha y + 2y^2 \mp 2\left(1 + 4\alpha y + \left(4\alpha^2 + 2\beta^2\right) y^2\right) \mp 2\left(3\alpha^2 - \frac{1}{8} - 10\alpha^4 - 8\beta^2\alpha^2\right) y^4 \\
&\simeq 2 + 8\alpha y + 2y^2 \mp \left(2 + 8\alpha y + \left(2 - 4\beta^2\right) y^2\right) \mp 2\left(3\alpha^2 - \frac{1}{8} - 10\alpha^4 - 8\beta^2\alpha^2\right) y^4 \\
d_+ &\simeq 2 + 8\alpha y + 2y^2 - 2 - 8\alpha y - \left(2 - 4\beta^2\right) y^2 - 2\left(3\alpha^2 - \frac{1}{8} - 10\alpha^4 - 8\beta^2\alpha^2\right) y^4 \\
&\simeq 4\beta^2 y^2 - 2\left(3\alpha^2 - \frac{1}{8} - 10\alpha^4 - 8\beta^2\alpha^2\right) y^4 \\
&\simeq 4\beta^2 y^2 - 2\left(3\alpha^2 - \frac{1}{8} - 10\left(\frac{1}{16} - \beta^4 - 2\alpha^2\beta^2\right) - 8\beta^2\alpha^2\right) y^4 \\
&\simeq 4\beta^2 y^2 - 2\left(3\alpha^2 - \frac{3}{4} + 10\beta^4 + 12\alpha^2\beta^2\right) y^4 \\
&\simeq 4\beta^2 y^2 - \left(-6\beta^2 + 20\beta^4 + 24\alpha^2\beta^2\right) y^4 \\
&\simeq 4\beta^2 y^2 \left(1 + \frac{6}{4} y^2 - 5\beta^2 y^2 - 6\alpha^2 y^2\right) \\
&\simeq 4\beta^2 y^2 \left(1 + 6\alpha^2 y^2 + 6\beta^2 y^2 - 5\beta^2 y^2 - 6\alpha^2 y^2\right) \\
&\simeq 4\beta^2 y^2 \left(1 + \beta^2 y^2\right) \\
d_- &\simeq 2 + 8\alpha y + 2y^2 + 2 + 8\alpha y + \left(2 - 4\beta^2\right) y^2 + 2\left(3\alpha^2 - \frac{1}{8} - 10\alpha^4 - 8\beta^2\alpha^2\right) y^4 \\
&\simeq 4 + 16\alpha y + 4\left(1 - \beta^2\right) y^2
\end{aligned}
$$

Note that a fourth order expansion of λ was needed for d_+, but not for d_-. Now let's expand the inverse square root $\frac{1}{\sqrt{d}}$:

$$d_+^{-\frac{1}{2}} \simeq \left(\sqrt{4\beta^2y^2\left(1+\beta^2y^2\right)}\right)^{-1} \simeq \frac{1}{2\beta y}\left(1-\frac{\beta^2}{2}y^2\right) \tag{E.107}$$

$$d_-^{-\frac{1}{2}} \simeq \left(4+16\alpha y+4\left(1-\beta^2\right)y^2\right)^{-\frac{1}{2}} \tag{E.108}$$

$$\simeq \frac{1}{2}\left(1+4\alpha y+\left(1-\beta^2\right)y^2\right)^{-\frac{1}{2}} \tag{E.109}$$

$$\simeq \frac{1}{2}\left(1-\left(\frac{4\alpha}{2}\right)y+\left(\frac{3\cdot 16\alpha^2}{8}-\frac{1-\beta^2}{2}\right)y^2\right) \tag{E.110}$$

$$\simeq \frac{1}{2}\left(1-2\alpha y+\left(6\alpha^2-\frac{1}{2}+\frac{\beta^2}{2}\right)y^2\right) \tag{E.111}$$

$$\simeq \frac{1}{2}\left(1-2\alpha y+\left(\frac{6}{4}-6\beta^2-\frac{1}{2}+\frac{\beta^2}{2}\right)y^2\right) \tag{E.112}$$

$$\simeq \frac{1}{2}\left(1-2\alpha y+\left(1-\frac{11}{2}\beta^2\right)y^2\right) \tag{E.113}$$

Note that all of the square roots take the positive root. Now let's consider the numerators:

$$n_1^{\pm} = 2\beta y \tag{E.114}$$

$$n_2^{\pm} = 1+2\alpha y\mp\lambda \tag{E.115}$$

$$\simeq 1+2\alpha y\mp\left(1+2\alpha y+2\beta^2y^2-4\beta^2\alpha y^3\right) \tag{E.116}$$

$$n_2^{+} \simeq 1+2\alpha y-1-2\alpha y-2\beta^2y^2+4\beta^2\alpha y^3 \tag{E.117}$$

$$\simeq -2\beta^2y^2+4\beta^2\alpha y^3 \tag{E.118}$$

$$n_2^{-} \simeq 1+2\alpha y+1+2\alpha y+2\beta^2y^2 \tag{E.119}$$

$$\simeq 2+4\alpha y+2\beta^2y^2 \tag{E.120}$$

Finally let's calculate the the mixing coefficients:

$$
\begin{aligned}
a_1^+ &= \frac{n_1^+}{\sqrt{d_+}} = \frac{2\beta y}{\sqrt{\left(1+2\alpha y-\lambda\right)^2+4\beta^2 y^2}} && \text{(E.121)}\\
&= \left(2\beta y\right)\frac{1}{2\beta y}\left(1-\frac{\beta^2}{2}y^2\right) && \text{(E.122)}\\
&\simeq 1-\frac{\beta^2}{2}y^2 && \text{(E.123)}\\
a_2^+ &= \frac{n_2^+}{\sqrt{d_+}} = \frac{1+2\alpha y-\lambda}{\sqrt{\left(1+2\alpha y-\lambda\right)^2+4\beta^2 y^2}} && \text{(E.124)}\\
&= \left(-2\beta^2 y^2+4\beta^2\alpha y^3\right)\frac{1}{2\beta y}\left(1-\frac{\beta^2}{2}y^2\right) && \text{(E.125)}\\
&\simeq -\left(\beta y-2\alpha\beta y^2\right)\left(1-\frac{\beta^2}{2}y^2\right) && \text{(E.126)}\\
&\simeq -\beta y+2\alpha\beta y^2 && \text{(E.127)}\\
a_1^- &= \frac{n_1^-}{\sqrt{d_-}} = \frac{2\beta y}{\sqrt{\left(1+2\alpha y+\lambda\right)^2+4\beta^2 y^2}} && \text{(E.128)}\\
&\simeq \left(2\beta y\right)\frac{1}{2}\left(1-2\alpha y+\left(1-\frac{11}{2}\beta^2\right)y^2\right) && \text{(E.129)}\\
&\simeq \beta y-2\alpha\beta y^2 && \text{(E.130)}\\
a_2^- &= \frac{n_2^-}{\sqrt{d_-}} = \frac{1+2\alpha y+\lambda}{\sqrt{\left(1+2\alpha y+\lambda\right)^2+4\beta^2 y^2}} && \text{(E.131)}\\
&\simeq \left(2+4\alpha y+2\beta^2 y^2\right)\frac{1}{2}\left(1-2\alpha y+\left(1-\frac{11}{2}\beta^2\right)y^2\right) && \text{(E.132)}\\
&\simeq \left(1+2\alpha y+\beta^2 y^2\right)\left(1-2\alpha y+\left(1-\frac{11}{2}\beta^2\right)y^2\right) && \text{(E.133)}\\
&\simeq 1-2\alpha y+\left(1-\frac{11}{2}\beta^2\right)y^2+2\alpha y-4\alpha^2 y^2+\beta^2 y^2 && \text{(E.134)}\\
&\simeq 1 \quad +\left(1-\frac{11}{2}\beta^2-4\alpha^2+\beta^2\right)y^2 && \text{(E.135)}\\
&\simeq 1+\left(1-\frac{11}{2}\beta^2+4\beta^2-1+\beta^2\right)y^2 && \text{(E.136)}\\
&\simeq 1-\frac{\beta^2}{2}y^2 && \text{(E.137)}
\end{aligned}
$$

As expected $a_1^{\pm} = \pm a_2^{\mp}$. For notational convenience, we'll drop the $\pm$ on the mixing coefficients. This gives, for the $\left\{\left|m_J^{\pm}\right\rangle\right\}$ states to second order in y (field):

$$\begin{aligned}
a_1 &= \frac{2\beta y}{\sqrt{(1+2\alpha y-\lambda)^2+4\beta^2 y^2}} = \frac{1+2\alpha y+\lambda}{\sqrt{(1+2\alpha y+\lambda)^2+4\beta^2 y^2}} \\
&\simeq 1-\frac{\beta^2}{2}y^2 \qquad \text{(E.138)} \\
a_2 &= \frac{1+2\alpha y-\lambda}{\sqrt{(1+2\alpha y-\lambda)^2+4\beta^2 y^2}} = \frac{-2\beta y}{\sqrt{(1+2\alpha y+\lambda)^2+4\beta^2 y^2}} \\
&\simeq -\beta y+2\alpha\beta y^2 \qquad \text{(E.139)} \\
\frac{\beta^2}{2} &= \frac{1}{8}\left(1-\frac{4m_J^2}{[L]^2}\right) \qquad \text{(E.140)} \\
2\alpha\beta &= \frac{m_J}{[L]}\sqrt{1-\frac{4m_J^2}{[L]^2}} \qquad \text{(E.141)} \\
|L_+, m_J\rangle &= a_1\left|L\pm\frac{1}{2}, m_J\right\rangle + a_2\left|L\mp\frac{1}{2}, m_J\right\rangle \qquad \text{(E.142)} \\
|L_-, m_J\rangle &= a_1\left|L\mp\frac{1}{2}, m_J\right\rangle - a_2\left|L\pm\frac{1}{2}, m_J\right\rangle \qquad \text{(E.143)}
\end{aligned}$$

where $\pm$ refers to the value of $J = L \pm \frac{1}{2}$ for the zero field eigenstate that $\left|m_J^{\pm}\right\rangle$ approaches as the field approaches zero.

In the lowest three RS terms for alkali metals, only the $m_J = \pm\frac{1}{2}$ of the $P_{\frac{1}{2}}$ and

$P_{\frac{3}{2}}$ terms mix:

$$a_1 \simeq 1 - \frac{y^2}{9} \tag{E.144}$$

$$a_2^{\pm} \simeq -\frac{\sqrt{2}}{3} y \left(1 \mp \frac{y}{3}\right) \tag{E.145}$$

$$\left|P_-, -\frac{1}{2}\right\rangle = a_1 \left|P_{\frac{1}{2}}, -\frac{1}{2}\right\rangle - a_2^- \left|P_{\frac{3}{2}}, -\frac{1}{2}\right\rangle \tag{E.146}$$

$$\left|P_+, -\frac{1}{2}\right\rangle = a_1 \left|P_{\frac{3}{2}}, -\frac{1}{2}\right\rangle + a_2^- \left|P_{\frac{1}{2}}, -\frac{1}{2}\right\rangle \tag{E.147}$$

$$\left|P_-, +\frac{1}{2}\right\rangle = a_1 \left|P_{\frac{1}{2}}, +\frac{1}{2}\right\rangle - a_2^+ \left|P_{\frac{3}{2}}, +\frac{1}{2}\right\rangle \tag{E.148}$$

$$\left|P_+, +\frac{1}{2}\right\rangle = a_1 \left|P_{\frac{3}{2}}, +\frac{1}{2}\right\rangle + a_2^+ \left|P_{\frac{1}{2}}, +\frac{1}{2}\right\rangle \tag{E.149}$$

where $\pm$ now refers to $m_J = \pm\frac{1}{2}$.

E.2.5 Transition Frequencies: Optical Spectrum

Transitions that occur between RS terms are electric dipole transitions. As will be discussed in more detail in the next section, these transitions have to conserve angular momentum and must result in a change of parity. All the possible transitions will be listed in groups labeled by the polarization of the incident light. D1 transitions refer to ones between the $S_{\frac{1}{2}}$ states and the $P_{\frac{1}{2}}$ states; whereas, D2 transitions refer to ones between the $S_{\frac{1}{2}}$ states and the $P_{\frac{3}{2}}$ states. Most of the energy difference between these states is due to electrostatic interactions. It will be convenient to express these frequencies with respect to the zero field D1 and D2 transition

frequencies:

$$\omega^0_{\frac{1}{2}} = \frac{E^P_0 - E^S_0}{\hbar} - \left(\frac{2}{3}\right)\omega_{\rm so} = 2\pi\nu^0_{\frac{1}{2}} \tag{E.150}$$

$$\omega^0_{\frac{3}{2}} = \frac{E^P_0 - E^S_0}{\hbar} + \left(\frac{1}{3}\right)\omega_{\rm so} = 2\pi\nu^0_{\frac{3}{2}} \tag{E.151}$$

$$\omega_{\rm so} = \omega^0_{\frac{3}{2}} - \omega^0_{\frac{1}{2}} = \left(\frac{1}{3} - -\frac{2}{3}\right)\omega_{\rm so} = 2\pi\nu_{\rm so} \tag{E.152}$$

$$\omega_{\frac{1}{2}} = \omega^0_{\frac{1}{2}} + \delta\omega_{\frac{1}{2}} \tag{E.153}$$

$$\omega_{\frac{3}{2}} = \omega^0_{\frac{3}{2}} + \delta\omega_{\frac{3}{2}} \tag{E.154}$$

$$\delta\omega = \delta\omega_{\frac{3}{2}} - \delta\omega_{\frac{1}{2}} \tag{E.155}$$

where the $\delta\omega$ terms are "added by hand" to account for the shift in the lines due to the presence of a buffer gas such as ^{3}He & N_2. Note that in the following, bracketed $[\cdots]$ terms evaluate to 1 when the approximation $g_S = -2$ is made. For light left circularly polarized perpendicular to the B-field (which has -1 unit of angular momentum), the possible transitions are:

$$\left|S_{\frac{1}{2}}, -\frac{1}{2}\right\rangle \leftrightarrow \left|P_{\frac{3}{2}}, -\frac{3}{2}\right\rangle \implies \omega = \omega_{\frac{3}{2}} - \frac{y\omega_{\rm so}}{\left[-1 - g_S\right]} \tag{E.156}$$

$$\left|S_{\frac{1}{2}}, +\frac{1}{2}\right\rangle \leftrightarrow a_1\left|P_{\frac{1}{2}}, -\frac{1}{2}\right\rangle - a_2^-\left|P_{\frac{3}{2}}, -\frac{1}{2}\right\rangle \implies \omega = \omega_{\frac{1}{2}} - \frac{4y}{3}\left(\left[\frac{\frac{1}{2} - \frac{g_S}{4}}{-1 - g_S}\right] + \frac{y}{6}\right)\omega_{\rm so} \tag{E.157}$$

$$\left|S_{\frac{1}{2}}, +\frac{1}{2}\right\rangle \leftrightarrow a_1\left|P_{\frac{3}{2}}, -\frac{1}{2}\right\rangle + a_2^-\left|P_{\frac{1}{2}}, -\frac{1}{2}\right\rangle \implies \omega = \omega_{\frac{3}{2}} - \frac{5y}{3}\left(\left[\frac{\frac{1}{5} - \frac{2g_S}{5}}{-1 - g_S}\right] - \frac{2y}{15}\right)\omega_{\rm so} \tag{E.158}$$

For light linearly polarized parallel to the B-field (which has 0 units of angular momentum), the transition frequencies are:

$$\left|S_{\frac{1}{2}},-\frac{1}{2}\right\rangle \leftrightarrow a_1\left|P_{\frac{1}{2}},-\frac{1}{2}\right\rangle - a_2^-\left|P_{\frac{3}{2}},-\frac{1}{2}\right\rangle \implies \omega=\omega_{\frac{1}{2}}+\frac{2y}{3}\left(1-\frac{y}{3}\right)\omega_{\text{so}} \tag{E.159}$$

$$\left|S_{\frac{1}{2}},-\frac{1}{2}\right\rangle \leftrightarrow a_1\left|P_{\frac{3}{2}},-\frac{1}{2}\right\rangle + a_2^-\left|P_{\frac{1}{2}},-\frac{1}{2}\right\rangle \implies \omega=\omega_{\frac{3}{2}}+\frac{y}{3}\left(1+\frac{2y}{3}\right)\omega_{\text{so}} \tag{E.160}$$

$$\left|S_{\frac{1}{2}},+\frac{1}{2}\right\rangle \leftrightarrow a_1\left|P_{\frac{1}{2}},+\frac{1}{2}\right\rangle - a_2^+\left|P_{\frac{3}{2}},+\frac{1}{2}\right\rangle \implies \omega=\omega_{\frac{1}{2}}-\frac{2y}{3}\left(1+\frac{y}{3}\right)\omega_{\text{so}} \tag{E.161}$$

$$\left|S_{\frac{1}{2}},+\frac{1}{2}\right\rangle \leftrightarrow a_1\left|P_{\frac{3}{2}},+\frac{1}{2}\right\rangle + a_2^+\left|P_{\frac{1}{2}},+\frac{1}{2}\right\rangle \implies \omega=\omega_{\frac{3}{2}}-\frac{y}{3}\left(1-\frac{2y}{3}\right)\omega_{\text{so}} \tag{E.162}$$

For light right circularly polarized perpendicular to the B-field (which has $+1$ unit of angular momentum), the transition frequencies are:

$$\left|S_{\frac{1}{2}},-\frac{1}{2}\right\rangle \leftrightarrow a_1\left|P_{\frac{1}{2}},+\frac{1}{2}\right\rangle - a_2^+\left|P_{\frac{3}{2}},+\frac{1}{2}\right\rangle \implies \omega=\omega_{\frac{1}{2}}+\frac{4y}{3}\left(\left[\frac{\frac{1}{2}-\frac{g_S}{4}}{-1-g_S}\right]-\frac{y}{6}\right)\omega_{\text{so}} \tag{E.163}$$

$$\left|S_{\frac{1}{2}},-\frac{1}{2}\right\rangle \leftrightarrow a_1\left|P_{\frac{3}{2}},+\frac{1}{2}\right\rangle + a_2^+\left|P_{\frac{1}{2}},+\frac{1}{2}\right\rangle \implies \omega=\omega_{\frac{3}{2}}+\frac{5y}{3}\left(\left[\frac{\frac{1}{5}-\frac{2g_S}{5}}{-1-g_S}\right]+\frac{2y}{15}\right)\omega_{\text{so}} \tag{E.164}$$

$$\left|S_{\frac{1}{2}},+\frac{1}{2}\right\rangle \leftrightarrow \left|P_{\frac{3}{2}},+\frac{3}{2}\right\rangle \implies \omega=\omega_{\frac{3}{2}}+\frac{y\omega_{\text{so}}}{\left[-1-g_S\right]} \tag{E.165}$$

E.3 The Hyperfine Structure of Alkali Atoms

E.3.1 Zero Field Eigenbasis

Adding nuclear spin $\vec{I}$ to the system introduces the hyperfine interaction:

$$\mathcal{H}_{hfs} = A_{hfs}\vec{I}\cdot\vec{J} \tag{E.166}$$

A_{hfs} hides all the factors that don't depend on the spins. IJ-coupling causes states with different m_J to mix. Since $m_F\left(=m_I+m_J\right)$ is conserved, the $\{|F,m_F\rangle\}$ states form a natural eigenbasis. This is more easily seen with a little arithmetic:

$$\vec{F}^2 = (\vec{I}+\vec{J})^2 = \vec{I}^2 + 2\vec{I}\cdot\vec{J} + \vec{J}^2 \tag{E.167}$$

$$\mathcal{H}_{hfs} = \frac{A_{hfs}}{2}(\vec{F}^2 - \vec{I}^2 - \vec{J}^2) \tag{E.168}$$

The hyperfine interaction splits the ${}^2S_{\frac{1}{2}}$, ${}^2P_{\frac{1}{2}}$, and ${}^2P_{\frac{3}{2}}$ terms into 2, 2, and 4 manifolds which are labeled by F. This is called the *hyperfine structure*. Note that many calculations to follow will be identical to those done for the fine structure mixing. Table (E.1) depicts the analogy.

E.3.2 Hamiltonian

The Hamiltonian describing the atom in a magnetic field $\vec{B}$ is

$$\mathcal{H} = \mathcal{H}_0 + \mathcal{H}_{hfs} - \vec{\mu}_I\cdot\vec{B} - \vec{\mu}_J\cdot\vec{B} \tag{E.169}$$

To recap:

Spin-Orbit	**Hyperfine**
$\vec{L}$	$\vec{I}$
$\vec{S}$	$\vec{J}$
$\vec{J}$	$\vec{F}$
mixes states with different J	mixes states with different F
mixes states with same m_J	mixes states with same m_F
A_{so}	A_{hfs}
$\nu_{\text{so}} \approx 10^7$ MHz	$\nu_{hfs} \approx 10^3$ MHz
y	x
$y \approx 1 \rightarrow B \approx 10^7$ gauss	$x \approx 1 \rightarrow B \approx 10^3$ gauss

Table E.1: Analogy between spin-orbit and hyperfine coupling.

- The first term H_0 contains all the terms that do not involve the nuclear spin.
- The second term is the hyperfine interaction.
- The third and fourth terms are the Zeeman terms for the nuclear spin and the total electronic angular momentum respectively.

Using $\vec{B} = B\hat{z}$ & $F_z = I_z + J_z$ and some rearrangement results in,

$$\mathcal{H} = \mathcal{H}_0 + \left(-\frac{A_{hfs}}{2}\left(\vec{I}^2 + \vec{J}^2\right) - g_I \mu_N B F_z\right) + \left(\frac{A_{hfs}}{2}\vec{F}^2 + \left(g_I \mu_N - g_J \mu_B\right) B J_z\right) \tag{E.170}$$

The Hamiltonian is separated into three terms intentionally. States within a $n^{2S+1}L_J$ term with the same m_F but on different manifolds F are mixed by the Zeeman interaction. This means that the first two terms are diagonal simultaneously in the $\{|F, m_F\rangle\}$ basis and the eigenbasis of $\mathcal{H}$. Therefore, the last term has to be diagonalized. (make some comment about how fine structure mixing effects this stuff)

E.3.3 Energies: Derivation of the Breit-Rabi Equation

Diagonalization

The Breit-Rabi equation, first derived in 1931 [6,7], gives the energies of the ground state hyperfine levels of atoms and ions with a single valence electron in the presence of a magnetic field. Let's specialize to this case $L = 0, S = \frac{1}{2}, J = \frac{1}{2}$. F can be $I \pm \frac{1}{2}$. Therefore in the $\{|F, m_F\rangle\}$ basis, the J_z term is block diagonal with subblocks no greater than 2 by 2 in size. The 2 by 2 subblocks are made of the states with different F and same m_F. For the special case of $m_F = \pm F_{max} = \pm\left(I + \frac{1}{2}\right)$, there are no other states to mix with. Thus, they reside in subblocks of size 1 by 1. To diagonalize $\mathcal{H}$, we only have to diagonalize each subblock of $\mathcal{H}'$,

$$\mathcal{H}' = \frac{A_{hfs}}{2}\vec{F}^2 + \left(g_I\mu_N - g_S\mu_B\right)BJ_z \tag{E.171}$$

$$\hat{\mathcal{H}}' = \frac{A_{hfs}}{2}\begin{bmatrix} \left(I+\frac{1}{2}\right)\left(I+\frac{3}{2}\right) & 0 \\ 0 & \left(I-\frac{1}{2}\right)\left(I+\frac{1}{2}\right) \end{bmatrix} + \left(g_I\mu_N - g_S\mu_S\right)B\begin{bmatrix} \alpha_+ & \beta_- \\ \beta_+ & \alpha_- \end{bmatrix} \tag{E.172}$$

$$\alpha_\pm = \left\langle I \pm \frac{1}{2}, m_F \middle| \hat{J}_z \middle| I \pm \frac{1}{2}, m_F \right\rangle \tag{E.173}$$

$$\beta_\pm = \left\langle I \mp \frac{1}{2}, m_F \middle| \hat{J}_z \middle| I \pm \frac{1}{2}, m_F \right\rangle \tag{E.174}$$

The first term can be simplified to give:

$$\frac{A_{hfs}}{2}\hat{\vec{F}}^2 = \frac{A_{hfs}}{2}\left(I+\frac{1}{2}\right)\left(I+\frac{1}{2}+\begin{bmatrix} 1 & 0 \\ 0 & -1 \end{bmatrix}\right) \tag{E.175}$$

$\alpha_\pm$ & $\beta_\pm$ in the second term are most easily calculated in the $\{|I,m_I\rangle\,|J,m_J\rangle\}$ basis:

$$|I,m_I\rangle\,|J,m_J\rangle = |m_I,m_J\rangle \tag{E.176}$$

$$|F,m_F\rangle = \sum |m_I,m_J\rangle \underbrace{\langle m_I,m_J|F,m_F\rangle}_{\text{Clebsch}-\text{Gordon}} \tag{E.177}$$

Using the formulas for Clebsch-Gordon coefficients (E.31):

$$\begin{aligned}\left\langle m_F \mp \frac{1}{2}, \pm\frac{1}{2}|I+\frac{1}{2},m_F\right\rangle &= \frac{1}{\sqrt{[I]}}\sqrt{I+\frac{1}{2}\pm m_F} \\ \left\langle m_F \mp \frac{1}{2}, \pm\frac{1}{2}|I-\frac{1}{2},m_F\right\rangle &= \frac{\mp 1}{\sqrt{[I]}}\sqrt{I+\frac{1}{2}\mp m_F}\end{aligned} \tag{E.178}$$

which gives:

$$\alpha_\pm = \pm(\alpha) = \pm\left(\frac{m_F}{[I]}\right) \tag{E.179}$$

$$\beta_\pm = -(\beta) = -\left(\frac{\sqrt{\left(I+\frac{1}{2}\right)^2 - m_F^2}}{[I]}\right) \tag{E.180}$$

To solve for the energies, we only need to diagonalize the last term in $\mathcal{H}'$:

$$\mathcal{H}' = \frac{A_{hfs}}{2}\left(I+\frac{1}{2}\right)^2 + \frac{A_{hfs}}{2}\left(I+\frac{1}{2}\right)\begin{bmatrix} 1+2\alpha x & -2\beta x \\ -2\beta x & -(1+2\alpha x)\end{bmatrix} \tag{E.181}$$

$$x = \left(g_I\mu_N - g_S\mu_B\right)\frac{2B}{A[I]} \tag{E.182}$$

This is easily done and, just like fine structure mixing, gives the eigenvalues:

$$\pm\left(\lambda = \sqrt{1+4\alpha x + x^2}\right) \tag{E.183}$$

The total energy is therefore:

$$E = E_0 - \frac{A_{hfs}}{2}\left(I(I+1) + \frac{1}{2}\left(\frac{1}{2}+1\right)\right) - g_I \mu_N m_F B + E' \tag{E.184}$$

$$E' = \frac{A_{hfs}}{2}\left(I+\frac{1}{2}\right)^2 \pm \frac{A_{hfs}}{2}\left(I+\frac{1}{2}\right)\lambda \tag{E.185}$$

In this case, E_0 is the energy of the (possibly mixed) spin-orbit coupled states. The $\pm\lambda$ eigenvalue is used for states evolving from the $F = I \pm \frac{1}{2}$ manifold. In the zero field case, $B = 0$, we find the hyperfine splitting between the two manifolds is:

$$\Delta E = \frac{A_{hfs}[I]}{2} = h\nu_{hfs} \tag{E.186}$$

Dropping E_0 and relating A_{hfs} to the zero field hyperfine splitting $h\nu_{hfs}$, we get the celebrated Breit-Rabi equation:

$$E = -\frac{h\nu_{hfs}}{2[I]} - g_I \mu_N B m_F \pm \frac{h\nu_{hfs}}{2}\sqrt{1 + \frac{4m_F}{[I]}x + x^2} \tag{E.187}$$

$$x = \left(g_I \mu_N - g_S \mu_B\right)\frac{B}{h\nu_{hfs}} \tag{E.188}$$

where $\pm$ refers to states in the $F = I \pm \frac{1}{2}$ manifold. Note that x is a unitless quantity that gives a relative measure of the size of the Zeeman interaction with respect to the hyperfine interaction. For example, the Zeeman interaction is comparable to the hyperfine interaction ($x \approx 1$) for potassium-39 and rubidium-85 when $B \approx$ 165 gauss & 1080 gauss respectively.

We'll discuss two special cases now. The energies of the $m_F = \pm(I + \frac{1}{2})$ states

(aka "edge" states) in the $F = I + \frac{1}{2}$ manifold (aka "upper" manifold) are:

$$E_{\pm(I+\frac{1}{2})} = \frac{I}{[I]} h\nu_{hfs} \pm \left(\begin{bmatrix} g_S \\ -2 \end{bmatrix} \mu_B - g_I \mu_N I \right) B \tag{E.189}$$

where $\pm$ now refers to m_F. A low field ($B < 165$ gauss & 1080 gauss for potassium-39 and rubidium-85 respectively) expansion of the energies for the the $F = I \pm \frac{1}{2}$ manifolds can be performed using:

$$\begin{aligned} \sqrt{1+2ax+x^2} &= 1 + \frac{1}{2}x(2a+x) - \frac{1}{2\cdot 4}x^2(2a+x)^2 + \frac{1\cdot 3}{2\cdot 4\cdot 6}x^3(2a+x)^3 \\ &\quad - \frac{1\cdot 3\cdot 5}{2\cdot 4\cdot 6\cdot 8}x^4(2a+x)^4 \\ &\quad + \frac{1\cdot 3\cdot 5\cdot 7}{2\cdot 4\cdot 6\cdot 8\cdot 10}x^5(2a+x)^5 \\ &\quad - \frac{1\cdot 3\cdot 5\cdot 7\cdot 9}{2\cdot 4\cdot 6\cdot 8\cdot 10\cdot 12}x^6(2a+x)^6 + \cdots \end{aligned} \tag{E.190}$$

Expanding each factor of $(2a+x)^n$ and reducing the coefficients in front of each term:

$$\begin{aligned} \sqrt{1+2ax+x^2} &= 1 + \frac{1}{2}x(2a+x) - \frac{1}{8}x^2\left(4a^2+x^2+4ax\right) \\ &\quad + \frac{1}{16}x^3\left(8a^3+12a^2x+6ax^2+x^3\right) \\ &\quad - \frac{5}{128}x^4\left(16a^4+32a^3x+24a^2x^2+8ax^3+x^4\right) \\ &\quad + \frac{7}{256}x^5\left(32a^5+80a^4x+80a^3x^2+40a^2x^3+10ax^4+x^5\right) \\ &\quad - \frac{21}{1024}x^6\left(64a^6+192a^5x+240a^4x^2+160a^3x^3+60a^2x^4+12ax^5+x^6\right) \end{aligned} \tag{E.191}$$

Keeping only the terms up to sixth order in the dimensionless field parameter x:

$$\begin{aligned}\sqrt{1+2ax+x^2} &= 1+\frac{1}{2}x\left(2a+x\right)-\frac{1}{8}x^2\left(4a^2+x^2+4ax\right)\\ &\quad+\frac{1}{16}x^3\left(8a^3+12a^2x+6ax^2+x^3\right)\\ &\quad-\frac{5}{16}x^4\left(2a^4+4a^3x+3a^2x^2\right)+\frac{7}{16}x^5\left(2a^5+5a^4x\right)\\ &\quad-\frac{21}{16}x^6a^6+O(x^7)\end{aligned} \tag{E.192}$$

Collecting all the terms order by order:

$$\begin{aligned}\sqrt{1+2ax+x^2} &= 1+(a)\,x+\left(\frac{1}{2}-\frac{a^2}{2}\right)x^2+\left(-\frac{a}{2}+\frac{a^3}{2}\right)x^3\\ &\quad+\left(-\frac{1}{8}+\frac{3a^2}{4}-\frac{5a^4}{8}\right)x^4+\left(\frac{3a}{8}-\frac{5a^3}{4}+\frac{7a^5}{8}\right)x^5\\ &\quad+\left(\frac{1}{16}-\frac{15a^2}{16}+\frac{35a^4}{16}-\frac{21a^6}{16}\right)x^6+O(x^7)\end{aligned} \tag{E.193}$$

Pulling out common factors:

$$\begin{aligned}\sqrt{1+2ax+x^2} &= 1+ax+\frac{1}{2}\left(1-a^2\right)x^2-\frac{a}{2}\left(1-a^2\right)x^3-\frac{1}{8}\left(1-6a^2+5a^4\right)x^4\\ &\quad+\frac{3a}{8}\left(1-\frac{10a^2}{3}+\frac{7a^4}{3}\right)x^5\\ &\quad+\frac{1}{16}\left(1-15a^2+35a^4-21a^6\right)x^6+O(x^7)\end{aligned} \tag{E.194}$$

Note that when $a=\pm1$, the stuff under the square root is a perfect square:

$$\sqrt{1+2ax+x^2}=\sqrt{1\pm2x+x^2}=\sqrt{(1\pm x)^2}=1\pm x \tag{E.195}$$

In this case ($a=\pm1$), all terms second order or higher in x have to disappear order

by order. Using this insight, a factor $(1-a^2)$ is pulled out of each higher order term:

$$\begin{aligned}\sqrt{1+2ax+x^2} &= 1+ax+\frac{1}{2}\left(1-a^2\right)x^2-\frac{a}{2}\left(1-a^2\right)x^3-\frac{1}{8}\left(1-5a^2\right)\left(1-a^2\right)x^4 \\ &\quad +\frac{3a}{8}\left(1-\frac{7a^2}{3}\right)\left(1-a^2\right)x^5 \\ &\quad +\frac{1}{16}\left(1-14a^2+21a^4\right)\left(1-a^2\right)x^6+O(x^7) \end{aligned} \tag{E.196}$$

Making the substitution $a = 2m_F/[I]$, dividing both sides of the Breit-Rabi equation (E.187) by $h\nu_{hfs}$, and using the sixth order expansion that was just calculated gives:

$$\pm\frac{E_\pm}{h\nu_{hfs}} = a_0+a_1x+\left[1-\left(\frac{2m_F}{[I]}\right)^2\right]\left[\sum_{n=2}^{6}a_nx^n\right] \tag{E.197}$$

$$x = \left(g_I\mu_N-g_S\mu_B\right)\frac{B}{h\nu_{hfs}} \tag{E.198}$$

$$[I] = 2I+1 \tag{E.199}$$

$$a_0 = \left(\frac{I+\frac{1}{2}\mp\frac{1}{2}}{[I]}\right) \tag{E.200}$$

$$a_1 = \frac{m_F}{[I]}\left(\frac{1\pm\frac{g_I\mu_N}{g_S\mu_B}\left([I]\mp1\right)}{1-\frac{g_I\mu_N}{g_S\mu_B}}\right)\approx\frac{m_F}{[I]}+O(10^{-3}) \tag{E.201}$$

$$a_2 = +\frac{1}{4} \tag{E.202}$$

$$a_3 = -\frac{m_F}{2[I]} \tag{E.203}$$

$$a_4 = -\frac{1}{16}\left[1-5\left(\frac{2m_F}{[I]}\right)^2\right] \tag{E.204}$$

$$a_5 = +\frac{3m_F}{8[I]}\left[1-\frac{7}{3}\left(\frac{2m_F}{[I]}\right)^2\right] \tag{E.205}$$

$$a_6 = +\frac{1}{32}\left[1-14\left(\frac{2m_F}{[I]}\right)^2+21\left(\frac{2m_F}{[I]}\right)^4\right] \tag{E.206}$$

where $\pm$ refers to the $F = I \pm \frac{1}{2}$ manifold. Note that eqn. (E.189) shows that the energy for the edge states in the upper manifold $\left(F = I + \frac{1}{2} \;\&\; |m_F| = I + \frac{1}{2}\right)$ is linear in field. Therefore, for the edge states, $\left(2m_F/[I]\right)^2 = 1$ and all terms of order two or higher in field in eqn. (E.197) must disappear order by order. Consequently eqn. (E.197) is written such that the disappearance of higher order terms is evident. Finally, we'll note that the order of the states from highest energy to lowest energy are $F = I + 1/2, m_F = I + 1/2$ down to $-(I + 1/2)$ and then $F = I - 1/2, m_F = -(I + 1/2)$ up to $+(I + 1/2)$.

E.3.4 Eigenstates: Hyperfine Mixing

At low field, it is useful to label states by F and m_F because F is almost a good quantum number. Therefore, at low field, we'll refer to two groups of states as "manifolds" which are labeled by F. Within each manifold, states are distinguished by their m_F. At high field, the nuclear spin and total electronic angular momentum decouple. This is because the Zeeman interaction becomes much larger than the hyperfine interaction. Because the electron magnetic moment is much larger than the nuclear magnetic moment, it is useful to groups states by their m_J, which at high field is almost a good quantum number. These groupings are called Zeeman multiplets. Each state within a multiplet is distinguished by it's m_I, which at high field is also almost a good quantum number. Note that regardless of the magnitude of the field, m_F is always a good quantum number. For most of this document, we'll be working in the low field limit where the most appropriate quantum numbers are F and m_F. Figure (E.1) depicts a qualitative energy level diagram for the most abundant isotope of Rubidium.

(The following is analogous to fine structure mixing with $y \to x$) Since we are

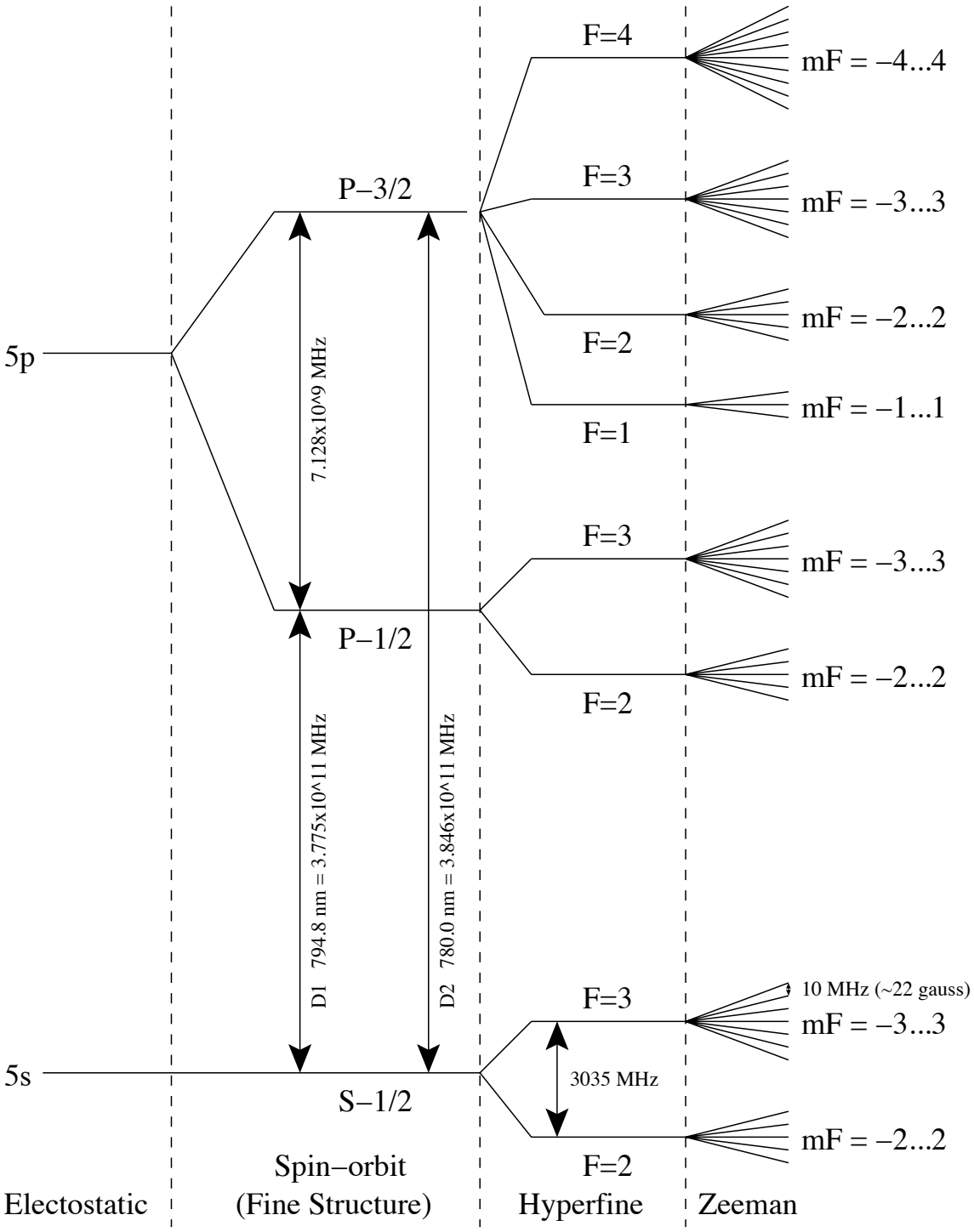

Figure E.1: Qualitative Energy Level Diagram for Rubidium-85 $\left(I = 5/2\right)$ in a Weak Field

considering the ground state term of an alkali metal atom, there is no fine structure mixing. However the field B does result in hyperfine structure mixing (states with the same m_F but different F):

$$|m_F^{\pm}\rangle = a_1^{\pm}\left|I+\frac{1}{2},m_F\right\rangle + a_2^{\pm}\left|I-\frac{1}{2},m_F\right\rangle \tag{E.207}$$

$$|F,m_F\rangle = \sum_{m_J=-\frac{1}{2}}^{+\frac{1}{2}} |m_F-m_J,m_J\rangle\langle m_F-m_J,m_J \mid F,m_F\rangle \tag{E.208}$$

$$b_1^{\pm}(m_F) = \left\langle m_F-\frac{1}{2},+\frac{1}{2}|I\pm\frac{1}{2},m_F\right\rangle \tag{E.209}$$

$$b_2^{\pm}(m_F) = \left\langle m_F+\frac{1}{2},-\frac{1}{2}|I\pm\frac{1}{2},m_F\right\rangle \tag{E.210}$$

$$\left|I\pm\frac{1}{2},m_F\right\rangle = b_1^{\pm}\left|m_F-\frac{1}{2},+\frac{1}{2}\right\rangle + b_2^{\pm}\left|m_F+\frac{1}{2},-\frac{1}{2}\right\rangle \tag{E.211}$$

The values for $a_{1,2}^{\pm}$ come from the diagonalization of eqn. (E.181) where $\lambda_{\pm}$ are the eigenvalues given by eqn. (E.183, α and β are defined by eqns. (E.179) and (E.180), and $b_{1,2}^{\pm}$ are from eqns. (C.9) and (C.10):

$$a_1^{\pm} = \frac{2\beta x}{\sqrt{(1+2\alpha x\mp\lambda)^2+4\beta^2x^2}} \tag{E.212}$$

$$a_2^{\pm} = \frac{1+2\alpha x\mp\lambda}{\sqrt{(1+2\alpha x\mp\lambda)^2+4\beta^2x^2}} \tag{E.213}$$

$$a_1^{\pm} = \pm a_2^{\mp} \tag{E.214}$$

$$b_1^{\pm} = \pm\sqrt{\frac{I\pm m_F+\frac{1}{2}}{[I]}} \tag{E.215}$$

$$b_2^{\pm} = +\sqrt{\frac{I\mp m_F+\frac{1}{2}}{[I]}} \tag{E.216}$$

The $\pm$ sign is taken for transitions within the $F=I\pm\frac{1}{2}$ manifold. For simplicity

(due to orthogonality):

$$a_1 \equiv a_1^+ = a_2^- \tag{E.217}$$

$$a_2 \equiv a_2^+ = -a_1^- \tag{E.218}$$

$$b_1 \equiv b_1^+ = b_2^- \tag{E.219}$$

$$b_2 \equiv b_2^+ = -b_1^- \tag{E.220}$$

$$\left| I \pm \frac{1}{2}, m_F \right\rangle = b_1 \left| m_F \mp \frac{1}{2}, \pm\frac{1}{2} \right\rangle \pm b_2 \left| m_F \pm \frac{1}{2}, \mp\frac{1}{2} \right\rangle \tag{E.221}$$

$$|m_F^\pm\rangle = a_1 \left| I \pm \frac{1}{2}, m_F \right\rangle \pm a_2 \left| I \mp \frac{1}{2}, m_F \right\rangle \tag{E.222}$$

Eqn. (E.222) represents the decomposition of the eigenstates $\{|m_F^\pm\rangle\}$ in the zero field hyperfine coupled basis $\{|F, m_F\rangle\}$, whereas eqn. (E.223) represents the decomposition in the zero field uncoupled IJ basis $\{|m_I, m_J\rangle\}$:

$$\begin{aligned} |m_F^\pm\rangle &= a_1 \left| I \pm \frac{1}{2}, m_F \right\rangle \pm a_2 \left| I \mp \frac{1}{2}, m_F \right\rangle \\ &= a_1 \left(b_1 \left| m_F \mp \frac{1}{2}, \pm\frac{1}{2} \right\rangle \pm b_2 \left| m_F \pm \frac{1}{2}, \mp\frac{1}{2} \right\rangle \right) \\ &\quad \pm a_2 \left(b_1 \left| m_F \pm \frac{1}{2}, \mp\frac{1}{2} \right\rangle \mp b_2 \left| m_F \mp \frac{1}{2}, \pm\frac{1}{2} \right\rangle \right) \\ &= (a_1 b_1 - a_2 b_2) \left| m_F \mp \frac{1}{2}, \pm\frac{1}{2} \right\rangle \pm (a_1 b_2 + a_2 b_1) \left| m_F \pm \frac{1}{2}, \mp\frac{1}{2} \right\rangle \end{aligned} \tag{E.223}$$

E.3.5 Transition Frequencies: EPR Spectrum

Introduction

EPR stands for *E*lectron *P*aramagnetic *R*esonance. At low field, it refers to the transitions between adjacent states within a particular manifold. Transitions between $m_F \leftrightarrow m_F - 1$ will be labeled by the higher state m_F. For example, refer to

Isotope	$F = I - \frac{1}{2}$	**transition**			$F = I + \frac{1}{2}$	**transition**			m_F
^{39}K					2	$+2$	$\leftrightarrow$	$+1$	$+2$
	1	$+1$	$\leftrightarrow$	0	2	$+1$	$\leftrightarrow$	0	$+1$
	1	0	$\leftrightarrow$	-1	2	0	$\leftrightarrow$	-1	0
					2	-1	$\leftrightarrow$	-2	-1
^{85}Rb					3	$+3$	$\leftrightarrow$	$+2$	$+3$
	2	$+2$	$\leftrightarrow$	$+1$	3	$+2$	$\leftrightarrow$	$+1$	$+2$
	2	$+1$	$\leftrightarrow$	0	3	$+1$	$\leftrightarrow$	0	$+1$
	2	0	$\leftrightarrow$	-1	3	0	$\leftrightarrow$	-1	0
	2	-1	$\leftrightarrow$	-2	3	-1	$\leftrightarrow$	-2	-1
					3	-2	$\leftrightarrow$	-3	-2

Table E.2: Transitions are labeled by the higher m_F state.

table (E.2) for the applicable transitions within the ground state for potassium-39 and rubidium-85. Recall that:

$$g_S = -2\left[1 + O(10^{-3})\right] \tag{E.224}$$

$$x = \left(g_I \mu_N - g_S \mu_B\right) \frac{B}{h\nu_{hfs}} \tag{E.225}$$

The frequency corresponding to these transitions within the $F = I \pm \frac{1}{2}$ manifold are:

$$\nu_+ = -\frac{g_I \mu_N B}{h} + \frac{\nu_{hfs}}{2}\left(\sqrt{1 + \frac{4m_F}{[I]}x + x^2} - \sqrt{1 + \frac{4(m_F - 1)}{[I]}x + x^2}\right) \tag{E.226}$$

$$-\nu_- = -\frac{g_I \mu_N B}{h} - \frac{\nu_{hfs}}{2}\left(\sqrt{1 + \frac{4m_F}{[I]}x + x^2} - \sqrt{1 + \frac{4(m_F - 1)}{[I]}x + x^2}\right) \tag{E.227}$$

$$\nu_- = +\frac{g_I \mu_N B}{h} + \frac{\nu_{hfs}}{2}\left(\sqrt{1 + \frac{4m_F}{[I]}x + x^2} - \sqrt{1 + \frac{4(m_F - 1)}{[I]}x + x^2}\right) \tag{E.228}$$

$$\nu_\pm = \mp\frac{g_I \mu_N B}{h} + \frac{\nu_{hfs}}{2}\left(\sqrt{1 + \frac{4m_F}{[I]}x + x^2} - \sqrt{1 + \frac{4(m_F - 1)}{[I]}x + x^2}\right) \tag{E.229}$$

where the overall sign was chosen to give a positive frequency for $\nu_{\pm}$.

End Transition Frequencies

Transitions involving the edge states are called "end" transitions. The frequencies for these transitions can be written in a simpler form by taking advantage of this formula:

$$m_F = \pm\left(I+\frac{1}{2}\right) \rightarrow 4m_F = \pm 2[I] \rightarrow \sqrt{1+\frac{4m_F}{[I]}x+x^2} = 1 \pm x \tag{E.230}$$

The frequency of the $m_F = I + 1/2 \leftrightarrow I - 1/2$ end transition is:

$$\nu_{+I+1/2} = -\frac{g_I \mu_N B}{h} + \frac{\nu_{hfs}}{2}\left(1+x-\sqrt{1+\frac{4\left(I-1/2\right)}{[I]}x+x^2}\right) \tag{E.231}$$

while the frequency of the $m_F = -(I+1/2)+1 \leftrightarrow -(I+1/2)$ end transition is:

$$\nu_{-I-1/2} = -\frac{g_I \mu_N B}{h} + \frac{\nu_{hfs}}{2}\left(\sqrt{1-\frac{4\left(I-1/2\right)}{[I]}x+x^2}-1+x\right) \tag{E.232}$$

We can collapse both of equations into one equation to give:

$$\nu_{\pm} = \frac{\nu_{hfs}}{2}\left[x\left(\frac{1+\frac{g_I\mu_N}{g_S\mu_B}}{1-\frac{g_I\mu_N}{g_S\mu_B}}\right) \pm 1 \mp \sqrt{1 \pm 2\left(\frac{2I-1}{2I+1}\right)x+x^2}\right] \tag{E.233}$$

where the $\pm$ now refers to edge state $m_F = \pm\left(I+\frac{1}{2}\right)$ involved in the end transition.

End Transition Frequency Inversion Formula

Because the equation for the frequency of an end transition involves only one square root term, the equation can be inverted to give the field as a function of frequency. Expressing eqn. (E.233) in terms of x and isolating the square root term:

$$\nu_{\pm} = \frac{\nu_{hfs}}{2}\left[\underbrace{x\left(\frac{1+\frac{g_I\mu_N}{g_S\mu_B}}{1-\frac{g_I\mu_N}{g_S\mu_B}}\right)}_{a} \pm 1 \mp \sqrt{1 \pm 2\underbrace{\left(\frac{2I-1}{2I+1}\right)}_{b}x + x^2}\right] \quad \text{(E.234)}$$

$$\nu = \frac{\nu_{hfs}}{2}\left(ax + s - s\sqrt{1+2sbx+x^2}\right) \quad \text{(E.235)}$$

$$s = \pm 1 \rightarrow s^2 = 1 \quad \text{(E.236)}$$

$$n = 2\frac{\nu}{\nu_{hfs}} = ax + s - s\sqrt{1+2sbx+x^2} \quad \text{(E.237)}$$

$$n - ax - s = -s\sqrt{1+2sbx+x^2} \quad \text{(E.238)}$$

Now both sides of the equation can be squared, leaving an equation that is second order in x:

$$\begin{aligned}
(n-ax-s)^2 &= \left(-s\sqrt{1+2sbx+x^2}\right)^2 \\
n^2 + a^2x^2 + 1 - 2nax - 2sn + 2sax &= 1 + 2sbx + x^2 \\
0 &= 2sbx + x^2 - n^2 - a^2x^2 + 2nax + 2sn - 2sax \\
0 &= \left(1-a^2\right)x^2 + 2\left(sb - sa + na\right)x + 2sn - n^2 \\
0 &= \left(1-a^2\right)x^2 - 2s\left(a - b - san\right)x + sn(2 - sn)
\end{aligned}$$

This is solved by using the quadratic formula from section 5.5 of *Numerical Recipes* [8]:

$$\mathcal{A}x^2 + \mathcal{B}x + \mathcal{C} = 0 \tag{E.239}$$

$$q \equiv -\frac{1}{2}\left[\mathcal{B} + \mathrm{sgn}(\mathcal{B})\sqrt{\mathcal{B}^2 - 4\mathcal{A}\mathcal{C}}\right] \tag{E.240}$$

$$x_1 = \frac{q}{\mathcal{A}} \quad \& \quad x_2 = \frac{\mathcal{C}}{q} \tag{E.241}$$

In principle, the "traditional" quadratic formula is formally equivalent to the solutions (E.241). However, in practice, solutions to the quadratic formula are typically computed on devices that are susceptible to round off errors caused the subtraction of two very nearly identical numbers. The solutions of the form given above are robust against round off errors.

Only one of the two solutions is correct. Since the B field defined the axis of quantization used to derive the Breit-Rabi equation, it is positive by definition. Therefore the correct solution is the one for which $B > 0$. Since $\mu_B \gg \mu_N$, the sign of x is given by the sign of $-g_S B$. Since $g_S \approx -2$, x and B have the same sign. The sign of x_1 is given by the sign of $-\mathcal{B}/\mathcal{A}$ while the sign of x_2 is given by the sign of $-\mathcal{C}/\mathcal{B}$.

The value of the parameter a is 1 with a small correction of order 10^{-3} whose sign depends on g_I. Consequently, $\mathcal{A}$ is nearly 0 and the sign of $\mathcal{A}$ is equal to the sign of g_I. The value of the parameter b is always less than 1. If $2I \ll 10^3$, then $b < a$. If we also stipulate that $0 < \nu < \nu_{hfs}/2$, then $n < 1$. All this put together insures $(a - b - san) > 0$ which implies $\mathcal{B}$ has the same sign as $-s$. Finally, the sign of $\mathcal{C}$ is s because $(2 - sn) > 0$. Therefore, under these conditions, the sign of x_1 is s/g_I, whereas the sign of x_2 is positive. Since the correct solution must be positive

regardless of s, it is $x_2 = \mathcal{C}/q$.

The discriminant $\mathcal{B}^2 - 4\mathcal{A}\mathcal{C}$ is given by:

$$\begin{aligned}[-2s\,(a-b-san)]^2 - 4\left[1-a^2\right][sn(2-sn)] &= 4\left[b^2+a^2-2ab+2absn-2sn+n^2\right] \\ &= 4\left[(a-b)^2-2sn(1-ab-sn/2)\right]\end{aligned} \tag{E.242}$$

Plugging this into q, canceling factors of 2 inside q, and canceling a factor of s in $\mathcal{C}$ & q gives:

$$x = \left(g_I\mu_N - g_S\mu_B\right)\frac{B}{h\nu_{hfs}} = \frac{C}{q} = \frac{n(2-sn)}{a(1-sn)-b+\sqrt{(a-b)^2-2sn(1-ab-sn/2)}} \tag{E.243}$$

where $s = \pm 1$ and as a reminder:

$$n = 2\nu/\nu_{hfs} \qquad a = \frac{1+\frac{g_I\mu_N}{g_S\mu_B}}{1-\frac{g_I\mu_N}{g_S\mu_B}} \qquad b = \frac{2I-1}{2I+1} = \frac{[I]-2}{[I]} \tag{E.244}$$

Multiplying the top and bottom by $[I]$, writing a as $1-\epsilon$, and solving for B gives:

$$B = \left(\frac{[I]h\nu}{g_I\mu_N}\right)\frac{\epsilon(1-f)}{1-[I]\left\{f(1-\epsilon)+\frac{\epsilon}{2}\right\}+\sqrt{\left(1-[I]\frac{\epsilon}{2}\right)^2-2f[I]\left(1-\epsilon+[I]\frac{(\epsilon-f)}{2}\right)}} \tag{E.245}$$

where $s = \pm 1$ is the sign of the edge state involved in the transition and:

$$[I] = 2I+1 \qquad f = s\nu/\nu_{hfs} \qquad \epsilon = 1-a = \frac{2g_I\mu_N}{g_I\mu_N - g_S\mu_B} = g_I\frac{\mu_N}{\mu_B}\left[\frac{-2}{g_S}\right]\left(1-\frac{g_I\mu_N}{g_S\mu_B}\right)^{-1} \tag{E.246}$$

Isotope	I	**upper** F	**End Transition**	g_I	ν_{hfs} MHz
^{6}Li	1	3/2	$s3/2 \leftrightarrow s1/2$	+0.822 056	228.205 26
^{7}Li	3/2	2	$s2 \leftrightarrow s1$	+2.170 960	803.504 09
^{23}Na	3/2	2	$s2 \leftrightarrow s1$	+1.478 347	1 771.626 13
^{39}K	3/2	2	$s2 \leftrightarrow s1$	+0.260 973	461.719 72
^{40}K	4	9/2	$s9/2 \leftrightarrow s7/2$	−0.324 5	-1 142.92
^{41}K	3/2	2	$s2 \leftrightarrow s1$	+0.143 247	254.013 87
^{85}Rb	5/2	3	$s3 \leftrightarrow s2$	+0.541 208	3 035.732 00
^{87}Rb	3/2	2	$s2 \leftrightarrow s1$	+1.834 133	6 834.682 60
^{133}Cs	7/2	4	$s4 \leftrightarrow s3$	+0.736 857	9 192.631 77

Table E.3: Upper Manifold End Transitions for which Equation (E.245) is valid with $s = \pm$

Twin Transition Frequency Difference

The upper manifold has two more $\Delta m_F = \pm 1$ transitions than the lower manifold. These extra transitions are the end transitions. All other upper manifold transitions have a "twin" transition in the lower manifold. The twins transitions sit side by side on the same row in table (E.2). The difference in frequencies between twin transitions depends only on the magnitude of the field:

$$\Delta\nu_{\text{twin}} = \nu_{\text{lower}} - \nu_{\text{upper}} = +2g_I \frac{\mu_N}{h} B \tag{E.247}$$

Note that for any pair of twin transitions, the lower manifold transition has the larger frequency. For example, the twin frequency differences for ^{39}K and ^{85}Rb at

10 Gauss are:

$$^{39}\mathrm{K} \quad : \quad \nu\left(F=1, m_F=\pm 1 \leftrightarrow 0\right) - \nu\left(F=2, m_F=\pm 1 \leftrightarrow 0\right) = 3.98 \text{ kHz} \tag{E.248}$$

$$^{85}\mathrm{Rb} \quad : \quad \nu\left(F=2, m_F=\pm 2 \leftrightarrow \pm 1 \leftrightarrow 0\right) - \nu\left(F=3, m_F=\pm 2 \leftrightarrow \pm 1 \leftrightarrow 0\right) = 8.25 \text{ kHz} \tag{E.249}$$

Low Field Frequency Expansion

To expand the frequency at low field up to sixth order in x:

$$\begin{aligned}
\nu_{\pm} &= \frac{\nu_{hfs}}{2}\Delta \mp \frac{g_I \mu_N B}{h} \\
\Delta &= \sqrt{1+2ax+x^2} - \sqrt{1+2a'x+x^2} \\
&= \left(a-a'\right)x + \left(-\frac{a^2-a'^2}{2}\right)x^2 \\
&\quad + \left(-\frac{a-a'}{2} + \frac{a^3-a'^3}{2}\right)x^3 \\
&\quad + \left(3\frac{a^2-a'^2}{4} - 5\frac{a^4-a'^4}{8}\right)x^4 \\
&\quad + \left(3\frac{a-a'}{8} - 5\frac{a^3-a'^3}{4} + 7\frac{a^5-a'^5}{8}\right)x^5 \\
&\quad + \left(-15\frac{a^2-a'^2}{16} + 35\frac{a^4-a'^4}{16} - 21\frac{a^6-a'^6}{16}\right)x^6
\end{aligned} \tag{E.250}$$

The difference in each term is with $b = [I]$:

$$a^n - a'^n = \left(\frac{2m_F}{[I]}\right)^n - \left(\frac{2\left(m_F-1\right)}{[I]}\right)^n = \left[\frac{2}{b}\right]^n \left[m_F^n - (m_F-1)^n\right] \tag{E.251}$$

Factoring out b^n from each term:

$$\begin{aligned}\frac{\Delta}{2} &= \frac{x}{b}+[1-2m_F]\frac{x^2}{b^2}+2\left[1-3m_F+3m_F^2-\frac{b^2}{4}\right]\frac{x^3}{b^3}\\ &+\left[5\left(1-4m_F+6m_F^2-4m_F^3\right)-\frac{3b^2}{2}\left(1-2m_F\right)\right]\frac{x^4}{b^4}\\ &+\left[14\left(1-5m_F+10m_F^2-10m_F^3+5m_F^4\right)-5b^2\left(1-3m_F+3m_F^2\right)+\frac{3b^4}{8}\right]\frac{x^5}{b^5}\\ &+\left[42\left(1-6m_F+15m_F^2-20m_F^3+15m_F^4-6m_F^5\right)\right]\frac{x^6}{b^6}\\ &+\left[-\frac{35b^2}{2}\left(1-4m_F+6m_F^2-4m_F^3\right)+\frac{15b^4}{8}\left(1-2m_F\right)\right]\frac{x^6}{b^6} \qquad \text{(E.252)}\end{aligned}$$

Putting this altogether gives (to sixth order in x), the frequency of transition for the $F = I \pm 1/2$ manifold at a given (low) field B:

$$\frac{\nu_\pm}{\nu_{hfs}} = \sum_{n=1}^{6} c_n \frac{x^n}{[I]^n} \qquad \text{(E.253)}$$

$$x = \left(g_I\mu_N - g_S\mu_B\right)\frac{B}{h\nu_{hfs}} \qquad \text{(E.254)}$$

$$[I] = 2I+1 \qquad \text{(E.255)}$$

$$c_1 = \frac{1\pm\frac{g_I\mu_N}{g_S\mu_B}\left([I]\mp 1\right)}{1-\frac{g_I\mu_N}{g_S\mu_B}} = 1\mp O(10^{-3}) \qquad \text{(E.256)}$$

$$c_2 = 1-2m_F \qquad \text{(E.257)}$$

$$c_3 = 2\left(1-3m_F+3m_F^2-\frac{[I]^2}{4}\right) \qquad \text{(E.258)}$$

$$c_4 = 5\left(1-4m_F+6m_F^2-4m_F^3\right)-\frac{3[I]^2}{2}\left(1-2m_F\right) \qquad \text{(E.259)}$$

$$c_5 = 14\left(1-5m_F+10m_F^2-10m_F^3+5m_F^4\right)-5[I]^2\left(1-3m_F+3m_F^2\right)+\frac{3[I]^4}{8} \qquad \text{(E.260)}$$

$$\begin{aligned}c_6 &= 42\left(1-6m_F+15m_F^2-20m_F^3+15m_F^4-6m_F^5\right)\\ &-\frac{35[I]^2}{2}\left(1-4m_F+6m_F^2-4m_F^3\right)+\frac{15[I]^4}{8}\left(1-2m_F\right) \qquad \text{(E.261)}\end{aligned}$$

where $\pm$ refers to the manifold.

Low Field Frequency Inversion Formula

If we drop all terms higher than second order, then we can get an inversion formula for equation (E.253) for *any* transition at low field. Thus applying the quadratic formula (E.241) and noting that $\mu_N/\mu_B \ll 1 \rightarrow c_1 \approx 1$ and $g_S \approx -2$, we get the field corresponding to a particular transition frequency at low fields:

$$B \approx \left(\frac{h\nu}{\mu_B}\right) \frac{[I]}{1+\sqrt{1+4(1-2m_F)\nu/\nu_{hfs}}} \tag{E.262}$$

Table (E.4) illustrates how accurate this approximate equation is. For ^{85}Rb, its better than 0.25% up to $\nu = 16$ MHz. For ^{39}K, its better than 0.50% up to $\nu = 10$ MHz.

Low Field Adjacent Transition Frequency Difference

At low fields to lowest order, the frequency difference between two adjacent transitions depends on B^2:

$$\left|\frac{\nu\left(m_F+1 \leftrightarrow m_F\right)-\nu\left(m_F \leftrightarrow m_F-1\right)}{\nu_{hfs}}\right| = 2\frac{x^2}{[I]^2} = 2\left[\left(g_I\mu_N - g_S\mu_B\right)\frac{B}{[I]h\nu_{hfs}}\right]^2 \tag{E.263}$$

At $B = 10$ G, $\Delta\nu = 14.4$ kHz for ^{85}Rb and $\Delta\nu = 212$ kHz for ^{39}K.

^{39}K		$\nu = 10$ MHz			$\nu = 25$ MHz		
F	m_F	B (full)	B (E.262)	% diff.	B (full)	B (E.262)	% diff.
2	-1	13.422	13.465	$+0.32$	30.923	31.276	$+1.14$
1	0	14.011	13.993	-0.13	34.514	33.974	-1.56
2	0	14.018	13.993	-0.18	34.532	33.974	-1.62
1	$+1$	14.633	14.613	-0.13	38.564	37.901	-1.72
2	$+1$	14.642	14.613	-0.19	38.590	37.901	-1.79
2	$+2$	15.292	15.363	$+0.46$	43.095	44.883	$+4.15$
^{85}Rb		$\nu = 6.5$ MHz			$\nu = 16$ MHz		
F	m_F	B (full)	B (E.262)	% diff.	B (full)	B (E.262)	% diff.
3	-2	13.779	13.786	$+0.05$	33.403	33.436	$+0.10$
2	-1	13.814	13.844	$+0.22$	33.700	33.769	$+0.21$
3	-1	13.838	13.844	$+0.04$	33.758	33.769	$+0.03$
2	0	13.873	13.903	$+0.21$	34.057	34.116	$+0.17$
3	0	13.898	13.903	$+0.04$	34.116	34.116	-0.00
2	$+1$	13.933	13.962	$+0.21$	34.417	34.478	$+0.18$
3	$+1$	13.957	13.962	$+0.03$	34.479	34.478	-0.00
2	$+2$	13.992	14.023	$+0.22$	34.781	34.855	$+0.21$
3	$+2$	14.017	14.023	$+0.04$	34.845	34.855	$+0.03$
3	$+3$	14.078	14.085	$+0.05$	35.215	35.250	$+0.10$

Table E.4: Comparison of calculation of B given ν. All the fields are in gauss. The "full" calculation is solving Eqn. (blah) numerically. The approximate calculation is Eqn. (E.262). Comparisons are made at $B \approx 15$ G & 35 G. For ^{39}K this corresponds to $\nu = 10$ MHz & 25 MHz. For ^{85}Rb this corresponds to $\nu = 6.5$ MHz & 16 MHz.

Low Field Frequency Derivative with respect to Field

The derivative of the frequency with respect to the field is:

$$\frac{d\nu}{dB} = \mp\frac{g_I\mu_N}{h} + \frac{\left(g_I\mu_N - g_S\mu_B\right)}{2h[I]}\left(\frac{2m_F + [I]x}{\sqrt{1+\frac{4m_F}{[I]}x+x^2}} - \frac{2m_F - 2 + [I]x}{\sqrt{1+\frac{4(m_F-1)}{[I]}x+x^2}}\right) \quad \text{(E.264)}$$

The derivative can be "expanded" in x at low field by taking the derivative of equation (E.253) term by term. To fifth order in field, the derivative of the frequency with respect to the field is:

$$\begin{aligned}
\frac{d\nu_\pm}{dB} &= \frac{\left(g_I\mu_N - g_S\mu_B\right)}{h[I]}\sum_{n=0}^{5} b_n \frac{x^n}{[I]^n} && \text{(E.265)}\\
x &= \left(g_I\mu_N - g_S\mu_B\right)\frac{B}{h\nu_{hfs}} && \text{(E.266)}\\
[I] &= 2I+1 && \text{(E.267)}\\
b_0 &= \frac{1 \pm \frac{g_I\mu_N}{g_S\mu_B}\left([I]\mp 1\right)}{1-\frac{g_I\mu_N}{g_S\mu_B}} = 1 \mp O(10^{-3}) && \text{(E.268)}\\
b_1 &= 2\left(1-2m_F\right) && \text{(E.269)}\\
b_2 &= 6\left(1-3m_F+3m_F^2-\frac{[I]^2}{4}\right) && \text{(E.270)}\\
b_3 &= 20\left(1-4m_F+6m_F^2-4m_F^3\right) - 6[I]^2\left(1-2m_F\right) && \text{(E.271)}\\
b_4 &= 70\left(1-5m_F+10m_F^2-10m_F^3+5m_F^4\right) - 25[I]^2\left(1-3m_F+3m_F^2\right) + \frac{15[I]^4}{8} && \text{(E.272)}\\
b_5 &= 252\left(1-6m_F+15m_F^2-20m_F^3+15m_F^4-6m_F^5\right) \\
&\quad -105[I]^2\left(1-4m_F+6m_F^2-4m_F^3\right) + \frac{45[I]^4}{4}\left(1-2m_F\right) && \text{(E.273)}
\end{aligned}$$

These coefficients have simple forms for the end transitions. Plugging in $m_F = I + 1/2$ for $I + 1/2 \leftrightarrow I - 1/2$ and $m_F = -I + 1/2$ for $-I + 1/2 \leftrightarrow -I - 1/2$, the

coefficients for the expansion of the derivative of the EPR frequency are:

$$b_0 = \frac{1+\frac{g_I\mu_N}{g_S\mu_B}(2I)}{1-\frac{g_I\mu_N}{g_S\mu_B}} = 1 - O(10^{-3}) \quad \text{(E.274)}$$

$$b_1 = \mp 4I \quad \text{(E.275)}$$

$$b_2 = 6I(2I-1) \quad \text{(E.276)}$$

$$b_3 = \mp 8I\left(4I^2 - 6I + 1\right) \quad \text{(E.277)}$$

$$b_4 = 10I(2I-1)\left(4I^2 - 10I + 1\right) \quad \text{(E.278)}$$

$$b_5 = \mp 12I\left(16I^4 - 80I^3 + 80I^2 - 20I + 1\right) \quad \text{(E.279)}$$

where $\pm$ refers to the edge state $m_F = \pm\left(I + \frac{1}{2}\right)$ involved in the transition.

E.4 The Structure of Polarized Light

E.4.1 Representing Electromagnetic Plane Waves

Real Representation

The electric and magnetic field components of an electromagnetic plane wave traveling in the z-direction with arbitrary polarization in a uniform and isotropic medium can be written as:

$$\vec{E}(\vec{r},t) = E_x(z,t)\hat{x} + E_y(z,t)\hat{y} = E_{0x}\hat{x}\cos(kz-\omega t) + E_{0y}\hat{y}\cos(kz-\omega t+\phi) \quad \text{(E.280)}$$

$$\vec{B}(\vec{r},t) = \sqrt{\mu\epsilon}\left[\hat{z}\times\vec{E}(\vec{r},t)\right] = \mu\vec{H}(\vec{r},t) \quad \text{(E.281)}$$

$$= \sqrt{\mu\epsilon}\left[E_{0x}\hat{y}\cos(kz-\omega t) - E_{0y}\hat{x}\cos(kz-\omega t+\phi)\right] \quad \text{(E.282)}$$

In SI, the energy flux (energy per unit time per unit area or instantaneous power density) associated with the EM wave is given by the Poynting vector:

$$\begin{aligned}
\vec{S}(\vec{r},t) &= \vec{E}(\vec{r},t)\times\vec{H}(\vec{r},t)=\frac{1}{\mu}\vec{E}(\vec{r},t)\times\vec{B}(\vec{r},t)=\sqrt{\frac{\epsilon}{\mu}}\vec{E}(\vec{r},t)\times\left[\hat{z}\times\vec{E}(\vec{r},t)\right] && \text{(E.283)}\\
&= \sqrt{\frac{\epsilon}{\mu}}\left(\hat{z}\left[\vec{E}(\vec{r},t)\cdot\vec{E}(\vec{r},t)\right]-\vec{E}(\vec{r},t)\left[\hat{z}\cdot\vec{E}(\vec{r},t)\right]\right) && \text{(E.284)}\\
&= \hat{z}\sqrt{\frac{\epsilon}{\mu}}\left[\vec{E}(\vec{r},t)\cdot\vec{E}(\vec{r},t)\right] && \text{(E.285)}\\
&= \hat{z}\sqrt{\frac{\epsilon}{\mu}}E_{0x}^2\left[\cos^2(kz)\cos^2(\omega t)+\sin^2(kz)\sin^2(\omega t)+\frac{1}{2}\sin(2kz)\sin(2\omega t)\right]\\
&\quad +\hat{z}\sqrt{\frac{\epsilon}{\mu}}E_{0y}^2\left[\cos^2(kz+\phi)\cos^2(\omega t)+\sin^2(kz+\phi)\sin^2(\omega t)\right.\\
&\quad \left.+\frac{1}{2}\sin(2kz+2\phi)\sin(2\omega t)\right] && \text{(E.286)}
\end{aligned}$$

We'll define the intensity as the magnitude of the time averaged energy flux (or time averaged power density):

$$\begin{aligned}
I &\equiv \frac{\omega}{2\pi}\int_0^{\frac{2\pi}{\omega}}\hat{z}\cdot\vec{S}(\vec{r},t)\,\mathrm{d}t && \text{(E.287)}\\
\frac{1}{2} &= \frac{\omega}{2\pi}\int_0^{\frac{2\pi}{\omega}}\cos^2(\omega t)\mathrm{d}t=\frac{\omega}{2\pi}\int_0^{\frac{2\pi}{\omega}}\sin^2(\omega t)\mathrm{d}t && \text{(E.288)}\\
I &= \sqrt{\frac{\epsilon}{\mu}}\left(\frac{E_{0x}^2}{2}\left[\cos^2(kz)+\sin^2(kz)\right]+\frac{E_{0y}^2}{2}\left[\cos^2(kz+\phi)+\sin^2(kz+\phi)\right]\right)\\
&= \frac{1}{2}\sqrt{\frac{\epsilon}{\mu}}\left[E_{0x}^2+E_{0y}^2\right]=\sqrt{\frac{\epsilon}{\mu}}\left\langle\left|\vec{E}\right|^2\right\rangle_{\text{time}} && \text{(E.289)}
\end{aligned}$$

where the time averaged magnitude of the electric field vector is given as:

$$\sqrt{\left\langle\left|\vec{E}\right|^2\right\rangle_{\text{time}}} = \sqrt{\frac{E_{0x}^2+E_{0y}^2}{2}} \qquad \text{(E.290)}$$

Complex Representation: The Jones Calculus

We will use the Jones calculus [9–11] for defining the polarization state of the light (vectors) and the action of the various optical elements (matrices). This convention uses complex number representation and a linear polarization basis. The electric field component of a monochromatic electromagnetic plane wave with propagation vector $\vec{k} = k\hat{z}$ at time t is:

$$\begin{aligned} \vec{E}(z,t) &= E_x(z,t)\hat{x} + E_y(z,t)\hat{y} = |E\rangle\, e^{ikz-i\omega t} && \text{(E.291)} \\ E_x(z,t) &= E_{0x}\exp\left(ikz - i\omega t + i\alpha_x\right) && \text{(E.292)} \\ E_y(z,t) &= E_{0y}\exp\left(ikz - i\omega t + i\alpha_y\right) && \text{(E.293)} \\ |E\rangle &\equiv \begin{bmatrix} E_{0x}e^{i\alpha_x} \\ E_{0y}e^{i\alpha_y} \end{bmatrix} && \text{(E.294)} \end{aligned}$$

where the relative phase shift is $\alpha = \alpha_x - \alpha_y$. *Note that it is assumed that the real part of $\vec{E}$ is taken when the physical field is needed.* At a fixed point is space and over one period ($= \frac{2\pi}{\omega}$) in time, $\vec{E}$ sweeps out an ellipse in the xy-plane given by (Born, Max and Emil Wolf. Principles of Optics, 7th (Expanded) Edition. Cambridge: Cambridge University Press, 1999. page 26, equation 15):

$$\left(\frac{E_x}{E_{0x}}\right)^2 + \left(\frac{E_y}{E_{0y}}\right)^2 - 2\left(\frac{E_x}{E_{0x}}\right)\left(\frac{E_y}{E_{0y}}\right)\cos(\alpha) = \sin^2(\alpha) \qquad \text{(E.295)}$$

In this representation, computing the modulus square of the electric field vector gives:

$$\vec{E}^* \cdot \vec{E} = \langle E|E\rangle = E_{0x}^2 + E_{0y}^2 \qquad \text{(E.296)}$$

The time averaged modulus squared of electric field vector is therefore:

$$\left|\vec{E}\right|^2_{\text{time}} \equiv \frac{\vec{E}^* \cdot \vec{E}}{2} = \frac{E_{0x}^2 + E_{0y}^2}{2} \tag{E.297}$$

and finally the intensity is:

$$I = \sqrt{\frac{\epsilon}{\mu}} \left\langle \vec{E}^* \cdot \vec{E} \right\rangle_{\text{time}} = \sqrt{\frac{\epsilon}{\mu}} \frac{\langle E \mid E \rangle}{2} = \frac{\langle B \mid B \rangle}{2\mu\sqrt{\epsilon\mu}} \tag{E.298}$$

E.4.2 Linear Polarization

For linear polarization, the relative phase shift is an integer multiple of half a wave,

$$\alpha = \pm n\pi \tag{E.299}$$

or in other words the two components are in phase. Eqn. (E.295) becomes degenerate,

$$\left(\frac{E_x}{E_{0x}}\right)^2 + \left(\frac{E_y}{E_{0y}}\right)^2 \mp 2\left(\frac{E_x}{E_{0x}}\right)\left(\frac{E_y}{E_{0y}}\right) = 0 \tag{E.300}$$

with solutions

$$\frac{E_y}{E_{0y}} = \mp \frac{E_x}{E_{0x}} \tag{E.301}$$

Two specific solutions are the orthogonal axes of the xy-plane which correspond to horizontal and vertical linearly polarized light. Horizontal linearly polarized light is denoted by

$$|\mathcal{P}\rangle = |x\rangle = \begin{bmatrix} 1 \\ 0 \end{bmatrix} \tag{E.302}$$

Vertical linearly polarized light is denoted by

$$|\mathcal{S}\rangle = |y\rangle = \begin{bmatrix} 0 \\ 1 \end{bmatrix} \tag{E.303}$$

Linear polarization at an angle θ counterclockwise from the x-axis is

$$|\theta\rangle = \begin{bmatrix} \cos(\theta) \\ \sin(\theta) \end{bmatrix} \tag{E.304}$$

E.4.3 Circular Polarization

When the relative phase shift is a quarter wave,

$$\alpha = \pm(2n+1)\frac{\pi}{2} \tag{E.305}$$

and the magnitudes of the two components are identical,

$$E_{0x} = E_{0y} \tag{E.306}$$

then eqn. (E.295) reduces to an equation for a circle:

$$E_x{}^2 + E_y{}^2 = 1 \tag{E.307}$$

The two orthogonal states are labeled by their helicity, namely the sign of the projection of the spin to the propagation vector. Right circularly polarized light,

$$|\mathcal{R}\rangle = |+\rangle = \frac{\sqrt{2}}{2}\begin{bmatrix} 1 \\ +i \end{bmatrix} \tag{E.308}$$

following the right hand rule such that the spin is parallel to the direction of propagation. Left circularly polarized light,

$$|\mathcal{L}\rangle = |-\rangle = \frac{\sqrt{2}}{2}\begin{bmatrix} 1 \\ -i \end{bmatrix} \tag{E.309}$$

is anti-parallel. Note that the standard optics convention is opposite to the helicity convention. In the helicity convention, for right circularly polarized light, $\vec{E}$ rotates counterclockwise in the xy-plane at a fixed point in space. In the standard optics convention, for right circularly polarized light, $\vec{E}$ rotates counterclockwise in the xy-plane at a fixed moment in time as you move forward in the direction of propagation. See fig. (4.15). Unless otherwise noted, *the helicity convention* will be used. See page 400 of *Waves* [12] for further discussion regarding handedness convention and also 4.5.3.

E.4.4 Stokes Parameters

Since the polarization vector of light has two components with complex coefficients, four real numbers are required to describe it completely. These real numbers are called Stokes parameters. Unfortunately many different conventions exist in the literature. For our purposes, the most useful convention in the circular po-

larization basis for arbitrarily polarized light is:

$$|E\rangle = E_0 e^{i\phi_p}\left[\sqrt{\frac{1+P}{2}}e^{-i\theta}\,|\mathcal{R}\rangle + \sqrt{\frac{1-P}{2}}e^{+i\theta}\,|\mathcal{L}\rangle\right] \tag{E.310}$$

where ϕ_p is just an overall phase factor that rarely contains any useful information about the light. Equivalently in the linear polarization basis, it is written as:

$$|E\rangle = E_0 e^{i\phi_p}\left[\left(\sqrt{1-P}\frac{e^{+i\theta}}{2} + \sqrt{1+P}\frac{e^{-i\theta}}{2}\right)|\mathcal{P}\rangle + \left(\sqrt{1-P}\frac{e^{+i\theta}}{2i} - \sqrt{1+P}\frac{e^{-i\theta}}{2i}\right)|\mathcal{S}\rangle\right] \tag{E.311}$$

The magnitude of $\vec{E}$ is:

$$\sqrt{\langle E|E\rangle} = \sqrt{\langle E_{\mathcal{R}}|E_{\mathcal{R}}\rangle + \langle E_{\mathcal{L}}|E_{\mathcal{L}}\rangle} = \sqrt{\left(\frac{1+P}{2}\right)E_0^2 + \left(\frac{1-P}{2}\right)E_0^2} = E_0 \tag{E.312}$$

The degree of circular polarization of the light is:

$$\frac{\langle E_{\mathcal{R}}|E_{\mathcal{R}}\rangle - \langle E_{\mathcal{L}}|E_{\mathcal{L}}\rangle}{\langle E|E\rangle} = \frac{\left(\frac{1+P}{2}\right)E_0^2 - \left(\frac{1-P}{2}\right)E_0^2}{E_0^2} = P \tag{E.313}$$

where $P = +(-)1$ for pure right (left) circular polarization and $P = 0$ for pure linear polarization. In the linear basis for pure linear polarization:

$$\begin{aligned} |E\rangle &= E_0 e^{i\phi_p}\left[\left(\frac{e^{+i\theta}}{2} + \frac{e^{-i\theta}}{2}\right)|\mathcal{P}\rangle + \left(\frac{e^{+i\theta}}{2i} - \frac{e^{-i\theta}}{2i}\right)|\mathcal{S}\rangle\right] \\ &= E_0 e^{i\phi_p}\left[\cos(\theta)\,|\mathcal{P}\rangle + \sin(\theta)\,|\mathcal{S}\rangle\right] \end{aligned} \tag{E.314}$$

where θ is the angle of the linear polarization vector with respect to the $|\mathcal{P}\rangle$-axis. In general for elliptically polarized light, θ is the angle that the major axis of the polarization ellipse makes with the $|\mathcal{P}\rangle$-axis.

E.4.5 Mirrors

Mirrors are produced by applying one or more layers of a thin film coating onto a substrate. The index of refraction and thickness of the thin film is chosen to maximize reflection. The reflectivity of the mirror and the phase shift induced in the light depends on the polarization of the light and its angle of incidence. The mirrors we commonly use (Newport Corporation, 1791 Deere Ave, Irvine, CA 92606, 1-800-222-6440) have a minimum reflectivity of 99% for $\mathcal{P}$ polarized light and 98% for $\mathcal{S}$ polarized light in the 700–950 nm range for angles from 0–45 degrees (broadband dielectric coating BD.2). Specifically, at 45 degrees and at a wavelength of around 800 nm, the relflectivities for $\mathcal{P}$ & $\mathcal{S}$ polarized light are 99.5% and 99.9%. Since the reflectivity is defined as the ratio of output to input intensities, the reflection coefficient is the square root of the reflectivity:

$$r_P = \sqrt{R_P} \approx 0.9975 \tag{E.315}$$

$$r_S = \sqrt{R_S} \approx 0.9995 \tag{E.316}$$

If the light is circularly polarized or a mix of $\mathcal{S}$ and $\mathcal{P}$ linear polarizations, then it is necessary to include a small relative phase shift factor, δ_m. Unfortunately, this value is not given in the optics catalogs and must be obtained empirically if needed. A simplified form for the mirror matrix is then:

$$\hat{M} = \begin{bmatrix} r_P & 0 \\ 0 & r_S e^{i\delta_m} \end{bmatrix} \tag{E.317}$$

A fully general mirror matrix would be, in principle, complex and may even contain small non-zero off diagonal elements.

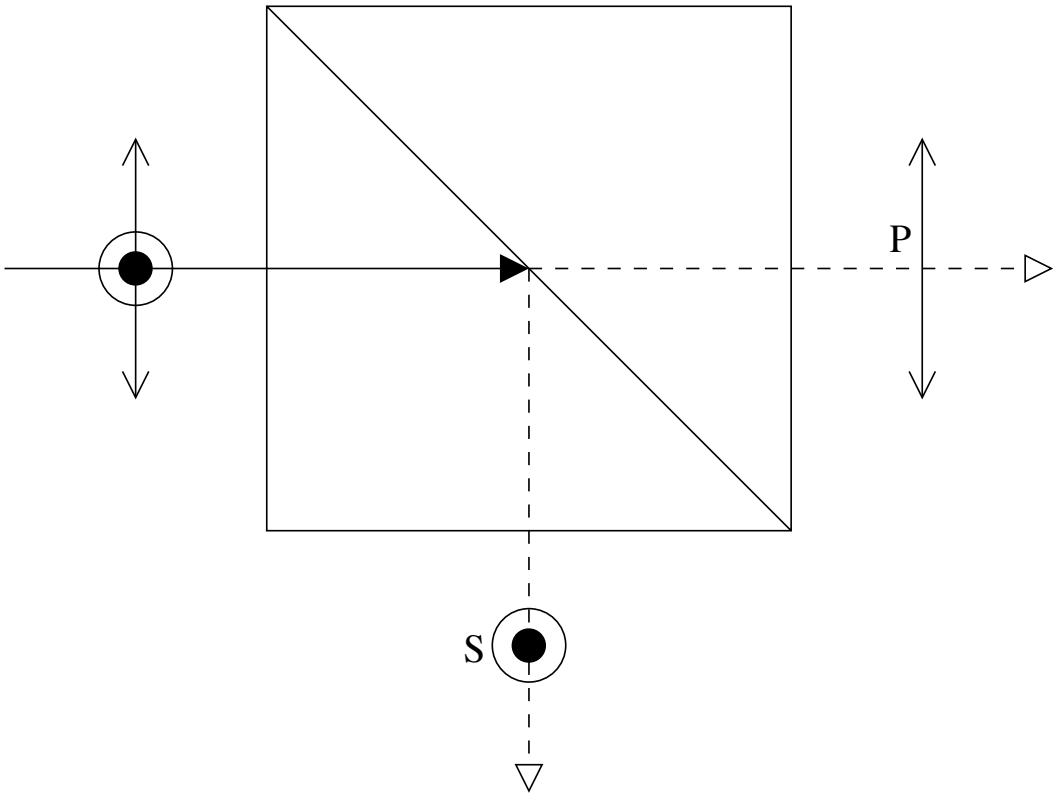

Figure E.2: Top view of BSPC

E.4.6 Beam Splitting Polarizing Cubes

Matrix Representation

An ideal beam splitting polarizing cube (BSPC) simply splits an incoming beam into it's two linearly polarized components. Once separated, the two beam paths are orthogonal, see fig. (E.2). The transmitted beam is selected by

$$\hat{C}_t = \begin{bmatrix} 1 & 0 \\ 0 & 0 \end{bmatrix} \tag{E.318}$$

and the reflected beam is selected by

$$\hat{C}_r = \begin{bmatrix} 0 & 0 \\ 0 & 1 \end{bmatrix} \tag{E.319}$$

For the ideal case, the transmitted and reflected beams are pure $\mathcal{P}$ & $\mathcal{S}$ linear polarizations respectively. In practice the splitting and polarizing are imperfect. According to RMI (Dr. Zhiming Lu, zlu@rmico.com, Rocky Mountain Instruments, 106 Laser Drive, Lafayette, CO, 80026, 303-664-5000), our 2″ BSPC has an extinction ratio for the transmitted beam of $\geq 1000:1$ whereas for the reflected beam it is $\leq 20:1$. The transmittance is about $\geq 95\%$, whereas the reflectance is about $\geq 99.9\%$. Therefore a more realistic form of $\hat{C}$ can be written. For example, for the transmitted beam:

$$\hat{C}_t = \begin{bmatrix} t_1 & 0 \\ 0 & t_2 \end{bmatrix} \tag{E.320}$$

$$T_t = \frac{I_{\text{transmitted}}}{I_{\text{input}\mathcal{P}}} = t_1^2 + t_2^2 \tag{E.321}$$

$$e_t = \frac{I_{\text{transmitted}\mathcal{P}}}{I_{\text{transmitted}\mathcal{S}}} = \frac{t_1^2}{t_2^2} \tag{E.322}$$

where t is the transmittance and e_t is the extinction ratio for the transmitted beam. Solving for t_1 & t_2 in terms of t & e_t and doing the same for the reflected beam, the

more general cube matrices become:

$$\hat{C}_t = \begin{bmatrix} \sqrt{\frac{T_t}{1+e_t^{-1}}} & 0 \\ 0 & \sqrt{\frac{T_t}{1+e_t}} \end{bmatrix} \tag{E.323}$$

$$\hat{C}_r = \begin{bmatrix} \sqrt{\frac{T_r}{1+e_r}} & 0 \\ 0 & \sqrt{\frac{T_r}{1+e_r^{-1}}} \end{bmatrix} \tag{E.324}$$

Given the specifications for our cube, the matrices are:

$$\hat{C}_t \approx \begin{bmatrix} 0.974 & 0 \\ 0 & 0.031 \end{bmatrix} \tag{E.325}$$

$$\hat{C}_r \approx \begin{bmatrix} 0.213 & 0 \\ 0 & 0.951 \end{bmatrix} \tag{E.326}$$

The fully general cube matrices could be, in principle, complex and have non-zero off diagonal elements.

Measuring the degree of circular polarization

One can measure the degree of circular polarization of a beam of light by using a rotatable beam splitting polarizing cube. Note that an input light polarization angle of θ with respect to the cube axis is equivalent to having the cube axis be $-\theta$ from the light polarization $\mathcal{P}$ axis. Therefore varying θ is equivalent to rotating the cube. If the incident light is normal to the cube, then the intensity of the light

transmitted through the cube is given by:

$$\begin{aligned} I_t &= \left|\hat{\mathcal{C}}_t\left|E\right\rangle\right|^2 = t_1^2\left\langle E_{\mathcal{P}}|E_{\mathcal{P}}\right\rangle + t_2^2\left\langle E_{\mathcal{S}}|E_{\mathcal{S}}\right\rangle \\ &= \frac{E_0^2 T_t e_t}{1+e_t}\left(\frac{1-P+1+P+2\sqrt{1-P^2}\cos(2\theta)}{4}\right) \\ &\quad + \frac{E_0^2 T_t}{1+e_t}\left(\frac{1-P+1+P-2\sqrt{1-P^2}\cos(2\theta)}{4}\right) \\ &= \frac{E_0^2 T_t}{2}\left[1+\left(\frac{e_t-1}{e_t+1}\right)\sqrt{1-P^2}\cos(2\theta)\right] \end{aligned} \tag{E.327}$$

The maximum and minimum transmitted intensities are:

$$I_{\max} = \frac{E_0^2 T_t}{2}\left[1+\left(\frac{e_t-1}{e_t+1}\right)\sqrt{1-P^2}\right] \tag{E.328}$$

$$I_{\min} = \frac{E_0^2 T_t}{2}\left[1-\left(\frac{e_t-1}{e_t+1}\right)\sqrt{1-P^2}\right] \tag{E.329}$$

Defining the cube efficiency f_c and forming the cube asymmetry A_c yields a polarization "Pythagorean" expression:

$$f_c \equiv \frac{e_t-1}{e_t+1} \tag{E.330}$$

$$A_c \equiv \frac{I_{\max}-I_{\min}}{I_{\max}+I_{\min}} = f_c\sqrt{1-P^2} \tag{E.331}$$

$$1 = P^2 + \left(\frac{A_c}{f_c}\right)^2 \tag{E.332}$$

where P is the degree if circular polarization.

E.4.7 Waveplates

Matrix Representation

A waveplate is an optical element that has different indices of refraction along two orthogonal axes, see fig. (E.3). This results in a net phase shift between the linear components of the polarization vector. First, the polarization vector has to be expressed in the basis of the waveplate. Therefore, a passive or coordinate system rotation of angle ϕ radians is performed,

$$\hat{R}(\phi) = \begin{bmatrix} \cos(\phi) & \sin(\phi) \\ -\sin(\phi) & \cos(\phi) \end{bmatrix} \tag{E.333}$$

followed by a relative phase retardation of β radians,

$$\hat{W}(\beta) = \begin{bmatrix} \exp\left(+i\frac{\beta}{2}\right) & 0 \\ 0 & \exp\left(-i\frac{\beta}{2}\right) \end{bmatrix} \tag{E.334}$$

and finally a rotation back to the original basis, $\hat{R}(-\phi)$. The complete waveplate operator is thus:

$$\begin{aligned} \hat{W}(\phi,\beta) &= \hat{R}(-\phi)\hat{W}(\beta)\hat{R}(\phi) = \exp\left(-i\frac{\beta}{2}\right) \times \\ &\begin{bmatrix} 1+2i\exp\left(i\frac{\beta}{2}\right)\sin\left(\frac{\beta}{2}\right)\cos^2(\phi) & i\exp\left(i\frac{\beta}{2}\right)\sin\left(\frac{\beta}{2}\right)\sin(2\phi) \\ i\exp\left(i\frac{\beta}{2}\right)\sin\left(\frac{\beta}{2}\right)\sin(2\phi) & 1+2i\exp\left(i\frac{\beta}{2}\right)\sin\left(\frac{\beta}{2}\right)\sin^2(\phi) \end{bmatrix} \end{aligned} \tag{E.335}$$

Note that for one complete wave, $\beta = 2\pi$. Typically the fast axis is taken to be vertical.

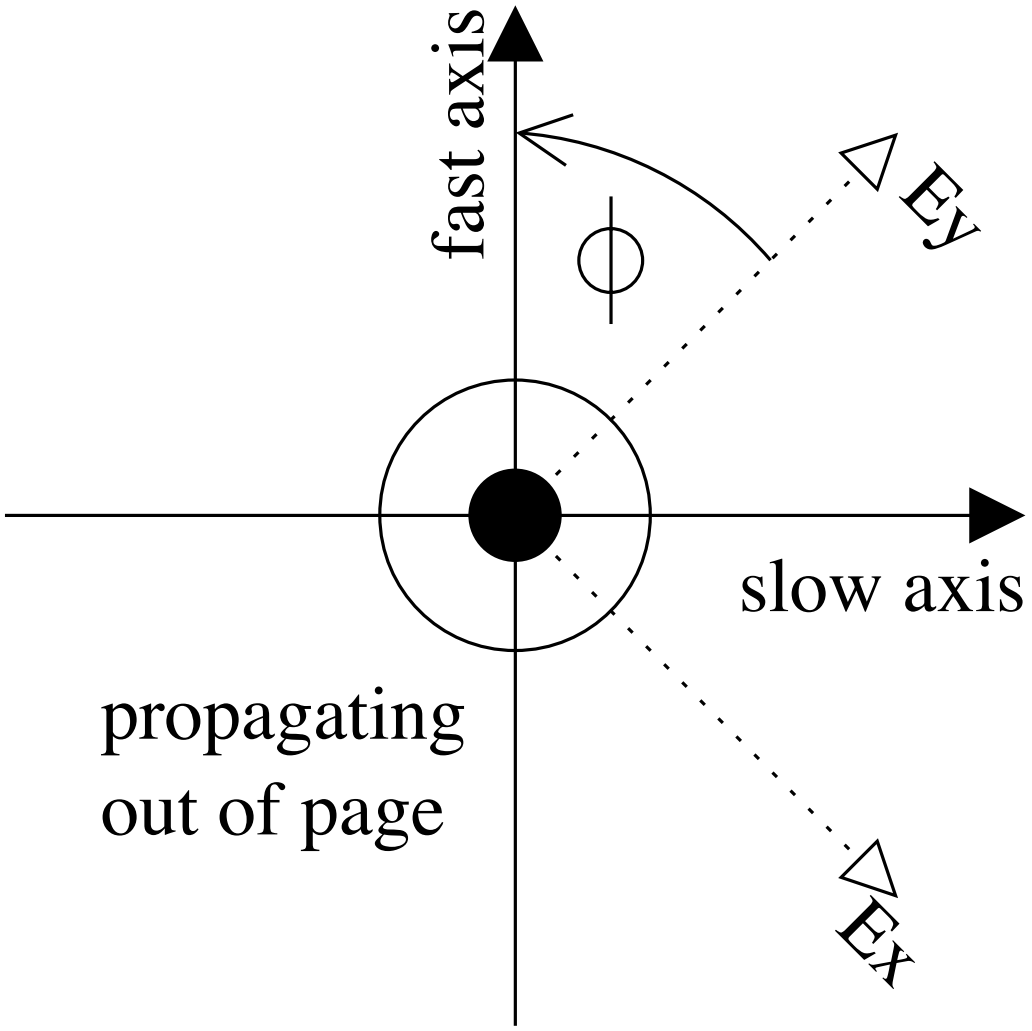

Figure E.3: Coordinate System of a Waveplate space convention fast axis

Half Waveplate

A half-waveplate has a retardance $\beta = \frac{2\pi}{2} = \pi$. When it is orientated at an angle of ϕ from a set of reference axes, the waveplate matrix becomes:

$$\hat{W}_{\frac{1}{2}}(\phi) = i \begin{bmatrix} \cos(2\phi) & \sin(2\phi) \\ \sin(2\phi) & -\cos(2\phi) \end{bmatrix} \tag{E.336}$$

This operation implies that each linear polarization component of some arbitrarily polarized light is rotated by twice the angle between the linear polarization axis and the waveplate fast axis. If the the linear polarization is either $\mathcal{S}$ or $\mathcal{P}$, then a half-waveplate at an angle ϕ with respect to the polarization axis rotates the linear polarization by an angle of 2ϕ. A half-waveplate at $\pm 45^{\text{o}}$ simplify flips $\mathcal{P} \leftrightarrow \mathcal{S}$. For pure circularly polarized light, a half-waveplate orientated at *any* angle simply flips $\mathcal{L} \leftrightarrow \mathcal{R}$.

Quarter Waveplate

For a quarter-waveplate with retardance $\beta = \frac{2\pi}{4} = \frac{\pi}{2}$, orientated at an angle of 45^{o}, the matrix becomes:

$$\hat{W}_{\frac{1}{4}}\left(\frac{\pi}{4}\right) = \frac{\sqrt{2}}{2} \begin{bmatrix} 1 & i \\ i & 1 \end{bmatrix} \tag{E.337}$$

To be explicit, a quarter-waveplate with its fast axis rotated counterclockwise by 45° turns horizontal linearly polarized light into right circularly polarized light,

$$\hat{W}_{\frac{1}{4}}\left(\frac{\pi}{4}\right)|\mathcal{P}\rangle = |\mathcal{R}\rangle \tag{E.338}$$

$$\hat{W}_{\frac{1}{4}}\left(\frac{\pi}{4}\right)|\mathcal{R}\rangle = i|\mathcal{S}\rangle \tag{E.339}$$

$$\hat{W}_{\frac{1}{4}}\left(\frac{\pi}{4}\right)|\mathcal{S}\rangle = i|\mathcal{L}\rangle \tag{E.340}$$

$$\hat{W}_{\frac{1}{4}}\left(\frac{\pi}{4}\right)|\mathcal{L}\rangle = |\mathcal{P}\rangle \tag{E.341}$$

and so forth following the simple pattern $\mathcal{P} \to \mathcal{R} \to \mathcal{S} \to \mathcal{L} \to \mathcal{P}$. An angle of -45° simply reverses the direction of the arrows. Note that in the RHS of the two middle equations, there is an overall phase factor (i) which for our purposes is unimportant.

Photoelastic Modulator

A photoelastic modulator is a variable retardance waveplate. The retardance can be fixed at a constant value or (more importantly) modulated at a frequency ν_{mod} $\left(= \Omega_{\text{mod}}/2\pi\right)$:

$$\beta(t) = \beta_0 \sin\left(\Omega_{\text{mod}} t + \phi_{\text{mod}}\right) \tag{E.342}$$

The PEM that we have (Hinds Instruments, 3175 NW Aloclek, Hillsboro, OR 97124, 503-690-2000) oscillates at 50 kHz. The ability to modulate the phase retardance and therefore modulate the polarization of the incident light makes a PEM (in conjunction with a lock-in amplifier) useful as a high precision polarimeter. Note the

following useful relationships from p. 361 of *Abramowitz & Stegun* [13]:

$$\begin{aligned}
\sin\left(\beta_0 \sin\left(\Omega_{\text{mod}} t\right)\right) &= 2\sum_{n=0}^{\infty} J_{2n+1}\left(\beta_0\right) \sin\left((2n+1)\Omega_{\text{mod}} t\right) \\
&= 2J_1\left(\beta_0\right) \sin\left(\Omega_{\text{mod}} t\right) + \cdots \qquad \text{(E.343)} \\
\sin\left(\beta_0 \cos\left(\Omega_{\text{mod}} t\right)\right) &= 2\sum_{n=0}^{\infty} (-)^n J_{2n+1}\left(\beta_0\right) \cos\left((2n+1)\Omega_{\text{mod}} t\right) \\
&= 2J_1\left(\beta_0\right) \cos\left(\Omega_{\text{mod}} t\right) - \cdots \qquad \text{(E.344)} \\
\cos\left(\beta_0 \sin\left(\Omega_{\text{mod}} t\right)\right) &= J_0\left(\beta_0\right) + 2\sum_{n=1}^{\infty} J_{2n}\left(\beta_0\right) \cos\left(2n\Omega_{\text{mod}} t\right) \\
&= J_0\left(\beta_0\right) + 2J_2\left(\beta_0\right) \cos\left(2\Omega_{\text{mod}} t\right) + \cdots \qquad \text{(E.345)} \\
\cos\left(\beta_0 \cos\left(\Omega_{\text{mod}} t\right)\right) &= J_0\left(\beta_0\right) + 2\sum_{n=1}^{\infty} (-)^n J_{2n}\left(\beta_0\right) \cos\left(2n\Omega_{\text{mod}} t\right) \\
&= J_0\left(\beta_0\right) - 2J_2\left(\beta_0\right) \cos\left(2\Omega_{\text{mod}} t\right) + \cdots \qquad \text{(E.346)}
\end{aligned}$$

E.5 The Effect on Alkali Atoms Due to Polarized Light

E.5.1 Density Matrix

Definition & Basic Properties

To discuss the change in the relative populations of different states due to transitions, it is useful to first introduce the density matrix [14–18]. The density matrix is often used to represent a large ensemble of systems in a statistical mixture of pure quantum states, for example, a vapor of polarized alkali atoms. To be explicit, given a statistical probability p_k of being in the pure quantum state $|\psi_k\rangle$, the density matrix is defined as

$$\rho \equiv \sum_k p_k \left|\Psi_k\right\rangle \left\langle\Psi_k\right| \qquad \text{(E.347)}$$

where $|\Psi_k\rangle$ is, in general, a superposition of eigenstates:

$$|\Psi_k\rangle = \sum_n c_{kn}(t)\,|n\rangle \qquad \& \qquad \langle\Psi_k| = \sum_m c^*_{km}(t)\,\langle m| \tag{E.348}$$

The complex coefficients $c_{kn}(t)$ contain all of the time dependence. For notational convenience we'll drop the (t) and expanding the density matrix in this eigenbasis gives

$$\rho = \sum_{k,m,n} p_k c^*_{km} c_{kn}\,|n\rangle\,\langle m| \tag{E.349}$$

where the matrix elements are

$$\rho_{ba} = \langle b|\,\rho\,|a\rangle = \sum_{k,m,n} p_k c^*_{km} c_{kn}\,\langle b\mid n\rangle\,\langle m\mid a\rangle = \sum_k p_k c^*_{ka} c_{kb} \tag{E.350}$$

The diagonal elements ($b = a$) have a simple and straightforward physical interpretation: they are the combined statistical and quantum mechanical probabilities of being in the eigenstate $|a\rangle$. We've assumed that everything has been normalized properly:

$$\sum_n c^*_{kn} c_{kn} = \sum_n |c_{kn}|^2 = 1 \qquad \& \qquad \sum_k p_k = 1 \tag{E.351}$$

Off-diagonal elements ($b \neq a$) are called coherences and are complex conjugates of each other

$$\rho_{ba} = \rho^*_{ab} \quad \rightarrow \quad \rho = \rho^\dagger \tag{E.352}$$

which implies that the density matrix is Hermitian, by construction.

Time Evolution: Liouville Equation

The time evolution of the density matrix is easily derived by first differentiating with respect to time t

$$\frac{d\rho}{dt} = \dot{\rho} = \sum_k p_k \left(\frac{\partial |\Psi_k\rangle}{\partial t} \langle \Psi_k| + |\Psi_k\rangle \frac{\partial \langle \Psi_k|}{\partial t} \right) \tag{E.353}$$

and then applying Schrodinger equation

$$\frac{\partial |\Psi_k\rangle}{\partial t} = -\frac{i}{\hbar} \mathcal{H} |\Psi_k\rangle \qquad \& \qquad \frac{\partial \langle \Psi_k|}{\partial t} = +\frac{i}{\hbar} \langle \Psi_k| \mathcal{H} \tag{E.354}$$

where $\mathcal{H}$ is the full Hamiltonian of the system. The end result is known as the Liouville equation:

$$\dot{\rho} = -\frac{i}{\hbar} \left(\mathcal{H}\rho - \rho\mathcal{H} \right) = -\frac{i}{\hbar} \left[\mathcal{H}, \rho \right] \tag{E.355}$$

We'll write $\mathcal{H}$ as the sum of the free Hamiltonian $\mathcal{H}_0$ and the interaction term $\mathcal{W}$:

$$\mathcal{H} = \mathcal{H}_0 + \mathcal{W} \qquad \& \qquad \mathcal{H}_0 |n\rangle = \hbar\omega_n |n\rangle \tag{E.356}$$

where the energy associated with the eigenstate n in the free Hamiltonian is $\hbar\omega_n$. Expanding ρ in the eigenbasis of $\mathcal{H}_0$ and collecting terms gives:

$$\dot{\rho} = -\frac{i}{\hbar} \sum_{k,n,m} p_k c^*_{km} c_{kn} \left\{ \left(\hbar\omega_{nm} + \mathcal{W} \right) |n\rangle \langle m| - |n\rangle \langle m| \mathcal{W} \right\} \tag{E.357}$$

where we've set $\omega_{nm} = \omega_n - \omega_m$. Placing this result inside $\langle b| \cdots |a\rangle$ gives the projection:

$$\dot{\rho}_{ba} = -\frac{i}{\hbar} \sum_{k,n,m} p_k c^*_{km} c_{kn} \left\{ \left(\hbar\omega_{nm} \langle b \mid n\rangle + \langle b| \mathcal{W} |n\rangle \right) \langle m \mid a\rangle - \langle b \mid n\rangle \langle m| \mathcal{W} |n\rangle \right\} \tag{E.358}$$

Reducing the sums over n and m by noting $\langle j \mid k\rangle = \delta_{jk}$ gives a set of coupled differential equations:

$$\dot{\rho}_{ba} = -i\omega_{ba}\rho_{ba} - \frac{i}{\hbar} \sum_n \left(\rho_{na} \langle b| \mathcal{W} |n\rangle - \rho_{bn} \langle n| \mathcal{W} |a\rangle \right) \tag{E.359}$$

where we've relabeled the dummy variable of the last term $m \to n$. When there is no interaction ($\mathcal{W} = 0$), the equations become uncoupled:

$$\dot{\rho}_{ba} = -i\omega_{ba}\rho_{ba} \tag{E.360}$$

and are easily solved:

$$\rho_{ba}(t) = \rho_{ba}(0) \exp\left(-i\omega_{ba}t\right) \quad \text{for coherences } (b \neq a) \tag{E.361}$$

$$\rho_{aa}(t) = \rho_a(t) = \rho_a(0) = \text{constant} \quad \text{for populations } (b = a) \tag{E.362}$$

Expectation Values: Trace

The expectation value of some operator $\mathcal{U}$ for a state $|\Psi_k\rangle$ is given by $\langle \mathcal{U} \rangle_k = \langle \Psi_k| \mathcal{U} |\Psi_k\rangle$. For a system in a statistical mixture of pure quantum states, we have

to average $\langle \mathcal{U} \rangle_k$ over all k:

$$\langle \mathcal{U} \rangle = \sum_k p_k \langle \mathcal{U} \rangle_k = \sum_k p_k \langle \Psi_k | \mathcal{U} | \Psi_k \rangle = \sum_{k,n,m} p_k c_{km}^* c_{kn} \langle m | \mathcal{U} | n \rangle = \sum_{n,m} \langle n | \rho | m \rangle \langle m | \mathcal{U} | n \rangle \tag{E.363}$$

We can write this sum in a more illuminating way by inserting three copies of the complete projection operator $1 = \sum_a |a\rangle \langle a|$:

$$\sum_{n,m} \langle n | \rho | m \rangle \langle m | \mathcal{U} | n \rangle = \sum_{n,m} \langle n | \left(\sum_a |a\rangle \langle a| \right) \rho \left(\sum_b |b\rangle \langle b| \right) |m\rangle \langle m | \mathcal{U} \left(\sum_\ell |\ell\rangle \langle \ell| \right) |n\rangle \tag{E.364}$$

When we group the sums appropriately, we find:

$$\sum_n \langle n | \left(\sum_{a,b} |a\rangle \langle a| \rho |b\rangle \langle b| \right) \left(\sum_{m,\ell} |m\rangle \langle m| \mathcal{U} |\ell\rangle \langle \ell| \right) |n\rangle = \sum_n \langle n | \rho \mathcal{U} | n \rangle \tag{E.365}$$

The action defined by $\sum_n \langle n | (\cdots) | n \rangle$ is simply the sum of the diagonal elements of the enclosed matrix, in other words: the trace $\mathrm{Tr}(\cdots)$. To summarize, in the density matrix formulation, the expectation value of some operator $\mathcal{U}$ is given by the trace of the product $\rho\mathcal{U}$:

$$\langle \mathcal{U} \rangle = \mathrm{Tr}(\mathcal{U}\rho) = \mathrm{Tr}(\rho\mathcal{U}) = \sum_{n,m} \langle n | \rho | m \rangle \langle m | \mathcal{U} | n \rangle \tag{E.366}$$

E.5.2 General Electromagnetic Dipole Interaction

Dipole Moment Operator

The interaction of light with an alkali atom can be written semiclassically as:

$$\mathcal{W} = -\vec{m} \cdot \Re \vec{F}(\vec{r}, t) \tag{E.367}$$

where $\vec{F}$ is the field component of the incident light *in the complex representation* and $\vec{m}$ is a dipole moment operator of the form:

$$\vec{m} = \sum_q m_0 \mathcal{U}_q \hat{\varepsilon}_q^* \tag{E.368}$$

where m_0 is magnitude of the moment and $\{\hat{\varepsilon}_q^*\}$ are unit basis vectors. The operator associated with the dipole moment, $\mathcal{U}_q$, connects the eigenstate m with the eigenstate $m+q$:

$$\mathcal{U}_q = \sum_{m,n} \delta_{m+q,n} \left|n\right\rangle \left\langle n\right| \mathcal{U}_q \left|m\right\rangle \left\langle m\right| = \sum_m \left|m+q\right\rangle \left\langle m+q\right| \mathcal{U}_q \left|m\right\rangle \left\langle m\right| \tag{E.369}$$

A subtle point to note is that the interaction depends only on *the real part of the field*. To be explicit, the real part of the field in the complex representation is:

$$\Re\vec{F}(\vec{r},t) = \Re\vec{F}_0 \exp(i\vec{k}\cdot\vec{r} - \omega t) = F_0 \left[\hat{F}_0 \exp(i\vec{k}\cdot\vec{r} - i\omega t) + \hat{F}_0^* \exp(-i\vec{k}\cdot\vec{r} + i\omega t)\right] \tag{E.370}$$

where F_0 is the real magnitude of the field, $\hat{F}_0$ is the complex unit polarization vector, $\vec{k}$ is the wave vector of the light, $\vec{r}$ is its direction of propagation, and ω is the angular frequency.

Dipole Approximation

We'll make the dipole approximation by noting:

$$|\vec{k}\cdot\vec{r}| \;=\; kr = \frac{2\pi r}{\lambda} \approx \frac{2\pi 5 a_0}{\lambda} \approx \frac{2\pi 5(0.053\text{ nm})}{780\text{ nm}} \approx 0.002 \ll 1 \tag{E.371}$$

where a_0 is the Bohr radius ($5a_0$ is the characteristic scale of an K or Rb atom) and λ is the wavelength of the light. Shorter wavelengths correspond to the transitions with the larger energy differences. The transitions with the largest energy differences that we'll be discussing are the $D1$ and $D2$ transitions of alkali atoms. For K and Rb, this is around 780 nm, therefore, the dipole approximation is a very good one under our conditions. Physically, this means that the amplitude of the electromagnetic wave hitting the atom does not vary much in amplitude over the size scale of the atom. As a consequence, we'll drop the $\vec{k}\cdot\vec{r}$ term and write the interaction as:

$$\mathcal{W} = -m_0 F_0 \sum_q \mathcal{U}_q \left[\hat{\varepsilon}_q^* \cdot \hat{F}_0 \exp(-i\omega t) + \hat{\varepsilon}_q^* \cdot \hat{F}_0^* \exp(+i\omega t)\right] = -\hbar\Omega \sum_{q,s} \left\{u_q^s \exp(+is\omega t)\mathcal{U}_q\right\} \tag{E.372}$$

where $s = \pm 1$ and we've made the following substitutions:

$$\hbar\Omega = m_0 F_0 \quad u_q^- = \hat{\varepsilon}_q^* \cdot \hat{F}_0 \quad u_q^+ = \hat{\varepsilon}_q^* \cdot \hat{F}_0^* \tag{E.373}$$

Since $\mathcal{W}$ is Hermitian, $(\mathcal{U}_q)^\dagger = \mathcal{U}_{-q}$ and consequently $\left(u_q^s\right)^* = u_{-q}^{-s}$.

Coherences

Plugging the general dipole interaction, Eqn. (E.372), into the Liouville equation, Eqn. (E.359), gives:

$$\begin{aligned}
\dot{\rho}_{ba} &= -i\omega_{ba}\rho_{ba} + i\Omega \sum_{q,s,n,m} u_q^s \exp(+is\omega t)\{\cdots\} \qquad \text{(E.374)}\\
\cdots &= \rho_{na}\langle b \mid m+q\rangle \langle m+q|\,\mathcal{U}_q\,|m\rangle \langle m \mid n\rangle - \rho_{bn}\langle n \mid m+q\rangle \langle m+q|\,\mathcal{U}_q\,|m\rangle \langle m \mid a\rangle
\end{aligned}$$

Reducing the sum over n and m gives:

$$\dot{\rho}_{ba} = -i\omega_{ba}\rho_{ba} + i\Omega\sum_{q,s} u_q^s \exp(+is\omega t)\left\{\rho_{b-q,a}\left\langle b\right|\mathcal{U}_q\left|b-q\right\rangle - \rho_{b,a+q}\left\langle a+q\right|\mathcal{U}_q\left|a\right\rangle\right\} \tag{E.375}$$

For the $q = b - a$ term in the sum, the matrix elements of ρ in that term are populations. For the remaining terms in the sum, $q \neq b - a$ and the matrix elements of ρ in those terms are coherences. As we'll see shortly, this is a vital difference, so we'll explicitly separate the $q = b - a$ term from the sum:

$$\dot{\rho}_{ba} = -i\omega_{ba}\rho_{ba} + i\Omega\sum_{s}\exp(+is\omega t)\left(U_{\text{pop}}^{s,q=b-a} + \sum_q U_{\text{coh}}^{s,q\neq b-a}\right) \tag{E.376}$$

$$U_{\text{pop}}^{s,q=b-a} = u_{b-a}^s\left(\rho_a - \rho_b\right)\left\langle b\right|\mathcal{U}_{b-a}\left|a\right\rangle \tag{E.377}$$

$$U_{\text{coh}}^{s,q\neq b-a} = u_q^s\left\{\rho_{b-q,a}\left\langle b\right|\mathcal{U}_q\left|b-q\right\rangle - \rho_{b,a+q}\left\langle a+q\right|\mathcal{U}_q\left|a\right\rangle\right\} \tag{E.378}$$

Relaxation

Up to now, we've only considered transitions due to our interaction term $\mathcal{W}$. In reality, there are other processes that cause transitions that drive the system toward thermodynamic equilibrium. We'll account for these "relaxation" processes by adding a relaxation term "by-hand:"

$$\dot{\rho}_{ba} = -i\omega_{ba}\rho_{ba} - \gamma_{ba}\rho_{ba} + i\Omega\sum_{s}\exp(+is\omega t)\left(U_{\text{pop}}^{s,q=b-a} + \sum_q U_{\text{coh}}^{s,q\neq b-a}\right) \tag{E.379}$$

where γ_{ba} is the relaxation rate and, by construction, $\gamma_{ba} = \gamma_{ab}$.

Solving this set of differential equations would be much easier if they weren't coupled (contained different coherences). To a very good approximation, we can decouple these equations by making the following arguments. First, we'll make an

educated guess for the form of the coherences $\rho_{ba}(t)$. When there is no interaction, the entire time dependence of the coherences is given by $\exp(-i\omega_{ba}t)$. Since we're now driving the system with a frequency of ω, it is not unreasonable to think that the time dependence of the coherences is now $\exp(\mp i\omega t)$, where the negative (positive) sign is chosen when ω_{ba} is positive (negative). Plugging in $C_{ba}(t)\exp(\mp i\omega t)$ for the coherences $b \neq a$ on both sides of the equation give:

$$\begin{aligned}(\mp i\omega C_{ba} + \dot{C}_{ba})\exp(\mp i\omega t) &= -i\left(\omega_{ba} - i\gamma_{ba}\right)C_{ba}\exp(\mp i\omega t) \\ &\quad + i\Omega\sum_s \exp(+is\omega t)\left(U_{\text{pop}}^{s,q=b-a} + \exp(\mp i\omega t)\sum_q \bar{U}_{\text{coh}}^{s,q\neq b-a}\right)\end{aligned} \tag{E.380}$$

where the terms in the sum over q proportional to coherences is given by:

$$\bar{U}_{\text{coh}}^{s,q\neq b-a} = u_q^s\left\{C_{b-q,a}\left\langle b\right|\mathcal{U}_q\left|b-q\right\rangle - C_{b,a+q}\left\langle a+q\right|\mathcal{U}_q\left|a\right\rangle\right\} \tag{E.381}$$

Multiplying both sides by $\exp(\pm i\omega t)$, dividing by i, and moving a few things around gives:

$$-i\dot{C}_{ba} = (\pm\omega - \omega_{ba} + i\gamma_{ba})C_{ba} + \Omega\sum_s \exp(+i(s\pm 1)\omega t)\times \tag{E.382}$$

$$\left(U_{\text{pop}}^{s,q=b-a} + \exp(\mp i\omega t)\sum_q \bar{U}_{\text{coh}}^{s,q\neq b-a}\right) \tag{E.383}$$

Rotating Wave Approximation

We're now in a position to take the second step, which is called the rotating wave approximation [19]: we simply drop any of the remaining oscillatory terms, namely

ones with a factor of $\exp(\pm ni\omega t)$ with $n \neq 0$:

$$-i\dot{C}_{ba} = (\pm\omega - \omega_{ba} + i\gamma_{ba})C_{ba} + \Omega U_{\text{pop}}^{s=\mp,q=b-a} \tag{E.384}$$

This is a completely uncoupled set of equations! The only term left that could possibly have any time dependence is C_{ba}. The last step in solving these equations is to choose C_{ba} to be a constant:

$$\begin{aligned} -i\dot{C}_{ba} = 0 &= (\pm\omega - \omega_{ba} + i\gamma_{ba})C_{ba} + \Omega U_{\text{pop}}^{s=\mp,q=b-a} && \text{(E.385)} \\ &= (\pm\omega - \omega_{ba} + i\gamma_{ba})C_{ba} + \Omega u_{b-a}^{\mp}(\rho_a - \rho_b)\langle b|\,\mathcal{U}_{b-a}\,|a\rangle && \text{(E.386)} \end{aligned}$$

This is just an algebraic equation which is solved very simply by:

$$C_{ba} = \frac{u_{b-a}^{\mp}\Omega(\rho_b - \rho_a)\langle b|\,\mathcal{U}_{b-a}\,|a\rangle}{\pm\omega - \omega_{ba} + i\gamma_{ba}} \tag{E.387}$$

which immediately gives:

$$\rho_{ba} = \frac{u_{b-a}^{\mp}\Omega(\rho_b - \rho_a)\langle b|\,\mathcal{U}_{b-a}\,|a\rangle}{\pm\omega - \omega_{ba} + i\gamma_{ba}}\exp(\mp i\omega t) \tag{E.388}$$

Changes in Population

Since we have a solution for the coherences ($b \neq a$), we now consider the coupled differential equations for the populations ($b = a$):

$$\begin{aligned} \dot{\rho}_a &= -i\omega_{aa}\rho_a + i\Omega\sum_s \exp(+is\omega t)\left(U_{\text{pop}}^{s,q=a-a} + \sum_q U_{\text{coh}}^{s,q\neq a-a}\right) && \text{(E.389)} \\ U_{\text{pop}}^{s,q=a-a} &= u_{a-a}^{s}(\rho_a - \rho_a)\langle a|\,\mathcal{U}_{a-a}\,|a\rangle = 0 && \text{(E.390)} \\ U_{\text{coh}}^{s,q\neq a-a} &= u_q^s\left\{\rho_{a-q,a}\langle a|\,\mathcal{U}_q\,|a-q\rangle - \rho_{a,a+q}\langle a+q|\,\mathcal{U}_q\,|a\rangle\right\} && \text{(E.391)} \end{aligned}$$

Up to now, we've been a little sloppy with the notation $q = b - a$, etc. What we have meant is that the operator associated with q is the "difference" between eigenstates b and a. In practice, q, b, and a can be made into numbers if b and a happen to be observables and not just labels for the eigenstates. This can be done if we label eigenstates as J, m where J & m represent eigenvalues associated with that eigenstate. Before going on, we should rewrite the coherences in this new notation:

$$\rho_{Ka+qJa} = \frac{u_q^{\mp}\Omega\left(\rho_{Ka+q} - \rho_{Ja}\right)\langle K, a+q|\,\mathcal{U}_q\,|J,a\rangle}{\pm\omega - \omega_{Ka+qJa} + i\gamma_{Ka+qJa}}\exp(\mp i\omega t) \tag{E.392}$$

where we've made the substitution $b = a + q$. The complex conjugate of this coherence is:

$$\rho^*_{Ka+qJa} = \rho_{JaKa+q} = \frac{\left(u_q^{\mp}\right)^*\Omega\left(\rho_{Ka+q} - \rho_{Ja}\right)\langle J, a|\,\mathcal{U}_{-q}\,|K,a+q\rangle}{\pm\omega - \omega_{Ka+qJa} - i\gamma_{JaKa+q}}\exp(\pm i\omega t) \tag{E.393}$$

Dropping terms that contain $\omega_{aa} = 0$ & $(\rho_a - \rho_a)$, the differential equations for the populations is rewritten as:

$$\dot{\rho}_{Ja} = i\Omega\sum_{K,s,q} u_q^s \exp(+is\omega t)\left\{\rho_{Ka-q,Ja}\langle J, a|\,\mathcal{U}_q\,|K,a-q\rangle - \rho_{Ja,Ka+q}\langle K, a+q|\,\mathcal{U}_q\,|J,a\rangle\right\} \tag{E.394}$$

These equations are coupled only to coherences, which we already have expressions for. Before plugging in the coherences, we'll derive an alternate form of the first sum by reversing the sum by $s, q \to -s, -q$ using the Hermiticity of $\mathcal{W}$ & ρ in

the form of $u_{-q}^{-s} = \left(u_q^s\right)^*$, $\rho_{Ka+q,Ja} = \rho_{Ja,Ka+q}^*$, & $\mathcal{U}_{-q} = \mathcal{U}_q^\dagger$:

$$\begin{aligned}
&\sum_{s,q} u_q^s \exp(+is\omega t)\rho_{Ka-q,Ja} \langle J,a| \mathcal{U}_q |K,a-q\rangle \\
&= \sum_{s,q} u_{-q}^{-s} \exp(-is\omega t)\rho_{Ka+q,Ja} \langle J,a| \mathcal{U}_{-q} |K,a+q\rangle \\
&= \sum_{s,q} \left[u_q^s \exp(+is\omega t)\rho_{Ja,Ka+q} \langle K,a+q| \mathcal{U}_q |J,a\rangle\right]^*
\end{aligned}$$

This shows that the first sum is just the complex conjugate of the second sum. Using the identity $z^* - z = -2i\Im\{z\}$, we can now write $\dot{\rho}_{Ja}$ as just the imaginary part of the second sum:

$$\dot{\rho}_{Ja} = 2\Omega \sum_{K,s,q} \Im\left\{u_q^s \exp(+is\omega t)\rho_{Ja,Ka+q} \langle K,a+q| \mathcal{U}_q |J,a\rangle\right\} \tag{E.395}$$

Plugging in the form of the coherence $\rho_{Ja,Ka+q} = \rho_{Ka+q,Ja}^*$, gives:

$$\begin{aligned}
\dot{\rho}_{Ja} \;=\; & 2\Omega^2 \sum_{K,s,q} \Im\Big\{u_q^s (u_q^{\mp})^* \exp(+i(s\pm 1)\omega t) \\
& \times \frac{\left(\rho_{Ka+q} - \rho_{Ja}\right) \langle K,a+q| \mathcal{U}_q |J,a\rangle^*}{\pm\omega - \omega_{Ka+qJa} - i\gamma_{Ka+qJa}} \langle K,a+q| \mathcal{U}_q |J,a\rangle \Big\}
\end{aligned} \tag{E.396}$$

Applying the rotating wave approximation once again, namely keeping only the $s = \mp 1$ terms, gives:

$$\dot{\rho}_{Ja} = 2\Omega^2 \sum_{K,q} \left|u_q^{\mp}\right|^2 \left(\rho_{Ka+q} - \rho_{Ja}\right) \left|\langle K,a+q| \mathcal{U}_q |J,a\rangle\right|^2 \Im\left\{\left(\pm\omega - \omega_{Ka+qJa} - i\gamma_{Ka+qJa}\right)^{-1}\right\} \tag{E.397}$$

After collecting all common factors, we find that the denominator is the only complex quantity. We can find the imaginary part of it by multiplying the top & bottom

by the complex conjugate of the bottom. This finally gives:

$$\dot{\rho}_{Ja} = 2\Omega^2 \sum_{K,q} \frac{\gamma_{Ka+qJa} \left(\rho_{Ka+q} - \rho_{Ja}\right) \left|u_q^{\mp}\right|^2 \left|\langle K, a+q| \, \mathcal{U}_q \, |J, a\rangle\right|^2}{\left(\pm\omega - \omega_{Ka+qJa}\right)^2 + \gamma_{Ka+qJa}^2} \tag{E.398}$$

Expectation Value of the Dipole Moment Operator

It is often useful to calculate the expectation value of the very operators causing the transitions. For the case of a general harmonic interaction, this means calculating the expectation value of $\mathcal{U}_q$:

$$\langle \mathcal{U}_q \rangle = \sum_{K,n,J,m} \langle K, n| \, \rho \, |J, m\rangle \, \langle J, m| \, \mathcal{U}_q \, |K, n\rangle = \sum_{K,n,J} \langle K, n| \, \rho \, |J, n+q\rangle \, \langle J, n+q| \, \mathcal{U}_q \, |K, n\rangle \tag{E.399}$$

There are two different cases which result in either a sum over populations or a sum over coherences. For the case ($K = J$ & $q = 0$), we get a sum over populations:

$$\langle \mathcal{U}_0 \rangle = \sum_{n,J} \rho_{Jn} \, \langle J, n| \, \mathcal{U}_0 \, |J, n\rangle \tag{E.400}$$

For all cases other than ($K = J$ & $q = 0$), we get a sum over coherences due to $\sum_q \mathcal{U}_q$, which we've already calculated, and plugging them in gives:

$$\langle \mathcal{U}_q \rangle = \sum_{K,n,J} \left\{ \frac{\Omega \left(\rho_{Jn+q} - \rho_{Kn}\right) \left(u_q^{\mp}\right)^* \left|\langle J, n+q| \, \mathcal{U}_q \, |K, n\rangle\right|^2}{\pm\omega - \omega_{Jn+qKn} - i\gamma_{Jn+qKn}} \times \exp(\pm i\omega t) \right\} \tag{E.401}$$

Electric Dipole Interaction for the $^{2S+1}L_J$ Orbital States

The interaction between the atom and the electric field component of the light is:

$$\mathcal{W} = -\vec{d} \cdot \Re\vec{E}(\vec{r}, t) \tag{E.402}$$

The electric dipole operator $\vec{d}$ is given by the sum $\sum_k q_k \vec{r}_k$, where q_k & $\vec{r}_k$ are the charge & relative position of the k-th particle in the atom. If we take the nucleus to be infinitely heavy and measure the position of the electrons relative to it, then the dipole operator is reduced to the sum over all electrons. Since we're only going to be considering transitions of the single valence electron of an alkali atom, the sum further reduces to a single term which results in $\vec{d} = -e\vec{r}$. The position vector of the valence electron, $\vec{r}$, can be expanded in the irreducible spherical vector basis $\sum_{q=-1}^{+1} r_q \hat{\varepsilon}_q^*$. We can now identify the parameters from the general dipole interaction Eqn. (E.372) as:

$$\mathcal{U}_q = r_q \quad \hbar\Omega = -eE_0 \quad u_q^- = \hat{\varepsilon}_q^* \cdot \hat{E}_0 \quad u_q^+ = \hat{\varepsilon}_q^* \cdot \hat{E}_0^* \tag{E.403}$$

The relevant atomic states are the $S_{1/2}$ ground state and the mixed $P_{1/2}$ & $P_{3/2}$ excited states, see Sec. (E.2.4). Therefore the electric dipole transition matrix elements are $\langle P_\pm, m+q | \, r_q \, | S, m \rangle$ and their complex conjugates for all m & q.

Magnetic Dipole Interaction for the $|F, m\rangle$ Hyperfine States

The interaction between the atom and the magnetic field component of the light is:

$$\mathcal{W} = -\vec{\mu} \cdot \Re\vec{B}(\vec{r}, t) \tag{E.404}$$

In this case, the light is in the form of radio-frequency (RF) waves. The magnetic moment operator is the sum of nuclear magnetic moment $\vec{\mu}_I$ and the total electronic magnetic moment $\vec{\mu}_J$. Since $|\vec{\mu}_I| \ll |\vec{\mu}_J|$, we'll ignore the coupling to the nuclear spin. In the $S_{1/2}$ ground state of an alkali atom, $J = S = 1/2 (L = 0)$ and therefore the magnetic moment can written in terms of the spin-1/2 angular momentum operators:

$$\vec{\mu} = g_S \mu_B \vec{S} = -g_S \mu_B \left(S_x \hat{x} + S_y \hat{y} + S_z \hat{z} \right) = g_S \mu_B \left(S_+ \hat{\varepsilon}_+^* + S_- \hat{\varepsilon}_-^* + S_z \hat{\varepsilon}_0^* \right) \tag{E.405}$$

where $S_\pm = S_x \pm i S_y$ and the unit vectors $\hat{\varepsilon}_q$ are *not* the same unit vectors used for the electric dipole operator from the previous section:

$$\hat{\varepsilon}_\pm^* = \frac{\hat{x} \mp i\hat{y}}{2} \qquad \hat{\varepsilon}_0 = \hat{z} \tag{E.406}$$

We can now identify the parameters from the general dipole interaction Eqn. (E.372) as:

$$\mathcal{U}_q = S_q \quad \hbar\Omega = g_S \mu_B B_{\mathtt{rf}} \quad u_q^- = \hat{\varepsilon}_q^* \cdot \hat{B}_{\mathtt{rf}} \quad u_q^+ = \hat{\varepsilon}_q^* \cdot \hat{B}_{\mathtt{rf}}^* \tag{E.407}$$

The relevant atomic states are the mixed hyperfine states in the $F = I \pm 1/2$ manifolds, see Sec. (E.3.4). We will only consider RF frequencies small enough to induce transitions *within* a manifold and *not between* manifolds. Therefore the magnetic dipole transition matrix elements are $\langle F, m+q | S_q | F, m \rangle$ and their complex conjugates for all m & q.

E.5.3 Electric Dipole Matrix Elements: Oscillator Strength

Wigner-Eckart Theorem

The probability that an electric dipole transition occurs from an initial state a to a final state b is proportional to the modulus squared matrix element of the component of the dipole operator that is parallel to the polarization vector of the light:

$$\left|\langle b|\,\vec{\varepsilon}\cdot\hat{\vec{d}}|a\rangle\right|^2 = \left|\langle b|\,\vec{\varepsilon}\cdot\left(-e\hat{\vec{r}}\right)|a\rangle\right|^2 = e^2\left|\langle b|\,\vec{\varepsilon}\cdot\hat{\vec{r}}|a\rangle\right|^2 \tag{E.408}$$

When the dipole operator, or analogously the radius vector operator, is written as a tensor of rank one using the Wigner-Eckart theorem. The theorem was originally derived from group theory considerations and factorizes the matrix element of a tensor operator T_q^k between states labeled with quantum numbers n_i, n_f and angular momentum (J_i, m_i) and $\left(J_f, m_f\right)$ into two parts:

$$\left\langle J_f, m_f\right|\hat{T}_q^k\left|J_i, m_i\right\rangle = \text{CG}\left(\vec{J_i}+\vec{k}=\vec{J_f}\;;\; m_i, q, m_f\right)\times\ \text{R.M.E.}\left(n_f, J_f; n_i, J_i\right) \tag{E.409}$$

The first part is simply a Clebsch-Gordon coefficient for the addition of angular momenta such that $\vec{J_i}+\vec{k}=\vec{J_f}$ with m_i, m_f, q. The second part, called the reduced matrix element, is a term *with the essential property that it is independent of* m_i, q, m_f. The exact form of the reduced matrix element is somewhat arbitrary so long as it is independent of m_i, q, m_f and behaves mathematically appropriately. By this, we mean that the matrix element is a complex number or equivalently the modulus square matrix element is non-negative. One form of the reduced matrix element

that is often *chosen* in textbooks (for example equation XIII.125 of *Messiah* [20]) is:

$$\text{R.M.E.} = \frac{1}{\sqrt{[J_f]}} \times \left\langle n_f, J_f \middle\| T^k \middle\| n_i, J_i \right\rangle \tag{E.410}$$

For the present discussion, we will drop the n_i and n_f labels because the D1 and D2 transitions of alkali metals occur within the same n. To insure positive definiteness of the modulus square matrix element, we'll explicitly give ourselves flexibility with the phase:

$$\text{R.M.E.} = \frac{(\pm)_{fi}}{\sqrt{[J_f]}} \times i \times \left\langle J_f \middle\| T^k \middle\| J_i \right\rangle \tag{E.411}$$

The phase ambiguity of the reduced matrix element is related to the choice made in defining the phase convention of the Clebsch-Gordon coefficients. Using the notation of *Messiah*, the Wigner-Eckart Theorem [21, 22] can be expressed as:

$$\left\langle J_f, m_f \middle| \hat{T}^k_q \middle| J_i, m_i \right\rangle = i \frac{(\pm)_{fi}}{\sqrt{[J_f]}} \left\langle (J_i, k)\, m_i, q \middle| J_f, m_f \right\rangle \left\langle J_f \middle\| T^k \middle\| J_i \right\rangle \tag{E.412}$$

Phase Convention and Positive Definiteness

Care must be taken in *choosing* the phase convention when evaluating these matrix elements using the Wigner-Eckart theorem. Let's consider the modulus square matrix element of a component q of the radius vector operator $\hat{\vec{r}}$ in the spherical tensor basis ($k = 1$):

$$\begin{aligned}
\left| \left\langle J_f, m_f \middle| r_q \middle| J_i, m_i \right\rangle \right|^2 &= \left\langle J_f, m_f \middle| r_q \middle| J_i, m_i \right\rangle^* \left\langle J_f, m_f \middle| r_q \middle| J_i, m_i \right\rangle && \text{(E.413)} \\
&= \left\langle J_i, m_i \middle| r^*_q \middle| J_f, m_f \right\rangle \left\langle J_f, m_f \middle| r_q \middle| J_i, m_i \right\rangle && \text{(E.414)} \\
&= (-1)^q \left\langle J_i, m_i \middle| r_{-q} \middle| J_f, m_f \right\rangle \left\langle J_f, m_f \middle| r_q \middle| J_i, m_i \right\rangle && \text{(E.415)}
\end{aligned}$$

Before expanding these matrix elements using the WET, we'll introduce the Wigner $3j$ symbol [22] which is related to the Clebsch-Gordon coefficients by:

$$\begin{pmatrix} J_i & k & J_f \\ m_i & q & -m_f \end{pmatrix} = \frac{(-1)^{J_i-k+m_f}}{\sqrt{[J_f]}} \left\langle (J_i,k)\, m_i, q | J_f, m_f \right\rangle \delta_{m_i+q=m_f} \tag{E.416}$$

where the Kronecker Delta insures that angular momentum is conserved ($m_i + q = m_f$). Their utility lies in the fact that they make the symmetry properties of Clebsch-Gordon coefficients more apparent under the cyclic permutation of all three columns, the interchange of two columns, and the replacement of the second row with its negative:

$$\begin{pmatrix} J_i & k & J_f \\ m_i & q & -m_f \end{pmatrix} = \begin{pmatrix} J_f & J_i & k \\ -m_f & m_i & q \end{pmatrix} = \begin{pmatrix} k & J_f & J_i \\ q & -m_f & m_i \end{pmatrix} \tag{E.417}$$

$$= (-1)^{J_i+k+J_f} \begin{pmatrix} k & J_i & J_f \\ q & m_i & -m_f \end{pmatrix} \tag{E.418}$$

$$= (-1)^{J_i+k+J_f} \begin{pmatrix} J_i & k & J_f \\ -m_i & -q & m_f \end{pmatrix} \tag{E.419}$$

Expanding the modulus squared matrix element using Wigner $3j$ symbol, en-

forcing $m_f = m_i + q$, and moving things around:

$$\begin{aligned}
\left|\langle r_q \rangle\right|^2 &= (-1)^q \langle J_i, m_i | r_{-q} | J_f, m_i + q \rangle \langle J_f, m_i + q | r_q | J_i, m_i \rangle && \text{(E.420)} \\
&= (-1)^q i (\pm)_{if} (-1)^{J_f - 1 + m_i} \begin{pmatrix} J_f & 1 & J_i \\ m_i + q & -q & -m_i \end{pmatrix} \langle J_i \| r \| J_f \rangle \\
&\quad \times (i)(\pm)_{fi} (-1)^{J_i - 1 + m_i + q} \begin{pmatrix} J_i & 1 & J_f \\ m_i & q & -(m_i + q) \end{pmatrix} \langle J_f \| r \| J_i \rangle && \text{(E.421)} \\
&= (\pm)_{fi} (\pm)_{if} (-1)^{J_f + J_i + 2m_i + 1} \begin{pmatrix} J_f & 1 & J_i \\ m_i + q & -q & -m_i \end{pmatrix} \\
&\quad \times \begin{pmatrix} J_i & 1 & J_f \\ m_i & q & -(m_i + q) \end{pmatrix} \left|\langle J_f \| r \| J_i \rangle\right|^2 && \text{(E.422)} \\
&= (\pm)_{fi} (\pm)_{if} (-1)^{2J_f + 2J_i + 2m_i + 2} \begin{pmatrix} J_i & 1 & J_f \\ -m_i & -q & m_i + q \end{pmatrix} \\
&\quad \times \begin{pmatrix} J_i & 1 & J_f \\ m_i & q & -(m_i + q) \end{pmatrix} \left|\langle J_f \| r \| J_i \rangle\right|^2 && \text{(E.423)} \\
&= (\pm)_{fi} (\pm)_{if} (-1)^{3J_f + 3J_i + 2m_i + 1} \begin{pmatrix} J_i & 1 & J_f \\ m_i & q & -(m_i + q) \end{pmatrix} \\
&\quad \times \begin{pmatrix} J_i & 1 & J_f \\ m_i & q & -(m_i + q) \end{pmatrix} \left|\langle J_f \| r \| J_i \rangle\right|^2 && \text{(E.424)} \\
&= (\pm)_{fi} (\pm)_{if} (-1)^{3J_f + 3J_i + 2m_i + 1} \begin{pmatrix} J_i & 1 & J_f \\ m_i & q & -(m_i + q) \end{pmatrix}^2 \left|\langle J_f \| r \| J_i \rangle\right|^2 && \text{(E.425)}
\end{aligned}$$

The last two terms are positive. For the left hand side of the equation to be positive

(as it should be), the following must be true for D1 transitions ($J_i, |m_i|, J_f = \frac{1}{2}$):

$$
\begin{aligned}
+1 &= [(\pm)_{fi}(\pm)_{if}]_{\frac{1}{2}}(-1)^{\frac{3}{2}+\frac{3}{2}\pm 1+1} && \text{(E.426)}\\
&= [(\pm)_{fi}(\pm)_{if}]_{\frac{1}{2}}(-1)^{4\pm 1} && \text{(E.427)}\\
&= -[(\pm)_{fi}(\pm)_{if}]_{\frac{1}{2}} && \text{(E.428)}\\
s_1 &= \left[(\pm)_{fi}\right]_{\frac{1}{2}} = -[(\pm)_{if}]_{\frac{1}{2}} && \text{(E.429)}
\end{aligned}
$$

For D2 transitions, the corresponding relations are ($J_i, |m_i| = \frac{1}{2}; J_f = \frac{3}{2}$):

$$
\begin{aligned}
+1 &= [(\pm)_{fi}(\pm)_{if}]_{\frac{3}{2}}(-1)^{\frac{9}{2}+\frac{3}{2}\pm 1+1} && \text{(E.430)}\\
&= [(\pm)_{fi}(\pm)_{if}]_{\frac{3}{2}}(-1)^{7\pm 1} && \text{(E.431)}\\
&= [(\pm)_{fi}(\pm)_{if}]_{\frac{3}{2}} && \text{(E.432)}\\
s_2 &= \left[(\pm)_{fi}\right]_{\frac{3}{2}} = [(\pm)_{if}]_{\frac{3}{2}} && \text{(E.433)}
\end{aligned}
$$

In both cases, we have hidden the sign in an s factor. The positive definiteness of the modulus square matrix element defines for the phase convention of the reduced matrix element. For a D1 transition, the reduced matrix elements for a matrix element and its complex conjugate must have opposite signs. However, the reduced matrix elements for a D2 matrix element and its complex conjugate must have the same sign.

Connecting the Radial Integral to Physical Observables

The double barred term $\langle b \| T^k \| a \rangle$ of the reduced matrix element (also sometimes called the reduced matrix element itself) is a radial integral. In practice, rather than being calculated from first principles, the value of the radial integral for the radius

vector between atomic states is inferred from measurements of the natural atomic lifetimes. The spontaneous decays of the $P_{\frac{1}{2}}$ and $P_{\frac{3}{2}}$ excited states for neutral alkali atoms are dominated by the D1 and D2 transitions. Therefore the lifetime τ of these states are nearly equal to the inverse of the spontaneous decay probability rate (as known as the Einstein A coefficient), see equation 4.23 of *Corney* [23]:

$$\tau_b^{-1} = A_b = \frac{e^2\omega_{ab}^3}{3\pi\epsilon_0\hbar c^3}\frac{\sum_{m_b}}{[J_b]}\sum_{m_a}\left|\langle J_a, m_a|\,\hat{\vec{r}}\,|J_b, m_b\rangle\right|^2 \tag{E.434}$$

$$= \frac{4\alpha\omega_{ab}^3}{3c^2}\underbrace{\frac{\sum_{m_b}}{[J_b]}}_{\text{mean}}\underbrace{\sum_{m_a}}_{\text{sum}}\left|\langle J_a, m_a|\,\hat{\vec{r}}\,|J_b, m_b\rangle\right|^2 \tag{E.435}$$

where A_b is averaged over all the initial (upper m_b) states and summed over all the final (lower m_a) states. Typical lifetimes for alkali metals are tens of nanoseconds, see table blah. Another form of the averaged, summed modulus square matrix element is the oscillator strength. In the classical picture, an atom is modeled as a collection of many damped oscillators with frequencies that correspond to all possible atomic transitions. An atom in a state a can make transitions to other states through a subset of oscillators that connect that state with all other states. The fraction of oscillators that connect state a to another state b is called the oscillator strength. For absorption (emission), the oscillator strength is chosen to be positive (negative) by convention. Just as for the probability rate, the modulus square matrix element is averaged over initial (lower m_a) states and summed over final (upper m_b) states. For transitions from initial state a to final state b, where the sign is chosen based on the physical process under consideration, the oscillator strength is:

$$f_{a\to b} = \pm\frac{2m\omega_{ab}}{3\hbar}\frac{\sum_{m_a}}{2J_a+1}\sum_{m_b}|\langle J_a, m_b|\,\vec{r}\,|J_a, m_b\rangle|^2 \tag{E.436}$$

By convention, we will always refer to the absorption oscillator strength unless otherwise noted. In addition, since we will always be discussing transitions from the $S_{\frac{1}{2}}$ ground states to one of either the $P_{\frac{1}{2}}$ or $P_{\frac{3}{2}}$ excited states, the oscillator strength will simply be labeled by the J of the final excited state.

Both the oscillator strength and the spontaneous decay rate involve sums over the initial and final m states. This sum, which depends only on J_a, J_b, and the reduced matrix element, is called the line strength (first introduced on page 98 of *Condon & Shortley* [24]) and for transitions between the lower state a and the higher state b, it is given by:

$$
\begin{aligned}
S_{ab} = S_{ba} &= \sum_{m_a}\sum_{m_b}\left|\langle J_a, m_a|\, e\hat{\vec{r}}|J_b, m_b\rangle\right|^2 && \text{(E.437)}\\
&= \sum_{m_a}\sum_{m_b}\left|\langle J_b, m_b|\, e\hat{\vec{r}}|J_a, m_a\rangle\right|^2 && \text{(E.438)}\\
&= \frac{3\hbar e^2}{2m\omega_{ab}}\cdot[J_a]f_b && \text{(E.439)}\\
&= \frac{3c^2[J_b]e^2}{4\alpha\omega_{ab}^3}\cdot\frac{1}{\tau_b} && \text{(E.440)}\\
&= \frac{3\pi\epsilon_0\hbar c^3[J_b]}{\omega_{ab}^3}\cdot A_b && \text{(E.441)}
\end{aligned}
$$

Note that the line strength is explicitly defined as a positive quantity. This insures that the absorption oscillator strength f_b, spontaneous lifetime τ_b, and the sponta-

neous probability rate are all positive. Evaluating the line strength using WET:

$$
\begin{aligned}
S_{ab} &= \sum_{m_a}\sum_{m_b}\left|\langle J_b, m_b|\, e\hat{\vec{r}}|J_a, m_a\rangle\right|^2 && \text{(E.442)}\\
&= \sum_{m_a}\sum_{m_b}\left|\langle J_b, m_b|\, e\sum_q(-1)^q\hat{r}_q\hat{\varepsilon}_{-q}\,|J_a, m_a\rangle\right|^2 && \text{(E.443)}\\
&= \sum_{m_a}\sum_{m_b}\langle J_a, m_a|\, e\sum_{q'}(-1)^{q'}\hat{r}_{q'}\hat{\varepsilon}_{-q'}\,|J_b, m_b\rangle\cdot\langle J_b, m_b|\, e\sum_q(-1)^q\hat{r}_q\hat{\varepsilon}_{-q}\,|J_a, m_a\rangle && \text{(E.444)}\\
&= \sum_{m_a}\sum_{m_b}\sum_q(-1)^q\langle J_a, m_a|\, e\hat{r}_{-q}\,|J_b, m_b\rangle\langle J_b, m_b|\, e\hat{r}_q\,|J_a, m_a\rangle && \text{(E.445)}\\
&= \pm s_{a,b}^2 i^2\sum_{m_a,m_b,q}(-1)^q\frac{\langle(J_b,1)\, m_b, -q|J_a, m_a\rangle}{\sqrt{[J_a]}}\langle J_a||er||J_b\rangle\frac{\langle(J_a,1)\, m_a, q|J_b, m_b\rangle}{\sqrt{[J_b]}}\langle J_b||er||J_a\rangle && \text{(E.446)}\\
&= |\langle J_b||er||J_a\rangle|^2\cdot\varsigma_b && \text{(E.447)}\\
\varsigma_b &= \mp\sum_{m_a,q}\frac{(-1)^q}{\sqrt{[J_a][J_b]}}\langle(J_b,1)\, m_a+q, -q|J_a, m_a\rangle\langle(J_a,1)\, m_a, q|J_b, m_a+q\rangle && \text{(E.448)}
\end{aligned}
$$

where the lower (upper) sign is taken for D1 (D2) transitions to insure positive definiteness. Again since we will always be discussing transitions from the $S_{\frac{1}{2}}$ ground states to one of either the $P_{\frac{1}{2}}$ or $P_{\frac{3}{2}}$ excited states, the Clebsch-Gordon sum ς will simply be labeled by the J of the final excited state. This gives us the following equivalent relationships between the modulus squared reduced matrix element (which is difficult to calculate accurately from theory) with physical observables (which we determine empirically) for transitions from the lower level a to the

higher level b:

$$|\langle J_b||r||J_a\rangle|^2 = \frac{S_{ab}}{\varsigma_{ab}e^2} \tag{E.449}$$

$$= \frac{3\hbar}{2m\omega_{ab}} \cdot \frac{[J_a]f_b}{\varsigma_b} \tag{E.450}$$

$$= \frac{3c^2}{4\alpha\omega_{ab}^3} \cdot \frac{[J_b]}{\varsigma_b\tau_b} \tag{E.451}$$

$$= \frac{3\pi\epsilon_0\hbar c^3}{e^2\omega_{ab}^3} \cdot \frac{[J_b]A_b}{\varsigma_b} \tag{E.452}$$

Evaluation of the Clebsch-Gordon Coefficients and Sums

The general forms of the D1 matrix elements are:

$$\begin{aligned}\left\langle P_{\frac{1}{2}}, q\pm\frac{1}{2}\middle| r_q \middle| S_{\frac{1}{2}}, \pm\frac{1}{2}\right\rangle &= \left\langle\left(\frac{1}{2},1\right)\pm\frac{1}{2},q|\frac{1}{2},q\pm\frac{1}{2}\right\rangle\left(i\frac{s_1}{\sqrt{2}}\right)\left\langle P_{\frac{1}{2}}\middle\| r \middle\| S_{\frac{1}{2}}\right\rangle \\ &= -i\frac{s_1}{\sqrt{2}}\left\langle\left(1,\frac{1}{2}\right)q,\pm\frac{1}{2}|\frac{1}{2},q\pm\frac{1}{2}\right\rangle\left\langle P_{\frac{1}{2}}\middle\| r \middle\| S_{\frac{1}{2}}\right\rangle \\ &= \pm is_1\sqrt{\frac{1\mp q}{6}}\left\langle P_{\frac{1}{2}}\middle\| r \middle\| S_{\frac{1}{2}}\right\rangle \end{aligned} \tag{E.453}$$

$$\begin{aligned}\left\langle S_{\frac{1}{2}}, q\pm\frac{1}{2}\middle| r_q \middle| P_{\frac{1}{2}}, \pm\frac{1}{2}\right\rangle &= \left\langle\left(\frac{1}{2},1\right)\pm\frac{1}{2},q|\frac{1}{2},q\pm\frac{1}{2}\right\rangle\left(-i\frac{s_1}{\sqrt{2}}\right)\left\langle S_{\frac{1}{2}}\middle\| r \middle\| P_{\frac{1}{2}}\right\rangle \\ &= i\frac{s_1}{\sqrt{2}}\left\langle\left(1,\frac{1}{2}\right)q,\pm\frac{1}{2}|\frac{1}{2},q\pm\frac{1}{2}\right\rangle\left\langle S_{\frac{1}{2}}\middle\| r \middle\| P_{\frac{1}{2}}\right\rangle \\ &= \mp is_1\sqrt{\frac{1\mp q}{6}}\left\langle S_{\frac{1}{2}}\middle\| r \middle\| P_{\frac{1}{2}}\right\rangle \end{aligned} \tag{E.454}$$

The general forms of the D2 matrix elements are:

$$\begin{aligned}
\left\langle P_{\frac{3}{2}}, q \pm \frac{1}{2} \middle| r_q \middle| S_{\frac{1}{2}}, \pm\frac{1}{2} \right\rangle &= \left\langle \left(\frac{1}{2}, 1\right) \pm \frac{1}{2}, q | \frac{3}{2}, q \pm \frac{1}{2} \right\rangle \left(i\frac{s_2}{2}\right) \left\langle P_{\frac{3}{2}} \middle\| r \middle\| S_{\frac{1}{2}} \right\rangle \\
&= i\frac{s_2}{2} \left\langle \left(1, \frac{1}{2}\right) q, \pm\frac{1}{2} | \frac{3}{2}, q \pm \frac{1}{2} \right\rangle \left\langle P_{\frac{3}{2}} \middle\| r \middle\| S_{\frac{1}{2}} \right\rangle \\
&= is_2 \sqrt{\frac{2 \pm q}{12}} \left\langle P_{\frac{3}{2}} \middle\| r \middle\| S_{\frac{1}{2}} \right\rangle \qquad \text{(E.455)} \\
\left\langle S_{\frac{1}{2}}, m \pm 1 \middle| r_\pm \middle| P_{\frac{3}{2}}, m \right\rangle &= \left\langle \left(\frac{3}{2}, 1\right) m, \pm 1 | \frac{1}{2}, m \pm 1 \right\rangle \left(i\frac{s_2}{\sqrt{2}}\right) \left\langle S_{\frac{1}{2}} \middle\| r \middle\| P_{\frac{3}{2}} \right\rangle \\
&= is_2 \sqrt{\frac{\left(\frac{1}{2} \mp m\right)\left(\frac{3}{2} \mp m\right)}{24}} \left\langle S_{\frac{1}{2}} \middle\| r \middle\| P_{\frac{3}{2}} \right\rangle \\
\left\langle S_{\frac{1}{2}}, \pm\frac{1}{2} \middle| r_0 \middle| P_{\frac{3}{2}}, \pm\frac{1}{2} \right\rangle &= \left\langle \left(\frac{3}{2}, 1\right) \pm \frac{1}{2}, 0 | \frac{1}{2}, \pm\frac{1}{2} \right\rangle \left(i\frac{s_2}{\sqrt{2}}\right) \left\langle S_{\frac{1}{2}} \middle\| r \middle\| P_{\frac{3}{2}} \right\rangle \\
&= -is_2 \sqrt{\frac{1}{6}} \left\langle S_{\frac{1}{2}} \middle\| r \middle\| P_{\frac{3}{2}} \right\rangle \qquad \text{(E.456)}
\end{aligned}$$

The D1 matrix elements are:

$$\begin{aligned}
\left\langle S_{\frac{1}{2}}, +\frac{1}{2} \middle| r_+ \middle| P_{\frac{1}{2}}, -\frac{1}{2} \right\rangle &= \left\langle P_{\frac{1}{2}}, -\tfrac{1}{2} \middle| r_- \middle| S_{\frac{1}{2}}, +\tfrac{1}{2} \right\rangle &&= +is_1 \sqrt{\frac{1}{3}} \left\langle P_{\frac{1}{2}} \middle\| r \middle\| S_{\frac{1}{2}} \right\rangle \\
-\left\langle S_{\frac{1}{2}}, +\frac{1}{2} \middle| r_0 \middle| P_{\frac{1}{2}}, +\frac{1}{2} \right\rangle &= \left\langle P_{\frac{1}{2}}, +\tfrac{1}{2} \middle| r_0 \middle| S_{\frac{1}{2}}, +\tfrac{1}{2} \right\rangle &&= +is_1 \sqrt{\frac{1}{6}} \left\langle P_{\frac{1}{2}} \middle\| r \middle\| S_{\frac{1}{2}} \right\rangle \\
-\left\langle S_{\frac{1}{2}}, -\frac{1}{2} \middle| r_0 \middle| P_{\frac{1}{2}}, -\frac{1}{2} \right\rangle &= \left\langle P_{\frac{1}{2}}, -\tfrac{1}{2} \middle| r_0 \middle| S_{\frac{1}{2}}, -\tfrac{1}{2} \right\rangle &&= -is_1 \sqrt{\frac{1}{6}} \left\langle P_{\frac{1}{2}} \middle\| r \middle\| S_{\frac{1}{2}} \right\rangle \\
\left\langle S_{\frac{1}{2}}, -\frac{1}{2} \middle| r_- \middle| P_{\frac{1}{2}}, +\frac{1}{2} \right\rangle &= \left\langle P_{\frac{1}{2}}, +\tfrac{1}{2} \middle| r_+ \middle| S_{\frac{1}{2}}, -\tfrac{1}{2} \right\rangle &&= -is_1 \sqrt{\frac{1}{3}} \left\langle P_{\frac{1}{2}} \middle\| r \middle\| S_{\frac{1}{2}} \right\rangle \\
\left\langle S_{\frac{1}{2}} \middle\| r \middle\| P_{\frac{1}{2}} \right\rangle &= \left\langle P_{\frac{1}{2}} \middle\| r \middle\| S_{\frac{1}{2}} \right\rangle && \qquad \text{(E.457)}
\end{aligned}$$

The D2 matrix elements are:

$$\begin{aligned}
\left\langle S_{\frac{1}{2}},+\frac{1}{2}\right| r_+ \left|P_{\frac{3}{2}},-\frac{1}{2}\right\rangle &= \left\langle P_{\frac{3}{2}},-\tfrac{1}{2}\right| r_- \left|S_{\frac{1}{2}},+\tfrac{1}{2}\right\rangle &&= +is_2\sqrt{\frac{1}{12}}\left\langle P_{\frac{3}{2}}\right\| r \left\|S_{\frac{1}{2}}\right\rangle \\
\left\langle S_{\frac{1}{2}},-\frac{1}{2}\right| r_+ \left|P_{\frac{3}{2}},-\frac{3}{2}\right\rangle &= \left\langle P_{\frac{3}{2}},-\tfrac{3}{2}\right| r_- \left|S_{\frac{1}{2}},-\tfrac{1}{2}\right\rangle &&= +is_2\frac{1}{2}\left\langle P_{\frac{3}{2}}\right\| r \left\|S_{\frac{1}{2}}\right\rangle \\
-\left\langle S_{\frac{1}{2}},+\frac{1}{2}\right| r_0 \left|P_{\frac{3}{2}},+\frac{1}{2}\right\rangle &= \left\langle P_{\frac{3}{2}},+\tfrac{1}{2}\right| r_0 \left|S_{\frac{1}{2}},+\tfrac{1}{2}\right\rangle &&= +is_2\sqrt{\frac{1}{6}}\left\langle P_{\frac{3}{2}}\right\| r \left\|S_{\frac{1}{2}}\right\rangle \\
-\left\langle S_{\frac{1}{2}},-\frac{1}{2}\right| r_0 \left|P_{\frac{3}{2}},-\frac{1}{2}\right\rangle &= \left\langle P_{\frac{3}{2}},-\tfrac{1}{2}\right| r_0 \left|S_{\frac{1}{2}},-\tfrac{1}{2}\right\rangle &&= +is_2\sqrt{\frac{1}{6}}\left\langle P_{\frac{3}{2}}\right\| r \left\|S_{\frac{1}{2}}\right\rangle \\
\left\langle S_{\frac{1}{2}},-\frac{1}{2}\right| r_- \left|P_{\frac{3}{2}},+\frac{1}{2}\right\rangle &= \left\langle P_{\frac{3}{2}},+\tfrac{1}{2}\right| r_+ \left|S_{\frac{1}{2}},-\tfrac{1}{2}\right\rangle &&= +is_2\sqrt{\frac{1}{12}}\left\langle P_{\frac{3}{2}}\right\| r \left\|S_{\frac{1}{2}}\right\rangle \\
\left\langle S_{\frac{1}{2}},+\frac{1}{2}\right| r_- \left|P_{\frac{3}{2}},+\frac{3}{2}\right\rangle &= \left\langle P_{\frac{3}{2}},+\tfrac{3}{2}\right| r_+ \left|S_{\frac{1}{2}},+\tfrac{1}{2}\right\rangle &&= +is_2\frac{1}{2}\left\langle P_{\frac{3}{2}}\right\| r \left\|S_{\frac{1}{2}}\right\rangle \\
\left\langle S_{\frac{1}{2}}\right\| r \left\|P_{\frac{3}{2}}\right\rangle &= \left\langle P_{\frac{3}{2}}\right\| r \left\|S_{\frac{1}{2}}\right\rangle
\end{aligned} \tag{E.458}$$

Note that the radial integral is real. Putting these results together allows us to evaluate the Clebsch-Gordon sums:

$$\varsigma_{\frac{1}{2}} = s_1^2\left[-\frac{i}{\sqrt{3}}\frac{i}{\sqrt{3}}+\frac{-i}{\sqrt{6}}\frac{i}{\sqrt{6}}+\frac{i}{\sqrt{6}}\frac{-i}{\sqrt{6}}-\frac{-i}{\sqrt{3}}\frac{-i}{\sqrt{3}}\right] = +1 \tag{E.459}$$

$$\varsigma_{\frac{3}{2}} = s_2^2\left[-\frac{i}{\sqrt{12}}\frac{i}{\sqrt{12}}-\frac{i}{2}\frac{i}{2}+\frac{-i}{\sqrt{6}}\frac{i}{\sqrt{6}}+\frac{-i}{\sqrt{6}}\frac{i}{\sqrt{6}}-\frac{i}{\sqrt{12}}\frac{i}{\sqrt{12}}-\frac{i}{2}\frac{i}{2}\right] = +1 \tag{E.460}$$

Therefore the radial integrals for the D1 and D2 transitions are:

$$\left|\left\langle P_J\right\| r \left\|S_{\frac{1}{2}}\right\rangle\right|^2 = \frac{3\hbar}{m\omega_J}f_J \tag{E.461}$$

The Radial Integral in the coupled LS basis

In the uncoupled basis, there is only one radial integral between the S and P states. First we must fix the phase convention of the uncoupled matrix elements:

$$
\begin{aligned}
|\langle r_q \rangle|^2 &= (-1)^q \left\langle \pm\frac{1}{2}\right|_S \langle 0|_L \, r_{-q} \, |q\rangle_L \left|\pm\frac{1}{2}\right\rangle_S \left\langle \pm\frac{1}{2}\right|_S \langle q|_L \, r_q \, |0\rangle_L \left|\pm\frac{1}{2}\right\rangle_S && \text{(E.462)}\\
&= (-1)^q \langle 0|_L \, r_{-q} \, |q\rangle_L \langle q|_L \, r_q \, |0\rangle_L && \text{(E.463)}\\
&= (\pm)_{PS}(\pm)_{SP}(-1)^{3+1} \begin{pmatrix} 0 & 1 & 1 \\ 0 & q & -q \end{pmatrix}^2 |\langle P \| \, r \, \| S\rangle|^2 && \text{(E.464)}\\
+1 &= (\pm)_{PS}(\pm)_{SP}(-1)^4 && \text{(E.465)}\\
&= (\pm)_{PS}(\pm)_{SP} && \text{(E.466)}\\
s &= (\pm)_{PS} = (\pm)_{SP} && \text{(E.467)}
\end{aligned}
$$

When the radial integral is evaluated in the coupled LS basis J, there is radial integral for each J. The relationship between the radial integrals evaluated in the two different basis sets can be shown by an expansion in the uncoupled basis and

by application of the WET:

$$\left\langle P_{\frac{3}{2}}, +\frac{3}{2}\middle| r_+ \middle| S_{\frac{1}{2}}, +\frac{1}{2}\right\rangle = \langle +1|_L \left\langle +\frac{1}{2}\middle|_S r_+ |0\rangle_L \middle| +\frac{1}{2}\right\rangle_S \tag{E.468}$$

$$= \langle +1| r_+ |0\rangle_L \left\langle +\frac{1}{2}| +\frac{1}{2}\right\rangle_S \tag{E.469}$$

$$= \langle (0,1)\, 0, +1|1, +1\rangle \left(\frac{is}{\sqrt{3}}\right) \langle P\| r \|S\rangle \tag{E.470}$$

$$= \frac{is}{\sqrt{3}} \langle P\| r \|S\rangle \tag{E.471}$$

$$= +is_2 \frac{1}{2} \left\langle P_{\frac{3}{2}}\middle\| r \middle\| S_{\frac{1}{2}}\right\rangle \tag{E.472}$$

$$\left\langle P_{\frac{1}{2}}, +\frac{1}{2}\middle| r_+ \middle| S_{\frac{1}{2}}, -\frac{1}{2}\right\rangle = \left(\sqrt{\frac{2}{3}} \langle +1|_L \left\langle -\frac{1}{2}\middle|_S - \sqrt{\frac{1}{3}} \langle 0|_L \left\langle +\frac{1}{2}\middle|_S\right) r_+ |0\rangle_L \middle| -\frac{1}{2}\right\rangle_S \tag{E.473}$$

$$= \sqrt{\frac{2}{3}} \langle +1| r_+ |0\rangle_L \left\langle -\frac{1}{2}| -\frac{1}{2}\right\rangle_S - \sqrt{\frac{1}{3}} \langle 0| r_+ |0\rangle_L \left\langle +\frac{1}{2}| -\frac{1}{2}\right\rangle_S \tag{E.474}$$

$$= \sqrt{\frac{2}{3}} \langle +1| r_+ |0\rangle_L \tag{E.475}$$

$$= \sqrt{\frac{2}{3}} \langle (0,1)\, 0, +1|1, +1\rangle \left(\frac{is}{\sqrt{3}}\right) \langle P\| r \|S\rangle \tag{E.476}$$

$$= \frac{is\sqrt{2}}{3} \langle P\| r \|S\rangle \tag{E.477}$$

$$= -is_1 \sqrt{\frac{1}{3}} \left\langle P_{\frac{1}{2}}\middle\| r \middle\| S_{\frac{1}{2}}\right\rangle \tag{E.478}$$

We can do the same calculation for the complex conjugates of the same matrix elements:

$$\left\langle S_{\frac{1}{2}}, +\frac{1}{2}\middle| r_- \middle| P_{\frac{3}{2}}, +\frac{3}{2}\right\rangle = \langle 0|_L \left\langle +\frac{1}{2}\middle|_S r_- |+1\rangle_L \middle| +\frac{1}{2}\right\rangle_S \tag{E.479}$$

$$= \frac{is}{\sqrt{3}} \langle S \| r \| P \rangle \tag{E.480}$$

$$= +is_2 \frac{1}{2} \left\langle S_{\frac{1}{2}} \middle\| r \middle\| P_{\frac{3}{2}} \right\rangle \tag{E.481}$$

$$\left\langle S_{\frac{1}{2}}, -\frac{1}{2}\middle| r_- \middle| P_{\frac{1}{2}}, +\frac{1}{2}\right\rangle = \langle 0|_L \left\langle -\frac{1}{2}\middle|_S r_+ \left(\sqrt{\frac{2}{3}} |+1\rangle_L \middle| -\frac{1}{2}\right\rangle_S - \sqrt{\frac{1}{3}} |0\rangle_L \middle| +\frac{1}{2}\right\rangle_S \right)$$

$$= \frac{is\sqrt{2}}{3} \langle S \| r \| P \rangle \tag{E.482}$$

$$= -is_1 \sqrt{\frac{1}{3}} \left\langle S_{\frac{1}{2}} \middle\| r \middle\| P_{\frac{1}{2}} \right\rangle \tag{E.483}$$

Note that the reduced matrix element in the uncoupled LS basis does not have any sign ambiguity due to positive definiteness, because for the transitions under consideration, the Clebsch-Gordon coefficient is always $+1$. Note also that the radial integral in the uncoupled basis is real. Since the radial integral is independent of m_L and m_J, we only had to evaluate one matrix element for each J. Summarizing these results:

$$s_2 \left\langle P_{\frac{3}{2}} \middle\| r \middle\| S_{\frac{1}{2}} \right\rangle = +s \frac{2}{\sqrt{3}} \langle P \| r \| S \rangle \tag{E.484}$$

$$s_2 \left\langle S_{\frac{1}{2}} \middle\| r \middle\| P_{\frac{3}{2}} \right\rangle = +s \frac{2}{\sqrt{3}} \langle S \| r \| P \rangle \tag{E.485}$$

$$s_1 \left\langle P_{\frac{1}{2}} \middle\| r \middle\| S_{\frac{1}{2}} \right\rangle = -s \sqrt{\frac{2}{3}} \langle P \| r \| S \rangle \tag{E.486}$$

$$s_1 \left\langle S_{\frac{1}{2}} \middle\| r \middle\| P_{\frac{1}{2}} \right\rangle = -s \sqrt{\frac{2}{3}} \langle S \| r \| P \rangle \tag{E.487}$$

where $s_1^2 = s_2^2 = s^2 = +1$. This implies the following relationships between the quantities relating to D1 and D2 transitions:

$$s_1 s_2 = -1 \tag{E.488}$$

$$\frac{\left\langle P_{\frac{3}{2}} \middle\| r \middle\| S_{\frac{1}{2}} \right\rangle}{\left\langle P_{\frac{1}{2}} \middle\| r \middle\| S_{\frac{1}{2}} \right\rangle} = -\sqrt{2}\frac{s_1}{s_2} = +\sqrt{2} \tag{E.489}$$

$$\langle P_J \| r \left\| S_{\frac{1}{2}} \right\rangle = \left\langle S_{\frac{1}{2}} \middle\| r \| P_J \right\rangle = +\sqrt{\frac{3\hbar}{m\omega_J} f_J} \tag{E.490}$$

$$\frac{S_{\frac{3}{2}}}{S_{\frac{1}{2}}} = 2 \tag{E.491}$$

$$\frac{f_{\frac{3}{2}}}{f_{\frac{1}{2}}} = 2\left(\frac{\omega_{\frac{3}{2}}}{\omega_{\frac{1}{2}}}\right) \tag{E.492}$$

$$\frac{\tau_{\frac{3}{2}}}{\tau_{\frac{1}{2}}} = \left(\frac{\omega_{\frac{1}{2}}}{\omega_{\frac{3}{2}}}\right)^3 \tag{E.493}$$

$$\frac{A_{\frac{3}{2}}}{A_{\frac{1}{2}}} = \left(\frac{\omega_{\frac{3}{2}}}{\omega_{\frac{1}{2}}}\right)^3 \tag{E.494}$$

Explicit Forms of the Matrix Elements

First we'll calculate the modulus square matrix elements neglecting fine structure mixing. This is easily done given the following matrix elements in terms of the

oscillator strength. The D1 matrix elements are:

$$\left\langle S_{\frac{1}{2}},+\frac{1}{2}\right| r_+ \left|P_{\frac{1}{2}},-\frac{1}{2}\right\rangle = \left\langle P_{\frac{1}{2}},-\frac{1}{2}\right| r_- \left|S_{\frac{1}{2}},+\frac{1}{2}\right\rangle = +is_1\sqrt{\frac{\hbar}{m}\frac{f_{\frac{1}{2}}}{\omega_{\frac{1}{2}}}} \quad \text{(E.495)}$$

$$-\left\langle S_{\frac{1}{2}},+\frac{1}{2}\right| r_0 \left|P_{\frac{1}{2}},+\frac{1}{2}\right\rangle = \left\langle P_{\frac{1}{2}},+\frac{1}{2}\right| r_0 \left|S_{\frac{1}{2}},+\frac{1}{2}\right\rangle = +is_1\sqrt{\frac{\hbar}{2m}\frac{f_{\frac{1}{2}}}{\omega_{\frac{1}{2}}}} \quad \text{(E.496)}$$

$$-\left\langle S_{\frac{1}{2}},-\frac{1}{2}\right| r_0 \left|P_{\frac{1}{2}},-\frac{1}{2}\right\rangle = \left\langle P_{\frac{1}{2}},-\frac{1}{2}\right| r_0 \left|S_{\frac{1}{2}},-\frac{1}{2}\right\rangle = -is_1\sqrt{\frac{\hbar}{2m}\frac{f_{\frac{1}{2}}}{\omega_{\frac{1}{2}}}} \quad \text{(E.497)}$$

$$\left\langle S_{\frac{1}{2}},-\frac{1}{2}\right| r_- \left|P_{\frac{1}{2}},+\frac{1}{2}\right\rangle = \left\langle P_{\frac{1}{2}},+\frac{1}{2}\right| r_+ \left|S_{\frac{1}{2}},-\frac{1}{2}\right\rangle = -is_1\sqrt{\frac{\hbar}{m}\frac{f_{\frac{1}{2}}}{\omega_{\frac{1}{2}}}} \quad \text{(E.498)}$$

The D2 matrix elements are:

$$\left\langle S_{\frac{1}{2}},+\frac{1}{2}\right| r_+ \left|P_{\frac{3}{2}},-\frac{1}{2}\right\rangle = \left\langle P_{\frac{3}{2}},-\frac{1}{2}\right| r_- \left|S_{\frac{1}{2}},+\frac{1}{2}\right\rangle = +is_2\sqrt{\frac{\hbar}{4m}\frac{f_{\frac{3}{2}}}{\omega_{\frac{3}{2}}}} \quad \text{(E.499)}$$

$$\left\langle S_{\frac{1}{2}},-\frac{1}{2}\right| r_+ \left|P_{\frac{3}{2}},-\frac{3}{2}\right\rangle = \left\langle P_{\frac{3}{2}},-\frac{3}{2}\right| r_- \left|S_{\frac{1}{2}},-\frac{1}{2}\right\rangle = +is_2\sqrt{\frac{3\hbar}{4m}\frac{f_{\frac{3}{2}}}{\omega_{\frac{3}{2}}}} \quad \text{(E.500)}$$

$$-\left\langle S_{\frac{1}{2}},+\frac{1}{2}\right| r_0 \left|P_{\frac{3}{2}},+\frac{1}{2}\right\rangle = \left\langle P_{\frac{3}{2}},+\frac{1}{2}\right| r_0 \left|S_{\frac{1}{2}},+\frac{1}{2}\right\rangle = +is_2\sqrt{\frac{\hbar}{2m}\frac{f_{\frac{3}{2}}}{\omega_{\frac{3}{2}}}} \quad \text{(E.501)}$$

$$-\left\langle S_{\frac{1}{2}},-\frac{1}{2}\right| r_0 \left|P_{\frac{3}{2}},-\frac{1}{2}\right\rangle = \left\langle P_{\frac{3}{2}},-\frac{1}{2}\right| r_0 \left|S_{\frac{1}{2}},-\frac{1}{2}\right\rangle = +is_2\sqrt{\frac{\hbar}{2m}\frac{f_{\frac{3}{2}}}{\omega_{\frac{3}{2}}}} \quad \text{(E.502)}$$

$$\left\langle S_{\frac{1}{2}},-\frac{1}{2}\right| r_- \left|P_{\frac{3}{2}},+\frac{1}{2}\right\rangle = \left\langle P_{\frac{3}{2}},+\frac{1}{2}\right| r_+ \left|S_{\frac{1}{2}},-\frac{1}{2}\right\rangle = +is_2\sqrt{\frac{\hbar}{4m}\frac{f_{\frac{3}{2}}}{\omega_{\frac{3}{2}}}} \quad \text{(E.503)}$$

$$\left\langle S_{\frac{1}{2}},+\frac{1}{2}\right| r_- \left|P_{\frac{3}{2}},+\frac{3}{2}\right\rangle = \left\langle P_{\frac{3}{2}},+\frac{3}{2}\right| r_+ \left|S_{\frac{1}{2}},+\frac{1}{2}\right\rangle = +is_2\sqrt{\frac{3\hbar}{4m}\frac{f_{\frac{3}{2}}}{\omega_{\frac{3}{2}}}} \quad \text{(E.504)}$$

The modulus squared matrix elements for transitions involving the absorption of photon with helicity $+1$ are calculated below:

$$\left|\left\langle P_{\frac{1}{2}},+\frac{1}{2}\right| r_+ \left|S_{\frac{1}{2}},-\frac{1}{2}\right\rangle\right|^2 = \frac{\hbar}{m}\frac{f_{\frac{1}{2}}}{\omega_{\frac{1}{2}}} \tag{E.505}$$

$$\left|\left\langle P_{\frac{3}{2}},+\frac{1}{2}\right| r_+ \left|S_{\frac{1}{2}},-\frac{1}{2}\right\rangle\right|^2 = \frac{\hbar}{4m}\frac{f_{\frac{3}{2}}}{\omega_{\frac{3}{2}}} \tag{E.506}$$

$$\left|\left\langle P_{\frac{3}{2}},+\frac{3}{2}\right| r_+ \left|S_{\frac{1}{2}},+\frac{1}{2}\right\rangle\right|^2 = \frac{3\hbar}{4m}\frac{f_{\frac{3}{2}}}{\omega_{\frac{3}{2}}} \tag{E.507}$$

The modulus squared matrix elements for transitions involving the absorption of photon with helicity 0 are calculated below:

$$\left|\left\langle P_{\frac{1}{2}},-\frac{1}{2}\right| r_0 \left|S_{\frac{1}{2}},-\frac{1}{2}\right\rangle\right|^2 = \frac{\hbar}{2m}\frac{f_{\frac{1}{2}}}{\omega_{\frac{1}{2}}} \tag{E.508}$$

$$\left|\left\langle P_{\frac{1}{2}},+\frac{1}{2}\right| r_0 \left|S_{\frac{1}{2}},+\frac{1}{2}\right\rangle\right|^2 = \frac{\hbar}{2m}\frac{f_{\frac{1}{2}}}{\omega_{\frac{1}{2}}} \tag{E.509}$$

$$\left|\left\langle P_{\frac{3}{2}},-\frac{1}{2}\right| r_0 \left|S_{\frac{1}{2}},-\frac{1}{2}\right\rangle\right|^2 = \frac{\hbar}{2m}\frac{f_{\frac{3}{2}}}{\omega_{\frac{3}{2}}} \tag{E.510}$$

$$\left|\left\langle P_{\frac{3}{2}},+\frac{1}{2}\right| r_0 \left|S_{\frac{1}{2}},+\frac{1}{2}\right\rangle\right|^2 = \frac{\hbar}{2m}\frac{f_{\frac{3}{2}}}{\omega_{\frac{3}{2}}} \tag{E.511}$$

The modulus squared matrix elements for transitions involving the absorption of photon with helicity -1:

$$\left|\left\langle P_{\frac{1}{2}},-\frac{1}{2}\right| r_- \left|S_{\frac{1}{2}},+\frac{1}{2}\right\rangle\right|^2 = \frac{\hbar}{m}\frac{f_{\frac{1}{2}}}{\omega_{\frac{1}{2}}} \tag{E.512}$$

$$\left|\left\langle P_{\frac{3}{2}},-\frac{1}{2}\right| r_- \left|S_{\frac{1}{2}},+\frac{1}{2}\right\rangle\right|^2 = \frac{\hbar}{4m}\frac{f_{\frac{3}{2}}}{\omega_{\frac{3}{2}}} \tag{E.513}$$

$$\left|\left\langle P_{\frac{3}{2}},-\frac{3}{2}\right| r_- \left|S_{\frac{1}{2}},-\frac{1}{2}\right\rangle\right|^2 = \frac{3\hbar}{4m}\frac{f_{\frac{3}{2}}}{\omega_{\frac{3}{2}}} \tag{E.514}$$

Because some of the excited eigenstates are mixed, now we'll evaluate the modulus squared matrix element in a general form.

$$
\begin{aligned}
|\langle r_q \rangle|^2 &= \left| \left(c_1^* \left\langle P_{\frac{3}{2}}, m+q \right| + c_2^* \left\langle P_{\frac{1}{2}}, m+q \right| \right) r_q \left| S_{\frac{1}{2}}, m \right\rangle \right|^2 && \text{(E.515)} \\
&= \left| c_1^* \left\langle P_{\frac{3}{2}}, m+q \right| r_q \left| S_{\frac{1}{2}}, m \right\rangle + c_2^* \left\langle P_{\frac{1}{2}}, m+q \right| r_q \left| S_{\frac{1}{2}}, m \right\rangle \right|^2 && \text{(E.516)} \\
&= |c_1|^2 \left| \left\langle P_{\frac{3}{2}}, m+q \right| r_q \left| S_{\frac{1}{2}}, m \right\rangle \right|^2 + |c_2|^2 \left| \left\langle P_{\frac{1}{2}}, m+q \right| r_q \left| S_{\frac{1}{2}}, m \right\rangle \right|^2 \\
&\quad + c_1^* \left\langle P_{\frac{3}{2}}, m+q \right| r_q \left| S_{\frac{1}{2}}, m \right\rangle \cdot c_2 \left\langle S_{\frac{1}{2}}, m \right| r_q^* \left| P_{\frac{1}{2}}, m+q \right\rangle \\
&\quad + c_1 \left\langle S_{\frac{1}{2}}, m \right| r_q^* \left| P_{\frac{3}{2}}, m+q \right\rangle \cdot c_2^* \left\langle P_{\frac{1}{2}}, m+q \right| r_q \left| S_{\frac{1}{2}}, m \right\rangle && \text{(E.517)}
\end{aligned}
$$

The c_1 and c_2 are the fine mixing coefficients which are real:

$$
\begin{aligned}
|\langle r_q \rangle|^2 &= c_1^2 \left| \left\langle P_{\frac{3}{2}}, m+q \right| r_q \left| S_{\frac{1}{2}}, m \right\rangle \right|^2 + c_2^2 \left| \left\langle P_{\frac{1}{2}}, m+q \right| r_q \left| S_{\frac{1}{2}}, m \right\rangle \right|^2 \\
&\quad + (-1)^q c_1 c_2 \left\langle P_{\frac{3}{2}}, m+q \right| r_q \left| S_{\frac{1}{2}}, m \right\rangle \left\langle S_{\frac{1}{2}}, m \right| r_{-q} \left| P_{\frac{1}{2}}, m+q \right\rangle \\
&\quad + (-1)^q c_1 c_2 \left\langle S_{\frac{1}{2}}, m \right| r_{-q} \left| P_{\frac{3}{2}}, m+q \right\rangle \left\langle P_{\frac{1}{2}}, m+q \right| r_q \left| S_{\frac{1}{2}}, m \right\rangle && \text{(E.518)}
\end{aligned}
$$

Noting the following relationship:

$$
\langle P_J, m+q | r_q \left| S_{\frac{1}{2}}, m \right\rangle = (-1)(-1)^q \left\langle S_{\frac{1}{2}}, m \right| r_{-q} | P_J, m+q \rangle \qquad \text{(E.519)}
$$

the cross terms can be written:

$$\begin{aligned}
\text{cross terms} &= (-1)^q c_1 c_2 \left\langle P_{\frac{3}{2}}, m+q \right| r_q \left| S_{\frac{1}{2}}, m \right\rangle \left\langle S_{\frac{1}{2}}, m \right| r_{-q} \left| P_{\frac{1}{2}}, m+q \right\rangle \\
&\quad + (-1)^q c_1 c_2 \left\langle S_{\frac{1}{2}}, m \right| r_{-q} \left| P_{\frac{3}{2}}, m+q \right\rangle \left\langle P_{\frac{1}{2}}, m+q \right| r_q \left| S_{\frac{1}{2}}, m \right\rangle \qquad \text{(E.520)} \\
&= (-1)^q c_1 c_2 \left\langle P_{\frac{3}{2}}, m+q \right| r_q \left| S_{\frac{1}{2}}, m \right\rangle (-1)(-1)^q \left\langle P_{\frac{1}{2}}, m+q \right| r_q \left| S_{\frac{1}{2}}, m \right\rangle \\
&\quad + (-1)^q c_1 c_2 (-1)(-1)^q \left\langle P_{\frac{3}{2}}, m+q \right| r_q \left| S_{\frac{1}{2}}, m \right\rangle \left\langle P_{\frac{1}{2}}, m+q \right| r_q \left| S_{\frac{1}{2}}, m \right\rangle \\
& \qquad \text{(E.521)} \\
&= (-1)^{1+q+q} 2 c_1 c_2 \left\langle P_{\frac{3}{2}}, m+q \right| r_q \left| S_{\frac{1}{2}}, m \right\rangle \left\langle P_{\frac{1}{2}}, m+q \right| r_q \left| S_{\frac{1}{2}}, m \right\rangle \qquad \text{(E.522)} \\
&= -2 c_1 c_2 \left\langle P_{\frac{3}{2}}, m+q \right| r_q \left| S_{\frac{1}{2}}, m \right\rangle \left\langle P_{\frac{1}{2}}, m+q \right| r_q \left| S_{\frac{1}{2}}, m \right\rangle \qquad \text{(E.523)}
\end{aligned}$$

Therefore the general form of the modulus square matrix element accounting for fine structure mixing is:

$$\begin{aligned}
\left| \langle r_q \rangle \right|^2 &= c_1^2 \left| \left\langle P_{\frac{3}{2}}, m+q \right| r_q \left| S_{\frac{1}{2}}, m \right\rangle \right|^2 + c_2^2 \left| \left\langle P_{\frac{1}{2}}, m+q \right| r_q \left| S_{\frac{1}{2}}, m \right\rangle \right|^2 \\
&\quad - 2 c_1 c_2 \left\langle P_{\frac{3}{2}}, m+q \right| r_q \left| S_{\frac{1}{2}}, m \right\rangle \left\langle P_{\frac{1}{2}}, m+q \right| r_q \left| S_{\frac{1}{2}}, m \right\rangle \qquad \text{(E.524)}
\end{aligned}$$

For the following, we've used equations (E.87) and (E.492). For the transitions involving light with -1 helicity:

$$\begin{aligned}
\left| \left\langle P_+, -\frac{3}{2} \right| r_- \left| S_{\frac{1}{2}}, -\frac{1}{2} \right\rangle \right|^2 &= \frac{3\hbar}{4m} \frac{f_{\frac{3}{2}}}{\omega_{\frac{3}{2}}} \qquad \text{(E.525)} \\
\left| \left\langle P_-, -\frac{1}{2} \right| r_- \left| S_{\frac{1}{2}}, +\frac{1}{2} \right\rangle \right|^2 &= \left(\frac{\hbar}{m} \frac{f_{\frac{1}{2}}}{\omega_{\frac{1}{2}}} \right) \left[1 + a_1 a_2^+ \sqrt{2} - \frac{\left(a_2^+\right)^2}{2} \right] \qquad \text{(E.526)} \\
\left| \left\langle P_+, -\frac{1}{2} \right| r_- \left| S_{\frac{1}{2}}, +\frac{1}{2} \right\rangle \right|^2 &= \left(\frac{\hbar}{4m} \frac{f_{\frac{3}{2}}}{\omega_{\frac{3}{2}}} \right) \left[1 - a_1 a_2^+ 2\sqrt{2} + \left(a_2^+\right)^2 \right] \qquad \text{(E.527)}
\end{aligned}$$

For the transitions involving light with 0 helicity:

$$\left|\left\langle P_-,-\frac{1}{2}\right| r_0 \left|S_{\frac{1}{2}},-\frac{1}{2}\right\rangle\right|^2 = \left(\frac{\hbar}{2m}\frac{f_{\frac{1}{2}}}{\omega_{\frac{1}{2}}}\right)\left[1-a_1a_2^-2\sqrt{2}+\left(a_2^-\right)^2\right] \quad \text{(E.528)}$$

$$\left|\left\langle P_+,-\frac{1}{2}\right| r_0 \left|S_{\frac{1}{2}},-\frac{1}{2}\right\rangle\right|^2 = \left(\frac{\hbar}{2m}\frac{f_{\frac{3}{2}}}{\omega_{\frac{3}{2}}}\right)\left[1+a_1a_2^-\sqrt{2}-\frac{\left(a_2^-\right)^2}{2}\right] \quad \text{(E.529)}$$

$$\left|\left\langle P_-,+\frac{1}{2}\right| r_0 \left|S_{\frac{1}{2}},+\frac{1}{2}\right\rangle\right|^2 = \left(\frac{\hbar}{2m}\frac{f_{\frac{1}{2}}}{\omega_{\frac{1}{2}}}\right)\left[1+a_1a_2^+2\sqrt{2}+\left(a_2^+\right)^2\right] \quad \text{(E.530)}$$

$$\left|\left\langle P_+,+\frac{1}{2}\right| r_0 \left|S_{\frac{1}{2}},+\frac{1}{2}\right\rangle\right|^2 = \left(\frac{\hbar}{2m}\frac{f_{\frac{3}{2}}}{\omega_{\frac{3}{2}}}\right)\left[1-a_1a_2^+\sqrt{2}-\frac{\left(a_2^+\right)^2}{2}\right] \quad \text{(E.531)}$$

For the transitions involving light with $+1$ helicity:

$$\left|\left\langle P_-,+\frac{1}{2}\right| r_+ \left|S_{\frac{1}{2}},-\frac{1}{2}\right\rangle\right|^2 = \left(\frac{\hbar}{m}\frac{f_{\frac{1}{2}}}{\omega_{\frac{1}{2}}}\right)\left[1-a_1a_2^-\sqrt{2}-\frac{\left(a_2^-\right)^2}{2}\right] \quad \text{(E.532)}$$

$$\left|\left\langle P_+,+\frac{1}{2}\right| r_+ \left|S_{\frac{1}{2}},-\frac{1}{2}\right\rangle\right|^2 = \left(\frac{\hbar}{4m}\frac{f_{\frac{3}{2}}}{\omega_{\frac{3}{2}}}\right)\left[1+a_1a_2^-2\sqrt{2}+\left(a_2^-\right)^2\right] \quad \text{(E.533)}$$

$$\left|\left\langle P_+,+\frac{3}{2}\right| r_+ \left|S_{\frac{1}{2}},+\frac{1}{2}\right\rangle\right|^2 = \frac{3\hbar}{4m}\frac{f_{\frac{3}{2}}}{\omega_{\frac{3}{2}}} \quad \text{(E.534)}$$

E.5.4 Magnetic Dipole Matrix Elements

The main field B defines the z-axis. In order to probe $\Delta m_F \pm 1$ transitions, a small set of coils creates an RF field in a direction *transverse* to the main B-field. In our lab, the RF field produced at the center of our cell by a 1.3 cm radius, 20 turn coil with a resistance of 3.9 Ω & an inductance of 0.5 μH driven at 16 VPP at a frequency of about 7 MHz is on order of hundreds of microgauss to a few milligauss. Therefore, we can treat the RF field $\vec{B}_{rf}$ as a time dependent perturbation to our

original Hamiltonian:

$$\mathcal{H}_{EPR} = \mathcal{H} + \mathcal{W} \tag{E.535}$$

$$\mathcal{W} = -\vec{\mu_I} \cdot \vec{B}_{rf} - \vec{\mu_J} \cdot \vec{B}_{rf} \tag{E.536}$$

We'll choose the rf-field to be in the $\hat{x}$ direction. After expressing the angular momentum operators as ladder operators $\left(\hat{J}_x = \frac{1}{2}\left(\hat{J}_+ + \hat{J}_-\right)\right)$ and treating only the case of stimulated emission ($m_F \rightarrow m_F - 1$), the matrix element of interest becomes:

$$W_{fi} = \frac{\hbar}{2}\left\langle m_F - 1\right| \omega_I \hat{I}_- + \omega_J \hat{J}_- \left|m_F\right\rangle \tag{E.537}$$

$$= \frac{\hbar}{2}\left\langle m_F - 1\right| \omega_I \hat{F}_- + \left(\omega_J - \omega_I\right) \hat{J}_- \left|m_F\right\rangle \tag{E.538}$$

$$= \frac{\hbar}{2}\left\langle f\right| \omega_I \hat{F}_- + \left(\omega_J - \omega_I\right) \hat{J}_- \left|i\right\rangle \tag{E.539}$$

$$\omega_I = -\frac{g_I \mu_N B_{RF}}{\hbar} \tag{E.540}$$

$$\omega_J = -\frac{g_S \mu_B B_{RF}}{\hbar} \tag{E.541}$$

To start with, let's calculate the matrix element of $\hat{F}_-$:

$$\begin{aligned}
\left\langle \hat{F}_- \right\rangle &= \langle m_F^{\pm} - 1 | \hat{F}_- | m_F^{\pm} \rangle && \text{(E.542)} \\
&= \left[a_1 (m_F - 1) \left\langle I \pm \frac{1}{2}, m_F - 1 \right| \pm a_2 (m_F - 1) \left\langle I \mp \frac{1}{2}, m_F - 1 \right| \right] \\
&\quad \hat{F}_- \left[a_1 (m_F) \left| I \pm \frac{1}{2}, m_F \right\rangle \pm a_2 (m_F) \left| I \mp \frac{1}{2}, m_F \right\rangle \right] && \text{(E.543)} \\
&= \left[a_1 (m_F - 1) \left\langle I \pm \frac{1}{2}, m_F - 1 \right| \pm a_2 (m_F - 1) \left\langle I \mp \frac{1}{2}, m_F - 1 \right| \right] \\
&\quad \left[f_{\pm} a_1 (m_F) \left| I \pm \frac{1}{2}, m_F - 1 \right\rangle \pm f_{\mp} a_2 (m_F) \left| I \mp \frac{1}{2}, m_F - 1 \right\rangle \right] && \text{(E.544)} \\
&= f_{\pm} a_1 (m_F) a_1 (m_F - 1) + f_{\mp} a_2 (m_F) a_2 (m_F - 1) && \text{(E.545)} \\
&= f_{\pm} a_{1f} a_{1i} + f_{\mp} a_{2f} a_{2i} && \text{(E.546)} \\
f_{\pm} &= \sqrt{\left(I + \frac{1}{2} \right) \left(I + \frac{1}{2} \pm 1 \right) - m_F (m_F - 1)} && \text{(E.547)}
\end{aligned}$$

Now let's calculate the matrix element of $\hat{f}_-$:

$$\begin{aligned}
\left\langle \hat{f}_- \right\rangle^{\pm} &= \langle m_F^{\pm} - 1 | \hat{f}_- | m_F^{\pm} \rangle && \text{(E.548)}\\
&= \left(a_{1f}b_{1f} - a_{2f}b_{2f}\right) \left\langle m_F - 1 \mp \frac{1}{2}, \pm\frac{1}{2} \right| \pm \left(a_{1f}b_{2f} + a_{2f}b_{1f}\right) \\
&\quad \times \left\langle m_F - 1 \pm \frac{1}{2}, \mp\frac{1}{2} \right| \big] \hat{f}_- \big[\left(a_{1i}b_{1i} - a_{2i}b_{2i}\right) \\
&\quad \times \left| m_F \mp \frac{1}{2}, \pm\frac{1}{2} \right\rangle \pm \left(a_{1i}b_{2i} + a_{2i}b_{1i}\right) \left| m_F \pm \frac{1}{2}, \mp\frac{1}{2} \right\rangle && \text{(E.549)}\\
\left\langle \hat{f}_- \right\rangle^{+} &= \left(a_{1f}b_{1f} - a_{2f}b_{2f}\right) \left\langle m_F - \frac{3}{2}, +\frac{1}{2} \right| + \left(a_{1f}b_{2f} + a_{2f}b_{1f}\right) \\
&\quad \times \left\langle m_F - \frac{1}{2}, -\frac{1}{2} \right| \Bigg] \sqrt{\frac{1}{2}\frac{3}{2} + \frac{1}{2}\frac{1}{2}} \Bigg[\left(a_{1i}b_{1i} - a_{2i}b_{2i}\right) \left| m_F - \frac{1}{2}, -\frac{1}{2} \right\rangle && \text{(E.550)}\\
&= \left[a_{1f}b_{2f} + a_{2f}b_{1f}\right] \times \left[a_{1i}b_{1i} - a_{2i}b_{2i}\right] && \text{(E.551)}\\
\left\langle \hat{f}_- \right\rangle^{-} &= \left(a_{1f}b_{1f} - a_{2f}b_{2f}\right) \left\langle m_F - \frac{1}{2}, -\frac{1}{2} \right| - \left(a_{1f}b_{2f} + a_{2f}b_{1f}\right) \\
&\quad \times \left\langle m_F - \frac{3}{2}, +\frac{1}{2} \right| \Bigg] \sqrt{\frac{1}{2}\frac{3}{2} + \frac{1}{2}\frac{1}{2}} \Bigg[- \left(a_{1i}b_{2i} + a_{2i}b_{1i}\right) \left| m_F - \frac{1}{2}, -\frac{1}{2} \right\rangle \\
&= \left[a_{2f}b_{2f} - a_{1f}b_{1f}\right] \times \left[a_{1i}b_{2i} + a_{2i}b_{1i}\right] && \text{(E.552)}
\end{aligned}$$

Note the following relations:

$$\begin{aligned}
b_{2f}b_{1i} &= \frac{\sqrt{\left(I + \frac{1}{2}\right)\left(I + \frac{3}{2}\right) - m_F\left(m_F - 1\right)}}{2I+1} = \frac{f_+}{2I+1} && \text{(E.553)}\\
b_{1f}b_{2i} &= \frac{\sqrt{\left(I + \frac{1}{2}\right)\left(I - \frac{1}{2}\right) - m_F\left(m_F - 1\right)}}{2I+1} = \frac{f_-}{2I+1} && \text{(E.554)}\\
b_{1f}b_{1i} &= \frac{\sqrt{\left(I + \frac{1}{2}\right)\left(I - \frac{1}{2}\right) + m_F\left(m_F - 1\right) + 2m_F\left(I + \frac{1}{2}\right)}}{2I+1} = \frac{g_-}{2I+1} && \text{(E.555)}\\
b_{2f}b_{2i} &= \frac{\sqrt{\left(I + \frac{1}{2}\right)\left(I + \frac{3}{2}\right) + m_F\left(m_F - 1\right) - 2m_F\left(I + \frac{1}{2}\right)}}{2I+1} = \frac{g_+}{2I+1} && \text{(E.556)}\\
g_\pm &= \sqrt{\left(I + \frac{1}{2}\right)\left(I + \frac{1}{2} \pm 1\right) + m_F\left(m_F - 1\right) \mp 2m_F\left(I + \frac{1}{2}\right)} && \text{(E.557)}
\end{aligned}$$

Going back to $\langle \hat{J}_- \rangle^{\pm}$:

$$\begin{aligned}
\langle \hat{J}_- \rangle^{+} &= \left[a_{1f}b_{2f} + a_{2f}b_{1f}\right] \times \left[a_{1i}b_{1i} - a_{2i}b_{2i}\right] && \text{(E.558)}\\
&= a_{1f}a_{1i}\frac{f_+}{2I+1} + a_{2f}a_{1i}\frac{g_-}{2I+1} - a_{1f}a_{2i}\frac{g_+}{2I+1} - a_{2f}a_{2i}\frac{f_-}{2I+1} && \text{(E.559)}\\
\langle \hat{J}_- \rangle^{-} &= \left[a_{2f}b_{2f} - a_{1f}b_{1f}\right] \times \left[a_{1i}b_{2i} + a_{2i}b_{1i}\right] && \text{(E.560)}\\
&= a_{2f}a_{1i}\frac{g_+}{2I+1} - a_{1f}a_{1i}\frac{f_-}{2I+1} + a_{2f}a_{2i}\frac{f_+}{2I+1} - a_{1f}a_{2i}\frac{g_-}{2I+1} && \text{(E.561)}\\
\langle \hat{J}_- \rangle^{\pm} &= \pm a_{1f}a_{1i}\frac{f_\pm}{2I+1} + a_{2f}a_{1i}\frac{g_\mp}{2I+1} - a_{1f}a_{2i}\frac{g_\pm}{2I+1} \mp a_{2f}a_{2i}\frac{f_\mp}{2I+1} && \text{(E.562)}
\end{aligned}$$

Putting this altogether,

$$\begin{aligned}
W_{fi} &= \frac{\hbar}{2}\omega_I\left(f_\pm a_{1f}a_{1i} + f_\mp a_{2f}a_{2i}\right) + \frac{\hbar}{2}\left(\omega_J - \omega_I\right)\\
&\quad \times\left(\pm a_{1f}a_{1i}\frac{f_\pm}{2I+1} + a_{2f}a_{1i}\frac{g_\mp}{2I+1} - a_{1f}a_{2i}\frac{g_\pm}{2I+1} \mp a_{2f}a_{2i}\frac{f_\mp}{2I+1}\right) && \text{(E.563)}\\
&= \frac{\hbar}{2}\left(\frac{2I\omega_I + (1\mp 1)\omega_I \pm \omega_J}{2I+1}\right) f_\pm a_{1f}a_{1i} + \frac{\hbar}{2}\left(\frac{2I\omega_I + (1\pm 1)\omega_I \mp \omega_J}{2I+1}\right)\\
&\quad \times f_\mp a_{2f}a_{2i} + \frac{\hbar}{2}\left(\frac{\omega_J - \omega_I}{2I+1}\right)\left(g_\mp a_{2f}a_{1i} - g_\pm a_{1f}a_{2i}\right) && \text{(E.564)}
\end{aligned}$$

Using the small field approximations from before:

$$\begin{aligned}
a_1 &= 1 - \frac{\beta^2}{2}x^2 && \text{(E.565)}\\
a_2 &= -\beta x + 2\alpha\beta x^2 && \text{(E.566)}
\end{aligned}$$

We're interested in the mod square of the matrix element to first order in x:

$$\begin{aligned}
\left|W_{fi}\right|^2 &\simeq \frac{\hbar^2}{4}\left(\frac{2I\omega_I + (1\mp 1)\omega_I \pm \omega_J}{2I+1}\right)^2 f_\pm^2 - \frac{\hbar^2}{4}\left(\frac{2I\omega_I + (1\mp 1)\omega_I \pm \omega_J}{2I+1}\right)\\
&\quad \times\left(\frac{\omega_J - \omega_I}{2I+1}\right) f_\pm\left(g_\mp\beta_f - g_\pm\beta_i\right)x + O(x^2) && \text{(E.567)}
\end{aligned}$$

E.5.5 Population Differences & Atomic Polarization

Two State Systems: Polarization

For a system with only two states, for example the two Zeeman levels $m_J = \pm 1$ of the $S_{1/2}$ ground state, we can label the populations as $\rho_\pm$. Their sum and difference are given by:

$$\rho_+ + \rho_- = \mathrm{Tr}(\rho) = 1 \qquad \rho_+ - \rho_- = P \tag{E.568}$$

where P is called the polarization. Using these two equations, it is straightforward to find the populations of the two states:

$$\rho_\pm = \frac{1 \pm P}{2} \tag{E.569}$$

The polarization P and the expectation value of S_z are related by:

$$\langle S_z \rangle = \mathrm{Tr}\left(\rho S_z\right) = \mathrm{Tr}\left\{ \begin{bmatrix} \rho_+ & 0 \\ 0 & \rho_- \end{bmatrix} \begin{bmatrix} +\frac{1}{2} & 0 \\ 0 & -\frac{1}{2} \end{bmatrix} \right\} \tag{E.570}$$

$$= \mathrm{Tr}\left\{ \begin{bmatrix} +\frac{\rho_+}{2} & 0 \\ 0 & -\frac{\rho_-}{2} \end{bmatrix} \right\} \tag{E.571}$$

$$= \frac{\rho_+ - \rho_-}{2} = \frac{P}{2} \tag{E.572}$$

Thermal Equilibrium

At thermal equilibrium, for a canonical ensemble (fixed number of particles in equilibrium with a heat reservoir at a common temperature T), the population of

each state is given by:

$$\rho_n = \frac{\exp\left(-\frac{E_n}{kT}\right)}{Z} \qquad Z = \sum_n \exp\left(-\frac{E_n}{kT}\right) \tag{E.573}$$

where Z is the partition function. Specifying to our two level case, the energies for $S_{1/2}$ states are:

$$E_\pm = E\left(\left|S_{\frac{1}{2}}, \pm\frac{1}{2}\right\rangle\right) = E_0^S \pm \left[\frac{g_S}{-2}\right]\mu_B B \tag{E.574}$$

This gives for the relative population of each state at thermodynamic equilibrium:

$$\begin{aligned}
Z &= \exp\left(-\frac{E_+}{kT}\right) + \exp\left(-\frac{E_-}{kT}\right) && \text{(E.575)}\\
&= \exp\left(-\frac{E_0^S + \left[\frac{g_S}{-2}\right]\mu_B B}{kT}\right) + \exp\left(-\frac{E_0^S - \left[\frac{g_S}{-2}\right]\mu_B B}{kT}\right) && \text{(E.576)}\\
&= \exp\left(-\frac{E_0^S}{kT}\right)\left[\exp\left(-\left[\frac{g_S}{-2}\right]\frac{\mu_B B}{kT}\right) + \exp\left(+\left[\frac{g_S}{-2}\right]\frac{\mu_B B}{kT}\right)\right] && \text{(E.577)}\\
\rho_\pm &= \frac{\exp\left(-\frac{E_0^S}{kT}\right)\exp\left(\mp\left[\frac{g_S}{-2}\right]\frac{\mu_B B}{kT}\right)}{\exp\left(-\frac{E_0^S}{kT}\right)\left[\exp\left(+\left[\frac{g_S}{-2}\right]\frac{\mu_B B}{kT}\right) + \exp\left(-\left[\frac{g_S}{-2}\right]\frac{\mu_B B}{kT}\right)\right]} && \text{(E.578)}\\
&= \frac{\exp\left(\mp\left[\frac{g_S}{-2}\right]\frac{\mu_B B}{kT}\right)}{\exp\left(+\left[\frac{g_S}{-2}\right]\frac{\mu_B B}{kT}\right) + \exp\left(-\left[\frac{g_S}{-2}\right]\frac{\mu_B B}{kT}\right)} && \text{(E.579)}\\
&= \frac{\exp\left(m_J\beta\right)}{\exp\left(+\frac{\beta}{2}\right) + \exp\left(-\frac{\beta}{2}\right)} && \text{(E.580)}
\end{aligned}$$

We have introduced the β parameter which we'll call the "spin temperature," even though it is a unitless quantity, is inversely proportional to temperature at thermal equilibrium, and is, in this case, negative. It's usefulness far outweighs those peccadilloes and will be more apparent when we discuss the role of nuclear spin in spin-exchange collisions in section (E.5.5). For the $S_{\frac{1}{2}}$ ground states at thermal

equilibrium, the spin temperature is:

$$\beta = \frac{g_S \mu_B B}{kT} = \left[\frac{g_S}{-2}\right]\left(\frac{-2\mu_B B}{kT}\right) \tag{E.581}$$

We can express the polarization as a function of the spin temperature:

$$\begin{aligned} P &= \frac{\exp\left(+\frac{\beta}{2}\right)}{\exp\left(+\frac{\beta}{2}\right)+\exp\left(-\frac{\beta}{2}\right)} - \frac{\exp\left(-\frac{\beta}{2}\right)}{\exp\left(+\frac{\beta}{2}\right)+\exp\left(-\frac{\beta}{2}\right)} && \text{(E.582)} \\ &= \frac{\exp\left(+\frac{\beta}{2}\right)-\exp\left(-\frac{\beta}{2}\right)}{\exp\left(+\frac{\beta}{2}\right)+\exp\left(-\frac{\beta}{2}\right)} && \text{(E.583)} \\ P &= \tanh\left(\frac{\beta}{2}\right) && \text{(E.584)} \end{aligned}$$

We'll see later on that this result is true regardless of the mechanism that producing the polarization. Inverting to get the spin temperature as a function of polarization:

$$\begin{aligned} P &= \frac{\exp\left(+\frac{\beta}{2}\right)-\exp\left(-\frac{\beta}{2}\right)}{\exp\left(+\frac{\beta}{2}\right)+\exp\left(-\frac{\beta}{2}\right)} = \frac{x-\frac{1}{x}}{x+\frac{1}{x}} = \frac{x^2-1}{x^2+1} && \text{(E.585)} \\ Px^2+P &= x^2-1 && \text{(E.586)} \\ (P-1)x^2 &= -P-1 && \text{(E.587)} \\ x^2 &= \left[\exp\left(+\frac{\beta}{2}\right)\right]^2 = \frac{1+P}{1-P} && \text{(E.588)} \\ \beta &= \log\left(\frac{1+P}{1-P}\right) && \text{(E.589)} \end{aligned}$$

Multiple State Systems: Spin Temperature

It has been shown [25] that under the optical pumping, spin exchange, high pressure conditions that exist within a cell, the populations are given by:

$$\rho_{m_F} = \frac{e^{\beta m_F}}{Z_F} = \frac{e^{\beta m_J}}{Z_J}\frac{e^{\beta m_I}}{Z_I} \tag{E.590}$$

where $m_F = m_J + m_I$ and the partition function, in general, is given by [26]:

$$Z_J = \sum_{m=-J}^{+J} e^{\beta m} = \frac{\sinh(\beta[J]/2)}{\sinh(\beta/2)} = \frac{(1+P)^{[J]} - (1-P)^{[J]}}{2P(1-P^2)^J} \tag{E.591}$$

where P is the polarization and $[J] = 2J + 1$.

The motivation of using β, spin temperature, is best described by the original 1959 reference by Anderson, Pipkin, & Baird [27]:

> Direct substitution into these equations shows that in the steady state the solution is given by
>
> $$\begin{aligned} a_{\frac{3}{2}} : a_{\frac{1}{2}} : a_{-\frac{1}{2}} : a_{-\frac{3}{2}} &= \alpha^3 : \alpha^2 : \alpha : 1 \\ b_{\frac{1}{2}} : b_{-\frac{1}{2}} &= \alpha : 1 \end{aligned}$$
>
> This solution suggests the general form of the steady-state solution for all spin-exchange problems. It is the most probable way in which two sets of particles can be arranged so that the number of particles in each set is a constant and so that the total z component of angular momentum is a constant. This implies that the density matrix for a system of

Na and N in spin-exchange equilibrium is given by

$$\rho = \frac{\exp\left[-\left(I_{1z} + S_{1z}\right)\beta\right]\exp\left[-\left(I_{2z} + S_{2z}\right)\beta\right]}{\mathrm{Tr}\left\{\exp\left[-\left(I_{1z} + S_{1z}\right)\beta\right]\exp\left[-\left(I_{2z} + S_{2z}\right)\beta\right]\right\}},$$

where β is such that the total z component of the angular momentum of the system is given by $Tr[(I_{1s} + S_{1z} + I_{2z} + S_{2z})\rho]$. The parameter β might be called an angular momentum spin temperature.

They were discussing spin-exchange between sodium and nitrogen, but it is perfectly applicable to other spin-exchange systems including "pure" and "hybrid" cells.

To calculate the population difference between states m and $m-1$, we first must calculate the population of states with m. In our case, $J = S = 1/2$ & $[J] = 2$, and consequently $Z_{1/2}$ is

$$Z_{1/2} = \frac{(1+P)^2 - (1-P)^2}{2P\sqrt{1-P^2}} = \frac{2}{\sqrt{(1-P)(1+P)}} = \frac{2}{1+P}\sqrt{\frac{1+P}{1-P}} = \frac{2\exp(\beta/2)}{1+P} \tag{E.592}$$

Plugging this in for the population of the m state gives [28]:

$$\rho_m = \frac{\exp(\beta m)}{Z_I Z_S} = \frac{\exp(\beta(m-1/2))}{Z_I}\frac{1+P}{2} = Q_{I\bar{m}}\frac{1+P}{2} \qquad Q_{I\bar{m}} = \frac{\exp(\beta\bar{m})}{Z_I} \tag{E.593}$$

where P is the polarization, I is the nuclear spin, and $\bar{m} = (m + m - 1)/2 = m - 1/2$ is the mean m of the transition. For the adjacent state $m-1$, the population is:

$$\begin{aligned} \rho_{m-1} &= \frac{\exp(\beta(m-1-1/2))}{Z_I}\frac{1+P}{2} = Q_{I\bar{m}}\frac{1+P}{2}\exp(-\beta) \\ &= Q_{I\bar{m}}\frac{1+P}{2}\left(\frac{1-P}{1+P}\right) = Q_{I\bar{m}}\frac{1-P}{2} \end{aligned} \tag{E.594}$$

Putting this altogether gives the population difference between the states m and $m-1$ as:

$$\rho_m - \rho_{m-1} = Q_{I\tilde{m}} \left(\frac{1+P}{2} - \frac{1-P}{2} \right) = Q_{I\tilde{m}} P \tag{E.595}$$

E.6 The Effect on Polarized Light Due to Spin Polarized Alkali Atoms

E.6.1 General Formula for Atomic Polarizability

As we've seen before, we can write the electric field component of an electromagnetic wave in the complex representation as:

$$\vec{E} = E_0 \hat{E}_0 \exp(i\vec{k} \cdot \vec{r} - i\omega t) \tag{E.596}$$

The speed of wave is given the ratio $\omega/|\vec{k}|$. The effect of a uniform, isotropic, and linear medium on a beam of light is given by the (possibly complex) index of refraction of the medium, n:

$$\left|\vec{k}\right| = \frac{\omega}{c} n = \frac{2\pi n}{\lambda_{\text{vac}}} \tag{E.597}$$

where $\vec{k}$ is the wave vector of the light and λ_{vac} is the wavelength of the light in vacuum. However, in general, different components of the light polarization vector have different values of $\vec{k}$ depending on the symmetry properties of an anisotropic medium. The symmetry of a vapor of alkali metal in a magnetic field is described by the spherical vector basis; therefore there are in general three different wave

vectors of the light in an alkali vapor:

$$\left|\vec{k}_q\right| = \frac{\omega}{c} n_q \tag{E.598}$$

where $q = 0, \pm 1$ labels the components relative to the atomic coordinate system. If $\vec{k}$ is imaginary, then its useful to split it into its real and imaginary parts:

$$\vec{E} = E_0 \hat{E}_0 \exp(-\Im\{\vec{k} \cdot \vec{r}\}) \exp(i\Re\{\vec{k} \cdot \vec{r}\} - i\omega t) \tag{E.599}$$

The real part of the index of refraction yields the dispersion relation which affects the phase of the wave. A difference in the real part for $q = \pm 1$ gives rise to circular birefringence; whereas, a difference in the real part between the $q = 0$ and $q = \pm$ gives rise to linear birefringence. The imaginary part of the index of refraction yields the attenuation constant which affects the amplitude of the wave. A difference in the imaginary part for $q = \pm 1$ gives rise to circular dichroism; whereas, a difference in the imaginary part between $q = 0$ and $q = \pm 1$ gives rise to linear dichroism. The details of the atomic system, beyond its symmetry, are hidden in the index of refraction:

$$n_q = \sqrt{\frac{\epsilon_q \mu_q}{\epsilon_0 \mu_0}} \tag{E.600}$$

where ϵ_q & μ_q are the dielectric constant & permeability of the medium and ϵ_0 & μ_0 are the dielectric constant & permeability of free space.

Applying Maxwell's equations, *in the complex representation*:

$$\vec{D} = \overleftrightarrow{\epsilon}\, \vec{E} = \epsilon_0 \vec{E} + \vec{P} = \epsilon_0 \vec{E} + [\mathcal{A}] \left\langle \vec{d} \right\rangle \tag{E.601}$$

where $\vec{P}$ is the electric polarization of the medium and $[\mathcal{A}]$ is the atomic number

density of the medium. The dipole moment, $\vec{d}$, is evaluated as the expectation value of the quantum mechanical dipole operator averaged over every atom or molecule in the medium [29]. The expectation value for the electric dipole operator is given by:

$$\Re\left\langle \vec{d} \right\rangle = -e\left\langle \vec{r} \right\rangle = -e\sum_{q}\left\langle r_q \right\rangle \varepsilon_q^* \tag{E.602}$$

Plugging in the result from Eqn. (E.401), where $\mathcal{U}_q = r_q$:

$$\Re\left\langle \vec{d} \right\rangle = -e\sum_{K,n,J,q}\left\{ \frac{\Omega\left(\rho_{Jn+q}-\rho_{Kn}\right)\left(u_q^{\mp}\right)^*\left|\left\langle J,n+q\right|r_q\left|K,n\right\rangle\right|^2}{\pm\omega-\omega_{Jn+qKn}-i\gamma_{Jn+qKn}}\times\exp(\pm i\omega t)\right\}\varepsilon_q^* \tag{E.603}$$

Using Eqn. (E.403) to identify the rest of the parameters:

$$\begin{aligned}\Re\left\langle \vec{d} \right\rangle &= \frac{e^2}{\hbar}\sum_{K,n,J,q}\hat{\varepsilon}_q^*\left\{\frac{\left(\rho_{Jn+q}-\rho_{Kn}\right)\left|\left\langle J,n+q\right|r_q\left|K,n\right\rangle\right|^2}{\pm\omega-\omega_{Jn+qKn}-i\gamma_{Jn+qKn}}\right\}\varepsilon_q\cdot E_0\hat{E}_0^{\pm}\exp(\pm i\omega t)\\ &= \frac{e^2}{\hbar}\left(\Sigma_1+\Sigma_2\right)\end{aligned} \tag{E.604}$$

where $\left(u_q^{\mp}\right)^* = \hat{\varepsilon}_q\hat{E}_0^{\pm}$ and $\hat{E}_0 = \hat{E}_0^-$ & $\hat{E}_0^* = \hat{E}_0^+$. When $|K,n\rangle$ are the $|S,\pm 1/2\rangle$ ground states, then the sum becomes:

$$\Sigma_1 = \sum_{n,s,q}\hat{\varepsilon}_q^*\left\{\frac{\left(\rho_{Psn+q}-\rho_{Sn}\right)\left|\left\langle P_s,n+q\right|r_q\left|S,n\right\rangle\right|^2}{+\omega-\omega_{Psn+qSn}+i\gamma_{Psn+qJn}}\right\}\varepsilon_q\cdot E_0\hat{E}_0^*\exp(+i\omega t) \tag{E.605}$$

where $s = \pm$ labels the mixed fine structure state. When $|J,n+q\rangle$ are the $|S,\pm 1/2\rangle$ ground states, then the sum becomes:

$$\Sigma_2 = \sum_{s,n,q}\hat{\varepsilon}_q^*\left\{\frac{\left(\rho_{Sn+q}-\rho_{Psn}\right)\left|\left\langle S,n+q\right|r_q\left|P_s,n\right\rangle\right|^2}{-\omega-\omega_{Sn+qPsn}-i\gamma_{Sn+qPsn}}\right\}\varepsilon_q\cdot E_0\hat{E}_0\exp(-i\omega t) \tag{E.606}$$

Reversing the sum, relabeling the sum variables, and multiplying the top & bottom by -1, the sum becomes:

$$\Sigma_2 = \sum_{s,n,q} \hat{\varepsilon}_q^* \left\{ \frac{\left(\rho_{Psn+q} - \rho_{Sn}\right) \left|\langle P_s, n+q| \, r_q \, |S,n\rangle\right|^2}{+\omega - \omega_{Psn+qSn} + i\gamma_{Psn+qSn}} \right\} \varepsilon_q \cdot E_0 \hat{E}_0 \exp(-i\omega t) \tag{E.607}$$

Finally, putting the two sums together again, we get:

$$\begin{aligned} \Re\left\langle \vec{d} \right\rangle &= \frac{e^2}{\hbar} \sum_{s,n,q} \hat{\varepsilon}_q^* \left\{ \frac{\left(\rho_{Sn} - \rho_{Psn+q}\right) \left|\langle P_s, n+q| \, r_q \, |S,n\rangle\right|^2}{\omega_{Psn+qSn} - \omega - i\gamma_{Psn+qSn}} \right\} \varepsilon_q \\ &\quad \cdot \left[E_0 \hat{E}_0 \exp(-i\omega t) + \left(E_0 \hat{E}_0 \exp(-i\omega t) \right)^* \right] \end{aligned} \tag{E.608}$$

The relationship between the induced dipole moment and the applied electric field defines the atomic polarizability tensor:

$$\Re\vec{d} = \overleftrightarrow{\alpha} \cdot \Re\vec{E} = \sum_q \hat{\varepsilon}_q^* \alpha_q \hat{\varepsilon}_q \left[\frac{\vec{E} + C.C.}{2} \right] \tag{E.609}$$

which immediately yields the components of the atomic polarizability tensor:

$$\alpha_q = \frac{e^2}{\hbar} \sum_{s,n} \left\{ \frac{\left(\rho_{Sn} - \rho_{Psn+q}\right) \left|\langle P_s, n+q| \, r_q \, |S,n\rangle\right|^2}{\omega_{Psn+qSn} - \omega - i\gamma_{Psn+qSn}} \right\} \tag{E.610}$$

E.6.2 Explicit Calculation of Atomic Polarizability

Description of Terms

To calculate the polarizability, we need to use many of the results from the previous sections:

1. the populations of the states, Sec. (E.5.5)

2. the transition matrix elements, Sec. (E.5.3)

3. the frequencies of the transitions, Sec. (E.2.5)

Putting these together, we see that every term in the sum looks like this:

$$\left(\frac{e^2}{\hbar}\right)\frac{[(\Delta\rho)]\overbrace{\left[\left(\frac{T\hbar f_n}{m\omega_n}\right)\left(1+c_1a_1a_2+c_2a_2^2\right)\right]}^{\text{matrix element squared}}}{\omega_n-\delta_2-\omega-i\gamma_n}=\left(4\pi\epsilon_0 r_e c^2\right)\left(\frac{(\Delta\rho)Tf_n}{\omega_n}\right)\underbrace{\left(\frac{1+c_1a_1a_2+c_2a_2^2}{\omega_n-\delta_2-\omega-i\gamma_n}\right)}_{\text{field dependent}} \tag{E.611}$$

where ϵ_0 is the electric permittivity of free space, r_e is the classical electron radius, c is the speed of light in a vacuum, e is the elementary charge, $\hbar$ is Planck's constant divided b y 2π, $(\Delta\rho)$ is the difference in population between the ground & excited states, $T=\{1/4,1/2,3/4,1\}$, $c_1=\pm\{2,2\sqrt{2}\}$,& $c_2=\{-1/2,+1\}$ are numerical constants that depends on the specific transition, f_n is the oscillator strength for the Dn transition, m is the mass of the electron, ω_n is the zero-field transition frequency for the Dn transition, δ_2 is the frequency shift due to the magnetic field & depends on the specific transition, ω is the incident light frequency, γ is the full width half maximum for the Dn transition, and $a1$ & $a2$ are the fine structure mixing coefficients and depend on the specific transition. When we say "specific" transition, we mean that it depends on the specific m_Js involved; on the other hand, when we say "Dn" transition, it only depends on the L_Js involved, where $n=1$ or 2. The last term is magnetic field dependent.

We'll specify the populations of the $|S,\pm\rangle$, $|P_-,\pm\rangle$, & $|P_+,(\pm1/2,\pm3/2)\rangle$ states. Under our spin-exchange optical pumping conditions inside the cells, the optical pumping rate is 1 MHz or less and the non-radiative quenching rate due to N_2 molecules is 1 GHz. This limits the populations of the $|P_\pm,(\pm1/2,\pm3/2)\rangle$ excited

states to $\approx 1/1000$. We can safely treat this as zero and set $\rho_{Psn+q} = 0$. Therefore, we only need to calculate the population of the $|S, \pm\rangle$ ground states. These are given by the electron spin polarization P as:

$$\rho_{S,\pm} = \frac{1 \pm P}{2} \tag{E.612}$$

Note that we can write everything in terms of the D1 oscillator strength f_1 by using:

$$f_n/\omega_n = n f_1/\omega_1 \qquad C^{-1} = 4\pi\epsilon_0 r_e c^2 f_1/\omega_1 \tag{E.613}$$

Expansion to Second Order in Magnetic Field

Before we can expand the last term to second order in field, we'll first need to specify the field dependence of each parameter. For convenience, the field will be represented by the fine structure scaling parameter y. We are considering the fine structure mixing for the P states, so $L = 1$ and taking $g_S = -2$ gives $y = \mu_B B/(\hbar\omega_{\mathtt{so}})$, where the fine structure splitting is given by $A_{\mathtt{so}}[L]/2 = \hbar\omega_{\mathtt{so}}$. The field dependence of the fine structure mixing coefficients a_1 & a_2 and frequency shift δ_2 to second order in y (field) is:

$$a_1 = 1 - \beta_0 y^2 \tag{E.614}$$

$$a_2 = -\beta_1 y + \beta_2 y^2 \tag{E.615}$$

$$\delta_2 = \omega_{\mathtt{so}}(ay + by^2) \tag{E.616}$$

where $\beta_0 = 1/9$, $\beta_1 = \sqrt{2}/3$, $\beta_2 = \pm\sqrt{2}/9$, $a = \pm\{1/3, 2/3, 1, 4/3, 5/3\}$, and $b = \pm 2/9$ depending on the transition involved. First we'll multiply the top and bot-

tom by the complex conjugate of the bottom:

$$G = G(y) = \frac{1 + c_1 a_1 a_2 + c_2 a_2^2}{\omega_n - \delta_2 - \omega - i\gamma_n} = \left(\frac{1 + c_1 a_1 a_2 + c_2 a_2^2}{\omega_n - \delta_2 - \omega - i\gamma_n}\right)\left(\frac{\omega_n - \delta_2 - \omega + i\gamma_n}{\omega_n - \delta_2 - \omega + i\gamma_n}\right) \tag{E.617}$$

which allows us to write G as a sum of its real and imaginary parts:

$$G = \frac{\left(1 + c_1 a_1 a_2 + c_2 a_2^2\right)(\omega_n - \omega - \delta_2 + i\gamma_n)}{(\omega_n - \omega - \delta_2)^2 + \gamma_n^2} = \frac{\left(1 + c_1 a_1 a_2 + c_2 a_2^2\right)(-\Delta_n - \delta_2 + i\gamma_n)}{(-\Delta_n - \delta_2)^2 + \gamma_n^2} \tag{E.618}$$

where $\Delta_n = \omega - \omega_n$ is the detuning. We now need to remove the field dependence from the bottom. To separate the bottom into a sum of field dependent and independent terms, we expand the square:

$$(-\Delta_n - \delta_2)^2 + \gamma_n^2 = \Delta_n^2 + 2\Delta_n\delta_2 + \delta_2^2 + \gamma_n^2 = D_n^2 + \delta_1 \tag{E.619}$$

where $D_n^2 = \Delta_n^2 + \gamma_n^2$ and $\delta_1 = 2\Delta_n\delta_2 + \delta_2^2$. Expanding the bottom to second order in y:

$$\frac{1}{D_n^2 + \delta_1} = D_n^{-2}\left(1 + \frac{\delta_1}{D_n^2}\right)^{-1} = D_n^{-2}\left(1 - \frac{\delta_1}{D_n^2} + \frac{\delta_1^2}{D_n^4}\right) \tag{E.620}$$

where $D_n^2 = \Delta_n^2 + \gamma_n^2$ is the field independent denominator of G. Altogether, this gives:

$$\begin{aligned} G &= \frac{\left(1 + c_1 a_1 a_2 + c_2 a_2^2\right)(-\Delta_n - \delta_2 + i\gamma_n)}{(-\Delta_n - \delta_2)^2 + \gamma_n^2} \\ &= D_n^{-2}(-\Delta_n + i\gamma_n - \delta_2)\left(1 + c_1 a_1 a_2 + c_2 a_2^2\right)\left(1 - \frac{\delta_1}{D_n^2} + \frac{\delta_1^2}{D_n^4}\right) \end{aligned} \tag{E.621}$$

The part of the field dependence of the numerator that is common to both the real and imaginary parts of G comes from this product:

$$\begin{aligned}(1+c_1a_1a_2+c_2a_2^2)\left(1-\frac{\delta_1}{D_n^2}+\frac{\delta_1^2}{D_n^4}\right) &= 1+\left[c_1a_1a_2-\frac{\delta_1}{D_n^2}\right]+\left[\frac{\delta_1^2}{D_n^4}-\frac{\delta_1}{D_n^2}c_1a_1a_2+c_2a_2^2\right] \\ &= 1+A_1y+A_2y^2 \end{aligned} \tag{E.622}$$

where we've kept on term second order in y. For only the real part, there is an additional term:

$$\begin{aligned}-\delta_2(1+c_1a_1a_2+c_2a_2^2)\left(1-\frac{\delta_1}{D_n^2}+\frac{\delta_1^2}{D_n^4}\right) &= -\delta_2+\left[\frac{\delta_1\delta_2}{D_n^2}-c_1\delta_2a_1a_2\right] \\ &= \omega_{\mathsf{so}}\left(B_1y+B_2y^2\right) \end{aligned} \tag{E.623}$$

Now we have:

$$G(y)=\frac{(-\Delta_n+i\gamma_n)\left(1+A_1y+A_2y^2\right)+\omega_{\mathsf{so}}(B_1y+B_2y^2)}{\Delta_n^2+\gamma_n^2} \tag{E.624}$$

The second order expansion of the product of parameters are:

$$a_1 a_2 = -\beta_1 y + \beta_2 y^2 \tag{E.625}$$

$$a_2^2 = \beta_1^2 y^2 \tag{E.626}$$

$$\delta_2^2 = a^2 \omega_{\mathrm{so}}^2 y^2 \tag{E.627}$$

$$\delta_1 = 2\Delta_n \delta_2 + \delta_2^2 = 2\Delta_n \omega_{\mathrm{so}}(ay + by^2) + a^2 \omega_{\mathrm{so}}^2 y^2 \tag{E.628}$$

$$\delta_1^2 = = 4a^2 \Delta_n^2 \omega_{\mathrm{so}}^2 y^2 \tag{E.629}$$

$$\delta_1 \delta_2 = 2a^2 \Delta_n \omega_{\mathrm{so}}^2 y^2 \tag{E.630}$$

$$\delta_2 a_1 a_2 = -a\beta_1 \omega_{\mathrm{so}} y^2 \tag{E.631}$$

$$\delta_1 a_1 a_2 = -2a\beta_1 \Delta_n \omega_{\mathrm{so}} y^2 \tag{E.632}$$

Plugging these in and collecting them by powers of y allows us to identify A_1, A_2, B_1, & B_2:

$$A_1 = -c_1\beta_1 - \frac{2a\Delta_n \omega_{\mathrm{so}}}{D_n^2} \tag{E.633}$$

$$A_2 = +c_1\beta_2 + c_2\beta_1^2 + \frac{2(ac_1\beta_1 - b)\Delta_n \omega_{\mathrm{so}} - a^2\omega_{\mathrm{so}}^2}{D_n^2} + \frac{4a^2\Delta_n^2\omega_{\mathrm{so}}^2}{D_n^4} \tag{E.634}$$

$$B_1 = -a \tag{E.635}$$

$$B_2 = ac_1\beta_1 - b + \frac{2a^2\Delta_n\omega_{\mathrm{so}}}{D_n^2} \tag{E.636}$$

where the values for the parameters for all the transitions are listed in Tab. (E.5). We'll define a lorentzian and dispersive line shape in the following way:

$$\mathcal{L}_n = \frac{\gamma_n}{D_n^2} = \frac{\gamma_n}{\Delta_n^2 + \gamma_n^2} \qquad \mathcal{D}_n = \frac{-\Delta_n}{D_n^2} = \frac{-\Delta_n}{\Delta_n^2 + \gamma_n^2} \tag{E.637}$$

m	q	s	$m+q$	n	T	c_1	c_2	β_2	a	b	$-c_1\beta_1$	a^2	$(ac_1\beta_1 - b)$	$(c_1\beta_2 + c_2\beta_1^2)$
$-$	$-$	$+$	$-3/2$	2	3/4	0	0	0	$+1$	0	0	1	0	0
$+$	$-$	$-$	$-1/2$	1	1	$+\sqrt{2}$	$-1/2$	$-\sqrt{2}/9$	$+4/3$	$+2/9$	$-2/3$	16/9	$+2/3$	$-1/3$
$+$	$-$	$+$	$-1/2$	2	1/4	$-2\sqrt{2}$	$+1$	$-\sqrt{2}/9$	$+5/3$	$-2/9$	$+4/3$	25/9	-2	$+2/3$
$-$	0	$-$	$-1/2$	1	1/2	$-2\sqrt{2}$	$+1$	$-\sqrt{2}/9$	$-2/3$	$+2/9$	$+4/3$	4/9	$+2/3$	$+2/3$
$-$	0	$+$	$-1/2$	2	1/2	$+\sqrt{2}$	$-1/2$	$-\sqrt{2}/9$	$-1/3$	$-2/9$	$-2/3$	1/9	0	$-1/3$
$+$	0	$-$	$+1/2$	1	1/2	$+2\sqrt{2}$	$+1$	$+\sqrt{2}/9$	$+2/3$	$+2/9$	$-4/3$	4/9	$+2/3$	$+2/3$
$+$	0	$+$	$+1/2$	2	1/2	$-\sqrt{2}$	$-1/2$	$+\sqrt{2}/9$	$+1/3$	$-2/9$	$+2/3$	1/9	0	$-1/3$
$-$	$+$	$-$	$+1/2$	1	1	$-\sqrt{2}$	$-1/2$	$+\sqrt{2}/9$	$-4/3$	$+2/9$	$+2/3$	16/9	$+2/3$	$-1/3$
$-$	$+$	$+$	$+1/2$	2	1/4	$+2\sqrt{2}$	$+1$	$+\sqrt{2}/9$	$-5/3$	$-2/9$	$-4/3$	25/9	-2	$+2/3$
$+$	$+$	$+$	$+3/2$	2	3/4	0	0	0	-1	0	0	1	0	0

Table E.5: Low Field Expansion Parameters. Dn transition due to r_q from $|S, m\rangle$ to $|P_s, m+q\rangle$. For all transitions, $\beta_0 = 1/9$ and $\beta_1 = \sqrt{2}/3$.

Using this notation, we rewrite $G(y)$ and the parameters within it:

$$G(y) = (\mathcal{D}_n + i\mathcal{L}_n)\left(1 + A_1 y + A_2 y^2\right) + \frac{\omega_{\mathsf{so}}}{\gamma_n}\mathcal{L}_n(B_1 y + B_2 y^2) \tag{E.638}$$

$$A_1 = -c_1\beta_1 + 2a\omega_{\mathsf{so}}\mathcal{D}_n \tag{E.639}$$

$$A_2 = +(c_1\beta_2 + c_2\beta_1^2) - 2(ac_1\beta_1 - b)\omega_{\mathsf{so}}\mathcal{D}_n + a^2\omega_{\mathsf{so}}^2\left(4\mathcal{D}_n^2 - \frac{\mathcal{L}_n}{\gamma_n}\right) \tag{E.640}$$

$$B_1 = -a \tag{E.641}$$

$$B_2 = (ac_1\beta_1 - b) - 2a^2\omega_{\mathsf{so}}\mathcal{D}_n \tag{E.642}$$

The real part is written as:

$$\begin{aligned}\Re G = {} & \mathcal{D}_n\left\{1 + [-c_1\beta_1 + 2a\omega_{\mathsf{so}}\mathcal{D}_n]\, y\right. \\ & \left. + \left[(c_1\beta_2 + c_2\beta_1^2) - 2(ac_1\beta_1 - b)\omega_{\mathsf{so}}\mathcal{D}_n + a^2\omega_{\mathsf{so}}^2\left(4\mathcal{D}_n^2 - 3\frac{\mathcal{L}_n}{\gamma_n}\right)\right] y^2\right\} \\ & + \mathcal{L}_n\frac{\omega_{\mathsf{so}}}{\gamma_n}\left\{-ay + (ac_1\beta_1 - b)y^2\right\}\end{aligned} \tag{E.643}$$

The imaginary part is written as:

$$\begin{aligned}\Im G &= \mathcal{L}_n\left\{1+\left[-c_1\beta_1+2a\omega_{\mathrm{so}}\mathcal{D}_n\right]y\right.\\ &\left.+\left[(c_1\beta_2+c_2\beta_1^2)-2(ac_1\beta_1-b)\omega_{\mathrm{so}}\mathcal{D}_n+a^2\omega_{\mathrm{so}}^2\left(4\mathcal{D}_n^2-\frac{\mathcal{L}_n}{\gamma_n}\right)\right]y^2\right\}\end{aligned} \tag{E.644}$$

Imaginary Part of the Polarizability: Absorption

The imaginary part of each term in the sum is written as:

$$\begin{aligned}&\tfrac{nT(1\pm P)}{2C}\mathcal{L}_n\left\{1+y\times(\cdots)\right\}\\ \cdots &= -c_1\beta_1+2a\omega_{\mathrm{so}}\mathcal{D}_n+\left[(c_1\beta_2+c_2\beta_1^2)-2(ac_1\beta_1-b)\omega_{\mathrm{so}}\mathcal{D}_n+a^2\omega_{\mathrm{so}}^2\left(4\mathcal{D}_n^2-\tfrac{\mathcal{L}_n}{\gamma_n}\right)\right]y\end{aligned} \tag{E.645}$$

where as a reminder $1/C=4\pi\epsilon_0 r_e c^2 f_1/\omega_1$, n refers to the Dn transition, P is the polarization of the ground state, and the other parameters are obtained from Tab. (E.5). Plugging in the parameters for the $q=-1$ component gives:

$$\begin{aligned}C\Im\alpha_- &= \frac{3}{4}(1-P)\mathcal{L}_2\left\{1+\left[2\omega_{\mathrm{so}}\mathcal{D}_2\right]y+\left[\omega_{\mathrm{so}}^2\left(4\mathcal{D}_2^2-\frac{\mathcal{L}_2}{\gamma_2}\right)\right]y^2\right\}\\ &+\frac{1}{6}(1+P)\mathcal{L}_1\left\{3+\left[-2+8\omega_{\mathrm{so}}\mathcal{D}_1\right]y+\left[-1-4\omega_{\mathrm{so}}\mathcal{D}_1+\frac{16}{3}\omega_{\mathrm{so}}^2\left(4\mathcal{D}_1^2-\frac{\mathcal{L}_1}{\gamma_1}\right)\right]y^2\right\}\\ &+\frac{1}{12}(1+P)\mathcal{L}_2\left\{3+\left[4+10\omega_{\mathrm{so}}\mathcal{D}_2\right]y+\left[2+12\omega_{\mathrm{so}}\mathcal{D}_2+\frac{25}{3}\omega_{\mathrm{so}}^2\left(4\mathcal{D}_2^2-\frac{\mathcal{L}_2}{\gamma_2}\right)\right]y^2\right\}\end{aligned} \tag{E.646}$$

Combining the D2 terms while separating the polarization dependent terms gives:

$$
\begin{aligned}
C\Im\alpha_{-} &= \mathcal{L}_2\left\{1+\left[\frac{1}{3}+\frac{7}{3}\omega_{so}\mathcal{D}_2\right]y+\left[\frac{1}{6}+\omega_{so}\mathcal{D}_2+\frac{13}{9}\omega_{so}^2\left(4\mathcal{D}_2^2-\frac{\mathcal{L}_2}{\gamma_2}\right)\right]y^2\right\}\\
&\quad -\frac{P}{2}\mathcal{L}_2\left\{1+\left[-\frac{2}{3}+\frac{4}{3}\omega_{so}\mathcal{D}_2\right]y+\left[-\frac{1}{3}-2\omega_{so}\mathcal{D}_2+\frac{1}{9}\omega_{so}^2\left(4\mathcal{D}_2^2-\frac{\mathcal{L}_2}{\gamma_2}\right)\right]y^2\right\}\\
&\quad +\frac{(1+P)}{2}\mathcal{L}_1\left\{1+\left[-\frac{2}{3}+\frac{8}{3}\omega_{so}\mathcal{D}_1\right]y+\left[-\frac{1}{3}-\frac{4}{3}\omega_{so}\mathcal{D}_1+\frac{16}{9}\omega_{so}^2\left(4\mathcal{D}_1^2-\frac{\mathcal{L}_1}{\gamma_1}\right)\right]y^2\right\}
\end{aligned}
\tag{E.647}
$$

Plugging in the parameters for the $q=0$ component gives:

$$
\begin{aligned}
C\Im\alpha_{0} &= +\frac{1}{4}(1-P)\mathcal{L}_1\left\{1+\left[\frac{4}{3}-\frac{4}{3}\omega_{so}\mathcal{D}_1\right]y+\left[\frac{2}{3}-\frac{4}{3}\omega_{so}\mathcal{D}_1+\frac{4}{9}\omega_{so}^2\left(4\mathcal{D}_1^2-\frac{\mathcal{L}_1}{\gamma_1}\right)\right]y^2\right\}\\
&\quad +\frac{1}{2}(1-P)\mathcal{L}_2\left\{1+\left[-\frac{2}{3}-\frac{2}{3}\omega_{so}\mathcal{D}_2\right]y+\left[-\frac{1}{3}+\frac{1}{9}\omega_{so}^2\left(4\mathcal{D}_2^2-\frac{\mathcal{L}_2}{\gamma_2}\right)\right]y^2\right\}\\
&\quad +\frac{1}{4}(1+P)\mathcal{L}_1\left\{1+\left[-\frac{4}{3}+\frac{4}{3}\omega_{so}\mathcal{D}_1\right]y+\left[\frac{2}{3}-\frac{4}{3}\omega_{so}\mathcal{D}_1+\frac{4}{9}\omega_{so}^2\left(4\mathcal{D}_1^2-\frac{\mathcal{L}_1}{\gamma_1}\right)\right]y^2\right\}\\
&\quad +\frac{1}{2}(1+P)\mathcal{L}_2\left\{1+\left[\frac{2}{3}+\frac{2}{3}\omega_{so}\mathcal{D}_2\right]y+\left[-\frac{1}{3}+\frac{1}{9}\omega_{so}^2\left(4\mathcal{D}_2^2-\frac{\mathcal{L}_2}{\gamma_2}\right)\right]y^2\right\}
\end{aligned}
\tag{E.648}
$$

Combining the D1 & D2 terms while separating the polarization dependent terms gives:

$$
\begin{aligned}
C\Im\alpha_{0} &= +\frac{1}{2}\mathcal{L}_1\left\{1+\left[\frac{2}{3}-\frac{4}{3}\omega_{so}\mathcal{D}_1+\frac{4}{9}\omega_{so}^2\left(4\mathcal{D}_1^2-\frac{\mathcal{L}_1}{\gamma_1}\right)\right]y^2\right\}\\
&\quad +\mathcal{L}_2\left\{1+\left[-\frac{1}{3}+\frac{1}{9}\omega_{so}^2\left(4\mathcal{D}_2^2-\frac{\mathcal{L}_2}{\gamma_2}\right)\right]y^2\right\}\\
&\quad +P\left\{\mathcal{L}_1\left[-1+\omega_{so}\mathcal{D}_1\right]+\mathcal{L}_2\left[+1+\omega_{so}\mathcal{D}_2\right]\right\}\frac{2y}{3}
\end{aligned}
\tag{E.649}
$$

Plugging in the parameters for the $q=+1$ component gives:

$$
\begin{aligned}
C\Im\alpha_+ &= \frac{(1-P)}{2}\mathcal{L}_1\left\{1+\left[\frac{2}{3}-\frac{8}{3}\omega_{so}\mathcal{D}_1\right]y+\left[-\frac{1}{3}-\frac{4}{3}\omega_{so}\mathcal{D}_1+\frac{16}{9}\omega_{so}^2\left(4\mathcal{D}_1^2-\frac{\mathcal{L}_1}{\gamma_1}\right)\right]y^2\right\} \\
&+\frac{1}{4}(1-P)\mathcal{L}_2\left\{1+\left[-\frac{4}{3}-\frac{10}{3}\omega_{so}\mathcal{D}_2\right]y+\left[\frac{2}{3}+4\omega_{so}\mathcal{D}_2+\frac{25}{9}\omega_{so}^2\left(4\mathcal{D}_2^2-\frac{\mathcal{L}_2}{\gamma_2}\right)\right]y^2\right\} \\
&+\frac{3}{4}(1+P)\mathcal{L}_2\left\{1+\left[-2\omega_{so}\mathcal{D}_2\right]y+\left[\omega_{so}^2\left(4\mathcal{D}_2^2-\frac{\mathcal{L}_2}{\gamma_2}\right)\right]y^2\right\}
\end{aligned}
\tag{E.650}
$$

Combining the D2 terms while separating the polarization dependent terms gives:

$$
\begin{aligned}
C\Im\alpha_+ &= \frac{(1-P)}{2}\mathcal{L}_1\left\{1+\left[\frac{2}{3}-\frac{8}{3}\omega_{so}\mathcal{D}_1\right]y+\left[-\frac{1}{3}-\frac{4}{3}\omega_{so}\mathcal{D}_1+\frac{16}{9}\omega_{so}^2\left(4\mathcal{D}_1^2-\frac{\mathcal{L}_1}{\gamma_1}\right)\right]y^2\right\} \\
&+\mathcal{L}_2\left\{1+\left[-\frac{1}{3}-\frac{7}{3}\omega_{so}\mathcal{D}_2\right]y+\left[\frac{1}{6}+\omega_{so}\mathcal{D}_2+\frac{13}{9}\omega_{so}^2\left(4\mathcal{D}_2^2-\frac{\mathcal{L}_2}{\gamma_2}\right)\right]y^2\right\} \\
&+\frac{P}{2}\mathcal{L}_2\left\{1+\left[\frac{2}{3}-\frac{4}{3}\omega_{so}\mathcal{D}_2\right]y+\left[-\frac{1}{3}-2\omega_{so}\mathcal{D}_2+\frac{1}{9}\omega_{so}^2\left(4\mathcal{D}_2^2-\frac{\mathcal{L}_2}{\gamma_2}\right)\right]y^2\right\}
\end{aligned}
\tag{E.651}
$$

Putting all three results together gives for $q=0,\pm1$:

$$
\begin{aligned}
C\Im\alpha_q &= \frac{(1-qP)}{2}\mathcal{L}_1\left\{1+q\left[\frac{2}{3}-\frac{8}{3}\omega_{so}\mathcal{D}_1\right]y+\left[\frac{2}{3}-q^2-\frac{4}{3}\omega_{so}\mathcal{D}_1+\frac{4+12q^2}{9}\omega_{so}^2\left(4\mathcal{D}_1^2-\frac{\mathcal{L}_1}{\gamma_1}\right)\right]y^2\right\} \\
&+\mathcal{L}_2\left\{1-q\left[\frac{1}{3}+\frac{7}{3}\omega_{so}\mathcal{D}_2\right]y+\left[-\frac{1}{3}+\frac{q^2}{2}+q^2\omega_{so}\mathcal{D}_2+\frac{1+12q^2}{9}\omega_{so}^2\left(4\mathcal{D}_2^2-\frac{\mathcal{L}_2}{\gamma_2}\right)\right]y^2\right\} \\
&+\frac{qP}{2}\mathcal{L}_2\left\{1+q\left[\frac{2}{3}-\frac{4}{3}\omega_{so}\mathcal{D}_2\right]y+\left[-\frac{1}{3}-2\omega_{so}\mathcal{D}_2+\frac{1}{9}\omega_{so}^2\left(4\mathcal{D}_2^2-\frac{\mathcal{L}_2}{\gamma_2}\right)\right]y^2\right\} \\
&+(1-q^2)P\left\{\mathcal{L}_1\left[-1+\omega_{so}\mathcal{D}_1\right]+\mathcal{L}_2\left[+1+\omega_{so}\mathcal{D}_2\right]\right\}\frac{2y}{3}
\end{aligned}
\tag{E.652}
$$

Real Part of the Polarizability: Phase Shift

The real part of each term in the sum is written as the sum between one part that has an imaginary analogue:

$$\frac{nT(1\pm P)}{2}\mathcal{D}_n\left[1+[-c_1\beta_1+2a\omega_{\rm so}\mathcal{D}_n]\,y+\left[(c_1\beta_2+c_2\beta_1^2)-2(ac_1\beta_1-b)\omega_{\rm so}\mathcal{D}_n+a^2\omega_{\rm so}^2\left(4\mathcal{D}_n^2-3\frac{\mathcal{L}_n}{\gamma_n}\right)\right]y^2\right] \tag{E.653}$$

and an additional term that does not have an imaginary analogue:

$$\frac{nT(1\pm P)}{2}\mathcal{L}_n\frac{\omega_{\rm so}}{\gamma_n}\left\{-ay+(ac_1\beta_1-b)y^2\right\} \tag{E.654}$$

where again $1/C=4\pi\epsilon_0 r_e c^2 f_1/\omega_1$, n refers to the Dn transition, P is the polarization of the ground state, and the other parameters are obtained from Tab. (E.5) To be explicit, the three main differences between the calculation for the imaginary part (that we've already done) and this one for the real part are:

1. the overall $\mathcal{L}_n$ outside the brackets becomes $\mathcal{D}_n$
2. the last term in the y^2 bracket goes from $-\mathcal{L}_n\gamma_n$ to $-3\mathcal{L}_n/\gamma_n$
3. there is an additional term proportional to $\mathcal{L}_n\frac{\omega_{\rm so}}{\gamma_n}$ that we must work out as well

Using the results for the imaginary part, the first term (α_q^1) for the real part for the $q=0,\pm1$ component is:

$$\begin{aligned}
C\Re\alpha_q^1 \;=\;& \frac{(1-qP)}{2}\mathcal{D}_1\left\{1+q\left[\frac{2}{3}-\frac{8}{3}\omega_{\rm so}\mathcal{D}_1\right]y+\left[\frac{2}{3}-q^2-\frac{4}{3}\omega_{\rm so}\mathcal{D}_1+\frac{4+12q^2}{9}\omega_{\rm so}^2\left(4\mathcal{D}_1^2-3\frac{\mathcal{L}_1}{\gamma_1}\right)\right]y^2\right\}\\
&+\mathcal{D}_2\left\{1-q\left[\frac{1}{3}+\frac{7}{3}\omega_{\rm so}\mathcal{D}_2\right]y+\left[-\frac{1}{3}+\frac{q^2}{2}+q^2\omega_{\rm so}\mathcal{D}_2+\frac{1+12q^2}{9}\omega_{\rm so}^2\left(4\mathcal{D}_2^2-3\frac{\mathcal{L}_2}{\gamma_2}\right)\right]y^2\right\}\\
&+\frac{qP}{2}\mathcal{D}_2\left\{1+q\left[\frac{2}{3}-\frac{4}{3}\omega_{\rm so}\mathcal{D}_2\right]y+\left[-\frac{1}{3}-2\omega_{\rm so}\mathcal{D}_2+\frac{1}{9}\omega_{\rm so}^2\left(4\mathcal{D}_2^2-3\frac{\mathcal{L}_2}{\gamma_2}\right)\right]y^2\right\}\\
&+(1-q^2)P\left\{\mathcal{D}_1[-1+\omega_{\rm so}\mathcal{D}_1]+\mathcal{D}_2[+1+\omega_{\rm so}\mathcal{D}_2]\right\}\frac{2y}{3}
\end{aligned} \tag{E.655}$$

Now calculating the second term (α_q^2) for the real part for the $q=-1$ compo-

nent:

$$C\Re\alpha_{-}^{2} = \frac{3(1-P)}{4}\mathcal{L}_2\frac{\omega_{so}}{\gamma_2}\{-y\} + \frac{(1+P)}{2}\mathcal{L}_1\frac{\omega_{so}}{\gamma_1}\left\{-\frac{4}{3}y+\frac{2}{3}y^2\right\} + \frac{(1+P)}{4}\mathcal{L}_2\frac{\omega_{so}}{\gamma_2}\left\{-\frac{5}{3}y-2y^2\right\} \tag{E.656}$$

Combining the D2 terms while separating the polarization dependent terms gives:

$$C\Re\alpha_{-}^{2} = (1+P)\mathcal{L}_1\frac{\omega_{so}}{\gamma_1}\left\{-\frac{2}{3}y+\frac{1}{3}y^2\right\} + \mathcal{L}_2\frac{\omega_{so}}{\gamma_2}\left\{-\frac{7}{6}y-\frac{1}{2}y^2\right\} + P\mathcal{L}_2\frac{\omega_{so}}{\gamma_2}\left\{\frac{1}{3}y-\frac{1}{2}y^2\right\} \tag{E.657}$$

Now calculating the second term (α_q^2) for the real part for the $q=0$ component:

$$\begin{aligned} C\Re\alpha_0^2 &= \frac{(1-P)}{4}\mathcal{L}_1\frac{\omega_{so}}{\gamma_1}\left\{\frac{2}{3}y+\frac{2}{3}y^2\right\} + \frac{(1-P)}{2}\mathcal{L}_2\frac{\omega_{so}}{\gamma_2}\left\{\frac{1}{3}y\right\} \\ &\quad + \frac{(1+P)}{4}\mathcal{L}_1\frac{\omega_{so}}{\gamma_1}\left\{-\frac{2}{3}y+\frac{2}{3}y^2\right\} + \frac{(1+P)}{2}\mathcal{L}_2\frac{\omega_{so}}{\gamma_2}\left\{-\frac{1}{3}y\right\} \end{aligned} \tag{E.658}$$

Combining the D2 terms while separating the polarization dependent terms gives:

$$C\Re\alpha_0^2 = \mathcal{L}_1\frac{\omega_{so}}{\gamma_1}\left\{\frac{1}{3}y^2\right\} - P\mathcal{L}_1\frac{\omega_{so}}{\gamma_1}\left\{\frac{1}{3}y\right\} - P\mathcal{L}_2\frac{\omega_{so}}{\gamma_2}\left\{\frac{1}{3}y\right\} \tag{E.659}$$

Now calculating the second term (α_q^2) for the real part for the $q=+1$ component:

$$C\Re\alpha_{+}^{2} = +\frac{(1-P)}{2}\mathcal{L}_1\frac{\omega_{so}}{\gamma_1}\left\{\frac{4}{3}y+\frac{2}{3}y^2\right\} + \frac{(1-P)}{4}\mathcal{L}_2\frac{\omega_{so}}{\gamma_2}\left\{\frac{5}{3}y-2y^2\right\} + \frac{3(1+P)}{4}\mathcal{L}_2\frac{\omega_{so}}{\gamma_2}\{y\} \tag{E.660}$$

Combining the D2 terms while separating the polarization dependent terms

gives:

$$C\Re\alpha_+^2 = (1-P)\mathcal{L}_1\frac{\omega_{so}}{\gamma_1}\left\{\frac{2}{3}y+\frac{1}{3}y^2\right\}+\mathcal{L}_2\frac{\omega_{so}}{\gamma_2}\left\{\frac{7}{6}y-\frac{1}{2}y^2\right\}+P\mathcal{L}_2\frac{\omega_{so}}{\gamma_2}\left\{\frac{1}{3}y+\frac{1}{2}y^2\right\} \tag{E.661}$$

Putting this altogether gives:

$$\begin{aligned} C\Re\alpha_q^2 &= (1-qP)\mathcal{L}_1\frac{\omega_{so}}{\gamma_1}\left\{q\frac{2}{3}y+\frac{1}{3}y^2\right\}+\mathcal{L}_2\frac{\omega_{so}}{\gamma_2}\left\{q\frac{7}{6}y-q^2\frac{1}{2}y^2\right\} \\ &\quad -(1-q^2)P\mathcal{L}_1\frac{\omega_{so}}{\gamma_1}\left\{\frac{1}{3}y\right\}+P\mathcal{L}_2\frac{\omega_{so}}{\gamma_2}\left\{\frac{2q^2-1}{3}y+q\frac{1}{2}y^2\right\} \end{aligned} \tag{E.662}$$

Finally, combining both terms gives for the real part α_q where $q=0,\pm1$:

$$\begin{aligned} C\Re\alpha_q &= \frac{(1-qP)}{2}\mathcal{D}_1\left\{1+q\left[\frac{2}{3}-\frac{8}{3}\omega_{so}\mathcal{D}_1\right]y+\left[\frac{2}{3}-q^2-\frac{4}{3}\omega_{so}\mathcal{D}_1+\frac{4+12q^2}{9}\omega_{so}^2\left(4\mathcal{D}_1^2-3\frac{\mathcal{L}_1}{\gamma_1}\right)\right]y^2\right\} \\ &\quad +\mathcal{D}_2\left\{1-q\left[\frac{1}{3}+\frac{7}{3}\omega_{so}\mathcal{D}_2\right]y+\left[-\frac{1}{3}+\frac{q^2}{2}+q^2\omega_{so}\mathcal{D}_2+\frac{1+12q^2}{9}\omega_{so}^2\left(4\mathcal{D}_2^2-3\frac{\mathcal{L}_2}{\gamma_2}\right)\right]y^2\right\} \\ &\quad +\frac{qP}{2}\mathcal{D}_2\left\{1+q\left[\frac{2}{3}-\frac{4}{3}\omega_{so}\mathcal{D}_2\right]y+\left[-\frac{1}{3}-2\omega_{so}\mathcal{D}_2+\frac{1}{9}\omega_{so}^2\left(4\mathcal{D}_2^2-3\frac{\mathcal{L}_2}{\gamma_2}\right)\right]y^2\right\} \\ &\quad +(1-q^2)P\left\{\mathcal{D}_1\left[-1+\omega_{so}\mathcal{D}_1\right]+\mathcal{D}_2\left[+1+\omega_{so}\mathcal{D}_2\right]-\frac{1}{2}\mathcal{L}_1\frac{\omega_{so}}{\gamma_1}\right\}\frac{2y}{3} \\ &\quad +(1-qP)\mathcal{L}_1\frac{\omega_{so}}{\gamma_1}\left\{\frac{2q}{3}y+\frac{1}{3}y^2\right\}+\mathcal{L}_2\frac{\omega_{so}}{\gamma_2}\left\{\frac{7q}{6}y-\frac{q^2}{2}y^2\right\}+P\mathcal{L}_2\frac{\omega_{so}}{\gamma_2}\left\{\frac{2q^2-1}{3}y+\frac{q}{2}y^2\right\} \end{aligned} \tag{E.663}$$

E.6.3 Atomic Polarization Vector

Light Propagation At a Skew Angle

It is useful to know how light is effected by the presence of a polarized alkali vapor when (1) optical pumping or (2) measuring alkali polarization and densities using Faraday Rotation. We'll assume that the polarized alkali vapor is located within a magnetic field that orients the alkali angular momentum. In other words, the magnetic field provides one axis of a coordinate system that naturally describes

the alkali atoms. The light and the alkali atoms are connected through the atomic polarizability, which itself is related to the dielectric permittivity. We'll start with Maxwell's equations and end with a matrix eigenvalue equation. The solution to this equation will give the wave numbers and polarization vectors for the two eigenmodes of propagation through the vapor. An eigenmode of propagation has the property that its polarization vector does not change as it propagates through the alkali vapor.

In SI, Maxwell's equations are:

$$\begin{aligned} \vec{\nabla}\cdot\vec{D} &= \rho & \vec{\nabla}\times\vec{E} &= -\partial\vec{B}/\partial t \\ \vec{\nabla}\cdot\vec{B} &= 0 & \vec{\nabla}\times\vec{H} &= \vec{J}+\partial\vec{D}/\partial t \end{aligned} \tag{E.664}$$

and the constitutive relations for a linear medium between the electric vector $\vec{E}$ & the electric displacement $\vec{D}$ and between the magnetic induction $\vec{B}$ & the magnetic vector $\vec{H}$ are:

$$\vec{D} = \overleftrightarrow{\varepsilon}\cdot\vec{E} \qquad \vec{B} = \overleftrightarrow{\mu}\cdot\vec{H} \tag{E.665}$$

where $\overleftrightarrow{\varepsilon}$ & $\overleftrightarrow{\mu}$ are the dielectric permittivity & the magnetic permeability tensors, respectively. In our case, there are no free charges ρ and currents $\vec{J}$. Since the light has optical frequencies, the magnetic permeability tensor $\overleftrightarrow{\mu}$ is very nearly equal to the scalar free space value μ_0:

$$\begin{aligned} \vec{\nabla}\cdot\vec{D} &= 0 & \vec{\nabla}\times\vec{E} &= -\mu_0\partial\vec{H}/\partial t \\ \vec{\nabla}\cdot\vec{H} &= 0 & \vec{\nabla}\times\vec{H} &= \partial\vec{D}/\partial t \end{aligned} \tag{E.666}$$

Representing the spatial and time dependence of $\vec{E}$, $\vec{D}$, $\vec{B}$, & $\vec{H}$ in plane wave form,

such as $\vec{E} \rightarrow \vec{E}\exp\left[i\vec{k}\cdot\vec{r} - i\omega t\right]$, results in:

$$\begin{aligned} \vec{k}\cdot\vec{D} &= 0 \qquad & \vec{k}\times\vec{E} &= \omega\mu_0\vec{H} \\ \vec{k}\cdot\vec{H} &= 0 \qquad & \vec{k}\times\vec{H} &= -\omega\vec{D} \end{aligned} \tag{E.667}$$

where $\vec{k}$ is the wave number and $\omega = 2\pi\nu$ is the frequency. Combining the two cross product equations results in:

$$\vec{k}\times\left(\vec{k}\times\vec{E}\right) = \vec{k}\left(\vec{k}\cdot\vec{E}\right) - k^2\vec{E} = -\omega^2\mu_0\vec{D} \tag{E.668}$$

where we've used the identity $\vec{a}\times\left(\vec{b}\times\vec{c}\right) = \vec{b}(\vec{a}\cdot\vec{c}) - \vec{c}\left(\vec{a}\cdot\vec{b}\right)$. Finally, using the constitutive relation for $\vec{D}$, factoring out $\vec{E}$, and moving things around gives:

$$\left(\begin{bmatrix} k^2 & 0 & 0 \\ 0 & k^2 & 0 \\ 0 & 0 & k^2 \end{bmatrix} - \begin{bmatrix} k_1^2 & k_1k_2 & k_1k_3 \\ k_2k_1 & k_2^2 & k_2k_3 \\ k_3k_1 & k_3k_2 & k_3^2 \end{bmatrix} - \omega^2\mu_0 \overleftrightarrow{\varepsilon} \right) \cdot \vec{E} = 0 \tag{E.669}$$

The derivation of this equation can also be found in chapter 15 of *Born & Wolf* [30] and also *Yariv & Yeh* [31].

Wave Number Eigenvalues

The following calculation is a detailed extension to the one found in [32]. There are in general three coordinate systems that one could use to solve for the possible eigenvalues for k:

1. the atomic basis, namely one that reflects the symmetry of the alkali vapor $\left(\hat{r}_+^*;\hat{r}_-^*;\hat{r}_0^* = \hat{B}_0\right)$ which is determined by the magnetic field $\vec{B}_0$

2. the linear $\left(\mathcal{P};\mathcal{S};\mathcal{Z}=\hat{k}\right)$ or circular $(\mathcal{R};\mathcal{L};\mathcal{Z})$ polarization basis of the light

3. the polarization eigenvector basis, namely the one for which the matrix multiplying $\vec{E}$ is diagonal

Unfortunately, we usually do not know beforehand what the polarization eigenvector basis is. However, when the magnetic field and light propagation direction point in the same direction, all three coordinates systems happen to coincide. Therefore we'll take advantage of this fact and choose to work in the circular polarization basis of the light. Consequently, the wave number dyad is represented as:

$$\vec{k}\vec{k} = \begin{bmatrix} 0 & 0 & 0 \\ 0 & 0 & 0 \\ 0 & 0 & k^2 \end{bmatrix} \tag{E.670}$$

where $k_1 = k_2 = 0$ and $\sqrt{k_1^2 + k_2^2 + k_3^2} = k^2$ due to the orthonormality of the circular polarization basis.

In the atomic basis $\left(\hat{r}_+^*;\hat{r}_-^*;\hat{r}_0^*\right)$, the dielectric tensor is, by construction, diagonal and given as:

$$\overleftrightarrow{\varepsilon} = \varepsilon_0 \left(1 + \frac{[\mathrm{A}]}{\varepsilon_0} \begin{bmatrix} \alpha_+ & 0 & 0 \\ 0 & \alpha_- & 0 \\ 0 & 0 & \alpha_0 \end{bmatrix} \right) \tag{E.671}$$

where ε_0 is the dielectric permittivity of free space and $[A]$ is the alkali number density. When the magnetic field is zero, the polarizabilities are given by:

$$\alpha_q = \frac{\varepsilon_0 r_e c^2}{2\pi} \left[\underbrace{\frac{f_1/\nu_1}{\nu_1 - \nu - i\Gamma_1/2}\left(1 - qP_{\mathrm{A}}\right)}_{\text{D1 transition}} + \underbrace{\frac{f_2/\nu_2}{\nu_2 - \nu - i\Gamma_2/2}\left(1 + \frac{qP_{\mathrm{A}}}{2}\right)}_{\text{D2 transition}} \right] \tag{E.672}$$

where r_e is the classical electron radius, c is the speed of light in a vacuum, P_{A} is the alkali polarization, $q(=0,\pm1)$ is the amount of angular momentum transferred to an alkali atom, f_n is the oscillator strength, ν_n is the transition frequency, and Γ_n is the full width half maximum of the transition. The subscripts $n(=1,2)$ refer to the D1 and D2 transitions of the alkali atom.

We'll have to transform the polarizability tensor from the $\left(\hat{r}_+^*;\hat{r}_-^*;\hat{r}_0^*\right)$ basis to the $(\mathcal{R};\mathcal{L};\mathcal{Z})$ basis in the following way:

1. switch from the $\left(\hat{r}_+^*;\hat{r}_-^*;\hat{r}_0^*\right)$ basis to the $\left(\hat{x};\hat{y};\hat{z}\right)$ basis relative to the atomic system

2. rotate by an angle θ from the $\left(\hat{x};\hat{y};\hat{z}\right)$ basis relative to the atomic system to the $(\mathcal{P};\mathcal{S};\mathcal{Z})$ basis relative to the light polarization, where θ is the angle between the magnetic field and the light propagation direction as in $\hat{B}_0\cdot\hat{k}=\cos(\theta)$

3. switch from the $(\mathcal{P};\mathcal{S};\mathcal{Z})$ basis to the $(\mathcal{R};\mathcal{L};\mathcal{Z})$ basis relative to the light polarization

We'll note the following relationships between the different bases relative to the light system:

$$\mathcal{R}=\frac{\mathcal{P}+i\mathcal{S}}{\sqrt{2}}\qquad\qquad \mathcal{L}=\frac{\mathcal{P}-i\mathcal{S}}{\sqrt{2}} \tag{E.673}$$

between the different bases relative to the atomic system:

$$\vec{r}=r_+\hat{r}_+^*+r_-\hat{r}_-^*+r_0\hat{r}_0^*=x\hat{x}+y\hat{y}+z\hat{z} \tag{E.674}$$

$$r_+=-\left(\frac{x+iy}{\sqrt{2}}\right)\qquad\qquad r_-=\frac{x-iy}{\sqrt{2}}\qquad\qquad r_0=z \tag{E.675}$$

and finally between the atomic and light systems:

$$\hat{x} = \mathcal{P}\cos(\theta) - \mathcal{Z}\sin(\theta) \qquad \hat{z} = \mathcal{P}\sin(\theta) + \mathcal{Z}\cos(\theta) \tag{E.676}$$

Switching the basis of the polarizability tensor from the circular basis to linear basis relative to the atomic system gives:

$$\overleftrightarrow{\alpha} = \frac{1}{\sqrt{2}}\begin{bmatrix} -1 & +1 & 0 \\ -i & -i & 0 \\ 0 & 0 & +1 \end{bmatrix}\begin{bmatrix} \alpha_+ & 0 & 0 \\ 0 & \alpha_- & 0 \\ 0 & 0 & \alpha_0 \end{bmatrix}\frac{1}{\sqrt{2}}\begin{bmatrix} -1 & +i & 0 \\ +1 & +i & 0 \\ 0 & 0 & +1 \end{bmatrix} = \frac{1}{2}\begin{bmatrix} \sigma & -i\delta & 0 \\ i\delta & \sigma & 0 \\ 0 & 0 & 2\alpha_0 \end{bmatrix} \tag{E.677}$$

where σ & δ are the sum & difference of α_+ & α_-:

$$\sigma = \alpha_+ + \alpha_- = 2\alpha_0 \qquad \delta = \alpha_+ - \alpha_- \tag{E.678}$$

To simplify things, we'll break the the resulting matrix up into the following:

$$\overleftrightarrow{\alpha} = \frac{1}{2}\begin{bmatrix} \sigma & -i\delta & 0 \\ i\delta & \sigma & 0 \\ 0 & 0 & 2\alpha_0 \end{bmatrix} = \frac{\sigma}{2} + i\frac{\delta}{2}\begin{bmatrix} 0 & -1 & 0 \\ 1 & 0 & 0 \\ 0 & 0 & 0 \end{bmatrix} \tag{E.679}$$

Now we rotate by θ from the linear basis of atomic system to linear polarization basis of the light:

$$\begin{bmatrix} \cos(\theta) & 0 & \sin(\theta) \\ 0 & 1 & 0 \\ -\sin(\theta) & 0 & \cos(\theta) \end{bmatrix}\begin{bmatrix} 0 & -1 & 0 \\ 1 & 0 & 0 \\ 0 & 0 & 0 \end{bmatrix}\begin{bmatrix} \cos(\theta) & 0 & -\sin(\theta) \\ 0 & 1 & 0 \\ \sin(\theta) & 0 & \cos(\theta) \end{bmatrix} = \begin{bmatrix} 0 & -\cos(\theta) & 0 \\ \cos(\theta) & 0 & -\sin(\theta) \\ 0 & \sin(\theta) & 0 \end{bmatrix} \tag{E.680}$$

Finally we'll switch from the linear polarization basis of the light to the circular one:

$$\frac{1}{\sqrt{2}}\begin{bmatrix} +1 & -i & 0 \\ +1 & +i & 0 \\ 0 & 0 & +1 \end{bmatrix}\begin{bmatrix} 0 & -\cos(\theta) & 0 \\ \cos(\theta) & 0 & -\sin(\theta) \\ 0 & \sin(\theta) & 0 \end{bmatrix}\frac{1}{\sqrt{2}}\begin{bmatrix} +1 & +1 & 0 \\ +i & -i & 0 \\ 0 & 0 & +1 \end{bmatrix} \tag{E.681}$$

which gives:

$$\begin{bmatrix} -i\cos(\theta) & 0 & -\frac{i}{2}\sin(\theta) \\ 0 & +i\cos(\theta) & +\frac{i}{2}\sin(\theta) \\ +\frac{i}{2}\sin(\theta) & -\frac{i}{2}\sin(\theta) & 0 \end{bmatrix} \tag{E.682}$$

Therefore, the polarizability in the circular polarization basis is:

$$\begin{aligned} \overleftrightarrow{\alpha} &= \frac{1}{2}\begin{bmatrix} \sigma+\delta\cos(\theta) & 0 & +\frac{\delta}{2}\sin(\theta) \\ 0 & \sigma-\delta\cos(\theta) & -\frac{\delta}{2}\sin(\theta) \\ -\frac{\delta}{2}\sin(\theta) & +\frac{\delta}{2}\sin(\theta) & \sigma \end{bmatrix} \\ &= \begin{bmatrix} \alpha_{\mathcal{R}} & 0 & +\frac{\delta}{4}\sin(\theta) \\ 0 & \alpha_{\mathcal{L}} & -\frac{\delta}{4}\sin(\theta) \\ -\frac{\delta}{4}\sin(\theta) & +\frac{\delta}{4}\delta\sin(\theta) & \alpha_0 \end{bmatrix} \end{aligned} \tag{E.683}$$

and consequently the matrix equation is written as

$$\begin{bmatrix} k^2-k_{\mathcal{R}}^2 & 0 & -\Delta_k^2 \\ 0 & k^2-k_{\mathcal{L}}^2 & +\Delta_k^2 \\ +\Delta_k^2 & -\Delta_k^2 & -k_0^2 \end{bmatrix}\cdot\vec{E}=0 \tag{E.684}$$

where we have defined the following quantities:

$$k_{\mathcal{Q}}^2 = \frac{\omega^2}{c^2}\left(1 + \frac{[A]}{\varepsilon_0}\alpha_{\mathcal{Q}}\right) \qquad \Delta_k^2 = \frac{\omega^2}{c^2}\frac{[A]}{\varepsilon_0}\left(\frac{\alpha_+ - \alpha_-}{4}\right)\sin(\theta) \tag{E.685}$$

$$\alpha_{\mathcal{Q}} = \frac{\varepsilon_0 r_e c^2}{2\pi}\left[\frac{f_1/\nu_1}{\nu_1 - \nu - i\Gamma_1/2}\left(1 - qP_{\mathrm{A}}\cos(\theta)\right) + \frac{f_2/\nu_2}{\nu_2 - \nu - i\Gamma_2/2}\left(1 + \frac{qP_{\mathrm{A}}\cos(\theta)}{2}\right)\right] \tag{E.686}$$

where $q = +1, 0, -1$ for $\mathcal{Q} = \mathcal{R}, 0, \mathcal{L}$ respectively. This equation is solved by setting the determinant of the matrix to zero:

$$\begin{vmatrix} k^2 - k_{\mathcal{R}}^2 & 0 & -\Delta_k^2 \\ 0 & k^2 - k_{\mathcal{L}}^2 & +\Delta_k^2 \\ +\Delta_k^2 & -\Delta_k^2 & -k_0^2 \end{vmatrix} = \left(k^2 - k_{\mathcal{R}}^2\right)\left[-\left(k^2 - k_{\mathcal{L}}^2\right)k_0^2 + \Delta_k^4\right] + \Delta_k^4\left(k^2 - k_{\mathcal{L}}^2\right) = 0 \tag{E.687}$$

This can be rearranged to:

$$k^4 + k^2\left[-k_{\mathcal{L}}^2 - k_{\mathcal{R}}^2 - 2\Delta_k^4/k_0^2\right] + \left[k_{\mathcal{R}}^2 k_{\mathcal{L}}^2 + \left(k_{\mathcal{R}}^2 + k_{\mathcal{L}}^2\right)\Delta_k^4/k_0^2\right] = 0 \tag{E.688}$$

and is then solved using the quadratic equation:

$$k^2 = \frac{1}{2}\left[k_{\mathcal{R}}^2 + k_{\mathcal{L}}^2 + 2\Delta_k^4/k_0^2 \pm \sqrt{\left(k_{\mathcal{R}}^2 - k_{\mathcal{L}}^2\right)^2 + 4\Delta_k^8/k_0^4}\right] \tag{E.689}$$

The two eigenvalues for k^2 are given by the two solutions above. However, a more illuminating form for k^2 can be obtained if we compare the size of Δ_k^2 against two different scales:

$$\frac{\Delta_k^2}{k_0^2} = \frac{[A](\alpha_+ - \alpha_-)\sin(\theta)}{4\varepsilon_0\left(1 + \frac{[A]}{\varepsilon_0}\alpha_0\right)} \approx 10^{-3}\left(\frac{\sin(\theta)}{4}\right) \qquad \frac{\Delta_k^2}{k_{\mathcal{R}}^2 - k_{\mathcal{L}}^2} = \frac{\tan(\theta)}{4} \tag{E.690}$$

where we have used the fact that the maximum absolute value of the polarizability occurs at resonance for the D2 transition $\nu = \nu_2$ which corresponds to:

$$\begin{aligned}\left[\frac{[A]}{\varepsilon_0}\alpha_0\right]_{\max} &= \left[\frac{[A]}{\varepsilon_0}\left(\frac{\alpha_+ - \alpha_-}{P_{\mathtt{A}}}\right)\right]_{\max} = \frac{[A] r_e c \lambda_2 f_2}{\pi \Gamma_2} \\ &= 10^{-3} \times \left(\frac{[A]}{10^{15}\ \mathrm{cm}^{-3}}\right)\left(\frac{\lambda_2}{780\ \mathrm{nm}}\right)\left(\frac{140\ \mathrm{GHz}}{\Gamma_2}\right) \end{aligned} \quad \text{(E.691)}$$

and we have put in typical values for the alkali density and absorption line width. Therefore, the angle for which the two terms under the square root are equal, for $P_{\mathtt{A}} = 1$, is about $\theta = 89.993$. In almost all cases, the first term dominates over the second term under the square root and we can write the two solutions as:

$$k^2 = \left(k_{\mathcal{R}}^2 \text{ or } k_{\mathcal{L}}^2\right) + \Delta_k^4 / k_0^2 \quad \text{(E.692)}$$

Light Polarization Eigenvectors

The polarization eigenvectors that correspond to these wave number eigenvalues are found by solving the following system of equations:

$$\begin{aligned}\left(k^2 - k_{\mathcal{R}}^2\right) E_1 - \Delta_k^2 E_3 &= 0 \\ \left(k^2 - k_{\mathcal{L}}^2\right) E_2 + \Delta_k^2 E_3 &= 0 \\ \Delta_k^2 E_1 - \Delta_k^2 E_2 - k_0^2 E_3 &= 0 \end{aligned} \quad \text{(E.693)}$$

which can be rearranged to give the following useful ratios among the components of the eigenvectors:

$$\left(k^2 - k_{\mathcal{R}}^2\right) E_1 = -\left(k^2 - k_{\mathcal{L}}^2\right) E_2 \qquad E_3 = \frac{\Delta_k^2}{k_0^2}\left(E_1 - E_2\right) \quad \text{(E.694)}$$

Finally, the two eigenvectors in the circular polarization basis of the light ($\mathcal{R}$; $\mathcal{L}$; $\mathcal{Z}$) to lowest order in Δ_k^2 are:

$$k_{\mathcal{R}} \; : \; (\, 1 \; ; \, 0 \; ; \, 0 \,) + \frac{\Delta_k^2}{k_0^2} \left(\, 0 \; ; \, -\frac{\tan(\theta)}{4} \; ; \, +1 \, \right) \tag{E.695}$$

$$k_{\mathcal{L}} \; : \; (\, 0 \; ; \, 1 \; ; \, 0 \,) + \frac{\Delta_k^2}{k_0^2} \left(\, +\frac{\tan(\theta)}{4} \; ; \, 0 \; ; \, -1 \, \right) \tag{E.696}$$

This means that polarization eigenvector basis:

1. is very well approximated by the circular polarization basis of the light
2. has a small admixture of linear polarization
3. is slightly parallel to the propagation direction

Generalization to Atomic Polarization Vector

We've found that when we have a skew angle θ, the polarization P in the atomic polarizability is replaced by $P\cos(\theta)$. This is very suggestive, and following the argument of Dehmelt [33], we'll replace $P\cos(\theta)$ with $\hat{k} \cdot \vec{P}$ where $\hat{k}$ is the beam propagation direction and $\vec{P}$ is the polarization vector. The quantum mechanical form of this polarization vector is given by $\vec{P} = 2\left\langle \vec{S} \right\rangle$ where $\vec{S}$ is the vector spin-1/2 operator. Therefore, all instances of P should be replaced by $\hat{k} \cdot \vec{P}$:

$$P \rightarrow 2\left(k_x \langle S_x \rangle + k_y \langle S_y \rangle + k_z \langle S_z \rangle\right) \qquad k_x^2 + k_y^2 + k_z^2 = 1 \tag{E.697}$$

When the beam is parallel to the magnetic field, then $k_z = 1$ and $P \rightarrow 2\langle S_z \rangle$. Since S_z is parallel to the magnetic field by definition, its expectation value is since the difference in populations or P, as expected. On the other hand, when the beam is

perpendicular to the magnetic field, say $k_x = 1$, then $P \rightarrow 2\langle S_x \rangle$. The expectation value of S_x involves coherences. If there is no external RF field, then the coherences are oscillating at the Larmor frequency. If there is an external RF field, then the coherences will be oscillating at the frequency of the RF field. In either case, the expectation value of S_x will be oscillatory and as a consequence so will the polarizability.

A more rigorous derivation of this generalization involving group theoretical methods can be found in *Happer & Mathur* [34]. They derive an irreducible tensor decomposition of the atomic polarizability (in the linear polarization basis):

$$\overleftrightarrow{\alpha} = \alpha_S \overleftrightarrow{1} + \alpha_V \left(\langle \vec{\mu} \rangle \times \right) + \alpha_T \left\langle \overleftrightarrow{Q} \right\rangle \tag{E.698}$$

where $\alpha_{S,V,T}$ are the scalar, vector, & tensor polarizabilities, $\vec{\mu}$ is the magnetic dipole operator, and $\overleftrightarrow{Q}$ is the electric quadrupole operator. Dropping the electric quadrupole part, we can write atomic polarizability in matrix form:

$$\overleftrightarrow{\alpha} = \begin{bmatrix} \alpha_S & 0 & 0 \\ 0 & \alpha_S & 0 \\ 0 & 0 & \alpha_S \end{bmatrix} + \frac{\alpha_V g_S \mu_B}{2} \begin{bmatrix} 0 & -P_z & P_y \\ P_z & 0 & -P_x \\ -P_y & P_x & 0 \end{bmatrix} \tag{E.699}$$

where $\vec{\mu} = g_S \mu_B \vec{S}$, $P_n = 2\langle S_n \rangle$, and we used the matrix form of the cross product. This looks suspiciously like Eqn. (E.679):

$$\overleftrightarrow{\alpha} = \frac{1}{2} \begin{bmatrix} \sigma & -i\delta & 0 \\ i\delta & \sigma & 0 \\ 0 & 0 & 2\alpha_0 \end{bmatrix} = \frac{\sigma}{2} + i\frac{\delta}{2} \begin{bmatrix} 0 & -1 & 0 \\ 1 & 0 & 0 \\ 0 & 0 & 0 \end{bmatrix} \tag{E.700}$$

where we can equate $\sigma/2 = \alpha_0 = \alpha_S$, $i\delta/2 = \alpha_V g_s \mu_B P_z/2$, $P_x = P_y = 0$. We'll now proceed with the rest of the analysis from Sec.(E.6.3), but now with $P_x \neq 0$ and $P_y \neq 0$. As a reminder, we're starting in the linear atomic basis. We rotate by θ from the linear basis of atomic system to linear polarization basis of the light:

$$\begin{bmatrix} \cos(\theta) & 0 & \sin(\theta) \\ 0 & 1 & 0 \\ -\sin(\theta) & 0 & \cos(\theta) \end{bmatrix} \begin{bmatrix} 0 & -P_z & P_y \\ P_z & 0 & -P_x \\ -P_y & P_x & 0 \end{bmatrix} \begin{bmatrix} \cos(\theta) & 0 & -\sin(\theta) \\ 0 & 1 & 0 \\ \sin(\theta) & 0 & \cos(\theta) \end{bmatrix} \tag{E.701}$$

where we get:

$$P_z M_z + P_x M_x + P_y M_y = \begin{bmatrix} 0 & -P_z\cos(\theta) + P_x\sin(\theta) & P_y \\ +P_z\cos(\theta) - P_x\sin(\theta) & 0 & -P_z\sin(\theta) - P_x\cos(\theta) \\ -P_y & P_z\sin(\theta) + P_x\cos(\theta) & 0 \end{bmatrix} \tag{E.702}$$

Finally we'll switch from the linear polarization basis of the light to the circular one. We already know how to transform $P_z M_z$:

$$\begin{aligned} P_z M_z' &= \frac{1}{\sqrt{2}} \begin{bmatrix} +1 & -i & 0 \\ +1 & +i & 0 \\ 0 & 0 & +1 \end{bmatrix} P_z \begin{bmatrix} 0 & -\cos(\theta) & 0 \\ \cos(\theta) & 0 & -\sin(\theta) \\ 0 & \sin(\theta) & 0 \end{bmatrix} \\ &\quad \times \frac{1}{\sqrt{2}} \begin{bmatrix} +1 & +1 & 0 \\ +i & -i & 0 \\ 0 & 0 & +1 \end{bmatrix} \end{aligned} \tag{E.703}$$

which gives:

$$P_z M'_z = \begin{bmatrix} -iP_z\cos(\theta) & 0 & -\frac{i}{2}P_z\sin(\theta) \\ 0 & +iP_z\cos(\theta) & +\frac{i}{2}P_z\sin(\theta) \\ +\frac{i}{2}P_z\sin(\theta) & -\frac{i}{2}P_z\sin(\theta) & 0 \end{bmatrix} \tag{E.704}$$

If we make the substitutions $P_z\cos(\theta) \rightarrow -P_x\sin(\theta)$ and $P_z\sin(\theta) \rightarrow P_x\cos(\theta)$, then if can immediately transform M_x to M'_x to give:

$$P_x M'_x = \begin{bmatrix} +iP_x\sin(\theta) & 0 & -\frac{i}{2}P_x\cos(\theta) \\ 0 & -iP_x\sin(\theta) & +\frac{i}{2}P_x\cos(\theta) \\ +\frac{i}{2}P_x\cos(\theta) & -\frac{i}{2}P_x\cos(\theta) & 0 \end{bmatrix} \tag{E.705}$$

Finally, we need to transforms $P_y M_y$ in the following way:

$$P_y M'_y = \frac{1}{\sqrt{2}}\begin{bmatrix} +1 & -i & 0 \\ +1 & +i & 0 \\ 0 & 0 & +1 \end{bmatrix} P_y \begin{bmatrix} 0 & 0 & 1 \\ 0 & 0 & 0 \\ -1 & 0 & 0 \end{bmatrix} \frac{1}{\sqrt{2}}\begin{bmatrix} +1 & +1 & 0 \\ +i & -i & 0 \\ 0 & 0 & +1 \end{bmatrix} \tag{E.706}$$

which gives:

$$P_y M'_y = \begin{bmatrix} 0 & 0 & P_y/2 \\ 0 & 0 & P_y/2 \\ -P_y/2 & -P_y/2 & 0 \end{bmatrix} \tag{E.707}$$

Putting this altogether gives:

$$P_z M'_z + P_x M'_x + P_y M'_y = -i \begin{bmatrix} +\hat{k}\cdot\vec{P} & 0 & +p_{xz}/2 + iP_y/2 \\ 0 & -\hat{k}\cdot\vec{P} & -p_{xz}/2 + iP_y/2 \\ -p_{xz}/2 - iP_y/2 & +p_{xz}/2 - iP_y/2 & 0 \end{bmatrix} \tag{E.708}$$

where $P_z\cos(\theta) - P_x\sin(\theta) = \hat{k}\cdot\vec{P}$ and $p_{xz} = P_z\sin(\theta) + P_x\cos(\theta)$. Therefore, the polarizability in the circular polarization basis is:

$$\overleftrightarrow{\alpha} = \frac{1}{2}\begin{bmatrix} \sigma + \delta'\hat{k}\cdot\vec{P} & 0 & +\delta'(p_{xz} + iP_y)/2 \\ 0 & \sigma - \delta'\hat{k}\cdot\vec{P} & -\delta'(p_{xz} - iP_y)/2 \\ -\delta'(p_{xz} + iP_y)/2 & +\delta'(p_{xz} - iP_y)/2 & \sigma \end{bmatrix} \tag{E.709}$$

where $\delta' = \delta/P$ and compared to Eqn. (E.683):

$$\overleftrightarrow{\alpha} = \frac{1}{2}\begin{bmatrix} \sigma + \delta\cos(\theta) & 0 & +\frac{\delta}{2}\sin(\theta) \\ 0 & \sigma - \delta\cos(\theta) & -\frac{\delta}{2}\sin(\theta) \\ -\frac{\delta}{2}\sin(\theta) & +\frac{\delta}{2}\sin(\theta) & \sigma \end{bmatrix} \tag{E.710}$$

we see that (1) $\delta\cos(\theta)$ has been replaced by $\delta'\hat{k}\cdot\vec{P}$ and (2) the off diagonal elements $\delta\sin(\theta)/2$ have been replaced by $\delta'(p_{xz} \pm iP_y)$. Analogous to before, we'll define the following quantities:

$$k_Q^2 = \frac{\omega^2}{c^2}\left(1 + \frac{[A]}{\varepsilon_0}\alpha_Q\right) \tag{E.711}$$

$$\alpha_Q = \frac{\varepsilon_0 r_e c^2}{2\pi}\left[\frac{f_1/\nu_1}{\nu_1 - \nu - i\Gamma_1/2}\left(1 - q\hat{k}\cdot\vec{P}_A\right) + \frac{f_2/\nu_2}{\nu_2 - \nu - i\Gamma_2/2}\left(1 + \frac{q\hat{k}\cdot\vec{P}_A}{2}\right)\right] \tag{E.712}$$

where $q = +1, 0, -1$ for $\mathcal{Q} = \mathcal{R}, 0, \mathcal{L}$ respectively. Just as before, the eigenvalues are essentially $k_{\mathcal{R}}$ and $k_{\mathcal{L}}$ with very small corrections at the level of $\delta'^2(p_{xz} \pm iP_y)^2/(16k_0^2)$. Corrections due to a non-zero field slightly modify these very small corrections and therefore can safely be ignored as well.

Components Without An RF Field (Calculation of $\langle S_z \rangle$)

The components of the atomic polarization vector $\vec{P}$ are just the expectation values of the spin-1/2 operators S_x,S_y,&S_z. We'll work in the $|F, m\rangle$ basis To calculate the expectation values of S_z, S_x & S_y, we'll first calculate it for S_q ($S_0 = S_z$; $S_\pm = S_x \pm iS_y$) using:

$$\langle S_q \rangle = \sum_{F,F',m} \langle F', m| \rho |F, m \pm 1\rangle \langle F, m+q| S_q |F', m\rangle \tag{E.713}$$

The coherences are simply:

$$\langle F', m| \rho |F, m+q\rangle = \rho_{F'mFm+q}(0) \exp\left[-i\omega_{F'mFm+q}t\right] \tag{E.714}$$

For a large collection of atoms at equilibrium, the spins have all dephased and $\rho_{F'mFm+q}(0)$ is equal to zero. Therefore, all the coherences are zero. Consequently, the only nonzero terms are ones that involve populations:

$$\langle S_z \rangle = \sum_{F,m} \rho_m \langle F, m| S_z |F, m\rangle \tag{E.715}$$

Since we originally defined $P = 2\langle S_z \rangle$, we should obtain $\langle S_z \rangle = P_z/2$. To evaluate the S_z matrix element, we'll have to expand $|F, m\rangle$ in the $|(I, 1/2), m_I, \pm 1/2\rangle$ basis:

$$\begin{aligned}\langle S_z \rangle &= \sum_{F,m,m_S,m'_S} \frac{\exp(\beta m)}{Z_I Z_{1/2}} \times \\ &\quad \left\langle F, m \mid \left(I, \frac{1}{2}\right), m - m'_S, m'_S \right\rangle \langle m - m'_S, m'_S | \, S_z \, | m - m_S, m_S \rangle \\ &\quad \times \left\langle \left(I, \frac{1}{2}\right), m - m_S, m_S \mid F, m \right\rangle \end{aligned} \tag{E.716}$$

$$= \sum_{F,m,m_S} \frac{\exp(\beta m)}{Z_I Z_{1/2}} m_S \left[\left\langle F, m \mid \left(I, \frac{1}{2}\right), m - m_S, m_S \right\rangle \right]^2 \tag{E.717}$$

Since there are two manifolds $F = I \pm 1/2$, we'll split the sum into two pieces:

$$\begin{aligned}\langle S_z \rangle &= \sum_{m=-I-1/2}^{m=+I+1/2} \sum_{m_S=-1/2}^{+1/2} \frac{\exp(\beta m)}{Z_I Z_{1/2}} m_S \left[\left\langle I + 1/2, m \mid \left(I, \frac{1}{2}\right), m - m_S, m_S \right\rangle \right]^2 \\ &\quad + \sum_{m=-I+1/2}^{m=+I-1/2} \sum_{m_S=-1/2}^{+1/2} \frac{\exp(\beta m)}{Z_I Z_{1/2}} m_S \left[\left\langle I - 1/2, m \mid \left(I, \frac{1}{2}\right), m - m_S, m_S \right\rangle \right]^2 \end{aligned} \tag{E.718}$$

Using the Clebsch-Gordon formulas from Sec. (C.2):

$$\begin{aligned}
\langle S_z \rangle &= \sum_{m=-I-1/2}^{m=+I+1/2} \sum_{m_S=-1/2}^{+1/2} \frac{\exp(\beta m)}{Z_I Z_{1/2}} m_S \left[\frac{I+1/2+2m_S m}{[I]} \right] \\
&\quad + \sum_{m=-I+1/2}^{m=+I-1/2} \sum_{m_S=-1/2}^{+1/2} \frac{\exp(\beta m)}{Z_I Z_{1/2}} m_S \left[\frac{I+1/2-2m_S m}{[I]} \right] \\
&= \sum_{m=-I-1/2}^{m=+I+1/2} \sum_{m_S=-1/2}^{+1/2} \frac{\exp(\beta m)}{Z_I Z_{1/2}} \left[\frac{+2m_S^2 m}{[I]} \right] \\
&\quad + \sum_{m=-I+1/2}^{m=+I-1/2} \sum_{m_S=-1/2}^{+1/2} \frac{\exp(\beta m)}{Z_I Z_{1/2}} \left[\frac{-2m_S^2 m}{[I]} \right] \\
&= \sum_{m_S=-1/2}^{+1/2} \left(\frac{\exp(+\beta[I]/2)}{Z_I Z_{1/2}} \left[\frac{+2m_S^2[I]/2}{[I]} \right] + \frac{\exp(-\beta[I]/2)}{Z_I Z_{1/2}} \left[\frac{-2m_S^2[I]/2}{[I]} \right] \right)
\end{aligned} \tag{E.719}$$

where the symmetric sum over $m_S = \pm 1/2$ cancels the $m_S(I+1/2)/[I]$ terms and the $2m_S^2 m/[I]$ term from one manifold cancels the one from the other manifold, except for the edge states $m = I \pm 1/2$:

$$\begin{aligned}
\langle S_z \rangle &= \frac{2\exp(+\beta[I]/2)}{4Z_I Z_{1/2}} - \frac{2\exp(-\beta[I]/2)}{4Z_I Z_{1/2}} = \frac{\sinh(\beta[I]/2)}{Z_I Z_{1/2}} = \frac{\sinh(\beta/2)\sqrt{1-P_z^2}}{2} \\
&= \left(\sqrt{\frac{1+P_z}{1-P_z}} - \sqrt{\frac{1-P_z}{1+P_z}} \right) \frac{\sqrt{1-P_z^2}}{4} = \left(\frac{(1+P_z)-(1-P_z)}{\sqrt{1-P_z^2}} \right) \frac{\sqrt{1-P_z^2}}{4} = \frac{P_z}{2}
\end{aligned} \tag{E.720}$$

where we've used Eqns. (E.591) & (E.592) (with $P \to P_z$) and as expected $P_z = 2\langle S_z \rangle$.

Components With An RF Field (Calculation of $\langle S_x \rangle$ & $\langle S_y \rangle$)

In this section, we'll assume that there is an RF Field with frequency ω creating coherences only within a manifold. In other words, there are no RF fields that

induce $F = I + 1/2 \leftrightarrow F' = I - 1/2$ transitions. Therefore, the expectation value for S_z is the same as the last section. To calculate the expectation values of S_x and S_y, we'll first calculate $S_\pm = S_x \pm iS_y$ using Eqn. (E.401) in the form of:

$$\begin{aligned}\langle S_\pm \rangle &= \sum_m \left\{ \frac{\Omega\left(\rho_m - \rho_{m\mp1}\right)\left(u_\pm^\mp\right)^* \left|\langle F,m| \mathcal{U}_\pm |F,m\mp1\rangle\right|^2}{\pm\omega - \omega_{FmFm\mp1} - i\gamma_{FmFm\mp1}} \times \exp(\pm i\omega t) \right. \\ &\left. + \frac{\Omega\left(\rho_m - \rho_{m\mp1}\right)\left(u_\pm^\pm\right)^* \left|\langle F',m| \mathcal{U}_\pm |F',m\mp1\rangle\right|^2}{\mp\omega - \omega_{F'mF'm\mp1} - i\gamma_{F'mF'm\mp1}} \times \exp(\mp i\omega t) \right\}\end{aligned} \tag{E.721}$$

where we've split the sum over the two manifolds ($F = I + 1/2$ & $F' = I - 1/2$) and the population of each state depends only on m. As a reminder, $\pm$ is the sign of $\omega_{Fm+qFm} = \omega_{Fm+q} - \omega_{Fm}$. Finally, for the $F = I + 1/2$ manifold, the energy of the m state is higher than the energy of the $m-1$ state, whereas for the $F' = I - 1/2$ manifold, the opposite is true. Therefore the frequency of the transition $m \leftrightarrow m-1$ is positive for the $F = I + 1/2$ manifold, whereas its negative for the F' manifold. Since $S_x = (S_+ + S_-)/2$, we can write its expectation value as:

$$\begin{aligned}\langle S_x \rangle &= \sum_m \left\{ \frac{\Omega\left(\rho_m - \rho_{m-1}\right)\left(u_+^-\right)^* \left|\langle F,m| S_+ |F,m-1\rangle\right|^2}{+\omega - \omega_{FmFm-1} - i\gamma_{FmFm-1}} \times \frac{\exp(+i\omega t)}{2} \right. \\ &+ \frac{\Omega\left(\rho_m - \rho_{m+1}\right)\left(u_-^+\right)^* \left|\langle F,m| S_- |F,m+1\rangle\right|^2}{-\omega - \omega_{FmFm+1} - i\gamma_{FmFm+1}} \times \frac{\exp(-i\omega t)}{2} \\ &+ \frac{\Omega\left(\rho_m - \rho_{m-1}\right)\left(u_+^+\right)^* \left|\langle F',m| S_+ |F',m-1\rangle\right|^2}{-\omega - \omega_{F'mF'm-1} - i\gamma_{F'mF'm-1}} \times \frac{\exp(-i\omega t)}{2} \\ &\left. + \frac{\Omega\left(\rho_m - \rho_{m+1}\right)\left(u_-^-\right)^* \left|\langle F',m| S_- |F',m+1\rangle\right|^2}{+\omega - \omega_{F'mF'm+1} - i\gamma_{F'mF'm+1}} \times \frac{\exp(+i\omega t)}{2} \right\}\end{aligned} \tag{E.722}$$

where $\Omega = g_S \mu_B B_{\mathtt{rf}}/\hbar$, $u_q^- = \epsilon_q^* \cdot \hat{B}_{\mathtt{rf}}$, and $u_q^+ = \epsilon_q^* \cdot \hat{B}_{\mathtt{rf}}^*$. As mentioned before, we'll label the transition by the higher m involved. Relabeling the terms in the sum and moving a few minus signs around gives:

$$\begin{aligned}\langle S_x \rangle &= \sum_m \left\{ \frac{\Omega(\rho_m - \rho_{m-1})\left(u_+^-\right)^* |\langle F,m| S_+ |F,m-1\rangle|^2}{+\omega - \omega_{FmFm-1} - i\gamma_{FmFm-1}} \times \frac{\exp(+i\omega t)}{2} \right. \\ &+ \frac{\Omega(\rho_m - \rho_{m-1})\left(u_-^+\right)^* |\langle F,m-1| S_- |F,m\rangle|^2}{+\omega - \omega_{FmFm-1} + i\gamma_{Fm-1Fm}} \times \frac{\exp(-i\omega t)}{2} \\ &- \frac{\Omega(\rho_m - \rho_{m-1})\left(u_+^+\right)^* |\langle F',m| S_+ |F',m-1\rangle|^2}{+\omega - \omega_{F'm-1F'm} + i\gamma_{F'mF'm-1}} \times \frac{\exp(-i\omega t)}{2} \\ &\left. - \frac{\Omega(\rho_m - \rho_{m-1})\left(u_-^-\right)^* |\langle F',m-1| S_- |F',m\rangle|^2}{+\omega - \omega_{F'm-1F'm} - i\gamma_{F'm-1F'm}} \times \frac{\exp(+i\omega t)}{2} \right\}\end{aligned} \tag{E.723}$$

We've already calculated that:

$$\rho_m - \rho_{m-1} = Q_{I\bar{m}} P_z \tag{E.724}$$

$$|\langle F,m| S_\pm |F,m\mp 1\rangle|^2 = \frac{F(F+1) - m(m\mp 1)}{[I]} \tag{E.725}$$

So we just need to work out what this term looks like:

$$\frac{u^* \exp(+i\omega t)/2}{\omega - \omega_0 - i\gamma} + \frac{u \exp(-i\omega t)/2}{\omega - \omega_0 + i\gamma} = \Re\left\{\frac{u \exp(-i\omega t)}{\omega - \omega_0 + i\gamma}\right\} = \Re\left\{u\left[\cos(\omega t) - i\sin(\omega t)\right]\left[\mathcal{D} - i\mathcal{L}\right]\right\} \tag{E.726}$$

where the two terms are just complex conjugates of each other, which makes their sum just the real part of either term and we've made the substitutions:

$$\mathcal{D} = \frac{\omega - \omega_0}{(\omega - \omega_0)^2 + \gamma^2} \qquad \mathcal{L} = \frac{\gamma}{(\omega - \omega_0)^2 + \gamma^2} \tag{E.727}$$

Expanding this out and grouping terms by phase:

$$\Re\{u[\cos(\omega t) - i\sin(\omega t)][\mathcal{D} - i\mathcal{L}]\} = \left[\mathcal{D}\Re\{u\} + \mathcal{L}\Im\{u\}\right]\cos(\omega t) + \left[\mathcal{D}\Im\{u\} - \mathcal{L}\Re\{u\}\right]\sin(\omega t) \tag{E.728}$$

Using this, we can anticipate the final form of the expectation value of S_x:

$$\langle S_x\rangle = P_z\left[\langle S_x\rangle_c \cos(\omega t) + \langle S_x\rangle_s \sin(\omega t)\right] \tag{E.729}$$

where $c(s)$ refers to the cosine (sine) component, $\pm$ refers to the manifold, and we get:

$$\langle S_x\rangle_c = \frac{\Omega}{[I]}\sum_{(\pm),m}(\pm)Q_{I\bar{m}}\left[(I+1/2)(I+1/2\pm 1) - m(m-1)\right]\left[\mathcal{D}_m^{\pm}\Re\{u_{\pm}^{-}\} + \mathcal{L}_m^{\pm}\Im\{u_{\pm}^{-}\}\right] \tag{E.730}$$

$$\langle S_x\rangle_s = \frac{\Omega}{[I]}\sum_{(\pm),m}(\pm)Q_{I\bar{m}}\left[(I+1/2)(I+1/2\pm 1) - m(m-1)\right]\left[\mathcal{D}_m^{\pm}\Im\{u_{\pm}^{-}\} - \mathcal{L}_m^{\pm}\Re\{u_{\pm}^{-}\}\right] \tag{E.731}$$

where I is the nuclear spin, $\pm$ refers to the manifold, we sum over both m and $\pm$ and:

$$\mathcal{D}_m^{+} = \frac{\omega - \omega_{FmFm-1}}{(\omega - \omega_{FmFm-1})^2 + \gamma_{FmFm-1}^2} \tag{E.732}$$

$$\mathcal{L}_m^{+} = \frac{\gamma_{FmFm-1}}{(\omega - \omega_{FmFm-1})^2 + \gamma_{FmFm-1}^2} \tag{E.733}$$

$$\mathcal{D}_m^{-} = \frac{\omega - \omega_{F'm-1F'm}}{(\omega - \omega_{F'm-1F'm})^2 + \gamma_{F'm-1F'm}^2} \tag{E.734}$$

$$\mathcal{L}_m^{-} = \frac{\gamma_{F'm-1F'm}}{(\omega - \omega_{F'm-1F'm})^2 + \gamma_{F'm-1F'm}^2} \tag{E.735}$$

where $F = I + 1/2$ and $F' = I - 1/2$.

For $S_y = (S_+ - S_-)/(2i)$, we get terms that look like:

$$\begin{aligned}\frac{u^* \exp(+i\omega t)/(2i)}{\omega - \omega_0 - i\gamma} - \frac{u \exp(-i\omega t)/(2i)}{\omega - \omega_0 + i\gamma} &= -\Im\left\{\frac{u \exp(-i\omega t)}{\omega - \omega_0 + i\gamma}\right\} \\ &= -\Im\left\{u\left[\cos(\omega t) - i\sin(\omega t)\right]\left[\mathcal{D} - i\mathcal{L}\right]\right\}\end{aligned} \tag{E.736}$$

Expanding this out and grouping terms by phase:

$$-\Im\left\{u\left[\cos(\omega t) - i\sin(\omega t)\right]\left[\mathcal{D} - i\mathcal{L}\right]\right\} = \left[\mathcal{D}\Re\{u\} + \mathcal{L}\Im\{u\}\right]\sin(\omega t) - \left[\mathcal{D}\Im\{u\} - \mathcal{L}\Re\{u\}\right]\cos(\omega t) \tag{E.737}$$

This is the same as for S_x except we make the substitutions cos $\rightarrow$ sin and sin $\rightarrow -$ cos:

$$\left\langle S_y \right\rangle = P_z\left[\left\langle S_y \right\rangle_c \cos(\omega t) + \left\langle S_y \right\rangle_s \sin(\omega t)\right] \tag{E.738}$$

$$\left\langle S_y \right\rangle_c = \frac{\Omega}{[I]} \sum_{(\pm),m} (\mp) Q_{I\bar{m}} \left[(I + 1/2)(I + 1/2 \pm 1) - m(m-1)\right]\left[\mathcal{D}_m^{\pm}\Im\{u_{\pm}^-\} - \mathcal{L}_m^{\pm}\Re\{u_{\pm}^-\}\right] \tag{E.739}$$

$$\left\langle S_y \right\rangle_s = \frac{\Omega}{[I]} \sum_{(\pm),m} (\pm) Q_{I\bar{m}} \left[(I + 1/2)(I + 1/2 \pm 1) - m(m-1)\right]\left[\mathcal{D}_m^{\pm}\Re\{u_{\pm}^-\} + \mathcal{L}_m^{\pm}\Im\{u_{\pm}^-\}\right] \tag{E.740}$$

The expectation values contain both lorentzian $\mathcal{L}$) and dispersive ($\mathcal{D}$) line shapes. They both contain in-phase and out-of-phase terms. Finally, the two manifolds appear with opposite signs.

E.6.4 Synthesis

We're now in a position to write the wave vector k_q in terms of the polarizability:

$$k_q = \frac{\omega}{c} n_q = \frac{\omega}{c}\sqrt{\frac{\epsilon_q \mu_q}{\epsilon_0 \mu_0}} = \frac{\omega}{c}\sqrt{1 + \frac{[\mathrm{A}]\alpha_q}{\epsilon_0}} = \frac{\omega}{c}\left(1 + \frac{[A]\alpha_q}{2\epsilon_0} - \frac{[A]^2\alpha_q^2}{8\epsilon_0^2} + \cdots\right) \quad \text{(E.741)}$$

Expanding k_q in terms of its real and imaginary parts gives, up to second order:

$$k_q = \frac{\omega}{c}\left(1 + \frac{[A]}{2\epsilon_0}\left(\Re\alpha_q + i\Im\alpha_q\right) - \frac{[A]^2}{8\epsilon_0^2}\left\{(\Re\alpha_q)^2 - (\Im\alpha_q)^2 + 2i(\Re\alpha_q)(\Im\alpha_q)\right\}\right) \quad \text{(E.742)}$$

Under our typical densities, the second order term is quite small and keep only up to first order:

$$k_q = \frac{\omega}{c} + [A]2\pi r_e c f_1 \frac{\omega}{\omega_1}\left(\frac{\Re\alpha_q + i\Im\alpha_q}{4\pi\epsilon_0 r_e c^2 f_1/\omega_1}\right) = \frac{\omega}{c} + [A] r_e c f_1 \left(\frac{\omega}{\omega_1}\right)\left(2\pi C\Re\alpha_q + i2\pi C\Im\alpha_q\right) \quad \text{(E.743)}$$

where $1/C = 4\pi\epsilon_0 r_e c^2 f_1/\omega_1$. Making the substitution $P \to \hat{k}\cdot\vec{P}_{\mathrm{A}}$, the imaginary part of the polarizability is for $q = 0, \pm 1$:

$$\begin{aligned} C\Im\alpha_q \;=\; & \frac{(1 - q\hat{k}\cdot\vec{P}_{\mathrm{A}})}{2}\mathcal{L}_1\left\{1 + q\left[\frac{2}{3} - \frac{8}{3}\omega_{\mathrm{so}}\mathcal{D}_1\right]y + \left[\frac{2}{3} - q^2 - \frac{4}{3}\omega_{\mathrm{so}}\mathcal{D}_1 + \frac{4+12q^2}{9}\omega_{\mathrm{so}}^2\left(4\mathcal{D}_1^2 - \frac{\mathcal{L}_1}{\gamma_1}\right)\right]y^2\right\} \\ & + \mathcal{L}_2\left\{1 - q\left[\frac{1}{3} + \frac{7}{3}\omega_{\mathrm{so}}\mathcal{D}_2\right]y + \left[-\frac{1}{3} + \frac{q^2}{2} + q^2\omega_{\mathrm{so}}\mathcal{D}_2 + \frac{1+12q^2}{9}\omega_{\mathrm{so}}^2\left(4\mathcal{D}_2^2 - \frac{\mathcal{L}_2}{\gamma_2}\right)\right]y^2\right\} \\ & + \frac{q\hat{k}\cdot\vec{P}_{\mathrm{A}}}{2}\mathcal{L}_2\left\{1 + q\left[\frac{2}{3} - \frac{4}{3}\omega_{\mathrm{so}}\mathcal{D}_2\right]y + \left[-\frac{1}{3} - 2\omega_{\mathrm{so}}\mathcal{D}_2 + \frac{1}{9}\omega_{\mathrm{so}}^2\left(4\mathcal{D}_2^2 - \frac{\mathcal{L}_2}{\gamma_2}\right)\right]y^2\right\} \\ & + (1 - q^2)\hat{k}\cdot\vec{P}_{\mathrm{A}}\left\{\mathcal{L}_1\left[-1 + \omega_{\mathrm{so}}\mathcal{D}_1\right] + \mathcal{L}_2\left[+1 + \omega_{\mathrm{so}}\mathcal{D}_2\right]\right\}\frac{2y}{3} \end{aligned} \quad \text{(E.744)}$$

and similarly for the real part:

$$
\begin{aligned}
C\Re\alpha_q \;=\; & \frac{(1-q\hat{k}\cdot\vec{P}_{\mathtt{A}})}{2}\mathcal{D}_1\left\{1+q\left[\frac{2}{3}-\frac{8}{3}\omega_{\mathtt{so}}\mathcal{D}_1\right]y+\left[\frac{2}{3}-q^2-\frac{4}{3}\omega_{\mathtt{so}}\mathcal{D}_1+\frac{4+12q^2}{9}\omega_{\mathtt{so}}^2\left(4\mathcal{D}_1^2-3\frac{\mathcal{L}_1}{\gamma_1}\right)\right]y^2\right\}\\
& +\mathcal{D}_2\left\{1-q\left[\frac{1}{3}+\frac{7}{3}\omega_{\mathtt{so}}\mathcal{D}_2\right]y+\left[-\frac{1}{3}+\frac{q^2}{2}+q^2\omega_{\mathtt{so}}\mathcal{D}_2+\frac{1+12q^2}{9}\omega_{\mathtt{so}}^2\left(4\mathcal{D}_2^2-3\frac{\mathcal{L}_2}{\gamma_2}\right)\right]y^2\right\}\\
& +\frac{q\hat{k}\cdot\vec{P}_{\mathtt{A}}}{2}\mathcal{D}_2\left\{1+q\left[\frac{2}{3}-\frac{4}{3}\omega_{\mathtt{so}}\mathcal{D}_2\right]y+\left[-\frac{1}{3}-2\omega_{\mathtt{so}}\mathcal{D}_2+\frac{1}{9}\omega_{\mathtt{so}}^2\left(4\mathcal{D}_2^2-3\frac{\mathcal{L}_2}{\gamma_2}\right)\right]y^2\right\}\\
& +(1-q^2)\hat{k}\cdot\vec{P}_{\mathtt{A}}\left\{\mathcal{D}_1\left[-1+\omega_{\mathtt{so}}\mathcal{D}_1\right]+\mathcal{D}_2\left[+1+\omega_{\mathtt{so}}\mathcal{D}_2\right]-\frac{1}{2}\mathcal{L}_1\frac{\omega_{\mathtt{so}}}{\gamma_1}\right\}\frac{2y}{3}\\
& +(1-q\hat{k}\cdot\vec{P}_{\mathtt{A}})\mathcal{L}_1\frac{\omega_{\mathtt{so}}}{\gamma_1}\left\{\frac{2q}{3}y+\frac{1}{3}y^2\right\}+\mathcal{L}_2\frac{\omega_{\mathtt{so}}}{\gamma_2}\left\{\frac{7q}{6}y-\frac{q^2}{2}y^2\right\}+\hat{k}\cdot\vec{P}_{\mathtt{A}}\mathcal{L}_2\frac{\omega_{\mathtt{so}}}{\gamma_2}\left\{\frac{2q^2-1}{3}y+\frac{q}{2}y^2\right\}
\end{aligned}
\tag{E.745}
$$

and finally :

$$
\hat{k}\cdot\vec{P}_{\mathtt{A}}=P_{\mathtt{A}}\left[k_z+\left(k_x\left\langle S_x\right\rangle_c+k_y\left\langle S_y\right\rangle_c\right)\cos(\omega_{\mathtt{rf}}t)+\left(k_x\left\langle S_x\right\rangle_s+k_y\left\langle S_y\right\rangle_s\right)\sin(\omega_{\mathtt{rf}}t)\right]
\tag{E.746}
$$

where $P_z=P_{\mathtt{A}}$ and $\omega_{\mathtt{rf}}$ is the frequency of the RF field.

E.7 Accessing Observables Using Polarized Light

E.7.1 Modulating Polarized Light Using a PEM

The effect of the atomic interaction on the light is expressed by the complex index of refraction through the wave vector $\vec{k}$. The direction of $\vec{k}$ is always in the direction that the light is propagating. On the other hand, the magnitude of $\vec{k}$ depends on the details of the atomic system and the polarization vector of the light. Our general experiment will consist of polarized traveling through a PEM, then the alkali vapor, and finally a beam splitting polarizing cube for detection. We'll start with a

arbitrarily polarized plane wave:

$$\vec{E} = |E\rangle\, e^{i\vec{k}\cdot\vec{r}-i\omega t} \tag{E.747}$$

$$|E\rangle = E_0 e^{i\phi_p}\left[\left(\sqrt{1-P}\frac{e^{+i\theta}}{2}+\sqrt{1+P}\frac{e^{-i\theta}}{2}\right)|\mathcal{P}\rangle+\left(\sqrt{1-P}\frac{e^{+i\theta}}{2i}-\sqrt{1+P}\frac{e^{-i\theta}}{2i}\right)|\mathcal{S}\rangle\right] \tag{E.748}$$

Going through a photoelastic modulator:

$$|E\rangle = E_0 e^{i\phi_p}\left[\left(\sqrt{1-P}\frac{e^{+i\theta_+}}{2}+\sqrt{1+P}\frac{e^{-i\theta_-}}{2}\right)|\mathcal{P}\rangle+\left(\sqrt{1-P}\frac{e^{+i\theta_-}}{2i}-\sqrt{1+P}\frac{e^{-i\theta_+}}{2i}\right)|\mathcal{S}\rangle\right] \tag{E.749}$$

$$\theta_\pm = \theta \pm \frac{\beta(t)}{2} \tag{E.750}$$

Going back into the circular polarization basis, the right $(+)$ and left $(-)$ components are:

$$|E\rangle_\pm = +\frac{E_0}{2\sqrt{2}}e^{i(\phi_p)}\left[\left\{e^{+i\theta_-}\mp e^{+i\theta_+}\right\}\sqrt{1-P}-\left\{e^{-i\theta_+}\pm e^{-i\theta_-}\right\}\sqrt{1+P}\right] \tag{E.751}$$

Going through the atomic vapor, each polarization component q of the light propagates with wave vector $\vec{k}_q$:

$$\vec{E} = \sum_q |E\rangle_q\, \hat{\varepsilon}_q e^{i\left(\vec{k}_q\cdot\vec{r}-\omega t\right)} \tag{E.752}$$

After traversing a distance of l in the atomic vapor and reentering a uniform and isotropic medium with wave vector $\vec{k}$, we get:

$$\vec{E} = e^{i\left(\vec{k}\cdot\vec{r}-\omega t\right)} \sum_q |E\rangle_q \, \hat{\varepsilon}_q e^{ik_q l} \tag{E.753}$$

The time averaged intensity of the light is:

$$I = \sqrt{\frac{\epsilon}{\mu}} \frac{\vec{E}^* \cdot \vec{E}}{2} = \sqrt{\frac{\epsilon}{\mu}} \sum_q \frac{\langle E \mid E \rangle_q}{2} e^{i(k_q - k_q^*)l} = \sqrt{\frac{\epsilon}{\mu}} \sum_q \frac{\langle E \mid E \rangle_q}{2} e^{-2l\Im k_q} \tag{E.754}$$

The effect of the atomic vapor can be written in (a very suggestive) matrix form in the linear polarization basis in the light coordinate system:

$$|E\rangle_{\text{aft}} = \hat{M} |E\rangle_{\text{bef}} \tag{E.755}$$

$$\hat{M} = e^{i(k_+ + k_-)\frac{l}{2}} \begin{bmatrix} \cos\left(\frac{k_+ - k_-}{2} l\right) & \sin\left(\frac{k_+ - k_-}{2} l\right) \\ -\sin\left(\frac{k_+ - k_-}{2} l\right) & \cos\left(\frac{k_+ - k_-}{2} l\right) \end{bmatrix} \tag{E.756}$$

$$|E\rangle_{\text{bef}} = \frac{E_0 e^{i\phi_p}}{2} \begin{bmatrix} \sqrt{1-P} e^{+i\theta_+} + \sqrt{1+P} e^{-i\theta_-} \\ -i\left(\sqrt{1-P} e^{+i\theta_-} - \sqrt{1+P} e^{-i\theta_+}\right) \end{bmatrix} \tag{E.757}$$

The atomic vapor has the effect of creating an overall complex phase of $i(k_+ + k_-)l/2$ and a complex rotation through and angle $(k_+ - k_-)l/2$. Now we'll send the light through a half waveplate whose axis is at an angle ϕ_h:

$$\hat{W}_{\frac{1}{2}} \hat{M}_0 = i \begin{bmatrix} +\cos\left(\frac{k_+ - k_-}{2} l + 2\phi_h\right) & +\sin\left(\frac{k_+ - k_-}{2} l + 2\phi_h\right) \\ +\sin\left(\frac{k_+ - k_-}{2} l + 2\phi_h\right) & -\cos\left(\frac{k_+ - k_-}{2} l + 2\phi_h\right) \end{bmatrix} \tag{E.758}$$

The final polarization vector can be written as:

$$|E\rangle_{\mathrm{f}} = i\frac{E_0 e^{i\phi'_p}}{2}\begin{bmatrix} \sqrt{1-P}e^{+i\theta}\left(\cos(\psi)e^{+i\frac{\beta}{2}} - i\sin(\psi)e^{-i\frac{\beta}{2}}\right) + \sqrt{1+P}e^{-i\theta}\left(\cos(\psi)e^{+i\frac{\beta}{2}} + i\sin(\psi)e^{-i\frac{\beta}{2}}\right) \\ i\sqrt{1-P}e^{+i\theta}\left(\cos(\psi)e^{-i\frac{\beta}{2}} - i\sin(\psi)e^{+i\frac{\beta}{2}}\right) - i\sqrt{1+P}e^{-i\theta}\left(\cos(\psi)e^{-i\frac{\beta}{2}} + i\sin(\psi)e^{+i\frac{\beta}{2}}\right) \end{bmatrix} \tag{E.759}$$

$$\phi'_p = \phi_p + (k_+ + k_-)\frac{l}{2} \tag{E.760}$$

$$\psi = (k_+ - k_-)\frac{l}{2} + 2\phi_h \tag{E.761}$$

Noting that ψ is complex, the intensities of the two components are:

$$\zeta = \sqrt{\frac{\epsilon}{\mu}}\frac{E_0^2}{4}e^{-l\Im\{k_+ + k_-\}} \tag{E.762}$$

$$\frac{I_{\mathcal{P}}}{\zeta} = |\cos(\psi)|^2 + |\sin(\psi)|^2 + iP\left(\cos(\psi^*)\sin(\psi)e^{-i\beta} - \cos(\psi)\sin(\psi^*)e^{+i\beta}\right) + \sqrt{1-P^2}\times \Re\left\{e^{+2i\theta}\left[|\cos(\psi)|^2 - |\sin(\psi)|^2 - i\cos(\psi^*)\sin(\psi)e^{-i\beta} - i\cos(\psi)\sin(\psi^*)e^{+i\beta}\right]\right\} \tag{E.763}$$

$$\frac{I_{\mathcal{S}}}{\zeta} = |\cos(\psi)|^2 + |\sin(\psi)|^2 + iP\left(\cos(\psi^*)\sin(\psi)e^{+i\beta} - \cos(\psi)\sin(\psi^*)e^{-i\beta}\right) - \sqrt{1-P^2}\times \Re\left\{e^{+2i\theta}\left[|\cos(\psi)|^2 - |\sin(\psi)|^2 - i\cos(\psi^*)\sin(\psi)e^{+i\beta} - i\cos(\psi)\sin(\psi^*)e^{-i\beta}\right]\right\} \tag{E.764}$$

Using the following relations:

$$|\cos(\psi)|^2 = \cos(\psi)\cos(\psi^*) = \frac{1}{2}\left[\cosh(2\Im\psi) + \cos(2\Re\psi)\right] \tag{E.765}$$

$$|\sin(\psi)|^2 = \sin(\psi)\sin(\psi^*) = \frac{1}{2}\left[\cosh(2\Im\psi) - \cos(2\Re\psi)\right] \tag{E.766}$$

$$\sin(\psi)\cos(\psi^*) = \frac{1}{2}\left[+i\sinh(2\Im\psi) + \sin(2\Re\psi)\right] \tag{E.767}$$

$$\sin(\psi^*)\cos(\psi) = \frac{1}{2}\left[-i\sinh(2\Im\psi) + \sin(2\Re\psi)\right] \tag{E.768}$$

finally gives:

$$I_{\mathcal{P},\mathcal{S}} = \frac{I_\sigma \pm I_\delta}{2} \tag{E.769}$$

$$I_\sigma = 2\zeta\left[\cosh(2\Im\psi) + \sinh(2\Im\psi)\left(\sqrt{1-P^2}\sin(2\theta)\sin(\beta) - \cos(\beta)\right)\right] \tag{E.770}$$

$$I_\delta = 2\zeta\left[P\sin(\beta)\sin(2\Re\psi) + \sqrt{1-P^2}\left(\cos(2\theta)\cos(2\Re\psi) + \sin(2\theta)\sin(2\Re\psi)\cos(\beta)\right)\right] \tag{E.771}$$

Using the following expansions for the β terms:

$$\beta(t) = \beta_0\cos\left(\Omega_{\text{mod}}t\right) \tag{E.772}$$

$$\sin\left(\beta_0\cos\left(\Omega_{\text{mod}}t\right)\right) = 2J_1\left(\beta_0\right)\cos\left(\Omega_{\text{mod}}t\right) - \cdots \tag{E.773}$$

$$\cos\left(\beta_0\cos\left(\Omega_{\text{mod}}t\right)\right) = J_0\left(\beta_0\right) - 2J_2\left(\beta_0\right)\cos\left(2\Omega_{\text{mod}}t\right) + \cdots \tag{E.774}$$

we can extract the DC, the RMS AC1, and the RMS AC2 components of the sum (σ) and difference (δ) signals:

$$I_\sigma(\text{DC}) = 2\zeta\left[\cosh(2\Im\psi) - J_0(\beta_0)\sinh(2\Im\psi)\right] \tag{E.775}$$

$$I_\sigma(\text{AC1}) = 2\zeta\sqrt{2}J_1(\beta_0)\sinh(2\Im\psi)\sqrt{1-P^2}\sin(2\theta) \tag{E.776}$$

$$I_\sigma(\text{AC2}) = 2\zeta\sqrt{2}J_2(\beta_0)\sinh(2\Im\psi) \tag{E.777}$$

$$I_\delta(\text{DC}) = 2\zeta\sqrt{1-P^2}\left[\cos(2\theta)\cos(2\Re\psi) + J_0(\beta_0)\sin(2\theta)\sin(2\Re\psi)\right] \tag{E.778}$$

$$I_\delta(\text{AC1}) = 2\zeta\sqrt{2}J_1(\beta_0)P\sin(2\Re\psi) \tag{E.779}$$

$$I_\delta(\text{AC2}) = 2\zeta\sqrt{2}J_2(\beta_0)\sqrt{1-P^2}\sin(2\theta)\sin(2\Re\psi) \tag{E.780}$$

$$2\zeta = \sqrt{\frac{\epsilon}{\mu}}\frac{E_0^2}{2}e^{-l\Im\{k_+ + k_-\}} \tag{E.781}$$

$$\psi = (k_+ - k_-)\frac{l}{2} + 2\phi_h \tag{E.782}$$

where:

1. J_n is a Bessel function of the first kind or order n
2. $\beta_0 = 2\pi\beta_{\text{set}}\left(\frac{\lambda_{\text{set}}}{\lambda_{\text{light}}}\right)$ is the PEM retardation. If there is no PEM, then we can simply set $\beta_0 = 0$.
3. ϕ_h is the angle of the half waveplate axis with respect to the PEM axis
4. P is the degree of circular polarization of the light before the PEM
5. θ is the angle of linear polarization component of the light with respect to the PEM axis before the PEM
6. $\Re$ and $\Im$ refer to the real and imaginary parts of a complex number

The AC components can be picked out using a Lock-In Amplifier referenced to the PEM frequency (Ω_{mod}). The DC components can be picked out using a low pass filter with a time constant that is several times longer than the PEM period $1/\Omega_{\text{mod}}$. For the case where there is no atomic vapor ($l = 0$):

$$I_\sigma(\text{DC}) = \sqrt{\frac{\epsilon}{\mu}}\frac{E_0^2}{2} \tag{E.783}$$

$$I_\sigma(\text{AC1}) = 0 \tag{E.784}$$

$$I_\sigma(\text{AC2}) = 0 \tag{E.785}$$

$$I_\delta(\text{DC}) = I_\sigma(\text{DC})\sqrt{1-P^2}\,[\cos(2\theta)\cos(4\phi_h) + J_0(\beta_0)\sin(2\theta)\sin(4\phi_h)] \tag{E.786}$$

$$I_\delta(\text{AC1}) = I_\sigma(\text{DC})\sqrt{2}J_1(\beta_0)P\sin(4\phi_h) \tag{E.787}$$

$$I_\delta(\text{AC2}) = I_\sigma(\text{DC})\sqrt{2}J_2(\beta_0)\sqrt{1-P^2}\sin(2\theta)\sin(4\phi_h) \tag{E.788}$$

This gives a simple method for measuring the degree of circular polarization (Sec. (E.4.6)) using a rotatable half-waveplate (RHWP). As the RHWP is rotated, the signal $I_\delta(\text{AC1})/I_\sigma$ will oscillate between a maximum and minimum four times through one complete rotation. The normalized amplitude of this sinusoidal oscillation is $\sqrt{2}J_1(\beta_0)P$. If there is no PEM, then $J_0(0) = 1$ and $I_\delta(\text{DC})/I_\sigma$ will oscillate in the same way, this time with an amplitude of $\sqrt{1-P^2}$.

E.7.2 The Imaginary Part of the Polarizability Sum

The imaginary sum is given by:

$$\Im(k_+ + k_-) = \frac{[\mathrm{A}]2\pi r_e c f_1 \omega}{\omega_1} C\Im(\alpha_+ + \alpha_-) \tag{E.789}$$

The sum of the imaginary parts of the polarizability is given by:

$$\begin{aligned}
C\Im(\alpha_+ + \alpha_-) &= \frac{(1-\hat{k}\cdot\vec{P}_{\mathrm{A}})}{2}\mathcal{L}_1\left\{1+\left[\frac{2}{3}-\frac{8}{3}\omega_{\mathrm{so}}\mathcal{D}_1\right]y+\left[-\frac{1}{3}-\frac{4}{3}\omega_{\mathrm{so}}\mathcal{D}_1+\frac{4+12}{9}\omega_{\mathrm{so}}^2\left(4\mathcal{D}_1^2-\frac{\mathcal{L}_1}{\gamma_1}\right)\right]y^2\right\} \\
&\quad +\mathcal{L}_2\left\{1-\left[\frac{1}{3}+\frac{7}{3}\omega_{\mathrm{so}}\mathcal{D}_2\right]y+\left[-\frac{1}{3}+\frac{1}{2}+\omega_{\mathrm{so}}\mathcal{D}_2+\frac{1+12}{9}\omega_{\mathrm{so}}^2\left(4\mathcal{D}_2^2-\frac{\mathcal{L}_2}{\gamma_2}\right)\right]y^2\right\} \\
&\quad +\frac{\hat{k}\cdot\vec{P}_{\mathrm{A}}}{2}\mathcal{L}_2\left\{1+\left[\frac{2}{3}-\frac{4}{3}\omega_{\mathrm{so}}\mathcal{D}_2\right]y+\left[-\frac{1}{3}-2\omega_{\mathrm{so}}\mathcal{D}_2+\frac{1}{9}\omega_{\mathrm{so}}^2\left(4\mathcal{D}_2^2-\frac{\mathcal{L}_2}{\gamma_2}\right)\right]y^2\right\} \\
&\quad +(1-1)\hat{k}\cdot\vec{P}_{\mathrm{A}}\left\{\mathcal{L}_1[-1+\omega_{\mathrm{so}}\mathcal{D}_1]+\mathcal{L}_2[+1+\omega_{\mathrm{so}}\mathcal{D}_2]\right\}\frac{2y}{3} \\
&\quad +\frac{(1+\hat{k}\cdot\vec{P}_{\mathrm{A}})}{2}\mathcal{L}_1\left\{1-\left[\frac{2}{3}-\frac{8}{3}\omega_{\mathrm{so}}\mathcal{D}_1\right]y+\left[-\frac{1}{3}-\frac{4}{3}\omega_{\mathrm{so}}\mathcal{D}_1+\frac{4+12}{9}\omega_{\mathrm{so}}^2\left(4\mathcal{D}_1^2-\frac{\mathcal{L}_1}{\gamma_1}\right)\right]y^2\right\} \\
&\quad +\mathcal{L}_2\left\{1+\left[\frac{1}{3}+\frac{7}{3}\omega_{\mathrm{so}}\mathcal{D}_2\right]y+\left[-\frac{1}{3}+\frac{1}{2}+\omega_{\mathrm{so}}\mathcal{D}_2+\frac{1+12}{9}\omega_{\mathrm{so}}^2\left(4\mathcal{D}_2^2-\frac{\mathcal{L}_2}{\gamma_2}\right)\right]y^2\right\} \\
&\quad +\frac{-\hat{k}\cdot\vec{P}_{\mathrm{A}}}{2}\mathcal{L}_2\left\{1-\left[\frac{2}{3}-\frac{4}{3}\omega_{\mathrm{so}}\mathcal{D}_2\right]y+\left[-\frac{1}{3}-2\omega_{\mathrm{so}}\mathcal{D}_2+\frac{1}{9}\omega_{\mathrm{so}}^2\left(4\mathcal{D}_2^2-\frac{\mathcal{L}_2}{\gamma_2}\right)\right]y^2\right\} \\
&\quad +(1-1)\hat{k}\cdot\vec{P}_{\mathrm{A}}\left\{\mathcal{L}_1[-1+\omega_{\mathrm{so}}\mathcal{D}_1]+\mathcal{L}_2[+1+\omega_{\mathrm{so}}\mathcal{D}_2]\right\}\frac{2y}{3} \\
&= +\mathcal{L}_1\left\{1+\left[-\frac{1}{3}-\frac{4}{3}\omega_{\mathrm{so}}\mathcal{D}_1+\frac{16}{9}\omega_{\mathrm{so}}^2\left(4\mathcal{D}_1^2-\frac{\mathcal{L}_1}{\gamma_1}\right)\right]y^2\right\} \\
&\quad +2\mathcal{L}_2\left\{1+\left[\frac{1}{6}+\omega_{\mathrm{so}}\mathcal{D}_2+\frac{13}{9}\omega_{\mathrm{so}}^2\left(4\mathcal{D}_2^2-\frac{\mathcal{L}_2}{\gamma_2}\right)\right]y^2\right\} \\
&\quad -\hat{k}\cdot\vec{P}_{\mathrm{A}}\mathcal{L}_1\left[\frac{2}{3}-\frac{8}{3}\omega_{\mathrm{so}}\mathcal{D}_1\right]y+\hat{k}\cdot\vec{P}_{\mathrm{A}}\mathcal{L}_2\left[\frac{2}{3}-\frac{4}{3}\omega_{\mathrm{so}}\mathcal{D}_2\right]y
\end{aligned} \tag{E.790}$$

E.7.3 The Imaginary Part of the Polarizability Difference

The imaginary difference is given by:

$$2\Im\psi = 2\Im\left(k_+ - k_-\right)\frac{l}{2} = \frac{l[\mathrm{A}]2\pi r_e c f_1 \omega}{\omega_1} C\Im(\alpha_+ - \alpha_-) \tag{E.791}$$

The difference of the imaginary parts of the polarizability is given by:

$$\begin{aligned}
C\Im(\alpha_+ - \alpha_-) &= \frac{(1-\hat{k}\cdot\vec{P}_{\mathrm{A}})}{2}\mathcal{L}_1\left\{1+\left[\frac{2}{3}-\frac{8}{3}\omega_{\mathrm{so}}\mathcal{D}_1\right]y+\left[-\frac{1}{3}-\frac{4}{3}\omega_{\mathrm{so}}\mathcal{D}_1+\frac{4+12}{9}\omega_{\mathrm{so}}^2\left(4\mathcal{D}_1^2-\frac{\mathcal{L}_1}{\gamma_1}\right)\right]y^2\right\} \\
&\quad +\mathcal{L}_2\left\{1-\left[\frac{1}{3}+\frac{7}{3}\omega_{\mathrm{so}}\mathcal{D}_2\right]y+\left[-\frac{1}{3}+\frac{1}{2}+\omega_{\mathrm{so}}\mathcal{D}_2+\frac{1+12}{9}\omega_{\mathrm{so}}^2\left(4\mathcal{D}_2^2-\frac{\mathcal{L}_2}{\gamma_2}\right)\right]y^2\right\} \\
&\quad +\frac{\hat{k}\cdot\vec{P}_{\mathrm{A}}}{2}\mathcal{L}_2\left\{1+\left[\frac{2}{3}-\frac{4}{3}\omega_{\mathrm{so}}\mathcal{D}_2\right]y+\left[-\frac{1}{3}-2\omega_{\mathrm{so}}\mathcal{D}_2+\frac{1}{9}\omega_{\mathrm{so}}^2\left(4\mathcal{D}_2^2-\frac{\mathcal{L}_2}{\gamma_2}\right)\right]y^2\right\} \\
&\quad +(1-1)\hat{k}\cdot\vec{P}_{\mathrm{A}}\left\{\mathcal{L}_1\left[-1+\omega_{\mathrm{so}}\mathcal{D}_1\right]+\mathcal{L}_2\left[+1+\omega_{\mathrm{so}}\mathcal{D}_2\right]\right\}\frac{2y}{3} \\
&\quad -\frac{(1+\hat{k}\cdot\vec{P}_{\mathrm{A}})}{2}\mathcal{L}_1\left\{1-\left[\frac{2}{3}-\frac{8}{3}\omega_{\mathrm{so}}\mathcal{D}_1\right]y+\left[-\frac{1}{3}-\frac{4}{3}\omega_{\mathrm{so}}\mathcal{D}_1+\frac{4+12}{9}\omega_{\mathrm{so}}^2\left(4\mathcal{D}_1^2-\frac{\mathcal{L}_1}{\gamma_1}\right)\right]y^2\right\} \\
&\quad -\mathcal{L}_2\left\{1+\left[\frac{1}{3}+\frac{7}{3}\omega_{\mathrm{so}}\mathcal{D}_2\right]y+\left[-\frac{1}{3}+\frac{1}{2}+\omega_{\mathrm{so}}\mathcal{D}_2+\frac{1+12}{9}\omega_{\mathrm{so}}^2\left(4\mathcal{D}_2^2-\frac{\mathcal{L}_2}{\gamma_2}\right)\right]y^2\right\} \\
&\quad +\frac{\hat{k}\cdot\vec{P}_{\mathrm{A}}}{2}\mathcal{L}_2\left\{1-\left[\frac{2}{3}-\frac{4}{3}\omega_{\mathrm{so}}\mathcal{D}_2\right]y+\left[-\frac{1}{3}-2\omega_{\mathrm{so}}\mathcal{D}_2+\frac{1}{9}\omega_{\mathrm{so}}^2\left(4\mathcal{D}_2^2-\frac{\mathcal{L}_2}{\gamma_2}\right)\right]y^2\right\} \\
&\quad -(1-1)\hat{k}\cdot\vec{P}_{\mathrm{A}}\left\{\mathcal{L}_1\left[-1+\omega_{\mathrm{so}}\mathcal{D}_1\right]+\mathcal{L}_2\left[+1+\omega_{\mathrm{so}}\mathcal{D}_2\right]\right\}\frac{2y}{3} \\
&= +\mathcal{L}_1\left[\frac{2}{3}-\frac{8}{3}\omega_{\mathrm{so}}\mathcal{D}_1\right]y-\hat{k}\cdot\vec{P}_{\mathrm{A}}\mathcal{L}_1\left\{1+\left[-\frac{1}{3}-\frac{4}{3}\omega_{\mathrm{so}}\mathcal{D}_1+\frac{16}{9}\omega_{\mathrm{so}}^2\left(4\mathcal{D}_1^2-\frac{\mathcal{L}_1}{\gamma_1}\right)\right]y^2\right\} \\
&\quad -2\mathcal{L}_2\left[\frac{1}{3}+\frac{7}{3}\omega_{\mathrm{so}}\mathcal{D}_2\right]y+\hat{k}\cdot\vec{P}_{\mathrm{A}}\mathcal{L}_2\left\{1+\left[-\frac{1}{3}-2\omega_{\mathrm{so}}\mathcal{D}_2+\frac{1}{9}\omega_{\mathrm{so}}^2\left(4\mathcal{D}_2^2-\frac{\mathcal{L}_2}{\gamma_2}\right)\right]y^2\right\}
\end{aligned} \tag{E.792}$$

E.7.4 The Real Part of the Polarizability Sum

The real sum is given by:

$$\Re(k_+ + k_-) = \frac{[\mathrm{A}]2\pi r_e c f_1 \omega}{\omega_1} C\Re(\alpha_+ + \alpha_-) \tag{E.793}$$

The sum of the real parts of the polarizability is given by:

$$\begin{aligned}
C\Re(\alpha_+ + \alpha_-) &= \frac{(1-\hat{k}\cdot\vec{P}_{\mathrm{A}})}{2}\mathcal{D}_1\left\{1+\left[\frac{2}{3}-\frac{8}{3}\omega_{\mathrm{so}}\mathcal{D}_1\right]y+\left[-\frac{1}{3}-\frac{4}{3}\omega_{\mathrm{so}}\mathcal{D}_1+\frac{4+12}{9}\omega_{\mathrm{so}}^2\left(4\mathcal{D}_1^2-3\frac{\mathcal{L}_1}{\gamma_1}\right)\right]y^2\right\} \\
&\quad +\mathcal{D}_2\left\{1-\left[\frac{1}{3}+\frac{7}{3}\omega_{\mathrm{so}}\mathcal{D}_2\right]y+\left[-\frac{1}{3}+\frac{1}{2}+\omega_{\mathrm{so}}\mathcal{D}_2+\frac{1+12}{9}\omega_{\mathrm{so}}^2\left(4\mathcal{D}_2^2-3\frac{\mathcal{L}_2}{\gamma_2}\right)\right]y^2\right\} \\
&\quad +\frac{\hat{k}\cdot\vec{P}_{\mathrm{A}}}{2}\mathcal{D}_2\left\{1+\left[\frac{2}{3}-\frac{4}{3}\omega_{\mathrm{so}}\mathcal{D}_2\right]y+\left[-\frac{1}{3}-2\omega_{\mathrm{so}}\mathcal{D}_2+\frac{1}{9}\omega_{\mathrm{so}}^2\left(4\mathcal{D}_2^2-3\frac{\mathcal{L}_2}{\gamma_2}\right)\right]y^2\right\} \\
&\quad +(1-1)\hat{k}\cdot\vec{P}_{\mathrm{A}}\left\{\mathcal{D}_1[-1+\omega_{\mathrm{so}}\mathcal{D}_1]+\mathcal{D}_2[+1+\omega_{\mathrm{so}}\mathcal{D}_2]-\frac{1}{2}\mathcal{L}_1\frac{\omega_{\mathrm{so}}}{\gamma_1}\right\}\frac{2y}{3} \\
&\quad +(1-\hat{k}\cdot\vec{P}_{\mathrm{A}})\mathcal{L}_1\frac{\omega_{\mathrm{so}}}{\gamma_1}\left\{\frac{2}{3}y+\frac{1}{3}y^2\right\}+\mathcal{L}_2\frac{\omega_{\mathrm{so}}}{\gamma_2}\left\{\frac{7}{6}y-\frac{1}{2}y^2\right\}+\hat{k}\cdot\vec{P}_{\mathrm{A}}\mathcal{L}_2\frac{\omega_{\mathrm{so}}}{\gamma_2}\left\{\frac{2-1}{3}y+\frac{1}{2}y^2\right\} \\
&\quad +\frac{(1+\hat{k}\cdot\vec{P}_{\mathrm{A}})}{2}\mathcal{D}_1\left\{1-\left[\frac{2}{3}-\frac{8}{3}\omega_{\mathrm{so}}\mathcal{D}_1\right]y+\left[-\frac{1}{3}-\frac{4}{3}\omega_{\mathrm{so}}\mathcal{D}_1+\frac{4+12}{9}\omega_{\mathrm{so}}^2\left(4\mathcal{D}_1^2-3\frac{\mathcal{L}_1}{\gamma_1}\right)\right]y^2\right\} \\
&\quad +\mathcal{D}_2\left\{1+\left[\frac{1}{3}+\frac{7}{3}\omega_{\mathrm{so}}\mathcal{D}_2\right]y+\left[-\frac{1}{3}+\frac{1}{2}+\omega_{\mathrm{so}}\mathcal{D}_2+\frac{1+12}{9}\omega_{\mathrm{so}}^2\left(4\mathcal{D}_2^2-3\frac{\mathcal{L}_2}{\gamma_2}\right)\right]y^2\right\} \\
&\quad +\frac{-\hat{k}\cdot\vec{P}_{\mathrm{A}}}{2}\mathcal{D}_2\left\{1-\left[\frac{2}{3}-\frac{4}{3}\omega_{\mathrm{so}}\mathcal{D}_2\right]y+\left[-\frac{1}{3}-2\omega_{\mathrm{so}}\mathcal{D}_2+\frac{1}{9}\omega_{\mathrm{so}}^2\left(4\mathcal{D}_2^2-3\frac{\mathcal{L}_2}{\gamma_2}\right)\right]y^2\right\} \\
&\quad +(1-1)\hat{k}\cdot\vec{P}_{\mathrm{A}}\left\{\mathcal{D}_1[-1+\omega_{\mathrm{so}}\mathcal{D}_1]+\mathcal{D}_2[+1+\omega_{\mathrm{so}}\mathcal{D}_2]-\frac{1}{2}\mathcal{L}_1\frac{\omega_{\mathrm{so}}}{\gamma_1}\right\}\frac{2y}{3} \\
&\quad +(1+\hat{k}\cdot\vec{P}_{\mathrm{A}})\mathcal{L}_1\frac{\omega_{\mathrm{so}}}{\gamma_1}\left\{-\frac{2}{3}y+\frac{1}{3}y^2\right\}+\mathcal{L}_2\frac{\omega_{\mathrm{so}}}{\gamma_2}\left\{-\frac{7}{6}y-\frac{1}{2}y^2\right\}+\hat{k}\cdot\vec{P}_{\mathrm{A}}\mathcal{L}_2\frac{\omega_{\mathrm{so}}}{\gamma_2}\left\{\frac{1}{3}y-\frac{1}{2}y^2\right\} \\
&= +\mathcal{D}_1\left\{1+\left[-\frac{1}{3}-\frac{4}{3}\omega_{\mathrm{so}}\mathcal{D}_1+\frac{16}{9}\omega_{\mathrm{so}}^2\left(4\mathcal{D}_1^2-3\frac{\mathcal{L}_1}{\gamma_1}\right)\right]y^2\right\}-\hat{k}\cdot\vec{P}_{\mathrm{A}}\mathcal{D}_1\left[\frac{2}{3}-\frac{8}{3}\omega_{\mathrm{so}}\mathcal{D}_1\right]y \\
&\quad +2\mathcal{D}_2\left\{1+\left[\frac{1}{6}+\omega_{\mathrm{so}}\mathcal{D}_2+\frac{13}{9}\omega_{\mathrm{so}}^2\left(4\mathcal{D}_2^2-3\frac{\mathcal{L}_2}{\gamma_2}\right)\right]y^2\right\}+\hat{k}\cdot\vec{P}_{\mathrm{A}}\mathcal{D}_2\left[\frac{2}{3}-\frac{4}{3}\omega_{\mathrm{so}}\mathcal{D}_2\right]y \\
&\quad +\mathcal{L}_1\frac{\omega_{\mathrm{so}}}{\gamma_1}\left\{\frac{2}{3}y^2\right\}-\mathcal{L}_2\frac{\omega_{\mathrm{so}}}{\gamma_2}y^2+\hat{k}\cdot\vec{P}_{\mathrm{A}}\mathcal{L}_2\frac{\omega_{\mathrm{so}}}{\gamma_2}\frac{2}{3}y-\hat{k}\cdot\vec{P}_{\mathrm{A}}\mathcal{L}_1\frac{\omega_{\mathrm{so}}}{\gamma_1}\left\{\frac{4}{3}y\right\}
\end{aligned} \tag{E.794}$$

E.7.5 The Real Part of the Polarizability Difference

The real difference is given by:

$$2\Re\psi = 2\Re\left(k_+ - k_-\right)\frac{l}{2} + 4\phi_h = \frac{l[\mathrm{A}]2\pi r_e c f_1 \omega}{\omega_1} C\Re(\alpha_+ - \alpha_-) + 4\phi_h \tag{E.795}$$

The difference of the real parts of the polarizability is given by:

$$\begin{aligned}
C\Re(\alpha_+ - \alpha_-) &= \frac{(1-\hat{k}\cdot\vec{P}_{\mathrm{A}})}{2}\mathcal{D}_1\left\{1+\left[\frac{2}{3}-\frac{8}{3}\omega_{\mathrm{so}}\mathcal{D}_1\right]y+\left[-\frac{1}{3}-\frac{4}{3}\omega_{\mathrm{so}}\mathcal{D}_1+\frac{4+12}{9}\omega_{\mathrm{so}}^2\left(4\mathcal{D}_1^2-3\frac{\mathcal{L}_1}{\gamma_1}\right)\right]y^2\right\} \\
&\quad +\mathcal{D}_2\left\{1-\left[\frac{1}{3}+\frac{7}{3}\omega_{\mathrm{so}}\mathcal{D}_2\right]y+\left[-\frac{1}{3}+\frac{1}{2}+\omega_{\mathrm{so}}\mathcal{D}_2+\frac{1+12}{9}\omega_{\mathrm{so}}^2\left(4\mathcal{D}_2^2-3\frac{\mathcal{L}_2}{\gamma_2}\right)\right]y^2\right\} \\
&\quad +\frac{\hat{k}\cdot\vec{P}_{\mathrm{A}}}{2}\mathcal{D}_2\left\{1+\left[\frac{2}{3}-\frac{4}{3}\omega_{\mathrm{so}}\mathcal{D}_2\right]y+\left[-\frac{1}{3}-2\omega_{\mathrm{so}}\mathcal{D}_2+\frac{1}{9}\omega_{\mathrm{so}}^2\left(4\mathcal{D}_2^2-3\frac{\mathcal{L}_2}{\gamma_2}\right)\right]y^2\right\} \\
&\quad +(1-1)\hat{k}\cdot\vec{P}_{\mathrm{A}}\left\{\mathcal{D}_1\left[-1+\omega_{\mathrm{so}}\mathcal{D}_1\right]+\mathcal{D}_2\left[+1+\omega_{\mathrm{so}}\mathcal{D}_2\right]-\frac{1}{2}\mathcal{L}_1\frac{\omega_{\mathrm{so}}}{\gamma_1}\right\}\frac{2y}{3} \\
&\quad +(1-\hat{k}\cdot\vec{P}_{\mathrm{A}})\mathcal{L}_1\frac{\omega_{\mathrm{so}}}{\gamma_1}\left\{\frac{2}{3}y+\frac{1}{3}y^2\right\}+\mathcal{L}_2\frac{\omega_{\mathrm{so}}}{\gamma_2}\left\{\frac{7}{6}y-\frac{1}{2}y^2\right\}+\hat{k}\cdot\vec{P}_{\mathrm{A}}\mathcal{L}_2\frac{\omega_{\mathrm{so}}}{\gamma_2}\left\{\frac{2-1}{3}y+\frac{1}{2}y^2\right\} \\
&\quad -\frac{(1+\hat{k}\cdot\vec{P}_{\mathrm{A}})}{2}\mathcal{D}_1\left\{1-\left[\frac{2}{3}-\frac{8}{3}\omega_{\mathrm{so}}\mathcal{D}_1\right]y+\left[-\frac{1}{3}-\frac{4}{3}\omega_{\mathrm{so}}\mathcal{D}_1+\frac{4+12}{9}\omega_{\mathrm{so}}^2\left(4\mathcal{D}_1^2-3\frac{\mathcal{L}_1}{\gamma_1}\right)\right]y^2\right\} \\
&\quad -\mathcal{D}_2\left\{1+\left[\frac{1}{3}+\frac{7}{3}\omega_{\mathrm{so}}\mathcal{D}_2\right]y+\left[-\frac{1}{3}+\frac{1}{2}+\omega_{\mathrm{so}}\mathcal{D}_2+\frac{1+12}{9}\omega_{\mathrm{so}}^2\left(4\mathcal{D}_2^2-3\frac{\mathcal{L}_2}{\gamma_2}\right)\right]y^2\right\} \\
&\quad -\frac{-\hat{k}\cdot\vec{P}_{\mathrm{A}}}{2}\mathcal{D}_2\left\{1-\left[\frac{2}{3}-\frac{4}{3}\omega_{\mathrm{so}}\mathcal{D}_2\right]y+\left[-\frac{1}{3}-2\omega_{\mathrm{so}}\mathcal{D}_2+\frac{1}{9}\omega_{\mathrm{so}}^2\left(4\mathcal{D}_2^2-3\frac{\mathcal{L}_2}{\gamma_2}\right)\right]y^2\right\} \\
&\quad -(1-1)\hat{k}\cdot\vec{P}_{\mathrm{A}}\left\{\mathcal{D}_1\left[-1+\omega_{\mathrm{so}}\mathcal{D}_1\right]+\mathcal{D}_2\left[+1+\omega_{\mathrm{so}}\mathcal{D}_2\right]-\frac{1}{2}\mathcal{L}_1\frac{\omega_{\mathrm{so}}}{\gamma_1}\right\}\frac{2y}{3} \\
&\quad -(1+\hat{k}\cdot\vec{P}_{\mathrm{A}})\mathcal{L}_1\frac{\omega_{\mathrm{so}}}{\gamma_1}\left\{-\frac{2}{3}y+\frac{1}{3}y^2\right\}-\mathcal{L}_2\frac{\omega_{\mathrm{so}}}{\gamma_2}\left\{-\frac{7}{6}y-\frac{1}{2}y^2\right\}-\hat{k}\cdot\vec{P}_{\mathrm{A}}\mathcal{L}_2\frac{\omega_{\mathrm{so}}}{\gamma_2}\left\{\frac{1}{3}y-\frac{1}{2}y^2\right\} \\
&= +\mathcal{D}_1\left[\frac{2}{3}-\frac{8}{3}\omega_{\mathrm{so}}\mathcal{D}_1\right]y-\hat{k}\cdot\vec{P}_{\mathrm{A}}\mathcal{D}_1\left\{1+\left[-\frac{1}{3}-\frac{4}{3}\omega_{\mathrm{so}}\mathcal{D}_1+\frac{16}{9}\omega_{\mathrm{so}}^2\left(4\mathcal{D}_1^2-3\frac{\mathcal{L}_1}{\gamma_1}\right)\right]y^2\right\} \\
&\quad -2\mathcal{D}_2\left[\frac{1}{3}+\frac{7}{3}\omega_{\mathrm{so}}\mathcal{D}_2\right]y+\hat{k}\cdot\vec{P}_{\mathrm{A}}\mathcal{D}_2\left\{1+\left[-\frac{1}{3}-2\omega_{\mathrm{so}}\mathcal{D}_2+\frac{1}{9}\omega_{\mathrm{so}}^2\left(4\mathcal{D}_2^2-3\frac{\mathcal{L}_2}{\gamma_2}\right)\right]y^2\right\} \\
&\quad +\mathcal{L}_2\frac{\omega_{\mathrm{so}}}{\gamma_2}\left\{\frac{7}{3}y\right\}+\hat{k}\cdot\vec{P}_{\mathrm{A}}\mathcal{L}_2\frac{\omega_{\mathrm{so}}}{\gamma_2}y^2+\mathcal{L}_1\frac{\omega_{\mathrm{so}}}{\gamma_1}\left\{\frac{4}{3}y\right\}-\hat{k}\cdot\vec{P}_{\mathrm{A}}\mathcal{L}_1\frac{\omega_{\mathrm{so}}}{\gamma_1}\left\{\frac{2}{3}y^2\right\}
\end{aligned} \tag{E.796}$$

E.8 D1 & D2 Absorption Spectroscopy

E.8.1 Experimental Signal: The Absorption Cross Section

For absorption measurements:

1. The intensity of the probe beam is kept very small so that there is essentially no optical pumping. Therefore the alkali polarization is thermal and essentially zero, $P_{\mathtt{A}} = 0$.

2. The alkali vapor is subject only to the earth's magnetic field. This is less than a gauss, so we take the field to be zero, $B = y = 0$.

3. A PEM will not be used, therefore, $\beta_0 = 0$ and $J_n(0) = \delta_{n0}$.

4. There is no analyzer half-wave plate, $\phi_h = 0$.

5. Only the total (sum) intensity before and after the alkali vapor is measured.

The transmitted intensity is therefore given by:

$$I_t = 2\zeta\left[\cosh(2\Im\psi) - \sinh(2\Im\psi)\right] \qquad 2\zeta = I_0 e^{-l\Im\{k_+ + k_-\}} \qquad \psi = \Im\left(k_+ - k_-\right)\frac{l}{2} \tag{E.797}$$

where I_0 is the intensity of the probe beam before the alkali vapor and the imaginary sum & difference of the polarizabilities are given by:

$$\Im(\alpha_+ - \alpha_-) = 0 \qquad \Im(\alpha_+ + \alpha_-) = \mathcal{L}_1 + 2\mathcal{L}_2 \tag{E.798}$$

We'll now introduce the absorption cross section:

$$\sigma(\nu) = \frac{\Im(k_+ + k_-)}{[\mathtt{A}]\ell} = 2\pi r_e c \left[\left(\frac{\omega}{\omega_1} \right) f_1 \mathcal{L}_1 + \left(\frac{\omega}{\omega_2} \right) f_2 \mathcal{L}_2 \right] \tag{E.799}$$

We'll make the approximations $\omega \approx \omega_1$ & $\omega \approx \omega_2$ and the substitutions $\nu = \omega/(2/\pi)$ & $\Gamma/2 = \gamma/(2\pi)$ to get:

$$\sigma(\nu) = r_e c \left[\frac{f_1 \Gamma_1/2}{(\nu - \nu_1)^2 + \Gamma_1^2/4} + \frac{f_2 \Gamma_2/2}{(\nu - \nu_2)^2 + \Gamma_2^2/4} \right] \tag{E.800}$$

where ν is the laser frequency, r_e is the classical electron radius, c is the speed of light in a vacuum, $f_{1(2)}$ is the D1(2) oscillator strength, $\nu_{1(2)}$ is the D1(2) transition frequency, and $\Gamma_{1(2)}$ is the full width at half maximum pressure broadening D1(2) line width.

The probe beam from the Ti:Sapphire (aka Single Frequency aka Ring) laser has a frequency dependent intensity which is modulated by an optical chopper at a frequency ω_{mod}:

$$I_0(\nu, t) = I_0(\nu) \left[\frac{1}{2} + \frac{2}{\pi} \sum_{k=1}^{\infty} \frac{\sin((2k-1)\omega_{\text{mod}} t)}{2k-1} \right] \tag{E.801}$$

where we've explicitly written the Fourier decomposition of the square wave produced by the chopper. The reference and transmitted intensities are converted into AC voltages (due to the chopper) by the photodiodes, amplified by the "photodiode box," converted into DC signals by the Lock-In amplifiers (referenced to ω_{mod}),

and finally digitized by the "autoscan interface box:"

$$N_{\text{ref}}(\nu) = G_{\text{PD1}} G_{\text{PD1-box}} G_{\text{lockin}-1} G_{\text{ADC}} I_0(\nu) \tag{E.802}$$

$$N_{\text{trans}}(\nu) = G_{\text{PD2}} G_{\text{PD2-box}} G_{\text{lockin}-2} G_{\text{ADC}} I_t(\nu) \tag{E.803}$$

where N is the number of bits from 0 to 4095 that the data channel reads. The raw data recorded in the ".SCN" file are the frequencies and the values of N_{ref} and N_{trans} in binary format. Before analysis, they have to be converted into ASCII format using a LabVIEW vi called "readscn.vi." We ultimately want to fit to $\sigma(\nu)$. Therefore the analysis program first makes the following transformation:

$$x = \nu \qquad y = \log\left(\frac{N_{\text{trans}}}{N_{\text{ref}}}\right) = -[A]\sigma(x)l + \log\left(\frac{G_{\text{PD2}} G_{\text{PD2-box}} G_{\text{lockin}-2}}{G_{\text{PD1}} G_{\text{PD1-box}} G_{\text{lockin}-1}}\right) \tag{E.804}$$

E.8.2 Corrections to the Line Shape

Introduction

Eqn. (E.800) implies that the line shape is a sum of pure lorentzian curves. However, it neglects:

1. An oscillatory background due to imperfect cancellation of the interference pattern produced by the cover of the photodiodes.
2. Natural line width
3. Doppler broadening
4. Finite hyperfine splittings of the ground and excited states.
5. Natural isotopic composition of the alkali vapor

6. Possible "leakage" of the wings of nearby absorption lines

Since we claim that the PB method is accurate at the 1 percent level (or even less), we'll discuss the above points more carefully.

When trying to determine how small of an effect is small enough to ignore, it's important to keep in mind the relative scales of the line shape. The FWHM of the absorption curve is about 20 GHz/amagat; so, an 8 amagat cell has about a 160 GHz FWHM. The frequency resolution (frequency jitter/noise and line width) of the Ti:Sapphire is about 1 MHz. Data is acquired in about 1 GHz intervals. The accuracy of the Autoscan Wavemeter is in principle easily sub-GHz. However, in practice, the frequency can be shifted by as much as 20 GHz with the shift being independent of frequency. The quantities of interest are *insensitive* to the absolute frequency. This is because we only use the width of the line (and not the shift of the line) to determine the noble gas density. In addition, the alkali density is derived from the "size" of the dip and not from the "location." As a final note, it's important to mention that the data acquisition time interval and lock-in time constant are chosen carefully to minimize lock-in time averaging signal shaping effects (minimum time between points $>$ five lock-in time constants).

Natural Line width

The natural line width is given by the spontaneous emission rate. For both lines of potassium and rubidium, the excited state lifetimes are all about $\tau \approx 30$ ns. Therefore the natural line width is about $\gamma_{\text{nat}} = \tau^{-1} \approx 0.03$ GHz. This is negligible.

Doppler Broadening

Doppler broadening of a spectral line is due to the Doppler shift. The Doppler width is obtained from the width of the velocity distribution of the gas molecules or atoms. In our case, this is the Maxwell velocity distribution, which is Gaussian. The FWHM as a fraction of the transition frequency is given by the formula (Demtroder, page 68, eq 3.43c):

$$\frac{\delta\nu_D}{\nu_0} = 7.16 \times 10^{-7} \sqrt{\frac{T \text{ (in Kelvin)}}{M \text{ (in grams per mole)}}} \tag{E.805}$$

For the D2 lines of Potassium and Rubidium at 150 C, the doppler widths are 0.91 GHz and 0.60 GHz respectively. These widths are less than one percent of the pressure broadened widths and are therefore negligible(?). For much lower pressure broadened widths, this is not negligible and the data must be fit to a Voigt profile, which is a convolution of a lorentzian line shape (pressure broadening) with a Gaussian line shape (Doppler broadening). An alternative is to simulate the effect and determine a Doppler correction factor.

Effect of Buffer Gas Collisions

When the collision between the alkali metal atom and perturbing atom occurs instantaneously ($T_d = 0$), then the absorption line shape is written as:

$$L(\Delta) = \frac{1}{2\pi} \frac{\gamma}{\Delta^2 + \gamma^2/4} \tag{E.806}$$

$$\Delta \equiv \omega - \omega_0 - \delta\omega(T) \tag{E.807}$$

$$\gamma = \gamma_{\text{nat}} + \langle \sigma v \rangle_{\text{pb}} (T)[N] \tag{E.808}$$

where γ is the FWHM broadening rate, Δ is the detuning from resonance ($\omega_0 + \delta\omega$), $\delta\omega$ is the temperature dependent resonance detuning shift due to collisions, γ_{nat} is the natural line width, $\langle\sigma v\rangle_{\text{pb}}(T)$ is the temperature dependent velocity averaged collisional cross section, and $[N]$ is the perturber density. This is called the impact approximation. Generalizing to finite collision times ($T_d \neq 0$) results in a detuning dependent broadening rate:

$$L(\Delta) = \frac{1}{2\pi}\frac{\gamma(x(T))}{\Delta^2 + \gamma(0)^2/4} \tag{E.809}$$

$$x(T) \equiv \Delta(T)T_d(T) \tag{E.810}$$

The exact form of $\gamma(x)$ depends on the interatomic potentials between the alkali atom and the perturber atom. If a van der Waals potential of the form:

$$\hbar\left(V_{\text{excited}} - V_{\text{ground}}\right) = \hbar\Delta V(R) = -\frac{C_6}{R^6} \tag{E.811}$$

is assumed to be the interatomic potential (where R is the interatomic separation) and working the low perturber density regime ($T_d\gamma \ll 1$), then Walkup et al [35] showed that the broadening rate could be written as:

$$\gamma(x) = \gamma_{\text{nat}} + \langle\sigma v\rangle_{\text{pb}}(x(T))[N] \tag{E.812}$$

$$\langle\sigma v\rangle_{\text{pb}}(x(T)) = 8\pi R_{\text{th}}^2(T)v_{\text{th}}(T)f(x(T)) \tag{E.813}$$

$$v_{\text{th}}(T) = \sqrt{\frac{2kT}{\mu}} \tag{E.814}$$

$$R_{\text{th}}(T) = \sqrt[5]{|C_6|v_{\text{th}}^{-1}} \tag{E.815}$$

$$T_d(T) \equiv \frac{R_{\text{th}}}{v_{\text{th}}} = \sqrt[5]{|C_6|v_{\text{th}}^{-6}} \tag{E.816}$$

where v_{th} is the most probable thermal velocity in the center of mass system, μ is the reduced mass, R_{th} is the effective collision radius, T_d is the temperature dependent effective collision duration time, and $f(x,T)$ is a dimensionless function that contains the detuning dependence.

Walkup et al calculated $f(x,T)$ in three regimes:

$$f(x,T) \approx \left\{ \begin{array}{cc} \frac{\pi}{6}\sqrt{x} & x < -2.4 \\ 0.3380 - 0.2245x & -1.5 < x < 0.5 \\ 0.8464\sqrt{x}\exp\left[-2.1341x^{\frac{5}{9}}\right] & x > 2.4 \end{array} \right\} \tag{E.817}$$

Near resonance, $x \approx 0$, the FWHM in the numerator should be replaced with:

$$\Gamma_n \rightarrow \Gamma_n \left[1 - \left(\frac{0.2245}{0.3380}\right) T_d^n 2\pi \left(\nu - \nu_n\right)\right] \tag{E.818}$$

where n refers to the Dn transition & T_d^n is the effective collision time.

Finite Hyperfine Splitting, Isotopic Composition, and Wing Leakage

Table A.6 lists the hyperfine splittings of all the alkali metal isotopes (AIV_{77} = Arimondo et al, RMP, 49, p31-75 (1977)). The natural abundance of each of these isotopes is listed in table A.5 (NIST_{x} = NIST websites). The hyperfine interaction between the nuclear spin and electron angular momentum causes an additional small splitting of the spectral line. This splitting, if not accounted for, would appear as a slight additional broadening. All the excited state hyperfine splittings are less that 0.5 GHz and therefore will be neglected. The ground state hyperfine splitting for both isotopes of Rb are larger than 3 GHz, see table A.6. The energy

shifts due to the hyperfine splitting of ground state are given by:

$$\frac{\Delta E_F}{h} = \Delta\nu_F = \Delta x_F = \frac{A}{2}\left[F(F+1) - I(I+1) - \frac{3}{4}\right] \tag{E.819}$$

where I is the nuclear spin of the isotope and $F = I \pm \frac{1}{2}$.

This is large enough to worry about for Rb and therefore each line of Rb should be fit to a set of *four* Lorenztians, two for the hyperfine splitting and one for each isotope:

$$\begin{aligned} y = {} & 0.7217c_0\left(\left[\frac{7}{12}\right]\frac{[1+0.664\times 2\pi c_1(x-c_2+1.264887)]}{(x-c_2+1.264887)^2+\frac{c_3^2}{4}}\right. \\ & \left.+\left[\frac{5}{12}\right]\frac{[1+0.664\times 2\pi c_1(x-c_2-1.770844)]}{(x-c_2-1.770844)^2+\frac{c_3^2}{4}}\right) \\ & +0.2783c_0\left(\left[\frac{5}{8}\right]\frac{[1+0.664\times 2\pi c_1(x-c_2+2.563005)]}{(x-c_2+2.563005)^2+\frac{c_3^2}{4}}\right. \\ & \left.+\left[\frac{3}{8}\right]\frac{[1+0.664\times 2\pi c_1(x-c_2-4.271676)]}{(x-c_2-4.271676)^2+\frac{c_3^2}{4}}\right)+c_4 \end{aligned} \tag{E.820}$$

where x, the laser frequency, is in units of GHz and the parameters c_0,c_1,c_2,c_3 & c_4 are:

$$\int_0^\infty \sigma(\nu)\mathrm{d}\nu = \sigma_0 = \pi r_e c f \tag{E.821}$$

$$c_0 = -\frac{[A]l\sigma_0\Gamma}{2\pi} \quad \left(\mathrm{GHz}^2\right) \tag{E.822}$$

$$c_1 = T_d \quad \left(\mathrm{GHz}^{-1}\right) \tag{E.823}$$

$$c_2 = \nu_0 \quad (\mathrm{GHz}) \tag{E.824}$$

$$c_3 = \Gamma \quad (\mathrm{GHz}) \tag{E.825}$$

$$c_4 = \log\left(\frac{G_{\mathrm{PD2}}G_{\mathrm{PD2-box}}G_{\mathrm{lockin-2}}}{G_{\mathrm{PD1}}G_{\mathrm{PD1-box}}G_{\mathrm{lockin-1}}}\right) \quad (\text{unitless}) \tag{E.826}$$

Only one isotope of K has a hyperfine splitting of greater than 1 GHz. However, that isotope (^{40}K) is naturally abundant only at the ppm level, which is negligible. The more abundant isotopes of K have negligible (< 1 GHz) hyperfine splittings. The potassium D1 and D2 lines are very close (≈ 1700 GHz) compared to the expected widths (≈ 160 GHz). Note that this is not a problem for Rb, because the D1 and D2 lines are well separated (≈ 7100 GHz) compared to their widths (≈ 160 GHz). Although the D1 line for K and the D2 line for Rb are well separated (≈ 5000 GHz) compared to their widths (≈ 160 GHz), the relative size of the "peaks" is expected to be about 10 to 1 favoring K. This may mean that the K D1 line leaks into the Rb D2 line. We'll have to see what the data looks like, but if this is the case, then we'll need to fit the K D1, K D2, and Rb D2 lines altogether. If that is not the case, then the Rb D2 can be fit separately but the K D1 and D2 lines still should be fit together (neglecting the small hyperfine splitting for K):

$$y = \underbrace{\frac{c_0\left[1+0.664\times 2\pi c_1\left(x-c_2\right)\right]}{\left(x-c_2\right)^2+\frac{c_3^2}{4}}}_{\text{D1}} + \underbrace{\frac{c_5\left[1+0.664\times 2\pi c_6\left(x-c_7-1730.32\right)\right]}{\left(x-c_7-1730.32\right)^2+\frac{c_8^2}{4}}}_{\text{D2}} + c_4 \tag{E.827}$$

where, for K, (c_0,c_1,c_2,c_3) refer to the D1 transition and analogously (c_5,c_6,c_7,c_8) refer to the D2 transition.

E.8.3 ^{3}He Density: Pressure Broadening

The density of the buffer gas is proportional to the FWHM (full-width half maximum) of the line shape and for Rubidium [36]:

$$c_3 = \Gamma = \langle\sigma v\rangle_{\mathrm{Rb}-^3\mathrm{He}}[^3\mathrm{He}] + \langle\sigma v\rangle_{\mathrm{Rb}-\mathrm{N_2}}[\mathrm{N_2}] \tag{E.828}$$

$$\langle\sigma v\rangle_{\mathrm{Rb}-\mathrm{D_1}-^3\mathrm{He}} = 18.7\left(\frac{T}{353\ \mathrm{K}}\right)^{0.05,0.11} \frac{\mathrm{GHz}}{\mathrm{amagat}} \tag{E.829}$$

$$\langle\sigma v\rangle_{\mathrm{Rb}-\mathrm{D_1}-\mathrm{N_2}} = 17.8\left(\frac{T}{353\ \mathrm{K}}\right)^{0.30} \frac{\mathrm{GHz}}{\mathrm{amagat}} \tag{E.830}$$

$$\langle\sigma v\rangle_{\mathrm{Rb}-\mathrm{D_2}-^3\mathrm{He}} = 20.8\left(\frac{T}{353\ \mathrm{K}}\right)^{0.53,0.34} \frac{\mathrm{GHz}}{\mathrm{amagat}} \tag{E.831}$$

$$\langle\sigma v\rangle_{\mathrm{Rb}-\mathrm{D_2}-\mathrm{N_2}} = 18.1\left(\frac{T}{353\ \mathrm{K}}\right)^{0.30} \frac{\mathrm{GHz}}{\mathrm{amagat}} \tag{E.832}$$

To get the correct helium density, one has to know the temperature of the cell and the nitrogen density (gotten from filling data). (Reference: Romalis, Miron, and Cates, PRA Vol 56 Num 6 p4569 (1997)) For Potassium, we've cross calibrated the number for Helium-3, but assumed the same for Nitrogen:

$$\langle\sigma v\rangle_{\mathrm{K}-\mathrm{D_1}-^3\mathrm{He}} = 14.4\left(\frac{T}{353\ \mathrm{K}}\right)^{0.41} \frac{\mathrm{GHz}}{\mathrm{amagat}} \tag{E.833}$$

$$\langle\sigma v\rangle_{\mathrm{Rb}-\mathrm{D_1}-\mathrm{N_2}} = 17.8\left(\frac{T}{353\ \mathrm{K}}\right)^{0.30} \frac{\mathrm{GHz}}{\mathrm{amagat}} \tag{E.834}$$

$$\langle\sigma v\rangle_{\mathrm{K}-\mathrm{D_2}-^3\mathrm{He}} = 20.15\left(\frac{T}{353\ \mathrm{K}}\right)^{0.23} \frac{\mathrm{GHz}}{\mathrm{amagat}} \tag{E.835}$$

$$\langle\sigma v\rangle_{\mathrm{Rb}-\mathrm{D_2}-\mathrm{N_2}} = 18.1\left(\frac{T}{353\ \mathrm{K}}\right)^{0.30} \frac{\mathrm{GHz}}{\mathrm{amagat}} \tag{E.836}$$

E.8.4 Alkali Density: Total Absorption

The alkali density is proportional to the size of the the "absorption dip" of the line shape:

$$[A] = -c_0 \frac{2\pi}{l\sigma_0\Gamma} = -c_0 \frac{2\pi}{l\pi r_e c f c_3} = -\frac{c_0}{c_3}\frac{2}{l r_e c f} \tag{E.837}$$

where l is the path length through the cell, $r_e = 2.817940325 \times 10^{-15}$ m (classical electron radius), c is the speed of light, and f is the oscillator strength of the transition. For both rubidium and potassium, $f = 1/3$ for the D1 transition and $f = 2/3$ for the D2 transition.

In principle, one can also get the alkali density by integrating over the line shape:

$$\int_{c_2-\Delta x}^{c_2+\Delta x} y(x)\,\mathrm{d}x = \int_{c_2-\Delta x}^{c_2+\Delta x} \frac{c_0}{(x-c_2)^2 + \frac{c_3^2}{4}} + \frac{c_0 0.664 \times 2\pi c_1 (x-c_2)}{(x-c_2)^2 + \frac{c_3^2}{4}} + c_4\,\mathrm{d}x \tag{E.838}$$

$$\lim_{\Delta x\to\infty} \int_{c_2-\Delta x}^{c_2+\Delta x} \frac{c_0}{(x-c_2)^2 + \frac{c_3^2}{4}}\,\mathrm{d}x = 2\pi\frac{c_0}{c_3} \tag{E.839}$$

$$\int_{c_2-\Delta x}^{c_2+\Delta x} \frac{x-c_2}{(x-c_2)^2 + \frac{c_3^2}{4}}\,\mathrm{d}x = 0 \text{ (by symmetry)} \tag{E.840}$$

$$\int_{c_2-\Delta x}^{c_2+\Delta x} c_4\,\mathrm{d}x = 2c_4\Delta x \tag{E.841}$$

where the alkali density is gotten from:

$$p \equiv \int_{c_2-\Delta x}^{c_2+\Delta x} y(x)\,\mathrm{d}x \approx 2\pi\frac{c_0}{c_3} + 2c_4\Delta x \tag{E.842}$$

$$[A] \approx -\frac{\left(p - 2c_4\Delta x\right)}{l\pi r_e c f} \tag{E.843}$$

To do this, one must be very certain that the background integrates to zero ($c_4 \approx 0$) or to some well known value.

E.9 Paramagnetic Faraday Rotation

E.9.1 Experimental Signal: The Rotation Angle

To measure the Faraday rotation induced by the alkali vapor:

1. The detector is a rotatable half-wave plate mounted in front a beam splitting polarizing cube. The intensity of each beam from the cube is measured by a photodiode.

2. The rotation angle is encoded in the difference of the intensities.

3. The intensity of the beam must be normalized because there the intensity has a strong wavelength dependence. This is due to both the probe laser itself and the absorption by the alkali vapor itself. This can be obtained from the sum of the intensities.

4. Any remaining normalization factors can be obtained by rotating the HWP.

The sum and difference intensities are given by:

$$I_\sigma(\text{DC}) = 2\zeta\left[\cosh(2\Im\psi) - J_0(\beta_0)\sinh(2\Im\psi)\right] \tag{E.844}$$

$$I_\delta(\text{DC}) = 2\zeta\sqrt{1-P^2}\left[\cos(2\theta)\cos(2\Re\psi) + J_0(\beta_0)\sin(2\theta)\sin(2\Re\psi)\right] \tag{E.845}$$

$$I_\delta(\text{AC1}) = 2\zeta\sqrt{2}J_1(\beta_0)P\sin(2\Re\psi) \tag{E.846}$$

$$2\zeta = \sqrt{\frac{\epsilon}{\mu}}\frac{E_0^2}{2}e^{-l\Im\{k_+ + k_-\}} \tag{E.847}$$

$$\psi = (k_+ - k_-)\frac{l}{2} + 2\phi_h \tag{E.848}$$

From these equations, we see for the case where a PEM isn't used ($\beta_0 = 0$):

$$\frac{I_\delta(\text{DC})}{I_\sigma(\text{DC})} = \underbrace{\left[\frac{\sqrt{1-P^2}}{\cosh(2\Im\psi) - \sinh(2\Im\psi)}\right]}_{\text{normalization}} \cos(2\theta - 2\Re\psi) \tag{E.849}$$

With no PEM, we're interested in the DC difference over the DC sum and the probe beam must be linearly polarized, $P = 0$. When we do use a PEM and a Lock-In Amplifier for the difference signal (referenced to the PEM frequency):

$$\frac{I_\delta(\text{AC1})}{I_\sigma(\text{DC})} = \underbrace{\left[\frac{\sqrt{2}J_1(\beta_0)P}{\cosh(2\Im\psi) - J_0(\beta_0)\sinh(2\Im\psi)}\right]}_{\text{normalization}} \sin(2\Re\psi) \tag{E.850}$$

With a PEM, we're interested in the AC difference over the DC sum and the probe beam must be circularly polarized, $P = \pm 1$. Both rotation formulas contain the term $\Re\psi$. The Faraday rotation angle is defined by $\phi = \Re\psi - 2\phi_h = \Re\,(k_+ - k_-)\,\frac{l}{2}$. This implies that:

1. the electric field polarization vector rotates by an angle of ϕ due to the atomic vapor
2. the observable quantity is 2ϕ from the reference axis
3. Faraday rotation (ϕ) can be canceled by a half waveplate with an angle of $-\phi/2$ between the its axis and the reference axis

We'll now calculate the Faraday rotation angle ϕ starting with:

$$\phi = \Re\psi - 2\phi_h = \Re\,(k_+ - k_-)\,\frac{l}{2} = \frac{l[\text{A}]\pi r_e c f_1 \omega}{\omega_1} C\Re(\alpha_+ - \alpha_-) \tag{E.851}$$

Since we're making these measurements at very low field ≤ 40 gauss, we'll only keep terms up to first order in field, y, which gives for the difference of the real parts of the polarizability:

$$\begin{aligned} C\Re(\alpha_+ - \alpha_-) &= -\frac{y\omega_{\mathtt{so}}}{3}\left[7\left(2\mathcal{D}_2^2 - \frac{\mathcal{L}_2}{\gamma_2}\right) + 4\left(2\mathcal{D}_1^2 - \frac{\mathcal{L}_1}{\gamma_1}\right) - 2\left(\frac{\mathcal{D}_1 - \mathcal{D}_2}{\omega_{\mathtt{so}}}\right)\right] \\ &\quad + \hat{k}\cdot\vec{P}_{\mathtt{A}}\left[\mathcal{D}_2 - \mathcal{D}_1\right] \end{aligned} \tag{E.852}$$

There is a natural separation between the rotation due to the magnetic field (y) and the alkali polarization ($P_{\mathtt{A}}$). Traditionally, Faraday rotation refers to the part due to the field only and the constant of proportionality is called the Verdet constant. The rotation due to the alkali polarization is called paramagnetic Faraday rotation and under our conditions will be the dominant term. Making the approximation $\omega \approx \omega_1$, making the substitution $y\omega_{\mathtt{so}} = \mu_B B/\hbar$, using $\Delta_n = 2\pi(\nu - \nu_n)$ where ν is the probe laser frequency, using $\gamma_n = 2\pi\Gamma_n/2$ where Γ_n is the pressure broadened FWHM, and noting the following:

$$2\pi\mathcal{L}_n = \frac{\Gamma_n/2}{(\nu-\nu_n)^2 + \Gamma_n^2/4} \qquad 2\pi\mathcal{D}_n = \frac{(\nu_n - \nu)}{(\nu-\nu_n)^2 + \Gamma_n^2/4} \tag{E.853}$$

we can write down the rotation formulas:

$$\begin{aligned} \phi_B &= -l[\mathrm{A}]B\left(\frac{r_e c f_1 \mu_B}{6h}\right)\left[7\left\{\frac{(\nu-\nu_2)^2 - \Gamma_2^2/4}{\left[(\nu-\nu_2)^2 + \Gamma_2^2/4\right]^2}\right\} + 4\left\{\frac{(\nu-\nu_1)^2 - \Gamma_1^2/4}{\left[(\nu-\nu_1)^2 + \Gamma_1^2/4\right]^2}\right\}\right. \\ &\quad \left. - \left(\frac{2}{\nu_1 - \nu_2}\right)\left\{\frac{(\nu-\nu_1)}{(\nu-\nu_1)^2 + \Gamma_1^2/4} - \frac{(\nu-\nu_2)}{(\nu-\nu_2)^2 + \Gamma_2^2/4}\right\}\right] \end{aligned} \tag{E.854}$$

$$\phi_P = l[\mathrm{A}]P_{\mathtt{A}}\cos(\theta)\left(\frac{r_e c f_1}{2}\right)\left[\frac{(\nu-\nu_1)}{(\nu-\nu_1)^2 + \Gamma_1^2/4} - \frac{(\nu-\nu_2)}{(\nu-\nu_2)^2 + \Gamma_2^2/4}\right] \tag{E.855}$$

When the probe laser frequency is far from resonance $(\nu - \nu_n) \gg \Gamma_n/2$ for both Dn transitions, then these formulas can be simplified even further to [37]:

$$\phi_B = -l[\mathrm{A}]B\left(\frac{r_e c f_1 \mu_B}{6h}\right)\left[\frac{7}{(\nu-\nu_2)^2} + \frac{4}{(\nu-\nu_1)^2} - \frac{2}{(\nu-\nu_1)(\nu-\nu_2)}\right] \quad \text{(E.856)}$$

$$\phi_P = -\left(\frac{r_e c f_1 \nu_{\mathtt{so}}}{2}\right)\left[\frac{l[\mathrm{A}]P_{\mathtt{A}}\cos(\theta)}{(\nu-\nu_1)(\nu-\nu_2)}\right] \quad \text{(E.857)}$$

where $\nu_{\mathtt{so}}$ is the spin-orbit splitting in frequency. The scales for these two rotations are given by:

$$\left(\frac{180\ \mathrm{deg}}{\pi}\right)\left(\frac{r_e c f_1 \mu_B}{6h}\right) = \frac{\left(3.76\ \mathrm{millidegrees}\right)\left(1000\ \mathrm{GHz}\right)^2}{\left(1\ \mathrm{cm}\right)\left(10^{14}\ \mathrm{cm}^{-3}\right)\left(1\ \mathrm{gauss}\right)} \quad \text{(E.858)}$$

$$\left(\frac{180\ \mathrm{deg}}{\pi}\right)\left[\frac{r_e c f_1 \nu_{\mathtt{so}}}{2}\right]_{\mathrm{Rb}} = \frac{\left(57.5\ \mathrm{degrees}\right)\left(1000\ \mathrm{GHz}\right)^2}{\left(1\ \mathrm{cm}\right)\left(10^{14}\ \mathrm{cm}^{-3}\right)} \quad \text{(E.859)}$$

$$\left(\frac{180\ \mathrm{deg}}{\pi}\right)\left[\frac{r_e c f_1 \nu_{\mathtt{so}}}{2}\right]_{\mathrm{K}} = \frac{\left(14.0\ \mathrm{degrees}\right)\left(1000\ \mathrm{GHz}\right)^2}{\left(1\ \mathrm{cm}\right)\left(10^{14}\ \mathrm{cm}^{-3}\right)} \quad \text{(E.860)}$$

(E.861)

E.9.2 Alkali Number Density

The alkali number densities are obtained by simply fitting the paramagnetic Faraday rotation angle vs frequency:

$$y = lP_{\mathtt{A}}\cos(\theta)\left(\frac{r_e c f_1}{2}\right)\left\{[\mathrm{K}]F_{\mathrm{K}} + [\mathrm{Rb}]F_{\mathrm{Rb}}\right\} \quad \text{(E.862)}$$

where the function F_X is given by:

$$F_X = \left(\frac{(x-\nu_1)}{(x-\nu_1)^2 + \Gamma_1^2/4} - \frac{(x-\nu_2)}{(x-\nu_2)^2 + \Gamma_2^2/4}\right) \quad \text{(E.863)}$$

To extract the alkali densities, you must know:

1. the alkali polarization, which is assumed to be the same for K and Rb
2. the laser beam path length through the cell
3. the skew angle which is usually a small correction
4. the absolute calibration of the angle obtained from the normalization with the RHWP

E.10 Probing EPR RF Transitions

E.10.1 Experimental Signal: Change in the Alkali Polarization

The EPR transitions are driven using a small RF coil producing an RF field perpendicular to the main holding field. When the RF coil frequency is held constant, the holding field is swept changing the transition frequencies. To obtain an alkali EPR RF spectrum, we need some observable that indicates that an RF transition is being driven. When the alkali atoms are polarized due to optical pumping, then driving an RF transition is depolarizing. As the magnetic field is swept, the alkali polarization is lowered when the transition frequency matches the RF coil frequency. These dips or peaks in the alkali polarization correspond to a particular EPR RF transition that can be identified provided we know magnitude of the magnetic field.

The alkali polarization is given by:

$$P_{\mathtt{A}}(z) = \frac{R(z)}{R(z) + \gamma + \gamma_{\mathtt{rf}}(z)} \tag{E.864}$$

where $R(z)$ is the position dependent optical pumping rate, γ is the spin relaxation rate, and $\gamma_{\mathtt{rf}}(z)$ is the position dependent effective relaxation rate due to the RF coil.

There are two different ways that we can measure the relative alkali polarization:

1. the paramagnetic Faraday rotation angle
2. the intensity of the D2 fluorescence emitted by the alkali vapor during optical pumping

When the Faraday rotation angle is canceled out by the RHWP, the difference signal will be zero. Therefore, small changes in the alkali polarization will result in a small changes in the rotation angle. Under the "small" condition, the change in the difference signal will be proportional to the change in rotation angle $I_\delta \propto \sin(\Delta\phi) \approx \Delta\phi$. Therefore the zeroed difference signal is directly a probe of the relative change in the alkali polarization:

$$\begin{aligned} \Delta\phi &\propto \Delta P_{\mathtt{A}} = P_A - P_A^0 = \frac{R}{R+\gamma+\gamma_{\mathtt{rf}}} - \frac{R}{R+\gamma} \\ &\approx \frac{R}{R+\gamma}\left[1 - \frac{\gamma_{\mathtt{rf}}}{R+\gamma}\right] - \frac{R}{R+\gamma} = -P_A^0\left[\frac{\gamma_{\mathtt{rf}}}{R+\gamma}\right] \end{aligned} \tag{E.865}$$

where P_A^0 is the alkali polarization when the RF coil is off or the RF coil frequency is off resonance.

Although the presence of N_2 molecules greatly suppresses the number of radiative decays, a few percent of the transitions back to the ground state still occur radiatively. The amount of D1 and D2 fluorescence is essentially the same because of collisional mixing of the excited states. However, a filter is placed in front of

a photodiode to allow transmission of only the D2 fluorescence. This is because the large D1 background from the pump laser light could potentially saturate the photodiode.

Therefore, the signal detected in the photodiode consists mainly of D2 fluorescence. A strong DC component is present due to the D2 light reaching the photodiode from parts of the cell that are minimally effected by the EPR excitation coil and due to the fact that the EPR excitation is very small and therefore the alkali polarization is not changing much. More important is the AC component that is at the modulation frequency of the EPR excitation coil. For the alkali polarization measurement, the amplitude of the RF coil is modulated; wheres, for the He-3 polarization measurement, the frequency of the RF coil is modulated. Either way, a lock-in amplifier is used to detect this small AC signal. The intensity of the D2 fluorescence detected by a photodiode observing the cell an be estimated by:

$$I_{\mathrm{D2}} \approx h\nu_2 \left(\frac{\Delta\Omega}{A_{\mathrm{pd}}}\right)\left(\frac{1}{1+\Gamma_{\mathrm{non}}\tau_{\mathrm{spon}}}\right) V[A]\,\langle R\rangle\,(1-\langle P_{\mathtt{A}}\rangle) \tag{E.866}$$

where Γ_{non} is the non-radiative quenching rate, $\tau_{\mathrm{spon}}^{-1}$ is the spontaneous emission rate, V is the volume of the pumping chamber, $\Delta\Omega$ is the solid angle subtended by the photodiode, A_{pd} is the area of the photodiode, and the brackets $<>$ refer to a volume average over the whole pumping chamber. Rewriting $\langle R\rangle\,(1-\langle P_{\mathtt{A}}\rangle)$ as $\langle P_A\rangle\,(\gamma+\gamma_{\mathtt{rf}})$ can be used to give the change in the D2 intensity due to the RF coils:

$$\Delta I_{\mathrm{D2}} \approx h\nu_2 \left(\frac{\Delta\Omega}{A_{\mathrm{pd}}}\right)\left(\frac{1}{1+\Gamma_{\mathrm{non}}\tau_{\mathrm{spon}}}\right) V[A]\,\langle P_A^0\rangle\,\gamma_{\mathtt{rf}} \tag{E.867}$$

where the D2 fluorescence intensity depends on $\langle\gamma_{\mathtt{rf}}\rangle$ the volume averaged effective relaxation rate due to the RF coil. In both cases, the observable is proportional

to the effective relaxation rate due to the RF coil.

E.10.2 Effective Relaxation Rate Due to EPR RF Transitions

We've already calculated the change in populations due to a dipole interaction, see Sec. (E.5.2). For an RF field in the x direction, where the holding field is in the z direction, the change is population is given by:

$$\dot{\rho}_{Fm} = 2\Omega_{\mathtt{rf}}^2 \left\{ \frac{\gamma_m \left(\rho_{Fm+1} - \rho_{Fm}\right) \left|u_+^-\right|^2 \left|\langle F, m+1| \, S_+ \, |F, m\rangle\right|^2}{\left(\omega - \omega_{Fm+1Fm}\right)^2 + \gamma_m^2} + \frac{\gamma_m \left(\rho_{Fm-1} - \rho_{Fm}\right) \left|u_-^+\right|^2 \left|\langle F, m-1| \, S_- \, |F, m\rangle\right|^2}{\left(-\omega - \omega_{Fm-1Fm}\right)^2 + \gamma_m^2} \right\} \tag{E.868}$$

The effective relaxation rate is given by the amount of change in $\langle S_z \rangle$ times the transition rate. The change in $\langle S_z \rangle$ for every $m \leftrightarrow m-1$ transition is $1/[I]$. There the effective relaxation rate is given as:

$$\frac{dP_A}{dt} = \frac{d2\left\langle S_z \right\rangle}{dt} = \frac{4\Omega_{\mathtt{rf}}^2}{[I]} \sum_{F,m} \frac{\gamma_m \left(\rho_{Fm-1} - \rho_{Fm}\right) \left|u_-^+\right|^2 \left|\langle F, m-1| \, S_- \, |F, m\rangle\right|^2}{\left(-\omega - \omega_{Fm-1Fm}\right)^2 + \gamma_m^2} \tag{E.869}$$

where we've labeled the transitions with the higher m value, ω is the RF coil frequency, and we've summed over all $m \leftrightarrow m-1$ transitions in both manifolds $F = I \pm 1/2$. Since $S_x = (S_+ + S_-)/2$, $\left|u_-^+\right|^2 = 1/4$ and plugging in values for the matrix element & population difference, we find:

$$\frac{dP_A}{dt} = -P_A \frac{\Omega_{\mathtt{rf}}^2}{[I]^2} \sum_{\pm,m} Q_{I\bar{m}} \left((I+1/2)(I+1/2 \pm 1) - m(m-1) \right) \mathcal{L}_m^{\pm} = -\gamma_{\mathtt{rf}} P_{\mathtt{A}} \tag{E.870}$$

where $\mathcal{L}_m^{\pm}$ is the lorentzian line shape associated with the $m \leftrightarrow m-1$ transition in the $F = I \pm 1/2$ manifold:

$$\mathcal{L}_m^{\pm} = \frac{\gamma_m}{(\omega - \omega_{FmFm-1})^2 + \gamma_m^2} \tag{E.871}$$

where ω_{FmFm-1} is the transitions frequency. The effective spin relaxation rate is given by the sum:

$$\gamma_{\mathtt{rf}} = \frac{\Omega_{\mathtt{rf}}^2}{[I]^2} \sum_{\pm,m} Q_{I\bar{m}} \left((I+1/2)(I+1/2 \pm 1) - m(m-1) \right) \mathcal{L}_m^{\pm} \tag{E.872}$$

E.10.3 Alkali Polarization: Ratio of Areas

The observable (rotation angle or D2 light intensity) is proportional to the effective spin relaxation rate which is given by the sum:

$$\frac{\Omega_{\mathtt{rf}}^2}{[I]^2} \sum_{\pm,m} Q_{I\bar{m}} \left((I+1/2)(I+1/2 \pm 1) - m(m-1) \right) \mathcal{L}_m^{\pm} \tag{E.873}$$

When the field is high enough, the transitions frequency are spaced far enough apart, relative to the width γ_m, that only one term dominated the effective relaxation rate. In other words, the peaks corresponding to the different transitions are well resolved. In practice, we can make adjacent transitions ($m \leftrightarrow m-1$ and $m-1 \leftrightarrow m-2$) well resolved, but the twin transitions ($F = I+1/2, m \leftrightarrow m-1$ and $F = I-1/2, m \leftrightarrow m-1$) are unresolved.

The area under each peak is given by [28,37]:

$$A_{Fm} = A_0 f_I[A] \left[\frac{B_{\mathtt{rf}}}{2I+1} \right]^2 [F(F+1) - m(m-1)] \frac{\exp(\beta \bar{m})}{Z_I} \tag{E.874}$$

where F labels the manifold, m is refers to the $m \leftrightarrow m-1$ transition, A_0 is area factor common to all transitions, f_I is the isotopic fraction of the alkali species, I is the nuclear spin of that species, β is the spin temperature, and $\bar{m} = m - 1/2$ is the mean m of the transition.

The ratio of the area of two peaks for the same alkali species is given by:

$$r = \frac{A_{Fm} + A_{F'm}}{A_{Fm'} + A_{F'm'}} = \left[\frac{F(F+1) - m(m-1) + F(F-1) - m(m-1)}{F(F+1) - m'(m'-1) + F(F-1) - m'(m'-1)}\right] \exp\left(\beta[m - m']\right) \tag{E.875}$$

where $F = I + 1/2$, $F' = I - 1/2$, and $\exp(\beta) = (1 + P_A)/(1 - P_A)$. We add the areas of the twin transitions together because we are assuming that they are unresolved. In addition, there is no $m = F \leftrightarrow F - 1$ transition for the F' manifold. Note however that $F(F-1) - F(F-1) = 0$ so the formula still holds. For the case $m - m' = 1$, we find:

$$r = \left[\frac{F(F+1) - m(m-1) + F(F-1) - m(m-1)}{F(F+1) - (m-1)(m-2) + F(F-1) - (m-1)(m-2)}\right] \left(\frac{1 + P_A}{1 - P_A}\right) \tag{E.876}$$

which can be solved for P_A to give:

$$P_A = \frac{\left[F^2 - (m-1)(m-2)\right] r - \left[F^2 - m(m-1)\right]}{\left[F^2 - (m-1)(m-2)\right] r + \left[F^2 - m(m-1)\right]} \tag{E.877}$$

When the twin transitions are unresolved and we take ratios involving the end transitions, then for a nuclear spin $I = 3/2$ isotope like K-39 or Rb-87:

$$P_A = \frac{2r-1}{2r+1} \quad r = \frac{A_{22}}{A_{21} + A_{11}} \tag{E.878}$$

$$P_A = \frac{r-2}{r+2} \quad r = \frac{A_{20} + A_{10}}{A_{2-1}} \tag{E.879}$$

whereas for a nuclear spin $I = 5/2$ isotope like Rb-85:

$$P_A = \frac{7r-3}{7r+3} \quad r = \frac{A_{33}}{A_{32}+A_{22}} \tag{E.880}$$

$$P_A = \frac{3r-7}{3r+7} \quad r = \frac{A_{3-1}+A_{2-1}}{A_{3-2}} \tag{E.881}$$

E.10.4 Alkali Density Ratio: Ratio of Areas

If we look at the same transition for two different alkali species with the same nuclear spin, then the ratio of areas gives the ratio of densities:

$$r = \frac{A^i_{Fm} + A^i_{F'm}}{A^k_{Fm} + A^k_{F'm}} = \frac{f_i[A_i]}{f_k[A]_k} \tag{E.882}$$

where $f_{i,(k)}$ is the natural isotopic fraction of alkali species i (k). For example, K-39, Rb-87, K-41, and Na-23 all have $I = 3/2$. Therefore the ratio of K-39 to Rb-87 for the same transition would give:

$$r = \frac{(0.93258)[\mathrm{K}]}{(0.2783)[\mathrm{Rb}]} = 3.35 \cdot D \tag{E.883}$$

where D is the ratio of K to Rb. On the other hand, we can take the ratio of K-39 to K-41 for the same transition:

$$r = \frac{(0.93258)[\mathrm{K}]}{(0.06730)[\mathrm{K}]} = 13.9 \tag{E.884}$$

If natural abundance K is being used, then the ratio should be equal to 13.9. This is a powerful cross check of the method.

Bibliography

[1] Norman F. Ramsey. *Molecular Beams*. Oxford University Press, London, 1964.

[2] G. K. Woodgate. *Elementary Atomic Structure*. Oxford University Press, Oxford, 2nd edition, 2002.

[3] Christopher J. Foot. *Atomic Physics*. Oxford University Press, Oxford, 2005.

[4] H. N. Russell and F. A. Saunders. New Regularities in the Spectra of the Alkaline Earths. *Astrophysical Journal*, 61:38–69, 1925.

[5] Murray R. Spiegel. *Mathematical Handbook of Formulas and Tables*. Schaum's Outline Series. McGraw-Hill, New York, 1993.

[6] G. Breit and I. I. Rabi. Measurement of Nuclear Spin. *Physical Review*, 38(11):2082–2083, Dec 1931.

[7] H. Kopfermann. *Nuclear Moments*. Academic Press, New York, 1958.

[8] William H. Press, Brian P. Flannery, Saul A. Teukolsky, and William T. Vetterling. *Numerical Recipes in C: The Art of Scientific Computing*. Cambridge University Press, Cambridge, 1st edition, 1988.

[9] R. Clark Jones. A New Calculus for the Treatment of Optical Systems, I. Description and Discussion of the Calculus. *Journal of the Optical Society of America*, 31(7):488–493, 1941.

[10] Henry Hurwitz Jr. and R. Clark Jones. A New Calculus for the Treatment of Optical Systems, II. Proof of Three General Equivalence Theorems. *Journal of the Optical Society of America*, 31(7):493–495, 1941.

[11] R. Clark Jones. A New Calculus for the Treatment of Optical Systems, III. The Sohncke Theory of Optical Activity. *Journal of the Optical Society of America*, 31(7):500–503, 1941.

[12] Frank S. Crawford Jr. *Waves*. McGraw-Hill, New York, 1968.

[13] Milton Abramowitz and Irene A. Stegun. *Handbook of Mathematical Functions with Formulas, Graphs, and Mathematical Tables*. Dover Publications, New York, 1965.

[14] U. Fano. Description of States in Quantum Mechanics by Density Matrix and Operator Techniques. *Reviews of Modern Physics*, 29(1):74–93, Jan 1957.

[15] D Ter Haar. Theory and applications of the density matrix. *Reports on Progress in Physics*, 24(1):304, 1961.

[16] Alain Omont. Irreducible components of the density matrix. Application to optical pumping. *Progress in Quantum Electronics*, 5:69 – 138, 1979.

[17] K. Blum. Density matrix formalism and applications in spectroscopy. In W. Hanle and H. Kleinpoppen, editors, *Progress in Atomic Spectroscopy: Part A*. Plenum Press, New York, 1978.

[18] W. E. Baylis. Collisional depolarization in the excited state. In W. Hanle and H. Kleinpoppen, editors, *Progress in Atomic Spectroscopy: Part B*. Plenum Press, New York, 1979.

[19] I. I. Rabi, N. F. Ramsey, and J. Schwinger. Use of Rotating Coordinates in Magnetic Resonance Problems. *Reviews of Modern Physics*, 26(2):167–171, Apr 1954.

[20] Albert Messiah. *Quantum Mechanics, Vols. I & II*. John Wiley & Sons, New York, 1966.

[21] Carl Eckart. The Application of Group theory to the Quantum Dynamics of Monatomic Systems. *Reviews of Modern Physics*, 2(3):305–380, Jul 1930.

[22] Eugene P. Wigner. *Group Theory and Its Application to the Quantum Mechanics of Atomic Spectra*. Academic Press, New York, 1959.

[23] Alan Corney. *Atomic and Laser Spectroscopy*. Clarendon Press, Oxford, 1977.

[24] E.U.Condon and G.H. Shortley. *The Theory of Atomic Spectra*. Cambridge University Press, London, 1967.

[25] A. R. Young, S. Appelt, A. Ben-Amar Baranga, C. Erickson, and W. Happer. Three-dimensional imaging of spin polarization of alkali-metal vapor in optical pumping cells. *Applied Physics Letters*, 70(23):3081–3083, 1997.

[26] S. Appelt, A. Ben-Amar Baranga, C. J. Erickson, M. V. Romalis, A. R. Young, and W. Happer. "theory of spin-exchange optical pumping of ^{3}He and ^{129}Xe". *Physical Review A*, 58(2):1412–1439, Aug 1998.

[27] L. Wilmer Anderson, Francis M. Pipkin, and James C. Baird. N14-N15 Hyperfine Anomaly. *Physical Review*, 116(1):87–98, Oct 1959.

[28] A. Ben-Amar Baranga, S. Appelt, C. J. Erickson, A. R. Young, and W. Happer. Alkali-metal-atom polarization imaging in high-pressure optical-pumping cells. *Physical Review A*, 58(3):2282–2294, Sep 1998.

[29] B. S. Mathur, H. Y. Tang, and W. Happer. Light propagation in optically pumped alkali vapors. *Phys. Rev. A*, 2(3):648–660, Sep 1970.

[30] Max Born and Emil Wolf. *Principles of Optics*. Cambridge University Press, Cambridge, 7th (expanded) edition, 1999.

[31] Amnon Yariv and Pochi Yeh. *Optical Waves in Crystals: Propagation and Control of Laser Radiation*. John Wiley & Sons, Hoboken, 2003.

[32] B. Chann, E. Babcock, L. W. Anderson, and T. G. Walker. Skew light propagation in optically thick optical pumping cells. *Physical Review A*, 66(3):033406, Sep 2002.

[33] H. G. Dehmelt. Modulation of a Light Beam by Precessing Absorbing Atoms. *Physical Review*, 105(6):1924–1925, Mar 1957.

[34] W. Happer and B. S. Mathur. Effective Operator Formalism in Optical Pumping. *Physical Review*, 163(1):12–25, Nov 1967.

[35] R. Walkup, B. Stewart, and D. E. Pritchard. Collisional line broadening due to van der Waals potentials. *Physical Review A*, 29(1):169–173, Jan 1984.

[36] M. V. Romalis, E. Miron, and G. D. Cates. Pressure broadening of Rb $D1$ and $D2$ lines by ^{3}He, ^{4}He, N_2, and Xe: Line cores and near wings. *Physical Review A*, 56(6):4569–4578, Dec 1997.

[37] B. Chann, E. Babcock, L. W. Anderson, and T. G. Walker. Measurements of ^{3}He spin-exchange rates. *Physical Review A*, 66(3):032703, Sep 2002.